



# NIGERIAN SOCIETY OF CHEMICAL ENGINEERS (NSChE) (A Division of NSE)



## Annual International Conference & Annual General Meeting


*Harmony* 2022

Ilorin, Kwara State, Nigeria

**THEME** ► Rejuvenation of the Nigerian Industrial Sector:  
The Chemical Engineering Perspectives

## CONFERENCE PROCEEDINGS

 De Peace Hotel, Ilorin,  
Kwara State

 Thursday 10 – Saturday 12  
November, 2022



**THE NIGERIAN SOCIETY  
OF  
CHEMICAL ENGINEERS**



**PROCEEDINGS OF THE 52ND ANNUAL CONFERENCE  
ON**

**REJUVENATION OF THE NIGERIAN INDUSTRIAL SECTOR:  
THE CHEMICAL ENGINEERING PERSPECTIVES**

**November 10 – 12, 2022  
ILORIN, NIGERIA**



# NSChE



**HARMONY 2022**

## **ANNUAL INTERNATIONAL CONFERENCE & AGM/EXHIBITION**

**2022**

**ISBN: 978-978-57244-5-5**

### **Book of Proceedings**

**Host Chairman**

Prof. Elijah A. Taiwo

**Conference Chairman**

Prof. Sulayman A. Abdulkareem

**Conference Vice-Chairman**

Prof. David S. Ogunniyi

**Conference Technical Committee Chairman**

Assoc. Prof. Ajiboye S. Osunleke

**Conference Technical Committee Co-Chairman**

Prof. Abdulwahab Giwa

2022 – Oyo/Osun/Kwara Chapter Harmony '22, Ilorin, Kwara State,  
Nigeria

<https://www.nsche.org.ng>

## PREFACE

Dear Colleagues and Friends,

I appreciate your participation at the International Conference and Annual General Meeting organized by the Nigerian Society of Chemical Engineers (NSChE) between 10 and 12 November 2022 with the theme **Rejuvenation of the Nigerian Industrial Sector: The Chemical Engineering Perspectives**. From every obvious indication, I can see that the NSChE has really made this international conference a Nigerian Industrial Section Rejuvenation affair!

I wish to thank the Keynote Speakers for sharing their experiences and unique knowledge on process development and applications in several areas of our national economy and needs towards our national industrial sector rejuvenation. I recognize that you have taken time and made the extra effort to prepare the presentations and for this I wish to commend your golden contributions. I also thank those who have accepted to collaborate with NSChE in making this conference goal on process development and applications for sustainable industrial sector rejuvenation a realizable one. The planning and organizing efforts of the local organizing committee are specially appreciated!

The main role of chemical engineers in a national economy has been identified in advanced and developing economies as mostly important for any nation to survive! Chemical Engineers are uniquely known for designing and troubleshooting processes for the production of chemicals, foods, fuels, biologicals, and pharmaceuticals, to name just a few. Their expertise is largely needed and employed by large-scale manufacturing plants to maximize productivity and product quality while minimizing costs and putting environmental and safety factors in proper perspectives, giving an effective instrument of law, policy, and dedicated enforcement. To this end, the professional chemical engineers have gathered in their hundreds in the state of harmony, deliberated and made plausible and technical decisions on how Nigerian industrial sectors can be rejuvenated.

The outcome of the conference which culminated in this compendium of knowledge in form of academic contributions which is here published as Proceeding Book for the conference, without doubt will contribute immensely to national development as envisaged by the Society. As usual, I am sure that the conference has not only provided us the ample opportunities to share and exchange our experiences but at the same time has candidly questioned our current methods on industrialization and the yardsticks we use to measure success. We should therefore put in place mechanisms to monitor and assess ourselves by applying the reporting and monitoring systems that we have discussed in this conference.

Thank you.



**Prof. S. A. Abdulkareem**  
Chairman, LOC NSChE 2022

## ACKNOWLEDGEMENTS

Dear Guests & Participants,

On behalf of the Oyo/Osun/Kwara chapter, I acknowledge our National President, Engr. Saidu A. Mohammed, the Deputy National President, Engr. Anthony U. Ogbuigwe, the Immediate Past President, Engr. Onochie A. Anyaoku, all past presidents and national executive members, board of directors, as well as the council members for their full support in hosting this conference (Harmony 2022).

I want to specially appreciate the Executive Secretary, Engr. Anthony K. Ogheneovo for his praxis and the dedication during this outing, which served as his inaugural conference. All our sponsors, donors, chairmen of sessions, keynote speakers, technical paper contributors and delegates are equally highly appreciated.

This acknowledgement will remain incomplete without recognizing the onerous efforts of the Local Organizing Committee led by Prof. S. A. Abdulkareem under whose leadership this success of hosting and executing the 52<sup>nd</sup> international Conference and AGM of the Society was recorded. We appreciate immensely Prof. D. O. Ogunniyi (the LOC Vice-chairman), Dr. Jamiu A. Adeniran (the LOC Secretary), all chairmen and members of the LOC subcommittees. Your various contributions and participations, no doubt, has culminated to this unprecedented compendium of knowledge, detailing the discussions, and has articulated the pathway towards rejuvenation of Nigeria industrial sector. This effort will forever be indelible in the annals of the Nigerian Society of Chemical Engineers (NSChE).

Lastly, the robust review process put together by the Technical Committee led by the duo of Dr. A. S. Osunleke (chairman) and Prof. A. Giwa (co-chairman), and the commitment of the team is highly appreciated.

Thank you and God bless.



**Prof. Elijah A. Taiwo,**  
Chairman, Oyo/Osun/Kwara Chapter.

## COMMUNIQUE OF THE 52ND INTERNATIONAL CONFERENCE OF THE NIGERIAN SOCIETY OF CHEMICAL ENGINEERS (NSChE)

The Nigerian Society of Chemical Engineers (NSChE) held its 52nd International Conference and Annual General Meeting tagged Harmony 2022 between 10 and 12 November 2022 at De-Peace Hotel and Suite, Ilorin, Kwara State Nigeria. This hybrid Conference (both physical and virtual) was a gathering of Chemical Engineering professionals, Technocrats, Policy makers, Captains of industries, Academia, Manufacturers, Students and stakeholders across the globe.

The theme of the Conference is **“Rejuvenation of the Nigerian Industrial Sector: The Chemical Engineering Perspectives”**. In addition to the three (3) keynote presentations on the main theme, seventy-seven (72) papers delivered under various sub-themes framed the deliberations of the Conference. The hub of these deliberations is the pursuit of reinventing Nigeria's ailing industrial sector through capacity building, process development, and economic networking for sustainable competitiveness in the emerging world.

In both developed and developing economies, Chemical Engineers have been identified as catalysts of economic survival. They have reputation for developing and troubleshooting process systems which is why almost all process facilities heavily rely on their expertise to increase productivity and improve product quality safely and economically. Hence, the reason why all the afore-mentioned categories of participants in the last three days have x-rayed the past, present and future of the Nigerian Industrial sector within the context of the current challenging global economy. This is to put forward technical and feasible decisions that are capable of birthing a new frontier of the sustainable, competitive and profitable industrial sector in Nigeria. Therefore, we participants in the Conference:

1. Congratulate the NSChE for successfully organizing the 52nd International Conference and Annual General Meeting dedicated to addressing the challenges of Industrialization in Nigeria.
2. Applaud the recent development in the oil and gas industry of Nigeria and globally ranging from the Petroleum Industry Act (PIA) and the emerging energy transition discourse. Energy transition discourse should however revolve around the implementation of a fair, equitable and sustainable energy mix that entrenches the principles of inclusiveness and guarantees energy security.
3. Identified the following seven solutions to ensure effective governance for industrial progress:
  - i. reduce the scope of the state: quality of public services and its independence from politics,
  - ii. invest more deliberately in infrastructure for industrial manufacturing,
  - iii. redouble efforts on industrialization and building technological innovation capacity,
  - iv. economic diversification in deeds not words,
  - v. prioritize the security of agricultural and industrial assets,
  - vi. the credibility of the government's commitment to visions and industrial policies; and
  - vii. bridge the trust deficit between the government and citizens.

4. Acknowledge the prospect of Nanotechnology in the fourth Industrial Revolution and the need for commercialization of the research outputs from the various Educational Institutions under the Society to enhance global outlook and more economic reward; and
5. Resolve to work together to surmount the real challenges hindering the growth and relevance of the Nigerian Industrial sector for continental relevance within a globally competitive environment.
- 6.

NSCHe

# 52<sup>ND</sup> ANNUAL INTERNATIONAL CONFERENCE & AGM - NSCHE 2022 LOC MEMBERS

## **Chairman**

Prof. S. A. Abdulkareem

## **Vice-Chairman**

Prof. D.S. Ogunniyi

## **Host Chairman**

Prof. E. A. Taiwo

## **Secretary**

Dr. J.A. Adeniran

Dr. A. S. Osunleke, Obafemi Awolowo  
University, Ile-Ife

Prof. J. A. Sonibare, Obafemi Awolowo  
University, Ile-Ife

Prof. O. A. A. Eletta, University of Ilorin,  
Ilorin, Kwara

Prof. O. O. Ogunleye, Ladoke Akintola  
University of Technology, Ogbomoso

Prof. T. J. Afolabi, Ladoke Akintola  
University of Technology, Ogbomoso

Dr. Mrs. F. N. Osuolale, Ladoke  
Akintola University of Technology,  
Ogbomoso

Dr. Tope Odetoeye, University of Ilorin,  
Ilorin, Kwara

Dr. G. Adeniyi, University of Ilorin,  
Ilorin, Kwara

Prof. A. Giwa, Afe Babalola University  
Ado-Ekiti, Ado-Ekiti

Engr. Barrister S. Adetona, MNSChE

Dr. A. Alade, Ladoke Akintola  
University of Technology, Ogbomoso

Prof. L. A. Jimoda, Ladoke Akintola  
University of Technology, Ogbomoso

Prof. M.O. Aremu, Ladoke Akintola  
University of Technology, Ogbomoso

Prof. D. O. Araromi, Ladoke Akintola  
University of Technology, Ogbomoso

Prof. S. E. Agarry, Ladoke Akintola  
University of Technology, Ogbomoso

Prof. G. K. Latinwoc, Ladoke Akintola  
University of Technology, Ogbomoso

Dr. R. O. Yusuf, University of Ilorin,  
Ilorin, Kwara

Dr. Salawudeen, University of Ilorin,  
Ilorin, Kwara

Dr. O. Sanda, Obafemi Awolowo  
University, Ile-Ife

Dr. K. K. Salam, Ladoke Akintola  
University of Technology, Ogbomoso

Dr. S. I. Mustapha, University of  
Ilorin, Ilorin, Kwara

Dr. F. A. Aderibigbe, University of  
Ilorin, Ilorin, Kwara

Dr. B. Fakinle, Landmark University,  
Omu-Aran, Kwara

Dr. Mrs. A. O. Ajani, University of  
Ilorin, Ilorin, Kwara

Dr. A. Arinkoola, Ladoke Akintola  
University of Technology, Ogbomoso

Dr. Mrs. Oyewole, Landmark  
University, Omu-Aran, Kwara

Dr. O. E. Ajala, University of Ilorin,  
Ilorin, Kwara

Engr. M. A. Amoloye, University of  
Ilorin, Ilorin, Kwara

Dr. Mrs. E. Babatunde, University of  
Ilorin, Ilorin, Kwara

Dr. Mrs. Aworanti, University of Ilorin,  
Ilorin, Kwara

Dr. K. Babatunde, Federal University  
of Technology, Akure

Dr. A. Bamimore, Obafemi Awolowo  
University, Ile-Ife



Dr. O. J. Odejobi, Obafemi Awolowo  
University, Ile-Ife  
Dr. E. F. Aransiola, Obafemi Awolowo  
University, Ile-Ife  
Dr. Mojirade Oloruntoba, PEDI, Ilesa

Dr. O. Agbede, Ladoke Akintola  
University of Technology, Ogbomoso  
Dr. Falowo Abiodun, Landmark  
University, Omu-Aran, Kwara  
Dr. Mrs. O. Akinwumi, University of  
Ilorin, Ilorin, Kwara  
Dr. Mrs. T. L. Adewoye, University of  
Ilorin, Ilorin, Kwara  
Dr. A. O. Adesina, Afe Babalola  
University Ado-Ekiti, Ado-Ekiti  
Dr. Aminat A. Sulayman, Ladoke  
Akintola University of Technology,  
Ogbomoso  
Engineer Olanlege, MNSChE

Engr. M. A. Amoloye, University of  
Ilorin, Ilorin, Kwara

Dr. Taiwo Abiola, Landmark  
University, Omu-Aran, Kwara  
Engr. Femi Ehinmitola, Obafemi  
Awolowo University, Ile-Ife  
Mrs. M. A. Ajala, University of Ilorin,  
Ilorin, Kwara

### **Advisors**

Emeritus Prof. S. A. Sanni, Obafemi  
Awolowo University, Ile-Ife  
Prof. A. N. Anozie (rtd), Obafemi  
Awolowo University, Ile-Ife  
Prof. O. Taiwo (rtd), Obafemi Awolowo  
University, Ile-Ife  
Prof. F. A. Akeredolu, Obafemi  
Awolowo University, Ile-Ife  
Prof. B. O. Solomon, Obafemi  
Awolowo University, Ile-Ife

# **TECHNICAL/EDITORIAL BOARD**

## **Chief Editor**

Dr. A.S. Osunleke

## **Co-Chief Editor**

Prof. A. Giwa

## **Editors**

Prof. D. O. Araromi

Prof. E. A. Taiwo

Dr. J. A. Adeniran

Dr. B. Fakinle

Dr. E. F. Aransiola

Dr. O. Sanda

Dr. K. K. Salam

Dr. S. I. Mustapha

Dr. A. Alade

NSCHE

## KEYNOTES

S/N	Presenter	TITLE OF PRESENTATION
1.	<b>Engr. Gbenga Komolafe</b> Commission Chief Executive, Nigerian Upstream Petroleum Regulatory Commission (NUPRC), Abuja	Recent Development in the Oil and Gas Industry
2.	<b>Prof. Oyebanji Oyelaran-Oyeyinka</b> , Chief of Staff and Special Adviser to the President, African Development Bank (AfDB), Abidjan Côte d'Ivoire	Raw Material development: Agro- Industry & Solid Raw materials
3.	<b>Prof. Ambali Saka AbdulKareem</b> , Department of Chemical Engineering, Federal University of Technology (FUT), Minna	Industrial Application of Nanotechnology
4.	<b>Prof. Dr. Mohammed Saedi Jami</b> , CEng, FIChemE, Head, Department of Chemical Engineering & Sustainability, Faculty of Engineering, International Islamic University Malaysia (IIUM), Kuala Lumpur, Malaysia	State of the Art and Recent Progresses in Water and Wastewater Treatment

# TABLE OF CONTENTS

CONTENTS	PAGE
<b>PREFACE</b>	<b>ii</b>
<b>WELCOME MESSAGE</b>	<b>iii</b>
<b>52<sup>ND</sup> ANNUAL INTERNATIONAL CONFERENCE &amp; AGM - NSCHE 2022 LOC MEMBERS</b>	<b>iv</b>
<b>TECHNICAL/EDITORIAL BOARD</b>	<b>vi</b>
<b>KEYNOTES</b>	<b>vii</b>
<b>INVESTIGATIONS ON THE SUITABILITY OF THE LANGMUIR ISOTHERMS IN THE ADSORPTION OF NITROPHENOL, NAPHTHALENE AND METHYLENE BLUE FROM AQUEOUS MEDIA ONTO ACTIVATED BENTONITE CLAY</b>	<b>1</b>
Ayobami O. AJANI, Wasiat O. BELLO, Tinuade J. AFOLABI, Funmilayo N. OSUOLALE, Olufunmilayo A. AWORANTI, Mujidat O. AREMU, Victoria A. ADEYI, Adeola R. AMOLE, and Abass O. ALADE	
<b>SIMULATION OF PYROLYSIS REACTOR TO PRODUCE BIO-FUEL FROM SELECTED BIOMASS</b>	<b>7</b>
Ebenezer O. DADA, Oluchukwu C. OYEKA, Ifeoluwa O. GBOLAHAN, Temitope S. OLAWALE, Victor O. OLALEYE, Akinola, D. OGUNSOLA, Kamoru O. OLADOSU, and Abass O. ALADE	
<b>BIO-ELECTROCHEMICAL TREATMENT OF PHARMACEUTICAL WASTEWATER AND SUSTAINABLE BIOELECTRICITY GENERATION USING MICROBIAL FUEL CELL</b>	<b>13</b>
Odunayo D. AKINWUMI, Samuel E. AGARRY, Mujidat O. AREMU, Abass O. ALADE, Abiola O. AWORANTI	
<b>AN APPROACH TO SCALE UP OF NEEM SEED OIL SOLVENT EXTRACTION PILOT PLANT</b>	<b>20</b>
John G. USMAN, Paul C. OKONKWO, Bello MUKHTAR, Abdul BABA	
<b>FLOW AND COMPACTION PROPERTIES OF EXCIPIENTS DEVELOPED FROM BIOPOLYMER WASTE SNAIL SHELL AND INFLUENCING FACTORS</b>	<b>26</b>
Babatunde K. ADEOYE, Elizabeth F. ARANSIOLA, Gbenga ALEBIOWU, Micheal O. OSUNGUNNA	
<b>ADSORPTION OF NICKEL (II) CATION FROM AQUEOUS SOLUTION USING MAIZE COB-ACTIVATED CARBON: OPTIMIZATION AND KINETIC STUDIES</b>	<b>33</b>
Mayowa A. LALA, Zainab O. OLOMOWEWE, Adekunle T. ADENIYI, Abdulwahab GIWA	
<b>SYNTHESIS AND APPLICATION OF CLINOPTILOLITE FOR THE PURIFICATION OF BIOGAS FROM COW DUNG</b>	<b>41</b>
Emmanuel O. EHINMITOLA, Olayinka SANDA, Elijah A. TAIWO, Ridwan A. OSENI, Azeez O. RAIFU, Oladele S. MATUWO and Samuel O. ADEBAYO	
<b>EXTRACTION OF BIOEMULSIFIER FROM CANDIDA TROPICALIS ISOLATED FROM BANANA (MUSA X PARADISIACA L.)</b>	<b>47</b>
Abigail O. ADETOYESE, Elizabeth F. ARANSIOLA, Hezekiah A. ADENIRAN	

<b>APPLICATION OF BOX-BEHNKEN DESIGN IN THE LEACHING KINETICS OF DOLOMITE IN HYDROCHLORIC ACID (HCL)</b>	54
Isaac Adekunle JOSEPH, Elijah Olawale AJALA, AHMED El-Imam Amina, Mary Adejoke AJALA	
<b>EXERGY ANALYSIS OF A NOVEL BIODIESEL PRODUCTION PROCESS INTEGRATED WITH POWER GENERATION</b>	59
Olajide, G. I. and Usman, M. A.	
<b>DIGESTATE VALORIZATION: A VALUE ADDITION TO ANAEROBIC BIODIGESTION TECHNOLOGY</b>	65
Minister Obonukut, Sunday Alabi, Jock Alexander, Kingsley Egemba and Benedict Edenseting	
<b>REDUCTION OF COD FROM TANNERY WASTEWATER USING CNTS MODIFIED ALBIZIA LEBBECK PODS</b>	71
Tunmise Latifat ADEWOYE, Salimah OMARI, Sarat Ayodele ATANDA, Oladipupo Olaosebikan OGUNLEYE, Taofeek Olalekan SALAWUDEEN, Ambali Saka ABDULKAREEM, Sherif Ishola MUSTAPHA	
<b>OPTIMISATION OF REMOVAL EFFICIENCY OF PALM KERNEL SHELL ASH IN THE TREATMENT OF MULTICOMPONENT DYES IN SIMULATED WASTEWATER</b>	78
Abass O. ALADE, Aduragbemi, G. OYELADE, Dauda O. ARAROMI, Taofik O. SALAWUDEEN, Rebecca A. OLAOYE, Temitope E. ODETOYE, Monsur O. DAUDA, and Tinuade J. AFOLABI	
<b>SUITABILITY OF ADSORPTIVE CELLULOSE DERIVED FROM TITHONIA DIVERSIFOLIA XYLEM FOR THE TREATMENT OF MULTICOMPONENT PHARMACEUTICAL WASTEWATER: ADSORPTION CAPACITY OPTIMIZATION</b>	84
Olusesan A. OLU-AROTIOWA, Abdulganiy O. YUSUF, Monsur O. DAUDA, Omodele A.A. ELETTA, Kazeem K. SALAM, Rasheed O. ADETORO, Lekan T. POPOOLA, Tinuade J. AFOLABI and Abass O. ALADE	
<b>VALOURISATION OF WASTE PARKIA PENDULA INFLORESCENCE AS BIOSORBENT FOR THE TREATMENT OF SYNTHETIC WASTEWATER CONTAINING PESTICIDES</b>	90
Tinuade J. AFOLABI, Hekram, A. SADIQ, Adewemimo, O. POPOOLA, Sunday, O. OLADUNNI, O. Monsur, O. DAUDA, Omotayo, S. AMUDA, Abolaji, G. FAROMBI, Esther O. AWOTONA, and Abass O. ALADE	
<b>ADSORPTION OF PARACETAMOL FROM PHARMACEUTICAL WASTEWATER USING GROUNDNUT (ARACHIS HYPOGAEA) SHELL ACTIVATED CARBON</b>	96
I. OLOWONYO, K. K SALAM, M. AREMU and A. LATEEF	
<b>ADSORPTION STUDIES ON WASTE PLANTAIN PEEL ASH AS ADSORBENT FOR SORPTION OF PHARMACEUTICAL WASTEWATER</b>	101
Dauda O. ARAROMI, Sofiat O. GANIYU, Ademola T. ADENIJI, Damilola O. ADEBUKOLA, Ayobami O. AJANI, Oluseye O. AGBEDE, Kehinde A. BABATUNDE, Solomon O. ALAGBE <sup>1</sup> , Samuel E. AGARRY, Taofik A, ADEDOSU, Ganiyu K. LATINWO, Abass O. ALADE, and Tinuade J. AFOLABI	
<b>SEASONAL VARIATION AND HEALTH RISKS OF PARTICULATES AT AND AROUND TRAFFIC HOTSPOTS IN IBADAN -A MODEL AFRICAN METROPOLIS</b>	108
Emmanuel T. ODEDIRAN, Jamiu A. ADENIRAN, Rafiu O. Yusuf	
<b>SIMULATION OF SAFETY HAZARDS DUE TO THERMAL RADIATION FROM REFINERY FLARE SYSTEM</b>	117
S. MUSA; U. Abubakar Zaria; P.C. Okonkwo	

<b>APPLICATION OF QUATERNARY COMPOSITE ADSORBENTS PREPARED FROM SELECTED WASTE PLASTIC FOR REMOVAL OF PESTICIDE MIXTURE FROM WASTEWATER</b>	123
Sunday O. OLADUNNI, Dauda O. ARAROMI, Akeem O. ARINKOOLA, Funmilayo N. OSUOLALE, Oladipupo, O. OGUNLEYE, Wasiat O. BELLO, Victoria, A. ADEYI, Adeola, R. AMOLE, Tinuade J. AFOLABI, Abass O. ALADE	
<b>AIR QUALITY IMPLICATION OF SOLID WASTE INCINERATION IN LAGOS</b>	130
Jacob A. SONIBARE, Abiodun J. ADEWALE, Daniel O. OKE	
<b>ASSESSMENT OF REMOVAL EFFICIENCY OF AG2O-TIO2-KAOLINITE CLAY HYBRID NANOCOMPOSITE DEVELOPED FOR THE TREATMENT OF MN(II), FE (III), PB(II) AND CU(II) IN MINING WASTEWATER</b>	137
Mary A. AJALA, Ambali S. ABDULKAREEM, Abdulsalami S. KOVO, Jimoh O. TIJANI, AJALA, Olawale Elijah	
<b>ELECTROCHEMICAL AND THERMODYNAMIC EVALUATIONS OF SPONDIAS MOMBIN LEAVES EXTRACT AS GREEN INHIBITOR FOR MILD STEEL CORROSION IN ACIDIC MEDIUM</b>	143
Kenneth K. ADAMA, Benedict I. ONYEACHU, Ebijuwa M. IGHO	
<b>PRODUCTION OF BIODIESEL FROM ORANGE PEEL AND AVOCADO SEED OILS; EFFECT OF REACTION PARAMETERS ON PRODUCTION EFFICIENCY</b>	149
Sylvester O. ANYIKWA, Stanley M. NWAKAUDU, Angela A. NWAKAUDU, Boniface C. NGOLUBE, Chigoziri N. NJOKU	
<b>ANALYSIS OF LIQUID PRODUCTS OF PYROLYZED LOW DENSITY POLYETHYLENE</b>	155
Aishat Ayoola OSIGBESAN, Adebola Femi ADE-AJAYI, Ephraim Akuaden AUDU, Zaharaddeen Sani GANO <sup>1</sup> , Jeffrey Tsware BARMINAS	
<b>SYNTHESIS AND CHARACTERIZATION OF FE DOPED MORDENITE AS A PROSPECTIVE CATALYST FOR PYROLYSIS OF WASTE PLASTICS</b>	162
Ephraim Akuaden Audu, Zaharaddeen Sani Gano, Aishat Ayoola Osigbesan, Adebola Femi Ade-Ajayi, Jeffrey T. Barminas	
<b>CHARACTERIZATION OF CHAR DERIVED FROM PYROLYSIS OF LOW-DENSITY POLYETHYLENE WASTE</b>	167
Adebola F. ADE-AJAYI, Aishat A. OSIGBESAN, Ephraim A. AUDU, Zaharaddeen Z. GANO, Jeffery T. BARMINAS	
<b>QUANTIFICATION OF 5-HYDROXYMETHYLFURFURAL AND LACTIC ACID FROM HYDROTHERMAL CARBONIZATION OF SUGAR CANE BAGASSE AND CORN COB</b>	171
Opeoluwa O. FASANYA, Dan Mallam A. ADAMU, Abdulazeez R. ISA, Chidimma D. NWAKUBA, Elizabeth WINFUL, Olanikpekun IDOWU, Elijah A. ADEGBE, Saheed A. IBRAHEEM, Ephraim A. AUDU, Yusuf O. USMAN, Mas'ud J. MUSA, Uzo B. AGUNWA, Jeffrey T. BARMINAS	
<b>PRODUCTION OF FUELS FROM GUINEA-CORN STRAW AND WASTE PLASTICS</b>	176
Adeola Grace OLUGBENGA <sup>1</sup> , Rasheed BABALOLA	
<b>PERFORMANCE OF DEEP EUTECTIC SOLVENTS IN THE EXTRACTION OF LACTIC ACID FROM SUGARCANE BAGASSE AND CORNCOB</b>	182
John E. OGUCHE, Alewo O. AMEH, Tajudeen K. BELLO and Nehemiah S. MAINA	
<b>APPLICATION OF MACHINE LEARNING XGBOOST MODEL FOR THE PREDICTION OF DYE ADSORPTION ONTO AGRO-WASTE-BASED ACTIVATED CARBONS</b>	188
Abass O. ALADE, Christopher I. ONI, Oladipupo O. OGUNLEYE, Samuel E. AGARRY, Ganiyu K. LATINWO, Aminah A. SULAYMAN, Monsur O. DAUDA, Teslim B. ASAFA, Tinuade J. AFOLABI and Sanni, A.O. OGIRIMA	

<b>UTILIZATION OF COSMO-RS FOR VALUABLE METAL EXTRACTION FROM SPENT LITHIUM-ION BATTERIES</b>	194
Hussein K. AMUSA, Ahmad S. DARWISH, Tarek LEMAOU, Hassan A. ARAFAT, Inas M. NASHEF	
<b>SYNTHESIS AND CHARACTERIZATION OF ZINC CHLORIDE MODIFIED ACTIVATED CARBON AND OTHER DERIVATIVE ADSORBENTS FROM VITEX DONIANA SEED</b>	200
Oluwadayo A. FRANCIS, Emeka C. NWORIE, Kevin S. OTOIKHIAN	
<b>SOLVENT EXTRACTION OF ACETIC ACID FROM AQUEOUS MEDIA USING TRIOCTYL PHOSPHINE OXIDE (TOPO) – BASED SOLVENT SYSTEMS</b>	207
O. SANDA, Emmanuel. O. EHINMITOLA, Bamidele S. FAKINLE and Elijah. A. TAIWO	
<b>VALORIZATION OF GARCINIA KOLA FRUIT POD EXTRACT AS A GREEN INHIBITOR FOR MILD STEEL IN ACIDIC MEDIA</b>	214
Innocent O. OBOH, Anselm I. IGBAFE, Joshua A. ADAM	
<b>ADSORPTION OF MALACHITE GREEN ONTO CELLULOSE SYNTHESIZED FROM BAOBAB POD</b>	221
Victoria A. ADEYI, Samuel E. AGARRY, Adeola R. AMOLE, Wasiat O. BELLO, Tinuade J. AFOLABI, Azeez G. AKINYEMI, Monsuru O. DAUDA, Olufunmilayo A. AWORANTI, Esther O. AWOTONA and Abass O. ALADE	
<b>EFFICIENT HIGH TEMPERATURE ACID CORROSION PROTECTION OF SS 316L STAINLESS STEEL USING AN IMIDAZOLE + KI INHIBITOR MIXTURE</b>	228
Aremiyau S. MOMOH, Kenneth K. ADAMA, Ikenna B. ONYEACHU	
<b>CHARACTERIZATION OF BAMBU CLAY: AS A POTENTIAL SOURCE FOR ZEOLITE Y SYNTHESIS</b>	233
Abdullahi A. MUSA, Haruna M. SANI, Mohammed U. GARBA, Elizabeth J. ETERIGHO, Mohammed ALHASSAN	
<b>INVESTIGATION OF GEOCHEMICAL PROPERTIES OF LATERITES IN SELECTED AREAS IN JOS-NORTH</b>	238
Yohanna A. ALIYUDA <sup>1</sup> , Lucas A. J. HAMIDU, Friday I. APEH <sup>1</sup> , Pyendang S. ZACHARIAH <sup>1</sup> , Yakubu ISHENI <sup>1</sup> , FelixACHEMA	
<b>PRODUCTION OPTIMIZATION OF A NIGERIAN OILWELL</b>	244
Ajiboye OSUNLEKE, Ayorinde BAMIMORE, Francis CHUKWUNTA, Nafees SANI, Ibrahim Abiola BADMUS	
<b>ASSESSING THE RISKS DUE TO LIQUEFIED PETROLEUM GAS PLANTS USING BOTH QUANTITATIVE AND QUALITATIVE TECHNIQUES</b>	252
Charles C. ANIGBOGU, Usman ABUBAKAR-ZARIA, Saidu M. WAZIRI	
<b>ISOLATION AND IDENTIFICATION OF POTENTIAL HYDROCARBON DEGRADING MICROBES FROM NON-HYDROCARBON CONTAMINATED SOURCES FOR CRUDE OIL SPILL CLEAN-UP</b>	259
Elizabeth WINFUL, Opeoluwa O. FASANYA, Jibrin ABDULKADIR, Balli GAUJE, Ugochi J. OKODUWA, Simon I. ADAMUN, Ephraim AUDU, Judy ADUDU, Hauwa A. MOHAMMED, Olalekan ADESINA, Jeffrey T. BARMINAS	
<b>PRELIMINARY INVESTIGATION ON DEMULSIFICATION OF NIGERIAN CRUDE OIL EMULSION USING SYNTHESIZED BIO-DEMULSIFIER</b>	265
Deborah. C NWAKUBA, Ibrahim Ali MOHAMMED-DABO, Haruna IBRAHIM	
<b>ADSORPTION BEHAVIOUR OF NAPHTHALENE, ANTHRACENE AND PYRENE IN AQUEOUS MEDIUM ONTO RICE HUSK ASH: REMOVAL EFFICIENCY OPTIMIZATION</b>	270

Ayobami O. AJANI, Ismahil K. SOKUNBI, Damilola I. ADEBUKOLA, Sofiat, O., GANIYU, Haleema O. ADEDOSU, Elizabeth F. ARANSIOLA, Tinuade J. AFOLABI, and Abass O. ALADE

**STUDY ON ELECTRICAL AND THERMAL CONDUCTIVITIES OF OPTIMISED RICE HUSK PARTICLEBOARD** 277  
Lucas HAMIDU, Umar AROKE, Odeh OSHA and Idris MUHAMMAD

**EXTRACTION OF KERATIN PROTEIN FROM CHICKEN FEATHERS: AN OPTIMIZATION STUDY** 285  
Favour Oluwabukunmi KAYODE, Benjamin ADEREMI, Olayomi Abiodun FALOWO

**OPTIMIZATION OF AVOCADO SEED OIL EXTRACTION USING FIVE-LEVEL RESPONSE SURFACE METHODOLOGY DESIGN** 293  
Saidat O. GIWA, Fatima Y. Abdullahi, Olukayode G. OLOYEDE, Saidu IBRAHIM, Abdulwahab GIWA

**DESIGN OF EXPERIMENT AS AN EXPERIMENTAL KEY IN THE OPTIMISATION OF THE OIL YIELD FROM FLUIDISED CATALYTIC CRACKING OF OIL SHALE USING ZSM-5 CATALYST** 298  
B. O. UMEH, P.E. DIM, A. G. OLUGBENGA and M.B. BABA

**MODELLING, SIMULATION AND OPTIMIZATION OF A REACTIVE DISTILLATION COLUMN** 303  
Chinenye S. UKPAI, Mufliah G. OMOFOYEWA, Idowu I. OLATEJU, Saidat O. GIWA, Abdulwahab GIWA

**PROCESS SIMULATION AND OPTIMIZATION OF PALM OIL FROM SPENT BLEACHING EARTH VIA SUPERCRITICAL EXTRACTION FOR SUSTAINABLE DEVELOPMENT** 310  
Wasiu A. OLADOSU, Mohammed S. HARUNA, Alaba A. SALAMI

**INVESTIGATION OF ADSORPTION CAPACITY OF EGGSHELL-BASED CHITOSAN IN THE TREATMENT OF MULTICOMPONENT AROMATIC ORGANIC POLLUTANTS** 315  
Azeez G. AKINYEMI, Arinkoola O. AKEEM, Shukurat B. OLABIYI, Monsuru O. DAUDA, Monsurat O. JIMOH, Odunola D. AKINWUMI, Sunday O. OYEKUNLE, Tinuade J. AFOLABI and Abass O. ALADE,

**IMPACTS OF METAL RECYCLING PLANT OPERATIONS ON AMBIENT AIR AND NOISE QUALITIES** 322  
Bamidele S. FAKINLE, Jacob A. SONIBARE, Funso A. AKEREDOLU and Ebenezer L. ODEKANLE

**AIR AND NOISE QUALITY ASSESSMENT AROUND LUBE BLENDING AND INSECTICIDE PRODUCTION PLANT** 328  
Jacob A. SONIBARE, Funso A. AKEREDOLU<sup>1</sup>, Ebenezer L. ODEKANLE and Bamidele S, FAKINLE

**EMISSION OF AIR POLLUTANTS IN THE PAPER RECYCLING PLANTS: MEASUREMENT RESULTS FROM A NIGERIAN MAJOR PAPER RECYCLING PLANT PRODUCTION FLOORS** 335  
Funso A. AKEREDOLU, Bamidele S. FAKINLE, Ebenezer L. ODEKANLE and Jacob A. SONIBARE

**ELEMENTAL CHARACTERIZATION OF POLLUTANTS EMANATED FROM COMBUSTION OF SELECTED AGRICULTURAL REMNANTS** 342  
Temilade, T. ADEBISI, Adejoke O. ALAMU Sunday A. ADEBANJO, Olusesan A. OLU-AROTIOWA, Kazeem K. SALAM, Lukuman, A. JIMODA and Abass O. ALADE



<b>AIR EMISSIONS FROM STEPWISE CO-PYROLYSIS OF PLASTIC MIXTURES</b> Atilade A. OLADUNNI, Oludare J. ODEJOBI, Jacob A. SONIBARE	348
<b>MODELING OF GASEOUS POLLUTANT EMISSIONS FROM SAVANNAH VEGETATION FIRES</b> Khadijat A. ABDULRAHEEM, Jamiu A. ADENIRAN and Adeniyi S. AREMU	353
<b>THREE-BOX SEQUENTIAL MODELLING OF THE EMISSION, DECAY AND TRANSPORTATION OF VOLATILE ORGANIC COMPOUNDS IN BEAUTY SHOPS</b> Sarat Ayodele ATANDA, Jamiu Adetayo ADENIRAN, Tunmise Latifat ADEWOYE	360
<b>FUZZY LOGIC CONTROLLER DESIGN FOR TEMPERATURE CONTROL OF SERVO SYSTEMS USING SIMULINK</b> Ajiboye OSUNLEKE, Ayorinde BAMIMORE, Sunrise EZEKIKWU, Ismail OYEHAN, Nafees SANNNI	367
<b>FUZZY LOGIC CONTROLLER DESIGN: A GENERAL APPRAISAL</b> Ajiboye OSUNLEKE, Ayorinde BAMIMORE, Ayodeji AJANI, Nafees SANNNI, Ibrahim Abimbola BADMUS	375
<b>A NEW IMPLICIT MODEL FOR PREDICTING ECONOMIC PIPE DIAMETER IN A FULLY DEVELOPED TURBULENT SINGLE-PHASE PIPE FLOW</b> Joseph U. OKON, Emmanuela O. AINERUA, Innocent O. OBOH and Anselm I. IGBAFE	384
<b>MODELLING OF LIQUEFIED NATURAL GAS AND PROPANE PRODUCTION USING NONLINEAR AUTOREGRESSIVE WITH EXOGENOUS INPUT NEURAL NETWORK</b> Azubuike Shedrack ASHINZE, Adekunle Tirimisiyu ADENIYI, Abdulwahab GIWA	393
<b>EVALUATION OF NATURAL GAS LIQUEFACTION PROCESS USING NONLINEAR AUTOREGRESSIVE NEURAL NETWORK AND NONLINEAR INPUT-OUTPUT NEURAL NETWORK: A COMPARATIVE STUDY</b> Azubuike Shedrack ASHINZE, Adekunle Tirimisiyu ADENIYI, Abdulwahab GIWA	399
<b>DESIGN AND DEVELOPMENT OF ARDUINO-BASED TEMPERATURE MONITORING SYSTEM FOR A PORTABLE HAEMODIALYSIS SYSTEM</b> Aminah A. SULAYMAN, Dauda O. ARAROMI, Olugbenga E. AYODELE	406
<b>FUZZY LOGIC CONTROL OF TOMATO CONVERSION IN A TRIPLE-EFFECT EVAPORATOR</b> Mojirade M. OLORUNTOBA and Folahan P. IBITOYE	412
<b>PROCESS DEVELOPMENT FOR THE PRODUCTION OF LOWER OLEFINS FROM LEVULINIC ACID USING 2 SEC-BUTYL PHENOL RECOVERY STRATEGY</b> Aramide A. ADESINA, David LOKHAT and Kamilu F. OYEDEKO	419
<b>RESPONSE MODELLING AND OPTIMIZATION OF PRODUCED PARTICLEBOARDS FROM SAWDUST SOFTWOOD USING R7AD2 ADHESIVE</b> Lucas HAMIDU and Umar AROKE	428
<b>ANN PREDICTION OF SELECTED OLEOPHILIC BACTERIAL GROWTH IN CRUDE OIL BIOREMEDIATION</b> Ajiboye S. OSUNLEKE, Nafees O. SANNNI, Mumeenah O. Mustapha, Elizabeth F. ARANSIOLA	435
<b>THERMODYNAMICS STUDIES OF ADSORPTION OF SELECTED ANTIBIOTICS MIXTURE FROM AQUEOUS SOLUTION USING <i>DELONIX REGIA</i> POD</b> Ilesanmi A. OJO, Ayobami O. AJANI, Wasiat O. BELLO, Tinuade J. AFOLABI, Abdulrazaq, ABDULLAHI, Akeem O. OLAYIWOLA, Ameen N AKINSOLA, and Abass O. ALADE	443

<b>EQUILIBRIUM STUDY OF METHYLENE BLUE ADSORPTION BY <i>VITEX DONIANA</i> ACTIVATED CARBON</b>	449
Kevin S. OTOIKHIAN, Oluwadayo A. FRANCIS, Emeka C. NWORIE	
<b>THERMODYNAMIC ACTIVITY COEFFICIENT MODELLING OF LIQUID-LIQUID EQUILIBRIUM DATA FOR TROPICAL ALMOND OIL BIODIESEL SYSTEM</b>	455
Kenneth K. ADAMA, Rilva S. SANTIAGO-AGUIAR, Regiane S. PINHEIRO, Robson A. C. da SILVA, Emmanuel O. ALUYOR, Thomas O.K. AUDU	
<b>PROFIT MAKING THROUGH PINCH ANALYSIS OF FEED GAS CIRCUIT IN LIQUEFACTION SYSTEM OF NATURAL GAS.</b>	461
Babatunde O. OLALEYE, Micheal S. OLAKUNLE, Adegboyega S. OLAWALE	

NSCHE

# PAPERS

NSCHE



## Investigations on the Suitability of the Langmuir Isotherms in the Adsorption of Nitrophenol, Naphthalene and Methylene Blue from Aqueous Media onto Activated Bentonite Clay

Ayobami O. AJANI<sup>1</sup>, Wasiat O. BELLO<sup>1,2</sup>, Tinuade J. AFOLABI<sup>1,2</sup>, Funmilayo N. OSUOLALE<sup>1,2</sup>, Olufunmilayo A. AWORANTI<sup>1,2</sup>, Mujidat O. AREMU<sup>1,2</sup>, Victoria A. ADEYI<sup>1,2</sup>, Adeola R. AMOLE<sup>1,2</sup>, and Abass O. ALADE<sup>1,2,3\*</sup>

<sup>1</sup> Department of Chemical Engineering, Faculty of Engineering, Ladoko Akintola University of Technology, (LAUTECH), Ogbomoso, Nigeria

<sup>2</sup> Bioenvironmental, Water and Engineering Research Group (BWERG, (LAUTECH), Ogbomoso, Nigeria

<sup>3</sup> Science and Engineering Research Group (SAERG), (LAUTECH), Ogbomoso, Nigeria

[aajani@lautech.edu.ng](mailto:aajani@lautech.edu.ng), [waasiabintbello@gmail.com](mailto:waasiabintbello@gmail.com), [tjafolabi@lautech.edu.ng](mailto:tjafolabi@lautech.edu.ng), [waasiabintbello@gmail.com](mailto:waasiabintbello@gmail.com)

\*Corresponding: [aalade@lautech.edu.ng](mailto:aalade@lautech.edu.ng)

### ABSTRACT

The presence of industrial effluents containing various pollutants (such as naphthalene, nitrophenol, and methylene blue (NNM)) in wastewater is a prime concern in the environment due to their toxic, carcinogenic and mutagenic effects on man. This research was aimed at investigating the best Langmuir isotherm that fits the adsorption process of NNM from an aqueous solution using modified bentonite clay. A composite of ratio 40:30:30 of acid, base and salt-modified bentonite clay was used for the adsorption process. Six Langmuir isotherms were investigated to know which best fit the adsorption process. The correlation coefficient ( $R^2$ ) of the linearized form of Langmuir isotherm models gave 0.965, 0.947 and 0.924 for Naphthalene, Nitrophenol and Methylene blue respectively. Langmuir 2 was most suitable for the adsorption of Naphthalene and Methylene blue while Langmuir 6 fit better the adsorption of Nitrophenol from the multicomponent solution. This means the adsorption of NNM took place at a specific homogeneous site within the adsorbent.

**Keywords:** Bentonite, Langmuir, Naphthalene, Nitrophenol, Methylene blue.

### 1. INTRODUCTION

Polycyclic aromatic hydrocarbons (PAHs), phenolic compounds, and dyes are major industrial effluents mostly discharged into water bodies. They are hazardous organic pollutants because of their toxic, mutagenic, and carcinogenic properties (Crini and Lichtfouse, 2018; Lasota *et al.* 2021). Toxicological studies have revealed that the presence of Nitrophenol, Naphthalene, and Methylene blue in wastewater has an adverse effect on human and aquatic life (Pazdro, 2014; Zhang *et al.* 2016; Porhemmat *et al.* 2017; Crini and Lichtfouse, 2018; Lasota *et al.* 2021). These organic pollutants need to be urgently removed from the water environment. However, the removal process has been a major environmental task because of the difficulties in treating such wastewater.

Various techniques have been developed for the removal of these organic pollutants from wastewater. Some of these include adsorption, flocculation, ion exchange, chemical precipitation, membrane-based filtration, photodegradation, solvent extraction, and reverse osmosis (Zhu *et al.* 2019). However, multi-component mixtures (dyes, PAHs) are difficult to remove using some of these traditional purification processes (Korbahti *et al.* 2011). Therefore, adsorption technology is considered the most promising for removing a variety of multicomponent pollutants (Rani *et al.* 2017; Mishra and Maiti, 2018; Boeykens *et al.* 2019). Research shows that adsorbents like activated carbons, natural and synthetic polymers, clays, zeolites, biomass and agricultural waste have been used to remove PAHs, dyes and phenolic compounds from solutions (Alabi *et al.* 2020; Okeowo *et al.* 2020; Berez *et al.* 2014). However, natural clay such as bentonite, kaolinite, and smectite is better adsorbents for the removal of multicomponent pollutants in water due to their low cost, high efficiency, porosity, availability, thermal stability, and non-toxicity (Puri and Sumana, 2018). Bentonite clay has been proven to be efficient, the majority of the adsorption process reported was on mono-component systems while a limited emphasis has been given to multi-component systems. Wu *et al.* (2020) reported the adsorption of naphthalene and phenanthrene using activated carbon, Giraldo *et al.* (2022) prepared orange peel to remove Methylene blue and Cadmium and Shihab *et al.* (2021) also remove p-nitrophenol using aidoxime-modified poly (acrylonite-co-acrylic acid). Bentonite clay had been used also to remove naphthalene and methylene blue as reported by Rennane *et al.* 2019 and Kelechi *et al.* 2022 respectively. This research work was aimed at using a composite

generated from acid, base and salt-activated bentonite clay as an adsorbent for the removal of multicomponent pollutants (Naphthalene, Nitrophenol and Methylene blue) from the aqueous solution which has not been previously reported. Adsorption isotherms were also investigated to investigate the best Langmuir isotherms that fit the adsorption process.

## 2. MATERIALS AND METHODS

The basic materials used was Raw Bentonite Clay Sample (RBCS) sourced from its deposits in Uturu, (5° 78'N / 7° 43' E), Abia State, Nigeria. The reagents used which include Phosphoric acid, Nitric acid, Methylene blue, Sodium Hydroxide, Barium chloride, Nitrophenol, Naphthalene and Ethanol were all analytical grade. RBCS was modified with Phosphoric acid, Sodium hydroxide and Barium chloride separately. Simplex Lattice Design (SLD) of the Mixture Methodology (MM) of Design Expert (DOE 12.0.1) was adopted to generate different mixing ratios of the three activated clay samples (Sadaf *et al.* 2014). The minimum and maximum percentage compositions were set to 30 and 40%, respectively for each of the modified clay. These ranges were fed into the Design Expert (DOE 12.0.1) based on the SLD to generate unbiased mixture ratios for the three activated clay samples as shown in Table 1.

### 2.1 Batch Adsorption

The adsorbate was prepared by dissolving an appropriate amount of Methylene blue, Nitrophenol and Naphthalene respectively in 1000 ml of distilled water. The resulting mixture is a typical composition of wastewater effluent from plastic and related industries (Khan, 2020). One gram of each of the components in Table 1 was mixed with 100 ml of the adsorbate prepared and shaken on a rotary shaker at a specific agitation rate of 120 rpm. The mixture was centrifuged and the supernatant was analyzed with UV spectrometer Model UV752(D)) at 270, 410 and 663 nm, to quantify the amount of Naphthalene, Nitrophenol and Methylene Blue respectively unadsorbed in the solution. The adsorption capacity and removal efficiency were evaluated by equations 1 and 2

$$q_e = \frac{C_o - C_e}{m} \times V \quad (1)$$

$$\% \text{ removal} = \frac{C_o - C_t}{C_o} \times 100 \quad (2)$$

Where  $C_o$  is the initial concentration of the adsorbate (methylene blue, Naphthalene and Nitrophenol) (100 mg/l),  $C_e$  is the equilibrium concentration of the adsorbate (mg/L),  $C_t$  is the concentration of the adsorbate at time  $t$ ,  $V$  is the volume of a targeted adsorbate (100 ml),  $m$  is the mass of the Bentonite Clay Geosorbent Composite (BCGC) (1 g).

### 2.2 Investigation of Suitable Adsorption Isotherm models

An adsorption isotherm is important to describe how adsorbates interact with adsorbents. The correlation between the experimental data and the model-predicted values was evaluated using the correlation coefficient ( $R^2$ ).

#### Langmuir isotherm model

Langmuir isotherm is the most used isotherm in presenting data of adsorption from solution. It assumes basically that adsorption takes place at specific homogeneous sites within the adsorbent. Literature usually presents four linear forms of the Langmuir isotherm (Bolster and Hornberger 2007; Parimal *et al.* 2010), although it is possible to write down at least six distinct linear forms, as presented in Table 1 (Osmari *et al.* 2013). The linear form of the Langmuir isotherm model is written in six different forms (Langmuir 1, Langmuir 2, Langmuir 3, Langmuir 4, Langmuir 5, and Langmuir 6) as expressed in Equations 4– 9 (Table 1). The linearized form of Langmuir equations used in this study were presented in Table 1. Furthermore, a dimensionless constant called the Langmuir equilibrium parameter ( $R_L$ ) was used to determine the nature of the adsorption process (Jawad *et al.*, 2020).

$$R_L = \frac{1}{K_L C_o + 1} \quad (3)$$

where  $C_o$  and  $K_L$  are the initial concentration of the pollutants ( $\text{mg L}^{-1}$ ) and Langmuir adsorption constant ( $\text{L mg}^{-1}$ ), respectively.

Table 1: Langmuir Isotherm Models

Model	Equation	Plot	Evaluation		Equation no
			Slope	Intercept	
Langmuir 1	$\frac{1}{q_e} = \frac{1}{q_m} + \frac{1}{q_m K_L C_e}$	$\frac{1}{q_e}$ against $\frac{1}{C_e}$	$\frac{1}{q_m K_L}$	$\frac{1}{q_m}$	4
Langmuir 2	$\frac{1}{C_e} = -K_L + q_m K_L \frac{1}{q_e}$	$\frac{1}{C_e}$ against $\frac{1}{q_e}$	$q_m K_L$	$-K_L$	5
Langmuir 3	$q_e = q_m - \frac{1}{K_L} \frac{q_m}{C_e}$	$q_e$ against $\frac{1}{C_e}$	$-\frac{q_m}{K_L}$	$q_m$	6

Langmuir 4	$\frac{q_e}{C_e} = q_m K_L - K_L q_e$	$\frac{q_e}{C_e}$ against $q_e$	$-K_L$	$q_m K_L$	7
Langmuir 5	$C_e = -\frac{1}{K_L} + q_m \frac{C_e}{q_e}$	$C_e$ against $\frac{C_e}{q_e}$	$q_m$	$-\frac{1}{K_L}$	8
Langmuir 6	$\frac{C_e}{q_e} = \frac{1}{q_m K_L} + \frac{1}{q_m} C_e$	$\frac{C_e}{q_e}$ against $C_e$	$\frac{1}{q_m}$	$\frac{1}{q_m K_L}$	9

where  $C_e$  (mg/L) is the concentration of adsorbate at equilibrium,  $q_e$  (mg/g) is adsorption capacity at equilibrium solute concentration,  $q_m$  (mg/g) is maximum adsorption capacity corresponding to complete monolayer coverage,  $K_L$  (mg/g) is Langmuir constants related to adsorption capacity

### 3. RESULTS AND DISCUSSION

#### 3.1 Development of an effective geosorbent

The mix ratio with the highest adsorption capacity and removal efficiency was chosen as the desired geosorbent. From Table 2, it was revealed that run 11 with a mix ratio of 40:30:30 of acid, base and salt-modified clay has the highest adsorption capacity and removal efficiency.

Table 2: Experimental Matrix generated for mixed ratios of BCGC

Run	Modified geosorbent Clay composition (%)			Naphthalene		Nitrophenol		Methylene blue	
	A: H <sub>3</sub> PO <sub>4</sub>	B: NaOH	C: BaCl <sub>2</sub>	q <sub>e</sub> (mg/g)	R E (%)	q <sub>e</sub> (mg/g)	R E (%)	q <sub>e</sub> (mg/g)	R E (%)
1	35	30	35	5.783	57.83	4.763	47.63	9.148	91.48
2	33	33	34	5.300	53.00	5.463	54.63	9.270	92.70
3	34	36	30	4.783	47.83	4.125	41.25	9.260	92.60
4	30	40	30	5.500	55.00	2.575	25.75	8.982	89.82
5	37	32	31	5.783	57.83	4.612	46.13	8.957	89.57
6	30	30	40	5.550	55.50	4.550	45.50	9.225	92.25
7	32	30	38	5.817	58.17	5.500	55.00	9.100	91.00
8	35	35	30	6.800	68.00	2.550	25.50	8.804	88.04
9	30	32	38	5.300	53.00	4.350	43.50	8.773	87.73
10	39	31	30	3.767	37.67	5.475	54.75	8.973	89.73
11	40	30	30	5.000	50.00	6.563	65.63	8.981	89.81
12	30	35	35	6.567	65.67	3.462	34.63	9.296	92.96
13	33	32	35	5.450	54.50	2.563	25.63	9.285	92.85
14	35	30	35	5.100	51.00	2.800	28.00	9.248	92.48
15	30	35	35	6.000	60.00	3.188	31.88	8.906	89.06
16	31	37	32	5.917	59.17	3.575	35.75	9.319	93.19

#### 3.2 Adsorption isotherm

The values of  $q_m$  and  $K_L$  (presented in Table 2) were determined from the slopes and intercepts of the plots presented in Fig 1. **Langmuir 1 and 2:** Figure 1 (a) and (b) show the plots of Langmuir 1 and 2. The adsorption capacities,  $q_m$ , and Langmuir isotherm parameter,  $K_L$ , as well as the correlating coefficient ( $R^2$ ) were obtained from the plots. The adsorption capacities of Naphthalene, Nitrophenol and Methylene blue increase in the order of their molar masses (Methylene blue (17.483, 22.241) > nitrophenol (6.817, 7.113) > naphthalene (5.083, 5.213)) for both Lang.1 and 2. The  $R_{sq}$  values obtained were 0.965, 0.936 and 0.924 for Naphthalene, Nitrophenol and Methylene blue respectively. It was equally observed that the Langmuir separation factor ( $R_L$ ) values indicated that the adsorption is favourable for the multicomponent pollutants since ( $R_L$ ) obtained for all is less than 1 ( $R_L < 1$ ) (Jawad *et al*, 2020).

**Langmuir 3 and 4:** Figure 1 (c) and (d) shows the plots of Langmuir 3 and 4. The adsorption capacities,  $q_m$ , and Langmuir isotherm parameter,  $K_L$ , as well as the correlating coefficient ( $R^2$ ) were obtained from the plots. The adsorption capacities of Naphthalene, Nitrophenol and Methylene blue equally increase in the order of their molar masses (Naphthalene < Nitrophenol < Methylene blue) for both Lang.3 and 4 from Table 3. Despite the high adsorption capacities and the  $R_L$  values indicating that the adsorption is favourable, the percentage errors obtained are too much (22.8%, 21.3 % and 67.3 % for Naphthalene, Nitrophenol and Methylene blue respectively) which makes Langmuir 3 and 4 unfit for the adsorption of these pollutants.

**Langmuir 5 and 6:** Figure 1 (e) and (f) shows the plots of Langmuir 5 and 6. The adsorption capacities,  $q_m$ , and Langmuir isotherm parameter,  $K_L$ , as well as the correlating coefficient ( $R^2$ ) were obtained from the plots. The molar masses have the same effect on the adsorption process as the previous isotherms. The adsorption capacities were at their best at Langmuir 6 for all pollutants but the  $R^2$  values of MB were incredibly small with an error of 60.31 % and that of Nitrophenol was at its best (0.947). This makes Langmuir 5 and 6 unfit for the adsorption of MB but the best for Nitrophenol because of the high adsorption capacity (8.467).

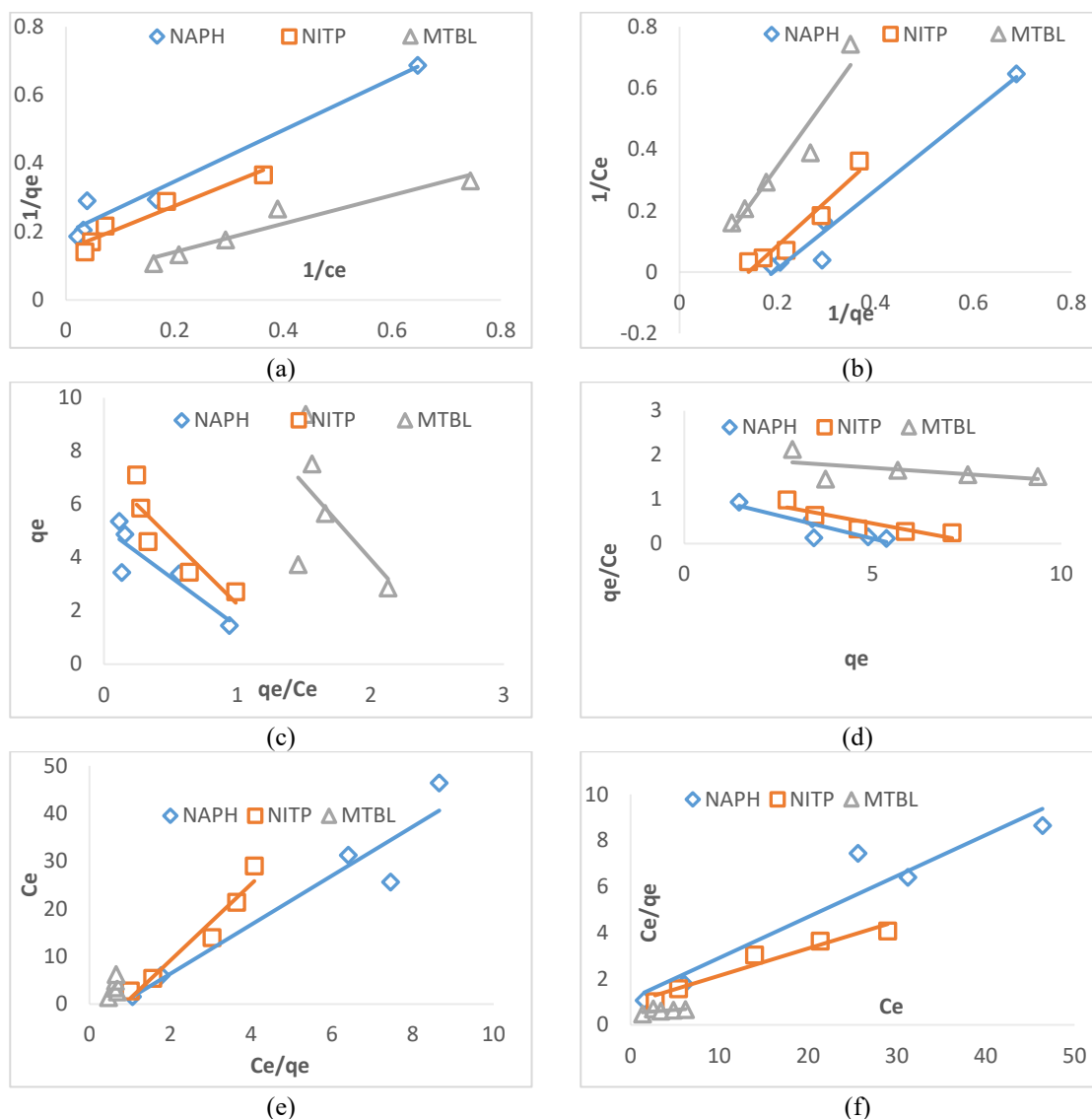


Figure 1 The plot of (a)  $1/C_e$  against  $1/q_e$  (Langmuir 1 isotherm model) (b)  $1/q_e$  against  $1/C_e$  (Langmuir 2 isotherm model) (c)  $q_e/C_e$  against  $q_e$  (Langmuir 3 isotherm model) (d)  $q_e$  against  $q_e/C_e$  (Langmuir 4 isotherm model) (e)  $C_e/q_e$  against  $C_e$  (Langmuir 5 isotherm model) (f)  $C_e$  against  $C_e/q_e$  (Langmuir 6 isotherm model).

Table 3: Langmuir Isotherm parameters and the  $R^2$  values obtained from the plots.

Isotherms	Pollutants	$q_m$	$K_L$	$R_L$	$R^2$
Langmuir 1	Naphthalene	5.083	0.262	0.428	0.965
	Nitrophenol	6.817	0.228	0.392	0.936
	Methylene Blue	17.483	0.138	0.294	0.924
Langmuir 2	Naphthalene	5.213	0.246	0.438	0.965
	Nitrophenol	7.113	0.204	0.408	0.936
	Methylene Blue	22.241	0.099	0.310	0.924
Langmuir 3	Naphthalene	5.119	1.384	0.124	0.773

Investigations on the Suitability of the Langmuir Isotherms in the Adsorption of Nitrophenol, Naphthalene and Methylene Blue from Aqueous Media onto Activated Bentonite Clay

Langmuir 4	Nitrophenol	7.208	1.454	0.087	0.787
	Methylene Blue	15.223	2.698	0.023	0.327
	Naphthalene	5.534	0.209	0.464	0.773
Langmuir 5	Nitrophenol	7.875	0.159	0.444	0.787
	Methylene Blue	34.575	0.058	0.333	0.327
	Naphthalene	5.149	0.254	0.433	0.915
Langmuir 6	Nitrophenol	8.019	0.145	0.462	0.947
	Methylene Blue	13.987	0.204	0.259	0.397
	Naphthalene	5.628	0.157	0.530	0.915
	Nitrophenol	8.467	0.124	0.488	0.947
	Methylene Blue	35.211	0.0056	0.337	0.397

Collectively, the correlation coefficients ( $R^2$ ) and adsorption capacities of Naphthalene (0.965 and 5.213) and Methylene blue (0.924 and 22.241) are high at Langmuir 2 suggesting the Langmuir 2 model to best fit the adsorption of Naphthalene and MB. The high  $R^2$  values suggest that the activated bentonite clay exhibit monolayer coverage (Alabi *et al.*, 2020). The adsorption of Naphthalene, Nitrophenol and Methylene has been investigated elsewhere using different adsorbents and the results are compared with those obtained from this work as shown in Table 4.

Table 4: Langmuir parameters for the adsorption of Naphthalene, Nitrophenol and Methylene blue onto various adsorbents.

Adsorbent	Adsorbate	Langmuir Parameters		$R^2$	Study
		$q_m$ (mg/g)	$K_L$ (L/mg)		
Walnut shell AC	Naphthalene	110.28	0.24	0.972	Wu <i>et al.</i> , 2020
Sand/Bentonite mixture		0.482	0.766	0.970	Rennane <i>et al.</i> , 2019
Activated Bentonite Clay		5.213	0.246	0.965	This study
AO-modified poly(An-co-AA)	Nitrophenol	143.06	0.020	0.994	Saber <i>et al.</i> , 2021
Activated Bentonite Clay		8.47	0.124	0.947	This study
Orange peel	Methylene blue	250.6	5.44	0.98	Giraldo <i>et al.</i> , 2022
Periodate modified nanocellulose		90.91	0.075	0.965	Kara <i>et al.</i> , 2021
Activated Bentonite Clay		22.24	0.099	0.924	This study

#### 4. CONCLUSION

This study was conducted to determine the suitability of Langmuir isotherm on the adsorption of Naphthalene, Nitrophenol and Methylene blue from an aqueous solution using chemically activated bentonite clay. The chemical activation of bentonite clay was successfully done in this study. Langmuir 1 to 6 were applied to find the best fitting for representing the adsorption of Naphthalene, Nitrophenol and Methylene blue onto the chemically activated clay. The adsorption capacity depends on the molar masses and the solubility of the pollutants. The adsorption process is favourable and presents different Langmuir isotherms for the different pollutants in the aqueous solution.

#### REFERENCES

- Alabi, O., Alade, A.O., and Afolabi, T.J. (2020). Process optimization of adsorption of Cr (VI) on adsorbent prepared from Bauhinia rufescence pod by Box-Behnken Design. *J. Sep. Sci. Technol.* 55, pp.47–60, DOI: <https://doi.org/10.1080/01496395.2019.1577436>.
- Berez A., Ayari, F. Abidi N., Schafer G., and Trabelsi-Ayadi M. “Adsorption-desorption processes of azo dye on natural bentonite: batch experiments and modelling”. *Clay Minerals*, (2014) 49, pp.747–763.
- Boeykens, S. P., Redondo, N., Obeso, R. A., Caracciolo, N., and Vazquez, C. (2019). Chromium and lead adsorption by avocado seed biomass study through the use of total reflection X-Ray fluorescence analysis. *Applied Radiation and Isotopes*, 153(108809). DOI: 10.1016/j.apradiso.2019.
- Crini, G., and Lichtfouse, E. (2018). Advantages and disadvantages of techniques used for wastewater treatment. *Environmental Chemistry Letters*, 17(1), pp.145-155.
- Giraldo, S., Acelas, N.Y., Ocampo-Pérez, R., Padilla-Ortega, E., Flórez, E., Franco, C.A. Cortés, F.B, Forgionny, A. (2022). Application of Orange Peel Waste as Adsorbent for Methylene Blue and Cd<sup>2+</sup> Simultaneous Remediation. *Molecules*, 27, 5105. <https://doi.org/10.3390/molecules27165105>.
- Jawad, A.H., Mubarak, N. S. A., and Abdulhameed, A.S. (2020). Microwave Enhanced Synthesis of Sulfonated Chitosan-montmorillonite for Effective Removal of Methylene Blue, *J. Polym. Environ.*, 28, pp. 624–637.



- Kara, H.T., Anshebo, S.T., Sabir, F.K., and Workineh, G.A. (2021). Removal of Methylene Blue Dye from Wastewater Using Periodiated Modified Nanocellulose. *International Journal of Chemical Engineering*, <https://doi.org/10.1155/2021/9965452>.
- Khan, A. A., and Mondal, M. (2021). Low-cost adsorbents, removal techniques, and heavy metal removal efficiency. In *New Trends in Removal of Heavy Metals from Industrial Wastewater*, 2021, pp.83-103. doi:<https://doi.org/10.1016/C2019-0-04585-2>.
- Korbahti, B.K., Artut, K., Gecgel, C., Ozer, A. (2011). Electrochemical decolorization of textile dyes and removal of metal ions from textile dye and metal ion binary mixtures. *Chem. Eng. J.* 173, pp. 677–688.
- Lasota, J., Łyszczarz, S., Kempf, P., Kempf, M., and Błońska, E. (2021). Effects of Species Composition on Polycyclic Aromatic Hydrocarbon (PAH) Accumulation in Urban Forest Soils of Krakow Water, Air, Soil Pollution. *Water Air Soil Pollut*, 232(74), pp. 1-12. doi:<https://doi.org/10.1007/s11270-021-05043-0>.
- Mishra, S., and Maiti, A. (2018). The efficacy of bacterial species to decolourise reactive azo, anthraquinone and triphenylmethane dyes from wastewater: a review. *Environmental Science and Pollution Research*, pp. 1-29.
- Okeowo, I.O., Balogun E.O., Ademola, A.J., Alade, A.O., Afolabi, T.J., Dada, E.O., Farombi, A.G. (2020). Adsorption of Phenol from Wastewater Using Microwave-Assisted Ag–Au Nanoparticle-Modified Mango Seed Shell-Activated Carbon, *Int. J. Environ. Res.* 14 pp. 215–233, DOI: <https://doi.org/10.1007/s41742-020-00244-7>.
- Pazdro, K. (2014). Persistent Organic Pollutants in Sediments from the Gulf of Gdańsk. *Annu. Set Environ. Prot.*, 6, pp. 63–76.
- Porhemmat, S., Ghaedi, M., Rezvani, A., Azghandi, M., and Bazrafshan, A. (2017). Nanocomposites: Synthesis, characterization and its application to removal azo dyes using ultrasonic assisted method: Modeling and optimization 530-543. *Ultrasonics Sonochemistry*, pp. 540-543.
- Puri, C., Sumana, G. (2018). Highly Effective Adsorption of Crystal Violet dye from Contaminated Water using Graphene Oxide Intercalated Montmorillonite Nanocomposite, *Appl. Clay Sci.* 166, pp. 102-112.
- Rani, B., Anees, A., and Muhammad, S. (2017). Mechanism of Adsorption on Nanomaterials. *The Royal Society of Chemistry, Detection Science Series No.9*, pp. 90-112. DOI: <https://www.researchgate.net/publication/3107718>.
- Rennane, S., Bendjaballah-Lalaoui, N., Trari, M. (2019). Comparative removal of naphthalene by adsorption on different sand/bentonite mixtures, *Bulgarian Chemical Communications*, 51(3), pp. 315-325 DOI:10.34049/bcc.51.3.4897.
- Saber, S.E.M., Md Jamil, S.N.A., Abdullah, L.C., Yaw, C., Tasman Ting, T.M, (2021), Insights into the p-nitrophenol adsorption by amidoxime-modified poly(acrylonitrile-co-acrylic acid): characterization, kinetics, isotherm, thermodynamic, regeneration and mechanism study, *Royal Society of Chemistry Adv.*, 11, pp. 8150-8162.
- Sadaf, S., Bhatti, H. N., Arif, M., Amin, M., Nazar, F., and Sultan, M. (2014). Box–Behnken design optimization for the removal of Direct Violet 51 dye from aqueous solution using lignocellulosic waste, *Desalination and Water Treatment*, 56(9), pp. 2425-2437.
- Wu, Z, Sun, Z, Liu, P, Li, Q, Yang, R and Yang, X (2020) Competitive Adsorption of Naphthalene and Phenanthrene on Walnut Shell Based Activated Carbon and the verification via theoretical calculation, *Royal Society of Chemistry Adv.*, 10, 10703-10714.
- Zhang, X., Duan, C., Jia, X., and Dai, B. (2016). Carboxylation kapok fiber as a low-cost, environmentally friendly adsorbent with remarkably enhanced adsorption capacity for cationic dyes. *Res. Chem. Intermed.*, 42, pp. 5069-5085.
- Zhu, Y., Fan, W., Zhou, T., and Li, X. (2019). Removal of chelated heavy metals from aqueous solution: A review of current methods and mechanisms Science of the Total Environment. *Sci Total Environ.*, 678, pp. 253-266. doi:10.1016/j.scitotenv.2019.04.416



## Simulation of Pyrolysis Reactor to Produce Bio-Fuel from Selected Biomass

Ebenezer O. DADA<sup>1,2</sup>, Oluchukwu C. OYEKA<sup>1</sup>, Ifeoluwa O. GBOLAHAN<sup>1</sup>, Temitope S. OLAWALE<sup>1</sup>, Victor O. OLALEYE<sup>1</sup>, Akinola, D. OGUNSOLA,<sup>3</sup> Kamoru O. OLADOSU<sup>4,5</sup> and Abass O. ALADE,<sup>1,2,5\*</sup>

<sup>1</sup>Chemical Engineering Department, Ladoké Akintola University of Technology, P.M.B. 4000, Ogbomoso, Nigeria.

<sup>2</sup>Bioenvironmental, Water and Engineering Research Group (BWERG), Ladoké Akintola University of Technology, P.M.B. 4000, Ogbomoso, Nigeria

<sup>3</sup>Department of Mechanical Engineering, Ladoké Akintola University of Technology, P.M.B. 4000, Ogbomoso, Nigeria

<sup>4</sup>Department of Mechanical Engineering, Kwara State University, Malete, P.M.B 1530 Ilorin, Nigeria

<sup>5</sup>Science and Engineering Research Group, (SEARG), Ladoké Akintola University of Technology, P.M.B. 4000, Ogbomoso, Nigeria

\*Corresponding author: [aolade@lautech.edu.ng](mailto:aolade@lautech.edu.ng)

---

### ABSTRACT

Numerical simulation of the rice straw and sugarcane bagasse was based on the data from the previous literature on biomass pyrolysis simulation, to determine the efficiency of the pyrolysis reactor, the effect of the feedstock and the operating conditions of the process. The simulation was carried out using Aspen plus. The product yield of fast pyrolysis of lignocellulosic biomass was calculated from developed pyrolysis reactions. The total mass flows rate of the liquid stream, gas stream and char stream compositions at 500 °C were 34.6737, 22.2392 and 15.3268 kg/h, respectively, while the heating rates for the samples were 10 and 60 °C/min. The yield of biochar at different pyrolysis temperatures of rice straw in the simulation is more than that of the sugarcane bagasse because of the size of particles and moisture content. The result of this model showed that it was suitable for predicting fast pyrolysis reactions for lignocellulosic biomass feedstock at high temperatures (500-600 °C).

**Keywords:** Biochar, Biomass, Pyrolysis, Simulation.

### 1. INTRODUCTION

Renewable energy sources are being projected globally as a possible replacement for fossil fuel-based energy sources. Biomass as a significant renewable energy source material is expected to play a prominent role in this process. It is readily and widely available, as well as contributes to global CO<sub>2</sub> reduction. Biomass has a high energy content (Dada *et al.*, 2021). However, issues bothering environmental protection and optimal production are holding biomass energy back from wider adoption and until these issues are addressed, it is unlikely that biomass energy will become a viable alternative to fossil fuels (Adeniyi *et al.*, 2019). Pyrolysis, the thermal degradation of organic material in an oxygen-deficient atmosphere of temperature between 400-900 °C, into gas, liquid, and solid products is one of the techniques used in the thermochemical conversion of biomass into biofuels (Tsai *et al.* 2006). The yield and composition of the products are influenced by a range of pyrolysis process parameters, including the type of waste, reactor system, gas residence time, contact time, heating rate, temperature, pressure ranges, and presence of catalysts (Velghe *et al.*, 2011). Sugarcane bagasse is an agro-allied waste product from the sugar industry found readily available after the extraction of raw cane sugar. It is a highly fibrous, low-density 'waste' material. Specifically, 100 kg of every 1000 kg of sugar cane produces about 100 tons of raw sugar and approximately 270 kg of bagasse (Drummond and Drummond, 1996). Generating power by direct combustion of sugar cane bagasse in boilers has a maximum efficiency of 26%.

The energy recovery processes will generate useful products such as hydrogen-rich synthesis gas, pyrolysis bio-oil, and char. Rice straw is a residual by-product of rice production at harvest time. The total bagasse of this residue depends on different factors such as diversities, soils and nutrient management and weather (Van Hung *et al.*, 2020). Rice straw has high fiber content and, consequently, has been used as animal feed in many countries worldwide (Ragab and Zhongli, 2019) Rice straw has immense potential to create bioenergy, an alternative renewable source of power. (Van Hung *et al.*, 2020). Due to the lack of actual plant data, system analysis of pyrolysis processes is normally based on process simulation.

Existing technical and environmental assessments use approximations applying a few model compounds, significantly simplifying the bio-oil characteristics. Predictive simulations are capable of dealing with a wide range of different lignocellulosic Kinetic reaction models based on thermodynamic equilibrium calculations are flexible and have proven to be unsuitable for predicting pyrolysis reactions (Pavel and Aloy, 2016). Current approaches for modelling pyrolysis

processes focus strongly on computational fluid dynamic (CFD) (Papadikis *et al.*, 2009; Aramideh *et al.*, 2015; Lee *et al.*, 2015;) or single particle models (Haseli *et al.*, 2012; Xue *et al.*, 2016), while others consider isolated biomass components (an example is lignin) (Hough *et al.*, 2016). This work was aimed at developing simulation models to obtain energy from rice straw and sugar cane bagasse with the use of aspen. The models were projected at harnessing optimum and high-quality yield. Experimental results within the contexts of the predictions earlier made were used to validate the models. The effect of the process variables on the product yield was determined, while the composition of bio-char, bio-oil and bio-gas was observed in the product).

## 2. MATERIALS AND METHODS

Rice Straw and Sugarcane Bagasse were used as the biomass feedstock for the simulation developed on the Aspen Plus V10 Modelling Software.

### 2.1 Simulation Process

The simulation process was modelled using Aspen plus V10 which is a large-scale general-purpose process simulation system for production plant design, steady-state simulation, and optimization. The data of feedstock for the simulation were based on experimental data collected from the literature on the pyrolysis of biomass (please cite the literature ???). The gas residence time in the pyrolysis reactor was 1.5 seconds for all runs. Figure 1 shows a flowsheet of the simulation used for reproducing the experimental runs.

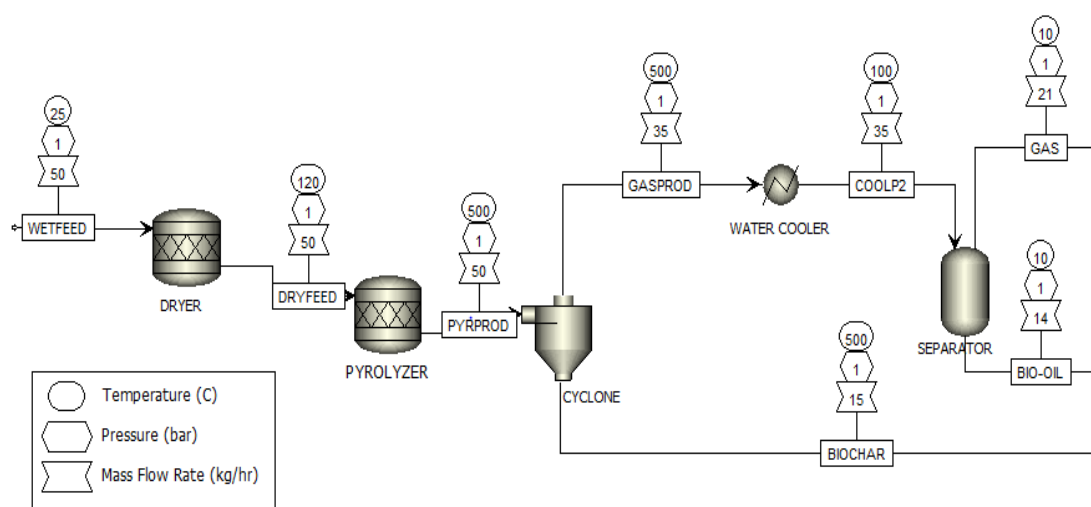


Figure 1: Flowsheet of the pyrolysis of biomass at 500 °C, and 1 atm

The reaction model terms are described in Table 1 and the pyrolysis reactor as represented on the flowsheet is required for modelling the pyrolysis reactions as described previously. The simulation further uses one cyclone and the gas-liquid separation is modelled by a flash at ambient pressure and ambient temperature. For this purpose, the condenser cools the quenched product stream down to 25 °C. Furthermore, the lignin composition of the feedstock was determined as input for the reaction model. This is done by the iterative calculation procedure implemented in MS Excel which adjusts the lignin composition to the given elemental and biochemical composition of the biomass. The biomass was set as an unconventional component and other components as conventional components, enthalpy and density are the only attributes calculated for unconventional components, which are calculated by empirical correlation.

Table 1: Reaction Model Description

Model	Description
Dryer	Dry the material to remove the moisture in the biomass before pyrolysis
RGibbs	It is the only reactor module that can handle the three-phase equilibrium of vapor, liquid and solid, based on the principle of minimum Gibbs free energy.
Cyclone	It is used to separate biochar from the fluid gas stream.
Cooler	Reduces the temperature of the gas stream before it enters the separator,
Flash	Based on strict vapor-liquid balance, moisture and biomass materials are separated.

The dried biomass stream from the dryer stream enters the 'RGibbs reactor' for pyrolysis. The R Gibbs reactor performs pyrolysis of biomass based on the principle of minimizing Gibbs free energy. By changing the temperature of the 'RGibbs reactor', the relationship between biochar yield and pyrolysis temperature as discussed was sustained.

### 3. RESULTS AND DISCUSSION

#### 3.1 Feedstock Characterization

The product yield of fast pyrolysis of lignocellulosic biomass was calculated from developed pyrolysis reactions. The result of this model showed that it was suitable for predicting fast pyrolysis reactions for lignocellulosic biomass feedstock at high temperatures (500-600 °C) (Rahman and Aziz, 2018). The oxygen and nitrogen content in the feedstock was not too high. The heating value (HHV) of biomass was found to be 30.3 MJ/kg which was within the literature study of  $28 \times 10^{40}$  MJ/kg (Huang and Lo, 2020).

#### 3.2 Products Characterization

The differential thermogravimetric (DTG) behaviour of biomass was achieved over the temperature range of 650 °C using a Pyris Diamond DTG analyser (Perkin Elmer). The samples (200 g) were heated at two different constant heating rates of 10 and 60 °C/min while maintaining a constant nitrogen flow rate of 100 mL per minute. The proximate analysis of the feedstock and products was carried out according to ASTM D1762-84 mechanisms.

#### 3.3 Bio-Oil Product Composition

The influence of reactor temperature on the pyrolysis products can be observed in Figure 2, with the liquid yield achieving a maximum of around 680 °C. The result obtained from the simulation at 500 °C is illustrated in Table 2. The simulation results agree nearly well with the experimental findings from the literature, with the highest correlation around 500 °C and slightly increasing deviation for temperatures above and below. The temperature behavior of the simulation, in general, is observed to be slightly less pronounced than in the experiments.

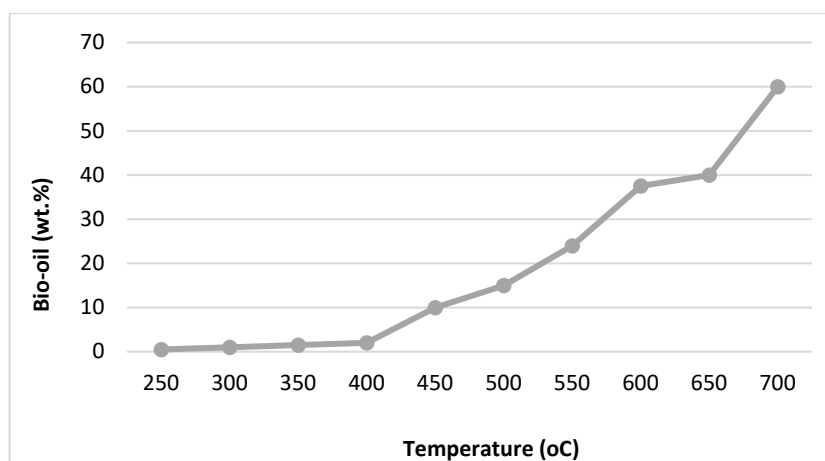


Figure 2: plot of temperature against bio-oil

Table 2: Stream composition at 500 °C

Component	Stream Mass Flow Rate (kg/h)		
	Liquid	Gas	Char
Biomass	0	0	0
Bio-oil	2.624989578	$6.37 \times 10^{-7}$	$6.37 \times 10^{-7}$
CH <sub>4</sub>	3.619075964	3.61407	3.61407
CO <sub>2</sub>	8.154093556	8.09921	8.09921
CO	8.859366861	8.85418	8.85418
NH <sub>3</sub>	0.005293403	0.005093	0.005093
H <sub>2</sub> S	0.079399728	0.077749	0.077749
N <sub>2</sub>	0.129275232	0.129205	0.129205
H <sub>2</sub>	0.275435679	0.275424	0.275424
H <sub>2</sub> O	10.92681736	1.18425	1.18425

##### 3.3.1 Gas product result

The yield of gas in the simulated model results depicts that there was almost a uniform output for the temperature range of 250–400 °C. As illustrated in Figure 3, the increment in gas yield compensates for the reduced value in solid products within the same temperature range that is considered. The composition of the gas stream at 500 °C is shown in Table 2

where CO has the highest value and is followed closely by CO<sub>2</sub> which has a negligible amount of liquid (bio-oil) rate of flow.

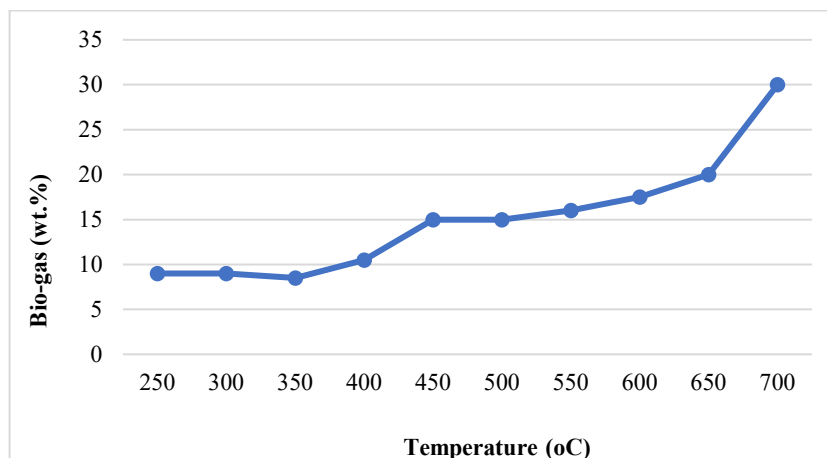


Figure 3: plot of temperature against bio-gas

### 3.3.2 Solid product result

Rice straw and sugarcane bagasse showed significantly different conversion and reactivity profiles. The sugarcane bagasse char had an increased rate of reaction in the later part of char conversion, with a clear dependence on operating temperature. With increased temperature, the effect seems to diminish. Meanwhile, rice straw char had a decrease in char conversion rates at later stages of the conversion, and more deactivation was observed with increased temperature; this coincides with more extensive melting of residual ash. These trends, as shown in Figure 4, might be explained by chemical phase transformations of catalytically active potassium carbonate taking place in that temperature range, others have described this mechanism (Zubek *et al.*, 2018).

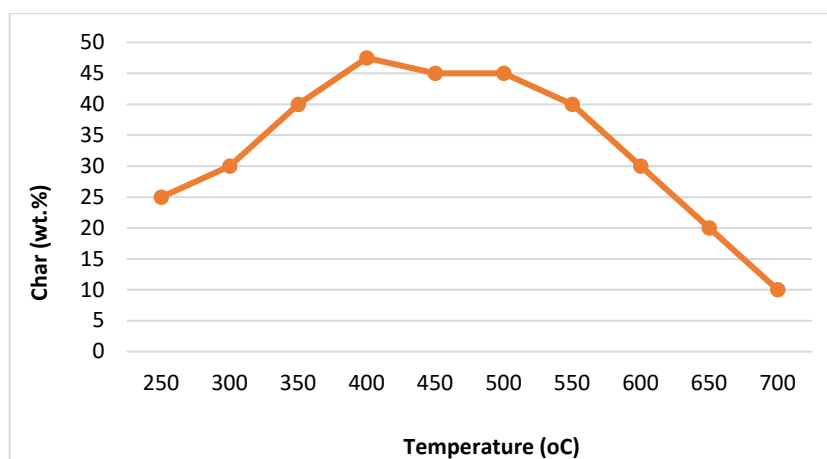


Figure 4: plot of temperature against bio-char

### 3.3.3 Result Comparison

To validate the reaction model as a predictive tool, it is first tested and cross-checked against data published in the literature. The results in Table 3 from the simulation of the modeled process of this research work at 250 °C show that the amount of char obtained is higher than the bio-oil and biogas yields, and this correlates with the experimental result achieved by Mohammed *et al.* (2017) used municipal green waste (MGW) as the feedstock. The results at 300 °C for this study and Mohammed *et al.* (2017) follow the same trend as that of 250 °C, but the experimental results from Pavel and Aloy (2016), using spruce sawdust as feedstock, ultimately oppose that trend as the gas yield accounts for up to 40-50% of the total output.

Table 3: Pyrolysis product of biomass at different temperatures

Reference	Temperature	Feedstock	Sample Products		
			Char	Oil	Gas
Mohammed <i>et al.</i> (2017)	At 250 °C	Municipal green waste	52	11	37
This Study		Rice straw	47	20.5	32.5

Mohammed <i>et al.</i> (2017)	At 300 °C	Municipal green waste	50.8	13.2	36
Pavel and Aloy (2016)	At 300 °C	Spruce sawdust	24	36	40
This Study		Rice straw	50	21	29
Pavel and Aloy (2016)	At 350 °C	Spruce sawdust	23.5	35	41.5
This Study		Rice straw	56	18.5	25.5
Pavel and Aloy (2016)	At 400 °C	Spruce sawdust	23.5	32.5	44
This Study		Rice straw	59.5	16	24.5
Pavel and Aloy (2016)	At 500 °C	Spruce sawdust	26	23	51
Ward <i>et al.</i> (2014)		Studded grain waste	17.08	58.01	24.9
		Pine chips	35.41	42.77	21.81
		Wood	35.15	42.97	21.88
Chawanaat <i>et al.</i> (2020)	At 450 °C	Municipal waste	50	38	12
Pavel and Aloy (2016)		Spruce sawdust	22.5	31	46.5
This Study		Rice straw	63	14.5	22.5
Chawanaat <i>et al.</i> (2020)	At 500 °C	Lignocellulosic biomass (sawdust)	26	52	22
Pavel and Aloy (2016)	At 500 °C	Spruce sawdust	26	23	51
Ward <i>et al.</i> (2014)		Shredded green waste	17.08	58.01	24.90
		Pine chips	35.41	42.77	21.81
		Wood	35.15	42.97	21.88
This Study		Rice straw	53.3	23.4	23.3
Chawanaat <i>et al.</i> (2020)	At 550 °C	Lignocellulosic Biomass (Sawdust)	12	63	25
Pavel and Aloy (2016)	At 580 °C	Spruce Sawdust	24	20	56
This Study		Rice Straw	46.67	30.68	22.65
Chawanaat <i>et al.</i> (2020)	At 600 °C	Lignocellulosic Biomass (Sawdust)	13	62	25
Pavel and Aloy (2016)	At 600 °C	Spruce Sawdust	22	18	60
This Study		Rice Straw	35	42.5	22.5

#### 4. CONCLUSION

Aspen Plus V10 software was used to simulate the pyrolysis process of rice straw and sugarcane bagasse. The biochar production at 300, 400, 500, 600, and 700 °C temperatures were simulated, and the results showed that as the temperature increased, the biochar yield showed a downward trend. Below 500 °C, the downward trend is mild, when the temperature is higher than 500 °C, the downward trend is more obvious. This is due to the secondary cracking of biochar to produce more pyrolysis gas at higher temperatures. At the same time, the heat duty of the RGibbs reactor at different pyrolysis temperatures was compared. Rice straw is an exothermic reaction at 300 and 400 °C, and an endothermic reaction when the pyrolysis temperature is higher than 500 °C. Sugarcane bagasse is an exothermic reaction only at 300 °C, and an endothermic reaction when the pyrolysis temperature is higher than 400 °C. Comparing the two biomasses, rice straw requires less heat energy during the pyrolysis process and can generate more biochar. Based on the simulation, a pyrolysis reactor was used to pyrolyse the rice straw and sugarcane bagasse. This work is significant in that without experimentation, the biochar production and the optimal pyrolysis temperature can be predicted by measuring the components of biomass.

#### REFERENCES

- Adeniyi, A. G., Ighalo, J. O. and Abdulsalam, A. (2019). Modelling of integrated processes for the recovery of the energetic content of sugar cane bagasse. *Biofuels Bioproducts and Biorefining*. 13(4), pp. 1-11.
- Aramideh, S., Xiong, Q., Kong, S. C. and Brown, R. C. (2015). Numerical simulation of biomass fast pyrolysis in an auger reactor. *Fuel*. 156(1), pp. 234–242.
- Dada E. O., Alade A. O., Adeniji A. T. and Afolabi T. J. (2021) Effect of Rice-Bran Pre-treatment in Biohydrogen Production. *Current Journal of Applied Science and Technology*, 40(16), pp. 12 -19.
- Drummond A. F. and Drummond I. W. (1996). Pyrolysis of sugar cane Bagasse in a wire-mesh reactor. *Industrial and Engineering Chemistry Research* 35(1), pp. 1263–1268

- Haseli, Y., Van Oijen, J. A. and De Goey, L. P. (2012). A simplified pyrolysis model of a biomass particle based on infinitesimally thin reaction front approximation. *Energy Fuels*. 26(1), pp. 3230–3243.
- Hough, B. R., Schwartz, D. T. and Pfaendtner, J. (2016). Detailed kinetic modelling of lignin pyrolysis for process optimization. *Industrial and Engineering Chemistry Research*. 55(34), pp. 9147–9153.
- Huang, Y. and Lo, S. (2020). Predicting heating value of lignocellulosic biomass based on elemental analysis. *Energy*, 19(1), DOI:10.1016/j.energy.2019.116501
- Lee, Y. R., Choi, H. S., Park, H. C. and Lee, J. E. (2015). A numerical study on biomass fast pyrolysis process: a comparison between full lumped modelling and hybrid modelling combined with CFD. *Computers and Chemical Engineering*. 82(2), pp. 202–215.
- Mohammed, M., Ozbay, I. and Durmusoglu, E. (2017). Bio-drying of green waste with high moisture content. *Process Safety and Environmental Protection*, 3(1) pp. 420–427,
- Papadikis, K., Gu, S., Bridgwater, A.V. and Gerhauser, H. (2009). Application of CFD to model fast pyrolysis of biomass. *Fuel Process Technology*. 90(1), pp. 504–512.
- Pavel, L. and Aloy P. (2016). Wood pyrolysis using aspen plus simulation and industrially applicable model. *GeoScience Engineering* 42(1), pp. 11–17.
- Rahman M.A. and, Aziz M.A (2018) Solar pyrolysis of scrap tire: Optimization of operating parameters. *Journal of Material Cycles and Waste Management*, 20(2), pp. 1207-1215.
- Tsai, W. T., Lee, M. K. and Chang, Y. M. (2006) Fast pyrolysis of rice straw, sugarcane bagasse and coconut shell in an induction-heating reactor. *Journal of Analytical and Applied Pyrolysis*. 72(2), pp. 230–237.
- Van Hung, N., Maguyon-Detras, M. Migo, M., Quilloy, R., Balingbing, C., Chivenge, P., Gummert, M. and Douthwaite, B. (2020). Rice Straw Overview: Availability, Properties, and Management Practices. *Sustainable Rice Straw Management*. 8(2), pp. 1-13.
- Velghe, I., Carleer, R., Yperman, J. and Schreurs, S. (2011). Study of the pyrolysis of municipal solid waste for the production of valuable products. *Journal of Analytical and Applied Pyrolysis*, 92(2), pp. 366-375.
- Ward, J. D., Rasul, M. and Bhuiya, M. M. (2014). Energy recovery from biomass by fast pyrolysis. *Procedia Engineering*, 90(1), pp. 669-674.
- Xue, A., Pan, J., Tian, M., and Yi, X. (2016). Pyrolysis model of single biomass pellet in downdraft gasifier. *Transactions of Tianjin University*. 22(1), pp. 174–181.
- Zubek, K., Czernski, G. and Porada, S. (2018). Determination of optimal temperature and amount of catalysts based on alkali and alkaline earth metals for steam gasification process of bituminous coal. *Thermochimica Acta*, 66(5), pp. 60-69



## Bio-Electrochemical Treatment of Pharmaceutical Wastewater and Sustainable Bioelectricity Generation Using Microbial Fuel Cell

Oduayo D. AKINWUMI\*, Samuel E. AGARRY<sup>1</sup>, Mujidat O. AREMU<sup>1</sup>, Abass O. ALADE<sup>1</sup>, Abiola O. AWORANTI<sup>1</sup>

<sup>1</sup>Department of Chemical Engineering, Ladoké Akintola University of Technology, Ogbomoso, Oyo State, Nigeria

<sup>1\*</sup>[aoakinwumi@lautech.edu.ng](mailto:aoakinwumi@lautech.edu.ng), <sup>1</sup>[seagarry@lautech.edu.ng](mailto:seagarry@lautech.edu.ng), <sup>1</sup>[moaremu@lautech.edu.ng](mailto:moaremu@lautech.edu.ng), <sup>1</sup>[aalade@lautech.edu.ng](mailto:aalade@lautech.edu.ng),  
<sup>1</sup>[aoworanti@lautech.edu.ng](mailto:aoworanti@lautech.edu.ng)

\*Corresponding author

---

### ABSTRACT

This study was conducted to evaluate the performance of bio-electrochemical treatment of pharmaceutical wastewater and the simultaneous production of bioelectricity using dual-chamber microbial fuel cells (MFCs). The anodic chamber was loaded with pharmaceutical wastewater (PWW), while the cathodic chamber contained a prepared buffer solution. The system was operated at varying pH (4.5, 5.5, 6.5 and 7.5), temperature (25, 35, 45 and 60 °C), and fruit waste additives (10, 20, 30, 40 and 50 g). The initial Chemical Oxygen Demand (COD) and Biological Oxygen Demand (BOD) for the PWW were 1346.17 and 1025.01 mg/L, respectively. Maximum power generations of 775 mV, 652 mV, and 1012 mV were achieved at a pH of 7.5; temperature of 35 °C; and mixed fruit wastes additive. The highest BOD and COD removals of 96.25 and 97.99% were attained at 100 Ω resistance of MFC. The results from this study further intensify the industrial wastewater treatment and bioelectricity generation potentials of the MFC technology.

**Keywords:** Additives, BOD, bioelectricity generation, COD, microbial fuel cells.

### 1. INTRODUCTION

Wastewater is any water that its quality has been adversely affected by anthropogenic activities. Industrial wastewater poses a potential hazard to natural water bodies as it contains both organic and inorganic contaminants that are toxic to various forms of life in the ecosystem (Surti, 2016). Contamination of natural water bodies resulting from industrial wastewater has emerged as a major challenge in developing and high-density-populated countries, such as Nigeria (Samdipta and Manswini, 2020). Wastewater treatment is a high-cost and energy-intensive process not only due to large numbers of pollutants but also for the large volumes of water to be treated, which are mainly generated by human activities and different industries.

There is a huge demand for electricity all around the globe presently. Then, renewable energy sources get a massive attraction due to the polluting nature of fossil fuels. Microbial Fuel Cells (MFCs) are a new type of renewable and sustainable technology for electricity generation since it recovers energy from renewable materials that can be difficult to dispose of such as organic wastes and industrial wastewater (Kasirajan *et al.*, 2021). MFC is one of the biological electrochemical systems with a promising capability to treat waste generated from industries and, in return, produce electricity. It consists of anode and cathode sections, which are separated by a specific membrane. The MFC technology has been researched intensively in the recent decade because it offers a solution for environmental sustainability, simultaneously performing pollutant removal and energy production (Egbadon *et al.*, 2016).

Thus, integrated waste-management technologies must be designed to address both issues, which cannot only treat wastewater but also generate energy from the wastewater using microorganisms as a catalyst (Gotovtsev *et al.*, 2016). Microorganisms grow and degrade waste according to the prevailing microenvironment (Samdipta and Manswini, 2020). MFCs and microbial electrolysis cells (MECs) are two examples of speedily developing biotechnology, generally known as bioelectrochemical systems (BES), that combine biological and electrochemical processes to generate electricity, hydrogen, or other valuable chemicals (Maitreyi *et al.*, 2018). The pharmaceutical industry is engaged in manufacturing drugs and personal care products. Liquid and solid effluent from the pharmaceutical industry is toxic to the various life forms of the ecosystem. They also have a complex mixture of chemicals whose behaviour toward the biological system can differ. Hence, wastewater from pharmaceutical industries poses several problems for successful biological treatment (Sima and Abadi 2021).



MFCs, as one of the promising biological treatments, have arisen as a viable solution for chemical oxygen demand (COD) and biological oxygen demand (BOD) removals and simultaneous electricity generation. Therefore, this study is aimed at bioelectricity generation and microbial pharmaceutical wastewater treatment using MFC technology.

## 2. MATERIALS AND METHODS

### 2.1 Collection of Pharmaceutical Wastewater and Fruit Waste Samples

The pharmaceutical wastewater (PWW) used for this study was obtained from a pharmaceutical industry located in the South-Western region of Nigeria. The collected wastewater was left undisturbed for 24 h at room temperature (25°C) under anaerobic conditions for the suspended particulate to settle (Egbadon *et al.*, 2016). Samples were taken according to APHA 1992 for physicochemical characterization, including BOD and COD. The different fruit (Pineapple, Orange and Mango) wastes used as co-substrate additives were collected from a major fruit market in Ogbomoso, Oyo State.

### 2.2 Preparation of co-substrate additives (Fruit wastes)

The collected fruit wastes were cleaned and washed with distilled water to minimize loss of glucose. All the different fruit wastes were sun-dried for one week and then oven dried at 50 °C for 6 h to a constant weight (Mathuriya and Sharma, 2009). The different dried fruit wastes were milled to homogenous size and stored in a container for subsequent usage.

### 2.3 Preparation of Proton Exchange Membrane (PEM)

The proton exchange membrane (PEM) was prepared according to the following procedure. Agar-agar was dissolved in distilled water at a concentration of 40 g/l, then sodium chloride (NaCl) was added to the prepared agar-agar (7.5 g of NaCl in 40 g/L of agar-agar) and the agar-agar-NaCl mixture was autoclaved at a temperature of 121°C for 15 minutes to form a gelatinous mixture (Mohan *et al.* 2008). The autoclaved agar-agar-NaCl mixture, while still warm before it thickens, was poured inside a plastic pipe sealed at one end and was then allowed to cool and solidify after 30 min (Onuabuchi *et al.*, 2014).

### 2.4 Construction of Dual-Chamber MFC

The dual-chamber MFC was constructed using two identical plastic drums as shown in Figure 1: the anaerobic anode chamber and the aerobic cathode chamber, with a total working volume of 10,000 mL. The working volume of the anode and cathode compartments was 5000 mL each. The two chambers were connected by a hollow tube disc (50-mm diameter) made from a pre-treated Nafion 117 sheet (Nafion TM 117, Sigma- Aldrich). The PEM was fixed between clamps in the hollow tube. Plain graphite plates (5 cm x 5 cm; 10-mm thickness) without any coating were used as electrodes for both the anode and cathode chamber. The cathode has a projected surface area of 70 cm<sup>2</sup> and the anode was provided with uniform holes of 0.1-cm diameter to increase the overall surface area (83.56 cm<sup>2</sup>). Prior to use, the electrodes were soaked in distilled water for a period of 24 hr, and it was positioned at a distance of 6 cm on either side of the PEM. Each chamber was designed to have sample ports, wire point input provision (top), inlet and outlet ports (Borah *et al.*, 2013).

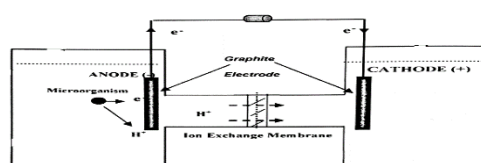


Figure 1: Schematic Diagram of MFC; Source: Modified from Mohan *et al.* (2008)

### 2.5 MFC Operation: Electricity Generation and Monitoring of BOD and COD Reduction

The MFC's anode chamber was flushed continually with distilled water to maintain anoxic conditions. The anode chamber was filled with PWW up to its working capacity (5 L), while a buffer solution was introduced into the cathode chamber with the working capacity maintained at 5 L, as provided in Figure 2. The experimental set up was left for at most 30 min to allow for stabilization and deflection. The MFC treatment of a full strength PWW was performed at varying pH (4.5, 5.5, 6.5 and 7.5), temperature (25, 35, 45 and 60 °C) and fruit wastes (from pineapple, mango and orange, used singly and in mixed form). The pH was adjusted by dropwise addition of sulphuric acid and/or sodium hydroxide. The bacteria for the bio-electrochemical treatment were the indigenous bacterial groups present in the PWW (Akinwumi *et al.*, 2020). After the setting up of the experiment, the MFC was continuously monitored for 166 days. The PWW in the anode chamber was periodically analysed at every 3 days interval for COD and BOD. The COD and BOD of PWW were monitored by using a test kit and a reader. The polarization curve of MFCs was measured by varying the external resistance from 33000 to 33  $\Omega$ . The voltage potential and current across the external load were simultaneously measured at intervals of 8 h using a connected digital multi-meter (Kusam, model DT-830D).



Figure 2: Experimental Microbial Fuel Set up

The COD reduction was calculated according to Equation 1.

$$E_{COD} = \frac{COD_{In} - COD_{Out}}{COD_{In}} \times 100\% \quad (1)$$

Where  $COD_{in}$  is the influent COD and  $COD_{out}$  is the effluent COD.

### 3. RESULTS AND DISCUSSION

#### 3.1 Physical Characterization

The results of physical characterization of the raw PWW are shown in Table 1. pH is a measure of acidity or alkalinity and is one of the stable parameters that specify a relative amount of free hydrogen and hydroxyl ions in the water (Akinwumi *et al.*, 2020). It is vital because it influences chemical reactions in the aquatic environment (Akinwumi *et al.*, 2020). Similarly, aquatic organisms are sensitive to pH changes and biological treatment. The pH of PWW obtained was 5.4 (Table 1), showing that the wastewater was relatively acidic (Gebrihans and Abadi, 2020). The colour rating for PWW was milky white and this indicate the extent that it has been sewer. The temperature of discharged PWW was 31 °C which falls within the standard (less than 40 °C) stipulated by WHO (WHO, 2008). Moreover, BOD (1025.10 mg/L) and COD (1346.17 mg/L) values in the PWW are relatively high and indicate that the level of pollution of water by oxygen depletion (Awotoye *et al.*, 2011). These levels were severely more than the WHO standard limit value of 50 mg/L.

Table 1: Physicochemical Characteristics of PWW

Parameters	Units	Measured values (PWW)	WHO Maximum Permissible Unit
PH	-	5.4	6-6.95
Temperature	°C	31	20-35
BOD	mg/L	1025.01	50
COD	mg/L	1346.17	100
Electrical conductivity	$\mu S / cm$	640	1400
TDS	mg/L	320	30
Colour	-	Milky White	-
Odour	-	Bad Odour	-

#### 3.2 Effect of pH on Bioelectricity generation using MFC

The pH of wastewater entering the anode chamber and the phosphate buffer entering the cathode chamber is one of the parameters that affect the current intensity in the MFC system and also affects and also affects the bioelectricity generation (Elakkiya and Matheswaran, 2013; Salam *et al.*, 2020). The effect of pH on PWW treatment under maximum voltage, current and power generated by MFCs operating at pH 4.5, 5.5, 6.5, and 7.5 as shown in Figure 3 were 344 mV, 420 mV 466 mV and 775 mV: 0.299 mA, 0.387 mA, 0.421 mA and 0.421 mA; 212 mW, 217 mW, 336 mW, 624 mW, respectively are shown in Figure 2a-c. The voltage generation increased continuously at pH 7.5, with a corresponding increase in the current generation. As the voltage values decreased from 775 mV to 405 mV with a decrease in the current generation, the voltage increased while the current and power generation also increased. This trend is similar to the observation reported by Agarry *et al.* (2016). The decrease in current generation at acidic pH (low pH) in comparison to alkaline pH may be because at low pH, microorganisms are deactivated, and thus microbial activity is reduced, which leads to low transfer of protons to the other side of the salt bridge and ultimately decreases the MFC efficiency.

#### 3.3 Effect of Temperature on Bioelectricity generation using MFC

The voltage, current and power generated from PWW as shown in Figure 4 were at 25 °C (402 mV, 0.344 mA and 161.604 mW) for 149 days, 35 °C (527 mV, 0.466 mA, and 277.79 mW) at 50 days, 45 °C (374 mV, 0.31 mA and 139.626 mW) for 12 days and 60 °C (230 mV, 0.181 mA and 47.961 mW) for 10 days. The bioelectricity parameter values were observed to reduce with an increase in temperature. The highest values were reported at temperature of 35 °C for PWW,

while the lowest values were obtained at 60 °C. A similar observation was reported by Chennappa *et al.* (2021), where voltage increased as temperature increased from 25 °C to 35 °C but decreased with an increase in temperature from 35 °C to 45 °C. This may likely be because most microorganisms are active in the temperature range of 30-35 °C.

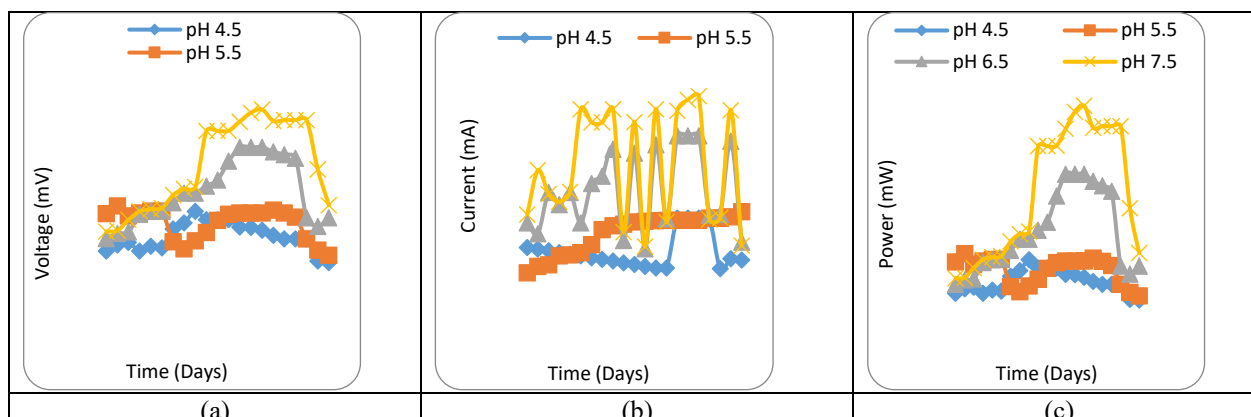


Figure 3: Plot of (a) Voltage versus Time (b) Current versus Time and (c) Power versus time for bioelectricity generation using PW at pH 4.5-7.5

Kjeang *et al.* (2009) and Jana *et al.* (2010) reported that the increase in temperature resulted in less cell multiplication and growth, which also affected the availability of catalysts leading to electrons released by the oxidation of wastewater and ultimately resulting in less current, voltage and power generation. However, during long operating times when bacteria are subjected to high temperatures, important compounds in cells, including nucleic acid and other material susceptible to temperature increment, may get damaged irreversibly, leading to an intense deterioration of cell function or cell death.

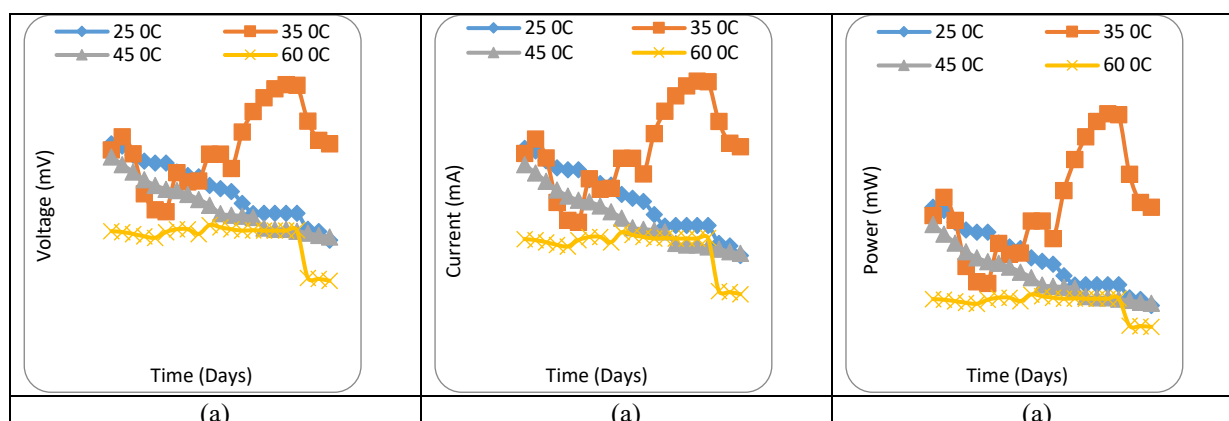


Figure 4: Plot of (a) Voltage versus Time (b) Current versus Time and (c) Power versus Time for Bioelectricity Generation using PWW at Temperature of 25 °C- 60 °C

### 3.4 Effect of additives (Fruit wastes)

The effect of additives (pineapple, orange and mango wastes) on bioelectricity generation from PWW (Figure 5) shows that there was an increase in voltage and current by the addition of each fruit waste to the PWW. Amongst the fruit wastes added singly as co-substrate to the PWW, the pineapple fruit waste (PFW) resulted in the highest bioelectricity generation (voltage: current: and power:) while the mixed fruit wastes addition to the PWW produced the highest bioelectricity (voltage: 1,012 mV; current: 0.95 mA; power: 1200 mW). Also, as shown in Figure 5, it was observed that the values of voltage, current and power generated from PWW with the addition of fruit wastes (singly or mixed form) were higher compared to the values of voltage, current and power generated from the PWW without the addition of fruit wastes (i.e., additives). This indicated that adding fruit wastes as co-substrates (additives) enhanced the bioelectricity generation from PWW. This may be due to the increase in carbon source in the wastewater, which led to an increase in microbial activities and, as a result, boosted the voltage, current and power generation. This result was supported by Mathuriya and Sharma (2009).

### 3.5 Coulombic Efficiency and removal of BOD and COD in the Presence of Additives

The percentage of BOD and COD removed, and coulombic efficiency as the main function of BOD and COD concentration are shown in Figures 6 and 7.

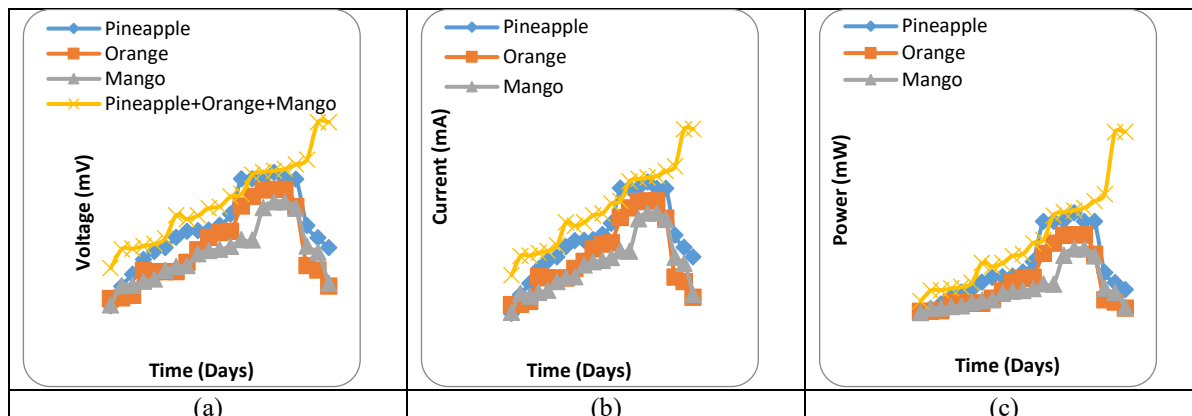


Figure 5: Plot of (a) Voltage versus Time, (b) Current versus Time and (c) Power versus Time for Bioelectricity Generation from PWW with Additives

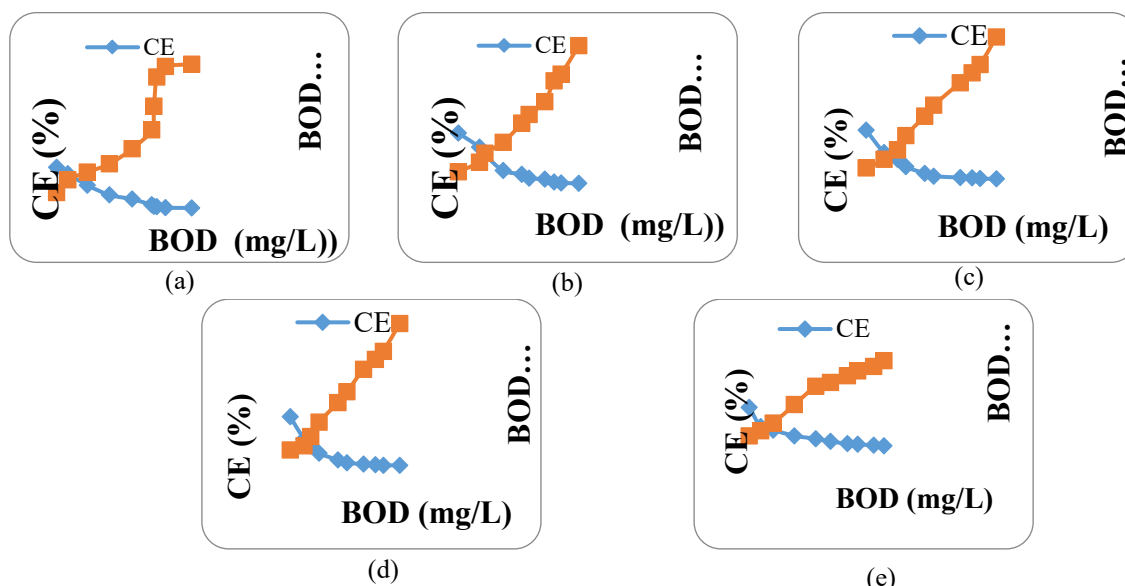


Figure 6: Coulombic Efficiency and BOD Removal from PW as function of BOD for (PWW, Only), (b) (PFW), (c) (OFW) (d) (MFW) and (e) (AFW)

It was observed that BOD and COD were 79.86%; 92.25% PWW only, 92.13%; 96.65% (PFW), 88.96; 95.78% (OFW), 81.5% ; 94.98% (MFW) and 96.25% ; 97.99% (AFW) while the CE are 22.5;20.69 (PWW only), 33.61 ; 29.5 (PFW), 30.56 ; 27.69 (OFW), 28.39 ; 20.69 (MFW) and 41.67 ; 37.79 (AFW) for PWW treatment at different BOD and COD concentration in the presence of PWW alone, PFW, OFW, MFW and AFW, respectively. A maximum BOD and COD removal of 96.65% : 97.89% was obtained for AFW followed by PFW (92.13% ; 96.65%). This showed that as the BOD and COD concentration of organic loading is decreased, the maximum CE of MFC is increased which is supported by Najiaowa et al., 2016. Also, the CE values obtained in this study are relatively higher than the CE obtained by Adeniran et al. (2016) (5% to 7%), and this may be because the reactor was efficient in converting the organic matter in wastewater to energy. Figure 6 and 7 shown that BOD and COD removal is proportional to wastewater concentration, and the results indicate the potential of the MFC as a wastewater treatment technique.

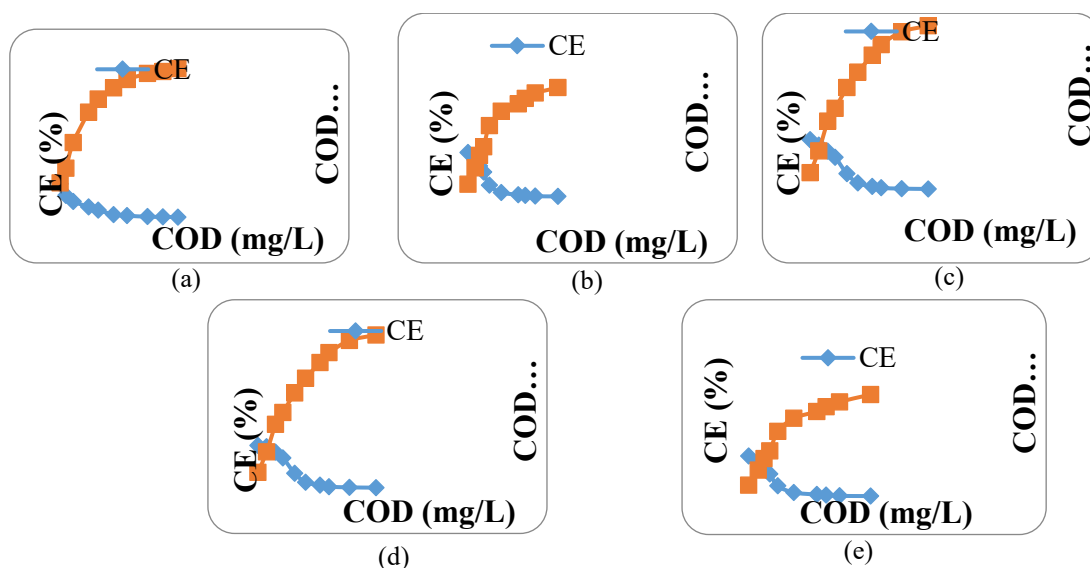


Figure 7: Coulombic Efficiency and COD Removal of PW as function of COD for (PW, Only), (b) (PFW), (c) (OFW), (d) (MFW), and (e) (AFW)

#### 4. CONCLUSION

Electricity was generated from PWW using MFC technology aided by microorganisms already in the wastewater. Optimum bioelectricity was generated at a pH of 7.5 and temperature of 35 °C using a 100% full strength PWW. The addition of a co-substrate such as fruit wastes (pineapple, orange and mango) to PWW enhanced power or bioelectricity generation as well as COD and BOD reductions. The bioelectricity generation through MFC technology is still in an early stage of development and shows great promise as a new method to accomplish both bioelectricity generation and wastewater treatment, which is affordable for both developing and developed countries. Thus, combining wastewater treatment and electricity generation could be a cost-effective way of wastewater treatment.

#### REFERENCES

- Adeniran, J.A., Huberts R, De-Koker., J.J, Arotiba, O.A., Olorundare, O.F. and Van-Zyl E. (2016). 'Energy Generation from Domestic Wastewater using Sandwich Dual-Chamber Microbial Fuel Cell with Mesh Current collector Cathode'. *International Journal of Environmental Science and Technology*, 13; 2209-2218.
- Agarry, S.E., Oghenejoboh, K.M., and Solomon, B.O (2016). 'Bioelectricity Production from Cassava Mill Effluents using Microbial Fuel Cell Technology'. *Nigerian Journal of Technology*, 35 (2): 329-336.
- Akinwumi, O.D., Aremu, M.O. and Agarry, S.E. (2020). 'Characterization of Brewery and Pharmaceutical Industrial Wastewater as Potential for Bioelectricity Generation'. *Research Journal of Engineering and Environmental Sciences*, 5 (20): 950-962.
- APHA. (1992). *Standard Methods for the Examination of Water and Wastewater*, 10<sup>th</sup> Edition, Washington D.C.
- Awotoye, O., Dada, A.C and Arowomo, G.A.O. (2011). Impact of Palm Oil Processing Effluent Discharge on the Quality of Receiving Soil and River in South-Western Nigeria. *Journal of Applied Science Research*, 7 (2). 111-118.
- Borah D, More, Sejal and Yadaf, R.N.S (2013). Construction of double chambered MFC using household materials and *Bacillus Megatarium* isolate from tea garden soil. *Journal of Microbial, Biotechnology and Food Sciences*, 3(1): 84-86.
- Chennappa, G., Vandana, H.B., Netravati, B.P., Chaitra Kumari, B.P., Nanje Gowda, N.A., Hanumantharaju., K.N. and Lokesh, A.C. (2021). Microbial Fuel Cells; An Alternate Approach for Bioelectricity Generation Waste Management. *Journal of Pure and Applied Microbiology*, 15 (4): 1833-1845.
- Egbadon, E.O., Akujobi, C.O., Nweke, C.O., Braide, W., Akaluka, C.K. and Adeleye, S.A, (2016). Simultaneous Generation of Bioelectricity and Treatment of Swine Wastewater in a Microbial Fuel Cell. *International Letters of Natural Sciences*, 54, 100-107
- Elakkiya, E. and Matheswaran, M. (2013). 'Comparison of Anodic Metabolism in Bioelectricity Production during Treatment of Dairy Wastewater in Microbial Fuel Cell. *Bioresource Technoogy*, 136: 407-412.
- Gebrihans, H.G and Abadi G.H. (2020). Physico-Chemical and Microbiological Analysis of Potable Ground Water in MIT and Abala, Afar Regional State, Ethiopia. *International Journal of Scientific and Engineering Research*. 11:4, 2229-5518
- Gotovtsev, P. and Dyakov, A. (2016). Biotechnology and Internet of things for Green Smart City 409 Application 2016 IEEE 3rd World Forum on Internet of Things (WF-IoT) 542–546.

## Bio-Electrochemical Treatment of Pharmaceutical Wastewater and Sustainable Bioelectricity Generation Using Microbial Fuel Cell

- Jana, P. S., Behera, M. and Ghangrekar, M.M. (2010). 'Performance Comparison of Up- Flow Microbial Fuel Cells Fabricated using Proton Exchange Membrane and Earthen Cylinder'. *International Journal of Hydrogen Energy*, 35, 5681-5686.
- Kasirajan, K., Saigeetha, S., Anthony, V.S., Abirami, S., Remitta, R.E. and Dhiva, S. (2021). Bioelectricity Production using Microbial Fuel Cells'. A Review. *Journal of Bioinference Research in Applied Chemistry*, 11 (2). 9420-9431.
- Kjeang, E., Djilali, N. and Sinton, D. (2009). 'Microfluidic Fuel Cells: A review'. *Journal of Power Sources*, 186, 353-369.
- Maitreyi, N., Praveen, S. and Rajeev, K.S. (2018). 'Treatment of Sewage (Domestic wastewater or municipal wastewater) and Electricity Production by Integrating Constructed Wetland with Microbial Fuel Cell'. *Intechopen*. DOI 10, 5772-75658.
- Mathuriya, A.S. and Sharma, V.N. (2009). 'Bioelectricity Production from Paper Industry Waste using a Microbial Fuel Cell by *Clostridium species*'. *Journal of Biochemical Technology*, 1 (2): 49-52.
- Mohan, S.V., Raghuvulu, S.V., Mohanakrishna, G. and Sarma, P.N. (2008). Bioelectricity production from wastewater treatment in dual chambered microbial fuel cell (MFC) using selectively enriched mixed microflora: effect of catholyte, *Bioresource Technology*, 99, 596-603
- Najiaowa, Y., Defeng, X., Wei, Yang, Y., Zhen, Yiran and Nanqi R. (2016). Electricity and Methane Production from Soybean Edible Oil Refinery Wastewater using Microbial Electrochemical Systems. *International Journal of Hydrogen Energy*, 42; 96-102
- Onuabuchi, A., Opara, C.C., Oji, A. (2014). Generation of Bio-electricity from Ammonia Fertilizer Plant Liquid Effluent. *Journal of Biochemistry and Biochemistry and Biotechnology*, 1 (1): 001-017
- Salam, RA., Amber, K. P., Ratyal, N.I, Alam, M., Akram, N., Munoz, C. Q.G. and Marquez, F. P.G. (2020). 'An Overview on Energy and Development of Energy and Development of Energy Integration in Major South Asian Countries: The Building Sector'. *Journal of Energies*, 13:21. <https://doi.org/10.3390/en13215776>.
- Sima, M. and Seyed, A. M. (2021). A review of the Operating Parameters on the Microbial Fuel Cell for Wastewater Treatment and Electricity Generation'. *Journal of water science and Technology*, 84 (6) 1309 <https://doi.org/10216./wst.2021.333>
- Somdipta, B. and Manswini, B. (2020). 'Pharmaceutical Wastewater Treatment in Microbial Fuel Cells'. DOI. 10.1016/B978-0-12-817493.00006.
- Surti, H.S. (2016). 'Physico- Chemical and Microbial Analysis of Wastewater from different Industries and COD Reduction Treatment of Industrial Wastewater by using Selective Microorganism'. *International Journal of Current Microbiology and Applied Science*, 5 (6) :707-717.



## An Approach to Scale Up of Neem Seed Oil Solvent Extraction Pilot Plant

John G. USMAN<sup>1\*</sup>, Paul C. OKONKWO<sup>2</sup>, Bello MUKHTAR<sup>3</sup>, Abdul BABA<sup>4</sup>

<sup>1</sup>Department of Chemical Engineering, Kaduna Polytechnic, Nigeria.

<sup>2,3,4</sup>Department of Chemical Engineering, Ahmadu Bello University, Zaria, Nigeria.

<sup>1\*</sup>[johngoji@yahoo.com](mailto:johngoji@yahoo.com), <sup>2</sup>[chemstprom@yahoo.com](mailto:chemstprom@yahoo.com), <sup>3</sup>[beloonline@yahoo.com](mailto:beloonline@yahoo.com), <sup>4</sup>[4olubababdul@gmail.com](mailto:4olubababdul@gmail.com)

\*Corresponding author

---

### ABSTRACT

The current mechanical expression of oil from neem seed cannot satisfy the ever-increasing demand of the neem oil. The futuristic solution to the shortage of neem oil is the successful scale up of the solvent extraction pilot plant to larger commercial plant to boost the production capacity. The scale up approach is based on the pilot plant study and the use of existing model equations. The similarities values for the scale up are 21.69 W/m<sup>2</sup>, 0.125, 0.029, 0.21 and  $7.5831 \times 10^{11}$  as power per volume, shape factor, Froude number, impeller speed and Reyleigh number respectively. Scaling up the agitation pilot plant, using ethanol at an extraction temperature of 50 °C and separation of the miscella at 50 °C under reduced pressure of 207.02 mmHg will reduce the recovery time and retain the oil quality. ASPEN PLUS V10 is recommended for simulation and the fractional compositions of neem seed kernel are 0.45% neem oil and 0.55% neem seed cake, while for ethanol are 96% pure ethanol and 4% water. The concept of overall heat transfer coefficient will be used for design and sizing of the condenser heat exchanger.

**Keywords:** *Neem tree, Solvent extraction, Scale up, Power per volume number and Reyleigh number.*

### 1. INTRODUCTION

The neem tree belongs to the mahogany family and its botanical name is '*Azadirac dita Indica*'. It is highly medicinal and extensively found in India and Indonesia (Oluwole *et al.*, 2015). The neem tree is found as plantation in Kano, Katsina and Jigawa states of Nigeria in West African subcontinent to check desertification and it provide materials base for industrial development (Nde & Foncha, 2020; Orsar *et al.*, 2016). The quality of neem oil is expressed in terms of iodine, acid and saponification values; and these values are affected by extraction temperature (Baboo, 2016; Workneh, 2011).

Agitation and mixing increase the mass and heat transfer (Usman *et al.*, 2013) and two processes are considered similar if they possess geometric, kinematic and dynamic similarities (Belwal *et al.*, 2016). Simulation process is used to predict the performance of the scaled-up equipment before construction (Maria, 1997) and ASPEN PLUS V10 is suitable for the simulation. Despite the abundant availability of neem seed in Nigeria, the major problem and challenges of neem oil extraction is the lack of processing equipment (Oluwole *et al.*, 2015). The current extraction process (mechanical press) cannot meet the increasing demand due to low yield extraction rate (Nkouam *et al.*, 2017). The demand on neem oil is ever increasing (Orsar *et al.*, 2016) and scale up to large scale production will meet the ever-increasing demand for the neem oil (Nde & Foncha, 2020; Oluwole *et al.*, 2015). Scale up of the solvent neem seed oil extraction pilot plant to large scale will boost the production capacity to meet the increasing demand of neem seed oil.

The scaling up procedure will largely depends on the pilot scale plant study. Prospectively, a futuristic recommendation on how to scale up the process to large extraction plant in order to meet the ever – increasing demand and preserve the quality of the extracted oil is presented. The most conventional method of extracting neem seed oil is the mechanical expression which leaves 6% to 14% of oil in the cake (Workneh, 2011) and needs additional solvent extraction method to maximize yield (Tsfaye & Tefera, 2017). The solvent extraction method leaves 0.5% of oil in the cake (Workneh, 2011) and the Soxhlet apparatus is the most popular equipment use for continuous solid – liquid extraction of oil from seed (Subramanian *et al.*, 2017). It gives higher yield and less turbid product when compared to mechanical method (Tsfaye & Tefera, 2017).

The neem kernel is dried in an oven at a temperature of 40 – 55 °C (Subramanian *et al.*, 2017; Tsfaye & Tefera, 2017; Jessinta *et al.*, 2014; Workneh, 2011). N-hexane and ethanol are the most commonly used solvent for extraction of neem seed oil. Subramanian *et al.* (2017) used n- hexane and ethanol in a Soxhlet apparatus at 70 °C and obtained

percentage yield of 45, 46, 47.5 and 49%; 40, 42, 45 and 46% at extraction time of 120, 180, 240 and 300 minutes respectively. Tesfaye and Tefera, (2017) used ethanol at 70, 78 and 86 °C and obtained percentage yield of 41.08, 41.89 and 42.41% respectively. Workneh, (2011) extracted neem seed oil in an agitated laboratory vessel at an extraction temperature of 30, 40 and 50 °C using ethanol and n-hexane. The percentage yield obtained were 26.9, 31.1 and 33.2%; 39.2, 44.8 and 47.3% respectively. At same temperature and solvents the iodine values were 66.58, 65.79 and 61.32 I<sub>2</sub>/g; 72.62, 68.41 and 62.83 I<sub>2</sub>/g respectively. The acid values were 32.8, 36 and 40; 96.4, 102 and 122 mg KOH/g respectively. The saponification values were 175.71, 194.3 and 205.84 mgKOH/g; 184.03, 209.30 and 221.93 mgKOH/g respectively.

Table 1 shows the work done by Usman *et al.* (2013) and Workneh, 2011 to extract oil from neem seed in an agitated media. Usman *et al.* (2013) used an agitated ethanol pilot plant with capacity of 9.65 kg/day of neem seed kernel to extract oil at a rate of 174.33 g/h within 40 minutes at 50°C with a maximum yield of 36.86% using flat blade turbine impeller at 84 rpm; while Workneh, (2011) reported an extraction rate of 6.63 g/h when agitated laboratory beaker was used at 50°C, with a yield of 33.19 and 47.32% for using ethanol and n – hexane respectively as seen from Table 1. The extraction rate of 174.33 g/h of neem oil reported by Usman *et al.* (2013) is greater than 6.63 g/hr of neem oil reported by Workneh, (2011). The major components of the pilot plant are mixer (extractor), evaporator, double – pipe condenser and a chiller. A flat blade turbine impeller was shown to be better than the Rhuston blade turbine impeller at 84 rpm due to the absent of a disc on the flat blade turbine impeller. It took 4 hr 25 minutes to separate the oil from the miscella (Usman *et al.*, 2013; Usman and Okonkwo, 2013).

Table 1: Effect of impeller speed and impeller type on the yield of oil from neem seed

Author	Solvent used	Impeller type	Impeller speed (RPM)	Extraction time	Yield	Extraction rate (g/hr)
Usman <i>et al.</i> , 2013a; Usman and Okonkwo, 2013b.	Ethanol	Flat blade turbine impeller	37	20	24.28	174.3
			84	40	28.64	
		Rhuston turbine impeller	20	20	29.32	
			40	40	36.86	
			37	20	20.95	
			84	40	23.95	
Workneh, 2011.	Ethanol	Stirrer	84	20	25	6.633
			40	40	31.25	
			40	180	33.19	
			180	180	47.32	

ASPEN PLUS is simulation software that is used base on mass balance and application of property method. The property method is easily applied because it depends on process parameters such as temperature, flow rate and fractional composition of the materials (Hachhach *et al.*, 2019).

Based on the published work by Usman *et al.* (2013), the following recommendations are made for scale up of the pilot plant.

### 1.1 Scale – up of solid – liquid mixer (Extractor).

**a. Geometric similarity:** Geometric similarity is attained by keeping the ratios of different dimensions such as impeller diameter to vessel diameter constant upon scale – up (Yavuz and Sandeep, 2019). The scale – up ratio in term of volume is expressed as:

$$R = \left(\frac{V_2}{V_1}\right)^{1/3} \quad (1)$$

In Equation (1), R = scale – up ratio,  $V_1$  = volume of pilot plant and  $V_2$  = volume of larger plant (Yavuz and Sandeep, 2019). Geometric similarity is obtainable when the impeller speed is greater than just suspended speed (critical speed), the power per volume and shape factor of the pilot and large plants are equaled (Megawati *et al.*, 2018; McCabe, 1993).

The impeller power number,  $N_p$ , is the flow of momentum associated with the bulk motion of the fluid. It is used to predict the power of the mixer, P directly.

$$N_p = \frac{P}{\rho N^3 D^5} \quad (2)$$

In Equation (2),  $N_p$  = Power number, P = Power of mixer (Watt), D = Diameter of impeller (m), N = Revolution per second and  $\rho$  = Density of the liquid, Kg m<sup>-3</sup> (McCabe, 1993).

The power number at a given Reynolds number, number of baffles in the extractor, number of blade and shape factor is obtained using Figure 1.

**b. Kinematic similarity: Velocity ratios at corresponding points are same.**

$$\text{The impeller tip speed is expressed as: } \pi D_1 N_1 = D_2 N_2 \quad (3)$$



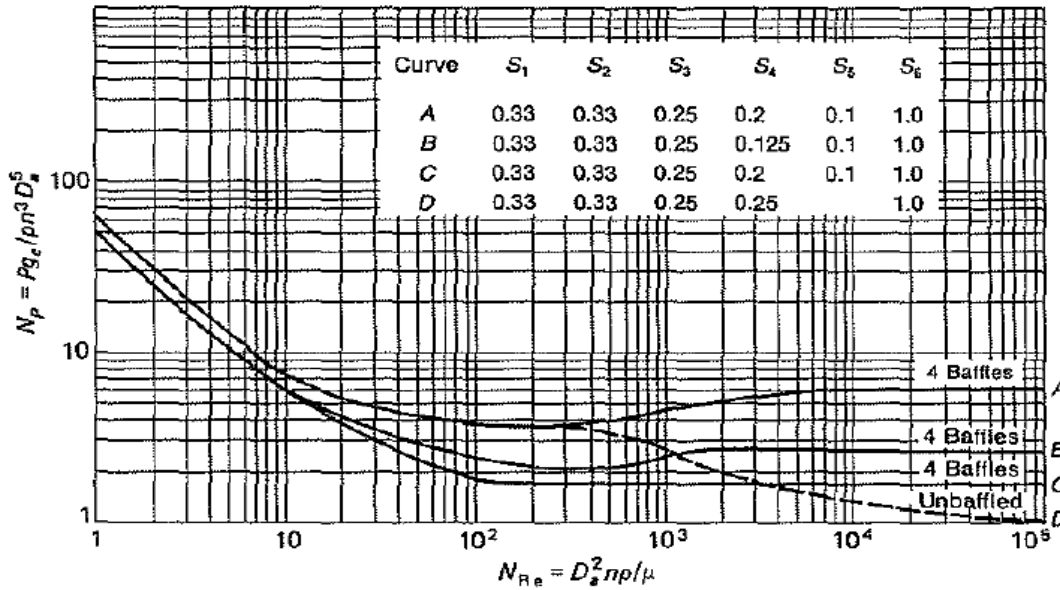
In Equation (3),  $N_1$  = impeller speed of pilot plant,  $N_2$  = impeller speed of large scale and  $D_1$  = impeller diameter of pilot plant and  $D_2$  = impeller diameter of large plant.

$$\text{Impeller Speed Scale up: } N_2 = N_1 \left(\frac{1}{R}\right)^n \quad (4)$$

In Equation (4),  $n = \frac{2}{3}$ , for systems having equal rates of mass transfer (equal power per unit volume) (Scaleup of Mixing system (n.d))

c. **Dynamic similarity:** Similarities in internal collision energy or same ratio of forces between corresponding sites in two systems. The Froude number is use to evaluate the dynamic similarity (Jang *et al.*, 2020).

$$\text{Froude number, (Fr)} = \frac{\text{Inertia force}}{\text{Gravitational force}} = \left(\frac{N^2 \times D}{g}\right)_{\text{pilot plant}} = \left(\frac{N^2 \times D}{g}\right)_{\text{large plant}} \quad (5)$$



Source: (McCabe, 1993)

Figure 1: Chart for Power number,  $N_p$  versus Reynold number,  $N_{Re}$  for six-blade turbines.

### 1.2 Scale up of evaporator.

The mode of heat transfer during separation of solvent from the extracted neem oil is natural convection (Usman *et al.*, 2013). Fluid motion and heat transfer phenomena are related in the evaporator and governed by the dimensionless quantities such as Grashof and Prandtl numbers. The Grashof (Gr) and Prandtl (Pr) number are connected by the Rayleigh number (Ra) as shown in Equation (6) to (8).

$$\text{Gr} = \frac{g\beta(T_w - T_a)Dt^3}{\nu^2} \quad (6)$$

$$\text{Pr} = \frac{\nu}{\alpha} \quad (7)$$

$$\text{Ra} = \text{Gr} \times \text{Pr} = \frac{g\beta(T_w - T_a)Dt^3}{(\nu \times \alpha)} \quad (8)$$

In Equations (6) to (8),  $\beta$  = coefficient of thermal expansion =  $1/T_a$  ( $^{\circ}\text{C}^{-1}$ ),  $T_a$  = ambient temperature ( $^{\circ}\text{C}$ ),  $T_w$  = wall temperature ( $^{\circ}\text{C}$ ),  $Dt$  = extractor diameter (m),  $k$  = thermal conductivity of air at average temperature ( $\text{W}/\text{m}^{\circ}\text{C}$ ),  $\nu$  = kinematic viscosity ( $\text{m}^2/\text{s}$ ) and  $\alpha$  = thermal diffusivity ( $\text{m}^2/\text{s}$ ) (Janna, 1986).

The evaporator for separating the extracted oil required low heating temperature and short residence time of the miscella. This is achieved by minimizing the volume of the miscella and operating the evaporator at a reduced pressure (Glover, 2004). The vapour pressure of ethanol at  $50^{\circ}\text{C}$  is 276 mbar (207.02 mmHg) (Rütti and Heierli, 2012).

### 1.3 Design of 1-2 shell-and-tube heat exchanger.

The pilot plant used by Usman *et al.* (2013) employs the usage of a double – pipe condenser. For scale up of the pilot plant to large plant, there is need for design of a condenser in the form of 1-2 shell-and-tube heat exchanger to reduce the condenser length and to enhance heat transfer for faster condensation. The 1 – 2 exchanger means one shell – side and two tube – side passes (Backhurst and Harker, 1983). The concept of overall heat transfer coefficient can be adopted for calculating the heat transfer area of the 1 – 2 shell-and-tube heat exchanger and its sizing. The basic equation for calculating heat transfer in a heat exchanger is

$$Q = UA\Delta T_m \quad (9)$$

In Equation (9), Q = Quantity of heat transferred (W), U = Design value of overall heat transferred coefficient (W/m<sup>2</sup>°C), A = Area for heat transfer (m<sup>2</sup>) and ΔT<sub>m</sub> = Logarithmic mean temperature difference (°C)

The approximate or assumed overall heat transfer coefficient is given by

$$U_a = \frac{0.7 \times h_i \times h_o}{h_i + h_o} \quad (10)$$

The overall design heat transfer coefficient is obtained from the individual film heat transfer coefficients. Neglecting pipe wall resistance and scale resistance, the equation is given as

$$\frac{1}{U_D} = \frac{1}{h_{io}} + \frac{1}{h_o} \quad (11)$$

In Equations (10) to (11),  $h_i$  = inside film coefficient (W/m<sup>2</sup> °C) and  $h_o$  = outside film coefficient (W/m<sup>2</sup> °C),  $h_{io}$  = inside film coefficient based on the outside diameter (W/m<sup>2</sup>°C) (Backhurst and Harker, 1983).

Data from the pilot plant used by Usman *et al.*, (2013) for the purpose of scale up include the following:

#### **Extractor**

- i. Number of blades on the flat blade turbine impeller = 6
- ii. Extractor diameter = 0.300 m
- iii. Impeller diameter = 0.150 m
- iv. Height of mixture = 0.306 m
- v. Height of extractor = 0.390 m
- vi. Extractor volume = 0.02121 m<sup>3</sup>
- vii. Width of impeller = 0.0188 m
- viii. Width of baffle = 0.025 m
- ix. Number of baffles in the extractor = 4
- x. Impeller speed = 84 rpm (1.40 rps)
- xi. Density of ethanol at 35°C ( $\frac{20+50}{2}$ ) = 788.38 kg/m<sup>3</sup>
- xii. Viscosity of ethanol at 35°C = 0.000882 kg/ms
- xiii. Reynolds number = 28,155.71
- xiv. Extraction temperature = 50°C

#### **Evaporator**

- i. Miscella temperature,  $T_w = 78^\circ\text{C}$
- ii. Ambient temperature,  $T_a = 20^\circ\text{C}$
- iii. Diameter of cylindrical evaporator,  $D_t = 0.2346$  m
- iv. Height of evaporator,  $H = 0.6744$  m
- v. Acceleration due to gravity,  $g = 9.81$  m/s<sup>2</sup>
- vi. Coefficient of thermal expansion,  $\beta = 1/T_a = 1/20 = 0.05$  °C<sup>-1</sup>
- vii. Kinematic viscosity of ethanol at 49°C,  $\nu = 0.9198 \times 10^{-6}$  m<sup>2</sup>/s
- viii. Thermal conductivity of ethanol at 49°C,  $k = 1.0210$  W/m°C
- ix. Density of ethanol at 49°C,  $\rho = 679.98$  kg/m<sup>3</sup>
- x. Specific heat capacity of ethanol at 49°C,  $C_p = 2850.5$  J/kg°C
- xi. Thermal diffusivity,  $\alpha = 5.2675 \times 10^{-7}$  (m<sup>2</sup>/s)

## **2. METHODOLOGY**

Based on the data obtained from the pilot plant used by Usman *et al.* (2013); the shape factor is evaluated based on the width and diameter of the impeller, the power number  $N_p$  is obtained from Figure 1 using curve B and shape factor of 0.125 at a Reynolds number of 28,155.71. The required power is evaluated using equation 2. The geometric similarity based on powers per volume of 21.69 W/m<sup>2</sup> and shape factor of 0.125 were obtained for the pilot plant for comparison with the future scaled up plant. Similarly, the Froude Number, 0.029 (Dynamic similarity) and the impeller tip speed of 0.21 (Kinematic similarity) were calculated for comparing the dynamic and kinematic similarities of the scaled-up plant respectively. The scale up ratio is obtainable using equation 1 and is based on the known volume of solvent used in the pilot plant and the volume of solvent for the scaled-up plant. The evaporator Reyleigh number of  $7.5831 \times 10^{11}$  is evaluated for comparison with the scale up evaporator to ensure scale up similarity. The condenser can be designed using the concept of overall heat transfer coefficient to calculate the area and size the 1-2 shell-and-tube heat exchanger (condenser) while the chiller is replaceable with an independent cooling water supply.

The ASPEN – PLUS V10 is recommended for correlating the existing models used is scaled up calculations. The ASPEN – PLUS V10 will be used for simulation of the scaled up plant before construction based on the flow rate of neem seed kernel and ethanol solvent (flow rate values depend on the scaled up capacity of the future commercial plant), fractional composition of neem seed kernel (neem seed oil = 0.45% and neem seed cake = 0.55%) and fractional composition of ethanol solvent (96% pure ethanol and 4% water), operating temperature (50°C) and operating pressures (760 mmHg for extraction in the extractor and 207.02 mmHg for separation in the evaporator) as requirement for running the ASPEN PLUS V10.

The 4hr 25 minutes used by Usman *et al.* (2013) for separating the miscella at 760 mmHg will be reduced in the scale up plant by incorporating a vacuum pump. Separation will take place at lower temperature of 50 °C under reduced pressure of 207.02 mmHg to reduce the recovery time and preserve the quality of the neem oil.

### 3. RESULTS AND DISCUSSION

The Geometric (Power per volume and shape factor), Dynamic (Froude number), Kinematic (Impeller tip speed) similarities and the Rayleigh number of the pilot plant are shown in Table 2.

Table 2: Calculated similarities values and Rayleigh numbers for future scale up

Plant	Power per Volume (W/m <sup>3</sup> )	Shape factor	Froude number	Impeller Speed	Tip Rayleigh Number
Pilot Plant	21.69	0.125	0.029	0.21	7.5831× 10 <sup>11</sup>

The oven drying at 50 °C is commonly used for drying the neem seed kernel because it preserves the quality of the neem seed (Azwanida, 2015) and the most commonly used solvents are ethanol and n – hexane with an extraction yield range of 26.9 - 46% and 39.2 – 49% respectively within the extraction temperature range of 30 – 86 °C. The quality of neem oil is affected by extraction temperature as seen from the work of Workneh, (2011). The iodine, acid and saponification values changes from 66.58 to 61.32 gI<sub>2</sub>/g, 32.8 to 40 mg KOH/g and 175.71 to 205.84 mg KOH/g as extraction temperature increases from 30 to 50 °C respectively using ethanol as the extraction solvent. The increase in temperature brings about decrease of iodine value due to formation of more saturate compounds, and this will make the oil less reactive. Extraction yield of neem oil in an agitation vessel is affected by the level of agitation. This is clearly seen from the work of Usman *et al.* (2013) in Table 1; at 84 rpm for 40 minutes extraction time, a yield of 36.86% was achieved as compared to 28.64% yield at 37 rpm for 40 minutes extraction time.

The successful operation and calculation of geometric, dynamic, kinematic and Reyleigh values of the pilot plant for similarities comparison potent the success toward the scale up of the pilot plant to commercial scale.

### 4. CONCLUSION

The scale up of the pilot plant used by Usman *et al.* (2013) to commercial scale is possible due to successful calculated values for similarity comparison. Such values include: 21.69 W/m<sup>2</sup> (Power per volume) and 0.125 (Shape factor) for geometric similarity; 0.029 (Froude number) for Dynamic similarity; 0.21 (Impeller tip speed) for kinematic similarity and 7.5831× 10<sup>11</sup> as Reyleigh number for the evaporator scaled up. The 1-2 shell – and – tube heat exchanger (condenser) can be designed and sized using the overall heat transfer coefficient technique. For future extraction of large quantity of good neem seed oil; the geometric, dynamic and kinematic similarities should be implored for the scale up of the pilot plant to commercial plant.

### REFERENCES

- Azwanida, N. N. (2015). A Review on The Extraction Methods Use in Medicinal Plants, Principle, Strength and Limitation. *Journal of Medicinal and Aromatic Plants*, 4(3). DOI:10.4172/2167-0412.1000196
- Baboo, P. (2016). Advancement In Neem Oil Extraction Process. Downloaded From [https://www.researchgate.net/publication/292392229\\_Advancement\\_In\\_Neem\\_Oil\\_Extraction\\_Process/Link/56ae169f08ae19a38515f831/Download\\_on\\_17/7/2020](https://www.researchgate.net/publication/292392229_Advancement_In_Neem_Oil_Extraction_Process/Link/56ae169f08ae19a38515f831/Download_on_17/7/2020) By 10:08am.
- Backhurst, J.R. and Harker, J.H. (1983). *Process Plant Design*. Heinemann Chemical Engineering Series, London, Pp. 64 - 71.
- Belwal, S., Revanth, V., Dinesh, K.S.V.V., Reddy, B.V. And Bhagvanth, M. R. (2016). Development And Scale Up of A Chemical Process In Pharmaceutical Industry: A Case Study. *International Journal of Engineering Research And Application*, 6(7), Pp. 81-88.
- Hachhach, M., Akram, H., Hanafi, M., Achak, Q And Chafik, T. (2019). Simulation And Sensitivity Analysis of Molybdenum Disulfide Nanoparticle Production Using Aspen Plus. *International Journal of Chemical Engineering*. Volume 2019, Article Id 3953862, 8 Pages. <https://doi.org/10.1155/2019/3953862>.
- Jang, E.H, Park, Y.S, Kim, M And Choi, D.Y. (2020). Model-Based Scale-Up Methodologies For Pharmaceutical Granulation. *Journal of Pharmaceutics*. 12, 453; Doi:10.3390/Pharmaceutics12050453.
- Janna, W.S. (1986). *Engineering Heat Transfer*. Pws Publishers, United States of America. Pages 453 - 454.
- Jessinta, S., Azhari, H.N., Saiful, N.T. And Abdurahman, H. N. (2014). Impact of Geographic Variation on Physicochemical Properties of Neem (*Azadirachta Indica*) Seed Oil. *International Journal of Pharmaceutical Sciences And Research*, 5(10), Pp. 4406-4413.
- Maria, A. (1997). Introduction To Modeling and Simulation. Proceedings of the 1997 Winter Simulation Conference. State University of New York At Binghamton. Department of Systems Science and Industrial Engineering, Binghamton, Ny 13902-6000, U.S.A. Pages 7 – 13. Available on [www.acqnotes.com](http://www.acqnotes.com).
- Mccabe, W.L., Smith, J.C., and Harriott, P. (1993). *Unit Operation of Chemical Engineering*. 5th Edition, Mcgraw-Hill Book Company, Singapore. Pages 248 – 250, 429 – 440.

- Nde, D.B. and Foncha, A.C. (2020). Optimization Methods For The Extraction of Vegetable Oils: A Review. *Journal of Processes*. 8(209), Doi:10.3390/Pr8020209 [www.mdpi.Com/Journal/Processes](http://www.mdpi.Com/Journal/Processes).
- Nkouam, G.B., Musongo, B., Boubou, A. A., Tchatchueng, J. B., Kapseu, C. and Barth, D. (2017). Traditional Techniques of Oil Extraction from Kapok (*Ceiba Pentandra Gaertn*), Mahogany (*Khaya Senegalensis*) and Neem (*Azadirach Indica A. Jus.*) Seeds From The Far-North Region of Cameroon. *International Journal of Environment, Agriculture and Biotechnology*, 2(4), Pp. 2207 – 2213.
- Oluwole, F.A; Oumarou, M.B. and Abdulrahim, A.T. (2015). Traditional Method of Neem Seed Oil Extraction In Northeastern Nigeria: Challenges and Prospect. *Continental Journal of Engineering Sciences*, 10(1), Pp. 1 – 8.
- Orsar, T. J., Tyowua, B. T. and Asemave, J.T. (2016). Neem (*Azadirachta Indica A. Juss*) Fruit Yield Determination in Makurdi, Benue State, Nigeria. *Journal of Research In Forestry, Wildlife & Environment*, 8(2), Pp. 145 – 156.
- Rütti, D. and Heierli, M. (2012). Multivapor Application Guide. Buchi Labortechnik Ag, Switzerland, Pp. 6 & 39. Retrieved From [https://static1.buchi.com/sites/default/files/application\\_guide\\_multivapor\\_1205...](https://static1.buchi.com/sites/default/files/application_guide_multivapor_1205...) on 25/04/2020 By 3.53 P.M.
- Subramanian, S., Salleh, A. S., Bachmann, R. T., Idrus, N. M. and Hossain, M. S. (2017). Optimising *Azadirachtin* Yield from Neem Tree Seeds and Leaves using a Binary Solvent System for Potential Pest Control Application. *International Conference on Environmental Research and Technology*. Universiti Kuala Lumpur, Malaysian Institute of Chemical and Bioengineering Technology, Gajah, Malaysia, Pp. 481 – 486.
- Tesfaye, B. and Tefera, T. (2017). Extraction of Essential Oil from Neem Seed By Using Soxhlet Extraction Methods. *International Journal of Advanced Engineering, Management and Science*, 3(6), Pp. 646 – 649.
- Usman, J.G., Okonkwo, P.C. and Mukhtar, B. (2013a). Design and Construction of Pilot Scale Process Solvent Extraction Plant For Neem Seed Oil. *Nigerian Journal of Technology (Nijotech)*, 32(3), Pp. 528 – 537.
- Usman J.G. and Okonkwo P.C. (2013b). Pilot Scale Extraction of Neem Oil Using Ethanol As Solvent. *International Journal of Engineering Research & Technology*, 2(9), Pp. 1716 – 1733.
- Workneh, W. (2011). Extraction and Characterization of Essential Oil From Morgosa Seed. Addis Ababa University, School of Graduate Studies, Addis Ababa Institute of Technology, Department of Chemical Engineering, Ethiopia, Retrieved From [www.libsearch.com/search/soxhlet%25](http://www.libsearch.com/search/soxhlet%25).
- Yavuz, N. and Sandeep, K.P. (2019). Scale-Up of Shear Thinning Fluid Mixing In An Unbaffled Stirred Vessel With Eccentrically Located and Modified Impellers. *International Journal of Chemical Reactor Engineering*. Doi: 10.1515/Ijcre-2018-0205
- Scaleup of Mixing System (N.D). From [http://www.uobabylon.edu.iq/uobcoleges/ad\\_downloads/5\\_4801\\_857.pdf](http://www.uobabylon.edu.iq/uobcoleges/ad_downloads/5_4801_857.pdf). Downloaded on 5/5/2020 By 9.05p.m.



## Flow and Compaction Properties of Excipients Developed from Biopolymer Waste Snail Shell and Influencing Factors

Babatunde K. ADEOYE<sup>1\*</sup>, Elizabeth F. ARANSIOLA<sup>2</sup>, Gbenga ALEBIOWU<sup>3</sup>, Micheal O. OSUNGUNNA<sup>3</sup>

<sup>1</sup>Department of Food Science and Technology, Federal University of Technology, Akure, Nigeria.

<sup>2</sup>Department of Chemical Engineering, Obafemi Awolowo University, Ile-Ife, Nigeria

<sup>3</sup>Department of Pharmaceutics, Faculty of Pharmacy, Obafemi Awolowo University, Ile-Ife, Nigeria

<sup>1\*</sup>[bkadeoye@futa.edu.ng](mailto:bkadeoye@futa.edu.ng), <sup>2</sup>[aransiolaef@gmail.com](mailto:aransiolaef@gmail.com), <sup>3</sup>[galebiowu@gmail.com](mailto:galebiowu@gmail.com), <sup>3</sup>[mowole@oauife.edu.ng](mailto:mowole@oauife.edu.ng)

\*Corresponding author

---

### ABSTRACT

This study developed functional excipients from biopolymer materials and evaluated their flow and compaction properties for preparation of tablet. Chitosan, a based excipient was extracted from snail shell and a compositional experimental design under the pharmaceutical dosage framework with corn-starch and lactose was used to study the singular and interaction effects of influencing parameters (Density; Hausner ratio; Carr's index; angle of repose; angle of internal friction; The Kawakita model; Consolidation index and Rate of consolidation) on the co-processed excipients, as well as, individual excipients. X-ray diffraction profiles showed that the chitosan produced was rich in or mostly made up of calcium silicate ( $\text{CaSiO}_3$ ). The novel functional excipients developed had substantially better flow with Hausner's ratio ranging from 1.254 to 1.327, Carr's index from 20.272 to 24.627, angle of repose from 26.06 to 36.32° and angle of internal friction from 38.84 to 44.82°. The novel excipients also had improved compaction properties with compressibility values ranging from 0.390 to 0.537, consolidation rate from 0.559 to 0.675 and consolidation index from -1.466 to -1.268, which were advantageous in tableting. The role of pressure as the most significant parameters influencing the compaction and consolidation rate was also established. The results suggest that the better rate of flow and compaction properties of co-process excipients can be achieved with high volume of chitosan at moderate mixing ratio.

**Keywords:** Excipients, biopolymer, flow, compaction, chitosan, consolidation.

### 1. INTRODUCTION

Recently, there has been a surge in clinical evidence regarding local material selection for the development of suitable excipients for probiotics encapsulation in dosage form. Excipients are components other than the active substances intentionally added to formulation of a dosage form (Goh *et al.*, 2018). However, compacting composite excipients into tablets, on the other hand, is difficult because powder flow involves frictional contact of individual particles, which often lead to structural changes and densification during compression.

A wide range of studies have been conducted to investigate the complex interaction of crystal structure, particle shape, particle size distribution, and single and multi-forces within the particles of single and composite excipients. Most of them were conducted in developed countries while a limited number of studies have been conducted in Africa (Builders and Arhewoh, 2016). Development of excipients from biopolymer materials available in Africa may generate many arguments than the western production. This is due to characteristics of powders (largely unrefined), different production techniques and weak regulation on the qualities of other binder, diluents and lubricant combinations imported into the continent. Also, the method of production is mostly uncontrolled as most people still use uncleaned production apparatus (i.e. mortar, pestle, firewood for cooking), mostly in poor ventilated space, which in turns give structural damage and contamination to the produced excipients. The extent to which these features alter powder flowability is still a difficult task.

This study aimed at investigating the combined effect of different proportion naturally extracted chitosan, industrial grade corn-starch and lactose for probiotics excipient development. Also, the singular and interaction effects of influencing parameters (Density; Hausner's ratio; Carr's index; angle of repose; angle of internal friction; The Kawakita model; Consolidation index and Rate of consolidation) on the flow and compaction properties of excipients' formulations were investigated. The result of this study could serve as eye-opener to the relevant stakeholders and enhance further research on untapped natural biopolymer materials available for excipients development.

## 2. MATERIALS AND METHODS

### 2.1 Source of Materials

The snail shells used were obtained from Oja Tuntun, Ile-Ife, Osun State, Nigeria. Lyophilized *Lactobacillus delbruiikii* ( $10^8$  -  $10^{10}$  CFU/g) isolated from fermented Bambara groundnut (*Vigna subterranea* (L.) Verdc.) was used as the model bacterial in this experiment. All other chemicals utilized were of analytical grade.

### 2.2 Methods

#### 2.2.1. Extraction and characterization of chitosan

Chitosan was extracted from snail shell. The basic processes involved were pulverization using a Rocklabs mill, deproteinization using 0.1 M sodium hydroxide, decolourization in pure acetone, demineralization using 0.5 M hydrochloric acid and deacetylation by boiling in 0.2 M sodium hydroxide. Characterization of the extracted chitosan was carried out using Fourier Transform Infrared Spectroscopy (FTIR).

#### 2.2.2. Determination of density attributes

The particle density was measured using a solvent pycnometry technique as described by Adeoye and Alebiowu, 2013. The average of three determinations was used to arrive at the final outcome.

#### 2.2.3. Determination of flow characteristics

The angle of repose, Hausner's ratio (HR), and compressibility index were used to evaluate the excipients' flow properties. Equation 1 was used to compute the angle of repose, which is the best angle that can be achieved between the self-supporting cone of the powder heap and the flat plain.

$$\theta = \tan^{-1} \frac{h}{r} \quad (1)$$

where h is the powder pile's or cone's height in cm, r is the radius of the cone's base in cm, and  $\theta$  is the angle of repose. The Hausner's ratio (HR) was calculated from the bulk and tapped densities using Equation 2, whereas the compressibility index was calculated using Equation 3.

$$\text{Hausner's ratio} = \frac{\text{Tapped density}}{\text{Bulk density}} \quad (2)$$

$$\text{Carr's index} = \frac{\text{Tapped density} - \text{Bulk density}}{\text{Tapped density}} \times 100 \quad (3)$$

#### 2.2.4. Evaluation of Compaction Properties

The packing and cohesive qualities of the excipients were measured by Kawakita equation shown in Equation 4.

$$\frac{N}{c} = \frac{N}{a} + \frac{1}{ab} \quad (4)$$

where N is the number of taps, and a and b denote the compressibility and cohesiveness of powders (1/b), respectively. Term C was calculated using equation 5 to describe the volume loss during tapping.

$$C = \frac{V_o - V_N}{V_o} \quad (5)$$

Where  $V_o$  is the powder's loose volume before tapping and  $V_N$  is the powder's volume after set numbers of taps

#### 2.2.5. Estimation of consolidation index and rate

The consolidation behaviour of the co-excipients and their constituent excipients was investigated adopting the approach outlined by Neumann *et al.* (1967) in equation 6, by measuring the proportionate decline in powder volume and density as a response to applied load.

$$\frac{\log(\rho_T - \rho_B)}{\rho_T} = K \log N + C \quad (6)$$

where,  $\rho_T$  and  $\rho_B$  are the tapped and bulk densities, respectively, N is the number of taps, C is the consolidation index, and K is the consolidation rate.

#### 2.2.6. Angle of internal friction measurement (AIF)

By graphing the porosity factor,  $\varepsilon^2 N / 1 - \varepsilon$  in (Equation 7) versus N, The AIF was calculated using the relationship between porosity and the number of taps (N) used to induce powder bed consolidation. The AIF was computed by determining the angle created between the straight path and the abscissa when  $K - K_o$  was re-plotted against N (Adeoye and Alebiowu, 2013)

$$k = \varepsilon^2 N / 1 - \varepsilon \quad (7)$$

N is the number of taps, and  $K_o$  will represent the intercept of the plot of K versus N.

#### 2.2.7. Preparation of probiotics-loaded tablets

This was done according to the method described by Alebiowu and Itiola (2007) with slight modification.

Formulations 1 – 8 (F1-F8) were prepared with the polymers in different ratios and the required active pharmaceutical ingredients (API) dose by mixing thoroughly in a mortar as shown in Table 1.

Table 1: Formulation of 450 mg Probiotic Powder

Excipients	F1	F2	F3	F4	F5	F6	F7	F8
API	4.5	4.5	4.5	4.5	4.5	4.5	4.5	4.5
Chitosan	225	225	225	225	270	270	270	270
Corn-Starch	166.5	121.5	76.5	144	121.5	76.5	54	99
Lactose	45	90	135	67.5	45	90	112.5	67.5
Magnesium stearate	4.5	4.5	4.5	4.5	4.5	4.5	4.5	4.5
Talc	4.5	4.5	4.5	4.5	4.5	4.5	4.5	4.5

F1-F8 are formulations 1-8, API-active pharmaceutical ingredient

### 3. RESULTS AND DISCUSSION

#### 3.1. Physical and morphological characteristics of extracted chitosan

Figures 1 - 3 shows X-ray diffraction spectra, elemental weight composition, scanning electron microscope (SEM) images of extracted chitosan respectively. Figure 4a and 4b shows the FTIR spectra of both extracted and conventional chitosan respectively. The morphological properties of excipients have been reported to be affected by the particle engineering process (Adeoye and Alebiowu, 2013). Figure 2 revealed the elemental composition of the samples. It allowed a quick guess that the sample analysed was rich or essentially made up of calcium silicate ( $\text{CaSiO}_3$ ). Calcium silicate has been demonstrated to have no adverse effects in short-term toxicity study in rats (Liu *et al.*, 2011).

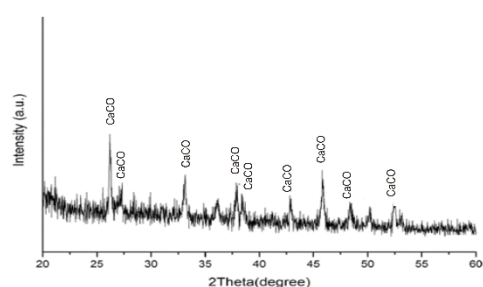


Figure 1: X-ray Diffraction of Chitosan

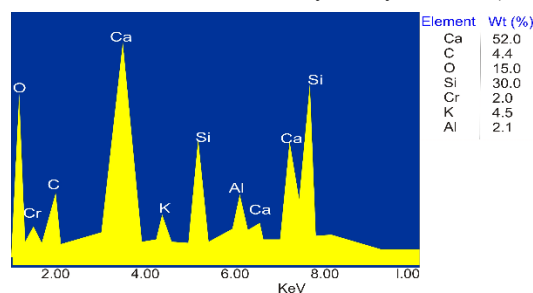


Figure 2: Elemental Weight of Chitosan

It also revealed that the sample analysed is free from heavy metal contamination, having undergone further purification to remove chromium contained in its composition, and is therefore safe for human health. The revealed chitosan particles appeared to be dense, with particles near the surface having distinguishable shapes. Spheres, ovals, and short cylinders are the most visible shapes. As illustrated in Figure 3, all of the shapes have a smooth appearance. The absence of sharp edges indicates a useful property necessary for smooth blood vessel transport as contained in US Pharmacopeia guidelines. In transportation, a smooth surface suggests low wear and friction. This implies that there will be less wear and degradation, which is common with drug-loaded micro-particles when delivering active pharmaceutical ingredient to ailing locations. Another advantage derivable from the smoothness of the micro-particles surface is reduced systemic circulation time to forestall premature drug release, having recognised that micro-particles tend to arrive their tumor-destination with little stress and at a shorter time under active tumor targeting scheme (Liu *et al.*, 2011).

Spectra of the chitosan produced have no much characteristic different from the spectra of the chitosan standard as shown in Figures 4a and 4b respectively. The increase in adsorption effectiveness is due to the bending vibrations of functional groups such as C=O (H bound) and N-H (1 amide). The results are in agreement with the work of Puvvada *et al.*, (2012) and Zvezdova, (2010). In case of conventional, broad bands observed at 3441.01 and 2974.23  $\text{cm}^{-1}$  are due to O-H stretching vibrations whereas a band at 1240  $\text{cm}^{-1}$  is due to O-H bending vibration. The bands in the region 1404.18–1311.59  $\text{cm}^{-1}$  are attributed to C-H stretching vibrations, while the one observed at 2927.94  $\text{cm}^{-1}$  is due to C-H stretching vibrations.

The bands at 1662.64 and 1554.63  $\text{cm}^{-1}$  are due to stretching vibrations of aromatic structure C=C. In case of chitosan produced, a broad band at 3442  $\text{cm}^{-1}$ , with a larger intensity compared to standard, is due to the presence of more crosslinked hydroxyl groups.

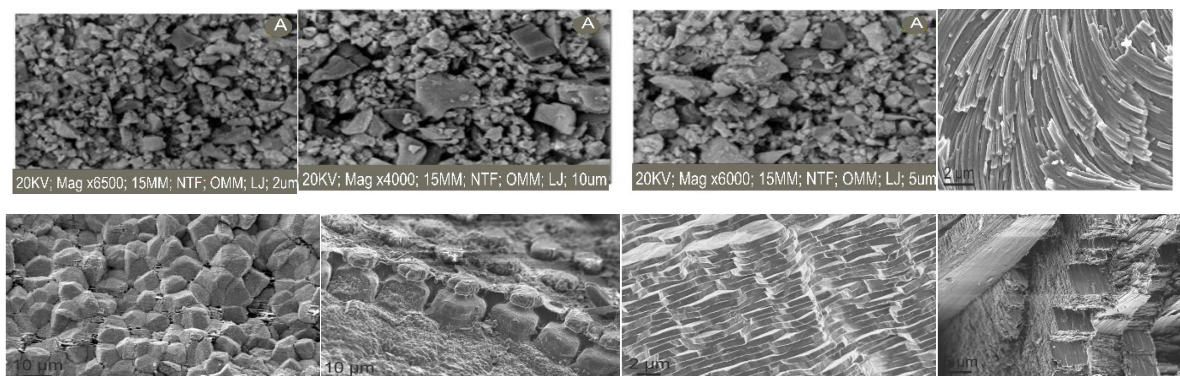


Figure 3: Scanning Electron Microscopy (SEM) Images of Chitosan at Different Magnitude

Intense bands that appeared at  $2926.82$  and  $2517.41\text{ cm}^{-1}$  are due to aliphatic C-H stretching vibrations. The bands at  $1798.72$  and  $1427.63\text{ cm}^{-1}$  are assigned to C-H bending vibrations. The bands appearing at  $872.86\text{ cm}^{-1}$  are due to the presence ring stretching ( $\text{NH}_2$  Amines groups). The new band  $707.82$  denote cis = C-H out-of-plane bending. In all, FT-IR confirms the crosslinking reaction.



Figure 4a: FTIR spectra of extracted chitosan

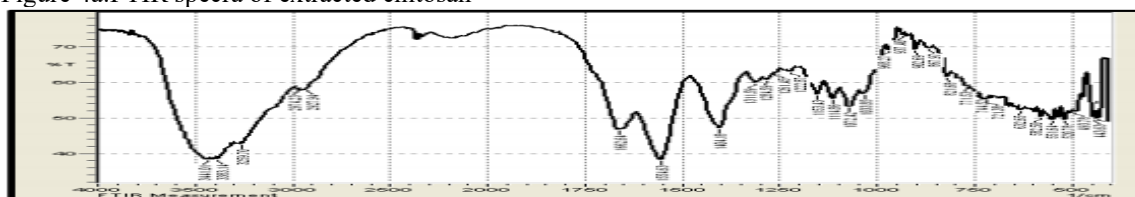


Figure 4b: FTIR spectra of chitosan standard

### 3.2. Fundamental and Derived Properties of The Excipients

#### 1. Densities of the excipients

The density of powders affects their behaviour during use and have been used in the characterization of some derived properties of powder system such as Hausner's ratio, Carr's index, porosity, packing fraction among others. Particle density has an impact on the packing behaviour of materials during tableting, notably during the initial compression phase, which is also known as the elasto-plastic flow phase (Okunola and Odeku, 2009). The results in Table 2 showed that the novel excipients' bulk density and tapped densities in formulation 1 -8 were higher than native excipients. The higher values of bulk and tapped densities of chitosan could have probably have influenced the increase in values found in novel excipient. More increase in values were noticed when the concentration of chitosan in the excipients' formulation was increased. This is advantageous in engineering design aspect of tablet manufacturing because the fill volume of the die is reduced at higher bulk density value (Okunola and Odeku, 2009). Improved consolidated bulk density is advantageous in tableting because it minimizes die load volume and enhances flow rates, all of which contribute to improved tablet homogeneity (Ogunjimi and Alebiowu, 2013; Okunola and Odeku, 2009). When compared to native excipients, this means that the novel excipients developed would form tablets at a higher compression force of  $1.8\text{N}$

#### 2. Derived flow properties

The excipients' flow attributes were assessed employing these important flow features i.e. Hausner's ratio (HR), Carr's index (CI), bulkiness, packing percentage, angle of repose and angle of internal friction (AIF) as their values shown in Table 3. Quantifying the resistance of the powder mass to flow, the angle of repose gives an indicator of the inter-particulate frictional forces working within the powder system (Adeoye and Alebiowu, 2013). Free flow is indicated by an angle of  $30^\circ$  or less, while poor flow is indicated by an angle of  $40^\circ$  or more (Huh and Scriven, 1971). The particle size distribution has an effect on the angle of repose, which normally increases as particle size decreases. For solid dose technology, values below around  $30^\circ$  are generally thought to be suitable (Adeoye and Alebiowu, 2013).



Table 2: Density Properties of the Excipients

Excipient	True density (g/ml)	Bulk density (g/cm <sup>3</sup> )	Tapped density (g/cm <sup>3</sup> )	Bulk volume (cm <sup>3</sup> )	Tapped volume (cm <sup>3</sup> )
Chitosan	2.760	0.989	1.353	30.314	22.17
Corn starch	1.734	0.53	0.614	56.556	48.864
Lactose	2.420	0.729	0.961	41.173	31.219
F1	2.302	0.881	1.105	33.934	27.147
F2	2.470	0.934	1.184	32.124	25.337
F3	2.439	0.947	1.239	31.671	24.206
F4	2.336	0.908	1.163	33.029	25.79
F5	2.404	0.947	1.228	31.671	24.432
F6	2.473	0.975	1.275	30.766	23.527
F7	2.507	1.036	1.326	28.957	22.622
F8	2.439	0.961	1.275	31.219	23.527

The novel excipients, as shown by the angle of repose ranged from 26.06° to 36.32°, have better flow qualities than the native excipients, which ranged from 29.34° to 32.89° as shown in the Table 3, corresponding to excipient in formulations 2 (F2) and 8(F8) respectively. It can be said that formulations 2, 3, 4, 5 and 7 have good flow properties while formulations 1, 6 and 8 have fair flow properties. A Hausner's ratio (HR) of less than 1.2 indicates acceptable powder flowability, but HRs of 1.5 or higher indicate poor powder flowability (Hausner, 1967).

Table 3: Flow Properties of the Excipient

Excipient	Hausner's ratio	Carr's index (%)	Bulkiness (cm <sup>3</sup> /g)	Packing fraction	Porosity	Angle of repose	Angle of internal friction
Chitosan	1.367	26.859	1.011	0.358	0.642	32.89	49.02
Corn starch	1.158	13.681	1.887	0.306	0.694	29.34	57.57
Lactose	1.318	24.142	1.372	0.301	0.699	31.38	57.36
F1	1.254	20.272	1.135	0.383	0.617	34.71	44.82
F2	1.268	21.115	1.071	0.394	0.606	26.06	42.99
F3	1.308	23.567	1.056	0.388	0.612	32.99	43.99
F4	1.281	21.926	1.101	0.389	0.611	28.91	42.78
F5	1.297	22.883	1.056	0.394	0.606	31.24	42.99
F6	1.308	23.529	1.026	0.394	0.606	34.13	42.99
F7	1.28	21.87	1.965	0.413	0.587	31.29	38.84
F8	1.327	24.627	1.041	0.394	0.606	36.32	42.99

The values of HR showed that both the native and the novel excipients have good flow. The HR is the proportion of bulk densities that have been tapped to those that have been aerated. The HR's values for formulation 8 was 1.327, which was very high. Formulations 1, 2, 4, 5, and 7 had Hausners' ratios of 1.254, 1.268, 1.281, 1.297, and 1.280, respectively, demonstrating a better flow than the original state. Carr's index is an assessment of the compressive strength of a powder and an intuitive determinant of the fluidity of a substance. The higher the value, the more firmed the powder is, signifying that there isn't enough flow. Carr's indexes of 16 to 25% indicate excellent flow characteristics but levels beyond 25% indicate cohesiveness or poor flow performance (Carr, 1965). All the novel excipients had carr's index values lower than those of chitosan and lactose. The values obtained ranges from 20.272 to 24.627 corresponding to excipients in formulations 1 and 8 respectively. Chitosan had the highest values with CI of 26.859 and HR of 1.367 indicating poor compressibility but a fair flow. Corn-starch and lactose on the other hand had lower CI values of 13.681 and 24.142 respectively while their HR are 1.158 and 1.318, which implies good compressibility and better flow. The synergy brought about by these complementary effects might be the reason for good compressibility and flows found in the novel excipient. This shows that mixing chitosan with corn-starch and lactose could aid in the creation of excipients with improved flow properties, which would be more effective in direct compression.

It has been argued that the degree of internal friction, rather than the angle of repose is a better indicator of flow arrangement due to the limited repeatability of the angle formed by the powders. This accumulates to a high angle and then drops to a comparatively deep angle (Neather, 2016). Varthalis and Pilpel (1976) proved that the angle of internal friction is one of the fundamental flow characteristics of the bulk solids which characterize the failure properties of the particle assemblage under load. Each particle roughness is present in powder flow, and this cross friction has been proven to have a significant consequence on powder packing. (Goh *et al.*, 2018).

From Table 3, the ranking for angle of internal friction is  $Cs > Ls > Ch > F1 > F3 > F2, F5, F6, F8 > F7$ . The estimates of the angle of internal friction demonstrated that the novel excipients produced had substantially improved flow characteristics in comparison to single original excipients. A higher value of the angle of internal friction denotes greater cohesiveness of the particle and the creation of bridges and arches in the powder, both of which restrict flow (Adeoye and Alebiowu, 2013; Juneja *et al.*, 2014). The observations imply that elevating particular quantities of chitosan in the excipient could assist to minimize patches of unwanted air in tablets, which can induce capping and/or lamination of the tablets, particularly while using in direct compression of tablets. This is in agreement with the work of Niranjana, (2013) who studied the sliding wear behaviour in composite mixture and concluded that increase in cohesiveness of particles can be the result of higher values of angle of internal frictions.

### 3.3 Packing and Cohesive Properties of the Novel Excipients

Compactibility refers to a material's ability to form compact tablets with acceptable tensile strength when subjected to densification. As the porosity of a compact decreases, its tensile strength increases (Sun, 2006). The Kawakita's model in Equation 4 reflects the amount of shrinkage in a powder bed to the tapping pressure. The model could be used to comprehend powder redevelopment, based on the established linearity relationship. The Kawakita coefficient 'a' denotes the powder bed's minimal porosity prior to application of load, which is related to its compressibility. The powder is packed thicker the initial time it was fed into the cylinder, if the value of 'a' is low. The value of 'b' is the inverted assessment of cohesiveness calculated from the plot's intercept. The higher the powder's 'a' value, the better the compressibility, which is important for direct tablet compression. The Plots of N/C against the number of taps for native excipients, F1-F4 and F1-F8 respectively, were done to determine the values of a, i.e. the volume reduction after tapping as percentages derived from straight line gradient as shown in Table 4. The rank order of "a" is  $F6 > F4 > F3 > F8 > F7 > F2 > F1$ . Since tapping did not result in a significant improvement in packing, the low values in some formulations indicate that the powders were sufficiently packed prior to tapping. The result presented in Table 4 showed that chitosan had the highest values. Tapping reduces voids in powders with a low value of "a" by removing air from the build platform without changing the particle structure or shape (Adeoye and Alebiowu, 2013).

### 3.4 Consolidation Index and Rate of Consolidation

The correlations between both the log of density variations and the log frequency of taps as shown in Equation 6 were respectively used to derive the consolidation index and rate of consolidation for native excipients, F1-F4 and for F5-F8. Both the rate of consolidation, K (an indicator of the efficiency of packing powder), and the consolidation index, C (a reflection of the influence of packing on flow) are both improved when the amount of chitosan or corn-starch in the novel excipient was increased. The finding could be linked to the combination's influence, which culminated in less unevenly shaped particles with a lower fraction of corn-starch or lactose, making particle reorganization simpler and resulting in a greater consolidation index. Reduced quantities of corn-starch starch or lactose in the novel excipients may have caused particle dimension reconfiguration, lessening the cohesive solid–solid association and reducing the consolidation rate, K. Because powder flow entails frictional contact between individual particles as well as a reduction in the Van der Waals forces's influence on cohesion, this inevitably means that flowability is increased, resulting in an improvement in the consolidation index. The degree of splitting and fracture at particle interaction locations, as well as the amplitude and severity of forces of attraction among connecting particles, all impact the flow feature of a powder mixture (Ogunjimi and Alebiowu, 2013). The rank order for C is  $Ch > F7 > F3 > F8 > F5 > F4 > F2 > F1$  and  $F6 > L > Cs$ , as seen in Table 4.

The highest C value was found in chitosan, denoting that it has an increased cohesiveness and the capacity to infuse excellent mechanical properties in dosage forms, while the lowest were found in corn-starch. A lower lactose value also implies that native excipients are more cohesive and that corn-starch particles are more likely to reorganize and fill vacant spaces after tapping. When particles are tapped or vibrated, the rate of consolidation provides an indication of how quickly they pack together.  $Cs > L > F6 > Cs > F4 > F5 > F1 > F2$  and  $F8 > F3 > F7$  are the rank order for consolidation rates.

## 4. CONCLUSION

In this study, the combined effect of different proportion naturally extracted chitosan, industrial grade corn-starch and lactose for probiotics excipient development was investigated. Singular and interaction effects of influencing parameters were also studied on the flow and compaction properties of excipients formulated. Our results showed from the estimates of the all micromeritics properties that the functional novel excipients developed had substantially better flow and compaction properties as well as improved consolidation characteristic when the amount of chitosan or corn-starch in the novel excipient was increased. Pressure plays the most significant impact in reducing the frictional contact between individual particles as well as the Van der Waals forces's influence on cohesion during tapping, leading to increase in flowability and subsequent improvement in the consolidation index. If the extracted chitosan could meet all US Pharmacopoeia specifications (such as limits of inorganic impurities and specific tests), then the novel excipients of chitosan, corn-starch and lactose could be suitable for use as less expensive alternatives to imported directly compressible excipients for probiotic tablet. Obtained results could serve as an eye-opener for relevant stakeholders by

providing them relevant information required to evaluate and harness local biopolymer available for excipients development.

Table 4: Compaction Properties of Powders and Processed Excipient

Excipient Formulation	Compressibility (a)	Cohesiveness (b)	Consolidation Rate (K)	Consolidation Index (CI)
Chitosan	0.530	0.033	0.570	-1.204
Corn-starch	0.525	0.013	1.671	-4.178
Lactose	0.494	0.032	0.812	-1.887
F1	0.390	0.036	0.584	-1.466
F2	0.396	0.035	0.578	-1.410
F3	0.469	0.035	0.566	-1.281
F4	0.471	0.033	0.614	-1.403
F5	0.462	0.032	0.586	-1.345
F6	0.537	0.023	0.675	-1.466
F7	0.450	0.030	0.559	-1.268
F8	0.463	0.031	0.578	-1.322

## REFERENCES

- Adeoye, O. and Alebiowu, G. (2013). Flow, packing and compaction properties of novel coprocessed multifunctional directly compressible excipients prepared from tapioca starch and mannitol. *Pharmaceutical Development and Technology*, 19(8), pp. 901-910.
- Alebiowu, G. and Itiola, O. A. (2003). The influence of pregelatinized starches disintegrants on interacting variables that act on disintegrant properties. *Pharmaceutical Technology*, 27, pp 28-31
- Antunes, F., Andrade, F., Araújo, F., Ferreira, D., and Sarmiento, B. (2013). Establishment of a triple co-culture in vitro cell models to study intestinal absorption of peptide drugs. *European Journal of Pharmaceutics and Biopharmaceutics*, 83(3), pp. 427-435.
- Builders, P. F., and Arhehwoh, M. I. (2016). Pharmaceutical applications of native starch in conventional drug delivery. *Starch-Stärke*, 68(9-10), pp. 864-873.
- Carr, R. L. (1965). Evaluating flow properties of solids. *Chemical Engineering Journal*, pp. 72: 163-
- Goh, H. P., Heng, P. W. S., and Liew, C. V. (2018). Comparative evaluation of powder flow parameters with reference to particle size and shape. *International Journal of Pharmaceutics*, 547(1-2), pp.133-141.
- Huh, C., and Scriven, L. E. (1971). Hydrodynamic model of steady movement of a solid/liquid/fluid contact line. *Journal of Colloid and Interface Science*, 35(1), pp. 85-101.
- Hausner H. H. (1967). Friction conditions in a mass of metal powder. *International Journal Powder Metall*, 3: pp. 7-13.
- Juneja, P., Kaur, B., Odeku, O. A., and Singh, I. (2014). Development of Corn Starch-Neusilin UFL2 conjugate as tablet superdisintegrant: Formulation and evaluation of fast disintegrating tablets. *Journal of Drug Delivery*, 2014.
- Kawakita, K., and Lüdde, K.-H. (1971). Some considerations on powder compression equations. *Powder Technology*, 4(2), pp. 61-68.
- Leonida, M., Ispas-Szabo, P., and Mateescu, M. A. (2018). Self-stabilized chitosan and its complexes with carboxymethyl starch as excipients in drug delivery. *Bioactive materials*, 3(3), pp. 334-340.
- Liu, T., Li, L., Teng, X., Huang, X., Liu, H., Chen, D., and Tang, F. (2011). Single and repeated dose toxicity of mesoporous hollow silica nanoparticles in intravenously exposed mice. *Biomaterials*, 32(6), pp. 1657-1668.
- Neather, A. C. (2016). Experimental investigations of granular matter flow regimes leading to insight into lahar flow dynamics: a Ph.D thesis presented in partial fulfilment of the requirements for the degree of Doctor of Philosophy in Earth Science at Massey University, Manawatū, New Zealand. Massey University.
- Niranjan, P. (2013). *Formulation and Invitro Evaluation of Sustained Release Matrix Tablets of Ibuprofen*. Adhiparasakthi College of Pharmacy, Melmaruvathur, Tamil Nadu, India.
- Ogunjimi, A. T., and Alebiowu, G. (2013). Flow and consolidation properties of neem gum coprocessed with two pharmaceutical excipients. *Powder technology*, 246, pp. 187-192.
- Okunola, A., and Odeku, O. (2009). Compressional Characteristic and Tabeting properties of Starches obtained from four dioscora species. *Famacia*, 57, pp. 756-769.
- Puvvada, Y. S., Vankayalapati, S., and Sukhavasi, S. (2012). Extraction of chitin from chitosan from exoskeleton of shrimp for application in the pharmaceutical industry. *International Current Pharmaceutical Journal*, 1(9), pp. 258-263.
- Varthalis, S., and Pilpel, N. (1976). Anomalies in some properties of powder mixtures. *Journal of Pharmacy and Pharmacology*, 28(5), pp. 415-419.
- Zvezdova, D. (2010). Synthesis and characterization of chitosan from marine sources in Black Sea. *Научни Трудове На Русенския Университет*, 49(9), pp. 65-69.



## Adsorption of Nickel (II) Cation from Aqueous Solution using Maize Cob-Activated Carbon: Optimization and Kinetic Studies

Mayowa A. LALA<sup>1\*</sup>, Zainab O. OLOMOWEWE<sup>1</sup>, Adekunle T. ADENIYI<sup>1</sup>, Abdulwahab GIWA<sup>1</sup>

<sup>1</sup>Department of Chemical and Petroleum Engineering, Afe Babalola University, Ado-Ekiti, Ekiti State, Nigeria

<sup>1\*</sup>[alam@abuad.edu.ng](mailto:alam@abuad.edu.ng), <sup>2</sup>[zainabwewe@gmail.com](mailto:zainabwewe@gmail.com), <sup>3</sup>[adenivia@abuad.edu.ng](mailto:adenivia@abuad.edu.ng), <sup>4</sup>[agiwa@abuad.edu.ng](mailto:agiwa@abuad.edu.ng)

\*Corresponding author

### ABSTRACT

This work has been carried out to study the adsorption of nickel (II) from a solution using an activated carbon developed from maize cob. The maize cob activated carbon (MCAC) was prepared by chemical activation. Afterwards, the MCAC was characterized and used as an adsorbent for batch adsorption of nickel (II) from aqueous solution. Three adsorption process variables, namely initial adsorbate concentration, contact time and adsorbent dosage were considered as the input parameters. The experiments carried out were designed using central composite design (CCD) of response surface methodology. The model developed from the experimental data using regression analysis was optimized with the aid of MATLAB. The analysis of variance (ANOVA) revealed that all the considered independent process variables had significant effect on the adsorption process. The optimum conditions obtained from MATLAB were found to be 9.75 mg/L for initial nickel (II) concentration, 120 min for contact time and 0.803 g for adsorbent dosage, and the application of the optimum conditions led to 100% removal of the nickel (II). Moreover, the experimental data were observed to be fitted best with pseudo-second-order kinetic model.

**Keywords:** Nickel, maize cob, MATLAB, response surface, statistical analysis.

### 1. INTRODUCTION

Anthropogenic activities resulting from high rate of urbanization and industrialization have been the major sources of environmental pollution (Bradl, 2002). The persistence increase of heavy metals in water bodies can be attributed to the exponential increase in the use of heavy metal containing compounds in domestic, agricultural and industrial applications (Yusuff *et al.*, 2019). Studies have shown that operations such as mining, smelting, metal galvanizations, coal burning in power plants, metal processing in refineries as well as activities in wood preservation and some agricultural products processing release unacceptable amount of toxic metals into the environment (Ahmed *et al.*, 2019).

Heavy metals are relatively high density (usually 3.5 to 7 g cm<sup>-3</sup>) metallic and metalloid elements, capable of inducing toxicity to human and the environment at some level of exposure (Tchounwou *et al.*, 2014). Heavy metals can be considered as either essential or non-essential. Essential heavy metals such as cobalt (Co), copper (Cu), chromium (Cr), iron (Fe), magnesium (Mg), manganese (Mn), molybdenum (Mo), selenium (Se) and zinc (Zn), help with metabolism activities in human body and also exert biochemical and physiological functions in plants and animals. This is possible when they are present in trace quantity; otherwise, they induce serious concern (Gautam *et al.*, 2014). The non-essential metals which include; lithium (Li), nickel (Ni), platinum (Pt), silver (Ag), strontium (Sr), tellurium (Te), thallium (Tl), tin (Sn), etc are those with little or no recognized biological functions, and their excessive exposure has also been noticed to cause cellular and tissue damage, hence, resulting into diverse side effects (Chang 1996).

Nickel, a very common and predominant metal, occurs naturally in the crust of the earth and is also present in cigarettes as nickel carbonyl. Nickel and its water-soluble salts are used in many industrial applications such as in electroplating, batteries, automobile and aircraft parts, spark plugs, coins, cosmetics, stainless steel, and also in the industrial scale production of nickel-cadmium batteries. The water soluble salts of nickel are the main problem of pollution in aquatic bodies (Gautam *et al.*, 2014), and study also showed that soluble micron nickel are more toxic compared to nickel nanoparticles (Zhou *et al.*, 2016). Nickel gains access to water bodies through mining, fuel combustion, waste incineration, rock weathering, and discharges from paint formulation and enamelling industries, and through the discharge of other nickel and its salt related industries (Buxton *et al.*, 2019). Nickel helps in red blood cells synthesis if present in very trace amount, but become toxic when exposed to higher doses for longer time. Nickel decreases body weight, damages liver and heart. It also causes reduction in cell growth, cancer and nervous

system damage (Gautam *et al.*, 2014). Hence, it is highly important to treat heavy nickel-contaminated waste before being discharged into water bodies. Nickel thresholds level corresponding to some human health and environmental compartment are; 0.44  $\mu\text{g Ni/cm}^2$  skin/day for human allergic contact dermatitis (Fischer *et al.*, 2005), 0.1 mg Ni/m<sup>3</sup> inhalable aerosol for human respiratory cancer (Oller *et al.*, 2014), 0.5  $\mu\text{g Ni/m}^3$  ng/m<sup>3</sup> PM10 aerosol for human respiratory cancer (Buekers *et al.*, 2015) and 4  $\mu\text{g Ni/L}$  bioavailability-based for freshwater (EU, 2013).

Studies have shown the effectiveness of reverse osmosis, ion exchange, electrocoagulation, electrochemical, membrane filtration, bioremediation, heterogeneous photocatalysts and adsorption process for the removal of nickel and some other heavy metals from wastewater (Yusuff *et al.*, 2019). Among the many techniques, adsorption has been widely accepted because of its effectiveness, simplicity, possibility of using different low-cost materials as adsorbent, and also because the method is highly environmentally friendly (Osasona *et al.*, 2018). Adsorption process is a unit operation in which the concentration of a fluid is altered by passing it through a porous material called adsorbent. Adsorbents such as agricultural waste particles (Singh and Rattan, 2011), activated carbon (Osasona *et al.*, 2018), zeolite (Kussainova *et al.*, 2018), molecular sieve (Rao *et al.*, 2015), silica gel (Tzvetkova and Nickolov, 2012), etc have been utilised for removing heavy metals from wastewater. At present time, different industrial wastes and biomass are utilized to prepare activated carbon (Reza *et al.*, 2020; Heidarinejad *et al.*, 2020). The preparation of activated carbon involves carbonization and activation process. Activation of the carbonized material can be physical activation (using heat with gas such as N<sub>2</sub>, CO<sub>2</sub> and H<sub>2</sub>O), chemical activation (using H<sub>3</sub>PO<sub>4</sub>, KOH, NaOH, ZnCl<sub>2</sub>, etc), physiochemical activation (using heat and chemical), and microwave-assisted activation (using microwave radiation) (Reza *et al.*, 2020). Among all the activation method, chemical activation is more economical as it requires shorter time for processing, lower activation temperature and higher carbon efficiency (Heidarinejad *et al.*, 2020).

In recent time, the removal of nickel (II) ion from wastewater has been proven possible by utilising low-cost wastes, some of which include natural and acid-treated neem sawdust (Krishnaiah *et al.*, 2006), and acid-treated lignin obtained from black liquor in pulp and paper industry (Pérez, 2006). Activated charcoal, clay and wood charcoal (Choksi and Joshi, 2007) and rice bran treated with acid (Zafar *et al.*, 2007) were also considered by some researchers for nickel (II) ion removal from water/wastewater.

The effectiveness of an adsorbent for the removal of heavy metals from aqueous solution depends on the adsorbent functional groups and how the adsorbent is modified. Studies on the characterization of maize cob, for example, indicated the presence of carboxyl, hydroxyl and amide groups which contribute positively to adsorption process (Herrera-Barros *et al.*, 2018). Also, adsorbent modification influences the surface area and adsorption capacities. The study of Al<sub>2</sub>O<sub>3</sub> nanoparticles modified maize cob by Herrera-Barros *et al.* (2018) revealed 86% removal of nickel (II) from aqueous solution. This was found to be higher than those obtained using maize cob particles (Herrera-Barros *et al.*, 2018).

Maize is a staple agricultural product in Nigeria. It serves as a major ingredient for the production of various types of food and can also be consumed directly when boiled or roasted. Maize cob on the other hand is one of the natural wastes from maize plant and can constitute high level of environmental pollution, if not properly handled. The ratio of maize grain to the cob is given as 100:18 (Hartmann *et al.*, 2012). This can lead to useless accumulation of large amounts of the cobs globally and, particularly, in Nigeria, if not properly utilized.

Therefore, this present work has been carried out to focus on NaOH-treated activated carbon produced from maize cob as a low-cost adsorbent for removing nickel (II) ion from aqueous solutions. Statistical and adsorption kinetics analysis were carried out to develop models that could describe the process.



Figure 1: Maize cob

## 2. MATERIALS AND METHODS

### 2.1 Materials

Maize cobs used for this research work were gathered from a local farm close to Afe Babalola University, Ado-Ekiti, Ekiti State, Nigeria. All the chemical compounds used, including nickel nitrate hexa-hydrate ( $Ni(NO_3)_2 \cdot 6H_2O$ ) and sodium hydroxide (NaOH) were of analytical grade, and were procured from Topjay Chemical Enterprise, Ado-Ekiti, Nigeria. A stock solution of 1000 mg/L nickel (II) was prepared by dissolving 5.82 g of the salt in 1000 mL deionized water. Various solutions of needed initial nickel (II) concentrations were obtained by diluting the stock solution with required amount of deionized water.

### 2.2 Preparation of the adsorbent (MCAC)

The maize cobs were washed thoroughly with clean tap water to remove sand and all other impurities. Subsequently, they were washed with distilled water to avoid the composition of the material being altered and, then, dried by heating up to 105 °C for 3 hours in an oven. The dried maize cobs were collected and crushed with mortar and pestle. Subsequently, the maize cob size was further reduced with the aid of a laboratory grinding mill. The sample obtained was then screened using a laboratory sieve-shaker to obtain 300 µm uniform-sized particles. Afterwards, 300 g of the pulverized maize cob was poured into a beaker containing 1000 cm<sup>3</sup> of 1.0 M sodium hydroxide (NaOH) solution. The mixture was left for 24 hr for proper impregnation. The resulting activated maize cob was washed with deionized water and filtered. Further, it was dried in the oven at 105 °C for 3 hours and later carbonized at 240 °C for 5 min in a muffle furnace. Finally, the derived maize cob activated carbon was screened again using the laboratory sieve-shaker to obtain 300 µm uniform-sized particles labelled MCAC.

### 2.3 Characterization of the maize cob based activated carbon (MCAC)

Compositions of C (Carbon), H (Hydrogen), O (Oxygen), N (Nitrogen) and S (Sulphur) in maize cob were determined based on existing standard procedures (García *et al.*, 2012). Also, proximate analysis was performed on the MCAC to determine its moisture content (% w/w), volatile matter content (% w/w), ash content (% w/w) and fixed carbon (% w/w) as described in the researches of Dada *et al.* (2012) and Wilde *et al.* (1972). Bulk density (g/cm<sup>3</sup>) and pH of the MCAC were determined using the method adopted by Dada *et al.* (2012). Moreover, scanning electron microscope (SEM) was used to determine MCAC morphology before and after adsorption. This was carried out using SEM-JEOL-JSM 7600F microscope.

### 2.4 Adsorption studies

#### 2.4.1 Experimental design and statistical analysis

Response Surface Methodology (RSM) was employed to study the influence of three process variables on the adsorption of nickel (II) on MCAC. Central Composite Design (CCD), an important optimization tool of the RSM was used, where initial concentration of nickel (II),  $C$  in mg/L, contact time,  $t$  in min, and MCAC dosage,  $d$  in g were considered as the independent process variables. The effects of these three variables on the removal efficiency of nickel (II) from aqueous solution were analysed. In Central Composite Design (CCD), each numeric factor was varied over 5 levels: plus and minus alpha (axial points), plus and minus 1 (factorial points) and the centre point. For the present study, a three-factor case was considered. Hence, the CCD was characterized by 6 axial points, 8 factorial points and 1 replicate at the centre which gave a total of 15 experiments. The levels generated by the CCD tool embedded in Design Expert 12.0 for the three factors studied are shown in Table 1. The removal efficiency, which was the response, was determined using batch adsorption of nickel (II) in aqueous solution onto the prepared MCAC and was used to develop a mathematical model. The model showed the relationship between the dependent variable ( $R$ ) and the three independent variables as represented by Equation (1), where  $a_1$ ,  $a_2$ ,  $a_3$ ,  $a_4$ ,  $a_5$  and  $a_6$  are the coefficients for the model. The variables  $C$ ,  $t$  and  $d$  are the actual values of the experimental independent variables.

$$R = a_0 + a_1C + a_2t + a_3d + a_4tC + a_5dC + a_6td \quad (1)$$

Table 1: Experimental process parameters and levels

Factor	Symbol	Level				
		1	2	3	4	5
Initial concentration of nickel (II) (mg/L)	$C$	9.85	10.06	10.26	10.47	10.67
Contact time (min)	$T$	60	75	90	105	120
MCAC dosage (g)	$D$	0.2	0.4	0.6	0.8	1.0

### 2.4.2 Experimental procedures

Stock solution of nickel (II) was prepared by dissolving  $Ni(NO_3)_2 \cdot 6H_2O$  in deionized water. Adsorption experiments with the prepared MCAC were performed by batch tests to observe the effects of initial concentration of nickel (II), contact time and MCAC dosage on Ni removal from aqueous solutions. The batch experiments were carried out in 250 mL beakers containing 50 mL aqueous solutions of nickel ions of various concentrations unto which activated carbon were added. The suspensions were shaken at room temperature using a mechanical shaker for a prescribed time at 120 rpm. The solutions were filtered using whatman 42 filter paper and the absorbance of the solutions after the process was determined. The absorbance was determined using *Buck Scientific 211 VGP* Atomic Absorption Spectrophotometer (AAS) situated at the Chemistry laboratory, Afe-Babalola University, Ado-Ekiti, Nigeria (ABUAD). The amount of nickel (II) adsorbed at equilibrium and the removal efficiency of nickel (II) in the solution were calculated using Equations (2) and (3), where  $R\%$  is the removal efficiency of nickel (II) in the aqueous solution,  $qt$  is the adsorption capacity at any time  $t$ ,  $C_0$  is the initial concentration of the metal ion (mg/L),  $C_e$  is the equilibrium concentration of the metal ion (mg/L),  $C_t$  is the metal concentration at any time  $t$  (mg/L),  $V$  is the volume of the adsorbate solution (mL) and  $m$  is the mass of MCAC (g) used.

$$R\% = \frac{C_0 - C_t}{C_0} * 100\% \quad (2)$$

$$qt = \frac{C_0 - C_t}{m} * V \quad (3)$$

### 2.4.3 Kinetic modelling

The determination of the mechanism involved in the adsorption of Ni ions onto the prepared MCAC was considered using three kinetic models; pseudo-first order, pseudo-second order and intra-particle diffusion. The non-linear equations of the three stated kinetic models are given respectively in Equations (4), (5) and (6), where  $k_1$  is the pseudo-first-order kinetic rate constant ( $\text{min}^{-1}$ ),  $k_2$  is the pseudo-second order rate constant ( $\text{g}^{-1} \text{min}^{-1}$ ),  $k_e$  is the diffusion constant ( $\text{mg} \cdot \text{g}^{-1} \cdot \text{min}^{-1/2}$ ), and  $q_e$  and  $qt$  are the amounts of adsorbate adsorbed in equilibrium and over time  $t$  (mg/g) respectively.

$$qt = q_e(1 - \exp^{-k_1 t}) \quad (4)$$

$$qt = \frac{t}{\left(\frac{1}{k_2 * q_e^2}\right) + \left(\frac{t}{q_e}\right)} \quad (5)$$

$$qt = k_e * t^{\frac{1}{2}} \quad (6)$$

## 3. RESULTS AND DISCUSSION

### 3.1 Adsorbent characterization

Presented in Table 2 are the chemical and physical parameters of the MCAC. The elemental composition shows lower values of nitrogen (0.35%) and sulphur (0.23%) compared to oxygen (44.62%), carbon (49.50%) and hydrogen (5.32%). According to the literature, higher values of carbon, oxygen and hydrogen in biomass favour adsorption process; hence the prepared MCAC has a good tendency to be effective for the removal of nickel (II) ion from aqueous solution. Moreover, the reported bulk density of 0.482 is within the range of the one reported in literature for materials suitable as an adsorbent, and the presented particle size of 300  $\mu\text{m}$  indicated that the prepared MCAC will be an effective adsorbent. Figure 2 presents the SEM images of MCAC before and after the adsorption of nickel (II). The more undefined, clouds-like and rough structure of micrograph in Figure 2(a) compared to Figure 2(b) showed the adsorption of nickel (II) on the MCAC surface given in Figure 2(b).

### 3.2 Central composite design (CCD) model and data analysis

The 3-Factor CCD design comprising the adsorption variables and values of the corresponding responses are presented in Table 3. The suggested CCD model by the software was a 2FI model. This was adopted for the removal response and used to develop the correlation between MCAC and the nickel (II) ion uptake. The equation developed in actual units for the removal efficiency of nickel (II) is given by Equation (7). The appearance of two variables in the equation implies a double factor effect.

$$R = 63.700018 - 6.0923C + 2.21684t - 23.0035d - 0.14728tC + 6.61364dC - 0.32981td \quad (7)$$

The authenticity of the developed model was examined based on its correlation coefficient ( $R^2$ ) and standard deviation values for this study. These are given in the analysis of variance (ANOVA) Table 3. The  $R^2$  value for the model equation was obtained to be 0.9984 which is considered high as it is close to unity. The standard deviation of the model was 0.7456 and it is agreeably small, thus, indicating that the predicted responses have accurate values and are similar to those of the actual response.

Table 2: Physicochemical properties MCAC

Description	Value				
Elemental composition (MC)	C: 49.50%	O: 44.62%	H: 5.30%	N: 0.35%	S: 0.23%
pH	7.8				
Moisture content (% w/w)	7.5				
Volatile matter (% w/w)	46.3				
Ash content (% w/w)	9.2				
Fixed carbon (% w/w)	36.7				
Bulk density (g/cm <sup>3</sup> )	0.482				
Particle size	300 μm				

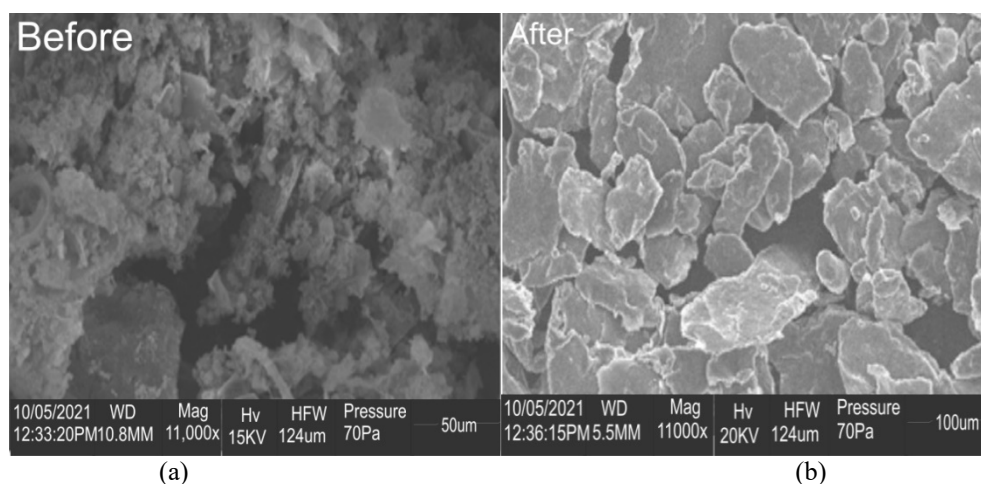


Figure 2: SEM micrographs of MCAC (a) before and (b) after adsorption of nickel (II)

Table 3: Analysis of variance (ANOVA) for adsorption efficiency

Source	Sum of Squares	Df	Mean square	F-value	p-value	Remark	Contribution
Model	2784.74	6	464.12	834.88	< 0.0001	Significant	
C	337.98	1	337.93	607.97	< 0.0001	Significant	12.14%
T	1972.83	1	1972.83	3548.80	< 0.0001	Significant	70.85%
D	312.95	1	312.95	562.95	< 0.0001	Significant	11.24%
tC	26.25	1	26.25	47.23	0.0001	Significant	0.94%
dC	9.41	1	9.41	16.93	0.0035	Significant	0.34%
Td	125.31	1	125.31	225.41	< 0.0001	Significant	4.50%
Residual	4.45	8	0.5559				
Cor Total	2789.19	14					
Adeq. Pre	20.3737						
R <sup>2</sup>	0.9984						
Adj. R <sup>2</sup>	0.9972						
Pred-R <sup>2</sup>	0.9653						
Std. Dev.	0.7456						
Adeq. Pre	108.4077						



Figure 3 presents the predicted values versus the experimental values for nickel (II) ions removal from aqueous solution. It was indicated that there was a good capture of the relationship between the adsorption parameters and the responses given by the developed model. It also shows a good relationship between the experimental and predicted values of the responses within the range of the operating parameters.

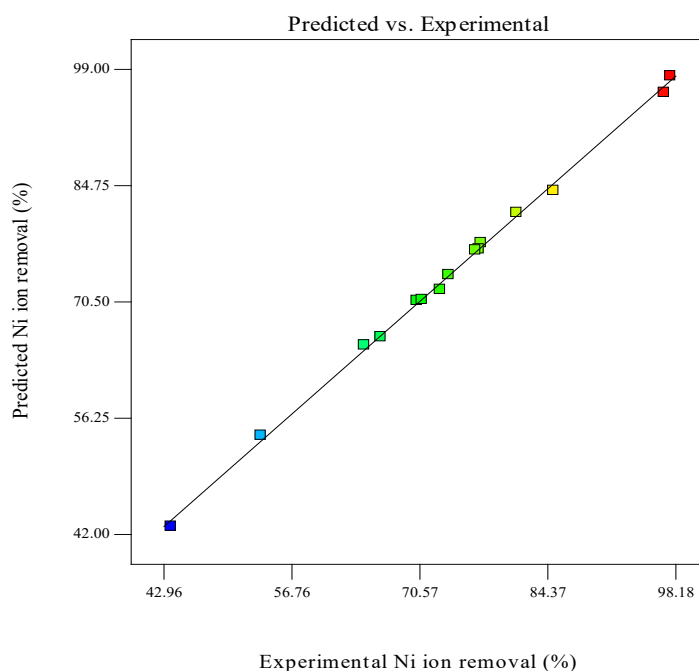


Figure 3: Graph of predicted vs. experimental Ni ion removal (%)

### 3.3 Process Optimization Using MATLAB

It is important to simulate the response and behaviour of a system based on relevant input parameters. In this study, the initial concentration, contact time and adsorbent dosage were considered as the input parameters for the modelling of the system. Regression analysis was carried out to fit the experimental data to a model with the aid of MATLAB. The correlation coefficient of the developed model,  $R^2$  was obtained as 0.9840. This implied that the model agreed reasonably with the data and was suitable for describing the process. Furthermore, MATLAB program was used to simulate the process and develop the responses given in Figure 4.

Optimization was carried out on the developed model to get the optimal conditions of the three variables studied within a desired range and initial conditions, and the optimum adsorption condition were obtained to be 9.75 mg/L for initial nickel (II) concentration, 120 min for contact time and 0.803 g for MCAC dosage. These conditions gave 100% nickel (II) removal. The optimization was based on the highest desirability and the optimal conditions show that long contact time, high MCAC dosage and low nickel (II) concentration is more adequate for the adsorption of nickel (II) from aqueous solution using MCAC.

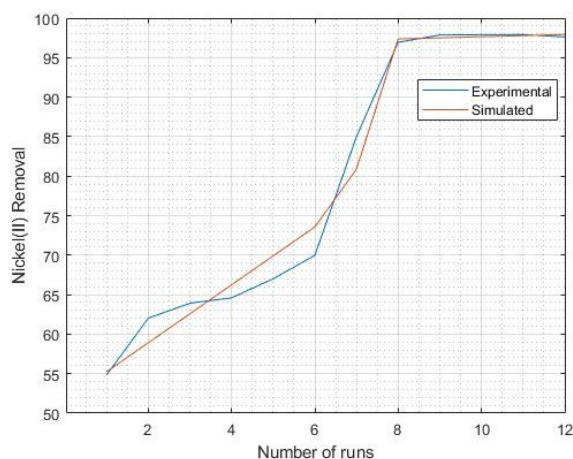


Figure 4: Experimental and the simulated responses

### 3.4 Adsorption kinetics analysis

The model parameters obtained from the non-linear kinetic model plots are presented in Table 4. The most suitable model was selected based on the fitted coefficient of determination,  $R^2$ . The higher  $R^2$  value, 0.9704 for pseudo-second-order model compared to 0.9156 for pseudo-first-order and 0.9191 for intra-particle diffusion signified that pseudo-second-order model fitted best to the experimental data. Also, the evaluated  $q_e$  for pseudo-second-order was the closest to that of experimental data. Hence, it can be concluded that the adsorption of nickel (II) on MCAC was chemisorption controlled.

Table 4: Kinetic model parameters for the adsorption of nickel (II) on MCAC

Kinetic models	$q_e$ (mg/g)	$k_1$ ( $\text{min}^{-1}$ )	$k_2$ ( $\text{g.mg}^{-1}\text{min}^{-1}$ )	$k_e$ ( $\text{mg.g}^{-1}.\text{min}^{-1/2}$ )	C	$R^2$
Experimental	0.6030					
Pseudo-first order	0.3597	0.0941				0.9156
Pseudo-second order	0.3888		0.4995			0.9704
Intra-particle diffusion				0.0118	0.2638	0.9191

## 4. CONCLUSION

The results obtained indicated that the developed maize cob activated carbon (MCAC) was very suitable in removing nickel (II) ion from aqueous solution as an effective adsorbent. It was also discovered that contact time contributed more to the adsorption process (70.85%), and the interaction between MCAC dosage and contact time contributed more (4.50%) when parameter interaction is considered. Furthermore, 9.75 mg/L initial nickel (II) concentration, 120 mins contact time and 0.803 g adsorbent dosage were found to give total removal of the nickel (II) from the solution. Finally, the experimental data fitted better to pseudo-second-order kinetic model. Therefore, it can be inferred that maize cob activated carbon is highly effective for the removal of Ni(II) from aqueous solution and the adsorption process is chemisorption controlled.

## REFERENCES

- Ahmed A.Y, Yasser A.M.A., Norhan S.S. and Farida M.S.E. (2019). Removal of cadmium ions from wastewaters using corn cobs supporting nano-zero valent iron, *Separation Science and Technology*, DOI: 10.1080/01496395.2019.1708109.
- Bradl, H., (2002). *Heavy Metals in the Environment: Origin, Interaction and Remediation Volume 6*. London: Academic Press.
- Buekers, J., De Brouwere, K., Lefebvre, W., Willems, H., Vendenbroele, M., Van Sprang, P., Eliat-Eliat, M., Hicks, K., Schlekot, C. E. and Oller, A. R. (2015), Assessment of human exposure to environmental sources of nickel in Europe: Inhalation exposure. *Sci. Total Environ*, 521–522, 359–371.
- Buxton, S., Garman, E., Heim, K. E., Lyons-Darden, T., Schlekot, C. E., Taylor, M. D. and Oller, A. R. (2019), Concise Review of Nickel Human Health Toxicology and Ecotoxicology, *Inorganics*, 7, 89; doi:10.3390/inorganics7070089.
- Chang, L.W., Magos, L., Suzuki, T. (1996). *Toxicology of Metals*. Boca Raton, FL, USA: CRC Press; 1996.
- Choksi, P.M. and Joshi, V.Y. (2007). Adsorption kinetic study for the removal of nickel (II) and aluminum (III) from an aqueous solution by natural adsorbents. *Desalination* 208, 216–231.
- Dada, A., Inyinbor, A. and Oluyori, A. (2012). Comparative adsorption of dyes unto activated carbon prepared from maize stems and sugar cane stems. *Journal of Applied Chemistry*, 2(3), 38-43. <https://doi.org/10.9790/5736-0233843>
- European Union (EU) (2013). Directive 2013/39/EU of the European Parliament and of the Council. *Off. J. Eur. Union*, 226, 338–436.
- Fischer, L. A., Menné, T. and Johansen, J. D. (2005), Experimental nickel elicitation thresholds—A review focusing on occluded nickel exposure. *Contact Dermat*, 52, 57–64.
- García, R., Pizarro, C., Lavín, A.G. and Bueno, J.L. (2012). Characterization of Spanish biomass wastes for energy use, *Bioresource Technology* 103, 249–258. doi:10.1016/j.biortech.2011.10.004.
- Gautam, R.K., Sharma, S.K., Mahiyab, S. and Chattopadhyaya, M.C. (2014). *Heavy Metals in Water: Presence, Removal and Safety*, Royal Society of Chemistry, <http://pubs.rsc.org> | doi:10.1039/9781782620174-00001.
- Hartmann M, Khalil S. and Bernet T. (2012). *Organic agriculture in Saudi Arabia*. *Sect Study*. 2012;10:1–48.
- Heidarinejad, Z., Dehghani, M. H., Heidari, M., Javedan, G., Ali, I. and Sillanpää, M. (2020), Methods for preparation and activation of activated carbon: a review, *Environmental Chemistry Letters*, online, DOI 10.1007/s10311-019-00955-0.
- Herrera-Barros, A., Tejada-Tovar, C., Villabona-Ortiz, A., Gonzalez-Delgado, A.D. and Alvarez-Calderon, J. (2018). Adsorption of Nickel and Cadmium by Corn Cob Biomass Chemically Modified with Alumina

- Nanoparticles, *Indian Journal of Science and Technology*, Vol 11(22), DOI: 10.17485/ijst/2018/v11i22/126125.
- Krishnaiah, A., Rao, P.S., Reddy, K.V.N.S. and Kalyani, S. (2006). Comparative sorption of copper and nickel from aqueous solutions by natural neem (*Azadirachta indica*) sawdust and acid treated sawdust. *Wood Sci. Technol.* 41 (5), 427–442.
- Kussainova, M.Z., Chernyakova, R.M., Jussiphekov, U.Z., Temel, H., Pasa, S., Kaiybayeva, R. A. and Agatayeva, A.A. (2018), Sorption removal of Pb<sup>2+</sup>, Cd<sup>2+</sup>, Cu<sup>2+</sup> from diluted acid solution by chitosan modified zeolite. *J Chem Technol Met* 53(1):94–100.
- Oller, A. R., Oberdörster, G. and Seilkop, S. K. (2014), Derivation of PM<sub>10</sub> size-selected human equivalent concentrations of inhaled nickel based on cancer and non-cancer effects on the respiratory tract. *Inhal. Toxicol*, 26, 559–578.
- Osasona, I., Aiyedatiwa, K., Johnson, J.A., Faboya, O.L. (2018). Activated carbon from spent brewery barley husks for cadmium ion adsorption from aqueous solution. *Indones J Chem* 18(1):145–152. <https://doi.org/10.22146/ijc.22422>
- Pérez, N.A., Rincón, A. and Delgado, L.A. (2006). Use of biopolymers for the removal of heavy metals produced by the oil industry –a feasibility study. *Adsorption* 12, 279–286.
- Rao, G.B., Prasad, M.K., Murthy, C.V.R. (2015). Cobalt (II) removal from aqueous solutions by adsorption onto molecular sieve. *Int J Chem Sci* 13(4):1893–1910.
- Reza, M. S., Yun, C. S., Afroze, S., Radenahmad, N., Bakar, M. S. A., Saidur, R., Taweekun, J. and Azad, A. K. (2020), Preparation of activated carbon from biomass and its' applications in water and gas purification, a review, *Arab Journal of Basic and Applied Sciences*, 27:1, 208-238, DOI: 10.1080/25765299.2020.1766799.
- Singh, H., Rattan, V.K. (2011). Adsorption of nickel from aqueous solutions using low cost biowaste adsorbents, *Water Quality Research Journal of Canada* | 46.3 | 2011.
- Tchounwou, P.B., Yedjou, C.G., Patlolla, A.K. and Sutton, D.J. (2014). Heavy Metals Toxicity and the Environment, NIH-RCMI Center for Environmental Health, College of Science, Engineering and Technology, EXS. 2012; 101: 133–164. doi:10.1007/978-3-7643-8340-4\_6.
- Tzvetkova, P. and Nickolov, R. (2012). Modified and unmodified silica gel used for heavy metal ions removal from aqueous solutions. *J. Uni. Chem. Tech. Met.* 47(5):498–504.
- Wilde, S.A., Voigt, G.K. and Iyer, J.J. (1972). Chesters (Ed.), *Soil and Plant Analysis for Tree Culture*, 4th ed., Oxford and IBH Publishing Co., New Delhi.
- Yusuff, A.S., Popoola, L.T. and Babatunde, E.O. (2019). Adsorption of cadmium ion from aqueous solutions by copper-based, *Applied Water Science* 9:106.
- Zafar, M.N., Nadeem, R. and Hanif, M.A. (2007). Biosorption of nickel from protonated rice bran. *J. Hazard. Mater.* 143, 478–485.
- Zhou, C., Vitiello, V., Casals, E., Puentes, V. F., Iamunno, F., Pellegrini, D., Changwen, W., Benvenuto, G. and Buttino, I. (2016), Toxicity of nickel in the marine calanoid copepod *Acartia tonsa*: Nickel chloride versus nanoparticles. *Aquat. Toxicol*, 170, 1–12.



## Synthesis and Application of Clinoptilolite for the Purification of Biogas from Cow Dung

\*Emmanuel O. EHINMITOLA, Olayinka SANDA, Elijah A. TAIWO, Ridwan A. OSENI, Azeez O. RAIFU, Oladele S. MATUWO and Samuel O. ADEBAYO

Department of Chemical Engineering, Obafemi Awolowo University, Ile-Ife, Nigeria

[fehinmi@oauife.edu.ng](mailto:fehinmi@oauife.edu.ng)

\*Corresponding author

### ABSTRACT

This study batch-synthesized clinoptilolite using silica derived from rice husk and bamboo leaves, with a view to using it as purification media for biogas produced from cattle droppings. Silica gels synthesized from rice husk and bamboo leaves were impregnated with NaOH and Al(OH)<sub>3</sub> without seeding, to constitute the clinoptilolite samples. Analysis of the unseeded products by x-ray fluorescence (XRF) indicated high Si to Al ratio of > 4 while x-ray diffraction (XRD) patterns indicated the presence of minerals of the same family as clinoptilolite. The porosity values of the products from rice husk and bamboo leaves were found to be 0.773 and 0.800 respectively. The synthesized clinoptilolite samples were used as absorbers attached to biogas generators generating biogas from cattle droppings and it was found that the CO<sub>2</sub> contents reduced in all the test cases. It can be concluded from the study that clinoptilolite produced from silico-alumina rich wastes have potentials of use as biogas purifiers.

**Keywords:** clinoptilolite, zeolite, crystallinity, biogas, porosity.

### 1. INTRODUCTION

Clinoptilolite is naturally occurring microporous zeolite. It could as well be synthesized forming microporous silica and alumina arrangement in a complex tetrahedral structure. It is usually formed as white to reddish crystals with a Mohr's hardness of 3.5 to 4, and commonly occurs as a devitrification product of volcanic glass shards in tuff and as vesicle fillings in basalts, andesites and rhyolites (Englert and Rubio, 2005). The geological formation of natural zeolites depends on the location viz-a-viz the occurrence of the natural phenomenon of release of heat from molten magma below the earth surface (Mastinu *et al.*, 2019). The aluminosilicate layer of zeolites makes them useful as separators in purification, among other applications. Clinoptilolite is abundant in Ukraine around the Carpathian Mountain with the general formula as  $(K_{2.3}Na_{0.5}Ca_{2.1}Mg_{0.6}Fe(III)_{0.9}Fe(II)_{0.2}Ti_{0.2}) \times (Si_{31.4}Al_{6.5}O_{44}) \times 21.8H_2O$  (Korkuna *et al.*, 2006). However, studies have shown that the general chemical formula is  $(Na,K)_6Al_6Si_{30}O_{72} \cdot 20H_2O$  and the Si/Al ratio may vary from 4.0 to 5.3 (Kowalczyk *et al.*, 2006, Dimitrijević *et al.*, 2019).

Although the mining of clinoptilolite from natural resources has been popular for many years, its artificial creation has been investigated in the last decades by many scientists due to the demand for high quality and purity of clinoptilolite. Consequently, a significant number of studies have focused on the synthesis of clinoptilolite (Luna *et al.*, 2018). A well reported and reproducible batch formulation of synthetic Na- and K-clinoptilolite is  $2.1MOH \cdot [Al(OH)_3(5SiO_2) \cdot 5.25H_2O]$ , where M is Na or K (Chi and Sand, 1983, Güvenir, 2005).

The synthesis of clinoptilolite has been reported to have helped in overcoming the problem of proximity to the various sources of natural clinoptilolite. Likewise, thermal modification of the natural clinoptilolite has helped establish the influence of temperature on the purification performance of the clinoptilolite in application for separation purposes (Ambrozova *et al.*, 2017). Clinoptilolite, both the natural and the synthetic has significant selectivity for CO<sub>2</sub> compared to CH<sub>4</sub> due to the high permeability ratio at almost all conditions (Castruita-de León *et al.*, 2018). The pore size of clinoptilolite among other zeolites averaged at 3.5 Å while the molecular sizes of CO<sub>2</sub> and CH<sub>4</sub> has been reportedly averaged at 3.3 and 4.0 Å, respectively. This indicates tendencies of favourable diffusing of CO<sub>2</sub> through clinoptilolite and the rejection of CH<sub>4</sub> (Farjoo *et al.*, 2015, Blankenship and Mokaya, 2022). According to Chi and Sand (1983), the batch synthesis of clinoptilolite requires having silica gel and a suitable salt of aluminium or sodium. There are, few sources of silica-rich materials (such as rice husk, bamboo leaves, green beans, banana peels among others) regarded as wastes. These can be harnessed for the synthesis of clinoptilolite as aimed in this present study, to achieve cleaner environment with wealth creation from the wastes. The source of gas mixture to be purified will be crude biogas. Rice husk and bamboo leaves were adopted in this study due to their very high proportion of silica in the synthesis of silica gel while biogas production utilized cow dung as feedstock.

## 2. MATERIALS AND METHODS

### 2.1. Materials

The materials used for this study include the agro-wastes (rice husk and bamboo leaves, for the synthesis of silica gel and cow dung, for biogas production), the consumables for the synthesis of clinoptilolite. The Rice husk, the main component for a batch synthesis of silica gel was obtained from Erin-Ijesha, Osun state while the bamboo leaves were collected within Obafemi Awolowo University, Ile-Ife Osun state. The animal waste was obtained from an abattoir in Ile-Ife. Sodium hydroxide pellet and Aluminum hydroxide powder which served as alkali source and alumina source respectively were supplied by Merck (Mumbai, India), while concentrated trioxonitrate (V) and tetraoxosulphate (VI) acids were supplied by Loba Chemie (Mumbai, India). The silica gel used was synthesized from rice husk and bamboo leaves, while water (distilled) was collected in the laboratory.

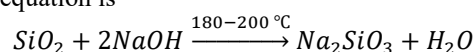
### 2.2 Synthesis of Clinoptilolite

The clinoptilolite preparation began with the synthesis of the silica gel a precursor agent, and the procurement of the alkali and alumina sources. The silica source (amorphous, reactive silica (SiO<sub>2</sub>)) was synthesized using rice husk and bamboo leaves separately as the starting materials, and then impregnated with NaOH, and Al(OH)<sub>3</sub>.

#### 2.2.1 Silica Gel Synthesis

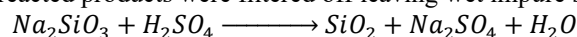
The rice husk and the bamboo leaves were collected, washed with distilled water and oven dried at 105 °C for 6 hours in batches. The rice husk and bamboo leaves were each calcined at 700 °C for 4 h to get the characteristic white rice husk ash (RHA) and bamboo leaves ash (BLA). The RHA and BLA were weighed and recorded, then leached with nitric acid (HNO<sub>3</sub>) by boiling each of the ashes in 500 mL of 2M concentrated HNO<sub>3</sub> (in batches) for 1 h for demineralization at about 83 °C. The leached RHA and BLA were filtered to remove the unreacted acid and the oxidized metallic impurities. The leached RHA and BLA were washed with distilled water, filtered and dried at room temperature. The resulting products were weighed, and the masses recorded.

Fifty gram of the dried acid-leached RHA and BLA were each contacted with 50 g of NaOH pellets per 500 mL distilled water. Each mixture was boiled at 180 °C in 2M NaOH solution for 1 h, so that sodium trioxosilicate (IV) (Na<sub>2</sub>SiO<sub>3</sub>) is precipitated (Prasad and Pandey, 2012). The resulting solution from each reaction was filtered to recover the precipitated trioxosilicate (IV) salt. The reaction equation is



The product from each sodium hydroxide washing stage was washed with distilled water, filtered, dried, weighed and recorded as sodium trioxosilicate (Na<sub>2</sub>SiO<sub>3</sub>).

The dried product from each washing stage was boiled in 2 M sulphuric acid (H<sub>2</sub>SO<sub>4</sub>) at 100 °C to produce a white precipitate of silica in solution of sodium sulphate. The precipitated silica in sodium hydroxide solution was filtered so that H<sub>2</sub>O, Na<sub>2</sub>SO<sub>4</sub>, and other unreacted products were filtered off leaving wet impure silica:



The filtered silica was dried at room temperature to give amorphous silica which is almost white in colour.

#### 2.2.2 Formulation of the synthetic clinoptilolite

A batch formulation with a molar composition of 2.01Na<sub>2</sub>O.10SiO<sub>2</sub>.Al<sub>2</sub>O<sub>3</sub>.110.1H<sub>2</sub>O was adopted from Güvenir (2005). Calculated amount of sodium hydroxide pellets (NaOH) was dissolved in distilled water in duplicate. Whitish clear solutions were obtained when aluminum hydroxide was added by stirring the mixture vigorously and heating to 90 °C for 1 hour. The silica obtained from RHA and BLA was each slowly added into the separate clear solutions and stirred. A snow-like consistency was obtained. This was further stirred for 1 h. The resulting mixture was each autoclaved for 15 min at 121 °C and 15 *psi* and left in the autoclave for about 48 hours during which the system cools to the room temperature. Each mixture was then be filtered off and placed in a desiccator till it becomes properly dried.

## 2.3. Characterization of the Synthetic Clinoptilolite

### 2.3.1 Bulk density measurement

A piece of empty measuring cylinder was weighed. A known mass of the clinoptilolite was poured into it and compacted to minimize voidage. The recorded volume in the measuring cylinder was taken and the resulting mass to volume ratio was recorded as the bulk density.

### 2.3.2 True density measurement

This was measured by water displacement method. A measured volume of water was poured into a measuring cylinder after which a weighed mass of the synthesized clinoptilolite was poured into the cylinder and the displaced volume was recorded. The resulting mass to volume ratio was taken to be the true density.

### 2.3.3 Porosity determination

Porosity of the synthesized clinoptilolite was determined using the bulk and true densities using the relation below:

$$\text{porosity } (\varepsilon) = 1 - \frac{\text{Bulk density}}{\text{True density}} \quad (1)$$

### 2.3.4 Sample characterization by XRD and XRF

The unseeded synthesized clinoptilolite from each of the rice husk based and bamboo leaves based silica gels were subjected to X-ray fluorescence (Shimadzu EDXRF-720HS) for the determination of the elemental composition, to establish the Si:Al ratio. Samples of the clinoptilolite were also subjected to x-ray diffraction (XRD) (Shimadzu XDS 2400H) diffractometer with Cu anode,  $\lambda_{\text{Cu}} = 1.541838 \text{ [\AA]}$  for crystallinity evaluation and determination of the type of zeolite formed. The XRD analysis was carried out using Cu-K alpha at wavelength of 40 kV and 40 mA.

## 2.4 Application of the Clinoptilolite in the Purification of Biogas from Cow Dung

The powdered crude synthetic clinoptilolite was applied using an approximately uniform thickness of 1 mm, on a porous support layer, folded and inserted into a pipe, connected to each batch digester. The pipe holding the clinoptilolite was drilled to create permeate paths positioned at certain interval distance from each other for the permeated molecules. Figure 1 shows the experimental rig configuration, while the schematic diagram of the flow chamber for the gas purification is shown in Figure 2. The composition of the feed and the reject streams were recorded at intervals from the in-situ measurements as before and after purification respectively over certain time using E-instrument industrial combustion analyzer (E-8500).

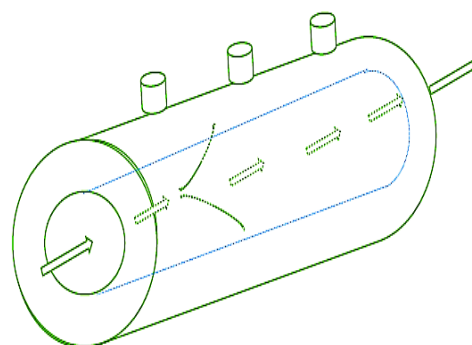
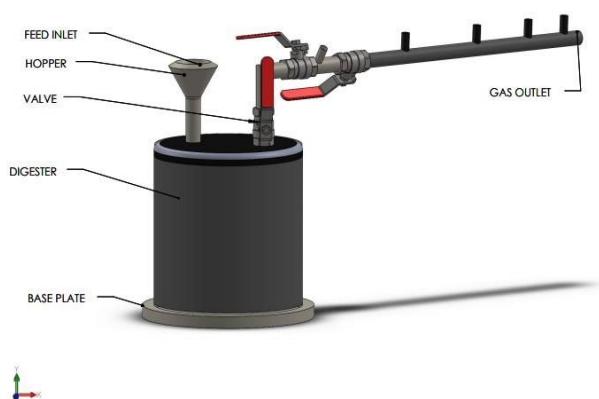


Figure 1: Set up of the biogas purification test rig at ambient conditions

Figure 2: The flow chamber for the biogas purification

## 3. RESULTS AND DISCUSSION

### 3.1. Characterization of the clinoptilolite

The unseeded clinoptilolite synthesized showed some intrinsic properties in terms of porosity, elemental and mineral compositions. It was very porous with a porosity value of 0.773 and 0.800 for rice husk and bamboo based products respectively. This indicates that it can sufficiently allow the flow of carrier-solvent of recoverable soluble gaseous solutes from it through its interstices. The bamboo based synthesized product is more favoured in this case.

The XRF analyses presented in Tables 1 and 2 show that the Si:Al ratio in the unseeded products in both syntheses is greater than 4, a major criterion in establishing the type of zeolite produced. The ratio is higher in the synthesis from rice husk compared with that from bamboo leaves.

The XRD analysis for each product of the syntheses has the crystallinity of 98.88% for the product from rice husk based formulation and mineral content similar to those reported for the family of clinoptilolite while the crystallinity of the bamboo leaves based formulation is 96.63% with more minerals of the clinoptilolite family than the rice husk based formulation as shown in Tables 3 and 4. The XRD result further reveals that consequent to the absence of seed crystals of natural clinoptilolite during the syntheses, no significant crystals of clinoptilolite was found, rather the family members. Cristobalite is one of the detected members of the family of clinoptilolite present in both products as quartz. Quartz had the sharpest peaks in both product at low  $2\theta$  values as seen on the diffraction patterns in Figures 3 and 4.

### 3.2. Application of the clinoptilolite in biogas purification

The gas purification unit was set up such that the thickness of the clinoptilolite samples, along with the fabric support and the holding wire mesh do not exceed 1 mm. The biogas generated from the digesters used composed mainly of carbon dioxide (CO<sub>2</sub>) and methane (CH<sub>4</sub>). The analyzed initial compositions of the biogas from the two digesters set up under similar conditions before purification were 48% carbon dioxide and 52% methane for digester I, and 71% carbon dioxide and 29% methane for digester II. After 95 min of passage of the feed gas from digester II through the purification unit containing the RHA – based clinoptilolite sample, the composition of the reject stream was 43% carbon dioxide and 57% methane. Likewise, after 90 min of passage of the feed gas from digester I through the purification unit containing the BLA – based clinoptilolite sample, the composition of the reject stream was the same as that with the RHA based unit.

Table 1: XRF Results showing the elemental composition of synthesized clinoptilolite using RHA as silica source

Major components	Formulae	% Composition	Trace elements	Composition (ppm)
Silicon Oxide	SiO <sub>2</sub>	94.32	Lead (Pb)	21.00
Aluminum Oxide	Al <sub>2</sub> O <sub>3</sub>	0.21	Copper (Cu)	12.97
Ferric Oxide	Fe <sub>2</sub> O <sub>3</sub>	0.19	Rubidium (Rb)	98.25
Titanium Oxide	TiO <sub>2</sub>	0.02	Cerium (Ce)	90.74
Calcium Oxide	CaO	0.55	Zinc (Zn)	34.19
Phosphorus Oxide	P <sub>2</sub> O <sub>5</sub>	0.92	Lanthanum (La)	17.03
Manganese Oxide	MnO	0.10	Strontium (Sr)	218.31
Magnesium Oxide	MgO	0.35	Yttrium (Y)	39.44
Sulphide	SO <sub>3</sub>	0.15	Barium (Ba)	564.82
Sodium Oxide	Na <sub>2</sub> O	0.01	Zirconium (Zr)	518.04
Potassium Oxide	K <sub>2</sub> O	1.24		
<b>Loss on Ignition (LOI): 1.91%</b>				

Table 2: XRF Results showing the elemental composition of synthesized clinoptilolite using BLA as silica source

Major components	Formulae	% Composition	Trace elements	Composition (ppm)
Silicon Oxide	SiO <sub>2</sub>	72.21	Lead (Pb)	18.24
Aluminum Oxide	Al <sub>2</sub> O <sub>3</sub>	8.12	Copper (Cu)	22.63
Ferric Oxide	Fe <sub>2</sub> O <sub>3</sub>	1.93	Rubidium (Rb)	112.39
Titanium Oxide	TiO <sub>2</sub>	0.09	Cerium (Ce)	120.64
Calcium Oxide	CaO	3.45	Zinc (Zn)	21.20
Phosphorus Oxide	P <sub>2</sub> O <sub>5</sub>	0.22	Lanthanum (La)	38.22
Manganese Oxide	MnO	0.07	Strontium (Sr)	401.02
Magnesium Oxide	MgO	0.64	Yttrium (Y)	41.17
Sulphide	SO <sub>3</sub>	0.36	Barium (Ba)	875.62
Sodium Oxide	Na <sub>2</sub> O	0.23	Zirconium (Zr)	512.48
Potassium Oxide	K <sub>2</sub> O	3.67		
<b>Loss on Ignition (LOI): 8.02 %</b>				

Table 3: XRD Results showing the mineral composition of synthesized clinoptilolite using RHA as silica source

S/N	2 $\theta$ /degree	Plane	Intensity	d-Value (Å)	Minerals
1	11.99	2 1 1	93.81	7.3808	Quartz
2	12.26	1 0 1	34.00	7.2183	Cristobalite
3	21.01	1 1 1	24.06	4.2289	Tridymite
4	55.16	3 1 1	29.79	1.6651	Mordenite

Table 4: XRD Results showing the mineral composition of synthesized clinoptilolite using BLA as silica source

S/N	2 $\theta$ /degree	Plane	Intensity	d-Value (Å)	Minerals
1	15.99	2 1 1	96.01	5.5422	Quartz
2	16.62	2 1 2	54.26	5.3332	Kaolinite

3	20.99	0 1 2	24.35	4.2323	Mullite
4	27.98	0 1 3	57.80	3.1889	Mordenite
5	28.36	0 0 4	58.48	3.1473	Cristobalite
6	29.99	0 2 2	25.70	2.9794	ZSm-5
7	47.99	3 1 0	23.97	1.8959	Aragonite
8	53.20	2 2 2	20.36	1.7218	Albite

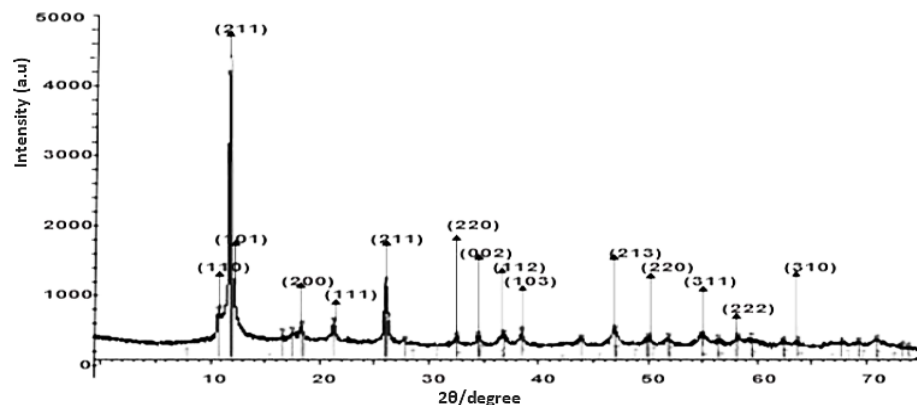


Figure 3: XRD Pattern of batch synthesized clinoptilolite using RHA as silica source

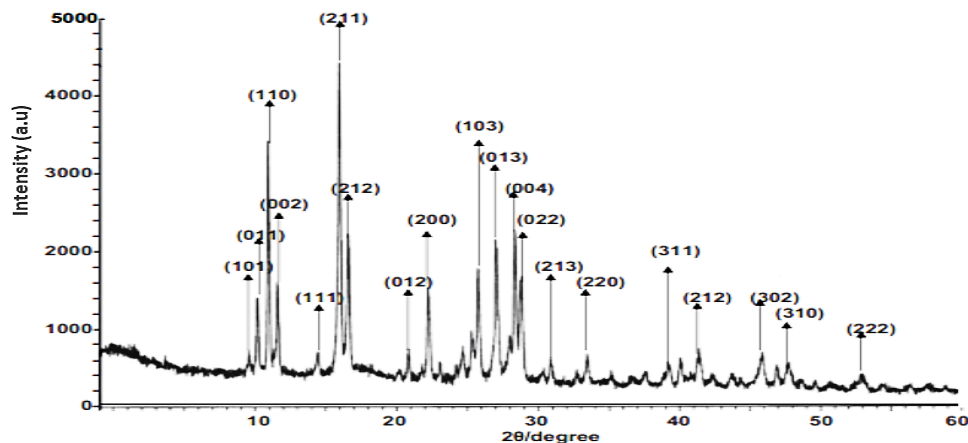


Figure 4: XRD Pattern of batch synthesized clinoptilolite using BLA as silica source

The in-place determination of the compositions of the reject stream at intervals reveals increasing composition of  $\text{CH}_4$  until after about 60 min before a noticeable increase in the  $\text{CO}_2$  fraction of the stream. This indicates the possibility of continuous permeation of  $\text{CO}_2$  through the axial path of the flowing gas stream this causes the reject stream to be leaner in  $\text{CO}_2$  and consequently richer in  $\text{CH}_4$ . The combined minerals of cristobalite, tridymite and mordenite present in the product from rice husk seems to be more potent for the purification of  $\text{CO}_2$  heavily laden stream as found in digester II. However, similar result was produced by the combination of cristobalite, mordenite, mullite, aragonite, albite and zsm-5 present in the product from bamboo leaves.

#### 4. CONCLUSION

Synthetic clinoptilolite and other family members of zeolite of almost similar properties with some natural clinoptilolite can be conveniently sourced from various silico-alumina based materials. Many of the silico-alumina based materials are cheaply available as wastes or unwanted or neglected materials but with valuable importance. The results reveals that unseeded synthetic product of the batch formulation of Chi and Sand (1983) from rice husk and bamboo leaves have the potentials to remove  $\text{CO}_2$  from biogas, even with no significant presence of clinoptilolite but with the presence minerals in its family group. The purification consequently guarantees cleaner biogas with greater calorific value and hence greater wealth and energy from wastes.

#### ACKNOWLEDGEMENTS

The authors would like to acknowledge the technical staff and the project students of the Department of Chemical Engineering, Obafemi Awolowo University for the various roles played in the course of the research.



## REFERENCES

- Ambrozova, P., Kynicky, J., Urubek, T. and Nguyen, V. D. (2017). Synthesis and modification of clinoptilolite. *Molecules*, 22, 1107.
- Blankenship, L. S. and Mokaya, R. (2022). Modulating the porosity of carbons for improved adsorption of hydrogen, carbon dioxide, and methane: a review. *Materials Advances*, 3, pp.1905 - 1930
- Castruita-De León, G., Meléndez-Ortiz, H. I., Hernández-Silva, G. C., García-Rodríguez, S. P., García-Cerda, L. A. and Montes-Luna, A. D. J. (2018) Effect of chemically modified clinoptilolite on the thermal, morphological, and gas separation properties of mixed matrix membranes. *Journal of Applied Polymer Science*, 135, 45659.
- Chi, C.-H. and Sand, L. (1983). Synthesis of Na- and K-clinoptilolite endmembers. *Nature*, 304, pp. 255-257.
- Dimitrijević, M. V., Miladinović, D. L., Ćirić, S. A., Krstić, N. S., Nikolić, J. S., Mitić, V. D. and Jovanović, V. P. S. (2019). Elemental and morphological features of thermally modified clinoptilolite as an efficient sorbent for benzo (a) pyrene extraction from water preceding GC-MS analysis. *Chemia Naissensis*, 3(2), pp. 1-23
- Englert, A. and Rubio, J. (2005). Characterization and environmental application of a Chilean natural zeolite. *International Journal of Mineral Processing*, 75, pp. 21-29.
- Farjoo, A., Sawada, J. A. And Kuznicki, S. M. (2015). Manipulation of the pore size of clinoptilolite for separation of ethane from ethylene. *Chemical Engineering Science*, 138, pp. 685-688.
- Güvenir, Ö. (2005). *Synthesis and characterization of clinoptilolite*. <https://open.metu.edu.tr/handle/11511/15333> [Accessed 28 July, 2022]
- Korkuna, O., Leboda, R., Skubiszewska-Zie, B. J., Vrublevs'ka, T., Gun'ko, V. and Ryczkowski, J. (2006). Structural and physicochemical properties of natural zeolites: clinoptilolite and mordenite. *Microporous and Mesoporous Materials*, 87, pp. 243-254.
- Kowalczyk, P., Sprynskyy, M., Terzyk, A. P., Lebedynets, M., Namieśnik, J. and Buszewski, B. (2006). Porous structure of natural and modified clinoptilolites. *Journal of colloid and interface science*, 297, pp. 77-85.
- Luna, A. D. J. M., De León, G. C., Rodríguez, S. P. G., López, N. C. F., Camacho, O. P. and Mercado, Y. A. P. (2018). Na<sup>+</sup>/Ca<sup>2+</sup> aqueous ion exchange in natural clinoptilolite zeolite for polymer-zeolite composite membranes production and their CH<sub>4</sub>/CO<sub>2</sub>/N<sub>2</sub> separation performance. *Journal of Natural Gas Science and Engineering*, 54, pp. 47-53.
- Mastinu, A., Kumar, A., Maccarinelli, G., Bonini, S. A., Premoli, M., Aria, F., Gianoncelli, A. and Memo, M. (2019). Zeolite clinoptilolite: Therapeutic virtues of an ancient mineral. *Molecules*, 24, 1517.
- Prasad, R. and Pandey, M. (2012). Rice husk ash as a renewable source for the production of value added silica gel and its application: an overview. *Bulletin of Chemical Reaction Engineering and Catalysis*, 7, pp. 1-25.



## Extraction of Bioemulsifier from *Candida tropicalis* Isolated from Banana (*Musa x paradisiaca* L.)

Abigail O. ADETOYESE<sup>1</sup>, Elizabeth F. ARANSIOLA<sup>1\*</sup>, Hezekiah A. ADENIRAN<sup>2</sup>

<sup>1</sup> Department of Chemical Engineering, Obafemi Awolowo University, Ile-Ife, Nigeria.

<sup>2</sup> Department of Food Science and Technology, Obafemi Awolowo University, Ile-Ife, Nigeria.

<sup>1</sup> [abylarry2@gmail.com](mailto:abylarry2@gmail.com), <sup>1\*</sup> [aransiolaef@gmail.com](mailto:aransiolaef@gmail.com), <sup>2</sup> [hexadeniran@gmail.com](mailto:hexadeniran@gmail.com)

\*Corresponding author

---

### ABSTRACT

Given the high expense of producing chemical-based emulsifying agents, the risk to human health, and the rising demand for natural products, biotechnologically-based compounds are gradually replacing these chemically synthesized emulsifiers. This work aimed to extract bioemulsifier from yeast strains isolated from available local fruits. Different fruit samples were collected randomly and allowed to grow on Potato Dextrose Agar (PDA) medium supplemented with 0.1 mg mL<sup>-1</sup> chloramphenicol. The expected yeast isolates were then screened by using the same medium. This resulted in 18 isolates. These isolates were identified and characterized based on morphological and biochemical tests. Isolate E3 from ripe bananas showed the best result and this was used for molecular characterization. The Blast results from the molecular test revealed 98.78% similarity with *Candida tropicalis* MN450877.1 in the NCBI database. Based on this, the strain was identified as *Candida tropicalis*. The bioemulsifier was extracted from the *Candida tropicalis* using the autoclaving method. The yield of bioemulsifier was 0.34g/3g dry yeast and emulsion activity after 24 h was 66.67%. This study has provided information on the potential, technological properties and suitability of *Candida tropicalis* isolated from ripe banana as bioemulsifier.

**Keywords:** Banana; Bioemulsifiers; *Candida tropicalis*; Yeast isolates.

### 1. INTRODUCTION

Biotechnologically-based compounds are gradually replacing the chemically produced surface-active compounds through either microbiological or enzymatic syntheses (Ahamed and Prasad, 2021). It should be obvious that water and oil do not mix. Owing to their distinct advantages over chemical surfactants, such as biodegradability, biocompatibility, non-toxicity, efficiency at low concentrations, foaming, and good selectivity at various temperatures, pH and salinities. Bioemulsifiers are known as surface active biopolymers compounds that are that are capable of stabilizing oil-in-water emulsions and are critical in a variety of industrial applications (Thraeib *et al.*, 2022). Bioemulsifiers are produced by bacteria, moulds, and yeast and may be found in a variety of natural resources. Bioemulsifier has a greater molecular weight than biosurfactants (Ribeiro *et al.*, 2020). In general, high-molecular-mass biosurfactants outperform low-molecular-mass biosurfactants as emulsifiers.

Due to the wide application of yeasts and it is Generally Regarded as Safe (GRAS) status, it is more easily accepted than other microorganisms in bioemulsifier production. Although yeast is present everywhere, it is most typically isolated from samples that are high in sugar. Fruits, berries, and plant exudates are a few excellent examples. Some yeast varieties are connected to soil and insects. It is necessary to consider certain physiological characteristics while evaluating a yeast strain for industrial usage. Numerous insoluble substrates have been fermented using *Candida* species, and they produce surface-active compounds (Alizadeh-Sani *et al.*, 2018). A rich source of mannoproteins, -glucans and glucomannan with anti-neoplastic, anti-genotoxic, and antioxidative effects is the biomass of *Candida* yeasts. The generation of extracellular metabolites such as ethanol, erythritol, citric acid, biosurfactants, xylitol and exopolysaccharides are one of the numerous uses of *Candida* yeasts in biotechnology. These ingredients are employed in the cosmetic, food processing and pharmaceutical industries (Kieliszek *et al.*, 2017). One of the most significant *Candida* species is *Candida tropicalis*. As an osmotolerant microorganism with the capacity to endure high salt concentrations, *C. tropicalis* may be crucial for the persistence of fungi in saline settings. This species is appropriate for use in biotechnology procedures because of its physiological trait. This study aims at extracting bioemulsifier from

yeast strains isolated from available local fruits and vegetables such as Banana, Orange, Plantain, Apple, Grapes and Tomatoes.

## 2. METHODOLOGY

### 2.1 Isolation of Yeast Strains from various Fruit Sources

Yeast strains are frequently connected to an environment where there is a lot of sugar. Fruit samples of Banana, Orange, Plantain, Apple, Grape and Tomatoes were collected randomly from the new market of Obafemi Awolowo University. The fruits' seeds were removed after being peeled. The samples were aseptically pressed or mashed as necessary, and the fruit pulp was sieved using a clean, sterile muslin cloth. They were then put into containers and kept in the refrigerator for future use. Yeast isolates were obtained using the dilution plate count technique (Bakare *et al.*, 2019). The serial dilution was prepared using sterile distilled water as diluents and about 1ml of each fruit pulp was used as a yeast source. This was further serially diluted in a test tube using 10 ml of sterile distilled water until dilution of  $10^{-6}$  dilutions. About 0.1 ml of each of the odd number serial dilutions were spread on top of  $39 \text{ g L}^{-1}$  PDA (potato dextrose agar) with chloramphenicol added at  $0.1 \text{ mg mL}^{-1}$ . Then, the composition was further incubated for 24-48 h at  $30 \text{ }^{\circ}\text{C}$ .

### 2.2 Yeast Screening

Using potato dextrose agar supplemented with chloramphenicol ( $0.1 \text{ g L}^{-1}$ ), yeast isolates were screened. According to the procedures outlined by Nasir *et al.* (2017), the selected isolates' cell morphology and how it appears on the PDA medium were studied. After being cultivated for 18 to 24 h, yeast isolates were aseptically selected, streaked on a PDA medium, and then incubated for 48 h at  $30 \text{ }^{\circ}\text{C}$ . All of the isolates produced were tested as yeast cultures and then evaluated further for their capacity to break down glucose, lactose, and sucrose mixed with the substrate without aeration at  $30 \text{ }^{\circ}\text{C}$ .

### 2.3 Yeast Identification

The characteristics of the yeast isolates were determined macroscopically by observing and taking note of the surface, shape, elevation, color, and morphology of the yeast isolates. The yeast isolates were also viewed under a microscope using the wet mount techniques cited by Nasir *et al.* (2017).

### 2.4 Biochemical Characterization of the Yeast Isolate

The yeast isolates can be identified by the changes in the indicator color when the yeast culture assimilates carbohydrates or fermentation tests, ethanol tolerance and thermo-tolerance.

#### 2.4.1 Sugar fermentation tests

The isolated yeasts were subjected to a sugar fermentation test which involves the use of 1% each of glucose, sucrose and lactose using 0.1% of Bromocresol purple indicator. The bromocresol was added to  $8 \text{ g L}^{-1}$  of yeast extract and the sugars were added too. Ten millilitres (10 ml) of each of the prepared sugars was introduced into the test tubes. Inverted Durham tubes were introduced into the test tubes and autoclaved. A sterile inoculating loop was used to pick colonies of each isolate and aseptically inoculated into the test tubes, then incubated for 48 h at  $37 \text{ }^{\circ}\text{C}$ .

#### 2.4.2 Ethanol tolerance

The yeast isolates were screened for their efficiency in ethanol; by enabling yeast to grow in 5%, 10%, and 20% ethanol broth, the tolerance of each isolate was investigated. The ethanol broth composes of 8 g/l of yeast extract, 0.1% bromocresol and absolute ethanol (5%, 10%, 20%). Each test tube received 10 ml of the prepared medium, which was then sterilized in an autoclave at  $121 \text{ }^{\circ}\text{C}$  for 15 mins. After allowing it to cool, the medium in the flasks was inoculated with a loop full of yeast isolates aseptically, and then incubated at  $37$  for 48 h (Bakare *et al.*, 2019). After incubation, the color change was indicative of a positive reaction.

#### 2.4.3 Detection of thermotolerance

Thermotolerance of the selected yeast isolates was detected using the PDA liquid medium. Test tubes containing ten milliliters of the medium were autoclaved and cooled. A 48-h-old selection of yeast isolates was then inoculated into a half loop. Every 24 h, the optical density of each tube was measured against a blank medium using a spectrophotometer set to 600 nm. All cultures were incubated at 30, 37, and  $43.5 \text{ }^{\circ}\text{C}$  for three days.

#### 2.4.4 Detection of Growth with Time

To detect the growth of the isolates with time, the isolates were inoculated into a 5% sterile glucose solution. The samples were withdrawn every 24 h for 72 h, and absorbance was taken with a spectrophotometer.

### 2.5 Molecular Characterization of Yeast Strains

Some fungal isolates cannot be taxonomically identified from phenotypic characteristics. To prevent mistakes in the identification of organisms with similar biochemical profiles, a molecular analysis of isolates is still necessary. By

analyzing the nuclear DNA's (rDNA) through the Internal Transcribed Spacer (ITS) region, yeast isolates may be identified. DNA of the 48 h old test organism was first extracted with a test kit. The Quick-DNA™ Fungal/Bacterial Miniprep Kit (Zymo Research, Catalogue No. D6005) was used to extract genomic DNA from the cultures.

The 16S target area was amplified using the universal primer 27F and 1492R (White *et al.*, 1990). The respective sequence of these primers is ITS-1: 5'-TCCGTAGGTGAACCTGCGG-3' and ITS-4: 5' TCCTCCGCTTATTGATATGC-3'. Using the primers highlighted above and One Taq® Quick-Load® 2X Master Mix (NEB, Catalogue No. M0486), the ITS target area was amplified. The PCR results were run on a gel, and the extracted fragments were then purified using Zymo Research's ZR-96 DNA Sequencing Clean-up Kit™ (Catalogue No. D4050) and forward and reverse sequenced using Nimagen's Brilliant Dye™ Terminator Cycle Sequencing Kit V3.1, BRD3-100/1000. For each reaction and each sample, the purified fragments were examined using the ABI 3500xl Genetic Analyzer (Applied Biosystems, ThermoFisher Scientific). Sequences were subsequently employed for taxonomic identification using a BLAST search and compared to the Gen Bank database (<http://www.ncbi.nlm.nih.gov/BLAST/>).

## 2.6 Extraction of Bioemulsifier

The technique of Torabizadeh *et al.* was modified to extract the bioemulsifier from *Candida tropicalis* cells. The technique was used to purify the bioemulsifier (Dikit *et al.*, 2010). The supernatant was mixed with three volumes of acidic ethanol (ethanol that contains 95% alcohol and 10 mL/L acetic acids) and incubated for the duration of the precipitation at 3–4 °C. Once the precipitate has been centrifuged for 10 mins at 10,000 rpm, it will then be freeze-dried.

## 2.7 Analysis of Bioemulsifier

The bioemulsifier's molecular weight was estimated using the (SDS-PAGE) sodium dodecyl sulphate gel electrophoresis method with 100 g L<sup>-1</sup> resolving gel (Dikit *et al.*, 2010). BSA was used as the standard to quantify protein using the Folin-Ciocalteu reagent as outlined by (Lowry *et al.*, 1951) (Spectrophotometer Perkin, Elmer). The technique of Dubois *et al.* (1956) was used to colorimetrically measure total carbohydrates.

# 3. RESULTS AND DISCUSSIONS

## 3.1 Isolation of Yeasts

By using a PDA medium, 12 microbial isolates were recovered from each substrate (tomatoes, oranges, apples, bananas, plantains and grapes), and each of the isolates was further screened by subculturing using a selective medium to obtain pure yeast colonies. Previous research has revealed that samples high in sugar, such as flowers, leaves, tree exudates, sweet fruits, roots, grain, dung, and soil, and insects are commonly associated with yeast (Tikka *et al.*, 2013).

## 3.2 Yeast Screening

Further screening in the PDA medium supplemented with chloramphenicol resulted in 18 isolates, being able to show the yeast's morphological character. The eighteen isolates (A1, and A9 from over ripe oranges, B1, B6 and B10 from overripe plantain, C2, C8 and C10 from overripe apple, D4, D6 and D11 from rotten tomatoes, E3, E4, E7 and E12 from overripe banana, F4, F8 and F11 from fermented grape juice) were selected after being cultivated on PDA agar at 30 °C. Therefore, those 18 isolates were continuously assayed for their capability to use.

## 3.3 Growth of Isolates

After 3 days of incubation at 30 °C, colonies were cream, smooth, and yeast-like on the surface of the PDA media. The summary of the results is shown in Table 1.

## 3.4 Microscopic Observation

The cell morphology of the selected isolates observed under the microscope shows the presence of round yeasts with single, pairs, or triple budding, and the germination consists of small, medium, and large types of budding. After 48 h of incubation at 30 °C, the isolates were found to be at the budding stage with cream color and the elevation raised. The microscopic morphology of isolates in the form of blastopores that are round, cylindrical, or ovoid short and long affected by its strain and confirmed to be yeast.

## 3.5 Biochemical Characterization

### 3.5.1 Sugar fermentation test

The isolated yeast varied in terms of three distinct sugars (Table 1). The strain used glucose (dextrose), and sucrose, but fail to grow on lactose indicating they are diverse in sugar utilization. The fermentation was verified by the change in the media color from wine to yellow. Observations were made following a 48-h inoculation.

### 3.5.2 Ethanol tolerance

The isolate was chosen because it passed the ethanol tolerance test for yeast. It was shown that B3 and E3 can grow faster in 5%, slightly in 10% and weakly in 20% containing liquid media of yeast extract and bromocresol (Table 2).

Table 1: Sugar fermentation

Code	A1	A2	A3	B1	B2	B3	C1	C2	C3	D1	D2	D3	E1	E2	E3	F1	F2	F3
Glucose	++	++	+	+	-	++	+	+	+++	-	++	++	++++	++	+++	-	+++	+++
Gas production	Yes	Yes	Yes	Yes	Yes	Yes	Yes	Yes	Yes	Yes	Yes	Yes	Yes	Yes	Yes	Yes	Yes	Yes
Lactose	-	-	-	-	-	-	-	-	-	-	-	-	-	-	-	-	-	-
Gas production	No	No	No	No	No	No	No	No	No	No	No	No	No	No	No	No	No	No
Sucrose	++	++	+	+	+	++	+	+	-	-	+	+	++++	++	+++	-	-	-
Gas production	No	No	No	No	No	No	No	No	No	No	No	No	No	No	No	No	No	No

- No change    + weak yellow    ++ Dark yellow    +++ light yellow    ++++ Bright yellow

Table 2: Ethanol tolerance

Code	A1	A2	A3	B1	B2	B3	C1	C2	C3	D1	D2	D3	E1	E2	E3	F1	F2	F3
5% ethanol-containing media	++	++	++	++	++	++	+	+	+	++	++	++	++	++	++	++	++	++
10% ethanol-containing media	+	+	+	+	+	++	+	+	+	++	+	-	+	+	++	+	+	+
20% ethanol-containing media	+	+	+	+	+	+	+	+	+	+	+	-	+	+	++	-	+	+

- No change    + weak yellow    ++ Dark yellow

The two isolates' highest growth was observed in 5% ethanol-containing media. The change in color shows the growth after 7 days at 5%, 10%, and 20% of ethanol-containing liquid media. The concentrations of ethanol play a significant role in regulating the fermentation process. It has been proven that fermentation cultures with incredibly high ethanol concentrations can depress or hinder the fermentation process. A similar result with Nasir *et al.* (2017) for E3 isolates that tolerated up to 20% ethanol was seen in the present investigation, which is much more consistent with the other results (Table 2).

### 3.5.3. Effect of temperature on growth

Eighteen media containing yeast cells were incubated for 48 h at 30 °C, 37 °C, and 43 °C. From Figure 2, all isolates were able to grow at 30 °C up to 37 °C and some up to 43 °C. The maximum growth was found to be 37 °C with code E3 with the highest growth. The isolates can be classified as mesophilic. The effect of temperature is consistent with earlier research (Sulman and Rehman, 2013). For this reason, the operating temperature in standard yeast fermentation reactors must be kept between 30 and 35 °C. It has been observed from previous studies that yeast cell viability was

adversely affected by high temperatures. However, there are few reports on the effective selection and isolation of yeasts capable of growing or fermenting at temperatures of at least 40 °C (Nasir *et al.*, 2017).

### 3.5.4 Effect of time on growth

The growth pattern was studied by growing the isolates in a 5% sterile glucose solution, and the optical density was observed for each isolate at an interval of 24 h (Figure 3). The growth curve was shown for the best three isolates.

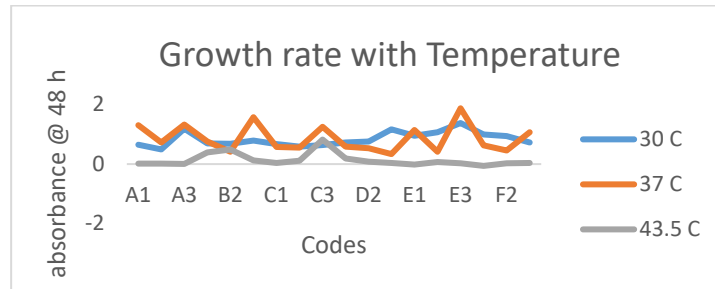


Figure 2: Effect of temperature on Growth rate

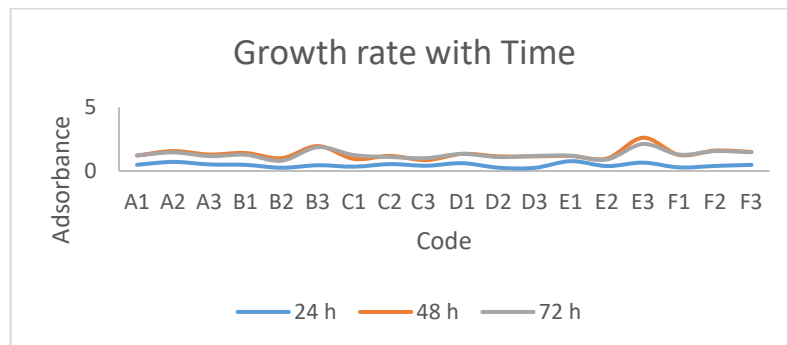


Figure 3: Effect of time on Growth rate

### 3.6 Molecular Identification of Yeast Strains

Due to the high accuracy of identification by molecular techniques, it was used in parallel with biochemical tests for the identification of species. After the isolates were identified and characterized based on morphological and biochemical tests, Isolate E3 from ripe bananas showed the best result and this was used for molecular identification. The results of the sequencing domain of the universal primer 27F and 1492R are used to amplify the 16S target region. Agarose gel electrophoresis was performed to resolve the amplified products, the photographic image of an agarose gel indicating the amplification of the ITS target region. The Blast results correspond to the similarity between the sequence queried and the biological sequences within the NCBI database. It revealed 98.78% similarity with *C. tropicalis* MN450877.1. Based on the result, the strain was identified as *Candida tropicalis*.

### 3.7 Extraction of bioemulsifier

The results of the autoclaving time at 2 h had a not very clear band with a range of molecular weights at 7.5 KDa, 16.90 KDa, and 34.2 KDa in gel electrophoresis (Figures 4 and 5). The yield of bioemulsifier was 0.34 g/3 g and emulsion activity after 24 h was 66.67%. The protein and carbohydrate content of this bioemulsifier are estimated to be 30.41 mg g<sup>-1</sup> (11.32%) and 238.54 mg g<sup>-1</sup> ( 88.675%) respectively which is similar to the composition of structural mannoprotein (approximately 10% protein and 90 %) (Barriga *et al.*, 1999) .

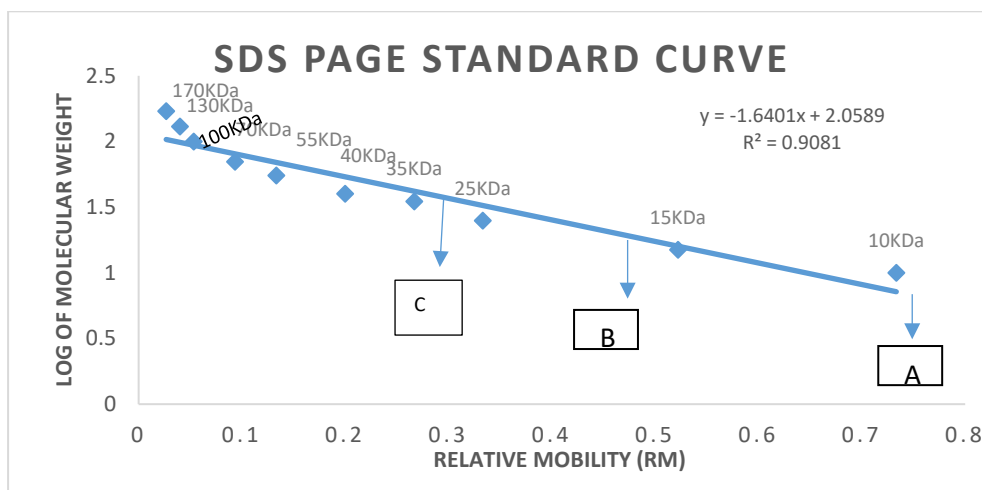


Figure 4: Standard Plots for the Determination of Molecular weight of bioemulsifier

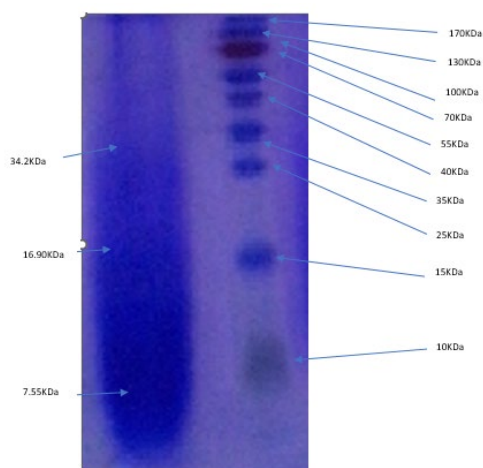


Figure 5: SDS-PAGE with Coomassie brilliant blue staining of bioemulsifiers extracted after 2 h of autoclaving and standard prestaining.

#### 4.CONCLUSION

This work has revealed that a biotechnologically useful yeast could be isolated from an underutilized, readily available waste product like overripe fruits; where bioemulsifier could be extracted. Different yeast strains were isolated, screened, and characterized biochemically and molecularly. This study has provided information on the potential, technological properties and suitability of *Candida tropicalis* isolated from ripe banana as bioemulsifier.

## REFERENCES

- Ahamed, M. I. and Prasad, R. (2021). *Microbial Biosurfactants: Preparation, Properties and Applications*, Springer Nature.
- Alizadeh-Sani, M., Hamishehkar, H., Khezerlou, A., Azizi-Lalabadi, M., Azadi, Y., Nattagh-Eshstivani, E., Fasihi, M., Ghavami, A., Aynehchi, A. and Ehsani, A. (2018). Bioemulsifiers Derived from Microorganisms: Applications in the Drug and Food Industry. *Advanced pharmaceutical bulletin*, 8, 191.
- Bakare, V., Abdulsalami, M., Onusiriuka, B., Appah, J., Benjamin, B. and Ndibe, T. (2019). Ethanol Production from Lignocellulosic Materials by Fermentation Process Using Yeast. *Journal of Applied Sciences and Environmental Management*, 23, 875-882.
- Barriga, J. A., Cooper, D. G., Idziak, E. S. and Cameron, D. R. (1999). Components of the Bioemulsifier from *S. Cerevisiae*. *Enzyme and Microbial Technology*, 25, 96-102.
- Dikit, P., Maneerat, S., Musikasang, H. and H-Kittikun, A. (2010). Emulsifier Properties of the Mannoprotein Extract from Yeast Isolated from Sugar Palm Wine. *Science Asia*, 36, 312-318.
- Dubois, M., Gilles, K. A., Hamilton, J. K., Rebers, P. T. and Smith, F. (1956). Colorimetric Method for Determination of Sugars and Related Substances. *Analytical chemistry*, 28, 350-356.
- Kieliszek, M., Kot, A. M., Bzducha-Wróbel, A., Błażejczak, S., Gientka, I. and Kurcz, A. (2017). Biotechnological Use of *Candida* Yeasts in the Food Industry: A Review. *Fungal Biology Reviews*, 31, 185-198.
- Lowry, O., Rosebrough, N., Farr, A. and Randall, R. (1951). Protein Measurement with the Phenol Folin Reagent. *J Biol Chem*, 193, 265-275.
- Nasir, A., Rahman, S. S., Hossain, M. M. and Choudhury, N. (2017). Isolation of *Saccharomyces Cerevisiae* from Pineapple and Orange and Study of Metal's Effectiveness on Ethanol Production. *European Journal of Microbiology and Immunology*, 7, 76-91.
- Ribeiro, B. G., Guerra, J. M. and Sarubbo, L. A. (2020). Biosurfactants: Production and Application Prospects in the Food Industry. *Biotechnology Progress*, 36, e3030.
- Sulman, S. and Rehman, A. (2013). Isolation and Characterization of Cellulose Degrading *Candida Tropicalis* W2 from Environmental Samples. *Pak J Zool*, 45, 809-16.
- Thraeib, J. Z., Altemimi, A. B., Jabbar Abd Al-Manhel, A., Abdelmaksoud, T. G., El-Maksoud, A. a. A., Madankar, C. S. and Cacciola, F. (2022). Production and Characterization of a Bioemulsifier Derived from Microorganisms with Potential Application in the Food Industry. *Life*, 12, 924.
- Tikka, C., Osuru, H. P., Atluri, N., Raghavulu, P. C. V., Mannur, I. S., Prasad, U. V., Aluru, S. and Bhaskar, M. (2013). Isolation and Characterization of Ethanol Tolerant Yeast Strains. *Bioinformation*, 9, 421.
- Torabizadeh, H., Shojaosadati, S. and Tehrani, H. (1996). Preparation and Characterisation of Bioemulsifier From *Saccharomyces Cerevisiae* and Its Application in Food Products. *LWT-Food Science and Technology*, 29, 734-737.





## Application of Box-Behnken Design in the Leaching Kinetics of Dolomite in Hydrochloric Acid (HCl)

Isaac Adekunle JOSEPH<sup>1\*</sup>, Elijah Olawale AJALA<sup>1</sup>, AHMED El-Imam Amina<sup>2</sup>, Mary Adejoke AJALA<sup>1</sup>

<sup>1</sup>Department of Chemical Engineering, University of Ilorin, Nigeria

<sup>2</sup>Department of Microbiology, University of Ilorin, Nigeria

<sup>1\*</sup>[isaacchemeng@yahoo.com](mailto:isaacchemeng@yahoo.com), <sup>1</sup>[olawaleola01@yahoo.com](mailto:olawaleola01@yahoo.com), <sup>2</sup>[amkmusty@yahoo.com](mailto:amkmusty@yahoo.com), <sup>1</sup>[ajala.ma@unilorin.edu.ng](mailto:ajala.ma@unilorin.edu.ng)

\* Correspondence author

### ABSTRACT

A more simplified approach of kinetic study of the leaching of dolomite in HCl using Box-Behnken Design was investigated in this study. Atomic absorption spectroscopy analysis shows that 54.14% calcium and 39.66% magnesium are the major elemental composition of dolomite, while the remaining 6.20 % is considered to be impurities. Dolomite was leached in a solution of HCl at an acid concentration between 0.5 and 2.5 M, temperature between 30 and 80 °C and reaction time between 10 and 40 minutes. The impurities were separated by filtration. A quadratic model with a coefficient of determination ( $R^2$ ) of 0.9465, an **adjusted  $R^2$**  of 0.9222, and a **predicted  $R^2$**  of 0.8615 best represent the leaching study. The analysis of variance revealed that acid concentration and leaching time enhanced the leaching process. At 50 °C, 10 minutes and 2 M, leaching efficiency of 97.67 % was predicted, while 96.998 % was achieved. Atomic absorption spectroscopy confirms the concentration of calcium and magnesium ions in the filtrate at optimum to be 232.545 ppm and 18.087 ppm, respectively. The developed quadratic model equation in this study was used to study the leaching kinetics of dolomite under different process conditions. The exponential curve model confirms the first order kinetics of the leaching process. Hence, Box-Behnken Design is a suitable novel approach to determine reaction kinetics.

**Keywords:** Acid concentration, Dolomite, Kinetics, Temperature, Time.

### 1.0 INTRODUCTION

The usefulness of dolomite ore is limited without a proper understanding of the appropriate process conditions for leaching and the chemistry behind the leaching process. The leaching process enhance the removal of silica as the major impurity (Baba *et al.*, 2014; Pultar *et al.*, 2019; Are *et al.*, 2021) is separated from the dolomite while the soluble components such as calcium carbonate and magnesium carbonate (Pultar *et al.*, 2019; Are *et al.*, 2021; Ajala *et al.*, 2019) go into the solution. Establishing the appropriate leaching conditions and the kinetics of the leaching process will help the process engineers in designing a suitable reactor with the appropriate size and volume as well as also putting the necessary safety measures in place for the smooth operation of the reactor (Faraji *et al.*, 2020).

Several attempts have been made in the metallurgical industry to develop useful products out of the naturally occurring mineral deposits across the globe (Massaro *et al.*, 2018; Faraji *et al.*, 2020; Tang *et al.*, 2021). The outcome of some of the studies is not implementable due to the high cost of implementation resulting from the process conditions, and inaccurate and inadequate experimental data (Faraji *et al.*, 2020). On the other hand, some of the studies only rely on the crude method of generating experimental data from laboratory studies. This is not only time-consuming and cumbersome but comes with the high cost of conducting research. The choice of Box-Behnken Design (BD) is due to better design levels between the independent variables and the lower number of experimental runs under response surface methodology (Chellapan *et al.*, 2021; Challadurai *et al.*, 2021). BD has been reported in several studies (Joseph *et al.*, 2021; Omonije *et al.*, 2021) but its use has been narrowed down to predicting only experimental conditions. For a novel application of BD, this study was used to established the kinetics of the reaction between HCl and dolomite from the developed model equation of BD without the conventional cumbersome experimental work.

### 2.0 MATERIALS AND METHODOLOGY

#### 2.1 Materials

Composite sample of the dolomite ore was collected from Oreke village, Ifelodun Local Government, Kwara State, Nigeria and milled into powder. Analytical grade hydrochloric acid produced by Guangdany Guanghai Chemical Factory Co. Ltd. Shanfau, Guandang, China was used for the study.

#### 2.2 Methodology

##### 2.2.1 Leaching study

Prior to the leaching of dolomite, elemental analysis using atomic absorption spectroscopy was carried out to determine its composition. The numerical factors that are required for Design Expert 11.0 to carry out the experimental design using Box-Behnken Design are presented in Table 1. Dolomite leaching was carried out in a 500 ml conical flask reactor. The reactor containing 100 ml of the known concentration was preheated on a magnetic stirrer to the reaction temperature. 3 g of the dolomite ore was poured into the reactor and the content was stirred at a constant agitation speed of 900 revolutions per hour. The reaction was allowed to continue until it reaches the specified reaction time. After the reaction, the reactor mixture was filtered and subjected to AAS analysis while the residue oven-dried before its weight determination and calculation of the leaching efficiency in equation 1. The entire procedure was repeated for the remaining experimental conditions in Table 2.

$$\text{Leaching Efficiency (\%)} = \frac{\text{Mass of dissolved dolomite} \times 100 \%}{\text{Initial Mass of dolomite}} \quad (1)$$

Table 1: Independent numerical variables for the leaching of dolomite in HCl

Factor	Name	Minimum	Maximum	Coded Low	Coded High	Mean	Std. Dev.
A	Temperature (°C)	30.00	80.00	-1 ↔ 30.00	+1 ↔ 80.00	55.00	17.68
B	Time (Minutes)	10.00	40.00	-1 ↔ 10.00	+1 ↔ 40.00	25.00	10.61
C	Conc (M)	0.5000	2.50	-1 ↔ 0.50	+1 ↔ 2.50	1.50	0.7071

### 2.2.2 The kinetic study of dolomite leaching in HCl via Box-Behnken Design

The leaching kinetic was carried out by imputing the different variations of acid concentration from 0.5 to 2.5 M and reaction time from 10 to 50 minutes at constant optimum temperature into the developed model equation 2 from Box-Behnken Design.

## 3.0 RESULTS AND DISCUSSION

The atomic absorption spectroscopy shows that the dolomite ore contain calcium (54.14 %) and magnesium (39.66 %) as the major metallic elements, while the remaining 6.20 % is considered to be impurities. The filtrate at the optimum leaching efficiency is expected to contain the highest amounts of elemental composition. Hence, at the optimum leaching efficiency, the concentration of calcium and magnesium ions in the filtrate are 232.545 ppm and 18.087 ppm, respectively.

### 3.1 Statistical optimization of the leaching of dolomite in HCl

The leaching conditions at each of the experimental runs and the leaching efficiency is presented in Table 2. The lowest leaching efficiency of 62 % was recorded at the temperature of 80 °C, time of 25 minutes, and acid concentration of 0.5 M. However, a higher leaching efficiency of 67.85 % was predicted by Design Expert Software with a residual of -5.85. The highest actual leaching efficiency of 96.7 % was achieved at leaching conditions of 30 °C, 25 minutes, and an acid concentration of 2.5 M. A very close leaching efficiency of 96.8 % was predicted by the Design Expert 11.0 software with a residual value of -4.2954. The total residual value of -0.02 is in the neighborhood of zero, this is an indication that the predicted leaching efficiency is very close to the actual leaching efficiency.

The ANOVA for the leaching of dolomite in HCl is presented in Table 3. According to Joseph *et al.* (2021), significant model terms (P-values less than 0.05) are the independent variable that had either positive or negative influence on the leaching of dolomite in HCl. In this study, time (B) and acid concentration are the only individual factors with significant model terms. Interaction between time and acid concentration (BC) also well as the square of the acid concentration (C<sup>2</sup>) all have a significant effect on the leaching efficiency. A significant model equation is used to determine the value of the dependent variable if the values of the independent variables are specified. In this study, significant model equations 2 and 3 with a P-Value of < 0.0001 are the developed coded and actual factor equations for predicting the value of the leaching efficiency of dolomite in HCl. This is a more simplified approach to obtaining the leaching efficiency of dolomite in mineral acids without undergoing cumbersome laboratory experiment equations. The Fit statistic shows that the developed quadratic equations 2 have a high predicted R<sup>2</sup> of 0.8615 which is close to the adjusted R<sup>2</sup> of 0.9222 and R<sup>2</sup> of 0.9465. The adequate precision value of 17.6317 in this study is much higher than the minimum base value of 4 required for a good model (Omonije *et al.*, 2021). This is an indication that the developed model equation has high prediction efficiency.

### Final Equation in Terms of Actual Factors

$$\text{Leaching Efficiency (\%)} = +30.76577 + 0.003950 \text{ Temperature} + 0.587833 \text{ Time} + 56.80417 \text{ Conc} - 0.266667 \text{ Time} * \text{ Conc} - 11.99042 \text{ Conc}^2 \quad (2)$$

Table 2: Dependent and independent variables for the leaching of dolomite in HCl

Run	A: Temperature (°C)	B:Time (Minutes)	C:Conc (M)	Leaching Efficiency (%)		
				Actual	Predicted	Residual
1	55	25	1.5	95.20	93.9	1.29
2	80	25	0.5	62.00	67.85	-5.85
3	80	40	1.5	96.00	96.82	-0.82
4	55	40	0.5	76.00	74.57	1.43
5	55	25	1.5	95.20	93.91	1.29
6	80	25	2.5	95.33	96.18	-0.85
7	30	40	1.5	92.33	96.63	-4.30
8	55	25	1.5	95.00	93.91	1.09
9	55	40	2.5	96.00	94.91	1.10
10	80	10	1.5	95.13	91.19	3.94
11	30	25	2.5	96.67	95.98	0.69
12	55	25	1.5	95.30	93.91	1.39
13	30	10	1.5	86.00	90.99	-4.99
14	55	10	0.5	60.33	60.93	-0.60
15	30	25	0.5	72.67	67.65	5.02
16	55	10	2.5	96.33	97.27	-0.94
17	55	25	1.5	95.00	93.91	1.09

Table 3: ANOVA for reduced quadratic model of dolomite leaching in HCl

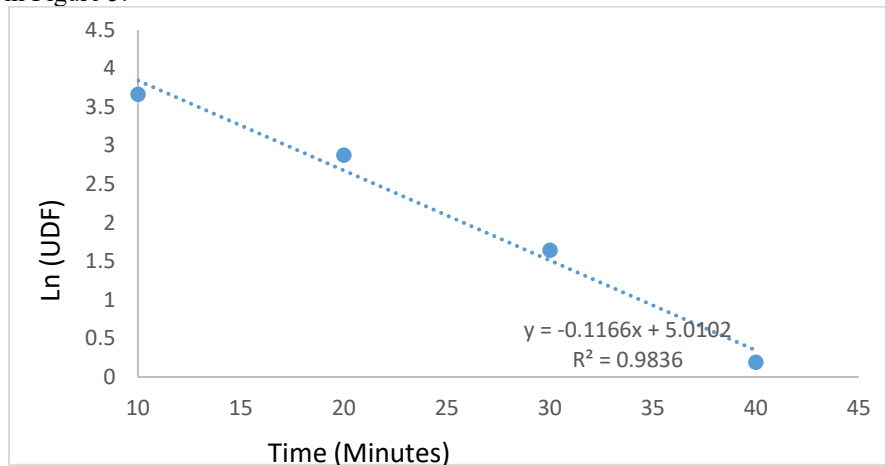
Source	Sum of Squares	Df	Mean Square	F-value	p-value	Remarks
Model	2341.95	5	468.39	38.93	< 0.0001	significant
A-Temperature	0.0780	1	0.0780	0.0065	0.9373	in significant
B-Time	63.51	1	63.51	5.28	0.0422	Significant
C-Conc	1605.46	1	1605.46	133.44	< 0.0001	Significant
BC	64.00	1	64.00	5.32	0.0416	Significant
C <sup>2</sup>	608.91	1	608.91	50.61	< 0.0001	Significant
Residual	132.34	11	12.03			
Lack of Fit	132.27	7	18.90	1049.75	< 0.0001	
Pure Error	0.0720	4	0.0180			
Cor Total	2474.29	16				

### 3.1.2 Optimum point determination for the leaching of dolomite in hydrochloric acid

The optimum point gives the best set of conditions between the dependent and independent variables for any process. Sequel to the analysis of variance on the experimental outcome, the identification of the optimum point for the leaching of dolomite in HCl will further provide useful information that will save time, energy, and cost in dolomite ore processing. At optimization constraints, the temperature was kept constant at 50 °C, since its effect does not show an appreciable effect on the leaching efficiency. From the analysis of the single effect of time on the leaching efficiency, time has little contribution to the leaching process. Therefore, at minimum reaction time, a high leaching efficiency could still be achieved. The acid concentration was kept constant at 2 M as a result of the highest leaching show at that point. At the optimum leaching conditions (20 °C, 10 minutes, and 2 M), 97.1549 % leaching efficiency was predicted and this was validated at 96.998 %. This is above the 88 % leaching efficiency of dolomite in nitric acid at 40 °C and 0.1 M by Pultar *et al.* (2019). The optimum leaching of dolomite in HCl from this study is comparable to the 99.3 % leaching efficiency reported by Baba *et al.* (2014), however, a higher leaching temperature of 80°C and time of 120 minutes were involved at 2 M HCl concentration. Abali *et al.* (2011), reported 83 % leaching of dolomite in 2 M HCl, 50 °C, and 5 minutes leaching time.

### 3.2 Evaluation of the kinetics of dolomite leaching in HCl via the use of Box-Behnken Design.

The order of any chemical reaction is an important determinant factor on how fast the chemical reaction proceeds. As the reaction between dolomite and HCl proceeds, the total starting fraction of unreacted dolomite decreases while the fraction of dolomite leached into the HCl increases as reaction time increases. A simple approach of determining if a reaction is first-order kinetics is to use an exponential profile approach (Peijun *et al.*, 2004; Vincent *et al.*, 2011). The plot of the natural logarithm of the unreacted dolomite fraction (UDF) against time (Figure 3) gave a linear curve with  $R^2$  value of 0.9836 while that of the UDF against time gave (Figure 4) an exponential curve. This is an indication that the leaching of dolomite in HCl follows first-order kinetics and is in agreement with the first-order kinetics predicted by Yildirim (2008) and Baba *et al.* (2004) using shrinking core model. An inverse relationship exist between the UDF and the reacted dolomite fraction in Figure 5.



UDF: Unreacted Dolomite Fraction

Figure 3: Plot of  $\ln(\text{UDF})$  against time for the leaching of dolomite in HCl

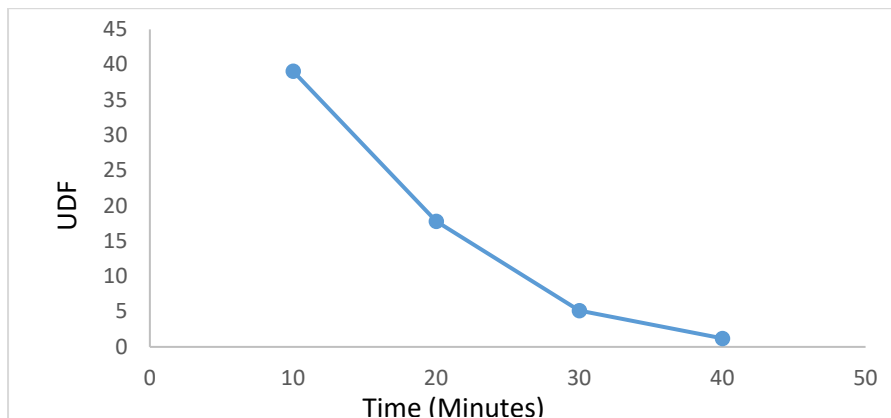


Figure 4: First order profile for the leaching of dolomite in HCl

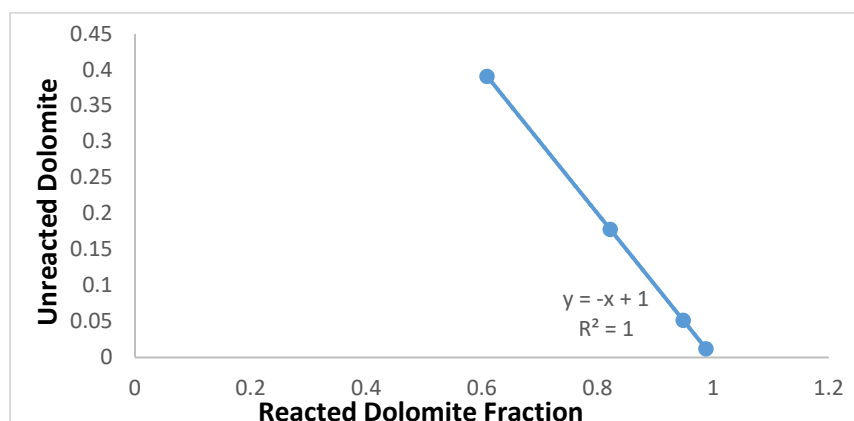


Figure 5: Plot of UDF and the reacted dolomite fraction

#### 4.0 CONCLUSION

The optimization and kinetics of dolomite leaching in hydrochloric acid were investigated. The outcome of the analysis of variance shows that the developed model equation is significant. Both leaching time and acid concentration have both single and interactive effects on the leaching process. At the optimum leaching condition of 50 °C, 10 minutes, and 2 M HCl concentration, 97.67 % leaching efficiency was predicted, while 96.998 % was validated. The developed model equation from Box-Behnken Design was able to predict the kinetics of the leaching process with a first-order reaction kinetics based on exponential profile model.

#### REFERENCES

- Abali, Y., Bayca, S. U., Arisoy, K. and Vaizogullar, A. I., 2011. Optimization of dolomite ore leaching in hydrochloric acid solutions. *Physicochemical Problems of Mineral Processing*, 46(1), pp.253-262.
- Ajala, E.O., Ajala, M.A., Odetoeye, T. E. and Okunlola, A.T., 2019. Synthesis of solid catalyst from dolomite for biodiesel production using palm kernel oil in an optimization process by definitive screening design. *Brazilian Journal of Chemical Engineering*, 36, pp.979-994.
- Are, C.T., Suleiman, M.A.T., Yisa, J., Auta, M. and Joseph, I. A., 2021. Kinetic study of reaction between dolomite ore and trioxonitrate (V) Acid (HNO<sub>3</sub>). *GeoScience Engineering*, 67(1).
- Baba, A. A., Omipidan, A.O., Adekola, F.A., Job, O., Alabi, A.G., Baral, A. and Samal, R., 2014. Optimization study of a Nigerian dolomite ore dissolution by hydrochloric acid. *Journal of Chemical Technology and Metallurgy*, 49(3), pp.280-287.
- Chellapan, S., Datta, D., Kumar, S. and Uslu, H., 2022. Statistical modeling and optimization of itaconic acid reactive extraction using response surface methodology (RSM) and artificial neural network (ANN). *Chemical Data Collections*, 37, p.100806.
- Chelladurai, S.J.S., Murugan, K., Ray, A.P., Upadhyaya, M., Narasimharaj, V. and Gnanasekaran, S., 2021. Optimization of process parameters using response surface methodology: A review. *Materials Today: Proceedings*, 37, pp.1301-1304.
- Faraji, F., Alizadeh, A., Rashchi, F. and Mostoufi, N., 2022. Kinetics of leaching: a review. *Reviews in Chemical Engineering*, 38(2), pp.113-148.
- Joseph, I.A., Eterigho, E.J., Okafor, J.O. and Are, C.T., 2021. Alternative Approach of Gold Extraction using Modified Borax. *Iranian Journal of Chemistry and Chemical Engineering (IJCCE)*.
- Massaro, M., Colletti, C.G., Lazzara, G. and Riela, S., 2018. The use of some clay minerals as natural resources for drug carrier applications. *Journal of functional biomaterials*, 9(4), p.58.
- Omonije, O.O., Chidi, E. E., K. Y. Adamu, Y. K. and M. Olutoye, M. A., 2021. Response Surface Optimization for Microwave-Assisted Alkaline Pretreatment of Plantain Pseudostem Biomass for Bioethanol Production. *Chemsearch Journal*, 12(2), pp 113-128.
- Peijun, L. V., Tieheng, S. F., Z. Chungui, Z. Hairong, X. Xianzhe, A. Graeme, M. Xuejun. and A. Mayumi. 2004. Field-Scale Bioremediation of Soil Contaminated with Crude Oil, *Environmental Engineering Science*, 19(5), pp 277-289.
- Pultar, M., Vidensky, J. and Sedlarova, I., 2019. Study of the reaction between dolomite and nitric acid. *Physicochemical Problems of Mineral Processing*, 55.
- Tang, X., Tang, R., Xiong, S., Zheng, J., Li, L., Zhou, Z., Gong, D., Deng, Y., Su, L. and Liao, C., 2021. Application of natural minerals in photocatalytic degradation of organic pollutants: A review. *Science of The Total Environment*, p.152434.
- Vincent, A.O., Felix, E., Weltime, M.O., Ize-iyamu, O.K. and Daniel, E.E., 2011. Microbial degradation and its kinetics on crude oil polluted soil. *Research Journal of Chemical Sciences*. ISSN, 2231, p.606X.
- Yildirim, M., 2008. Dissolution kinetics of Icel-Aydincik dolomite in hydrochloric acid. *South African Journal of Chemistry*, 61, pp.127-132.



## Exergy Analysis of a Novel Biodiesel Production Process Integrated WITH Power Generation

G. I., OLAJIDE<sup>1</sup> and M. A. USMAN<sup>2</sup>

Department of Chemical Engineering, University of Lagos, Lagos, Nigeria

<sup>1</sup>[gbolagade.olajide@live.unilag.edu.ng](mailto:gbolagade.olajide@live.unilag.edu.ng), <sup>2</sup>[musman@unilag.edu.ng](mailto:musman@unilag.edu.ng)

\*Corresponding author

---

### ABSTRACT

Biodiesel is often said to be part of the solution to the energy crisis. A major stumbling block to its widespread commercialization is the dilemma in the disposal of glycerol – if it is thrown away it harms the environment; if it is combusted it produces little energy. A third option, though, is to use it, and this option has attracted a lot of research recently. Mehrpooya *et al.* (2020) have proposed and simulated processes to reform the glycerol, producing electricity. In this paper, exergy analysis was carried out on one of the proposed processes, in order to make it more energy-efficient. The process route was simulated, and the necessary data was then extracted from the simulation results and used to carry out exergy analysis. The exergy analysis revealed that the components to be targeted for optimization are the distillation column for purification of the esterification products (T100), the series of splitters used to purify the bottom product of the above-mentioned column (SP100 and SP101), and the neutralizer (R200). This equipment are the sources of 95, 58.5, 160.2- and 64.5-kW exergy destruction respectively: together causing over 57% of the entire process's energy inefficiencies. Optimization of these equipment will result in a much more energy-efficient process route.

**Keywords:** Exergy destruction, biodiesel, exergy, glycerol reforming, exergy analysis.

### 1. INTRODUCTION

Environmental degradation and climate change are widely acknowledged as two of the most pressing concerns of our time. Much of the blame for these two ills lies with the use of fossil fuels (a form of hydrocarbons commonly combusted to produce energy (Kopp, 2020)). Davidson (1989) has outlined two of the many issues arising from the use of fossil fuels:

- i. *Air pollution:* from the release of toxic gases such as carbon monoxide. These gases can cause serious health problems.
- ii. *Climate change:* The combustion of fossil fuels releases greenhouse gases into the atmosphere. These gases act like a blanket trapping heat within the atmosphere.

Furthermore, the combustion of fossil fuels is inherently unsustainable, as the rate at which they are being consumed is much higher than the rate at which they are formed (millions of years). The world, therefore, has to turn to alternative energy sources.

A promising alternative energy source is biodiesel, a fuel produced from animal fats or vegetable oils, and an alcohol – via transesterification (a reaction between triglycerides and three molecules of an alcohol to produce glycerol and a mixture of esters – called biodiesel). Biodiesel is renewable, non-toxic, biodegradable, and has low carbon footprint (Van Gerpen *et al.*, 2004). In the production of biodiesel, glycerol results as a by-product and has to be taken care of. Crude glycerol can be used as a fuel; however, it has a low calorific value. Refining it into useful chemicals increases its cost and hence the total cost of biodiesel, making biodiesel less economically viable than petrodiesel. Therefore, the development of a scheme to use crude glycerol profitably is crucial to making biodiesel cost competitive (Mehrpooya *et al.*, 2020). Certain researchers – such as Pairojpiriyakul *et al.* (2010) – have proposed to convert the glycerol into hydrogen, which is a clean, renewable fuel, and use the hydrogen to power the biodiesel production plant, thus making the production process less costly. Mehrpooya *et al.* (2020) carried out an investigation on a process of biodiesel production with the steam reforming of glycerol to produce hydrogen (which is then used as fuel in a solid oxide fuel cell power plant to provide thermal and electrical energy for the biodiesel production plant, and electricity to the power grid) and concluded that the proposed process is feasible.

The study by Mehrpooya et al. (2020) is representative of some of the research that has taken place on the simultaneous production of biodiesel and power. However, there has been no exergetic evaluation of the authors' proposed process. An exergetic evaluation is very important as it reveals the sources of inefficiencies within the system, so that they can be corrected. This is the gap that this research seeks to fill. Thus, the aim of this study is to evaluate the exergetic performance of the process, hence pointing out the sources and magnitudes of inefficiencies in it. This will then enable the optimization of the process, clearing the way to its implementation, hence a drastic reduction in the cost of biodiesel.

## 2. MATERIALS AND METHODS

### 2.1 process Simulation Methodology

Process simulators are software used to simulate the behavior of real-world systems. Aspen Plus and HYSYS are two of the best-known of such software. The waste cooking oil is canola oil, which is mainly composed of triolein: hence triolein is used to represent it. Methyl oleate is used to represent the resulting biodiesel since it is its dominant compound. As both methyl oleate and triolein are found in the HYSYS library, neither of them needed to be created. However, CaO and CaSO<sub>4</sub> are missing from the library, hence they were created as solid components with the properties in Table 1 Note that HYSYS requires only two properties to be mandatorily specified for an hypothetical solid component.

Table 1. Properties used for creating CaO and CaSO<sub>4</sub> in HYSYS

Component	Property	
	Density (kg/m <sup>3</sup> )	Molecular weight (kg/kmole)
CaO	3340	56.08
CaSO <sub>4</sub>	2960	136.14

The conversion of biodiesel into products is assumed to be 97% as it is reported in Zhang et al. (2003). The following assumptions are also made: steady-state operation; no pressure drop in heat exchangers, and column reboilers and condensers; all heat exchangers are single-pass; 100% tray efficiencies in distillation columns; adiabatic efficiency of 70%, 80%, and 75% for compressors, turbines, and pumps respectively; and no heat loss from any of the units. Due to the presence of polar compounds like glycerol, NRTL (Non-Random Two Liquid) model is chosen as the base method for calculating the activity coefficients. The UNIFAC (Universal Quasi-chemical Functional-group Activity Coefficients) method is used to estimate the missing temperature-dependent binary parameters. In the steam reforming process, the PSRK (Predictive Soave-Redlich-Kwong) model is employed as equation of state, due to the high temperatures encountered here.

### 2.2. Process Description

Methanol and sulphuric acid are fed to an esterification reactor. Waste cooking oil (WCO) is preheated in a heat exchanger then fed to the esterification reactor. The product from this reactor is sent to a distillation tower (T100), for purification. The overhead product from T100 is composed mainly of methanol, along with some impurities. The methanol is condensed in a condenser; part of it is recycled to the top of the column, and the other part is pumped to mix with the inlet methanol and sulphuric acid. The bottom product from T100 is composed of biodiesel (major product), sulphuric acid, glycerol, methanol, and unconverted oil. It is sent to a splitter (SP100), where a hexane-water mixture is used to extract most of the sulphuric acid, water, methanol, and glycerol. The upper layer of SP100 then goes to another splitter (SP101) to be washed with methanol-water mixture (in order to prevent the dissolution of hexane). It is then sent to a distillation column (T200), whose bottom product is the unreacted oil and whose top product is hexane and biodiesel. The hexane is vaporized in a flash drum and is recycled to the hexane-water washing in SP100. Thus, biodiesel is left in the drum. The lower layer of SP100 – a mixture of sulphuric acid, water, methanol, and glycerol – is sent to a reactor where it reacts with calcium oxide, thoroughly neutralizing the sulphuric acid to produce calcium sulphate and water. This product enters a splitter (SP102) which separates the CaSO<sub>4</sub> out. The top layer of SP102 contains methanol, glycerol, and water and enters a distillation column which has glycerol and water as its bottom product to be sent to the glycerol reforming process.

The glycerol is first diluted with water, in order to reduce its viscosity and aid pumping. In the reformer, the following reaction takes place:



Other reactions occur to form a small amount of methane. The produced synthesis gas formed goes to the solid oxide fuel cell power plant. Compressed air enters the cathode and the below reaction takes place:



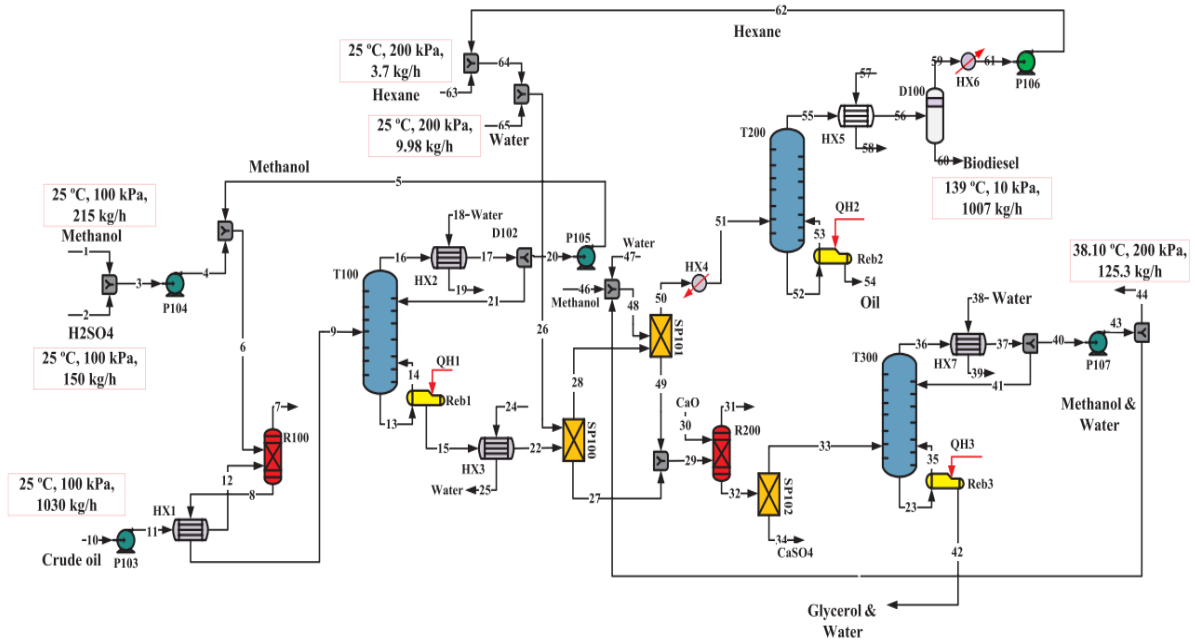
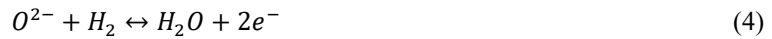


Figure 1. Process flowsheet: biodiesel production section (Mehrpooya et al., 2020)

At the anode, carbon monoxide and hydrogen react with oxygen anions:



Side reactions of methane and carbon monoxide with steam to form hydrogen, carbon dioxide, and carbon monoxide also occur at the anode. The exhaust gases from the anode are burned off in the combustor. The flue gases from the combustor are passed through a series of heat exchangers, and then transfer heat to the working fluid of the ORC (Organic Rankine Cycle) in an evaporator. The fluid (R113, which has now been vaporized by heat transferred) turns the blades of a turbine, generating electricity.

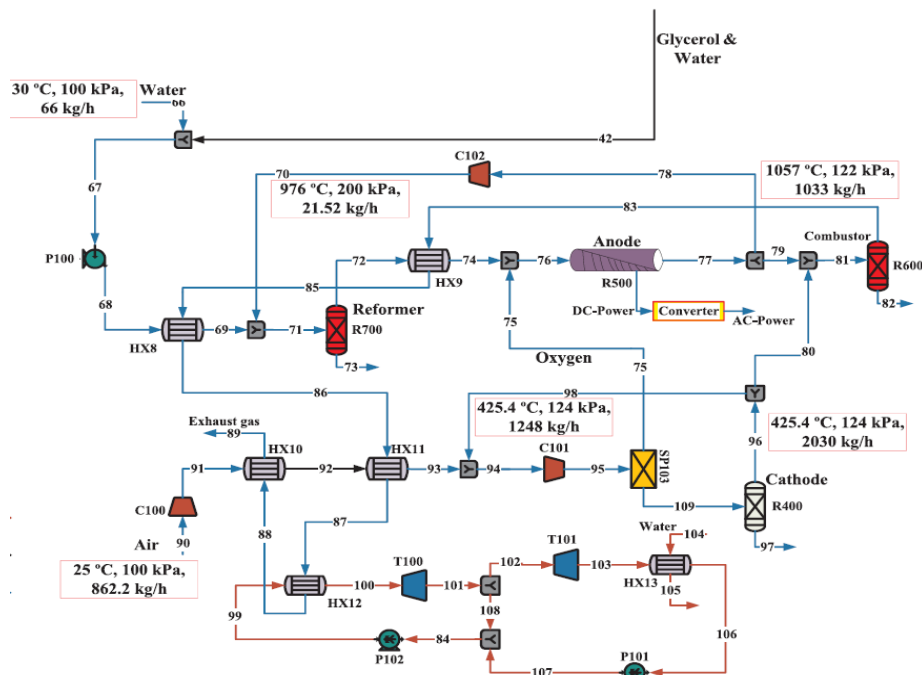




Figure 2. Process flowsheet: glycerol reforming section (Mehrpooya et al., 2020)

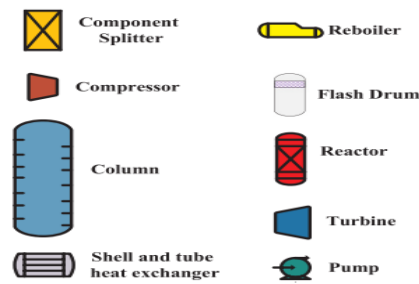


Figure 2.2. Process flowsheet: legend (Mehrpooya et al., 2020)

### 2.3. Exergy Analysis

The general unsteady-state exergy balance is given by Taner (2018) as:

$$\text{Exergy accumulated} = \text{Exergy input} - \text{Exergy output} - \text{Exergy destroyed} \quad (5)$$

As exergy accumulated = 0, equation 5 becomes:

$$\text{Exergy destroyed} = \text{Exergy input} - \text{Exergy output} \quad (6)$$

Since the exergy input and output are already known, the exergy destruction for each component can thus be derived. The exergy flow of a stream is the maximum work that can be derived when the stream is brought to mechanical and thermal equilibrium with its environment. It is given as:

$$Ex_{flow} = (H - H_0) - T_0(S - S_0) \quad (7)$$

Where  $Ex_{flow}$  = exergy flow;  $H$  = enthalpy of the stream;  $H_0$  = enthalpy of the stream's dead state;  $S$  = entropy of the stream; and  $S_0$  = entropy of the stream's dead state

Aspen Plus makes the application of equation 7 unnecessary, as it already gives the physical exergy ( $EXERGYXL$ ) for each stream.

Work exergy is the exergy transfer accompanying work and is given by:

$$Ex_{work} = W \quad (8)$$

Where  $W$  = work and  $Ex_{work}$  = work exergy

Equation 8 is a logical consequence of the fact that exergy is the maximum work that can be extracted from a given amount of energy. Hence, exergy of work is simply equal to work.

Thermal exergy is the exergy transfer accompanying heat transfer and is given by:

$$Ex_{heat} = \left(1 - \frac{T_0}{T}\right) q \quad (9)$$

Where  $Ex_{heat}$  = thermal exergy and  $q$  = heat transfer from/to system

Exergy efficiency of a system is the system's efficiency compared to that of an ideal version of it. Tatiana and George (2013) gave the following equation (using different symbols) for exergy efficiency:

$$\varphi_k = \frac{E_{p,k}}{E_{f,k}} = 1 - \frac{E_{d,k}}{E_{f,k}} \quad (10)$$

Where  $\varphi_k$  = exergy efficiency of kth component;  $E_{p,k}$  = product exergy of kth-component;  $E_{f,k}$  = fuel exergy of kth-component; and  $E_{d,k}$  = exergy destruction of kth-component.

## 3. RESULTS

### 3.1. Process Simulation Results

Below are the key results from the simulation of the process:

Table 2. Key results derived from the simulation of the process

	Key result	Simulation result	Result from literature	% correspondence
1	Biodiesel yield (kg product/kg reactant)	0.9816	0.9777	99.6
2	WCO recovered (kg/h)	31.37	31.19	99.42
3	Total power generated by turbines in the ORC (kW)	14.77	16.17	91.34

The closeness of this work's simulation results with those in literature validate this simulation.

### 3.2. Results of Exergy Analysis

Below are presented the results of the exergy balance carried out on each unit of the process:

Table 3. Results of exergy analysis of the process

Component	Exergy of fuel (kW)	Exergy of product (kW)	Exergy of destruction (kW)	% destruction	Exergy	Exergy (%)	efficiency
<b>PUMPS</b>							
P100	0.339	0.340	0.007	0.001		12.050	
P101	0.019	0.026	0.232	0.035		2.930	
P102	9.350	9.599	0.631	0.096		28.300	
P103	1.410	0.092	1.398	0.212		11.540	
P104	0.075	0.087	0.027	0.004		31.453	
P105	0.965	1.076	0.668	0.101		62.260	
P106	2.962	2.953	0.022	0.003		75.440	
P107	0.018	0.025	0.011	0.002		0.500	
<b>COMPRESSORS</b>							
C100	0.000	6.303	2.359	0.358		38.640	
C101	74.391	77.387	0.479	0.073		86.210	
C102	148.745	19.875	3.334	0.506		92.670	
<b>TURBINES</b>							
Turbine1	33.090	26.445	1.018	0.154		84.680	
Turbine2	13.857	2.575	2.143	0.325		81.003	
<b>HEAT EXCHANGERS</b>							
HX1	159.606	156.503	3.106	0.471		98.020	
HX3	36.022	20.993	15.029	2.279		61.430	
HX4	3.271	1.147	2.124	0.322		35.072	
HX6	2.962	2.275	0.688	0.104		76.788	
HX8	122.334	97.039	25.295	3.837		79.323	
HX9	312.071	311.245	0.826	0.125		99.735	
HX10	34.279	28.808	5.471	0.830		84.040	
HX11	83.645	75.323	8.322	1.262		90.051	
HX12	65.984	61.066	4.918	0.746		92.547	
HX13	2.575	0.951	1.624	0.246		36.932	
<b>COLUMNS</b>							
T100	195.124	100.097	95.026	14.413		51.299	
T200	11.47	2.80	1.315	1.315		8.568	
T300	46.229	12.636	33.593	5.095		27.334	
<b>REACTORS</b>							
R100	153.425	141.582	11.843	1.796		92.281	
R700	209.058	150.509	58.549	8.880		71.143	
Anode	236.066	228.840	7.223	1.096		96.342	
Combustor	164.214	161.600	2.647	0.402		97.422	
Cathode	99.103	83.679	15.424	2.339		92.422	
R200	16.035	7.040	8.995	1.364		43.903	
<b>SPLITTERS</b>							
SP103	241.625	225.663	15.962	2.421		79.374	
SP1	228.839	148.745	160.190	24.296		30.000	
SP2	83.679	51.454	64.450	9.775		22.979	
SP3	26.445	13.857	25.176	3.818		4.799	
TEE100	7.181	7.181	0.000	0.000		99.994	
SP101	5.374	1.100	4.274	0.648		20.466	
X101	7.040	7.040	0.000	0.000		99.995	
V100	31.755	10.059	21.696	3.291		31.677	
<b>MIXERS</b>							
M1	0.755	0.521	0.234	0.035		69.007	
M2	214.470	202.892	11.578	1.756		94.602	

M3	211.370	197.449	13.921	2.111	93.414
M4	112.319	102.665	9.654	1.464	91.405
M5	75.421	74.323	1.098	0.167	98.544
M6	12.614	9.350	3.264	0.495	74.124
M7	0.075	0.075	0.000	0.000	99.970
M8	135.968	130.884	5.084	0.771	96.261
M9	0.103	0.100	0.003	0.000	96.888
M10	0.100	0.009	0.091	0.014	9.483
M11	3.448	3.387	0.061	0.009	98.222
M12	8.179	7.322	0.856	0.130	89.529

#### 4. DISCUSSION

The figure below shows each equipment's contribution to the total exergy destruction.

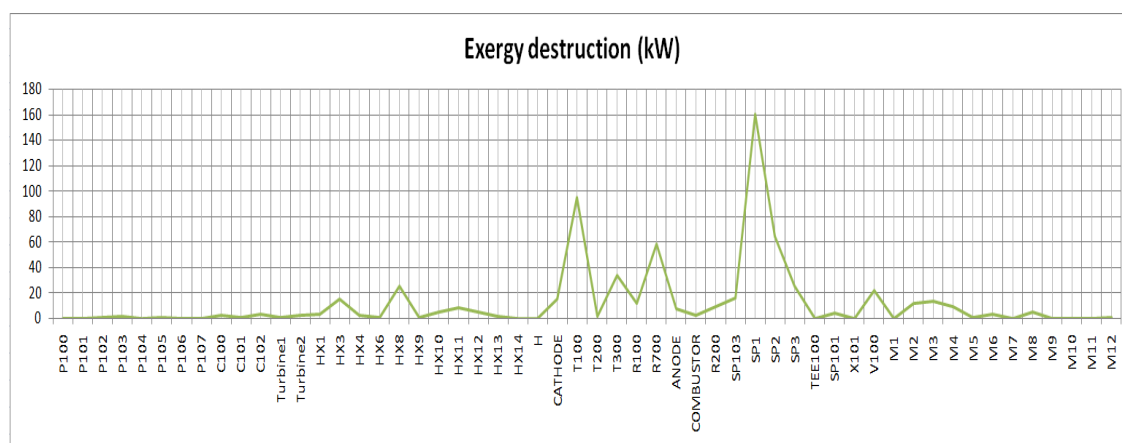


Figure 4.0. Exergy destruction of each component of the process

The above graph shows that the majority of the exergy inefficiencies are caused by distillation column T100, reactor R700, and splitters SP1 and SP2. These equipment are the sources of 95.0, 58.5, 160.2, and 64.5 kW exergy destruction respectively; together contributing to 57.4% of the entire process's energy inefficiency.

#### 5. CONCLUSION

From the analysis conducted, it is concluded that distillation column T100, reactor R700, and splitters SP1 and SP2 are the equipment most in need of thermodynamic optimization, as they are the source of over half of the system's overall exergy destruction. Hence, future development (before final implementation) of this process should explore the thermodynamic optimization of these components.

#### REFERENCES

- Davidson, A. (1989). *Fossil Fuel Consumption and the Environment*. Oxford: Oxford Institute for Energy Studies, pp. 6 – 16.
- Kopp, O. C. (2020). *Fossil fuel*. [online] Available at: <https://www.britannica.com/science/fossil-fuel> [Accessed August 31<sup>st</sup>, 2022].
- Mehrpooya, M., Ghorbani, B., and Abedi, H. (2020). Biodiesel production integrated with glycerol steam reforming process, solid oxide fuel cell (SOFC) power plant. *Energy Conversion and Management*, 206: 112467.
- Pairojpiriyaku, T., Kiatkittipong, W., Wiyaratn, W., Sootitantawat, A., Arpornwichanop, A., Laosiripojana, N., Croiset, E., and Assabumrun, S. (2010). Effect of mode of operation on hydrogen production from glycerol at thermal neutral conditions: Thermodynamic analysis. *International Journal of Hydrogen Energy*, 35: 10257-10270.
- Taner, T. ed., 2018. *Application of Exergy*. 1st ed. London: IntechOpen, pp.109 – 123.
- Tatiana, M., and George, T. (2013). Exergoenvironmental analysis is a new tool for evaluation of an energy conversion system. *Енергетика і автоматика*, 4: 3 - 14.
- Van Gerpen, J., Shanks, B., and Pruszko, R. (2004), *Biodiesel Production Technology*. NREL/SR-510-36244. [online] Colorado, NREL, pp. 1 – 2. Available at: <https://www.nrel.gov/docs/fy04osti/36244.pdf> [Accessed August 31<sup>st</sup> 2022].
- Zhang, Y., Dube, M. A., McLean, D. D., and Kates, M. (2003). Biodiesel production from waste cooking oil: 1. Process design and technological assessment. *Bioresource Technology*, 89: 1 - 16.

## Digestate Valorization: A Value Addition to Anaerobic Biodigestion Technology

<sup>†</sup>Minister Obonukut, Sunday Alabi, Jock Alexander, Kingsley Egemba and Benedict Edenseting

<sup>+</sup>Department of Chemical Engineering, Topfaith University, Mkpatak, Nigeria  
 Department of Chemical and Petroleum Engineering, University of Uyo, Nigeria

[\\*minister.obonukut@topfaith.edu.ng](mailto:minister.obonukut@topfaith.edu.ng)

\*Corresponding author

### ABSTRACT

Anaerobic digestion technology, exploited to transform diverse bio-sourced feedstocks into valuable products, is challenged by Gregory effect/Dutch disease. Digestate, the leftover product after biogas generation, is mostly discarded as its valorization is domiciled within fertilizer application. The consumption rate for fertilizer generation is reported to be one-tenth of its production rate. This review found that large-scale bio-fertilizer production is confronted with high operational and transportation costs, greenhouse gas emissions during storage, and improper nutrient content. It becomes necessary to examine the potential of digestate beyond bio-fertilizer application. It was found that the digestate liquor is suitable for microalgae cultivation due to its rich nutritional content. Due to its rich cellulose content, the digestate filtrate is a suitable culture medium for bioethanol production with the additional advantages of about 33% energy reduction with fewer inhibitory compounds. In the case of the digestate residue, strong complementary role of thermochemical process was showcased. It was found that several valuable products with superior properties were produced. These valuable products are exploited as: soil amender, adsorbent, activated carbon, particle board, and nanocellulose. However, the processes are still in their infancy and, as expected, have some drawbacks. Consequently, more studies to overcome these challenges are recommended.

**Keywords:** Digestate Valorization, Biofertilizer, Biochar, Bioethanol, Activated Carbon.

### 1.0 INTRODUCTION

The growing interest in meeting the energy needs globally leads to a shift from fossil fuels to biofuels while keeping the environment pollution free (Turkiewicz *et al.*, 2013; Obonukut and Inyang, 2022). Studies, (Kozo *et al.*, 1996; Oparaku *et al.*, 2013), showcased the anaerobic digestion process to proffer a solution to not only the energy and environmental needs of the society but also an attractive "waste-to-wealth" strategy via digestate valorization, as shown in Figure 1.

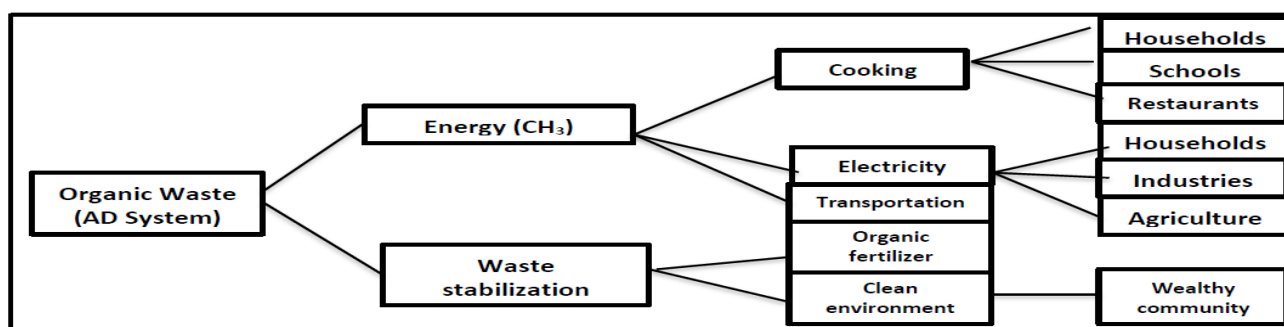


Figure 1: Anaerobic Digestion Technology: A waste-to-wealth strategy

Anaerobic Digestion (AD) Technology involves the degradation and stabilization of organic materials under anaerobic (oxygen-deficient) conditions by a microbial consortium leading to the production of an energy rich biogas and digestate. However, AD technology has been bedevilled by the Dutch disease/Gregory effect. The Dutch Disease/Gregory Effect describes a situation in which growth in one sector causes neglect in the other. In other words, the strong demand for a particular resource causes a knock-on effect on the other (Warr, 2006). The impacts of the Gregory effect on AD technology not only defeat the essence of the technology but also adversely affect its profitability. This is critical and should be urgently addressed, hence the need for this review.

Specifically, AD technology is widely known because biogas generation is designed to convert biomass into recoverable methane-rich gas and a stabilized digestate using a complex anaerobic biological process. Biomass refers to biodegradable organic materials of plant and animal origin. It extends beyond the remains/residue of animals/plants to their waste, especially agricultural waste products, which are principally used as the feedstock for the AD process (Eboibi *et al.*, 2020). The advances in technological development reveal that these biological materials are highly valuable feedstock for the industrial production of chemicals, fuel, and other related products. Hence, they are regarded as bio-sourced feedstocks (Edenseting *et al.*, 2020; Issah *et al.*, 2020)).

AD produces two valuable outputs: biogas and digestate. However, biogas is considered more valuable and highly sought-after than its counterpart (Abila, 2012). Akinbami *et al.* (2001) reported that Methane, the primary component of natural gas, is present in high concentrations in biogas (50 to 75 percent). Biogas, like natural gas, is energy-rich (fuel) and provides heat, generate electricity, and power cooling systems, among other uses (Akinbami *et al.*, 2001). Moreover, biogas, when purified by removing inert or low-value constituents, is considered cleaner and more environmentally friendly than natural gas (Andrade *et al.*, 2019). Consequently, most AD plants are widely known as biogas plants, as if biogas is the only product generated from this technology (Dariusz *et al.*, 2012).

Profit maximization of any process depends on the total valorization of all its products, ensuring zero wastage. Of all AD products, digestate is one of the most neglected and unexploited (Szwaja *et al.*, 2019). In this paper, digestate valorisation for fertilizer application and its challenges are reviewed (section 2). Thermochemical processes with a complementary role in the digestate residue will be presented (section 3). This is followed by a detailed description of alternative routes of digestate valorization other than fertilizer applications (section 4).

## 2.0 DIGESTATE VALORISATION FOR FERTILIZER APPLICATION AND ITS CHALLENGES

Digestate is mechanically separated into liquid and solid fractions that are stored separately for easy handling and transport. The liquid fraction (digestate filtrate) contains a large part of N and K, whereas the solid fraction (digestate residue) is composed of a large amount of residual fiber and phosphorous (Lied *et al.*, 2006). These are the reasons behind their applications as fertilizer or soil improvers (Tambone *et al.*, 2010; Rodriguez-Navas *et al.*, 2013).

Clearly, as a stabilized and homogeneous product from the anaerobic digestion of organic matter, the mineralization of fertilizing elements in the digestate liquor (filtrate) makes it a product of choice for soil nutrition (Insam *et al.*, 2015). The utilization of digestate for agricultural purposes represents economic and environmental benefits. Biofertilizer is of prime importance in the recycling of limiting nutrients (e.g., phosphorous) and is a better substitute for commercial fertilizer (Suominen *et al.*, 2014). Walsh *et al.* (2012) indicated that, contrary to commercial fertilizers, digestate improves yields from grassland cultures and concurrently reduces nutrient losses to the environment (Monlau *et al.*, 2015). Studies have shown that digestate (bio-fertilizer) from the AD process is superior to that of aerobic digestion in terms of bioavailability as its nutrients are more accessible to crops (Manlay, 2000; Dioha *et al.*, 2005). Despite the edge over others, less than one-tenth of the digestate produced is utilized for bio-fertilizer, and the remaining is discarded due to the following drawbacks attributed to fertilizer application.

Firstly, storing digestate for future application is challenging as its consumption rate is limiting the growth stages of crops, soil size/type, and stabilization levels (Ndiaye *et al.*, 2010). In most cases, the digestate is stored in uncovered tanks releasing greenhouse gases into the atmosphere (Sambusiti *et al.*, 2013). The gases (CH<sub>4</sub>, CO<sub>2</sub>, and N<sub>2</sub>O), affect the global environment and climate, while NH<sub>3</sub> contributes to general atmospheric pollution (Bonetta *et al.*, 2014). Secondly, commercial production of digestate is challenged by the high cost of transporting the digestate (Ndiaye *et al.*, 2010). The quantity of bio-fertilizer supplied per farm is small according to regulations on nutrient loading per hectare based on fertilization plan (Holm-Nielsen *et al.*, 2009). Once the costs of transportation and spreading are taken into account, the value of the digestate can be close to zero and it may even become an expense for the farmer (Monlau *et al.*, 2015). Thirdly, environmental pollutants (pathogens, heavy metals, pesticides, steroid hormones, and organic compounds) may be found in bio-fertilizers (Bonetta *et al.*, 2014; Insam *et al.*, 2015). This is one of the challenges negating its application, making it unattractive for storage. However, with good agricultural practices, optimal environmental and economic benefits can be achieved using bio-fertilizers (Holm-Nielsen *et al.*, 2009).

Proper characterization of the digestate before its application as fertilizer would prevent contamination of soil, which would eventually lead to food chain contamination (Zirkler *et al.* 2014). This would reveal the irregularity attributed to an unbalanced nutrient as well as the presence of contaminants.

## 3.0 COMPLEMENTARY ROLE OF THERMOCHEMICAL PROCESSES ON DIGESTATE RESIDUE

Thermochemical processes (including combustion, hydrothermal carbonization, and pyrolysis) have played a complementary role in various biological processes; including anaerobic digestion process (Szwaja *et al.*, 2019). Several researchers have investigated the impacts of thermal processes on anaerobic digestate and found that valuable products

can be produced, which eventually improves the overall energy efficiency of AD processes translating to increased profitability (Hoffman *et al.*, 2013; Li *et al.*, 2014; Monlau *et al.*, 2015; Szwaja *et al.*, 2019). Table 1 shows these thermochemical processes and digestates exploited.

Table 1: Thermochemical processes of anaerobic digestates +

Digestate Residue	Thermal Process Parameters	Products Distribution (% DM)		Source(s)
		Gas + Bio-Oil	Pyrochar	
Separated anaerobic digestate Residue	HTC realized in a custom-built autoclave at 180 °C for 4 h	25.7	74.3	Oliveira <i>et al.</i> , 2013
Anaerobic digestate from wheat straw digested in upflow anaerobic solid-state continuous reactors at 55 °C	HTC realized in 1 L stirred pressure reactor at 190 °C for 6 h	NA	66	Funke <i>et al.</i> , 2013
Whole anaerobic digestate from a mesophilic anaerobic plant treating 70% corn stillage and 30% cow manure	HTC realized in 18.75 L stainless reactor at 230 °C for 6 h. Solid loading: 5%	NA	53.5	Funke <i>et al.</i> , 2013b
Whole anaerobic digestate from mesophilic anaerobic plant treating 70% corn stillage and 30% cow manure	VTC realized in 18.75 L stainless reactor at 230 °C for 6 h. Solid loading: 25%	NA	64.5	Funke <i>et al.</i> , 2013b
Anaerobic digestate from maize silage digested in two-stage solid state reactors at 55 °C	HTC realized in 1 L stirred pressure reactor at 190 °C for 6 h	NA	70.1	Munme <i>et al.</i> , 2011
Sugar beet tailings digested in anaerobic two-stage reactor at 55 °C	Bench-scale slow pyrolyzer. Temperature of 600 °C, heating rate of 10 °C min <sup>-1</sup> and residence time of 2 h	54.5	45.5	Yao <i>et al.</i> , 2011
Sugarcane bagasse digested in anaerobic batch at 55 °C	Laboratory mini tubular pyrolyzer reactor, temperature of 600 °C, heating rate of 10 °C min <sup>-1</sup> and residence time of 1.5 h	82	18	Inyang <i>et al.</i> , 2010
Chicken manure and corn stover digested in CSTR reactor at mesophilic temperature	Laboratory pyrolysis tube reactor. Temperature of 800 °C, heating rate of 50 °C min <sup>-1</sup> and residence time of 3 h	72	28	Li <i>et al.</i> , 2014
Mix of slurry and energy crops	Thermo catalytic reforming plant: pyrolysis reactor connected to a reformer. Temperature from 150 °C to 500 °C in the pyrolysis reactor. Temperature of 600 °C in the reformer	NA		Neumann <i>et al.</i> , 2014
Pig manure digested in real anaerobic plant operating at mesophilic conditions and HRT of 20–30 days	Laboratory scale pyrolysis reactor Temperature of 600 °C and residence time of 15 min	NA		Troy <i>et al.</i> , 2013
Mix of manure and agricultural residues digested in real anaerobic plant operating at 45 °C and HRT of 62 days	Laboratory Rotary Kiln pyrolysis reactor. Temperature of 500 °C, heating rate of 20 °C min <sup>-1</sup> and residence time of 10 min	NA		Monlau <i>et al.</i> , 2015

+HTC: hydrothermal carbonization; VTC: vapothermal carbonization; NA: Not Available

Source: Monlau *et al.* (2015).

#### 4.0 EMERGING OPPORTUNITIES FOR DIGESTATE VALORIZATION

Clarification (i.e., dewatering) and further thermal processing of digestate have been investigated and promising valorization alternatives are reported as presented in this section.

##### 4.1: Digestate Valorization: Emerging Opportunities for Microalgae Cultivation

The impact of anaerobic digestion on algae growth dates to the 1950s. Golueke *et al.* (1957) suggested that the anaerobic digestion process would promote the conversion of sunlight into chemical energy. However, no further research was conducted to investigate the idea until recently when experiments were carried out to evaluate the feasibility of digestates as a nutrient source in microalgae cultivation was investigated and the outcome was promising (Monlau *et al.*, 2015).

The hike in food prices promoted algae cultivation especially when algae (i.e. 4<sup>th</sup> generation bio-sourced feedstock) was found to be a suitable alternative to first-generation counterparts (i.e., edible crops) for biofuel production (Edensting *et al.*, 2020). However, algae cultivation for biofuel production was initially uneconomical as production and extraction costs were found to be too high (Monlau *et al.*, 2015). Several strategies geared towards cost reduction and possibly improving the viability of algae cultivation economically have been exploited. Alternative valorization of anaerobic digestate via nutrient recovery has been well-reported as the most attractive strategy (Norsker *et al.*, 2011). Specifically,

microalgae were assessed for their ability to grow on digestates and the most prominent ones among them are presented in Table 2.

Table 2: Digestates valorization for algae cultivation

Algae	Digestate Source (Pretreatment)	Growth rate $\mu$ (d <sup>-1</sup> )	Source(s)
Mix culture (mainly Chlorella and Scenedesmus)	D-M (S/L separation, dilution)	0.05	Bchir <i>et al.</i> , 2011;
Spongiochloris sp.	Slaughter house (S/L separation, nutrients addition)	0.0155	Chen <i>et al.</i> , 2012
Mix Oocystis sp., Scenedesmus, Chlorella sp., Protoderma sp., Chlamydomonas sp. (mixed with activated sludge)	SW-M (S/L separation, Dilution)	(a) 1.34	Gonzalez-Fernandez <i>et al.</i> , 2010; Molinuevo-Salces <i>et al.</i> , 2010
Scenedesmus sp.	(b) codigestion of SW-M and Nannochloropsis	(b) 1.62	Bjornsson <i>et al.</i> , 2013
	(c) SW-M with nutrients	(c) 0.851	
	(d) SW-M with lake water	(d) 1.66	
Nannochloris spp with bacteria	Synthetic digestate	0.13–0.72	Vasseur <i>et al.</i> , 2012
Mixed (Scenedesmus dominant)	Synthetic digestate (dilution)	0.04–0.9	Uggetti <i>et al.</i> , 2014
Scenedesmus obliquus	Codigestion C-M and cheese whey (S/L separation, dilution)	0.49–0.64 0.23–0.44 0.26–0.37	Franchino <i>et al.</i> , 2013
Chlorella sp.	D-M (S/L separation, dilution)	0.282–0.409	Wang <i>et al.</i> , 2010
		Increasing with the dilution factor	
Spirulina maxima, mutant strain (short filaments)	SW-D (S/L separation, dilution)	0.04–0.08 (on TS); 0.12–0.18 (on chlorophyll); 0.09–0.13 (on protein)	Olguin <i>et al.</i> , 1994
Mixed bacteria and microalgae (mainly: Scenedesmus sp., Chlorella sp., Synechocystis sp.)	Livestock wastes (S/L separation, dilution, Nutrient correction)	0.78	Marcilhac <i>et al.</i> , 2014
Chlorella sp. Scenedesmus Obliquus	SW-D (dilution)		de la Noue and Basse'eres, 1989
Phormidium bohneri	Cheese production	0.36–0.58	Blier <i>et al.</i> , 1995; Blier <i>et al.</i> , 1996
Micractinium pusillum	(S/L separation, dilution)	0.35	

However, turbidity of the media due to dissolved and suspended materials in the digestates is one of the major drawbacks to digestates' valorization via algae cultivation (Wang *et al.*, 2010). Ammonia inhibition is another critical issue of concern as microalgae are known to use ammonium as a source of nitrogen (Uggetti *et al.*, 2014). More so is bacterial contamination, as it may induce sanitary issues for downstream biomass valorization (Chen *et al.*, 2012). The contamination is inevitably due to microbe-medium interactions, either symbiotically or competitively. It is believed that bacterial growth will alter the turbidity, pH, dissolved oxygen, nutrient apportionment (mineral or organic), and chemical nature (oxidation state) of the media.

#### 4.2 Digestate Valorization: Emerging Opportunities in Soil Amendment

The endearing properties (stability, porosity, mineral content, etc.) of pyrochars are exploited to improve soils with fragile structures, waterlogged soil, and attenuate the drought stress of semi-arid regions of the world. The porous structure of pyrochars not only improves soil structure but also provides shelter for beneficial soil microorganisms and, as well, influences positively the binding effect between nutritive cations and anions (Monlau *et al.*, 2015). The application of pyrochar to soil has been reported to minimize the dispersal of pesticides and the leaching of heavy metals with their subsequent accumulation in plants (Uchimiya *et al.*, 2010).

The environmental implications of using pyrochar from AD digestate in agricultural soils have been well-reported by many researchers. These include: pyrochar from digested dairy waste (DW) with BET surface area and total pore volume of 161.2 m<sup>2</sup> g<sup>-1</sup> and 0.147 cm<sup>3</sup> g<sup>-1</sup> while whole sugar beet (SB) was 48.6 m<sup>2</sup> g<sup>-1</sup> and 0.034 cm<sup>3</sup> g<sup>-1</sup> (Inyang *et al.*, 2012). Yao *et al.* (2011) reported that pyrochar obtained from anaerobically digested biomass has a higher accessible surface area (336 m<sup>2</sup> g<sup>-1</sup>) than pyrochar produced from raw feedstock (2.6 m<sup>2</sup> g<sup>-1</sup>). Pituello *et al.* (2014) reported that a pyrochar produced using a digestate from cattle manure and silage combo exhibited a higher phosphorus concentration than the initial feedstock, suggesting that they can be used for low nutrient release as phosphorus is an important element for plant growth. Therefore, the development of pyrochars with superlative properties using anaerobic digestate is an added advantage to the AD process.

Despite this potential of exploiting pyrochars produced from digestate as soil amenders, there are some aggressive components of the digestate which can have negative effects on the soil, crops, and even the environment. In view of this, characterization of digestates after the AD process as well as pyrochars produced from the digestate is necessary. Before application, these bioavailable compounds should be known and their potential negative effects isolated and carefully addressed.

#### 4.3 Digestate Valorization: Emerging Opportunities for Activated Carbon Development

The adsorption capacity of pyrochars can be further improved by converting them into activated carbons (ACs). However, the activation process requires two further stages of pyrolysis of the carbon at a temperature below 800 °C, followed by a steam activation process (Ioannidou and Zabaniotou, 2007). The activation process promotes not only the stability of

the material but also its porosity and surface area. In view of this, ACs from digestate residues have been found to exhibit a much higher accessible surface area and porosity than pyrochars (Monlau *et al.*, 2015).

Specifically, activated carbons from the digestate residues of the AD process using dairy manure exhibited a high accessible surface area and pore volume of  $1950 \text{ m}^2 \text{ g}^{-1}$  and  $232 \text{ cm}^3 \text{ g}^{-1}$ , respectively (Yuan *et al.*, 2011). Presently, there is a greater demand for activated carbon due to the emerging non-biodegradable contaminants from industrial wastes constituting an environmental issue (vide supra). Activated carbon is the most efficient adsorbent that removes these contaminants, and its consumption has been reported to have dramatically increased recently (Monlau *et al.*, 2015). Commercial activated carbons are produced from expensive but nonrenewable materials (coal, etc.), making the ACs expensive and much more expensive if not produced locally. AD digestate residue is suitable for the production of low-cost value-added ACs (Yuan *et al.*, 2011).

#### 4.4 Digestate Valorization: Emerging Opportunities in Bioethanol Production

Anaerobic digestate residue has an edge over the conventional feedstock exploited for bioethanol production. Two types of anaerobic digesters (CSTR and PFR) as reported by Yue *et al.* (2011) were exploited for bioethanol production using AD digestates. It was found that  $105 \text{ g kg}^{-1}$  dry digestate and  $85 \text{ g kg}^{-1}$  dry digestate of bioethanol were produced from CSTR and PFR, respectively (Yue *et al.*, 2011). The higher bioethanol production from the CSTR digestate was due to its higher cellulose content than in the PFR digestate (Yue *et al.*, 2011). Similar results were obtained during switchgrass bioethanol fermentation (Yue *et al.*, 2010). Digestate residue after co-digestion of corn stover and swine manure (40 and 60% fresh material, respectively), as reported by MacLellan *et al.* (2013), produced  $152 \text{ g CH}_4$  and  $50 \text{ g ethanol kg}^{-1} \text{ DM}$  via coupling AD and the bioethanol production process.

AD Digestates perform better than the conventional feedstock for bioethanol production as the digestate has been hydrolyzed during AD process (Yue *et al.*, 2011). At this stage, its lignin content is not only enriched with cellulose but also enhanced its accessibility (Monlau *et al.*, 2015). AD process with low hydraulic retention time (HRT) has equally been exploited as a biological pretreatment process to alter the composition of the fibrous feedstock, making it suitable as a cellulosic feedstock for ethanol production (Yue *et al.*, 2011). This strategy is a relatively new concept and its role is still controversial in the literature (Vancov *et al.*, 2015).

However, in an attempt to advance this strategy, Yue *et al.* (2011) showed that anaerobically digested manure contains less hemicellulose (11%) and more cellulose (32%) than raw manure and it presents better enzymatic digestibility than switch-grass. This strategy needs to be probed further. Meanwhile, the conventional bioethanol production process involves mechanical fractionation and/or thermo-chemical pretreatment followed by enzymatic hydrolysis-ethanolic fermentation (Monlau *et al.*, 2015). In a related study by Motte *et al.* (2015), it was found that anaerobic biological degradation prior to mechanical fractionation could significantly reduce the energy requirement of the milling step from  $142 \text{ kWh t}^{-1}$  for initial feedstock to  $95 \text{ kWh t}^{-1}$  for digestate.

#### 5.0 CONCLUSION

Generally, effective utilization of any process output or effluent requires its full valorization into a product of higher value. Anaerobic digestion technology is not an exception, as the full valorization of its products (biogas and digestate streams) is a necessity. This paper concludes that digestate valorization beyond bio-fertilizer application is the way forward to prevent the Gregory effect confronting the AD process. Valorization of the AD digestate increases the economic prospects and curtails the impending environmental issue of an AD/biogas project. However, most of the digestate valorization processes reviewed are challenged as the technology is still in its nascent state. Intensive research in this direction is the way forward to ensure that AD technology is not a waste generation strategy but a waste disposal/treatment strategy.

#### REFERENCES

- Abila, N. (2012) Biofuels development and adoption in Nigeria: synthesis of drivers, incentives and enablers. *Energy Policy*; 43:387–95.
- Akinbami, J. F. K., Ilori, M. O., Oyebisi, T. O., Akinwumi, I. O., Adeoti, O. (2001) Biogas energy use in Nigeria: Current status, future prospects and policy implications. *Renewable and Sustainable Energy Review*, 5: 97-112.
- [Andrade, C. I.](#), [Lucianode, M.](#), [Ariadne, N.](#), [João, V.](#), [Larissa, R.](#), [Nádia, H.](#), [Rebeca, Y.](#), [Ram, N.](#), [Renan, F.](#) and [Luiz, F.](#) (2019). A new approach using an open-source low cost system for monitoring and controlling biogas production from dairy wastewater. *Journal of Cleaner Production* 241:23-34.
- Bchir, F. S., Gannoun, H., El Herry, S. and Hamdi, M. (2011). *Bioresour. Technol.*, 102: 3869–3876.
- Bjornsson, W. J., Nicol, R. W., Dickinson, K. E. and McGinn, P. J. (2013) *J. Appl. Phycol.*, 25: 1523–1528.
- Blier, R., Laliberte, G. and de la Noue, J. (1996). *Process Biochem.*, 31: 587–593.
- Bonetta, S., Bonetta, S., Ferretti, E., Fezia, G., Gilli, G. and Carraro, E. (2014). *Water, Air, Soil Pollut.*, 225: 3–11.
- Chen, R., Li, R., Deitz, L., Liu, Y., Stevenson, R. J. and Liao, W. (2012). *Biomass Bioenergy*, 39: 128–138.



- Dariusz, W., Janusz, G., Andrzej, B. (2012). The pyrolysis and gasification of digestate from agricultural biogas plant. *Archives of Environmental Protection* 41(3): 70–75.
- Dioha, I. J., Eboatu .A. N., Akpuaka M.U., Abdullahi .D. Arinze R.U. and Okoye P.A.C. (2005). Comparative studies of the Effects of Brands of cow dung and NPK fertilizers on the growth of okra plants. *Nigerian Journal of Solar Energy* 16: 15 – 18.
- Eboibi, B., Atikpo, E., Ihueghian, P. and Ogiribo, P. (2020). Characteristics of Products from Anaerobic Digestion of Cassava Waste for Biogas Production Biogas Production, *Journal of Experimental Research*, 8 (2): 36-45
- Edenseteng, B. O., Obonukut, M. E. and Oboh, I. O. (2020). Bio-Sourced Feedstocks for Biofuel Production: Nigeria as a Case Study. *Journal of Scientific and Engineering Research*, 7(12): 1-18.
- Franchino, M., Comino, E., Bona, F. and Riggio, V. A. (2013) *Chemosphere*, 92: 738–744.
- Funke, A., Mumme, J., Koon, M. and Diakite, M. (2013). *Biomass Bioenergy*, 58: 229–237.
- Golueke, C. G. and Oswald, W. J. (1957). *Appl. Microbiol.*, 7: 219–227.
- Gonzalez-Fernandez, C., Molinuevo-Salces, B. and Garcia-Gonzalez, M. C. (2010) *Ecol. Eng.*, 36, 1497–1501.
- Holm-Nielsen, J. B., Al Seadi, T. and Oleskowicz-Popiel, P. (2009). *Bioresour. Technol.*, 100: 5478–5484.
- Insam, H., Gomez-Brandon, M. and Ascher, J. (2015). *Soil Biol. Biochem.*, 84: 1–14.
- Inyang, M., Gao, B., Yao, Y., Xue, Y., Zimmerman, A. R., Pullammanappallil, P. and Cao, X. (2011) *Bioresour. Technol.*, 110: 50-56.
- Ioannidou, O., Zabaniotou, A., Antonakou, E. V., Papazisi, K. M., Lappas, A. A. and Athanassiou, C. (2009) *Renewable Sustainable Energy Rev.*, 13: 750–762.
- Issah, A., Kabera, F. and Kemausuor, T. (2020). Biogas optimisation processes and effluent quality: A review. *Biomass and Bioenergy*. 133: 42-67.
- Li, Y., Zhang, Y., He, C. Zhang, X. Liu, C. Chen and Liu, G. (2014). *Bioresour. Technol.*, 156: 342–347.
- Lied, B. E., Bombardiere, I. J. and Chatfield, J. M. (2006). *Water Sci. Technol.*, 53(8): 69–79.
- MacLellan, J., Chen, R., Kraemer, R., Zhong, Y. Y. Liu and Liao, W. (2013). *Bioresour. Technol.*, 130, 418–423.
- Manlay R. (2000) Organic matter dynamics in mixed-farming systems of the West African savanna: A village case study from south Senegal. In *Ecole Nationale du Genie Rural, des Eaux et Forets Centre de Montpellier*, vol Doctorat. Montpellier, pp. 42 - 52.
- Monlau, F., Kaparaju, P., Trably, E., Steyer, J. P. and Carrere, H. (2015). *Chem. Eng. J.*, 260: 377–385.
- Motte, J. C., Sambusiti, C., Dumas, C. and Barakat, A. (2015). *Appl. Energy*, 147: 67–73.
- Mumme, J., Eckervogt, L., Pielert, J., Diakite, M., Rupp, F. and Kern, J. (2011). *Bioresour. Technol.*, 102: 9255–9260.
- Ndiaye, M. L., Niang, S., Pfeifer, H. R., Peduzzi, R., Tonolla, and M. and Dieng, Y. (2010) Effect of irrigation water and processing on the microbial quality of lettuces produced and sold on markets in Dakar (Senegal). In: Sons JW, ed. *Irrigation and Drainage*, Wiley: NY, pp. 35 – 56.
- Norsker, N. H., Barbosa, M. J., Vermue, M. H. and Wijffels, R. H. (2011). *Biotechnol. Adv.*, 29: 24–27.
- Obonukut, M. E. and Inyang, U. E. (2022). Advances and Challenges of Anaerobic Biodigestion Technology, *London Journal of Engineering Research* 22(1): 23 - 40
- Oparaku, N. F., Ofomatah, A. C. and Okoroigwe, E. C. (2013) Biodigestion of cassava peels blended with pig dung for methane generation *Academic Journals*, 12(40): 5956-5961.
- Pituello, C., Francioso, O., Simonetti, G., Pisi, A., Torreggiani, A., Berti, A. and Morari, F. (2014). *J. Soils Sediments*, 4: 792–804.
- Rodriguez-Navas, C., Bjorklund, E., Halling-Sorensen, B. and Hansen, M. (2013). *Environ. Pollut.*, 180: 368–371.
- Sambusiti, C., Ficara, E., Malpei, F., Steyer, J. and Carrere, H. (2013). *Bioresour. Technol.*, 144, 149-155.
- Suominen, K., Verta, M. and Marttinen, S. (2014). *Sci. Total Environ.*, 491–492: 192–199.
- Szwaja, S., Magdziarz, A., Zajemska, M., Poskart, A. and Musia, D. (2019). Investigation on Thermal Decomposition of Biogas Digestate to Producer Gas. 2<sup>nd</sup> International Conference on the Sustainable Energy and Environmental Development, Poland.
- Tambone, F., Scaglia, B., D’Imporzano, G., Schievano, A., Orzi, V., Salati, S. and Adani, F. (2010). *Chemosphere*, 81: 577–583.
- Uchimiya, M., Lima, I. M., Klasson, K. T. and Wartelle, L. H. (2010). *Chemosphere*, 80: 935–940.
- Uggetti, E., Sialve, B., Trably, E. and Steyer, J. P. (2014). *Biofuels, Bioprod. Biorefin.*, 8: 516–529.
- Vancov, T., Schneider, R. C., Palmer, J., McIntosh, S. and Stuetz, R. (2015). *Bioresour. Technol.*, 183: 120–128.
- Walsh, J. J., Jones, D. L., Edwards-Jones, G. and Williams, A. P. (2012). *J. Plant Nutr. Soil Sci.*, 175: 840–845.
- Wang, S., Dai, G., Yang, H. and Luo, Z. (2017). Lignocellulosic Biomass Pyrolysis Mechanism: A State-of-the-Art Review. *Progress in Energy and Combustion Science*, 62, 33-86.
- Warr, P. (2006). The Gregory Thesis Visits the Tropics, PhD Thesis, Australian National University
- Yao, Y., Gao, B., Inyang, M., Zimmerman, A. R., Cao, X., Pullammanappallil, P. and Yang, L. (2011). *Bioresour. Technol.*, 102: 6273–6278.
- Yuan, X. Z., Shi, X. S., Zeng, S. J. and Wei, Y. L. (2011). *J. Chem. Technol. Biotechnol.*, 86, 361–366.
- Yue, Z., Teater, C., MacLellan, J., Liu, Y. and Liao, W. (2011). *Biomass Bioenergy*, 35: 1946–1953.
- Zirkler, D., Peters, A. and Kaupenjohann, M. (2014). *Biomass Bioenergy*, 67: 89–98.



## Reduction of COD from Tannery Wastewater using CNTs Modified *Albizia Lebbeck* Pods

Tunmise Latifat ADEWOYE<sup>1,4\*</sup>, Salimah OMARI<sup>1</sup>, Sarat Ayodele ATANDA<sup>1</sup>, Oladipupo Olaosebikan OGUNLEYE<sup>2</sup>, Taofeek Olalekan SALAWUDEEN<sup>2</sup>, Ambali Saka ABDULKAREEM<sup>3,4</sup>, Sherif Ishola MUSTAPHA<sup>1</sup>

<sup>1</sup> Department of Chemical Engineering, University of Ilorin, PMB 1515 Ilorin, Kwara Nigeria

<sup>2</sup> Department of Chemical Engineering, Ladoko Akintola University, PMB 4000 Ogbomoso, Oyo State

<sup>3</sup> Department of Chemical Engineering, Federal University of Technology, PMB 65 Minna, Niger State, Nigeria

<sup>4</sup> Nanotechnology Research Group, Africa Centre of Excellence for Mycotoxin & Food Safety, Federal University of Technology, PMB 65 Minna, Niger State, Nigeria

<sup>1,4</sup> [adewoye.tl@unilorin.edu.ng](mailto:adewoye.tl@unilorin.edu.ng), <sup>1</sup> [salimaomari@gmail.com](mailto:salimaomari@gmail.com), <sup>1\*</sup> [sarat.morenikeji@gmail.com](mailto:sarat.morenikeji@gmail.com), <sup>2</sup> [ooogunleye@lautech.edu.ng](mailto:ooogunleye@lautech.edu.ng),  
<sup>2</sup> [tosalawudeen@lautech.edu.ng](mailto:tosalawudeen@lautech.edu.ng), <sup>3,4</sup> [kasaka2003@futminna.edu.ng](mailto:kasaka2003@futminna.edu.ng), <sup>1</sup> [mustapha.si@unilorin.edu.ng](mailto:mustapha.si@unilorin.edu.ng)

\*Corresponding author

### ABSTRACT

Tannery effluent, which contains a large quantity of organic and inorganic contaminants has a detrimental effect on health and the environment when discharged directly into the water bodies. The adsorption potential of unmodified and modified carbonized *Albizia Lebbeck* pods for the reduction of chemical oxygen demand (COD) in tannery wastewater was investigated in this study. *Albizia Lebbeck* pods were carbonized and modified with purified carbon nanotubes (CNTs) to produce carbonized *Albizia Lebbeck* (ALC) and modified *Albizia lebbeck* (MALC) adsorbents. The developed adsorbents were characterized by Brunauer–Emmett–Teller (BET), high-resolution scanning electron microscopy (HRSEM), energy dispersive X-ray spectrometry (EDS) and X-ray diffraction (XRD). The batch adsorption process was conducted to investigate the effect of, pH, contact time, adsorbent dosage and temperature on the uptake of COD from tannery wastewater onto the adsorbents. The BET surface area of the ALC and MALC were 638 and 616 m<sup>2</sup>/g, respectively. HRSEM revealed that the adsorbents have good morphology while the XRD showed that the adsorbents are highly crystalline. The maximum adsorption efficiency of MALC and ALC are 95 and 93%, respectively. It can be deduced that modification of carbonized *Albizia Lebbeck* (ALC) with CNT slightly improved the adsorption potential of the ALC adsorbent.

**Keywords:** Tannery, Wastewater, COD, Adsorption and *Albizia lebbeck*.

### 1. INTRODUCTION

Water is a significant natural resource used for drinking and other purposes in our daily lives hence, the need for the availability of pure water (Haseena, Malik, Javed, Arshad, & Asif, 2017). About 80% of the world's population is facing threats from polluted water (Owa, 2013). Leather tanning involves the use of a large quantity of water and chemicals which result in the generation of toxic effluent which poses a threat to the nearby ecosystem and humans (Barman, Juel, & Hashem, 2016; Muhammad, Rakhshan, Ikhtiar, & Asma, 2015). The wastewater generated by tanning industries is usually dark brown and contains microorganisms, heavy metals, organic pollutants, and toxic chemicals which vary based on the chemicals used in the tanning process (Durai & Rajasimman, 2011). Tannery wastewater is characterized by its salinity, conductivity, high chemical oxygen demand (COD), high biological oxygen demand (BOD), inorganic matters, suspended solids (SS), total dissolved solids (TDS), heavy metals and organic pollutants which are recognized as a serious environmental threat due to high chemical levels. COD is the total measurement of all chemicals in the water that can be oxidized and the high COD concentrations in wastewater are toxic to biological life and will affect the aquatic environment such as aquatic plants and fishes (Nayl *et al.*, 2017), it is therefore important to treat the effluents from the tannery industry before discharging them into the environment.

A large number of researchers used conventional methods for the reduction of COD from wastewater (Ademiluyi, Amadi, & Amakama, 2009; Badalians Gholikandi, Baneshi, Dehghanifard, Salehi, & Yari, 2010; Mustapha *et al.*, 2019). Out of all the methods, the adsorption technique is simple, has low cost and reduces the generation of secondary pollutants (Olufemi, 2018). Different adsorbents have been used for adsorption which includes activated carbon (Ademiluyi *et al.*, 2009), silica gel (Yan & Wang, 2018), zeolite (Badalians Gholikandi *et al.*, 2010) and lots more. The

major shortcoming in using some of these adsorbents is the cost of production (Gawande & Kaware, 2016), hence, there is a need to use an alternative material such as an adsorbent derived from agricultural waste for the reduction of COD from tannery water.

Agricultural waste is an alternative because they are inexpensive, abundant in nature, and readily available waste material from the waste industry (Dai *et al.*, 2018). Some of the agricultural waste material that has been explored includes Rice husk (Mohamed & Alfalous, 2020), Sugarcane bagasse (Karnitz Jr *et al.*, 2007), Wheat bran (Özer, 2007) and maize cob (Opeolu, 2009). However, these agricultural wastes have limitations as their unmodified forms have low adsorption capacities, it is, therefore, necessary to modify them before they are used as adsorbents. Carbon Nanotubes (CNTs) have been reported to have wide specific surface areas, hollow and layered structures which make them a perfect adsorption material for wastewater treatment (Kumar & Saravanan, 2018; Moosa, Ridha, M., & Abdulla, 2015). The application of CNTs is limited by their cost, nevertheless, it can be employed to modify the agricultural waste adsorbent to improve the adsorption efficiency.

This work focuses on the use of purified CNTs modified *Albizia Lebbeck* pod to efficiently reduce COD from tannery wastewater. The objectives of this research are; to purify carbon nanotubes (MWCNTs), and modify carbonized *Albizia Lebbeck* pods with the purified MWCNTs.

## 2. MATERIAL AND METHODS

### 2.1 Collection of Samples

The *Albizia Lebbeck* seed pods used in this study were collected from Mimosa trees around the Oke-Odo area, Ilorin, Kwara State. The seeds were removed from the pods and the pods were washed with distilled water to remove dust and other adhering impurities after which the washed pods were air-dried. The tannery wastewater sample was collected from a tannery in Zaria, Kaduna State. The water sample was collected in a sealed sterile plastic container and then placed in a refrigerator at 4°C for further use.

### 2.2 Characterization of Tannery Wastewater Sample

The pH, turbidity, COD, BOD, colour, heavy metals, TDS and conductivity of the wastewater sample were determined. The COD and BOD were carried out using standard procedures (Nayl *et al.*, 2017). The pH was determined using a pH meter. Turbidity, TDS, and conductivity were determined using the Turbidity meter, TDS meter and Conductivity meter, respectively.

### 2.3 COD Analysis

About 5 ml each of  $K_2Cr_2O_7$  was added to the wastewater sample and distilled water in a conical flask in triplicate. The six flasks were kept in a boiling water bath (100°C) for an hour and then allowed to cool. Potassium iodide (5 ml) was added to all six flasks and then 10 ml of  $H_2SO_4$ . The contents of each flask were titrated with 0.1(M)  $Na_2S_2O_4$  until it turns yellow. After which, 1 ml of starch solution was added to all the flasks until the solution turned blue. The sample obtained was then titrated with 0.1 (M) sodium thiosulphate endpoint until the blue colour disappeared. The COD was calculated as

$$COD = \frac{(A-B)*N*8000}{S} \quad (1)$$

Where; COD represents COD in the sample in mg/litre, B is the volume in ml of the titrant used for the sample, A is the volume in ml of titrant used as blank, S represents the volume of the water sample and N is the normality of sodium thiosulphate.

### 2.4 Purification of CNT

The procured CNT was purified to remove residual metals and other impurities absorbed in the CNTs (Egbojiuba, 2022). The CNT was purified with a mixture of acetic acid and sulphuric acid in the ratio of 3:1 (V/V); 100 mg of CNTs was poured into the prepared mixture and the sample was then placed in a sonicator for 3 h at 30°C. After which the mixture was brought out and washed with distilled water till a pH of 7 was attained. It was then filtered and oven-dried at 110°C. The obtained purified CNT (A.N CNT) was stored in an airtight, sterile sample bottle for further use.

### 2.5 Preparation, Modification and Characterization of *Albizia Lebbeck* adsorbent

The obtained *Albizia Lebbeck* sample was ground into powder, sieved using a sieve size of 225  $\mu$ m, and washed again with distilled water until the colourless filtrate was attained to remove any traces of absorbed salt (Ullah *et al.*, 2019). The residue gotten from the filtration was then dried in an oven at 105°C for 8 h (Ibrahim & Umar, 2016). The dried sample was calcined in a muffle furnace at 550°C for 3 h to obtain carbonized *Albizia Lebbeck* pods (ALC)

For the modified adsorbent, ALC sample (5.0 g) was dispersed in 250 ml of ethanol solution and sonicated for 10 mins, then 0.05 g of purified MWCNTs (1% weight) was added into the mixture and it was further sonicated for 20 mins (Parlayıcı, Eskizeybek, Avcı, & Pehlivan, 2015). It was then filtered and placed in an oven to dry at 80°C for 3 h. The obtained (sample MALC) was then placed in a desiccator for the adsorption experiment. The obtained samples were characterized for their surface morphologies/composition, surface area, functional group and crystallinity using Zeiss Auriga HRSEM, NOVA 4200e surface area and pore size analyser, PerkinElmer FTIR spectrometer and XRD spectrometer.

## 2.6 Batch Adsorption Experiments

Batch adsorption studies were conducted to examine the effect of contact time, temperature, adsorbent dosage and pH on the reduction of COD using modified *Albizia Lebbeck* carbon (MALC) and unmodified *Albizia Lebbeck* carbon (ALC). 100 ml of the wastewater sample was taken into 250 ml Erlenmeyer flasks in several places. The kinetics of the adsorption experiment was studied at different time intervals (5-30 min) using 0.5 g of adsorbents. Different doses of adsorbents ranging from 0.5 – 0.9 g were separately mixed with 100 ml of wastewater sample put into 250 ml Erlenmeyer. The effect of temperature was investigated at different temperatures ranging from 30-50°C. The effect of pH was also studied by varying the pH of the water sample (4-12) either with 0.1 M NaOH or 0.1M H<sub>2</sub>SO<sub>4</sub>. The mixture was shaken constantly using a water bath shaker at 150 rpm. The mixture obtained was filtered and the residual concentration of the COD content was then analyzed and the reduction efficiencies were determined using

$$\% \text{ removal} = \frac{C_0 - C_e}{C_0} \times 100 \quad (2)$$

Where, C<sub>0</sub> and C<sub>e</sub> (mg/l) are the concentration of COD present in the tannery wastewater sample at the initial stage and equilibrium, respectively. The equilibrium amount (Q<sub>e</sub>) of COD removed per mass of adsorbent was evaluated using equation 3.

$$Q_e = \frac{(C_0 - C_e)V}{W} \times 100 \quad (3)$$

Where; Q<sub>e</sub> (mg/g) is the amount of metal ions adsorbed per unit mass of adsorbent at equilibrium. V(l) is the volume of the solution and W(g) is the mass of the adsorbent used.

### 2.6.1 Adsorption isotherm model

The equilibrium relationship between the adsorbate concentration in the solution and on the surface of the adsorbent at a specified condition is described through adsorption isotherm models. Langmuir, Freundlich and Temkin isotherm models were used to describe the equilibrium characteristic of both adsorbents in this adsorption study.

## 3. RESULTS AND DISCUSSION

### 3.1 Characterization of Wastewater Sample

Analysis was carried out on the tannery wastewater (TW) to determine its BOD, COD, pH, conductivity, TDS and heavy metals using a standard method. The results showed that BOD, Zinc, Copper, Manganese, Iron and pH were within the permissible limits set by Federal Environmental Protection (FEPA), on the other hand, COD (1200 mg/l), TDS (10400 mg/l) and Lead (0.2 mg/l) were above the permissible limit for the discharge of wastewater into surface water. The results obtained were similar to the results reported (Hossain *et al.*, 2019) for tannery wastewater. High COD values of the effluent may indicate the high organic pollution potential of the effluent (Hossain *et al.*, 2019). Hence, this research is concentrated on reducing the concentration of COD as their high concentration in the effluent impacts lives negatively when discharged into surface water without treatment.

### 3.2 Characterization of the Adsorbents

Purified CNTs (A.N CNT), calcined *Albizia Lebbeck* pods (ALC) and the modified calcined *Albizia Lebbeck* pods (MALC) were characterized for the surface area using BET analysis and the result is presented in Table S1. The result revealed that the adsorbents had a large area of 799, 638 and 616 m<sup>2</sup>/g for A.NCNT, ALC and MALC, respectively which indicates a high adsorption capacity (Okeola, Odebunmi, & Ameen, 2012). The result obtained was similar to what was reported by Liu, Sun, Xu, Qu, and Qu (2020). The average pore size of the adsorbents were in the range of 6.181-6.247 nm which appears to be mesoporous (2-50 nm). It was also observed that the surface area of MALC was a bit lower than that of ALC. This observation may be a result of the formation functional group on the surface of MALC due to the incorporation of the CNT.

A High-Resolution scanning electron microscope was used to study the morphology/composition of the adsorbents and the results are presented in Figure 1. The HRSEM images showed a densely wormlike structure of CNTs and the tubes could be seen in Figure 1a. The HRSEM results for ALC are shown in Figure 1b, and it is seen to have an irregular sheet-like morphology which is similar to the HRSEM results of the activated *Albizia Lebbeck* reported by Ullah *et al.* (2019).

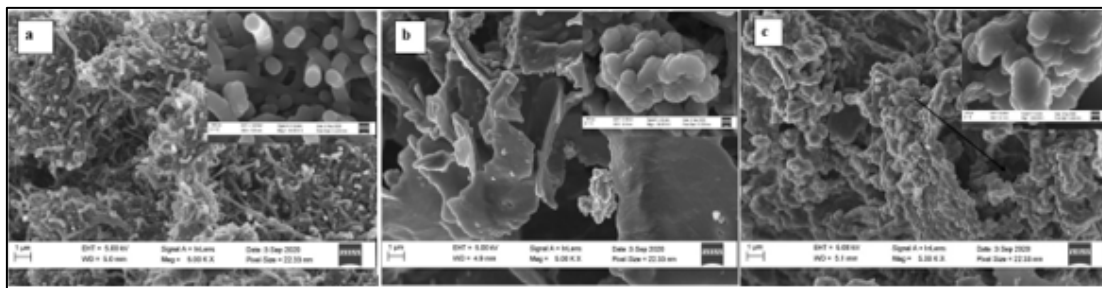


Figure 1: HRSEM images for (a) A.N CNT (b) ALC (c) MALC

The HRSEM results obtained for MALC (Figure 1c) showed irregular aggregate morphology with large pore openings (arrow) which may be a result of the modification. This irregular texture may be responsible for the observed improved stability and reduction efficiency of the MALC adsorbent presented in the subsequent section.

The Energy Dispersive X-ray Spectroscopy (EDX) results presented in Figure 2 showed that carbon is dominantly present in the three adsorbents. A.N CNT is seen to contain some other elements which could be remnants of its impurities. There was a slight increase in the Carbon weight in MALC which could be attributed to the modification with A.N CNT. The results also revealed that ALC and MALC adsorbents have oxygen-containing functional groups which may act as active sites for the adsorption of COD.

X-ray Diffraction (XRD) studies show variations in the crystallinity of the adsorbents and Figure 3 depicts the XRD spectra for the ALC and MALC adsorbents.

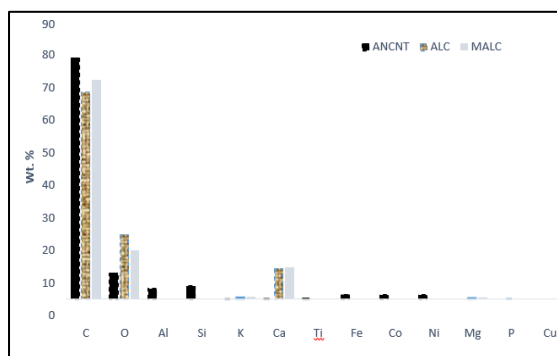


Figure 2: EDX results for A.N CNT, ALC and MALC

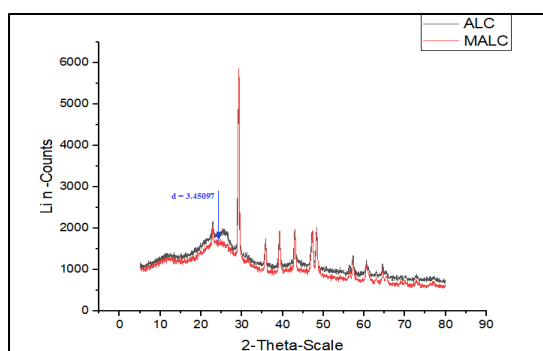


Figure 3: XRD spectra of ALC and MALC

It was observed that well-defined peaks of both adsorbents around  $2\theta$  of  $29.5$  ( $002$ ) show the crystalline nature of the developed adsorbents. The intensity of the peak CNTs around  $2\theta$  of  $29.5$  ( $002$ ) planes was higher in the modified adsorbent than the unmodified adsorbent and, the d-spacing of  $3.45097$  corresponding to CNT observed in the XRD spectral of MALC adsorbent confirmed that A.N CNT was well incorporated into the matrix of MALC adsorbent which is in agreement with the HRSEM result (Das *et al.*, 2014).

### 3.3 Batch Experiment Studies

The effect of adsorption process parameters such as pH, contact time, adsorbent dosage and solution temperature on the efficiency of ALC and MALC adsorbents for the reduction of COD from tannery wastewater was investigated and the results are depicted in Figure 4. The effect of pH on the adsorption of COD was studied by carrying out the adsorption process at different pH values under constant adsorbent dosage (0.5g) and contact time (20 min). It was observed from Figure 4a that as pH increases, the reduction efficiency of COD increased for both adsorbents and maximum reduction was achieved at a pH of about 6 corresponding to 86 and 88% for ALC and MALC, respectively. Generally, at a low pH, the positively charged  $H^+$  ions are high and they tend to bind to the adsorbents by electrostatic adsorption of both  $H^+$  and oxygen and have a strong affinity for each other to take up the binding sites. However, when the pH was increased beyond 6, the removal rate of COD decreased as a result of the abundance of  $OH^-$  ions, using higher hindrance to diffusion of organics contributing to COD.

The effect of time was studied in the range of 5-30 min using 0.5 g of adsorbents at 30°C. The results obtained from the studies showed that the sorption efficiency of the two adsorbents was instantaneous as more than 70% of COD was adsorbed at the initial stage, an indication that the two adsorbents have very good potential for the reduction of COD from Tannery wastewater. The sorption efficiency increased considerably with time and at approximately 20 mins, equilibrium was reached as a further increase in time caused a decrease in the reduction of COD. The maximum reduction efficiencies were 85 and 87% for ALC and MALC, respectively. The decrease in reduction efficiency observed in Figure 4b may be due to the filling of pores of adsorbents with water molecules (Parlayici *et al.*, 2015). Hence, the retention time of 20 mins was chosen as the optimum time in this study. In addition, MALC showed a slightly higher maximum adsorption efficiency and better stability compared to ALC under the same batch adsorption conditions. The enhanced stability and adsorption efficiency may be due to the improved morphology of the MALC as shown in Figure 1(c).

The effect of ALC and M.ALC dosage on the percentage reduction of COD was studied at 30°C for 20 min. The adsorbent dosage was varied from 0.5 - 0.9g/100 ml as shown in Figure 4b. It was observed that the reduction efficiency increased with increasing adsorbent dose until the optimum dosage of 0.8 g/100 ml for MALC and 0.7 g/100 ml for ALC corresponding to 95 and 93%, respectively. The increase in the reduction efficiency may be ascribed to the increase in the functional groups and the total surface area of the adsorbents due to the increase in dosage, and hence, more active sites on the adsorbents were available for the adsorption of COD from the wastewater (Jain, Garg, & Kadirvelu, 2010). The decrease in removal efficiency observed with further increase in dosage (Figure 4c) was probably due to the aggregation of adsorbent as adsorbent dosage increases and therefore, the accessible adsorption sites might decrease as well due to the adsorption density (Edet & Ifelegebu, 2020). Comparing both adsorbents, it could be seen that both adsorbents showed good performances with MALC adsorbents having a slightly higher COD reduction efficiency. the improved morphology of the MALC as shown in Figure 1(c).

The temperature has strong effects on the intermolecular forces between the adsorbate and adsorbent particles. From Figure 4d, it is seen that the rate of reduction of COD decreases as the temperature increases for both adsorbents which indicated that the adsorption is exothermic (Edet & Ifelegebu, 2020). The decrease in adsorption capacity is due to the fact that at low temperatures, the kinetic energy of the particle is low and the intermolecular attractive forces are strong, hence, the molecules of the adsorbate are easily and strongly attracted to the surface of the adsorbent which gives a higher adsorption efficiency and vice versa.

### 3.4 Adsorption Isotherms

The relation between COD adsorption capacities ( $Q_e$ ) with ALC and MALC and the residual amounts ( $C_e$ ) of COD at equilibrium was analyzed with different isotherm models at a constant temperature. Linear plots of Langmuir, Freundlich and Temkin are shown in Figures S3, S4 and S4 and the goodness-of-fit of the isotherms was accessed by  $R^2$ . Table S3 shows that Langmuir had the best  $R^2$  (0.8957 for ALC and 0.9364 for MALC) values for the reduction of COD for both adsorbents which indicated a physical sorption mechanism (physisorption) (Edet & Ifelegebu, 2020).

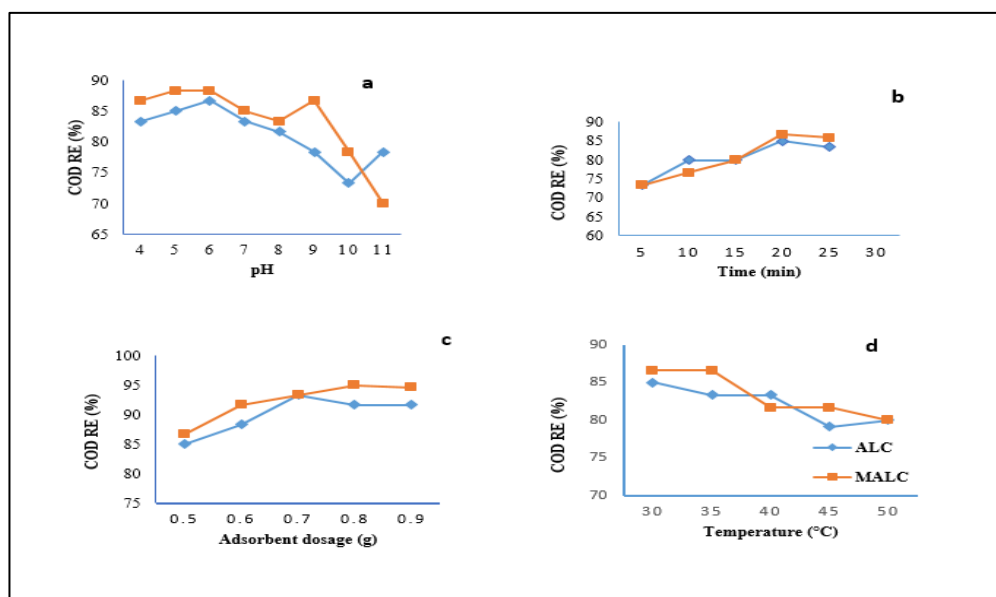


Figure 4: Effect of (a) pH (b) contact time (c) adsorbent dosage and (d) Temperature on the reduction efficiency of COD using ALC and MALC.

#### 4. CONCLUSION

This study presented the preparation and modification of carbonized *Albizia Lebbeck* pods (ALC) as adsorbents for the reduction of COD in tannery wastewater. The results obtained revealed that the properties of the ALC adsorbent were enhanced after the modification. The pore structure and surface area of the ALC were altered after modification with purified MWCNTs. HRSEM image of the MALC adsorbent revealed visible large pore openings resulting from the modification with MWCNTs. The XRD results confirmed that MALC showed a better crystallinity after the modification. The studies demonstrated that activated carbon prepared from *Albizia Lebbeck* can be used as an effective, low cost and natural adsorbent for the adsorption of COD from tannery wastewater. However, MALC showed slightly better efficiency removal, probably due to its modification with purified CNT. In addition, MALC showed better stability, morphology and crystallinity. The results of the batch experiments showed that the adsorption process was dependent on adsorbent dose, contact time, solution pH, and temperature.

#### REFERENCES

- Ademiluyi, F., Amadi, S., & Amakama, N. J. (2009). Adsorption and Treatment of Organic Contaminants using Activated Carbon from Waste Nigerian Bamboo. *Journal of Applied Sciences and Environmental Management*, 13(3).
- Badalians Gholikandi, G., Baneshi, M. M., Dehghanifard, E., Salehi, S., & Yari, A. R. (2010). Natural zeolites application as sustainable adsorbent for heavy metals removal from drinking water. *Iranian Journal of toxicology*, 3(3), 302-310.
- Barman, B. C., Juel, M. A. I., & Hashem, M. A. (2016). *Tannery Wastewater Treatment by Simple Coagulation-Filtration Process Using Low Cost Coagulants*. Paper presented at the International Conference on Mechanical, Industrial and Energy Engineering.
- Dai, Y., Sun, Q., Wang, W., Lu, L., Liu, M., Li, J., . . . Xu, J. (2018). Utilizations of agricultural waste as adsorbent for the removal of contaminants: A review. *Chemosphere*, 211, 235-253.
- Durai, G., & Rajasimman, M. (2011). Biological treatment of tannery wastewater-a review. *Journal of Environmental science and Technology*, 4(1), 1-17.
- Edet, U. A., & Ifelegegu, A. O. (2020). Kinetics, isotherms, and thermodynamic modeling of the adsorption of phosphates from model wastewater using recycled brick waste. *Processes*, 8(6), 665.
- Egboosiuba, T. (2022). Incorporation of zero-valent silver and polyvinyl acetate on the surface matrix of carbon nanotubes for the adsorption of mercury and chromium from industrial wastewater. *Nigerian Journal of Technology*, 41(1), 158-168-158-168.
- Gawande, P. R., & Kaware, J. P. (2016). Preparation and activation of activated carbon from waste materials-a review. *International Journal for Research in Applied Science and Engineering Technology*, 4(12), 1-4.
- Haseena, M., Malik, M. F., Javed, A., Arshad, S., & Asif, N. (2017). Water pollution and human health. *Health*, 1(3), 16-19.
- Ibrahim, M., & Umar, A. (2016). Adsorption thermodynamics of some basic dyes uptake from aqueous solution using *Albizia lebbeck* shells. *Chemsearch Journal*, 7(1), 43-51.
- Jain, M., Garg, V. K., & Kadirvelu, K. (2010). Adsorption of hexavalent chromium from aqueous medium onto carbonaceous adsorbents prepared from waste biomass. *Journal of environmental management*, 91, 949-957.

- Karnitz Jr, O., Gurgel, L. V. A., De Melo, J. C. P., Botaro, V. R., Melo, T. M. S., de Freitas Gil, R. P., & Gil, L. F. (2007). Adsorption of heavy metal ion from aqueous single metal solution by chemically modified sugarcane bagasse. *Bioresource Technology*, 98(6), 1291-1297.
- Kumar, P. S., & Saravanan, A. (2018). Environmental Detoxification Using Carbonaceous Composites. *Carbonaceous Composite Materials*, 42, 205-230.
- Liu, Z., Sun, Y., Xu, X., Qu, J., & Qu, B. (2020). Adsorption of Hg (II) in an aqueous solution by activated carbon prepared from rice husk using KOH activation. *ACS omega*, 5(45), 29231-29242.
- Mohamed, F., & Alfalous, K. (2020). The effectiveness of activated silica derived from rice husk in coagulation process compared with inorganic coagulants for wastewater treatment. *The Egyptian Journal of Aquatic Research*, 46(2), 131-136.
- Moosa, M. A., , Ridha, A. A., M., A., & Abdullha, I. N. (2015). Chromium Ions Removal from Wastewater Using Carbon Nanotubes Chromium Ions Removal from Wastewater Using Carbon Nanotubes. (March). *Research gate*, 1-7.
- Muhammad, A., Rakhshan, K., Ikhtiar, K., & Asma, S. (2015). Effect of Heavy Metals from Tannery Effluent on the Soil and Groundwater using Multivariate Analysis in District Sheikhpura, Pakistan. 1-10.
- Mustapha, S., Ndamitso, M., Abdulkareem, A., Tijani, J., Mohammed, A., & Shuaib, D. (2019). Potential of using kaolin as a natural adsorbent for the removal of pollutants from tannery wastewater. *Heliyon*, 5(11), e02923.
- Nayl, A. E. A., Elkhashab, R. A., Malah, T. E., Yakout, S. M., El-Khateeb, M. A., Ali, M. M. S., & Ali, H. M. (2017). Adsorption studies on the removal of COD and BOD from treated sewage using activated carbon prepared from date palm waste. *Environment Science Pollution Resources*, 1-10.
- Okeola, O., Odebunmi, E., & Ameen, O. (2012). Comparison of sorption capacity and surface area of activated carbon prepared from *Jatropha curcas* fruit pericarp and seed coat. *Bulletin of the Chemical Society of Ethiopia*, 26(2).
- Olufemi, A. S. (2018). Agricultural Waste Adsorbents for Heavy Metals Removal from Wastewater Agricultural Waste Adsorbents for Heavy Metals Removal from Wastewater., 1-7.
- Opeolu, B. O. (2009). Utilization of maize (*Zea mays*) cob as an adsorbent for lead (II) removal from aqueous solutions and industrial effluents. *African Journal of Biotechnology*, 8(8).
- Owa, F. (2013). Water pollution: sources, effects, control and management. Department of Integrated Science, Federal College of Education, Okene, Kogi State, Nigeria. *Mediterr J Soc Sci MCSEER Publishing, Rome-Italy*, 4(8).
- Özer, A. (2007). Removal of Pb (II) ions from aqueous solutions by sulphuric acid-treated wheat bran. *Journal of Hazardous Materials*, 141(3), 753-761.
- Parlayıcı, S., Eskizeybek, V., Avcı, A., & Pehlivan, E. (2015). Removal of chromium (VI) using activated carbon-supported-functionalized carbon nanotubes. *Journal of Nanostructure in Chemistry*, 5(3), 255-263.
- Ullah, M., Nazir, R., Khan, M., Khan, W., Shah, M., Afridi, S. G., & Zada, A. (2019). The effective removal of heavy metals from water by activated carbon adsorbents of *Albizia lebbeck* and *Melia azedarach* seed shells. *Soil and Water Research*, 15(1), 30-37.
- Yan, K., & Wang, Q. (2018). *Adsorption characteristics of the silica gels as adsorbent for gasoline vapors removal*. Paper presented at the IOP Conference Series: Earth and Environmental Science.





## Optimisation of Removal Efficiency of Palm Kernel Shell Ash in the Treatment of Multicomponent Dyes in Simulated Wastewater

Abass O. ALADE<sup>1,2,5\*</sup>, Aduragbemi, G. OYELADE<sup>1,2</sup>, Dauda O. ARAROMI<sup>1</sup>, Taofik O. SALAWUDEEN<sup>1</sup>, Rebecca A. OLAOYE<sup>3</sup>, Temitope E. ODETOYE<sup>4</sup>, Monsur O. DAUDA<sup>1,2</sup>, and Tinuade J. AFOLABI<sup>1,2</sup>

<sup>1,3</sup>Department of Chemical Engineering, Ladoke Akintola University of Technology, P.M.B. 4000, Ogbomoso, Nigeria

<sup>2</sup>Bioenvironmental, Water and Engineering Research Group, (BWERG), Ladoke Akintola University of Technology, P.M.B. 4000, Ogbomoso, Nigeria

<sup>4</sup>Department of Chemical Engineering, University of Ilorin, Ilorin, Nigeria

<sup>3</sup>Science and Engineering Research Group, (SEARG), Ladoke Akintola University of Technology, P.M.B. 4000, Ogbomoso, Nigeria

\*Corresponding author: [aolade@lautech.edu.ng](mailto:aolade@lautech.edu.ng) +2347037885961

### ABSTRACT

Synthetic dyes are mostly employed in the textile industries creating a risk to the environment for both plants and animals. The removal efficiency of ashed Palm Kernel Shell (APKS) adsorbent for the removal of Malachite green (MG), Methyl Orange (MO), and Crystal Violet (CV) from simulated wastewater was examined in this study. The palm kernel shell (PKS) was washed, sun-dried, and milled to a consistent size. The milled PKS was ashed in a muffled furnace at 700 °C for 4 h. The feasible mixtures of the selected dyes were developed based on the Design Expert (12.0) software, Optimal Design feature. The solution (100 mL) of the mixed pollutants was mixed with 1 g of the APKS in a 250 mL flask and agitated at 150 rpm for 1 h. The unadsorbed concentration was quantified with a UV-visible spectrometer at the wavelength of 624 nm, 464 nm, and 579 nm and the maximum Removal Efficiency was 99.52 %, 74.64 %, and 98.46 % for MG, MO, and CV respectively. The  $R^2$  of the model generated were 0.8046, 0.9850, and 0.9482 for MG, MO, and CV respectively. The APKS developed demonstrated satisfactory removal efficiency for the treatment of dye mixture in wastewater.

**Keywords:** Adsorption, Dye, Optimization, Palm Kernel Ash, Wastewater

### 1. INTRODUCTION

Dyes are used to colour a variety of things, including paper, cosmetics, tannery, and textile fibres. The massive amounts of this toxic wastewater generated by the dyeing processes in the textile industries make it challenging to treat. The dye industries often produce massive amounts of toxic wastewater. As a result, when released in untreated or partially treated forms into the environment (air, soil, plants, and water), they have negative effects that contribute to several human disorders (Slama et al., 2021). Dye wastewater is currently one of the major sources of serious pollution issues due to the rising demand for textile products, the corresponding growth in their production, and the usage of synthetic colours (Drumond Chequer et al., 2013). Because of the negative effects on receiving waterways, the treatment of wastewater containing such dyes is important (Rafatullah et al., 2010).

There have been various documented physical, chemical, and biological decolourization techniques during the past three decades, but only a small number of them have been approved by the paper and textile sectors. Adsorption is the method of choice and produces the best results among the various dye removal processes because it can be used to remove a variety of colouring components. Adsorption is a well-known equilibrium separation technique that works effectively for decontaminating water. In comparison to other methods for reusing water, adsorption is more advantageous due to its low initial cost, adaptability, and simplicity of design, as well as its ease of operation and insensitivity to harmful pollutants. Many strategies have recently been researched to create more affordable and efficient adsorbents. Several researchers have proposed a wide range of non-traditional low-cost adsorbents, including natural materials, biosorbents, and waste products from industry and agriculture. These substances could be employed as adsorbents to take colours out of solutions (Rafatullah et al., 2010).

Palm Kernel Shell which is the waste product left behind from processing palm kernel is a form of adsorbent used in this study. The shell encloses the palm kernel and is a fleshy fiber that carries palm oil around the shell. Thus, after processing the fibrous, meaty fruit to produce palm oil, the palm kernel shell is produced. To determine whether the

biomaterial is suitable for use in a variety of applications, numerous researchers have looked at the characteristics of palm kernel shells. Porosity, moisture content, lignin content, cellulose and Nanocellulose fractions, solid density, and carbon content are a few of these intriguing characteristics (Baffour-Awuah et al., 2021).

The most effective way to combine the dyes to get an effective result was determined via optimization. Depending on the situation, measuring a function's maximum or minimum value is the main goal of employing optimization techniques. The Design Expert (12.0) software's Optimal Design tool was used to design and meticulously conduct 14 experimental runs to develop the workable mixes of the chosen dyes (Alabi et al., 2020). This research aimed to produce calcinated Palm Kernel Shell for the removal of multi-component dye from simulated wastewater.

## 2. MATERIALS AND METHODS

### 2.1. Procurement of Material, Reagents and Chemical

Palm Kernel Shell was collected from a local farm in Aroje town, Ogbomosho, Oyo state, Nigeria (467M+7HF, 210101, Ogbomosho). Malachite Green (chemical formula  $C_{23}H_{25}ClN_2$  and molecular weight of 364.911 g/mol), Methyl Orange (chemical formula  $C_{14}H_{12}N_3O_3NaS$  and molecular weight of 327.34g/mol), and Crystal Violet (chemical formula  $C_{25}H_{30}ClN_3$  and molecular weight of 407.99 g/mol) were used as adsorbate in this study.

### 2.2 Methodology

Palm Kernel Shell was regularly cleaned with distilled water to get rid of debris like dirt and dust. After being cleansed, the shell was sun-dried for one week to remove the moisture content in the shell. The shell was milled into smaller particle sizes after being sun-dried to increase the material's surface area. The automated sieve shaker and US Tyler standard screen Mesh 40 and 60 were utilized to achieve uniform particle diameter. The particles retained on meshes 40 and 60 had sizes of 0.420 mm and 0.250 mm, respectively. The recovered particles were mixed and given a 4hour ash treatment in a muffled furnace operating at 700 °C to calcinate the Palm kernel Shell to increase the adsorbing power of the material. To make 250mg/L of each dye solution, 0.25g of Malachite Green MG, Methyl Orange MO, and Crystal Violet CV powder were combined with 1L of distilled water in a separate two-liter flask. The Design Expert (12.0) software's Optimal Design tool was used to produce and meticulously conduct 14 experimental runs to develop the practical mixtures of the MG, MO, and CV dyes. To start the adsorption procedure, 100mL of the dye mixture made from MG, MO, and CV was poured into 1g of the Ashed Palm Kernel Shell (APKS) in a 250 mL flask. After 14 hours, the Adsorption process was discontinued and the solution of APKS and mixed dye was centrifuged at the speed of 1000 rpm at 10 mins. The UV-visible spectrometer was employed to find out how much dye was left unadsorbed, at peak wavelengths of 624 nm, 464 nm, and 579 nm for MG, MO, and CV, respectively the quantity of Pesticides adsorbed per unit weight of adsorbent,  $q_e$  ( $mg\ g^{-1}$ ), was performed to decide the ideal adsorption limit. The calculation for the adsorption capacity ( $q_e$ ) was done using the relation

$$REMOVAL\ EFFICIENCY = \frac{C_0 - C_e}{C_e} \times 100 \quad (1)$$

Where,  $C_0$  is the initial concentration (mg/l),  $C_e$  is the experimental concentration (mg/l),  $V$  is the volume of the diluted adsorbate (L) and  $m$  is the mass of the composite (g).

## 3.0 RESULTS AND DISCUSSION

### 3.1 Removal Efficiency (RE) of APKS

The Design Expert (12.0) software's Optimal Design tool used Arose for the experimental design for the adsorption of MG, MO and CV onto APKS in this study. A linear, quadratic model and special quartic model were chosen for MG, MO, and CV respectively from the fourteen (14) experimental runs that the design generated. Power Transform was done for the RE of MO on APKS. After which run 11 of the optimal design of Experiment proved to have the highest removal efficiency of 99.524% for MG, 74.640% for MO at run 5, and 98.458% for CV at run 10 and with an average removal efficiency of 88.814% at run 5 (Alabi et al., 2020). The highest RE recorded for MG is 99.52% at run 11 (40.15%MG, 39.85%MO and 20.00% of CV), 74.64% RE of MO at run 5 (26.78%MG, 47.17%MO and 26.05%CV) and 98.46% RE of CV at run 10 (40.10%MG, 20.00%MO and 39.90%CV) respectively. While the lowest RE of MG, MO and CV was generated at run 1, run 14 and run 1 respectively. (Table 1). The maximum RE of APKS unto MG at run 11(99.52%) of the present study indicates that APKS has better Removal Efficiency than RE of APKS unto MO at run 5 (74.64%) and APKS unto CV at run 10 (98.46%).

Table 1: Batch adsorption research response and experimental design matrix

Run	Component (%)			Removal Efficiency (%)		
	A: Malachite Green	B: Methyl Orange	C: Crystal Violet	(Malachite Green)	(Methyl Orange)	(Crystal Violet)
1	20.00	20.00	60.00	87.26	66.30	93.42
2	20.00	60.00	20.00	98.73	64.66	96.07
3	20.00	39.89	40.11	95.54	53.27	95.18
4	20.77	39.49	39.74	91.72	51.68	96.00

5	26.78	47.17	26.05	96.79	74.64	95.01
6	27.49	24.87	47.64	96.29	61.44	97.27
7	33.39	33.24	33.37	99.14	66.21	97.49
8	39.42	39.78	20.80	96.36	41.05	95.73
9	39.54	21.03	39.43	95.89	52.74	94.62
10	40.10	20.00	39.90	98.33	54.75	98.46
11	40.15	39.85	20.00	99.52	58.23	96.84
12	49.81	30.19	20.00	98.08	39.63	97.09
13	50.00	20.00	30.00	97.26	51.42	94.53
14	60.00	20.00	20.00	97.03	34.18	94.96

### 3.2. Fit Summary

The fit summary obtained from the DOE optimal design tool for the model of Malachite Green (MG), Methyl Orange (MO) and Crystal Violet (CV) can be found in Tables 2. The Linear model to be the suggested model for the removal of Malachite Green, with a standard deviation of 2.40, an adjusted  $R^2$  and predicted  $R^2$  value of 0.4546 and 0.1232, respectively, while table 3 shows that the Linear and Quadratic models to be the suggested model for the removal of Methyl Orange with the standard deviation of 4.594E-06 and 3.387E-06 respectively and Table 4 shows that Special Quartic model to be the suggested model for the removal of Crystal Violet with the standard deviation of 0.3891.

Table 2: Fit summary for Malachite Green, Methyl Orange and Crystal Violet

Source		Std. Dev.	$R^2$	Adjusted $R^2$	Predicted $R^2$	PRESS
Malachite Green	Linear	2.40	0.5385	0.4546	0.1232	119.93*
	Quadratic	1.91	0.7868	0.6536	-0.3438	183.81
	Special Cubic	1.95	0.8044	0.6368	-0.4589	199.56
	Cubic	2.18	0.8607	0.5471	0.1699	113.55
	Special Quartic	2.00	0.8535	0.6192	-0.4214	194.42
Methyl Orange	Linear	4.594E-06	0.5528	0.4715	0.2220	4.038E-10*
	Quadratic	3.387E-06	0.8232	0.7126	0.1879	4.215E-10*
	Special Cubic	3.562E-06	0.8288	0.6821	0.0622	4.867E-10
	Cubic	3.976E-06	0.8782	0.6041	-4.3587	2.781E-09
	Special Quartic	4.004E-06	0.8456	0.5984	-6.4458	3.864E-09
Crystal Violet	Linear	1.23	0.1492	-0.0399	-0.5725	25.29
	Quadratic	1.29	0.3768	-0.1426	-8.5016	152.79
	Special Cubic	1.25	0.5104	-0.0771	-7.7876	141.31
	Cubic	0.6319	0.9503	0.7269	-648.9544	10451.85
	Special Quartic	0.3891	0.9718	0.8964	-5.2198	100.02*

### 3.3 Analysis of Variance

The Model F-value of 7.45 for the linear model implies the model is significant. There is only a 1.42% chance that an F-value this large could occur due to noise (Table 3). While the Model F-value of 7.45 for the Quadratic Model implies the model is significant. There is only a 0.70% chance that an F-value this large could occur due to noise. And The Model F-value of 12.90 implies the model is significant. There is only a 2.96% chance that an F-value this large could occur due to noise. P-values less than 0.0500 indicate model terms are significant. In the case of the Linear Model, A, B, and C are significant model terms. While for the Quadratic model, A, and AC are significant model terms. And for the Special Quartic model, cases A, B, C,  $AB^2C$ , and  $ABC^2$  are significant model terms. Values greater than 0.1000 indicate the model terms are not significant. Model reduction may enhance the model if there are numerous unnecessary terms.

Table 3: ANOVA of Linear, Quadratic and Special Quartic Models for the Removal of Malachite Green, Methyl Orange and Crystal Violet

Source		Sum of Squares	df	Mean Square	F-value	p-value
Malachite Green	Model	73.66	2	36.83	6.42	0.0142*
	<sup>(1)</sup> Linear Mixture	73.66	2	36.83	6.42	0.0142
	Residual	63.12	11	5.74		
	Cor Total	136.79	13			
Methyl Orange	Model	4.272E-10	5	8.544E-11	7.45	0.0070*
	<sup>(1)</sup> Linear Mixture	2.869E-10	2	1.434E-10	12.50	0.0035
	AB	2.222E-11	1	2.222E-11	1.94	0.2015
	AC	1.146E-10	1	1.146E-10	9.99	0.0134

	BC	7.253E-12	1	7.253E-12	0.6322	0.4495
	Residual	9.178E-11	8	1.147E-11		
	Cor Total	5.190E-10	13			
	Model	15.63	8	1.95	12.90	0.0296*
	<sup>(1)</sup> Linear Mixture	2.40	2	1.20	7.92	0.0635
	AB	0.8915	1	0.8915	5.89	0.0936
	AC	0.1429	1	0.1429	0.9440	0.4029
Crystal Violet	BC	0.4049	1	0.4049	2.67	0.2005
	A <sup>2</sup> BC	0.0207	1	0.0207	0.1365	0.7363
	AB <sup>2</sup> C	1.54	1	1.54	10.19	0.0496
	ABC <sup>2</sup>	5.92	1	5.92	39.07	0.0083
	Residual	0.4542	3	0.1514		
	Cor Total	16.08	11			

\* Significant

### 3.3.1. Model Equations

The model Equations (1) and (2), obtained in terms of L pseudo component and real component, respectively, in the Removal Efficiency of Malachite Green shows that the equation in terms of coded factors can be used to make predictions about the response for given levels of each factor. By default, the high levels of the mixture components are coded as +1 and the low levels are coded as 0. The coded equation is useful for identifying the relative impact of the factors by comparing the factor coefficients. While Equation 3 and 4, obtained in terms of L pseudo component and Real Component for the Removal Efficiency of Methyl Orange respectively shows that the equation in terms of coded factors can be used to make predictions about the response for given levels of each factor. By default, the high levels of the mixture components are coded as +1 and the low levels are coded as 0. The coded equation is useful for identifying the relative impact of the factors by comparing the factor coefficients. And Equation 5 obtained in terms of pseudo component for the Removal Efficiency of Crystal Violet shows that the equation in terms of coded factors can be used to make predictions about the response for given levels of each factor. By default, the high levels of the mixture components are coded as +1 and the low levels are coded as 0. The coded equation is useful for identifying the relative impact of the factors by comparing the factor coefficients.

$$\text{REMOVAL EFFICIENCY (MALACHITE GREEN)} = +99.21A + 98.06B + 91.09C \quad (1)$$

$$\begin{aligned} (\text{REMOVAL EFFICIENCY (METHYL ORANGE)})^{-3} = & +0.0000A + 3.053 \times 10^{-6}B + 4.548 \times 10^{-6} - \\ & 0.0000AB - 0.0000AC + 0.0000BC \quad (3) \end{aligned}$$

$$\begin{aligned} \text{REMOVAL EFFICIENCY (CRYSTAL VIOLET)} = & +95.07A + 96.04B + 93.35C + 3.91AB - 1.88AC + \\ & 2.64BC - 31.07A^2BC - 154.01AB^2C + 344.82ABC^2 \quad (5) \end{aligned}$$

A=Malachite Green, B=Methyl Orange and C= Crystal Violet

### 3.3.2. Fit Statistics

The difference between the Predicted R<sup>2</sup> of 0.1232 and the Adjusted R<sup>2</sup> of 0.4546 is not as great for Malachite Green. While for Methyl Orange, as one may typically anticipate, the Predicted R<sup>2</sup> of 0.1879 is not as near to the Adjusted R<sup>2</sup> of 0.7126. It is more than 0.2, in other words, this might point to a significant block effect or suggest that the model and/or the data have a flaw. Model reduction, response transformation, outliers, and other factors should all be taken into account. And for Crystal Violet, a negative Predicted R<sup>2</sup> implies that the overall mean may be a better predictor of the response than the current model. Adeq Precision measures the signal-to-noise ratio. A ratio greater than 4 is desirable. A sufficient signal is shown by the ratio of 7.323 for Malachite Green, 9.413 for Methyl Orange and 12.117 for Crystal Violet. To move around the design space, these models can be utilized.

Table 4: Fit statistics for Malachite Green, Methyl Orange and Crystal Violet

	Malachite green	Methyl orange	Crystal violet
Std. Dev.	2.40	3.387E-06	0.3891
Mean	96.28	8.004E-06	95.59
C.V. %	2.49	42.32	0.4070
R <sup>2</sup>	0.5385	0.8232	0.9718
Adjusted R <sup>2</sup>	0.4546	0.7126	0.8964
Predicted R <sup>2</sup>	0.1232	0.1879	-5.2198
Adeq Precision	7.3233	9.4132	12.1173

### 3.4. Diagnostic Case Study

## Optimisation of Removal Efficiency of Palm Kernel Shell Ash in the Treatment of Multicomponent Dyes in Simulated Wastewater

Diagnostic case studies for the responses (RE) of Malachite Green, Methyl Orange and Crystal Violet adsorption onto the Ashed Palm Kernel Shell (APKS) at different optimized mixture shows the actual values obtained from the experimental procedure and predicted values generated by the software (Table 4). Runs 2, 3, 6, 7, 9, 10, 11, and 13 have positive residuals while runs 1, 4, 5, 8, 12, and 14 have negative residuals for the RE.

Table 5: Diagnostic Report on Actual Value, Predicted Value and Residual of Malachite Green, Methyl Orange and Crystal Violet

Run Order	Malachite Green			Methyl Orange			Crystal Violet		
	Actual Value	Predicted Value	Residual	Actual Value	Predicted Value	Residual	Actual Value	Predicted Value	Residual
1	87.26	91.09	-3.83	3.432E-06	4.548E-06	-1.116E-06	93.42	93.35	0.0714
2	98.73	98.06	0.6680	3.699E-06	3.053E-06	6.454E-07	96.07	96.04	0.0313
3	95.54	94.55	0.9864	6.614E-06	6.404E-06	2.106E-07	95.18	95.35	-0.1610
4	91.72	94.64	-2.92	7.246E-06	6.161E-06	1.085E-06	96.00	95.78	0.2197
5	96.79	97.20	-0.4107	2.405E-06	4.899E-06	-2.494E-06	95.01	95.13	-0.1216
6	96.29	93.46	2.83	4.311E-06	3.412E-06	8.987E-07	97.27	97.43	-0.1576
7	99.14	96.12	3.03	3.446E-06	5.403E-06	-1.957E-06	97.49	97.32	0.1673
8	96.36	98.48	-2.11	0.0000	8.805E-06	5.651E-06	95.73	96.05	-0.3278
9	95.89	95.24	0.6558	6.817E-06	4.602E-06	2.215E-06	94.62	94.79	-0.1701
10	98.33	95.17	3.16	6.094E-06	4.501E-06	1.593E-06	96.84	96.53	0.3113
11	99.52	98.64	0.8850	5.066E-06	9.263E-06	-4.198E-06	94.53	94.28	0.2468
12	98.08	98.92	-0.8357	0.0000	0.0000	7.297E-07	94.96	95.07	-0.1097
13	97.26	97.18	0.0805	7.354E-06	0.0000	-4.386E-06			
14	97.03	99.21	-2.18	0.0000	0.0000	1.123E-06			

### 3.4.1. Actual, Predicted and Residual Values

The plot of the Normal Plot of Residuals for Removal Efficiency of Malachite Green, Methyl Orange and Crystal Violet (Fig. 1a-c) shows how well spread the points are on the graph. Malachite Green has less stacking compared to Methyl Orange and Crystal Violet making Malachite Green have minimal error compared to Methyl Orange and Crystal Violet. Figure 2 related the residual value with Table 8, where the runs for the residual values are positive and where some are negative. Each point above the line in Figure (2a-c) shows the number of runs for the residual values that are positive and every point below the line shows the runs for the negative residual values

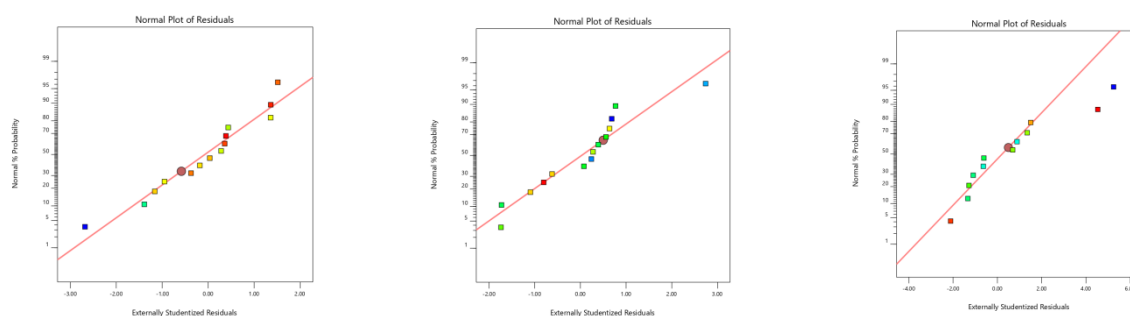


Figure 1: Normal plot for residual of (a) Malachite Green, (b) Methyl Orange and (c) Crystal Violet

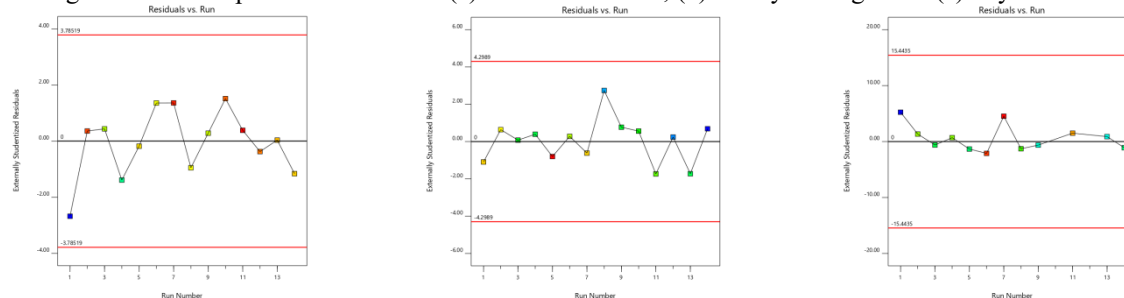


Figure 2: Residual vs Run plot for (a) Malachite Green, (b) Methyl Orange and (c) Crystal Violet

## Response Surface Plot

Figures 3-4 describe the state of the equation model for each of the RE of MG, MO and CV. The flat surfaces of the 3D areas describe that the equation is linear while the contours on the 3D areas indicate that the equation is either quadratic or special quartic. The Red region of the figures shows the feasible region where the adsorption process is taking place while the blue region is the point where the least adsorption process is taking place and the green region is where the adsorption process is feasible.

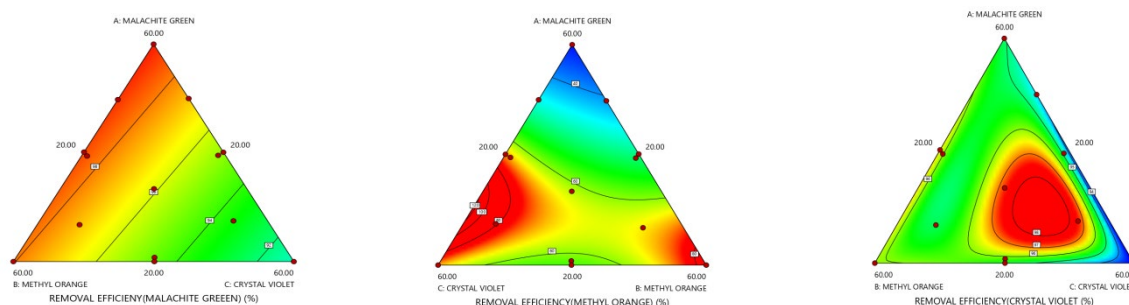


Figure 3: 2D view of the Removal Efficiency for (a) Malachite Green, (b) Methyl Orange and (c) Crystal Violet

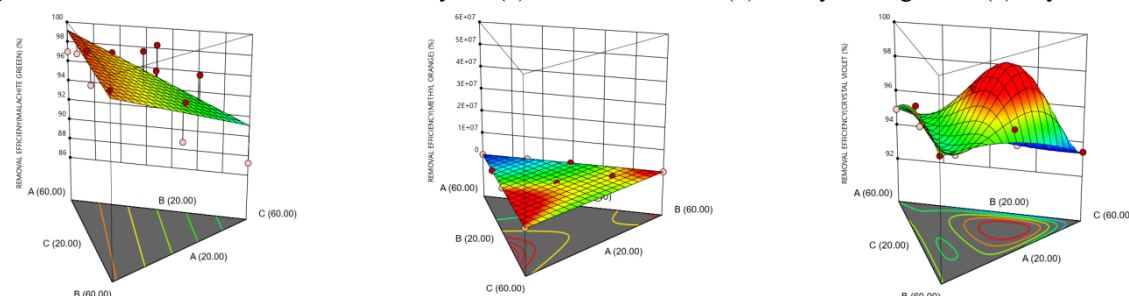


Figure 4: 3D view of the Removal Efficiency for (a) Malachite Green, (b) Methyl Orange and (c) Crystal Violet

## CONCLUSION

The removal of Malachite Green, Methyl Orange, and Crystal Violet from wastewater using APKS was successfully studied utilizing the DOE optimal design tool. Malachite Green, Methyl Orange, and Crystal Violet had the greatest RE of the APKS at Runs 11, 5, and 10 correspondingly, with 99.52%, 74.64%, and 98.46% obtained. For process optimization and statistical experimental designs, the linear model, quadratic model, and special quartic model were established. These models were shown to help predict and comprehend the interacting effects of the chosen process parameters.

## REFERENCES

- Alabi, O., Alade A.O., & Afolabi, T. J. (2020). Process optimization of adsorption of Cr(VI) on adsorbent prepared from Bauhinia rufescence pod by Box-Behnken Design. *Separation Science and Technology (Philadelphia)*, 55(1), 47–60.
- Baffour-Awuah, E., Akinlabi, S. A., Jen, T. C., Hassan, S., Okokpujie, I. P., & Ishola, F. (2021). Characteristics of Palm Kernel Shell and Palm Kernel Shell-Polymer Composites: A Review. *IOP Conference Series: Materials Science and Engineering*, 1107(1), 012090.
- Drumond Chequer, F. M., de Oliveira, G. A. R., Anastacio Ferraz, E. R., Carvalho, J., Boldrin Zanoni, M. V., & Oliveir, D. P. (2013). Textile Dyes: Dyeing Process and Environmental Impact. *Eco-Friendly Textile Dyeing and Finishing*. <https://doi.org/10.5772/53659>
- Rafatullah, M., Sulaiman, O., Hashim, R., & Ahmad, A. (2010). Adsorption of methylene blue on low-cost adsorbents: A review. *Journal of Hazardous Materials*, 177(1–3), 70–80.
- Slama, H. ben, Bouket, A. C., Pourhassan, Z., Alenezi, F. N., Silini, A., Cherif-Silini, H., Oszako, T., Luptakova, L., Golińska, P., & Belbahri, L. (2021). Diversity of synthetic dyes from textile industries, discharge impacts and treatment methods. *Applied Sciences (Switzerland)*, 11(14), 1–21. <https://doi.org/10.3390/app11146255>



## Suitability of Adsorptive Cellulose derived from *Tithonia diversifolia* Xylem for the Treatment of Multicomponent Pharmaceutical Wastewater: Adsorption Capacity Optimization

Olusesan A. OLU-AROTIOWA<sup>1</sup>, Abdulganiy O. YUSUF<sup>1,2</sup>, Monsur O. DAUDA<sup>1,2</sup>, Omodele A.A. ELETTA<sup>3</sup>, Kazeem K. SALAM<sup>1</sup>, Rasheed O. ADETORO<sup>4</sup>, Lekan T. POPOOLA<sup>5</sup>, Tinuade J. AFOLABI<sup>1,2</sup> and Abass O. ALADE<sup>1,2,6\*</sup>,

<sup>1</sup>Department of Chemical Engineering, Ladoke Akintola University of Technology, P.M.B. 4000, Ogbomoso, Nigeria

<sup>2</sup>Bioenvironmental, Water and Engineering Research Group, (BWERG), Ladoke Akintola University of Technology, P.M.B. 4000, Ogbomoso, Nigeria

<sup>3</sup>Department of Chemical Engineering, University of Ilorin, Ilorin, Nigeria

<sup>4</sup>Department of Pure and Applied Chemistry, Osun State University, Osogbo, Nigeria

<sup>5</sup>Department of Chemical and Petroleum Engineering, College of Engineering, Afe Babalola University Ado-Ekiti, ABUAD, Ado-Ekiti, Ekiti State, Nigeria

<sup>6</sup>Science and Engineering Research Group, (SEARG), Ladoke Akintola University of Technology, P.M.B. 4000, Ogbomoso, Nigeria

\*Corresponding author: [aalade@lautech.edu.ng](mailto:aalade@lautech.edu.ng) +2347037885961

### ABSTRACT

The presence of residual pharmaceutical products in the surface water is detrimental to the plant and animal lives, thus there is growing agitation for their removal. Raw *Tithonia Diversifolia* (sunflower) Xylem (TDX) was employed to develop a cellulose-based adsorbent for the treatment of wastewater containing mixtures of Tetracycline, Metronidazole and Cotrimoxazole. The raw TDX obtained was washed, dried, uniformly milled and treated with 4 wt.% NaOH at 80 °C for 2 h, before being acetylated and treated with NaClO<sub>2</sub> for 24 h. The residue was washed, dried at 50 °C and then treated with H<sub>2</sub>O<sub>2</sub> (30 %). The product was neutralized and dried as TDX cellulose. Simplex Lattice Design of the Design-Expert (12.0.1) software was employed to simulate possible mixing ratios of the three selected pharmaceuticals in the ranges of 25–50 mg L<sup>-1</sup>. The batch adsorption experiment was carried out at room temperature, 150 rpm and 60 mins. The residual concentration of the pharmaceutical mixture was determined using 357 nm, 340 nm and 520 nm wavelengths in a UV-visible spectrophotometer, for Tetracycline, Metronidazole and Co-trimoxazole, respectively. The data generated were analysed statistically with the Design-Expert software. The maximum Adsorption Capacity (*q<sub>e</sub>*) obtained were 4.7715, 4.2259 and 4.8372 mg/g respectively. The linear model developed gave R<sup>2</sup>, adjusted R<sup>2</sup> and standard deviation of (1.0000, 1.0000 and 0.0037), (0.0630, 0.9992 and 0.9951) and (0.1174, 0.9833 and 0.9858) for Tetracycline, Metronidazole and Co-trimoxazole respectively. The developed TDX cellulose adsorbent demonstrated satisfactory adsorption capacity for remediating wastewater containing pharmaceutical pollutants.

Keywords: Adsorption, Cellulose, Optimization, Pharmaceutical, *Tithonia diversifolia*.

### 1. INTRODUCTION

Due to industrial development across the world and the rapid growth of industries, several toxic waste materials are regularly released into the aquatic environment from industries (Li et al. 2020). Such pollutants include heavy metals, radioactive substances, dyes, pesticides, pharmaceuticals, chiral chemicals as well as oil contaminants (Ahmed and Hameed 2018; Alharbi et al. 2018; Basheer 2018; Eze et al. 2019a, b; Sarim et al. 2019; Umeh et al. 2019).

Water is a raw material that is used in the pharmaceutical industry for the production, manufacturing, extraction, processing, purification and packaging of chemical and biological materials, such as solids and liquids to be used as a medication for humans and animals. Wastewaters in the pharmaceutical manufacturing industry usually originate from the washing of the floor and the equipment used during the production process. For example, antibiotic drugs which are commonly used for treating or preventing human and animal diseases can find their way to water bodies through human activities (Liu et al. 2012). Recently, water pollution from pharmaceuticals and drug residues has also been increasing at an alarming rate (Wharfe et al. 2010; Bahar et al. 2018). They are referred to as emerging pollutants and are undesirable due to their genetic, hormonal and endocrine nature of disturbance (Wharfe et al. 2010; Bahar et al. 2018).

Pharmaceutical contaminants in general, when present in the aqueous environment, build drug resistance in organisms (Ahmed and Hameed 2018; Akpomie et al. 2019a). There have been many technologies to deal with antibiotics from wastewater, such as membrane separation, oxidation, electrochemistry, photodegradation, biodegradation and adsorption (Aydin et al. 2016; Radjenovic & Petrovic 2017). However, the adsorption method has become the main method in practical applications due to its high efficiency, simple operation and low energy consumption. Nowadays, research is aimed at utilizing effective, easily obtainable and low-cost adsorbents for the adsorption process such as cellulose, zeolites, chitosan, etc.

In this study, sustainable cellulose was used as an adsorbent which was derived from *tithonia diversifolia* (sunflower) xylem for the treatment of multicomponent pharmaceutical wastewater. The experimental model was designed with the use of a Simplex Lattice Design from the mixture (Design Expert v 12.0) in which the factors that affect adsorption such as the effect of time and initial concentration on adsorption capacity were studied also adsorption isotherms and kinetics were also examined.

## 2.0 MATERIALS AND METHODS

### Preparation of TDX Cellulose Derived Adsorbent

The TDX used in this study was obtained within the Yusuf Oladuni and Co-operation (YOACO) area, Ogbomosho-Ilorin Expressway Ogbomosho Oyo state. All the reagents were of analytical grade. Sodium hydroxide (NaOH), Ethanoic acid (CH<sub>3</sub>COOH), Sodium chlorite (NaClO<sub>2</sub>) and Hydrogen peroxide (H<sub>2</sub>O<sub>2</sub>) were supplied by Labtech Scientific Company.

The TDX obtained was washed, dried, milled and sieved (10 µm) before being treated with NaOH of 4 wt.% to dissolve the unwanted materials in the wood leaving relatively pure cellulose at 80 °C for 2 h, treated with CH<sub>3</sub>COOH and NaClO<sub>2</sub> to remove lignin on plant and agitated for 24h at room temperature. The residue was washed till neutral and dried to steady weight. Finally, treated with (30%) H<sub>2</sub>O<sub>2</sub> which is used to remove coloured lignin and decomposed chromophoric materials from the cellulose residue. Cellulose derived was used for the adsorption process without any modification or activation.

## 2.1 BATCH ADSORPTION STUDIES

### Adsorbate Preparation

For the synthesis of tetracycline (100 mg), 0.11g was weighed and diluted with distilled water of 1000 ml, for metronidazole (100 mg), 0.24 g was weighed and diluted with distilled water of 1000 ml, for co-trimoxazole (100 mg), 0.13 g was weighed and diluted with a distilled water of 1000 ml, after which they were shaken till uniform dissolution. The batch adsorption study was carried out in a mechanical shaker at ambient temperature in which 1g of TDX cellulose was mixed with 100 ml of 100 mg/L of tetracycline, metronidazole and cotrimoxazole at 25%, 50% and 25% respectively for 60 mins at 150 rpm was carried out to access the effectiveness of the cellulose. The solution after 60 mins was decanted and centrifuged at 1000 rpm for 5 min. The precipitate form was decanted and analysed at a maximum wavelength of 357 nm, 340 nm and 520 nm for tetracycline, metronidazole and co-trimoxazole respectively. The adsorption capacity was calculated using;

$$\text{Adsorption capacity} = \frac{C_0 - C_e}{M} \times V \quad (1)$$

Where C<sub>0</sub> is the initial concentration (mg/L), C<sub>e</sub> is the final concentration (mg/L), M is the mass of the sample (g) and V is the volume (L).

## 2.2 EXPERIMENTAL MODEL

Simple Lattice Design was employed to optimize the experimental runs of the adsorption of multicomponent pharmaceutical wastewater onto the TDX cellulose. The mixtures chosen for the study were tetracycline, metronidazole and cotrimoxazole by which the response to be determined is adsorption capacity (q<sub>e</sub>) mg/g. The experiment was conducted within the range of 25-50% as shown in Table 1

Table 1: Mix ratio of tetracycline, metronidazole and co-trimoxazole within 25-50 %

Component	Unit	Level	
		Low	High
A – Tetracycline	%	25	50
B – Metronidazole	%	25	50
C – Co-trimoxazole	%	25	50

## 3. RESULTS AND DISCUSSION



### 3.1 Responses from the Experimental Data

The Design Expert software helps in the study of the adsorption capacity for the tetracycline, metronidazole and cotrimoxazole mixture. The response in terms of adsorption capacity for tetracycline, metronidazole and cotrimoxazole ranges from (2.21-4.77 mg/g), (1.76-4.23 mg/g) and (2.28-4.84 mg/g) respectively. The highest and lowest  $q_e$  for tetracycline can be found in run 2 and run 10 respectively, for the highest and lowest  $q_e$  for metronidazole can be found in run 11 and run (2/6) respectively, for the highest and lowest  $q_e$  for cotrimoxazole can be found in run 1 and run 6 respectively (Table 2).

Table 2: Response from the Experimental runs Simplex Lattice Design

Runs	Mixtures (%)			Response (adsorption capacity (mg/g))		
	Tetracycline	Metronidazole	Cotrimoxazole	Tetracycline	Metronidazole	Cotrimoxazole
1	25.00	25.00	50.00	2.27	1.89	4.84
2	50.00	25.00	25.00	4.77	1.76	2.30
3	33.33	33.33	33.33	3.09	2.54	2.98
4	37.50	37.50	25.00	3.50	2.92	2.43
5	37.50	37.50	25.00	3.50	2.92	2.49
6	50.00	25.00	25.00	4.76	1.76	2.28
7	25.00	25.00	50.00	2.27	1.89	4.83
8	25.00	37.50	37.50	2.27	2.90	3.41
9	41.67	29.17	29.17	3.92	2.18	2.84
10	25.00	50.00	25.00	2.21	3.98	2.30
11	25.00	50.00	25.00	2.21	4.23	2.46
12	29.17	41.67	29.17	2.63	3.39	2.86
13	29.17	29.17	41.67	2.72	2.19	4.05
14	37.50	25.00	37.50	3.48	1.78	3.72

### 3.2 Analysis of Variance (ANOVA) for Tetracycline

The adequacy of the model was further examined by analysis of variance. The ANOVA for the special quartic model of tetracycline, metronidazole and co-trimoxazole are given in Tables 3-5. The model  $F$ -values were 97155.60, 1115.45 and 383.15 for tetracycline, metronidazole and co-trimoxazole, respectively, implying the model is significant. There is only a 0.01 % chance that an  $F$ -value this large could occur due to noise.  $P$ -values less than 0.05 indicate model terms are significant. In the case of tetracycline, A, B, C, AB, AC, BC, AB<sup>2</sup>C, and ABC<sup>2</sup> are significant model terms. While A, B, and C are significant for both metronidazole and co-trimoxazole are significant model terms. Values greater than 0.10 indicate the model terms are not significant. If there are many insignificant model terms (not counting those required to support hierarchy), model reduction may improve your model.

The Lack of Fit  $F$ -values of 7.46, 0.26 and 4.68 for tetracycline, metronidazole and cotrimoxazole, respectively, imply there is 5.24, 94.05 and 7.73 % for tetracycline, metronidazole and co-trimoxazole, respectively, chance that a Lack of Fit  $F$ -value this large could occur due to noise. Lack of fit is bad for both tetracycline and co-trimoxazole, while a non-significant lack of fit is good for metronidazole, we want the model to fit. This relatively low probability (<10 %) is troubling.

Table 3: ANOVA for Special Quartic model of Adsorption capacity (Tetracycline)

Source	SOS	DF	MS	F-value	p-value	
Model	10.74	8	1.34	97155.60	< 0.0001	significant
<sup>(1)</sup> Linear Mixture	10.74	2	5.37	3.884E+05	< 0.0001	
AB	0.0003	1	0.0003	21.37	0.0057	

AC	0.0010	1	0.0010	71.79	0.0004	
BC	0.0006	1	0.0006	45.61	0.0011	
A <sup>2</sup> BC	6.745E-06	1	6.745E-06	0.4879	0.5160	
AB <sup>2</sup> C	0.0018	1	0.0018	127.61	< 0.0001	
ABC <sup>2</sup>	0.0025	1	0.0025	180.26	< 0.0001	
Residual	0.0001	5	0.0000			
Lack of Fit	0.0000	1	0.0000	7.46	0.0524	NS
Pure Error	0.0000	4	6.031E-06			
Cor Total	10.74	13				

Table 4: ANOVA for Linear model Adsorption capacity (Metronidazole)

Source	SOS	DF	MS	F-value	p-value	
Model	8.86	2	4.43	1115.45	< 0.0001	significant
<sup>(1)</sup> Linear Mixture	8.86	2	4.43	1115.45	< 0.0001	
Residual	0.0437	11	0.0040			
Lack of Fit	0.0138	7	0.0020	0.2625	0.9405	NS
Pure Error	0.0299	4	0.0075			
Cor Total	8.91	13				

Table 5: ANOVA for Linear model for adsorption capacity (Co-trimoxazole)

Source	SOS	DF	MS	F-value	p-value	
Model	10.56	2	5.28	383.15	< 0.0001	significant
<sup>(1)</sup> Linear Mixture	10.56	2	5.28	383.15	< 0.0001	
Residual	0.1516	11	0.0138			
Lack of Fit	0.1351	7	0.0193	4.68	0.0773	NS
Pure Error	0.0165	4	0.0041			
Cor Total	10.71	13				

NS - Not Significant, DF - Degree of Freedom, SOS - Sum of Squares, MS - Mean Square

### 3.3 Fit Statistic

The Predicted R<sup>2</sup> of 0.9995, 0.9903 and 0.9796 for tetracycline, metronidazole and cotrimoxazole, respectively, are in reasonable agreement with the Adjusted R<sup>2</sup> of 1.0000, 0.9942 and 0.9833 for tetracycline, metronidazole and cotrimoxazole, respectively. That is, the difference is less than 0.2. Adeq Precision measures the signal-to-noise ratio. A ratio greater than 4 is desirable. Your ratio of 857.742, 80.232 and 45.094 indicate adequate signals. The models can be used to navigate the design space. The plot of predicted vs actual R<sup>2</sup> justifies the correlation coefficient R<sup>2</sup>, which shows most of the points are closer to the straight line expressed in the plot (Figures 1, 3 and 5) and the model graph (Figures 2, 4 and 6). Thus, this is the reason for the high value of R<sup>2</sup>.

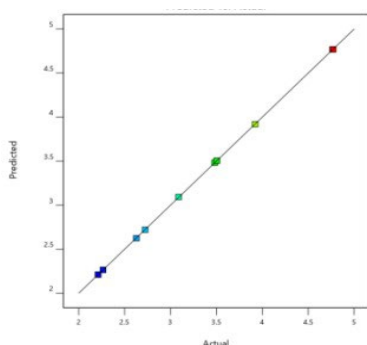


Figure 1: Graph of predicted vs actual

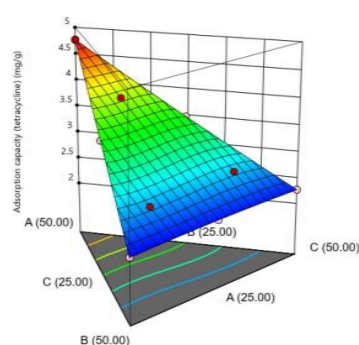


Figure 2: 3D model graph

## Suitability of Adsorptive Cellulose derived from *Tithonia diversifolia* Xylem for the Treatment of Multicomponent Pharmaceutical Wastewater: Adsorption Capacity Optimization

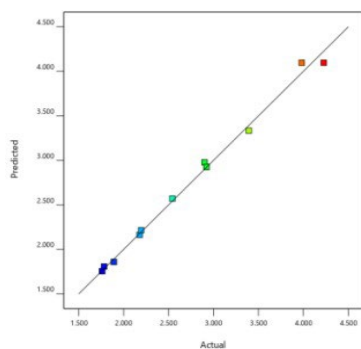


Figure 3: Graph of predicted vs actual

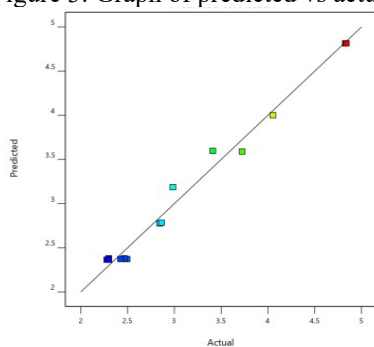


Figure 5: Graph of predicted vs actual

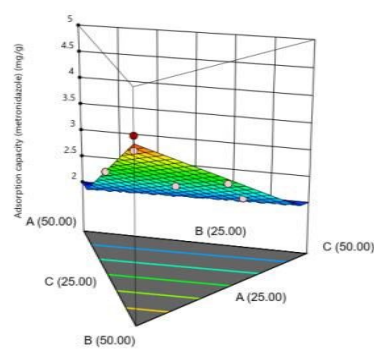


Figure 4: 3D Model graph

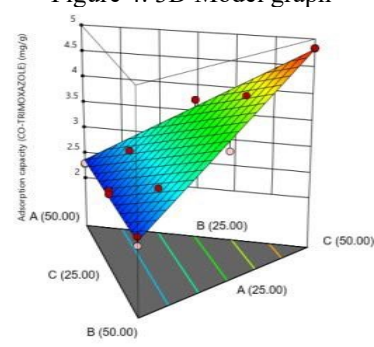


Figure 6: 3D Model graph

### 3.4 Model Equations Generated

The equation in terms of coded factors can be used to make predictions about the response for given levels of each factor. The coded equation is useful for identifying the relative impact of the factors by comparing the factor coefficients. The final equation derived from the statistical analysis of the adsorption capacity ( $q_e$ ) is expressed in equations 1, 2 and 3 for tetracycline, metronidazole and cotrimoxazole respectively

$$q_e = 4.77A + 2.21B + 2.27C + 0.0595AB - 0.1402AC + 0.1118BC - 0.2566A^2BC - 4.15AB^2C + 5.00ABC^2 \quad (1)$$

$$q_e = 1.76A + 4.10B + 1.86C \quad (2)$$

$$q_e = 2.36A + 2.38B + 4.82C \quad (3)$$

where  $q_e$  is the Adsorption Capacity in mg/g, A, B and C are tetracycline, metronidazole and co-trimoxazole are in % respectively, the positive signs show favorability of the factor for increased responses while negative signs show opposition to increased responses (Alade *et al.*, 2012).

A comparison of TDX cellulose developed to other adsorbents employed for the removal of various antibiotics is presented in Table 6 and the TDX cellulose developed showed an acceptable performance in terms of its maximum adsorption capacity ( $q_{max}$ ), compared with others

Table 6: Comparison of the performance of TDX cellulose with other adsorbents

Adsorbent	Dosage ( $g L^{-1}$ )	Antibiotic	Optimum Time (min)	$Q_{max}$ ( $mg g^{-1}$ )	Reference
Au-TiO <sub>2</sub> @ZnFe <sub>2</sub> O <sub>4</sub>	1.0	Tetracycline	240	-	Jia, et al., (2017)
ZnFe <sub>2</sub> O <sub>4</sub> /Ag/PEDOT	0.002	Tetracycline	120	1.47	Lu, et al., (2017)
Fe-modified Sepiolite	0.2	Metronidazole	15	5.62	Ding, and Bian,(2015)
Nanocellulose	1.5	Tetracycline	120	7.73	Rathod, et al.,(2017)
Fe <sub>3</sub> O <sub>4</sub> -chitosan MIPs	0.01	Sulfamethoxazole	30	4.32	Qin, et al., (2015)
TDX cellulose	1.0	Tetracycline,		4.78	
		Metronidazole	60	4.23	Current study
		Co-trimoxazole		4.84	

### 4.0 CONCLUSION

The Cellulose produced from *tithonia diversifolia* xylem has shown a great effect in the removal of multicomponent pharmaceutical wastewater and the use of simplex lattice design under the mixture design of the Design Expert (12.0.1) has been successfully employed to test the adsorption capacity. A special quartic model was used for the analysis of variance (ANOVA) for tetracycline while a linear model was used for metronidazole and cotrimoxazole. Therefore,

the optimization of adsorptive cellulose derived from tithonia diversifolia has shown an effective usage for the removal of multicomponent pharmaceutical wastewater.

## REFERENCES

- Ahmed MJ, Hameed BH (2018) Removal of emerging pharmaceutical contaminants by adsorption in a fixed bed column: a review. *Ecotoxicol Environ Safe* 149:pp. 257–266.
- Akpomie KG, Fayomi OM, Ezeofor CC, Sha’Ato R, Vanzyl WE (2019) Insights into the use of metal complexes of thiourea derivatives as highly efficient adsorbents for ciprofloxacin from contaminated water. *Trans R Soc South Afr* 74(2) pp.180-188.
- Alharbi OM, Khattab RA, Ali I (2018) Health and environmental effects of persistent organic pollutants. *J Mol Liq* 263: pp.442–453. <https://doi.org/10.1016/j.molliq.2018.05.029>
- Aydin, E. et al. 2016 Chlortetracycline removal by using hydrogen-based membrane biofilm reactor. *Journal of Hazardous Materials* 320, pp. 88–95.
- Bahar MM, Mahbub KR, Naidu R, Megharaj M (2018) As(V) removal from aqueous solution using a low-cost adsorbent coir pith ash: equilibrium and kinetic study. *Environ TechnolInnov* 9, pp.198–209. <https://doi.org/10.1016/j.eti.2017.12.005>
- Basheer AA (2018) Chemical chiral pollution: impact on the society and science and need of the regulations in the 21<sup>st</sup> century. *Chirality* 30(4), pp. 402–406
- Ding, H., and Bian, G. (2015) Adsorption of metronidazole in aqueous solution by Fe-modified sepiolite, *Desalination and Water Treatment*, 55, pp.1620 -1628.
- Eze SI, Akpomie KG, Ezeofor CC, Mmadubuike MV, Ojo FK (2019) Remediation of oil spill polluted water from Niger Delta Nigeria by sorption onto ammonium sulfate modified *Dialiumguineense* seed husk. *Petrol Sci Technol* 37(15), pp. 1830–1838.
- Eze SI, Akpomie KG, Ezeofor CC, Osunkunle AA, Maduekwe OB, Okenyeka OU (2019b) Isotherm and kinetic evaluation of *dialium guineense* seed husk and its modified derivative as efficient sorbent for crude oil polluted water treatment. *Water Conserv Sci Eng.* 4, pp. 21–31. <https://doi.org/10.1007/s41101-019-00065-6>
- Jia, Y., J. Liu, S. Cha, S. Choi, Y.C. Park, C. Liu, (2017) Magnetically separable AuTiO<sub>2</sub>/nanocube ZnFe<sub>2</sub>O<sub>4</sub> composite for chlortetracycline removal in wastewater under visible light, *Journal of Industrial and Engineering Chemistry*, 47, pp. 303-314.
- Li D, Wang MQ, Lee C (2020) The waste treatment and recycling efficiency of industrial waste processing based on two-stage data envelopment analysis with undesirable inputs. *J Clean Prod* 242, pp. 118279. <https://doi.org/10.1016/j.jclepro.2019.118279>
- Lu, Z. Yu, J. Dong, M. Song, Y. Liu, X. Liu, Z. Ma, H. Su, Y. Yan, P. Huo, (2018) Facile microwave synthesis of a Z-scheme imprinted ZnFe<sub>2</sub>O<sub>4</sub>/Ag/PEDOT with the specific recognition ability towards improving photocatalytic activity and selectivity for tetracycline, *Chemical Engineering Journal*, 337, pp. 228-241.
- Qin, S., L. Su, P. Wang, and Y. Gao, (2015) Rapid and selective extraction of multiple sulfonamides from aqueous samples based on Fe<sub>3</sub>O<sub>4</sub>-chitosan molecularly imprinted polymers, *Analytical Methods*, 7, pp. 8704-8713.
- Radjenovic, J. & Petrovic, M. 2017 Removal of sulfamethoxazole by electrochemically activated sulfate: implications of chloride addition. *J. of Hazar. Materials* 333, pp. 242.
- Rathod, M., S. Haldar, and S. Basha, (2015) Nanocrystalline cellulose for removal of tetracycline hydrochloride from water via biosorption: Equilibrium, kinetic and thermodynamic studies, *Ecological Engineering*, 84, pp.240-249
- Sarim KM, Kukreja K, Shah I, Choudhary CK (2019) Biosorption of direct textile dye Congo red by *Bacillus subtilis* HAU-KK01. *Bioremed J* 23(3) , pp. 185-195.
- Tao, J. Yang, C. Ma, J. Li, K. Du, Z. Wei, C. Chen, Z. Wang, C. Zhao, and X. Deng, (2020) Cellulose nanocrystals/graphene oxide composite for the adsorption and removal of levofloxacin hydrochloride antibiotic from aqueous solution, *R Soc Open Sci*, 7, pp. 200857200857
- Umeh C, Asegbeloyin JN, Akpomie KG, Oyeka EE, Ochonogor AE (2019) Adsorption properties of tropical soils from Awka north Anambra Nigeria for lead and cadmium ions from aqueous media. *Chem Afr.* <https://doi.org/10.1007/s42250-019-00109-3>
- Wharfe ES, Winder CL, Jarvis RM, Goodacre R (2010) Monitoring the effects of chiral pharmaceuticals on aquatic microorganisms by metabolic fingerprinting. *Appl Environ Microbiol* 76(7), pp. 2075– 2085. <https://doi.org/10.1128/AEM.02395-09>
- Xu, J.; Krietemeyer, E.F.; Boddu, V.M.; Liu, S.X.; Liu, W.C. (2018). Production and characterization of cellulose nanofibril (CNF) from agricultural waste corn stover. *Carbohydr. Polym.*, 192, pp. 202–207.



## Valourisation of Waste *Parkia Pendula* Inflorescence as Biosorbent for the Treatment of Synthetic Wastewater Containing Pesticides

Tinuade J. AFOLABI<sup>1,2</sup>, Hekram, A. SADIQ<sup>1,2</sup>, Adewemimo, O. POPOOLA<sup>1</sup>, Sunday, O. OLADUNNI<sup>1,2</sup>, O. Monsur, O. DAUDA<sup>1,2</sup>, Omotayo, S. AMUDA<sup>3</sup>, Abolaji, G. FAROMBI<sup>4</sup>, Esther O. AWOTONA<sup>1,2</sup>, and Abass O. ALADE<sup>1,2,5\*</sup>

<sup>1</sup> Department of Chemical Engineering, Ladoke Akintola University of Technology, P.M.B. 4000, Ogbomoso, Nigeria

<sup>2</sup> Bioenvironmental, Water and Engineering Research Group, (BWERG), Ladoke Akintola University of Technology, P.M.B. 4000, Ogbomoso, Nigeria

<sup>3</sup> Analytical/Environmental Chemistry Unit, Department of Pure and Applied Chemistry, Ladoke Akintola University of Technology, Ogbomoso, Nigeria

<sup>4</sup> Department of Science Laboratory Technology, Osun State Polytechnic, Iree, Nigeria

<sup>5</sup> Science and Engineering Research Group, (SEARG), Ladoke Akintola University of Technology, P.M.B. 4000, Ogbomoso, Nigeria

Corresponding Author: [aolade@lautech.edu.ng](mailto:aolade@lautech.edu.ng) +2347037885961

### ABSTRACT

The increasing presence of pesticides in the water bodies, due to the surge in their uses in modern day agricultural activities, is deleterious to the aquatic lives and humans. This study examined the resourcefulness of the inflorescence of *Parkia pendula* which is shed and wasted annually without any usefulness, the possibility of being used as biosorbent for the treatment of wastewater containing pesticides attracts the interest of this study. The shed *Parkia pendula* inflorescence was collected, washed, sun-dried, milled to uniform particle size, and activated with H<sub>2</sub>O<sub>2</sub> (20 wt. %) for 120 h to produce *Parkia Pendula* Inflorescence Biosorbent (PPIB), which was used in the treatment of wastewater containing predominantly used pesticides [Glyphosate (GLY), Chlorpyrifos (CPF), and Lambda-Cyhalothrin (LCT)]. The three pesticides were mixed at different ratios (20–60%) based on the mixture methodology of the Design-Expert (12.0.0) software to simulate various the pesticides composition. Batch adsorption of the mixture was conducted and the maximum  $q_e$  obtained for Lambda-Cyhalothrin, CPF, and GLY removal were 6.503, 6.407, and 2.994 mg/g respectively. The Analysis of Variance of the models generated is significant at Coefficient of Determination ( $R^2$ ) 1.0000; 0.99611 and 0.9958, for LCT, CPF, and GLY, respectively. This study shows that the *Parkia biglobosa* inflorescence is very resourceful in the remediation of wastewater containing pesticide component.

**Keywords:** Biosorption, Optimization, *Parkia Pendula*, Pesticide, Wastewater

### 1. INTRODUCTION

A rising number of perilous normal combinations are being delivered into the environment, in present-day culture. Among these toxins, pesticides have been of unprecedented worry because of their standard plant applications and their over-the-top toxicity as well as persistency in the environment. The levels of pesticides in water have extended because of their preposterous use in the state-of-the-art cultivating space.

Due to its huge surface area and well-developed internal micro-porosity, activated carbon is frequently utilized as an adsorbent in adsorption procedures for the removal of various organic and inorganic pollutants from wastewater. However, using activated carbon is difficult since it is expensive and the adsorbent is difficult to regenerate (Alade *et al.* 2012a). Therefore, it is necessary to create an alternative adsorbent from cheap, easily accessible material that is useful in removing pollutants and has high surface areas and pore volumes. Several commonly available and inexpensive agricultural products, including cotton, nutshells, rice husks, chitosan, brewery waste, corn husks, and rice husks, have been effectively tested as substitute adsorbents. (Alade *et al.*, 2012a, 2012b).

Biosorption is also becoming a promising alternative to replace or supplement the present removal processes of organic pollutants from wastewater. Biosorption is the process of adhering different pollutants to biological agents' cell walls; it excludes the use of either aerobic or anaerobic metabolism for oxidation (Arumugam *et al.*, 2018). *Parkia biglobosa* also known as the African locust bean, is a perennial deciduous tree of the family Fabaceae, in the genus *Parkia* (Jacq.) R.Br. ex G. Don). It is widely distributed in most African communities and is primarily grown for its pods that contain

both sweet pulp and valuable seeds. Amongst the fruit of the *Parkia biglobosa* is the *Parkia* Pendula Inflorescence (PPI) which was used in this study. The inflorescence was used because it only sheds down from its pulp which is a waste and has no economic importance to the environment. The objective of this study is to remove CPF, LCT, and GLY from wastewater using biosorbent produced from the waste inflorescence of *Parkia* Pendula(USDA).



Figure 1: *Parkia* Pendula Inflorescence

## 2. MATERIALS AND METHODS

### 2.1 Material and Reagents

The main material used for this study was *Parkia* Pendula Inflorescence (PPI) collected from the premises of Ladoko Akintola University of Technology, Ogbomoso, Oyo State, Nigeria, and the pesticides (GLY, CPF, and LCT) with the Ultraviolet (UV) absorbance of 254 nm, 290 nm, and 460 nm, respectively. The reagents used include Distilled Water, analytical-grade Hydrogen Peroxide ( $H_2O_2$ ), and Sodium Hydroxide.

### 2.2 Biosorbent Preparation and Chemical Modification

#### 2.2.1. Material Pre-treatment

The waste PPI Inflorescence material was washed slightly with water and rinsed with distilled water to remove the sand particles and eliminate contaminants from it. The washed material was sun-dried till the materials became very dry and were then milled to reduce their surface area (Alade et al., 2017). The Automatic Sieve Shaker D403 and US Tyler Standard Screens were used to obtain uniform particle diameter.

#### 2.2.2. Activation of Biosorbent

Hydrogen Peroxide ( $H_2O_2$ ) 20 wt.% was used for the chemical activation of PPI with an impregnation ratio of 6 grams to 100 mL. The 20 wt.% of the  $H_2O_2$  was prepared by mixing 400mL of it with 600mL of distilled water. The PPI was then soaked in the solution for 120h and the mixture was treated to neutrality (pH 6.9-7.1) with 0.1 M of NaOH. Immediately after the neutralization process the material was filtered and drained very well. The material was then sun-dried and kept in the desiccators as PPI biosorbent (PPIB).

### 2.3 Preparation of Synthetic Pesticide Wastewater

The Design of Experiment software was used in optimizing the experimental runs for the adsorption of the multicomponent pesticides onto the PPIB. The Design Expert (12.0.0) software generated thirteen (13) experimental runs for the design. The three-level factorial design in the Design Expert Software (12.0.0) was used to generate the number of the experimental run at random for selected factors. The selected factors were the mix ratio of the pesticides (GLY, CPF, and LCT) ranging between (20–60%) (Table 1) and the response determined was adsorption capacity ( $q_e$ ) (mg/g). The best model that has the highest order of polynomials with significant added terms without alias was selected. The fitness of the models was ascertained based on the square of their coefficient of determination ( $R^2$ ).

Table 1: Mix ratio of GLY, CPF, and LCT

Component	Unit	Level	
		Level	High
GLY	mg/L	20	60
CPF	mg/L	20	60
LCT	mg/L	20	60

All of the Pesticide solutions were prepared with distilled water. The Pesticides were used without further purification. A stock solution of  $1000 \text{ mg l}^{-1}$  was first prepared by dissolving 10 mL of CPF, 40 mL of LCT, and 5.56 mL of GLY Pesticides each in 2000 mL distilled water. The experimental solution ( $100 \text{ mg l}^{-1}$ ) was prepared by diluting the stock

solution with distilled water. The concentration of GLY, CPF, and LCT was then determined at 254 nm, 290 nm, and 460 nm respectively by the UV–visible spectrophotometer.

### 2.4 Batch Biosorption Experiment

The PPIB (1.0 g) was mixed with 100 mL, and a concentration of 100 mg/L of pesticides arranged in a 250 mL conical flask at room temperature in a combination containing GLY, CPF, and LCT in different ratios gotten from the Design of Experiment (DOE). The flasks were shaken in a rotary shaker at 150 rpm for 60 minutes. The flasks were removed from the shaker and the residual concentration in the response mixture was resolved to utilize a UV-visible spectrophotometer set at the highest frequency of 254 nm, 290 nm, and 460 nm for GLY, CPF and LCT respectively. The standard curve was gotten by plotting the absorbance limit against the known concentration of Pesticides. The quantity of Pesticides adsorbed per unit weight of adsorbent,  $q_e$  ( $\text{mg g}^{-1}$ ), was performed to decide the ideal adsorption limit. The calculation for the adsorption capacity ( $q_e$ ) was done using the relation

$$q_e = \frac{C_0 - C_e}{m} V \quad (1)$$

Where,  $C_0$  is the initial concentration (mg/l),  $C_e$  is the experimental concentration (mg/l),  $V$  is the volume of the diluted adsorbate (L) and  $m$  is the mass of the composite (g).

### 3.0 RESULTS AND DISCUSSION

The concentration of the pesticide solution at equilibrium was gotten using a standard curve from the plot of absorbance capacity against concentration. The maximum adsorption capacity of 6.400 mg/g (Run 3) was obtained for LCT when the percentage mixture of CPF, LCT and GLY was 70, 15 and 15 % for CPF, LCT and GLY, respectively (Table 1). The maximum adsorption capacity of 6.503mg/g (Run 2) was obtained for CPF when the percentage composition of the pesticide mixture was 15, 70 and 15 % for CPF, LCT and GLY, respectively, while maximum adsorption capacity of 2.994mg/g (Run 11) was obtained for GLY at the percentage composition of 15, 42.50 and 42.50 % for CPF, LCT and GLY, respectively. The maximum adsorption capacity demonstrated by the PPIB, on the average, is 3.524 mg/g and falls on Run 2. The adsorption capacity of the removal of composition of the adsorbent composite that gave the best adsorption capacity (mg/g) values is Run 12 of  $Q_e$  of 88.781 and  $Q_e$  of 2.994 with 15% of material A (CPF) to 42.5% of material B (LCT) to 42.5% of the material C (GLY). The PPIB biosorbent developed demonstrated satisfactory efficiency for Pesticides removal as compared with other biosorbent used for the treatment of wastewater containing pesticides (Table 3).

Table 2: Experimental design and responses value at different runs of the multi-component organic pollutant removal

Run	Components			Adsorption Capacity (mg/g)			
	A:CPF	B:LCT	C:GLY	CPF	LCT	GLY	Average
1	42.50	42.50	15.00	3.561	3.567	2.783	3.304
2	15.00	70.00	15.00	1.102	6.503	2.967	3.524
3	70.00	15.00	15.00	6.400	0.867	2.822	3.363
4	15.00	70.00	15.00	1.096	6.502	2.950	3.516
5	42.50	15.00	42.50	3.551	0.881	2.793	2.408
6	15.00	15.00	70.00	1.176	0.931	2.959	1.689
7	42.50	42.50	15.00	3.554	3.567	2.780	3.300
8	24.17	51.67	24.17	1.904	4.596	2.919	3.139
9	24.17	24.17	51.67	2.058	1.737	2.895	2.230
10	51.67	24.17	24.17	4.615	1.775	2.842	3.077
11	15.00	42.50	42.50	1.275	3.588	2.994	2.619
12	33.33	33.33	33.33	2.557	2.748	2.785	2.697
13	15.00	15.00	70.00	1.173	0.931	2.958	1.687

Table 3: Adsorption capacities of various sustainable adsorbents for pesticides

Adsorbent	Target pesticide	Adsorption capacity (mg/g)	References
Walnut shell powder	Carbofuran	$0.89 \pm 0.033^b$	Memon (2014)
	Chlorpyrifos	$0.99 \pm 0.016^b$	
Sunflower seed shell powder	Simazine	$4.20 \pm 1.03$	Rojas et al. (2015)
Rice husk powder	Chlorfenvinphos	$6.42 \pm 2.08$	
Biochar from soybean	Atrazine	1.348	Liu et al. (2015)
Biochar from bagasse	Chlorpyrifos	3.2	Jacob et al. (2020)
	Lambda-Cyhalothrin	6.503	This study
	Chlorpyrifos	6.400	

<i>Parkia</i> Inflorescence (PPIB)	Pendula Biosorbent	Glyphosate	2.994
--	-----------------------	------------	-------

### 3.2 Statistical Analysis

The best fit model condition of the  $R^2$  and the adjusted  $R^2$  is (0.9990, 1.0000, and 0.9143) and (0.9974, 0.9999, and 0.8608) for CPF, LCT and GLY respectively. The  $R^2$ , which ought to be near one (1), exhibits the degree to which the reaction in the model has reduced. Enormous  $R^2$  esteem suggests that the produced model condition mirrors the interaction sensibly and can be utilized for hypothetical model portrayal. The connection between the autonomous and subordinate (reaction) factors is introduced as coded units in the equations below for CPF, LCT, and GLY separately.

Table 4: ANOVA of the different models for the removal of CPF, LCT, and GLY

	CPF				LCT				GLY			
	Sum of Squares	Mean Square	F-value	p-value	Sum of Squares	Mean Square	F-value	p-value	Sum of Squares	Mean Square	F-value	p-value
Model	45.63	5.70	632.690	0.0001	2342.45	292.81	24818.000	0.0001	0.0760	0.0152	17.08	0.0004
<sup>(1)</sup> Linear Mixture	45.48	22.74	2522.170	0.0001	2087.42	1043.71	88463.780	0.0001	0.0487	0.0244	27.39	0.0003
AB	0.0464	0.0464	5.150	0.0725	98.35	98.35	8335.860	0.0001	0.0173	0.0173	19.39	0.0023
AC	0.0375	0.0375	4.160	0.0970	1.22	1.22	103.520	0.0002	0.0096	0.0096	10.75	0.0112
BC	0.0209	0.0209	2.320	0.1879	38.61	38.61	3272.350	0.0001	0.0009	0.0009	0.9868	0.3496
A <sup>2</sup> BC	0.0038	0.0038	0.41630	0.5472	18.18	18.18	1541.310	0.0001	26.72	NA	NA	NA
AB <sup>2</sup> C	0.0198	0.0198	2.200	0.1982	0.8858	0.8858	75.080	0.0003	NA	NA	NA	NA
ABC <sup>2</sup>	9.8E-06	9.8E-06	0.00110	0.9750	0.6415	0.6415	54.380	0.0007	NA	NA	NA	NA
Residual	0.0451	0.0090	NANA		0.0590	0.0118	NANA		0.0071	0.0009	NA	NA
Lack of Fit	0.0450	0.0450	2696.480	0.0001	0.0543	0.0543	45.880	0.0025	0.0070	0.0017	44.90	0.0014
Pure Error	0.0001	0.0000	NANA		0.0047	0.0012	NANA		0.0002	0.0000	NA	NA
Cor Total	45.68	NA	NANA		2342.51	NA	NANA		0.0831	NA	NA	NA

NA = Not Available, CPF = Chlorpyrifos, LCT = Lambda Cyhalothrin, GLY = Glyphosate

$$\text{Adsorption Capacity (CPF)} = 6.41A + 1.11B + 1.18C - 0.7475AB - 0.8620AC + 0.6444BC + 6.05A^2B - 13.91AB^2C - 0.3140ABC^2 \quad (2)$$

$$\text{Adsorption Capacity (LCT)} = 0.8656A + 6.50B + 0.9299C - 0.4755AB - 0.0859AC - 0.5292BC + 3.16A^2B - 7.48AB^2C - 3.92ABC^2 \quad (3)$$

$$\text{Adsorption Capacity (GLY)} = 2.83A + 2.96B + 2.96C - 0.4313AB - 0.3849AC + 0.1166BC \quad (4)$$

The Mixture Component coding for CPF, LCT, and GLY is L Pseudo, while the Sum of squares for each is also Type III - Partial. The Model F-value of 632.69 suggests the model of CPF is huge, while for LCT, the Model F-value of 3222.42 considers the model as basic and the Model F-value of 17.08 for GLY implies the model is significant. F-value this huge has just a 0.01% chance to occur for both CPF and LCT and a 0.04% chance for GLY because of noise. P-values under 0.0500 show model terms are critical. For this situation A, B, and C are huge model terms for CPF, A, B, C, AB, BC, AB<sup>2</sup>C, and ABC<sup>2</sup> are model terms for LCT, and A, B, C, AB, and AC are significant model terms for GLY. Values more prominent than 0.1000 shows the model terms are not huge. Assuming there are numerous



## Valourisation of Waste *Parkia* Pendula Inflorescence as Biosorbent for the Treatment of Synthetic Wastewater Containing Pesticides

immaterial model terms (not including those expected to help the progressive system), a model decrease might improve the model.

The Lack of Fit F-value of 2696.48, 2278.46, and 44.90 for CPF, LCT, and GLY respectively infers the Lack of Fit is Significant. The chance of the Lack of Fit F-value to be this huge due to noise is just 0.01% for CPF and LCT and 0.014% chance for GLY, which makes the Lack of Fit insignificant. The effect of the mixture of the pesticides on the adsorption capacity of the biosorbent is illustrated in contour plots. The contour lines (Figure 3a, b, and c) are not absolutely parallel, as seen, they slightly curve towards the right end of the figure, and thus the equation can be assumed quadratic. The three-dimensional (3D) representations of these trends (Figure 4) for the pesticides (Chlorpyrifos, Lambda-Cyhalothrin, and Glyphosate).

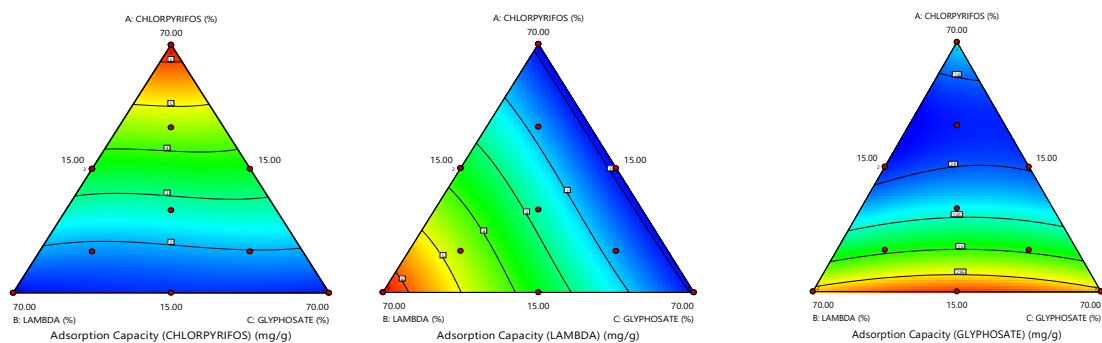


Figure 3a: Contour plot of Adsorption capacity for (CPF), (LCT) and (GLY)

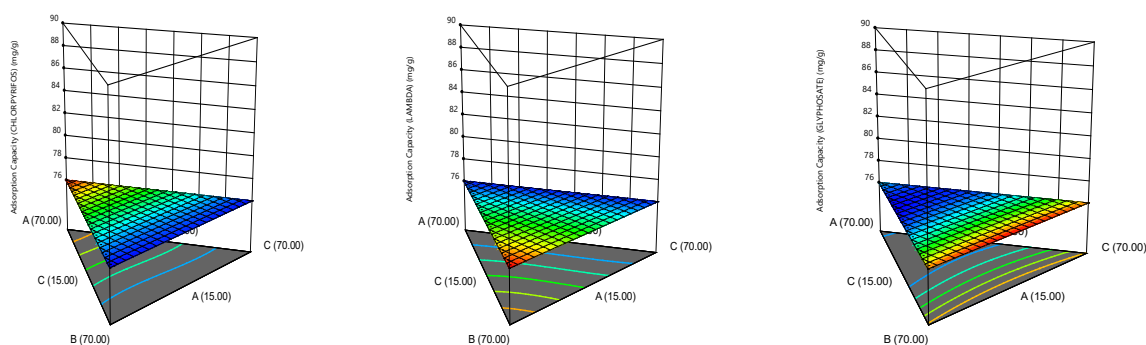


Figure 4: 3D Plot of Adsorption capacity for (CPF), (LCT) and (GLY)

## CONCLUSION

The potential of waste *Parkia* Pendula Inflorescence (PPI) as a resourceful precursor for the production of biosorbent for the effective treatment of pesticide (Chlorpyrifos, Lambda Cyhalothrin, and Glyphosate) contaminant in wastewater sample has been attempted. This study has demonstrated that PPIB has a maximum adsorption capacity of 4.118 to 6.503 mg/g for the pesticides within the contact time of 120 mins. The statistical analysis indicated that adsorption capacities of the PPIB demonstrated a quadratic relationship for the pesticides with high Correlation Coefficient (0.9990, 1.0000, and 0.9143). These findings outlined the newly developed PPIB as an excellent adsorbent for the on-site remediation of pesticide contaminated wastewater. It will improve the waste-to-wealth drive in the rural area.

## REFERENCES

- Abdoulaye, D.N., Youssef, A.E, Mostafa, M.A., Mohamed, S.K., & Driss, F. (2020). Adsorption of Methylene Blue from aqueous solution using Senegal River *Typha australis*. *Mediterranean Journal of Chemistry*, 10(1), pp. 22-32. doi:http://dx.doi.org/10.13171/mjc10102001221185adn
- AjoySaha, V.T. Gajbhiye, S.G., Rajesh, K., and Rakesh, K.G., Simultaneous Removal of Pesticides from Water by Rice Husk Ash: Batch and Column Studies. <https://doi.org/10.2175/106143014X14062131178358>.
- Alade, A.O., Amuda, O.S., Afolabi, T.J., and Okoya, A.A. (2012). Adsorption of Naphthalene onto Activated Carbon Derive from Milk Bush Kernel Shell and Flamboyant Pod. *Journal of Environmental Chemistry and Ecotoxicology*, 4(7),pp. 124-132

- Alade, A.O., Amuda, S.O.; Ogunleye, O.O., and Okoya, A.A. (2012). Evaluation of Interaction of Carbonization Temperatures and Concentration on the Adsorption Capacities and Removal Efficiencies of Activated Carbon Using Response Surface Methodology (RSM). *Journal of Biodegradation*, 3(1),pp 1-8.
- Andrunik, M.; and Bajda, T. (2021). Removal of Pesticides from Waters by Adsorption: Comparison between Synthetic Zeolites and Mesoporous Silica Materials. A Review. *Materials* 14, pp. 3532. <https://doi.org/10.3390/ma14133532>.
- Araromi, D.O., Alade, A.O., Bello, M.O., Bakare, T., Akinwande, B.A., Jameel, A.T., Adegbola, S.A., (2017): Optimization of Oil Extraction from Pitanga (*Eugenia Uniflora* L) Leaves Using Simplex Centroid Design (SCD). *Sep. Sci. and Tech.*
- Aremu, O.M., Aonughe, I.U., Alade A.O., and Araromi D.O., (2019) Optimization of the operating variables for the extraction of soy oil in a single screw expeller using a central composite design (CCD); [https:// DOI: 10.17508/CJFST.2019.11.2.1](https://doi.org/10.17508/CJFST.2019.11.2.1).
- Arumugan, N., Chelliapan, S., Kamyab, H., Thirugana, S., Othman, N., Nasri, N.S., (2018). Treatment of wastewater using seaweed: A review. *Int. J. Environ. Res. Public Health*. 15(12),pp. 2851; <https://doi.org/10.3390/ijerph15122851>
- Jacob MM, Ponnuchamy M, Kapoor A, Sivaraman P (2020) Bagasse based biochar for the adsorptive removal of chlorpyrifos from contaminated water. *J Environ Chem Eng* 8:103904. <https://doi.org/10.1016/j.jece.2020.103904>
- Liu N, Charrua A.B., and Weng C.H. (2015) Characterization of biochars derived from agriculture wastes and their adsorptive removal of atrazine from aqueous solution: A comparative study. *Bioresour Technol* 198: pp. 55–62. <https://doi.org/10.1016/j.biortech.2015.08.129>
- Memon G.Z. (2014) Adsorption of Selected Pesticides from Aqueous Solutions Using Cost Effective Walnut Shells. *IOSR J Eng* 4 :pp., 43–56. <https://doi.org/10.9790/3021-041014356>
- Obi, F., Ugwuishiwu, B., & Nwakaire, J. (2016). Agricultural Waste Concept, Generation, Utilization and Management. *Nigerian Journal of Technology*, 35(4) pp., 957. <https://doi.org/10.43114/mjt.v35i4.34>.
- Ojo, O.S., Agbede, O.O., Ogunleye, O.R., Adeyi, V.A., Afolabi, T.J., and Alade, A.O. (2021). Optimization of Biosorptive Removal of Dichlorvos Removal from Synthetic Wastewater by Acid-Activated *Tithonia diversifolia* Xylem. *Journal of Materials and Environmental Science*, 13, pp.461-478.
- Parkia biglobosa*. Germplasm Resources Information Network (GRIN). Agricultural Research Service (ARS), United States Department of Agriculture (USDA).
- Rojas R, Morillo J, and Usero J. (2015) Adsorption study of low-cost and locally available organic substances and a soil to remove pesticides from aqueous solutions. *J Hydrol* 520:4pp. 61–472. <https://doi.org/10.1016/j.jhydrol.2014.10.046>
- Saleh, I.A., Zouari, N. and Al-Ghouti, M.A.(2020) *Environmental Technology & Innovation* 19. 101026. <https://doi.org/10.1016/j.eti.2020.101026>.
- Salman. J.M. (2014). Optimization of preparation conditions for activated carbon from palm oil fronds using response surface methodology on the removal of pesticides from aqueous solution". *Arabian Journal of Chemistry*, 7: pp. 101–108. <https://doi.org/10.1016/j.arabjc.2013.05.033>
- Santoso, E., Ediati, R., Kusumawati, Y., Bahruji, H., Sulistiono, D.O., & Prasetyoko, D. (2020). Review on recent advances of carbon-based adsorbent for methylene blue removal from wastewater. *Materials Today Chemistry*, 16. doi:100233. doi: 10.1016/j.mtchem.
- Vacca, A., Mais, L., Mascia, M., Usai, E.M., and Palmas, S. (2020). Design of Experiment for the Optimization of Pesticide Removal from Wastewater by Photo-Electrochemical Oxidation with TiO<sub>2</sub> Nanotubes. *Catalysts*, 10(5): pp. 512. <https://doi.org/10.3390/catal10050512>



## Adsorption of Paracetamol from Pharmaceutical Wastewater Using Groundnut (*Arachis hypogaea*) Shell Activated Carbon

I. OLOWONYO<sup>1</sup>, K. K SALAM<sup>1,2</sup>, M. AREMU<sup>1</sup> and A. LATEEF<sup>1</sup>

<sup>1</sup>Ladoke Akintola University, Ogbomosho, Oyo State

<sup>2</sup>FEDDO Integrated Services

[idayatolowonyo@gmail.com](mailto:idayatolowonyo@gmail.com)

\*Corresponding author

---

### ABSTRACT

Groundnut shell activated carbon (GNSAC) was investigated for the removal of paracetamol from pharmaceutical wastewater and the effect of temperature and contact time on percentage removal of paracetamol were studied in a batch experiment. The GNSAC was characterized using FTIR and proximate analysis. The optimum paracetamol removed was 90 % at optimum conditions (dosage, temperature and time) of 0.7g, 28°C and 42 min respectively. The thermodynamics of paracetamol adsorption onto GNSAC indicated that the adsorption was spontaneous and endothermic in nature.

**Keywords:** Carbonization, ANOVA, Wastewater treatment, Optimization, Absorbance.

### 1. INTRODUCTION

Paracetamol is a non-prescribed analgesic used worldwide for the treatment of minor pain, fever and rheumatic disorder which results in digestive problems, diarrhea, and fatigue when abused or used in excess. It has been detected at low concentration in surface and groundwater throughout the world (Al-hindi *et al.*, 2017). However, inappropriate disposal of untreated waste water from pharmaceutical industries into water bodies causes serious environmental implication which leads to disruption in the metabolism of the biota by increasing and altering the antioxidant mechanism (Žur *et al.*, 2018; Nunes, 2020). Thus, it is important to treat wastewater containing these pollutants before releasing it into the environment. Compare to all other treatment methods, adsorption techniques is preferable because of its flexibility, better efficiency and relatively cheap (Aremu *et al.*, 2020).

For commercial feasibility, efforts have been directed to develop low-cost adsorbents by using agricultural residues such as fruits, rice husk, straw, coconut wastes, coffee waste, vegetable peels, etc. Agricultural wastes are now becoming viable alternatives due to easy availability, low purchase costs and good adsorption potential for the removal of drugs (Dhiman and Sharma, 2019). In this study, groundnut shell activated carbon was tested as an effective adsorbent for removal of paracetamol from pharmaceutical wastewater.

### 2. METHODOLOGY

#### 2.1 Material and Reagents

Groundnuts (GN) were obtained from Arada market in Ogbomosho, Oyo State, Nigeria. The reagents used include sodium hydroxide (NaOH), distilled water, hydrochloric acid (HCl) and paracetamol tablets. The equipment used include Furnace (Carbolite ELF 11/68), FTIR (FT/IR-4600), weighing balance (ZC20602), UV-vis (UV752D), Water Bath Shaker, and Electric Oven (Techmel TT-9083, USA).

#### 2.2 Preparation and Characterization of Groundnut shell activated carbon (GNSAC)

Groundnuts were deseeded and the shells were washed with distilled water to remove dust. The washed shells were dried in an oven at 100 °C for 4 hours and then finely ground for easy activation. The milled groundnut shell was subjected to sieve analysis and particles in the size range of 100 –225 µm were activated using 1M Sodium hydroxide (NaOH). 100 grams of dried milled groundnut shell (GNS) sample was activated by soaking it in 100 ml of 1M NaOH in a beaker and then carbonized in an oven at temperature and time of 200°C and 1 hour respectively (Imam and Abdullahi, 2017). For proper activation, the mixture was kept overnight. The produced GNS activated carbon (GNSAC) was washed to neutral level (pH 7), dried at 110 °C for two hours, cooled at room temperature, and then stored for further use. The produced activated carbons was analyzed for their moisture content, ash content, volatile matter and fixed carbon according to the method adopted by Onawumi *et al.* (2021). Fourier transform infra-red (FTIR) spectrophotometer was used to identify the different functional groups available on the adsorbent sites.

### 2.3 Batch Adsorption Studies

The method adopted in the research of Lung *et al.* (2021) was modified and used for the batch adsorption studies. The temperature (25-35 °C), adsorbent dose (0.5 - 1.5 gL<sup>-1</sup>), contact time (10 - 50 min) ranges were gotten from literature (Lung *et al.*, 2021).. After a certain temperature and time with agitation at 400 rpm, the solution was filtered and filtrate analyzed with UV-visible spectrophotometer at wavelength of 243 nm to determine the reduction of paracetamol in the wastewater. Equation (1) was used to convert the result of absorbance obtained to concentration at time t ( $c_e$ ) using intercept and slope gotten from the calibration curve. Percentage removal (% removal) of paracetamol was evaluated using equation (2) (Yang *et al.*, 2019)

$$c_e \left( \frac{mg}{L} \right) = \frac{y-c}{M} \quad (1)$$

$$\% \text{ Removal} = \frac{(c_o - c_e)}{c_o} \times 100 \quad (2)$$

Where: y = absorbance (nm), c = intercept obtained from calibration curve, M = Slope obtained from calibration curve,  $c_o$  = initial concentration of paracetamol solution (mg/L),  $c_e$  = paracetamol equilibrium concentration (mg/L), M = mass of adsorbent in gram, v = volume of aqueous solution (ml).

Table 1: Process variables and their levels

Factors	Unit	Level	
		Low	High
Adsorbent dosage	G	0.5	1.5
Temperature	°C	25	35
Contact time	Min	10	50

### 2.4 Kinetic study

Pseudo-first and Pseudo-second order were used to analyze the kinetic data needed to understand the adsorption mechanism and predict diffusion and kinetic transport that controls the adsorption rate. The linearized form of pseudo-first and pseudo-second order are presented in equation (3) and (4) respectively.

$$\log(q_e - q_t) = \log q_e - \left( \frac{k_1}{2.303} \right) t \quad (3)$$

$$\frac{t}{q_t} = \frac{1}{k_2 q_e^2} + \left( \frac{1}{q_e} \right) t \quad (4)$$

Where:  $q_t$  = adsorption capacity at time t (mg/g),  $q_e$  = adsorption capacity at equilibrium (mg/g),  $k_1$  = pseudo-first order rate constant (  $min^{-1}$ ),  $k_2$  = rate constant of pseudo-second order (  $g/mg \text{ min}$  ), t = time in minutes

### 2.5 Thermodynamic Study

Thermodynamic studies are used to describe a reaction in a better way. In the present study, thermodynamic studies were performed and the parameters, namely free energy change ( $\Delta G^0$ ), enthalpy ( $\Delta H^0$ ), and entropy ( $\Delta S^0$ ), were determined at different temperatures (shown in Table 2). These parameters were calculated using equation (5) – (7)

$$\Delta G = -RT \ln K_c \quad (5)$$

$$\ln K_c = \frac{\Delta S}{R} - \frac{\Delta H}{RT} \quad (6)$$

$$\Delta G^0 = \Delta H^0 - T\Delta S \quad (7)$$

where  $K_c$  is the equilibrium constant, R is the universal gas constant (8.314 J/molK), T is the absolute temperature (K).

## 3. RESULTS AND DISCUSSION

### 3.1 Standard curve

Paracetamol solution was prepared at different concentrations to the mark line in a series of 10 ml volumetric flasks, and the absorbance of the solution was measured. The standard curve of paracetamol using concentration and absorbance was plotted as shown in Figure 1.

Where y is absorbance and x are paracetamol solution concentration (mg /L). Fitting the absorbance to the paracetamol solution concentration as a function of equation (8),  $R^2 = 0.979$ , which proves a good fit.

$$y = 0.009x + 0.019 \quad (8)$$

### 3.2 Characterization of GNSAC

The produced GNSAC was observed to have low moisture, ash and volatile content of 9.89, 8.1 and 10.9 % respectively. The fixed carbon of the Adsorbent was 71.11%. Low volatile matter content increases char yield while low inorganic content such as ash is responsible for high fixed carbon content observed (Aremu *et al.*, 2020). Activated carbon with lower moisture content and high fixed carbon greater than 65% has been reported to have more adsorption efficiency (Onawumi *et al.*, 2021). The values gotten were in agreement with the results reported by Onawumi *et al.* (2021) and Malik *et al.* ( 2007).

The FTIR analysis of GNS and GNSAC is given in Figures 2a and b, respectively. The FTIR spectra show shift in peaks, appearance and disappearance of some new peaks due activation and carbonization. The band at 3416 - 3436 .98  $\text{cm}^{-1}$

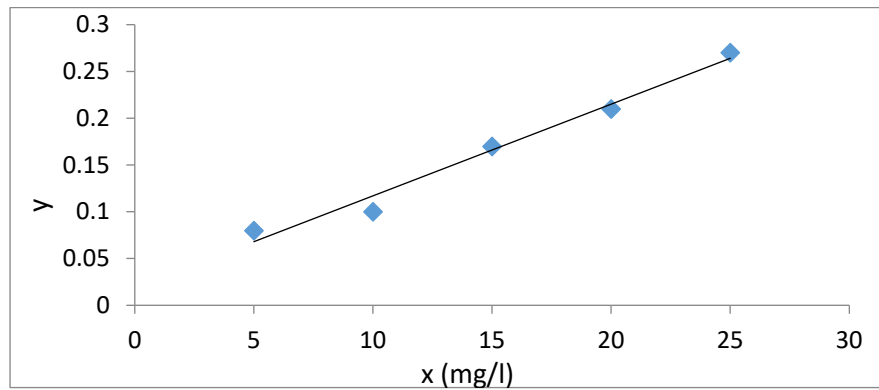


Fig 1: Standard curve of paracetamol solution concentration versus absorbance.

depicts O-H (hydroxyl) groups. A C-H stretching band of an alkane group was also observed at 2925 - 2926.54  $\text{cm}^{-1}$ . The peak at range of 1644.19 – 1630.66  $\text{cm}^{-1}$  signifies a strong C - O stretching of alkyl aryl ester. The band noticed at 1258.17 – 1054.09  $\text{cm}^{-1}$  is assigned to C-N. Similarly, the peak range 418.56 – 451.36  $\text{cm}^{-1}$  belongs to a strong C-CL. The changes observed in the FTIR spectra of the GNSAC confirm the effect of base activation on the raw samples; this is an indication that these samples will be a useful adsorbent in waste water treatment (Bello *et al.*, 2017).

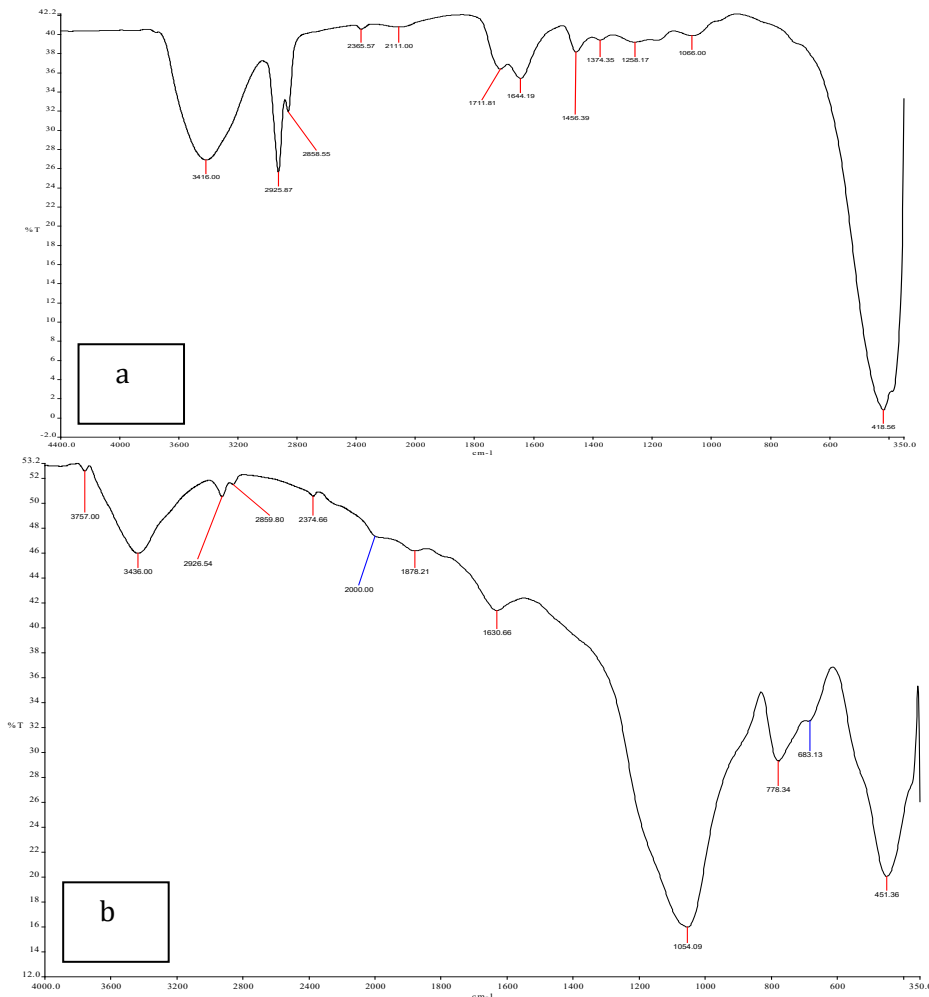


Figure 2: FTIR Spectrum of (a) GNS (b) groundnut shell activated carbon

### 3.3 Batch Adsorption Study

Table 2 is the design matrix for the Box-Behnken method showing the 17 experimental runs performed for optimization. The factors selected include adsorbent dosage (0.5-1.5 $\text{gL}^{-1}$ ), temperature (25-35  $^{\circ}\text{C}$ ) and contact time (10 -50 min).The results of the studies showed that adsorption factors (adsorbent dosage, temperature and contact time) has a significant

effect on the percentage of paracetamol removed using GNSAC. The results also showed that the maximum and minimum amount of paracetamol removed were 89.75 and 52.14 % at run 4 and 10 respectively.

### 3.4 Data Analysis

The results in table 2 was analyzed using ANOVA at 95% confidence interval ( $\alpha = 0.05$ ). It was revealed that the linear model was suitable to approximate percentage removal of paracetamol with correlation coefficient and adjusted correlation coefficient of 99.63 and 99.272 % respectively. The Model F-values of 271.81 implied that the linear model selected was significant. There is only a 0.01% chance that F-values this large could occur due to noise. P-values less than 0.0500 indicate model terms are significant. In this case B, C, AB, AC, A<sup>2</sup>, B<sup>2</sup> were significant model terms. The Lack of Fit F-value of 12139.95 implied that the Lack of Fit was significant relative to the pure error. The final equation for percentage removal is given as:

$$\begin{aligned} \% \text{ Removal} = & + 84.29 + 0.0300 * \text{Adsorbent dosage} - 4.32 * \text{Temp} + 8.53 * \text{contact time} + 20.55 \\ & * \text{Adsorbent dosage} * \text{Temp} - 3.40 * \text{Adsorbent dosage} * \text{Contact time} \\ & - 6.73 \text{ Adsorbent dosage}^2 - 20.37 \text{ Temp}^2 \end{aligned} \quad (9)$$

### 3.5 Optimization of Selected Adsorption Factors

Optimization was performed by maximizing paracetamol percentage removal approximated by equations 4 subjected to the experimental constraints. This is carried out to give the optimum mass of adsorbent. The numerical technique method embedded in the Design Expert (version 13) was employed using desirability function criteria. At optimum conditions of 0.7g, 42 min, and 28°C for adsorbent dosage, contact time and temperature respectively, 90% of paracetamol was removed with 100 % desirability. Table 3 shows the validated experiments performed in triplicates at the optimum process condition. The closeness of simulated and experimental values for GNSAC pointed to the reliability of the developed equation for predicting percentage removal of paracetamol from pharmaceutical wastewater.

### 3.6 Kinetic studies

Table 4 shows the experimental data and parameters for the two models used in this study. It is obvious that pseudo-second-order kinetic model has higher coefficient of correlation ( $R^2 = 0.998$ ) than pseudo-first-order kinetic model ( $R^2 = 0.948$ ) for paracetamol adsorption. The calculated value of  $qe$  for pseudo-second-order kinetic model is very close to the experimental value. This indicates that that pseudo-second order fits the equilibrium data for paracetamol adsorption onto GNSAC from pharmaceutical waste water (Shirsath and Shirivastava, 2015).

Table 2: Experimental Response for Adsorption of paracetamol onto produced GNS Adsorbents

Run	Adsorbent dosage (g)	Temp. (°C)	Contact time (min)	%Removal
1	1	30	30	84.30
2	1	30	30	84.30
3	1	30	30	84.27
4	0.5	30	50	89.75
5	1.5	35	30	72.66
6	1	30	30	84.29
7	1	25	10	59.99
8	1.5	30	50	83.80
9	1	35	50	67.85
10	1	35	10	52.14
11	.5	25	30	82.80
12	1	25	50	75.69
13	1	30	30	84.30
14	1.5	30	10	72.16
15	.5	35	30	86.00
16	1.5	25	30	56.46
17	.5	30	10	64.52

Table 3: Simulation and Experimental values of paracetamol % removal by GNSAC

	Process variables			%Removal
	Dosage (g)	Time ( min)	Temp. (°C)	
Simulation	0.7	42	28	91.74
Experimental	0.7	45	30	90.23

Table 4: Kinetic studies Parameters of paracetamol adsorption onto GNSAC

q <sub>e</sub> (exp) (mg/g)	Pseudo-first-order			Pseudo-second-order		
	q <sub>e</sub> (cal) (mg/g)	K <sub>1</sub> (min <sup>-1</sup> )	R <sup>2</sup>	q <sub>e</sub> (cal) (mg/g)	K <sub>2</sub> (mg/gmin)	R <sup>2</sup>
56.57	0.1336	0.014	0.948	62.5	0.0047	0.998

### 3.7 Thermodynamic studies

Table 5 shows the values of thermodynamic parameters determined. Positive value of entropy change ( $\Delta S^0$ ) and enthalpy change ( $\Delta H^0$ ) indicates the endothermic nature of paracetamol adsorption onto GNSAC. The parameter  $\Delta G^0$  was negative so the process is feasible and spontaneous. It was also noted that values of standard Gibbs free energy ( $\Delta G^0$ ) decreases with increasing temperature.

Table 5: Thermodynamic Parameters for paracetamol adsorption onto GNSAC

$\Delta H^0$ (KJ/mol)	$\Delta S^0$ (KJ/mol)	$\Delta G^0$ (KJ/mol)				
32.092	0.126	298K	303k	308k	313k	318k
		-5.456	-6.086	-6.716	-7.346	-7.976

## 4. CONCLUSION

The results obtained in this research demonstrated that activated carbon prepared from groundnut shell has high adsorption abilities for adsorption of paracetamol from real wastewater. FTIR shows the presence of stretches of C-H, C-O, C-Cl, C-N and O-H on the adsorbents. An upward shift in peak values of the bands indicated changes that occur during the process of activation and carbonization. 90% of paracetamol was removed at optimum conditions of 0.7g, 28°C and 42 min for adsorbent dosage, temperature and time respectively. The kinetic studies indicated paracetamol adsorption onto GNSAC followed pseudo-second-order. The thermodynamic results showed the adsorption was spontaneous and endothermic.

## REFERENCES

- Al-hindi, F. M. M., Yahfoufi, R. and Ayoub, G. M. (2017) 'The use of activated carbon for the removal of pharmaceuticals from aqueous solutions: a review', *Reviews in Environmental Science and Bio/Technology*. doi: 10.1007/s11157-017-9456-8.
- Aremu, M. O., Arinkoola, A.O., Olowonyo, I.A. and Salam, K.K. (2020) 'Heliyon Improved phenol sequestration from aqueous solution using silver nanoparticle modified Palm Kernel Shell Activated Carbon', *Heliyon*, 6(May), p. e04492. doi: 10.1016/j.heliyon.2020.e04492.
- Bello, O. S., Owojuyigbe, E.S., Babatunde, M.A., and Folaranmi, F.E. (2017) 'Sustainable conversion of agro-wastes into useful adsorbents', *Applied Water Science*, 7(7), pp. 3561–3571. doi: 10.1007/s13201-016-0494-0.
- Dhiman, N. and Sharma, N. (2019) 'Batch adsorption studies on the removal of ciprofloxacin hydrochloride from aqueous solution using ZnO nanoparticles and groundnut (*Arachis hypogaea*) shell powder: a comparison\*', *Indian Chemical Engineer*, 61(1), pp. 67–76. doi: 10.1080/00194506.2018.1424044.
- Imam, S. S. and Abdullahi, M. (2017) 'Adsorptive Removal of Methylene Blue Using Groundnut Shell Activated Carbon Coated With Fe<sub>2</sub>O<sub>3</sub>', 10(4), pp. 12–21. doi: 10.9790/5736-1004011221.
- Lung, I., Soran, M. and Stegarescu, A. (2021) 'Evaluation of CNT-COOH/MnO<sub>2</sub>/Fe<sub>3</sub>O<sub>4</sub> nanocomposite for ibuprofen and paracetamol removal from aqueous solutions', *Journal of Hazardous Materials*, 403(July), p. 123528. doi: 10.1016/j.jhazmat.2020.123528.
- Malik, R., Ramteke, D. S. and Wate, S. R. (2007) 'Adsorption of malachite green on groundnut shell waste based powdered activated carbon', *Waste Management*, 27(9), pp. 1129–1138. doi: 10.1016/j.wasman.2006.06.009.
- Nunes, B. (2020) 'Ecotoxicological Effects of the Drug Paracetamol: A Critical Review of Past Ecotoxicity Assessments and Future Perspectives', *Handbook of Environmental Chemistry*, 96, pp. 131–145. doi: 10.1007/978-2020-546.
- Onawumi, O. O. E., Sangoremi, A. A. and Bello, O. S. (2021) 'Preparation and characterization of activated carbon from groundnut and egg shells as viable precursors for adsorption', *Journal of Applied Sciences and Environmental Management*, 25(9), pp. 1707–1713. doi: 10.4314/jasem.v25i9.24.
- Shirsath, D. S. and Shirivastava, V. S. (2015) 'Adsorptive removal of heavy metals by magnetic nano-adsorbent: an equilibrium and thermodynamic study', *Applied Nanoscience (Switzerland)*, 5(8), pp. 927–935. doi: 10.1007/s13204-014-0390-6.
- Yang, P., Xu, Y., Tuo, J., Li, A., Liu, L. and Shu, H. (2019) 'Preparation of modified pomelo peels pulp adsorbent and its adsorption to uranyl ions', *Royal Society Open Science*, 6(3). doi: 10.1098/rsos.181986.
- Żur, J., Wojcieszynska, D., Hupert-Kocurek, K., Marchewicz, A. and Guzik, U. (2018) 'Paracetamol – toxicity and microbial utilization. *Pseudomonas moorei* KB4 as a case study for exploring degradation pathway', *Chemosphere*, 206, pp. 192–202. doi: 10.1016/j.chemosphere.2018.04.179.



## Adsorption Studies on Waste Plantain Peel Ash as Adsorbent for Sorption of Pharmaceutical Wastewater

Dauda O. ARAROMI<sup>1</sup>, Sofiat O. GANIYU<sup>1,2</sup>, Ademola T. ADENIJI<sup>1,2,3</sup>, Damilola O. ADEBUKOLA<sup>1,2</sup>, Ayobami O. AJANI<sup>1,2</sup>, Oluseye O. AGBEDE<sup>1</sup>, Kehinde A. BABATUNDE<sup>1</sup>, Solomon O. ALAGBE<sup>1</sup>, Samuel E. AGARRY<sup>1</sup>, Taofik A, ADEDOSU<sup>4</sup>, Ganiyu K. LATINWO<sup>1</sup>, Abass O. ALADE<sup>1,2,5\*</sup>, and Tinuade J. AFOLABI<sup>1,2</sup>

<sup>1</sup>Department of Chemical Engineering, Ladoke Akintola University of Technology, P.M.B. 4000, Ogbomoso, Nigeria

<sup>2</sup>Bioenvironmental, Water and Engineering Research Group, (BWERG), Ladoke Akintola University of Technology, P.M.B. 4000, Ogbomoso, Nigeria

<sup>3</sup>Department of Chemistry, University of Porto, Porto, Portugal

<sup>4</sup>Department of Pure and Applied Chemistry, Ladoke Akintola University of Technology, Ogbomoso, Nigeria

<sup>5</sup>Science and Engineering Research Group, (SEARG), Ladoke Akintola University of Technology, P.M.B. 4000, Ogbomoso, Nigeria

\*Corresponding author: [aalade@lautech.edu.ng](mailto:aalade@lautech.edu.ng) +2347037885961

### ABSTRACT

Unregulated use of pharmaceutical products has created a huge threat to all life forms in the biosphere, although they have been credited with benefits such as extending life spans, alleviating diseases, and improving quality of life. This study aims to perform optimization studies of some selected emerging pharmaceutical contaminants from wastewater using adsorbents developed from Plantain peel waste. The plantain peel used was obtained from a local market at Ladoke Akintola University of Technology (LAUTECH), Ogbomoso, Nigeria. washed thoroughly to remove dirt particles, dried, grounded, screened, and ashed in a muffled furnace at a temperature of 600 °C for 3 h. Ibuprofen, Doxycycline, and Chloroquine (IDC) mixtures were prepared and 100mL of IDC was mixed with Plantain peel Ash (PPA) and optimization study was carried out and Adsorption capacity (AC) was evaluated as the response. The maximum AC (3.35 mg/g) for Ibuprofen was obtained at Run 7 and 8, the maximum AC (3.15 mg/g) for Doxycycline was obtained at Run 14, and for Chloroquine, the maximum AC (3.51 mg/g) was obtained at Run 5. The Plantain Peel Ash adsorbent developed showed great efficacy in the removal of IDC from an aqueous solution.

**Keywords:** Adsorption, Ash, Chloroquine, Doxycycline, Ibuprofen, *Musa paradisiaca*

### 1. INTRODUCTION

The most basic elements for a healthy lifestyle are a clean-living environment and safe drinking water. Clean water is necessary for residential, industrial, and agricultural use. Increased water consumption would result in bigger wastewater effluents. Although water covers more than 70% of the planet, only 3% of it is fit for human consumption, with the remaining 97 percent being salty water (Rashid *et al.*, 2021). The global trend of industrialization, urbanization and the release of innumerable dangerous compounds are the primary causes of water contamination (Kaur *et al.*, 2021). Pharmaceutical pollution of surface and wastewater includes the presence of pharmaceuticals in ground and drinking water sources, exposing humans and the broader ecosystem. They can be found in amounts ranging from ng/L to g/L in aquatic systems (Patel *et al.*, 2021) and can have unanticipated ecotoxicological effects on non-targeted animals and humans (Waleng and Nomngongo, 2022). Traditional wastewater treatment plants, on the other hand, are incapable of eradicating such large pollutant groupings, necessitating extra cost-effective water treatment. Therefore, a cost-effective tertiary treatment technique is presented because typical primary and secondary treatment facilities fail to eliminate or degrade these hazardous substances. Adsorption is a popular method for removing contaminants worldwide because of its installation cost, significant effectiveness, and simple operational design (Rathi and Kumar, 2021).

Adsorption is superior to alternative wastewater treatment systems in terms of initial cost, design simplicity, ease of usage, and resistance to dangerous compounds. As a result, adsorption prevents harmful compounds from forming (Rafatullah *et al.*, 2010). Plantain peels, on the other hand, are wastes that have been proven to be a good source of phytochemicals and dietary fibers that are helpful to the human body and have shown to have effects on therapeutically significant agents, as well as being useful as adsorbents (Felix *et al.*, 2018). Plantain being a commonly produced food crop in nations within the West African sub-region, plantain peel is abundant and can be easily obtained from trash



sites, local farmers, and dealers in the tropics. Furthermore, plantain peel when compared to the creation of charcoal from bones and woody materials, takes less time and consumes less energy (Oluyemi *et al.*, 2009).

The cost of preparation and raw materials is the biggest issue with activated carbon; however, this drawback can be overcome by using inexpensive materials, such as plantain peel, which has become crucial. Because of their great sorption and complexation abilities, plantain peel ash has thus been widely examined while considering activated-carbon limitation. This study aims to perform optimization studies of some selected emerging pharmaceutical contaminants from wastewater using adsorbents developed from Plantain peel waste.

## 2. MATERIALS AND METHODS

### Materials

The plantain peels used were obtained from a trader within Ladoko Akintola University of Technology (LAUTECH), Ogbomoso, Nigeria premises, Doxycycline (Chemical Formula:  $C_{22}H_{44}N_2O_8$ , Molecular Weight: 444.4 g/mol, Solubility in water: 630 mg/L, Ultraviolet (UV) Absorbance Value: 407nm), Ibuprofen (Chemical Formula:  $C_{13}H_{18}O_2$ , Molecular Weight: 206.29 g/mol, Solubility in water: 0.021mg/cm<sup>3</sup>, Ultraviolet (UV) Absorbance Value: 247nm) and Chloroquine were obtained from JMK Pharmaceuticals, Under-g, Ogbomoso, Oyo State, Nigeria.

### Adsorbent preparation

On collection of the plantain peels, they were washed to remove dirt from the plantain peel samples, sundried for 5 d, crushed using a laboratory mortar and pestle, and ground into smaller particles. The samples were then sieved to 60  $\mu$ m particle size, 270 g of the samples were ashed in a crucible in a muffled furnace at a temperature of 600  $^{\circ}$ C for 3 h and 29 g of the samples were retrieved.

### Adsorbates preparation

The Pharmaceuticals used for this experiment were Ibuprofen, Doxycycline and Chloroquine. The maximum wavelengths of these drugs are 222 nm, 407 nm, and 345 nm respectively. Ibuprofen, Doxycycline and Chloroquine solution for the adsorption experiment was prepared from a stock solution, 0.14g of Ibuprofen, 0.16g of Doxycycline and 0.16g of Chloroquine respectively were mixed with 1000 mL of distilled water. The solution was stirred until it dissolves to obtain a homogenous solution. The solution was then diluted to mark a 1000 mL volumetric flask for each component. The different concentrations needed for the research work were taken from the 1000 mg/L solution by serial dilution.

### Adsorption of IDC Mixtures

The adsorption process was carried out according to the procedures described with some modifications (Alade *et al.*, 2012). The prepared adsorbent (1g) of plantain peel ash was mixed in 100 mL Ibuprofen, Doxycycline and Chloroquine (IDC) - mixtures in different ratios obtained from Design of Experiment (DOE) and left for 4 h. the solution was decanted and taken for UV analysis using a UV spectrophotometer to obtain the absorbance.

The final concentration was calculated from the standard curve with known concentrations. The standard curve was constructed with the absorbance versus the known concentration of Ibuprofen, Doxycycline and Chloroquine. The analysis of variance (ANOVA) procedure was used to determine the significance of variables and to substantiate the adequacy of the quadratic regression model obtained in this study. The Adsorption Capacity ( $q_e$ ) was calculated using equation 1.

$$q_e = \frac{C_o - C_e}{M} \times V \quad (1)$$

Where  $q_e$  is the Adsorption Capacity,  $C_o$  and  $C_e$  are the initial and equilibrium concentration (mg/L) respectively,  $V$  is the volume of the solution (mL) and  $M$  is the mass of the adsorbent composite (g).

### Design of Experiment

The experiment design is generally undertaken to minimize the time, materials, and, invariably, cost involved in experimental design. Design-Expert software (Version 12.0) was used for the experimental design. The experimental design information is expressed in Tables 1 and 2.

Table 1: Experimental Design Information

Design Information	
Study Type	Mixture
Design Type	Simplex Lattice
Design Model	Quadratic

Build Time (ms)	194.00
Subtype	Randomized
Runs	14
Blocks	No Blocks

Table 2: Independent variable levels used in this research for experimental design

Component Name	Units	Minimum	Maximum
Ibuprofen	mg/L	20.00	60.00
Doxycycline	mg/L	20.00	60.00
Chloroquine	mg/L	20.00	60.00

### 3. RESULTS AND DISCUSSION

#### Adsorption experiment of IDC on plantain peel ash

The result of the average adsorption capacity and removal efficiency of the pharmaceutical contaminants (IDC) onto the surface of the plantain peel ash adsorbent are relayed in Table 3. The adsorption capacity explains the amount of adsorbate solute in the solution taken up by the adsorbent particles during the adsorption experiment. Run 5 gave the highest average adsorption capacity (1.38 mg/g) with a large contribution from chloroquine. Run 7 and 8 also gave a high average adsorption capacity (1.35 mg/g) with most of the contribution coming from Ibuprofen (3.51 mg/g). Run 4 gave the lowest average adsorption capacity with an almost equal contribution from each of the adsorbate compositions. These different optimization results indeed showed that adsorption capacity is insufficient to explain the best combination of the solute. To better understand the result, the average removal efficiency expressed in percentage was calculated for each of the clay compositions. This was done by finding the ratio of the difference between the equilibrium concentration and initial concentration to the initial concentration for each of the solutes present in the individual composition. The results were expressed as percentages and averaged. Run 2, 7 and 8 gave removal efficiency greater than 90 %. Initially, run 5 gave the maximum average adsorption capacity, however, the large contribution of Chloroquine resulted in low average removal efficiency. The % composition in run 2 was taken as the most optimized composition and is used in the future study of this research project.

Table 3: The multi-component pharmaceuticals pollutant adsorption capacity experimental setup and responses values during various runs

Runs	% Composition			Adsorption Capacity (mg/g)				Removal Efficiency (%)
	I	D	C	I	D	C	Average	Average
1	46.67	26.67	26.67	1.96	0.62	0.67	1.08	90.4
2	40.00	20.00	40.00	1.43	0.35	1.52	1.10	91.0
3	40.00	40.00	20.00	1.33	1.35	0.36	1.01	85.9
4	33.33	33.33	33.33	0.95	1.00	1.03	0.99	89.2
5	20.00	20.00	60.00	0.29	0.34	3.51	1.38	85.2
6	40.00	40.00	20.00	1.33	1.35	0.36	1.01	85.9
7	60.00	20.00	20.00	3.35	0.35	0.36	1.35	90.1
8	60.00	20.00	20.00	3.35	0.35	0.36	1.35	90.1
9	26.67	46.67	26.67	0.56	1.99	0.63	1.06	86.3
10	20.00	60.00	20.00	0.26	3.09	0.35	1.24	80.1
11	26.67	26.67	46.67	0.55	0.61	2.06	1.07	85.8
12	20.00	40.00	40.00	0.28	1.41	1.50	1.06	84.1
13	20.00	20.00	60.00	0.30	0.35	3.42	1.36	86.0
14	20.00	60.00	20.00	0.26	3.15	0.34	1.25	78.9

I – Ibuprofen

D- Doxycycline

C- Chloroquine

#### Regression Model and Analysis of Variance (ANOVA)

By fitting the adsorption experimental data to the special quartic, special quartic, and linear regression models using the Design Expert statistical software version 12, the coefficients of the model equation given in Table 4 were found. The coefficient estimate, which assumes that all other factors remain constant, shows the estimated change in response per unit change in factor value. The intercept in an orthogonal design is the mean response across all runs. The adsorption capacity as a function of ibuprofen, doxycycline, and Chloroquine to obtain Eq. (2-4). The factor settings are used to modify the average using the coefficients. The equation considers both the relevant and the insignificant model terms.

$$\text{Absorption Capacity}_{Ibu} = 3.35 A + 0.2612 B + 0.2967 C - 1.89 AB - 1.57 AC + 0.0075 BC + 2.04 A^2BC + 2.98 AB^2C - 2.99 ABC^2 \quad (2)$$

$$\text{Absorption Capacity}_{Doxy} = 0.3527 A + 3.12 B + 0.3457 C - 1.54 AB + 0.0321 AC - 1.3 BC - 0.9536 A^2BC + 8.92 AB^2C - 4.00 ABC^2 \quad (3)$$

$$\text{Absorption Capacity}_{Chloro} = 0.3573 A + 0.3456 B + 3.47 C - 1.54 AB - 1.58 AC - 1.61 BC + 1.40 A^2BC - 1.17 AB^2C - 1.17 ABC^2 \quad (4)$$

Where, respectively, A, B, and C are ibuprofen, doxycycline, and Chloroquine. The models' fit was tested using the Fischer test (F-value), probability value (p-value), and correlation coefficient (R<sup>2</sup>), which is a measure of fit goodness (Table 4).

Table 4: Coefficient of model for Adsorption capacity of selected pharmaceuticals (A – Ibuprofen, B – Doxycycline & C – Chloroquine)

Component	Ibuprofen			
	Coefficient Estimate	Standard Error	95% CI Low	95% CI High
A	3.35	0.0033	3.34	3.34
B	0.2612	0.0033	0.2526	0.2526
C	0.2967	0.0033	0.2882	0.2882
AB	-1.89	0.0163	-1.93	-1.93
AC	-1.57	0.0209	-1.63	-1.63
BC	0.0075	0.0209	-0.0463	-0.0463
A <sup>2</sup> BC	2.04	0.4644	0.8457	0.8457
<AB <sup>2</sup> C	2.98	0.4644	1.79	1.79
ABC <sup>2</sup>	-2.99	0.4710	-4.20	-4.20
	Doxycycline			
	Coefficient Estimate	Standard Error	95% CI Low	95% CI High
A	0.3527	0.0135	0.3181	0.387
B	3.12	0.0135	3.09	3.16
C	0.3457	0.0135	0.3110	0.380
AB	-1.54	0.0660	-1.71	-1.37
AC	0.0321	0.0849	-0.1862	0.250
BC	-1.30	0.0849	-1.52	-1.08
A <sup>2</sup> BC	-0.9536	1.88	-5.80	3.89
<AB <sup>2</sup> C	8.92	1.88	4.08	13.76
ABC <sup>2</sup>	-4.00	1.91	-8.91	0.914
	Chloroquine			
	Coefficient Estimate	Standard Error	95% CI Low	95% CI High
A	0.3573	0.0202	0.305	0.4092
B	0.3456	0.0202	0.293	0.3975
C	3.47	0.0202	3.42	3.52
AB	0.0324	0.0990	-0.22	0.2869
AC	-1.58	0.1274	-1.91	-1.26
BC	-1.61	0.1274	-1.94	-1.28
A <sup>2</sup> BC	1.40	2.83	-5.86	8.67
<AB <sup>2</sup> C	-1.17	2.83	-8.44	6.09
ABC <sup>2</sup>	-1.17	2.87	-8.54	6.20

For Ibuprofen, Doxycycline, and Chloroquine (IDC) respectively, the model equation developed for their adsorption capacities is special quartic with standard deviation, R<sup>2</sup>, and Adjusted R<sup>2</sup> values of (0.0047, 1.0000, and 1.0000), (0.0191, 0.9999, and 0.9996), (0.0286, 0.9997, and 0.9993). The comparatively high values of R<sup>2</sup> show that the experimentally observed values and anticipated values exhibit a strong association.

The "Pred R<sup>2</sup>" values of 0.9993, 0.9952, and 0.9990 are reasonably in agreement with the corresponding "Adj R<sup>2</sup>" values of 1.0000, 0.9996, and 0.9993 for Ibuprofen, Doxycycline, and Chloroquine, respectively, proving that the model is adequate. Since "Adeq Precision" measures the signal-to-noise ratio and a ratio greater than 4 is preferred, the Adequate (Adeq) Precision values of 819.4264, 181.5044, and 136.1791 obtained for the adsorption capacities of Ibuprofen, Doxycycline, and Chloroquine, respectively, by the plantain peel ash, indicate an adequate signal. The Model F-values of 84989.88, 4262.68, and 2467.23 for the adsorption capabilities of Ibuprofen, Doxycycline, and Chloroquine by the plantain peel ash adsorbent, respectively, show the regression models' high significance (Table 7). There is only a 0.01% chance that a "Model F-value" this large could occur due to noise.

The low probability value of the F-extremely test in the analysis of variances for regression models (ANOVA) demonstrated that the models were highly significant (0.0001) Model terms are regarded as being insignificant when Prob > F values are more than 0.1000 but less than 0.05. The linear mixture terms are significant models in each of the developed regression model equations, based on the p values of the regression coefficients.

Table 5: Results of ANOVA for selected pharmaceuticals (A – Ibuprofen, B – Doxycycline & C – Chloroquine) by plantain peel ash

	Ibuprofen			
	Sum of Squares	Mean Square	F-value	p-value
Model	15.02	1.88	84989.83	<1E-4
<sup>(1)</sup> Linear Mixture	14.55	7.27	3.292E+5	<1E-4
AB	0.2991	0.2991	13535.11	< 1E-4
AC	0.1246	0.1246	5640.48	< E-4
BC	2.807E-06	2.8E-6	0.1270	0.7361
A <sup>2</sup> BC	0.0004	0.0004	19.29	0.0071
AB <sup>2</sup> C	0.0009	0.0009	41.22	0.0014
ABC <sup>2</sup>	0.0009	0.0009	40.34	0.0014
Residual	0.0001	0.0000	NA	NA
Lack of Fit	0.0001	0.0001	18.09	0.0131
Pure Error	0.0000	5.002E-06	NA	NA
Cor Total	15.02	NA	NA	NA
	Doxycycline			
	Sum of Squares	Mean Square	F-value	p-value
Model	12.40	1.55	4262.7	< 0.0001
<sup>(1)</sup> Linear Mixture	12.10	6.05	16633.5	< 0.0001
AB	0.1982	0.1982	545.17	< 0.0001
AC	0.0001	0.0001	0.1428	0.7210
BC	0.0851	0.0851	233.94	< 0.0001
A <sup>2</sup> BC	0.0001	0.0001	0.2562	0.6343
AB <sup>2</sup> C	0.0082	0.0082	22.43	0.0052
ABC <sup>2</sup>	0.0016	0.0016	4.38	0.0907
Residual	0.0018	0.0004	NA	NA
Lack of Fit	0.0005	0.0005	1.33	0.3123
Pure Error	0.0014	0.0003	NA	NA
Cor Total	12.40	NA	NA	NA
	Chloroquine			
	Sum of Squares	Mean Square	F-value	p-value
Model	16.16	2.02	2467.23	<0.0001
<sup>(1)</sup> Linear Mixture	15.78	7.89	9636.82	<0.0001
AB	0.0001	0.0001	0.1068	0.7571
AC	0.1265	0.1265	154.60	<0.0001
BC	0.1311	0.1311	160.19	<0.0001
A <sup>2</sup> BC	0.0002	0.0002	0.2467	0.6404
AB <sup>2</sup> C	0.0001	0.0001	0.1723	0.6953
ABC <sup>2</sup>	0.0001	0.0001	0.1664	0.7002
Residual	0.0041	0.0008	NA	NA
Lack of Fit	5.6E-06	5.6E-06	0.0055	0.9445
Pure Error	0.0041	0.0010	NA	NA
Cor Total	16.16	NA	NA	NA

### Model Validity

To ascertain whether the chosen model provides a sufficient approximation of the real system, several diagnostic data analyses based on actual and expected values were carried out. While the actual values were achieved by experimentation, the projected values came from the model equations. Figures 1a, 2a, and 3a use a normal plot to display the model's predicted and actual responses for the deletion of all medications under investigation. Figures 1b, 2b, and 3b show the disparities between the actual and predicted responses for the deletion of IDC, together with the results of plotting the expected value versus the actual value. A better agreement between actual and anticipated values may be seen in Figure 2a. When every data point is represented as a straight line, the data are uniformly distributed.

Figure 2b illustrates how close the residuals are. The correlation between the 3D distribution of IDC utilizing the developed models is shown in Figures 1c, 2c, and 3c, respectively. Additionally, it showed how closely the chosen model resembles the real system.

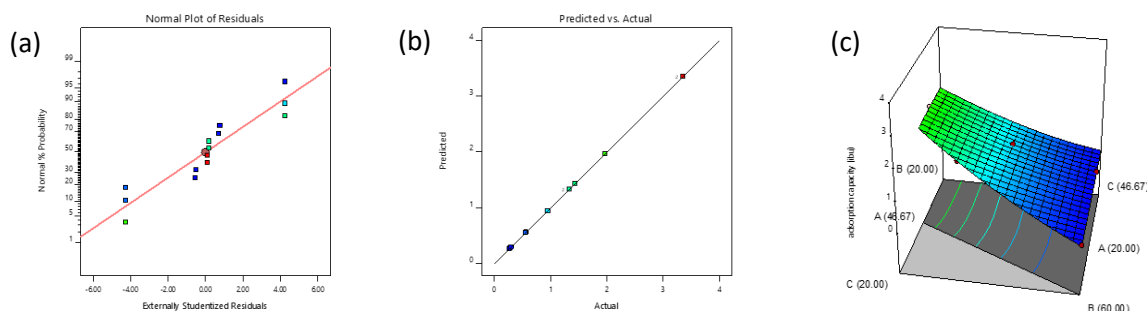


Figure 1: Ibuprofen graphs of (a) Normal % probability versus Externally studentized residuals, (b) Actual versus Predicted value, and (c) 3D surface distribution

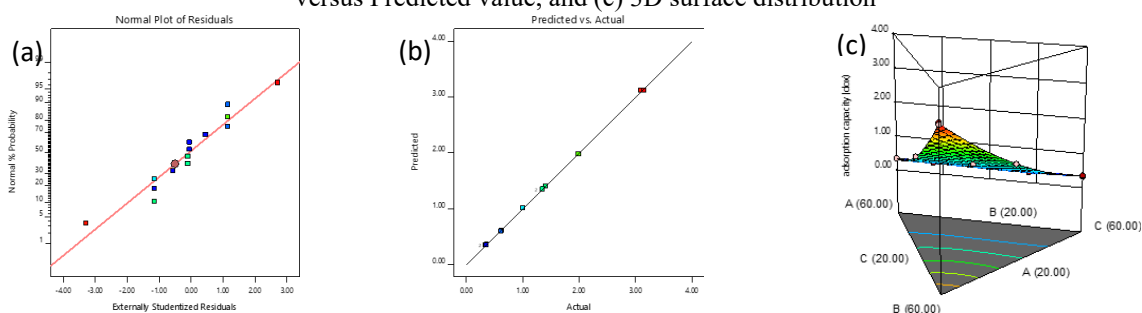


Figure 2: Doxycycline graphs of (a) Normal % probability versus Externally studentized residuals, (b) Actual versus Predicted value, and (c) 3D surface distribution

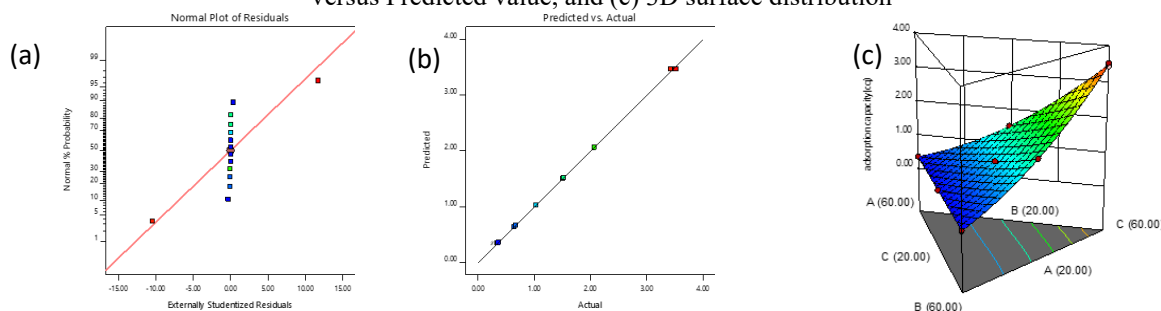


Figure 3: Chloroquine graphs of (a) Normal % probability versus Externally studentized residuals, (b) Actual versus Predicted value, and (c) 3D surface distribution

## CONCLUSION

The adsorption of ibuprofen, doxycycline, and Chloroquine as well as the individual and combined impacts of their concentrations were effectively examined using Design Expert Software's Simplex Lattice of the Mixture approach. The investigation has shown that a selective adjustment in the content of Ibuprofen, Doxycycline, and Chloroquine has a significant effect on the ability of the Plantain peel ash adsorbent. The Plantain Peel Ash adsorbent developed showed great efficacy in the removal of IDC from an aqueous solution.

## REFERENCES

- R. Rashid, I. Shafiq, P. Akhter, M. J. Iqbal, and M. Hussain, (2021). A state-of-the-art review on wastewater treatment techniques: the effectiveness of adsorption method. *Environ Sci Pollut Res*, 28(8) pp. 9050–9066, DOI: 10.1007/s11356-021-12395-x.
- G. Kaur, N. Singh, and A. Rajor. (2021). Efficient Adsorption of Doxycycline Hydrochloride Using Deep Eutectic Solvent Functionalized Activated Carbon Derived from Pumpkin Seed Shell. *Chemistry Select*, 6(13), pp. 3139–3150, DOI: 10.1002/slct.202100182.
- M. Patel, R. Kumar, C. U. Pittman, and D. Mohan, (2021). Ciprofloxacin and acetaminophen sorption onto banana peel biochars: Environmental and process parameter influences. *Environmental Research*, 201, pp. 111218, DOI: 10.1016/j.envres.2021.111218.
- N. J. Waleng and P. N. Nomngongo. (2022). Occurrence of pharmaceuticals in the environmental waters: African and Asian perspectives,” *Environmental Chemistry and Ecotoxicology*, 4, pp. 50–66, DOI: 10.1016/j.enceco.2021.11.002.

- B. S. Rathi and P. S. Kumar. (2021). Application of adsorption process for effective removal of emerging contaminants from water and wastewater. *Environmental Pollution*, 280, pp.116995, DOI: 10.1016/j.envpol.2021.116995.
- Mohd. Rafatullah, O. Sulaiman, R. Hashim, and A. Ahmad, (2010). Adsorption of methylene blue on low-cost adsorbents: A review. *Journal of Hazard. Materials*, 177, (1-3): pp.70–80, DOI: 10.1016/j.jhazmat.2009.12.047.
- N. Felix, L. Nwabue, I. Ikelee and A. O. Ogah, (2018). Activated Plantain Peel Biochar as Adsorbent for Removal of Zinc (II) Ions from Aqueous Solution: Equilibrium and Kinetics Studies.,” *Journal of the Turkish Chemical Society, Section A: Chemistry*, pp. 1257–1270, DOI: 10.18596/jotcsa.438332.
- E. A. Oluyemi, J. A. O. Oyekunle, and S. O. Olasoji, (2009). A Comparative Study of the Removal of Heavy Metal Ions from Synthetic Wastewaters Using Different Adsorbents. *Adsorption Science & Technology*, vol. 27, no. 5, pp. 493–501, DOI: 10.1260/0263-6174.27.5.493.
- A.O. Alade, O.S. Amuda, T.J. Afolabi and A.A. Okoya, (2012) Adsorption of naphthalene onto activated carbons derived from milk bush kernel shell and flamboyant pod. *Journal of Environmental Chemistry and Ecotoxicology* 4 (7):pp. 124-132



## Seasonal Variation and Health Risks of Particulates at and around Traffic Hotspots in Ibadan -a Model African Metropolis

Emmanuel T. ODEDIRAN<sup>1\*</sup>, Jamiu A. ADENIRAN<sup>1</sup>, Rafiu O. Yusuf<sup>1</sup>

<sup>1</sup>Environmental Engineering Research Laboratory, Department of Chemical Engineering, University of Ilorin, Nigeria

<sup>1\*</sup>[odedirantolu@yahoo.com](mailto:odedirantolu@yahoo.com), <sup>1</sup>[adeniran.ja@unilorin.edu.ng](mailto:adeniran.ja@unilorin.edu.ng), <sup>1</sup>[yusuf.ro@unilorin.edu.ng](mailto:yusuf.ro@unilorin.edu.ng)

\*Corresponding author

### ABSTRACT

Fewer studies have investigated incidents of pollution from vehicular traffic in African cities compared to other parts of the world. This study assessed variation in seasonal concentrations and exposure to health risks of particulates ( $PM_1$ ,  $PM_{2.5}$ ,  $PM_{10}$  & TSP) at and around twenty-five (25) major traffic Intersections (TIs) within Ibadan City, a typical urban environment in Sub-Saharan Africa. The 24h mean concentration of  $PM_1$ ,  $PM_{2.5}$ ,  $PM_{10}$  and TSP sampled at 25 TIs in Ibadan during the dry season were 1.57, 2.29, 4.19 and 4.09 times their corresponding values during the rainy season. The Pearson's correlations of total vehicle on-road with  $PM_1$  and  $PM_{2.5}$  were positive while that of  $PM_{10}$  and TSP gave negative correlations. Statutory Limit Breach (SLB) values were above the set standards of regulatory agencies at several TIs. Total Respiratory Deposition Doses (TRDD) of  $PM_1$ ,  $PM_{2.5}$  &  $PM_{10}$  were higher during the dry season by 35.15%, 56.89% and 78.27% than those during the rainy season. SLB and TRDD estimates showed that road users are significantly at risk of exposure to particulates from traffic-related sources.

**Keywords:** Particulate, Traffic Intersection, Season, Rush and Non-rush hour, Deposition dose.

### 1. INTRODUCTION

The primary sources of urban air pollution are road traffic and industrial activities (Adiang *et al.*, 2017). Globally, over one billion people are exposed to urban air pollution each year (Zhang and Day, 2015). India and China reported more than one million premature deaths per year due to incidences of urban air pollution (Dockery and Evans, 2017). Urban vehicular congestions occur mostly at Traffic Intersections (TIs) resulting in adverse human health effects in cities (Police *et al.*, 2016). Therefore, TIs are foremost traffic hotspots (Adeniran *et al.*, 2017), where vehicular emissions are deposited and dispersed over time (Gunawardena *et al.*, 2013). Exhaust emissions from internal combustion engines of vehicles are significantly gaseous and particulate pollutants which may include: un-burnt fuel, particulate matters (PM), carbon monoxide (CO), carbon dioxide (CO<sub>2</sub>), volatile organic compounds (VOCs), polycyclic aromatic hydrocarbons (PAHs), oxides of nitrogen (NO<sub>x</sub>), oxides of sulphur (SO<sub>x</sub>), lead (Pb), heavy metals and other hydrocarbons (Ugbebor and John, 2018).

The variation in spatial and temporal characteristics and the fate of atmospheric pollutants in a locality are mainly affected by meteorological factors (such as ambient temperature, relative humidity, precipitation, wind speed and direction) and topography. Poor air quality in many African cities caused by urbanization, surge in population, industrialization and increased vehicular emissions impacts poor citizens more negatively (Das *et al.*, 2015; Delkash and Mir, 2016; Singh *et al.*, 2014). Although Africa's urban population is experiencing very rapid growth, studies on urban air pollution in sub-Saharan Africa (especially across West Africa) are very few (Dolumbia *et al.*, 2018).

Proportionate urban pollution impacts fluctuate with vehicle type. The large population of vehicles in many African cities predominantly imported automobiles from America and Europe generate high emissions in traffic (Kumar and Barrett, 2008). Emissions from vehicles have adverse effects on visibility, public health and global climate change. Considerable harmful emissions are released by automobiles that are not well-maintained during rush-hour traffic (Essiet and Mmom, 2014).

Prior epidemiological studies have associated traffic-related air pollution with asthma, lung malfunction, and other respiration difficulties in people (Adiang *et al.*, 2017; Gordian *et al.*, 2006; Vallero, 2014). Pollutants generated from fuel combustion activities pose significant health problems, accounting for more than half of the overall traffic emissions of PM in urban areas (Han and Naehar, 2006).

Some researchers have investigated pollutants ambient concentrations in cities across the world (Adeniran *et al.*, 2017; Djossou *et al.*, 2018; Fenech and Aquilina, 2020; Kumar *et al.*, 2021; Morakinyo *et al.*, 2017; Njoku *et al.*, 2016; Olajire *et al.*, 2011; Owoade *et al.*, 2015; Pal *et al.*, 2012; Polednik and Piotrowicz, 2020; Singh *et al.*, 2014; Torkmahalleh *et al.*, 2020; Triantafyllou *et al.*, 2020). However, regardless of the global effort to tackle this key air pollution challenge, little progress has been made in Africa where the problem is prevalent. Pollution from vehicular traffic remains one of the many environmental problems that need consideration in many cities across Africa. The evaluation of the likely exposure risks to air pollutants from road traffic requires data on their ambient concentration levels in the environment. Insufficient statistics on air pollutants related to traffic and their connections with climatic factors in several countries in Africa (including Nigeria) makes it difficult to develop a reliable emission control strategy. Therefore, this study investigated the seasonal concentration levels and exposure health risks of particulates (PM<sub>1</sub>, PM<sub>2.5</sub>, PM<sub>10</sub> & TSP) in and around major traffic pollution hotspots of Ibadan Metropolis- one of the largest cities in Africa. Monitoring pollutant concentration levels will help relevant government establishments and concerned stakeholders to develop essential mitigation policies to check future deleterious impacts on human health and ensure exposure reduction.

## 2. MATERIALS AND METHODS

### 2.1 Study Area Description

Ibadan is positioned between longitudes 7°2'E to 7°40'E and latitudes 3°35'N to 4°10'N (Figure 1). Ibadan is the capital of Oyo State in Nigeria and one of the biggest African cities (Ajayi *et al.*, 2012). The city is located in the south-western part of Nigeria (Ayeni, 1994). Ibadan is heavily populated with more than 3.8 million occupants (NPC, 2006). Ibadan exhibits tropical rainy and dry climate. The rainy period spans between March and October of each year whereas its dry season comes with the cool dry wind (harmattan) covering the months of November to February. Rainfall of about 1420.06mm drops within an average of 109 days. June and September are the two months with the highest rainfall. The city's temperature fluctuates between 20.10°C and 40°C, atmospheric pressure varies from 754.6 to 762.3mmHg and the relative humidity extended from 49.2 to 83.58% (Yusuf *et al.*, 2022). The city has elevations extending from 152 to 213m with a land radius of 12,000m. The lowest and highest wind speed values observed during the dry season vary from 1.1 to 17 km/h. Environmental pollution in Ibadan is triggered by emissions from anthropogenic activities including road traffic in addition to commercial and industrial activities (Liu *et al.*, 2019; Wei *et al.*, 2015).

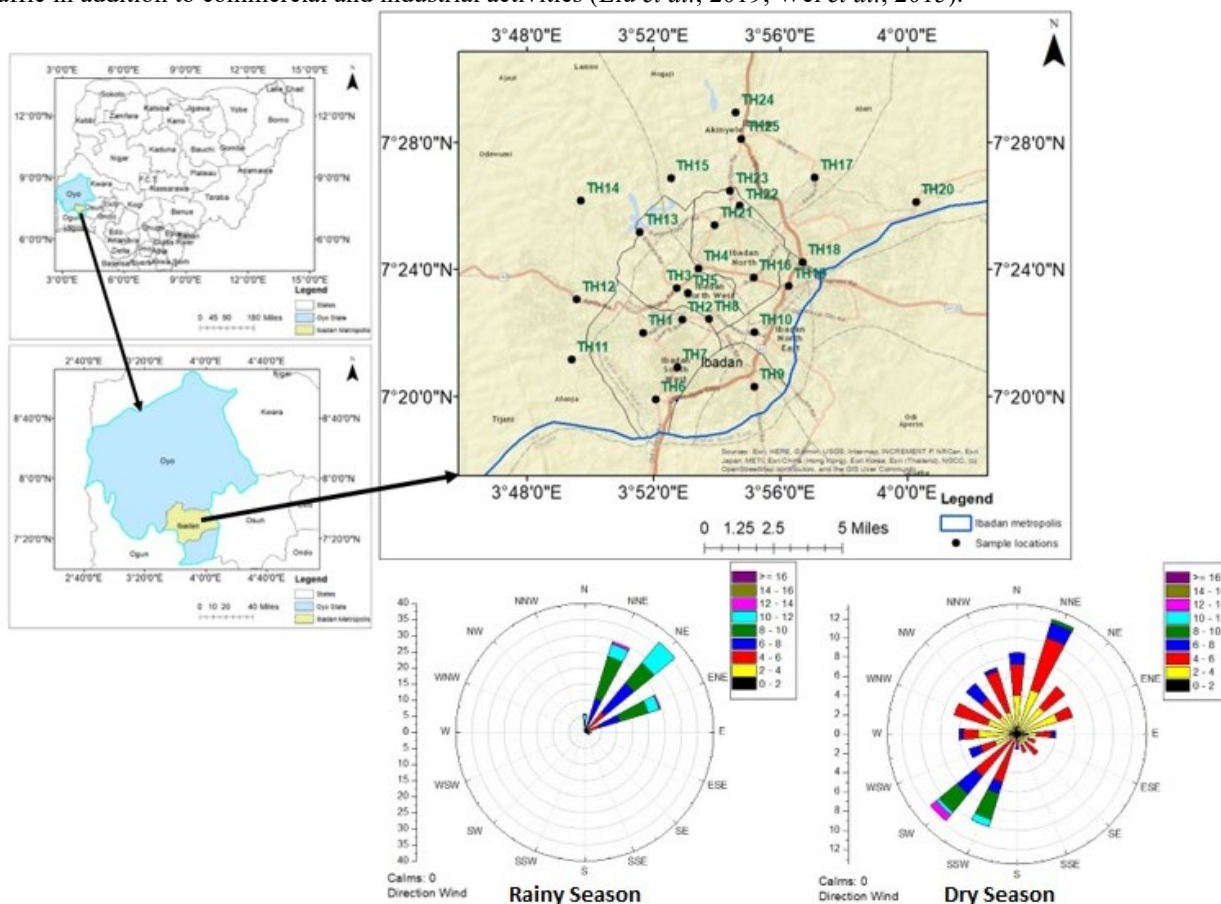


Figure 1: Study location with wind rose of rainy and dry seasons



## 2.2 Sampling Protocol for PM Pollutants

Particulate matter (PM<sub>1</sub>, PM<sub>2.5</sub>, PM<sub>10</sub> & TSP) was sampled in twenty-five (25) major traffic hotspots during the rainy (wet) and dry seasons in Ibadan. Selected sampling sites were the TIs, evenly and spatially distributed within the Ibadan metropolis, having land use patterns such as industrial, commercial and residential activities (Supplementary Table S1).

This study adopted sampling method used by Adeniran *et al.* (2017). Ambient PM sizes of PM<sub>1</sub>, PM<sub>2.5</sub>, PM<sub>10</sub> & TSP were measured with Aerocet 531S particle counter/mass monitor, placed within the breathing zone of 1-1.5m above the ground level at the selected TIs. This battery-operated, handheld Met One Instruments measured concurrently six mass concentration ranges (PM<sub>1</sub>, PM<sub>2.5</sub>, PM<sub>4</sub>, PM<sub>7</sub>, PM<sub>10</sub> and TSP) or five particle count sizes (0.3, 0.5, 1.0, 5.0 and 10 µm). Data sample history was displayed on the screen in either mode after capturing of particle. For the rainy and dry seasons data, monitoring of selected PM and gaseous pollutants were carried out simultaneously in all the TIs during heavy traffic (rush hour) and light vehicular traffic (non-rush hour) periods. Atmospheric pressure, ambient temperature and relative humidity were measured for the entire sampling duration using Kestrel 4500 Weather Tracker.

Information on equipment operation and calibration, adjustment of PM values for relative humidity, correction achieved from the correlation of PM data obtained from Hazdust™ sampler and gravimetric analysis with results obtained from Aerocet 531S particle counter have been described in other studies (Adeniran *et al.*, 2017; Adeniran *et al.*, 2018).

## 2.3 Human Exposure Risk Assessment

Assessments of human exposure risk to airborne pollutants at the TIs were estimated using Statutory Limit Breach (SLB) and the total respiratory deposition dose (TRDD) estimates.

SLB was considered particulate matter (PM<sub>2.5</sub>, PM<sub>10</sub> & TSP) using Equation 1. SLB is the ratio of concentrations of sampled PM to their corresponding ambient statutory limits. The ambient air quality guidelines or statutory limits taken into consideration include those of the World Health Organization (WHO) (WHO, 2006), the US Environmental Protection Agency (USEPA, 2012) and Nigeria's National Environmental Standards and Regulations Enforcement Agency (NESREA) formerly Federal Ministry of Environment (FMENV) (Gazette FRN, 1991; NESREA, 2020).

$$SLB = \frac{C_{SP}}{P_{SL}} \quad (1)$$

where C<sub>SP</sub> is the pollutant concentration of sampled PM and P<sub>SL</sub> is the pollutant concentration of statutory limit of PM. The equation was used to compute SLB value. The value of SLB greater than 1 is significant and worrisome.

The respiratory deposition dose (RDD) rates for PM<sub>10</sub>, PM<sub>2.5</sub> and PM<sub>1.0</sub> were estimated by using the approach used by Adeniran *et al.* (2017) and Kumar and Goel (2016) as shown in Equation (2):

*Deposited doses (in thoracic, tracheobronchial, alveolar regions of PM fractions)*

$$= (V_T \times f) \times DF_i \times PM_i \quad (2)$$

$$DF = IF \times \left( 0.058 + \frac{0.911}{1 + \exp(4.77 + \ln d_p)} + \frac{0.943}{1 + \exp(0.508 - 2.58 \ln d_p)} \right) \quad (3)$$

$$IF = 1 - 0.5 \left( 1 - \frac{1}{1 - 0.00076 d_p^{2.8}} \right) \quad (4)$$

where V<sub>T</sub> is defined as tidal volume, f is known as breathing frequency. DF<sub>i</sub> and PM<sub>i</sub> are known as the fraction of deposition and mass concentration of particle size *i* in micrometre, respectively. For light exercise conditions, men's values f and V<sub>T</sub> were taken as 0.35 and 800 cm<sup>3</sup> per breath, respectively, (Hinds, 1999; Kumar and Goel, 2016). DF<sub>i</sub> and IF (inhalable fraction) for PM<sub>1</sub>, PM<sub>2.5</sub> and PM<sub>10</sub> were evaluated using equations 3 and 4 suggested by Hinds (1999).

## 3. RESULTS AND DISCUSSION

### 3.1 Meteorological Parameters

The seasonal meteorological parameters of the study area obtained during the rush and non-rush hours using the Kestrel 4500 weather tracker (Supplementary Table S2) were consistent with the historical climate data of the Nigeria Meteorological Agency (NIMET, 2019). In the rainy season, the mean temperature ranged between 21.7 and 30.3°C for all the TIs. The relative humidity (RH) ranged from 63 to 98%. Atmospheric pressure was between 757.1 and 762.3mmHg. The highest and lowest recorded wind speeds (WS) were 4.72 and 0.83m/s, respectively. In the dry season, the mean temperature for all TIs ranged between 20.1 and 38°C, RH varied from 12 - 97%, Atmospheric pressure recorded was in the range of 754.6 - 759.8mmHg while wind speed varied from 0.31 to 4.72m/s.

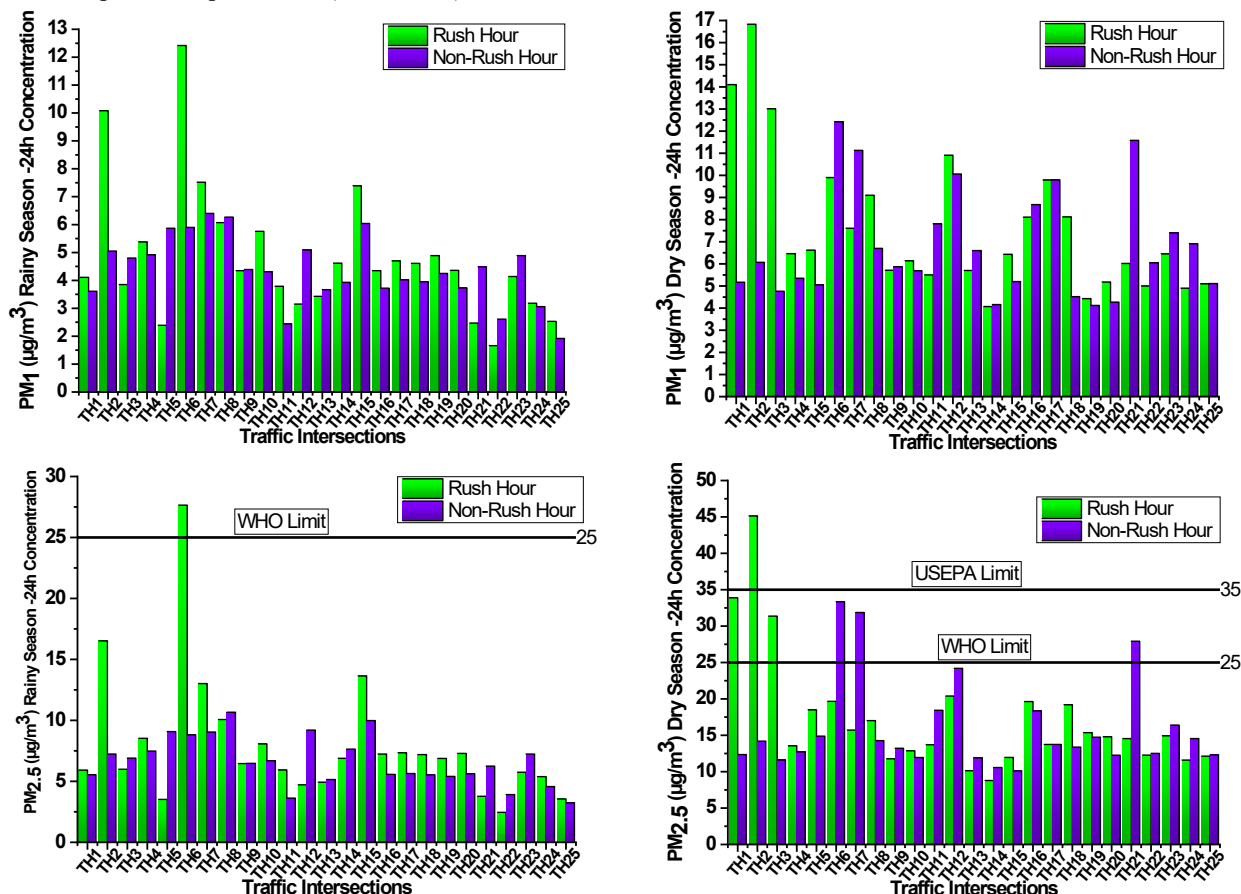
### 3.2 PM Concentration Variations during Traffic Flow Intensity

The seasonal variation of PM (PM<sub>1</sub>, PM<sub>2.5</sub>, PM<sub>10</sub> & TSP) mass concentrations during the rush and non-rush hours in Ibadan are illustrated in Figure 2. The 24h mean concentrations of PM<sub>1</sub>, PM<sub>2.5</sub>, PM<sub>10</sub> & TSP in Ibadan during rush hours of rainy season were 4.85±1.43, 7.95±2.57, 33.69±13.85 and 60.87±25.51 µg/m<sup>3</sup>, respectively while the corresponding values during non-rush hours of the rainy season were 4.37±1.51, 6.66±2.66, 36.17±16.07, 72.83±33.89 µg/m<sup>3</sup>, respectively. During the rainy season, 24h concentrations of PM<sub>1</sub> ranged from 1.66µg/m<sup>3</sup> (TH22) to 12.42µg/m<sup>3</sup> (TH6) during rush hours and 5.13µg/m<sup>3</sup> (TH25) to 6.40µg/m<sup>3</sup> (TH7) during non-rush hour, PM<sub>2.5</sub> concentration ranged from 2.46µg/m<sup>3</sup> (TH22) to 27.65µg/m<sup>3</sup> (TH6) during rush hour and 3.24µg/m<sup>3</sup>(TH25) to 10.67µg/m<sup>3</sup> (TH8) during non-rush hour. PM<sub>10</sub> ranged from 10.5µg/m<sup>3</sup> (TH21) to 146.28µg/m<sup>3</sup> (TH15) during rush hours and 11.84µg/m<sup>3</sup> (TH22) to 93.43µg/m<sup>3</sup> (TH14) during non-rush hours. TSP 24h concentration varied from 16.17µg/m<sup>3</sup> (TH21) to 345.93µg/m<sup>3</sup> (TH15) during rush hour and 19.87µg/m<sup>3</sup> (TH16) to 234µg/m<sup>3</sup> (TH15) during non-rush hours.

During the dry season, PM<sub>1</sub> 24h concentration extended from 4.07µg/m<sup>3</sup> (TH14) to 16.83µg/m<sup>3</sup> (TH2) during rush hours and 4.16µg/m<sup>3</sup> (TH14) to 12.42µg/m<sup>3</sup> (TH6) during non-rush hours, PM<sub>2.5</sub> ranged from 8.79µg/m<sup>3</sup>(TH14) to 45.13µg/m<sup>3</sup> (TH2) during rush hour and 19.2µg/m<sup>3</sup>(TH14) to 145.2µg/m<sup>3</sup> (TH12) during non-rush hour. PM<sub>10</sub> ranged from 34.9µg/m<sup>3</sup> (TH17) to 285.2µg/m<sup>3</sup> (TH19) during rush hours and 34.9µg/m<sup>3</sup> (TH17) to 306.03µg/m<sup>3</sup> (TH9) during non-rush hours and the concentration of TSP ranged from 57.31µg/m<sup>3</sup> (TH17) to 572.79µg/m<sup>3</sup> (TH11) during rush hours and correspondingly 57.31µg/m<sup>3</sup> (TH17) to 670.78µg/m<sup>3</sup> (TH9) during non-rush hours. The 24h mean concentration of PM<sub>1</sub>, PM<sub>2.5</sub>, PM<sub>10</sub> & TSP during rush hour of the dry season were 7.65±1.99, 17.31±4.39, 140±31.50 and 268.27±77.53 µg/m<sup>3</sup> respectively while the corresponding values are 6.82±1.40, 16.07±3.19, 152.40±58.06 and 277.93±95.22 µg/m<sup>3</sup> during non-rush hours.

In the rainy seasons, the highest 24h mean concentrations of PM<sub>1</sub>, PM<sub>2.5</sub>, PM<sub>10</sub> & TSP were found at TH6, TH6, TH15 and TH15 during rush hours and TH7, TH8, TH14 and TH15 during the non-rush hours, respectively. Similarly, the PM<sub>1</sub>, PM<sub>2.5</sub>, PM<sub>10</sub> & TSP highest mean concentrations in the dry season were recorded at TH2, TH2, TH19 and TH11 during rush hours and TH6, TH6, TH9 and TH9 during non-rush hours, respectively.

Elevated concentrations of airborne PM recorded at TIs in Ibadan may be from vehicular exhausts, road dust suspension by pedestrians and moving vehicles, vehicular body wears, wears of tyre, brake and engine parts, waste and bush burning near roads, back-up generators used in roadside shops and commercial buildings and mobile telecommunication base transceiver stations (Adeniran *et al.*, 2017). Heavy vehicular traffic in the city has been identified as a major source of atmospheric air pollutants. (Etim, 2016).



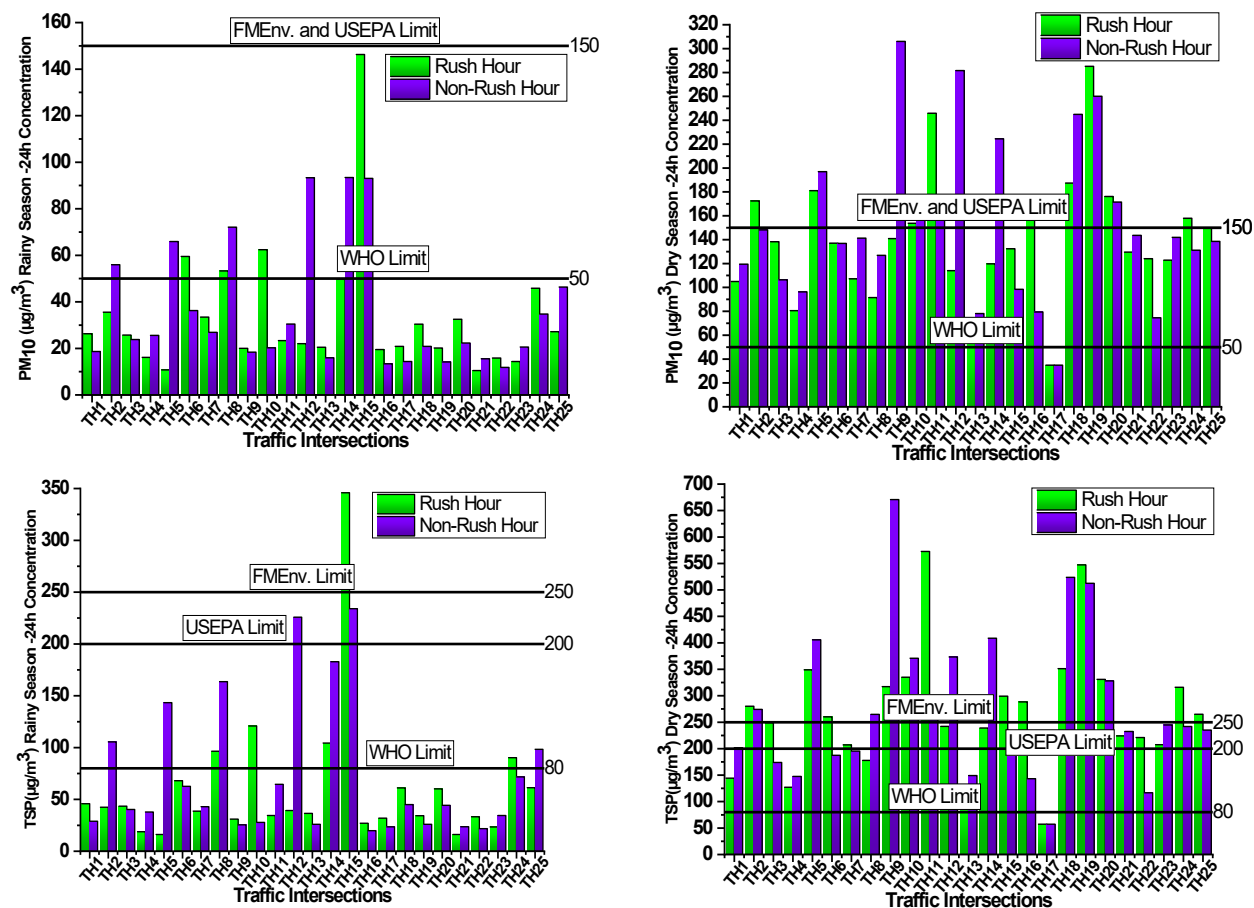


Figure 2: Seasonal variation of PM<sub>1</sub>, PM<sub>2.5</sub>, PM<sub>10</sub> and TSP (24h) mass concentrations during Non-rush and Rush hour periods in Ibadan

Temperature inversion contributes to higher PM concentrations during the early morning hours and late-night periods due to calmer night winds caused by an absence of solar irradiation, thus, leading to a lower temperature of the air which hinders the diffusion of PM having different densities (Saebo *et al.*, 2017).

The average concentration levels of PM<sub>1</sub>, PM<sub>2.5</sub>, PM<sub>10</sub> & TSP during rush hour periods were higher than in non-rush hour periods at 64%, 60%, 60% and 56% of 25 TIs studied, respectively during the rainy season and correspondingly 52%, 52%, 44% and 48% of 25 TIs studied during the dry seasons. Apart from a few exceptions, PM during traffic congestion or rush hours was generally higher than those during free-flow traffic or non-rush hours in this study (Zhang *et al.*, 2017). The free movement of vehicles on the road results in the re-suspension of road dust while the slow movement of vehicles at traffic intersections (TIs) causes incomplete combustion of fuel (Gokhale and Raokhande, 2008; Shirmohammadi *et al.*, 2017).

### 3.3 Seasonal Variations in Concentrations of PM

According to Chowdhury *et al.* (2019), ambient PM loads are usually influenced by seasonal variation effects. In this study, the 24h mean concentrations of PM<sub>1</sub>, PM<sub>2.5</sub>, PM<sub>10</sub> and TSP sampled at 25 TIs in Ibadan during the dry season were 1.57, 2.29, 4.19 and 4.09 times their corresponding values during the rainy season (Supplementary Table S3). Many related studies reported that re-suspended particles have varied impacts during the rainy and dry seasons, due to many factors including relative humidity, wind speed, rainfall, sunshine, categories of vehicles and traffic flow type (Adeniran *et al.*, 2018; Fernandez *et al.*, 2017). Forced deposition of particles may be accelerated during the rainy season than the dry season as a result of high relative humidity, temperature drop, rainfall, wind speed and lush vegetation (Chate, 2005; Jones and Harrison, 2004; Ranjan *et al.*, 2016).

### 3.4 PM Ratios

In this study, the ratios of PM<sub>1</sub> to PM<sub>2.5</sub>, PM<sub>2.5</sub> to PM<sub>10</sub> and PM<sub>10</sub> to TSP were estimated to assess the ambient PM fractions and their exposure consequences on residents as shown in Supplementary Figure S1. In the rainy season PM<sub>1</sub>/PM<sub>2.5</sub> ratio ranged from 0.5 to 0.74, PM<sub>2.5</sub>/PM<sub>10</sub> ratio varied from 0.09 to 0.39 and PM<sub>10</sub>/TSP ratio extended from 0.41 to 0.74. Similarly, during the dry season, PM<sub>1</sub>/PM<sub>2.5</sub> ratios varied from 0.28 to 0.56; PM<sub>2.5</sub>/PM<sub>10</sub> ratios stretched from 0.05 to 0.21 and PM<sub>10</sub>/TSP ratios extended from 0.4 to 0.65. High ratios of PM<sub>1</sub>/PM<sub>2.5</sub> and PM<sub>10</sub>/TSP were observed during both rainy and dry seasons, implying particulate levels in Ibadan may generally influenced by emissions from crustal particles,

automobile exhausts, road dust resuspension in addition to brake, tyre and engine wears during rainy and dry seasons in Ibadan (Odediran *et al.*, 2021).

The high percentages of ultrafine particles ( $PM_1$ ) in respirable (fine) PM fractions ( $PM_{2.5}$ ) during the two seasons studied confirmed that ultrafine particles are the main contributor to urban air pollution from fine particles. PM outdoor emissions are majorly caused by human activities which include fossil fuel combustion in internal combustion engines of generators and vehicles in addition to industrial activities at and around TIs (Adeniran *et al.*, 2018). Similarly, the high percentage of coarse particles ( $PM_{10}$ ) in total suspended particles (TSP) during the two seasons implies coarse particles were formed from particulates coagulation, accretion, agglomeration and other processes of secondary formation. Thus, demonstrating the dominant contribution of non-exhaust sources (such as road dust suspension and re-suspension, crustal particles, wear of brake, tyre, engine and vehicle body parts) to  $PM_{10}$  urban air pollution in this study.

### 3.5 Statutory Limit Breach (SLB) for PM

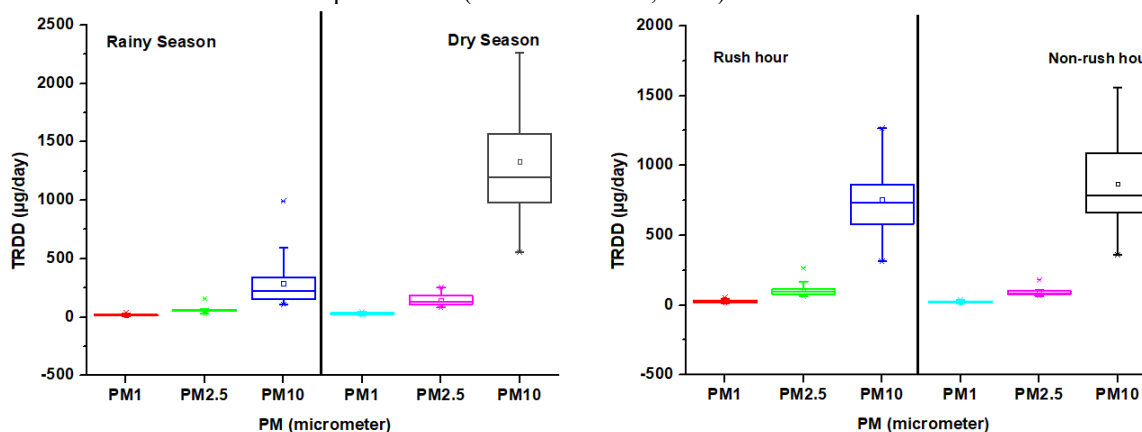
The SLB results of PM sampled in 25 TIs in Ibadan were presented in Figure 2, In the rainy season, The SLB of  $PM_{2.5}$  with reference to FMENV Standard of  $25 \mu\text{g}/\text{m}^3$  (Gazette FRN, 1991) at one TI (TH6) during rush hour only. Emissions of  $PM_{10}$  exceeded WHO limits of  $50 \mu\text{g}/\text{m}^3$  (WHO, 2006) at 4 TIs (TH6, TH8, TH10 & TH15) during the rush hour and 6 TIs during the non-rush hour. SLB results of TSP show that 1 TI (TH15) breached FMENV limit of  $250 \mu\text{g}/\text{m}^3$  (NESREA, 2020) during rush hour only, USEPA limits of  $200 \mu\text{g}/\text{m}^3$  for TSP (USEPA, 2012) were exceeded at 1 TI (TH15) during rush hour and 2 TIs (TH12 and TH15) during non-rush hour. In addition, 5 TIs (TH8, TH10, TH14, TH15 & TH24) during rush hour and 7 TIs (TH2, TH5, TH8, TH12, TH14, TH15, TH25) during non-rush hour breached WHO concentrations limit ( $80 \mu\text{g}/\text{m}^3$ ) of TSP (WHO, 2006) in this study.

In the dry season, SLB estimates as shown in Figure 2 indicated that  $PM_{2.5}$  limits ( $35 \mu\text{g}/\text{m}^3$ ) of USEPA were breached at 1 TI (TH2) during rush hour while the  $PM_{2.5}$  WHO limit ( $25 \mu\text{g}/\text{m}^3$ ) was exceeded at 3 TIs each during the rush and non-rush hour periods. FMENV and USEPA limits ( $150 \mu\text{g}/\text{m}^3$ ) of  $PM_{10}$  were breached at 8 and 7 TIs during the rush and non-rush hours, respectively. The standard WHO limits of  $PM_{10}$  ( $50 \mu\text{g}/\text{m}^3$ ) and TSP ( $80 \mu\text{g}/\text{m}^3$ ) were exceeded at 24 TIs out of 25 TIs studied during the rush and non-rush hour periods whereas FMENV limits ( $250 \mu\text{g}/\text{m}^3$ ) of TSP were breached at 13 and 10 TIs during the rush and non-rush hours, respectively.

### 3.6 Total Respiratory Deposition Dose (TRDD) of PM

The average on-road TRDD rates estimates at TIs during the rainy season were  $19 \pm 6.68$ ,  $62.57 \pm 27.6$ , and  $289.72 \pm 197.30 \mu\text{g}/\text{day}$  for  $PM_1$ ,  $PM_{2.5}$ , and  $PM_{10}$ , respectively while the corresponding values at TIs during the dry season were  $29.3 \pm 8.7$ ,  $145.15 \pm 45.45$  and  $1333.28 \pm 569.55 \mu\text{g}/\text{day}$ . Figure 3 illustrates the average TRDD for  $PM_1$ ,  $PM_{2.5}$ , and  $PM_{10}$  for the two seasons studied and different traffic flow intensities. The average on-road TRDD rates of  $PM_1$ ,  $PM_{2.5}$ , and  $PM_{10}$  at all TIs during the dry season were higher than those during the rainy season by 35.16%, 56.89% and 78.27%.

Likewise, the TRDD rates for  $PM_1$ ,  $PM_{2.5}$ , and  $PM_{10}$  at TIs during the rush hours were  $25.88 \pm 9.93$ ,  $109.43 \pm 46.86$ , and  $755 \pm 234.76 \mu\text{g}/\text{day}$ , respectively, and the corresponding non-rush hours TRDD rates were  $22.61 \pm 6.20$ ,  $98.30 \pm 30.91$  and  $868.38 \pm 436.12 \mu\text{g}/\text{day}$ . Rates of average TRDD estimated for  $PM_1$  and  $PM_{2.5}$  during rush hours were found to be 12.64% and 10.18% greater than those estimated during the non-rush hours while the average TRDD rate of  $PM_{10}$  during non-rush hours was higher than that obtained during rush hours by 13.02%. This implies that faster movement of on-road vehicles during non-rush hours results in re-suspension of more coarse particulates from road dust during non-rush hours than rush hours. TRDD estimates were used to evaluate the exposure of pedestrians, roadside traders, traffic wardens, vehicle inspection officers and road safety professionals who regularly spend long hour at TIs. RDD and TRDD rates may be high and severe during traffic congestion (rush hour), triggering serious health ailments such as asthma, sneezing and coughing (Day, 2006). Ultrafine particulates ( $PM_1$ ) and fine particulates ( $PM_{2.5}$ ) could cause widespread adverse respiratory-related ailments when inhaled deeply into the lungs reaching the Alveoli while inflammatory responses are associated with inhalation of coarse particulates (Zwozdziak *et al.*, 2017).



(a) (b)

Figure 3: Average TRDD rate of PM<sub>1</sub>, PM<sub>2.5</sub> and PM<sub>10</sub> for (a) seasonal variation and (b) traffic flow intensity

### 3.7 Effect of Climatic Parameters on Urban Air Pollution

Supplementary Table S4 presents the result of Pearson's correlation used to test the relationship of the PM mass concentration levels (PM<sub>1</sub>, PM<sub>2.5</sub>, PM<sub>10</sub> and TSP) with meteorological parameters (temperature, Relative Humidity, Atmospheric pressure, wind speed and wind direction) and vehicle traffic density (cars, buses, trucks, bicycles, tricycles and total vehicle on road per hour). The correlation coefficient obtained among all the PM sizes ranging from 0.53 to 1 showed a positive strong relationship signifying smaller particles are fragments of larger particles. Results showed that positive and negative correlations existed among the PM sizes, vehicle traffic densities and meteorological parameters. Effects of wet deposition may cause the negative coefficients obtained from the correlations of particulates with relative humidity during the washout process. Rainfall limits the possibility of PM re-suspension by increasing the humidity of the ecosystem and triggering a drop in outdoor PM concentrations. Wind speed interrupts the turbulence close to the land, thus reducing fine particulates in the air compared to coarse particulates. The rise or decline in wind speed determines the rate of PM dilution and dispersion in the air (Mkoma and Mjemah, 2011; Owoade *et al.*, 2012). Furthermore, wind direction enhances PM variation and movement from various upwind regions to the TIs. Ambient temperature and atmospheric pressure stimulate warmer air masses, which aids PM dispersion more than cold air masses.

As anticipated, relative humidity and wind speed showed positive correlations. A strong negative correlation of -0.82 was exhibited between temperature and relative humidity. The relationships of total vehicle on-road with PM<sub>1</sub> and PM<sub>2.5</sub> were positive whereas the correlation of total vehicle on-road with PM<sub>10</sub> and TSP gave negative correlations (Supplementary Table S4). This demonstrates that ultrafine (PM<sub>1</sub>) and fine (PM<sub>2.5</sub>) particle emissions from vehicle exhausts rise as the time that vehicles spend in rush hours traffic increases whereas coarse (PM<sub>10</sub>) particle rises more from road dust resuspension instigated by high-speed vehicles during non-rush hours.

## 4. CONCLUSION

This study revealed the seasonal variation in exposure to particulate matter (PM<sub>1</sub>, PM<sub>2.5</sub>, PM<sub>10</sub> & TSP) at and around traffic hotspots in a model African metropolitan area. Pollutant concentration levels measured at and around twenty-five major traffic Intersections (TIs) in Ibadan was considerably more hazardous to public health during the dry season than the rainy season. Dispersion of particulates was influenced by the dominating northern wind during the rainy season while the blend of northern and southern wind-aided pollutant dispersion in the dry season. Estimates of Statutory Limit Breach (SLB) showed that the average concentrations of PM pollutants exceeded the threshold limits set by environmental regulatory agencies at many TIs. Total Respiratory Deposition Dose (TRDD) of PM<sub>1</sub>, PM<sub>2.5</sub> & PM<sub>10</sub> were higher during the dry season by 35.15%, 56.89% and 78.27% than those during the rainy season. In this study, TRDD estimates during traffic congestion (Rush hour) for PM<sub>1</sub> & PM<sub>2.5</sub> were greater than those during traffic free-flow (non-rush hour) by 12.64% and 10.18%, respectively whereas TRDD values for PM<sub>10</sub> during non-rush hour were higher than rush hour TRDD by 13.02%. Pearson's correlation indicated that PM<sub>1</sub> & PM<sub>2.5</sub> emissions from vehicle exhausts increased as traffic congestion rose whereas PM<sub>10</sub> emission increased with road dust re-suspension during free-flow traffic. SLB and TRDD values indicated that pedestrians, road professionals and residents at and around the studied 25 TIs in Ibadan were exposed to particulate emissions considered harmful during the two seasons studied. Data of this study are suitable for developing integrated traffic pollution abatement policies for a model African metropolis. Alternate routes for traffic reduction, usage of cleaner combustible fuels from sustainable renewables and the enforcement of obligatory automobile inspection and maintenance schedules could be incorporated as essential (quick fix) remedies to Africa's urban air pollution.

## 5. REFERENCES

- Adeniran, J., Yusuf, R. & Olajire, A. (2017). Exposure to coarse and fine particulate matter at and around major intra-urban traffic intersections of Ilorin metropolis, Nigeria. *Atmospheric environment*, 166, 383-392.
- Adeniran, J. A., Aremu, A. S., Saadu, Y. O. & Yusuf, R. O. (2018). Particulate matter concentration levels during intense haze event in an urban environment. *Environmental monitoring and assessment*, 190(1), 41.
- Adiang, C. M., Monkam, D., Lenouo, A., Njeugna, E. & Gokhale, S. (2017). Evaluating impacts of two-wheeler emissions on roadside air quality in the vicinity of a busy traffic intersection in Douala, Cameroon. *Air Quality, Atmosphere & Health*, 10(4), 521-532.
- Ajayi, O. O., Charles-Davies, M. A. & Arinola, O. G. (2012). Progesterone, selected heavy metals and micronutrients in pregnant Nigerian women with a history of recurrent spontaneous abortion. *Afr Health Sci*, 12(2), 153-159. doi:10.4314/ahs.v12i2.12
- Ayeni, B. (1994). The metropolitan area of Ibadan: its growth and structure. *Ibadan region*, 72-84.
- Chate, D. (2005). Study of scavenging of submicron-sized aerosol particles by thunderstorm rain events. *Atmospheric environment*, 39(35), 6608-6619.
- Chowdhury, S., Dey, S., Di Girolamo, L., Smith, K. R., Pillarisetti, A. & Lyapustin, A. (2019). Tracking ambient PM<sub>2.5</sub> build-up in Delhi national capital region during the dry season over 15 years using a high-resolution (1 km) satellite aerosol dataset. *Atmospheric environment*, 204, 142-150.

- Das, R., Khezri, B., Srivastava, B., Datta, S., Sikdar, P. K., Webster, R. D. & Wang, X. (2015). Trace element composition of PM<sub>2.5</sub> and PM<sub>10</sub> from Kolkata—a heavily polluted Indian metropolis. *Atmospheric Pollution Research*, 6(5), 742-750.
- Day, R. J. (2006). Traffic-related air pollution and perceived health risk: lay assessment of an everyday hazard. *Health, Risk & Society*, 8(3), 305-322.
- Delkash, M. & Mir, H. M. (2016). Examining some potential actions in mitigating gaseous emissions from vehicles, case study: Tehran. *Air Quality, Atmosphere & Health*, 9(8), 909-921.
- Djossou, J., Akpo, A. B., Liousse, C., Yoboué, V., Bedou, M., Bodjrenou, M., Chiron, C., Galy-Lacaux, C., Gardrat, E. & Abbey, M. (2018). Mass concentration, optical depth and carbon composition of particulate matter in the major southern West African cities of Cotonou (Benin) and Abidjan (Côte d'Ivoire). *Atmospheric Chemistry and Physics*, 18(9), 6275-6291.
- Dockery, D. W. & Evans, J. S. (2017). Tallying the bills of mortality from air pollution. *Lancet*, 389(10082), 1862-1864. doi:10.1016/S0140-6736(17)30884-X
- Doumbia, M., Toure, N. D. E., Silue, S., Yoboue, V., Diedhiou, A. & Hauhouot, C. (2018). Emissions from the Road Traffic of West African Cities: Assessment of Vehicle Fleet and Fuel Consumption. *Energies*, 11(9), 2300.
- Essiet, U. & Mmom, P. C. (2014). Spatio-temporal variations in urban vehicular emissions in Uyo City, Akwa Ibom State, Nigeria. *Journal of Sustainable Development*, 7(4), 272-281.
- Etim, E. U. (2016). Air pollution emission inventory along a major traffic route within Ibadan Metropolis, southwestern Nigeria. *African Journal of Environmental Science and Technology*, 10(11), 432-438.
- Fenech, S. & Aquilina, N. J. (2020). Trends in ambient ozone, nitrogen dioxide, and particulate matter concentrations over the Maltese Islands and the corresponding health impacts. *Sci Total Environ*, 700, 134527. doi:10.1016/j.scitotenv.2019.134527
- Fernandez, J.-M., Meunier, J.-D., Ouillon, S., Moreton, B., Douillet, P. & Grauby, O. (2017). Dynamics of suspended sediments during a dry season and their consequences on metal transportation in a coral reef lagoon impacted by mining activities, New Caledonia. *Water*, 9(5), 338.
- Gazette FRN. (1991). Federal Republic of Nigeria Official Gazette.
- Gokhale, S. & Raokhande, N. (2008). Performance evaluation of air quality models for predicting PM<sub>10</sub> and PM<sub>2.5</sub> concentrations at urban traffic intersection during winter period. *Science of the Total Environment*, 394(1), 9-24.
- Gordian, M. E., Haneuse, S. & Wakefield, J. (2006). An investigation of the association between traffic exposure and the diagnosis of asthma in children. *Journal of exposure science & environmental epidemiology*, 16(1), 49-55.
- Gunawardena, J., Egodawatta, P., Ayoko, G. A. & Goonetilleke, A. (2013). Atmospheric deposition as a source of heavy metals in urban stormwater. *Atmospheric environment*, 68, 235-242.
- Han, X. & Naeher, L. P. (2006). A review of traffic-related air pollution exposure assessment studies in the developing world. *Environ Int*, 32(1), 106-120. doi:10.1016/j.envint.2005.05.020
- Hinds, W. C. (1999). *Aerosol technology: properties, behavior, and measurement of airborne particles*: John Wiley & Sons.
- Jones, A. M. & Harrison, R. M. (2004). The effects of meteorological factors on atmospheric bioaerosol concentrations—a review. *Science of the Total Environment*, 326(1-3), 151-180.
- Kumar, A. & Barrett, F. (2008). Stuck in traffic: Urban transport in Africa. *AICD Background paper*, 1.
- Kumar, P. & Goel, A. (2016). Concentration dynamics of coarse and fine particulate matter at and around signalised traffic intersections. *Environmental Science: Processes & Impacts*, 18(9), 1220-1235.
- Kumar, P., Hama, S., Nogueira, T., Abbass, R. A., Brand, V. S., Andrade, M. F., Asfaw, A., Aziz, K. H., Cao, S. J., El-Gendy, A., Islam, S., Jeba, F., Khare, M., Mamuya, S. H., Martinez, J., Meng, M. R., Morawska, L., Muula, A. S., Shiva Nagendra, S. M., Ngowi, A. V., Omer, K., Olaya, Y., Osano, P. & Salam, A. (2021). In-car particulate matter exposure across ten global cities. *Sci Total Environ*, 750, 141395. doi:10.1016/j.scitotenv.2020.141395
- Liu, E., Wang, X., Liu, H., Liang, M., Zhu, Y. & Li, Z. (2019). Chemical speciation, pollution and ecological risk of toxic metals in readily washed off road dust in a megacity (Nanjing), China. *Ecotoxicol Environ Saf*, 173, 381-392. doi:10.1016/j.ecoenv.2019.02.019
- Mkoma, S. L. & Mjemah, I. C. (2011). Influence of meteorology on ambient air quality in Morogoro, Tanzania. *International Journal of Environmental Sciences*, 1(6), 1107-1115.
- Morakinyo, O. M., Adebowale, A. S., Mokgobu, M. I. & Mukhola, M. S. (2017). Health risk of inhalation exposure to sub-10 µm particulate matter and gaseous pollutants in an urban-industrial area in South Africa: an ecological study. *BMJ open*, 7(3), e013941.
- NESREA. (2020). NESREA, 2020 National Environmental (Air Quality Control) Regulations, 2020 Schedule XIII Ambient Air Quality Standards.
- NIMET. (2019). Nigerian Meteorological Agency (NiMeT) 2019 Seasonal Rainfall Prediction (SRP). Retrieved from <https://fscluster.org/nigeria/document/nigerian-meteorological-agency-nimet> website:
- Njoku, K. L., Rumide, T. J., Akinola, M. O., Adesuyi, A. A. & Jolaoso, A. O. (2016). Ambient air quality monitoring in metropolitan city of Lagos, Nigeria. *Journal of Applied Sciences and Environmental Management*, 20(1), 178-185-178-185.

- NPC. (2006). National Population Commission (2006). *Federal Republic of Nigeria Official Gazette*, 96(2).
- Odediran, E. T., Adeniran, J. A., Yusuf, R. O., Abdurraheem, K. A., Adesina, O. A., Sonibare, J. A. & Du, M. (2021). Contamination Levels, Health Risks and Source Apportionment of Potentially Toxic Elements in Road Dusts of a Densely Populated African City. *Environmental Nanotechnology, Monitoring & Management*, 100445. doi:10.1016/j.enmm.2021.100445
- Olajire, A., Azeez, L. & Oluyemi, E. (2011). Exposure to hazardous air pollutants along Oba Akran Road, Lagos–Nigeria. *Chemosphere*, 84(8), 1044-1051.
- Owoade, K. O., Hopke, P. K., Olise, F. S., Ogundele, L. T., Fawole, O. G., Olaniyi, B. H., Jegede, O. O., Ayoola, M. A. & Bashiru, M. I. (2015). Chemical compositions and source identification of particulate matter (PM<sub>2.5</sub> and PM<sub>2.5-10</sub>) from a scrap iron and steel smelting industry along the Ife–Ibadan highway, Nigeria. *Atmospheric Pollution Research*, 6(1), 107-119. doi:10.5094/apr.2015.013
- Owoade, O., Olise, F., Ogundele, L., Fawole, O. & Olaniyi, H. (2012). Correlation between particulate matter concentrations and meteorological parameters at a site in Ile-Ife, Nigeria. *Ife Journal of Science*, 14(1), 83-93.
- Pal, S. K., Wallis, S. G. & Arthur, S. (2012). Emission patterns of traffic-related metals and associated contamination in road deposited sediment. *International journal of global environmental issues*, 12(2-4), 229-241.
- Polednik, B. & Piotrowicz, A. (2020). Pedestrian exposure to traffic-related particles along a city road in Lublin, Poland. *Atmospheric Pollution Research*, 11(4), 686-692.
- Police, S., Sahu, S. K. & Pandit, G. G. (2016). Chemical characterization of atmospheric particulate matter and their source apportionment at an emerging industrial coastal city, Visakhapatnam, India. *Atmospheric Pollution Research*, 7(4), 725-733.
- Ranjan, O., Menon, J. S. & Nagendra, S. S. (2016). Assessment of air quality impacts on human health and vegetation at an industrial area. *Journal of Hazardous, Toxic, and Radioactive Waste*, 20(4), A4016002.
- Saebo, A., Janhäll, S., Gawronski, S. & Hanslin, H. M. (2017). Urban forestry and pollution mitigation. *Routledge Handbook of Urban Forestry*. Routledge, London, 112-122.
- Shirmohammadi, F., Wang, D., Hasheminassab, S., Verma, V., Schauer, J. J., Shafer, M. M. & Sioutas, C. (2017). Oxidative potential of on-road fine particulate matter (PM<sub>2.5</sub>) measured on major freeways of Los Angeles, CA, and a 10-year comparison with earlier roadside studies. *Atmospheric environment*, 148, 102-114.
- Singh, P., Saini, R. & Taneja, A. (2014). Physicochemical characteristics of PM<sub>2.5</sub>: Low, middle, and high-income group homes in Agra, India—a case study. *Atmospheric Pollution Research*, 5(3), 352-360.
- Torkmahalleh, M. A., Hopke, P. K., Broomandi, P., Naseri, M., Abdrakhmanov, T., Ishanov, A., Kim, J., Shah, D. & Kumar, P. (2020). Exposure to particulate matter and gaseous pollutants during cab commuting in Nur-Sultan city of Kazakhstan. *Atmospheric Pollution Research*.
- Triantafyllou, E., Diapouli, E., Korras-Carraca, M., Manousakas, M., Psanis, C., Floutsi, A., Spyrou, C., Eleftheriadis, K. & Biskos, G. (2020). Contribution of locally-produced and transported air pollution to particulate matter in a small insular coastal city. *Atmospheric Pollution Research*, 11(4), 667-678.
- Ugbebor, J. & John, I. L. (2018). Impact of vehicular traffic on ambient air quality in selected junctions in Port Harcourt, Nigeria. *Science World Journal*, 13(4), 39-43.
- USEPA. (2012). Integrated Risk Information System.
- Vallero, D. A. (2014). *Fundamentals of air pollution*: Academic Press.
- Wei, C., Bandowe, B. A., Han, Y., Cao, J., Zhan, C. & Wilcke, W. (2015). Polycyclic aromatic hydrocarbons (PAHs) and their derivatives (alkyl-PAHs, oxygenated-PAHs, nitrated-PAHs and azaarenes) in urban road dusts from Xi'an, Central China. *Chemosphere*, 134, 512-520. doi:10.1016/j.chemosphere.2014.11.052
- WHO. (2006). *Air quality guidelines: global update 2005: particulate matter, ozone, nitrogen dioxide, and sulfur dioxide*: World Health Organization.
- Yusuf, R. O., Odediran, E. T., Adeniran, J. A. & Adesina, O. A. (2022). Polycyclic aromatic hydrocarbons in road dusts of a densely populated African city: spatial and seasonal distribution, source, and risk assessment. *Environmental Science and Pollution Research*, 1-16.
- Zhang, H., Huang, B., Dong, L., Hu, W., Akhtar, M. S. & Qu, M. (2017). Accumulation, sources and health risks of trace metals in elevated geochemical background soils used for greenhouse vegetable production in southwestern China. *Ecotoxicol Environ Saf*, 137, 233-239. doi:10.1016/j.ecoenv.2016.12.010
- Zhang, J. J. & Day, D. (2015). Urban air pollution and health in developing countries *Air Pollution and Health Effects* (pp. 355-380): Springer.
- Zwozdziak, A., Gini, M. I., Samek, L., Rogula-Kozłowska, W., Sowka, I. & Eleftheriadis, K. (2017). Implications of the aerosol size distribution modal structure of trace and major elements on human exposure, inhaled dose and relevance to the PM<sub>2.5</sub> and PM<sub>10</sub> metrics in a European pollution hotspot urban area. *Journal of Aerosol Science*, 103, 38-52.

## Simulation of Safety Hazards Due to Thermal Radiation from Refinery Flare System

S. MUSA<sup>1</sup>; U. Abubakar Zaria<sup>2,\*</sup>; P.C. Okonkwo<sup>3</sup>

<sup>1</sup>Department of Chemical Engineering, Ahmadu Bello University, Zaria

E-mails: [uabubakar@abu.edu.ng](mailto:uabubakar@abu.edu.ng) & [augayya@yahoo.com](mailto:augayya@yahoo.com); [mshuaibu@abu.edu.ng](mailto:mshuaibu@abu.edu.ng);

Tel.: +234(0)8033690787

\*Corresponding author

### ABSTRACT

Gas flaring is one of the most difficult energy and environmental issues today. Environmental consequences of gas flaring have serious impacts on personnel and equipment. This often results in equipment damage and serious health problems. In this study, simulation of the thermal radiation hazards due to flare system was carried out. Flaresim Software 5.0 was used. Results show that, the lower level of thermal radiation intensity determined to be 1.577 kW/m<sup>2</sup>, could have a radius falling in the range 200 –400 m the Upper level of the radiation intensity, which was determined to be 6.309 kW/m<sup>2</sup>, could be in the range 40- 130 m, presenting high risks at the base of the flare stack. This study recommends that all safety critical pressure safety valves in the unit should be serviced and recalibrated. Also, operational and emergency flare igniters should be moved to a secure area.

**Keywords:** Flare System, Thermal radiation, Personnel Protective Equipment (PPE), Hazards Simulation.

### 1. INTRODUCTION

Flaring is the combustion process which has been and remained the traditional method for the safe disposal of large quantities of unwanted flammable gases and vapors in the oil industry Li *et.al.*, (2021), API, (2014), Brzustowski, (1976), Dubnowski and Davis, (1983). The primary function of a flare is to use combustion to convert flammable, toxic or corrosive vapors to less objectionable compounds API, (1990). The high elevation reduces potential flaring hazards because ground level radiation is lower and better dispersion of gases occurs should the flame be snuffed out Dubnowski and Davis, (1983). The fraction of heat radiated expresses the total radiant power output of a flare as a fraction of the total chemical power input Cooke *et al.*, (1987b). The fraction of heat radiated is an overall characteristic of the flame, which can be affected by the following variables Schwartz and White, (1996).

Gas composition, flame type, state of air-fuel mixing, soot/smoke formation, Quantity of fuel being burned, flame temperature and flare burner design. A flare system from the Kaduna Refining and Petrochemical Company (KRPC) limited was used in this study.

### 2. METHODOLOGY

Kaduna Refining and Petrochemical Company (KRPC) limited Flare System Unit is shown in Plates A and B There are two elevated flares at KRPC, namely: flare 61SO1 for Normal Operations and flare 61SO2 for Emergency situations.



Plate A  
KRPC Flares on Operation



Plate B  
KRPC Flares at Shutdown



## 2.1 Thermal Radiation Simulation

Both thermal radiation from the flare system and sun radiation are included in the total radiation. Flaresim Software developed by Softbit Consultant was used to simulate thermal radiation. Flaresim Software already had solar radiation simulations built in. The requirements for input data for Flaresim software are summarized in Table 2. The hazard connected with thermal radiation can have an impact on personnel/equipment without direct contact with the fire/hot surface at a place where the flare system is heightened because of the increased temperature intensity. To calculate thermal radiation levels, knowing the fraction of heat released by flares is critical. The fraction of heat radiated in the vicinity of a flame is determined by mathematical expression, some of the models considered in this paper were based on theoretical derived equations and relationships that were created based on API (1969) suggested derived equation approach. Radiation intensity standard exposure and time were shown in Table 1.

Table 1: Thermal radiation intensity and API recommended exposure limit

Heat radiation intensity (kW/m <sup>2</sup> )	API standard 521
9.49	Required urgent emergency action. Radiation shielding and/or special protective apparel (e.g. a fire approach suit) required.
6.31	Emergency actions lasting up to 30s without shielding but with appropriate clothing.
4.73	Emergency actions <b>lasting 2 min to 3 min</b> without shielding but with appropriate clothing.
1.58	personnel with appropriate clothing can be <b>continuously exposed</b>

The American Petroleum Institute Recommended Practice, Section 521 API, (1969) gives the following equation for calculating the minimum distance from a flare to an object whose exposure must be limited:

$$D = \sqrt{\frac{\tau F Q}{4\pi K}} \quad (1)$$

where,

$D$  = minimum distance from the midpoint of the flame to the object being considered, in feet

$\tau$  = fraction of heat intensity transmitted,  $F$  = fraction of heat radiated

$Q$  = net heat release (lower heating value), in British thermal units per hour (kilowatts)

$K$  = allowable radiation, in British thermal units per hour per square foot (kilowatts per square meter,  $\pi$  = Constant

Rearranging for the fraction of heat radiated gives:

$$F = \frac{4\pi K D^2}{\tau Q} \quad (2)$$

To calculate the F-Factor in Equation (2) then  $K$  becomes actual radiation received at ground level rather than allowable radiation. The model adopted presented above is more commonly called the single-point model, due to some of the assumption list below, that all the heat is radiated from a single point location.

Assumptions:

- i. Equation 2 ignores wind effects.
- ii. It is assumed that the flame can be treated as a single point source located at the centre of the flame which radiation is at the base of the flame (at the flare tip), not in the centre.
- iii. The location where thermal radiation must be limited is at the base of the flare.  $K$  becomes actual radiation received at ground level rather than allowable radiation.

Table 2: Required input parameter and specification for Flaresim configuration

Parameter	Configuration
Methane	0.8726 mole
Ethane	0.0416 mole
Nitrogen	0.0336 mole
Carbon dioxide (CO <sub>2</sub> )	0.0202 mole
Propane	0.019 mole
Butane	0.0067 mole
Water (H <sub>2</sub> O)	0.0017 mole
Pentane	0.0028 mole
Hydrogen Sulphide (H <sub>2</sub> S)	0.001 mole
n-Hexane	0.0008 mole
Minimum Flowrate (emergency).	178,682 kg/hr.
Average Flowrate (emergency).	461,880 Kg/hr.
Maximum Flowrate (emergency).	580,252 kg/hr.
Temperature:	45°C
Reference Pressure:	0.35Bar
Wind speed:	5.46 m/s
Wind direction:	57°
Average Solar radiation:	5.7 kW/m <sup>2</sup>
Ambient temperature:	29 °C
Humidity:	50 %
Grid Plane:	Northing-Easting
Northing:	1024m
Easting:	918m
Stack Length:	65m
Angle to Horizontal:	90°
Angle to North:	0°
Tip type:	Pipe
Number of Burner:	1(one)
Seal Type:	Fluidic 1
Seal Diameter Basis:	Tip
Tip Length:	4.050m
Assist Fluid Type:	Steam
Flow Calculation:	Smokeless
Smokeless Method:	API
Exit Diameter Emergency Flare:	1372mm
Exit Diameter Normal Flare:	762mm
Burner Opening:	100%
Riser Diameter:	863.6mm
Sterile Radius of interest:	200 m
Scenario:	Thermal Radiation Hazard
Intensity levels API:	1.577, 3.155, 4.732, 6.309 kW/m <sup>2</sup>
Software Version:	Flaresim 5.0

### 3. RESULTS AND DISCUSSION

The thermal radiation at the combustion zone (flare tip) was simulated using KRPC flow rate at various stages (minimum, average, and maximum). The surrounding flare stacks base directly impacted by the radiation's strength (sterile region), equipment around the base, and personnel.

Table 3: Thermal radiation intensity standard and KRPC model result@ min. 178,682 (kg/hr.)

Thermal radiation (kW/m <sup>2</sup> )	Temperature (°C)	Distance (m)
1.577	25	231.0
3.155	50	118.4
4.732	75	75.39
6.309	100	40.10

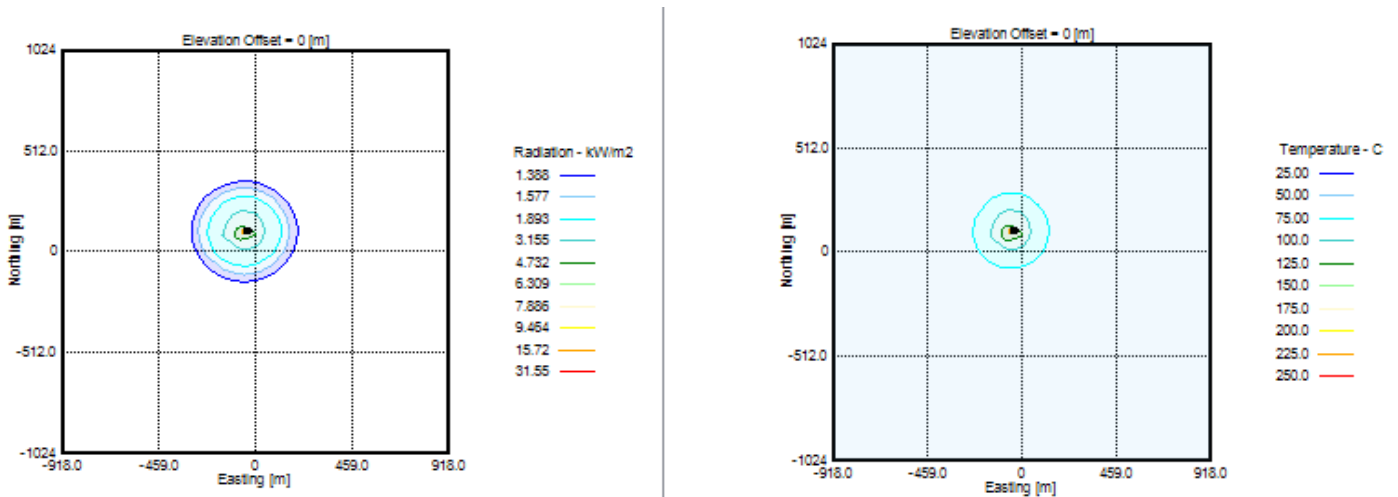


Figure 1: Radiation and temperature isopleth for KRPC minimum

Result for the minimum operation with the corresponding temperature difference is shown in Table 3 and Figure 1 shows thermal intensities of 1.577 kW/m<sup>2</sup>, 3.155 kW/m<sup>2</sup>, 4.732 kW/m<sup>2</sup>, and 6.309 kW/m<sup>2</sup> at distances of 231.0 m, 118.4 m, 75.39 m, and 40.10 m, respectively, with temperatures of (25, 50, 75, and 100) °C at the flare tip to the surrounding, the result indicate high release of thermal radiation at base and personnel only last for few minutes with appropriate protective cloth.

Table 4: Thermal radiation intensity standard and KRPC model result@ average 461,880 (kg/hr.)

Thermal radiation (kW/m <sup>2</sup> )	Temperature (°C)	Distance (m)
1.577	25	377.8
3.155	50	207.2
4.732	75	149.7
6.309	100	116.4

Table 4 shows the Model result for average operation with the corresponding temperature difference Figure 2 indicate the thermal intensity of 1.577 kW/m<sup>2</sup>,3.155 kW/m<sup>2</sup>,4.732 kW/m<sup>2</sup> and 6.309 kW/m<sup>2</sup>with the distance of 377.8 m, 207.2 m, 149.7 m and 116.4 m with the Corresponding temperature of (25, 50, 75 and 100) °C at the flare tip to the surrounding, also for the average thermal radiation is high at base personnel only last for few seconds with appropriate safety clothing.

Table 5 shows the Model result operation with the corresponding temperature difference Figure 3 indicate the thermal intensity of 1.577 kW/m<sup>2</sup>,3.155 kW/m<sup>2</sup>,4.732 kW/m<sup>2</sup> and 6.309 kW/m<sup>2</sup>with the distance of 423.6 m, 234.1 m, 171.2 m and 134.7 m with the corresponding temperature of (25,50,75 and 100) °C at the flare tip to the surrounding. Table 6 summarizes the results of the thermal radiation simulation.

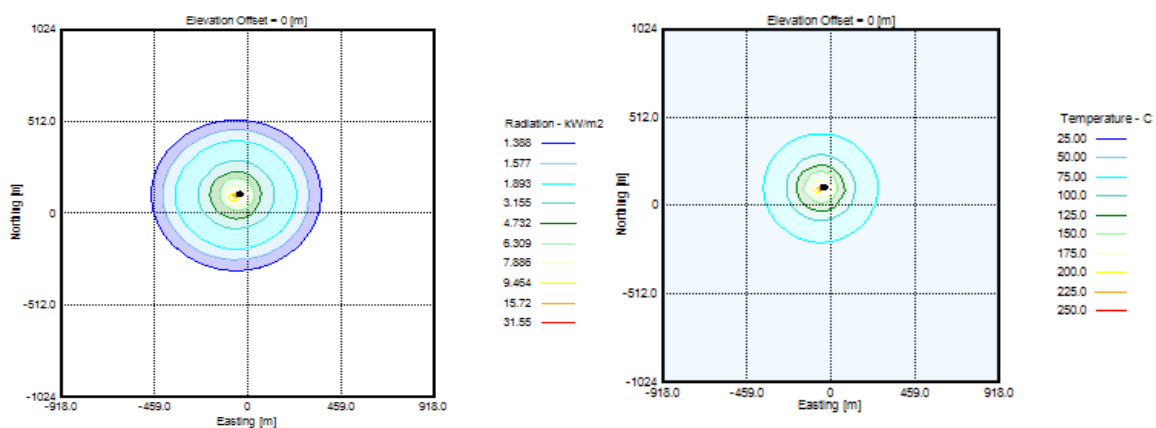


Figure 2: Radiation and temperature isopleth for KRPC (Average mass flow rate)

Table 5: Thermal radiation intensity standard and KRPC model result@ maximum. 580,252 (kg/hr.)

Thermal radiation (kW/m <sup>2</sup> )	Temperature (°C)	Distance (m)
1.577	25	423.6
3.155	50	234.1
4.732	75	171.2
6.309	100	134.7

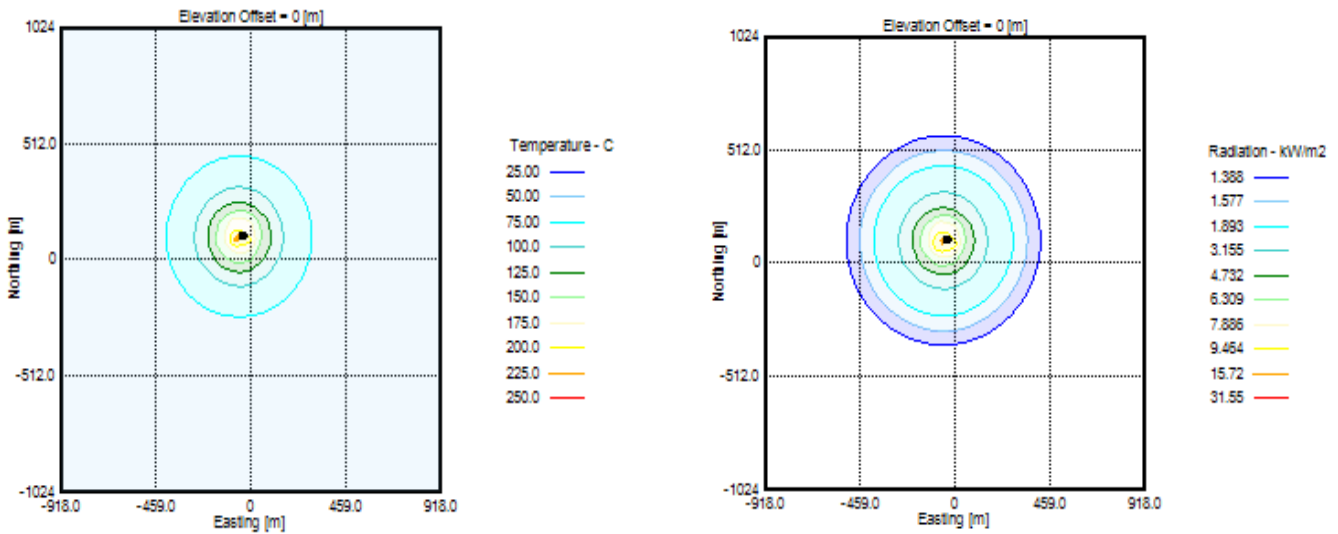


Figure 3: Radiation and temperature isopleth for KRPC at maximum mass flow rate

Table 6: Overall Thermal radiation intensity model result at different flow rate (mass basis)

Recommended level	KRPC Flow rate (kg/hr.)		
Thermal Radiation Intensity level (kW/m <sup>2</sup> )	178,682	461,880	580,252
1.577	231.0	377.8	423.6
3.155	118.4	207.2	234.1
4.732	75.39	149.7	171.2
6.309	40.10	116.4	134.7

Table 6 shows the permissible recommended thermal radiation intensity standard truncated at 6.309 kW/m<sup>2</sup> against the overall mass flow rate of KRPC data with their corresponding distance covers in (meter) each, from the standard the minimum radiation intensity of 1.577 kW/m<sup>2</sup> covers a distance of 231.0, 377.8, 423.6 at different stage was identify, indicate radiation intensity is high at the stack base and it beyond the KRPC design sterile region of 200 m, and equipment at the stack base such as pilot ignition channel, water seal drum, pumps etc. were directly affected due to activities of the flare, Personnel working around the stack base for maximum radiant heat intensity at any location with appropriate clothing may continuously exposed.

#### 4. CONCLUSION

The higher radiation intensity of 6.309 kW/m<sup>2</sup> covered a distance of 40.10 m to 134.7 m and was found to be high at the base of the flare stack. Additionally, the thermal radiation intensity was above the KRPC sterile area of 200 meters. The lower level of thermal radiation intensity was 1.577 kW/m<sup>2</sup>, covering a distance of 231.0 m to 423.6 m. It is recommended that the operating and emergency flare igniters should be relocated to safer location (away from the flare stack base and Service and recalibrate all safety critical Pressure Safety Valve (PSVs) in the unit.

#### REFERENCE

- Lai Xuejiang, Yang Yi, Huang Li, Li Liang (2021) . Thermal Radiation and Noise Safety Assessment of an Offshore Platform Vent Pipe. *Journal of Energy, Environmental & Chemical Engineering* Vol. 6, No. 3, pp. 88-93. doi: 10.11648/j.jeece.20210603.16.
- Miller, D. (2017). New model for predicting thermal radiation from flares and high-pressure jet fires for hydrogen and syngas. *Process Safety Progress*, 36(3), 237– 251. doi:10.1002/prs.11867.
- Peng, W., An-feng, Y., Wen-yi, D. *et al* (2016). Modeling Thermal Radiation of an Enclosed Ground Flare. *Chem Technol Fuels Oils* 52, 331–339 <https://doi.org/10.1007/s10553-016-0712-3>
- API RP 521(January, 2014) Pressure-relieving and Depressuring Systems, American Petroleum institute, sixth edition.
- Brzustowski, T. A. (1976). ‘Flaring In the Energy Industry’, *Progress in Energy and Combustion Science*, Volume 2, p129-144.
- Cook, D. K., Fairweather, M., Hammonds, J. and Hughes, D. J. (1987) ‘Size and Radiative Characteristics of Natural Gas Flares. Part 2-Empirical Model’, *Chemical Engineering, Research and Design*, Volume 65, pp. 310-317
- Dubnowski, J. J. and Davies, B. C. (1983). ‘Flaring Combustion Efficiency: A Review of the State of Current Knowledge’, *Proceedings of the Annual Meeting Air Pollution Control Association*, Atlanta, Georgia, 76th, Volume 4, Published by APCA, Pittsburgh, Pa, USA 83-52. 10, 27p.
- Schwartz, R. E. and White, J. W. (1996). ‘Flare Radiation Prediction: A Critical Review’. 30th Annual Loss Prevention Symposium of the American Institute of Chemical Engineers, Session 12: Flare Stacks and Vapor Control Systems.
- Softbits Consultants. Retrieved from <https://softbits.com/>
- US Environmental Protection Agency: *The CAMEO Software System – ALOHA – user’s manual*. National Oceanic and Atmospheric Administration, 2007.



## Application of Quaternary Composite Adsorbents Prepared from Selected Waste Plastic for Removal of Pesticide Mixture from Wastewater

Sunday O. OLADUNNI<sup>1,2</sup>, Dauda O. ARAROMI<sup>1</sup>, Akeem O. ARINKOOLA<sup>1</sup>, Funmilayo N. OSUOLALE<sup>1</sup>, Oladipupo, O. OGUNLEYE<sup>1</sup>, Wasiat O. BELLO<sup>1,2</sup>, Victoria, A. ADEYI<sup>1,2</sup>, Adeola, R. AMOLE<sup>1,2</sup>, Tinuade J. AFOLABI<sup>1,2</sup>, Abass O. ALADE<sup>1,2,3\*</sup>

<sup>1</sup> Department of Chemical Engineering, Ladoke Akintola University of Technology, Ogbomosho, Nigeria

<sup>2</sup> Bioenvironmental, Water and Engineering Research Group (BWERG), Ladoke Akintola University of Technology, Ogbomosho, Nigeria

<sup>3</sup> Science and Engineering Research Group (SAERG), Ladoke Akintola University of Technology, Ogbomosho, Nigeria

<sup>1</sup>[soladunni2005@yahoo.com](mailto:soladunni2005@yahoo.com), <sup>2</sup>[doararomi@lautech.edu.ng](mailto:doararomi@lautech.edu.ng), <sup>3</sup>[waasiahbintbello@gmail.com](mailto:waasiahbintbello@gmail.com), <sup>4</sup>[tjafolabi@lautech.edu.ng](mailto:tjafolabi@lautech.edu.ng),  
<sup>5</sup>[aoarinkoola@lautech.edu.ng](mailto:aoarinkoola@lautech.edu.ng), <sup>6</sup>[fosuolale@lautech.edu.ng](mailto:fosuolale@lautech.edu.ng), <sup>7</sup>[ooogunleye@lautech.edu.ng](mailto:ooogunleye@lautech.edu.ng), <sup>8</sup>[victoria\\_adeyi@yahoo.com](mailto:victoria_adeyi@yahoo.com),  
<sup>9</sup>[amoleadeola1@gmail.com](mailto:amoleadeola1@gmail.com), <sup>10</sup>[aalade@lautech.edu.ng](mailto:aalade@lautech.edu.ng)

\* [aalade@lautech.edu.ng](mailto:aalade@lautech.edu.ng)

### ABSTRACT

The discarded plastics of plastic chairs (WPCG), polyvinyl chloride pipes (WPVC), jerry cans (WJCG) and waste electronics casing (WECG) were collected and mixed into a composite for the treatment of an aqueous solution containing a mixture of pesticide Chlorpyrifos and Dichlorvos (DDVP) because the mixture is generated as industrial effluents. Each waste plastic sample was washed, milled to 840um size and acetylated to obtain Activated Waste Plastic Granules (AWPGs). The Mixture Methodology (MM) of Design Expert (DOE 12.0.1) was adopted to generate different mixing ratios (15 to 55%) of the four AWPGs samples leading to AWPG composite (AWPGC), which were used for the removal of the pesticide (Chlorpyrifos and DDVP) mixture from aqueous solution in a batch study. Results showed that the maximum adsorption capacity (2.6091mg/g) and removal efficiency (52.18%) were obtained in Run 2 when the mixture ratio of WPCG: WPVC: WJCG: WECG is 35:35:15:15 % (w/w). This investigation demonstrated that the WPCG: WPVC: WJCG: WECG composite developed has the potential for the removal of strong pesticide (Chlorpyrifos and DDVP) samples from polluted surface water.

**Keywords:** Chlorpyrifos, Composite, DDVP, Mixture Methodology, Waste plastic.

### 1. INTRODUCTION

Pesticides are poisonous chemicals, chemical mixtures, or biological agents that are used to kill, prevent, deter, control, destroy, repel, or mitigate insects, weeds, rodents, fungus, or other harmful pest populations in agricultural, domestic, and industrial settings (Coppock and Dziwenka, 2020). Pesticides function as regulators or moderators to eliminate pests. In agricultural fields, insecticides are used to reduce pest and pest-related disease outbreaks and boost the quality of yield (Arihilar & Arihilar 2019). Insecticides, fungicides, fumigants, and rodenticides are the four main categories of pesticides that are frequently utilized. The overuse and misuse of pesticides lead to serious health issues, financial loss, and a variety of environmental issues. The health issues caused by pesticides include cancer, birth defects, reproductive issues, liver, renal, and neurological issues, among others (Rasheed *et al.*, 2019). In many countries, pesticides are not properly used and this had endangered human health and the environment. On the other hand, excessive pesticide use contributes to environmental damage, leading to the soil, water, and air pollution, and upsets the ecosystem (Vela *et al.*; 2019). Although a pesticide can enter the body through ingestion, inhalation, or skin penetration, the majority of people are afflicted by eating pesticide-contaminated food (Mahmood *et al.*; 2015).

One of the current environmental concerns across the world is the removal of pesticides and their compounds from the environment. Since so many different kinds of pesticides are used, it is quite challenging to create a single, all-encompassing technique for getting rid of them. Pesticide cleanup techniques fall into one of three categories: biological, chemical, or physical. Physical remediation is primarily based on the adsorption process, which is one of the most widely used techniques for water purification due to its capacity, efficacy, and scalability (Ahmad *et al.*; 2010). Adsorption is a well-known (successful) equilibrium separation method for water decontamination. Due to its low starting cost, versatility, and straightforward design, as well as its simplicity of use therefore adsorption is more favorable than other techniques for reusing water (Rafatullah *et al.*, 2010) (Okeowo *et al.*; 2020).

According to a UNEP report from 2021, 300 million tonnes of waste plastic are produced annually. The degradation of plastic waste materials can take 50–500 years or longer, depending on interior structure and components (Muller et al., 2001). Researchers in previous years have proven plastic waste to be a suitable adsorbent in the adsorption process having an adsorption capacity ranging from 60.625–67.9 mg/g (Yuliusman *et al.*; 2017). This research is therefore aimed to produce Activated Waste Plastic Granules Composite for the removal of Bi-component pesticides from simulated wastewater.

## 2. MATERIALS AND METHODS (OR METHODOLOGY)

### 2.1 Material and Procurement

Waste plastics, [plastic chairs (WPCG), polyvinyl chloride pipes (WPVC), jerry can (WJCG) and (WECG)] were collected from a waste plastic collection site in the Ogbomoso (8° N and 4° E) and transported to Ladoko Akintola University of Technology, Ogbomoso, Oyo State. The reagents used include phosphoric acid, nitric acid, ethanol and pesticide samples (Chlorpyrifos and DDVP).

### 2.2 Methods

Each waste plastic sample was shredded and cleaned with water and then soaked in ethanol solution for 24 h to remove surface contamination and washed to neutrality with distilled water (Khorram et al., 2017). The second activation was done by soaking the plastic sample in 1.0 M acetic acid for 24 h and washing it to neutrality and sun-dried it to obtain Activated Waste Plastic Granules (AWPGs). The Mixture Methodology (MM) of Design Expert (DOE 12.0.1) was adopted to generate different mixing ratios (15 to 55%) of the four AWPGs samples (Table 1).

### 2.3 Batch Adsorption

Chlorpyrifos solution was prepared by mixing 120 ml of Chlorpyrifos in 1080 ml of distilled water in a 1 dm<sup>3</sup> standard flask and the mixture was stirred continuously for 10 mins to give room for proper mixing. DDVP solution was also prepared by mixing 120 ml of DDVP in 1080 ml of distilled water in a 1 dm<sup>3</sup> standard flask. The mixture was stirred thoroughly for complete dissolution. The two prepared solutions (Chlorpyrifos and DDVP) were transferred into two 1 dm<sup>3</sup> standard flasks. Thus, the resulting mixture contained 100 mg/l of Chlorpyrifos and 100 mg/l of DDVP, which is the typical composition of wastewater effluent from plastic and related industries (Suleiman and Abdulkadir 2017). One gram of the component mixtures derived from the software was mixed with 100 ml of the simulated, wastewater and shaken on a rotary shaker at 120 rpm. The mixture was centrifuged and the supernatant was analyzed using a UV spectrometer (Model UV752 (D)) to quantify the amount of the Chlorpyrifos and DDVP, before (100 mg/L) and after adsorption. The adsorption capacity and removal efficiency were evaluated from Eqns. 1 and 2

$$q_e = \frac{C_o - C_e}{m} \times V \quad (1)$$

$$\% \text{ removal} = \frac{C_o - C_t}{C_o} \times 100 \quad (2)$$

Where  $C_o$  is the initial concentration of the adsorbate (Chlorpyrifos and DDVP (100 mg/l)),  $C_e$  is the equilibrium concentration of the adsorbate (mg/L),  $C_t$  is the concentration of the adsorbate at time  $t$ ,  $V$  is the volume of a targeted adsorbate (100 ml),  $m$  is the mass of the AWPG Composite (AWPGC).

## 3. RESULTS AND DISCUSSION

### 3.1 Adsorption Capacity (AC) and Removal Efficiency (RE) Waste Plastic Granules Composite (AWPGC) of Activated

The adsorption of Chlorpyrifos and DDVP unto the AWPGCs developed was processed as a special cubic model with eighteen (18) experimental runs, under the design tool of the software. Power transform was done for the RE and AC of (chlorpyrifos+DDVP) on AWPGC. The maximum AC (2.6091mg/g) and RE (52.18%) were obtained in Run 2 of the experimental run, while the minimum AC (1.4216 mg/g) and RE (28.43%) were generated in Run 9 (Table 1).

### 3.2 Analysis of Variance for AC and RE of Chlorpyrifos and DDVP

The data displayed in Table 2 shows the Analysis of Variance (ANOVA) for the AC and RE of Chlorpyrifos and DDVP. The **Model F-value** of 6.94 for the AC implies the model is significant ( $p < 0.05$ ). There is only a 3.75% chance that an F-value this large could occur due to noise. **Model F-value** of 5.93 for the RE with  $p < 0.05$  implies the model is significant. There is only a 4.94% chance that an F-value this large could occur due to noise. **P-values** less than 0.0500 indicate model terms are significant, for both cases, A, B, C, D, AB, AD, ABC, ACD, and BCD are significant model terms.

### 3.3 Model Equation for AC and RE of Chlorpyrifos and DDVP

The final equation for AC and RE of Chlorpyrifos and DDVP onto the AWPGCs is shown in equations 3 and 4 in terms of coded factors. The coded equation is useful for identifying the relative impact of the factors by comparing the factor coefficients.

Table 1. Batch adsorption research response and experimental design matrix of AC and RE of AWPGC for Chlorpyrifos +DDVP mixture

Run	Component				Space Type	Response	
	A: WPCG	B: WPVC	C: WJCG	D: WECG		Adsorption Capacity (mg/g)	Removal Efficiency (%)
1	15	15	15	55	Vertex	2.1069	42.14
2	35	35	15	15	CentEdge	2.6091	52.18
3	15	15	55	15	Vertex	2.2578	45.16
4	20	20	40	20	AxialCB	1.9022	38.04
5	25	25	25	25	Center	1.9334	38.67
6	15	15	55	15	Vertex	2.2793	45.59
7	15	15	15	55	Vertex	2.0228	40.46
8	40	20	20	20	AxialCB	1.9280	38.56
9	20	40	20	20	AxialCB	1.4216	28.43
10	35	15	35	15	CentEdge	1.4614	29.23
11	15	35	15	35	CentEdge	2.4841	49.68
12	15	15	35	35	CentEdge	2.4151	48.30
13	35	15	15	35	CentEdge	2.0099	40.20
14	20	20	20	40	AxialCB	1.7017	34.03
15	15	55	15	15	Vertex	2.2330	44.66
16	35	35	15	15	CentEdge	2.0185	40.37
17	15	35	35	15	CentEdge	1.8440	36.88
18	15	55	15	15	Vertex	1.8472	36.94

Table 2: ANOVA of AC and RE of Chlorpyrifos and DDVP

Source	Adsorption Capacity (AC)				Removal Efficiency (RE)			
	Sum of Squares	Mean Square	F-value	p-value	Sum of Squares	Mean Square	F-value	p-value
<b>Model</b>	0.1038	0.0080	6.94	0.0375	2.092E-08	1.609E-09	5.93	0.0494*
<sup>⊃</sup> Linear Mixture	0.0054	0.0018	1.57	0.3283	1.080E-09	3.601E-10	1.33	0.3828
AB	0.0110	0.0110	9.56	0.0365	2.244E-09	2.244E-09	8.27	0.0452*
AC	0.0069	0.0069	5.97	0.0710	1.401E-09	1.401E-09	5.16	0.0855
AD	0.0102	0.0102	8.86	0.0409	2.067E-09	2.067E-09	7.62	0.0509*
BC	0.0024	0.0024	2.07	0.2237	5.385E-10	5.385E-10	1.98	0.2317
BD	0.0023	0.0023	2.01	0.2288	5.595E-10	5.595E-10	2.06	0.2244
CD	0.0007	0.0007	0.5761	0.4901	1.632E-10	1.632E-10	0.6015	0.4813
ABC	0.0094	0.0094	8.19	0.0458	1.965E-09	1.965E-09	7.24	0.0546
ABD	0.0002	0.0002	0.1780	0.6948	4.755E-11	4.755E-11	0.1753	0.6970
ACD	0.0339	0.0339	29.51	0.0056	6.582E-09	6.582E-09	24.26	0.0079*
BCD	0.0151	0.0151	13.15	0.0222	3.064E-09	3.064E-09	11.29	0.0283*
<b>Pure Error</b>	0.0046	0.0011			1.085E-09	2.713E-10		
<b>Cor Total</b>	0.1084				2.201E-08			

\* Significant

$$\left( \text{Adsorption Capacity (CHLOROPYRIFOS + DDVP)} \right)^{-3} = +2.49A + 0.1242B + 0.0857C + 0.1139D - 4.88AB - 3.88AC - 4.72AD + 0.2182BC - 0.2152BD - 0.1151CD - 18.53ABC - 2.73ABD - 35.05ACD + 74.45BCD \quad (1)$$



$$\begin{aligned} \left[ \left( \text{Removal Efficiency (CHLOROPYRIFOS + DDVP)} \right) \right]^{-2.6} = & +0.0011A + 0.0001B + 0.0000C + \\ & 0.0001D - 0.0022AB - 0.0018AC - 0.0021AD + 0.0001BC - 0.0001BD - 0.0001CD - 0.0085ABC - \\ & 0.0013ABD - 0.0154ACD + 0.0335BCD \end{aligned} \quad (2)$$

### 3.4 Fit Summary

The fit summary of AC and RE of Chlorpyrifos and DDVP onto AWPGC is shown in Table 3. The difference between the **adjusted R<sup>2</sup>** is not as high for the AC and RE. The **predicted R<sup>2</sup>** of both AC and RE is not defined, it might be due to the leverage cases of both AC and RE having a value of 1.0. - A ratio greater than 4 is desirable and a sufficient signal is shown by the ratio of 9.4581 and 8.7501 obtained for AC and RE, respectively. Thus, the models obtained can be used for navigating the design space.

Table 3: Fit Summary for AC and RE of Chlorpyrifos and DDVP

Response	Statistical Properties						
	Std. Dev.	Mean	C.V. %	R <sup>2</sup>	Adjusted R <sup>2</sup>	Predicted R <sup>2</sup>	Adeq Precision
Adsorption Capacity	0.0339	0.1411	24.04	0.9576	0.8197	NA	9.4581
Removal Efficiency	0.0000	0.0001	22.04	0.9507	0.7904	NA <sup>(1)</sup>	8.7501

### 3.5 Diagnostic Case Study

Diagnostic case studies for the AC and RE responses of Chlorpyrifos and DDVP adsorption onto AWPGC at different optimized mixture shows the actual values obtained from the experimental procedure and predicted values generated by the software for AC and RE respectively (Table 4). Runs 3, 4, 5, 7, 8, 9, 10, 11, 12, 13, 14, 16, 17 and 18 have positive residuals for AC and RE while runs 1, 2, 6, and 15 have negative residuals for AC and RE. The Normal Plot of Residuals for AC and RE of Chlorpyrifos and DDVP (Fig. 1a&b) shows how well spread the points are on the graph. Both the AC and the RE have no stacking thereby making both of them have minimal error. Figure 2 related the residual value with Table 5, where each point above the line in Figures (2a&b) shows the number of runs for the residual values that are positive and every point below the line shows the runs with negative residual values.

Table 4: Diagnostic Report on Actual Value, Predicted Value and Residual of AC and RE of Chlorpyrifos and DDVP on AWPGC

Run Order	Adsorption Capacity (AC)			Removal Efficiency (RE)		
	AV	PV	Residual	AV	PV	Residual
1	0.1069	0.1139	-0.0069	0.0001	0.0001	-3.332E-06
2	0.0563	0.0889	-0.0326	0.0000	0.0001	-0.0000
3	0.0869	0.0857	0.0012	0.0000	0.0000	6.083E-07
4	0.1453	0.1453	0.0000	0.0001	0.0001	0.0000
5	0.1384	0.1384	0.0000	0.0001	0.0001	0.0000
6	0.0844	0.0857	-0.0012	0.0000	0.0000	-6.083E-07
7	0.1208	0.1139	0.0069	0.0001	0.0001	3.332E-06
8	0.1395	0.1395	0.0000	0.0001	0.0001	0.0000
9	0.3481	0.3481	0.0000	0.0002	0.0002	0.0000
10	0.3204	0.3204	0.0000	0.0002	0.0002	0.0000
11	0.0652	0.0652	0.0000	0.0000	0.0000	0.0000
12	0.0710	0.0710	0.0000	0.0000	0.0000	0.0000
13	0.1232	0.1232	0.0000	0.0001	0.0001	0.0000
14	0.2029	0.2029	0.0000	0.0001	0.0001	0.0000
15	0.0898	0.1242	-0.0344	0.0001	0.0001	-0.0000

Application of Quaternary Composite Adsorbents Prepared from Selected Waste Plastic for Removal of Pesticide Mixture from Wastewater

16	0.1216	0.0889	0.0326	0.0001	0.0001	0.0000
17	0.1595	0.1595	0.0000	0.0001	0.0001	0.0000
18	0.1587	0.1242	0.0344	0.0001	0.0001	0.0000

AV- Actual Value, PV- Predicted Value

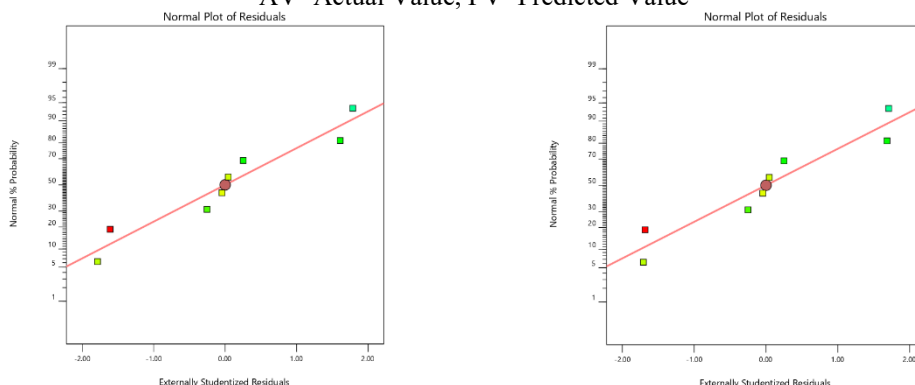


Figure 1. Normal plot for residual of AC and RE of chlorpyrifos and DDVP

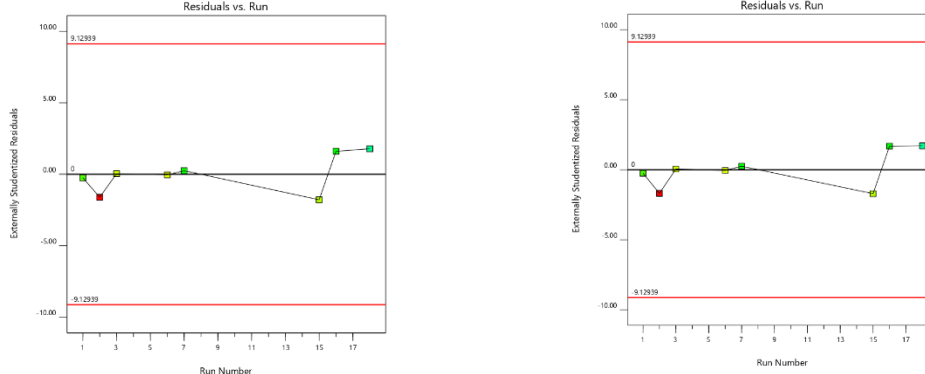


Figure 2. Residual vs Run plot for AC and RE of chlorpyrifos and DDVP

### 3.6 Response Surface Plot

Figure 3 describes the state of the equation model for AC and RE of Chlorpyrifos and DDVP. The red region of the figures shows the feasible region where the adsorption process is taking place while the blue region is the point where the least adsorption process is taking place and the green region is where the adsorption process is feasible.

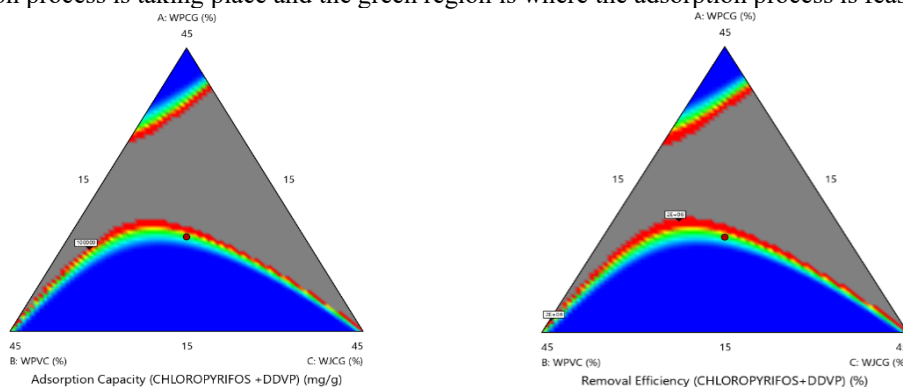


Figure 3. 2D view of the Special Cubic Model of AC and RE of Chlorpyrifos and DDVP

### 3.7 Process Optimization for Adsorption Capacity and Removal Efficiency of Activated Waste Plastic Granules Composites.

Adsorption of Chlorpyrifos and DDVP on the components of the AWPCG was optimized numerically using CCD under the Response Surface Methodology of the DOE software (12.0). The components of the AWPCG were set 'in ranges' while the responses of AC and RE of Chlorpyrifos and DDVP were both set for maximization. The software also generated the numerical value of 1.0 for the desirability factor which indicates that the response is on target (Figure 4).

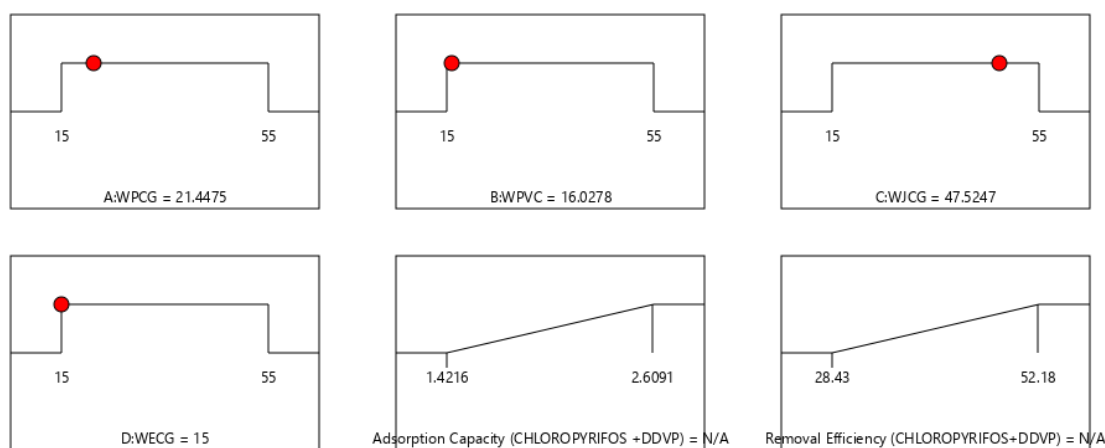


Figure 4. Desirability factor response of the Special Cubic Model

### 3.8 Overlay Plot

Figure 5 shows the overlay plot of the minimum AC and RE of the components of the APWGC. The yellow region depicts the 28.431% RE of Chlorpyrifos and DDVP while the ash region depicts the 1.42155 mg/g AC of Chlorpyrifos and DDVP.

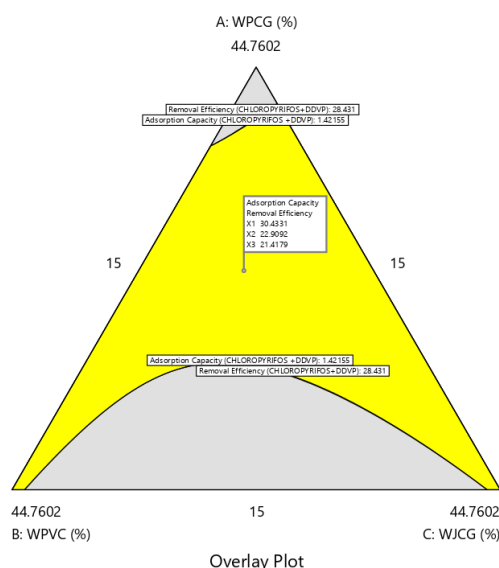


Figure 5. Overlay Plot of the Minimum AC and RE of the AWPGC

## 4. CONCLUSION

The removal of Chlorpyrifos and DDVP from wastewater using AWPGC was successfully studied utilizing the DOE simplex lattice design tool the highest AC and RE of 2.6091 mg/g and 52.18% respectively were successfully obtained. For process optimization and statistical experimental designs, a special cubic model was established. The model was shown to help predict and comprehend the interacting effects of the chosen process parameters.

## ACKNOWLEDGEMENT

Bioenvironmental Water and Engineering Research Group (BWERG) Laboratory, Ladok Akintola University of Technology, Ogbomoso is hereby acknowledged for the opportunity given to us to use the Laboratory.

## REFERENCES

- Ahmad, T., Rafatullah, M., Ghazali, A., Sulaiman, O., Hashim, R., & Ahmad A. (2010). Removal of Pesticides from Water and Wastewater by Different Adsorbents: A Review *Journal of Environmental Science of Health Part C- Environmental Carcinogenic Ecotoxicology*. 28, pp.231–271.
- Arihilam, N. & Arihilam, E. (2019). Impact and control of anthropogenic pollution on the ecosystem – A review. *Impact and control journal of Bioscience and Biotechnology. Discovery*, 4(4), pp.54–59.
- Blettler C.M., Abrial E., Khan F.R., Sivri, N., & Espinola L.A. (2019). Freshwater plastic pollution: Recognizing research biases and identifying knowledge gaps, *Environmental Journal* 108, pp78-83.
- Coppock, R., & Dziwenka, M. (2020). Threats to wildlife by chemical and warfare agents. *Handbook of Toxicology of Chemical Warfare Agents*, pp.1077–1087.
- Mahmood, I., Imadi, R.S. Shazadi, K., Gul, A., & Hakeem, R.K. (2015). Effect of pesticides in environment, *Journal of Environmental Science*, pp.253-269.
- Müller, R.J., Kleeberg, I., & Deckwer, W.D. (2001). Biodegradation of polyesters containing aromatic constituents. *Journal of Biotechnology* 86, pp.87–95
- Neelanjan, D., & Anirban G., (2022). Use of Waste Plastic Char as Adsorbent for Removal of Arsenic and COD from Aqueous Solution. *Environmental Journal* 124 pp 456-589
- Okeowo, I.O., Balogun, E.O., Ademola, A.J., Alade, A.O., Afolabi, T.J., Dada, E.O., & Farombi, A.G., (2020). Adsorption of phenol from wastewater using microwave-assisted Ag–Au nanoparticle-modified mango seed shell-activated carbon. *International Journal of Environmental Resources*. pp 234-238
- Rafatullah, M., Sulaiman, O., Hashim, R., and Ahmad, A. (2010). Adsorption of methylene blue on low-cost adsorbents: A review. *Journal of Hazardous Materials*, 177 pp70–80. <https://doi.org/10.1016/j.jhazmat.2009.12.047>
- Rasheed, T., Bilal, M., Nabeel, F., Adeel, M., & Iqbal, H. (2019). Environmentally-related contaminants of high concern: Potential sources and analytical modalities for detection, quantification, and treatment. *Environmental Journal*, 122, pp.52–66.
- Suleiman, H.A. & AbdulKadir, H. (2017). Consequences of Water Pollution and the Way Forward Among Local Communities in Nigeria. *The International Journal of Geography and Environmental Management*, 112, pp.15-23.
- Vela, N., Fenoll, J., Garrido, I., Pérez-Lucas, G., Flores, P., Hellín, P., & Navarro, S. (2019). Reclamation of agro-wastewater polluted with pesticide residues using sunlight-activated persulfate for agricultural reuse. *Science and Total Environment* pp. 923–930.
- Yuliusman, N., Sanal, A; Bernama, A., Haris, F., & Ramadhan, I. (2017). Preparation of activated carbon from waste plastics polyethylene terephthalate as adsorbent in natural gas, *Conference of Material Science and Engineering*. 012055.



## Air Quality Implication of Solid Waste Incineration in Lagos

Jacob A. SONIBARE<sup>1</sup>, Abiodun J. ADEWALE<sup>2\*</sup>, Daniel O. OKE<sup>3</sup>

<sup>1</sup>Department of Chemical Engineering, Obafemi Awolowo University, Ile-Ife, Nigeria

<sup>1</sup>[asonibar@oauife.edu.ng](mailto:asonibar@oauife.edu.ng), <sup>2</sup>[adewaleabiodun@pg-student.oauife.edu.ng](mailto:adewaleabiodun@pg-student.oauife.edu.ng), <sup>3</sup>[okedaniel097@gmail.com](mailto:okedaniel097@gmail.com)

\*[adewaleabiodun@pg-student.oauife.edu.ng](mailto:adewaleabiodun@pg-student.oauife.edu.ng)

### ABSTRACT

Solid waste incineration is a major source of air pollution in the atmosphere which has adverse effects on the environment, plants, animals, and nearby communities. This study carried out air quality implications on some incinerators in Lagos State, Nigeria. The study was undertaken using an emission inventory and ISC-AERMOD view (version 8.2.0) dispersion modeling tool considering five operating conditions scenarios. Impacts of the predicted ground-level concentrations emission of air pollutants including carbon monoxide, CO; oxides of nitrogen, NO<sub>x</sub>; sulfur dioxide, SO<sub>2</sub>; suspended particulate matter, SPM and hydrocarbons, HC on ambient air quality were investigated using the National Ambient Air Quality Standards (NAAQS) of criteria air pollutants. The study concluded that all the investigated air quality parameters were within their respective standards except the 24-hour averaging period SO<sub>2</sub> and the 1-hour averaging period NO<sub>x</sub>. However, modification of the incinerators' stack height from the proposed 6.2 m to 8 m reduces the daily averaging period SO<sub>2</sub> from 31.8 µg/m<sup>3</sup> breaching the 26 µg/m<sup>3</sup> limit to 23.9 µg/m<sup>3</sup> that is within it. Similarly, modification of the electric power generator stack from the proposed 6.2 m to 20 m will reduce the anticipated 1-hour NO<sub>x</sub> to its world bank group (WBG) limit.

**Keywords:** Incinerator, Particulate matter, Gaseous pollutants, Dispersion, Receptor.

### 1. INTRODUCTION

Air pollution has been reported as a cause of respiratory disease, cardiovascular and pulmonary diseases, cancer, stunted growth in plants, formation of ground-level ozone (O<sub>3</sub>) which is the key player in greenhouse gases that is responsible for climate change (Bălă *et al.*, 2021a, 2021b; Dehghani *et al.*, 2017; Fairbairn *et al.*, 1997; Katanoda *et al.*, 2011; Kim *et al.*, 2018a, 2018b; Mannucci *et al.*, 2015a, 2015b; Rodrigues *et al.*, 2021; ROKAW, 1961; Simkovich *et al.*, 2019; Zhu *et al.*, 2019). The daily activities of human beings involve the usage of material in liquid form, solid form, and gaseous form. Most of these materials have an end product which in most cases ended as waste (Garcia-Garcia, Stone, and Rahimifard, 2019). Wastes can be in solid, liquid, and gaseous forms which have implications for human health and the environment at large. Solid wastes have been a major source of air pollution globally, especially in Nigeria. Nigeria, a developing country with over 200 million population, is blessed with mineral resources crude oil inclusive of which plastic, nylon, and other useful materials are being produced from it. Solid wastes have been a major concern in Nigeria because of their menace to society (Orhorhoro & Oghoghorie, 2019). The objectives of this study are to predict ground-level concentrations of air pollutants associated with the emissions emanating from incinerators and determine the impacts of the predicted ground-level concentration of air pollutants on ambient air quality.

### 2. MATERIALS AND METHODS (OR METHODOLOGY)

#### 2.1 Incinerator locations and description

The incinerators were designed to handle combustible municipal solid wastes, sewage sludge, and medical wastes. An efficient incinerator, a world-class incinerator is used for this study, the two incinerators are located in Oshodi, Lagos state Nigeria. The incinerators have both electricity supply and fuel options of light oil or gas/liquefied petroleum gas (LPG) with 7 burners. The incinerators are powered by generators.

To the south of the incinerators are the following communities as shown in Figure 1: Surulere, FESTAC town, Satellite, Ikotun, Alimosho, Ojodu, and Ikeja are located to the northwest and north of the incinerator respectively shown in Figure 1. The coordinate of the incinerators and generator used for powering the incinerators are presented in Table 1.

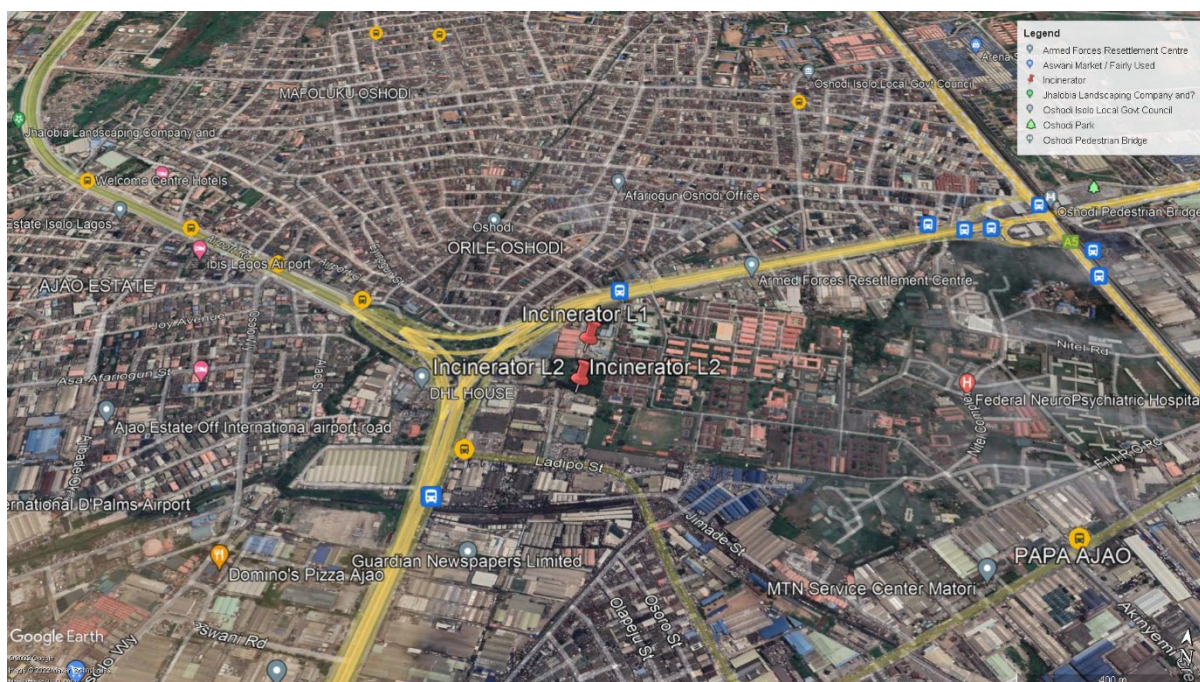


Plate 1: Location of the incinerators and the receptors around Oshodi, Lagos State, Nigeria

## 2.2 Gaseous pollutants monitoring

WolfPack™ Modular Area Monitor was used to measure gaseous pollutants. The equipment has data processing software and can continuously record data for as long as its battery pack lasts. The equipment was calibrated to continuously monitor 30 pollutants via 20 sensors. The sensors were positioned in each community area at a height of 2 m from ground level. Monitoring commenced 12 hours before emitter sources operation to determine background pollutant levels and eliminate the possibility of unaccounted emitter sources. The recorded results are given as time averages and weighted averages.

## 2.3 Suspended particulate matter (SPM) monitoring

The suspended particulate matter (SPM) which comprises  $PM_{10}$ ,  $PM_{2.5}$ ,  $PM_4$ ,  $PM_{10}$  and total suspended particle (TSP) was measured with AEROCET 831, supplied by MetOne instruments. Calibration equations were used for the adjustment of the SPM as reported by (Adeniran *et al.*, 2017, 2018).

## 2.4 Emission Modeling Protocol

The Industrial Source Complex (ISC) AMS/EPA Regulatory Model (AERMOD) is a steady-state Gaussian air dispersion model based on planetary atmospheric boundary layer theory that is state-of-the-art. The Plume Rise Model Enhancement (PRIME building) downwash algorithms, advanced depositional parameters, local terrain, and urban heat island effects, and advanced meteorological turbulence calculations are all fully integrated into AERMOD (Lakes Environmental, 2022). AERMOD is widely used to estimate pollution concentrations and deposition from a wide range of sources in a variety of locations around the world.

## 2.5 Emission Sources

All of the incinerator's sources of criteria air pollutants were assessed. carbon monoxide (CO), nitrogen oxides ( $NO_x$ ), sulfur dioxide ( $SO_2$ ), volatile organic compounds (VOCs) and suspended particle matter (SPM) were among the air contaminants modeled for ground-level concentrations. Emission rates and exhaust vent stack characteristics (height, diameter, exhaust temperature, and exit velocity) were gathered and utilized as model input parameters.

## 2.6 Scenarios considered for this Study

Five scenarios were considered for this study. For this study, two electric power generators are proposed. One of these is a 500 kva C15-500 generator and the other is a 250 kva GEH 250 power generator. They are both to be diesel-powered electric power generators. The emission source parameters is shown in Table 3.

**Scenario 1:** Assumed air emissions from one of the two proposed incinerators' operations.

**Scenario 2:** In this scenario air emissions from simultaneous operations of the two proposed waste incinerators (AQ1 and AQ2) were considered.

**Scenario 3:** Assumed air emissions from one of the two proposed incinerators operations simultaneously with the two power plants.

**Scenario 4:** In this scenario air emissions from simultaneous operations of the two proposed waste incinerators were considered with simultaneous operations of the two power plants, this scenario is considered the highest source emission of pollutants.

**Scenario 5:** In this scenario, air emissions from simultaneous operations of the two proposed power plants were considered.

Table 1: The Incinerators locations, the generator, and the host communities

Sampling Location					
Code	Source	Coordinates		Immediate Community	Upwing/Downwind
		Latitude	Longitude		
AQ1	Incinerator 1	6° 32' 55.8"	003° 20' 25.0"	Onipanu	
				Mushin	
				Ilupeju	
				Mafoluku	
				Oshodi	
				Papa Ajao	
				Isolo	
				Oshodi-Isolo	
				Isanga-Tedo	
				Kosofe	
AQ2	Incinerator	6° 32' 50.8"	003° 20' 25.0"	Gbagada	
				Somolu	
				Oworonshoki	
				Ikeja	
				Egbeda	
				Ikotun	
				Ijegun	
AQ3	Generator 1	6° 28' 47.8"	003° 18' 20.0"	FESTAC Town	
				Abule Ado	
				Lawanson	
				Surulere	
				Satellite Town	
				Lekki	
AQ4	Generator 2	6° 28' 37.8"	003° 18' 20.0"	Oto-Awori	
				Aiyetoto-Asogun	
				Irede	
				Ebuta Metta	
				Igbesa	
				Agbara	
				Alasia	
				Ikoyi	

### 3. RESULTS AND DISCUSSION

#### 3.1 Air Pollutants Ground Level Concentrations (GLCs) Associated with the Facilities

In all the five operation scenarios investigated the anticipated minimum GLCs air pollutant is SPM with NO<sub>x</sub> as the maximum for the three averaging periods. All these air pollutants will be within their respective Federal ministry of environment (FMEnv) limits except the 24-hour averaging period SO<sub>2</sub> which may slightly breach its limit in Phase 2 as shown in Table 2.

Table 2: Cumulative GLCs Impacts Associated with the Facilities

Air Pollutant	Averaging Period	Scenario	Concentration ( $\mu\text{g}/\text{m}^3$ )			% of Limit	
			Predicted	Measured	Total	FMEnv	WBG
CO	24-Hour	Scenario 1	7.19	0.0	7.19	0.06	-
		Scenario 2	15.9	0.0	15.9	0.14	-
		Scenario 3	23.5	0.0	23.5	0.21	-
		Scenario 4	26.7	0.0	26.7	0.23	-
		Scenario 5	21.5	0.0	21.5	0.19	-
SO <sub>2</sub>	1-Hour	Scenario 1	36.9	0.0	36.9	14.19	-
		Scenario 2	66.5	0.0	66.5	25.58	-
	24-Hour	Scenario 1	14.4	0.0	14.4	55.38	-
		Scenario 2	31.8	0.0	31.8	122.31	-
NO <sub>x</sub>	1-Hour	Scenario 1	73.8	1.9	75.7	-	37.85
		Scenario 2	132.9	1.9	134.8	-	67.40
		Scenario 3	228.8	1.9	230.7	-	115.35
		Scenario 4	229.2	1.9	231.1	-	115.55
		Scenario 5	228.0	1.9	229.9	-	114.95
	24-Hour	Scenario 1	28.8	0.6	29.4	26.02	-
		Scenario 2	63.6	0.6	64.2	56.81	-
		Scenario 3	86.3	0.6	86.9	76.90	-
		Scenario 4	99.5	0.6	100.1	88.58	-
		Scenario 5	69.5	0.6	70.1	62.04	-
-SPM	1-Hour	Scenario 1	5.54	72.2	77.74	12.96	-
		Scenario 2	9.98	72.2	82.18	13.70	-
		Scenario 3	5.57	72.2	77.77	12.96	-
		Scenario 4	9.99	72.2	82.19	13.70	-
		Scenario 5	2.05	72.2	74.25	12.38	-
	24-Hour	Scenario 1	2.16	21.8	23.96	9.58	-
		Scenario 2	4.77	21.8	26.57	10.63	-
		Scenario 3	2.67	21.8	24.47	9.79	-
		Scenario 4	4.80	21.8	26.6	10.64	-
		Scenario 5	0.87	21.8	22.67	9.07	-
VOCs	24-Hour	Scenario 1	4.31	0.0	4.31	2.69	-
		Scenario 2	9.54	0.0	9.54	5.96	-
		Scenario 3	4.33	0.0	4.33	2.71	-
		Scenario 4	9.56	0.0	9.56	5.98	-
		Scenario 5	0.58	0.0	0.58	0.36	-

Similarly, they will also be within their WBG limits except for the 1-hour averaging period NO<sub>x</sub> that may breach its limit during the simultaneous operations of the incinerators and the electric power generators.

The maximum predicted Ground Level Concentrations (GLCs) by the model are summarized in Table A1-A2. While the maximum 1-hour GLCs are 5.54 – 73.8  $\mu\text{g}/\text{m}^3$  in **scenario 1**, they are 9.98 – 132.9  $\mu\text{g}/\text{m}^3$  in **scenario 2** and 5.57 – 228.8  $\mu\text{g}/\text{m}^3$  in **scenario 3**. They are 9.99 – 229.2  $\mu\text{g}/\text{m}^3$  in **scenario 4** and 2.05 – 228.0  $\mu\text{g}/\text{m}^3$  in **scenario 5**. In **scenario 1**, the anticipated maximum 24-hour GLCs are 2.16 – 28.8  $\mu\text{g}/\text{m}^3$  with **scenario 2** levels of 4.77 – 63.6  $\mu\text{g}/\text{m}^3$ . Its **scenario 3**, **scenario 4** and **scenario 5** levels are 2.67 – 86.3  $\mu\text{g}/\text{m}^3$ , 4.80 – 99.5  $\mu\text{g}/\text{m}^3$  and 0.58 – 69.5  $\mu\text{g}/\text{m}^3$  respectively. The annual averaging period anticipated maximum GLCs of air pollutants from **scenario 1** is 0.5 – 6.52  $\mu\text{g}/\text{m}^3$  but 1.14 – 15.20  $\mu\text{g}/\text{m}^3$  in **scenario 2** and 0.76 – 34.4  $\mu\text{g}/\text{m}^3$  in **scenario 3** with **scenario 4** and **scenario 5** levels of 1.22 – 39.0  $\mu\text{g}/\text{m}^3$  and 0.32 – 28.5  $\mu\text{g}/\text{m}^3$  respectively.

### 3.2 Cumulative Air Pollutants GLCs from the Facilities

Results of the cumulative impacts investigated by the model using the present air quality status of the project site are reported in Table 4. The anticipated cumulative 1-hour GLCs are 36.9 – 77.74  $\mu\text{g}/\text{m}^3$  in **scenario 1**, 66.5 – 134.8  $\mu\text{g}/\text{m}^3$  in **scenario 2**, 77.77 – 230.7  $\mu\text{g}/\text{m}^3$  in **scenario 3**, 82.19 – 231.1  $\mu\text{g}/\text{m}^3$  in **scenario 4** and 74.25 – 229.9  $\mu\text{g}/\text{m}^3$  in **scenario 5**. The 24-hour cumulative GLCs are 4.31 – 29.40 in **scenario 1** but 9.54 – 31.80  $\mu\text{g}/\text{m}^3$  in **scenario 2** and 4.33 – 96.90  $\mu\text{g}/\text{m}^3$  in **scenario 3**. Its **scenario 4** GLCs are 9.56 – 100.10  $\mu\text{g}/\text{m}^3$  and 21.50 – 70.1  $\mu\text{g}/\text{m}^3$  in **scenario 5**. While the minimum 1-hour averaging period cumulative GLCs are from SO<sub>2</sub> in **scenarios 1** and **scenario 2**, they are from SPM in **scenarios 3 - 5**. The maximum is from SPM in **scenario 1** but NO<sub>x</sub> in **scenarios 2 – 5**. However, the minimum and maximum 24-hour averaging period GLCs are from VOCs and NO<sub>x</sub> respectively in all investigated scenarios. The AERMOD model predicted anticipated maximum cumulative GLCs are within their respective FMEnv



limits in all the investigated operations scenarios and for all the averaging periods except the 24-hour cumulative SO<sub>2</sub> that slightly breached its limit in **scenario 2**. Similarly, they will also all be within their WBG limits except the 1-hour averaging period NO<sub>x</sub> that may breach its limit during the simultaneous operations of the incinerators and the electric power generators. **Isopleths** of scenario one and scenario five investigated **averaging periods** are presented in Figure 2 – Figure 3.

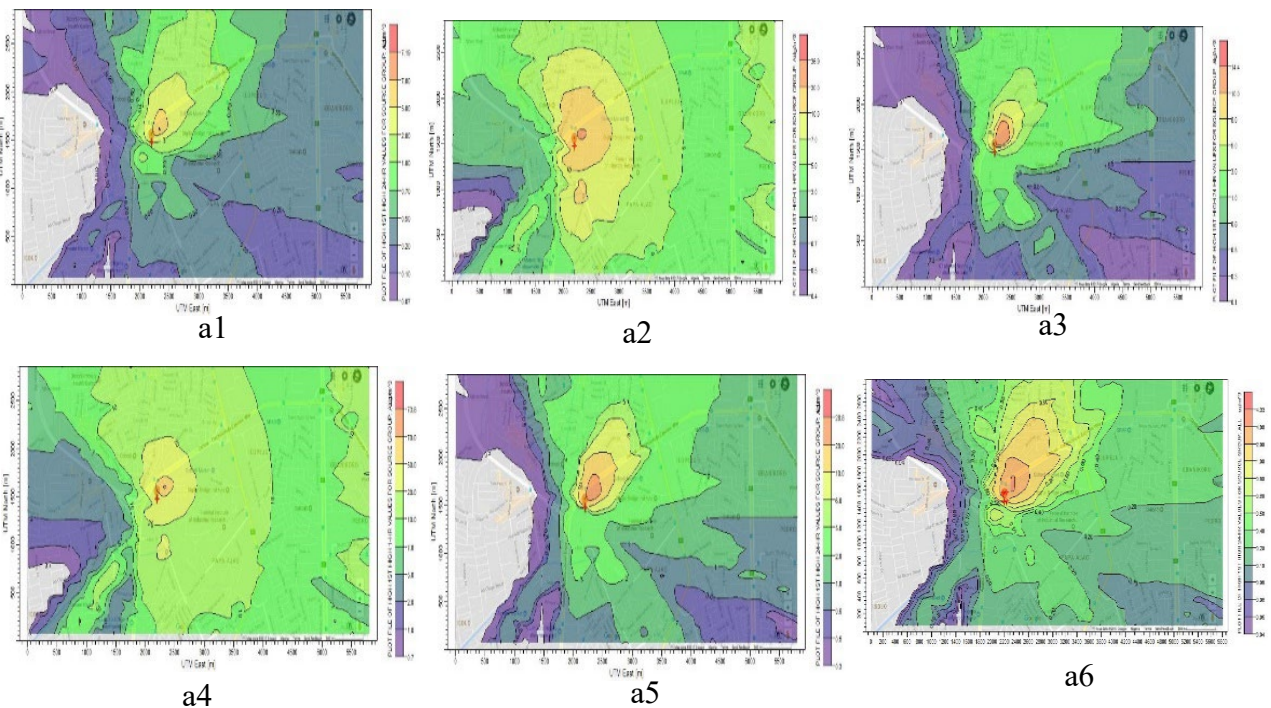


Figure 1: Isopleths of Ambient Pollutants Levels at the Incinerators Nearby Communities (Scenarios one (Point Sources)). a1 - 24-h CO; a2 - 1-h SO<sub>2</sub>; a3 - 24-h SO<sub>2</sub>; a4 - 1-h NO<sub>x</sub>; a5 - 24-h NO<sub>x</sub>; a6 - Annual NO<sub>x</sub>

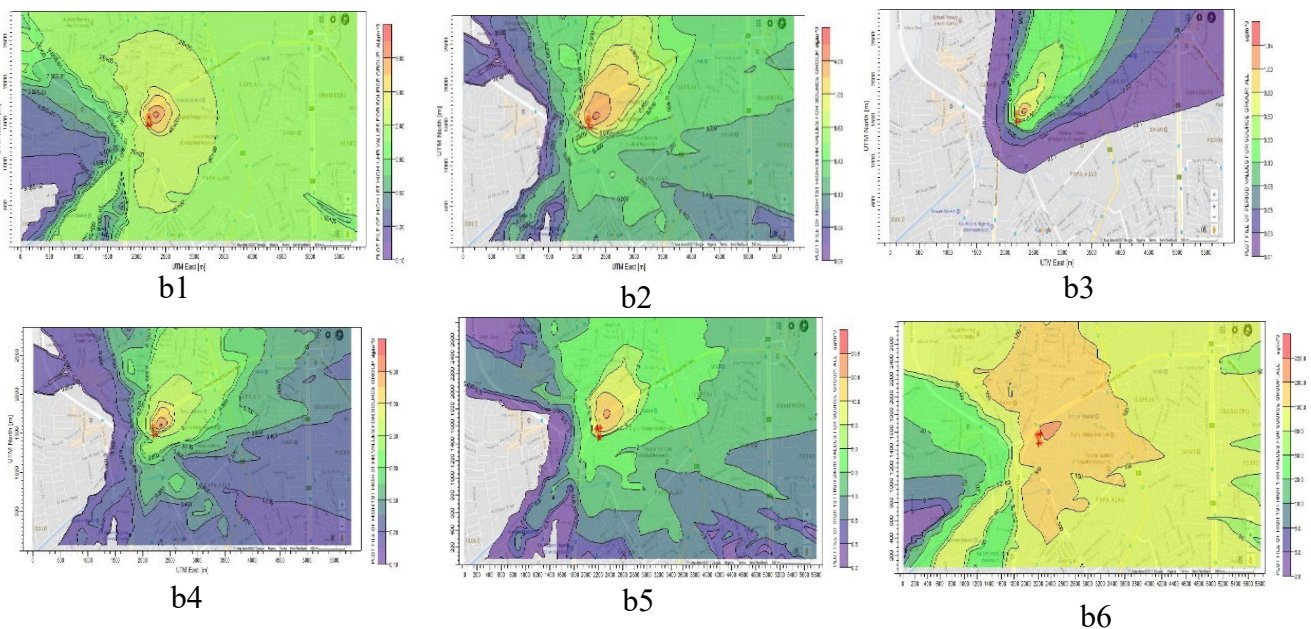


Figure 2: Isopleths of Ambient Pollutants Levels at the Incinerators Nearby Communities (All Scenarios (Point Sources)). b1 - 24-h CO; b2 - 1-h SO<sub>2</sub>; b3 - 24-h SO<sub>2</sub>; b4 - 1-h NO<sub>x</sub>; b5 - 24-h NO<sub>x</sub>; b6 – Annual.

Table 3: Incinerator Emissions characteristics and Air Emission Source Parameters used in the Modelling

S/No	Waste Type	Emission (g/s)					Gas Temperature (°C)	Stack Diameter (m)	Exit Velocity (m/s)	Release Height (m)
		CO	NO <sub>x</sub>	SO <sub>2</sub>	SPM	HC				
1	Medical*	0.2252	0.9008	0.4504	0.0676	0.1351				
2	Sewage Sludge*	0.2252	0.9008	0.4504	0.0676	0.1351	850	0.46	13.55	6.2
3	Combustibles MSW*	0.2252	0.9008	0.4504	0.0676	0.1351	850	0.46	13.55	6.2
4	500 kva Gen Set*	0.2266	4.5771	-	0.0103	0.0069	524	0.15	72.55	6
5	250 kva Gen Set*	0.1133	2.2886		0.0052	0.0034	576	0.15	36.82	6

\*Calculated from the provided emissions rates by the manufacturers

#### 4. CONCLUSION

Pollutants emanating from solid wastes is global pollution, especially in developing country like Nigeria. AERMOD a dispersion modeling tool was used for the prediction of the impact of the pollutants on the receptor communities of which five scenarios were considered. It can be concluded from these results that all the investigated parameters were within their respective standards except SO<sub>2</sub>. Though the concentrations from the operation of a unit of the incinerators are within the limit, its cumulative concentrations during simultaneous operations of the two incinerators breach it. However, changing the incinerators' stack height from the proposed 6.2 m to 8 m reduces the daily averaging period SO<sub>2</sub> from 31.8 µg/m<sup>3</sup> breaching the 26 µg/m<sup>3</sup> limit to 23.9 µg/m<sup>3</sup> within it. The results show the impact of the pollutants on the receptor communities.

#### REFERENCES

- Adeniran, J. A., Aremu, A. S., Saadu, Y. O., & Yusuf, R. O. (2018). Particulate matter concentration levels during intense haze event in an urban environment. *Environmental Monitoring and Assessment*, 190(1). <https://doi.org/10.1007/s10661-017-6414-4>
- Adeniran, J. A., Yusuf, R. O., Amole, M. O., Jimoda, L. A., & Sonibare, J. A. (2017). Air quality impact of diesel back-up generators (BUGs) in Nigeria's mobile telecommunication base transceiver stations (BTS). *Management of Environmental Quality: An International Journal*, 28(5), 723–744. <https://doi.org/10.1108/MEQ-09-2015-0168>
- Bălă, G. P., Râjnovceanu, R. M., Tudorache, E., Motișan, R., & Oancea, C. (2021a). Air pollution exposure—the (in)visible risk factor for respiratory diseases. *Environmental Science and Pollution Research*, 28(16), 19615–19628. <https://doi.org/10.1007/s11356-021-13208-x>
- Bălă, G. P., Râjnovceanu, R. M., Tudorache, E., Motișan, R., & Oancea, C. (2021b). Air pollution exposure—the (in)visible risk factor for respiratory diseases. *Environmental Science and Pollution Research*, 28(16), 19615–19628. <https://doi.org/10.1007/s11356-021-13208-x>
- Dehghani, M., Keshtgar, L., Javaheri, M. R., Derakhshan, Z., Conti, G. O., Zuccarello, P., & Ferrante, M. (2017). The effects of air pollutants on the mortality rate of lung cancer and leukemia. *Molecular Medicine Reports*, 15(5), 3390–3397. <https://doi.org/10.3892/mmr.2017.6387>
- Fairbairn, A. S., Reid, D. D., & Holland, W. W. (1997). Air pollution and other local factors in respiratory disease. *Journal of Epidemiology and Community Health*, 51(3), 216–226. <https://doi.org/10.1136/jech.51.3.216>
- Garcia-Garcia, G., Stone, J., & Rahimifard, S. (2019). Opportunities for waste valorisation in the food industry – A case study with four UK food manufacturers. *Journal of Cleaner Production*, 211, 1339–1356. <https://doi.org/10.1016/j.jclepro.2018.11.269>
- Katanoda, K., Sobue, T., Satoh, H., Tajima, K., Suzuki, T., Nakatsuka, H., Takezaki, T., Nakayama, T., Nitta, H., Tanabe, K., & Tominaga, S. (2011). An association between long-term exposure to ambient air pollution and mortality from lung cancer and respiratory diseases in Japan. *Journal of Epidemiology*, 21(2), 132–143. <https://doi.org/10.2188/jea.JE20100098>
- Kim, D., Chen, Z., Zhou, L., & Huang, S. (2018a). Air pollutants and early origins of respiratory diseases. *Chronic Diseases and Translational Medicine*, 4(2), 75–94. <https://doi.org/10.1016/j.cdtm.2018.03.003>
- Kim, D., Chen, Z., Zhou, L., & Huang, S. (2018b). Air pollutants and early origins of respiratory diseases. *Chronic Diseases and Translational Medicine*, 4(2), 75–94. <https://doi.org/10.1016/j.cdtm.2018.03.003>
- Lakes Environmental, S. (2022). *WRPLOT View - Lakes Environmental Software*. <https://www.weblakes.com/software/air-dispersion/aermod-view/>

- Mannucci, P. M., Harari, S., Martinelli, I., & Franchini, M. (2015a). Effects on health of air pollution: a narrative review. *Internal and Emergency Medicine*, 10(6), 657–662. <https://doi.org/10.1007/s11739-015-1276-7>
- Mannucci, P. M., Harari, S., Martinelli, I., & Franchini, M. (2015b). Effects on health of air pollution: a narrative review. *Internal and Emergency Medicine*, 10(6), 657–662. <https://doi.org/10.1007/s11739-015-1276-7>
- Orhorhoro, E. K., & Oghoghorie, O. (2019). Review on Solid Waste Generation and Management in Sub-Saharan Africa: A Case Study of Nigeria. *Journal of Applied Sciences and Environmental Management*, 23(9), 1729. <https://doi.org/10.4314/jasem.v23i9.19>
- Rodrigues, S. D., Ueda, R. M., Barreto, A. C., Zanini, R. R., & Souza, A. M. (2021). How atmospheric pollutants impact the development of chronic obstructive pulmonary disease and lung cancer: A var-based model. *Environmental Pollution*, 275. <https://doi.org/10.1016/j.envpol.2021.116622>
- Rokaw, S. N. (1961). Air pollution and chronic respiratory disease. *The American Review of Respiratory Disease*, 83, 572–574. <https://www.sciencedirect.com/science/article/pii/S0013935183710832>
- Simkovich, S. M., Goodman, D., Roa, C., Crocker, M. E., Gianella, G. E., Kirenga, B. J., Wise, R. A., & Checkley, W. (2019). The health and social implications of household air pollution and respiratory diseases. *Npj Primary Care Respiratory Medicine*, 29(1). <https://doi.org/10.1038/s41533-019-0126-x>
- Zhu, F., Ding, R., Lei, R., Cheng, H., Liu, J., Shen, C., Zhang, C., Xu, Y., Xiao, C., Li, X., Zhang, J., & Cao, J. (2019). The short-term effects of air pollution on respiratory diseases and lung cancer mortality in Hefei: A time-series analysis. *Respiratory Medicine*, 146, 57–65. <https://doi.org/10.1016/j.rmed.2018.11.019>



## Assessment of Removal Efficiency of Ag<sub>2</sub>O-TiO<sub>2</sub>-Kaolinite Clay Hybrid Nanocomposite developed for the treatment of Mn(II), Fe (III), Pb(II) And Cu(II) in Mining Wastewater

Mary A. AJALA<sup>1,2\*</sup>, Ambali S. ABDULKAREEM<sup>2</sup>, Abdulsalami S. KOVO<sup>2</sup>, Jimoh O. TIJANI<sup>3</sup>, AJALA, Olawale Elijah<sup>1</sup>

<sup>1</sup>Department of Chemical Engineering, University of Ilorin, Ilorin, Kwara State, Nigeria.

<sup>2</sup>Department of Chemical Engineering, Federal University of Technology, Minna, Niger State, Nigeria

<sup>3</sup>Department of Chemistry, Federal University of Technology, Minna

<sup>1\*</sup> [ajala.ma@unilorin.edu.ng](mailto:ajala.ma@unilorin.edu.ng); [maryjokes2002@yahoo.com](mailto:maryjokes2002@yahoo.com), <sup>2</sup>[kasaka2003@futminna.edu.ng](mailto:kasaka2003@futminna.edu.ng) <sup>3</sup>[kovo@futminna.edu.ng](mailto:kovo@futminna.edu.ng)  
<sup>4</sup>[jimohtijani@futminna.edu.ng](mailto:jimohtijani@futminna.edu.ng) <sup>5</sup>[ajala.oe@uniloirn.edu.ng](mailto:ajala.oe@uniloirn.edu.ng)

\*Corresponding author

### ABSTRACT

This study considered the synthesis of Ag<sub>2</sub>O-TiO<sub>2</sub>-kaolinite-clay nanocomposite by the combination of green and wet impregnation method, which involves the reduction of silver nitrate and titanium tetra isopropoxide to nanoparticles with aqueous extract of *Parkia biglobossa* leaf. These were then immobilised on acid-activated kaolinite clay. The prepared nanomaterials' phase structure, morphology, chemical composition, and oxidation states were determined using X-ray diffraction (XRD), high resolution scanning electrode microscopy (HRSEM), and X-ray photoelectric spectroscopy (XPS). The ability of the nanocomposite prepared to adsorb four heavy metal ions (Mn (II), Fe (III), Pb (II), and Cu (II)) from mining wastewater was examined by varying the contact time. The XRD pattern of the Ag<sub>2</sub>O-TiO<sub>2</sub>-clay reveals the synthesis of the rutile phase of TiO<sub>2</sub> embedded in the kaolinite clay, while the HRSEM shows evenly distributed arrangement of hemispherical stacks of kaolinites. The states of oxidation of Ag and Ti revealed by the XPS are +1 and +4 respectively either as binary or ternary nanocomposite. The Ag<sub>2</sub>O-TiO<sub>2</sub>-clay nanocomposite adsorbed 99.85%, 97.85% 95.18%, and 40% of Fe(III), Mn (II), Cu(II) and Pb(II) ions at 120 min from the mining wastewater respectively. The synergetic efforts of the Ag<sub>2</sub>O, TiO<sub>2</sub>, and acid-activated kaolinite clay was found responsible for the adsorptive capability and post-separation possibility of the Ag<sub>2</sub>O-TiO<sub>2</sub>-clay nanocomposite.

**Keywords:** Adsorption, Characterisation, Kaoline, Mining wastewater, Nanocomposite.

### 1.0 INTRODUCTION

There is a great concern about water safety and availability due to industrial activities that generate heavy metals and pollute water bodies (Wazwaz *et al.*, 2019). Amidst the heavy metals generating industries are; pharmaceutical, paints, electroplating, and mining industries. Heavy metals generated from mining activities include; Pb, Fe Zn, Cd, Mn, As, and Cu which are linked to dangerous environmental issues threatening life on earth (Hussain & Ali, 2021). These heavy metals are highly mobile, non-biodegradable, recalcitrant, and toxic at low concentrations and their continuous presence in the environment can cause physiological disturbances to both plants and animals (Balali-Mood *et al.*, 2021). Exposure to heavy metals such as Pb, Zn, Cd, Mn, and Cu in excess has been responsible for diarrhoea, abdominal pain, lethargy, nausea, anaemia, and eventual death (Ajala, Abdulkareem, Tijani, & Kovo, 2022), therefore, these heavy metals must be removed.

Many wastewater treatment techniques have been employed for heavy metal removal in wastewater. These include; electro dialysis, catalytic processes, chemical precipitation, membrane processes, ion exchange processes, and adsorption process. (Hussain & Ali, 2021) The adsorption process is a preferred alternative because of its high efficiency and simplicity (Adebayo, Adegoke, & Sidiq, 2020). Adsorption with nanoparticles and nanocomposites of chitosan, carbon nanotubes, zinc oxide, iron oxide, titanium oxide, and silver oxides have gained pre-eminence because of their unique physiochemical properties (Kumari, Alam, & Siddiqi, 2019). These nanomaterials are also considered all-encompassing, due to their antimicrobial properties and non-production of harmful disinfection by-products like conventional chemical disinfectants (Sushman & Richa, 2015).

Among the nanomaterials, TiO<sub>2</sub> nanoparticles and their composites have been employed for the mineralization and degradation of organic compounds, dyes, and other contaminants in water remediation processes (Dontsova *et al.*, 2020). Despite its uniqueness, the low surface area and agglomeration of TiO<sub>2</sub> limits its industrial applications as a

nano-adsorbent (Akinawo, 2019). To overcome the limitations, it is therefore doped with other materials like clay, silver, silver oxide nanoparticles (AgNPs/Ag<sub>2</sub>ONPs) (Akinawo, 2019; Ajala *et al.*, 2022). Ag<sub>2</sub>ONPs have wide applications as antimicrobial agents and demonstrated excellent catalytic performance in the degradation of anthropogenic pollutants present in the environment (Arya *et al.*, 2018; Christopher, Saswati, & Ezilrani, 2015). Meanwhile, AgNPs and Ag<sub>2</sub>ONPs have been previously successfully used to treat wastewater by incorporating them into materials such as; polyurethane foams, carbon/polymeric nanofibres, and clays (Kyomuhimbo *et al.*, 2019). Hence, the combination of silver with other metal nanoparticles such as TiO<sub>2</sub> can enhance the adsorption capacity for wastewater treatment (Yadav *et al.*, 2017). In addition, a possible combination of clay with metal nanoparticles is expected to perform multi-functionality such as adsorption, catalysis, disinfection, and overcome post-separation problems during the treatment of wastewater (Shivaraju, Egumbo, Madhusudan, Anil Kumar, & Midhun, 2018).

Clays possess desired properties of a good starting material for wastewater treatment and nano filter production. These properties include high cation exchange capacity and ease of surface modification to obtain the desired functionality required of a good adsorbent (Awasthi, Jadhao, & Kumari, 2019). Clays of different origins, compositions, and modifications have been used as adsorbents and as support for nanoparticles to treat wastewater (Hajjaji *et al.*, 2018). However, the use of silver immobilised titanium oxide nanocomposite supported on clay has not been reported for heavy metal removal in mining wastewater treatment. Therefore, this study focuses on the treatment of mining wastewater using silver-doped titanium oxide nanocomposite supported on clay to act as an adsorbent for the removal of heavy metal ions.

## 2.0 MATERIALS AND METHODS

### 2.1 Material collection

Analytical silver trioxo nitrate (V) (>97%), titanium (IV) isopropoxide solution (>98%), sodium hydroxide, hydrochloric acid (37%), and tetraoxosulphate (IV) acid (98%) were obtained from Sigma Aldrich. The fresh leaves of *Parkia biglobossa* were obtained from different locations in Ilorin, Kwara State (Nigeria) Metropolis and certified by a plant taxonomist. Clay samples were collected from deposits in Akerebiata, Ilorin. The mining wastewater was collected from artisanal gold mine in Chanchaga Local government Area, Minna, Niger State, Nigeria. The mining wastewater was collected into a clean 5000 cm<sup>3</sup> polythene bottle, transferred to the laboratory, and stored in a refrigerator before investigation. The heavy metal concentrations were quantified by Atomic Absorption Spectroscopy machine (AAS) (PG990).

### 2.2 Synthesis of Silver oxide/Titanium (IV) oxide immobilized on acid-activated kaolinite clay

The nanoparticles of TiO<sub>2</sub> were synthesized using the method of Ajala *et al.* (2022) with 50 cm<sup>3</sup> of *Parkia biglobossa* aqueous leaves extract, which has been confirmed rich in phenolic and flavonoid content, 50 cm<sup>3</sup> of titanium (IV) isopropoxide solution pH 8, stirred for 2 h on a magnetic stirrer at a speed of 2000 rpm. There was a development of precipitates accompanied by the color change. The resulting TiO<sub>2</sub> nanoparticles cake was filtered, washed, aged, oven-dried, and later calcined in a muffle furnace for 2 h at 550°C. Thereafter, 12 cm<sup>3</sup> of 0.005 M AgNO<sub>3</sub> aqueous solution was measured into a 250 cm<sup>3</sup> beaker followed by the addition of 6 cm<sup>3</sup> of aqueous leaf extract. The solution pH was adjusted to 8 using 2 M NaOH solution and 6 g of the already synthesized TiO<sub>2</sub> nanoparticles was added to the mixture. The mixture was stirred at 1000 rpm speed for 2 h, the solution completely changed from pale white to dark grey which indicated the reduction of metallic silver and the complete reduction of Ag<sup>+</sup> to Ag<sup>0</sup>. Evidence of silver loading onto titanium dioxide nanoparticles was also confirmed by the change in colour from white TiO<sub>2</sub> nanoparticles to grey Ag<sub>2</sub>O-TiO<sub>2</sub> slurry. The mixture was left overnight to age, oven dried at 100°C for 1 h before calcination for 2 hours at 450°C in the furnace to obtain Ag<sub>2</sub>O-TiO<sub>2</sub> nanocomposites. The Ag<sub>2</sub>O-TiO<sub>2</sub> nanocomposites were immobilized on 40 g of activated clay already prepared using the method of Ajala *et al.* (2022) via wet impregnation technique. The resultant slurry was calcined at 450°C to produce Ag<sub>2</sub>O-TiO<sub>2</sub>-clay hybrid nanocomposite.

### 2.3 Characterization of Ag<sub>2</sub>O-TiO<sub>2</sub> and Ag<sub>2</sub>O-TiO<sub>2</sub>-clay hybrid nanocomposite

A Bruker AXS D8 Advance X-ray diffractometer (XRD) employing Cu K radiation was used to examine the phases and crystallite sizes of the produced nanomaterials. The morphological disposition and elemental composition of the samples were also examined using a Zeiss Auriga HRSEM equipped with energy dispersive spectroscopy (EDS). The oxidation states of the surface elements of Ag<sub>2</sub>O-TiO<sub>2</sub> nanoparticles and Ag<sub>2</sub>O-TiO<sub>2</sub>-activated clay nanocomposites were investigated using X-ray photoelectron spectroscopy (XPS) with monochromated Mg K (1,253.6 eV) operated at 300 W and 15 eV.

### 2.4 Batch adsorption of metal ion onto Ag<sub>2</sub>O-TiO<sub>2</sub>-activated clay nanocomposites.

Batch adsorption treatment of the mining wastewater was carried out using the synthesized Ag<sub>2</sub>O-TiO<sub>2</sub>-activated clay. The process was carried out at temperature 30°C and 0.5 g adsorbent dose, while contact time was varied between 20 - 180 min to study the effect of contact time on the adsorption process. In doing this, 100 cm<sup>3</sup> of the mining wastewater was measured into 0.5 g of the Ag<sub>2</sub>O-TiO<sub>2</sub>-activated clay nanocomposite in a 250 cm<sup>3</sup> flask, the experiments were performed in duplicates. Sampling was done at an interval of 20 min and the resulting mixture was filtered. The

supernatant was analyzed for unwanted metal ions (Fe(III), Pb(II), Zn(II), and Cu(II) concentration by the AAS. Equations 1 and 2 were used to calculate the adsorbed phase concentration ( $q_t$ , in mgg<sup>-1</sup>) at a time (t) and the percentage of metal ion removal, given as:

$$q_t = \frac{(C_o - C_t)V}{m} \quad (1)$$

$$\text{Removal (\%)} = \frac{C_o - C_t}{C_o} \times 100\% \quad (2)$$

Where  $C_o$  and  $C_t$  represents the initial, final, and equilibrium metal ion concentrations in milligrams per liter (mgL<sup>-1</sup>) respectively; V represents the volume of the water sample (L) and m is the mass (g) of adsorbent used. (Guillaume, Chelaru, Visa, & Lassiné, 2018).

### 3.0 RESULTS AND DISCUSSION

#### 3.1 Metal ion concentration in wastewater

The heavy metal analysis from the artisanal gold mining wastewater revealed that, the water has heavy metal concentrations of 20.02 mg/L Fe (III), 4.29 mg/L Mn (II), 0.31 mg/L Cu (II), and 0.98 mg/L Pb (II) ions. These results are higher than the permissible limit (heavy metal) for industrial and drinking water by the WHO and NIS respectively (WHO, 2017) thus, the need for the mining wastewater treatment with Ag<sub>2</sub>O-TiO<sub>2</sub>-clay hybrid nanocomposite.

#### 3.2 Characterisation results of synthesised adsorbents

##### 3.2.1 XRD analysis

Figure 1a and b are the XRD spectral of the nanocomposites, which confirmed the effective interaction between the kaolinite clay structure and the rutile-phased titanium (IV) oxide doped with silver oxide nanoparticles. In Figure 1a, there is the presence of peaks at angle 2 $\theta$  and corresponding crystal planes of 27.4° (110), 36.1° (101), 39.2° (200), 41.2° (111), 44.0° (210), 54.3°(211), 56.8° (220) and 69.8° (112), these are assigned tetragonal, rutile-phase titania, with JCPDS number 00-021-1276 (**Key: K=kaolin, R=rutile-TiO<sub>2</sub>, Q=quartz C=calcite**).

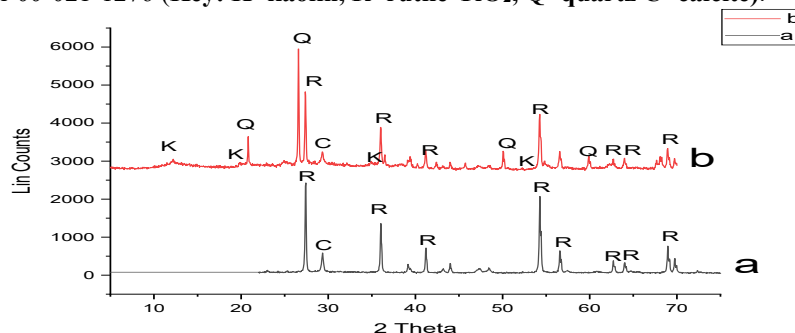


Figure 1: XRD spectral of (a) Ag<sub>2</sub>O-TiO<sub>2</sub> (b) Ag<sub>2</sub>O-TiO<sub>2</sub>/clay nanocomposite

The Ag<sub>2</sub>O peaks were not shown on the XRD pattern, which may be attributed to the low concentration and occurrence of silver oxide in the reduced form as nanoparticles (Shameli, Ahmad, Yunus, & Ibrahim, 2011). The non-detection of Ag<sub>2</sub>O by the XRD is perhaps due to insufficient Ag<sub>2</sub>O content in the composite to form an observable crystalline structure which follows research findings (Bagheri, Ramimoghdam, Yousefi, & Hamid, 2015). In Figure 1b are diffraction peaks at 2 theta values of 12.36°, 19.92°, 24.80° and 38.40° with miller indices; (001), (020), (002) and (-113) respectively corresponding with JCPDS 01-079-1570, which shows the clay is kaolinite. At 2  $\theta$  values of 20.93° (100), 26.59° (101), and 40.22 (111), there are strong and relatively powerful diffraction peaks in agreement with the literature (JCPDS card no 00-083-0539) indicative of quartz presence in the clay. The indices of; 27.52° (110), 36.08° (101), 41.22° (111), 44.05° (210), 54.32° (211), 56.70° (220), 62.90° (002), 64.03° (310), 69.28° (301) and 70.14° (112) matched well with a typical rutile phase of TiO<sub>2</sub> nanoparticles having JCPDS number, 00-021-1276. The XRD patterns of Figures 1a and b, obviously show that immobilizing the Ag<sub>2</sub>O-TiO<sub>2</sub> nanoparticles on Ag-TiO<sub>2</sub>-clay nanocomposites did not cause phase transformation from rutile to either anatase or brookite, but the TiO<sub>2</sub> rutile phase maintained. Only the various intensities of rutile-TiO<sub>2</sub> peaks were reduced and shifted, in Figure 1b. The diffraction peaks earlier noticed on Ag-TiO<sub>2</sub> were similarly represented on the Ag-TiO<sub>2</sub>-clay nanocomposites with the addition of kaolinite peaks. These peaks are evidence of clear interaction between the Ag<sub>2</sub>O- TiO<sub>2</sub>-clay composite.

##### 3.2.2 SEM/EDS results

The HRSEM image of the Ag<sub>2</sub>O-TiO<sub>2</sub> and Ag<sub>2</sub>O-TiO<sub>2</sub>-clay is presented in Figure 2a (i) and (ii). The image shown in Plate 2a (i) reveals the uniformly distributed spherical morphology. The structure of the Ag<sub>2</sub>O-TiO<sub>2</sub> maintains a cage-bell structure reported for TiO<sub>2</sub> without destruction after modification with Ag<sub>2</sub>O nanoparticles (Guo *et al.*, 2013).

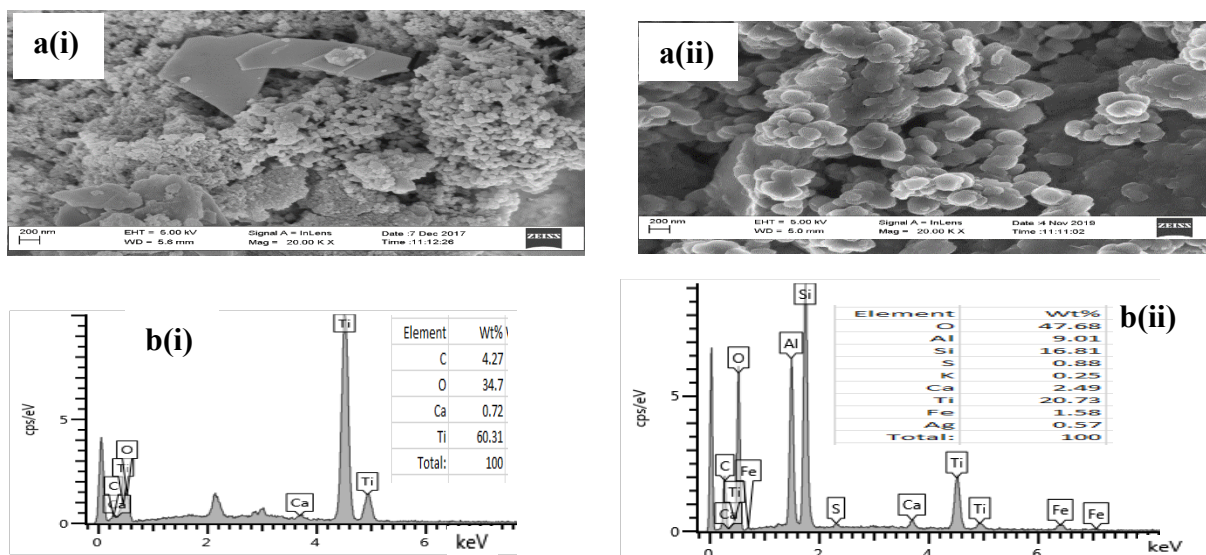


Figure 2: (a) SEM images of (i)  $\text{Ag}_2\text{O-TiO}_2$  (ii)  $\text{Ag}_2\text{O-TiO}_2/\text{clay}$  (b) EDS images of (i)  $\text{Ag}_2\text{O-TiO}_2$  (ii)  $\text{Ag}_2\text{O-TiO}_2/\text{clay}$

The image reveals porosity and also showed that the silver deposition did not cause lattice distortion on the synthesized  $\text{Ag}_2\text{O-TiO}_2$  (Pham & Lee, 2014). This indicates good silver dispersion on the  $\text{TiO}_2$  surface, as well as the fact that the doping impact affects the morphological layout of the nanoparticles generated (Oguzhan, Yildiz, Semih, & Ozge, 2016). The morphology of the  $\text{Ag}_2\text{O-TiO}_2/\text{clay}$  in Figure 2a (ii) shows an evenly distributed and interstitial arrangement of the clay lattice, which consists of hemispherical stacks of platelets structures of porous kaolinites similar to previous work (Mustapha *et al.*, 2019). The elemental composition of the  $\text{Ag}_2\text{O-TiO}_2$  (ii)  $\text{Ag}_2\text{O-TiO}_2/\text{clay}$  in Figure 2b (i) and (ii) at binding energy between 0-20 keV revealed the presence of C, O, Al, Si, S, K, Ti, Fe, Ag and Ca. Figure 2b (i) shows the presence of high composition of Ti (60.31%) with Oxygen (34.70%) in the nanocomposite. There is a complete absence of Ag, probably due to its minimal concentration in the doped composite, similar to the report of (Petrik, Missengue, Fatoba, Tuffin, & Sachs, 2012) and which corroborates the XRD results. In the  $\text{Ag}_2\text{O-TiO}_2/\text{clay}$  spectral, the presence of Ag was confirmed, having 0.57%, which shows that Ag was doped on the structure. The high percentage of Ti (20.73%) is attributed to the doping of  $\text{TiO}_2$  and its even distribution in the composite matrix. This is similar to the previous report where Zn was immobilised on the kaolinite clay surface (Mustapha *et al.*, 2020). The high percentage of oxygen reveals that the Si, Al, Fe, C, Ti, and Ag are present in a combined state as oxides. The entire element in Figure 2bii shows that the sample is an aluminosilicate material having  $\text{Ag}_2\text{O}$ , and  $\text{TiO}_2$  incorporated into the activated clay.

### 3.2.3 XPS analysis

The condition of oxidation number on the surface and orbital of the elements included in the samples were determined by XPS analysis of  $\text{Ag}_2\text{O-TiO}_2$  nanoparticles and  $\text{Ag}_2\text{O-TiO}_2/\text{clay}$  nanocomposite (Figure 3). Figures 3a (i) and (ii) are the general survey spectrum, while 3b and 3c are the peak deconvoluted for Ti and Ag in the (i)  $\text{Ag}_2\text{O-TiO}_2$  and (ii)  $\text{Ag}_2\text{O-TiO}_2/\text{clay}$  respectively. The XPS of the  $\text{Ag}_2\text{O-TiO}_2$  sample (Fig.3 ai), reveals the presence of titanium, oxygen, silver, and carbon at different binding energies on both spectra.

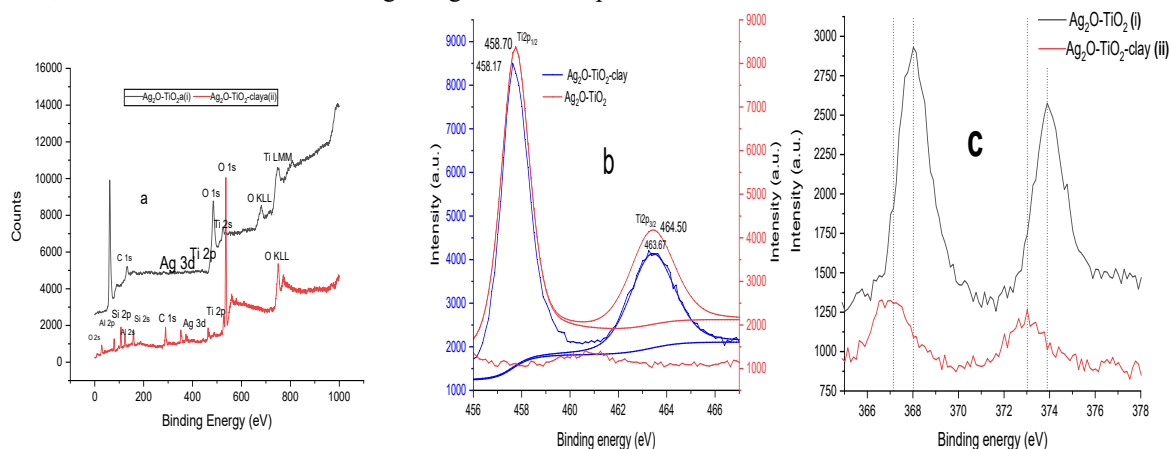


Figure 3: (a) General XPS spectrum (b) deconvoluted spectral of Ti (c) Ag (i)  $\text{Ag}_2\text{O-TiO}_2$  and (ii)  $\text{Ag}_2\text{O-TiO}_2/\text{clay}$

The presence of Ag 3d at binding energies 368.80 eV and 369.20 reveals evidence of  $\text{Ag}_2\text{O}$  doping on  $\text{TiO}_2$  nanoparticles at 464.50 eV and 463.67 eV in Figures 3a (i) and (ii) respectively. The titanium LMM Auger transition exhibits an

intense peak in the region of 880 eV and 760 eV indicating the presence of the TiO<sub>2</sub> crystal. Figure 3 a(ii) reveals the presence of Ag<sub>2</sub>O doped on the alumina-silicate clay structure which could not be seen in the XRD spectra. Figures 3 b(i), (ii) and 3 c(i), (ii) are the deconvoluted XPS spectra of Ti and Ag in Ag<sub>2</sub>O-TiO<sub>2</sub> and Ag<sub>2</sub>O-TiO<sub>2</sub>-clay samples, respectively. The figures reveal the presence of doublet peaks of Ti 2p<sub>1/2</sub> and Ti 2p<sub>3/2</sub> spin-orbital splitting photoelectrons in each of the two samples. These were located at similar binding energies of 458.70 eV and 464.50 eV on b(i) while at 458.17 eV and 463.67 eV on b(ii). The peaks show the difference of ~ 6 eV (5.8 and 5.58 eV) on Ag<sub>2</sub>O-TiO<sub>2</sub> and Ag<sub>2</sub>O-TiO<sub>2</sub>-clay respectively, which is an indication of the existence of Ti as TiO<sub>2</sub> framework in the oxidation state of +4, irrespective of the composite. Figure 3ci reveals the presence of two intense peaks at energy levels of 368.5 eV and 373.9 eV. The split peak observed were assigned to Ag 3d<sub>5/2</sub>(368.5 eV) and Ag 3d<sub>3/2</sub>(373.9 eV). The binding energy difference between the split 3d doublet and the singlet is roughly 6.0 eV. This indicates that the oxidation state present on the surface of Ag is zero and not the metallic silver as present in AgNO<sub>3</sub>. Irrespective of the ionic radius disparity between Ag (0.115 nm) and Ti (0.061 nm), it is clear that some Ag<sup>0</sup> species may have penetrated the TiO<sub>2</sub> framework, implying a mutual interaction between the dopant and the doped.

### 3.3 Adsorption study

#### 3.3.1 Effect of contact time

The result of the variation of contact time effect on the removal of Mn (II), Fe(III), Pb (II), and Cu (II) ions by Ag<sub>2</sub>O-TiO<sub>2</sub>-clay nano adsorbent is revealed in Figure 4. The percentage removal of Mn (II), Fe (III), and Cu (II) ions from mining wastewater increased drastically within the first 60 mins then became gradual from 80 to 120 minutes and thereafter the adsorption became constant for the four metal ions considered in this study. The rapid elevation in percentage removal of the metal ions at the onset of the adsorption exercise was ascribed to the high number of vacant adsorptive surfaces on Ag<sub>2</sub>O-TiO<sub>2</sub>-clay and this resulted in a higher solute concentration gradient (Mnasri-Ghnimi & Frini-Srasra, 2019). As time progresses between 80 to 120 minutes, the adsorptive surfaces became saturated with metal ions and further adsorption became difficult (Kazak, Eker, Bingol, & Tor, 2018). The low removal of Pb(II) ions may be attributed to its large ionic radii (0.06nm > Mn (II) 0.072 nm > Cu (II) 0.073nm > Pb (II) 0.119nm) because, ions with a large ionic radius diffuse slower (Ajala et al, 2022).

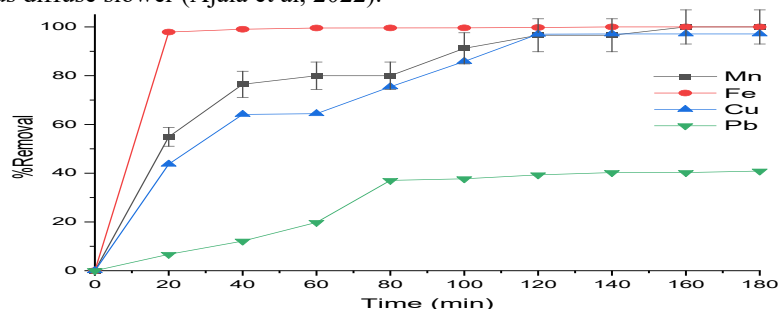


Figure 4: Effect of contact time on percentage removal of the metal ions.

### 4.0 CONCLUSION

The Ag<sub>2</sub>O-TiO<sub>2</sub> and Ag<sub>2</sub>O-TiO<sub>2</sub>-clay nanocomposite materials were successfully synthesized by a simplistic, green, efficient, and environment friendly procedure. The findings from this study confirmed the presence of Ag<sub>2</sub>O and TiO<sub>2</sub> in the interlayer of acid-activated kaolinite clay. The synthesised titanium was confirmed rutile TiO<sub>2</sub>, in the +4 oxidation state in both Ag<sub>2</sub>O-TiO<sub>2</sub> and Ag<sub>2</sub>O-TiO<sub>2</sub>-clay nanocomposites matrices and has a large surface area. The adsorptive effects studied revealed that time of contact affect the rate of removal of the metal ion onto the Ag<sub>2</sub>O-TiO<sub>2</sub>-clay surface. The Ag<sub>2</sub>O-TiO<sub>2</sub>-clay nanocomposite can therefore be used for the efficient removal of Mn (II), Fe (III), Pb (III) and Cu (II) ions from mining wastewater.

### REFERENCES

- Adebayo, G. B., Adegoke, H. I., & Sidiq, F. (2020). Adsorption of Cr(VI) ions onto goethite, activated carbon and their composite: kinetic and thermodynamic studies. *Applied Water Science*, 10, 213-231. doi:10.1007/s13201-020-01295-z
- Ajala, M. A., Abdulkareem, A. S., Tijani, J. O., & Kovo, A. S. (2022). Adsorptive behaviour of rutile phased titania nanoparticles supported on acid-modified kaolinite clay for the removal of selected heavy metal ions from mining wastewater. *Applied Water Science*, 12(19), 1-24. doi:10.1007/s13201-021-01561-8
- Akinnawo, S. (2019). Synthesis, Modification, Applications and Challenges of Titanium Dioxide Nanoparticles. *Research Journal of Nanoscience and Engineering*, 3(14), 10-22.
- Arya, G., Kumari, R. M., Gupta, N., Kumar, A., Chandra, R., & Nimesh, S. (2018). Green synthesis of silver nanoparticles using Prosopis juliflora bark extract: reaction optimization, antimicrobial and catalytic activities. *Artificial Cells, Nanomedicine, and Biotechnology*, 46(4), 985-993. doi:10.1080/21691401.2017.1354302



- Awasthi, A., Jadhao, P., & Kumari, K. (2019). Clay nano-adsorbent: structures, applications and mechanism for water treatment. *SN Applied Sciences*, *1*(1076), 1-21. doi:10.1007/s42452-019-0858-9
- Bagheri, S. B., Ramimoghdam, D., Yousefi, A. T., & Hamid, S. A. (2015). Synthesis, Characterization and Electrocatalytic Activity of Silver Doped-Titanium Dioxide Nanoparticles. *International Journal of Electrochemical Science*, *10*, 3088 - 3097.
- Christopher, J. D., Saswati, B., & Ezilrani, P. S. (2015). Optimization of Parameters for Biosynthesis of Silver Nanoparticles Using Leaf Extract of *Aegle marmelos*. *Brazilian Archives of Biology and Technology*, *58*(5), 702-710. doi:10.1590/S1516-89132015050106
- Dontsova, T. A., Kutuzova, A. S., Bila, K. O., Kyrii, S. O., Kosogina, I. V., & Nechyporuk, D. O. (2020). Enhanced photocatalytic activity of TiO<sub>2</sub>/SnO<sub>2</sub> binary nanocomposites. *Journal of Nanomaterials*, 2020.
- Guillaume, P. L. A., Chelaru, A., Visa, M., & Lassiné, O. (2018). Titanium Oxide-Clay” as Adsorbent and Photocatalysts for Wastewater Treatment. *Journal of Membrane Science and Technology*, *8*(1), 176-186. doi:10.4172/2155-9589.1000176
- Guo, H., wang, W., Liu, L., He, Y., Li, C., & Wang, Y. (2013). Shape-controlled synthesis of Ag@TiO<sub>2</sub> cage-bell hybrid structure with enhanced photocatalytic activity and superior lithium storage+. *Green Chemistry*, *15*, 2810-2816. doi:10.1039/c3g41280f
- Hajjaji, W., Andrejkovičová, S., Pullar, R. C., Tobaldi, D. M., Lopez-Galindo, A., Jammousi, F., . . . Labrincha, J. A. (2018). Effective removal of anionic and cationic dyes by kaolinite and TiO<sub>2</sub>/kaolinite composites. *Clay Minerals*, *51*(1), 19-27. doi:10.1180/claymin.2016.051.1.02
- Hussain, S. T., & Ali, S. A. K. (2021). Removal of Heavy Metal by Ion Exchange Using Bentonite Clay. *Journal of Ecological Engineering*, *22*(1), 104–111. doi:10.12911/22998993/128865
- Kazak, O., Eker, Y. R., Bingol, H., & Tor, A. (2018). Preparation of chemically-activated high surface area carbon from waste vinasse and its efficiency as adsorbent material. *Journal of Molecular Liquids*, *272*, 189-197. doi:10.1016/j.molliq.2018.09.085.
- Krishnan, B., & Mahalingam, S. (2017). Ag/TiO<sub>2</sub>/bentonite nanocomposite for biological applications: Synthesis, characterization, antibacterial and cytotoxic investigations. *Advanced Powder Technology*, *28*, 2265–2280. doi:http://dx.doi.org/10.1016/j.apt.2017.06.007
- Kumari, P., Alam, M., & Siddiqi, W. A. (2019). Usage of nanoparticles as adsorbents for waste water treatment: An emerging trend. *Sustainable Materials and Technologies*, *22*(2019), 1-14. doi:10.1016/j.susmat.2019.e00128
- Kyomuhimbo, H. D., Michira, I. N., Mwaura, F. B., Derese, S., Feleni, U., & Iwuoha, E. I. (2019). Silver–zinc oxide nanocomposite antiseptic from the extract of *Bidens pilosa*. *SN Applied Sciences*, *1*(681), 1-17. doi:10.1007/s42452-019-0722-y
- Mnasri-Ghnimi, S., & Frini-Srasra, N. (2019). Removal of heavy metals from aqueous solutions by adsorption using single and mixed pillared clays. *Applied Clay Science*, *179*(2019), 3-19. doi:10.1016/j.clay.2019.105151
- Mustapha, S., Ndamitso, M. M., Abdulkareem, A. S., Tijani, J. O., Shuaib, D. T., Ajala, A. O., & Mohammed, A. K. (2020). Application of TiO<sub>2</sub> and ZnO nanoparticles immobilized on clay in wastewater treatment: a review. *Applied Water Science*, *10*(49), 1-36. doi:10.1007/s13201-019-1138-y
- Oguzhan, A., Yildiz, B., Semih, G., & Ozge, K. (2016). Ag doped TiO<sub>2</sub> nanoparticles prepared by Hydrothermal Method and Coating of the Nanoparticles on the Ceramic Pellets for Photocatalytic Study: Surface Properties and Photoactivity. *Journal of Engineering Technology and Applied Sciences*, *1*(1), 1-12.
- Pham, T., & Lee, B. (2014). Feasibility of silver doped TiO<sub>2</sub>/glass fiber photocatalyst under visible irradiation as an indoor air germicide. *International Journal of environmental Research and Public Health*, *11*, 3271-3288.
- Shivaraju, H. P., Egumbo, H., Madhusudan, P., Anil Kumar, K. M., & Midhun, G. (2018). Preparation of affordable and multi-functional clay-based ceramic filter matrix for treatment of drinking water. *Environmental Technology*, 1-30. doi:10.1080/09593330.2018.1430853
- Wang, Z., Bao, J., Wang, T., Moryani, H. T., Kang, W., Zheng, J., . . . Xiao, W. (2021). Hazardous Heavy Metals Accumulation and Health Risk Assessment of Different Vegetable Species in Contaminated Soils from a Typical Mining City, Central China. *18*(5), 2617.
- WHO. (2017). *Guidelines for Drinking-water Quality: Fourth Edition Incorporating the First Addendum*. Retrieved from Geneva.



## Electrochemical and Thermodynamic Evaluations of *Spondias Mombin* Leaves Extract as Green Inhibitor for Mild Steel Corrosion in Acidic Medium

Kenneth K. ADAMA\*<sup>1</sup>, Benedict I. ONYEACHU<sup>2</sup>, Ebijuwa M. IGHO<sup>1</sup>

<sup>1</sup> Department of Chemical Engineering, Faculty of Engineering, Edo State University Uzairue, Edo State, Nigeria

<sup>2</sup> Department of Industrial Chemistry, Faculty of Science, Edo State University Uzairue, Edo State, Nigeria

\*Corresponding author: [adama.kenneth@edouniversity.edu.ng](mailto:adama.kenneth@edouniversity.edu.ng)

---

### ABSTRACT

Acid corrosion of steel-based structural equipment is a serious challenge for the chemical industry, especially, during descaling practices. Adding efficient corrosion inhibitors into the acid solution can significantly mitigate against this phenomenon. Currently, greener corrosion inhibitors, such as extracts of plant parts, have gained outstanding attention because they impact minimally when discharged into the environment. In this work, electrochemical and thermodynamic methods were employed to investigate the inhibitive efficiency of the water and ethanol extracts of *spondias mombin* leaves against the corrosion of typical industrial steel (C1020) in 1.0M HCl. Both extracts protect the steel surface by blocking anodic and cathodic reactions on the steel surface, and lowering the capacitive behavior of the steel-acid interface. The extracts adsorb according to the models of Langmuir and Freundlich isotherms. The ethanol extract performs better (with an efficiency 96–98 %) than the water extract (efficiency 36–38 %), and exhibits more negative  $\Delta G$  (-28.00 KJ/mol.) which is synonymous with more feasible and spontaneous adsorption.

Keywords: *Electrochemical, Thermodynamics, Corrosion inhibition, Green product, Spondias mombin extracts.*

### 1. INTRODUCTION

Carbon steel constitutes the most abundantly used alloy for fabricating major equipment in the chemical process industry due to its natural abundance, cheapness and strength (Palaniappan *et al.*, 2020; Verma *et al.*, 2019). Over time, inorganic scales would percolate on the surface of the steel-based equipment; interfering with production and diminishing the structural integrity of the equipment. Acid-cleaning, with dilute mineral acids like hydrochloric acid (HCl), is a common industrial practice that dislodges these scales and restores the efficiency of the equipment. However, the acid solution eventually impacts severe corrosion attack on the steel surface during acid-cleaning. Globally, the financial and material losses associated with this acid corrosion is enormous (Alrefae *et al.*, 2020; Marzorati *et al.*, 2019; Verma *et al.*, 2019). One of the most conventional ways to mitigate against this corrosion is to add effective corrosion inhibitors into the acid-cleaning solution.

Most chemical process industries usually add toxic chemicals to acid-cleaning solutions (Alrefae *et al.*, 2020; Muthukumarasamy *et al.*, 2020; Fouda *et al.*, 2019; Ishak *et al.*, 2019), but these chemicals impact dangerously on the environment (Alrefae *et al.*, 2020; Belakhdar *et al.*, 2020; Berrissoul *et al.*, 2020; Chen *et al.*, 2020; Asfia *et al.*, 2020; Bidi *et al.*, 2020). Identifying greener alternatives, with high inhibition efficiency, is important for the chemical industry since they would be excellent replacements for the toxic chemicals. The extracts of plant parts are remarkable in this regard (Ahanotu *et al.*, 2020, Akinbulumo *et al.*, 2020). They are naturally abundant, cheap and environmentally safe. They also contain phytochemicals which offer enormous active sites for interaction with metal atoms (Alrefae *et al.*, 2020; Chaudhary and Tak 2022). Several research works exist on the use of plant extracts as corrosion inhibitors for steel in acidic solutions (Marzorati *et al.*, 2019; Verma *et al.*, 2019; Ishak *et al.*, 2019; Chen *et al.*, 2020; Asfia *et al.*, 2020; Alrefae *et al.*, 2020; Ahanotu *et al.*, 2020). However, majority of reported works used only single (and toxic) solvents for their extraction. We have a concept that the amount/characteristics of phytoconstituents extracted from a plant part would influence its corrosion inhibition efficiency, and depends on the extracting solvent. Knowledge of this will guide the industry on the most preferable solvent for extraction. It is important, also, that these solvents (like water and ethanol) also exhibit green properties in case of eventual discharge to environment.

This work reports a study conducted to investigate the capability of water and ethanol extracts of *spondias mombin* leaves to ameliorate the acid corrosion of carbon steel C1020. Potentiodynamic polarization (PDP) and electrochemical

impedance spectroscopy (EIS) were utilized as electrochemical methods to understand the effect of extracts on the kinetics and mechanism of the steel corrosion in 1 M HCl solution. Thermodynamic assessment was performed based on adsorption isotherm and  $\Delta G$  calculations.

## 2. MATERIALS AND METHODS

### 2.1 Materials

The materials used include fresh samples of *spondias mombin* leaves, sterile plastic bags, industrial blender, solvents: acetone, distilled water and ethanol (98 %), rotary evaporator, steel coupons and polishing papers, acid/extract concentrations tested: 1 M HCl /100, 200, 300, and 500 ppm.

### 2.2 Methods

#### 2.2.1. Sample preparation

Coupons with surface area of 1.0 x 1.0 cm<sup>2</sup> were used for electrochemical measurement. Prior to use, they were abraded mechanically using abrasive polishing papers (successively) with 400 and 600 grit sizes, rinsed with distilled water and acetone, and dried using a Buchler Torrmet specimen dryer. Analytical grade HCl (36 wt. %) was dissolved in distilled water to prepare the corrodent (1 M HCl). Fresh samples of *Spondias mombin* leaves were obtained from the campus of Edo State University Uzairue and was validated by Dr. A.I. Anani of Biological Science Department, Edo State University Uzairue, Nigeria. The leaves were thoroughly washed with distilled water, dried at room temperature for fourteen days and then ground to powdered form using an industrial blender. The extraction was performed by soaking the powder for 72 h in ethanol and water as solvent in the ratio of 1:10 (plant powder (g): solvent volume (mL)). Thereafter, the mixture was filtered and the filtrate was concentrated using a rotary evaporator. The powder residue was also air-dried until a constant mass was obtained. The difference in powder mass before and after extraction was utilized to calculate the amount of plant phytochemical extracted by each solvent.

#### 2.2.2 Electrochemical and thermodynamic investigations

The electrochemical experiments were conducted on a Gamry Potentiostat/Galvanostat/ZRA Reference 600 work station following the method reported previously by Ahanotu *et al.* (2020). The setup comprises a three-electrode system where an epoxy-encapsulated C1020 steel functioned as the working electrode, the auxiliary electrode was a graphite rod, and the reference electrode was a Ag/AgCl electrode. The electrochemical experiments were performed after monitoring the variation of open circuit potential (OCP) for an hour. The electrochemical impedance spectroscopy (EIS) measurements were performed, at OCP, within the frequency range of 10<sup>5</sup> Hz to 10<sup>-3</sup> Hz with  $\pm 10$  mV amplitude signal. The signal amplitude perturbation was  $\pm 10$  mV. On the other hand, the potentiodynamic polarization (PDP) measurements were conducted by polarizing the working electrode within  $\pm 0.25$  V versus OCP using a scan rate of 0.166 mVs<sup>-1</sup>. The analysis of EIS data was done using Echem analyst while EC-lab software was used for PDP data analysis. The experiments were conducted in triplicates to achieve reproducibility. The inhibition efficiency (from EIS and PDP results) was calculated according to Solomon *et al.*, (2018) and Fang *et al.*, (2019), based on Equations (1) and (2).

$$\% IE_{EIS} = 1 - \frac{R_{ct}(\text{without inhibitor})}{R_f(\text{with inhibitor}) + R_{ct}(\text{with inhibitor})} \times 100\% \quad (1)$$

$$\% IE_{PDP} = 1 - \frac{i_{corr}(\text{with inhibitor})}{i_{corr}(\text{without inhibitor})} \times 100\% \quad (2)$$

Different adsorption isotherm models were adopted to investigate the thermodynamic interactions and properties of the inhibitor. From the investigated isotherm models, the Gibbs free energy was evaluated to understand the spontaneity and feasibility of inhibitor protection.

## 3. RESULTS AND DISCUSSION

### 3.1. Electrochemical studies

#### 3.1.1 Electrochemical impedance spectroscopy (EIS)

The analysis of the EIS is presented in the form of a Nyquist, Absolute impedance and Phase angle plots as shown in Figure 1. The addition of different concentrations of the *spondias mombin* leaf extracts caused the size of the Nyquist arcs to expand significantly in comparison to the size displayed by the uninhibited solution (blank solution). This is shown in Figure 1(a). This enlargement of the Nyquist arc size depicts lower rate of corrosion and increase in corrosion resistance. It can be seen that, at 500 ppm, the ethanol extract (with charge transfer resistance,  $R_{ct}$ , of 2004.10  $\Omega$  cm<sup>2</sup>) shows larger sizes than the water extract (with charge transfer resistance,  $R_{ct}$ , of 121.00  $\Omega$  cm<sup>2</sup>), which confirm that the ethanol extract exhibits greater protection of the steel surface than the water extract.

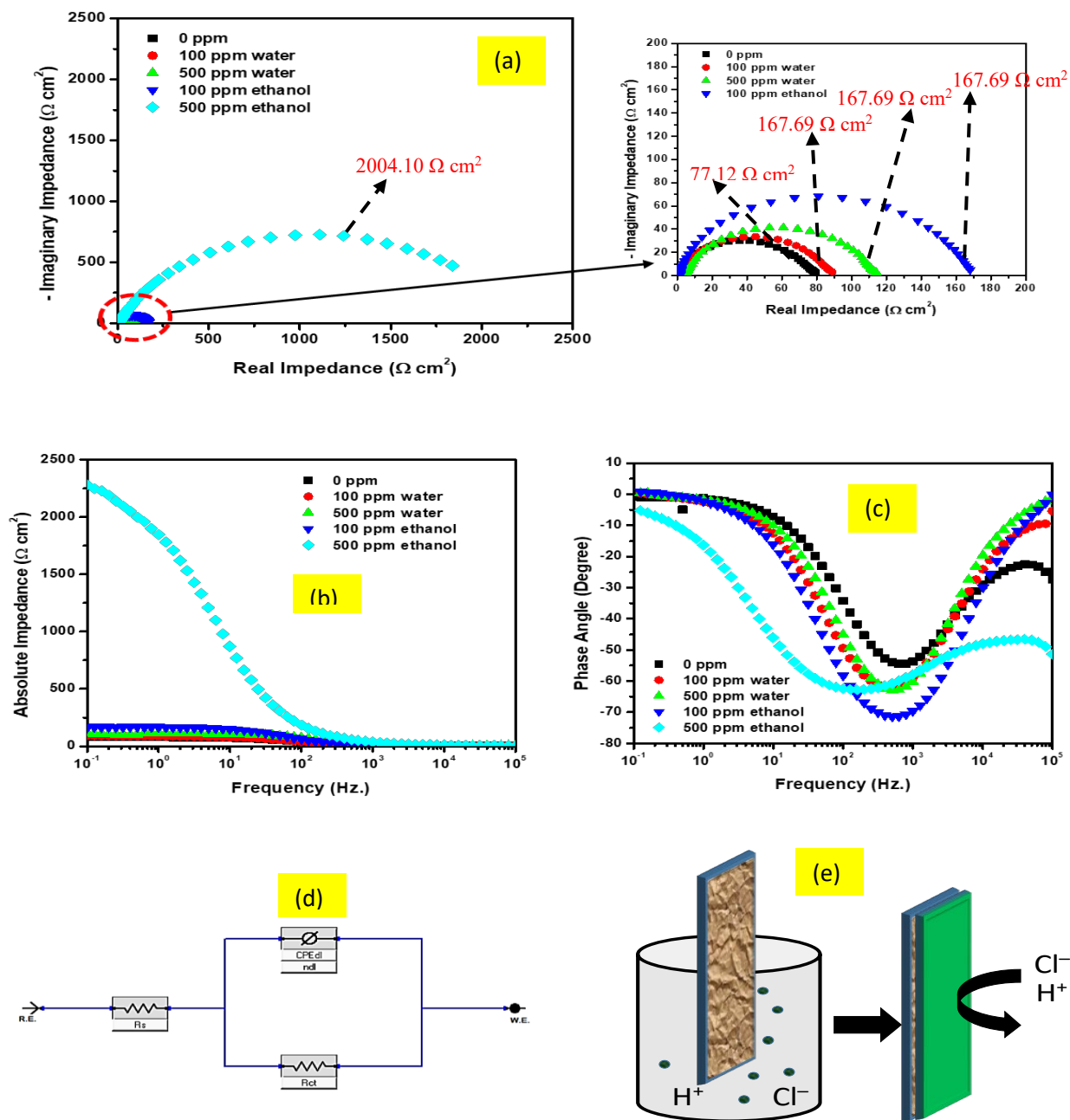


**Figure 1:** EIS analysis shown as (a) Nyquist ( $R_{ct}$  values in red font) (b) absolute impedance and (c) phase angle plots, along with (d) electrical equivalent circuit model and (e) schematic illustration of inhibition mechanism.

The Nyquist trend is also supported by the absolute impedance plots in Figure 1(b) whereby the addition of inhibitor extracts continuously increases the value of impedance at low frequency, compared with the blank solution. Also, the phase angle plots of Figure 1(c) reveal higher peaks in the presence of inhibitor extract. Higher peaks depict greater corrosion resistance. Consequently, the impedance behavior of the inhibited and uninhibited steel is modeled using the one-time electrical equivalent circuit in Figure 1(d). The model depicts that the extracts effectively modify the electric double layer at the steel-solution interface, by repelling water and chloride ions from the acid away from the steel surface, as depicted in Figure 1(e).

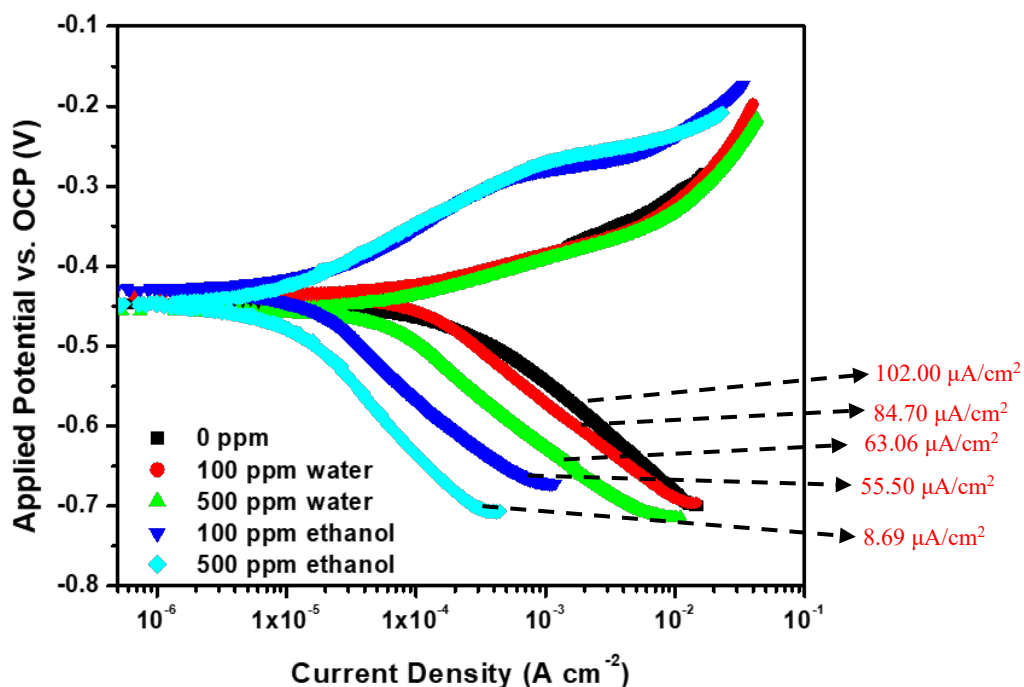


**Figure 2:** PDP analysis of C1020 steel in 1 M HCl containing water and ethanol extracts of *Spondias mombin* leaves at 25 °C (corrosion current,  $i_{\text{corr}}$ , values given in red font).

### 3.1.2 Potentiodynamic polarization (PDP)

The influence of the extracts on the anodic and cathodic reactions on the steel surface during the corrosion in the acid solution was investigated using the PDP technique. In the present study, the predominant anodic reaction is the oxidation of Fe to  $\text{Fe}^{2+}$  while that of the cathodic reaction is the reduction of  $\text{H}^+$  to  $\text{H}_2(\text{g})$ . Figure 2 shows the result of the polarization of the steel samples in the acid solution without and with concentrations of 100 and 500 ppm of the different extracts. The influence of both extracts on the corrosion potentials of the steel was observed to be minimal. This implies that the extracts had minimal influence on the thermodynamic propensity of the steel to corrode in the acid solution. However, the extracts significantly shifted both anodic and cathodic current to lower values. The implication is that the extracts exhibited mixed-type inhibitions since they were able to lower both anodic and cathodic reactions.

### 3.2. Adsorption Isotherm Analysis

The electrochemical results confirm that the ethanol extract of *Spondias mombin* leaf performed better than the water extract. This could be attributed to the fact the ethanol, being a more vigorous solvent, could extract more phytoconstituents from the leaves, compared with the less aggressive solvent (water). It has also been well documented that the plant constituents protect corroding metal surfaces by adsorbing on active sites to block the electrochemical reactions. Adsorption isotherms are usually employed to decipher the predominant adsorption mechanism by corrosion inhibitors. In this work, we have tested the extract adsorption using the Langmuir, Freundlich and Temkin isotherms (Equations (3)–(5), respectively), by focusing on the ethanol extract. The results are presented in Figure 3.

$$\frac{C}{\theta} = \frac{1}{K_{\text{ads}}} + C \quad (3)$$

$$\log \theta = \log K_{\text{ads}} + \frac{1}{n} \log C \quad (4)$$

$$\theta = -\frac{1}{2\alpha} \ln C - \frac{1}{2\alpha} K_{\text{ads}} \quad (5)$$

The most appropriate model is usually identified by the isotherm with the highest correlation coefficient ( $R^2$ ). Figure 3 shows that the Freundlich isotherm (0.9975) exhibited the highest value of  $R^2$ . This indicates that the extract components

adsorbed as single layer on roughened steel surface during the corrosion inhibition (Akinbulumo *et al.*, 2020; Chaudhary and Tak 2022).

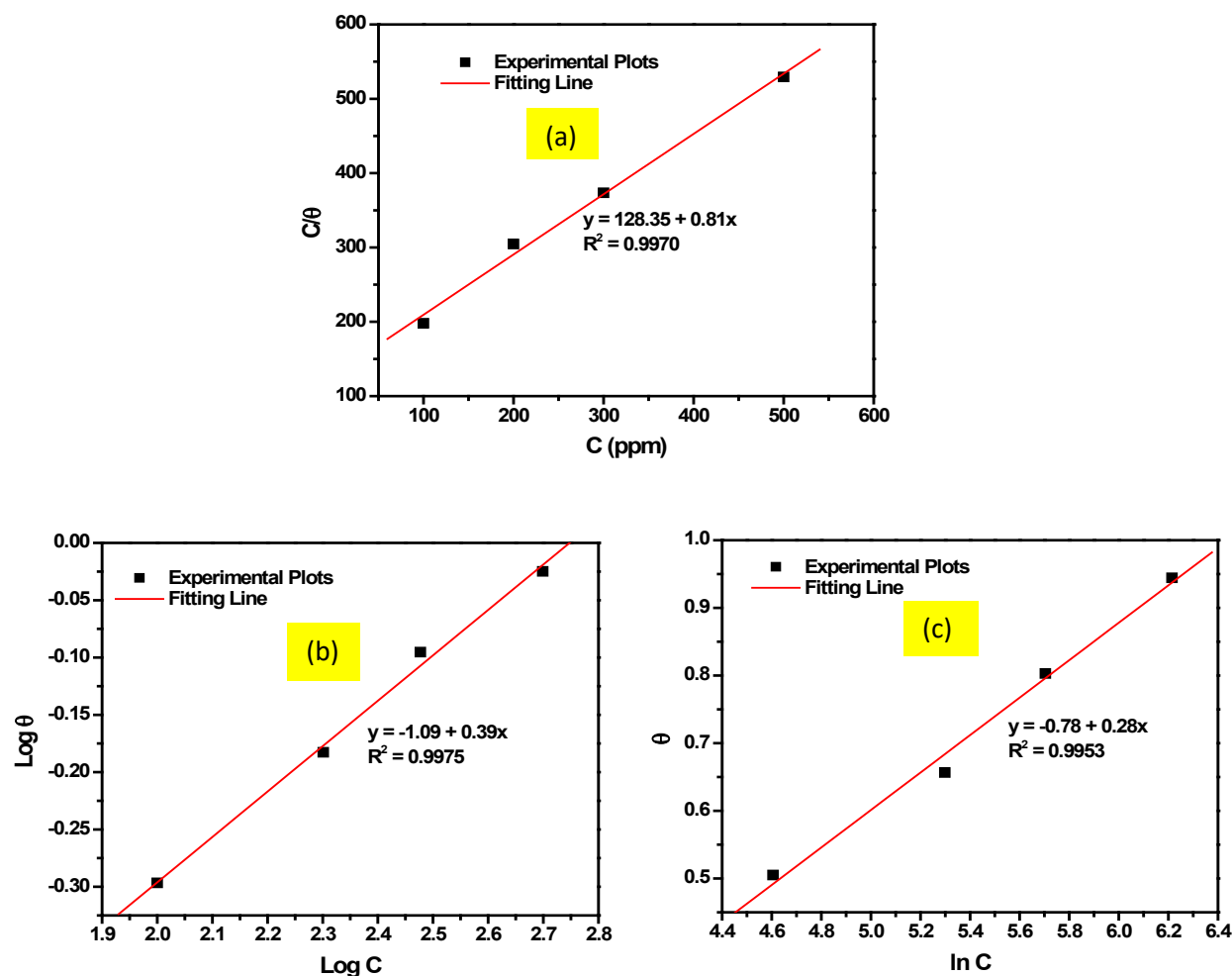


**Figure 3:** (a) Langmuir (b) Freundlich and (c) Temkin and isotherm plots for C1020 steel in 1 M HCl containing different concentrations of water extract of *Spondias mombin* leaves at 25 °C.

The adsorption constant,  $K_{ads}$ , can be extrapolated from the intercept of the Freundlich plot, according to the Equation (4), can be introduced into the following  $\Delta G_{ads} = -RT(10^6 K_{ads})$  to calculate the thermodynamic Gibbs free energy change which describes the feasibility and spontaneity of inhibitor adsorption. The adsorption equilibrium constant was calculated as 0.081 ppm mol.<sup>-1</sup> and, from this value, the Gibbs' free energy was deduced as -28.00 KJ mol.<sup>-1</sup>. The negative value confirms that the extract adsorption was spontaneous and feasible.

#### 4. CONCLUSIONS

This study examines current developments in the use of plant extracts as corrosion inhibitors based on the use of *Spondias mombin* leave extracts. Several plant extracts have been evaluated as inhibitors against metallic corrosion due to their environmentally friendly behavior and excellent inhibitory efficiency. The adsorption of the *Spondias mombin* leave extracts on the mild carbon steel was via Langmuir and Freundlich isotherm indicating the components adsorbed as single layer on very roughened steel surface during the corrosion process. The water extract had dominant effect on the anodic corrosion reactions while the ethanol extract had major effect on the cathodic corrosion reactions. The electrochemical analysis revealed lower rate of corrosion and increase in corrosion resistance of the extracts.

**REFERENCES**

- Ahanotu C.C., Onyeachu I.B., Solomon M.M., Chikwe I.S., Chikwe O.B., Eziukwu C.A. Pterocarpus Santalinoides Leaves Extract as Sustainable and Potent Inhibitor for Low Carbon Steel in a Simulated Pickling Medium, *Sustainable Chemistry and Pharmacy*, 15 (2020) 100196
- Akinbulumo O.A., Odejebi O.J., Odekanle E.L. Thermodynamics and Adsorption Study of the Corrosion Inhibition of Mild Steel by Euphorbia heterophylla L. Extract in 1.5M HCl, *Results in Materials*, 5 (2020) 100074
- Alrefaee S.H., Rhee K. Y., Verma C., Quraishi M. A., Ebenso E.E. Challenges and Advantages of Using Plant Extract as Inhibitors in Modern Corrosion Inhibition Systems: Recent Advancements, *Journal of Molecular Liquids*, (2020), 44-88.
- Asfia M.P., Rezaei M., Bahlakeh G. Corrosion Prevention of AISI 304 Stainless Steel in Hydrochloric Acid Medium Using Garlic Extract as Green Corrosion Inhibitor: Electrochemical and Theoretical Studies, *Journal of Molecular Liquids*, 315 (2020) 113679
- Belakhdar A., Ferkous H., Djellahi S., Sahraoui R., Lahbib H., Amor Y.B., Erto A., Balsamo M., Benguerba Y. Computational and Experimental Studies on the Efficiency of Rosmarinus officinalis Polyphenols as Green Corrosion Inhibitors for XC48 Steel in Acidic Medium, *Colloids and Surfaces A: Physicochemical and Engineering Aspects* 606 (2020) 125458
- Berrissoul A., Onarhach A., Benhiba F., Romane A., Zarrouk A., Guenbour A., Dikici B., Dafali A. Evaluation of Lavandula mairei Extract as Green Inhibitor for Mild Steel Corrosion in 1M HCl Solution – Experimental and Theoretical Approach, *Journal of Molecular Liquids*, (2020) 113493
- Bidi M.A., Azadi M., Rassouli M. A New Green Inhibitor for Lowering the Corrosion Rate of Carbon Steel in 1M HCl Solution Using Hyalomma tick Extract, *Materials Today Communication*, 24 (2020) 100996
- Chaudhary S., Tak R.K. Natural Corrosion Inhibition and Adsorption Characteristics of Tribulus terrestris Plant Extract on Aluminum in Hydrochloric Acid Environment. *Biointerface Res. Appl. Chem.* 12 (2) (2022) 2603-2617
- Chen S., Chen S., Zhu B., Huang C., Li W. Magnolia grandiflora Leave Extracts as a Novel Environmentally Friendly Inhibitor for Q235 Steel Corrosion in 1M HCl: Combining Experimental and Theoretical Researches, *Journal of Molecular Liquids* (2020) 113312
- Fang Y., Suganthan B., Ramasamy R.P. Electrochemical Characterization of Aromatic Corrosion Inhibitors from Plant Extracts. *J. Electroanal. Chem.* 840 (2019) 74-83
- Fouda A., Shalabi K., Shaaban M. Synergistic Effect of Potassium Iodide on Corrosion Inhibition of Carbon by Achillea santolina Extract in Hydrochloric Acid Solution, *Journal of Bio-and Tribo-Corrosion*, 5 (2019) 71.
- Ishak A., Adams F.V., Madu J.O., Joseph I.V., Olubambi P.A. Corrosion Inhibition of Mild Steel in 1M Hydrochloric Acid Using Haematostaphis barteri Leaves Extract, *Procedia Manufacturing*, 35 (2019) 1279-1285
- Marzorati S., Verotta L., Trasatti S.P. Green Corrosion Inhibitors from Natural Sources and Biomass Wastes, *Molecules*, 24 (2019) 48.
- Muthukumarasamy K., Pitchai S., Devarayan K., Nallathambi L. Adsorption and Corrosion Inhibition Performance of Tunbergia fragrans Extract on Mild Steel in Acid Medium, *Materials Today: Proceedings*, (2020) 23-31
- Palaniappan N., Cole I., Caballero-Briones F., Manickam S., Thomas K.J., Santos D. Experimental and DFT Studies on the Ultrasonic Energy-assisted Extraction of the Phytochemicals of Catharanthus roseus as Green Corrosion Inhibitors for Mild Steel in NaCl Medium, *RSC Advances*, 10 (2020) 5399-5411
- Solomon M.M., Umoren S.A., Obot I.B., Sorour A.A. Gerengi H. Exploration of Dextran for Application as Corrosion Inhibitor for Steel in Strong Acid Environment: Effect of Molecular Weight, Modification and Temperature on Efficiency. *ACS Appl. Mater. Interfaces* 10 (2018) 28112-28129
- Verma C., Ebenso E.E., Bahadur I., Quraishi M.A. Alkaloids as Green and Environmental Benign Corrosion Inhibitors: An Overview, *International Journal of Corrosion and Scale Inhibition*, 8 (2019) 512-528



## Production of Biodiesel from Orange Peel and Avocado Seed Oils; Effect of Reaction Parameters on Production Efficiency

Sylvester O. ANYIKWA<sup>1,2\*</sup>, Stanley M. NWAKAUDU<sup>1</sup>, Angela A. NWAKAUDU<sup>3</sup>, Boniface C. NGOLUBE<sup>1</sup>, Chigoziri N. NJOKU<sup>1,4\*</sup>

<sup>1</sup>Department of Chemical Engineering, Federal University of Technology, PMB 1526, Owerri, Nigeria

<sup>2</sup>Department of Chemical Engineering, Chukwuemeka Odumegwu Ojukwu University, PMB 02, Uli Nigeria

<sup>3</sup>Department of Food Science and Technology, Federal University of Technology, PMB 1526, Owerri, Nigeria

<sup>4</sup>Africa Center of Excellence in Future energies and Electrochemical System (ACE-FUELS), Federal University of Technology, PMB 1526, Owerri, Nigeria

<sup>1,2\*</sup>[anvikwasylvester@gmail.com](mailto:anvikwasylvester@gmail.com), <sup>1</sup>[stanley.nwakaudu@futo.edu.ng](mailto:stanley.nwakaudu@futo.edu.ng), <sup>3</sup>[angela.nwakaudu@futo.edu.ng](mailto:angela.nwakaudu@futo.edu.ng), <sup>1</sup>[boniface.ngolube@futo.edu.ng](mailto:boniface.ngolube@futo.edu.ng),  
<sup>1,4\*</sup>[chigoziri.njoku@futo.edu.ng](mailto:chigoziri.njoku@futo.edu.ng)

\*Corresponding author

---

### ABSTRACT

Comparative analysis of the effect of reaction parameters on the production of biodiesel from two different non-edible oils (orange peel oil and avocado seed oil) was carried out of the non-edible oils from the orange peel and avocado seed with the aid of a soxhlet extractor. (N-hexane was used for the extraction) Orange peel gave a percentage oil yield of 14.2%, while that of avocado seed was 20.5%. Transesterification reaction was carried out by a reaction between methanol and oil with sodium hydroxide (NaOH) as the catalyst. The varying reaction parameters considered were a temperature of 30-80°C, catalyst concentration of 0.03-0.3, and methanol to oil ratio of 1:3-1:95. For avocado oil, an optimum yield of 90.23% was obtained at a temperature of 45°C, catalysts concentration of 0.3 and alcohol to oil ratio 9:1; an increase in methanol to oil ratio has a greater effect on the yield than temperature. For the orange oil, to obtain an optimum yield of 91.03%, the optimum conditions are a temperature of 60°C, catalyst concentration of 0.36, and alcohol to oil ratio of 6:1. It was concluded that orange oil gives a greater biodiesel yield than avocado seed oil.

**Keywords:** Orange Peel Oil, Avocado Seed oil, Biodiesel, Transesterification, Response Surface Methodology

### 1. INTRODUCTION

The concern for the fast depletion of petroleum oil and its environmental impact has shifted interest to alternative sources of fuels, particularly fuels, which are renewable and environmentally friendly (Demirbas, 2008). Thus, varieties of virgin, non-edible, and waste vegetable oil have been sourced for the production of biofuels (Maniak *et al.*, 2009). The choice of biofuels over diesel fuel includes its portability, availability, renewability, higher combustion efficiency, higher octane number, higher biodegradability, high flash point, inherent lubricity, and lower sulfur and aromatic contents (Knothe, 2005).

The major percentage of energy used in the world today is from fossil fuel sources. These fossil fuels are nonrenewable resources that take millions of years, and their reserves are being depleted faster than they are being regenerated. They are the major contributor and sources of greenhouse gases, air pollution, and global warming. Some of the emissions generated from these fossil fuels: are CO, CO<sub>2</sub>, NO<sub>x</sub>, SO<sub>x</sub>, unburnt or partially burns HC, and particulate. Biodiesel, a form of biofuel is an answer to this call. It is a fuel derived from renewable biological sources to be used in a diesel engine. Biodiesel fuels are recently attracting increasing attention worldwide as a blending component or a direct replacement for diesel fuels in vehicle engines. B20 can be used in all diesel equipment and are compatible with most storage and distribution equipment. This low-level blend generally does not require any engine modifications. Higher blends, even B100, can be used in many engines built with little or no modifications. Though, biodiesel is gaining popularity more than 95% of the renewable resources used for its production are edible oils and this has been in conflict with food consumption and is also more expensive than petroleum diesel.

Due to this fact, it is necessary to look into non-edible oils which are not competitive for consumption and are also cheap. Globally, a large number of non-edible oil plants are readily available in nature. The Energy Policy Act (EPAct 1992 and 2005). The ideal vegetable for biodiesel must be readily available, its plants should be easy to cultivate, and its composition must include a high percentage of monounsaturated fatty acids. Based on this criterion, orange peels and avocado pear seeds be useful renewable sources for biodiesel production.



Biodiesel is referred to as vegetable oil or animal fat-based diesel fuel that is composed of long-chain alkyl (methyl, ethyl, and propyl) ester of long chain Fatty acid derived from renewable lipid sources. It is a diesel fuel substitute that is produced from renewable sources of energy. Biodiesel is manufactured from the process of trans-esterification as a result of the reaction between vegetable oil and animal fat with methanol and ethanol in the presence of a catalyst such as sodium hydroxides to yield glycerin and biodiesels. (The American Taxpayer Relief Act of 20 12 Public Law) There are two types of oils; edible and non-edible oils. Edible oils are the major sources to produce biodiesel fuels like sunflower, soybean, and palm oils. Due to higher prices of edible vegetable oils compared to diesel fuels, waste vegetable oils and non-edible crude vegetable oils (mango oil, orange oil, pumpkin oil, avocado oil, beniseed oil), etc., are now sued as biodiesel sources. However, there could be disadvantages to using edible oils such as higher viscosity, lower volatility, the reactivity of unsaturated hydrocarbon chains, etc. Due to these disadvantages, vegetable oils are not used directly as biodiesels, so there are methods to enhance vegetable oil's characteristics for biodiesel production by blending the biodiesel from these oils with ozonated vegetable oils which increases the acid value and decreases the viscosity of the oil and also prevent the agglomeration of biodiesel into the solidified materials, giving crystals. etc.

The aim and objective of this research work include but are not limited to improve air quality and the environment, provide safety benefits, and aid Engine operation. Figure 1 shows the total world energy consumption.

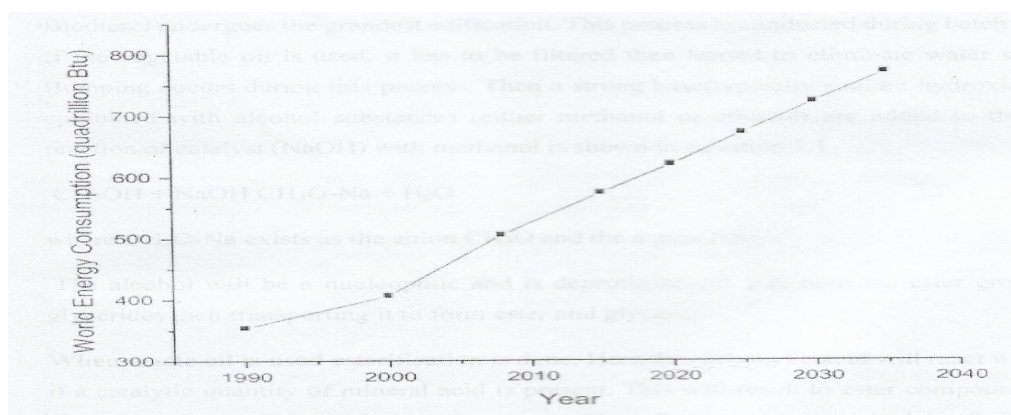


Figure 1: Total world energy consumption (1990-2035)  
(source: united states energy information administration)

## 2.0 MATERIALS AND METHOD

### 2.1 Materials

The following materials and equipment were used in this research work. Oil extracted from orange peel and avocados pear seeds n-hexane and methanol solution was used for extraction of the oil from the materials. Sodium hydroxide (NaOH) was used to vary the parameters. Distilled water was used for dilution sulphuric acid (H<sub>2</sub>SO<sub>4</sub>) used for temperature reduction. Electronic weighing balance was used for weighing the weight of the material while all other reagents and equipment used for the analysis were of standard grade.

### 2.2 Method

#### 2.2.1 Material preparation

Oranges and avocados pear were obtained from a local market in Owerri, Nigeria. The peels of the oranges and seeds of the avocado pears were removed and cut into smaller sizes and sun-dried for 72 hours to reduce the moisture content to obtain more oil. The dried orange peels were blended in an electronic blender and sieved with the aid of a mesh to remove the unwanted particulate substance. The final product should be an averagely coarse aggregate. The same method was repeated for avocado pear seed.

#### 2.2.2 Oil extraction

The coarse aggregate was then weighed with an electronic weighing balance and transferred to a soxhlet extraction set up and 300ml n-hexane was used as the extraction solvent at 68°C, (boiling temperature of hexane) for 48 hours in an electric heater. After the oil has been drained from the sample completely, it will be removed, and the chamber will be filled with a fresh weighed sample. This continued until a significant amount of oil was extracted. The resulting solution of the oil and hexane was heated to evaporate n-hexane and obtain pure orange oil. The same procedure will be repeated for the extraction of avocado pear seed oil. The percentage of the oil was calculated by using equation 2.1.

$$\text{Percentage oil yield} = \frac{\text{weight of oil}}{\text{weight of sample}} \times 100 \quad (2.1)$$

### 2.2.3 Determination of free fatty acid (FFA) of the oil for the production of biodiesel

1g of the oil was placed in a conical flask containing 25ml of propanoic isopropyl alcohol. Then 2 -3 drops of an indicator preferably phenolphthalein was added to the oil. Next, the oil indicator solution was titrated against 0.1M NaOH. The average titer value after three titrations was used to calculate the acid value and FFA value of the oil using equations 2.2 and 2.3 respectively.

$$\text{Acid value} = \frac{\text{titre value} \times \text{concentration of NaOH} \times 56.1}{\text{Weight of oil}} \quad (2.2)$$

$$\text{FFA} = \frac{\text{Acid value}}{2} \times 100 \quad (2.3)$$

### 2.2.4 Acid-catalyzed esterification reaction

When calculated, the FFA of avocado pear seed oil was 0.52% while that of orange oil was beyond 2%, the FFA of orange oil has to be reduced to 2% or even below.

The crude non-edible oil was heated at 60°C for about 10 minutes; sulphuric acid was used as a catalyst. The sulphuric acid and methanol were added to the preheated oil in a ratio of 6:1 (alcohol: oil) and the resulting mixture was stirred on a magnetic hot plate for 1 hour at 50°C, after which it was allowed to settle for 2 hours. Two layers were expected, the preheated oil was separated from the methanol-water phase at the top, and the bottom phase containing the oil was collected for base-catalyzed transesterification. The oil was tested again to ensure that the FFA has been reduced to 2% or less, following the test for FFA as described above.

### 2.2.5 Statistical analysis

The design expert software version 11 was employed to design the experiment and obtain the number of experimental runs using the central composite design (CCD) by varying the reaction parameters considered within the ranges as follows: Temperature: 30°C – 80°C, Oil-methanol ratio: 1:3 to 1:95. Catalyst concentration: 0.03 - 0.4M

### 2.2.6 Base-catalyzed transesterification (Biodiesel Production)

An oil quantity of 20g was used for each based catalyzed transesterification. 1% wt of 0.1M sodium hydroxide (NaOH) was used as a catalyst here, and methanol, still as the alcohol at a ratio of 3:1 (alcohol: oil). The alcohol base mixture was added to the oil and preheated in a water bath with a magnetic stirrer at 45°C for 1 hour. The phases of the transesterification product were separated with the bottom layer drained using a separation funnel. The top layer containing the oil methyl ester was collected. This entire experiment was repeated for each of the two different oils at temperatures of 30°C to 80°C, the molar ratio of alcohol to oil is 1:3 to 1:95, and the concentration of catalyst was 0.02 to 0.4 following the design of the experiment. The biodiesel yield (y) was recorded against the reaction parameters

$$\text{Biodiesel yield (\%)} = \frac{\text{Weight of Biodiesel}}{\text{Weight of oil}} \times 100 \quad (2.4)$$

## 3.0 RESULTS AND DISCUSSION

### 3.1 Free fatty acid level

The percentage yield of avocado oil was calculated to be 20.5%, while that of orange oil was 14.2%. Titration was carried out on both oils to determine the percentage of free fatty acid because this will determine if the oil will be acid esterified before use in producing biodiesel. If the free fatty acid level obtained is greater than 2%, then esterification will be carried out to reduce it after titration, the free fatty acid level of avocado oil was 1.7% while that of orange oil was 9.6%, esterification was carried out on the orange oil to reduce the FFA. After the esterification process, titration was carried out again on the oil, and the free fatty acid of the oil was reduced to 1.2%. The results of orange oil and avocado oil are shown in Table 1.

Table 1: Titration results obtained from orange and avocados oils

	1 <sup>st</sup> reading (cm <sup>3</sup> )		2 <sup>nd</sup> reading (cm <sup>3</sup> )		3 <sup>rd</sup> reading (cm <sup>3</sup> )				
	orange	Avocado	Orange	Avocado	Orange	avocado			
Initial reading	13.42	19.57	5.98	9.80	19.10	5.34	6.58	18.71	4.76
Final reading	16.85	20.00	6.58	13.42	19.57	5.95	9.80	19.10	5.34
Titre value	3.43	0.43	0.63	3.62	0.47	0.61	3.22	0.39	0.58

Orange<sup>•</sup> Pre-esterification; orange<sup>••</sup> = Post esterification

### 3.2 Design of Experimental Runs

The results shown in Table 2 were obtained from the design of experimental runs of orange oil using design software version 11.

Table 2: General Linear Model on Esterification of Orange oil with Biodiesel Yield as Response Variable.

Std	Run	Factor 1 A: methanol: oil ratio %w/w	Factor 2 B: Temperature (°C)	Factor 3 C: catalyst conc.	Response 1 Biodiesel yield (%)
16	1	0.825	60	0.2	85.88
13	2	0.825	60	0.0318207	82.26
20	3	0.825	60	0.2	85.88
14	4	0.825	60	0.368179	91.03
3	5	0.75	70	0.1	78.73
5	6	0.75	50	0.3	90.75
4	7	0.9	70	0.1	82.77
15	8	0.825	60	0.2	85.88
12	9	0.825	76.8179	0.2	84.89
7	10	0.75	70	0.3	81.74
17	11	0.825	60	0.2	85.04
18	12	0.825	60	0.2	85.88
8	13	0.9	70	0.3	85.00
1	14	0.75	50	0.1	81.45
10	15	0.951134	60	0.2	76.81
9	16	0.698866	60	0.2	75.54
19	17	0.825	60	0.2	85.88
2	18	0.9	50	0.1	78.80
11	19	0.825	43.1821	0.2	85.45
6	20	0.9	50	0.3	81.22

Table 3: Response to biodiesel yield

Source	Sum of square	Df	Mean square	F-value	Source	
Model	315.95	9	35.11	70.43	<0.0001	Significant
A-methanol: oil ratio	0.7293	1	0.7293	1.46	0.00023	
B-temperature	5.96	1	5.96	11.96	0.0061	
C-catalyst conc.	103.57	1	103.57	207.79	<0.0001	
AB	23.05	1	23.05	46.25	<0.0001	
AC	1.58	1	1.58	3.18	0.1050	
BC	19.16	1	19.16	38.43	0.0001	
A <sup>2</sup>	152.83	1	152.83	306.61	<0.0001	
B <sup>2</sup>	0.0840	1	0.040	0.1684	0.6902	
C <sup>2</sup>	2.86	1	2.86	5.73	0.0377	
Residual	4.98	10	0.4985			
Lack of fit	0.0727	5	0.0145	3.02	0.1254	Not significant
Pure error	0.0241	5	0.0048			
CorTotal	320.92	19				

Factor coding is **coded**; the Sum of squares is **type III- Partial**

The result in Table 3 shows the reaction parameter, obtaining the P-value and F-Value. The model F-Value of 70.43 implies the model is significant. There is only a 0.01% chance that an F-value this large could occur due to noise. A **P-value** less than 0.0500 indicate model terms are significant. In this case, B, C, AB, BC, A<sup>2</sup>, C<sup>2</sup> are significant model terms. Values greater than 0.1000 indicates the model terms are not significant. If there are many insignificant model terms (not counting those required to support hierarchy), model reduction may improve the model. The **lack of fit F-value** of 7.48 implies the lack of fit is significant. There is only a 2.28% chance that a lack of fit F-value this large could occur due to noise. A significant lack of fit is bad-we want the model to fit. The result in Table 4 reports the experimental runs and their corresponding actual and predicted values.

Production of Biodiesel from Orange Peel and Avocado Seed Oils; Effect of Reaction Parameters on Production Efficiency

Table 4: Report of the actual value and predicted value

Run order	Actual value	Predicted value	Residual	Leverage
1	85.88	85.72	0.1592	0.166
2	82.26	82.35	-0.0885	0.607
3	85.88	85.72	0.1592	0.166
4	91.03	91.61	-0.5814	0.607
5	78.73	78.59	0.1374	0.670
6	90.75	89.71	1.04	0.670
7	82.77	83.34	-0.5697	0.670
8	85.88	85.72	0.1592	0.166
9	84.89	84.39	0.4960	0.607
10	81.74	81.90	-0.1553	0.670
11	85.04	85.72	-0.6808	0.166
12	85.88	85.72	0.1592	0.166
13	85.00	84.86	0.1375	0.670
14	81.45	80.21	0.3362	0.670
15	76.81	76.90	-0.0886	0.607
16	75.54	76.12	-0.5813	0.607
17	85.88	85.72	0.1592	0.166
18	78.80	78.17	0.6290	0.670
19	85.45	86.62	-1.17	0.607
20	81.22	85.88	0.3363	0.670

Figures 2 and 3 show the three-dimensional diagram of the effect of reaction parameters on biodiesel yield. In both figures, the biodiesel yield increased with increase in the reaction parameters.

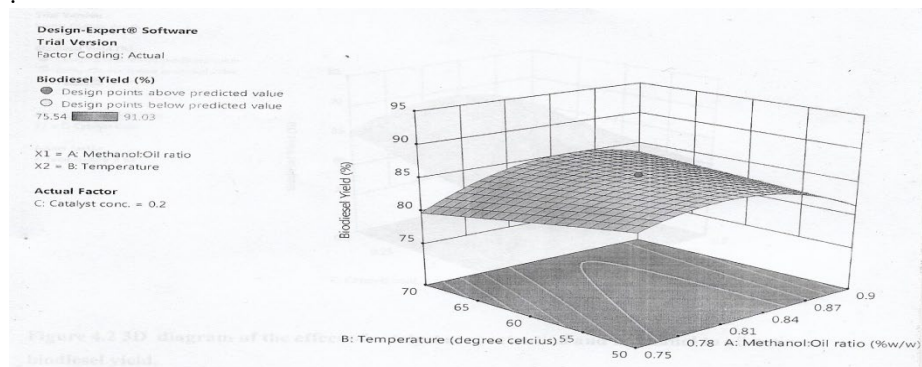


Figure 2: 3D Diagram of the effect of temperature and methanol to oil ratio in biodiesel yield.

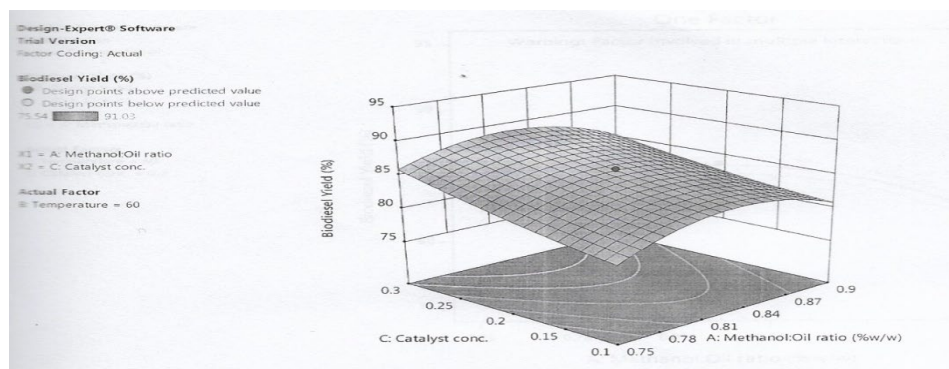


Figure 3: 3D Diagram of the effect of catalyst concentration and methanol to oil ratio on biodiesel yield.

#### 4.0 CONCLUSION

Biodiesel from avocado oil is obtained by the transesterification process while that of orange oil is obtained by the esterification process to reduce the FFA before it is used for the production of biodiesel. It was observed from the experimental runs for orange oil that to obtain an optimum yield of 91.03%, the optimum conditions are a temperature of 60°C, catalyst concentration of 0.36, and alcohol to oil ratio of 6:1. For avocado oil, to obtain an optimum yield of 90.23%, the optimum conditions are a temperature of 45°C, catalyst concentration of 0.3 and alcohol to oil ratio 9:1. For the orange oil, a temperature higher than 60°C resulted in methanol loss because of vaporization and also resulted in fewer methyl esters content, catalyst concentration does not play a significant role here. Transesterification is an exothermic reaction, so the temperature rise pushed the equilibrium into the reactants side this is under research.

#### REFERENCES

- Abdel, F.M, H.A Farag, M.E Osman (2012). Production of biodiesel from non-edible oil and effect of blending with fuel on fuel properties. *IRACST engineering science and technology. An international journal (ESTIJ), Vol 2 No 4 22250-3498.*
- Ahmad, A. L.; Yasin, N.H.M, Derek, C.J.C. and Lim, J.K (2011). Microalgae as a sustainable energy source for biodiesel production: *A review. Renewable and sustainable energy reviews. Vol. 15, No 1. Pp584-593.*
- Ahmad, M., Khan, M., Zafar, M and Sultana, S (2011). Biodiesel from non-edible oil seeds: a renewable source of bioenergy, economic effects of biofuels production.
- Ahmia, A.C F. Danane, R Bessah and I. Boumesbah (2014). Raw materials for biodiesel production volarization of used edible oils. *Center de development des nergiesrenouvelables (CDER). Vol. 17(2) 335-343.*
- Akpan, A (2012). The potential of orange oil with diethyl-ether (DEE) as an alternative fuel for compression ignition engines. B.Eng thesis.
- Alemayehu, G and Amanu, L (2014). Production of biodiesel from non-edible oils and its properties. Department of chemistry, faculty of natural and computational sciences. Vol 3. No 4, 1544-1562.
- Alnuami, W; Buthainah, A., Eti, C.J., Jassim, L. I and Gomes, G. A. (2014). Evaluation of different materials for biodiesel production. *International journal of innovative technology and exploring engineering, 3(8) 1-8.*
- Antony, Raija, S., Robinson Smart, D.S and Robert Lee, C (2014). Biodiesel production from Jatropha oil and its characterization. *Research Journal of chemical sciences. 1(1) 81-85.*
- Anusi, M.O., Umenweke, G.C., K.B Oyoh., Nkuzinna, O and Njoku, C.N (2018). Characterization of non-edible plants for biodiesel production. *American journal of engineering research (AJER). Vol. 7(4).32-36.*
- Aransiola, E.F., Betiku, E., Ikhomoregbe, D.I.O and Ojumu, T.V (2012). Production of biodiesel from crude neem oil feedstock and its emissions from internal combustion engines. *African journal of Biotechnology, 11(22), 6178-6186.*
- Aransiola, E.F., Ojumu, T.V., Onyekola, O. O. and Ikhomoregbe, D.I.O (2012). A study of biodiesel production from non-edible oil seeds: *a comparative study. Open conference proceeding journal Vol 3, 18-22.*
- Ayhan, D., Abdullah, B., Waper, A and Manzor, S (2016). Biodiesel production from non-edible oils. *Energy exploration and exploitation. Vol 34(2) 290-318.*
- Ayhan, D., (2008). Biofuels sources, biofuels policy, biofuels economy and global biofuels production. *Energy conversion and management. 49. 2106-2116.*
- Barnwal, B.K and Sharma, M.P (2005). Prospects of biodiesel production from vegetable oils in india. *Renewable and sustainable energy reveiw, 90(3) 63-78.*
- Bello, E.I. and Agge, M (2012). Biodiesel production from groundnut oil. *Journal of engineering trends in engineering and applied sciences, 3(2) 276-280.*
- Bioengineering resources incc. [www.bioenergy.com](http://www.bioenergy.com)
- Bull, O.S and Obunwo, C.C (2014), Biodiesel production from oil of orange (citrus sinensis). *Peels as livestock. Vol 18(3) 371-373.*



## Analysis of Liquid Products of Pyrolyzed Low Density Polyethylene

Aishat Ayoola OSIGBESAN<sup>1\*</sup>, Adebola Femi ADE-AJAYI<sup>1</sup>, Ephraim Akuaden AUDU<sup>1</sup>, Zaharaddeen Sani GANO<sup>1</sup>, Jeffrey Tsware BARMINAS<sup>1</sup>

<sup>1</sup>*Petrochemicals and Allied Department, National Research Institute of Chemical Technology, Zaria*

[aishatosigbesan2011@gmail.com](mailto:aishatosigbesan2011@gmail.com), [phemmistic@gmail.com](mailto:phemmistic@gmail.com), [ephrain.audu@yahoo.com](mailto:ephrain.audu@yahoo.com), [zaharaddeenn@gmail.com](mailto:zaharaddeenn@gmail.com),  
[bjtsware@gmail.com](mailto:bjtsware@gmail.com)

\*Corresponding author

---

### ABSTRACT

Waste Low Density Polyethylene (LDPE) was pyrolyzed and reformed in an integrated pyrolysis and fixed bed reactor system at 400 and 450 °C respectively. The reforming was carried out with and without mordenite – based catalyst. The oils samples obtained were collected and analysed using Fourier Transform Infrared Spectroscopy (FTIR), Gas Chromatography - Mass Spectroscopy (GC-MS) and bomb calorimetry. The calorimetric analysis of the catalysed sample showed that the oil has a High Heating Value (HHV) of 43.40 MJ/Kg. The FTIR spectra showed that peaks of aliphatic hydrocarbons in the uncatalysed oil are more prominent than in that of the catalysed oil. Conversely, the peaks of aromatic hydrocarbons appeared to be more in the catalysed oil than in the uncatalysed oil. The GC-MS analysis confirmed high presence of aliphatic (alkane and alkene) hydrocarbons in the uncatalysed sample, which were lower in the catalysed sample. These differences showed that reforming took place in the presence of the mordenite – based catalyst. These results would serve as a basis for further works on pyrolysis technology.

**Keywords:** *Pyrolysis, Reforming, Catalyst, Pyrolysis oil, Hydrocarbons.*

### 1. INTRODUCTION

Disposal and proper management of municipal and industrial waste are issues that keep gaining global attention. These wastes which include plastics usually cause environmental menace. In Nigeria, the use of plastics such as low-density polyethylene (LDPE) for packaging drinking water has contributed greatly to the environmental pollution due to their non – biodegradability (Kehinde *et al.*, 2020).

In order to eliminate or reduce the environmental problems caused by waste plastics, many approaches have been developed. However, the approach with high prospects is the pyrolysis technology, which is a chemical recycling method (Serrano *et al.*, 2004). This technology converts the waste plastics to valuable chemicals and fuels (Palos *et al.*, 2021). Usually, the products of pyrolysis are a mixture of gaseous, liquid and solid hydrocarbons (Obeid *et al.*, 2014) which are however, crude but can be further processed to target specific usage.

Typically, pyrolysis process takes place at high temperatures between 300 and 900 °C (Jouhara *et al.*, 2018). Elordi *et al.* 2007 carried out the catalytic pyrolysis of polyethylene in spouted bed reactor (Elordi *et al.*, 2007) and obtained products ranging from C<sub>2</sub> to C<sub>9</sub>. They concluded that the rate of weight loss is greatly influenced by the presence of catalyst. Nema and Ganesh Phrasad, 2002 studied the plasma pyrolysis of medical waste. Carbon II oxide (CO), hydrogen (H<sub>2</sub>) and Carbon (IV) oxide (CO<sub>2</sub>), as well as C<sub>1</sub>- C<sub>5</sub> (i.e. CH<sub>4</sub>, C<sub>2</sub>H<sub>6</sub>, C<sub>3</sub>H<sub>8</sub>, NC<sub>4</sub>, IC<sub>5</sub> NC<sub>3</sub>) were produced after pyrolysis. Tsuji *et al.* 2001 pyrolyzed polyethylene, polypropylene and polystyrene plastic pellets in a two- stage thermal degradation process. The main component of the product gas for polyethylene and polypropylene were methane and olefins such as ethane and propene with some aromatic oils as by products.

An advanced method of tertiary recycling is the two stages process involving pyrolysis as the first stage and catalytic reforming as the second stage. Mochamad Syamsiro *et al.* 2013 reported on passing the products of pyrolysis through a catalytic reforming unit. They obtained and analysed wide range of products. The catalysts tested for the two stages recycling process include synthesized mordenite from Malaysian clay and commercial mordenite.

Ponnusamy *et al.* 2015 established the effective reforming of products of pyrolysis using several catalysts. They include zeolites like ZSM – 5, mesoporous MCM-41, USY,  $\text{SiO}_2\text{Al}_2\text{O}_3$ , natural zeolites and so on; other forms of catalysts are metal impregnated on zeolite support like Nickel on ZSM -5, Cobalt on mordenite, etc.

Consequently, at the National Research Institute for Chemical Technology, Zaria, the pyrolysis technology has been taken further to a stage of designing and fabricating state of the art reactor that could enhance the achievement of waste to wealth conversion. The reactor, an Integrated Pyrolysis and Fixed Bed Reactor was used to process wastewater sachets (LDPE) to fuel oil using a mordenite – based catalyst. The obtained fuel oil which is the liquid product of pyrolysis shall be analysed.

## 2. MATERIALS AND METHODS

The materials, equipment and experimental procedures are described as follows.

### 2.1 Materials:

Wastewater sachets (LDPE) was collected from Zaria environs, mordenite catalyst supplied by the Zeolyst International, pure Nitrogen gas supplied by Desko Gases Enterprises, Kaduna and sample collector / holder was purchased from Cardinal Scientific Supplies, Zaria.

### 2.2 Equipment:

Weighing Balance, KERN EW6000 – 1M was used for weighing the mass of feedstock and catalyst. Drying Oven, GENLAB model MINO/75/F/DIG for drying items. Muffle Furnace, Gallenkomp England SXL-1008 model was employed for the calcination of the catalyst; Digital Bomb Calorimeter for the measurement of the calorific value of the liquid product, Shimadzu Fourier Transform Infrared (FTIR) 8400S model used for the identification of the functional groups present in the liquid products and Agilent Gas Chromatography – Mass Spectrometer (GC-MS) used for the identification of the chemical constituents of the liquid products.

### 2.3 Pyrolysis set up:

The integrated pyrolysis and fixed bed reactor system was designed, fabricated and patented at the National Research Institute for Chemical Technology (NARICT), Zaria. The process flow diagram of the reactor system and its picture are shown in Figures 1 and 2 respectively.

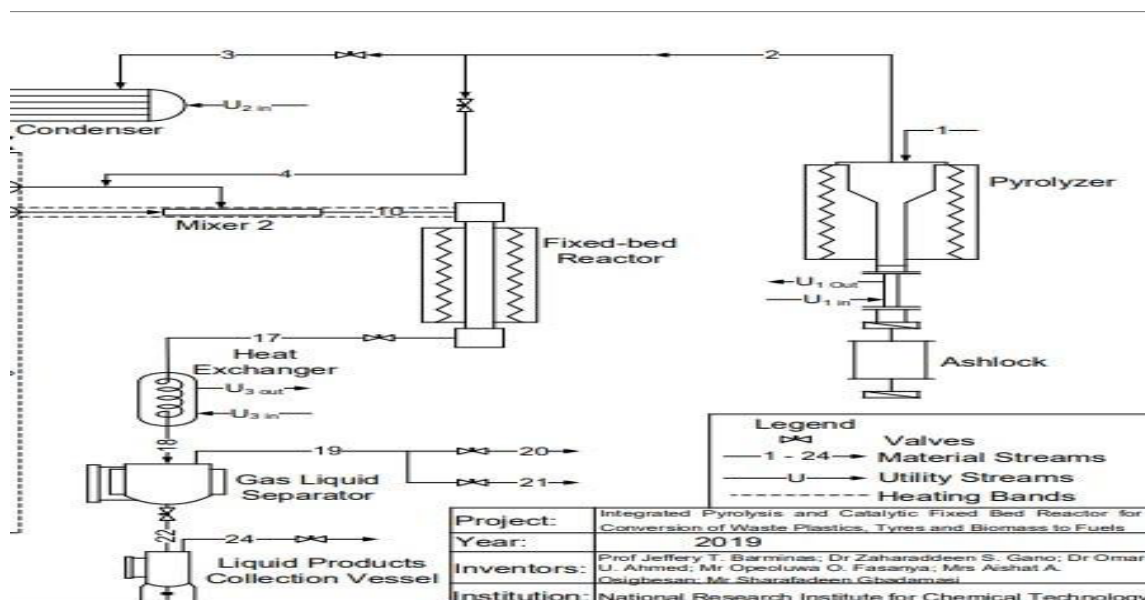


Figure 1: Process Flow Diagram of the Reactor System



Figure 2: The Integrated Pyrolysis and Fixed Bed Reactor System at the National Research Institute for Chemical Technology, Zaria.

#### 2.4 Experimental Procedures:

50 g of the waste LDPE was weighed and fed into the pyrolyzer whose internal temperature was set at 400 °C. Prior to the pyrolysis, the system was flushed with nitrogen gas for about 1 hour in order to create an inert system. Process activities in the reactor were monitored from the control panel. Reforming of the pyrolysis products took place in the fixed bed reactor loaded with 1 g of mordenite – based catalyst at a temperature of 450 °C. Products from the reformer were passed through a flash drum, condenser set at 13 °C and finally to the product collection tank.

#### 2.5 Characterization of the Liquid Products:

To determine the calorific value of the liquid product in this work, an Oxygen-Bomb Calorimeter was used.

#### 2.6 FTIR Analysis of the Liquid Products:

The liquid product obtained from each experimental run was analyzed using Fourier Transmission Infrared (FTIR) Spectrophotometer, Shimadzu IR-8400S. The functional groups present in the liquid sample were transmitted between the wavelength ranges of 4000 – 400  $\text{cm}^{-1}$ .

#### 2.7 GC-MS Analysis of the Liquid Products:

The chemical composition of the liquid product was analyzed using the Gas Chromatography – Mass Spectrometry technique as described by Medeiros, 2018 (Medeiros, 2018). The peaks were identified using the National Institute of Standards and Technology (NIST) reference database (library) of the GC-MS.

### 3. RESULTS AND DISCUSSION

For this work, two experiments were studied; uncatalyzed run (sample A) and catalyzed run (sample B). analysis of products from these experiments are as presented and discussed in the following subsections.

#### 3.1 Calorific Values:

High heating value (HHV) of the catalysed pyrolysis oil was found to be 43.40 MJ/Kg. Therefore, this suggests that this pyrolysis oil has heating values within the range reported for gasoline (42 – 46 MJ/Kg), diesel (42 – 45 MJ/Kg), kerosene (43.1 – 46.2 MJ/Kg) and heavy oil (40MJ/Kg) by works of Dash *et al.* (2015) and Rasul *et al.* (2021) (Dash *et al.*, 2015, Rasul *et al.*, 2021).

#### 3.2 Fourier Transform Infrared Spectroscopy Analysis

Figure 3 shows the FTIR spectra of liquid samples obtained from the pyrolysis of the LDPE without catalyst and with catalyst. Table 1 is an illustration of the functional groups of the HCs present in the oil samples as well as their corresponding wavebands.



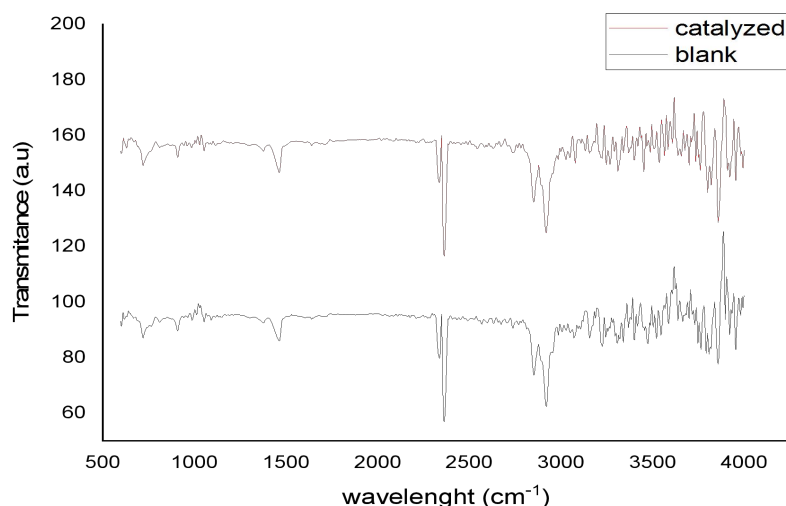


**Figure 3:** FTIR spectra of the liquid samples

**Table 1:** Prominent wavebands and their corresponding functional groups for the liquid products.

WAVEBANDS (cm <sup>-1</sup> )	BOND TYPE	FUNCTIONAL GROUPS
3020 – 3085	=C-H stretching	Aromatic
2845 – 2940	C-H Stretching	Aliphatic Alkane
2345 – 2370	C – C bending	Aliphatic
1640 – 1650	C = C stretching	Aromatic
1450 – 1490	C-C stretch (in – ring)	Aromatic
905 – 989	=C – H bending	Alkenes
695 – 775	C – H	Aromatic

The intensity of the aliphatic C-H (2915 – 2940 cm<sup>-1</sup>), aliphatic C-C (2345 – 2370 cm<sup>-1</sup>), symmetric methyl (2845 – 2860 cm<sup>-1</sup>) and CH<sub>2</sub> (1455 – 1465 cm<sup>-1</sup>) groups are much higher and prominent than that of the aromatic C=C (1640 – 1650 cm<sup>-1</sup>) and others. However, the intensities of the aromatic peaks in the catalysed product are more prominent than those in the uncatalysed product. This could be as a result of reforming that took place in the presence of the catalyst used. This result is in accordance with (Valiev and Zemskii, 2020).

The FTIR analysis therefore, shows that the use of catalyst greatly favoured the production of product fuels with significant intensity of alkane and alkene groups as well as of aromatic groups. This statement is in accordance with the report of Hakeem *et al.*, 2018 where various catalysts including mordenite were explored.

### 3.3 Gas Chromatography - Mass Spectroscopy (GC-MS) Analysis

The chemical compositions of the liquids obtained from the uncatalysed run and the catalysed run were analyzed by the GC-MS techniques. Figures 4a and 4b show the retention time and the abundance of the individual compounds detected and identified in the liquid products.

Figure 4a shows the chromatograph of the analyzed liquid obtained at 400 °C pyrolyser temperature. While figure 4b shows the chromatograph of the analysed liquid obtained from the reforming stage at 450 °C and 1 g of catalyst. These chromatographs moved from widely spread peaks of large hydrocarbons of retention time of almost 35 minutes to sharper peaks of lighter hydrocarbons of less retention time. This observation is further illustrated in Tables 2a and 2b.

## Analysis of Liquid Products of Pyrolyzed Low Density Polyethylene

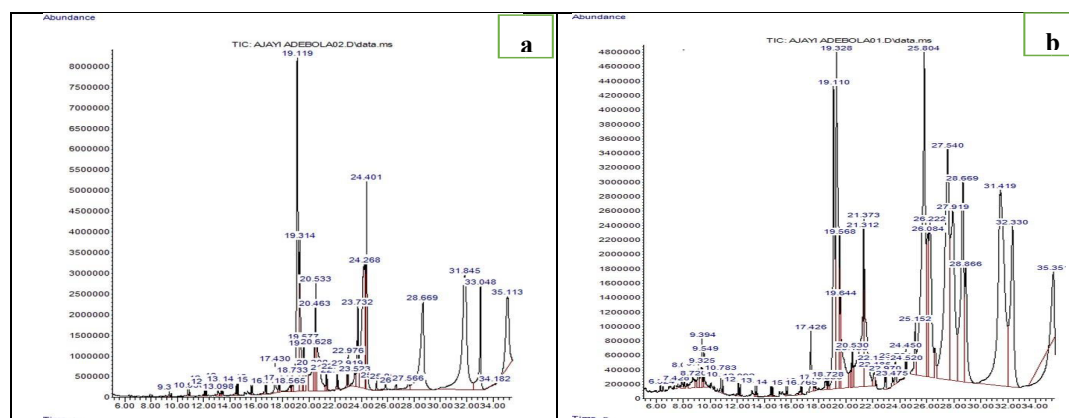


**Figure 4:** Chemical compositions of the liquid products obtained from GC – MS analysis of (a) uncatalysed (b) catalysed run.

**Table 2a:** The most abundant component of the GC-MS analysis of the liquid sample of LDPE at 400 °C

Uncatalysed (A)				
S / No.	Nomenclature	Retention Time (Minutes)	Hydrocarbon Type	No. Of Catoms
1	1-Tridecene	9.396	Olefin	C13
2	4-Tetradecene	10.786	Olefin	C14
3	Tetradecane	10.930	Paraffin	C14
4	9-Octadecene	12.096	Olefin	C18
5	Pentadecane	12.226	Paraffin	C15
6	Hexadecane	13.452	Paraffin	C16
7	Heptadecene	14.502	Olefin	C17
8	Heptadecane	14.614	Paraffin	C17
9	Eicosene	15.615	Olefin	C17
10	Octadecane	15.718	Paraffin	C20
11	Nonadecane	16.770	Paraffin	C18
12	Eicosane	17.774	Paraffin	C19
13	Hexadecadiene	18.565	Olefin	C16
14	Nonadecene	18.650	Olefin	C19
15	Heneicosane	18.733	Paraffin	C21
16	Docosane	19.652	Paraffin	C12
17	Tricosene	20.463	Olefin	C13
18	Tricosane	20.533	Paraffin	C13
19	1-Docosene	20.628	Olefin	C12
20	Tetracosane	21.377	Paraffin	C14
21	Heptacosane	22.192	Paraffin	C17
22	Hexacosene	24.268	Olefin	C16
23	Eicosene	26.639	Olefin	C20

**Table 2b:** The most abundant component of the GC-MS analysis of the reformed pyrolytic oil samples of LDPE at 450 °C

Catalysed (B)				
S /No.	Nomenclature	Retention Time (Minutes)	Hydrocarbon Type	No. of Catons
1	4-Undecene	6.324	Olefin	C11
2	Naphthalene	7.428	Cyclic	C10
3	1-Dodecene	7.912	Olefin	C12
4	Dodecane	8.081	Paraffin	C12
5	1-Cyclopenten-1-yl Benzene	8.720	Aromatic	C11
6	2-Methyl Naphthalene	9.325	Cyclic	C11
7	5-Tridecene	9.394	Olefin	C13
8	Tridecane	9.549	Paraffin	C13
9	4-Tetradecene	10.783	Olefin	C14
10	Undecane	10.926	Paraffin	C11
11	9-Octadecene	12.092	Olefin	C18
12	Pentadecane	12.223	Paraffin	C15
13	9-Eicosene	13.327	Olefin	C20
14	Hexadecane	13.448	Paraffin	C16
15	1-Heptadecene	14.497	Olefin	C17
16	Octadecane	15.712	Paraffin	C18
17	Nonadecane	16.765	Paraffin	C19
18	Eicosane	17.771	Paraffin	C20
19	Pyrene	18.556	Aromatic (PAH)	C16

Table 2a is an illustration of the composition of the pyrolysis oil obtained by blank run at 400 °C, the oil contains hydrocarbons, which are mainly olefins (C<sub>13</sub> – C<sub>20</sub>) and paraffin (C<sub>14</sub> – C<sub>21</sub>). While the oil obtained from the reforming (catalysed) stage consists of olefinic, paraffinic, cyclic and aromatic hydrocarbons. This composition is shown in table 2b. The olefins ranged from C<sub>11</sub> – C<sub>20</sub>, the paraffins ranged from C<sub>12</sub> – C<sub>20</sub>, 2-Methyl Naphthalene is the cyclic hydrocarbon, 1-Cyclopenten-1-yl Benzene is the aromatic hydrocarbon and pyrene is the polycyclic aromatic hydrocarbon (PAH).

The composition of the catalysed oil shows that cracking of some of the components of the uncatalyzed oil took place in the presence of the catalyst that was employed and at an elevated temperature of the fixed catalytic bed reactor. Thus, the GC-MS analysis confirms that using a suitable catalyst plays a key role in enhancing the cracking of the larger hydrocarbons leading to improving the quality of the liquid product. Furthermore, the liquid product can be said to contain kerosene range hydrocarbons (C<sub>11</sub> – C<sub>14</sub>), diesel and heavy fuel oil hydrocarbons (C<sub>11</sub> – C<sub>20</sub>).

#### 4. CONCLUSION

In this work, the liquid products of uncatalysed and catalysed pyrolysis of low-density polyethylene were analysed and compared. The uncatalysed and catalysed run proceeded at 400 and 450 °C respectively.

The high heating value (HHV) of the liquid product was found to be 43.40 MJ/Kg which is within the range of HHVs of some commercial fuel oils. The FTIR spectra of both samples showed strong absorption bands of stretching and bending vibrations of alkane, alkene and aromatic groups. However, the intensities of the absorption bands were more prominent in the catalysed product than in the uncatalysed. GC-MS analysis showed that the uncatalysed product constituted mostly aliphatic compounds mainly alkanes and alkenes of C<sub>13</sub> – C<sub>21</sub> while that of the catalysed process constituted alkanes,

alkenes and aromatics of C<sub>11</sub>–C<sub>20</sub>. This is an indication that reforming of the constituent compounds was achieved in the catalysed product. Hence, it can be concluded that employing a suitable catalyst and operating conditions can improve the quality of pyrolysis oil.

### ACKNOWLEDGEMENT

The authors sincere gratitude goes to the Director General of the National Research Institute for Chemical Technology, Zaria. Prof. J. T. Barminas for the financial and technical supports given the team to forge ahead in the continuous research on Pyrolysis Technology. The team leader is also acknowledged for his onward support to ensure the work continues favourably.

### REFERENCES

- Dash, A., Kumar, S. & Singh, R. K. 2015. Thermolysis of Medical Waste (Waste Syringe) to Liquid Fuel Using Semi Batch Reactor. *Waste and Biomass Valorization*, 6, 507-514.
- Elordi, G., Olazar, M., Aguado, R., Lopez, G., Arabiourrutia, M. & Bilbao, J. 2007. Catalytic pyrolysis of high density polyethylene in a conical spouted bed reactor. *Journal of Analytical and Applied Pyrolysis*, 79, 450-455.
- Hakeem, I. G., Aberuagba, F. & Musa, U. 2018. Catalytic pyrolysis of waste polypropylene using Ahoko kaolin from Nigeria. *Applied Petrochemical Research*, 8, 203-210.
- Jouhara, H., Ahmad, D., Van Den Boogaert, I., Katsou, E., Simons, S. & Spencer, N. 2018. Pyrolysis of domestic based feedstock at temperatures up to 300 °C. *Thermal Science and Engineering Progress*, 5, 117-143.
- KEHINDE, O., RAMONU, O. J., BABAREMU, K. O. & JUSTIN, L. D. 2020. Plastic wastes: environmental hazard and instrument for wealth creation in Nigeria. *Heliyon*, 6, e05131.
- Medeiros, P. M. 2018. Gas Chromatography–Mass Spectrometry (Gc–Ms). In: White, W. M. (ed.) *Encyclopedia of Geochemistry: A Comprehensive Reference Source on the Chemistry of the Earth*. Cham: Springer International Publishing.
- Nema, S. K. & Ganeshprasad, K. S. 2002. Plasma pyrolysis of medical waste. *Current Science*, 83, 271-278.
- Obeid, F., Zeaiter, J., Al-Muhtaseb, A. A. & Bouhadir, K. 2014. Thermo-catalytic pyrolysis of waste polyethylene bottles in a packed bed reactor with different bed materials and catalysts. *Energy Conversion and Management*, 85, 1-6.
- Palos, R., Gutiérrez, A., Vela, F. J., Olazar, M., Arandes, J. M. & BILBAO, J. 2021. Waste Refinery: The Valorization of Waste Plastics and End-of-Life Tires in Refinery Units. A Review. *Energy Fuels*, 35, 3529-3557.
- Ponnusamy, S. K., Bharathikumar, M., Prabhakaran, C., Vijayan, S. & Ramakrishnan, K. 2015. Conversion of waste plastics into low-emissive hydrocarbon fuels through catalytic depolymerization in a new laboratory scale batch reactor. *International Journal of Energy and Environmental Engineering*, 8.
- Rasul, S. B., Som, U., Hossain, M. S. & Rahman, M. W. 2021. Liquid fuel oil produced from plastic based medical wastes by thermal cracking. *Scientific Reports*, 11, 17048.
- Serrano, D., Aguado, J., Escola, J., Garagorri, E., Rodríguez, J., Morselli, L., Palazzi, G. & Orsi, R. 2004. Feedstock recycling of agriculture plastic film wastes by catalytic cracking. *Applied Catalysis B Environmental*, 49.
- Syamsiro, M., Hu, W., Komoto, S., Cheng, S., Noviasri, P., Prawisudha, P. & Yoshikawa, K. 2013. Co-Production of Liquid and Gaseous Fuels from Polyethylene and Polystyrene in a Continuous Sequential Pyrolysis and Catalytic Reforming System. *Energy and Environment Research*, 3.
- Tsuji, T., Tanaka, Y. & Itoh, H. 2001. Two-stage thermal gasification of polyolefins. *Journal of Material Cycles and Waste Management - J MATER CYCLES WASTE MANAG*, 3, 2-7.
- Valiev, A. & Zemskii, D. 2020. The catalytic cracking of the off-spec polyisoprene rubber thermolysis products. *E3S Web of Conferences*, 157, 02027.



## Synthesis and Characterization of Fe Doped Mordenite as a Prospective Catalyst for Pyrolysis of Waste Plastics

Ephraim Akuaden Audu<sup>a\*</sup>, Zaharaddeen Sani Gano<sup>a</sup>, Aishat Ayoola Osigbesan<sup>a</sup>, Adebola Femi Ade-Ajayi<sup>a</sup>, Jeffrey T. Barminas<sup>a</sup>

<sup>a</sup> National Research Institute for Chemical Technology, Basawa, Zaria, Kaduna State, Nigeria  
<sup>a\*</sup> [akuadenuadu@gmail.com](mailto:akuadenuadu@gmail.com), <sup>a</sup> [zaharaddeenn@gmail.com](mailto:zaharaddeenn@gmail.com), <sup>a</sup> [aishatosigbesan2011@gmail.com](mailto:aishatosigbesan2011@gmail.com), <sup>a</sup> [pheммistic@gmail.com](mailto:pheммistic@gmail.com),  
<sup>a</sup> [btsware@gmail.com](mailto:btsware@gmail.com)

\*Corresponding author

### ABSTRACT

In this work, metal doped on mordenite (MO) was synthesized using wet impregnation method for potential use as catalyst in the pyrolysis of waste plastics. Varying concentrations of iron was considered for catalyst formulations. The obtained catalyst samples were characterized using Fourier Transform Infrared (FTIR) spectroscopy, Energy Dispersive X-ray (EDX) and pyridine FTIR. The FTIR spectra revealed the presence of basic peaks 3411, 1640, 1250, 950, 769, 586 and 450  $\text{cm}^{-1}$  found in mordenite both in Fe doped and unmodified mordenite. EDX analysis confirmed the synthesis of Fe-MO and further gave iron concentrations of 0.99, 2.45 and 3.89 %wt corresponding to 1, 3, and 5 %wt that were prepared. Results of Pyridine FTIR on the samples revealed Bronsted acidic site at 1534  $\text{cm}^{-1}$ . Acidity of mordenite was improved as Fe loading increased signifying that the sample could promote cracking of pyrolysis products into shorter chain hydrocarbons. This suggests that Fe doped on mordenite has improved the characteristics of the catalyst which can enhance its activity, and selectivity towards lighter hydrocarbons in pyrolysis of plastics. Overall, the results showed iron doped mordenite exhibits properties that have high potential for application as catalysts in pyrolysis of plastics wastes.

**Keywords:** catalyst, mordenite, pyrolysis, acidity, impregnation.

### 1. INTRODUCTION

The use of catalyst in chemical processes not only reduces the time of reaction, it also helps in selectivity towards targeted products, decreases the quantity of by-products formed and cut down cost of production by making a catalysed reaction more energy efficient.

Pyrolysis of plastic wastes such as low-density polyethylene (LDPE), high density polyethylene (HDPE), polyethylene terephthalate (PET) and polystyrene (PS) have attracted considerable attention from researchers as observed in numbers of publications in that area. Getting the right catalyst for pyrolysis reaction is a major factor in obtaining desired product. The non-catalytic or thermal pyrolysis of plastics is a high energy, endothermic process requiring temperatures of at least 350–500 °C (Murata *et al.*, 2004). The mechanism in catalytic pyrolysis involves activities on the surface and in the pores of the solid acid catalyst which leads to cracking, isomerization, oligomerization, cyclisation and aromatization reactions. These mechanisms are mainly influenced by the acidity, density and porosity of the catalyst (Fadillah *et al.*, 2021). Catalytic pyrolysis has been widely recognized as a promising technique for the thermochemical conversion of waste polymers and lignocellulosic biomass to useful chemicals and fuel additives (Zhang *et al.*, 2018). Some works have reported temperatures range as high as 700–900 °C are needed to obtain reasonable pyrolysis (Mastral *et al.*, 2002). However, catalytic pyrolysis of plastics has been reported to be successful at lower temperature range (300–500 °C) with higher yield Panda *et al.* (2019), (Sriningsih *et al.*, 2014, Jan *et al.*, 2010).

Mordenite has desirable properties that make them to be used as catalyst and catalyst support (Maretto *et al.*, 2014). They are microporous, microcrystalline aluminosilicate materials (Neamtu *et al.*, 2004) with a three-dimensional structure and four-connected framework built from tetrahedral of  $[\text{SiO}_4]^{4-}$  and  $[\text{AlO}_4]^{5-}$  bonded together via the oxygen atoms.  $\text{Al}^{3+}$  can replace  $\text{Si}^{4+}$  resulting in a negatively charged framework (Blanco *et al.*, 2014). Mordenite is characterized by the presence of regular voids capable of allowing the adsorption of small and medium-sized ions and molecules due to their high internal surface area. The effect of loading Fe on to mordenite has been shown to reduce the activation energy for pyrolysis of plastics and also improve reactivity by increasing the surface area of the catalyst (Miskolczi *et al.*, 2019).

Literature has reported various routes for the synthesis of Fe-mordenite modified catalyst, they include methods like chemical vapour deposition (CVD) of volatile iron compounds (Hensen *et al.*, 2004), solid ion exchange (Rauscher *et al.*, 1999), wet ion exchange (Pieterse *et al.*, 2007) and wet impregnation (Kostyniuk *et al.*, 2019).

In this work, we carried out impregnation of Fe on mordenite (1, 3 and 5 wt%) and then characterized the obtained samples using SEM-EDX, FT-IR spectroscopy and acidity test for its applicability as catalyst in pyrolysis of plastics.

## 2. MATERIALS AND METHODS

### 2.1 Equipment, Materials and Reagents:

Iron III Nitrate Nonahydrate (CDH New Delhi, India), Mordenite purchased from Zeolyst (CBV21A Oosterhorn, Netherland), Hydrochloric acid (37% Sigma Aldrich), Distilled water from Water Still Aquatton (A8000) Distiller, Wattman No. 1 Filter paper. Equipment includes analytical weighing balance, digital hotplate magnetic Stirrer (Stuart CD 162), muffle furnace (SXL – 1008 Gallenkomp, England) and drying oven (Genlab). All reagent was used as supplied by the manufactures.

### 2.2 Synthesis of MO-Fe

#### 2.2.1 Acid treatment of the Mordenite

Mordenite 100 g was calcined in a muffle furnace at a temperature of 550 °C for 3 hours to burn off any inorganic material present and free up pore spaces. 50 g of the calcined mordenite was weighed out in a 250 mL conical flask and 500 mL of 1 M HCl solution was carefully added. The mixture was placed on a magnetic stirrer and agitated for 1 hour. On completion of agitation the mixture was filtered to remove residual HCl then it was dried in the oven at 120 °C for a duration of 3 hours (Syamsiro *et al.*, 2014). The acidified dried sample was crushed into powder after cooling.

#### 2.2.2 Doping of Iron into mordenite support

Fe was doped onto acidified mordenite support using the wet impregnation method. A calculated amount of the precursor (Iron III Nitrate Nonahydrate) was dissolved in 100ml of distilled water to obtain Iron III Oxide at different percentages (1, 3 and 5%). 20 g of acidified mordenite was placed in a beaker, the solution of the precursor was added and stirred at 300 RPM on a hotplate with magnetic stirrer at 70 °C until a paste is obtained. The paste was dried in an oven at 120 °C for 2 hours then crushed and further calcined at 550 °C for 3 hours.

### 2.3 Characterization Techniques

To confirm that the integrity of the mordenite functional groups is intact after impregnation, Infrared data was collected using a Shimadzu-8400S Fourier Transform Infrared Spectrometer (Kyoto, Japan) over the range of 4000–400  $\text{cm}^{-1}$ . Elemental composition of the sample was determined to ascertain the level of Fe doping on each sample using Phenom world SEM-EDX analyzer (Thermo Fischer. Waltham, U.S).

Acidity test using Pyridine FTIR method was done using 0.2 g of each sample was weighed in a small flat dish and placed in an oven for degassing at 200 °C for 2 hours. The degassed samples were immediately placed in a desiccator containing pyridine at the bottom. The set up was then connected to a vacuum pump. The pump was turned on and pyridine adsorption was allowed for 30 minutes. After the adsorption process, samples were quickly transferred into a second desiccator for stabilization. Thereafter, Fourier Transform Infrared Spectroscopy (FTIR) analysis was carried out on the samples using Attenuated Total Reflectance (ATR) in the range 1400 to 1700  $\text{cm}^{-1}$  (Rasheed and Meera, 2016).

## 3. RESULTS AND DISCUSSION

### 3.1 Fourier Transform Infrared Spectroscopy (FTIR) analysis

FTIR was carried out to ascertain if the modification by Fe impregnation has altered the original functional groups of the mordenite. Figure 1 displays the FTIR spectra of unmodified mordenite and Fe impregnated mordenite (1, 3, 5 wt%). Basic peaks of mordenite were all retained in the Fe modified mordenite regardless of the Fe wt% loading signifying that the effect of impregnation is nondestructive to the basic structure of the mordenite. The broad peak at 3411  $\text{cm}^{-1}$  and the peak at denotes a characteristic stretching vibration of hydroxyl (-OH) group due adsorbed water molecules within the mordenite framework. Similarly, the peak at 1640  $\text{cm}^{-1}$  depicts a stretching vibration of coordinated hydroxyl groups attached to mordenite surface (Gougazeh and Buhl, 2014). The high-intensity vibration frequency at the band 1065  $\text{cm}^{-1}$  falls between spectral ranges 1250 and 950  $\text{cm}^{-1}$  which suggests vibrations due to the tetrahedral asymmetric stretching of  $\text{TO}_4$  (T= Al, Si) bonds (Abidin *et al.*, 2017). A low intensity peak found at 769  $\text{cm}^{-1}$  band depicts a symmetric stretching vibration of Si-O-Si and Al-O-Si bonds. The peaks at 769 and 586 and 450 can be ascribed to the symmetric stretching and asymmetric stretching of crystalline mordenite (Kalhor *et al.*, 2020). Findings implies that doping of Fe into mordenite did not deform the parent mordenite structure. This suggests that the Catalytic activity of mordenite is still unaltered.

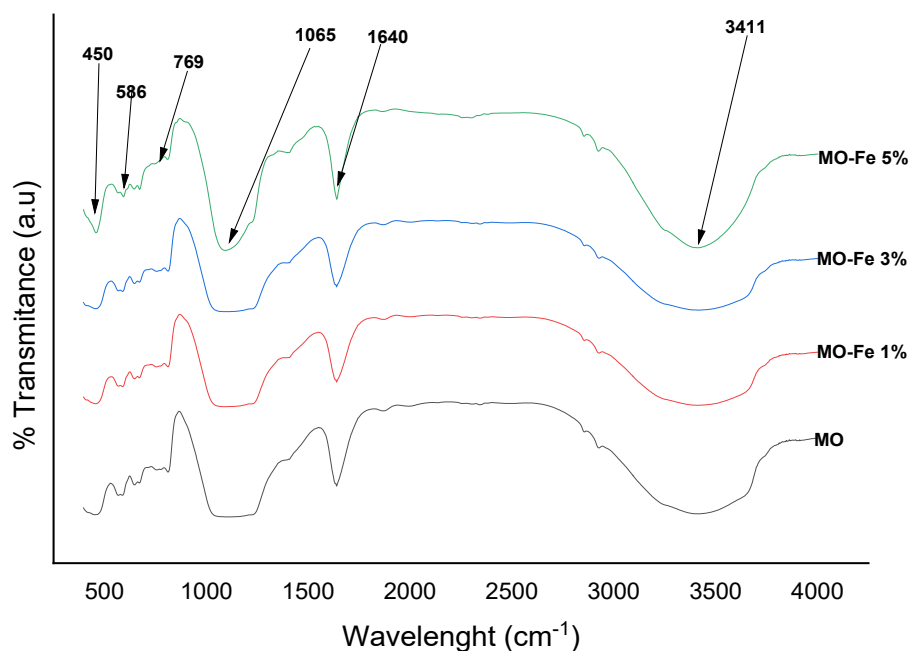


Figure 1: FTIR spectra of mordenite (MO) and Fe doped mordenite (MO- 1, 3, 5 wt%)

### 3.2 Elemental composition Analysis

In order to confirm the synthesis of Fe – MO and quantity of Fe doped on each of the samples after impregnation, SEM-EDX was performed. Table 1 shows the atomic weight of the elemental composition present in the samples. It can be seen that Fe was present in all the samples confirming the success of the doping. Also, as expected the quantity (atomic conc.) of Fe in the samples were found to be 0.99, 2.45 and 3.89 %wt for 1, 3 and 5 wt% respectively indicating that the impregnation was successful. This confirms that increasing metal loading resulted in a corresponding increase in concentration of Fe bonded into the mordenite framework. Similar finding was reported by the works of (Permata and Trisunaryanti, 2020).

Table 1: Elemental composition (atomic conc.) of Fe doped mordenite (1, 3, 5 wt%)

Element	MO	MO-1 wt%	MO- 3wt%	MO-5 wt%
Si	58.45	38.82	36.12	46.48
O	12.62	30.92	29.33	30.32
Fe	0.76	0.99	2.45	3.65
Al	4.48	-	3.12	4.68
C	4.21	18.49	17.85	9.90

### 3.3 Acidity Test

Pyridine FTIR was carried out in order to detect the acidity of the samples. Acidity is usually confirmed by the presence of Lewis acid (LA) and Bronsted acid (BA) sites in the samples (Penkova *et al.*, 2014).

Figure 2 shows the spectra of pyridine FTIR on mordenite impregnated with 1, 3 and 5 wt% Fe. The peaks located at 1534  $\text{cm}^{-1}$  suggest a characteristic adsorption peak which corresponds to a 19a vibration mode ascribed to pyridinium ions adsorbed on Bronsted sites (Cheng *et al.*, 2018). Interestingly, the effect of increase in metal loading was found to increase the acidity of the catalyst as shown from the corresponding increase in absorbance intensity (0.00934, 0.01432 and 1.21358 for 1, 3 and 5 wt% respectively). The presence of a Bronsted acid site on the surface of the catalyst provides more  $\text{H}^+$  ion for reaction with double bonds (Kalhor *et al.*, 2020). Acidic catalyst has high cracking ability and hence produces more shorter chain hydrocarbons (López *et al.*, 2011). This implies that Fe doped catalyst is suitable for application in cracking during plastics pyrolysis. Increasing Fe loading resulted in an increase in acidity suggesting an increase in cracking ability to promote production of shorter chain hydrocarbons.

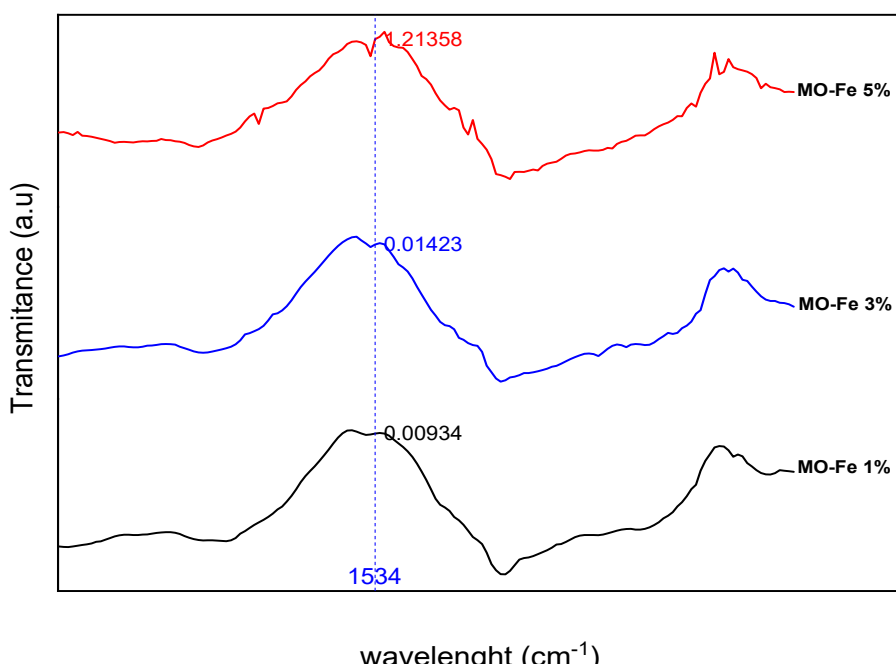


Figure 2: Pyridine FTIR spectra of 1, 3, and 5 wt% Fe doped mordenite.

#### 4. CONCLUSION

Iron doped mordenite (1, 3 and 5 wt%) were synthesized and characterized using FTIR, SEM-EDX and acidity using pyridine FTIR. Impregnation of Fe on mordenite did not alter the parent mordenite as all the basic peaks present in the original mordenite were present after the impregnation. EDX confirmed the synthesis of Fe-MO as atomic concentration of Fe was found to be 0.99, 2.45 and 3.89 for 1, 3, and 5 wt% Fe and signifying that increasing the wt% of Fe resulted in an increase in the quantity of Fe in the mordenite framework. Pyridine FTIR clearly showed that acidity of mordenite was improved as Fe loading increased. All the findings obtained showed that doping mordenite with Fe improved the acidity of the catalyst. This suggests that the samples synthesized could be used as catalyst for pyrolysis of plastics into fuel.

#### ACKNOWLEDGEMENT

The authors appreciate the National Research Institute for Chemical Technology (NARICT) for financial and technical supports rendered in carrying out this research.

#### REFERENCES

- Abidin, A. Z., Bakar, N. A., Ng, E. & Tan, W. 2017. Rapid degradation of methyl orange by Ag doped zeolite X in the presence of borohydride. *Journal of Taibah University for Science*, 11, 1070-1079.
- Blanco, M., Martinez, A., Marcaide, A., Aranzabe, E. & Aranzabe, A. 2014. Heterogeneous Fenton catalyst for the efficient removal of azo dyes in water. *American Journal of Analytical Chemistry*, 5, 490.
- Cheng, K., Song, W., Cheng, Y., Zheng, H., Wang, L., Liu, J., Zhao, Z. & Wei, Y. 2018. Enhancing the low temperature NH<sub>3</sub>-SCR activity of FeTiO<sub>x</sub> catalysts via Cu doping: a combination of experimental and theoretical study. *RSC advances*, 8, 19301-19309.
- Fadillah, G., Fatimah, I., Sahroni, I., Musawwa, M. M., Mahlia, T. M. I. & Muraza, O. 2021. Recent progress in low-cost catalysts for pyrolysis of plastic waste to fuels. *Catalysts*, 11, 837.
- Gougazeh, M. & Buhl, J.-C. 2014. Synthesis and characterization of zeolite A by hydrothermal transformation of natural Jordanian kaolin. *Journal of the Association of Arab Universities for Basic and Applied Sciences*, 15, 35-42.
- Hensen, E., Zhu, Q., Hendrix, M., Overweg, A., Kooyman, P., Sychev, M. & Van Santen, R. 2004. Effect of high-temperature treatment on Fe/ZSM-5 prepared by chemical vapor deposition of FeCl<sub>3</sub>: I. Physicochemical characterization. *Journal of Catalysis*, 221, 560-574.
- Jan, M. R., Shah, J. & Gulab, H. 2010. Catalytic degradation of waste high-density polyethylene into fuel products using BaCO<sub>3</sub> as a catalyst. *Fuel processing technology*, 91, 1428-1437.
- Kalhor, M., Zarnegar, Z., Janghorban, F. & Mirshokraei, S. A. 2020. Fe<sub>3</sub>O<sub>4</sub>@zeolite-SO<sub>3</sub>H as a magnetically bifunctional and retrievable nanocatalyst for green synthesis of perimidines. *Research on Chemical Intermediates*, 46, 821-836.
- Kostyniuk, A., Key, D. & Mdleleni, M. 2019. Effect of Fe-Mo promoters on HZSM-5 zeolite catalyst for 1-hexene aromatization. *Journal of Saudi Chemical Society*, 23, 612-626.



- lópez, A., De Marco, I., Caballero, B., Laresgoiti, M., Adrados, A. & Torres, A. 2011. Pyrolysis Of Municipal Plastic Wastes II: Influence Of Raw Material Composition Under Catalytic Conditions. *Waste Management*, 31, 1973-1983.
- Maretto, M., Bianchi, F., Vignola, R., Canepari, S., Baric, M., Iazzoni, R., Tagliabue, M. & PAPINI, M. P. 2014. Microporous and mesoporous materials for the treatment of wastewater produced by petrochemical activities. *Journal of cleaner production*, 77, 22-34.
- Mastral, F., Esperanza, E., Garcia, P. & Juste, M. 2002. Pyrolysis of high-density polyethylene in a fluidised bed reactor. Influence of the temperature and residence time. *Journal of Analytical and Applied Pyrolysis*, 63, 1-15.
- Miskolczi, N., Juzsakova, T. & Sója, J. 2019. Preparation and application of metal loaded ZSM-5 and  $\gamma$ -zeolite catalysts for thermo-catalytic pyrolysis of real end of life vehicle plastics waste. *Journal of the Energy Institute*, 92, 118-127.
- Murata, K., Sato, K. & Sakata, Y. 2004. Effect of pressure on thermal degradation of polyethylene. *Journal of Analytical and Applied Pyrolysis*, 71, 569-589.
- Neamtu, M., Zaharia, C., Catrinescu, C., Yediler, A., Macoveanu, M. & Kettrup, A. 2004. Fe-exchanged Y zeolite as catalyst for wet peroxide oxidation of reactive azo dye Procion Marine H-EXL. *Applied Catalysis B: Environmental*, 48, 287-294.
- Panda, A. K., Alotaibi, A., Kozhevnikov, I. V. & Shiju, N. R. 2019. Pyrolysis of Plastics to Liquid Fuel Using Sulphated Zirconium Hydroxide Catalyst. *Waste and Biomass Valorization*, 1-9.
- Penkova, A., Bobadilla, L. F., Romero-Sarria, F., Centeno, M. A. & ODRIOZOLA, J. A. 2014. Pyridine adsorption on NiSn/MgO–Al<sub>2</sub>O<sub>3</sub>: An FTIR spectroscopic study of surface acidity. *Applied surface science*, 317, 241-251.
- Pieterse, J. A., Pirngruber, G. D., Van Bokhoven, J. A. & Booneveld, S. 2007. Hydrothermal stability of Fe-ZSM-5 and Fe-BEA prepared by wet ion-exchange for N<sub>2</sub>O decomposition. *Applied Catalysis B: Environmental*, 71, 16-22.
- Rasheed, R. & Meera, V. 2016. Synthesis of iron oxide nanoparticles coated sand by biological method and chemical method. *Procedia Technology*, 24, 210-216.
- Rauscher, M., Kesore, K., Mönnig, R., Schwieger, W., Tissler, A. & Turek, T. 1999. Preparation of a highly active Fe-ZSM-5 catalyst through solid-state ion exchange for the catalytic decomposition of N<sub>2</sub>O. *Applied Catalysis A: General*, 184, 249-256.
- Sriningsih, W., Saerodji, M. G., Trisunaryanti, W., Armunanto, R. & Falah, I. I. 2014. Fuel production from LDPE plastic waste over natural zeolite supported Ni, Ni-Mo, Co and Co-Mo metals. *Procedia Environmental Sciences*, 20, 215-224.
- Syamsiro, M., Cheng, S., Hu, W., Saptoadi, H., Pratama, N. N., Trisunaryanti, W. & Yoshikawa, K. 2014. Liquid and gaseous fuel from waste plastics by sequential pyrolysis and catalytic reforming processes over indonesian natural zeolite catalysts. *Waste Technology*, 2, 44-51.
- Zhang, L., Bao, Z., Xia, S., Lu, Q. & Walters, K. B. 2018. Catalytic pyrolysis of biomass and polymer wastes. *Catalysts*, 8, 659.



## Characterization of Char Derived from Pyrolysis of Low-Density Polyethylene Waste

Adebola F. ADE-AJAYI<sup>1,a\*</sup>, Aishat A. OSIGBESAN<sup>2,a</sup>, Ephraim A. AUDU<sup>3,a</sup>, Zaharaddeen Z. GANO<sup>4,a</sup>,  
Jeffery T. BARMINAS<sup>5,a</sup>

<sup>a</sup> Petrochemicals and Allied Department, National Research Institute of Chemical Technology, Zaria

<sup>1</sup>[phemmistic@gmail.com](mailto:phemmistic@gmail.com), <sup>2</sup>[aishatosigbesan2011@gmail.com](mailto:aishatosigbesan2011@gmail.com), <sup>3</sup>[ephrain.audu@yahoo.com](mailto:ephrain.audu@yahoo.com), <sup>4</sup>[zaharaddeenn@gmail.com](mailto:zaharaddeenn@gmail.com),  
<sup>5</sup>[bitsware@gmail.com](mailto:bitsware@gmail.com)

\*Corresponding author

---

### ABSTRACT

Char (solid residue) from pyrolysis of Low-Density Polyethylene (LDPE) was collected and analysed to investigate its proximate properties, ultimate properties, High Heating Value (HHV), morphology, compositions, and functional groups using bomb calorimetry, Scanning Electron Microscopy – Energy Dispersive X-ray (SEM – EDX) and Fourier Transform Infrared (FTIR) spectroscopy. From the proximate analysis, the pyrolysis char had fixed carbon (80.56%), moisture (1.40%), volatile matter (5.52%) and ash (12.52%). The ultimate analysis showed that the percentages of C, H, N, O and S are 70%, 3.45%, 1.29%, 24.21% and 0.1%, respectively. The calorimetric analysis of the sample showed that the char has a High Heating Value (HHV) of 40.80 MJ/Kg. The elemental composition of the char as obtained from the SEM-EDX analysis showed the presence of Si (39.57%wt), Br (17.79%wt), Fe (8.23%wt) Cu (5.79%wt) with an average particle size of 47µm. The FTIR spectra showed the presence of hydrocarbons in the char. These results would serve as a basis for further works on pyrolysis char applications.

**Keywords:** Char, low density polyethylene, morphology, Pyrolysis, ultimate properties.

### 1. INTRODUCTION

Plastics are used extensively in daily life as well as in industries acting as an indispensable ingredient due to their versatility and low cost; thus, consumption of virgin plastics has increased exponentially over the past decades (Piñar *et al.*, 2021). In addition, the short life span of plastic accelerates the production of plastic waste on a daily basis (Sogancioglu *et al.*, 2017). The global plastic production was estimated at around 300 million tons per year and is continuously increasing every year (Ratnasari *et al.*, 2017). Most of plastic wastes in the municipal solid wastes are polyethylene (PE), and polypropylene (PP) corresponding to 68.74% and 16.10% of the total plastic wastes respectively (Sogancioglu *et al.*, 2017).

The most common types of polyethylene are low density polyethylene (LDPE) and high-density polyethylene (HDPE). They are produced as low- or high-density polyethylene by addition polymerization of the ethylene using organometallic catalyzers. LDPE has a high degree of short- and long-chain branching, which means that the chains do not pack into the crystal structure (Kurbanova *et al.*, 1997). Disposal of plastics takes away valuable land and creates numerous potential environmental problems. Waste-to-energy technologies can mitigate negative impacts of waste plastics and provide sustainable energy from low-cost feedstock. Examples of these technologies include incineration, gasification, anaerobic digestion, and pyrolysis (López *et al.*, 2010).

Pyrolysis is one of the processes used to convert plastic waste to different types of fuels. This pyrolysis process produces a liquid that can be assimilated to a fuel or raw material for obtaining chemical products of interest. The product; a gas with a low calorific value that is usually used to feed the pyrolysis own process and a solid product (char) that can be used as a solid fuel, an adsorbent or even used to improve soil nutrients (Harussani *et al.*, 2022).

The use or application of the char depends on the composition of the pyrolyzed material and its characteristic properties (Jamradloedluk and Lertsatitthanakorn, 2014). The most common use of char is as an adsorbent due to its properties such as surface area and porosity. Other applications of char include the productions of char based fuel briquettes, sensors and super capacitors, fabrication of graphene and its derivatives, nanocatalysts, nano-fillers for composite (Vivekanandhan, 2018, Piñar *et al.*, 2021).

## 2. MATERIALS AND METHODS

### 2.1 Equipment

Weighing balance (Kern-EW6000, with accuracy of 0.001g), digital hotplate with magnetic stirrer (Stuart CD 162), muffle furnace (SXL – 1008 Gallenkamp, England), hot air oven (Genlab, UK), Bomb Calorimeter, Shimadzu Fourier Transform Infrared (FTIR) 8400S.

### 2.2 Analysis of Char

Proximate analysis was conducted according to ASTM 3173, ASTM D 3175, ASTM3172-07, and ASTM D 3174 to determine the moisture content, volatile matter, fixed carbon and ash of the char respectively. Ultimate analysis was also conducted using ASTM D3176 as the determination of the carbon, hydrogen, nitrogen, and sulfur in the char, Calorific value was determined according to ASTM D 5865, using a bomb calorimeter.

### 2.3 Characterization of Char

Infrared data was collected using a Shimadzu-8400S Fourier Transform Infrared Spectrometer (Kyoto, Japan) over the range of 4000–400  $\text{cm}^{-1}$ . The constituent elements in the sample were determined using Phenom world SEM-EDX analyzer (Thermo Fischer, Waltham, U.S).

## 3.0 RESULTS AND DISCUSSIONS

### 3.1 Analysis of Char

Proximate analysis, ultimate analysis and calorific value of the char are shown in Table 1. From the proximate analysis it showed that the fixed carbon content is the highest percentage at 80.56% while the volatile content is 5.52%wt. The ash content for the char is 12.52%wt and moisture content is 1.4%wt high values of these two components in char which tends to reduce their excellent characteristics as fuels.

Since the char is from plastics which are hydrocarbons, carbon and nitrogen are the major elements. The ultimate analysis showed that the percentages of C, H, N, O and S are 70.95%, 3.45%, 1.29%, 24.21% and 0.1%, respectively. The High heating value (HHV) is 40.80 MJ/Kg, heating values depend not only on the carbon content but also on the volatile matter content of char (Luo *et al.*, 2010).

Table 1: Characteristics of Char derived from pyrolysis of LDPE waste

	<i>Moisture Content (%)</i>	$1.40 \pm 0.2$
	<i>Volatile Content (%)</i>	$5.52 \pm 0.8$
	<i>Fixed Carbon Content (%)</i>	$80.56 \pm 0.5$
	<i>Ash Content (%)</i>	$12.52 \pm 0.2$
<i>Ultimate analysis</i>	C (%)	$70.95 \pm 0.3$
	H (%)	$3.45 \pm 0.3$
	N (%)	$1.29 \pm 0.2$
	O (%)	$24.21 \pm 0.2$
	S (%)	$0.10 \pm 0.3$
<i>Calorific value</i>	HHV (MJkg <sup>-1</sup> )	40.80

### 3.2 SEM - EDX

The result obtained from the elemental analysis of the char is as shown in Table 2. The result shows that silicon (Si) is the element with the highest percentage of 39.57 wt% while other elements like Br (17.79 wt%), Fe (8.23 wt%) Cu (5.79 wt%) are lower. The presence of these metals may be as a result of additives and printing materials in the LDPE. On the other hand, the presence of Na, K and Ca (Table 2) suggests that this char can find its applications in soil enrichment, since they are nutrient elements for plant growth (Suárez-Hernández, 2017).

The SEM investigation shows the morphology of the samples at magnification of 80  $\mu\text{m}$  as shown in Plate 1. The image shows that the char appeared to have scattered pseudo-spherical shaped particles. A particle size distribution was obtained from the analysed SEM data using Image J software. The particle size for the pyrolysis char is within the range of 20 – 70  $\mu\text{m}$  with an average particle size of 47 $\mu\text{m}$ . This implies more surface area.

### 3.3 Fourier Transform Infrared Spectroscopy (FTIR)

Figure 2 shows the FTIR spectra of pyrolysis char of the LDPE. Table 3 presents the functional groups of the hydrocarbons present as well as their corresponding wavebands. The intensity of the alcohols O-H (3500 – 3150  $\text{cm}^{-1}$ ),

and aromatics ( $1450 - 1490 \text{ cm}^{-1}$ ,  $1640 - 1650 \text{ cm}^{-1}$ ) groups are much prominent than that of the amines N-H ( $3550 - 3250 \text{ cm}^{-1}$ ), alkenes ( $1625 - 1440 \text{ cm}^{-1}$ ) and others. This could be as a result of residual volatile matter left in the char.

Table 2: Elemental composition (% weight) of Char

Element	% wt
<i>Si</i>	39.57
<i>Br</i>	17.79
<i>O</i>	9.72
<i>Fe</i>	8.23
<i>Cu</i>	5.76
<i>Ca</i>	4.11
<i>Zn</i>	2.63
<i>Mg</i>	2.04
<i>S</i>	1.82
<i>Na</i>	1.80
<i>K</i>	1.48
<i>Cl</i>	1.26
<i>Cr</i>	1.17
<i>Mn</i>	0.72
<i>Ni</i>	0.69
<i>F</i>	0.68
<i>Co</i>	0.55

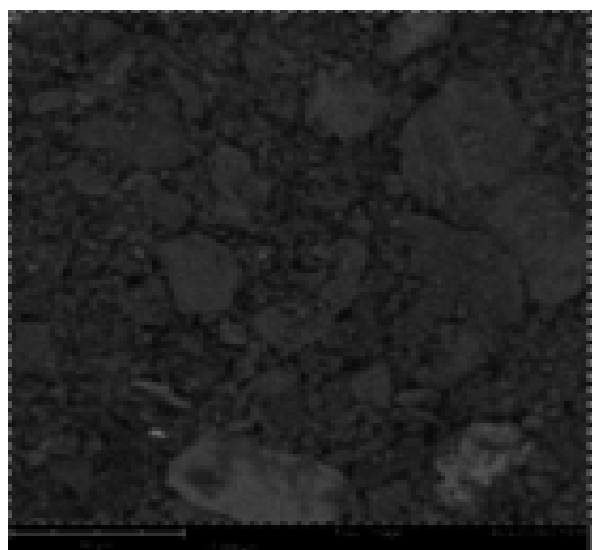


Plate 1: Morphology of char

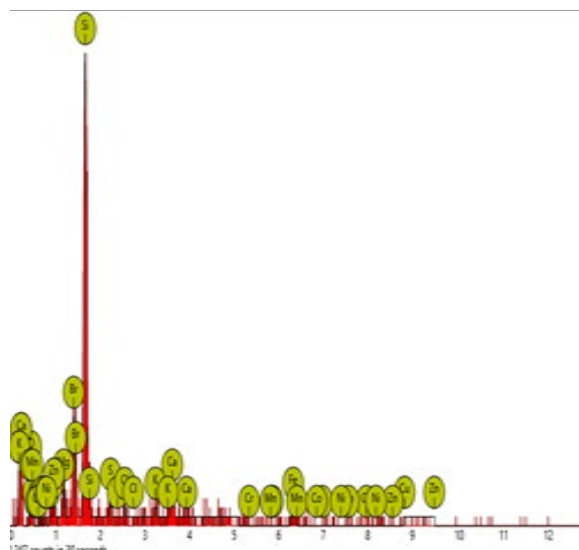


Figure 1: EDX of char

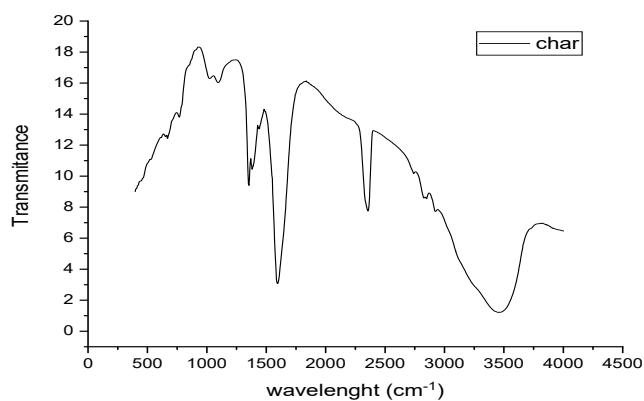


Figure 2: FTIR spectra of the char

Table 3: Prominent wavebands and their corresponding functional groups for the char

Wavebands (Cm <sup>-1</sup> )	Bond Type	Functional Groups
3500 – 3150	O-H stretching	Alcohols
3550 – 3250	N-H Stretching	Amines
1625 – 1440	C= C stretching	Alkenes
1640 – 1650	C = C stretching	Aromatic
1450 – 1490	C = C Stretching	Aromatic
1000 – 1400	C – F Stretching	Alkyls

### 3.4 Possible Applications of Char

Based on the obtained properties of the char, it can find application in the following areas: Agriculture; to enrich soil nutrients for plant growth, Energy; as briquette which is an alternative source of energy, Catalysis; as support in catalyst preparation and Water treatment; as an adsorbent in treatment of water.

### 4.0 CONCLUSION

Char obtained from the pyrolysis of Low-Density Polyethylene was analyzed. elemental proximate, ultimate, calorific analysis and morphology of the char were determined. Fixed carbon was found to be 80%. Carbon, hydrogen, nitrogen, oxygen and sulphur contents were found to be 70%, 3.45%, 1.29%, 24.21% and 0.1% respectively. High Heating Value (HHV) was found to be 40.80 MJ/Kg. The elemental analysis revealed the presence of Na, P, K. It can be concluded that char could be used as solid fuels and also for soil enrichments.

### REFERENCES

- harussani, M. M., Sapuan, S. M., Rashid, U., Khalina, A. & Ilyas, R. A. 2022. Pyrolysis of polypropylene plastic waste into carbonaceous char: Priority of plastic waste management amidst COVID-19 pandemic. *Science of The Total Environment*, 803, 149911.
- Jamradloedluk, J. & Lertsatitthanakorn, C. 2014. Characterization and Utilization of Char Derived from Fast Pyrolysis of Plastic Wastes. *Advanced Materials Research*, 931-932, 849 - 853.
- López, A., De Marco, I., Caballero, B. M., Laresgoiti, M. F. & Adrados, A. 2010. Pyrolysis of municipal plastic wastes: Influence of raw material composition. *Waste Manag*, 30, 620-7.
- Luo, S., Xiao, B., Hu, Z. & Liu, S. 2010. Effect of Particle Size on Pyrolysis of Single-Component Municipal Solid Waste in Fixed Bed Reactor. *International Journal of Hydrogen Energy - INT J HYDROGEN ENERG*, 35, 93-97.
- Piñar, A., Ligeró, A., Blázquez, G. & Calero, M. 2021. Characterization and use of char produced from pyrolysis of post-consumer mixed plastic waste. *Water (Switzerland)*, 13.
- Ratnasari, D. K., Nahil, M. A. & Williams, P. T. 2017. Catalytic pyrolysis of waste plastics using staged catalysis for production of gasoline range hydrocarbon oils. *Journal of Analytical and Applied Pyrolysis*, 124, 631-637.
- Sogancioglu, M., Yel, E. & Ahmetli, G. 2017. Pyrolysis of waste high density polyethylene (HDPE) and low density polyethylene (LDPE) plastics and production of epoxy composites with their pyrolysis chars. *Journal of Cleaner Production*, 165, 369-381.
- Suárez-Hernández, L., Ardila-A., A. N. And Barrera-Zapata, R. 2017. “Morphological and physicochemical characterization of biochar produced by gasification of selected forestry species”. *Revista Facultad de Ingeniería*, 26, 123–130.
- Vivekanandhan, S. 2018. Biochar Supercapacitors: Recent Developments in the Materials and Methods. *Green and Sustainable Advanced Materials*.



## Quantification of 5-Hydroxymethylfurfural and Lactic Acid from Hydrothermal Carbonization of Sugar Cane Bagasse and Corn Cob

Opeoluwa O. FASANYA<sup>1\*</sup>, Dan Mallam A. ADAMU<sup>2</sup>, Abdulazeez R. ISA<sup>3</sup>, Chidimma D. NWAKUBA<sup>2</sup>, Elizabeth WINFUL<sup>1</sup>, Olanikpekun IDOWU<sup>2</sup>, Elijah A. ADEGBE<sup>2</sup>, Saheed A. IBRAHEEM<sup>2</sup>, Ephraim A. AUDU<sup>2</sup>, Yusuf O. USMAN<sup>2</sup>, Mas'ud J. MUSA<sup>2</sup>, Uzo B. AGUNWA<sup>4</sup>, Jeffrey T. BARMINAS<sup>4</sup>

<sup>1</sup>Industrial and Environmental Pollution Department, National Research Institute for Chemical Technology, Zaria, Nigeria

<sup>2</sup>Scientific and Industrial Research Department, National Research Institute for Chemical Technology, Zaria, Nigeria

<sup>3</sup>Pilot Plant and Fabrication Department, National Research Institute for Chemical Technology, Zaria, Nigeria

<sup>4</sup>Directorate, National Research Institute for Chemical Technology, Zaria, Nigeria

\*Corresponding author: [ope.fasanya@narict.gov.ng](mailto:ope.fasanya@narict.gov.ng)

### ABSTRACT

The production of platform chemicals from biomass has gained wide acceptance in the scientific and industrial community. These chemicals are seen as a viable alternative to petrochemicals due to reduced pollution and cost competitiveness. Some of these include lactic acid (LA) and 5-hydroxymethylfurfural (5-HMF). The aqueous phase that is left behind during hydrothermal carbonization (HTC) of biomass is a potpourri of chemicals at different concentrations which depend on the starting material. In this paper, the presence of lactic acid and 5-HMF in the HTC liquor was determined and quantified. Hydrothermal carbonization was conducted on two different types of biomasses; corn cob and sugar cane bagasse at 200 °C. The effect of varying time on the LA and 5-HMF concentration in the liquor was determined. Sugar cane bagasse gave higher concentration of 1.64 g/L and 0.026 mg/mL for LA and 5-HMF respectively. The amount of 5-HMF and LA reduced with increase in processing time.

**Keywords:** Hydrothermal Carbonization, Lactic acid, 5- hydroxymethylfurfural, biomass valorization, platform chemicals

### 1. INTRODUCTION

Biomass is renewable, available in large quantity and has been found to contain valuable building blocks that can be used for the production of different chemicals. These building blocks are termed platform chemicals. The production of platform chemicals from biomass has the capacity to reduce dependency on crude oil thereby reducing environmental pollution stemming from extraction and processing of fossil fuels. The nature of the products extracted from biomass depends on the type of processing employed.

Hydrothermal carbonization (HTC) of biomass occurs in a closed system at temperatures between 120-300 °C (Czerwińska *et al.*, 2022, Erses Yay *et al.*, 2021). In the presence of hot compressed water, biomass gives rise to valuable products with higher energy and purity than the initial raw material (Ischia and Fiori, 2021). HTC has gained popularity as a result of ease of implementation, flexibility, mild operating conditions and probability of production of high value side products (Gallifuoco *et al.*, 2022). The solid product is termed hydrothermal char and has been used as catalyst support, adsorbent for pollutant clean up and fuel.

The liquid products contain a mixture of polyaromatics, carboxylic acids and oligosaccharides amongst others (Wu *et al.*, 2017). The liquid by product of HTC has a variety of uses. Some research has recommended its reuse in HTC to increase the carbon ratio of coal formed, while others have taken the route of anaerobic treatment for methane production due to its high organic content (Erses Yay *et al.*, 2021).

Two important platform chemicals are 5-Hydroxymethylfurfural (5-HMF) and lactic acid (LA). 5-HMF contains both hydroxyl and carbonyl groups in its structure. This endows on HMF the ability for catalytic transformation into multiple industrially relevant products (Soszka and Ruppert, 2020). The transformations occur via oxidation and reduction reactions yielding levulinic acid, dimethylfuran and 5-ethoxymethyl furfural (Siabbamrung *et al.*, 2021). Industrial production of 5-HMF was only recently achieved in 2014 via a modified HTC process (Krawielitzki and Kläusli, 2015). Lactic acid on the other hand is recognized as an emerging bioproduct which has application in food, pharmaceutical, medical and packaging industries because of its biocompatible and biodegradable properties (Li *et al.*, 2021). It is

produced predominantly by fermentation of first-generation sugars such as corn starch and sugar cane juice. Lignocellulose derived lactic acid has the potential to replace high volume and high energy and emission intensive fossil-based plastics and also reduce dependency on toxic solvents such as xylene, toluene and N-methyl-2-pyrrolidone (NMP). The quantity of HMF and LA produced depend on the type of biomass feedstock used in HTC in addition to the operating conditions.

Nigeria is blessed with a wide variety of agricultural biomass due the arable nature of land in her borders. As of 2011, Nigeria's arable land stands at roughly 37.3% of its total land mass (Abubakar, 2021). Depending on location, key crops grown within the country include but are not limited to maize, sorghum, yam, cassava, millet, sugar cane and cabbages. Maize (*Zea mays* L) also known as corn is one of the widely grown crops in Nigeria. As of 2018 maize production was put at 10.5 million metric tons (Kosemani and Bamgboye, 2021). This placed Nigeria as the highest producer of maize in that year (Kamara *et al.*, 2020).

Sugarcane (*Saccharum officinarum*), a tropical plant is grown freely in Brazil, India, China, south Africa and some parts of Nigeria (Ezeonuegbu *et al.*, 2021). In Nigeria, after extraction of the juice either by local sugar industries or leisure consumption, the bagasse is usually discarded or burnt. Depending on the type of processing involved, the high silica and cellulose content contained in the bagasse has been exploited as an adsorbent for heavy metal removal, water purification or catalyst support to mention a few.

This study aims to determine the amount of 5-HMF and lactic acid produced as by-products during the hydrothermal carbonization of corn cob and sugar cane bagasse. The study also characterizes other properties of the liquid product such as pH, conductivity and total dissolved solids. The determinations were carried out in duplicates, and the presented results correspond to average values.

## 2. MATERIALS AND METHODS (OR METHODOLOGY)

Materials and methodology employed in the course of this work are elucidated on in the following section. The methodology consists of cellulose, holocellulose and lignin content determination as well as quantifying lactic and 5-HMF in the process water used in hydrothermal carbonization.

### 2.1 Materials

Analar grade of chemicals and double distilled water were used throughout this work. Corn cob and sugar cane bagasse were gotten from farms in Zaria and Ikara respectively both located in Kaduna State. Double distilled water was used in all experiments and analyses.

### 2.2 Methods

#### 2.2.1 Holocellulose, Cellulose and Lignin Content

Holocellulose content was quantified using a method reported by (Song *et al.*, 2019). The procedure began with the transfer of 1g of each fiber into a 100 ml conical flask containing 30 ml solution of acetic acid and sodium chlorite. The flask was placed in a water bath at 75 °C for 1h after which it was cooled and filtered using Whatman 41 filter paper. The residue was washed thoroughly and allowed to dry in an oven at 60 °C for 24h. The percentage amount of holocellulose was calculated as

$$\text{Holocellulose}(\%) = \frac{M_2}{M_1} \times 100 \quad (1)$$

Where,  $M_2$  = final weight,  $M_1$  = initial weight

To determine cellulose, the holocellulose was treated with 17.5% NaOH solution for 5 h at 75 °C. At the end of 5 h the reaction was quenched rapidly by dipping the flask in an ice bath. A white powder was obtained and washed thoroughly until the filtrate attained a neutral pH. Percentage cellulose was calculated via equation 2

$$\text{Cellulose}(\%) = \frac{M_3}{M_1} \times 100 \quad (2)$$

Where,  $M_3$  = mass of white powder obtained.

Acid insoluble Lignin (AIL) was determined using the modified Klason lignin determination procedure as contained in the work by Fasanya *et al.* (2022). Approximately 3 mL of 72% sulfuric acid was added to 0.150 g of the sample in an Erlenmeyer flask. The sample was left to soak for an hour and stirred at intervals of 10 minutes to complete wetting and mixing. Subsequently, 84 mL of deionized water was added to the sample and autoclaved for 75 min at 123 °C. The autoclaved sample was cooled and filtered using No. 1 Whatman filter paper. The residue in the filter, which was the AIL, was washed with distilled water and oven-dried at 105 °C until a constant weight was recorded. The dried AIL was then subjected to gravimetric analysis. Calculations were performed as follows:

$$\text{AIL} = \frac{W_{\text{after}}}{W_{\text{before}}} \times 100 \quad (3)$$

Where,

AIL = acid-insoluble lignin content (%)

## Quantification of 5-Hydroxymethylfurfural and Lactic Acid from Hydrothermal Carbonization of Sugar Cane Bagasse and Corn Cob

$W_{\text{after}}$  = oven-dried weight of the residue in the filter (g)

$W_{\text{before}}$  = oven-dried weight of the sample (g)

UV spectroscopic method was used to determine Acid Soluble Lignin (ASL). Approximately 2 mL of 3% sulfuric acid was added to 2 mL of the filtrate, the solution was then filtered, and the mixture was analysed using a UV spectrophotometer at a wavelength of 205 nm.

Calculations were conducted as follows:

$$ASL = \frac{CV}{(1000 \times W_{\text{before}})} \times 100 \quad (4),$$

where,

ASL = acid-soluble lignin content (%).

C = concentration of soluble lignin in the filtrate (g/mL).

V = total volume of the filtrate (mL).

$W_{\text{before}}$  = oven-dried weight of extractive-free sample (g).

C, the concentration of ASL, was calculated as follows:

$$C = \frac{A}{110} \times \frac{V_{\text{final}}}{V_{\text{initial}}} \quad (5),$$

where,

A = absorbance at 205 nm.

$V_{\text{final}}$  = final volume of the solution (mL).

$V_{\text{initial}}$  = initial volume of the solution (mL).

### 2.2.2 Hydrothermal Carbonization Reactions

A stainless steel 250 ml, high pressure batch reactor was used for hydrothermal reactions. The ratio of water/biomass was constant at 10/1. For a typical experiment, 10 grams of dry biomass and 100 g of water was loaded into the reactor. The reactor was sealed and purged with  $N_2$  gas for several minutes. Two residence times of 1 h and 2 h were considered for this work at 200 °C for each biomass source. The reaction was terminated with by quenching in an ice bath after desired time was attained. The solids and liquids were separated by filtration using Whatman 41 filter paper. The liquid was sealed and stored in a refrigerator pending analysis. The optical density of the liquid was analysed using Shimadzu UV-Vis 2550 spectrophotometer.

### 2.2.3 Liquid Characterization

The pH of the liquid was measured using Milwaukee 150 pH meter while, electrical conductivity and total dissolved solids (TDS) was measured using Hanna Instruments Portable meter HI 9813-5.

#### 2.2.3.1 Lactic acid determination

Lactic acid was determined using the method proposed by Borshchevskaya et al. (2016). Briefly a test solution (50  $\mu$ L) containing lactic acid was added to 2 mL of a 0.2% solution of iron (III) chloride and stirred and absorbance was measured at 390 nm against the reference solution (2 mL of a 0.2%  $FeCl_3$  solution). The absorbance of the liquid was analysed using Shimadzu UV-Vis 2550 spectrophotometer which had previously been calibrated for lactic acid determination. The reaction and measurements were performed at  $25 \pm 5$  °C. The colour of the solution was stable for 15 min.

#### 2.2.3.2 5-HMF extraction and measurement

5-HMF was extracted using liquid-liquid extraction techniques. This involved mixing 10 ml of chloroform with 10 ml of the HTC liquor. The mixture was then stirred for 5 minutes at room temperature using a magnetic stirrer at a speed of 1100 rpm. The stirred mixture was then left undisturbed for 5 minutes to allow for formation of two solvent phases. A 4 ml aliquot of the chloroform phase was then collected, and the absorbance measured using a UV-Vis spectrophotometer. In order to quantify the 5-HMF calibration of the UV-Vis was required. Stock solution of 5-HMF of 12 mg/ mL was prepared and further diluted to 0.0012 mg/mL – 0.008 mg/mL. Absorbance of each solution was measured at wavelength of 284 nm and used to prepare a linear calibration curve with R2 value of 0.9993.

## 3. RESULTS AND DISCUSSION

The holocellulose, cellulose and lignin content of the raw fibres were first of all evaluated and presented in Table 1. Holocellulose is the carbohydrate fraction of biomass which includes the total polysaccharide fraction obtained after lignin and extractives have been removed from natural materials. Availability of these components at appreciable quantities in the raw biomass is important. Holocellulose and cellulose hydrolyse from temperatures of 180 °C and 200 °C respectively while lignin degrades at 200 °C. Hydrolysis reactions occur as a result of water ionization at elevated temperatures.

Corn cob had predominantly higher holocellulose, but both had the same amount of cellulose (35%). For lignin on the other hand, the acid insoluble fraction of lignin was much higher in the sugar cane bagasse with a value of 21.3%. Corn cob however had a higher amount of acid soluble lignin than the sugar cane bagasse. The presence of these three



components during HTC have been generally reported to lead to formation of furfural, 5-HMF and phenolic derivatives (Sharma *et al.*, 2020).

Table 1: Holocellulose, cellulose and lignin content of corn cob and sugar cane bagasse

	Holocellulose (%)	Cellulose (%)	Acid Insoluble Lignin (%)	Acid Soluble Lignin (%)
Corn Cob	82.7	35.2	12.9	4.1
Sugar Cane	72.7	35.0	21.3	1.7

The effect of time on product formation is shown in In Table 2. Lactic acid and 5-HMF content of the HTC liquor was shown alongside pH, conductivity and total dissolved solids. In corn cob, a 14.7% increase was observed in the quantity of lactic acid as time increased from 1 h to 2 h. The converse was the case for the sugar cane bagasse wherein a 14.6% reduction of lactic acid was observed. For both fibres, 5-HMF concentration decreased within the HTC liquor as time increased portending degradation or hydrolysis of HMF to other products.

Table 2: Effect of time on properties and products of HTC liquor

Sample	Time (h)	pH	Conductivity	Total Dissolved Solids	Lactic Acid (g/L)	HMF (mg/mL)
Corn cob	1	3.36	1.18	854	1.10	0.019
	2	3.89	1.74	1440	1.29	0.005
Sugar cane	1	3.39	1.21	870	1.64	0.026
	2	3.34	1.09	770	1.40	0.012

The formation of 5-HMF proceeds via breakage of amorphous cellulose into smaller molecules. One pathway to 5-HMF formation proceeds from isomerization of glucose, which forms from cellulose hydrolysis to fructose (Paksung *et al.*, 2020). Fructose is then rapidly converted to 5-HMF and furfural. The reduction of 5-HMF with time as seen in Table 2 was expected as levulinic acid and formic acid are formed by rehydration of 5-HMF (Oh *et al.*, 2015). The formation of these products may be responsible for the slight increase in acidity for corn cob though acetic acid is usually the predominant organic acid that is present in HTC liquor (Kambo *et al.*, 2018).

The concentration of lactic acid in the aqueous fraction is relatively low compared to yields from fermentation using microbes (Juturu and Wu, 2016). It is also low compared to chemo-catalytic treatments using catalysts such as Lanthanum Triflate and other acid catalysts some of which have yields between 4-8 g/L. One advantage of lactic acid via this route however is that unprocessed biomass is used as feedstock rather than cellulose or C<sub>3</sub>-C<sub>5</sub> sugars as is often the case for lactic acid production. Extraction of the lactic acid generated here could however be commercially viable depending on the overall quantity of biomass being processed and purity levels required.

In order to have a better understanding of cellulose and lignin conversion, characterization of the HTC char will be carried out in subsequent work. Table 1 showed an increase in total dissolved solids and conductivity for corn cob as time increased while the reverse was the case for sugar cane bagasse. This implies increased breakdown of either lignin or cellulose of the corn cob with longer reaction time.

It however appears that the total sugar content of sugar cane bagasse may be a contributing factor the higher LA and 5-HMF yield as compared to corn cob.

#### 4. CONCLUSION

Hydrothermal carbonization is a relatively inexpensive thermochemical process which is used in producing hydrothermal char. It has the advantage of formation of valuable by-products such as lactic acid and 5-HMF which have appreciable value in industrial markets. Short carbonization time has the potential of yielding appreciable quantities of 5-HMF and Lactic acid. Development of inexpensive separation techniques to extract pure 5-HMF and lactic acid from the aqueous phase of HTC has the potential of making the process more profitable.

## REFERENCES

- Abubakar, I. R. (2021). Predictors of inequalities in land ownership among Nigerian households: Implications for sustainable development. *Land Use Policy*, *101*, 105194. doi:https://doi.org/10.1016/j.landusepol.2020.105194
- Borshchevskaya, L. N., Gordeeva, T. L., Kalinina, A. N., & Sineokii, S. P. (2016). Spectrophotometric determination of lactic acid. *Journal of Analytical Chemistry*, *71*(8), 755-758. doi:10.1134/S1061934816080037
- Czerwińska, K., Śliz, M., & Wilk, M. (2022). Hydrothermal carbonization process: Fundamentals, main parameter characteristics and possible applications including an effective method of SARS-CoV-2 mitigation in sewage sludge. A review. *Renewable and Sustainable Energy Reviews*, *154*, 111873. doi:https://doi.org/10.1016/j.rser.2021.111873
- Erses Yay, A. S., Birinci, B., Açıklan, S., & Yay, K. (2021). Hydrothermal carbonization of olive pomace and determining the environmental impacts of post-process products. *Journal of Cleaner Production*, *315*, 128087. doi:https://doi.org/10.1016/j.jclepro.2021.128087
- Ezeonuegbu, B. A., Machido, D. A., Whong, C. M. Z., Japhet, W. S., Alexiou, A., Elazab, S. T., . . . Batiha, G. E.-S. (2021). Agricultural waste of sugarcane bagasse as efficient adsorbent for lead and nickel removal from untreated wastewater: Biosorption, equilibrium isotherms, kinetics and desorption studies. *Biotechnology Reports*, *30*, e00614. doi:https://doi.org/10.1016/j.btre.2021.e00614
- Fasanya, O. O., Adesina, O. B., Okoduwa, U. J., Abdulkadir, J., Winful, E., Obidah, T. Y., . . . Barminas, J. T. (2022). Characterization of Sansevieria Liberica & Urena Lobata Fibers as Potential Sorbent Materials for Crude Oil Clean Up. *Journal of Natural Fibers*, *19*(5), 1756-1771. doi:10.1080/15440478.2020.1788486
- Gallifuoco, A., Papa, A. A., Spera, A., Taglieri, L., & Di Carlo, A. (2022). Dynamics of liquid-phase platform chemicals during the hydrothermal carbonization of lignocellulosic biomass. *Bioresource Technology Reports*, *19*, 101177. doi:https://doi.org/10.1016/j.biteb.2022.101177
- Ischia, G., & Fiori, L. (2021). Hydrothermal Carbonization of Organic Waste and Biomass: A Review on Process, Reactor, and Plant Modeling. *Waste and Biomass Valorization*, *12*(6), 2797-2824. doi:10.1007/s12649-020-01255-3
- Juturu, V., & Wu, J. C. (2016). Microbial production of lactic acid: the latest development. *Critical Reviews in Biotechnology*, *36*(6), 967-977. doi:10.3109/07388551.2015.1066305
- Kamara, A. Y., Kamai, N., Omoigui, L. O., Togola, A., Ekeleme, F., & Onyibe, J. E. (2020). *Guide to maize production in northern Nigeria*. Retrieved from Ibadan, Nigeria:
- Kambo, H. S., Minaret, J., & Dutta, A. (2018). Process Water from the Hydrothermal Carbonization of Biomass: A Waste or a Valuable Product? *Waste and Biomass Valorization*, *9*(7), 1181-1189. doi:10.1007/s12649-017-9914-0
- Kosemani, B. S., & Bamgboye, A. I. (2021). Modelling energy use pattern for maize (*Zea mays* L.) production in Nigeria. *Cleaner Engineering and Technology*, *2*, 100051. doi:https://doi.org/10.1016/j.clet.2021.100051
- Krawielitzki, S., & Kläusli, T. M. (2015). Modified Hydrothermal Carbonization Process for Producing Biobased 5-HMF Platform Chemical. *Industrial Biotechnology*, *11*(1), 6-8. doi:10.1089/ind.2014.1543
- Li, Y., Bhagwat, S. S., Cortés-Peña, Y. R., Ki, D., Rao, C. V., Jin, Y.-S., & Guest, J. S. (2021). Sustainable Lactic Acid Production from Lignocellulosic Biomass. *ACS Sustainable Chemistry & Engineering*, *9*(3), 1341-1351. doi:10.1021/acssuschemeng.0c08055
- Oh, S. J., Park, J., Na, J. G., Oh, Y. K., & Chang, Y. K. (2015). Production of 5-hydroxymethylfurfural from agarose by using a solid acid catalyst in dimethyl sulfoxide. *RSC Advances*, *5*(59), 47983-47989. doi:10.1039/C5RA02911B
- Paksung, N., Pfersich, J., Arauzo, P. J., Jung, D., & Kruse, A. (2020). Structural Effects of Cellulose on Hydrolysis and Carbonization Behavior during Hydrothermal Treatment. *ACS Omega*, *5*(21), 12210-12223. doi:10.1021/acsomega.0c00737
- Sharma, R., Jasrotia, K., Singh, N., Ghosh, P., srivastava, S., Sharma, N. R., . . . Kumar, A. (2020). A Comprehensive Review on Hydrothermal Carbonization of Biomass and its Applications. *Chemistry Africa*, *3*(1), 1-19. doi:10.1007/s42250-019-00098-3
- Siabbamrung, P., Quitain, A. T., Kida, T., Laosiripojana, N., Boonnoun, P., & Shotipruk, A. (2021). Solid acid catalyst prepared via one-step microwave-assisted hydrothermal carbonization: Enhanced stability towards intensified production of 5-hydroxymethylfurfural in water/ $\gamma$ -valerolactone/NaCl. *Molecular Catalysis*, *512*, 111772. doi:https://doi.org/10.1016/j.mcat.2021.111772
- Song, K., Zhu, X., Zhu, W., & Li, X. (2019). Preparation and characterization of cellulose nanocrystal extracted from *Calotropis procera* biomass. *Bioresources and Bioprocessing*, *6*(1), 45. doi:10.1186/s40643-019-0279-z
- Soszka, E., & Ruppert, A. M. (2020). Separation procedures in the identification of the hydrogenation products of biomass-derived hydroxymethylfurfural. *Reviews in Analytical Chemistry*, *39*(1), 88-105. doi:doi:10.1515/revac-2020-0106.
- Wu, Q., Yu, S., Hao, N., Wells, T., Meng, X., Li, M., . . . Ragauskas, A. J. (2017). Characterization of products from hydrothermal carbonization of pine. *Bioresource Technology*, *244*, 78-83. doi:https://doi.org/10.1016/j.biortech.2017.07.138.



## Production of Fuels from Guinea-Corn Straw and Waste Plastics

Adeola Grace OLUGBENGA<sup>1\*</sup>, Rasheed BABALOLA<sup>2</sup>

<sup>1</sup>Department of Chemical Engineering, Faculty of Engineering, University of Abuja,

<sup>2</sup>Department of Chemical/ Petrochemical Engineering, Faculty of Engineering,

<sup>1</sup>[grace.olugbenga@uniabuja.edu.ng](mailto:grace.olugbenga@uniabuja.edu.ng), <sup>2</sup>[rasheedbabalola@aksu.edu.ng](mailto:rasheedbabalola@aksu.edu.ng)

\*Adeola Grace Olugbenga

---

### ABSTRACT

*The production of fuels from guinea - corn straw and waste plastics predominantly polyethylene during pyrolysis was studied. The effects of mixing ratio of guinea-corn straw and waste plastics, pyrolysis temperature, and gas passed over the pyrolysis reaction (CO<sub>2</sub> or N<sub>2</sub>) on the quantities of pyrolysis oil were studied. The results showed that pyrolysis of guinea-corn straw and waste plastics can increase the amount of produced oil due to the petroleum based content in the waste plastics. When a ratio of 1:4 for guinea-corn straw to waste plastics was used, the product fuel oil was as high as 52.1%, which was 4.5% more than the calculated value. At an increased temperature of decomposition, the product improved having its maximum at 485°C. The addition of 25% by weight of HZSM-5 catalyst reduced the proportion of oxygenates and promoted the generation of aromatic hydrocarbons. This study identified the theoretical basis for the comprehensive utilization of plastic and biomass energy because the pyrolysis of plastics has yielded pyrolysis oil and gas with improved hydrogen content and calorific value having lowered the oxygen content to an improved product properties.*

**Keywords:** Waste plastic; guinea-corn straw; co-pyrolysis; pyrolysis oils.

### 1. INTRODUCTION

The straw of cereal crops and their chaffs are of low economic value as they are low in nutritive value, where nutritive value is the product of nutrient intake, digestibility, and efficiency of use. Currently it is unexploited (Weir and Glasner, 2018) particularly in Nigeria. Guinea corn straw can be defined as the small cereal grain residues which are heterogeneous consisting of several botanical fractions including chaff, grain, leaf crown, leaf sheath, internode and node. These parts vary in composition; they are even low in nutritive value to the animals that feed on them. It is thought that since the straw is more than the cereal obtained after harvesting and there is already gathered straw as soon as the cereals are stripped off the crown. Obtaining the raw materials is prompt and is especially finding applications in producing fuels; it becomes an interesting engineering application to develop technique to produce fuels from this available non- edible biomass. The fuel content is usually low as such an important waste is the plastic materials which contain hydrocarbon materials that can add up the fuel contained in biomass. Therefore, we can produce an ideal synthetic liquid fuel. In this regard, the idea of co-pyrolysis of biomass is a feasible technique that shows good promise by meeting these two criteria. Co-pyrolysis of biomass has successfully improved the oil quality and quantity without any manipulation in the system process. In contrast to catalytic cracking, co-pyrolysis has shown promise for future application in industry because of its attractive performance/cost ratios, nearness to source of raw materials and very cheap feedstock (Olugbenga *et al.*, 2021).

The objective therefore is that solid waste management can be done by converting waste to fuel. This research fills the gap of the relatively slow pace of technological development that caters for waste management. Increased use of solid biomass can in-turn yield valuable resources that are under-utilized and which can be converted to energy.

The importance of this procedure predominantly lies with the synergistic impact which originates from the response of various materials during the procedure (Zhang, at al., 2016). A past report has reported that the yield of oil from plastic waste was higher than that gotten from wood or plant (Abnisa and Daud, 2014) alone and furthermore had a higher caloric worth, which originates from hydrocarbon polymers comprising of a non-condensable gas with high caloric worth, aromatics and, naphthens, olefins, isoparaffins, and paraffins (Panda *et al.*, 2010)

Unit costing and materials for bio-fuel production has been accounted for (Olugbenga *et al.*, 2018) mixing oil from biomass with oil from plastic wastes appears inconceivable (Abnisa and Daud, 2014) and may add to production cost. Oil from biomass cannot be totally blended in with oil from plastics or plastics waste due to the fact that pyrolysis oil

from biomass is not fully explored. On the off chance that these oils are combined, an unsteady oil mix is obtained, which form distinct phases after a short timeframe. On the off chance that pyrolysis of biomass and plastic happens freely or independently, more energy is required and the expense for oil production will fundamentally build (Abnisa and Daud, 2014). The pyrolysis processes are seen as progressively solid to deliver homogenous pyrolysis oil (Brebou *et al.*, 2010) than the techniques used in mixing of biomass with plastics to obtain product oil. The interaction of radicals during pyrolysis usually promotes the development of a steady pyrolysis oil that inhibit stage partition (Martínez *et al.*, 2014).

It was reported that few radicals during pyrolysis can be made via inception, secondary radical formation (de-polymerization, development of monomers, transfer of hydrogen which may or may not favour reactions, transfer of intermolecular hydrogen (arrangement of paraffin and dienes), isomerization through vinyl gathering) and end by a radical recombination or disproportionation (Önal *et al.*, 2014).

Further, the primary advantage of utilizing pyrolysis strategy is the way that the estimation of waste can be diminished altogether as increasingly waste plastics are expended as feedstock. It has the additional advantage of lessening the landfill required, sparing expenses for waste plastic recycling, and taking care of various ecological issues. Since the removal of waste in landfills is bothersome (Zia *et al.*, 2007) this landfill could be proposed as an elective waste administration anyway monetarily, co-pyrolysis has been reserve to be a promising alternative for a biomass transformation method to produce pyrolysis oil. It is advantageous because of the synergetic impacts of the co-pyrolysis of biomass with plastics has been environmentally friendly (Kuppens *et al.*, 2010). Which means that; the utilization of co-pyrolysis method is more beneficial than the pyrolysis of biomass alone and that it also has potential for business and enterprise advancement.

Plastic wastes contains polymers which are not known until they are determined, such polymers include, Polyacryl (PA), polyethylene terephthalate (PET), polycarbonate (PC), polypropylene (PP), low-density and high-density polyethylene (LDPE and HDPE), polystyrene (PS), polyvinyl chloride (PVC), and others. (Zhiwei *et al.*, 2021) The gap in knowledge remains that these plastics contain chemical structure characterized by different amounts of carbon, hydrogen and oxygen, their unique feature are based on the viscosity, the relative large amount of volatile content, and heating value, but know standard values has been reported on these. It remains a stiff challenge to prescribe the expected volume and quality of useful oil product from waste plastics. This research work included the addition of biomass as mixed feed to refine waste plastic in order to obtain improved oil properties where the oxygen content is controlled by catalysis.

## 2. MATERIALS AND METHODS (OR METHODOLOGY)

Guinea-corn straw (GS) was collected on Gidan kwano farm in Minna, Nigeria. The obtained GS was ground and sieved with 80-mesh sieve, and dried in a vacuum drying box at 60°C for 48 hours before pyrolysis. Polyethylene (PE) waste bags (pure water sachet) was collected from canteens, Minna, Niger state. The detailed method for the determination of the proximate and ultimate analyses of guinea-corn straw and waste plastics is provided by Sahito *et al.*, (2013). ZSM-5 (SiO<sub>2</sub>/Al<sub>2</sub>O<sub>3</sub> = 46) to the experiments, the ZSM-5 zeolite was converted to HZSM-5 by calcination in nitrogen at 485°C for 7 h. A pyrolysis reactor (Perkin Elmer 4000: Netherlands) was employed to decompose the raw materials. One side of the pyrolyzer is linked to gas inlet, connected to N<sub>2</sub> and CO<sub>2</sub>, for 30 minutes a mass flow rate of 100 ml/min N<sub>2</sub> and CO<sub>2</sub> was allowed before the heat was supplied, the gas was allowed to exit from the system. A reaction temperature (485°C) and heating time of 15 minutes was allowed to effect the reaction in the quartz tube containing the raw materials inside the pyrolysis kit. This is because the reaction time takes 15 minutes after which the gas begins to evolve. The evolving gas flowed through the condenser equipped with a refrigerant capable of attaining -30°C water to the collection catheter and gas was passed through dichloromethane to be washed. The condensed oil is the resulting pyrolysis oil. The constituents of pyrolysis oil were explored by using the element analyzer. For the hydrogen and carbon contents, data were obtained by combustion and the oxygen content was confirmed by mass difference. The C, H, O, N and S content was determined after the yield was determined using the method of Abnisa and Daud, (2014). At 101 kPa and 25°C which are standard conditions the gas sample obtained from pyrolysis was washed in water and further sent thorough the metal wool. The resulting samples were sent into the gas analyzer for analysis. The same procedure was followed for different guinea-corn straw to WP proportions (1:0, 4:1, 1:1, 1:4, 0:1) and the results are plotted.

### 3. RESULTS AND DISCUSSION

Table 1: Proximate and ultimate analysis of guinea-corn straw (GS) and waste plastics (WP)

Material	Proximate Analysis (Wt%)				Ultimate Analysis (Wt%)			
	moisture	ash	volatile	fixed carbon	C	H	O	N
GS	3.61	6.39	76.06	13.94	43.03	6.97	48.50	1.50
WP	0.00	0.06	99.82	0.12	85.43	14.57	0.00	0.00

Prior to the experimental research for the quality of fuels that can be obtained from guinea-corn straw and plastics, the proximate analysis and the ultimate analysis of the feedstock were determined separately. The values obtained for the moisture, ash, volatile and fixed carbon are presented in Table 1. For the ultimate analysis the carbon, hydrogen, oxygen and nitrogen values were 43.03, 6.97, 48.5 and 1.50 respectively for the guinea-corn straw. These values are somewhat reported for some other samples by (Yao *et al.*, 2018).

#### 3.1 Oil Yield at Different Proportions of Guinea-corn Straw (GS) and Waste Plastics (WP)

The yield of oil, char and gas obtained from pyrolysis of guinea-corn straw (GS) and waste plastics (WP) occurred at 485°C with different guinea-corn straw to WP proportions (1:0, 4:1, 1:1, 1:4, 0:1) and they are presented in Figure 1. The basis for the selection of this ratio is based on the optimized value which has been previously tested for guinea corn and waste plastics feed in previous laboratory work, the ratios are found to yield quality oil which contains the adequate proportion of C and H required in diesel or gasoline.

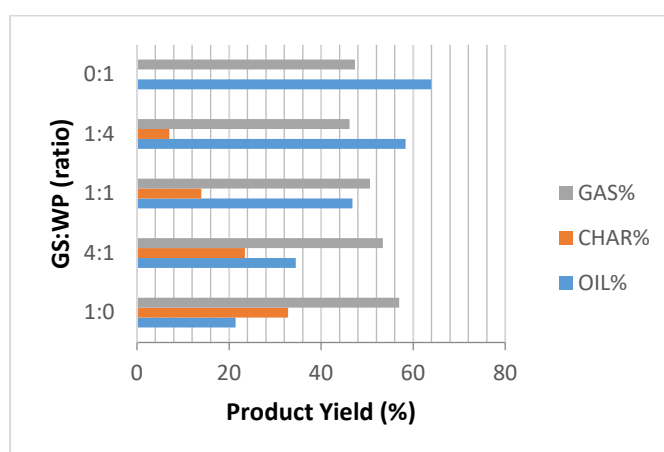


Figure 1: Experimental yield of different GS:WP ratio at 485°C

Normally, the petroleum based diesel are blended from several refinery streams, by using this idea, and noting that the guinea-corn straw contains pyrolysis oil that can be blended with waste plastic pyrolysis oil, the ratio of the two feed stock were researched. In fact in a refining process, components from other units, such as first crude oil cracking, are often used to improve diesel. In the initial refining unit, distillation occurs at atmospheric pressure, the process temperature is usually set to give maximum distillation. The ratio 1:4, 1:1, 4:1. and 0:1 examined in this research have similar quality of the streams blended in refining diesel. This is proven by the H and C content presented in Figure 2 where their HHV and deoxygenated percentage achieved reflect a range of properties of for pyrolysis oil similar to petro diesel.

At 485°C, the oil production rate of WP alone was (63.952 -21.392) 42.56%, more than that of guinea-corn straw pyrolysis alone, which was 21.4%. Since the WP is rich in volatiles because of the debris substance moderately low fixed carbon, the carbon produced by WP pyrolysis alone was 63.952%, with the addition of WP content in the pyrolysis, it is significant because the yield of pyrolysis oil rises from 21.392% to 58.352% as the waste plastic content increases from 25% to 75% of the feedstock. This is presented as GS:WP in Figure 1.

For less amount of guinea-corn straw, and more of waste plastics, the more significantly the carbon yield decreases. At the point when the GS:WP proportion was 1:4, the carbon yield was about 6.8%. From one viewpoint, the carbon created by waste plastics pyrolysis alone was lower than that of guinea-corn pyrolysis alone. Then again, in light of the fact that the C/H ratio of waste plastics is higher than guinea-corn straw, when the constituent of waste plastics

increased, the waste plastics is present as hydrogen giver and consolidates with the free radicals which are unstable and are created during pyrolysis of guinea-corn straw, which represses the polymerization and cross-connecting responses, prompting the reduction of carbon formed.

### 3.2 Synergetic Analysis of Product/Yield

The experimental and calculated yields of different GS:WP ratios which pyrolysis was done at 485°C are presented Figure 2. The gas, char and oil percentage obtained in Figure 1 were used to carry out the synergetic effect of oil quality on the mixed feedstock.

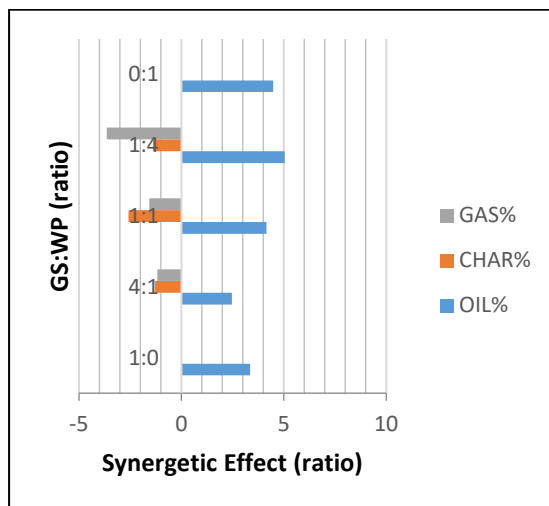


Figure 2: Analysis of the synergetic effect of blending at various guinea-corn straw to waste plastics ratio (GS:WP)

When the ratio of GS:WP was equals 1:1 during pyrolysis at 485°C, the determined yields of pyrolysis oil, carbon and gas were 46.82%, 13.99% and 50.62% respectively (these values are plotted in Figure 1 for the equal ratio of GS:WP (1:1), which is an equal proportion of feedstock, it does not imply that it should yield the maximum oil. The target is the environmental safety requiring the introduction of bio-fuel feedstock to fight the emission of green-house gases when the fuels and subjected to combustion. The emission of such gases is responsible for global warming. Although the pure waste plastics yielded the maximum oil, the use of waste plastics as pure feedstock should be discouraged because of the negative environmental effect of using such oil in machines). It is presented in Figure 2 that the carbon and gas yields were both lower than the hypothetical qualities, while the fluid yields were higher than the hypothetical qualities. This is because of the positive synergistic effect of guinea-corn straw and waste plastics' pyrolysis on the yield of pyrolysis oil, which is responsible for the improvement in the formation of the liquid product. Additionally, with the addition of waste plastics content into the pyrolysis reactor, the synergistic effect turned out to be increasingly articulated. Since pyrolysis happens through free radicals, the guinea-corn straw pyrolysis produces an enormous number of little free radicals, while the decomposition of the waste plastic creates moderately huge free radicals. At the point where guinea-corn straw and the waste plastics were made to go through co-pyrolysis, the little free radicals created by guinea-corn straw correspond with huge free radicals produced by the waste plastics to advance the development of high-atomic weight natural compound of oils, therefore restraining the production of low-molecular weight gas.

### 3.2 Basic Analysis of Pyrolysis Oil

The C, H, and O contained in the pyrolysis oil delivered from different GS:WP proportions at 485°C pyrolysis is presented in Figure 3.

The standard diesel and gasoline oil must contain approximately 86 wt-% of carbon and 14 wt-% of hydrogen (Wexler *et al.*, 2005) however the hydrogen to carbon ratio varies in gasoline and diesel depending on composition of the feedstock from which the fuel was produced. Figure 3 indicate that the carbon and hydrogen weight are within the standard the best is found for ratio 4:1 where the proportion of GS is 4 and the proportion of WP is 1. In this results C is 85.7 and H is 12.2.

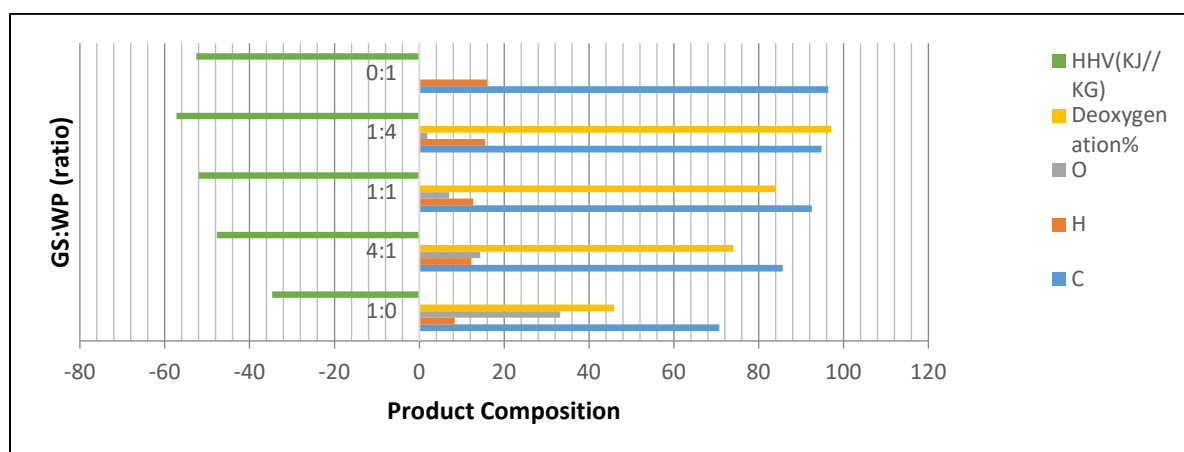


Figure 3: Composition of pyrolysis oil for ratio of GS:WP at 485°C

When 100% of the guinea-corn straw was subjected to pyrolysis, the oxygen content in pyrolysis oil was as high as 33.24 wt. %, while the de-oxidation pace of bio-oil was just 45.93%. When the ratio of GS:WP is equal (1:1) during pyrolysis, the created oils contained a significant amount of C and H, while the substance of oxygen (O) was just 7.07wt%, and the de-oxidation rate of pyrolysis oil was up to 84.11%. The high heating value (HHV) was calculated as  $(\text{MJ/kg}) = -0.3578C - 1.1357H + 0.0845O - 0.0594N - 0.1119S$ , where S, N, O, H and C are mass rates of sulphur, nitrogen, oxygen, hydrogen and carbon respectively. The high heat value (HHV) of the bio-oil pyrolysis carried out using guinea-corn straw alone was 31.94 MJ/kg. The high heating value of ratio 1:4 is due to the quality of the pyrolysis oil. The volatile and flammable gas accompanying the quality of oil is more in the sample than the other sample. The low HHV limits its far reaching use as a sustainable power source. The HHV of oil from the pyrolysis of waste plastics alone was 52.59 KJ/kg. Along these lines, the co-pyrolysis of biomass with plastic is an effective technique to improve the qualities of oil/fuels. When GS:WP was equal (1:1) the pyrolysis oil was analysed, the HHV of the pyrolysis oil was calculated based on this analysis and the value is 45 KJ/kg. This value is in agreement with the standard HHV of diesel (42–45 KJ/kg) and gasoline (42–46 KJ/kg) (Kumar and Pandey 2019).

#### 4. CONCLUSION

The adequate proportions of guinea-corn straw and waste plastics, pyrolysis temperature and catalyst addition and reaction atmosphere determine the properties of pyrolysis products. The examination of these criteria indicated that because of the connection among guinea-corn straw and waste plastics, the co-pyrolysis not just had an advancing effect on the creation of oil, yet in addition influenced an extraordinary change in properties of the fuel. Comparing the pyrolysis of guinea-corn straw alone, the co-pyrolysis oils had lower oxygen content and higher HHV, which are increasingly helpful for their application in industry. With the expansion of pyrolysis temperature, 485oC was beneficial for four ratios that yielded pyrolysis oil of bio-mixed quality which scenically means at the observed ratio C, H, and de-oxygenation can be incorporated reported for co-pyrolysis fuels. Most importantly, catalyst addition can enhance the quality of the pyrolysis oil; it improves the original nature of oil and advanced the processes necessary for converting mixture of petroleum based plastic and bio-oil based feed to produce useful hydrocarbons. The reaction N<sub>2</sub> air, CO<sub>2</sub> had a specific oxidation effect on the fractions of pyrolysis oil, which diminished the contribution of co-pyrolysis oil and advanced the expansion of oxygen-containing aromatics in co-pyrolysis oils.

#### REFERENCES

- Weiß, B. D., & Glasner, C. (2018). Evaluation of the process steps of pretreatment, pellet production and combustion for an energetic utilization of wheat chaff. *Frontiers in Environmental Science*, 6, 36.
- Olugbenga, A. G., Oluimi, J. O., Yahya, M. D. & Garba, M. U. (2018). Simulation and Unit Cost of Using Fluid Catalytic Cracking of Soyabeans Oil for the Production of Bio-Gasoline. *Covenant Journal of Entrepreneurship*, 2(2).
- Abnisa, F., & Daud, W. M. A. W. (2014). A review on co-pyrolysis of biomass: an optional technique to obtain a high-grade pyrolysis oil. *Energy Conversion and Management*, 87, 71-85.
- Panda, A. K., Singh, R. K., & Mishra, D. K. (2010). Thermolysis of waste plastics to liquid fuel: A suitable method for plastic waste management and manufacture of value added products—A world prospective. *Renewable and Sustainable Energy Reviews*, 14(1), 233-248.
- Abnisa, F., & Daud, W. M. A. W. (2014). A review on co-pyrolysis of biomass: an optional technique to obtain a high-grade pyrolysis oil. *Energy Conversion and Management*, 87, 71-85.

- Brebu, M., Ucar, S., Vasile, C., & Yanik, J. (2010). Co-pyrolysis of pine cone with synthetic polymers. *Fuel*, 89(8), 1911-1918.
- Zhang, X., Lei, H., Chen, S., & Wu, J. (2016). Catalytic co-pyrolysis of lignocellulosic biomass with polymers: a critical review. *Green Chemistry*, 18(15), 4145-4169.
- Martínez, J. D., Veses, A., Mastral, A. M., Murillo, R., Navarro, M. V., Puy, N., & García, T. (2014). Co-pyrolysis of biomass with waste tyres: Upgrading of liquid bio-fuel. *Fuel Processing Technology*, 119, 263-271.
- Önal, E., Uzun, B. B., & Pütün, A. E. (2014). Bio-oil production via co-pyrolysis of almond shell as biomass and high density polyethylene. *Energy conversion and management*, 78, 704-710.
- Zia, K. M., Bhatti, H. N., & Bhatti, I. A. (2007). Methods for polyurethane and polyurethane composites, recycling and recovery: A review. *Reactive and functional polymers*, 67(8), 675-692.
- Kuppens, T., Cornelissen, T., Carleer, R., Yperman, J., Schreurs, S., Jans, M., & Thewys, T. (2010). Economic assessment of flash co-pyrolysis of short rotation coppice and biopolymer waste streams. *Journal of environmental management*, 91(12), 2736-2747.
- Harasimowicz, M.; Orluk, P.; Zakrzewska-Trznadel, G. & Chmielewski, A. (2007). Application of polyimide membranes for biogas purification and enrichment, *Journal of Hazardous Materials*, Vol. 144, No. 3, June 2007, pp. 698-702, ISSN 0304-3894.
- Marchaim, U. (1992). *Biogas processes for sustainable development*, FAO, ISBN 92-5-103126-6, Rome, Italy
- Olugbenga, A. G., Yahya, M. D., Garba, M. U., Utilizing the Decomposition of Onelga Oil Shale to Fix Kinetics Parameter and Heat Energy for Pyrolyser-Reactor, (2021) *International Review of Mechanical Engineering (IREME)*, Praise worthy prize publisher (vol 15 No. 2).
- Wang, Z., Burra, K. G., Lei, T., & Gupta, A. K. (2021). Co-pyrolysis of waste plastic and solid biomass for synergistic production of biofuels and chemicals-A review. *Progress in Energy and Combustion Science*, 84, 100899..
- Sahito, A. R., Mahar, R. B., Siddiqui, Z., & Brohi, K. M. (2013). Estimating calorific values of lignocellulosic biomass from volatile and fixed solids. *International Journal of Biomass and Renewables*, 2(1), 1-6.
- Yao, D., Yang, H., Chen, H., & Williams, P. T. (2018). Co-precipitation, impregnation and so-gel preparation of Ni catalysts for pyrolysis-catalytic steam reforming of waste plastics. *Applied Catalysis B: Environmental*, 239, 565-577.
- Wexler, P., Anderson, B. D., Gad, S. C., Hakkinen, P. B., Kamrin, M., De Peyster, A., ... & Shugart, L. R. (Eds.). (2005). *Encyclopedia of toxicology (Vol. 1)*. Academic Press.
- Kumar, S., & Pandey, A. (2019). Current developments in biotechnology and bioengineering and waste treatment processes for energy generation: an introduction. In *Current developments in biotechnology and bioengineering* (pp. 1-9). Elsevier.





## Performance of Deep Eutectic Solvents in the Extraction of Lactic Acid from Sugarcane bagasse and Corncob

John E. OGUCHE<sup>1\*</sup>, Alewo O. AMEH<sup>1</sup>, Tajudeen K. BELLO<sup>1</sup> and Nehemiah S. MAINA<sup>1</sup>

<sup>1</sup>Department of Chemical Engineering, Ahmadu Bello University, Zaria, Nigeria

<sup>1\*</sup>mailoguchejohn@yahoo.com, alewoameh@yahoo.com, tjbelo27@gmail.com, nsmaina@yahoo.com

\*Corresponding author: mailoguchejohn@yahoo.com

### ABSTRACT

Recently, hydrophobic deep eutectic solvents (HDESs) are gaining attention as to conventional extracting solvents because of their low extraction efficiency, cost, and high toxicities. HDESs are green solvents and have advantages such as low toxicity, recyclability, low viscosity, ease of preparation, biodegradable and sustainable over conventional organics solvents. Three hydrophobic deep eutectic solvent (HDESs) were synthesized from decanoic acid, menthol and thymol using a molar ratio of 1:1 respectively and used to study the extraction of lactic acid produced from corncob and sugarcane bagasse respectively. Their physicochemical properties for all the synthesized HDESs were determined and the value are close to that reported in literature. Conventional solvents such as trioctylamine (TOA), butanol and benzene were also used as extractants for lactic acid in order to compare the performances with the newly prepared HDESs. The Synthesized HDESs showed higher extraction efficiencies of 90 %, 93 % and 89 % from corncob and 94 %, 97 % and 90 % from sugarcane bagasse for DES1, DES2 and DES3 respectively compare to 71-78 % for TOA, 59- 62% for butanol and 56-58 % for benzene from the same substrates. Therefore, HDESs synthesized performed better with higher extraction efficiency than conventional organic solvents used.

**Keywords:** Hydrophobic deep eutectic solvents (HDESs), Agricultural residues, Lactic acid and Extraction

### 1. INTRODUCTION

Lactic acids is one of the most essential raw material for production of diverse products in food, pharmaceutical, textile, chemical and cosmetics industries and also used for production of poly lactic acids which is also a platform chemical in the polymer industry (Pleissner *et al.*, 2015). Due to its versatile applications, the demand of lactic acid is very high hence the need to look for alternative method of improving the recovery of this versatile chemical.

Presently, the most widely used purification method for lactic acid production is the calcium lactate process involving calcium hydroxide precipitation, being applied by the world's largest producer of lactic acid (Nature Works and Purac) in lactic acid production from starch (Enrique *et al.*, 2018). However, this method is limited by high consumption of sulphuric acid, generation of gypsum and low productivity of lactic acid (LA). (Agata *et al.*, 2019). Also other methods such as distillation, membrane separation and filtration are limited due to fouling, high energy consumption, polarization and high cost of these methods (Ajala *et al.*, 2021). Although, solvent extraction has been proved to be an outstanding technique of separation because of its flexibility, low energy requirement, low operating cost, and high recovery (Abdullahi *et al.*, 2021), the efficiency of solvent extraction for LA production is limited by high cost, non-recyclability, and high toxicity of conventional organic and ionic liquids, all of which diminish LA yield (Urrea, 2019). While ionic liquids (ILs) and volatile conventional organic solvents (VOCs) have been widely utilized for various applications and extraction purposes, the "green" character of these solvents have often been questioned. This is mainly due to their poor biodegradability, stability, biocompatibility and sustainability (Abbott *et al.*, 2003).

In contrast to VOCs and ILs, DESs exhibit distinctive properties such as chemical and thermal stability, biodegradability, non-flammability, and cost effectiveness. These features account for their wide range of applications (Makoš *et al.*, 2019). DESs are synthesized through the complexation of two or more compounds through hydrogen bonding between the hydrogen bond donor (HBD) and the hydrogen bond acceptor (HBA). The aforementioned hydrogen bonding results in melting point depression (Abdullahi *et al.*, 2021). Hydrophilic DESs are miscible with water, which precludes their use for separation processes of aqueous samples. However, hydrophobic DESs offers this advantage because it forms a clear distinct layer when applied in aqueous samples and also minimizes solvent consumption which is one of the key objectives of green chemistry (Wei *et al.*, 2015). Previous studies have shown the successful application of hydrophobic DES for extraction purposes in aqueous samples, which include extraction of volatile fatty acids (VFAs) from water (Van Osch *et al.*, 2015), extraction of pesticides from water (Florindo *et al.*, 2014), extraction of polycyclic aromatic

hydrocarbons (Makoś *et al.*,2019) , micro-extraction of two auxins in water, fruit juice (Farajzadeh *et al.*,2017) and extraction of aromatic compounds (BTX) from contaminated water (Abdullahi *et al.*,2021).

So far, no DESs either hydrophobic or hydrophilic has been used for extraction of lactic acid from lignocellulosic materials hence this current work evaluate the performance of hydrophobic DESs for extraction of lactic acid.

## 2. MATERIALS AND METHODS

### 2.1 Materials:

Some of the reagents used in this work includes Menthol (Sigma Aldrich, 99.8%), Decanoic acid (Sigma Aldrich, 99.5%), Thymol (Sigma Aldrich, 98%), Trioctylamine (TOA) (Sigma Aldrich, 99 %), butanol (Sigma Aldrich, 99.8%) and benzene (Sigma Aldrich, 99.5%). The molar ratio of all the HDESs used in this work is 1:1 respectively. Some apparatus used includes weighing balance, heating mantle (GallenKamp model), magnetic stirrer, beakers, and viscometer (ModelNTV-E1), tensiometer (sigma 702, serial 72296) by Bionic scientific and pH meter were used to determine the viscosity, surface tension, density and pH of all the synthesized HDESs. Sugarcane bagasse and corncob were obtained from Markarfi, Kaduna state, dried and subsequently ball milled at department of Chemical Engineering, Ahmadu Bello University (ABU) Zaria.

### 2.2 Synthesis of DESs

The three HDESs were synthesized by heating method (Van Osch *et al.*, 2015). Both hydrogen bond acceptor (HBAs) and hydrogen bond donor (HBDs) were mixed at appropriate molar ratio at about 80 °C, stirred at 1000 rpm for 30minutes until homogeneous liquid was formed. The synthesis was in a closed vessel and stored in an air tight container to avoid absorption of water. Table 1 shows the various DESs sythensized with their names coded. The physicochemical characterization such as viscosity, electrical conductivity, density, surface tension and pH measurement of the synthesized DESs were carried out at 28 °C and each reading were repeated three times with their average values reported and their standard deviations calculated as shown in Table 1. Also the FTIR analysis of all the synthesized DESs was done using Shimadzu FTIR-8400s model at the department of Chemistry, ABU Zaria.

### 2.3 Production of lactic acid from the substrates:

Sugarcane bagasse and corncob was ball milled to about 0.5 mm while microorganism (*Bacillus coagulans*) used was cultured and a pure strain was obtained and used for fermentation. The production of lactic acid takes place in a batch reactor using water bath shaker at room temperature at 100 rpm for 24 hrs. After the fermentation, the broth was centrifuge and subsequently, titration method was used to determine the concentration of lactic acid produced from both the substrates (sugarcane bagasse and corncob) respectively.

### 2.4 Extraction of Lactic acid

A stock solution of lactic acid produced was utilized for the extraction process. Lactic acid was extracted using the synthesized Hydrophobic DESs and other conventional organic solvents (TOA, butanol and benzene).10 ml of lactic acid produced and 10 ml of each of the synthesized hydrophobic DESs were contacted and mixed vigorously in closed capped vials at room temperature on a hot plate equipped with a magnetic stirrer. After extraction experiments, the resulting mixture was left to settle for clear phase separation between the DESs and lactic acid. Subsequently, a separatory funnel was used to separate the DES phase and the aqueous phase. Lactic acid concentration in the aqueous phase was determined using a UV spectrometer (CGOLDEWALL 722n) at a wavelength of 390 nm and a calibration standard of pure LA was used before determination of concentration of the lactic acid produced using the absorbance curve from the calibration. A calibration curve in the range of 0.5g/l to 10 g/l of LA was used.

### 2.5 Calculation of Extraction Efficiencies

Extraction efficiencies were calculated for hydrophobic DESs by quantifying the concentration of Lactic acid in the water rich phase after extraction using equation (1)

$$\text{Extraction Efficiency, } Y(\%) = \frac{C_0 - C_1}{C_0} \times 100 \quad (1)$$

Where Y is the extraction efficiency,  $C_0$  is the initial LA concentration in the aqueous phase before extraction and  $C_1$  is the final LA concentration in the aqueous phase in ppm after extraction.

## 3. RESULTS AND DISCUSSION

### 3.1. Physical Properties of the Hydrophobic DES

The production of DESs were validated by FTIR tests and other physicochemical properties while the moisture contents of all the synthesized HDESs were determined and presented in Table 1

Table 1: Physical Properties of the synthesized hydrophobic DESs

Property (28 °C)	DES1	DES2	DES3	Literature Values
	Decanoic acid- Menthol	Decanoic acid- Thymol	Menthol-Thymol	
Moisture Content (%)	0.103 ± 0.90	0.075 ± 0.24	0.084 ± 1.40	0.22 (Van Osch <i>et al.</i> ,2019)
Density (g/cm <sup>3</sup> )	0.8967 ± 1.20	0.9291 ± 1.00	0.9366 ± 0.01	0.9147 (Lee <i>et al.</i> ,2019)
Viscosity (mPa.s)	42.00 ± 1.90	30.02 ± 0.10	53.14 ± 0.55	42 (Al-Akayleh <i>et al.</i> ,2019)
Surface Tension (mN/m)	27.00 ± 0.20	28.12 ± 0.20	27.59 ± 0.31	28.10 (Al-Akayleh <i>et al.</i> ,2019)
Conductivity(μS/cm)	1.2 ± 0.30	0.1 ± 1.10	0.7 ± 0.10	-
pH	5.7 ± 1.70	6.5 ± 0.23	5.55 ± 0.01	-

The presence of water in DESs is critical in determining their purity. Otherwise, the components of DESs would be solvated by water molecules and would not form ion pairs (Degam, 2017). As shown in Table 1, All the HDESs synthesized contained very low and insignificant amount of water. DES1 had the highest water content (0.103 %). This indicates that amount of water present in DESs is dependent mainly on the HBD. Van Osch *et al* 2019 recorded water content for DES1 (0.22%) and DES2 with 0.31% respectively. Also shown in Table 1, DES1 has the lowest density of 0.8967 g/cm<sup>3</sup> followed by DES2 (0.9291 g/cm<sup>3</sup>) while DES3 show the highest density (0.9366 g/cm<sup>3</sup>). This is attributed to the HBA (thymol). Viscosity relates to molecular and electrostatic interactions between the liquid components. Therefore, DES with low viscosity is very essential for extraction applications (Abdullahi *et al.*, 2021). The order of increasing viscosity among the DESs synthesized is DES2 <DES1 <DES3. The high viscosity of DES3 is due to its capability of coordination of the thymol and the formation of self-hydrogen bonds between thymol and menthol compare to decanoic acid. However, this increases the attractive forces between molecules, making DES3 more viscous than DES1 and DES2. As a result, DES3 may be less efficient in extraction. The low viscosity of DES2 (30.02mPa.s) would enhanced the mobility and mass transfer of lactic acid from the aqueous phase into the organic phase. In terms of density, DES1 and DES2 with density of 0.8967 g/cm<sup>3</sup> and 0.9291 g/cm<sup>3</sup> have a close values to that reported by Makos *et al.* (2019) with 0.8855 g/cm<sup>3</sup> for DES1, Fernando *et al.*(2022) recorded 0.9148 g/cm<sup>3</sup> while Lee *et al.* (2019) reported a value of 0.9147 g/cm<sup>3</sup> for DES2 respectively. Also, with respect to surface tension, Fernando *et al.* (2022) reported a value of 28.79 mN/m which is close to that obtained in this current work. Al-Akayleh *et al.* (2019) reported viscosity of 42.mPa.s, Van Osch *et al.* (2015) with 53.14 mPa.s and 30.02 mPa.s also reported by Fernando *et al.* (2022) were all close to the value of viscosities obtained for DES1,DES3 and DES2 respectively in this work.DES2 has highest pH of 6.5 followed by DES1 (5.7) and DES3 with 5.5 respectively.

### 3.2 FT-IR Characterization of the Synthesized HDESs

Fourier Transform-Infrared (FT-IR) are utilized to investigate the interface between dissimilar groups, investigate and classify constructions. The FT-IR spectra of all the DESs synthesized and the components is shown in Figure 1a to 1c. The formation of hydrogen bonds between the oxygen atom in menthol and the hydroxyl group in decanoic acid was the main force for the formation of DES1. As shown in Figure 1a the  $\nu$ -OH stretching vibration of pure decanoic acid was observed at 3497 cm<sup>-1</sup>, and the intensity of  $\nu$ -OH was shifted slightly in menthol-Decanoic acid in DES1. The FT-IR spectrum of menthol shows an OH stretching at 3244 cm<sup>-1</sup> of H-bonding, 2979 cm<sup>-1</sup> and 2847 cm<sup>-1</sup> (C-H stretching), and 1022 cm<sup>-1</sup> and 1220 cm<sup>-1</sup> (C-O stretching). Similar trends was reported by Hiba *et al.* (2019). The absorption bands at 835-992 cm<sup>-1</sup> depict the C-C stretching mode of the hexagonal ring. At 1376 cm<sup>-1</sup> to 1477 cm<sup>-1</sup> frequencies, menthol displayed C-H bending typical of methyl groups present within menthol. Bands at 660 and 768 cm<sup>-1</sup> are due to the skeletal mode vibrations of the hexagonal ring in the menthol structural unit.

As indicated in Figure 1a, menthol confirmed the intact structure of a hexagonal ring. The high degree of broadening of the menthol O-H groups indicates hydrogen bond formation. FT-IR band changes related to decanoic acid suggest a break-up of the methylene arrangement structure due to changes in the C-H band frequencies. The red shift encountered in C=O stretching band emphasizes hydrogen bond formation taking place between the oxygen atom of the hydroxyl group comprising the carboxylic moiety of decanoic acid and the hydrogen atom of menthol hydroxyl group (Hiba *et al.*, 2019).

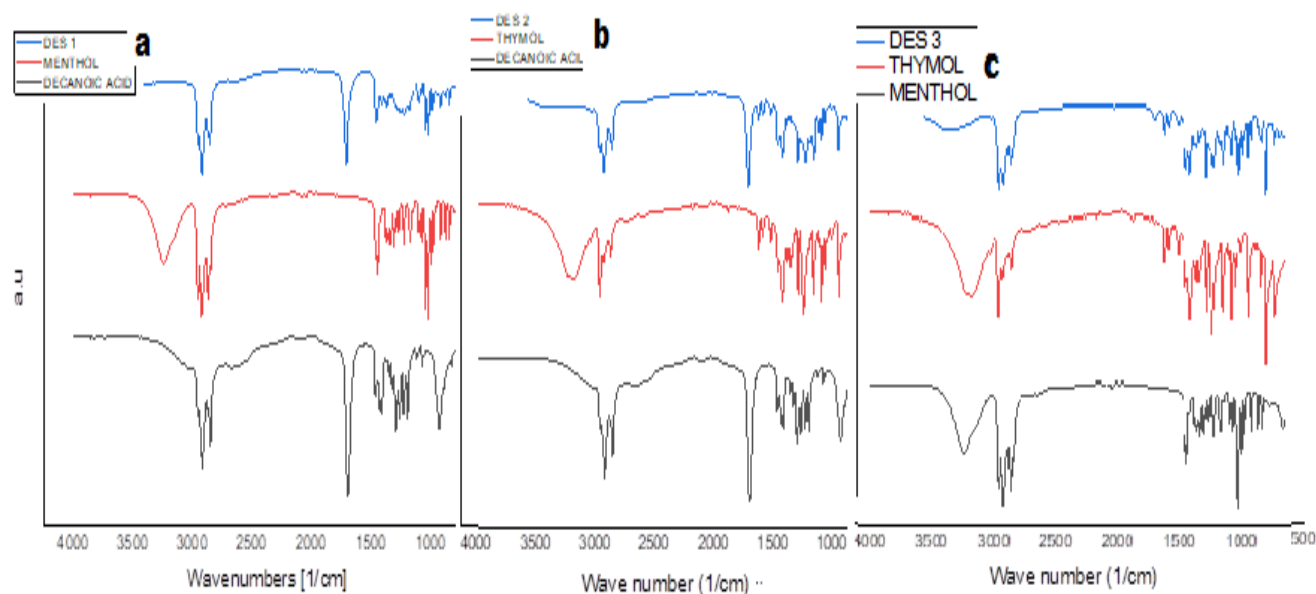


Figure 1: FT-IR of (a) Menthol, Decanoic acid and DES1 (b) Thymol, Decanoic acid and DES2 (c) Menthol, thymol and DES3

The decanoic acid component in DES1 showed a change in the vibration state because a portion of the cloud of electrons of the oxygen atom transfers to hydrogen bonding, thereby reducing the force constant. Hence, changes in the  $\nu$ -OH stretching vibration indicated the presence of hydrogen bonds between decanoic acid and menthol when DES1 was formed. This trends is similar to that reported by Yena and Row. (2020).

Decanoic acid presented a carboxylic acid compound strong stretching of O-H and C-H bands at  $2853\text{ cm}^{-1}$  and  $2913\text{ cm}^{-1}$  respectively while another strong C=O stretching band of the carbonyl group is depicted at  $1694\text{ cm}^{-1}$  as shown in Figure 1a and Figure 1b. In addition, the O-H bend modes are presented at  $1465\text{ cm}^{-1}$  and  $925\text{ cm}^{-1}$  bands. The last band which manifested a typical carboxylic acid compound is the stretching band of C-O at  $1297\text{ cm}^{-1}$ . Moreover, the bands in the range;  $932\text{--}1300\text{ cm}^{-1}$  assign the C-H stretching mode whereas bands in the range;  $1408\text{ cm}^{-1}$  and  $1468\text{ cm}^{-1}$  represent the C-C stretching of the hydrocarbon chain. It has to be noted that there is no appearance of dissociated carboxylate group ( $\text{COO}^-$ ) for capric acid at  $1697\text{ cm}^{-1}$  due to its dimeric form as also reported by Hiba *et al.* (2019). Figure 1b shows the shifts in the representative peaks and band broadening of the involved bonds of DES2 and its individual components. Initially, bands broadening between  $2752\text{ cm}^{-1}$  to  $2944\text{ cm}^{-1}$  represent structural disorder attributed to the loss in the crystalline structure of molecules. This can be attributed to the phase change that took place when the two solid components were mixed. Similar disorder is observed at the carbonyl group of decanoic acid displayed at  $1710\text{ cm}^{-1}$  whereby peak broadening was clearly dominant. The thymol ring structural encountered no change. Nevertheless, the appearance of new bands with broad transmittance at  $1221, 1365, 1425, 1455\text{ cm}^{-1}$  suggests C-H methylene wagging of the decanoic acid hydrocarbon chain. Such wagging usually arises upon re-orientation of the H atoms of the methylene groups which commonly takes place upon heating/melting of fatty acids (Hiba *et al.*,2019). The collapse of the methylene groups orientation is associated with the motion of the C=O and C-O electronic cloud which renders changes to their bond length resulting in broadening and shift of the C=O band at  $1677\text{ cm}^{-1}$  of decanoic acid to a higher wavenumber recorded at  $1713\text{ cm}^{-1}$  for the composite mixture. The spectrum of thymol in Figure 1c consists of the peaks of phenolic O-H ranged from  $3423$  to  $2787\text{ cm}^{-1}$  and centred at  $3195\text{ cm}^{-1}$ , C-H stretching vibrations at  $2954$  and  $2864\text{ cm}^{-1}$ , aromatic C=C stretching at  $1614$  and  $1578\text{ cm}^{-1}$ , C-H out-of-plane bending at  $802\text{ cm}^{-1}$ , C-O stretching at  $1236$ , and O-H bending vibrations at  $1351\text{ cm}^{-1}$ . Besides, aromatic C-H bending overtones that appeared at  $2214\text{--}1933\text{ cm}^{-1}$  confirm a tri-substituted aromatic ring. In DES3, the peak for the  $\text{--OH}$  stretching bond could be observed at  $3320\text{ cm}^{-1}$  while the saturated C-H stretch bond is presented at  $2972\text{ cm}^{-1}$ .

### 3.3 Extraction of Lactic Acid

Figure 2 present the extraction efficiency of all the DESs synthesized as well as that of conventional organic solvents like TOA, butanol and benzene from sugarcane baggasse and corncob respectively.

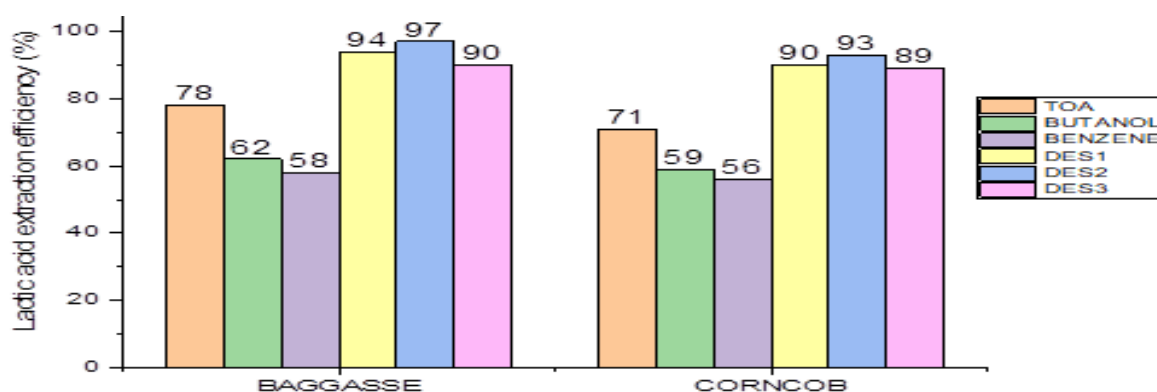


Figure 2: Performance evaluation of extraction capacity of DESs synthesized and that of conventional solvent

As shown in Figure 2, the performance evaluation was carried out on the synthesized DESs and compared with that of conventional solvent to ascertain whether DESs synthesized could perform better than the conventional solvents used. DES6 showed the highest extraction capacity for both sugarcane bagasse and corn cob with extraction efficiency of 97 % and 93 % respectively. The order of extraction efficiency for lactic acid for the three HDESs synthesized is  $DES3 < DES1 < DES2$ . From the performance test, it was clear that all the three DESs synthesized performed better than the conventional solvents used hence the HDESs synthesized can serve as a suitable replacement for the present practice of using conventional solvent. The high extraction efficiency of DESs compared to that of conventional organic solvents may be attributed to the interaction between the delocalized pi- electron clouds over the aromatic ring. Also it could be that a portion of the pi- electron cloud surrounds the partially positively charged H- atoms in the menthol, which contributes significantly to the binding of menthol to the aromatic compound. Cation- aromatic interaction facilitates the formation of a contact pair that is perhaps more stable than the ion pair between tetra alkyl quaternary ammonium ions and anionic residue of aqueous solution (Abdullahi *et al.*, 2021).

#### 4. CONCLUSIONS

Three hydrophobic deep eutectic solvents (HDES) were successfully synthesized and used for extraction of lactic acid from sugarcane bagasse and corncob. The formation of DESs was confirmed by FT-IR bands at  $3497\text{ cm}^{-1}$ ,  $3310\text{ cm}^{-1}$  and  $3423\text{ cm}^{-1}$  for DES1, DES2 and DES3 respectively. The highest viscosity of DES3 (53.14 mPa.s) compared to DES1 (42 mPa.s) and DES2 (30.02 mPa.s) can be attributed to the creation of more hydrogen bonds between menthol and thymol. In this work, conventional organic solvents (TOA, butanol and benzene) were used as extractant in order to compare with the newly prepared hydrophobic DESs.

The synthesized HDESs showed higher extraction efficiencies of 90 %, 93 % and 89 % for DES1, DES2 and DES3 from corncob and 94 %, 97 % and 90 % from sugarcane bagasse respectively compared to 71-78 % for TOA, 59- 62% for butanol and 56-58 % for benzene. From the performance test, it was clear that all the three DESs synthesized performed better than the conventional solvents used hence the HDESs synthesized can serve as a potential replacement for the present practice of using conventional solvent. DES2 showed the highest extraction capacity for both sugarcane bagasse and corn cob with extraction efficiency of 97 % and 93 % respectively.

#### REFERENCES

- Abbott, A.P., Capper, C., Davies, D.L., Rasheed, R.K. and Tambyrajah, V. (2003). Novel solvent properties of choline chloride/urea mixtures. *Chemical Communications* (1), 70–71.
- Abdullahi, Y., Zaharaddeen, S.G., Omar, U.A., Suleiman, M.S., Abdulazeez, Y.A., and Baba Y.J. (2021). Application of hydrophobic deep eutectic solvent for the extraction of aromatic compounds from contaminated water *Korean J. Chem. Eng.* DOI: 10.1007/s11814-021-0994-y pISSN: 0256-1115 eISSN: 1975-7220
- Agata, O.W., Maria, A., José, P. L-G., Roland, S., Michael, M. and Joachim, V. 1. (2019). Production and Purification of l-lactic Acid in Lab and Pilot Scales Using Sweet Sorghum Juice. *Fermentation* <http://www.mdpi.com> Vol 5, PP 36 -47
- Ajala, E. O., Ajala, M. A., Onoriemu, O. O., Akinpelu, S. G., and Bamidele, S. H. (2021). Lactic acid production: Utilization of yam peel hydrolysate as a substrate using *Rhizopus oryzae* in kinetic studies. *Biofuels, Bioproducts and Biorefining*. doi:10.1002/bbb.2213
- Al-Akayleh, F., Hiba, H.M A., Mowafaq, M. G., Mayyas, A. (2019). Therapeutic deep eutectic system of capric acid and menthol: Characterization and pharmaceutical application *Journal of Drug Delivery Science and Technology* 53 101-159 <https://doi.org/10.1016/j.jddst.2019.101159>
- Degam, G. (2017) Deep Eutectic Solvents Synthesis, Characterization and Applications in Pretreatment of Lignocellulosic Biomass <http://openprairie.sdstate.edu/etd>

- Enrique, C.C., Cristina, G.F., Mercedes, B., Elia, T.P. (2018). Biotechnological advances in lactic acid production by lactic acid bacteria: lignocellulose as novel substrate a review; *journal of biofuels products and biorefining*. (wileyonlinelibrary.com); doi: 10.1002/bbb.1852; *biofuels, bioprod. Biorefining*. 12:290–303.
- Farajzadeh, M. A., Sattari, D.M., Yadeghari, A. (2017). Deep Eutectic Solvent Based Gas-Assisted Dispersive Liquid-Phase Microextraction Combined with Gas Chromatography and Flame Ionization Detection for the Determination of Some Pesticide Residues in Fruit and Vegetable Samples. *J. Sep. Sci.* 2017, 40, 2253–2260. DOI: 10.1002/jssc.201700052.
- Fernando, B., Miguel, C., José, M.E., Carlos, L., Manuela, A. (2022). L-menthol-based eutectic solvents: Characterization and application in the removal of drugs from water. *Journal of Molecular Liquids* 3 52 <https://doi.org/10.1016/j.molliq.2022.118754> (2022) 118- 754
- Florindo, C.F., Oliveira, S. L., Rebelo, P. N., Ana, M., Fernandes, and Marrucho I. M. (2014). Insights into the Synthesis and Properties of Deep Eutectic Solvents Based on Cholinium Chloride and Carboxylic Acids. *ACS Sustainable Chemistry & Engineering* · October 2014 DOI: 10.1021/sc500439w
- Hiba, H.A., Mowafaq, M.G., Mayyas, A.R., Faisal,T.A.(2019). New insight into single phase formation of capric acid/menthol eutectic mixtures by Fourier-transform infrared spectroscopy and differential scanning calorimetry *Tropical Journal of Pharmaceutical Research February 2020; 19 (2): 361-369 ISSN: 1596-5996 (print); 1596-9827 (electronic) http://dx.doi.org/10.4314/tjpr.v19i2.19*
- Lee, J., Dasom, J., Keunbae, P. (2019). Hydrophobic deep eutectic solvents for the extraction of organic and inorganic analytes from aqueous environments. *Trends in Analytical Chemistry* 118 853e868 <https://doi.org/10.1016/j.trac.2019.07.008>
- Makos, P., Edyta, S. L., Jacek, G.Ā. (2019). Hydrophobic deep eutectic solvents in microextraction techniques—a review. *Microchemical Journal*. 2019, doi: <https://doi.org/10.1016/j.microc.2019.104384>
- Pleissner, D., Lau, K.Y., Schneider, R., Venus, J., Lin, C.S.K. (2015). Fatty acid feedstock preparation and lactic acid production as integrated processes in mixed restaurant food and bakery wastes treatment. *Food Res. Int.*, 73, 52–61
- Urrea, M.P. (2019). Concentration and Esterification of Lactic Acid in Complex Coacervates: Master Thesis Faculty of Science & Technology Nano biophysics group (NBP) Sustainable Process Technology group (SPT) P.O. Box 2177500 AE Enschede, The Netherlands. viable cosolvents for enzyme-catalyzed epoxide hydrolysis. *J. Biotechnol.* 147(3-4).
- Van Osch, D. J. G. P., Zubeir, L. F., van den Bruinhorst, A., Rocha, M. A. A., and Kroon, M. C. (2015).Hydrophobic deep eutectic solvents as water-immiscible extractants. *Green Chemistry*, 17(9), 4518–4521. <https://doi.org/10.1039/C5GC01451D>
- Wei, Z.F., Qi, X.L., Li, T.T., Luo, M., Wang, Zu, Y.G., Fu, Y.J. (2015). Application of natural deep eutectic solvents for extraction and determination of phenolics in *Cajanus cajan* leaves by ultra-performance liquid chromatography. *Sep. Purif. Technol.* 149, 237–244.
- Yena, A. and Kyung, H.R. (2020). Evaluation of Menthol-Based Hydrophobic Deep Eutectic Solvents for the Extraction of Bisphenol A from Environment Water, *Analytical Letters*, DOI: 10.1080/00032719.2020.1811716



## Application of Machine Learning Xgboost Model for the Prediction of Dye Adsorption onto Agro-Waste-Based Activated Carbons

Abass O. ALADE<sup>a,b,c,\*</sup>, Christopher I. ONI<sup>a,b</sup>, Oladipupo O. OGUNLEYE<sup>a</sup>, Samuel E. AGARRY<sup>a</sup>, Ganiyu K. LATINWO<sup>a</sup>, Aminah A. SULAYMAN<sup>a</sup>, Monsur O. DAUDA<sup>a,b</sup>, Teslim B. ASAFA<sup>c,d</sup>, Tinuade J. AFOLABI<sup>a,b</sup> and Sanni, A.O. OGIRIMA<sup>e</sup>

<sup>a</sup> Department of Chemical Engineering, Faculty of Engineering, Ladoke Akintola University of Technology, (LAUTECH), Ogbomoso, Nigeria

<sup>b</sup> Bioenvironmental, Water and Engineering Research Group (BWERG), (LAUTECH), Ogbomoso, Nigeria

<sup>c</sup> Science and Engineering Research Group (SAERG), (LAUTECH), Ogbomoso, Nigeria

<sup>d</sup> Department of Mechanical Engineering, Faculty of Engineering, Ladoke Akintola University of Technology, (LAUTECH), Ogbomoso, Nigeria

<sup>e</sup> Department of Information Systems, Ladoke Akintola University of Technology, Ogbomoso, Nigeria

\*Corresponding: [aolade@lautech.edu.ng](mailto:aolade@lautech.edu.ng) +2347037885961

### ABSTRACT

The machine learning (ML) method is an emerging and powerful tool to elaborate complicated multivariate relationships. Xgboost model of the ML was used to model thirty-nine adsorbents manufactured from sixteen types of agro-waste and Heat-map was used to demonstrate the association of variables with the target-independent variable in a dataset (350 sets) of adsorption trials (adsorbent efficiency). The ideal model parameters were also selected to enhance the outcome, after optimization and selection of the five most associated independent variables (initial concentration, agro-waste pH, surface area, pore volume, and particle size). The scores obtained for the initial concentration, agro-waste pH, surface area, pore-volume, and particle size are 0.351, 0.248, 0.245, 0.129, and 0.025, respectively. The initial concentration and agro-waste pH have the highest influence, while surface area and agro-waste pH were closely correlated. The R, MSE and RMSE of the trained data were 0.95, 0.037636 and 0.194, while those of the Test Data were 0.71, 0.018496 and 0.136, respectively. This study indicates that the Xgboost model is suitable to predict dye adsorption onto agro-waste-based activated carbons.

**Keywords:** Activated Carbon, Agricultural Waste, Dye, Machine Learning, Xgboost.

### 1. INTRODUCTION

Polycyclic aromatic hydrocarbons (PAHs), phenolic compounds, and dyes are major industrial effluents mostly discharged into water bodies. They are hazardous organic pollutants because of their toxic, mutagenic, and carcinogenic properties (Crini and Lichtfouse, 2018; Lasota *et al.* 2021). Toxicological studies have revealed that the presence of Nitrophenol, Naphthalene, and Methylene blue in wastewater has an adverse effect on human and aquatic life (Pazdro, 2014; Zhang *et al.* 2016; Porhemmat *et al.* 2017; Crini and Lichtfouse, 2018; Lasota *et al.* 2021). These organic pollutants need to be urgently removed from the water environment. However, the removal process has been a major environmental task because of the difficulties in treating such wastewater.

Various techniques have been developed for the removal of these organic pollutants from wastewater. Some of these include adsorption, flocculation, ion exchange, chemical precipitation, membrane-based filtration, photodegradation, solvent extraction, and reverse osmosis (Zhu *et al.* 2019). However, multi-component mixtures (dyes, PAHs) are difficult to remove using some of these traditional purification processes (Korbahti *et al.* 2011). Therefore, adsorption technology is considered the most promising for removing a variety of multicomponent pollutants (Rani *et al.* 2017; Mishra and Maiti, 2018; Boeykens *et al.* 2019). Research shows that adsorbents like activated carbons, natural and synthetic polymers, clays, zeolites, biomass and agricultural waste have been used to remove PAHs, dyes and phenolic compounds from solutions (Alabi *et al.* 2020; Okeowo *et al.* 2020; Berez *et al.* 2014). However, natural clay such as bentonite, kaolinite, and smectite is better adsorbents for the removal of multicomponent pollutants in water due to their low cost, high efficiency, porosity, availability, thermal stability, and non-toxicity (Puri and Sumana, 2018). Bentonite clay has been proven to be efficient, the majority of the adsorption process reported was on mono-component systems while a limited emphasis has been given to multi-component systems. Wu *et al.* (2020) reported the adsorption of naphthalene and phenanthrene using activated carbon, Giraldo *et al.* (2022) prepared orange peel to remove Methylene blue and Cadmium and Shihab *et al.* (2021) also remove p-nitrophenol using aidoxime-modified poly (acrylonite-co-acrylic acid). Bentonite clay had been used also to remove naphthalene and methylene blue as reported

by Rennane *et al.*, 2019 and Kelechi *et al.*, 2022 respectively. This research work was aimed at using a composite generated from acid, base and salt-activated bentonite clay as an adsorbent for the removal of multicomponent pollutants (Naphthalene, Nitrophenol and Methylene blue) from the aqueous solution which has not been previously reported. Adsorption isotherms were also investigated to investigate the best Langmuir isotherms that fit the adsorption process. Dye has been an important substance that chemically bonds to the substrate to which it is applied to add color to materials such that the coloring properties are not easily removed by any factors they are exposed (Abrahart and Stothers, 2019). The ubiquitous acceptance of dyes in commercial industries have positively contributed to the economy and at the same time poses great dangers to the environment. The large usage of dyes in the industries leads to their release as effluents that eventually contaminate the water bodies which in turn affect aquatic lives and creatures collecting the water for personal use.

In addition, various metals existing in dyes and clothing materials accumulate in our bodies and pose a great threat to vital organs in the body. This can also cause various skin problems and illnesses. Hence, it is very important to remove dyes before they are discharged into the environment due to their toxicity. Various methods such as coagulation, ion exchange, filtration and adsorption have been deployed for the treatment of such wastewater. However, adsorption has been generally considered to be the most prominent approach due to the actions performed on the surface and it is more advantageous over the other available methods because of its low cost, high efficiency, ease of operation and simple design (EL Alouani, 2018). Several adsorbents such as plant wastes silica gel, clay, activated carbon and rice husk have been studied for the adsorption of dye from aqueous solutions (Tahir Rauf, 2006; Altenor *et al.*, 2009; Samiey Toosi, 2010; Gupta and Kushwaha, 2011; Safa Bhatti, 2011). Among the above-mentioned adsorbents, activated carbon is a major dye removal adsorbent due to its large specific surface area, low density, chemical stability, suitability for large-scale production, variety of structural forms, and the ability to modify the pore structures (Okeowo *et al.*, 2017).

Machine Learning (ML) method is an emerging and powerful tool to elaborate the complicated multivariate relationships, especially with the rapid development of interpretable ML models (*e.g.*, decision tree, random forest, and gradient boosting trees) and interpretation methods for ML models (*e.g.*, local interpretable model-agnostic explanations) (Molnar, 2019; Zhu *et al.*, 2020). Zhu *et al.*, (2021) studied random forest (RF), gradient boosting trees (GBT), and artificial neural work (ANN) were applied to build the prediction models for evaluating the adsorption of the antibiotic on CBMs. Some of the areas of application of Machine Learning (ML) include waste-to-energy conversion, biochar for metal and organic compound sorption, municipal solid-waste treatment, and oxidation of micropollutants (Yuan *et al.*, 2021). Some of the often-used ML models include linear regression, support vector machines (SVMs), k-nearest neighbours, and artificial neural networks (ANNs). Tree-based ML models such as decision trees (DTs), random forest (RF), gradient boosting decision trees (GBDTs), light gradient boosting machines (LGBs), and extreme gradient boost (XGB), are subcategories of supervised ML methods, and they engage recursive binary splitting of data in which the residual sum of squares is minimized (Yuan *et al.*, 2021).

The traditional batch adsorption experiments are often time-consuming and cost-intensive, thus, building a general predictive model for evaluating the adsorption process would provide gainful insights into the relative importance of individual factor and their interactions on the adsorption properties of the selected adsorbent. In this manuscript, the Xgboost model was used to predict the adsorption capacity, and reveal the relationships of agro-waste-based activated carbons such as pH, pore volume, particle size, surface area, and others in the data, and their relative importance using feature selection in the prediction of adsorption capacity. Unlike other models' Gradient boost, Decision Tree, Multiple Linear Regression, and Random Forest, Xgboost uses more accurate approximations to find the best tree model, provides parallel tree boosting, and is the leading machine learning library for regression, classification, and ranking problems (Wang *et al.*, 2017). This study aims to predict the adsorption of dye onto agro-waste-based activated carbons using the machine learning Xgboost model. we believe this manuscript with the aid of the machine learning Xgboost model, the systematic approach deployed in getting the adsorption accuracy will be valuable for future applications of machine learning on agricultural waste-based activated carbons.

## 2. MATERIALS AND METHODS

### 2.1. Data Collection

Various adsorbents produced from agro-wastes of 16 kinds of agro-waste at the temperature range of 400-800 °C were modeled using Xgboost to predict the adsorption capacity. The experimental data (350 sets) of adsorption experimental data of different dyes on the agro-waste-based activated carbon were extracted from previous studies with the aid of Getdata 2.21 (He *et al.*, 2016; Selmi *et al.*, 2018; Tahir and Rauf, 2006; Archin and Sharifi, 2019; Gupta *et al.*, 2019; Shokry *et al.*, 2019; Alshabib, 2021;). The datasets contain some missing values, so it is important to treat the dataset and delete the missing values so that the missing values do not affect an accurate prediction of adsorption capacity. Each variable was visualized to show its relationship and a linear relationship was detected which means the dataset falls under regression analysis. In addition, the characteristics of the agro-wastes varied due to the different feedstock and pyrolysis conditions, where the statistical distributions of the factors related to the agro-waste characteristics were acquired via boxplots. Ten variables (Pyrolysis temperature, Agro-Waste pH, Particle Size, Surface Area, Pore Volume,



Adsorbent Temperature, Adsorbent pH, and initial concentration) of the adsorption process were modeled and the dyes' adsorption capacities (ACs) onto the agro-wastes predicted.

## 2.2. Data Pre-Processing and Model Estimator

The Pearson- Correlation and Heatmap were used to show and visualize the correlation, and study the relationship of the variables in determining their level of importance in achieving perfect accuracy, before fitting the variables in the prediction model. Variables with low positive and negative correlation values were eliminated while variables with high positive and negative values were retained. Variables with high positive and negative correlation revealed that there is a direct relationship between the values of the selected variables and the adsorption capacity. These relationships are very important in selecting variables that affect sorption capacity.

The predictors were normalized by SK-learn standard scalar before fitting in regression to eliminate the measurement unit. In this study, Xgboost was used to predict the adsorption capacity because it provides a parallel tree boosting, and is the leading machine learning library for regression, classification, and ranking problems to evaluate the accuracy of the model. The correlation coefficient (R), the Mean Squared Error (MSE) and the Root Means Squared Error (RMSE) were used to evaluate the performances of the data analysis. The Pearson correlation coefficient (PCC) measured the linear dependences between any two selected variables or between each feature and the target variable, which were calculated with Equations 1-4:

$$R = \frac{\sum_{i=1}^N (\hat{y}_i - y_i)}{\sqrt{\sum_{i=1}^N (\hat{y}_i - \bar{y})^2}} \quad (1)$$

$$MSE = \frac{1}{N} \sum_{i=1}^N (\hat{y}_i - y_i)^2 \quad (2)$$

$$RMSE = \sqrt{MSE} \quad (3)$$

$$r_{xy} = \frac{\sum_{i=1}^n (x_i - \bar{x}) \sum_{i=1}^n (y_i - \bar{y})}{\sqrt{\sum_{i=1}^n (x_i - \bar{x})^2} \sqrt{\sum_{i=1}^n (y_i - \bar{y})^2}} \quad (4)$$

where  $\bar{x}$  or  $\bar{y}$  = mean of factors x or y, respectively. Then, each variable's data were scaled into the range of 0 and 1 with Equation 5:

$$y = \frac{(x_i - x_{min})}{(x_{max} - x_{min})} \quad (5)$$

where y = normalized value of initial  $x_i$ ,  $x_{max}$  and  $x_{min}$  = maximum and minimum values of  $x_i$  respectively.

## 2.3. Model Built XGBOOST Method

Xgboost is an example of a gradient boosting (an **ensemble** of weak predictors, which are usually decision trees) framework. Xgboost uses the ensemble learning method which proffers systematic solutions to combine the predictive power of multiple learners. The concept of boosting in Xgboost emanates from its ability to improve on the deficiencies of the trees that are built in it. The ability to improve on the deficiencies enables the model to achieve high efficiency and performance. The data was split into training 80:20 for training and testing. Eighty percent of the data values were trained, while 20 percent were tested after hyperparameter tuning of the trained dataset to achieve the best accuracy and avoid overfitting. GridSearchCV was used to find the best parameter for the model and colsample\_bytree, gamma, learning rate, max depth, alpha, and o of estimators were supplied with a list of values individuals for the GridSearchCV to pick the best parameters from. Using the best parameters, the Xgboost model was fitted to the dataset and the accuracy of 95% was recorded on the trained data taste while the test dataset returned an accuracy of 71%.

## 3. RESULTS AND DISCUSSION

The Pearson Correlation matrix (also expressed as Heat Map) between any of the nine independent variables and adsorption efficiency is shown in Figure 1. The adsorption efficiency (same as adsorption capacity) is the targeted variable. A correlation value of -0.093663, -0.587663, 0.083903, 0.689945, 0.665779, -0.046671, 0.060306, and 0.738891 was obtained for Pyrolysis temperature, Agro-Waste pH, Particle Size, Surface Area, Pore Volume, Adsorbent Temperature, Adsorbent pH, and initial concentration, respectively. The correlation of each variable can also be determined to get its relationship with other variables but in this study, the remaining nine variables are the independent variables.

Pearson correlation matrix returned either the positive or negative correlation values of each variable. Variables with correlation values lower than -0.1 and 0.1 were dropped because they are assumed to have a relatively low correlation with the target. Particle Size is not dropped because the size of the particle is assumed to affect adsorption capacity, though its effect is inconspicuous as indicated by its correlation value. The initial concentration has the highest effect on the adsorption efficiency, an increase in concentration value will cause an increase in the adsorption efficiency. The agro-waste pH has the strongest negative correlation value with the target, and also shows a strong correlation with other agro-waste properties. The pore volume was found as the main factor of agro-waste over the other properties of agro-waste. Similarly, the surface area is the second important factor of agro-waste. A higher surface area could afford

more active sites and an enhanced carbon/substrate interaction to improve the adsorption efficiency (Moosavi, 2021; Wang *et al.*, 2017; He, 2016; Selmi, 2018).

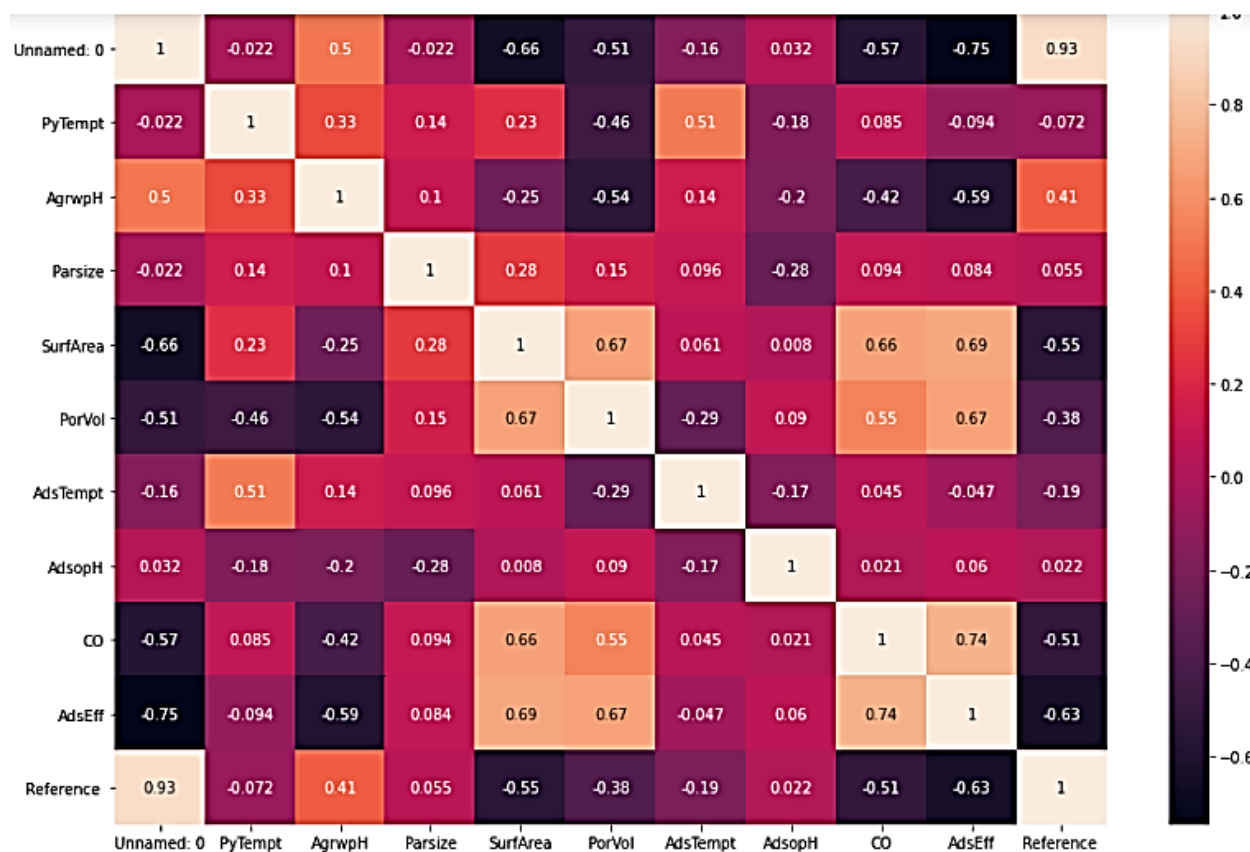


Figure 1 the correlation between each variable and the target variable using Heat Map.

The R, MSE and RMSE of the trained data were 0.95, 0.037636 and 0.194, while those of the Test Data were 0.71, 0.018496 and 0.136, respectively, after fitting the dataset with the Xgboost model (Table 1). The predicted adsorption efficiency versus experimental data using the Xgboost model is shown in Figure 2.

Table 1. Score (weight) of variables based on three Machine Learning (ML) methods

Index	R <sup>2</sup>	MSE	RMSE
Train Data	0.95	0.037636	0.194
Test Data	0.71	0.018496	0.136

The impact of surface area on the adsorption capacity increased within the range below 600 m<sup>2</sup>/g, but a further increase in the range of 600–1700 m<sup>2</sup>/g showed a restrained trend, and over 2000 m<sup>2</sup>/g, there was a sharp decrease in adsorption efficiency. A very large surface area (over 2000 m<sup>2</sup>/g) might have a negative impact on the other physicochemical characteristics of agro-waste like limited micropore accessibility, slow mass transfer, and diminished surface functional groups, which in turn affects the overall adsorption performance, unlike previous studies (Moosavi *et al.*, 2021; Arampatzidou and Deliyanni, 2016). The importance of the variables based on the Xgboost model is shown in descending order (Table 2).

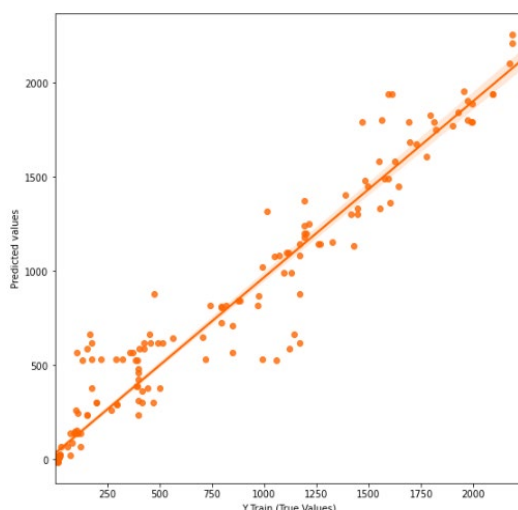


Figure 2: The predicted adsorption efficiency versus experimental data using the Xgboost model

**Table 2.** Score (Weight) of Variables Based on the Machine Learning (ML) Method

Variable	Score
Initial Concentration (C0)	0.351
Agro-waste Ph	0.248
Surface Area	0.245
Pore Volume	0.129
Particle Size	0.025

#### 4. CONCLUSION

Based on the level of correlation in the Pearson Correlation Matrix, this study modeled the five most significant variables (Initial Concentration, Particle Size, Pore Volume, Agro Waste pH, and Surface Area). The model scored an accuracy of 95% after a thorough parameter tuning on the selected variables. In order to reveal the level of importance of each variable with respect to how they assist in determining the adsorption capacity of agricultural waste, feature selection was performed on the dataset. In the result obtained, the role of the particle size was inconspicuous, the initial concentration was seen as the most influencing variable in the model and the surface area was in a close range with agro-waste pH, while the Pore Volume also had a considerable effect in the model. With the advantage of using agricultural waste-activated carbons in dye adsorption to achieve good removal of various dyes and high-quality treated effluent, the accuracy developed by this model could also reduce the experimental screening efforts in the laboratory, such as finding the importance of variables and their influence, and also predicting the dye adsorption efficiency using agricultural waste-activated carbon.

#### REFERENCES

- Abrahart, E.N., and Stothers, J.B. (2019) "dye". *Encyclopedia Britannica*, 5 Mar. (2019), <https://www.britannica.com/technology/dye>. Accessed 30 July 2022.
- Alshabib, M.; Oluwadamilare, M.A.; Tanimu, A.; Abdulazeez, I.; Alhooshani, K.; and Ganiyu, S.A (2021) Experimental and DFT investigation of ceria-nanocomposite decorated AC derived from groundnut shell for efficient removal of methylene blue from wastewater effluent. *Appl. Surf. Sci.* 536: pp.147749
- Altenor, S., Carene, B., Emmanuel, E., Lambert, J., and Ehrhardt, J. (2009). Adsorption studies of methylene blue and phenol onto vetiver roots activated carbon prepared by chemical activation. *J. Hazard. Mater.* 165, pp. 1029–1039
- Arampatzidou, A.C.; and Deliyanni, E.A.J. (2016) Comparison of activation media and pyrolysis temperature for activated carbons development by pyrolysis of potato peels for effective adsorption of endocrine disruptor bisphenol-A. *Colloid Interface Sci.* 466: pp.101–112.
- Archin, S., and Sharifi, S.H., (2019) Optimization and modeling of simultaneous ultrasound-assisted adsorption of binary dyes using activated carbon from tobacco residues: *Response surface methodology. Clean. Prod.* 239: pp.118136.
- EL Alouani, M., Alehyen, S., EL Achouri, M., and Taibi, M. (2018). Removal of Cationic Dye–Methylene Blue- from Aqueous Solution by Adsorption on Fly Ash-based Geopolymer. *J. Mater. Environ. Sci.*, 9(1) pp. 32-46.

- Gupta, K.; Gupta, D.; and Khatri, O.P. (2019), Graphene-like porous carbon nanostructure from Bengal gram bean husk and its application for fast and efficient adsorption of organic dyes. *Appl. Surf. Sci.*, 476: pp. 647–657.
- Gupta, N., and Kushwaha, A.M. ( 2011). Kinetics and thermodynamics of malachite green adsorption on banana pseudo-stem fibers. *J. Chem. Pharm. Res.* 3, pp. 284–296
- He, J.; Dai, J.; Zhang, T.; Sun, J.; Xie, A.; Tian, S.; Yan, Y.; and Huo, P (2016) Preparation of highly porous carbon from sustainable  $\beta$ -cellulose for superior removal performance of tetracycline and sulfamethazine from water. *RSC Adv.* 6: pp. 28023–28033
- Molnar, C. (2019). Interpretable machine learning. A Guide for Making Black Box Models Explainable, <https://christophm.github.io/interpretable-ml-book/>.
- Moosavi, S., Manta, O., El-Badry, Y.A., Hussein, E.E.; El-Bahy, Z.M., Mohd Fawzi, N.F.B., Urbonavičius, J., and Moosavi, S.M.H. (2021) A Study on Machine Learning Methods' Application for Dye Adsorption Prediction onto Agricultural Waste Activated Carbon. *Nanomaterials 11*: pp. 2734.
- Okeowo, I.O., Balogun, E.O., Alade, A.O., Afolabi, T.J., and Farombi, A.G. (2017). Optimization of Conditions for the Production of Activated Carbon from Mango Seed Shell Using Barium Chloride as the Activating Agent. Paper presented at the 7th International Biotechnology Conference, Exhibition and Workshop, Covenant University. Ota, Nigeria.
- Safa, Y., and Bhatti, H. (2011). Kinetic and Thermodynamic Modelling for the Removal of Direct Red 31 and Direct Orange 26 Dyes from Aqueous Solutions by Rice Husk. *Desalination*, 272: pp. 313-322.
- Samiey, B., and Toosi, A. (2010). Adsorption of malachite green on silica gel: effects of NaCl, pH and 2-propanol. *J. Hazard. Mater.* 184, pp. 739–745
- Selmi, T.; Sanchez-Sanchez, A.; Gadonneix, P.; Jagiello, J.; Seffen, M.; Sammouda, H.; Celzard, A.; and Fierro, V (2018) Tetracycline removal with activated carbons produced by hydrothermal carbonization of Agave americana fibers and mimosa tannin. *Ind. Crops Prod* 115: pp. 146–157.
- Shokry, H., Elkady, M., and Hamad, H (2019) Nano-activated carbon from industrial mine coal as adsorbents or removal of dye from simulated textile wastewater: Operational parameters and mechanism study. *J. Mater. Res. Technol.* 8: pp. 4477–4488.
- Tahir, S., and Rauf, N. ( 2006). Removal of a cationic dye from aqueous solutions by adsorption onto bentonite clay. *Chemosphere* 63: pp. 1842–1848.
- Wang, H.; Chu, Y.; Fang, C.; Huang, F.; Song, Y.; and Xue, X. (2017) Sorption of tetracycline on biochar from rice straw under different temperatures. *PLoS ONE* 12:e0182776.
- Yuan, X., Manu Suvarna, Sean Low, Pavani Dulanja Dissanayake, Ki Bong Lee, Jie Li, Xiaonan Wang, and Yong Sik Ok. (2021). Applied Machine Learning for Prediction of CO<sub>2</sub> Adsorption on Biomass Waste-Derived Porous Carbons. *Environ. Sci. Technol.*, 55, pp. 11925-11936
- Zhu, X., D.C.W. Tsang, L. Wang, Z. Su, D. Hou, L. Li, J. Shang, (2020). Machine learning exploration of the critical factors for CO<sub>2</sub> adsorption capacity on porous carbon materials at different pressures, *J. Clean. Product.* 273: pp. 122915.
- Zhu, X., D.C.W. Tsang, L. Wang, Z. Su, D. Hou, L. Li, J. Shang (2021) Machine learning for the selection of carbon-based materials for tetracycline and sulfamethoxazole adsorption. *Chemical Engineering Journal* 406: pp. 126782



## Utilization of COSMO-RS for Valuable Metal Extraction from Spent Lithium-ion Batteries

Hussein K. AMUSA<sup>ab\*</sup>; Ahmad S. DARWISH<sup>A</sup>, Tarek LEMAOUI<sup>C</sup>, Hassan A. ARAFAT<sup>A,b</sup>, Inas M. NASHEF<sup>A,b</sup>

<sup>a</sup> Department of Chemical Engineering, Khalifa University of Science and Technology, Abu Dhabi, United Arab Emirates.

<sup>b</sup> Center for Membranes and Advanced Water Technology, Khalifa University, P.O. Box 127788, Abu Dhabi, United Arab Emirates.

<sup>c</sup> Laboratoire des Matériaux Polymères Multiphasiques (LMPMP), Université Ferhat ABBAS Sétif-1, 19000 Sétif, Algeria.

\* Corresponding author: husseinkehindeamusa@gmail.com

---

### ABSTRACT

Lithium-ion batteries (LIBs) wide usage constitutes a disposal threat to the environment. As a result, several laws are being introduced to encourage the recycling of this waste, particularly, in lithium recovery. Deep eutectic solvent (DES) has been reported as an efficient solvent in valuable metal recovery from spent LIBs. However, efficient deep eutectic solvent design requires a smart selection of components. This study developed a COSMO-RS model to screen several components as DES starting material in lithium extraction from spent LIB. The model consists of 191 different constituents. The model is developed using the COSMOtherm software in the LIB application for the first time. The model uses lithium chemical potential to measure the affinity of lithium in the screened components. Overall, all the compounds show an affinity for lithium. The components are classified into ionic and non-ionic. The ionic compounds performed better than the non-ionic compounds. This is due to the coordinating ability of the ionic compounds with lithium. Further, this study highlights other properties such as reducibility, toxicity, and viscosity as screening strategies in DES component selection for lithium extraction. This is to implement the full green chemistry principle essential for industrial application.

**Keywords:** Lithium-ion battery; Lithium; Green technology; Deep eutectic solvents; COSMO-RS.

### 1. INTRODUCTION

Lithium possesses excellent properties such as high redox potential, specific heat capacity, and charge-to-weight ratio. This enables its wide use as an important element in several industries such as energy security, environmental safety, daily life, industrial consumption, and mental health treatment (Swain, 2017). Among the end consumer who uses lithium, lithium-ion batteries (LIBs) have the largest lithium market share value worldwide. This is owing to the increasing usage of LIBs for various applications such as portable electronic devices, stationary storage devices, and hybrid electric vehicles. It is estimated that the market value of LIBs would reach \$99.98 billion by the year 2030 (Fan *et al.*, 2020). This poses a major disposal threat to the environment.

In contrast, the recycling of spent LIBs could address the impending threat of environmental contamination from these wastes. In this regard, recovery of these end-of-life LIBs, particularly, lithium from the cathode material ensures twin benefits of conserving spent LIB and sustaining lithium production. Therefore, the research community continues to explore different lithium recycling strategies from spent LIBs.

Traditionally, the recycling methods of spent LIB cathode materials are based on pyrometallurgy and hydrometallurgy. Pyrometallurgy involves short operation steps. The method has been reported to give high efficiency of valuable metal extraction (Swain, 2017). However, the process is limited by high energy requirements, treatment of off-gas, and loss of lithium in the slag. On the other hand, hydrometallurgy is a promising lithium production technique due to its low energy requirements and high recovery rate. Unfortunately, this technique is limited by toxic and environmentally harmful solvents such as sulfuric, nitric, and hydrochloric acid in the leaching operation (Liu *et al.*, 2019). Hence, the need for a green solvent.

Deep eutectic solvent (DES) arises as a green solvent for efficient leaching of LIB cathode materials. (Tran *et al.*, 2019) first used DES as a green solvent for leaching LIB cathode material. Since then, more studies have emerged in

this area (Tang *et al.*, 2022). Deep eutectic solvents are obtained in the laboratory by incorporation of two or more components that exit as eutectic (Abbott *et al.*, 2006). Owing to their designers' nature, vast possible combinations of the DES constituents exist. Therefore, it is reasonable to devise a means to efficiently screen these constituents base on their affinity for lithium. This is to save researchers valuable time and experiment costs. In this regard, the application of computational models and molecular-level chemistry analyses is pertinent to suggest potential DES' components for lithium extraction from spent LIBs.

The Conductor-like screening model for realistic solvation (COSMO-RS) is a method based on quantum chemistry and a statistical model to screen solvents for different applications (Hou *et al.*, 2016). For example, (Adeyemi *et al.*, 2018) employed COSMO-RS to screen several probable deep eutectic solvents for CO<sub>2</sub> capture. It has also been used as a solvent screening tool in several liquid-liquid extraction processes (Jiang *et al.*, 2021). In lithium extraction, the use of COSMO-RS has been reported in a few studies. In one study, (Zhao *et al.*, 2018) utilized COSMO-RS to predict and screen probable ionic liquids (ILs) constituents that show an affinity for lithium from brine. In the study, the model was used to optimize the probable IL in extracting Li. In another investigation, (Olea *et al.*, 2022) used COSMO-RS to propose new ILs based on the experimental findings and correlations with COSMO-RS prediction. The two mentioned studies were based on lithium production from brine. To the best of the authors' knowledge, no prior study has been carried out on the use of COSMO-RS to screen and predict DES in lithium extraction from spent LIB.

Thus, this work aims to use COSMO-RS to screen several DES constituents for lithium extraction from spent LIB. The chemical potential of lithium was obtained by sigma profile analyses. Further, selected best DES constituents could lead to the design of novel DES over different parameters such as toxicity, viscosity, reducibility, and ability to form chelating compounds with lithium. Lastly, probable DES would be utilized for further experimental studies on LIB dissolution for lithium production.

## 2.0 MATERIALS AND METHODS

The COSMO-RS workflow is in two phases (figure 1) COSMO (uses quantum chemistry programs like TURBOMOLE) and Figure 2. COSMO-RS (COSMOTHERM). The COSMO surface can be used to qualitatively determine molecular properties such as activity coefficient at infinite dilution and chemical potential. Since Li is a cation, the model works to determine the chemical potential of lithium on DES constituents. Detailed information on the COSMO-RS working procedures can be found elsewhere (Adeyemi, Abu-Zahra and AlNashef, 2018).

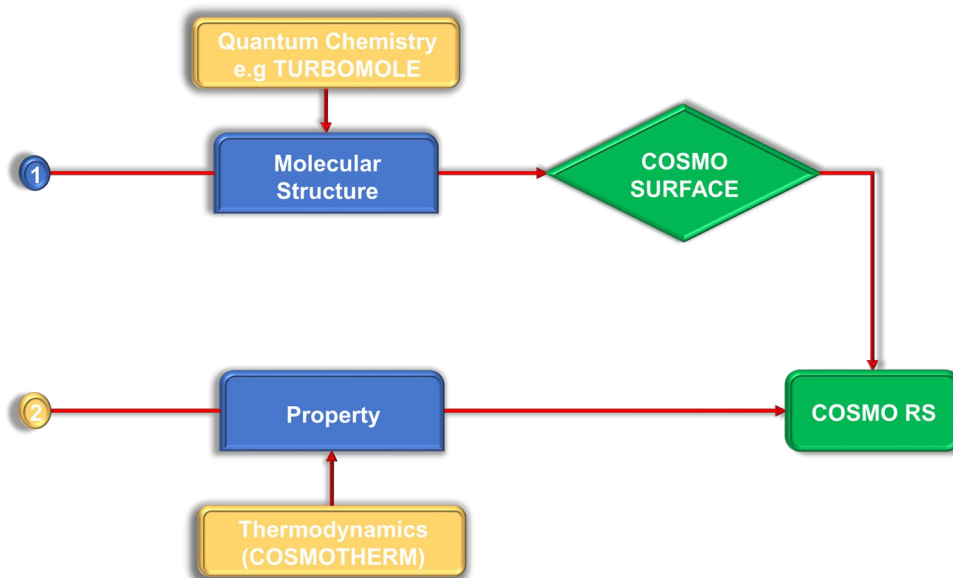


Figure 1: COSMO-RS workflow

### 2.1 Computation Details

To develop the COSMO-RS model used in this study, the Turbomole software version TmoleX19 4.5.1 was first utilized to draw the geometry of each DES component (Allouche, 2012). Subsequently, the density functional theory (DFT) calculations were used to optimize the geometrical structures of the components using the def-TZVP "triple-zeta valence polarized" basis with the Becke-Perdew (BP86) exchange-correlation functional (SCF convergence of  $1 \times 10^{-6}$  Hartree with 500 cycles (Bououden *et al.*, 2021). This procedure follows that reported by our former research group (Hadj-Kali *et al.*, 2016; Adeyemi *et al.*, 2020). Cosmo files are created and then imported into the 2022 BIOVA COSMO therm version software. The software assumes that each surface structure consists of a segment area

$a$ ; and characterizes the interaction between molecules as hydrogen bond interactions, van der Waal interactions, or having surface charge densities of  $\sigma_i$  with misfit electrostatic charge. In COSMO, the interaction is expressed mathematically as

$$\varepsilon_{vdW} = a_{eff} \cdot (\tau_{vdW} + \tau'_{vdW}) \quad (1)$$

Subsequently, these interactions are used to express the DES components ( $\mu_S$ ) defined in

$$\varepsilon_{hb} = a_{eff} \cdot c_{hb} \min(0; \min(0; \sigma_{donor} + \sigma_{hb}) \max(0; \sigma_{acceptor} + \sigma_{hb})) \quad (2)$$

$$\varepsilon_{mf} = a_{eff} \cdot \frac{\alpha'}{2} (\sigma + \sigma')^2 \quad (3)$$

$$\mu_S(\sigma) = \frac{-RT}{a_{eff}} \ln \left[ \int P_S(\sigma') \exp \left( \frac{a_{eff}}{RT} (\mu_S(\sigma') - \varepsilon_{mf} - \varepsilon_{hb} - \varepsilon_{vdW}) \right) d\sigma' \right] \quad (4)$$

Where ( $\mu_S$ ) is the DES constituents potential (kJ/g),

$\sigma$  And  $\sigma'$  represents the two surface segments (e/nm<sup>2</sup>)

$a_{eff}$  Is the area of effective contact (nm<sup>2</sup>),

$\tau_{vdW}$  Is the strength coefficient of dispersion,

$\sigma_{hb}$  Is the screening charge density threshold for hydrogen bonding (set to 0.008 e/Å<sup>2</sup> by default),

$c_{hb}$  Is the strength coefficient of hydrogen bonding,

$\sigma_{donor}$  And  $\sigma_{acceptor}$  are the surfaces of the hydrogen bond donor and acceptor (e/nm<sup>2</sup>),

$\alpha'$  Is a general interaction fitting parameter, and  $P_S$  the screening charge density distribution (e/Å<sup>2</sup>).

### 3. RESULTS AND DISCUSSION

#### 3.1 COSMO-RS Analyses

COSMO-RS analyses are based on two main principles- the sigmal profile, and the DFT structure of the molecules. The sigmal profile represents the degree to which a molecular surface segment gives a positive, negative, or neutral charge. Essentially, the sigmal profile provides information on the types of interaction in molecules. This is represented through the height, width, and location of the peaks in the sigmal profile. Fundamentally, the sigmal profile categorized molecules into three groups: region of positive polarity, negative polarity, and neutral surfaces. Further detail on the significance of the sigmal profile can be found elsewhere (Lemaoui *et al.*, 2020). The sigmal profile also reveals which constituents make a hydrogen bond donor or acceptor. Compounds that give peaks on both sides can act as both hydrogen bond acceptors (HBA) and hydrogen bond donors (HBD).

#### 3.2 Classification into ionic and non-ionic species

The screened constituents are broadly classified into ionic (HBAs) and non-ionic (HBDs). Table 1 shows the dissolution of selected DES constituents (in ascending order of Li chemical potential). The other DES constituents studied are available in the supplementary document. Interestingly, all the constituents can dissolve lithium. Therefore, both the hydrogen bond donors and hydrogen bond acceptors can influence the performances of the resulting DESs in the lithium leaching process (Wang *et al.*, 2016). The ionic compounds generally perform better than the non-ionic compound in their ability to dissolve lithium. This may be due to the presence of different anions and captions which aids the formation of coordinating complexes between the ionic compound and lithium. The next section expatiates the influence of the different anions and captions in the ionic compounds.

#### 3.3 Influence of Hbas

The HBAs studied in this work are mainly based on organic salts, metal halides, and natural-based HBAs (Table S1 of the supplementary document). Organic salts based on phosphonium and ammonium compounds as the central atom has a high influence on lithium extractability. Generally, the order of chemical affinity is higher in ammonium-based compared to phosphonium-based compounds. This may be due to higher densities in phosphonium-based compounds compared to ammonium-based compounds (Wazeer *et al.*, 2021). This higher density translates to a lower leaching rate and hence lower efficiency. Moreover, the charge density in the P=O group is influenced by the presence of radicals in the vicinity of the energy bonding (Blundell and Licence, 2014). On the other hand, high polarity and small volume of the central nitrogen atom in ammonium-based HBAs lead to high performance.

Table 1: Chemical potential of Li in Selected DES constituent

HBA	Ionic Compound	$\mu\text{Li}^+$ (kJ/g)	HBD	Non-Ionic Compound	$\mu\text{Li}^+$ (kJ/g)
A13	Tetrabutylammonium Chloride	5.130	D1	Polyethyleneglycol400	10.284
A14	Tetrabutylphosphonium Chloride	5.138	D2	Lidocaine	10.975
A19	Tetraethylphosphonium Chloride	5.712	D3	ethanolamine	11.417
A28	Tetraethylammonium Chloride	6.120	D7	Urea	11.976
A31	Benzethonium Chloride	6.630	D13	Camphor	12.459
A47	Carnitine	7.451	D15	Allantoicacid	12.580
A48	Betaine	7.509	D21	Thiourea	12.935
A49	Tetraethylphosphonium Bromide	7.584	D28	Glycol	13.150
A58	Tetraethylammonium Bromide	7.934	D45	Acetic acid	13.917
A62	Benzethonium Bromide	8.323	D47	Menthol	13.950
A64	Choline Chloride	8.739	D66	Formic acid	14.462
A69	Choline Bromide	10.112	D74	Citric acid	14.708

Furthermore, the length of the alkyl chain in the quaternary-based compounds also contributes to their dissolution ability. The chemical potential tends to increase with an alkyl chain length with Tetrapentylammonium (TPA) > Tetrahexylammonium (THA) > Tetraoctylammonium (TOA). However, for the lower alkyl group, the chemical potential decreases with alkyl chain length in the order Tetrabutylammonium (TBA) > Tetraethylammonium (TEA) > Tetramethylammonium (TMA). For phosphonium-based compounds, the result shows similar trends as ammonium-based compounds. However, comparing both types, ammonium-based compounds perform better than phosphonium-based molecules as discussed earlier. Several ring/phenyl group compounds were also predicted for their ability to dissolve lithium. In general, the HBA having rings shows a lower affinity for lithium compared to the straight-chain organic salts. This result may stem from the large steric hindrance in the ring-based compounds (Braun *et al.*, 2020). The HBA-containing halide plays a crucial role in the metal dissolution. This is because the leaching of metals could occur via coordination with halide ions in the HBA. For the halide compounds, the chlorine-containing compounds perform better than their bromine-containing compounds counterparts. This attribute can be ascribed to the more electronegativity in chlorine compared to bromine (Warrag *et al.*, 2017).

The metal salt containing the copper halide and hydrates of copper halide performed excellently in the target metal dissolution. This behavior may be attributed to the reduced ability of the copper (Peeters, Binnemans and Riaño, 2020). Since the leaching of cobalt is influenced by a reducing agent. Thus, copper in copper halide and hydrated copper halide as HBA may act as a potential component of a DES (Ghareh Bagh *et al.*, 2013). In addition, the presence of the halide is essential for the formation of a halo-metal complex during the leaching operation. Moreover, these results corroborated literature findings that metal halides increased the solubility of metals (Chanaka *et al.*, 2019). Although based on the COSMO-RS prediction, the metal halide group shows the best performance, it is also essential to assess their toxicity and whether this group would form a DES. This is because no prior study has established their usage in DES formation, or it may be a research gap.

In this study, several compounds including carnitine, betaine, glycine, alanine, proline, and choline chloride, etc. could form natural deep eutectic solvents (NADES) when paired with natural HBDS. Figure 3 presents examples of NADES forming HBAs. NADES could exhibit all the principles of green chemistry (Dai *et al.*, 2015). Among these compounds, those containing oxygen anion perform better than the cholinium-based HBA. Although betaine and choline chloride possess similar structures, the higher solubility in betaine may be attributed to the presence of the oxygen anion. This is because oxygen is a better electron acceptor compared to chlorine.



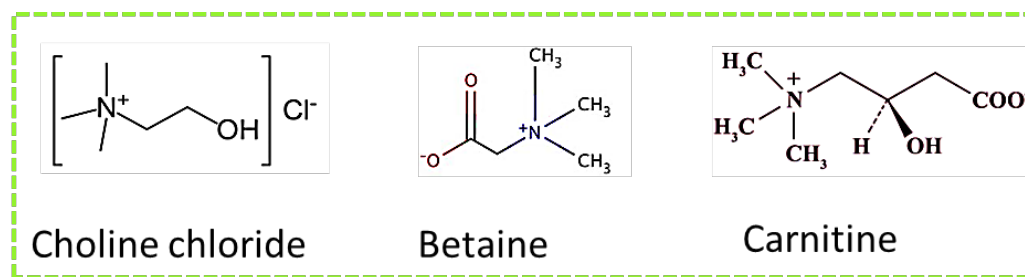


Figure 2: Examples of NADES forming HBAs

Overall, HBA component selection based on betaine and carnitine could lead to novel optimal green DES design. However, the choice of selected HBD is also an important consideration in optimum DES design. Hence, the next discussion presents the hydrogen bond donor influence on lithium extraction from spent lithium-ion batteries.

### 3.4 Influence of HBDs

The several HBDs (Table S2 of the supplementary document) studied also showed a great ability to solubilize lithium. This may be explained due to metal complexing ligand formation between lithium and the non-ionic compound (Schaeffer *et al.*, 2020). In HBD analysis, the alkyl chain length, functional group, and the presence of a ring or cyclic molecules further influence the extractability of the studied constituents.

Based on the functional group present in the HBD, no rigid trends were observed regarding the superior performance of a specific functional group. It appears that several other factors influence the performances of the solvents. However, compounds containing multifunctional groups tend to perform better than compounds with a single functional group. This behavior may be attributed to the specificity of each functional group's ability to solubilize lithium. Essentially, the amino-alcohol groups perform better than the other studied functional groups. This high performance may be related to the presence of the amine and alcohol groups.

## 4. CONCLUSION

A COSMO-RS model has been developed to predict lithium extractability with several DES components. The model can determine the affinity of any DES component comprising hydrogen bonds for lithium. The only input of the model is the chemical structure of these hydrogen bond-forming compounds. Among the 191 studied components, ionic compounds show a high affinity for lithium. This phenomenon is attributed to the coordination of lithium with these compounds. In addition, the presence of functional groups in non-ionic compounds is influential in the ion exchange mechanism with lithium. Thus, the COSMO-RS model can guide the appropriate selection of probable DES constituents from a pool of possible DES components for metal dissolution. Therefore, our future study will focus on the application of this model to other valuable metals in spent LIBs. Further, novel DES would be synthesized based on other desirous properties such as reduction ability, transport property, health, and ecological concerns.

## ACKNOWLEDGEMENTS

The authors would like to thank Khalifa University, Abu Dhabi, and the United Arab Emirates for providing the library resources required for this work.

## REFERENCES

- Abbott, A.P. *et al.* (2006) 'Solubility of metal oxides in deep eutectic solvents based on choline chloride', *Journal of Chemical and Engineering Data*, 51(4), pp. 1280–1282. Available at: <https://doi.org/10.1021/je060038c>.
- Adeyemi, I. *et al.* (2020) 'Removal of chlorophenols from aqueous media with hydrophobic deep eutectic solvents: Experimental study and COSMO RS evaluation', *Journal of Molecular Liquids*, 311, p. 113180. Available at: <https://doi.org/10.1016/j.molliq.2020.113180>.
- Adeyemi, I., Abu-Zahra, M.R.M. and AlNashef, I.M. (2018) 'Physicochemical properties of alkanolamine-choline chloride deep eutectic solvents: Measurements, group contribution and artificial intelligence prediction techniques', *Journal of Molecular Liquids*, 256, pp. 581–590. Available at: <https://doi.org/10.1016/j.molliq.2018.02.085>.
- Allouche, A. (2012) 'Software News and Updates Gabedit — A Graphical User Interface for Computational Chemistry Softwares', *Journal of computational chemistry*, 32, pp. 174–182. Available at: <https://doi.org/10.1002/jcc>.
- Blundell, R.K. and Licence, P. (2014) 'Quaternary ammonium and phosphonium based ionic liquids: A comparison of common anions', *Physical Chemistry Chemical Physics*, 16(29), pp. 15278–15288. Available at: <https://doi.org/10.1039/c4cp01901f>.

- Bououden, W. *et al.* (2021) ‘Surface adsorption of Crizotinib on carbon and boron nitride nanotubes as Anti-Cancer drug Carriers: COSMO-RS and DFT molecular insights’, *Journal of Molecular Liquids*, 338, p. 116666. Available at: <https://doi.org/10.1016/j.molliq.2021.116666>.
- Braun, M.G. *et al.* (2020) ‘Green Chemistry Articles of Interest to the Pharmaceutical Industry’, *Organic Process Research and Development*, 24(3), pp. 334–346. Available at: <https://doi.org/10.1021/acs.oprd.0c00036>.
- Chanaka, C.U. *et al.* (2019) ‘Insights into the speciation of heavy metals during pyrolysis of industrial sludge’, *Science of the Total Environment*, 691, pp. 232–242. Available at: <https://doi.org/10.1016/j.scitotenv.2019.07.095>.
- Dai, Y. *et al.* (2015) ‘Tailoring properties of natural deep eutectic solvents with water to facilitate their applications’, *Food Chemistry*, 187, pp. 14–19. Available at: <https://doi.org/10.1016/j.foodchem.2015.03.123>.
- Fan, E. *et al.* (2020) ‘Sustainable Recycling Technology for Li-Ion Batteries and Beyond: Challenges and Future Prospects’, *Chemical Reviews*. American Chemical Society, pp. 7020–7063. Available at: <https://doi.org/10.1021/acs.chemrev.9b00535>.
- Florindo, C. *et al.* (2014) ‘Insights into the synthesis and properties of deep eutectic solvents based on cholinium chloride and carboxylic acids’, *ACS Sustainable Chemistry and Engineering*, 2(10), pp. 2416–2425. Available at: <https://doi.org/10.1021/sc500439w>.
- Ghareh Bagh, F.S. *et al.* (2013) ‘Solubility of sodium salts in ammonium-based deep eutectic solvents’, *Journal of Chemical and Engineering Data*, 58(8), pp. 2154–2162. Available at: <https://doi.org/10.1021/jc400045d>.
- Hadj-Kali, M.K. *et al.* (2016) ‘Removal of Thiophene from Mixtures with n-Heptane by Selective Extraction Using Deep Eutectic Solvents’, *Industrial and Engineering Chemistry Research*, 55(30), pp. 8415–8423. Available at: <https://doi.org/10.1021/acs.iecr.6b01654>.
- Hou, D., Lu, L. and Ren, Z.J. (2016) ‘Microbial fuel cells and osmotic membrane bioreactors have mutual benefits for wastewater treatment and energy production’, *Water Research*, 98, pp. 183–189. Available at: <https://doi.org/10.1016/j.watres.2016.04.017>.
- Jiang, C. *et al.* (2021) ‘COSMO-RS prediction and experimental verification of 1,5-pentanediamine extraction from aqueous solution by ionic liquids’, *Green Energy and Environment*, 6(3), pp. 422–431. Available at: <https://doi.org/10.1016/j.gee.2020.12.011>.
- Lemaoui, T. *et al.* (2020) ‘Predicting the density and viscosity of hydrophobic eutectic solvents: Towards the development of sustainable solvents’, *Green Chemistry*, 22(23), pp. 8511–8530. Available at: <https://doi.org/10.1039/d0gc03077e>.
- Li, C. *et al.* (2022) ‘Densities and viscosities of, and solubilities of acidic gases (SO<sub>2</sub> and H<sub>2</sub>S) in natural deep eutectic solvents’, *Journal of Chemical Thermodynamics*, 167. Available at: <https://doi.org/10.1016/j.jct.2021.106713>.
- Liu, C. *et al.* (2019) ‘Recycling of spent lithium-ion batteries in view of lithium recovery: A critical review’, *Journal of Cleaner Production*, 228(1), pp. 801–813. Available at: <https://doi.org/10.1016/j.jclepro.2019.04.304>.
- Olea, F. *et al.* (2022) ‘Ionic Liquids for the Selective Solvent Extraction of Lithium from Aqueous Solutions: A Theoretical Selection Using COSMO-RS’, *Minerals*, 12(2). Available at: <https://doi.org/10.3390/min12020190>.
- Schaeffer, N. *et al.* (2020) ‘Non-ionic hydrophobic eutectics-versatile solvents for tailored metal separation and valorisation’, *Green Chemistry*, 22(9), pp. 2810–2820. Available at: <https://doi.org/10.1039/d0gc00793e>.
- Swain, B. (2017) ‘Recovery and recycling of lithium: A review’, *Separation and Purification Technology*, 172, pp. 388–403. Available at: <https://doi.org/10.1016/j.seppur.2016.08.031>.
- Tang, S., Zhang, M. and Guo, M. (2022) ‘A Novel Deep-Eutectic Solvent with Strong Coordination Ability and Low Viscosity for Efficient Extraction of Valuable Metals from Spent Lithium-Ion Batteries’, *ACS Sustainable Chemistry & Engineering*, pp. 975–985. Available at: <https://doi.org/10.1021/acssuschemeng.1c06902>.
- Tran, M.K. *et al.* (2019) ‘Deep eutectic solvents for cathode recycling of Li-ion batteries’, *Nature Energy*, 4(4), pp. 339–345. Available at: <https://doi.org/10.1038/s41560-019-0368-4>.
- Wang, S. *et al.* (2020) ‘A novel method for screening deep eutectic solvent to recycle the cathode of Li-ion batteries’, *Green Chemistry*, 22(14), pp. 4473–4482. Available at: <https://doi.org/10.1039/d0gc00701c>.
- Wang, Y. *et al.* (2016) ‘Roles of a hydrogen bond donor and a hydrogen bond acceptor in the extraction of toluene from n-heptane using deep eutectic solvents’, *Green Chemistry*, 18(10), pp. 3089–3097. Available at: <https://doi.org/10.1039/c5gc02909k>.
- Warrag, S.E.E., *et al.* (2017) ‘Separation of Thiophene from Aliphatic Hydrocarbons Using Tetrahexylammonium-Based Deep Eutectic Solvents as Extracting Agents’, *Journal of Chemical and Engineering Data*, 62(9), pp. 2911–2919. Available at: <https://doi.org/10.1021/acs.jced.7b00168>.
- Wazeer, I. *et al.* (2021) ‘The subtle but substantial distinction between ammonium- and phosphonium-based deep eutectic solvents’, *Journal of Molecular Liquids*. Available at: <https://doi.org/10.1016/j.molliq.2021.115838>.
- Zhao, X. *et al.* (2018) ‘Liquid-liquid extraction of lithium from aqueous solution using novel ionic liquid extractants via COSMO-RS and experiments’, *Fluid Phase Equilibria*, 459, pp. 129–137. Available at: <https://doi.org/10.1016/j.fluid.2017.11.038>.



## Synthesis and Characterization of Zinc Chloride Modified Activated Carbon and other Derivative Adsorbents from *Vitex Doniana* Seed

Oluwadayo A. FRANCIS<sup>1\*</sup>, Emeka C. NWORIE<sup>2</sup>, Kevin S. OTOIKHIAN<sup>3</sup>

<sup>1,3</sup>Department of Chemical Engineering, Edo State University, Uzairue, Nigeria

<sup>2</sup>Department of Chemical Engineering Technology, Auchi Polytechnic, Auchi, Nigeria

<sup>1\*</sup>[Francis.asokogene@edouniversity.edu.ng](mailto:Francis.asokogene@edouniversity.edu.ng), <sup>2</sup>[nocyka2016@gmail.com](mailto:nocyka2016@gmail.com), <sup>3</sup>[otoikhian.kevin@edouniversity.edu.ng](mailto:otoikhian.kevin@edouniversity.edu.ng)

\*Corresponding author

### ABSTRACT

This study evaluated the characteristics and adsorption performance of zinc chloride-modified activated carbon (VDZnCl<sub>2</sub>), its precursor (VDC), and sodium hydroxide (VDNaOH), hydrochloric acid (VDHCl) and thermally (VDT) modified adsorbents from vitex doniana. The adsorption performance of the adsorbents for methylene blue was in this order: VDZnCl<sub>2</sub> < VDNaOH < VDC < VDT < VDHCl. The VDZnCl<sub>2</sub> was characterized by Fourier transform infrared (FTIR), Brunauer-Emmett-Teller (BET), scanning electron microscope (SEM), energy-dispersive X-ray (EDAX) and thermal gravimetric analysis (TGA). The FTIR spectrum showed the presence of the O-H group and characteristics C=C group generally found in carbonaceous materials. The BET surface area remarkably increased from 14.02 m<sup>2</sup>/g to 933.25 m<sup>2</sup>/g and pore size from 0.92 to 18.9 Å which reflected enhanced specific surface area and porous nature of the adsorbent, and its ability to facilitate pore fillings of many molecules inside its carbon matrix during adsorption. The SEM micrograph showed varieties of pores with widened cavities. Therefore, VDZnCl<sub>2</sub> is a potential adsorbent substitute for wastewater treatment.

**Keywords:** *Vitex doniana*, characteristics, activated carbon, adsorption, carbonaceous materials.

### 1. INTRODUCTION

The growing trend of water contaminations resulting from growing population and industrialization is of great concern because they contaminate surface and groundwater, and also render them unfit for drinking and irrigation when they are discharged into streams, oceans and lakes by chemical, textile and other allied industries (Piriya *et al.*, 2021). These contaminants such as heavy metals, dyes, etc. in water limit sunlight penetration into water and aeration of water bodies which impact negatively photosynthesis and subsequently reduces the amount of dissolved oxygen in water (Piriya *et al.*, 2021; Imran *et al.* 2019). They also inject chemicals that lead to the death of most aquatic life, contamination of soils, and poisoning of drinking water which results in numerous health issues like dyscrasia, leukocytosis, anaemia, eye burn, damage to the liver, heart, spleen, kidney, lungs, bones and teratogenic effects (Alipour *et al.*, 2019; Piriya *et al.*, 2021).

Several treatment methods adopted for the removal of contaminants from wastewater include extraction, membrane separation, coagulation, ozonation, flocculation and adsorption (Asokogene *et al.*, 2019; Aslam *et al.*, 2017; Luo *et al.*, 2017; Wang *et al.*, 2017). Adsorption holds a special place in the treatment of wastewater because of its low cost, effectiveness and ability to selectively enrich certain compounds (Asokogene *et al.*, 2019; Pandey *et al.*, 2020; Piriya *et al.*, 2021). This has led researchers to develop low-cost and readily available adsorbents from several synthetic and natural biomass.

Activated carbon has gained wide attention as a brilliant adsorbent for the removal of aquatic pollutants due to its high surface area, stability, array of functional groups and excellent pore structures (Afshin *et al.*, 2019). It is produced from several agricultural wastes such as empty fruit bunch (Zaini *et al.*, 2016), wood (Nowicki, 2016) bamboo (Zhao *et al.*, 2017), palm shells (Zhao *et al.*, 2018), coconut shells (Singh *et al.*, 2017), rice husk (Li *et al.*, 2015), sawdust (Zhu *et al.*, 2014), apricot stones (Djilani *et al.*, 2015) and grape seeds (Okman *et al.*, 2014), etc. by chemical or physical activation. Chemical activation enhances its specific surface area and porosity (Piriya *et al.*, 2021). Zinc chloride has proven to be a better activating agent for most activated carbon adsorbents as it produces higher specific surface area and better adsorption results. For instance, ZnCl<sub>2</sub>-activated carbon from *sterculia gulata* shells had an adsorption capacity of 90.90 mg/g as against the precursor (*sterculia gulata* shells) of 45.45 mg/g (Rangabhashiyam and Selvaraju, 2015). Similarly, Zhang *et al.*, 2020 also reported that ZnCl<sub>2</sub> impregnated activated carbon from rice husk at an impregnation ratio of 1:1 had a higher surface area than its precursor.

Consequently, *vitexdoniana* seed, which is frequent waste in Nigeria (Ameh *et al.*, 2012; Kapooria and Aime, 2005) and obtained from commonly grown *vitex doniana* tree has been limitedly synthesized as activated carbon adsorbent for Zn (II) and Pb (II) removal (Ameh *et al.*, 2012) and as acid modified activated carbon for Cr (II) removal (Yusuf *et al.*, 2020) from wastewater, but no study has been done on the synthesis of ZnCl<sub>2</sub> modified activated carbon from *vitex doniana* seed and its adsorption potential for dye (methylene blue) from wastewater. Therefore, this study was a first-time attempt at the synthesis of zinc chloride (ZnCl<sub>2</sub>) modified activated carbon adsorbent from *vitex doniana*, removal of methylene blue dye from wastewater and comparing its adsorption performance of its precursor, sodium hydroxide (NaOH), hydrochloric acid (HCl) and thermally modified ones, with the view to encourage its use as an indigenous adsorbent for wastewater treatment, thus contributing to sustainable development goals. BET, SEM, EDX, FTIR and TGA were used to determine the properties of the adsorbent and its adsorption potential in batch mode was carried out on methylene blue removal from wastewater within a working concentration of 10 mg/L.

## 2.0 MATERIALS AND METHODS

### 2.1 Materials, Reagent and Instrument

*Vitex doniana* seeds were collected from the Auchi Polytechnic community in Edo State. The chemicals used were of analytical grade: hydrochloric acid (37 %, Fisher Scientific, USA), methylene blue powder (98.5 %, BDH, England), Zinc chloride pellet (99%, Merck, Germany) and distilled water (Chemical Engineering Laboratory, Auchi). Instruments used are analytical balance (Scout Pro, Ohaus, London, UK), pH meter (pH ep® pocket-sized pH meter, Hanna Instruments, Inc., USA), grinding mill (Biocotek, China), shaker (Ro-tap, England), stopwatch (Quartz, China), Thermometer (Pyrex Technico, England), Fourier transform infrared (FTIR) spectrometer (Thermo Scientific, Nicolet ISI 10, USA), scanning electron microscope (SEM)/ energy dispersive analysis of x-ray (EDX) spectrophotometer (Karl Zeiss, Germany), Brunauer-Emmett-Teller (BET) surfer machine (Thermo Scientific, USA), thermogravimetric analyser (Orton Simultaneous DTG/TGA, USA), UV-Vis spectrophotometer (Angstrom Advanced Inc, model 752, Massachusetts, USA) and muffle furnace (TT-EF-12, Techmel, USA).

### 2.2 Pre-treatment and Synthesis of *Vitex Doniana* Adsorbent

The exocarp and impurities of *vitex doniana* seed were washed off with running water. The seed was sun-dried for seven days, crushed, ground, and sieved to a size of 355 µm (Ameh *et al.*, 2012). A 100 g each of the pulverized *vitex doniana* was treated thermally at 800 °C (Mistar *et al.*, 2020) and chemically modified using ZnCl<sub>2</sub>, sodium hydroxide (NaOH) and hydrochloric acid (HCl) by adding 0.5 M solutions of each chemical to the pulverized samples in the ratio of 1:1 to form homogenize paste-like mixtures which were allowed to stay for 24 h for adequate impregnation. The mixtures were activated at 800°C for 2 h in a TT-EF-12 muffle furnace (Techmel, USA). The resultant activated carbon samples were allowed to cool, washed with distilled water to a pH of 7, dried in the oven at 105°C for 3 h and kept in a desiccator, except for the ZnCl<sub>2</sub> modified sample which was soaked in HCl (3 wt.%) for the 12 h to remove surface ash before washing (Mkungunugwa *et al.*, 2021; Mistar *et al.*, 2020; Jaria *et al.*, 2015; Khadiran *et al.*, 2015). These adsorbents were designated as VDC, VDT, VDZnCl<sub>2</sub>, VDNaOH and VDHCl for precursor, thermally treated, ZnCl<sub>2</sub> modified, NaOH modified and HCl modified *vitex doniana*, respectively.

### 2.3 Characterization of *Vitex Doniana* Adsorbent

The surface functional groups of VDZnCl<sub>2</sub> and VDC (precursor) adsorbent samples were determined using an FTIR analyser (Thermo Scientific Nicolet ISI 10, USA) at a wavenumber range of 4000-500 cm<sup>-1</sup>. The textural properties were measured using a Thermo Scientific (USA) surface area analyser. The SEM image of the adsorbent surface and texture was obtained by a Karl Zeiss (Germany) instrument. The thermal decomposition of the adsorbent sample was determined using the standard Orton simultaneous DTG/TGA analyser, USA by recording the differential thermal couple output and balance output signal over a temperature range of 30–1000°C. The elemental composition of the adsorbent was also obtained using EDX as individual fluorescent energies detected were specific to the elements that were present in the sample.

### 2.4 Experimental Procedure

For the batch adsorption study, 1 g of methylene blue powder was dissolved in 1000 mL of distilled water to make a stock solution and a working concentration of 10 mg/L was prepared by dilution. In Beatson bottles, 50 mL of the concentration was added to 50 mg of the adsorbents. Next, the bottles were sealed, shaken, and kept at 28°C for 72 h. The contact time was assumed to be long enough to achieve equilibrium adsorption (Asokogene *et al.*, 2019). The residual concentrations were calculated by measuring absorbance at 620 nm with an Angstrom Advanced Inc. (model 752) scientific ultraviolet-visible (UV-Vis) spectrophotometer. The pH of the methylene blue solution was kept at 4.8±0.3, as it should be. The adsorption capacity,  $q_e$  (mg/g), was determined from a mass balance equation,

$$q_e = \left( \frac{C_o - C_e}{m} \right) \times V \quad (1)$$

Where;  $C_o$  and  $C_e$  (mg/L) are the initial and equilibrium concentrations, respectively,  $V$  (L) is the volume of the solution, and  $m$  (g) is the mass of the adsorbent.

### 3. RESULTS AND DISCUSSION

The batch adsorption plots to determine the best among the series of prepared adsorbents from *vitex doniana* (VDNaOH, VDZnCl<sub>2</sub>, VDHCl, VDT and VDC) are presented in Figure 1. The result revealed that VDNaOH, VDZnCl<sub>2</sub>, VDHCl, VDT and VDC adsorbents had adsorption capacities of 8.57 mg/g, 9.08 mg/g, 5.01 mg/g, 5.40 mg/g and 7.98 mg/g, respectively. In other words, the adsorption capacities were of this order: VDZnCl<sub>2</sub> < VDNaOH < VDC < VDT < VDHCl. This better adsorption performance demonstrated by VDZnCl<sub>2</sub> can be attributed to the creation of better active reaction sites for the adsorption of methylene blue in VDZnCl<sub>2</sub> than VDNaOH, VDC, VDT and VDHCl (Ademiluyi and David-West, 2012).

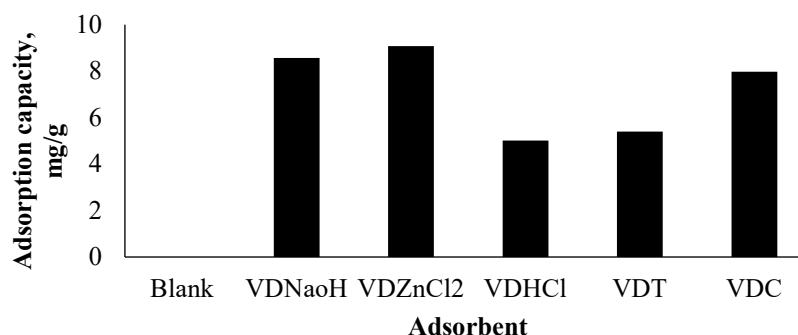


Figure 1: *Vitex doniana* adsorbents performance

The FTIR spectrum which gave insight into the surface functional groups and structure of VDZnCl<sub>2</sub> and VDC adsorbents over a frequency range of 4000-500 cm<sup>-1</sup> is presented in Figures 2 and 3. The signal at 3625–3605 cm<sup>-1</sup> in the FTIR spectrum corresponds to intermolecular hydrogen bonding of polymeric compounds such as alcohols, phenols, and carboxylic acids, showing the presence of free hydroxyl groups on the adsorbent surface of VDZnCl<sub>2</sub> and VDC. Asymmetric and symmetric C—H bending vibrations of the —CH<sub>2</sub> and —CH<sub>3</sub> (alkanes) are associated with a peak at 3300 cm<sup>-1</sup> of VDZnCl<sub>2</sub> while the peak at 2410.16 cm<sup>-1</sup> corresponds to the CH<sub>2</sub> (alkanes) group of C—H symmetric stretching vibration for VDC. Furthermore, the C=C stretching vibration of alkenyl is the characteristic of a peak at 2611 cm<sup>-1</sup> for VDZnCl<sub>2</sub>. Meanwhile, C=O stretching vibration in aldehydes, ester or ketones, and carboxyl groups are indicated by the peaks at 1877 cm<sup>-1</sup> and 1903.27 cm<sup>-1</sup>, respectively of VDZnCl<sub>2</sub> and VDC. Because of the carboxyl group, the peak at 1710.75 cm<sup>-1</sup> corresponds to C—O stretching vibrations, while the C—O stretching vibrations in alcohol, ether, or hydroxyl groups correlate to the peak at 1150.28 cm<sup>-1</sup> for VDC. The peak at 1551 cm<sup>-1</sup> of VDZnCl<sub>2</sub> corresponds to C=C stretching vibrations in the aromatic ring of alkenes, which are common in carbonaceous materials like activated carbon (Mkungunugwa *et al.*, 2021). Finally, the peak at 1298 cm<sup>-1</sup> of VDZnCl<sub>2</sub> belongs to C—H bending vibrations found in alkyl groups like CH<sub>3</sub>, which are lignin-like.

The functional groups contained in VDZnCl<sub>2</sub> and VDC revealed that the majority of the peaks in both adsorbent materials were comparable, with the exception of a peak at 1551.37 cm<sup>-1</sup>, which corresponds to C=C stretching vibrations in the aromatic ring of alkenes and is commonly detected in carbonaceous materials like activated carbon (Mkungunugwa *et al.*, 2021).

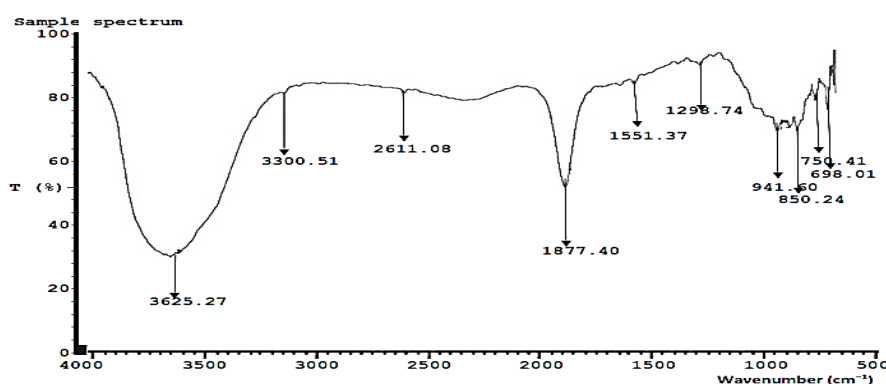


Figure 2: FTIR spectrum of zinc chloride modified vitex doniana activated carbon (VDZnCl<sub>2</sub>)

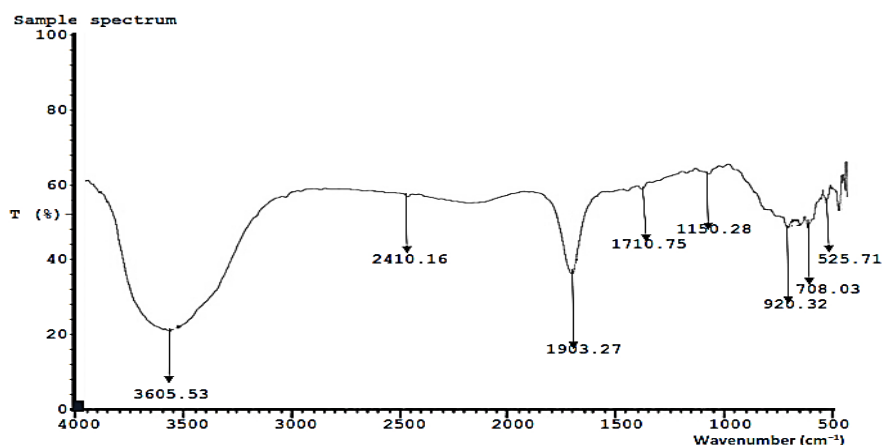


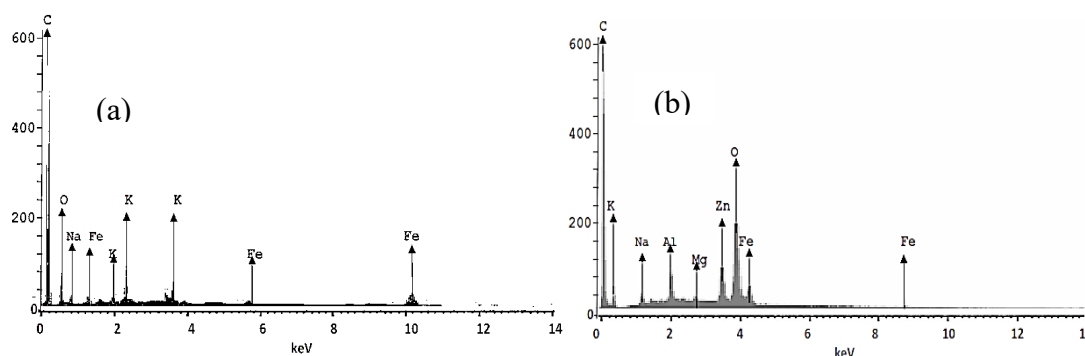
Figure 3: FTIR spectrum of vitex doniana precursor (VDC)

Table 1 summarizes the textural properties of VDZnCl<sub>2</sub> and VDC. The surface area of VDZnCl<sub>2</sub> increased dramatically from 14.0 to 933 m<sup>2</sup>/g. The pattern is consistent with other raw materials upon activation (Mistar *et al.*, 2020; Gonzalez, 2018). Accordingly, the pore volume increased by about three times, from 0.07 to 0.21 cm<sup>3</sup>/g (Mistar *et al.*, 2020; Sethia and Sayari, 2016). After activation, the pore size increased from 0.92 to 18.9 Å. Therefore, VDZnCl<sub>2</sub> will allow for pore fillings of numerous molecules inside its carbon matrix during adsorption ((Thommes *et al.*, 2015; Mistar *et al.*, 2020).

Table 1: Surface Textural Properties of VDZnCl<sub>2</sub> and VDC

BET Parameters	Samples	
	VDC	VDZnCl <sub>2</sub>
Surface area (m <sup>2</sup> g <sup>-1</sup> )	14.02	933.25
Pore volume (cm <sup>3</sup> g <sup>-1</sup> )	0.0683	0.207
Pore size (Å)	0.917	18.92

The SEM result of VDZnCl<sub>2</sub> adsorbent material which was characteristics of its surface morphology and texture at ×500 magnification is shown in Figure 4 and the EDX results of VDZnCl<sub>2</sub> and VDC are shown in Figures 5 (a) and (b), respectively.

Figure 4: SEM micrograph of VDZnCl<sub>2</sub> adsorbentFigures 5: EDX analysis of (a) VDZnCl<sub>2</sub> adsorbent and (b) VDC adsorbent

The SEM micrograph of VDZnCl<sub>2</sub> adsorbent showed thin plant boundary walls due to modification and the presence of varieties of pores with widened cavities which could be due to the removal of volatile matter and production of fixed carbon after activation (Ohimor *et al.*, 2021).

The EDX result revealed the dominance of C and O in the precursor (VDC) and activated carbon adsorbent (VDZnCl<sub>2</sub>). However, in VDC small proportion of Mg, Al, Ca and Zn were observed which were not present in VDZnCl<sub>2</sub>. These elements would have been removed along with other volatile materials during activation at 800°C. Alam *et al.*, 2017 reported similar results for activated carbon synthesized from *Eucalyptus lenceolata*.

The TGA/DTA result for ZnCl<sub>2</sub>-based *vitex doniana* activated carbon, which was characteristic of its thermal behaviour at a regulated temperature, is shown in Figure 6.

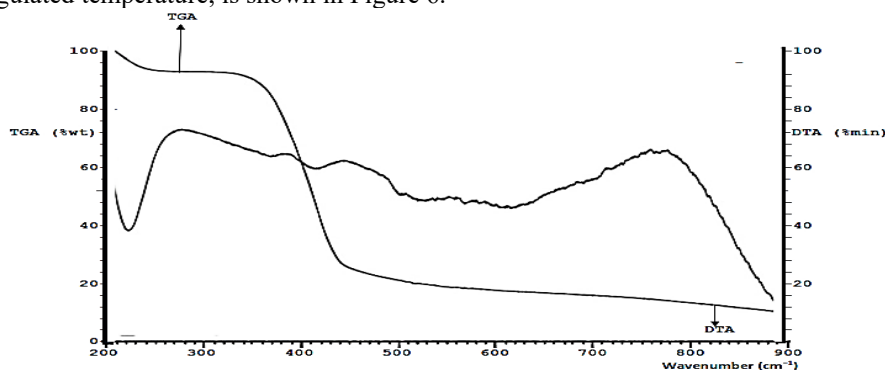


Figure 6: Thermal gravimetric profile of VDZnCl<sub>2</sub>

The curves showed three steps of weight loss (Figure 6) from 200 to 900°C and 48.90 to 68%. The first weight loss within a temperature range of 200-250°C could be due to the eradication of water vapour and light volatile matter (Piriya *et al.*, 2021). The second weight loss within the temperature range of 350 to 500°C could be a result of the liberation of organic constituents and other functional groups in the adsorbent. Finally, the less pronounced third weight loss within a temperature range of 650 to 700°C was probably due to heavy volatile matter eradication or disintegration of high-strength configuration (Piriya *et al.*, 2021). Nevertheless, decomposition of the adsorbent material occurred slowly from 200 to 900°C with most of its fraction being lignin and residual traces of possibly cellulose and hemicellulose (Piriya *et al.*, 2021; Cazetta *et al.*, 2011).

#### 4. CONCLUSION

Zinc chloride-modified activated carbon adsorbent (VDZnCl<sub>2</sub>) and other derivative adsorbents (VDC, VDT, VDNaOH and VDHCl) were synthesized from *vitex doniana* seeds which are common waste around Auchu Polytechnic community in Edo State. The adsorption performance of the adsorbents for methylene blue was in this order: VDZnCl<sub>2</sub> < VDNaOH < VDC < VDT < VDHCl. Therefore, VDZnCl<sub>2</sub> was characterized for its physicochemical properties. The presence of O-H group, characteristics C=C group generally found in carbonaceous materials, improved surface area and pores with widened cavities reflected its potential as an adsorbent for methylene blue. The textural properties showed a tremendous increase after modification from 14.0 to 933 m<sup>2</sup>/g, the pore volume increased by about three times, from 0.07 to 0.21 cm<sup>3</sup>/g and the pore size increased from 0.92 to 18.9 Å.

#### 5. ACKNOWLEDGEMENT

We wish to acknowledge the scientific and financial support made by our 2022 project students and the department of Chemical Engineering laboratory of Auchu Polytechnic.

#### REFERENCES

- Ademiluyi, F. T. and David-West, E. O. 2012. Effect of chemical activation on the adsorption of heavy metals using activated carbons from waste materials. *International Scholarly Research Network ISRN Chemical Engineering*, 674209, 1-6.
- Afshin, S., Rashtbari, Y., Shirmardi, M., Vosoughi, M. and Hamzehzadeh, A. 2019. Adsorption of basic violet 16 dye from aqueous solution onto mucilaginous seeds of *Salvia sclarea*: kinetics and isotherms studies. *Desalination and Water Treatment* 161, 365–375.
- Alam, S., Rehman, N., Amin, N., Shah, L. A., Mian, I. and Ullah, H. 2017. Removal of basic green 5 by carbonaceous adsorbent: adsorption kinetics. *Bulletin of Chemical Society Ethiopia*, 31(3), 411-422.
- Alipour, M., Vosoughi, M., Mokhtari, S. A., Sadeghi, H., Rashtbari, Y., Shirmardi, M. and Azad, R. 2019. Optimising the basic violet 16 adsorption from aqueous solutions by magnetic graphene oxide using the response surface model based on the Box–Behnken design. *International Journal of Environmental Analytical Chemistry*.

- Ameh, P. O., Odoh, R. and Oluwaseye, A. 2012. Equilibrium study on the adsorption of Zn(II) and Pb(II) ions from aqueous solution onto *vitex doniana* nut. *International Journal of Modern Chemistry*, 3(2): 82-97
- Aslam, S., Zeng, J., Subhan, F., Li, M., Lyu, F., Li, Y. and Yan, Z. 2017. In-situ one-step synthesis of Fe<sub>3</sub>O<sub>4</sub> @ MIL-100(Fe) core-shells for adsorption of methylene blue from water. *Journal of Colloid and Interface Science* 505, 186–95.
- Asokogene, F. O., Muhammad, A. A. Z., Misau, M. I., Surajudeen, A. and El-Nafaty, A. U. 2019. Methylene blue adsorption onto neem leave/chitosan aggregates: isotherm, kinetics and thermodynamics studies. *International Journal of Chemical Reactor Engineering*. pp 1-16.
- Cazetta, A. L., Vargas, A. M. M., Nogami, E. M., Kunita, M. H., Guilherme, M. R., Martins, A. C., Silva, T. L., Moraes, J. C. G. and Almeida, V. C. 2011. NaOH-activated carbon of high surface area produced from coconut shell: kinetics and equilibrium studies from the methylene blue adsorption. *Chemical Engineering Journal* 174 (1), 117–125.
- Djilani, C., Zaghdoudi, R., Djazi, F., Bouchekima, B., Lallam, A., Modarressi, A. and Rogalski, M. 2015. Adsorption of dyes on activated carbon prepared from apricot stones and commercial activated carbon. *Journal of Taiwan Institute of Chemical Engineering* 53, 112–121.
- Kapooria, R. G. and Aime, M. C. 2005. Report of oliverscirtula on *vitex doniana* in Zambia. *Africa Journal of Science and Technology*, 3: 57-60.
- González P. G. 2018. Activated carbon from lignocellulosics precursors: a review of the synthesis methods, characterization techniques and applications. *Renewable and Sustainable Energy Rev.*, 82(1), 1393–1414.
- Imran, M., Islam, A. U., Tariq, M. A., Siddique, M. H., Shah, N. S., Khan, Z. U. H., Amjad, M., Din, S. U., Shah, G. M., Naeem, M. A., Nadeem, M., Nawaz, M. and Rizwan, M. 2019. Synthesis of magnetite-based nanocomposites for effective removal of brilliant green dye from wastewater. *Environmental Science and Pollution Research* 26 (24), 24489–24502.
- Jaria, G., Calisto, V., Gil, M. V., Otero, M. and Esteves, V. I. 2015. Removal of fluoxetine from water by adsorbent materials produced from paper mill sludge. *Journal of Colloid and Interface Science* 448, 32–40.
- Khadiran, T., Hussein, M. Z., Zainal, Z. and Rusli, R. 2015. Textural and chemical properties of activated carbon prepared from tropical peat soil by chemical activation method. *Bioresources* 10 (1), 986–1007.
- Li, W., Ma, T., Zhang, R., Tian, Y. and Qiao, Y. 2015. Preparation of porous carbons with high- and low-pressure CO<sub>2</sub> uptake by KOH activation of rice husk char. *Fuel* 139, 68–70.
- Luo, L., Wu, X., Li, Z., Zhou, Y., Chen, T., Fan, M. and Zhao, W. 2019. Synthesis of activated carbon from biowaste of fir bark for methylene blue removal. *Royal Society Open Science* 6(190523), 1-14
- Luo, X. P., Fu, S. Y., Du, Y. M., Guo, J. Z. and Li, B. 2017. Adsorption of methylene blue and malachite green from aqueous solution by sulfonic acid group modified MIL-101. *Microporous and Mesoporous Materials* 237, 268–274.
- Mistar, E. M., Alfatah, T. and Supardan, M. D. 2020. Synthesis and characterization of activated carbon from *Bambusa vulgaris striata* using two-step KOH activation. *Journal of Materials Research and Technology*, 9 (3), 6278-6286.
- Mkungunugwa, T., Manhokwe, S., Chawafambira, A. and Shumba, M. 2021. Synthesis and characterization of activated carbon obtained from marula (sclerocaryabirrea) nutshell. *Journal of Chemistry* <https://doi.org/10.1155/2021/5552224>
- Nowicki, P. 2016. Effect of heat treatment on the physicochemical properties of nitrogen-enriched activated carbons. *Journal of Thermal Analysis and Calorimetry* 125(3), 1017-1024.
- Ohimor, E. O., Temisa, D. O. and Ononiwu, P. I. 2021. Production of activated carbon from carbonaceous agricultural waste material: coconut fibres. *Nigerian Journal of Technology*, 40(1), 19-24.
- Okman, I., Selhan, K., Tay, T. and Erdem, M. 2014. Activated carbons from grape seeds by chemical activation with potassium carbonate and potassium hydroxide. *Applied Surface Science* 293, 138-142.
- Pandey, S., Do, J. Y., Kim, J. and Kang, M. 2020. Fast and highly efficient catalytic degradation of dyes using κ-carrageenan stabilized silver nanoparticles nanocatalyst. *Carbohydrate Polymers* 230, 115597.
- Piriya, R. S., Jayabalakrishnan, R. M., Maheswari, M., Boomiraj, K. and Oumabady, S. 2021. Coconut shell-derived ZnCl<sub>2</sub> activated carbon for malachite green dye removal. *Water Science & Technology* in press. pp. 1-16
- Rangabhashiyam, S. and Selvaraju, N. 2015. Adsorptive remediation of hexavalent chromium from synthetic wastewater by a natural and ZnCl<sub>2</sub>-activated Sterculia guttata shell. *Journal of Molecular Liquids*, 207, 39-49.
- Sethia, G. and Sayari A. 2021. Activated carbon with optimum pore size distribution for hydrogen storage. *Nigerian Journal of Technology* 40 (1),19–24.
- Singh, G., Kim, I. Y., Lakhi, K. S, Srivastava, P., Naidu, R. and Vinu, A. 2017. Single-step synthesis of activated bio-carbons with a high surface area and their excellent CO<sub>2</sub> adsorption capacity. *Carbon* 116, 448–455.
- Thommes, M., Kaneko, K., Neimark, A. V., Olivier, J. P., Reinoso, F. R., Rouquerol, J. et al., 2015. Physisorption of gases, with special reference to the evaluation of surface area and pore size distribution (IUPAC Technical Report). *Pure and Applied Chemistry*, 87:1051–69.



Synthesis and Characterization of Zinc Chloride Modified Activated Carbon and other Derivative Adsorbents from *Vitex Doniana* Seed

- Wang, F., Zhang, L., Wang, Y., Liu, X., Rohani, S. and Lu, J. 2017. Fe<sub>3</sub>O<sub>4</sub> @ SiO<sub>2</sub> @ CS-TETA functionalized graphene oxide for the adsorption of methylene blue (MB) and Cu(II). *Applied Surface Science*, 420, 970–981.
- Zaini, M. A. A., Shu-Hui, T., Lin-Zhi, L. and Alias, N. 2016. Fate of chemical activators in the aqueous environment: What should we do about it? *Aceh International Journal of Science and Technology* 5(1), 18-20.
- Zhang, S., Zhu, S., Zhang, H., Liu, X. and Xiong, Y. 2020. Synthesis and characterization of rice husk-based magnetic porous carbon by pyrolysis of pre-treated rice husk with FeCl<sub>3</sub> and ZnCl<sub>2</sub>. *Journal of Analytical and Applied Pyrolysis* 147, 104806.
- Zhao, H., Zhong, H., Jiang, Y., Li, H., Tang, P., Li, D. and Feng, Y. 2022. Porous ZnCl<sub>2</sub>-activated carbon from Shaddock peel: methylene blue adsorption behaviour. *Materials*, 15(895), 1-16
- Zhao, W., Luo, Lu., Wang, H. and Fan, M. 2017. Synthesis of bamboo-based activated carbons with super-high specific surface area for hydrogen storage. *Bioresources* 12, 1246–1262.
- Zhao, W., Luo, L., Chen, T., Li, Z., Zhang, Z. and Fan, M. 2018. Activated carbons from oil palm shells for hydrogen storage. *Material Science Engineering*, 368, 012031.
- Zhu, X., Wang, P., Peng, C., Yang, J. and Yan, X. 2014. Activated carbon produced from paulownia sawdust for high-performance CO<sub>2</sub> sorbents. *Chin. Chem. Lett.* 25, 929–932.



## Solvent Extraction of Acetic Acid from Aqueous Media Using Trioctyl Phosphine Oxide (TOPO) – Based Solvent Systems

O. SANDA<sup>1,2\*</sup>, Emmanuel. O. EHINMITOLA<sup>1</sup>, Bamidele S. FAKINLE<sup>2</sup> and Elijah. A. TAIWO<sup>1</sup>

<sup>1</sup>Department of Chemical Engineering, Obafemi Awolowo University, Ile-Ife, Nigeria

<sup>2</sup>Department of Chemical, Landmark University, Omu-Aran, Kwara state, Nigeria

<sup>1,2\*</sup> [osanda@oauife.edu.ng](mailto:osanda@oauife.edu.ng), <sup>1</sup> [fehinmi@oauife.edu.ng](mailto:fehinmi@oauife.edu.ng), <sup>2</sup> [fakinle.bamidele@lmu.edu.ng](mailto:fakinle.bamidele@lmu.edu.ng), <sup>1</sup> [etaiwo@oauife.edu.ng](mailto:etaiwo@oauife.edu.ng)

\*Corresponding author

### ABSTRACT

Acetic acid is a very important commodity chemical with several applications in the chemical and food industry. Although acetic acid can be produced readily via fermentation processes, various factors such as low yield, the presence of secondary fermentation products and the rather complex separation requirements make the production high quality acetic acid via the fermentation route rather expensive. This study examined the reactive extraction of acetic acid from aqueous media using trioctyl phosphine oxide (TOPO) with *n* – hexane, toluene, methyl isobutyl ketone (MIBK) and methyl ethyl ketone (MEK) as diluents. Effect of various parameters such as phase ratios, and concentration of TOPO in the diluents on the degree of extraction of acetic acid were studied and the results obtained showed that while MEK on its own gave a higher extraction yield than MIBK, a reversal in trends was observed on adding TOPO to these solvents with the MIBK – TOPO system having a greater degree extraction, compared to the MEK – TOPO system. The extractions performed using *n*-hexane and toluene as diluents gave higher extraction yields with toluene. The degree of effectiveness of the diluents in the extraction of acetic acid from aqueous media is MIBK > MEK > Toluene > *n* – hexane.

**Keywords:** Acetic acid, MIBK, MEK, Reactive Extraction, TOPO.

### 1. INTRODUCTION

Frequently, chemical engineers and organic chemists must separate organic compounds of interest from a mixture of compounds, often derived from natural sources or product of synthetic reactions. One method commonly used to separate the mixture compounds called solvent extraction or liquid-liquid extraction (Cox and Rydberg, 2004; Wasewar, 2012; Ingle *et al.*, 2017; Sas *et al.*, 2018; Alves De Oliveira *et al.*, 2020). In separation and purification technology, liquid-liquid extraction plays an important role and has been successfully applied in the isolation of organic compounds such as lactic acid (Udachan and Sahoo, 2014; Komesu *et al.*, 2017; Li *et al.*, 2021), citric acid (Araújo *et al.*, 2017), itaconic acid (Kreyenschulte *et al.* 2018), and other valuable organic acids from fermentation broths. Another very important organic acid which can be recovered from fermentation media using this method is acetic acid.

Acetic acid is a commodity chemical with several applications in the food and chemical industry. Acetic acid is used in several industrial sectors such as chemical, pharmaceutical, textile, polymer and paints, food and beverages, with a substantial proportion of the global production being used in the production of cellulose acetate (Candido *et al.*, 2017) and vinyl acetate monomer (VAM) which is used in the production of a wide range of polymers and resins for paints, adhesives, films, and a myriad of other industrial and consumer applications (Das *et al.*, 2009; Li *et al.*, 2022). Acetic acid also finds uses in the food industry as food additive (code E260) as an acidulant and as a condiment (Derossi *et al.*, 2011; Awuchi *et al.*, 2020).

Acetic acid is produced industrially synthetically via the carbonylation of methanol (Haynes, 2006; Kalck *et al.*, 2020), oxidation of acetaldehyde (Han *et al.*, 2019) or by fermentative oxidation of ethanol (Gullo *et al.*, 2014). Unfortunately, the disadvantage of fermentation is that it produces rather dilute solutions of acetic acid due to the inhibitory nature of the acid to the fermentation microorganisms (Lin and Tanaka, 2006). In addition, the fermentation broth always contains many impurities including cell biomass, other organic acids, and unconsumed nutrients (Zi *et al.*, 2013; Zentou *et al.*, 2021). Recovery and purification of acetic acid from dilute media requires many steps and unit operations, which consequently contribute to high cost of production.

Reactive extraction has been one of the attractive methods for the recovery of carboxylic acids and has been studied by several researchers. Some extractants that have been investigated include tri-*n*-octylamine (Uslu, 2009; Inyang and Lokhat, 2020), tributyl phosphate (Djas and Henczka, 2018) and trioctyl phosphine oxide (Djas and Henczka, 2018) as well as neutral extractants with oxygen-containing polar groups (Djas and Henczka, 2018; Pandey and Kumar, 2018; Mungma *et al.*, 2019). This work studied the extraction of acetic acid with methyl isobutyl ketone (MIBK), methyl ethyl

ketone (MEK), trioctyl phosphine oxide (TOPO) and their blends. The objective is to examine the influence of different variables such as phase ratio, initial feed concentration and nature of organic extractant on the extraction of acetic acid.

### 1.1 Reactive Solvent extraction of carboxylic acids

The reactive extraction of a carboxylic acid (HA) with an extractant (E) gives a reaction complex, which remains in the organic phase (Mukherjee and Munshi, 2020):



Where HA represents the unassociated part of the acid present in the aqueous phase and the overbar represents the species in the organic phase. From equation (1), the equilibrium extraction constant  $k_{ex}$  can be written:

$$k_{ex} = \frac{\overline{(HA)(E)_n}}{[HA][\bar{E}]^n} \quad (2)$$

Where the square brackets are the concentrations of the respective species. The distribution coefficient of acetic acid in the aqueous and organic phases ( $K_D$ ) is defined by:

$$K_D = \frac{\overline{[HA]}}{[HA]} \quad (3)$$

where [HA] and  $\overline{[HA]}$  are the concentrations of the acid in the aqueous and organic phases, respectively. It is noteworthy that here,  $\overline{(HA)(E)_n}$  and  $\overline{[HA]}$  represent the same quantity. Thus, equation (2) becomes:

$$k_{ex} = \frac{K_D}{[\bar{E}]^n} \quad (4)$$

The value of the extraction constant can be determined from a plot of  $\log(K_D)$  against  $\log[\bar{E}]$  where (4) is written in a linear form:

$$\log k_{ex} = \log K_D - n \log[\bar{E}] \quad (5)$$

## 2. MATERIALS AND METHODS (OR METHODOLOGY)

Methyl isobutyl ketone (MIBK), methyl ethyl ketone (MEK), n-hexane and toluene were obtained from BDH chemicals while tri-n-octyl phosphine oxide (TOPO) was obtained from Sigma-Aldrich. All solvents used as organic phase or extractant were of analytical grade and were used without further purification. Glacial acetic acid (Merck) was used to prepare the various concentrations used in the study. All experiments were performed at  $300 \pm 2$  K. For the purpose of the experiment, isothermal condition was assumed.

Aqueous acetic acid solution was prepared by dissolving glacial acetic acid in distilled water until the desired concentration was achieved, with the highest concentration used in this study being 16.9 g/L (or, 0.28 mol/L). The initial concentration of acetic acid in the aqueous phase was determined by titration against 0.1 M NaOH using phenolphthalein as indicator. The extraction and stripping experiments were carried with 20 cm<sup>3</sup> of the aqueous phase shaken with specified volumes of the organic solvents in stoppered 250 ml glass flasks on a tabletop mechanical shaker at 300 rpm for 20 min, after which the mixtures were poured into 250 ml separating funnels and allowed to settle for 3 h for complete phase separation. The quantity of acetic acid left in the aqueous phase was determined by titration with 0.1 M NaOH solution, while the acid content of the organic phase was obtained by material balance. The process was repeated for 2, 3, 4 and 5 successive extractions using equal volume of aqueous and organic phases in each case for batch extraction in stages and varying volume of solvent for single batch extraction. This procedure was repeated for the various solvent blends used.

The level of extraction for each solvent system was expressed in terms of the percentage extraction which is defined as (Inyang and Lokhat, 2020):

$$\text{Percentage Extraction (\%E)} = \left( \frac{V_o C_o - V_{eq} C_{eq}}{V_o C_o} \right) \times 100 \quad (6)$$

Where  $V_o$  and  $V_{eq}$  are the initial and equilibrium volumes of the aqueous phase, respectively. In addition,  $C_o$  and  $C_{eq}$  are the initial and equilibrium concentrations of acetic acid in the aqueous phase, respectively.

### 3. RESULTS AND DISCUSSION

#### 3.1 Acetic acid extraction with MIBK and MEK

A comparison of the solvent extraction of acetic acid was made for both MIBK and MEK for single batch and crosscurrent extractions and the result obtained (Tables 1 and 2) shows MEK to be a better extractant than MIBK. The general trend is degree of extraction can be improved on using a stage-wise crosscurrent extraction systems, compared to single extraction batches with the volume of the organic phase ( $V_o$ ) increased as shown in Table 2. The equilibrium curves for the extraction of acetic acid using MIBK, MEK or their 1:1 blend (Figure 1) also showed MEK to be the better extractant.

Table 1: Single Batch Extraction of Acetic Acid into MEK and MIBK ( $C_o = 0.28$  Mol/L)

Phase Ratio ( $V_o:V_A$ )	%E		
	MIBK	MEK	1:1 blend of MIBK and MEK
1:1	31.80	41.61	36.16
2:1	48.41	64.02	57.18
3:1	59.07	77.70	67.67
4:1	65.43	85.46	76.44
5:1	71.14	89.14	79.86

$V_o$  = volume of organic phase.  $V_A$  = volume of aqueous phase.

Table 2: Batch-wise Extraction of Acetic Acid into MEK and MIBK ( $V_o:V_A = 1:1$ ) ( $C_o = 0.28$  Mol/L)

No. of batches	%E		
	MIBK	MEK	1:1 blend of MIBK and MEK
1	31.80	41.61	36.16
2	55.42	71.55	70.32
3	70.26	88.63	81.63
4	80.74	95.64	88.63
5	87.34	98.23	93.88

$V_o$  = volume of organic phase.  $V_A$  = volume of aqueous phase.

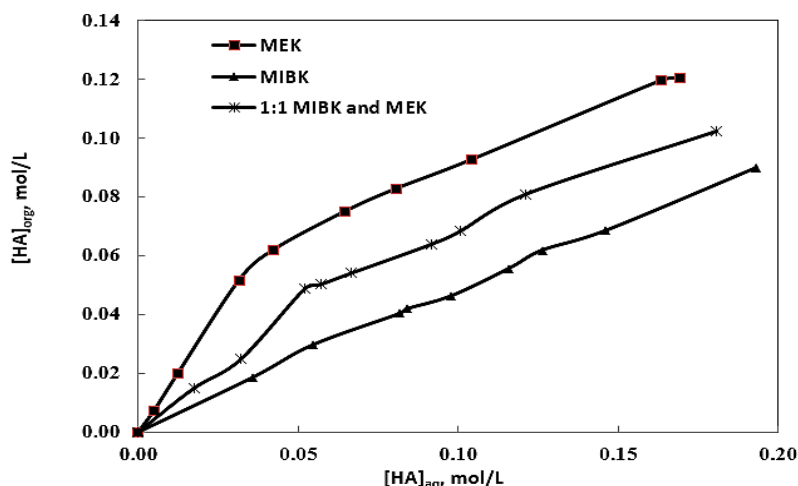


Figure 1: Distribution of acetic acid between phases for MIBK and MEK

#### 3.2 Effect of adding a second extractant

The addition of small amounts of a second extractant (TOPO) to the organic phases gave an even greater separation for acetic acid as shown by the equilibrium plots in Figure 2. The highest percentage extraction for an extractant containing 1 % v/v TOPO in MIBK was found to be 74.15 % for a phase ratio of 5:1, compared to pure MIBK which gave a 71.14% recovery for the same phase ratio (Table 1). Also, a 1% (v/v) TOPO–MIBK solvent blend gave 88.57% recovery of acetic acid, compared to pure MIBK which gave 87.34 % for the same number of extraction batches as shown in Tables 3 and 4. Thus, the interaction between TOPO and MIBK is synergistic with respect to the extraction of acetic acid from aqueous media. The addition of TOPO to MEK however had an antagonistic effect on the extraction of acetic acid as shown in Figure 3. The highest percentage extraction for a solvent system containing 1% TOPO in MEK was found to be 84.60 % for a phase ratio of 5:1 and 96.81 % for five extraction batches as shown in Tables 3 and 4.

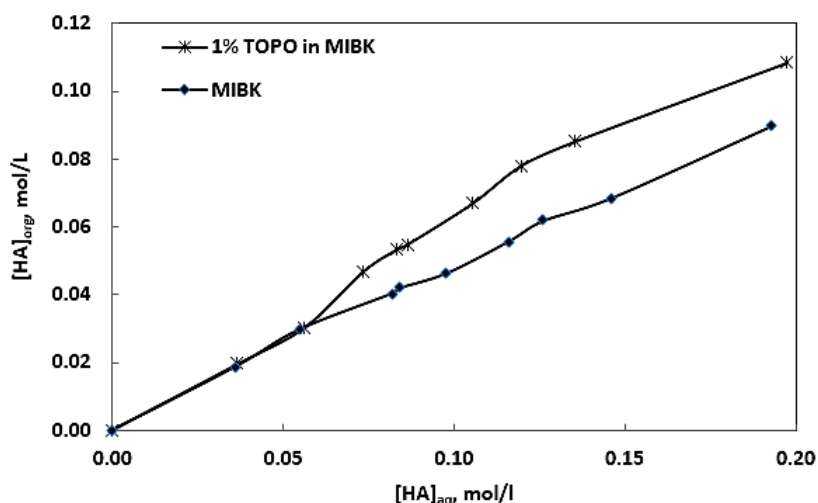


Figure 2: Distribution of acetic acid between phases using 1 % TOPO in MIBK as extractant

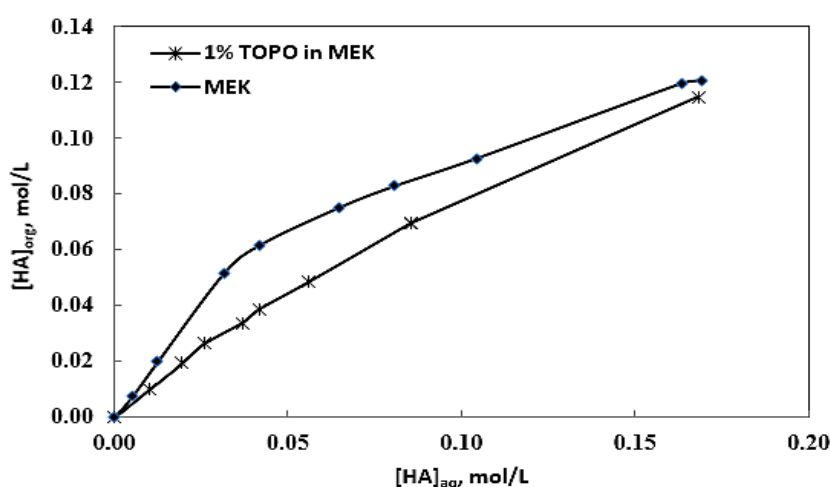


Figure 3: Distribution of acetic acid between phases using 1 % TOPO in MEK as extractant

Table 3: Single Batch Extractions of Acetic Acid with 1% TOPO in MEK and MIBK

Phase Ratio ( $V_o:V_A$ )	%E	
	1% TOPO in MIBK	1% TOPO in MEK
1:1	35.46	40.52
2:1	52.12	61.11
3:1	62.78	72.22
4:1	69.43	78.68
5:1	74.15	84.60

Table 4: Batch-wise Extraction of Acetic Acid 1% TOPO in MEK and MIBK ( $V_o:V_A = 1:1$ )

No. of batches	%E	
	1% TOPO in MIBK	1% TOPO in MEK
1	35.46	40.52
2	60.95	70.01
3	72.88	86.44
4	82.46	93.63
5	88.57	96.84

To further examine the extraction of acetic acid using TOPO, two additional solvents were introduced, which are n-hexane (an aliphatic hydrocarbon) and toluene (an aromatic solvent). Figure 4 illustrates the behavior of a 1 percent (w/v) solution of TOPO in n-hexane and toluene. From Figure 4, there use of toluene gave an increased extraction yield for acetic acid, when compared to n-hexane. These results are similar to those reported by Wasewar *et al.* (2011) and Inyang and Lokhat (2020).

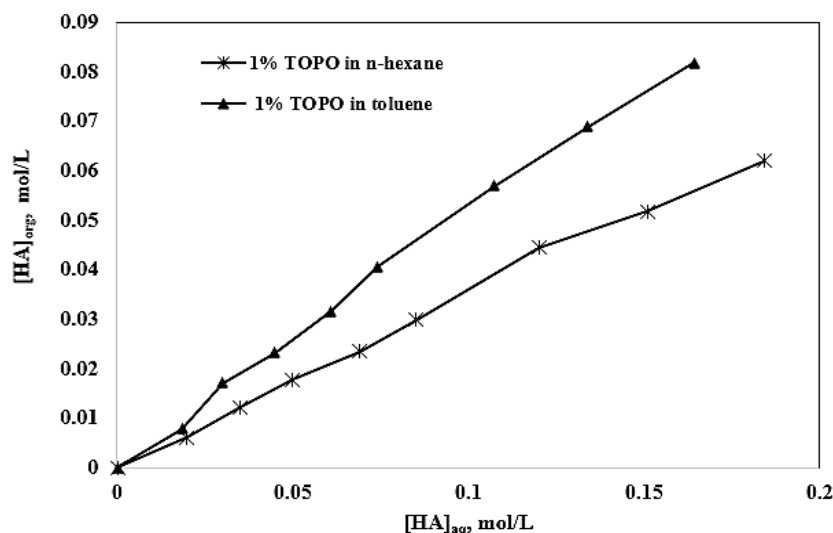


Figure 4: Distribution of acetic acid between phases using 1 % TOPO using toluene and n-hexane as extractants ( $V_O:V_A = 1:1$ )

Figure 5 shows the effect of increasing the concentration of TOPO on the acetic acid Extraction yield. The concentration of TOPO in the solvents were varied from 0.02 and 0.30 mol/L while the initial aqueous phase concentration of the acetic acid was kept constant at 0.28 mol/L. From Figure 5, it can be inferred that the use of active diluents such as MIBK and MEK gave higher extraction yields with TOPO, compared with what was extracted using inert such as n – hexane and toluene. This is in agreement with the results obtained by Pal and Keshav (2014), and Sprakel and Schuur (2019). The use of an aromatic diluent such as toluene gave higher extraction yields than those obtained using an aliphatic diluent such as n – hexane.

The plot of the distribution coefficient against the concentration of TOPO (Figure 5) was fitted to equation (4) to obtain the equilibrium extraction constant  $k_{ex}$  and the results obtained are presented in Table 5. The number of TOPO molecules per molecule of acetic acid extracted was found to decrease in the order MIBK < MEK < toluene < n – hexane and the extraction constant also follows that trend. This trend is similar to the one reported by Wasewar and Shende (2011) in the extraction of caproic acid using Aliquat 336, and Udachan and Sahoo (2014) for the extraction of lactic acid using trioctyl amine.

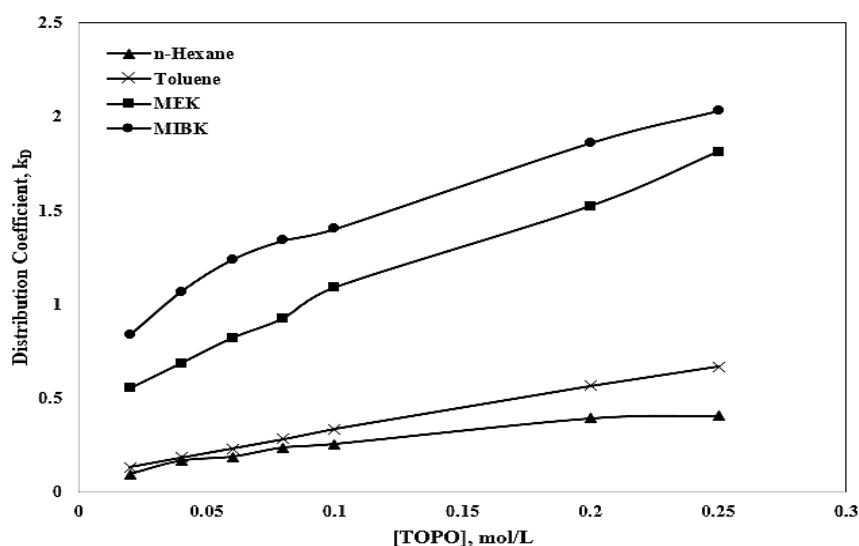


Figure 5: Effect of TOPO concentration on the extraction of acetic acid from aqueous media

Table 5: Extraction equilibrium parameters for each of the solvent systems

Diluent	Extraction constant ( $K_{ex}$ )	$n$	$R^2$
n- Hexane	0.954	0.57	0.9851
Toluene	1.579	0.66	0.9896
MEK	3.237	0.48	0.9829
MIBK	3.268	0.34	0.9964

#### 4. CONCLUSION

The extraction of acetic acid using trioctyl phosphine oxide in inert diluents (n – hexane and toluene) and active diluents (MEK and MIBK) were studied at room temperature and the following conclusions were made. MIBK and MEK on their own are good extractants for acetic acid with recovery for a phase ratio of 1:1 being 31.80% for MIBK and 41.61% for MEK, indicating that MEK is a better extractant for acetic acid from aqueous media, compared to MIBK. While synergistic extraction was observed on addition of small amounts of TOPO to MIBK, the addition of similar quantities of TOPO to MEK had an antagonistic effect, with the extraction yield dropping to 40.52 %. Although the recovery of acetic acid using TOPO in the inert diluents increased with increasing concentration of TOPO, higher solvent loading was observed when MEK and MIBK were used, with MIBK being better diluent than MEK. The degree of effectiveness of the diluents in the extraction of acetic acid from aqueous media is MIBK > MEK > Toluene > n – hexane.

#### ACKNOWLEDGEMENTS

The authors would like to acknowledge the technical staff and the project students of the Department of Chemical Engineering, Obafemi Awolowo University for the various roles played in the course of the research.

#### REFERENCES

- Alves De Oliveira, R., Alexandri, M., Komesu, A., Venus, J., Vaz Rossell, C. E., and Maciel Filho, R. (2020). Current advances in separation and purification of second-generation lactic acid. *Separation and Purification Reviews*, 49(2), pp. 159-175.
- Araújo, E. M. R., Coelho, F. E. B., Balarini, J. C., Miranda, T. L. S., and Salum, A. (2017). Solvent extraction of citric acid with different organic phases. *Advances in Chemical Engineering and Science*, 7(03), p.304.
- Awuchi, C. G., Twinomuhwezi, H., Igwe, V. S., and Amagwula, I. O. (2020). Food Additives and Food Preservatives for Domestic and Industrial Food Applications. *Journal of Animal Health*, 2(1), pp. 1-16.
- Candido, R. G., Godoy, G. G., and Goncalves, A. R. (2017). Characterization and application of cellulose acetate synthesized from sugarcane bagasse. *Carbohydrate polymers*, 167, pp. 280-289.
- Cox, M., and Rydberg, J. (2004). Introduction to solvent extraction. In *Solvent Extraction Principles and Practice, Revised and Expanded* (pp. 13-36). CRC Press.
- Das, C. K., Kumar, S., and Rath, T. (2009). 17 Vinyl Polymer Applications and Special Uses. *Handbook of Vinyl Polymers*, p. 541.
- Derossi, A., Fiore, A. G., De Pilli, T., and Severini, C. (2011). A review on acidifying treatments for vegetable canned food. *Critical reviews in food science and nutrition*, 51(10), pp. 955-964.
- Djas, M., and Henczka, M. (2018). Reactive extraction of carboxylic acids using organic solvents and supercritical fluids: A review. *Separation and Purification Technology*, 201, pp. 106-119.
- Gullo, M., Verzelloni, E., and Canonico, M. (2014). Aerobic submerged fermentation by acetic acid bacteria for vinegar production: Process and biotechnological aspects. *Process Biochemistry*, 49(10), pp. 1571-1579.
- Han, S., Shin, K., Henkelman, G., and Mullins, C. B. (2019). Selective oxidation of acetaldehyde to acetic acid on Pd–Au bimetallic model catalysts. *ACS Catalysis*, 9(5), pp. 4360-4368.
- Haynes, A. (2006). Acetic acid synthesis by catalytic carbonylation of methanol. *Catalytic Carbonylation Reactions*, pp. 179-205.
- Ingle, K. P., Deshmukh, A. G., Padole, D. A., Dudhare, M. S., Moharil, M. P., and Khelurkar, V. C. (2017). Phytochemicals: Extraction methods, identification and detection of bioactive compounds from plant extracts. *Journal of Pharmacognosy and Phytochemistry*, 6(1), pp. 32-36.
- Inyang, V., and Lokhat, D. (2020). Reactive extraction of malic acid using trioctylamine in 1–decanol: equilibrium studies by response surface methodology using Box Behnken optimization technique. *Scientific reports*, 10(1), pp. 1-10.
- Jones, B., Linnen, M., Tande, B., and Seames, W. (2015). The production of vinyl acetate monomer as a co-product from the non-catalytic cracking of soybean oil. *Processes*, 3(3), pp. 619-633.
- Kalck, P., Le Berre, C., and Serp, P. (2020). Recent advances in the methanol carbonylation reaction into acetic acid. *Coordination Chemistry Reviews*, 402, 213078.
- Komesu, A., Maciel, M. R. W., and Maciel Filho, R. (2017). Separation and purification technologies for lactic acid—A brief review. *BioResources*, 12(3), pp. 6885-6901.

- Kreyenschulte, D., Heyman, B., Eggert, A., Maßmann, T., Kalvelage, C., Kossack, R. and Büchs, J. (2018). In situ reactive extraction of itaconic acid during fermentation of *Aspergillus terreus*. *Biochemical Engineering Journal*, 135, pp. 133-141.
- Li, C., Gao, M., Zhu, W., Wang, N., Ma, X., Wu, C., and Wang, Q. (2021). Recent advances in the separation and purification of lactic acid from fermentation broth. *Process Biochemistry*, 104, pp. 142-151.
- Li, Z., Wang, K., Luo, X., and Xu, X. (2022). Optimization and simulation of vinyl acetate process based on Aspen Plus. In *International Conference on Optoelectronic Materials and Devices (ICOMD 2021)* (Vol. 12164, pp. 420-425). SPIE.
- Lin, Y., and Tanaka, S. (2006). Ethanol fermentation from biomass resources: current state and prospects. *Applied microbiology and biotechnology*, 69(6), pp. 627-642.
- Mukherjee, S., and Munshi, B. (2020). Experimental and theoretical analysis of reactive extraction of caproic acid by using TBP in green diluents. *Chemical Engineering and Processing-Process Intensification*, 153, 107926.
- Mungma, N., Kienberger, M., and Siebenhofer, M. (2019). Reactive extraction of lactic acid, formic acid and acetic acid from aqueous solutions with tri-n-octylamine/1-octanol/n-undecane. *ChemEngineering*, 3(2), pp. 43 – 51
- Pal, D., and Keshav, A. (2014). Extraction equilibria of pyruvic acid using tri-n-butyl phosphate: Influence of diluents. *Journal of Chemical and Engineering Data*, 59(9), pp. 2709 – 2716.
- Pandey, S., and Kumar, S. (2018). Reactive extraction of gallic acid using aminic and phosphoric extractants dissolved in different diluents: effect of solvent's polarity and column design. *Industrial and Engineering Chemistry Research*, 57(8), pp. 2976-2987.
- Sas, O. G., Domínguez, I., González, B., and Domínguez, Á. (2018). Liquid-liquid extraction of phenolic compounds from water using ionic liquids: Literature review and new experimental data using [C2mim] FSI. *Journal of environmental management*, 228, pp. 475 – 482.
- Sprakel, L. M. J., and Schuur, B. (2019). Solvent developments for liquid-liquid extraction of carboxylic acids in perspective. *Separation and purification technology*, 211, pp. 935 – 957.
- Udachan, I. S., and Sahoo, A. K. (2014). A study of parameters affecting the solvent extraction of lactic acid from fermentation broth. *Brazilian Journal of Chemical Engineering*, 31, pp. 821 – 827.
- Uslu, H. (2009). Reactive extraction of formic acid by using tri octyl amine (TOA). *Separation science and technology*, 44(8), pp. 1784–1798.
- Wasewar, K. L. (2012). Reactive extraction: an intensifying approach for carboxylic acid separation. *International Journal of Chemical Engineering and Applications*, 3(4), pp. 249 – 258
- Wasewar, K. L., and Shende, D. Z. (2011). Equilibrium for the reactive extraction of caproic acid using tri-n-butyl phosphate in methyl isobutyl ketone and xylene. *Journal of Chemical and Engineering Data*, 56(8), pp. 3318 – 3322.
- Wasewar, K. L., Shende, D., and Keshav, A. (2011). Reactive extraction of itaconic acid using quaternary amine Aliquat 336 in ethyl acetate, toluene, hexane, and kerosene. *Industrial and engineering chemistry research*, 50(2), pp. 1003 – 1011.
- Zentou, H., Zainal Abidin, Z., Yunus, R., Awang Biak, D. R., Abdullah Issa, M., and Yahaya Pudza, M. (2021). A new model of alcoholic fermentation under a byproduct inhibitory effect. *ACS omega*, 6(6), pp. 4137-4146.
- Zhang, X., Li, J., Kang, L., and Zhu, M. (2022). Theoretical study on the synthesis of vinyl acetate from acetylene and acetic acid over nonmetallic catalysts with different carbon-nitrogen ratios. *Molecular Catalysis*, 524, 112299.
- Zi, L. H., Liu, C. G., Xin, C. B., and Bai, F. W. (2013). Stillage backset and its impact on ethanol fermentation by the flocculating yeast. *Process Biochemistry*, 48(5-6), pp. 753-758.





## Valorization of *Garcinia kola* Fruit pod Extract as a Green Inhibitor for Mild Steel in Acidic Media

Innocent O. OBOH<sup>1\*</sup>, Anselm I. IGBAFE<sup>2</sup>, Joshua A. ADAM<sup>1</sup>

<sup>1</sup>Department of Chemical and Petroleum Engineering, University of Uyo, Uyo, Nigeria

<sup>2</sup>Department of Chemical and Petroleum Engineering, Afe Babalola University, Ado-Ekiti, Ekiti State, Nigeria

<sup>1\*</sup>[innocentoboh@uniuyo.edu.ng](mailto:innocentoboh@uniuyo.edu.ng), <sup>2</sup>[igbafesai@abuad.edu.ng](mailto:igbafesai@abuad.edu.ng), <sup>3</sup>[adamsmithsuccess@yahoo.com](mailto:adamsmithsuccess@yahoo.com)

\*Corresponding author

---

### ABSTRACT

Corrosion is a constant problem since it affects every sphere of the economy, specifically the manufacturing sector resulting in enormous economic loss. Extracts of *Garcinia Kola* fruit pods were screened for physicochemical and phytochemical properties. The corrosion behaviour and mechanism of mild steel in (1M HCl) hydrochloric acid solutions were examined in the presence of the plant extracts used as inhibitors. The results revealed that as extract concentrations increased, the inhibitors' effectiveness increased as well. Maximum inhibitory efficiency values of 94.4%, 93.4%, 83.4%, 76.9%, and 52.5% were achieved in 1M HCl environments for 500 mg/L, 400 mg/L, 300 mg/L, 200 mg/L, and 100 mg/L, respectively. From the findings, the plant extracts provided gave effective protection for mild steel.

**Keywords:** Mild steel, plant extract, Corrosion Inhibitor, Hydrochloric Acid.

### 1. INTRODUCTION

Corrosion is a natural phenomenon where metals and alloys try to revert to their more stable thermodynamics form due to reaction with the environment that surrounds them. (Shehata *et al.*, 2018). Corrosion leads to dangerous and expensive damage to industrial processes, such as in the petrochemical industries, and to bridges and public buildings (Shetty, 2018). According to the National Association of Corrosion Engineers (NACE), the cost of corrosion is close to 4.2% of the gross domestic product (GDP) of industrialised countries (Verma *et al.*, 2018). Corrosion causes enormous economic losses that range from 1 to 5% of the GDP of developed nations like the United States, China, and India, among others (Hu *et al.*, 2016; Verma *et al.*, 2017). Mild steel (MS), although being prone to corrosion, is a common building material for numerous sectors, including those that produce petroleum, power and water, refine and process chemicals, manufacture technical equipment, and build bridges. Due to its high ductility and malleability, good mechanical resistance, low price, and availability, mild steel is a crucial component of the infrastructure (Dutta *et al.*, 2017; El-Taib Heakal *et al.*, 2018). However, it must be regularly checked due to mild steel's indisputable disadvantage of being susceptible to corrosion in hostile conditions. In metal finishing, acid descaling, steel pickling, and oil well acidization at high temperatures, aggressive media like HCl and H<sub>2</sub>SO<sub>4</sub> is employed often (Zhang *et al.*, 2018).

Corrosion inhibitors are chemical substances which when introduced in small amounts to corrosive media, reduce or prevent the metal's reaction with the media (Stephen *et al.*, 2014). The use of inhibitors is a well-known strategy when metal corrosion needs to be prevented, controlled, or retarded. Green inhibitors are biodegradable, ecologically acceptable and renewable. Their valorization expands possible applications in industrial fields other than 'waste to energy' in the perspective of circular economy (Marzorati *et al.*, 2019). Green inhibitors are substances obtained from natural sources and used to stop aggressive dangerous metallic corrosion without damaging the ecosystem of the environment (Ahmed *et al.*, 2020).

Green inhibitors aid in the reduction of corrosion, such as phytoconstituents. They are inherently organic and frequently contain heterocyclic or aromatic compounds such as alkaloids, flavonoids, and tannins (Oguzie, *et al.*, 2008; Kesavan *et al.*, 2012). These chemicals formed a protective coating by adhering to the surface of the metal via their electroactive sites. The inhibition mechanisms of some green inhibitors have theories developed that demonstrate the behaviour of green inhibitors. One of these theories considered that the anions in acidic medium could be absorbed by the metallic surface to complete the cathodic process, which leads to reduced corrosion process (Ahmed, 2020).



$$C_1V_1 = C_2V_2 \quad (1)$$

$$V_{extract} = \frac{C_{dil}V_{350ml}}{C_{extract}} \quad (2)$$

Where;  $C_1 = C_{extract}$ ,  $V_1 = V_{extract}$ ,  $C_2 = C_{dil}$ , and  $V_2 = V_{350ml}$

### 2.3 Corrosion Rate Determination

Under total immersion conditions at room temperature, the test coupons used for the gravimetric studies had the following measurements: 30 mm x 30 mm x 1.5 mm. The weight of a Mild Steel (MS) specimen was measured to 4-digit accuracy in the corrosive medium both before and after using an analytical balance. The solution had inhibitor concentrations of 100 mg/L, 200 mg/L, 300 mg/L, 400 mg/L, and 500 mg/L. After a specified period of immersion. The specimen (Test coupons) were removed from the corrosion medium (1M HCl) at 24 h intervals and progressively for 144 h, after which it was immersed for 5 minutes in 1.0M NaOH solution to inhibit excessive acid on the metal surface, rinsed with distilled water, the metal was dried for 15 minutes at 100°C in an oven and cooled in a desiccator before final weight was taken. It is assumed that the weight difference represents metal loss due to corrosion. The corrosion rate (CR, mg/cm<sup>2</sup>/h) is calculated by dividing the weight loss (W, mg) from the experiments by the metal surface area in contact with the solution (A, cm<sup>2</sup>) and the immersion period (t, h) as represented by Equation 3 (William, 2007).

$$CR = \frac{87.6\Delta W}{DAT} \quad (3)$$

Where; W = weight loss in mg, D = density of the mild steel g/cm<sup>3</sup>, A = area in cm<sup>2</sup> and T = exposure time in hours.

### 2.4 Determination of Percentage Inhibition Efficiency (IE)

The inhibition efficiency (IE) can be calculated by using Equation (4), as previously stated (Ihebrodike *et al.*, 2010).

$$IE = \frac{CR_0 - CR}{CR_0} \times 100 \quad (4)$$

Where; CRO = corrosion rate in the absence of an inhibitor, CR = corrosion rate in the presence of an inhibition.

### 2.5 FT-IR Analysis

The functional groups contained in the *Garcinia kola* fruit pod were identified using FTIR. It was also used to identify the active compounds that had been adsorbed onto the metal surface and formed the protective coating. *Garcinia kola* fruit pod extract was deposited and exposed to infrared ray beams. The transmittance and reflectance of infrared (IR) photons at various frequencies were converted into an IR absorption plot with reverse peaks. To determine the functional group contained in the extract, the spectra pattern was evaluated and matched using an IR absorption table.

### 2.6 Phytochemical Screening of *Garcinia Kola* Pod Extract

The modified Harborne technique was adopted to screen the phytochemicals of *Garcinia kola* fruit pod extract in ethanol (Nuhu *et al.*, 2000; Ezeonu, 2005). Which was carried out in order to identify the heterocyclic chemicals found in *Garcinia kola* pods. The crude extract was tested for phytochemicals such as tannins, saponins, flavonoids, and alkaloids.

## 3.0 RESULTS AND DISCUSSION

### 3.1 Weight Loss Analysis

Figure 3 revealed that weight loss increased with increase in time as demonstrated in the 100 mg/L concentration where weight loss went from 0.0879 g after 24 h to 1.3234 g at 144 h. The results demonstrate that increase in time leads to increase in corrosion.

Figure 4 illustrates the corrosion rate (mm/yr) for steel specimens immersed in 1.0M HCl for a period of 144 h at 24-hour intervals for each of the six samples. It was found that the weight loss of the metal specimen was significantly high in the blank corrodent (control) and relatively low in the presence of the extract of *Garcinia Kola* Pod. From the findings, it shows that with an increase in inhibitor concentration, mild steel corrosion was successfully inhibited, as weight loss of the metal specimen was lowest at 400 mg/l and 500 mg/l concentrations. This is because a large number of active inhibitor molecules from the extract adhered to the metal surface and produced a thin coating to shield it from further attack from the corrosive environment; this is consistent with the findings of (Yawas, 2005).

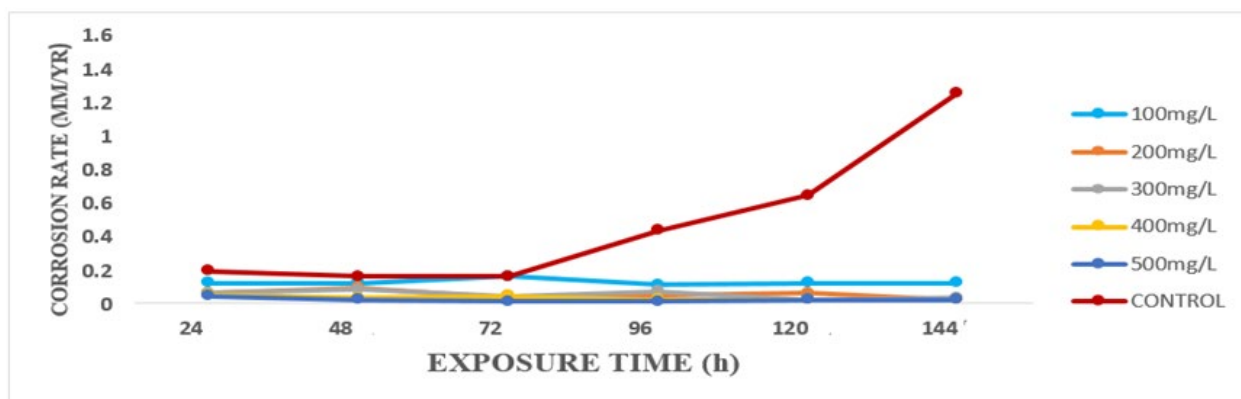


Figure 3: Corrosion rate – exposure time curve of mild Steel in the presence and absence of various concentrations of Garcinia kola pod extract

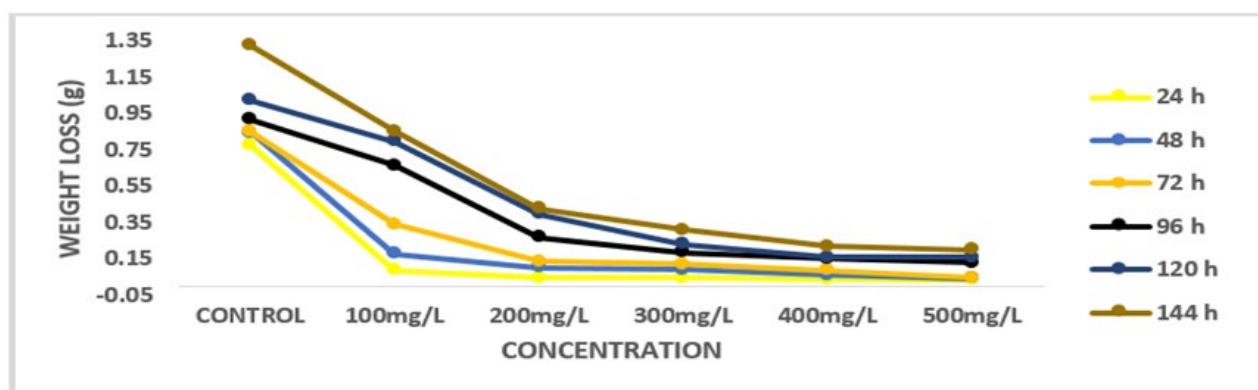


Figure 4. Weight loss-concentration curves of mild Steel in the presence and absence of various concentrations of Garcinia kola pod extract

The variation in weight loss over time for mild steel corrosion in 1.0 M HCl solution in both the presence and absence of Garcinia Kola pod extract is shown in Figure 5. A trend shows where an increase in inhibitor concentration resulted in a corresponding decrease in weight loss for the metal specimens, further demonstrating the inhibitory effect of Garcinia kola pod extract on mild steel. It was observed that weight loss increased over time, with the Blank Corroderent (control) experiencing the greatest increase in weight loss.

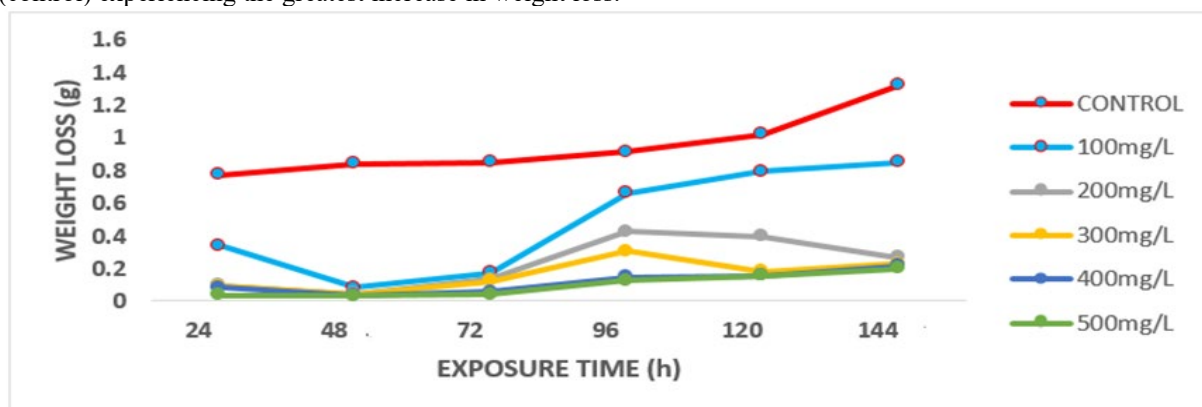


Figure 5. Weight loss curve of mild Steel in the presence and absence of various concentrations of Garcinia kola pod extract

### 3.2 Phytochemical analysis

Phytochemical analysis findings of the plant extract are summarised in Table 1. According to the findings, Garcinia kola pod extract contains saponins, flavonoids, tannins, and alkaloids among other chemical components. When compared to blank media (control), the acid medium's corrosion rate was significantly lower in the plant because of the presence of chemical compounds such as tannins, flavonoids, and saponins (control). Due to their increased basicity and electron density, functional groups like nitrogen (N), sulphur (S) and oxygen (O) found in plant extract molecules operate as the active centres for the adsorption of the inhibitor on the metal surface. It is made easier for electrons to transfer from the inhibitor to the surface of the metal because the functional groups of the inhibitor molecules contain non-bonded (lone

pair) and p-electrons. The observations described above are consistent with the findings of (Yawas 2005; Oki *et al.*, 2011; Nwabanne and Okafor, 2011).

Table 1: Phytochemical analysis of plants extract

Chemical Constituents	<i>Garcinia Kola fruit pod</i>
Tannin	+
Alkaloids	+
Flavonoids	+
Saponins	+

Key: Presence (+), Absence (-)

Several researchers have confirmed that the FT-IR spectrometer is a powerful tool for determining the type of bonding for organic inhibitors adsorbed on metal surfaces (Lalitha, *et al.*, 2005). The FT-IR spectrometer gave the specific functional groups present in the extract. The FT-IR absorption spectrum of *Garcinia Kola* Pod extract is shown in Figure 2, which displays the *Garcinia Kola* Pod band frequencies.

The FTIR analysis of the *Garcinia kola* pod confirmed the presence of compounds with major peaks at 3968.00, 1429.00, 3543.35, 1724.42, 1628.94, 1581.38, 3490.31, 1173.72, 2384.58, 1650.96, and 3285.66cm<sup>-1</sup>, respectively. These compounds include OH (Phenols, Hydroxyl group), C=O (Aldehyde, Ketones), C=C (Alkene), CH(CH<sub>3</sub>)<sub>2</sub> (Alkyls), O=C-O-C (Esters), Aromatic C-H bend, C-I (Alkyl halide). The absorption brought on by the hydroxyl group's (OH) presence, C=C stretching, and C-H bend.

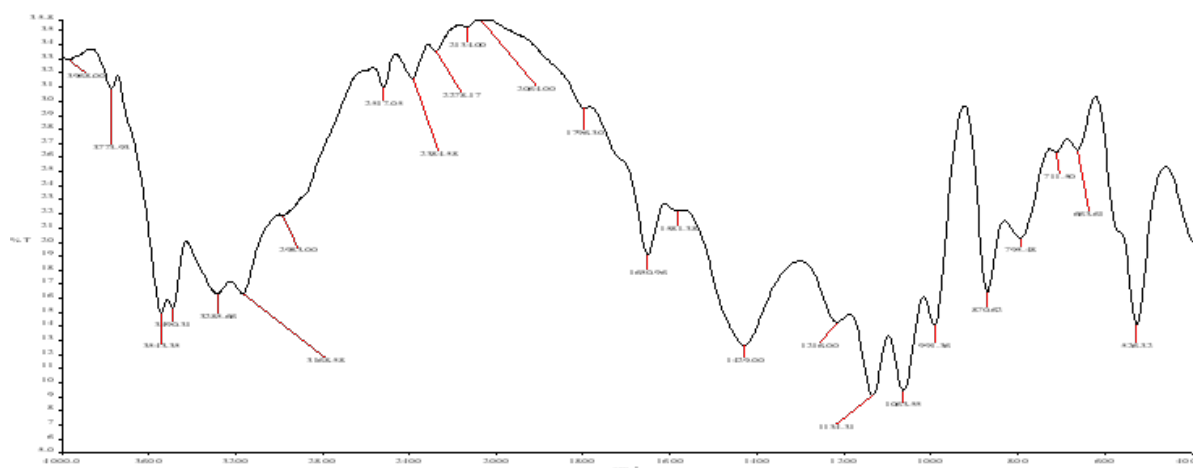


Figure 6. Fourier Transform Infrared Spectroscopy (FTIR) Analysis

### 3.3 Inhibition Efficiency

An evaluation of the inhibition efficiency (I.E) determined by Equation (4) was used to quantitatively characterise the inhibitory effect of *Garcinia Kola* pod extract on the corrosion of mild steel. Figure 6 depicts the variation in inhibitory effectiveness with concentration for mild steel corrosion in 1.0M HCl solution over a 144-hour period in both the presence and absence of *Garcinia Kola* Pod extract. It was observed that the highest concentration had the highest inhibition efficiency, whereas the lowest concentration had the lowest inhibition efficiency. This indicated that the acidic media increased the inhibitor's efficiency with increasing concentrations due to a greater surface coverage. The 400 mg/L and 500 mg/L concentrations showed a certain degree of uniformity, which suggested stability. Additionally, a sharp increase was seen from 100 mg/L to 300 mg/L, with an average efficiency of 80.5%. This showed that from a concentration of 400 mg/L to 500 mg/L, the ethanolic extract of *Garcinia Kola* pod increased its efficiency of inhibition by an average of 93.9%. According to the experimental data obtained, the *Garcinia kola* pod extract's inhibitive effectiveness occurred from 400 mg/L.

A significant indication, however, could be seen in Figure 7 where the inhibition efficiency decreased with time following continued immersion, going from 95.5% for 500mg/L after 24 h to 94.6% after 48 h, 95.3% after 72 h, 94.3% after 96 h, 94.2% after 120 h, and 94.2% for 144 h. Because of this, the ethanolic extract of *Garcinia kola* pod's inhibitory effectiveness was very time dependent and proportionally slowed down with progression of time. These indicated that mild steel would be inhibited more effectively in the higher the concentration of *Garcinia Kola* pod extract in 1.0MHCl acid solution. This corresponded to the findings of (Yawas 2005) and (Nwabanne and Okafor, 2011).

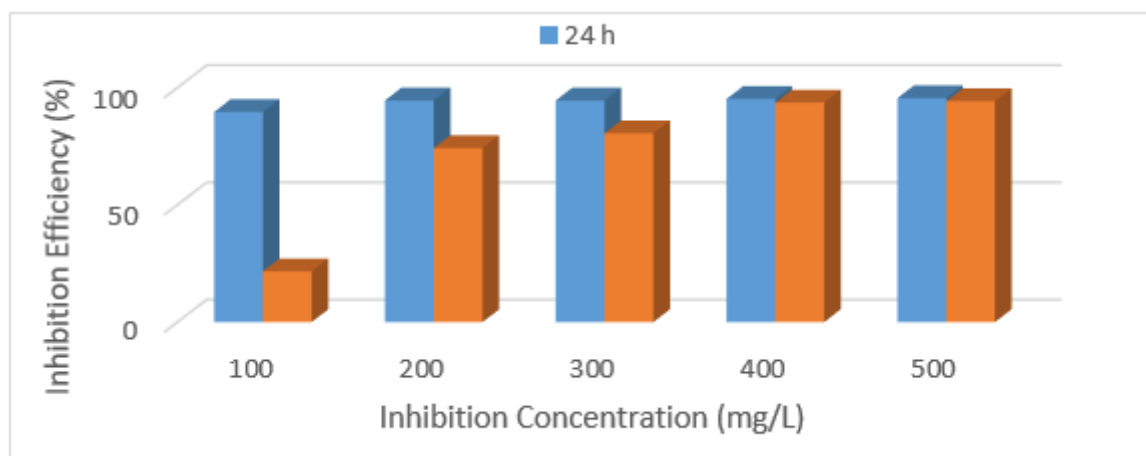


Figure 7: Inhibitor efficiency of mild Steel in 1.0M HCl in presence and absence of various concentrations of *Garcinia kola* pod extract at 24 h and 144 h.

#### 4. CONCLUSION

Extracts from *Garcinia Kola* pod proved to be very good eco-friendly corrosion inhibitors for mild steel in 1.0M HCl solution. Extract from the pod exhibits excellent inhibitory effectiveness. As the concentration of the plant inhibitor increased, so did its effectiveness. The inhibition was probably caused by the formation of a protective layer as a result of aromatic molecules such as tannins, flavonoids, saponins, and alkaloids adhering to the metal surface.

#### REFERENCES

- Adegboye MF, Akinpelu D.A, Okoh. (2008). the Bioactive and Phytochemical properties of *Garcinia kola* (Heckel) seed extraction on some pathogens. *African Journal of Biotechnology*. 7(21): pp.3934-3938.
- Ahmed, W. A, Al-Mashhadani, M. H., Abdallah, M, Hussain, Z, (2020). Eco-friendly green corrosion inhibitors in overview. *Advanced Sciences*. Volume 1(1), 7-16.
- Avwiri, G.O, and Igbo, P.O. (2003). Inhibitive Action of *Vernonia Amygdalina* on the Corrosion of Aluminium Alloys in Acidic Media. *Materials letters*, 57(22-23), pp. 3705- 3711.
- Dutta, A., Saha, S.K., Adhikari, U., Banerjee, P. and Sukul, D. (2017) Effect of Substitution on Corrosion Inhibition Properties of 2-(Substituted Phenyl) Benzimidazole Derivatives on Mild Steel in 1 M HCl Solution: A Combined Experimental and Theoretical Approach. *Corrosion Science*, 123, 256-266. <https://doi.org/10.1016/j.corsci.2017.04.017>.
- El-Taib Heikal F, and Amira M. Bakry. (2018). Corrosion Degradation of AXJ530 Magnesium Alloy in Simulated Physiological Fluid and Its Mitigation by Fluoride and Chitosan Coatings for Osteosynthetic Applications. *International Journal of Electrochemical Science*. Vol. 13. 7724 – 7747, doi: 10.20964/2018.08.67.
- Ezeonu, O.J (2005). "A preliminary comparative phytochemical analysis of evil (Bean) plant *Mucuna Flagellipes*", In: *Proceedings of Chemical Society of Nigeria*. pp,21-25
- Hu, Z., Meng, Y., Ma, X., Zhu, H., Li, J., Li, C., *et al.*, (2016) Experimental and Theoretical Studies of Benzothiazole Derivatives as Corrosion Inhibitors for Carbon Steel in 1 M HCl. *Corrosion Science*, 112, 563-575. <https://doi.org/10.1016/j.corsci.2016.08.012>
- Ihebrodike, M.M., Anthony, A.U., Kelechukwu, B.O., and Gregory, A.A. (2010). The Inhibitive Effect of *Solanum Melongena* L. Leaf Extract on the Corrosion of Al in H<sub>2</sub>SO<sub>4</sub>. *African Journal of Pure and Applied Chemistry*. 4(8), pp.158-165.
- Kesavan, M., Gopiraman C., N. Sulochana, (2012). "Green Inhibitors for Corrosion of Metals: A Review," *Chemical Science Review and Letters*, vol. I, no. 1, pp. 1-8,
- Lalitha, A., Ramesh, S., and Rajeswari, S. (2005): Surface protection of copper in acids medium by azoles and surfactants. *Electrochimica Acta*, Vol. 51, no. 1, pp 47-55.
- Loto R. T, Bryan U. Ayozie and Cleophas A. L (2019), Electrochemical study of the corrosion inhibition effect of a 3-cyanophenyl compound on 420 martensitic stainless steel in strong acid media, *Materials Science Engineering*. 613 012012
- Loto, R. T, C.A. Loto, A.P.I. Popoola (2012). Corrosion Inhibition of Thiourea and Thiazazole Derivatives: A Review, *Journal Materials Environmental Science*. 3 (5) (2012) 885-894.
- Marzorati, S, Verotta, L. and Trasatti, S. P. (2019). Green Corrosion Inhibitors from Natural Sources and Biomass Wastes. *Molecules*, 24, 48; doi:10.3390/molecules24010048
- Nuhu, A.M; Mshelia, M.S and Yakubu, V (2000). "Antimicrobial Screening of Bark Extract of *Pterocarpus Erinaceus* tree", *Journal of Chemical Society of Nigeria*, 25: pp.85-86.

- Nwabanne, J.T and Okafor V.N. (2011). Inhibition of the corrosion of mild steel in acidic medium by Vernonia Amygdalina: Adsorption and thermodynamics study Journal of Emerging Trends in Engineering and Applied Sciences, 2(4): 619-625.
- Oguzie, E.E. (2008). "Evaluation of the inhibitive effect of some plant extracts on the acid corrosion of mild steel," Corrosion Science, o. 50, pp.2993-2998,
- Oki, M, Charles, E, Alaka, C, and Oki, K. T, (2011). Corrosion Inhibition of Mild Steel in Hydrochloric Acid by Tannins from Rhizophora Racemosal Material Sciences and Applications, 2, 592-595.
- Otor, J. U., Abdulkadir, U. and Abu, M. A. (2001). Some biological activities of *Garcinia kola* in growing rats.71 (5): pp.287-297.
- Shehata, O. S., Korshed, L. A. and Attia, A. (2018). Green Corrosion Inhibitors, Past, Present, and Future. Chapter 6 from the book Corrosion Inhibitors, Principles and Recent Applications Published by Intechpp . Downloaded at <http://www.intechopen.com/books/corrosion-inhibitors-principlesand-recent-applications>
- Shetty, P. (2018). Hydrazide Derivatives: An Overview of their Inhibition Activity Against Acid Corrosion of Mild Steel. South African Journal Chemistry. Vol. (71), DOI: 10.17159/0379-4350/2018/v71a6
- Stephen, G.Y., Sylvester, O. A., Tersoo G. T., Ungwanen, J. A., Joseph A. G. (2014). Thermodynamic, Kinetic and Adsorptive parameters of corrosion inhibition of Aluminium using sorghum bicolor leaf extract in H<sub>2</sub>SO<sub>4</sub>. International Journal of Advanced Research in Chemical Science (IJARCS). Volume. (1). pp. 38-46.
- Verma, C., Ebenso, E.E., and Quraishi, M.A. (2017). Ionic liquids as green and sustainable corrosion inhibitors for metals and alloys: an overview. J. Mol. Liq. 233: 403–417, <https://doi.org/10.1016/j.molliq.2017.02.111>. Search in Google Scholar
- Verma, C., Obot, I.B., Bahadur, I., Sherif, E.M., and Ebenso, E.E. (2018). Choline based ionic liquids as sustainable corrosion inhibitors on mild steel surface in acidic medium: gravimetric, electrochemical, surface morphology, DFT and Monte Carlo simulation studies. Appl. Surf. Sci. 457: 149, <https://doi.org/10.1016/j.apsusc.2018.06.035>.
- William, D. (2007). Materials Science and Engineering: An Introduction 7th Edition, John Wiley and Sons, Inc.
- Yawas, D.S., (2005) " Suitability Assessment of some Plant Extracts and Fatty acid vegetable oils as corrosion inhibitors".Phd Dissertation in the Department of Mechanical Engineering, ABU, Zaria - Nigeria.
- Yong Hua, Amir Shamsa, Richard Barker and Anne Neville, (2018). Protectiveness, Morphology and Composition of Corrosion Products Formed on Carbon Steel in the Presence of Cl<sup>-</sup>, Ca<sup>2+</sup> and Mg<sup>2+</sup> in High Pressure CO<sub>2</sub> Environments. Applied Surface Science, 455. pp. 667-682. ISSN 0169-4332
- Zhang, K., Yang, W., Chen, Y., Xu, B., Yin, X., Liu, Y., and Zuo, H. (2018). Enhanced inhibitive performance of fluoro-substituted imidazolium-based ionic liquid for mild steel corrosion in hydrochloric acid at elevated temperature. J. Mater. Sci. 53: 14666–14680, <https://doi.org/10.1007/s10853-018-2616-6>.



## Adsorption of Malachite Green onto Cellulose Synthesized from Baobab Pod

Victoria A. ADEYI<sup>1,2</sup>, Samuel E. AGARRY<sup>1</sup>, Adeola R. AMOLE<sup>1,2</sup>, Wasiat O. BELLO<sup>1,2</sup>, Tinuade J. AFOLABI<sup>1,2</sup>, Azeez G. AKINYEMI<sup>1,2</sup>, Monsuru O. DAUDA<sup>1,2</sup>, Olufunmilayo A. AWORANTI<sup>1,2</sup>, Esther O. AWOTONA<sup>1,2</sup> and Abass O. ALADE<sup>1,2,3\*</sup>

<sup>1</sup> Department of Chemical Engineering, Faculty of Engineering, Ladoko Akintola University of Technology, (LAUTECH), Ogbomoso, Nigeria

<sup>2</sup> Bioenvironmental, Water and Engineering Research Group (BWERG), (LAUTECH), Ogbomoso, Nigeria

<sup>3</sup> Science and Engineering Research Group (SAERG), (LAUTECH), Ogbomoso, Nigeria

\*Corresponding: [aolade@lautech.edu.ng](mailto:aolade@lautech.edu.ng)

---

### ABSTRACT

. Wastewater generated from textiles, cosmetics and other industries includes different types of dyes used in colouring amongst other impurities and these dyes-laden wastewaters pose health hazards to aquatic life and humans when left in water sources unattended to. Therefore, the need for effective remediation through a suitable technique such as adsorption arises. This study, therefore, looked into the adsorption of Malachite Green (MG) by cellulose generated from the baobab pod. Waste baobab pod synthesized to Baobab Pod Cellulose (BPC) was used in batch adsorption of Malachite Green (MG) from synthetic wastewater. The data obtained were used to determine the adsorption isotherms (Henry, Freundlich and Langmuir) and Kinetic (the Pseudo-Second order) properties of the process. The removal efficiencies of the BPC for MG were in the range of 84.7-91.3% within contact time of 10-225 mins, while the adsorption capacity was 0-8.47 mg/g. The coefficient of determination ( $R^2$ ) for Henry, Freundlich and Langmuir isotherms were 0.9601, 0.9250 and 0.9349, respectively. The adsorption process follows the pseudo-second-order kinetic model Type 1 with its values as 0.99997, 0.99994 and 0.99993 for Pearson's  $r$ ,  $R$ -Square, Adj.  $R$ -Square, respectively. Based on the results gotten it can be concluded that baobab pod cellulose is a good adsorbent for adsorption processes.

**Keywords:** Baobab pod, Cellulose, Malachite green, Wastewater.

### 1. INTRODUCTION

Rubber, plastic, printing, textile, leather, and cosmetic companies amongst others use huge quantities of different dyes in their production processes which are non-biodegradable such as methylene blue, Rhodamine B, and malachite green amongst others (Ani *et al.*, 2020). Dye-polluted wastewater is therefore produced from the activities of these companies leading to water pollution (Aseel *et al.*, 2014). Malachite green is a cationic dye that has been employed as an antibacterial in aquaculture. It has mutagenic and carcinogenic properties which create unfavourable effects on the liver, gill, kidney, gut, gonads and pituitary cells. It also generates sinusoidal congestion and localized necrosis in the liver, damages mitochondria and creates nuclear alterations (Palukurty *et al.*, 2014). The removal of Malachite Green is a necessity because of its end effects on aquatic life and man. Various methods such as chemical coagulation, biological reduction, photocatalytic fermentation, ozone treatment, membrane filtering, electrolysis, reverse osmosis, and adsorption among others have been employed and are still being used in the removal of dyes and their constituents (Senthil *et al.*, 2022).

Adsorption has been ascertained to be one of the most effective ways of removing dye pollutants (Wong *et al.*, 2018). Adsorption technologies are effective in the removal of organics from water due to their high efficacy and ability to separate a wide range of chemical components. According to experts, adsorption procedures are now seen as the most practical method for removing pollutants from wastewater because they are relatively cheap and readily available, simple in design, high in efficiency, easy to use, biodegradability, and can handle dye in high concentration form (Kumaraswamy *et al.*, 2014). Adsorption processes require the use of adsorbents which are mostly derived from agricultural wastes and other available materials. Baobab whose botanical name is *Adansonia digitata L* is a large tree very indigenous to Africa. It is found in many African countries (Kabbashi *et al.*, 2017). The baobab tree has various use ranging from nutrition to medicine (Adenekan *et al.*, 2017; Tchikualaa *et al.*, 2017). Though almost all parts of the



baobab are useful, the pod is majorly the waste generated from the tree (Tchikualaa *et al.*, 2017). The pod of the baobab fruit is discarded majorly where it is harvested thereby littering the environment and has been reported to have no economic value (Kabbashi *et al.* 2017).

Most agricultural wastes have high cellulose content. Cellulose is an organic compound which is an important component of the primary cell wall of plants and wood (Nur *et al.*, 2020). Baobab pods have been found to be an abundant agricultural waste which is also a high source of cellulose (Ahmed and Taiseer, 2018) therefore based on this knowledge, this study looked into the production of cellulose from baobab pods for the removal of malachite green from simulated wastewater.

## 2. MATERIALS AND METHODS

### 2.1 Material and reagents

The baobab pod was gathered locally in Ogbomosho (8.142165 latitude and 4.245186 longitudes) while malachite green was gotten from a local source which is the adsorbate. The adsorbent was made using analytical grade solutions of sodium hydroxide, acetic acid, and hydrogen peroxide.

### 2.2 Preparation of cellulose from baobab pod

The baobab pod was obtained from the parent plant, washed, dried, ground and sieved (40  $\mu\text{m}$ ) before being treated with NaOH of 4wt% (1:25 biomass to NaOH) and stirred on a magnetic stirrer for 2 h at 80  $^{\circ}\text{C}$ . The material was further treated with acetic acid (1:10 acetic acid: distilled water) and then NaClO<sub>2</sub> and agitated at room temperature for 24h. The residue was sieved, washed with distilled water, and dried at 50  $^{\circ}\text{C}$  until steady weight, then treated with (30%) H<sub>2</sub>O<sub>2</sub>. The product was washed to neutrality and dried as Baobab Pod Cellulose (BPC).



Figure 1: Baobab pods on the parent tree ( Asogwa *et al.*, 2020)

### 2.3 Preparation of adsorbate

Malachite green dye was applied to make a simulation of malachite green wastewater. The stock solution was made in 1000 mg/L by carefully weighing 1.0g of malachite green and diluted in distilled water. The stock solution was then carefully wrapped using aluminium foil and kept in a dark position to avoid any decolourisation. The working standard was freshly established utilizing dilutions.

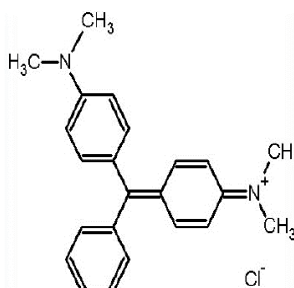


Figure 2: Structure of malachite green (Prabakaran and Arivoli, 2012)

#### 2.3.1 Batch Adsorption

All experiments were done in the batch manner, at a constant stirring intensity provided by a shaker. A stirring speed of 150 rpm was used at a temperature of 60 °C for 5hrs at 30 mins intervals. 1 g of the cellulose produced was introduced into 100 ml of 100 mg/l concentration of Malachite Green. The effect of alterations of numerous elements that may affect the adsorption process was examined, in order to gain the perfect circumstances for dye removal. NaOH (0.1 N) and HCl (0.1 N) solutions were employed for pH correction. The dye concentration was evaluated using a UV-VIS spectrophotometer. Three independent duplicates were done for each adsorption test. The following calculations were used to determine the amount that was adsorbed to the surface of the BPC ( $q_t$  (mg/g)) and the removal percentage (Rt (percent)) of the adsorbent (Slimani *et al.*, 2012).

$$Removal\ Efficiency(\%) = \frac{C_0 - C_E}{C_0} \times 100 \tag{1}$$

$$Adsorption\ Capacity(mg/g) = \frac{(C_0 - C_E)M}{V} \tag{2}$$

Where  $C_0$  and  $C_e$  represent the respective initial and ultimate concentrations,  $m$  is the mass of the adsorbent and  $v$  is the volume of the adsorbate.

### 2.3.2 Isotherm study

Selected isotherm models such as Henry, Freundlich and Langmuir (Eqns 3-6) (Table 1) were used to analyse the experimental isotherm data in this research work (Guo and Wang, 2019), (Laith, *et al.*, 2020). The Langmuir isotherm is characterised by a dimensionless parameter known as the separation factor,  $R_L$  (Eqn 6), which measures the suitability of the adsorbent for the adsorption process and the extent of the practicability of the adsorption [i.e., unfavourable ( $R_L > 1$ ), linear ( $R_L = 1$ ), favourable ( $0 < R_L < 1$ ) or irreversible ( $R_L = 0$ ).

Table 1: Langmuir Isotherm models

Model	Equation	Plot	Equation no
Henry	$q_e = K_H C_s$	$q_e$ against $C_e$	(3)
Freundlich	$log q_e = \frac{1}{n} log C_e + log K_f$	$log q_e$ against $log K_f$	(4)
Langmuir	$\frac{1}{q_e} = \frac{1}{q_m} + \frac{1}{q_m K_L C_e}$	$\frac{1}{q_e}$ against $\frac{1}{C_e}$	(5)
	$R_L = \frac{1}{(1 + K_L C_e)}$	NA	(6)

where  $C_e$  (mg/L) is the concentration of adsorbate at equilibrium,  $q_e$  (mg/g) is adsorption capacity at equilibrium solute concentration,  $q_m$  (mg/g) is maximum adsorption capacity corresponding to complete monolayer coverage,  $K_L$  (mg/g) is Langmuir constants related to adsorption capacity. NA= Not Applicable.

### 2.3.3 Pseudo-second-order kinetic model study

The Pseudo-second-order kinetic model (PSO) is widely applied to describe the adsorption processes. Most published studies utilized the PSO model to anticipate the adsorption experimental data and to calculate the adsorption rate constants (Uddin *et al.*, 2007). The Pseudo-second-order kinetics model is given in Table 2.

Table 2: Linear and nonlinear pseudo second order kinetic models

Pseudo Second Order	Equation	Number
Non-linear	$q_t = q_e \left[ 1 - \frac{1}{1 + k_2 t} \right]$	(7)
Linear		
Type 1	$\frac{1}{q_t} = \frac{1}{k_2 q_e^2} + \frac{t}{q_e}$	(8)
Type 2	$\frac{1}{q_t} = \frac{1}{k_2 q_e^2} - \frac{1}{t} + \frac{1}{q_e}$	(9)
Type 3	$\left( \frac{1}{q_t} - \frac{1}{q_e} \right) q_e^2 = \frac{1}{k_2 t}$	(10)
Type 4	$q_t = q_e - \left( \frac{1}{k_2 q_e} \right) \frac{q_t}{t}$	(11)
Type 5	$(q_t - q_e) q_e = - \left( \frac{q_t}{k_2 t} \right)$	(12)

Type 6	$\frac{q_t}{t} = k_2 q_e^2 - k_2 q_e q_t$	(13)
--------	---	------

### 2.3.4 Error Analysis

In this phase, the best-fitting equation is calculated using the well-known special functions to quantify the error deviation among experimental and predicted data. The mathematical formulae of such error functions are shown in Table 3.

Table 3: Error function for statistical analysis of kinetic models (Soheil *et al.* 2017)

Error function	Equation	Number
Residual Sum of Squares	$RSS = \sum_{i=1}^n  q_{exp} - q_{obs} ^2$	(14)
Coefficient of determination ( $R^2$ )	$R^2 = 1 - \frac{\sum_{i=1}^n (q_{e,exp} - q_{e,cal})^2}{\sum_{i=1}^n (q_{e,cal} - q_{e,exp})^2}$	(15)

## 3. RESULTS AND DISCUSSION

### 3.1 Effect of contact time

The effect of contact time for adsorption of the MG onto BPC developed (Fig.3), indicated a gradual increase in the removal efficiency from 84.7% to 91.3 % as the contact time increased (10-225 mins). There was a rapid change in the adsorption capacity within the first 10 mins from 0 to 8.47 mg/g, and a maximum adsorption capacity of 9.13 mg/g was recorded at 225<sup>th</sup> mins. These indicate the influence of the contact time on the adsorption properties of the BPC developed. This is due to the initial dye concentration providing the driving force to overcome the barrier to the mass transfer of dye between the aqueous liquid and the solid phase (Kumar *et al.* 2010). It can be observed from previous studies that there was a rapid increase in the removal of MG at the initial stage of the adsorption process. Adsorption Capacity and Removal efficiencies determined based on the contact time in comparison with other studies are indicated in Table 4.

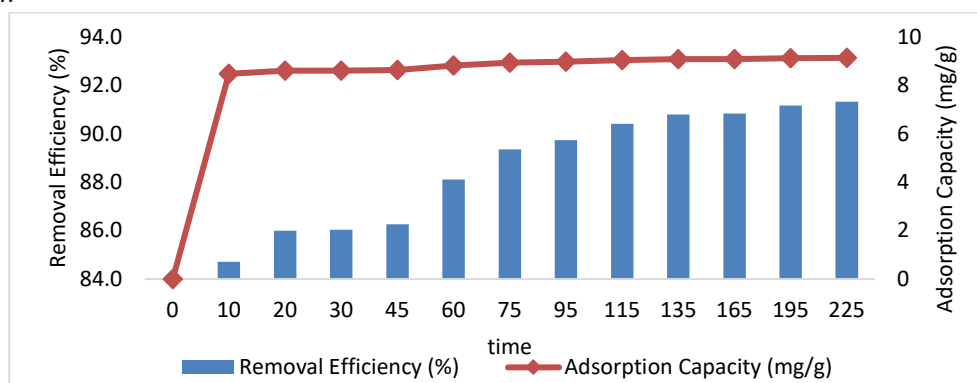


Figure 3: Adsorption capacity and removal efficiency of the BPC developed

Table 4: Comparison of other studies based on contact time, Isotherms and Kinetics

Adsorbent	Contact time			Isotherms	$R_L$	Kinetics	References
	Maximum Removal Rate time (mins)	Adsorption Capacity mg/g	Percentage Removal %				
Orange peel	NR	NR	NR	Henry	NS	Pseudo-Second Order	Zhul-quarnain <i>et al.</i> , 2018
<i>Ziziphus spina Christi</i> seeds	360	48	NR	Langmuir	0,02955-0.02491	Pseudo-Second Order	Mohammed <i>et al.</i> , 2019
<i>Catha edulis stem</i>	60	1.0	98.8	Freundlich	0.089-0.019	Pseudo-Second Order	Abate <i>et al.</i> , 2020
Durian peel	240-300	50.6	84	Freundlich	0.11-0.25	Pseudo-first Order	Yusop <i>et al.</i> , (2021)

Baobab pod cellulose	225	9.13	91.3	Henry	0.245-0.619	Pseudo-second Order Type 1	This Study
----------------------	-----	------	------	-------	-------------	----------------------------	------------

NR: Not Reported    NS: Not Stated

### 3.2 Isothermal study

The equilibrium data of the MG adsorption on of the BPC developed were fitted to Henry, Freundlich and Langmuir isotherm models displayed in Fig. 4a-c and evaluated in Table 5. The  $R^2$  of the Henry, Freundlich and Langmuir isotherms are 0.9601, 0.9290, and 0.9349 respectively, thus giving the order of suitability as Henry>Langmuir>Freundlich. The RL values (0.245-0.619) fall within the condition of  $0 < RL < 1$  and this indicated favourable adsorption (Yusop *et al.*, 2021) for the removal of MG by the BPC developed. In comparison with other studies as indicated in Table 4, BPC is highly favourable for adsorption purposes

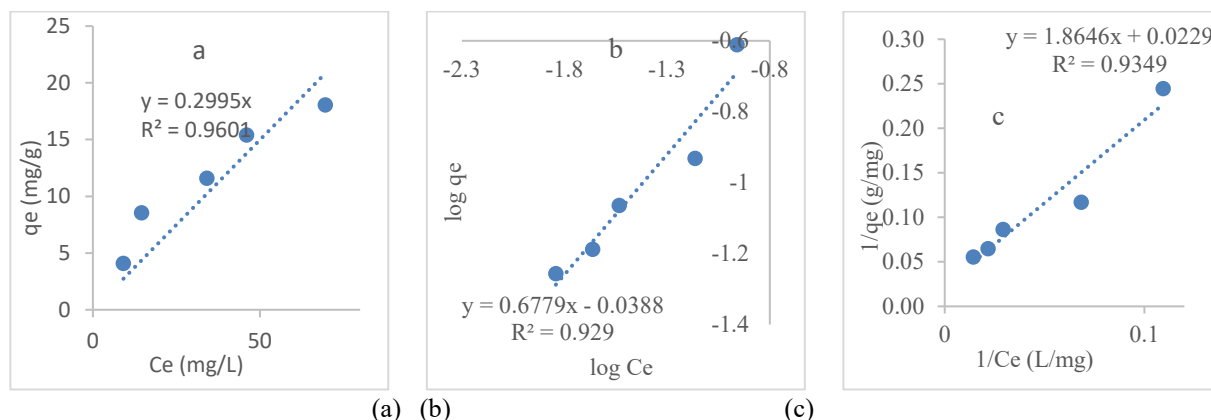


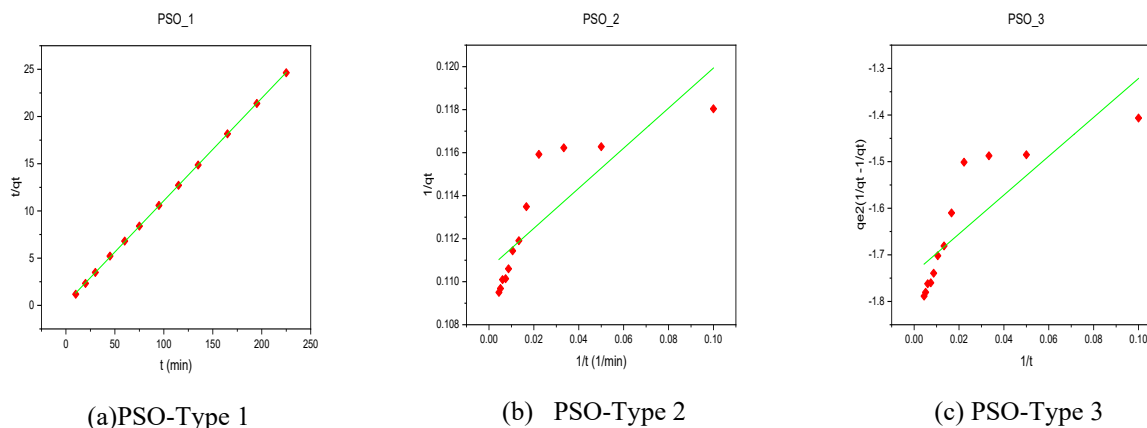
Figure 4. Plots of: (a) Henry (b) Freundlich and (c) Langmuir isotherm models for the sorption of MG dye onto BPC developed

Table 5: Error function analysis for different types of pseudo-second order kinetic models

Isotherm Models								
Henry		Freundlich			Langmuir			
$K_H$	$R^2$	$1/n$	$K_f$	$R^2$	$q_m$	$K_L$	$R_L$	$R^2$
0.2995 L/g	0.9601	0.6779	0.9145	0.929	43.67 mg/g	0.0123	0.245-0.619	0.9349

### 3.4 Pseudo-second-order kinetic model Analysis

The pseudo second order Type 2 & 6 satisfied the standard condition of the Residual sum of squares RSS with a value  $3.07 \times 10^{-5}$ , according to (Soheil *et al.* 2017). It stated that the standard condition requirement is satisfied by the model with the least value of RSS and according to Amtul *et al.*, (2017) for Pearson's (r), R-Square, Adj. R-Square has a similar standard condition of error value closest to unity. Pseudo second order kinetic model Type 1 satisfied the condition perfectly with values of 0.99997, 0.99994 and 0.99993 for Pearson's r, R-Square, Adj. R-Square respectively (Table 6). Most previous studies looked into gave Pseudo-Second Order as the best fit for their studies (Table 4).



(a) PSO-Type 1

(b) PSO-Type 2

(c) PSO-Type 3

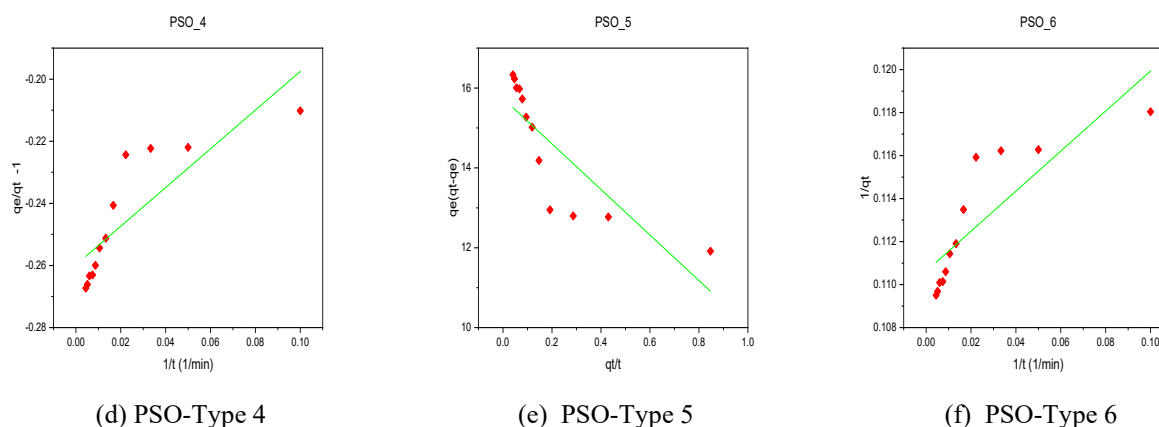


Figure 5: Plots of pseudo-second-order kinetics model for type 1-type 6

Table 6: Error Function Analysis for Different Types of Pseudo-Second Order Kinetic Models

Model	Residual Sum of Squares	Pearson's r	R-Square
PSO_1	$4.13 \times 10^{-2}$	0.99997	0.99994
PSO_2	$3.07 \times 10^{-5}$	0.83976	0.70519
PSO_3	$6.14 \times 10^{-2}$	0.83976	0.70519
PSO_4	$1.37 \times 10^{-3}$	0.83976	0.70519
PSO_5	$8.55 \times 10^0$	-0.83432	0.69609
PSO_6	$3.07 \times 10^{-5}$	0.83976	0.70519

#### 4. CONCLUSION

In this study, we observed that the longer the contact time between the adsorbent and its adsorbate, the greater the percentage of dye removal detected at any initial dye concentration which indicates that it has a high removal efficiency. Henry, Freundlich and Langmuir isotherms studied showed that  $R^2$  of the Henry, Freundlich and Langmuir isotherms were 0.9601, 0.9290, and 0.9349 respectively, thus giving the order of suitability as Henry>Langmuir> Freundlich. Based on the error functions studied for type-1 – type-6 of the pseudo second order kinetic model it was revealed that Type 1 fitted the experimental data best by satisfying the error functions parameters. Based on all parameters used in the study it can be deduced that BPC works favourably in adsorption processes.

#### ACKNOWLEDGEMENT

The authors acknowledged the opportunity given to use the Bioenvironmental Water and Engineering Research Group (BWERG) Laboratory, Ladoké Akintola University of Technology, Ogbomosó.

#### REFERENCES

- Abate, G.Y., Alene, A.N., Habte, A.T and Getahun, D.M. (2020). Adsorptive removal of malachite green dye from aqueous solution onto activated carbon of *Catha edulis* stem as a low-cost bio-adsorbent. *Environmental Systems Research*, 9(29), pp: 1-13
- Adenekan, M.K., Fadimu, G.J., Odunmbaku, L.A., Nupo S.S., Oguntoyinbo S.I. and Oke E.K. (2017). Chemical and Functional Characterization of Baobab (*Adansonia Digitata* L.) Seed Protein Concentrate using Alcohol Extraction Method. *International Journal of Environment, Agriculture and Biotechnology (IJEAB)*, 2(5), pp. 2554-2558
- Ahmed, A. A.Y and Taiseer, H, M. (2018). Synthesis and Characteristic of Carboxymethyl Cellulose from Baobab (*Adansonia Digitata* L.) Fruit Shell. *International Journal of Engineering and Applied Sciences (IJEAS)*, 5(12). pp. 1-10
- Amtul, Q., Syed, A.K., and Saeeda, N.A., (2017). Equilibrium Modelling for Adsorption of Aqueous Cd (II) onto Turmeric: Linear versus Nonlinear Regression Analysis, *Mor. J. Chem.*, 2, pp. 362-370
- Ani. J.U, Akpomie, K.G, Okoro, U.C, Aneke, L.E, Onukwuli, O.D and Ujam, O.T. (2020). Potentials of activated carbon produced from biomass materials for sequestration of dyes, heavy metals, and crude oil components from aqueous environment. *Applied Water Science*. 10(69), pp. 1-11
- Aseel, M.A., Abbas N.A., and Ayad F.A. (2014). Kinetics and equilibrium study for the adsorption of textile dyes on coconut shell-activated carbon. *Arabian Journal of Chemistry*, pp. 11-21

- Asogwa, I.S., Ibrahim, A.N and AGBAKA, J.I. (2020). African baobab: Its Role in Enhancing Nutrition, Health, and the Environment. *Trees, Forests and People*, pp. 1-34.
- Guo, X. and Wang, J. (2019). The phenomenological mass transfer kinetics model for Sr<sup>2+</sup> sorption onto spheroids primary microplastics. *Environmental pollution*, pp. 737– 745
- Kabbashi, N.A., Mirghani, M.E.S., Alam Md. Z, Qudsieh, S.Y and Bello, I.A. (2017). Characterization of the Baobab fruit shells as adsorption material. *International Food Research Journal*, 24(Suppl), pp. S472-S474
- Kumar, D.H., Harinath, Y., Seshiah, K., and Reddy, A.V.R. (2010). Biosorption of Pb (II) from aqueous solutions using chemically modified *Moringa oleifera* tree leaves. *Chemical Engineering Journal*. 162 (2), pp. 626-634
- Kumaraswamy, K., Dhananjanyulu, B.V., and Kumar, M.S.J. (2014). Adsorption studies of Congo red from aqueous solution onto rice husk. *Research Journal of Pharmaceutical, Biological and Chemical Sciences*. 5(1), pp. 317-325
- Mohammed, S.B., Mohammed, H. A. and Hanan, S.A. (2019). Removal of Malachite Green Dye from Aqueous Solution by Adsorption Using Modified and Unmodified Local Agriculture Waste. *Science Journal of Analytical Chemistry*, 7(2), pp. 42-56
- Nur, A. S., Norshahidatui, A. M. S., Ahmad, Z.A.S., Nurasmah, M. S., Mohammad, K.A.A.R., Mazlan, M., Mohamad, A. M. A., Wan, N. A. W. M., Abrar, I., An'Am, B. M. N. and Nor, H.A. (2020). Preparation & Characterization of Microcrystalline Cellulose from Agriculture Waste. *IOP Conference Series: Earth and Environmental Science*. 596, pp. 1-7. Malaysia: IOP Publishing
- Palukurty, M. A., Allu, T., Chitturi, A., and Somalanka, S. R. (2014). Adsorption of Malachite Green from Synthetic Waste Water onto Activated Carbon from Corn Cob. *Journal of Chemical, Biological and Physical Sciences*, 4(3), pp. 1910-1921
- Prabakaran, R and Arivoli, S. (2012). Thermodynamic and Isotherm Analysis on the Removal of Malachite Green Dye Using Thespesia Populnea Bark. *E-Journal of Chemistry*, 9(4), pp. 2575-2588
- Senthil, R. M., Vivek S., Sampathkumar, V., Gokulan, R., Premkumar, S., Veerapathran, M., Ravindaran, T., Gowri, S. R., Mukesh, P. and Selvakumar, P. (2022). Biosorption of Malachite Green from Aqueous Phase by Tamarind Fruit Shells Using FBR. *Advances in Materials Science and Engineering*, 2022, pp. 1-7
- Sharma, N., Tiwari, D.P., and Singh, S.K. (2012). Decolourisation of Synthetic Dyes by Agricultural Waste - A Review. *International Journal of Scientific & Engineering Research*, 3(2), pp. 1-10
- Slimani, M. S. Ahlafi, H. Moussout, H. Boukhelifi, F. and Zegaoui, O. (2012). Adsorption of hexavalent chromium and phenol onto bentonite modified with Hexadecyltrimethylammonium bromide (HDTMABr). *Journal of Advances in Chemistry*, 8(2), pp. 1602–1611
- Tchikualaa, E., Mourão, P and Nabais, J. (2017). Valorisation of Natural Fibres from African Baobab Wastes by the Production of Activated Carbons for Adsorption of Diuron. *The Procedia Engineering*, 200, pp. 399-407
- Uddin, M.T., Islam, M.S., and Abedin, M.Z. (2007). Adsorption of phenol from aqueous solution by water hyacinth ash. *ARNP Journal of Engineering and Applied Sciences* 2(2), pp. 11–17
- Wong, S., Ngadi, N., Inuwa, I.M., and Hassan, O., (2018). Recent advances in applications of activated carbon from biowaste for wastewater treatment: A short review. *J. Clean. Prod.* 175, pp. 361–375
- Yusop, M.F.R., Ahmad, M.A., Rosli, N.A., Gonawan, F.N and Abdullah, S.J. (2021). Scavenging Malachite Green Dye from Aqueous Solution Using Durian Peel Based Activated Carbon. *Malaysian Journal of Fundamental and Applied Sciences*, 17(1), pp. 95-103
- Zhul-quarnain, M., Ogemdi, I.K., Ilesanmi, M., Emuobosa, G. and Ekpunobi, E.C. (2018). Adsorption of Malachite Green Dye Using Orange Peel. *Journal of Biomaterials*, 2(2), pp. 31-40



## Efficient High Temperature Acid Corrosion Protection of SS 316L Stainless Steel using an Imidazole + KI Inhibitor Mixture

Aremiyau S. MOMOH<sup>1</sup>, Kenneth K. ADAMA<sup>1</sup>, Ikenna B. ONYEACHU<sup>2\*</sup>

<sup>1</sup>Department of Chemical Engineering, Edo State University Uzairue, Edo State, Nigeria

<sup>2</sup>Department of Chemistry, Edo State University Uzairue, Edo State, Nigeria

\*Corresponding author: [onyeachu.benedict@edouniversity.edu.ng](mailto:onyeachu.benedict@edouniversity.edu.ng).

### ABSTRACT

Protecting chemical reactor alloys is very important in the industry. Nowadays, the use of highly efficient and environmentally friendly chemicals is greatly encouraged. This work investigates the efficiency of a corrosion inhibitor mixture containing 1-benzylimidazole and potassium iodide (KI), for the protection of stainless steel SS 316L during acid corrosion at 60 °C. The inhibitor mixture significantly lowers the alloy corrosion rate and behaves like a mixed-type inhibitor with greater anodic inclination. The mixture delivers an efficiency > 80 %, as confirmed by weight loss, potentiodynamic polarization and cyclic voltammetry characterizations. The inhibitor mixture also enhances passivation of the alloy and mitigates against surface microstructural degradation, based on scanning electron microscopy (SEM) characterization.

**Keywords:** Stainless steel, Acid pickling, Imidazole, Cyclic voltammetry, Corrosion inhibition.

### 1. INTRODUCTION

Acid corrosion of chemical reactors is a serious challenge for the chemical industry. Most of these reactors are fabricated with stainless steel. It usually occurs when the reactor alloy makes contact with aqueous acid solutions, especially HCl, during industrial acid pickling (periodically performed to dissolve scales which have developed on the reactor surface over prolonged period of application) (Obot *et al.*, 2019). It is an electrochemical process that is sustained by simultaneous oxidation and reduction reactions occurring, respectively, at anodic and cathodic reactive sites on the alloy surface. The oxidation reactions usually cause the dissolution of metal atoms from the alloy surface ( $M - ne = M^{+ne}$ ), and they constitute the major cause of material loss during the corrosion (Obot *et al.*, 2019). For effectiveness, acid pickling is commonly conducted at temperature up to 60 °C, which makes the acid solution very aggressive.

To control acid corrosion and sustain the material integrity and service life of chemical reactor alloys, the chemical industries add low doses of corrosion inhibitors into the acid pickling solution. These inhibitors are largely organic molecules with the capability to adsorb and form protective films on the reactor surface, thereby simultaneously protecting the reactor surface during acid pickling (Onyeachu *et al.*, 2020). Unfortunately, most chemical companies usually apply corrosion inhibitor formulations containing propargyl alcohol, which has been reported to be very toxic to the environment (Thakur *et al.*, 2013). Therefore, identifying highly effective corrosion inhibitors with good environmental profile is imperative in order to sustain material protection against acid corrosion in the chemical industry.

In this work, we have tested 1-benzylimidazole (Fig. 1) and its mixture with potassium iodide (KI) as an effective corrosion inhibitor mixture for protecting SS316L stainless steel during corrosion in 1 M HCl acid at 60 °C. The techniques used in the present work include weight loss (WL), cyclic potentiodynamic polarization (CPDP), cyclic voltammetry (CV) and scanning electron microscopy (SEM). Our choice of 1-benzylimidazole and KI hinges on the promising electronic properties and pharmacological characteristics of 1-benzylimidazole (Onyeachu and Solomon, 2020), as well as the efficiency-boosting impact which KI is known to contribute when mixed with organic corrosion inhibitors in acid solutions (Umoren and Solomon, 2014). It is our expectation that the developed corrosion inhibitor mixture will be beneficial for the chemical industry during acid pickling of stainless steel chemical reactors.

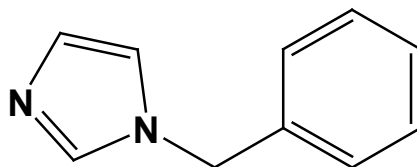


**Figure 1:** The molecular structure of 1-benzylimidazole.

## 2. MATERIALS AND METHODS

The acid solution (1 M HCl) without and with KI was prepared by diluting the concentrated acid with distilled water alone or already prepared KI solution. 2000 ppm of 1-benzylimidazole was prepared by diluting a stock solution (prepared in isopropanol) with the acid and acid + KI solutions. Preparation of the SS 316L alloy surface include polishing with up to 1000 grit size SiC paper, washing thoroughly with water/acetone and drying. Experiment at 60 °C temperature was achieved with a thermostatic water bath. The SS 316L samples for weight loss samples had total exposed surface area of 22.73 cm<sup>2</sup> while the electrochemical coupons had 1 cm<sup>2</sup> surface area. After immersion, the coupons were withdrawn from the solutions and cleaned according to ASTM G1-03 standard procedure (ASTM, 1997).

The weight loss after immersion ( $\Delta W$ ) was calculated as  $\Delta W$  (g) =  $W_{(\text{before immersion})} - W_{(\text{after immersion})}$ :

Where corrosion rate ( $v$ , mm/yr) was calculated as  $v$  (mm/yr) =  $\frac{\Delta W \times 87600}{A \times \rho \times T}$ ;

Whereby  $\rho$  = density of the stainless steel sample (7.99 g cm<sup>-3</sup>),  $T$  = immersion time (6 h), and  $A$  = surface area of the coupons (22.73 cm<sup>2</sup>).

The electrochemical tests, performed in a three-electrode system, were conducted on a Gamry Potentiostat/Galvanostat/ZRA Reference 600+ workstation and commenced with an open circuit potential (OCP) determination during 1800 s of free corrosion. The SS 316L alloy acted as working electrode while Ag/AgCl was reference electrode and a Pt. sheet was the counter electrode. Cyclic voltammetry measurements were carried out in the potential range of -0.6 V vs. Ag/AgCl to +0.6 V vs. Ag/AgCl using a sweep rate of 10 mV/s. Cyclic potentiodynamic polarization (CPDP) measurements were conducted using the following parameters: initial potential = -0.25 V/Ref; apex potential = 1 V/Ref; final potential = 0 V/Ref; forward and reverse scan rate = 0.5 mV/s.

The efficiency of inhibition (%  $IE$ ) was calculated from the CPDP results as  $\% IE_{\text{CPDP}} = 1 - \frac{i_{\text{corr}(\text{with inhibitor})}}{i_{\text{corr}(\text{without inhibitor})}} \times 100\%$

The extent by which the 1-benzylimidazole + KI mixture mitigates the SS 316L surface degradation due to corrosion, was characterized after the immersion period using scanning electron microscopy (SEM) JEOL JSM-6610 LV model operated at a voltage of 20 kV and irradiation current of 10 mA.

## 3. RESULTS AND DISCUSSION

### 3.1 Weight Loss Studies

After 6 h immersion in 1 M HCl with and without 1-benzylimidazole, KI and 1-benzylimidazole + KI at 60 °C, the corrosion rate experienced by the alloy has been represented in Figure 2(a). In the inhibitor-free acid solution the SS 316L experiences a corrosion rate of  $12.87 \pm 1.59$  mm/yr. The corrosion rate experienced in the presence of 2000 ppm of 1-benzylimidazole, 1 mM KI, and 1-benzylimidazole + 1 mM KI, is  $4.90 \pm 1.36$  mm/yr,  $3.21 \pm 0.46$  mm/yr, and  $3.21 \pm 0.46$  mm/yr, respectively. According to Figure 2(b), the calculated inhibition efficiency when 1-benzylimidazole, KI and 1-benzylimidazole + KI are added is, respectively,  $65.12 \pm 1.87$  %,  $59.91 \pm 1.42$  % and  $75.03 \pm 0.44$  %.

In the acid solution, the corrosion of SS 316L is attributed to dissolution of surface elements, especially Fe and Cr, from the reactive sites on the alloy surface (Maurice and Marcus, 2018; Strehblow, 2016). Through adsorption, the added 1-benzylimidazole lowers the corrosion rate experienced by alloy by blocking either (or both) anodic and cathodic sites from where Fe and Cr dissolve. Anodic sites are blocked when 1-benzylimidazole (as a protonated molecule in the acid solution (Onyeachu *et al.*, 2021; Cardona *et al.*, 2014), transfers electron from its electron-rich active centres (consisting of the electronegative N atom and C=C bonds) to incompletely-occupied d-orbitals of Fe and Cr. Cathodic sites (where H<sup>+</sup> reduction into H<sub>2</sub> dominates) are blocked by competitive adsorption of cationic 1-benzylimidazole to minimize the effect of H<sub>2</sub> formation. The adsorption of this cationic 1-benzylimidazole molecule is significantly boosted in the presence of iodide ions (flourished by KI) because pre-adsorbed iodide anions could charge the alloy surface negatively and promote electrostatic attraction of the inhibitor species (Onyeachu *et al.*, 2021).



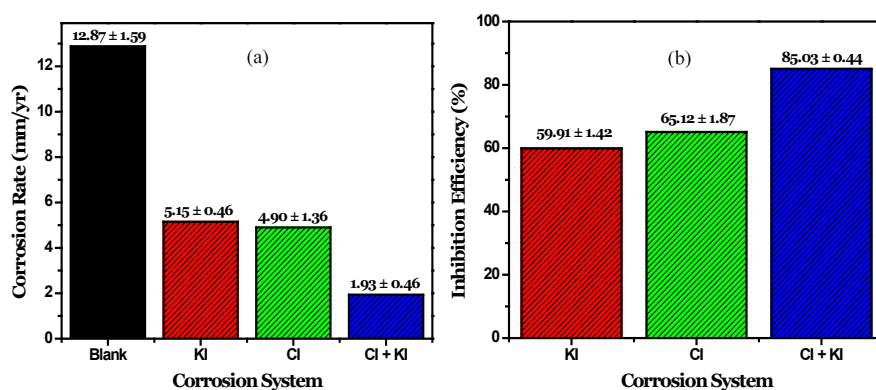


**Figure 2:** (a) Corrosion rate experienced by SS 316L after 6 h immersion at 60 °C in 1 M HCl without and with 1–benzylimidazole, KI and 1–benzylimidazole + KI, (b) corresponding inhibition efficiencies.

### 3.2 Electrochemical Studies

The CPDP plots of potential vs, current density during SS 316L corrosion in 1 M HCl solution without and with 1–benzylimidazole, KI, and 1–benzylimidazole + KI are presented in Fig. 3. Important polarization elements extrapolated from the plots include corrosion potential ( $E_{\text{corr}}$ ), corrosion current density ( $i_{\text{corr}}$ ), passivation potential ( $E_{\text{pass}}$ ), re-passivation potential ( $E_{\text{rp}}$ ) and pitting potential ( $E_{\text{pit}}$ ). The values of these elements are given in Table 1. Active corrosion phenomena are depicted by the forward potential while pitting and re-passivation phenomena are depicted by the reverse scan. With 1–benzylimidazole in the corrosion system, the stainless steel  $E_{\text{corr}}$  slightly shifts anodically from  $-247.09$  mV in the uninhibited solution to  $-232.55$  mV in the presence of inhibitor. Both anodic and cathodic currents are reduced. Therefore, the inhibitor is a mixed–type inhibitor with slightly more anodic impact. Similar impacts of 1–benzylimidazole has been reported on carbon steel (Onyeachu *et al.*, 2021). The anodic influence implies that 1–benzylimidazole effectively lowers the rate anodic oxidation reactions ( $\text{Fe} \rightarrow \text{Fe}^{2+}$  and  $\text{Cr} \rightarrow \text{Cr}^{3+}$ ). The reduced rate of anodic reactions blocks off the electron flow that sustains cathodic reduction of  $\text{H}^+$ . The addition of KI releases iodide ( $\text{I}^-$ ) ions which could pre-interact with the  $\text{Fe}^{2+}$  and  $\text{Cr}^{3+}$ , and then create templates which enhance the anchorage of 1–benzylimidazole molecules and boost their efficiency. Furthermore, the inhibition efficiencies calculated for 1–benzylimidazole, KI and 1–benzylimidazole + KI are consistent with the corrosion rate results. The 1–benzylimidazole and 1–benzylimidazole + KI both lower the pitting potential ( $E_{\text{pit}}$ ), which confirms the ability of the inhibitor systems to decrease rate of active corrosion on the alloy surface. However, some growing Fe/Cr–oxide/hydroxide products (during passivation) could infringe on the inhibitor–metal atoms interaction (which sustains inhibitor adsorption) and encourage its detachment to open new active sites which trigger localized pitting corrosion on the alloy surface. Nevertheless, negative hysteresis are recorded in the reverse CPDP scan, which shows some self-healing tendencies of the alloy corrosion layer, both without and with corrosion inhibitor (Esmailzadeh *et al.*, 2018).

The cyclic voltammograms obtained during SS 316L corrosion in the acid solution at 60 °C with and without the inhibitor systems, are given in Figure 4. Two anodic and cathodic peaks are obvious. The anodic peaks align with the resultant anodic currents from the oxidation of Fe and Cr into oxides and hydroxides (Mulimbayan and Mena, 2016; Knapp and Wren, 2012). The cathodic peaks are signals from reduction reactions like  $\text{H}^+ \rightarrow \text{H}_2$ ,  $\text{Fe}^{2+} \rightarrow \text{Fe}$  and  $\text{Cr}^{3+} \rightarrow \text{Cr}$  (Mulimbayan and Mena, 2016; Knapp and Wren, 2012). Higher current values exhibited in the absence of inhibitor imply more rapid corrosion rate and greater susceptibility to localized corrosion like pitting. Conversely, lower current values show slower rate of oxidation leading to slower rate (and more stable) rate of growth of the passive layer. Therefore, the Fig. 4 confirm that 1–benzylimidazole + KI corrosion inhibitor system impacts very high efficiency on lowering the SS 316L alloy corrosion in 1 M HCl at 60 °C.

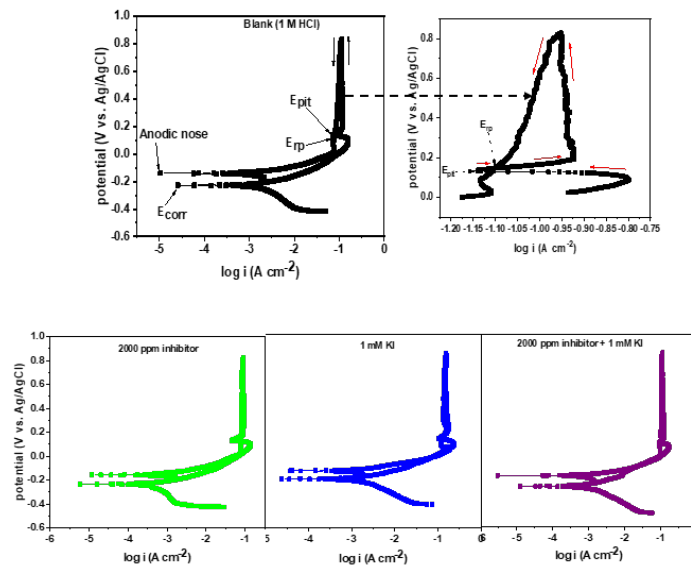


Figure 3: CPDP plots obtained for SS316L during corrosion in 1 M HCl at 60 °C without and with 1-benzylimidazole, KI and 1-benzylimidazole + KI.

Table 1: Polarization parameters for SS 316L during corrosion in 1 M HCl at 60 °C without and with 1-benzylimidazole, KI and 1-benzylimidazole + KI.

System	$-E_{corr}$ (mV <sub>Ag/AgCl</sub> )	$i_{corr}$ (mA cm <sup>-2</sup> )	$E_{pit}$ (mV <sub>Ag/AgCl</sub> )	$E_{rp}$ (mV <sub>Ag/AgCl</sub> )	$E_{pit}-E_{rp}$ (mV <sub>Ag/AgCl</sub> )	%IE
Blank	247.09	2.36	174.88	120.98	53.90	-
2000 ppm	232.55	0.69	133.24	22.51	110.73	70.76
1 mM KI	195.64	1.28	134.96	65.97	68.99	45.76
2000 ppm + 1 mM KI	181.67	0.44	124.54	21.65	102.89	81.36

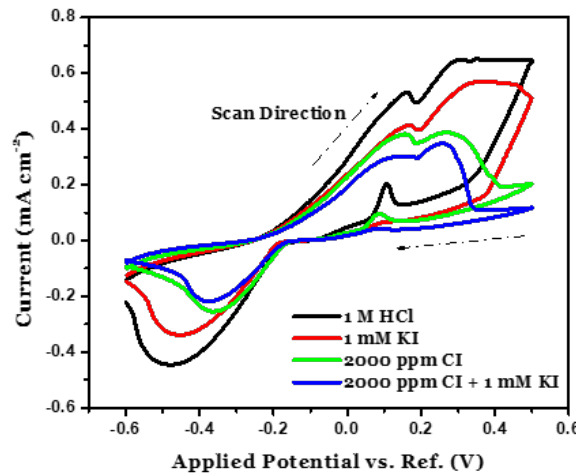
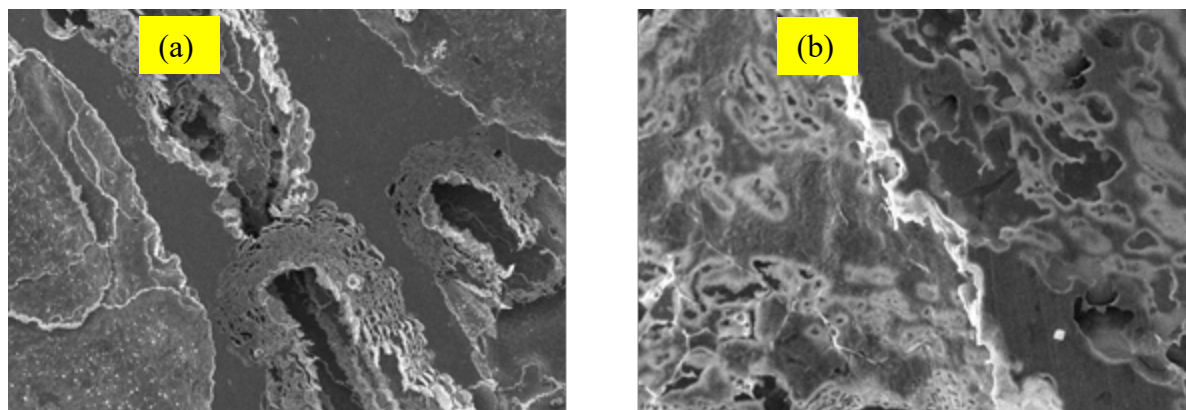


Figure 4: Cyclic voltammograms obtained during SS316L corrosion in 1 M HCl at 60 °C without and with 1-benzylimidazole, KI and 1-benzylimidazole + KI.

### 3.3 SEM Investigation

Surface morphologies of corroded SS 316L in the absence and presence of 1-benzylimidazole + KI are shown in Fig. 5. Without inhibitor system, the alloy surface corrodes significantly; showing a severely degraded microstructure with enormous pits on some portions and smoother characteristics at other portions. The smoother portions represent portions of minimal corrosion due to protective corrosion product formation on stainless steel alloy after 6 h immersion in 1 M HCl. However, when 1-benzylimidazole + KI is added to the acid solution, smaller and shallower pits are observed and the alloy surface is far smoother than in the absence of inhibitor. This confirms the adsorption of the corrosion inhibitor system, which eventually enhances re-passivation of the stainless steel during the acid corrosion, in agreement with the CPDP results.



**Figure 5:** SEM–EDX surface images ( $\times 1000$ ) for SS316L stainless steel after corrosion in 1 M HCl at 60 °C (a) without and (b) with 2000 ppm 1-benzylimidazole + 1 mM KI.

#### 4. CONCLUSIONS

The following conclusions can be drawn from the present work:

1-benzylimidazole is an efficient corrosion inhibitor for SS 316L during corrosion in 1 M HCl at 60 °C, however, addition of KI provides significant boost to this efficiency.

1-benzylimidazole + KI inhibitor system is a mixed-type inhibitor with greater inclination towards anodic activity

1-benzylimidazole + KI inhibitor system significantly mitigates effect of surface microstructural degradation caused by the acid corrosion at 60 °C.

#### REFERENCES

- ASTM-G 01–03, Standard practice for preparing, cleaning, and evaluation corrosion test specimens, ASTM Book of Standards (Re-approved 1997).
- Belakhdar A., Ferkous H., Djellahi S., Sahraoui R., Lahbib H., Amor Y.B., Erto A., Balsamo M., Benguerba Y. Computational and Experimental Studies on the Efficiency of Rosmarinus officinalis Polyphenols as Green Corrosion Inhibitors for XC48 Steel in Acidic Medium, *Colloids and Surfaces A: Physicochemical and Engineering Aspects* 606 (2020) 125458.
- Cardona C., Narváez L., Miranda J.M., Acosta A. Benzodimidazole and Imidazole as Corrosion Inhibitors of AISI 316L Stainless Steel in Sulphuric Acid Medium, In ECS Meeting Abstracts No. 13 (2014) 766. IOP Publishing.
- Esmailzadeh S., Aliofkhaezai M., Sarlak H. Interpretation of Cyclic Potentiodynamic Polarization Test Results for Study of Corrosion Behavior of Metals: A Review, *Prot. Met. Phys. Chem. Surf.* 54 (2018) 976.
- Knapp Q.W., Wren J.C. Film Formation on Type-316L Stainless Steel as a Function of Potential: Probing the Role of Gamma-radiation, *Electrochim. Acta* 80 (2012) 90–99.
- Maurice V., Marcus P. Progress in Corrosion Science at Atomic and Nanometric Scales, *Prog. Mater. Sci.* 95 (2018) 132–171.
- Mulimbayan F.M., Mena M.G. Cyclic Voltammetric Study of the Pitting Corrosion Behavior of Low-Nickel Austenitic Stainless Steels in Citric Acid, *Mater. Sci. Forum* 866 (2016) 191–195.
- Obot I.B., Meroufel A., Onyeachu I.B., Alenazi A., Sorour A.A. Corrosion Inhibitors for Acid Cleaning of Desalination Heat Exchangers: Progress, Challenges and Future Perspectives, *Mol. Liq.* 296 (2019) 111760.
- Onyeachu I.B., Obot I.B., Alamri A., Eziukwu C.A. Effective Acid Corrosion Inhibitors for X60 Steel Under Turbulent Flow Conditions Based on Benzimidazoles: Experimental, Theoretical, SEM, ATR-IR and XPS Investigations, *European Physical Journal Plus* 135 (2020) 129.
- Onyeachu I.B., Solomon M.M. Benzotriazole Derivative as an Effective Corrosion Inhibitor for Low Carbon Steel in 1 M HCl and 1 M HCl + 3.5wt.% NaCl Solutions, *Molecular Liquids* 313 (2020) 113536.
- Onyeachu I.B., Njoku D.I., Kaya S., El Ibrahim B., Nnadozie C.F. Sour Corrosion of C1018 Carbon Steel and Its Inhibition by 1-benzylimidazole: Electrochemical, SEM, FTIR and Computational Assessment, *J. Adhes. Sci. Technol.* 36 (2022) 774–794.
- Strehblow H.H. Passivity of Metals Studied by Surface Analytical Methods, A Review, *Electrochim. Acta* 212 (2016) 630–648.
- Thakur S.A., Flake G.P., Travlos G.S., Dill J.A., Grumbein S.L., Harbo S.J., Hooth M.J., Evaluation of Propargyl Alcohol Toxicity and Carcinogenicity in F344/N Rats and B6C3F1/N Mice following Whole-body Inhalation Exposure, *Toxicology* 314 (2013) 100.
- Umoren S.A., Solomon M.M. Effect of Halide Ions on the Corrosion Inhibition Efficiency of Different Organic Species– A Review, *J Ind. Eng. Chem.* 21 (2014) 81–100.



## Characterization of Bambu Clay: As a Potential Source for Zeolite Y Synthesis

Abdullahi A. MUSA<sup>1\*</sup>, Haruna M. SANI<sup>2</sup>, Mohammed U. GARBA<sup>3</sup>, Elizabeth J. ETERIGHO<sup>4</sup>, Mohammed ALHASSAN<sup>4</sup>

<sup>1</sup>Chemical Engineering Department, Federal University of Technology, Minna, Niger State, Nigeria.

<sup>2</sup>National Agency for Science and Engineering Infrastructure, PMB, 391, Idu, Garki Abuja. Nigeria

\*Corresponding author email: [abdulmusavespa@gmail.com](mailto:abdulmusavespa@gmail.com)

---

### ABSTRACT

Bambu clay has been intensively used in ceramics formulation and pot-making by the indigene of Bambu village in the Wamba Local Government Area in Nasarawa State north central of Nigeria. Clay mineral has several technological applications in the industry which include ceramics, cements, latex, paint, catalysts for petroleum refining, water treatment, cosmetics and others. In this study, the characterization analysis was conducted so as to determine the potential of Bambu clay for zeolite Y synthesis. The Bambu clay was subjected to preliminary treatment, beneficiation and thereafter subjected to calcination at 750°C for 3 hour in a chamber furnace for processing into metakaolin. The results of the analyses reveal that the raw Bambu clay is considered to be kaolinite with Si/Al ratio of approximately 1:8. The surface area of the raw Bambu clay is 159.40 m<sup>2</sup>g<sup>-1</sup>, pore volume 0.0780 cm<sup>3</sup>g<sup>-1</sup> and pore radius 2.920 nm. After subjected to calcination, the surface area increased from 159.40 to 530.40 m<sup>2</sup>g<sup>-1</sup>, pore volume increased from 0.0780 to 0.270 cm<sup>3</sup>g<sup>-1</sup> and pore radius increased from 2.920 to 3.217nm, respectively. Therefore, after the calcination, the kaolinite structure crumbled, and higher surface area was obtained as amorphous materials known as metakaolin. The result of the study was when compared with other research work where zeolite Y was synthesised from metakaolin, hence, Bambu clay is also potential source for zeolite Y synthesis.

**Keywords:** Bambu clay, Characterization, Calcination, Amorphous, Zeolite Y.

### 1.0 INTRODUCTION

Clay minerals are very tiny crystalline substances evolved primarily from chemical weathering of certain rock-forming minerals (Holtz and Kovacs, 2010). Bambu clay was mined from clay deposits in Wamba LGA (8°9600890 N', 8°6293780 E') in Nasarawa State of Nigeria. Clay minerals are hydrous aluminosilicates composed of crystal sheets which have a repeating atomic structure, and the sheets exist as tetrahedral silica and octahedral alumina. The fundamental sheets are mostly either arranged in 1:1 or 2:1 ratio of silica tetrahedron: alumina octahedron sheets. The sheets arranged in 1:1 are referred to as kaolinite group (Al<sub>2</sub>Si<sub>2</sub>O<sub>5</sub>(OH)<sub>4</sub>) (Holtz and Kovacs, 2010) and sheet arranged 2:1 are referred to as bentonite (montmorillonite) with general formula: M<sub>x</sub>(Al<sub>2-y</sub>Mg<sub>y</sub>)Si<sub>4</sub>O<sub>10</sub>(OH)<sub>2</sub>.nH<sub>2</sub>O (Cadene *et al.*, 2005). Similarly, illites has 2:1 arranged sheets with most important and extensive cation as potassium (K) which is of general formula: (K, H)Al<sub>2</sub>(SiAl)<sub>4</sub>O<sub>10</sub>(OH)<sub>2</sub>.XH<sub>2</sub>O (Uddin, 2008).

Zeolites are crystalline aluminosilicates minerals with distinctive three-dimensional structural shapes that form a uniformly sized interconnected pores of molecular dimensions which are widely used in industrial applications (Asmaa *et al.*, 2020). Zeolite X and Y are Faujasite class of zeolites which are known for remarkable stability and solid structure with large empty space (Olaremu, et al., 2018). It is widely used in catalytic cracking; hydro racking and isomerization process (Bai *et al.*, 2018). Zeolite X has Si/Al ratio from 1.0-1.5 while Zeolite-Y has Si/Al ratio from 2-5 (Xu, *et al.*, 2009). In this study, Bambu clay was characterized as possible source for synthesizing zeolite Y.

In accordance with the current work, the physical beneficiation and characterization of Bambu clay was carried out to ascertain its potential for synthesize zeolite Y. Zeolite Y synthesis could be determined by study the basic features like structural analysis, qualitative and quantitative compositions, pore volume and pore sizes, and functional group

## 2.0 MATERIAL AND METHODS

Bambu clay was collected from clay deposits in Wamba Local Government Area (LGA) of Nasarawa State located in the north central of Nigeria lying between Latitude: 8° 56' 29.51" N and Longitude: 8° 36' 11.34" E in of Nigeria. The clay was subjected to preliminary treatment and physical beneficiation. The treatment involved removal of all the dirt associated with clay and sun dried for one week. The beneficiation conducted by powdered the dried clay and soaked in de-ionized water of ratio 100g: 1dm<sup>3</sup> for two days. The slurry was blunged and screened through a 75µm mesh sieve and then allowed to settle thereafter, the water was siphoned-off and the clay was dried for three days for further use. The dried beneficiated clay was further calcined at 750°C for 3 hours in a chamber furnace for processing into metakaolin. Though, it was reported from the study of Nasuruddeen (2018) and Asmaa *et al.* (2020) that zeolite Y was produced from metakolin.

### 2.1 Characterization of Bambu Clay

In order to study the Bambu clay for synthesizing zeolite Y, the X-ray Diffraction (XRD) was used to determine crystallinity and phase identification, the Scanning Electron Micrograph (SEM) was used to know the morphology and X-ray Fluorescence (XRF) was used to determine chemical composition and mineralogy. Brunauer-Emmett-Teller (BET) analysis was conducted to measure the surface area and Fourier Transform Infrared Spectroscopy (FTIR) was used for surface functional groups present in the clay.

## 3.0 RESULTS AND DISCUSSION

### 3.1 X-Ray Fluorescence (XRF) Analysis

The chemical composition of Bambu clay, beneficiation and metakaolin obtained from XRF analysis are presented in Table 1. The XRF analysis usually indicate the presence of oxides as SiO<sub>2</sub> and AlO<sub>3</sub> predominately in high percentages than any other oxides. The analysis revealed that Bambu clay can be classified as kaolinite with Si/Al ratio of 1.80 as presented in the Table, though SiO<sub>2</sub>/AlO<sub>2</sub> ratio of clay is a function of the mineral phase. This implies that the structure of the Bambu clay consists of a tetrahedral sheet of silica (SiO<sub>2</sub>) inserting a central octahedral sheet of alumina in the structure (AlO<sub>3</sub>).

The mechanism of metakaonization involved dehydroxylation at temperature between 420°C to 450°C where water molecules diffuse out within the layers of the kaolinite structure that is the adjacent OH groups within the structure migrate through the crystal. At this temperature, outer OH groups are liberated resulted to the crystal structure to form microspores. At temperature increase to 750°C, the liberation of inner OH groups appear higher which lead to continuous disordered of internal structure of the kaolinite consequently, the porous size of kaolinite increased towards outer crystal layer structure and become an amorphous materials known as meta-kaolin (Kovo *et.al.* 2009). Metakaolin is highly reactive and has metastable phase which was suitable source for synthesizing zeolite Y Asmaa *et al.* (2020). The XRF analysis as presented in the Table Al<sub>2</sub>O<sub>3</sub> has decreased from 26.12 to 25.02. The decrease of Al<sub>2</sub>O<sub>3</sub> illustrated the alumina ions has diffuse out from lattice structure of kaolinite and resulted to hamper of octahedral structure. This analysis corroborated with the research work of feng *et al.*, (2009) that temperature range 600-800°C Al<sub>2</sub>O<sub>3</sub> octahedral structure does not maintained.

### 3.2 X-ray Diffractograms of Analysis

Figure 1. Presents the X-ray diffractograms of Bambu clay with different peaks, miller indices, lattice parameters at different diffraction angles and intensities. In Figure 1 (a) the first peaks at  $2\theta = 8.93^\circ$  indicated the presence of illite though, the intensity of the peak is not strong enough to justify the presence of illite in appreciable quantity. The second mineral peak at  $2\theta = 12.50^\circ$  indicated the presence of kaolinite, the fourth mineral peak at  $2\theta = 25.10^\circ$  indicated the presence of Albite and the fifth mineral peak at  $2\theta = 26.79^\circ$  indicated the presence of quartz which was the highest intensity on the diffraction pattern of Bambu clay.

Figure 1(b) shows the XRD pattern of metakaolinized Bambu clay which contains the Quartz as the most dominant peak. It reveals that kaolinite, illite and albite minerals were suppressed as a result of calcination which led their crystal lattice to collapsing and their peaks appearing very small in a crisscross pattern. This observation conforms to an earlier work of Abdullahi *et al.*, (2019) which reported that metakaolin is more reactive than other minerals present in the clay.

The Figure also shows that the quartz content of kaolinite was still inert after calcination at 750°C. Though, it was reported from previous work that, the crystalline silica is inert to calcination treatment even at 1050°C (Edomwonyi-Otu *et al.*, 2013).

### 3.3 Fourier Transform Infrared Spectra (FTIR) of Bambu Clay

The FTIR analysis of the clay was conducted at infrared wavelength of 4000-5000 cm<sup>-1</sup> to ascertain the various functional groups present in the Bambu clay. Figure 2 shows that the clay has well resolved (-OH) absorption bands in IR spectrum at peaks 3695.30, 3626.20, 3402.98, 1620.26 and 799.48 cm<sup>-1</sup>. These peaks are related to the -OH- stretching vibrating bands in the Bambu clay. These bands indicated the presence of kaolinite as it was revealed by Frost (1995). The result

was similar to the result obtained by (Patel, 2014). Appearance of peaks 1018.45, 799.84 and 678.97 $\text{cm}^{-1}$  at low region indicates the presence of quartz which agrees with the result obtained by Nwosu *et al.*, (2013). Therefore, bambu clay could be described to contain predominant of kaolinite which also confirmed in the XRD analysis in Figure 1.

**Table 1 X-ray Fluorescence (XRF) of the sample**

Compound	Raw clay (bambu)	Beneficiated clay	Meta-kaolin
SiO <sub>2</sub>	54.40	48.87	57.20
Al <sub>2</sub> O <sub>3</sub>	29.30	26.12	32.18
Fe <sub>2</sub> O <sub>3</sub>	4.20	4.14	5.32
CaO	0.41	0.51	0.24
V <sub>2</sub> O <sub>5</sub>	0.029		0.022
K <sub>2</sub> O	1.76	0.54	0.41
MnO	0.081	0.27	0.28
NaO <sub>2</sub>	0.80	0.60	0.50
TiO <sub>2</sub>	1.64	1.69	1.7
P <sub>2</sub> O <sub>5</sub>	ND	Nd	ND
SO <sub>3</sub>	ND	Nd	ND
CuO	0.028		0.034
MgO	0.007	0.004	0.004
NiO			
CuO			
ZnO	0.019		0.011
Ga <sub>2</sub> O <sub>3</sub>	0.012		0.021
Ta <sub>2</sub> O <sub>5</sub>			
Cl			
LOI (1000 <sup>o</sup> C)	7.31	12.14	2.08
Si/Al ratio	1.80	1.87	2.11

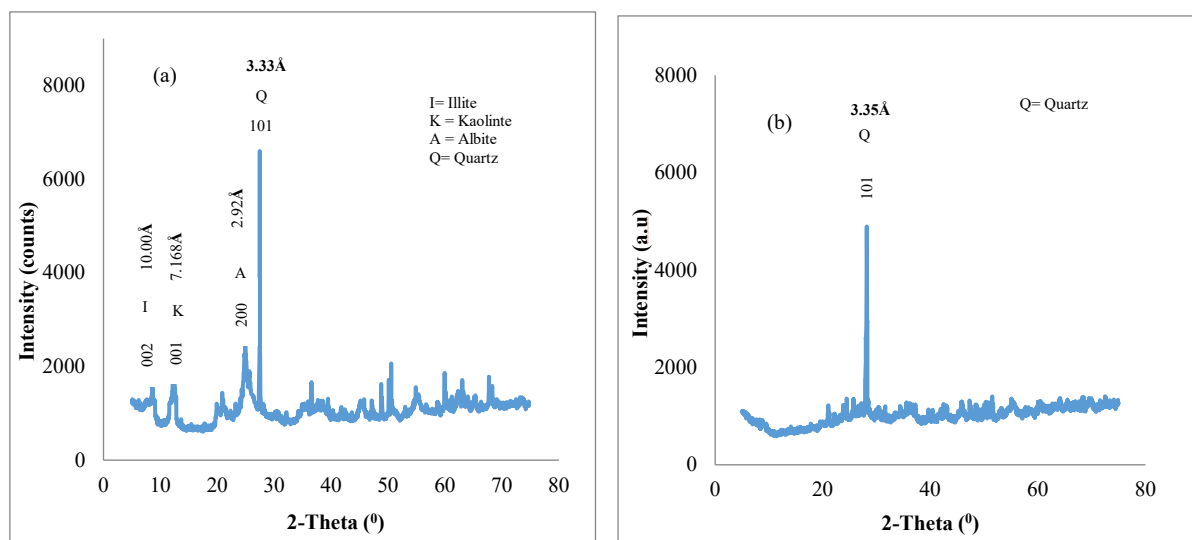


Figure 1: XRD patterns (a) Bambu clay (b) Metakaolin

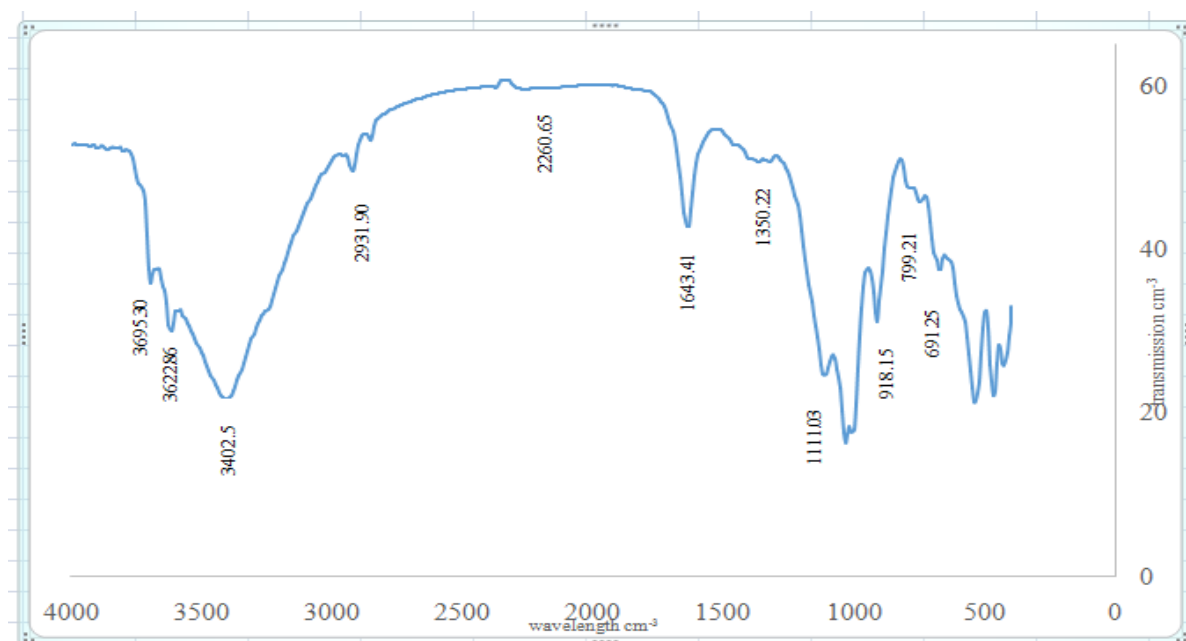


Figure 2: Fourier transform infrared spectra (FTIR) of raw Bambu clay

### 3.4 Scanning Electron Microscopy (SEM)

The morphology and crystallite size of Bambu clay and metakaolin were studied as a complimentary characterisation technique to the XRD using Scanning Electron Microscopy (SEM) and are presented in Figure 2. The morphology in Plate 1(a) shows that Bambu clay contains large stacks of highly packed kaolinite (Al-ani and Sarapaa, 2008). Present within the microstructure are also pseudo-hexagonal crystals characteristics of kaolinite minerals. Plate 1(b) shows that the collapse of other minerals resulted to the appearance of more platelet structures that are lumped together which indicated the presence of crystalline silica in the clay and it is evidence of amorphous materials.

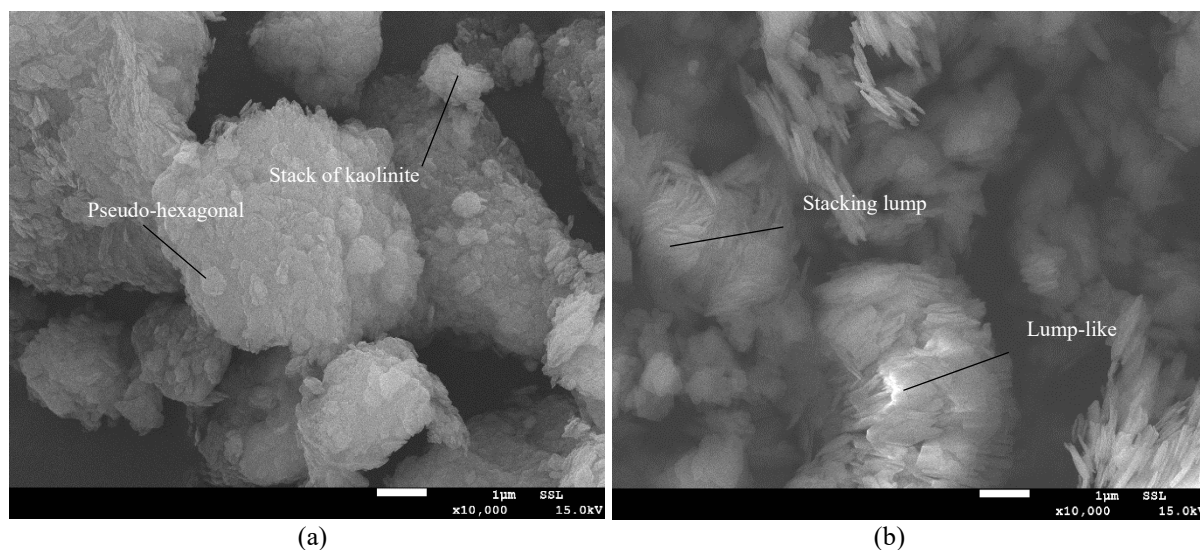


Plate 1: SEM (a) Bambu clay (b) Metakaolin

### 3.6 Brunauer-Emmett-Teller (BET) Analysis of Bambu Clay

The BJH method was considered in this research for BET analysis. The surface area of the raw Bambu clay as presented in the Table 2 is  $159.40 \text{ m}^2\text{g}^{-1}$ , pore volume  $0.0780 \text{ cm}^3\text{g}^{-1}$  and pore radius  $2.920 \text{ nm}$ . The surface area increased from  $159.40$  to  $530.40 \text{ m}^2\text{g}^{-1}$ , pore volume increased from  $0.0780$  to  $0.270 \text{ cm}^3\text{g}^{-1}$  and pore radius increased from  $2.920$  to  $3.217 \text{ nm}$  after structural changes as a result of calcination. This increase in the surface area may be attributed to the crumbling of stacking structure of kaolinite as a result of calcination which led to loss of crystallinity of the kaolinite. Therefore, exposed the kaolinite into higher surface area of an amorphous materials known as metakaolin. The order of increased is Bambu clay < metakaolin which is  $159.40 \text{ m}^2\text{g}^{-1} < 530.40 \text{ m}^2\text{g}^{-1}$  for BET surface area.

**Table 2: BET Results of the porous materials**

Samples	BET surface Area m <sup>2</sup> g <sup>-1</sup>	Pore Volume cm <sup>3</sup> g <sup>-1</sup>	Pore Radius (nm)
Raw Bambu clay	159.40	0.0780	2.920
Metakaolin	530.40	0.270	3.217

#### 4.0 Conclusion

This study discussed the characterization of Bambu clay. The XRF analysis indicated that raw Bambu clay can be classified as kaolinite with Si/Al ratio of approximately 1:80, but after dehydroxylation the ratio slightly increases to 2:1 hence, the clay could be a potential source for zeolite Y synthesis. Similarly, the clay contained mine kaolinite and quartz which was confirmed by the analysis of FTIR.

The surface area increased from 159.40 to 530.40 m<sup>2</sup>g<sup>-1</sup>, pore volume from 0.0780 to 0.270 cm<sup>3</sup>g<sup>-1</sup> and pore radius from 2.920 to 3.217 nm after structural changes as a result of calcination. In addition, The calcination resulted to crumbling of kaolinite structure and therefore exposed it to higher surface area of an amorphous materials known as metakaolin. Finally, the result obtained from this study for Si/Al ratio agreed with the result of Xu *et al.* (2009) and the Bambu clay is dominated with kaolinite. The values of the surface area and pore volume obtained in this study compared favourably with the surface area of result of study by Nasuruddeen (2015). Again, the structural changes and pore sizes corroborated with the research work of Asmaa *et al.* (2020) for zeolite Y synthesis.

#### 5.0 References

- Abdullahi, T., Harun, Z., Othman, M.H.D., Yusof, K.N., Rahmawati, A., Yunos, M.Z., Lajis, M.A. and Yusof, Y. (2019). Preliminary studies on hydrothermal synthesis of zeolite from Malaysian kaolinite clays. *Malaysian Journal of Fundamental and Applied Sciences*, **15**(3), 421- 425.
- Al-Ani, T. & Sarapaa, O. (2008). Clay and clay mineralogy: physical – chemical properties and industrial uses. *Geological Survey of Finland*. 1 – 94.
- Asmaa K. B., Helmy E. H., Ahmed A. M., Ahmed M. A., Manar H. M. (2020). Synthesis and characterization of zeolite-Y from natural clay of Wadi Hagul. *Egyptian Journal of Chemistry*. 290. <http://ejchem.journals.ekb.eg/>.
- Bai, Y., Wu, W., Bian, X. (2018). Dynamic synthesis route of zeolite Y with kaolin to improve yield. *Green Processing and Synthesis*, **7**(1), 23-29Å
- Cadene, A., Durand-Vidal, S., Turq, P.& Brendle, J. (2005). Study of individual Na-motmorillonite particle size, morphology and apparent charge. *Journal of Colloid and Interface Science*. 285, 719-730
- Djomgoue, P. & Njopwouo, D. (2013). FT-IR Spectroscopy applied for surface clays characterization. *Journal of Surface Engineered Materials and Advanced Technology*, **3**, 275-282. doi:10.4236/jsemat.2013.34037
- Feng, P. Y., Bu, X. H., & Stucky, G. D. (1997). Hydrothermal syntheses and structural characterization of zeolite analogue compounds based on cobalt phosphate. *Nature*, **388**, 735-741
- Frost, R., L. (1995). Fourier Transform Infrad Spectroscopy of kaolinite, dickite and halloysite. *Clays and Clay Minerals*. **43**(2), 191-195.
- Holtz, R. D. & Kovacs, W. D. (2010). An introduction to geotechnical engineering. New York. Prentice-Hall Civil Engineering and Engineering Mechanics Series.
- Kovo, A.S., Holmes, S. M. (2010). Effect of aging on the synthesis of kaolin-based zeolite Y from Ahoko Nigeria using a novel metakaolinization technique. *Journal of dispersion science and technology*, **31**(4), 442-448.
- Nasuradeen Salahudeen. (2018). Metakaolinization effect on the thermal and physiochemical properties of kankara kaolin. *KMUTNB Int J Appl Sci Technol*, vol. 11, no. 2, pp. 127-135-
- Nwosu, D. C., Ejikeme, P.C.N., & Ejikeme, E. M. (2013). Physic-chemical characterization of “NGWO”white clay for industrial use. *International Journal of Multidisciplinary Sciences and Engineering*, **4**(3) 11-14. Retrieved on line 13 October 2017 from [www.ijmse.org](http://www.ijmse.org)
- Olaremu, A.G., Odebunmi, E.O., Nwosu, F.O., Adeola, A.O. and Abayomi, T.G. (2018). Synthesis of zeolite from kaolin clay from Erusu Akoko southwestern. *Journal of Chemical Society of Nigeria*, **43**(3), 381-786.
- Patel, H. A. (2014). *Nanoclays: synthesis, characterisation and applications*. New Delhi: Astral International Pvt. Ltd.
- Uddin, F. (2008). Nanoclays and montmorillonite minerals. *Metallurgical and Materials Transaction A*. **39A**.2804-2814.
- Xu, R., Pang, W., Yu, J., Huo, Q. and Chen, J. (2009). *Chemistry of zeolites and related porous materials: synthesis and structure*. John Wiley & Sons





## Investigation of Geochemical Properties of Laterites in Selected Areas in Jos-North

Yohanna A. ALIYUDA<sup>1</sup>, Lucas A. J. HAMIDU<sup>1\*</sup>, Friday I. APEH<sup>1</sup>, Pyendang S. ZACHARIAH<sup>1</sup>, Yakubu ISHENI<sup>1</sup>, FelixACHEMA<sup>1</sup>

<sup>1</sup>Nigerian Building and Road Research Institute, 10 NBRI Way/I.T. Igbani Street, off Awolowo Way, Jabi, Abuja  
Nigeria

<sup>1</sup>[kiddogimba@gmail.com](mailto:kiddogimba@gmail.com), <sup>\*1</sup>[lucadohamidu@yahoo.com](mailto:lucadohamidu@yahoo.com), <sup>1</sup>[fiapah2@yahoo.com](mailto:fiapah2@yahoo.com), <sup>1</sup>[pyendangzach@gmail.com](mailto:pyendangzach@gmail.com),  
<sup>1</sup>[isheniwonders@gmail.com](mailto:isheniwonders@gmail.com), <sup>1</sup>[achemafelix@gmail.com](mailto:achemafelix@gmail.com)

\*Corresponding author

### ABSTRACT

This research investigated the geochemical properties of laterite soils in selected three (3) locations of Jos North Local Government Area, Plateau State (Zaria Road, Bauchi Road and Tudun Wada) using the global positioning system (GPS) device for the geographical coordinates locations (altitudes, latitudes and longitudes). The laterites soils were processed for the determination of moisture content, loss on ignition, organic carbon contents, oxides and elemental compositions. The results revealed that Zaria Road, Bauchi Road and Tudun Wada moisture contents were 0.82%, 0.33% and 0.23%, loss on ignition 0.06912%, 0.0456% and 0.004436%, and organic carbon contents were 0.002138%, 0.001963% and 0.007615% respectively. The XRF results for the oxide compositions ranges are SiO<sub>2</sub> (63.51 – 69.47%), MnO (0.09 – 0.34%), Fe<sub>2</sub>O<sub>3</sub> (5.38 – 10.77%), SO<sub>3</sub> (0.09 – 0.258%), CaO (0.82 – 1.67%), K<sub>2</sub>O (1.21 – 2.55%), Al<sub>2</sub>O<sub>3</sub> (15.90 – 17.66%), TiO<sub>2</sub> (1.71 – 2.55%), Cl (1.11 – 1.67%) and ZrO<sub>2</sub> (0.089 – 0.194) respectively. The absence of organic carbon matter and loss on ignition in the laterites revealed that the laterites are non-emitting and have a high potential for the formulation and optimization of the interlocking compressed stabilized earth block (ICSEB) production to complement the use of conventional Portland cement in infrastructural development.

**Keywords:** Geochemical properties, investigation, sub-grade soil, materials, infrastructure.

### 1. INTRODUCTION

Availability of natural resources is a nature's gift that contributes immensely to socio-economic development from both renewable and non-renewable materials (Jack, Nkwocha and Odubo 2016). Nigeria with over 200 million population is facing challenges of housing and poor road network infrastructure for easy access to human needs as a cardinal point in sustaining the achievement of the millennium development goals (MDGs) (Hamidu *et al.*, 2022). Different types of materials are used in the construction sector, which includes but is not limited to the following, sub-grade soil, granite, gravel, etc. A sub-grade soil is among the major natural resource that has been used in the building, and construction of earth dams and roads (Ojo *et al.*, 2012). It is formed from the weathered tropical soil, rich in a secondary oxide combination of iron, aluminum and manganese which is further categorized into laterite, lateritic and non-lateritic soils (Manasseh and Joseph, 2014).

According to Saing *et al.* (2016), laterite has wide varieties of red, brown to yellow, fine grain-sized residual granular structures with the composition of silica (SiO<sub>2</sub>) to oxide ratio of (Fe<sub>2</sub>O<sub>3</sub> + Al<sub>2</sub>O<sub>3</sub>) 1.33 and 2.0. Any value above this ratio is not considered as laterite and is categorized as low bearing capacity and low strength due to the high content of clay, which stability cannot be ascertained under load in the presence of moisture (Fitsum 2018). Based on the degree of lateralization, a critical consideration is given to swelling and shrinkage properties along with cracking patterns, laterite type and quantities of organic matter contained in molding.

It was revealed that attention was more on the geotechnical properties of sub-grade soil that forms the laterite rather than geochemical properties by several authors which include; (Netterberg 2014), Asa-Dam area Ilorin Southwestern Nigeria (Omotoso *et al.*, 2011). Study on the effect of different parent materials on the mineral characteristics by (Irmak *et al.*, 2007), stabilization with yam peel ash by (Ramonu *et al.*, 2018), geotechnical and environmental evaluation by (Ojuri *et al.*, 2017), use of shredded polyethylene by (Ojuri *et al.*, 2016), engineering properties of lateritic soils of Ado-Ekiti by (Oke and Olowoyo 2019), regression analysis of soil within Oshogbo by (Bello *et al.* 2015) and geochemistry characterization on the parameters for marine clay by (Samaila *et al.*, 2019) were carried out.

Other authors placed laterite as a clay-based geo-polymer which has the potential as an adsorbent for the removal of heavy metals (Ghani *et al.*, 2020), as a raw material for the production of compressed stabilized earth block (CSEB) (Olayemi and Van Rooy, 2016), as an admixture in the soil stabilization (Makusa, 2012), for the Road Packer Plus using Malaysian soil (Lilian, 2014), soil stabilization technique (Habiba, 2017), assessment and comparative study on the stabilizing effect of three materials, cement, sodium chloride and brick dust on clay soil (Obianigwe and Ngene, 2018), additive in the stabilization with eggshell powder, sodium silicate to construct light traffic pavement (Oke and Olowoyo, 2019) among others.

In a related development, the interlocking compressed stabilized earth block (ICSEB) produced by the Nigerian Building and Road Research Institute (NBRI) has shown in some cases walling cracks and water absorption. These observed defects could be attributed to several factors, such as component formulation, inadequate knowledge of the chemical composition of the material, and improper curing among others. Chemical compositions of laterite and lateritic soil from the original parent material were reported in separate publications by (Hamidu *et al.* 2022; Ghani *et al.*, 2020) gave an ideal chemical composition of the aforementioned materials.

This research aims to investigate the geochemical properties of laterite soils in three selected locations of Jos North Local Government Area, Plateau State (Bauchi Road, Tudun Wada and Zaria Road) for future optimization, for the production of interlocking compressed stabilized earth blocks which will not have the problems of cracks and water absorption on the wall's surface.

## 2.0 MATERIALS AND METHODS

### 2.1 Materials

The materials used in this work are laterite soil samples obtained at the following study areas: Zaria Road along Federal Government College Jos, Bauchi Road at Angwan Maigogge and Tudun Wada. The global positioning system (GPS) GRAMIN eTrex 20x model was used for the geographical coordinate locations i.e., altitude, latitude and longitude. The equipment used is a mini digger for excavation of the laterite soil, a shovel, stainless steel hand trowel, and metal mesh with a sieve 2.0 mm aperture size B.S/ISO.3310 model for sieving of the soil sample, digital weighing balance KL16001/11-D0630/16 model with precision accuracy of 0.0001 for weighing, porcelain crucibles and laboratory can for weighing. The Oven 10-D1390/10 model with a temperature range of 0 – 300 °C was used for the determination of moisture content, laboratory Gallenkamp Muffle Furnace Made in England with maximum temperature up to 1000°C was used for the loss on ignition and organic carbon content determinations. The laterite soil was powdered to a fine state using a laboratory pestle and mortar and sieved with 63 µm mesh size for the XRF characterisations using XRS-FP for oxides and elemental composition analyses.

### 2.2 Methods

#### 2.2.1 Geographical Location of Laterite Soil Samples for Study Areas

Table 1, presents the geographical locations at which the laterite soils were collected in the study areas A, B and C of Jos North Local Government Area of Plateau State at their respective coordinates (Latitude (N), Longitude (E) and Altitude (m)).

Table 1: Geographical Locations of A, B and C laterite Soils

Name of State	Site of Collection	Latitude (N)	Longitude (E)	Altitude (m)
Jos North Local Government	A	N 10° 01.025'	E 008° 55.682'	944
	B	N 09° 57.803'	E 008° 50.745'	1159
	C	N 09° 54.077'	E 008° 52.834'	1259

Where; A is Zaria Road, B is Bauchi Road and C is Tudun Wada

The laterite soils were obtained at a depth of 1000 mm according to Ogundele *et al.* (2015) from the study areas to ascertain their geochemical and physical properties. The soil samples were ground into fine particle sizes to reduce the lumps and processed according to Addis and Abewaw (2017) by oven drying at 80 °C for 24 h. Thereafter, the dried laterite soils were sieved using a 2.0 mm aperture mesh size for determination of moisture contents, loss on ignitions and organic carbon contents based on the ASTM D2974 test methods as shown in Figure 1 (Rasti, Pineda and Razavi 2020).

The moisture content was determined by weighing five grams (5 g) of laterite soil in an empty porcelain crucible, heated in the oven at the temperature of 105 °C for 24 h, thereafter the crucible containing the laterite soil was removed from the oven and placed in a desiccator to cool and reweighed gravimetrically by a direct method according to Pattnayak *et al.* (2019) and calculated in percentage as.

$$M.C = \left( \frac{W_1 - W_{105}}{W_1} \right) 100 \quad (1),$$

where; M. C is the moisture content expressed in percentage (%),  $W_1$  is the initial weight of laterite soil and  $W_{105}$  is the dry weight of laterite soil at 105 °C both measured in gram (g).



Figure 1: Processed A, B and C Laterite Soils for Characterisations

The loss on ignition (LOI) was carried out by weighing five grams (5 g) of the laterite soil in an empty porcelain crucible, heated at a steady temperature of 550 °C for 1 hour in the Muffle furnace, thereafter; the porcelain crucible containing the laterite soil was removed, cooled in the desiccators and reweighed. The LOI was determined using Equation 2 (Heiri, Lotter and Lemcke, 2001).

$$LOI_{550} = \left( \frac{W_{105} - W_{550}}{W_{105}} \right) 100 \quad (2)$$

Where;  $LOI_{550}$  is the loss on ignition at 550 °C expressed as a percentage,  $W_{105}$  is the initial weight before heating at 105 °C and  $W_{550}$  is the dry weight of the laterite after heating to 550 °C (both measurements are in gram). The organic carbonate content (OGC) was carried out by weighing five grams (5 g) of the laterite soil in a porcelain crucible, and heated for 1 hour in the Muffle furnace at the temperature of 950 °C, thereafter, the laterite soil was removed cooled in the desiccators and reweighed. The OGC was calculated in percentage using Equation (3) (Heiri, Lotter and Lemcke 2001).

$$OGC_{950} = \left( \frac{W_{550} - W_{950}}{W_{105}} \right) 100 \quad (3)$$

Where;  $OGC_{950}$  is the organic carbon content expressed in percentage,  $W_{950}$  is the dry wet of the laterite after heating at 950 °C. A minimum of three replicates determinations were carried out for each laterite soil.

Finely powdered laterite soil was sieved through 63 µm mesh for the oxides and elemental compositions using XRF conditioned to run at a lifetime of 60 seconds on automatic control mode using the standard detector in atmospheric air. At the end of the dead time counts, the results were exported to the periodic table software for the selection of the elements to be analyzed using the software application window.

### 3. RESULTS AND DISCUSSION

The results of the investigated physical properties of the laterite study areas are presented in Table 2.

Table 2: Percentage Moisture Content, Loss on Ignition and Organic Carbon of A, B and C

Samples	%M. C	%L. O. I	%O. G. C
A	0.82	0.06912	0.002138
B	0.33	0.0456	0.001963
C	0.23	0.004436	0.007615

#### 3.1 Moisture Content of A, B and C Laterites

Before the determination of the moisture contents, the laterites were ground using a pestle and mortar to reduce the lump size, oven dried and sieve with a mesh of 2 mm aperture. The initial weight of 5 g of each of the three (3) samples was weighed, followed by heating at a steady temperature of 105 °C for 24 h. Thereafter, the sample was removed from the oven and cooled in the desiccators. The final weight after 24 h of heating was weighed and determined using Equation 1. The results revealed that the moisture contents range from 0.23 to 0.83%. The highest M.C (0.83%) for Zaria Road and Tudun Wada (C) being the least with (0.23%) is lower than the M. C for similar studies in Iyuku (1.21 – 1.77%) according to Irabor and Okolo 2010 and that of Netterberg 2014 which is (5 – 20%). This has shown that the laterite soils possess low moisture content signifying that it is a non-problematic soil that will not expand when used as an engineering material in compressed stabilized earth blocks. In a situation where laterites show high moisture content, it is inferred that the soil contains much clay which could lead to water absorption resulting to swell and cracks on the wall's surface, or even on the road network that is not usually stabilized. In a separate publication by Pattnayak (*et al.* 2019), laterite soil with a high capacity of moisture and organic carbon contents will not make a better material for the production of compressed stabilized earth blocks since it affects the strength of the soil, it was also supported by Fitsum (2018) which recommended low moisture content as criteria that make good quality of laterite.

### 3.2 Loss on Ignition of A, B and C Laterites

The percentage loss on ignition (LOI) for A, B and C laterites, which is a measure of the presence of organic matters in the soil sediments and combustibility or loss of volatile salts, structural water, or inorganic carbon in the soil were in the ranges of 0.0044 to 0.0691%. The results revealed that the highest (0.06912%) and the lowest (0.004436%) are lower than the similar studies by Irabore and Okolo (2010) (4.08 – 8.35%) and Ghani *et al.* (2020) (0.64%). This implies that, at 550°C combustion, the soil property remains high with low emissive properties. This has demonstrated that the potentials of laterites are high for use as a green-free emission engineering material.

### 3.3 Organic Carbon Content of A, B and C Laterites

The degree of lateralization which is based on the organic carbon content matter responsible for swelling and shrinkage properties along with cracking was investigated. The laterites which were subjected to heating between 550 °C – 950°C for percentage organic carbon content revealed that the OGC was in the ranges of 0.001963 – 0.007615%. Tudun Wada which has the highest OGC (0.00762%) is lower than the similar studies by Pattnayak (*et al.* 2019) (1.1 – 1.3%). The presence of organic carbon content matter in the soil which is a major factor in soil quality and responsible for low bearing strength is virtually less than 0.01% showing that the laterites have a greater potential for the production of high-grade stabilized block and road construction material.

### 3.4 X-Ray Fluorescence of A, B and C Laterites

The results of oxides and chemical compositions of the sub-grade laterites presented in Tables 3 and 4 were detected at 30 kV, 20µA after 20 seconds of dead time based on an automatic detection module.

Table 3: Oxides Composition of Characterized Laterites A, B and C XRF

Oxides Composition	Concentration (mg/cm <sup>3</sup> )			Mole (%)		
	A	B	C	A	B	C
SiO <sub>2</sub>	50.587	48.169	56.482	65.947	63.651	69.465
MnO	0.089	0.303	0.088	0.098	0.339	0.092
Fe <sub>2</sub> O <sub>3</sub>	20.685	21.613	11.639	10.144	10.747	5.382
SO <sub>3</sub>	0.092	0.145	0.279	0.09	0.144	0.258
CaO	0.572	0.834	1.27	0.824	1.18	1.674
K <sub>2</sub> O	1.455	4.644	4.467	1.21	3.914	3.504
Al <sub>2</sub> O <sub>3</sub>	22.983	20.415	22.57	17.656	15.897	16.358
TiO <sub>2</sub>	1.983	2.564	1.849	1.945	2.549	1.711
Cl	0.754	0.495	0.538	1.665	1.109	1.122
ZrO <sub>2</sub>	0.27	0.139	0.324	0.172	0.089	0.194
Total				100	100	100

The results of the XRF studies of the A, B and C laterites in the three selected study areas of Jos North Local Government, Plateau State as presented in Table 3 are as follows: silicon oxide (SiO<sub>2</sub>) (63.65 – 69.47%), iron oxide (Fe<sub>2</sub>O<sub>3</sub>) (5.38 – 10.75%), aluminum oxides (Al<sub>2</sub>O<sub>3</sub>) (15.90 – 17.66%), potassium oxide (K<sub>2</sub>O) (1.21 – 3.91%), calcium oxide (CaO) (0.82 – 1.67%), Titanium Oxide (TiO<sub>2</sub>) (1.71 – 2.55%), Chlorine (Cl) (1.11 – 1.67%). The oxides of manganese, sulphides and zirconium are in traces. The investigation revealed that the composition of the major oxide which forms the geochemical properties of the laterites in the study areas is silicon which shows the presence of quartz, iron and aluminum being minerals present and Anatase detected. The presence of zirconium is of concern in the laterite since it is considered harmful being a radioactive material at a high level, but it is extremely resistant to heat and corrosion. The result shows that carbonaceous materials which can aid emission when combusted were not found, this also supports the low-level % LOI and %OGC which largely represent the volatile matters when the laterites were tested at 550 °C and 950 °C. The occurrence of soil sediments is based on the parent origin of the rock material or the weathering environment which varies from different locations. However; the investigated areas at Zaria Road, Bauchi Road and Tudun Wada both in Jos North Local Government Area, Plateau State which has shown low moisture and organic carbon contents in the laterites indicate a high potential material for building and road construction. Table 4 presented the elemental compositions of the characterized laterites from the three study areas A, B and C.

Table 4: Elemental Composition of Characterized Laterites A, B and C XRF

Element	Intensity (c/s)			Concentration (mg/cm <sup>2</sup> )		
	A	B	C	A	B	C
O	0	0	0	45.482	44.186	46.458
Al	38.128	36.517	55.719	12.164	10.805	11.946
Si	339.065	359.413	550.723	23.647	22.517	26.402
S	2.548	4.52	10.499	0.037	0.058	0.112
Cl	69.737	5.778	67.622	0.754	0.495	0.538
K	175.344	624.136	718.065	1.208	3.855	3.708
Ca	92.346	135.077	247.12	0.422	0.596	0.908
Ti	584.187	773.246	668.22	1.189	1.537	1.109
Mn	64.299	222.549	84.056	0.069	0.235	0.068
Fe	15353.63	16269.58	11794.73	14.468	15.116	8.141
Zr	194.884	102.297	393.249	0.2	0.103	0.24
Total				100	100	100

The XRF revealed that carbons were not found in all three sites of laterites investigated after exposure at different intensities in counts per second (c/s), the resulting composition shows various degrees of aluminum, iron, silicon and others in traces (Table 4) with more percentage of oxygen which could be beneficial to human. The geochemical properties of the laterites of the three study areas revealed that heavy metals were not detected, and thus, low loss on ignition and organic carbon content were obtained.

## CONCLUSION

This research investigated the geochemical properties of laterites in some selected areas of Jos North Local Government Area, Plateau State, Nigeria. The results revealed that the geochemical properties of the laterites varied from one location to the other. Zaria Road (A) in Jos had the highest moisture content of 0.82%, Loss on ignition of 0.06912% and Organic carbon content of 0.00214% but is within the standard range and non-problematic soils.

XRF revealed that the compositions of the oxide show Tudun Wada (C) has the highest silicon oxide (69.47%), Bauchi Road (B) had the highest iron oxide (10.75%) and Zaria Road (A) had aluminum oxide (13.66%). Furthermore; the elemental compositions revealed that more aluminum in Zaria Road (A) (12.16%), silicon in Tudun Wada (C) (26.402%) and iron in Bauchi Road (B) (15.12%) respectively. These show that the geochemical properties of the investigated laterites can be used for the production of interlocking compressed stabilized earth blocks (ICSEB) as sustainable building materials based on their locations.

## ACKNOWLEDGEMENT

The authors are grateful to the Director General/Chief Executive Officer and management of the Nigerian Building and Road Research Institute for using the Laboratory facilities at Jos Zonal Office, the Zaria Road community along Federal Government College Jos, Angwan Maigogge Community along Bauchi Road, Jos and Tudun Wada community for allowing the research team to access the samples.

## REFERENCES

- Addis, W. and Abebaw, A. (2017). Determination of Heavy Metal Concentration in Soils Used for Cultivation of *Allium sativum* L. (garlic) in East Gojjam Zone, Amhara Region, Ethiopia Cogent Chemistry, 3:1, 1419422; <https://doi.org/10.1080/23312009.2017.1419422>.
- Bello, A., Ige, J. and Ayodele, H. (2015). Stabilization of Laterite Soil with Cassava Peels Ash. *British Journal of Applied Science and Technology*, 7(6), pp. 642 -650. <https://doi.org/10.9734/bjast/2015/16120/>.
- Fitsum, M, D. (2018). Recent Literatures Review on Stabilization of Lateritic Soil. *International Journal of Scientific Research Engineering & Technology*, 7(11), November 2018.
- Ghani, U., Hussain, S., Noor-ul-Amin, Imtiaz, M. and Ali Khan, S. (2020). Laterite Clay-Based Geopolymer as a Potential Adsorbent for the Heavy Metals Removal from Aqueous Solutions. *Journal of Saudi Chemical Society*, 2020(24), pp. 874–884.
- Habiba, A. (2017). A Review on Different Types Soil Stabilization Techniques. *International Journal of Transportation Engineering and Technology*, 3(2), pp. 19-24. Doi: 10.11648/j.ijtet.20170302.12.

- Hamidu, L, A, J., Adamu, A, Y. and Ishan, Y. (2022).The Imperativeness of Laterite in Building and Road Construction Sectors for Sustainable Infrastructure in Nigeria: A Review of Laterite for Socio-Economic Development. *Path of Science*, 8(4), pp. 5001 – 5008. Doi:10.22178/pos.80-5.
- Heiri, O., Lotter, A, F. and Lemcke, G. (2001). Loss on Ignition as a Method for Estimating Organic and Carbonate Content in Sediments: Reproducibility and Comparability of Results. *Journal of Paleolimnology*, 25, pp.101–110, 2001.
- Irmak, S., Surucu, A, K. and Aydogdu, I, H. (2007).Effects of Different Parent Material on the Mineral Characteristics of Soils in the Arid Region of Turkey. *Pakistan Journal of Biological Sciences*, 10(4), pp. 528-536.
- Jack, J, T, C., B, Nkwocha, I, B. and Odubo, T, R. (2016). Natural Resource Exploitation and Socio-Economic Development in Nigeria. (1981-2015).
- Lilian, G. (2014). Lateritic Soil Stabilization by Using Road Packer Plus. Master's degree in Civil Engineering 2014.
- Makusa, G, P. (2012). State of the Art Review: Soil Stabilization Methods and Materials in Engineering Practice.
- Manasseh, J. and Joseph, E. (2014). Stabilization of Ikpayongo Laterite with Cement and Calcium Carbide Waste. *Global Journal of Pure and Applied Sciences*,20(2014), pp. 49-55. DOI: <http://dx.doi.org/10.4314/gjpas.v20i1.8>.
- Netterberg, F. (1994). Low-cost Local Road Materials in Southern Africa. *Geotechnical and Geological Engineering*, 12(1), pp. 35–42. <https://doi.org/10.1007/BF00425935>.
- Obianigwe, N. and Ngene, B, U. (2018). Soil Stabilization for Road Construction: Comparative Analysis of a Three-Prong Approach. *IOP Conf. Ser.: Mater. Sci. Eng.* 413 012023.
- Ogundele, D, T., Adio, A, A. and Oludele, O, E. (2015). Heavy Metal Concentrations in Plants and Soil along Heavy Traffic Roads in North Central Nigeria. *Journal of Environmental Analysis Toxicology*, 5(6), pp. 1 – 5. Doi: 4172/2161-0525.1000334.
- Olayemi, C, A. and Van Rooy, J, L. (2016). A Review of the Use of Lateritic Soils in the Construction/Development of Sustainable Housing in Africa: A Geological Perspective. Department of Geology, University of Pretoria.
- Ojo, O, J., Oladele, O. and Emmanuel, T, A. (2012). Engineering Properties of Lateritic Soils around Dall Quarry in Sango Area, Ilorin, Nigeria. DOI:10.5539/esr.v1n2p71.
- Ojuri, O, O., Adavi, A, A. and Oluwatuyi, O, E. (2017). Geotechnical and Environmental Evaluation of Lime–Cement Stabilized Soil–Mine Tailing Mixtures for Highway Construction. *Transportation Geotechnics*, 10, pp. 1–12. <https://doi.org/10.1016/j.trgeo.2016.10.001>.
- Ojuri, O, O. (2016). Improvement of Strength Characteristics of Lateritic Sub-Grade Soil with Shredded Polyethylene Waste. *Journal of Applied Science Environmental Management*, Sept. 2016, 20(3), pp. 660-666.
- Oke, J, A. and Olowoyo, M, K. (2019). Stabilization of Laterite Soil with Eggshell Powder and Sodium Silicate Used as Fill Material in Road Construction. *Arid Zone Journal of Engineering, Technology & Environment*, 15(3), pp. 586-597. Published by the Faculty of Engineering, University of Maiduguri, Nigeria.
- Omotoso, O, A., Mamodu, M, O. and Ojo, O, J. (2011). Evaluation of Geotechnical Properties of Laterite Soils in Asa-Dam Area, Ilorin, Southwestern Nigeria. *World Journal of Applied Science and Technology*, 3(2), pp. 1 – 9.
- Pattnayak, M., Kumar, S, C., Sahu, N, K., Dhal and Behera, R, K. (2019). Comparison of Soil Characteristics and Carbon Content of Contrastingly Different Moist-Mixed Deciduous and Evergreen Mangrove Forest in Odisha. *India, Geology, Ecology, and Landscapes*,3(4), pp. 239-246, DOI: 10.1080/24749508.2018.1545104.
- Ramonu, J, A, L., Ilevbaoje, J, O., Ayandalfedapo, S., Modupe, A, E., Adeniyi, O, M. and Adewole, T, A. (2018). Geotechnical Properties of Lateritic Soil Stabilized with Yam Peel Ash for Subgrade Construction. *International Journal of Civil Engineering and Technology (IJCIET)* 2018, pp.1666–1681, ISSN Online: 0976-6316.
- Rasti A., Pineda, M. and Razavi, M. (2020). Assessment of Soil Moisture Content Measurement Methods: Conventional Laboratory Oven versus Halogen Moisture Analyzer. *Journal of Soil Water Science* 4(1), pp. 151-160. DOI: [10.36959/624/440](https://doi.org/10.36959/624/440)
- Saing, Z., Samang, L., Harianto, T. and Patanduk, J. (2016). Strength Characteristic of Ferro Laterite Soil with Lime Stabilization as Subgrade Material. 10<sup>th</sup>International Symposium on Lowland Technology, September, pp. 15 – 17, 2016, at Mangalore, India.
- Samaila, S., Mohd, N, A, A., Nor, Z, M, Y., Kamarudin, A., Nazri, A., Dayang, Z, A, H. and Rini, A, A. (2019). Geochemistry characterization of marine clay. IOP Conf. Series: Materials Science and Engineering527 (2019) 012023, IOP Publishing doi:10.1088/1757-899X/527/1/012023.



## Production Optimization of a Nigerian Oil Well

Ajiboye OSUNLEKE<sup>1\*</sup>, Ayorinde BAMIMORE<sup>1</sup>, Francis CHUKWUNTA<sup>1</sup>, Nafees SANNI<sup>1</sup>, Ibrahim Abiola BADMUS<sup>2</sup>

<sup>1</sup>Department of Chemical Engineering, Obafemi Awolowo University, Ile-Ife, Nigeria

<sup>2</sup>Department of Process and Operations, Dangote Petroleum Refinery and Petrochemicals FZE, Lagos

<sup>1\*</sup>[aosunlek@oauife.edu.ng](mailto:aosunlek@oauife.edu.ng), <sup>2</sup>[abamimore@oauife.edu.ng](mailto:abamimore@oauife.edu.ng), <sup>3</sup>[cu9francis@gmail.com](mailto:cu9francis@gmail.com), <sup>4</sup>[nafeesolaitan@gmail.com](mailto:nafeesolaitan@gmail.com),  
<sup>5</sup>[ibrahimabiolabadmus@yahoo.com](mailto:ibrahimabiolabadmus@yahoo.com)

\*Corresponding author: [aosunlek@oauife.edu.ng](mailto:aosunlek@oauife.edu.ng)

---

### ABSTRACT

*Obtaining the most out of a hydrocarbon reservoir is not commonplace as it takes a lot of informed decisions to make. Over the last decade, there has been a constant growing demand for oil and gas, and a reduced discovery of large oil reservoir. Hence, a need to efficiently exploit existing ones. One possible way of improving production rate is through a wide array of techniques collectively termed Production Optimization. Production Optimization technique employed here was used to control undesired fluid production, increase the potential for greater oil recovery and predicting field performance, hence, enhance reservoir profitability. In this work, an optimal control to reservoir management, and in particular to reservoir production is applied. An open-source reservoir simulator (MATLAB Reservoir Simulator Toolbox, MRST) was used to simulate and run production optimization for a real reservoir model considering different well placements. Three different well placement scenarios were used with each scenario having multiple producer wells and either single or multiple injector wells. The performance criterion used for this work is water cut. For all scenarios considered, the well performance and simulation schedule over a 10-year period (total simulation time) was analysed. The profitability of each producer well in all the scenarios was found to depend on both its well placement and that of the injector wells. The volume and number of injector wells was also found to affect the volume of oil produced, and the profitability length. Scenario 1 with an injector well produced less oil but of greater profitability length in the simulated time. Scenarios 2 and 3 with three injector wells each had less profitability length but produced more oil than scenario 1 in 10 years.*

**Keywords:** Reservoir management; production optimization; Reservoir Simulation; well placement.

### 1. INTRODUCTION

Energy is playing a pivotal role in the prosperity of mankind and will in all probability continue to do so into the distant future. Worldwide economic growth is expected to be about 3% per year through 2030, a pace similar to the last 20 years and it is estimated that the energy demand will increase by 50% by the year 2030 (ExxonMobil Corporation, 2004). This undiminished growth in energy demand due to population growth, and increasing personal income, notably in developing countries, will accelerate the global demand for energy. The sustainability of our modern society depends crucially on a secure and accessible supply of energy, thus, the importance of energy to our modern world cannot be overemphasized.

Interestingly, oil and gas has been the predominant source satisfying almost 60% of the current energy demand worldwide. This percentage is expected to stay relatively stable in the future, at least to 2030, (ExxonMobil Corporation, 2004). Also, oil and gas have the advantages of being relatively more available, better performance, cheaper, and more convenient than the other sources listed in Figure 1. Hence, the need to maximally utilize this source of energy.

Unfortunately, most of the existing major oilfields are already at a mature stage, and the number of new significant discoveries per year is decreasing (Brouwer, 2004) and since oil is non-renewable, it will become increasingly harder to meet this ever-increasing demand for oil and gas. Although, smaller fields are still regularly found, but at the current oil price, it is often not economical to exploit them. As a direct result it becomes more and more difficult to maintain economic reserves at a desirable level. In order to satisfy the growing worldwide demand for oil and gas, it is becoming increasingly important to produce existing fields and new fields as efficiently as possible, while simultaneously decreasing development and operating costs (Najafiazar, 2014).

The current industry average for the recovery factor from an oil well is a meagre 35%, which is for reservoirs with favourable production conditions (Rossi, 2002). One possible way of improving production rate is through a wide array of techniques collectively termed “Production Optimization”.

The production optimization process is based on a sequence of activities that transform measured or collected data into optimal field management decisions. It is achieved by comparing measured data with predicted performance and executing a sequence of activities as iterative loops to ensure that the reservoir delivers to its maximum potential. Production optimization includes controlling wells in order to maximize (or minimize) some performance criteria. The ability to control wells provides the ability to control fluid flow behaviour within the reservoir, thereby enabling maximization or minimization of any criteria by which production performance can be measured.

This work seeks to determine the optimal reservoir production rate by optimising the net present value (NPV) of the reservoir. To achieve this, a water flooding method is used to control undesired fluid production and increase the potential for greater oil recovery thus enhance reservoir management and profitability. This is done by observing the profitability of different production wells at different locations in a field using water cut as the performance criterion.

## 2. RESERVOIR MODEL

The physical system to be modelled must be expressed in terms of appropriate mathematical equations. This process almost always involves assumptions. The assumptions are necessary from a practical standpoint in order to make the problem tractable (Najafiazar, 2014). In this work, the following simplifying assumptions are made in modelling the reservoir;

- i. the flow of oil and water only through a heterogeneous porous medium is considered
- ii. the reservoir is horizontal and of constant thickness
- iii. the gravity and capillary forces are negligible.
- iv. the reservoir is in its secondary recovery phase
- v. the pressures are above the bubble point pressure of the oil phase.
- vi. the fluids and rocks are incompressible, with no-flow boundaries, and are at isothermal conditions

Hence, there are two-phase immiscible flow (that is, no mass transfer between the two liquid phases).

The focus here is on water – flooding cases for a two-phase (oil and water) reservoir. To implement the reservoir model, MATLAB Reservoir Simulation Toolbox (MRST) was used.

MRST is developed by *SINTEF Applied Mathematics* and is a result of their research on the development of new (multiscale) computational methodologies. Version 2015a which was used in this study, is available online for free download under the terms of the GNU General Public License (GPL) (Lie *et al.*, 2012). The toolbox consists of two main parts: a core offering basic functionality and single and two-phase solvers, and a set of add-on modules offering more advanced models, viewers and solvers.

### 2.1 Reservoir Optimization

Reservoir production optimization is a complete or partial automation process for maximizing the development effect within the lifecycle of a reservoir by optimizing operational parameters (Hou *et al.*, 2015). Production optimization aims at achieving the best development performance for a given reservoir by optimizing well controls. In order to evaluate the performance of different development programs, various objectives have been proposed during the long research into production optimization. For example, Rosenwald & Green (1974) minimized the difference between the production-demand curve and the flow curve actually attained, Babayev (1975) provided minimum total cost per unit output; while Ladson *et al.* (1986)

- i. maximized the deliverability of a gas reservoir at a specified time,
- ii. minimized the total gas withdrawal shortfall between the demand schedule and the amount of gas that can actually be delivered in each month, and
- iii. optimized the weighted combinations of the above two objectives.

When optimizing production strategies, one often encounters multiple local maxima. This phenomenon may be a good thing sometimes because it means that there are extra degrees of freedom in the optimization problem, which can be used to accomplish other optimization objectives. For instance, Van Essen *et al.* (2011) incorporated short-term goals into the life-cycle optimization problem and proposed a hierarchical production optimization structure with multiple objectives. Chen *et al.* (2012) also optimized both long-term and short-term net present value. As more and more oilfields enter the high water cut period, the production costs increase gradually. Therefore, the net present value is commonly selected as the objective function for production optimization.



According to Hou *et al.*, (2015), in order to find out under which operational parameters at current reservoir conditions the oil production might be most efficient and profitable, automatic history matching and reservoir production optimization should be combined together.

### 3. MODEL DEVELOPMENT

To optimize a reservoir, a reservoir model needs to be developed. The system (reservoir) to be modelled must be expressed in terms of appropriate mathematical equations. This process almost always involves assumptions. The assumptions are necessary from a practical standpoint in order to make the problem tractable (Najafiazar, 2014). This follows two approaches: Subsurface flow modelling and then optimization of the process.

#### 3.1 Subsurface Flow Modelling Through Porous Media

The mass balance for a porous medium domain of volume  $V$  with boundary  $\partial\Omega$  of area  $s$ , for the conservation of some quantity  $c$  can be formulated as

$$\frac{\partial}{\partial t} \int c \, dV + \oint F \cdot n \, ds = \int q \, dV \quad (1)$$

The continuity equation is obtained using the Gauss' divergence theorem

$$\frac{\partial c}{\partial t} + \nabla \cdot F = q \quad (2)$$

Expressing Equation (2) in Darcy's law considering a two – phase (oil and water) fluid flow, the following were obtained

$$\frac{\partial(\rho_\alpha \phi S_\alpha)}{\partial t} + \nabla \cdot (\rho_\alpha v_\alpha) = \tilde{q}_\alpha \quad (3a)$$

$$v_\alpha = -\frac{k_{r\alpha}}{\mu_\alpha} K (\nabla p_\alpha - \rho_\alpha g \nabla d) \quad (3b)$$

Where  $K$  is the permeability tensor,  $\mu$  is the fluid viscosity,  $k_r$  is the relative permeability,  $\rho$  is pressure,  $g$  is the acceleration of gravity and  $d$  is the depth. The ratio  $\frac{k_{r\alpha}}{\mu_\alpha}$  is called the phase mobility represented as  $\lambda_\alpha$ . Since, no gravity assumption was employed, Darcy's law becomes

$$v_\alpha = -\lambda_\alpha K \nabla p_\alpha \quad (4)$$

For two – phase flow, there are unknowns ( $p_w, p_o, S_w, S_o$ ), four equations are required to complete the system description and solve Equations (3a) and (3b). The two additional equations are given by a closure equation which states that the sum of all fractional saturations must always be equal to one, and the oil-water capillary pressure equation, which gives a relation between phase pressures as function of water saturation. They are respectively given as:

$$S_w + S_o = 1 \quad (5a)$$

$$p_o - p_w = p_c(S_w) \quad (5b)$$

Equations (1) to (5) can be rearranged in such a way that the two-phase equations are formulated in terms of two state variables:  $p_o$ , the oil pressure, and  $S_w$  the water saturation.

In order to do that, one can apply the chain rule differentiation and the definitions of oil, water and rock compressibility yielding

$$\phi \frac{\partial S}{\partial t} + \nabla \cdot f_w(S) v = q_w \quad (6)$$

Equations (4) and (5) are called the pressure and saturation equations respectively. The pressure and saturation equations are referred to as the state equations. It is impossible to find an analytical solution of the state equations for typical reservoir models. Hence, one approximates the solutions by some numerical method (Aarnes *et al.*, 2007).

MRST applies a spatial discretization scheme based on finite differences using upstream weighting in the convection dominant terms. After discretization in space, each grid block is related to two states of the reservoir, that is oil pressures and water saturations. MRST implements an adjoint model consisting of a multi-scale pressure solver and a saturation solver which works on flow-adapted grids (Lie *et al.*, 2012). Each step of the discretized state equations can be written in a compact form as  $F(x, u)$  as

$$F^n(x^n, x^{n-1}, u^n) \quad (7)$$

Introducing an auxiliary function  $J_\alpha$  as

$$J_\alpha(x, u) = J(x, u) + \alpha^T F(x, u) \quad (8)$$

Where  $J(x, u)$  is the objective function,  $\nabla_u J$  the gradient of  $J$  with respect to  $u$ ,  $\alpha = \alpha(\alpha_v, \alpha_p, \alpha_s, \alpha_\pi)$  is a vector of Lagrange multipliers and the gradient  $\nabla_u J_\alpha$  is given by

$$\nabla_u J_\alpha^T = \frac{\partial J}{\partial u} + \frac{\partial J}{\partial x} \frac{\partial x}{\partial u} + \alpha^T \frac{\partial F}{\partial u} + \alpha^T \frac{\partial F}{\partial x} \frac{\partial x}{\partial u} + F^T \frac{\partial \alpha}{\partial u} \quad (9a)$$

$$\nabla_u J_\alpha^T = \frac{\partial J}{\partial u} + \alpha^T \frac{\partial F}{\partial u} \quad (9b)$$

While  $\alpha$  satisfies the adjoint equation

$$\frac{\partial F^T}{\partial x} \alpha = - \frac{\partial J^T}{\partial x} \quad (10)$$

From Equations (9a), (9b) and (10), the gradient with respect to time step  $n$  is computed from

$$\nabla_{u^n} J_\alpha = \frac{\partial J^T}{\partial u} + \frac{\partial F^{nT}}{\partial u^n} \alpha^n \quad (11)$$

The adjoint equations for time step  $n$  are obtained as Equations (11) and

$$\left[ I - \frac{\partial g(v^n, s^n)}{\partial s^n} \right]^T \alpha_s^n = \alpha_s^{n+1} - \frac{\partial J^{nT}}{\partial s^n} - \left[ \frac{\partial B(s^n) v^{n+1}}{\partial s^n} \right]^T \alpha_v^{n+1} \quad (12)$$

$$\begin{bmatrix} B(s^{n-1}) & C & D \\ C^T & 0 & 0 \\ D^T & 0 & 0 \end{bmatrix} \begin{bmatrix} \alpha_v^n \\ \alpha_p^n \\ \alpha_\pi^n \end{bmatrix} = \begin{bmatrix} -\frac{\partial J^{nT}}{\partial v^n} + \frac{\partial g(v^n, s^n)^T}{\partial v^n} \alpha_s^n \\ 0 \\ 0 \end{bmatrix} \quad (13)$$

Solving the adjoint equations, the gradient of the objective function  $J$  at a time step  $n$  is given by equation 14

$$\nabla_{u^n} J = \frac{\partial J^T}{\partial u^n} - A_D^{nT} \alpha_v^n - A_N^{nT} \alpha_\pi^n \quad (14)$$

The gradient Equation (14) can be used in any gradient-based methods.

### 3.2 Optimization Method

The goal of production optimization problem is finding the right combination of well settings, i.e., the bottom-hole pressure (BHP) and the flow rates, to maximize an economic objective function, namely the net present value (NPV) (Najafiazar, 2014).

For a given configuration of wells as in particular for a flooding scenario involving multiple injectors and producers, the well rates or pressures is used to optimize the flooding process over the life of the reservoir (Jansen, *et al.*, 2008).

MRST uses the *OptimizeObjective* function under its *adjoint* module which uses an aggressive line search based on the given gradient. The algorithm handles box constraints, and linear equality and inequality constraints. It performs on an iterative scheme, applying the constraints to the gradient until convergence is achieved. The algorithm makes use of the *gradient projection method*.

## 4. RESULTS AND DISCUSSION

In this work, water flooding scenarios were assessed for three test cases for the same well using real reservoir data from a field in the Niger Delta region of Nigeria.

### 4.1 The reservoir model

The reservoir model setup consists of a two-phase oil/water model with some compressibility through a heterogeneous porous medium. A reservoir of constant thickness is assumed with gravity and capillary forces neglected. For the different flooding scenarios of multiple injectors and producers, well rates and bottom – hole pressures (BHP) is used to optimize the flooding process over the entire life of the reservoir respectively. The reservoir area is about 12,500 m $\times$ 20,000 m and a thickness of approximately 5 m and modelled as 50 $\times$ 50 $\times$ 5 m. Typical pressure and saturation distribution in the well before simulation are shown in Figures 2 and 3.

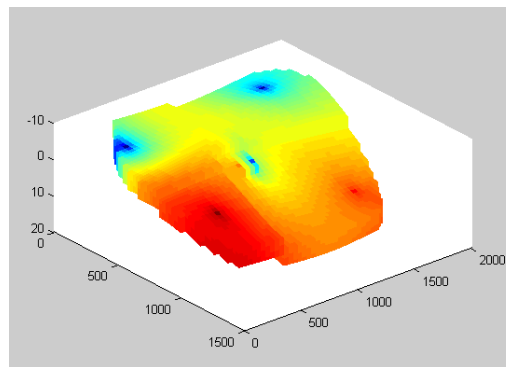


Figure 1: Pressure distribution in the modelled reservoir before simulation.

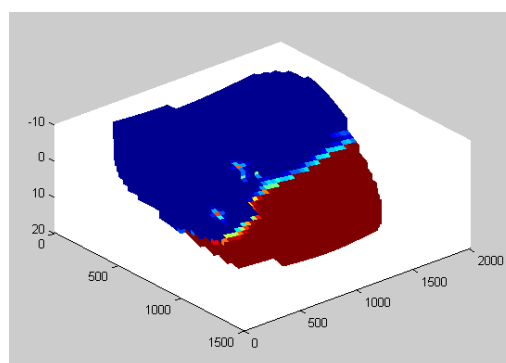


Figure 2: Saturation distribution in the modelled reservoir before simulation.

In Figure 2, the injector wells are seen as the deep red colouration at different positions while the producer wells are seen as the deep blue colourations. Different scenarios of well placements at different positions were considered and the results

were compared. The reservoir was modelled using the reservoir properties of the field. Each test scenario has injector wells and three producer wells. A simple NPV as economic object function was desired to be maximized; the oil revenue was set to \$50 per barrel and the water injection and production cost at \$10 per barrel. The water cut in the producer was set to be profitable at or below 70% (that is, the well is no longer profitable as the water cut in the producer exceeds about 0.70). Three different scenarios considered with well placement positions are:

- 1) The wells and simulation schedule are defined by three producer wells operating at the fixed bottom hole pressure and perforated throughout all layers of the model along with a single injector injecting one pore volume over 10 years (the total simulation length).
- 2) The wells and simulation schedule are defined by three producer wells operating at the fixed bottom hole pressure and three injector wells each injecting one pore volume over the total simulation length (10 years).
- 3) Three producer wells operating at the fixed bottom hole pressure and three injector wells each injecting one pore volume over the total simulation length (10 years) with different injector and producer wells as scenario (b).

The reference case is a constant rate/BHP case, with the all-producer BHPs at 250 bar ( $\approx 3700$  psia). The injection rate is constrained at a maximum rate of 3000 STBD per injector and the producer BHPs at a minimum of 200 bar ( $\approx 2910$  psia) and a maximum of 350 bar ( $\approx 5080$  psia). The initial simulation input is constant and equal rate for the all injectors and constant BHP for the producer. The initial simulation time is set to 3650 days (10 years). Figures 4, 5 and 6 show the accumulated water cut for the three production scenarios. For Scenario 1, The producer well, P1 was profitable for about 3500 days and produced about equal amount of oil and water between 2,300 to 2,400 days. The producer well, P2 was at no time profitable. From day 1 to 1000th day, only water was being produced. The producer well, P3 was profitable for the first 10 years (3650 days) of production and produced only oil for about the first 1,400 days (3.8 years). For Scenario 2, the producer well, P1 was profitable for about 1300 days and produced only oil for about the first 400 days. It produced about 50% oil and water after 1000 days. The producer well, P2 was also profitable for about 1300 and produced only oil for about the first 250 days. The producer well, P3 was only profitable for less than about 100 days. For Scenario 3, the producer well, P1 was profitable for about 1100 days and produced only oil for about the first 400 days. The producer well, P2 was at no time profitable. From day 1 to the 250th day, only water was being produced. The producer well, P3 was only profitable for about 1600 days and P2 produced only oil for about the first 400 days. The profitability days result for all the scenarios is given in Table 1.

Table 1: Producer wells profitability days for the different scenarios

Scenario	Profitability of Producer Wells (Days)		
	P1	P2	P3
1	3500	None	>3500
2	1300	1300	100
3	1100	None	1700

were compared. The reservoir was modelled using the reservoir properties of the field. Each test scenario has injector wells and three producer wells. A simple NPV as economic object function was desired to be maximized; the oil revenue was set to \$50 per barrel and the water injection and production cost at \$10 per barrel. The water cut in the producer was set to be profitable at or below 70% (that is, the well is no longer profitable as the water cut in the producer exceeds about 0.70). Three different scenarios considered with well placement positions are:

- 1) The wells and simulation schedule are defined by three producer wells operating at the fixed bottom hole pressure and perforated throughout all layers of the model along with a single injector injecting one pore volume over 10 years (the total simulation length).
- 2) The wells and simulation schedule are defined by three producer wells operating at the fixed bottom hole pressure and three injector wells each injecting one pore volume over the total simulation length (10 years).
- 3) Three producer wells operating at the fixed bottom hole pressure and three injector wells each injecting one pore volume over the total simulation length (10 years) with different injector and producer wells as scenario 2.

The reference case is a constant rate/BHP case, with the oil producer BHPs at 250 bar ( $\approx 3700$  psia). The injection rate is constrained at a maximum rate of 3000 STBD per injector and the producer BHPs at a minimum of 200 bar ( $\approx 2910$  psia) and a maximum of 350 bar ( $\approx 5080$  psia). The initial simulation input is constant and equal rate for the all injectors and constant BHP for the producer. The initial simulation time is set to 3650 days (10 years). Figures 4, 5 and 6 show the accumulated water cut for the three production scenarios. For Scenario 1, The producer well, P1 was profitable

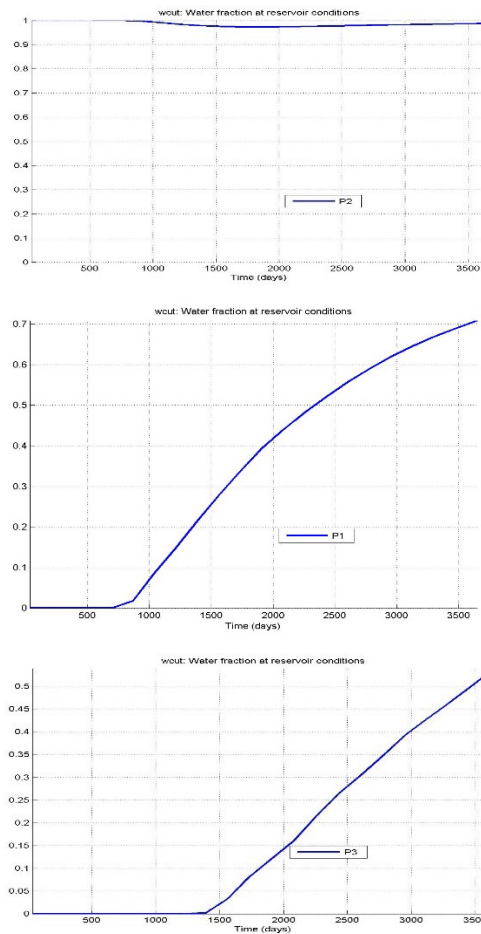


Figure 4: Accumulated water cut at reservoir conditions for Scenario 1

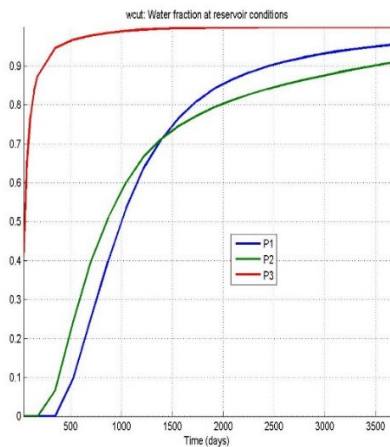


Figure 5: Accumulated water cut at reservoir conditions for scenario 2

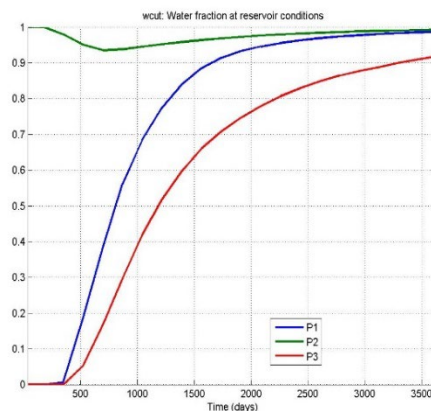


Figure 6: Accumulated water cut at reservoir conditions for scenario 3

From the water cut performance criterion, the optimal well placement positions for this reservoir can be chosen. For an optimal production for a period of 10 years, the production wells with the profitability over a 10-year period are chosen. For an optimal production less than 10 years, the production wells with profitability less than 10 years are chosen. Some wells that are not profitable at any point in time should not even be developed at all.

### 5.0 CONCLUSION AND RECOMMENDATIONS

This work employed an open-source simulator MRST as an efficient technique for reservoir production optimization. The effect of well placement on the NPV of a reservoir was investigated and it can be seen that Well placement (injector and producer wells) affects well productivity and profitability.

## ACKNOWLEDGEMENTS

Special appreciation to the important contributors to this work, including late Prof. A. A. Adepelumi and Dr. Oladele Bello for providing us with the required data for this work.

## REFERENCES

- Aarnes, J.E., Gimse, T. and Lie, K.A., 2007. An introduction to the numerics of flow in porous media using Matlab. In *Geometric modelling, numerical simulation, and optimization* (pp. 265-306). Springer, Berlin, Heidelberg.
- Babayev, D. A. (1975). Mathematical models for optimal timing of drilling on multilayer oil and gas fields. *Manage Science*, 12(21), pp. 1361-1369.
- Najafiazar, B., 2014. *Mathematical Optimization in Reservoir Management* (Master's thesis, Institutt for petroleumsteknologi og anvendt geofysikk)..
- Brouwer, D.R. and Jansen, J.D., 2002, October. Dynamic optimization of water flooding with smart wells using optimal control theory. In European petroleum conference. OnePetro.
- Brouwer, D R; Naevdal, G; Jansen, J D; Vefring, E H; van Kruijsdijk, C P. (2004). *Improved reservoir management through optimal control and continuous model updating*. Houston, Texas, s.n.
- Chen, C., Li, G. and Reynolds, A.C., 2012. Robust constrained optimization of short-and long-term net present value for closed-loop reservoir management. *SPE Journal*, 17(03), pp.849-864.
- ExxonMobil Corporation (2004). *ExxonMobil Corporation, Energy Outlook to 2030, technical report*. [Online] Available at: [www.exxonmobil.com/energyoutlook](http://www.exxonmobil.com/energyoutlook) [Accessed 15 September 2015].
- Heijn, T., Markovinovic, R. and Jansen, J.D., 2004. Generation of low-order reservoir models using system-theoretical concepts. *SPE Journal*, 9(02), pp.202-218.
- Hou, J., Zhou, K., Zhang, X.S., Kang, X.D. and Xie, H., 2015. A review of closed-loop reservoir management. *Petroleum Science*, 12(1), pp.114-128.
- Jansen, J., Bosgra, O. H. & den Hof, P. M. V. (2008). Model-based control of multiphase flow in subsurface oil reservoirs. *Journal of Process Control*, Volume 18, pp. 846 - 855.
- Lasdon, L., Coffman Jr, P.E., MacDonald, R., McFarland, J.W. and Sepehrnoori, K., 1986. Optimal hydrocarbon reservoir production policies. *Operations Research*, 34(1), pp.40-54.
- Lie, K A; Krogstad, S; Ligaarden, I S; Natvig, J R; Nilsen, H M; Skaflestad, B (2012). Open source matlab implementation of consistent discretisations on complex grids. *Computer Geosciences*, 16(2), pp. 297 - 322.
- Rosenwald, G. W. & Green, D. W. (1974). A method for determining the optimum location of wells in a reservoir using mixed-integer programming. *SPE Journal*, 1(14), pp. 44-54.
- Rossi, D. C. M. K. J. L. D. M. S. (2002). *Reservoir and Production Optimization, white paper*. [Online] Available at: [www.slb.com](http://www.slb.com) [Accessed 8 September 2015].
- Van den Hof, P.M., Jansen, J.D. and Heemink, A., 2012. Recent developments in model-based optimization and control of subsurface flow in oil reservoirs. *IFAC Proceedings Volumes*, 45(8), pp.189-200.
- Van Essen, G. M., Van den Hof, P. M. & Jansen, J. D. (2011). Hierarchical long-term and short-term production optimization. *SPE Journal*, 1(16), pp. 191-199.



## Assessing the Risks Due to Liquefied Petroleum Gas Plants using Both Quantitative and Qualitative Techniques

CHARLES C. ANIGBOGU<sup>1\*</sup>, Usman ABUBAKAR-ZARIA<sup>2</sup>, Saidu M. WAZIRI<sup>3</sup>

<sup>1, 2, 3</sup>Department of Chemical Engineering, Ahmadu Bello University, Zaria, Kaduna state, Nigeria

<sup>1\*</sup>[charles\\_anigbogu@yahoo.co.uk](mailto:charles_anigbogu@yahoo.co.uk), <sup>2</sup>[uabubakar@abu.edu.ng](mailto:uabubakar@abu.edu.ng), <sup>3</sup>[augayva@yahoo.com](mailto:augayva@yahoo.com)

\*Corresponding author

---

### ABSTRACT

Fire and overpressure hazards continue to be sources of serious concern in Liquefied Petroleum Gas (LPG) plants which is evidenced by several LPG plant explosion incidents. This research aims to assess fire and overpressure risks due to two case study LPG plants, namely: NAVGAS Sphere and SHIRASH Bullet LPG plants with holding capacities of 4189m<sup>3</sup> and 62.2 m<sup>3</sup> respectively. Quantitative risk assessment was carried out using the event tree method and ALOHA software tool. While the event tree generates the frequency of the different fire consequences obtainable, the ALOHA predicted the safe zone due to each fire. Based on the analyses, the maximum jet-fire length expected in both NAVGAS and SHIRASH LPG gas plants were 61m and 58m respectively from the epicenter, the safe zone in the event of overpressure for NAVGAS and SHIRASH LPG gas plant was 3300m, and 871m respectively, while maximum Blast overpressure radii were found to be 299m for NAVGAS sphere and 274m for SHIRASH Gas plant respectively. From the study, both plants present a danger to the population within their fire radii.

**Keywords:** Quantitative risk assessment, Event tree, Liquefied Petroleum Gas, Overpressure, Aerial Location of Hazardous Atmosphere (ALOHA).

### 1. INTRODUCTION

Liquefied Petroleum Gas (LPG) is a clean-burning and efficient fuel, and a vital source of energy for hundreds of millions of people globally, in terms of global LPG production about 60% is gotten from the crude oil and natural gas extraction process, while about 40% comes from the refinery production process. The Global production and consumption of LPG is estimated to be 280 million tonnes per annum (Paczuski *et al.*, 2016) (Amorin *et al.*, 2018) (Huang Beng, 2017). LPG has more than 1000 applications in the industrial, chemical, residential/ commercial, refinery, and transportation sectors (Raslavi *et al.*, 2014). In Nigeria, LPG is used for domestic cooking, metal workshops, fridge/air-conditioning repair shops, hotels, restaurants, and industrial power generation (Anandhan *et al.*, 2019) (Adolf *et al.*, 2015). LPG is also the source of many disastrous events such as the event of 15<sup>th</sup> March 2020 which occurred in Soba, Abule Ado in Lagos state, Nigeria, where over 23 people were reportedly killed while more than 50 houses, vehicles, and businesses were destroyed (Vanguardngr, 2020), while On 24<sup>th</sup> December 2015 reports suggested that over 100 people were killed in the district of Nnewi in Anambra State, Nigeria, the incident occurred when a gas tanker exploded at the Inter Corp Oil Limited gas plant while unloading LPG (business-humanrights, 2016). Tamil *et al.* (2015) worked on Fire, explosion, and dispersion modelling of automatic LPG distribution systems of high-rise building apartments. The analysis was done using a leading software tool called PHAST, while Gallab *et al.* in 2017 worked on Risk assessment in LPG loading operation simulation, AnyLogic platform based on Multi-Agent Systems was used to assess the safety of this supply chain, in their work ANYLOGIC software was used to model critical failure scenarios. Planas *et al.* (2015) analyzed the effect of boiling liquid expanding vapour explosion (BLEVE) in a transport tanker using mathematical models.

This work aims to assess the thermal risks posed by the NAVGAS sphere and SHIRASH LPG storage system. The different fire consequences expected with their frequencies within the NAVGAS sphere and SHIRASH LPG storage system were simulated using the event tree while possible safe zones due to each fire were determined using the areal location of hazardous atmosphere (ALOHA) software.

### 1.1 Quantitative Risk Assessment (QRA)

Several literature works have different definitions for Quantitative risk assessment, which is the numerical quantification of risk posed by a given system to individuals and societies (Selvan & Siddqui, 2017). Event tree has been utilized by several researchers in the quantitative identification of possible hazardous consequences, as seen in the works by (Hidayat & Hermansyah, 2018) and (Zwęgliński, 2022) while (Dadkani *et al.*, 2021), (Tseng *et al.*, 2012), and (Poluyan *et al.*, 2017) in the works demonstrated the significance of ALOHA in risk analysis. The presence of large storage of flammable and hazardous chemicals close to or even within residential centers is a source of concern (Nabhani & Hayati, 2020).

### 1.2 Damage Criteria

Tables 1 and 2 show a breakdown of critical damage levels for 10 seconds that can result in various degrees of injury obtained from the ALOHA software during simulation. Table 3 gives details on the site location data for the two facilities under consideration.

Table 1: Pressure levels and effects (Tamil & Siddqui, 2015)

S/N	Pressure levels (Psi)	Effect
1	1.5	Partial demolition of houses made uninhabitable
2	3.5	Steel frame buildings distorted and pulled away from the foundation
3	7.0	Loaded train cars overturned
4	10.0	Probable total building destruction: heavy machine tools moved and badly damaged
5	15-30	Range for 1-99% fatalities among the exposed population due to direct blast effect

Table 2: Damage criteria for Heat Radiation (Anandhan *et al.*, 2019)

S/N	Incident flux (kW/m <sup>2</sup> )	Extent of Damage
1	37.5	100% fatal, process equipment is damaged
2	25.0	100% lethal/ fatal minimum energy required to ignite wood
3	10.0	Potential lethal within 60 seconds
4	5.0	Second-degree burn within 60 seconds
5	2.0	Second-degree burn within 60 seconds
6	1.6	No discomfort for long exposure

Table 3: Site location data

S/N	LPG facility Name	Location	Coordinate
1	NAVGAS LPG Storage and Loading System	NavGas, Apapa Lagos state Nigeria.	Lat. 6.43 Long. 3.34
2	SHIRASH LPG Storage and Unloading System	Shirash, Zaria Kaduna state, Nigeria.	Lat. 11.12 Long. 7.7

### 1.3 NAVGAS LPG Facility- Operating Principle

The NAVGAS LPG depot is a facility that stores and distributes LPG to large retail plants, this facility is located in the Apapa local government area of Lagos state. NAVGAS LPG depot was designed with a storage capacity of 4189m<sup>3</sup>, from which LPG tank trucks of different capacities are loaded and distributed to different states in Nigeria. The normal design operating condition is a temperature 30°C and a pressure of 6bar, the NAVGAS LPG loading system starts from the 4189m<sup>3</sup> storage sphere through the centrifugal pump to the loading arm, the system also includes the link from the 4189m<sup>3</sup> storage sphere through the compressor to the vapour loading arm. The LPG sphere storage bay yard consists of unloading pipelines, a road tanker unloading bay, associated valves, fittings, and hoses. The Loading arm is composed of the Vapour line and the Liquid line, the Vapour line is connected to the compressor, while the Liquid line is connected to the centrifugal pump. A satellite view of NAVGAS facility is shown in Plate 1 below.



Plate 1: NAVGAS Aerial View from Google satellite



## 2. MATERIALS AND METHODS (OR METHODOLOGY)

The complete methodology is grouped into five stages, the process description gives a detailed description of the entire system under consideration, where major failure points would be identified. Then we move to the hazard identification within the system and a credible scenario that presents a danger to the system is selected. Fault tree modelling is done to show the chain of activities that could result in the initial scenario selected. An event tree is then prepared, which gives us the likely consequences expected due to the failure of the safety system put in place to protect the system, the probability/frequency of each consequence is also computed from the event tree. This consequence highlighted by the event tree is then carefully modeled using the ALOHA software. Figure 1 gives the block flow diagram of the research work.

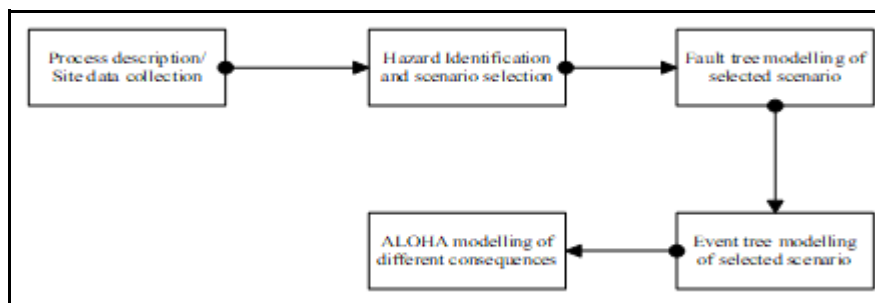


Figure 1: Detailed Block flow diagram for research work

In this work LPG bullet, catastrophic failure was selected as the hazardous scenario modeled, the leak was from a hole, with a 100mm diameter hole for catastrophic rupture as used by Lakshmi & Lakshmi, 2016.

### 2.1 Data Presentation

Table 4: Simulation chemical data

1	Chemical name	Butane
2	CAS Number	106-97-8
3	Molecular Weight	58.12 g/mol
4	AEGL-1 (60 min)	5500 ppm
5	AEGL-2 (60 min)	17000 ppm
6	AEGL-3 (60 min)	53000 ppm
7	LEL	16000 ppm
8	UEL	84000 ppm
9	Ambient Boiling Point	-0.5° C
10	Vapour Pressure at Ambient Temperature	greater than 1 atm
11	Ambient Saturation Concentration	1,000,000 ppm or 100.0%

Table 5: Simulation atmospheric data: (manual input of data)

1	Wind speed	6 meters/second from w at 6 meters
2	Ground Roughness	open country
3	Cloud Cover	5 tenths
4	Air Temperature	30° C
5	Stability Class	D
6	No Inversion Height	
7	Relative Humidity	50%

Table 6: Dimensions of NAVGAS sphere and SHIRASH Bullet

Description	NAVGAS sphere	SHIRASH Bullet
Diameter (m)	20	2.4
Length(m)		13.78
Volume(m <sup>3</sup> )	4189	62.2

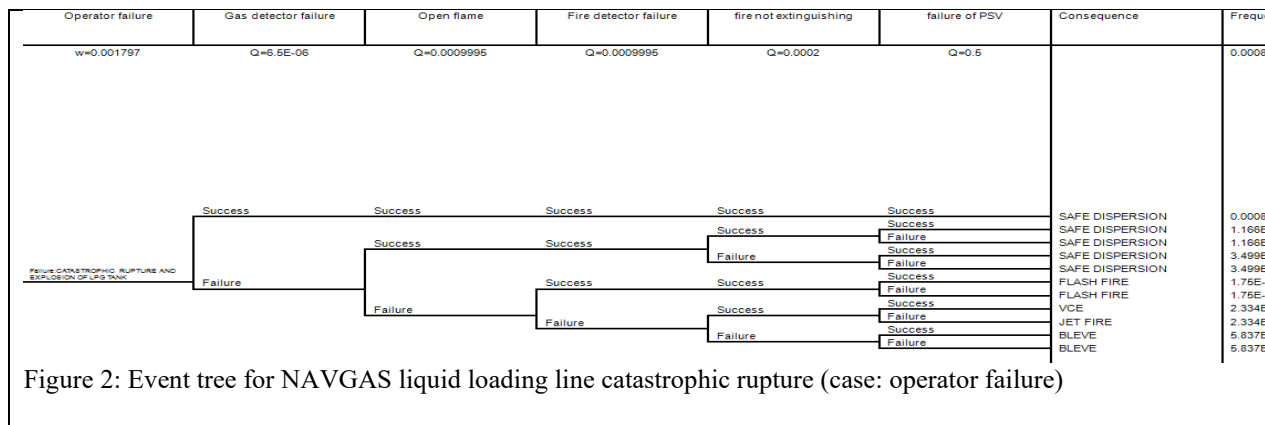
The capacities of tanks used in this work were assumed to be filled to 85% capacity and were assumed to be above ground level, the sphere pressure was set at 6bar while that of the bullet was at 4bar.

### 3. RESULTS AND DISCUSSION

The data from Tables 1 and Table 2 was used as the input for the ALOHA while the results generated are shown in the plots in Figures 2 through 6.

#### 3.1 Event tree analysis

Figure 3.1.1 is the event tree for expressing the Boiling Liquid Expanding Vapour Explosion (BLEVE) of the NAVGAS LPG loading system and SHIRASH LPG liquid unloading line arising from catastrophic rupture and eventual explosion, with a focus on operator failure and liquid outlet line failure. From the event tree, five consequences were observed to occur which are BLEVE, Vapour Cloud Explosion (VCE), Jet fire, flash fire, and safe dispersion. These consequences occur through a chain of different events, The BLEVE consequence was found to have an estimated frequency of 5.837E-18 for both cases which indicates that the likelihood of a BLEVE is relatively low, while (Ferdous *et al.*, 2011) in their work that focused on just LPG release recorded an event tree frequency of 5.5E-05, also (Hidayat & Hermansyah, 2018) in their work reported a fire frequency of 2.6E-3.



#### 3.2 The Thermal Radiation of BLEVE

The effect of BLEVE that could be caused by the NAVGAS and SHIRASH gas plant simulated using ALOHA is shown in Figures 3 and 4 respectively below.

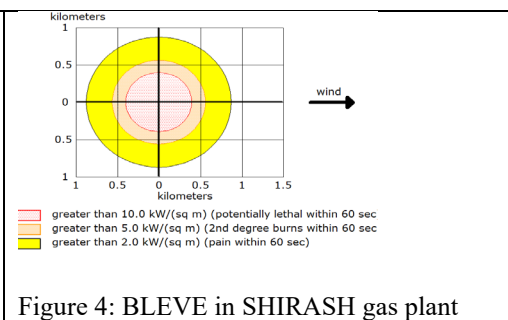
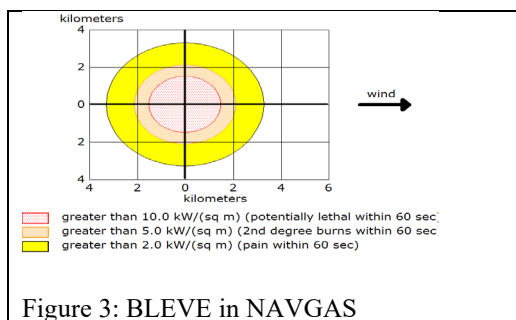


Table 7: Thermal Radiation threat Zone due to BLEVE

Source	Volume (m <sup>3</sup> )	Fireball Duration (sec)	Fireball Diameter (m)	Thermal Radiation Level		
				10(kW/m <sup>2</sup> ) for a radius of (m)	5(kW/m <sup>2</sup> ) for a radius of (m)	2(kW/m <sup>2</sup> ) for a radius of (m)
Sphere	4189	34	734	1500	2100	3300
Bullet	62.2	12	180	396	559	871

The thermal Radiation threat Zone due to BLEVE was presented in Figures 3 and 4, while specific detail of the threat zone and the lethal potential within each zone were presented in Table 7, the sphere had higher values for fireball duration, fireball diameter as well as thermal radiation level radius. This implies that the impacted zone is relatively higher for the NAVGAS sphere, indicating higher expected possible casualties as given in Figure 1 (Anandhan *et al.*, 2019). Planas *et al.* (2015) in their work, pointed out that regardless of the severity of the explosion or fireball as long as people are not within the expected impact zone, they will be safe. But outside the thermal threat zone is the safe zone. The boiling point temperature and the minimum ignition temperature is a major factor as proposed by (Sepp, 2014) and (Mohitpour *et al.*, 2016). Roberts *et al.* (2000) in their work, concluded that the resulting size and shape of the fireball following the BLEVE failure of a vessel was dependent on the amount of fuel in the vessel at the time of failure and the mode of failure.

### 3.3 The Jet Fire

An explosion will only occur if the explosion limit is between the lower and upper bound as reported by (Sadeghi et al., 2017). While Figures 3.3.1 and 3.3.2 are NAVGAS jet fire threat Zone and SHIRASH jet fire threat Zone while considering a storage tank with a given open diameter.

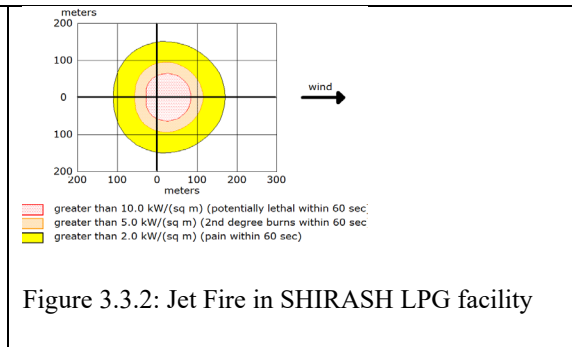
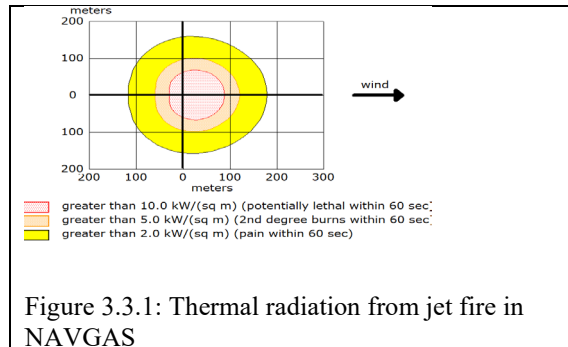


**Table 3.3.1 Thermal Radiation Threat Zone due to Jet Fires**

Source	Volume (m <sup>3</sup> )	Maximum Burn rate (Kg/min)	Duration (min)	Max Flame Length (m)	Thermal Radiation Level		
					10(kW/m <sup>2</sup> ) for a radius of (m)	5(kW/m <sup>2</sup> ) for a radius of (m)	2(kW/m <sup>2</sup> ) for a radius of (m)
Sphere	4,189	4,790	14	61	90	122	180
Bullet	62.2	4,310	14	58	86	116	172

From table 3.3.1 given above it could be deduced that from their respective flame length, both are equally hazardous to the operators and users within the facility. The Jet Fire Radiation threat was presented in figures 3.3.1 and 3.3.2 the lethal potential within each zone was presented in table 3.3.1, and the sphere had a higher value for Flame length as well as thermal radiation level radius (Bariha et al., 2016) reported in their work that population within the zone is likely to experience 1<sup>st</sup>-degree burn as a result of the radiation exposure.

### 3.4 The Blast Effect and Dispersion

Figure 5 represents NAVGAS overpressure threat Zone while Figure 6 represents the SHIRASH overpressure threat zone.

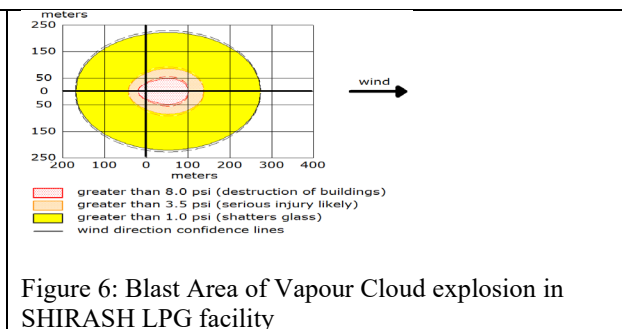
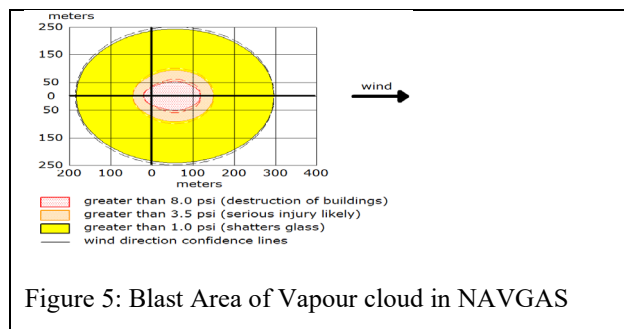


**Table 8 Blast Overpressure Zone due to Vapour Cloud Explosion**

Source	Volume (m <sup>3</sup> )	Release Duration (min)	Blast Overpressure Zone		
			8.0 psi up to the radius of (m)	3.5 psi up to the radius of (m)	1.0 psi up to the radius of (m)
Sphere	4,189	14	119	151	299
Bullet	62.2	14	102	139	274

The NAVGAS had higher Blast overpressure zones as shown in Table 8, from which we could infer that the NAVGAS sphere is relatively more hazardous. Both storage systems are hazardous and could cause serious injury and destruction of properties such as the shattering of glasses within its radius upon explosion, as the report in Table 1 by (Tamil & Siddiqui, 2015).

#### 4. CONCLUSION

From the work, the estimated safe zones in the event of BLEVE for NAVGAS and SHIRASH LPG gas plant were determined to be 3300m and 871m respectively from the epicenter, while Maximum jet-fire flame length expected due to NAVGAS and SHIRASH LPG gas plant were estimated to be 61m and 58m respectively, and above these distance, we have the safe zone where no impact is expected, the population and properties within the safe zone would not be impacted. The Maximum Blast overpressure radii effect were estimated to be ineffective above these distances 299m and 274m for NAVGAS and SHIRASH Gas plant respectively. Finally, looking at the safety instrumented systems integrated into NAVGAS and SHIRASH LPG plants, it is reasonable to conclude that safety gadgets were adequate but need to be inspected and services as and when due. Staff training on health safety and environmental management is also highly recommended to avoid accidents within the facilities.

#### REFERENCES

- Adolf, J., Balzer, C., Joedicke, A., & Schabla, U. (2015). *Shell LPG Study*. 1–15. <http://s05.static-shell.com/content/dam/shell-new/local/country/deu/downloads/pdf/shell-lpg-study-english-summary.pdf>
- Amorin, R., Broni-Bediako, E., Worlanyo, D., & Konadu, S. A. (2018). The Use of Liquefied Petroleum Gas (LPG) as a Fuel for Commercial Vehicles in Ghana: A Case Study at Tema Community 1. *Current Journal of Applied Science and Technology*, 29(2), 1–8. <https://doi.org/10.9734/cjast/2018/41531>
- Anandhan, M., Prabakaran, T., Muhaidheen, M., & Ragavendran, S. (2019). Quantitative risk assessment in LPG storage area for different fire scenarios. *International Journal of Mechanical Engineering and Technology*, 10(2), 1425–1435.
- Bariha, N., Mani, I., & Chandra, V. (2016). Journal of Loss Prevention in the Process Industries Fire and explosion hazard analysis during surface transport of liquefied petroleum gas (LPG): A case study of LPG truck tanker accident in Kannur, Kerala, India. *Journal of Loss Prevention in the Process Industries*, 40, 449–460. <https://doi.org/10.1016/j.jlp.2016.01.020>
- Dadkani, P., Noorzai, E., Ghanbari, A. H., & Gharib, A. (2021). Risk analysis of gas leakage in gas pressure reduction station and its consequences: A case study for Zahedan. *Heliyon*, 7(5), e06911. <https://doi.org/10.1016/j.heliyon.2021.e06911>
- Ferdous, R., Khan, F., Sadiq, R., Amyotte, P., & Veitch, B. (2011). Fault and Event Tree Analyses for Process Systems Risk Analysis: Uncertainty Handling Formulations. *Risk Analysis*, 31(1), 86–107. <https://doi.org/10.1111/j.1539-6924.2010.01475.x>
- Hidayat, M. E. N., & Hermansyah, H. (2018). Risk analysis of gas distribution pipelines in apartments using the event tree analysis method. *AIP Conference Proceedings*, 2021(2018). <https://doi.org/10.1063/1.5062721>
- Huang Beng, Y. (2017). *Quantitative Risk Analysis for Explosion Safety of Oil and Gas Facilities*. [http://research-repository.uwa.edu.au/files/20467204/thesis\\_doctor\\_of\\_philosophy\\_huang\\_Yimiao\\_2017.pdf](http://research-repository.uwa.edu.au/files/20467204/thesis_doctor_of_philosophy_huang_Yimiao_2017.pdf)
- Mohitpour, M., Jenkins, A., & Babuk, T. (2016). *Pipelining Liquefied Petroleum Gas (LPG)*. 1–8. <https://doi.org/IPC2006-10032>.
- New evidence points to pipeline in Lagos' March explosion. Esi-africa, 2020. Retrieved November 10, 2020, from <https://www.esi-africa.com/industry-sectors/business-and-markets/new-evidence-points-to-pipeline-in-lagos-march-explosion/>
- Nigeria: Several people killed and many others injured after gas tanker explodes, gas company negligence cited. business-humanrights, 2016. Retrieved June 20, 2020, from <https://www.business-humanrights.org/en/nigeria-several-people-killed-and-many-others-injured-after-gas-tanker-explodes-gas-company-negligence-cited>
- Nigeria gas tanker explosion kills dozens. Aljazeera (2018). Retrieved November 15, 2020, from <https://www.aljazeera.com/news/2018/9/11/nigeria-gas-tanker-explosion-kills-dozens>
- Nabhani, N., & Hayati, F. (2020). *Risk assessment of LPG pressure vessel by Fault Tree Analysis and consequence modelling with PHAST*. July.
- Paczuski, M., Marchwiany, M., Pulawski, R., Pankowski, A., Kurpiel, K., & Przedlacki, M. (2016). Liquefied Petroleum Gas (LPG) as a Fuel for Internal Combustion Engines. In *Alternative Fuels, Technical and Environmental Conditions* (Vol. 13, Issue March). <https://doi.org/10.5772/61736>
- Planas, E., Pastor, E., Casal, J., & Bonilla, J. M. (2015). Journal of Loss Prevention in the Process Industries Analysis of the boiling liquid expanding vapor explosion (BLEVE) of a liquefied natural gas road tanker: The Zarzalico accident. *Journal of Loss Prevention in the Process Industries*, 34, 127–138. <https://doi.org/10.1016/j.jlp.2015.01.026>.
- Poluyan, L. V., Syutkina, E. V., & Guryev, E. S. (2017). Software Systems for Prediction and Immediate Assessment of Emergency Situations on Municipalities Territories. *IOP Conference Series: Materials Science and Engineering*, 262(1). <https://doi.org/10.1088/1757-899X/262/1/012199>
- Raslavi, L., Mockus, S., Ker, N., & Starevi, M. (2014). *Liquefied petroleum gas (LPG) as a medium-term option in the transition to sustainable fuels and transport*. 32, 513–525. <https://doi.org/10.1016/j.rser.2014.01.052>
- Roberts, T., Gosse, A., & Hawksworth, S. (2000). Thermal radiation from fireballs on failure of liquefied petroleum gas storage vessels. *Process Safety and Environmental Protection: Transactions of the Institution of Chemical Engineers, Part B*, 78(3), 184–192. <https://doi.org/10.1205/095758200530628>

- Sadeghi, M., Mehranfar, H., Tadayon, A., Bagheri, M., & Kamali, A. (2017). Risk analysis of stationary rail cars containing hazardous materials; A Case Study. *International Journal of Railway Research*, 4(September), 1–9. <https://www.researchgate.net/publication/319876043>.
- Selvan, R. T., & Siddqui, N. A. (2017). Risk Assessment of Natural Gas Gathering Station & Pipeline Network. *International Journal of Theoretical and Applied Mechanics*, 12(2), 227–242.
- Tamil, R., & Siddqui, N. A. (2015). *Fire, Explosion and Dispersion Modelling of Automatic LPG Distribution System of High-Rise Building Apartment*. 2(4), 276–283.
- Tseng, J. M., Su, T. S., & Kuo, C. Y. (2012). Consequence evaluation of toxic chemical releases by ALOHA. *Procedia Engineering*, 45, 384–389. <https://doi.org/10.1016/j.proeng.2012.08.175>.
- Unravelling the Abule Ado blast. Vanguardngr, (2020). Retrieved June 20, 2020, from <https://www.vanguardngr.com/2020/03/unravelling-the-abule-ado-blast/>
- Zwęgliński, T. (2022). Conventional Event Tree Analysis on Emergency Release of Liquefied Natural Gas. *International Journal of Environmental Research and Public Health*, 19(5). <https://doi.org/10.3390/ijerph19052961>.



## Isolation and Identification of Potential Hydrocarbon Degrading Microbes from Non-Hydrocarbon Contaminated Sources for Crude Oil Spill Clean-Up

Elizabeth WINFUL<sup>1</sup>, Opeoluwa O. FASANYA<sup>1\*</sup>, Jibrin ABDULKADIR<sup>1</sup>, Balli GAUJE<sup>1</sup>,  
Ugochi J. OKODUWA<sup>1</sup>, Simon I. ADAMUN<sup>1</sup>, Ephraim AUDU<sup>2</sup>, Judy ADUDU<sup>2</sup>, Hauwa A.  
MOHAMMED<sup>1</sup>, Olalekan ADESINA<sup>1</sup>, Jeffrey T. BARMINAS<sup>3</sup>

<sup>1</sup>Industrial and Environmental Pollution Department, National Research Institute for Chemical Technology,  
Zaria, Nigeria

<sup>2</sup>Scientific and Industrial Research Department, National Research Institute for Chemical Technology, Zaria,  
Nigeria

<sup>3</sup>Directorate, National Research Institute for Chemical Technology, Zaria, Nigeria

<sup>1</sup>[modupewins@gmail.com](mailto:modupewins@gmail.com), <sup>2\*</sup>[ope.fasanya@narict.gov.ng](mailto:ope.fasanya@narict.gov.ng),

\*Corresponding author

---

### ABSTRACT

Pollution due to spillage of crude oil has resulted in appreciable levels of damage to many communities. Water sources as well as land are affected leading to destruction of natural fauna and flora. Hydrocarbon degrading microbes from non-crude oil contaminated environments were isolated and their potential degradation efficiency was studied. Morphological and biochemical characterization as well as molecular studies were used to identify the isolates. Preliminary qualitative studies were also carried out on the isolates to evaluate their ability to produce biosurfactants. The microbes were found to belong to Bacillaceae, Xanthomonadaceae and Saccharomycetaceae families. Highest crude oil degradation after 15 days in this study was 45 and 56% by 2 of the 12 isolates studied. This shows that microorganisms isolated from non-crude oil contaminated sites have the potential to degrade crude.

**Keywords:** Crude oil, Biosurfactants, Degradation, Bacteria, Yeast

### 1. INTRODUCTION

Microorganisms have been known to colonize diverse environments for thousands of years, including those that are considered “extreme” to most organisms (Peixoto *et al.*, 2011). Yeasts, bacteria, and fungi have been employed to digest and breakdown substances that are harmful to humans, animals and environment (Ojuederie and Babalola, 2017). The use of these microbes has generated research interests as they are a sustainable and cost-effective alternative to chemical treatment of a variety of contaminants. Due to their small size, these microbes are able to interact with contaminants easily, facilitating quick and effective degradation or reduction to a permissible concentration or less harmful state (Gao *et al.*, 2018).

Most of these microorganisms produce extracellular or membrane-associated surface-active compounds also known as biosurfactants. Biosurfactants are presently gaining tremendous attention because of their biodegradability ability and low toxicity. Other merits of biosurfactant use include low cost of synthesis from cheap raw materials as well as effectiveness at extreme conditions of temperature, pH and salinity (Shoeb *et al.*, 2013). The employment of biosurfactant-producing and hydrocarbon-utilizing microbes enhances the efficiency of the bioremediation process as biosurfactant plays an important role by making hydrocarbons bio-available for degradation (Patowary *et al.*, 2017).

Identification of microbes that play vital roles in hydrocarbon degradation is relevant to the development of optimal *in situ* bioremediation strategies. Significant milestones have been achieved with regards to isolating and identifying potential hydrocarbon degraders, as well as biosurfactant producers, characterizing their bacterial communities and their responses to pollutants (MacNaughton *et al.*, 1999). Numerous reviews have been written by different groups discussing progresses of petroleum hydrocarbon degradation by microbes (Xue *et al.*, 2015, Wartell *et al.*, 2021, Imron *et al.*, 2020).

Oil spills became a major environmental issue in the 1960's especially to the marine ecosystem as a result of increased crude oil exploration activity (Zhang *et al.*, 2019). These spills occur as a result of leakage of crude oil onto the surface of a large body of water or land (Elisha and Felix, 2021). Nigeria is the sixth-largest exporter of crude oil and correspondingly the sixth largest nation among the Organization of the Petroleum Exporting Countries (OPEC) (Albert *et al.*, 2018). Accompanying this status is the deluge of oil spills in oil producing areas with over 100,000 barrels of oil spilled in the Niger Delta and environs since 2018 (Albert *et al.*, 2018, Nuhu *et al.*, 2022). The multiple oil spills have had adverse effects on the natural fauna and flora in the area as well as negative impact of quality of life of residents in the area (Osuagwu and Olaifa, 2018, Onyena and Sam, 2020). The use of oil degrading microbes has been explored as a viable means of tackling crude oil pollution in these environs (Gao *et al.*, 2018). A large fraction of crude oil is biodegradable and can be consumed by microbes leaving CO<sub>2</sub> as an end product (Marchand *et al.*, 2017). This is one major advantage of bioremediation over other available methods of oil spill clean-up. Bioremediation is presently being encouraged because of the advantage of sustainability and the possibility of restoring the contaminated body (soil or water) to its original form. In this paper, data generated from preliminary investigations into crude oil degradation potential of some locally isolated microorganisms from non-marine sources for oil clean-up is presented.

## 2. MATERIALS AND METHODS

### 2.1 Materials

In this study, bacteria were isolated from soil collected from different locations within Zaria, while yeasts were isolated from fermented grapes purchased in Samaru Market, Zaria. Composition of mineral salt medium (MSM) used in this study are given below. \

#### 2.1.1 For isolation of hydrocarbon degraders

2.42 g/L KH<sub>2</sub>PO<sub>4</sub>, 5.60 g/L K<sub>2</sub>HPO<sub>4</sub>, 2.00 g/L (NH<sub>4</sub>)<sub>2</sub>SO<sub>4</sub>, 0.30 g/L MgSO<sub>4</sub>·7H<sub>2</sub>O, 0.04 g/L CaCl<sub>2</sub>·2H<sub>2</sub>O,  $4.5 \times 10^{-3}$  g/L MnSO<sub>4</sub>·7H<sub>2</sub>O,  $0.1 \times 10^{-3}$  g/L CuSO<sub>4</sub>·5H<sub>2</sub>O and  $0.1 \times 10^{-3}$  g/L FeSO<sub>4</sub>·7H<sub>2</sub>O (Xia *et al.*, 2019).

#### 2.1.2 For biosurfactant production:

0.2 g/L MgSO<sub>4</sub>, 0.02 g/L CaCl<sub>2</sub>, 1.0 g/L KH<sub>2</sub>PO<sub>4</sub>, 1.0 g/L K<sub>2</sub>HPO<sub>4</sub>, 1.0 g/L NH<sub>4</sub>NO<sub>3</sub>, and 0.5 g/L FeCl<sub>3</sub> supplemented with 1% (v/v) glucose (Parthipan *et al.*, 2017).

In addition to the MSM, nutrient agar, nutrient broth, Sabouraud dextrose agar, yeast extract, peptone, glucose, pseudomonas agar base was also used. All chemical reagents used were analytical grade and used without further purification. The Escarvos crude oil which was donated by Kaduna Refining and Petrochemical Company (KRPC).

The pH for all media was set at  $7.0 \pm 0.2$  (NaOH and HCl were used to adjust) then sterilized at 121 °C for 15 mins.

## 2.2 Methodology

### 2.2.1 Isolation of microorganisms

The process of isolation of *Bacillus* spp was carried out according to the steps highlighted by Akhavan *et al* (2008) while for *Pseudomonas* spp the methodology proposed by Su *et al.* (2018) was adopted. For the isolation of yeast, the procedure by Abioye *et al.* (2013) was employed. A total of 12 (8 bacterial isolates and 4 yeast isolates) were isolated and used in this study. Bacterial isolates were gotten from soil while yeast isolates were obtained from grapes that were kept for 3 days to ferment.

Codes used for isolates: Target *Bacillus* = B1, B2, B3, B4; Target *Pseudomonas* = P1, P2, P3, P4; Target Yeast = S1, S2, S3, S4

### 2.2.2 Identification

Morphological and biochemical characterizations were carried out according to Bergey's Manual of Systematic Bacteriology (Bergey, 1994). Molecular identification was subsequently done by PCR amplification using 16S rDNA sequencing and ITS1 & ITS2 for bacteria and yeast isolates respectively.

16S rDNA universal forward primers (GGACTACAGGGTATCTAAT) and reverse primer (AGAGTTTGATCCTGG) was employed for the bacteria isolates; and

ITS1 (5'-TCCGTAGGTGAACCTGCGG-3'), ITS4 (5'-TCCTCCGCTTATTGATATGC-3') for the 1st round and NL1 (GCA TAT CAA TAA GCG GAG GAA AAG) NL4 (GGT CCG TGT TTC AAG ACG G) for 2nd round was employed for the yeast isolates.

All sequences gotten for the twelve isolates were submitted to the Genetic Sequence Database at the National Centre for Biotechnical Information (NCBI).

### 2.2.3 Degradation Studies of Isolates

A 15-day degradation study of the isolates was carried out using modified procedures by Abioye *et al.* (2013) and Tian *et al.* (2018). Briefly, 1 ml of 24 h broth culture of each of the isolates was inoculated into an Erlenmeyer flask containing 50 mL sterile MSM and 1 g of crude oil (which serves as their sole carbon source). Positive and negative controls were equally set up. The positive control contained 50 mL sterile MSM and 1 g of crude oil without the isolates, while the negative control contained 50 mL sterile MSM and 1 mL 24 h broth culture of each of the isolates without crude oil. All flasks were incubated at 37 °C for the duration of the studies.

At 5-day intervals, optical density (OD) readings were taken using a UV-visible spectrophotometer (Shimadzu UV-2550) to determine rate of crude oil degradation. The culture medium was taken at OD600 nm, after which the crude was extracted using chloroform then optical density determined at 257 nm.

Oil degradation was calculated using the equation below.

$$C_d = 1 - C_a/C_o \times 100\% \quad (1)$$

where  $C_o$ ,  $C_a$ , and  $C_d$  represent the concentration of oil hydrocarbons in the sample culture, concentration of oil hydrocarbons in the control, and rate of oil degradation, respectively.

### 2.2.4 Biosurfactant production/screening

Production was aerobically carried out in 500 mL Erlenmeyer flasks containing 200 mL of sterile MSM (Parthipan *et al.*, 2017). The flasks were individually inoculated with 18 to 24h culture of the isolates, then incubated for 7 days at 37 °C. The content of the flasks was centrifuged for 20 min at 4000 x g and the supernatant was utilized for screening purposes. Preliminary screening of the biosurfactant was done using the oil displacement test according to Plaza *et al.* (2006). A volume of 100 µL of crude oil was dropped on the surface of 50 ml of distilled water contained in petri dishes. Subsequently 10 µL of the culture filtrates was added to the crude oil surface. The diameter of the clear zone on the oil surface was observed and measured using vernier callipers.

## 3. RESULTS AND DISCUSSION

Isolates were first identified based on their morphological and biochemical characteristics as presented in Table 1. These preliminary identification results showed that the isolates were significantly different from each other. Gene sequencing revealed that the similarities of homology of the amplicon was as high as 92% and 95%. Based on these identification processes, isolates were identified to belong to the following families: *Bacillaceae*, *Xanthomonadaceae* and *Saccharomycetaceae* respectively.

Isolates were aseptically introduced into the sterilized MSM containing 1% (w/v) crude oil then incubated for 15 days (the crude oil served as their sole carbon source). The growth rate of the microorganisms and level of crude oil degradation was monitored at 5-day intervals using UV spectrometry and readings taken. All 12 isolates were then screened for biosurfactant production using a primary screening method (oil displacement). Isolates S4 gave the highest clearance of 0.975mm (Plate 1) followed by B2 with a value of 0.875mm (Plate 2) and the lowest value obtained; 0.295mm was gotten by isolate P2. This method of screening confirmed the presence of biosurfactants produced by the isolates.



Plate 1: Oil displacement result for S4

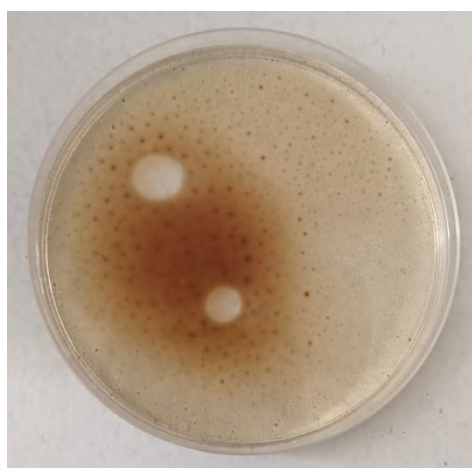


Plate 2: Oil displacement result for B2



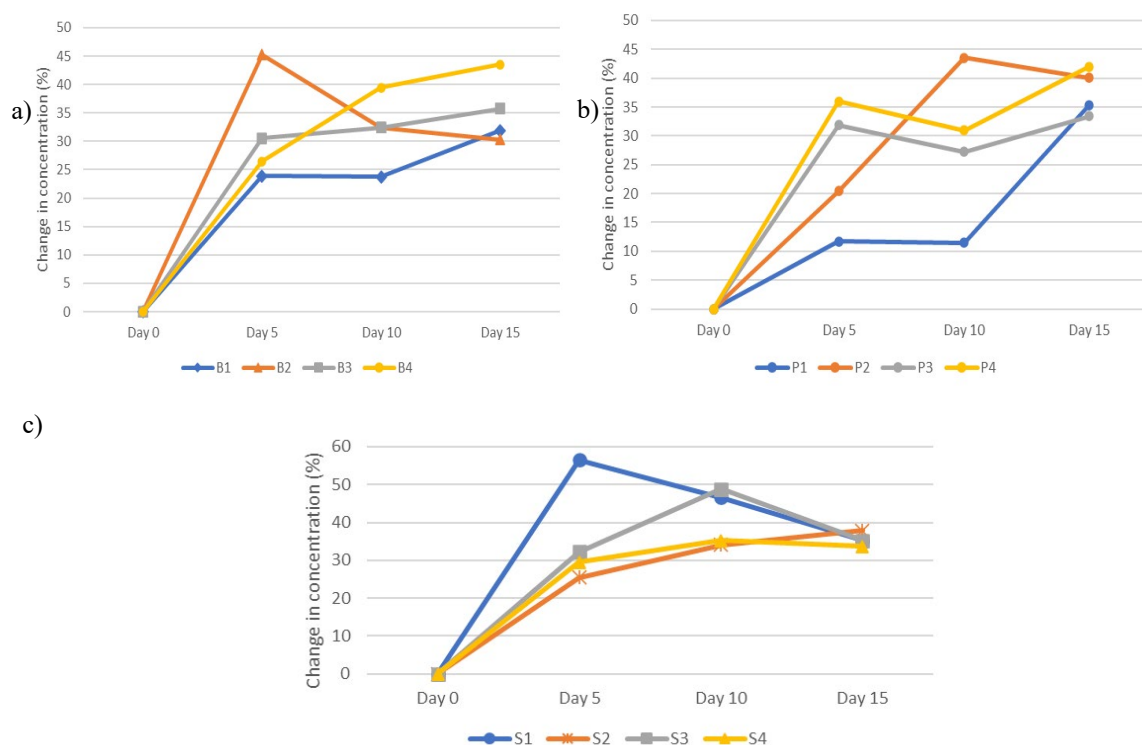


Figure 3: Crude oil degradation activity of the isolates for a) *Bacillus* b) *Pseudomonas* and c) Yeast

Table 1: Morphological and Biochemical Characteristics of Isolates

Isolate	B1	B2	B3	B4	P1	P2	P3	P4	S1	S2	S3	S4
Gram	P.L. R	P.L. R	P.L. R	P.L. R	N.S.R	N.S.R	N.S.R	N.S.R	S.Y.C	O.Y.C	O.Y.C	O.Y.C
Urease	+	+	+	+	-	-	+	-	-	+	+	+
Citrate	-	+	+	+	+	+	+	+	-	-	-	-
Indole	-	+	-	+	+	+	+	+	-	-	-	-
Nitrate	+	+	+	+	+	+	+	+	-	-	+	-
MR	+	+	+	+	+	+	-	+	-	-	-	-
VP	-	-	-	-	-	+	+	-	+	+	+	+
Starch	+	-	-	-	+	+	+	-	-	-	-	-
Catalase	+	+	+	+	+	+	+	+	-	+	+	+
Oxidase	-	-	-	-	-	-	-	-	-	-	-	-
Glucose	AG	AG	AG	AG	AG	A	AG	A	A	A	A	A
Maltose	-	AG	-	-	AG	-	AG	-	-	-	-	-
Mannitol	-	AG	-	-	AG	A	AG	-	-	-	-	-

S.Y.C = spherical yeast cells; P.L.R = positive long rods; N.S.R = negative short rods; - = Negative; + = Positive; AG = Acid & Gas; A = Acid only.

Table 2: Screening of Biosurfactant for Oil Displacement Test

Isolate	B1	B2	B3	B4	P1	P2	P3	P4	S1	S2	S3	S4
Clearance (mm)	0.4	0.87	0.362	0.377	0.33	0.29	0.47	0.252	0.4	0.387	0.377	0.97
	8	5	5	5	5	5	5	5	2	5	5	5

Figure 3 shows results of the rate of crude oil degradation which was monitored using a UV spectrophotometer at optical density 257 nm. All 12 isolates showed an appreciable level of degradation in the first 5 days with B2 and S1 giving the highest levels of degradation as 45.2 and 56.3% respectively. Interestingly, all isolates showed similar patterns of rate degradation through the 15-day study. As stated earlier, they started with a rise in rate of degradation within the first 5 days, then except the isolates S1-S4, there was a drop on day 10 and a rise again in percentage degradation on day 15. This shows that all isolates were able to utilize the crude oil as their sole carbon source.

The results obtained are much higher when compared to microbial degradation studies by Hossain *et al.* (2022) as well as the work of Ozyurek & Bilkay (2018) wherein degradation of 15% and 12.5% respectively were reported with differing operating conditions. The low values appear to follow the trend of aged crude degradation oil which are harder to degrade (Ullah *et al.*, 2021) as well non-rotary conditions (Bilen Ozyurek and Seyis Bilkay, 2018). Lack of rotatory movement implies reduced solubility and thereby presence of oxygen for the microorganisms.

When compared with data presented in Table 2 for the oil displacement test, the results for sample B2 are in agreement with regards to level of degradation and diameter of oil spread. This suggests a high level of biosurfactant activity by B2. Sample S4 which had the highest clearance did not however present high levels of degradation. This portends that the presence of an additive such as glucose may be required to boost overall degradation activity (Sharma *et al.*, 2019).

#### 4. CONCLUSION

The preliminary results obtained from this study show the ability of microbes isolated from non-hydrocarbon contaminated environments to degrade crude oil. The microbes in this study showed production of biosurfactants as well as relatively moderate levels of crude oil degradation. This was achieved without optimization and boosting of microbes. Extensive work will be done to identify, quantify test the potency of biosurfactants produced by the isolates as well as compare the efficiency of microbes isolated from non-hydrocarbon contaminated habitat and those isolated from crude oil contaminated sites. Kinetic studies on the degradation of crude oil as well as growth kinetics of the better performing microbes will also be carried out in subsequent studies.

#### REFERENCES

- Abioye, O., Akinsola, R., Aransiola, S., Damisa, D., & Auta, S. (2013). Biodegradation of crude oil by *saccharomyces cerevisiae* isolated from fermented zobo (locally fermented beverage in Nigeria). *Pak J Biol Sci*, *16*(24), 2058-2061.
- AKHAVAN, S. A., DEZHBAN, G. P. I., Emami, M., & Nakhoda, A. (2008). Isolation and characterization of Crude oil degrading *Bacillus* spp.
- Albert, O. N., Amaratunga, D., & Haigh, R. P. (2018). Evaluation of the impacts of oil spill disaster on communities and its influence on restiveness in Niger Delta, Nigeria. *Procedia engineering*, *212*, 1054-1061.
- Bilen Ozyurek, S., & Seyis Bilkay, I. (2018). Biodegradation of petroleum by *Klebsiella pneumoniae* isolated from drilling fluid. *International Journal of Environmental Science and Technology*, *15*(10), 2107-2116. doi:10.1007/s13762-017-1581-y
- Elisha, O., & Felix, M. (2021). Destruction of coastal ecosystems and the vicious cycle of poverty in Niger Delta region. *Journal of Global Agriculture and Ecology*, *11*, 7-24.
- Gao, H., Xie, Y., Hashim, S., Akhtar Khan, A., Wang, X., & Xu, H. (2018). Application of microbial technology used in bioremediation of urban polluted river: a case study of Chengnan River, China. *Water*, *10*(5), 643.
- Hossain, M. F., Akter, M. A., Sohan, M. S. R., Sultana, D. N., Reza, M. A., & Hoque, K. M. F. (2022). Bioremediation potential of hydrocarbon degrading bacteria: isolation, characterization, and assessment. *Saudi Journal of Biological Sciences*, *29*(1), 211-216. doi:https://doi.org/10.1016/j.sjbs.2021.08.069
- Imron, M. F., Kurniawan, S. B., Ismail, N. I., & Abdullah, S. R. S. (2020). Future challenges in diesel biodegradation by bacteria isolates: A review. *Journal of Cleaner Production*, *251*, 119716. doi:https://doi.org/10.1016/j.jclepro.2019.119716
- MacNaughton, S. J., Stephen, J. R., Venosa, A. D., Davis, G. A., Chang, Y.-J., & White, D. C. (1999). Microbial population changes during bioremediation of an experimental oil spill. *Applied and environmental microbiology*, *65*(8), 3566-3574.
- Marchand, C., St-Arnaud, M., Hogland, W., Bell, T. H., & Hijri, M. (2017). Petroleum biodegradation capacity of bacteria and fungi isolated from petroleum-contaminated soil. *International Biodeterioration & Biodegradation*, *116*, 48-57. doi:https://doi.org/10.1016/j.ibiod.2016.09.030
- Nuhu, M. M., Rene, E. R., & Ishaq, A. (2022). Remediation of crude oil spill sites in Nigeria: Problems, technologies, and future prospects. *Environmental Quality Management*, *31*(4), 165-175. doi:https://doi.org/10.1002/tqem.21793
- Ojuederie, O. B., & Babalola, O. O. (2017). Microbial and plant-assisted bioremediation of heavy metal polluted environments: a review. *International journal of environmental research and public health*, *14*(12), 1504.

- Onyena, A. P., & Sam, K. (2020). A review of the threat of oil exploitation to mangrove ecosystem: Insights from Niger Delta, Nigeria. *Global Ecology and Conservation*, 22, e00961. doi:<https://doi.org/10.1016/j.gecco.2020.e00961>
- Osuagwu, E. S., & Olaifa, E. (2018). Effects of oil spills on fish production in the Niger Delta. *PLOS ONE*, 13(10), e0205114. doi:10.1371/journal.pone.0205114
- Parthipan, P., Elumalai, P., Sathishkumar, K., Sabarinathan, D., Murugan, K., Benelli, G., & Rajasekar, A. (2017). Biosurfactant and enzyme mediated crude oil degradation by *Pseudomonas stutzeri* NA3 and *Acinetobacter baumannii* MN3. *3 Biotech*, 7(5), 1-17.
- Patowary, K., Patowary, R., Kalita, M. C., & Deka, S. (2017). Characterization of biosurfactant produced during degradation of hydrocarbons using crude oil as sole source of carbon. *Frontiers in microbiology*, 8, 279.
- Peixoto, R. S., Vermelho, A. B., & Rosado, A. S. (2011). Petroleum-Degrading Enzymes: Bioremediation and New Prospects. *Enzyme Research*, 2011, 475193. doi:10.4061/2011/475193
- Plaza, G. A., Zjawiony, I., & Banat, I. (2006). Use of different methods for detection of thermophilic biosurfactant-producing bacteria from hydrocarbon-contaminated bioremediated soils. *Journal of Petroleum Science and Engineering*, 50(1), 71-77.
- Sharma, S., Verma, R., & Pandey, L. M. (2019). Crude oil degradation and biosurfactant production abilities of isolated *Agrobacterium fabrum* SLAJ731. *Biocatalysis and Agricultural Biotechnology*, 21, 101322. doi:<https://doi.org/10.1016/j.bcab.2019.101322>
- Shoeb, E., Akhlaq, F., Badar, U., Akhter, J., & Imtiaz, S. (2013). Classification and industrial applications of biosurfactants. *Academic Research International*, 4(3), 243.
- Su, S. S., Lae, K. Z. W., & Ngwe, H. (2018). Isolation and Identification of *Pseudomonas aeruginosa* from the Clinical Soil. *University of Yangon Research Journal*, 8, 271-275.
- Tian, X., Wang, X., Peng, S., Wang, Z., Zhou, R., & Tian, H. (2018). Isolation, screening, and crude oil degradation characteristics of hydrocarbons-degrading bacteria for treatment of oily wastewater. *Water Science and Technology*, 78(12), 2626-2638.
- Ullah, S., Ali, N., Dawar, F., Nughman, M., Rauf, M., Khattak, M., & Kim, B. (2021). Biodegradation of petroleum by bacteria isolated from fishes of Indian Ocean. *Brazilian Journal of Biology*, 82.
- Wartell, B., Boufadel, M., & Rodriguez-Freire, L. (2021). An effort to understand and improve the anaerobic biodegradation of petroleum hydrocarbons: A literature review. *International Biodeterioration & Biodegradation*, 157, 105156. doi:<https://doi.org/10.1016/j.ibiod.2020.105156>
- Xia, M., Fu, D., Chakraborty, R., Singh, R. P., & Terry, N. (2019). Enhanced crude oil depletion by constructed bacterial consortium comprising bioemulsifier producer and petroleum hydrocarbon degraders. *Bioresource technology*, 282, 456-463.
- Xue, J., Yu, Y., Bai, Y., Wang, L., & Wu, Y. (2015). Marine Oil-Degrading Microorganisms and Biodegradation Process of Petroleum Hydrocarbon in Marine Environments: A Review. *Current Microbiology*, 71(2), 220-228. doi:10.1007/s00284-015-0825-7
- Zhang, B., Matchinski, E. J., Chen, B., Ye, X., Jing, L., & Lee, K. (2019). Marine oil spills—oil pollution, sources and effects. In *World seas: an environmental evaluation* (pp. 391-406): Elsevier.



## Preliminary Investigation on Demulsification of Nigerian Crude Oil Emulsion using Synthesized Bio-Demulsifier

Deborah. C NWAKUBA<sup>1\*</sup>, Ibrahim Ali MOHAMMED-DABO<sup>1\*</sup>, Haruna IBRAHIM<sup>1\*</sup>

National Research Institute for chemical Technology (NARICT), Zaria, Nigeria  
Ahmadu Bello University zaria, Nigeria  
Kaduna Polytechnic, Kaduna Nigeria

[chidimmanwakuba@gmail.com](mailto:chidimmanwakuba@gmail.com), [iroali@mail.ru](mailto:iroali@mail.ru), [ibrahimhauna@gmail.com](mailto:ibrahimhauna@gmail.com)

\*Corresponding author

---

### ABSTRACT

Commercial demulsifiers being used in Nigerian National Petroleum Corporation (NNPC) are not biodegradable which has made it of paramount importance to seek bio-demulsifiers that can be produced in Nigeria from Nigerian vegetable seed oils. In this study, three demulsifiers were produced from Nigerian vegetable seed oils using 15 g of oil, heated to 60 °C, 25 g of paraffin wax, 30 g of starch and 20 g of soap which were homogeneously stirred for 1 hour at 60 °C and tested alongside the commonly commercial demulsifiers being used in NNPC. They all performed very well at thermal test. Calabash demulsifier had high performance of 80% same as commercial demulsifier while Neem demulsifier had 75% and mahogany has 78%. They are, therefore, good enough to replace commercial demulsifiers at improved level.

**Keywords:** biodegradation, bio-demulsifier, demulsification, crude oils, performance

### 1. INTRODUCTION

An emulsion is the dispersion of one liquid on another liquid which are immiscible with one another as in water in crude oil (Venkatesham *et al.*, 2018). Crude oils are produced from the wells in most cases as an emulsion of water-in-oil. During the formation of crude oils in the reservoirs, both oil and water migrate through the porous sedimentary rocks into the reservoir wells, hence they are believed to have met along the path of their migration (Raynel *et al.*, 2021). The presence of water has damage effects on process equipment such as corrosion and poisoning of downstream catalyst in the refinery and the quality of oil products hence, has to be removed before refining processes (Alao *et al.*, 2021). Water-in-oil emulsion raises the viscosity of the fluid thereby increasing the energy required to transport the crude (Balsamo *et al.*, 2017). The concentration of water in crude oils varies depending on the origin and the location of the oil wells. The presence of active surfactants in oil and water such as fatty acids, asphaltenes, resins, solid particles and bases are believed to stabilize the emulsion of water in oils (Raynel *et al.*, 2021). Sometimes, the emulsions are prepared to aid the exploration of petroleum from deeper oil reservoirs (Long *et al.*, 2021). The introduction of the prepared emulsifiers enhances the recovery of the petroleum from the reservoirs by reduction of the viscosity of oil in water hence, facilitating the transportation of the oil (Vallejo-Cardona *et al.*, 2017). After the oils are recovered from the reservoirs, the emulsion has to be broken to obtain clear oils.

The methods used in the dissolution of emulsions in the petroleum industries include; chemical, electrical, thermal, and mechanical techniques (Alao, *et al.*, 2021). The most commonly used among these methods of demulsification is the chemical application (Sofiah *et al.*, 2020). The breaking down of the emulsion into the components is known as demulsification and this requires the application of demulsifiers as in chemical method, mechanical agitation as the mechanical method, electrostatic field application as in electrical method and thermal application as in thermal method. Among them, the chemical method which involves the application of demulsifiers is the easiest and cheapest cost method (Balsamo *et al.*, 2017). Some of the commercial demulsifiers commonly used in petroleum industries include; copolymers of polyoxyethylene and polyoxypropylene or alkylphenol- formaldehyde resins, alkoxyated amines, or mixtures of them as reported by Balsamo *et al.*, (2017). These petrochemical-based demulsifiers have adverse effects on the ecosystem into which the recovered waters are discharged as they are non-biodegradable.

In this investigation, three bio-demulsifiers were produced from three vegetable oils namely: Neem, Mahogany and Calabash growing in Nigeria soil. The three bio-demulsifiers were evaluated alongside commercial demulsifiers to ascertain their efficacies for use in refining.

There are other types of biodegradable demulsifiers which has also shown a good result in the treatment of crude oil emulsion. Lime was used which showed a good demulsification ability, which the concentrate caused water in oil emulsion whose stability increases with increasing concentrate volume to be formed (Folashade *et al.*, 2018). The stability increased with an increase in the concentration of the demulsifier. Another author (Ebikapaye 2018) worked on using glycerol, tri-ethanol amine and xylene, despite being all chemical demulsifiers, glycerol and tri-ethanol amine were reported as being better than xylene but the amount of separation increased with time. The specific gravity of crude oil is not dependent on the amount of brine in emulsion with the crude oil but on the amount of water in crude oil emulsion. Nigerian crude oils on static, dynamic, thermal and basic sediment and water tests.

## 2. MATERIALS AND METHODS

The materials, equipment and experimental procedures are described as follows.

### 2.1 Materials:

The materials used in the production of bio-demulsifiers includes camphor powder used as the lipophilic agent, paraffin oil as the bulking agent, cassava starch form the hydrophilic agent, liquid soap as a binder and distilled water as the solvent for starch (Venkatesham *et al.*, 2018).

### 2.2 Equipment:

Gallenkamp hot plate magnetic stirrer, Pyrex conical flask, Pyrex beaker, viscometer, water bath, syringe, measuring cylinder, pH meter and thermometer.

### 2.3 Extraction of vegetable oil:

The Mahogany and Neem seeds were collected within the premises of the National Research Institute for Chemical Technology (NARICT), Zaria environs while the calabash seeds were purchased from Katsina. The seeds were dehulled and extracted by mechanical pressing in the NARICT neem extraction laboratory (Francis *et al.*, 2016).

#### 2.3.1 preparation of oil field brine:

The synthetic emulsion was produced by dissolving Sodium chloride in deionized water to obtain the required salinity similar to the average Kaduna Refinery and Petrochemical Company (KRPC)'s which is about 2.4% salinity (Falode and Aduroja, 2015) as expressed in

$$Y = 8.3566X - 0.3582 \quad (1)$$

where,

$$Y = \text{Salinity (\%w/w)}; \% \text{ in per thousand}$$

$$X = \text{NaCl concentration (g/100 ml)}$$

The sodium chloride solution was mixed with the crude obtained from KRPC in a 1:1 ratio to obtain a water-in-oil emulsion. It was stirred with a mechanical stirrer for three hours at 1,300 rpm.

#### 2.3.2 preparation of liquid detergent:

A 125 g of Sodium Hydroxide (NaOH) was dissolved in 150 g of distilled water for 24 hours in a plastic bowl, 192 g of Sodium Laurel Sulphate (SLS), 270 g Sodium Trioxocarbonate (IV) ( $\text{Na}_2\text{CO}_3$ ) and 520 g of Sulphonic acid were mixed in another bowl. The two solutions were mixed to form liquid detergent. The mixture was gently stirred, and more distilled water was added to produce a homogeneous mixture of 10 litres with a pH of 9.0 (Francis *et al.*, 2016).

#### 2.3.3 Production of local starch from cassava:

Some quantity of dry cassava powder was purchased from a local market around Sabon Gari market in Zaria. A 262 g of the dry cassava starch was dissolved in 261 g of cold distilled water to form a solution. Boiled distilled water was added to the starch solution and gently stirred to form a paste-like solution (Francis *et al.*, 2016).

#### 2.3.4 Production of local demulsifiers:

The production of demulsifier was carried out using the method adopted from Francis *et al.* (2016) where a mass of 25 g of camphor powder was mixed with 15 g of Mahogany oil in a 500 ml beaker, placed on a heated hot plate magnetic stirrer at a temperature of 40 °C and gently stirred with the follower to completely dissolve the camphor. A mass of 10 g of paraffin wax was added to the hot camphorated Mahogany oil followed by 30 g of prepared cassava starch and 20 g

of prepared liquid detergent and stirred for further 60 minutes. This procedure was also applied to Neem and calabash oil.

### 2.3.5 Analysis of the demulsifiers

#### (a) Static test

Before the test, the emulsion was placed in a water bath at 60°C. 0.5ml of demulsifier was injected into 10 ml of emulsion sample in a centrifuge tube and labelled with the name of the demulsifier. The centrifuge tube is closed and shaken for 5 minutes continuously. After shaking, the sample was kept in the water bath again and the separation of water was noted down after 120 minutes, the experiment was repeated with 1.0, 1.5 and 2.0 ml of demulsifier as reported by Venkatesham *et al.*, (2018).

#### (b) Dynamic test

Dynamic test was carried out using the method adapted from Venkatesham et al (2018) where this 0.5 ml of demulsifier was added to 10 ml emulsion in a centrifuge tube and placed in the water bath for 10 minutes at 60°C as in (Venkatesham *et al.*, 2018). Thereafter, it was removed and placed in a bench centrifuge and spun for 10 minutes at 2,500 rpm. The separation of water was noted down immediately after the centrifuge was stopped. The experiment was repeated with 1.0, 1.5 and 2.0 ml of the demulsifier.

#### (c) Thermal test

The thermal test was conducted according to the method in Francis et al (20116) where a volume of 10 ml of emulsified crude was poured into a calibrated centrifuge tube and 0.5 ml of demulsifier was injected into it and stirred. The bottles were then placed in the water bath at 80°C with the water level at the 10 ml mark. After 120 minutes the volume of water separation was read for each demulsifier.

#### (d) Basic sediments and wastes (BS & W)

The basic sediment and waste test was conducted through adoption of the method used in Abel et al (2017) where five calibrated centrifuge tubes were filled with 10 ml of emulsified crude oil each, and 0.5, 0.1, 1.5, 2.0 and 2.5 ml of demulsifier. A volume of 5 ml of xylene was added to each and they were shaken to obtain a uniform mixture. They were then inserted in a centrifuge and spun for 10 mins at 3000 rpm. After 10 mins the tubes were brought out and the value of the basic sediment and water separated were read for each tube.

## 4. RESULTS AND DISCUSSION

The results of the static test demulsification of Nigerian crude oil by bio-demulsifiers and commercial shows good performance. Calabash seed oil demulsifier at 2 ml concentration had an equal performance as commercial one with 80 % of water removal. This was closely followed by neem seed oil with 75 % water removal with the same quantity as depicted in figure 1. With these results, Calabash seed oil demulsifiers can be a potential replacement commercial demulsifiers. For the sake of environmental degradation, Neem seed oil demulsifiers can also be considered to be better than the commercial ones.

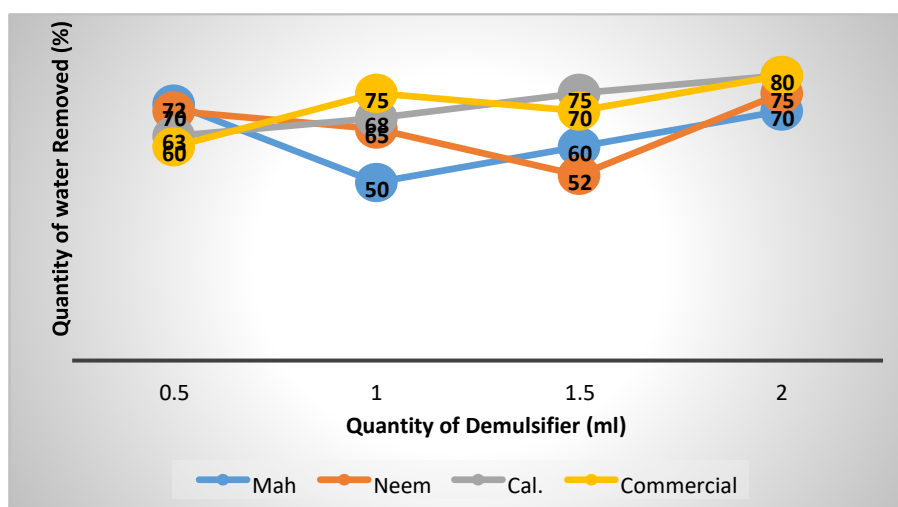


Figure 1: Static Test Performance of bio-demulsifiers and commercial demulsifier

None of the bio-demulsifiers could be compared with commercial demulsifiers for dynamic test performance. The commercial demulsifier had a performance of 60 % water removal with 0.5 ml and this increases with its quantity to 80 %. The bio-demulsifiers had a very low performance with the highest of 45 % water removal by Neem seed oil demulsifier with 0.5 and 1.5 ml. The other two had their highest performance of 40 % water removal as depicted in Figure 2.

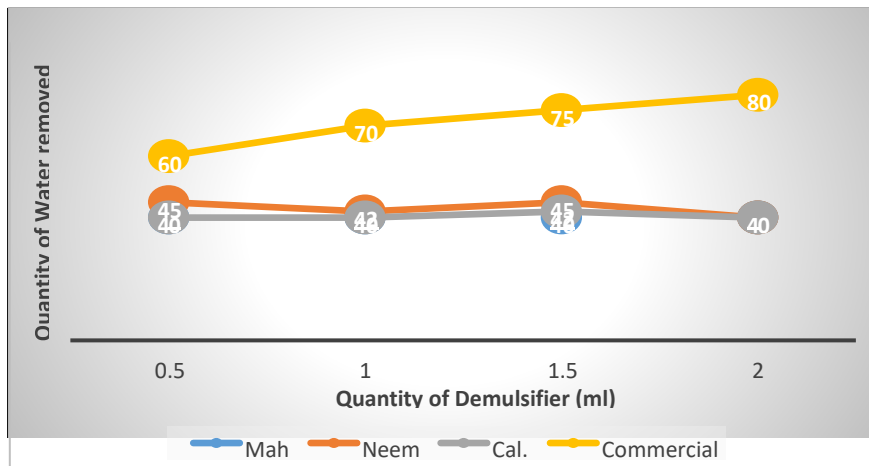


Figure 2: Dynamic Test Performance of bio-demulsifiers and commercial demulsifier

In the thermal test, all the bio-demulsifiers performed very well especially the calabash seed oil demulsifier which exhibited the same performance as commercial. Both have their best performance of 80 % water removal with the quantity of 2ml closely followed by Neem demulsifier, 75 % and Mahogany 70 %. Though Mahogany demulsifier best thermal performance is 72 % water removal with 0.5 ml which was the highest at that quantity among demulsifiers as depicted in Figure 3.

Basic sediment and water removal test shows that Neem seed oil demulsifier shows very good performance. At 1.5ml Neem seed oil demulsifier had 75% basic sediment and water removal while commercial demulsifier had 68% with quantity separated as 78% basic sediment and water as shown in Figure 4.

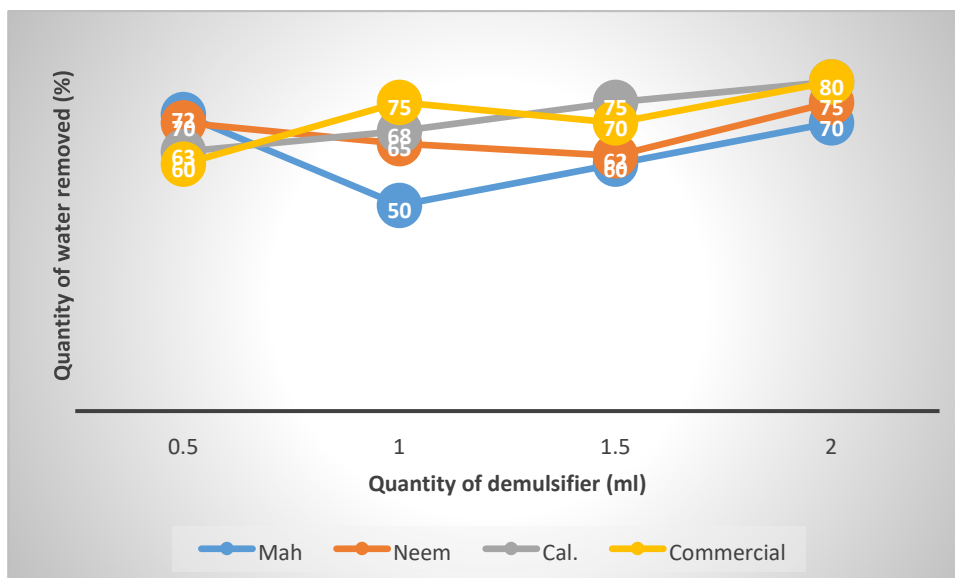


Figure 3: Thermal test performance of bio-demulsifiers and commercial demulsifier

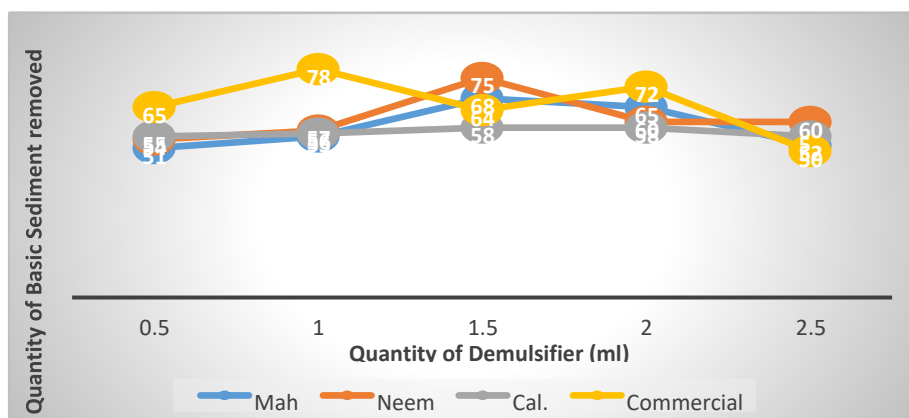


Figure 4: Basic Sediment and water Performance of bio-demulsifiers and commercial demulsifiers.

## 5. CONCLUSION

Three bio-based demulsifiers were prepared from vegetable seed oils grown in Nigeria. The three bio-demulsifiers were tested alongside commercial demulsifiers commonly used by NNPC, for static, dynamic, thermal and basic sediment and water removal. All the bio-demulsifiers performance was encouraging and has a great potential at an improved level, except the dynamic test which they all performed below average. Calabash demulsifier had an equal performance as commercial demulsifier on static and thermal tests with 80 % water removal. Neem demulsifier had the best performance on Basic sediment and water test among the bio-demulsifiers with 75% water removal while commercial demulsifier had 78%.

## REFERENCES

- Ebikapaye Jeffery Peretomode (2018), Demulsification of Crude Oil Emulsion Using Xylene, Polyhydric Alcohol (glycerol), and Tri-ethanol Amine (TEA). *Journal of Agriculture and Food Environment* volume 5(1):68-75
- Francis A.O, Sulaiman A. D.I, Abdusalam .S, (2016), Stability Study of Some Selected Nigerian Crude Oil Emulsion and the Effectiveness of Locally Produced Demulsifier. *Journal of Energy Technologies and Policy*.
- Venkatesham, V., Nasal, M., Robin, M. Joy., Ginto, G. M. 2018. Studies on Demulsification of Crude Oil Emulsion Using Plant Extracts as Green Demulsifiers. *Asian Journal of Applied Science and Technology (AJAST)* (Open Volume 2, Issue 2, Pages 999-1004.
- Raynel, G., Marques, D. S., Al-Khabaz, S., Al-Thabet, M., Oshinowo, L. 2021. A new method to select demulsifiers and optimize dosage at wet crude oil separation facilities. *Oil & Gas Science and Technology – Rev. IFP Energies Nouvelles* 76, 19; <https://doi.org/10.2516/ogst/2020096>
- Long, H., Chen, W., Tan, D., Yang, L., Zhang, S., Wang, S. 2021. Development of a High Temperature and High Pressure Oil-Based Drilling Fluid Emulsion Stability Tester. *Open Journal of Yangtze Gas and Oil*, ISSN Online: 2473-1900 6, 25-35 <https://www.scirp.org/journal/ojogas>.
- Vallejo-Cardona, A. A., M.Artôñez-Palou, R., Chañez-Goámez, B., Garcôaa-Caloca, G., Guerra-Camacho, J., Ceroân-Camacho, R., Reyes-Aâ Vila, J., Karamath, J. R. Aburto, J. 2017. Demulsification of crude oil-in-water emulsions by means of fungal spores. *PLOS ONE* | DOI: 10.1371 1-17
- Alao, K. T., Alara, O. R., Abdurahman, N. H. 2021. Trending approaches on demulsification of crude oil in the petroleum Industry. *Applied Petrochemical Research* <https://doi.org/10.1007/s13203-021-00280-0>
- Balsamo, M., Erto, A., Lancia, A. 2017. Chemical Demulsification of Model Water-in-Oil Emulsions with Low Water Content by Means of Ionic Liquids. *Brazilian Journal of Chemical Engineering*. Vol. 34, No. 01, pp. 273 - 282, dx.doi.org/10.1590/01046632.20170341s20150583.
- Falode, O. A., Aduroja, O. C. (2015). Development of Local Demulsifier for Water-in-Oil Emulsion Treatment. *International Journal of Sciences: Basic and Applied Research (IJSBAR)* ISSN 2307-4531 pp301-318.
- Sofiah Atira Raya, Ismail Mohd Saaid, Abdelazim, Abbas Ahmed, Abubakar Abubakar Umar (2020), A Creitical Review of Development and Demulsification Mechanism of Crude oil Emulsion in petroleum Industries. *Journal of Petroleum Exploration and Production and Production Technology*:101711 - 1728





## Adsorption Behaviour of Naphthalene, Anthracene and Pyrene in Aqueous Medium onto Rice Husk Ash: Removal Efficiency Optimization

Ayobami O. AJANI <sup>a,b</sup>, Ismahil K. SOKUNBI <sup>a,b</sup>, Damilola I. ADEBUKOLA <sup>a,b</sup>, Sofiat, O. GANIYU <sup>a,b</sup>,  
Haleema O. ADEDOSU <sup>c</sup>, Elizabeth F. ARANSIOLA <sup>d</sup>, Tinuade J. AFOLABI <sup>a,b</sup> and Abass O.  
ALADE <sup>a,b,e\*</sup>

<sup>a</sup> Department of Chemical Engineering, Faculty of Engineering, Ladoké Akintola University of Technology, Ogbomoso, Nigeria

<sup>b</sup> Bioenvironmental, Water and Engineering Research Group (BWERG), Ladoké Akintola University of Technology, Ogbomoso, Nigeria

<sup>c</sup> Department of Science Laboratory Technology, Faculty of Pure and Applied Sciences, Ladoké Akintola University of Technology, Ogbomoso, Nigeria

<sup>d</sup> Department of Chemical Engineering, Obafemi Awolowo University, Ile-Ife, Nigeria

<sup>e</sup> Science and Engineering Research Group (SAERG), Ladoké Akintola University of Technology, Ogbomoso, Nigeria

\*Corresponding Author Email: [aoalade@lautech.edu.ng](mailto:aoalade@lautech.edu.ng); Phone: +2347037885961

### ABSTRACT

Polycyclic Aromatic Hydrocarbons (PAHs) are two or more fused aromatic ring compounds that are toxic, carcinogenic and recalcitrant, thus posing risks to the environment and humans. The removal of PAHs from an aqueous solution via adsorption has undergone extensive research and this is extended to the removal of Naphthalene, Anthracene and Pyrene from an aqueous solution using Rice Husk Ash (RHA) as an adsorbent, in this work, under batch adsorption experiment. The raw RH was washed, sun-dried and ashed in a furnace at 700 °C for 4 h. Design Expert (12.1.0) software was employed to optimize the effective mixture ratio (10-80%) of the three samples' concentrations, under Simplex Lattice Design. The maximum removal efficiency of 92.31 %, 98.12 % and 92.06 % was obtained for Naphthalene, Anthracene and Pyrene. The Special-Quartic, Special-Quartic and Quadratic model equations with P-Values and Coefficient of Determination ( $R^2$ ) of 0.0009, 0.9785; < 0.0001, 0.9931; and 0.0046, 0.8416 were generated for Naphthalene, Anthracene and Pyrene, removal respectively. The feasibility of adsorption of PAHs in an aqueous medium using ash-based (rice husk) adsorbent is demonstrated based on the high removal efficiency of the batch adsorption process.

**Keywords:** Adsorption, Optimization, PAHs, Rice Husk Ash, Simplex Lattice Design

### 1. INTRODUCTION

Polycyclic aromatic hydrocarbons (PAHs) are a class of organic compounds that have more than two aromatic rings on their molecules. Incomplete combustion of organic material including wood, tobacco, and charbroiled meat results in the formation of compounds known as PAHs (Abdel-shafy *et al.*, 2016), which can be discharged into surface water from industrial and wastewater treatment facilities. The majority of PAHs are insoluble in water, which restricts their mobility in the environment. (Patel *et al.*, 2020). These compounds can be a threat to the environment and humans since they are recalcitrant, toxic and carcinogenic (Olayinka *et al.*, 2018).

Adsorption techniques are frequently used to remove contaminants from water and wastewater. Adsorption is one of the most efficient, fast and widely applicable remediation treatments (Gul Zaman *et al.*, 2021). Adsorption can be used to remove a variety of contaminants, including organic pollutants and heavy metals, choosing the adsorption type and adsorption conditions. Various types of adsorbents have been used for the removal of PAHs for example. Zeolites (Lemic *et al.*, 2007), and rice husk-activated carbon (Yakout *et al.*, 2013). Rice husk ash has also frequently been utilized as an adsorbent for water treatment.

The fact that rice husk is a cheap, renewable resource and a by-product of rice milling makes it a suitable material for removing various pollutants (Balati *et al.*, 2015). When this by-product builds up, it causes issues with solid waste management that, if not addressed, attract animals that spread illness, and raise the risk of fire (Balati *et al.*, 2015). Rice husk is a cellulose-based fiber and contains approximately 20% silica in amorphous form (Hu *et al.*, 2008). One of the best solutions for addressing the issue of rice husk as waste is the development of adsorbents from it. As a byproduct

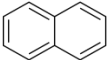
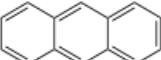
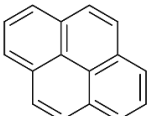
of burning rice husk, ash is produced. Due to its high silica content, rice husk ash (RHA) has good adsorption properties such as its highly porous structure and large specific surface area. An experiment on simultaneous methylene blue adsorption and PH neutralization of contaminated water onto rice husk ash (RAH) was done by (Teruhisa *et al.*, 2021). This experiment aims to evaluate the removal efficiency of ash from locally accessible material (rice husk), for adsorbing naphthalene (NA), anthracene (AN), and pyrene (PY).

## 2. MATERIALS AND METHODS

### 2.1 Chemical and Reagents

Analytical-grade naphthalene (NA), anthracene (AN), pyrene (PY), and distilled water were used. These PAHs were chosen due to their frequent occurrence in petroleum and their properties. These are considered to be examples of two, three and four-ringed PAHs. The three examined PAHs' environmental and biological behavior can best be described by some of their physicochemical properties (Table 1). The compounds have low solubility in water and their solubility in water decreases as the aromatic ring increases except for anthracene. The procedure specified was followed in the preparation of a stock solution of the adsorbate, NA, AN, and PY. Specifically, a known mass (0.25g) of NA, AN, and PY was dissolved in 1000ml of distilled water and then shaken for a homogenous mixture. Then the initial concentration of the PAHs used was 250 mg/l.

Table 1: PAH's Physicochemical Properties

Compound	Structure	Formula	Molecular weight(g/mol)	BP(°C)	Solubility(mg/l)	Log $K_{ow}$
Naphthalene		C <sub>10</sub> H <sub>8</sub>	128.17	218	31.7	3.30
Anthracene		C <sub>14</sub> H <sub>10</sub>	178.23	340	0.022	4.45
Pyrene		C <sub>16</sub> H <sub>10</sub>	202.26	404	0.146	5.1

### 2.2 Adsorbent

#### 2.2.1 Preparation of the Rice Husk

The rice husk in this experiment was collected at a rice milling factory in Ogbomoso, Oyo State, Nigeria. The rice husk was washed thoroughly with distilled water to remove dirt and then sun-dried for 48hr. To obtain uniform particle size Automatic Sieve Shaker and US Tyler Standard screen were used to sieve the rice husk and the size retained in mesh 40 which is (420µm) was used.

#### 2.2.2 Calcination Process of Rice Husk

The rice husk was burned at 700°C for 4h in a porcelain crucible inside an electric furnace to get the ash, which was then allowed to cool at ambient temperature. Since we are focused on amorphous silica and not crystalline silica, the chosen temperature and time (700°C for 4h) give the best characterization results in terms of ash content.

### 2.3 Experimental Design

Design of the Design Expert (DOE) (12.1.0) software was used to optimize the effective mix ratio of the mass composition of the adsorbates. The selected range of mixture used was between (10- 80) %, and it was run to generate the experimental run at random.

### 2.4 Adsorption studies

Adsorption experiments were carried out using batch techniques to examine and evaluate variables significant to the removal efficiency (%) of the three PAHs which are NA, AN, and PY. To start the adsorption, process the PAHs mixture made from NA, AN, and PY was 100ml in volume, which was poured into 1g of Rice Husk Ash (RHA) in a 250ml flask after 5mins, the adsorption process was discontinued and the solution of RHA and mixed PAHs was centrifuged at speed of 1000rpm for 10minutes. The residual PAH concentration in the reaction mixture was determined using a UV – Visible spectrophotometer with the wavelength of PAHs set at 315nm, 430nm, and 335nm for NA, AN, and PY respectively. The final concentration was calculated from the absorbance.

## 3.0 RESULTS AND DISCUSSION

### 3.1 Removal efficiency (RE) of Rice Husk Ash (RAH)

The Design Expert (12.0) software's Optimal Design tool was used for the experimental design for the adsorption of PY, NA, and AN onto RAH in this study. From the fourteen experimental runs generated by the design expert, the

## Adsorption Behaviour of Naphthalene, Anthracene and Pyrene in Aqueous Medium onto Rice Husk Ash: Removal Efficiency Optimization

maximum RE recorded for PY is 92.31% at Run 2 (80% PY, 10% NA and 10% AN), 98.12% RE for NA at Run 14 (10%PY, 80%NA and 10%AN) and 92.06% RE for AN at Run 3(21.67%PY, 56.67%NA and 21.67%AN) respectively.

While the minimum RE recorded for PY, NA and AN are 50.88%, 41.78% and 0.83% at Run 14, Run 6 and Run 2 respectively (Table 2). The maximum RE of RHA unto NA at run 14 which is 98.12% of this experiment shows that RAH has more affinity for NA compared to PY at Run 2 where it has a maximum RE to be 92.31% and AN at Run 3 where it has maximum RE to be 92.06. After which run 13 of the optimal design of the experiment provide to have the maximum removal efficiency of 92.31%, 98.12%, and 92.06% for NA, AN, and PY respectively.

Table 2: Batch adsorption research response and experimental design matrix

Run	Space Type	Component (%)			Removal Efficiency (%)		
		A: pyrene	B: naphthalene	C: atrazine	(Pyrene)	Naphthalene	Anthracene
1	Vertex	80	10	10	85.91	48.36	1.67
2	Vertex	80	10	10	92.31	45.54	0.83
3	AxialCB	21.67	21.67	56.67	72.11	66.63	92.06
4	AxialCB	21.67	56.67	21.67	81.24	93.29	10.77
5	CentEdge	45	45	10	78.41	78.4	16.67
6	CentEdge	45	10	45	91.05	41.78	54.07
7	CentEdge	45	45	10	78.72	81.85	30
8	CentEdge	10	45	45	59.72	94.78	57.96
9	AxialCB	56.67	21.67	21.67	83.41	64.46	78.08
10	Vertex	10	10	80	57.24	88.73	79.38
11	Vertex	10	80	10	51.24	92.96	67.5
12	Vertex	10	10	80	57.24	86.85	78.75
13	Center	33.33	33.33	33.33	75.19	80.42	87.25
14	Vertex	10	80	10	50.88	98.12	5

### 3.2 Response

It is shown in Table 3 that the model equation for the Removal efficiency of Pyrene, Naphthalene is Special quartic and for Anthracene it is Quadratic. It also shows in the table that the transform of Removal efficiency for Pyrene and Naphthalene is none while the transform of Removal efficiency for Anthracene is inverse sqrt. With a standard deviation of 14.52, 19.32 and 34.79 for Pyrene, Naphthalene and Anthracene respectively.

Table 3. Response to Removal Efficiency of Pyrene, Naphthalene and Anthracene

Response	Name	Units	Transform	Model
R1	Removal Efficiency (Pyrene) RE	%	None	Special Quartic
R2	Removal Efficiency (Naphthalene) RE	%	None	Special Quartic
R3	Removal Efficiency (Anthracene) RE	%	Inverse Sqrt	Quadratic

### 3.3 Fit Summary

Table 4 shows the fit summary for the PY, NA and AN model that was obtained from the DOE optimal design tool. Table 4 shows that Quadratic and Special quartic vs Quadratic are the suggested model for the removal of Pyrene and naphthalene with an adjusted R<sup>2</sup> to be 0.8435 and 0.9821 and predicted R<sup>2</sup> values to be 0.7547 and 0.7713. While Quadratic model is the suggested model for the removal of Anthracene with adjusted R<sup>2</sup> and predicted R<sup>2</sup> are 0.7427 and 0.4786 respectively. It is also shown in Table 4 that Cubic, Quartic vs Cubic and Quartic vs Special Quartic models are aliased.

### 3.4 Analysis of Variance

The model is suggested to be significant by the model F-value of 28.38 and 90.03 for the Special quartic model of pyrene and naphthalene respectively. A large F-value could occur due to noise with 0.09% and 0.01% chance for pyrene and naphthalene (Table 5). And the model F-value of 8.50 for the Quadratic model suggested the model is significant and a large F-value could occur due to noise with a 0.46% chance (Table 5). Model terms are significant when the P-value is less than 0.0050. In the case of the Special quartic model of pyrene, A, B, C, AB, AC, A<sup>2</sup>, BC, and AB<sup>2</sup>C are considered to be significant model terms. While for the Special quartic model of naphthalene, A, B, C, AB, AC, A<sup>2</sup>, BC, and ABC<sup>2</sup> are considered to be significant model terms. And for the Quadratic model of anthracene A, B, AB, and AC are considered to be significant model terms. A value higher than 0.1000 implies the model terms are not significant.

Table 4: Fit Summary for Pyrene, Naphthalene and Anthracene

Source	Sequential p-value	Adjusted R <sup>2</sup>	Predicted R <sup>2</sup>	
Linear	0.0006	0.6974	0.5721	
Quadratic	0.0412	0.8435	0.7547	Suggested
Special Cubic	0.8339	0.8223	-0.1609	
Cubic	0.0241	0.9440	-0.7059	Aliased
Special Quartic vs Quadratic	0.0442	0.9440	-0.7059	Suggested
Linear	0.0001	0.7692	0.7024	
Quadratic	0.0064	0.9265	0.8912	
Special Cubic	0.1352	0.9403	0.7205	
Cubic	0.0213	0.9821	0.7713	Aliased
Special Quartic vs Quadratic	0.0175	0.9821	0.7713	Suggested
Quartic vs Cubic	0.3094	0.9833		Aliased
Quartic vs Special Quartic	0.3094	0.9833		Aliased
Linear	0.0246	0.3976	0.0880	
Quadratic	0.0199	0.7427	0.4786	Suggested
Special Cubic	0.8636	0.7072	-0.3164	
Cubic	0.2580	0.7616	0.6274	Aliased
Special Quartic vs Quadratic	0.3958	0.7616	0.6274	

Table 5: ANOVA of Special Quartic Model (Pyrene), (Naphthalene) and Quadratic Model (Anthracene)

Source	Sum of Squares	Df	Mean Square	F-value	p-value	
Model	2682.25	8	335.28	28.38	0.0009	Significant
Linear Mixture	2039.52	2	1019.76	86.32	0.0001	
AB	100.99	1	100.99	8.55	0.0329	
AC	277.09	1	277.09	23.46	0.0047	
BC	31.25	1	31.25	2.65	0.1648	
A <sup>2</sup> BC	102.12	1	102.12	8.64	0.0322	
AB <sup>2</sup> C	164.03	1	164.03	13.88	0.0136	
ABC <sup>2</sup>	16.65	1	16.65	1.41	0.2884	
Residual	59.07	5	11.81			
Lack of Fit	38.45	1	38.45	7.46	0.0524	not significant
Pure Error	20.62	4	5.16			
Model	4818.03	8	602.25	90.03	< 0.0001	Significant
<sup>(1)</sup> Linear Mixture	3904.04	2	1952.02	291.82	< 0.0001	
AB	102.92	1	102.92	15.39	0.0112	
AC	541.29	1	541.29	80.92	0.0003	
BC	6.37	1	6.37	0.9521	0.3740	
A <sup>2</sup> BC	100.50	1	100.50	15.02	0.0117	
AB <sup>2</sup> C	20.40	1	20.40	3.05	0.1412	
ABC <sup>2</sup>	58.48	1	58.48	8.74	0.0316	
Residual	33.45	5	6.69			
Lack of Fit	8.45	1	8.45	1.35	0.3094	not significant
Pure Error	24.99	4	6.25			
Model	0.9773	5	0.1955	8.50	0.0046	Significant
<sup>(1)</sup> Linear Mixture	0.5693	2	0.2846	12.38	0.0036	
AB	0.2292	1	0.2292	9.97	0.0134	
AC	0.1756	1	0.1756	7.64	0.0245	
BC	0.0000	1	0.0000	0.0006	0.9803	
Residual	0.1839	8	0.0230			
Lack of Fit	0.0775	4	0.0194	0.7284	0.6169	not significant
Pure Error	0.1064	4	0.0266			

### 3.5 Model Equations

The model equation (1), (2), and (3) were obtained in terms of the L pseudo component in the Removal efficiency of pyrene, naphthalene and Anthracene respectively. This implies that making predictions about the reaction for specific levels of each factor is possible using the equation in terms of coded factors. By default, the mixture's high levels are represented as +1, and its low levels are coded as 0. The coded equation can be used to compare the factor coefficients and determine the relative importance of the components.

$$\text{Removal Efficiency (Pyrene)} = 89.33A + 51.28B + 57.46C + 34.78AB + 11AC + 24.87BC - 998.37A2BC + 1265.27AB2C - 408.93ABC2 \quad (1)$$

$$\text{Removal Efficiency (Naphthalene)} = 46.85A + 95.44B + 87.69C + 35.11AB - 103.58AC + 11.24BC + 990.39A2BC + 446.26AB2C - 766.32ABC2 \quad (2)$$

$$(\text{Removal Efficiency (Anthracene)})^{1/2} = 0.90024A + 0.3082B + 0.1196C - 1.57AB - 1.65AC - 0.0152BC \quad (3)$$

Where A = Pyrene, B = Naphthalene and C = Anthracene

### 3.6 Fit Statistics

For Pyrene the negative According to predicted  $R^2$ , the overall mean might be a more accurate predictor of response than the current model. Sometimes a higher-level model can also predict more accurately. While for Naphthalene the Adjusted  $R^2$  of 0.9821 and the Predicted  $R^2$  of 0.7713 are more than 0.2 apart, which is not as close as one may often expect. This might point to a significant block effect or suggest that there is an issue with your model and/or data. Model reduction, response transformation, outliers, and other factors should be taken into account. And for Anthracene the Predicted  $R^2$  of 0.4786 is not as near to the Adjusted  $R^2$  of 0.7427 as one may typically anticipate; the discrepancy is greater than 0.2. This can suggest a significant block effect or point to a potential issue with the model and/or data. The signal-to-noise ratio is measured by Adeq precision. A ratio greater than 4 is preferred. The ratio of 14.749 for Pyrene, 26.071 for Naphthalene, and 8.540 for Anthracene indicate that there is a sufficient signal. These models can be used to move the design space.

Table 6: Fit statistics table of PY, NA and AN

	Pyrene	Naphthalene	Anthracene
Std. Dev.	3.44	2.59	0.1516
Mean	72.48	75.87	0.2849
C.V. %	4.74	3.41	53.23
$R^2$	0.9785	0.9931	0.8416
Adjusted $R^2$	0.9440	0.9821	0.7427
Predicted $R^2$	-0.7059	0.7713	0.4786
Adeq Precision	14.7491	26.0713	8.5403

#### 3.7.1 Actual, Predicted and Residual Values

The plot of the Normal plot of residuals for removal efficiency of Pyrene, Naphthalene and Anthracene in (Fig. 1a, b and c) shows how well spread the points are on the graph. It shows on the graph that the point on the Naphthalene graph is well spread compared to that of Pyrene and Anthracene. Anthracene has less stacking compared to Naphthalene and Pyrene has more stacking making it have maximum error compared to Naphthalene and Anthracene. Figure 2 is related to the residual value (Table 7). Where all the points above the line in Figures (2a-c) indicate the number of runs for the residual values that are positive and all points below the line indicates the number of runs for the residual values that are negative.

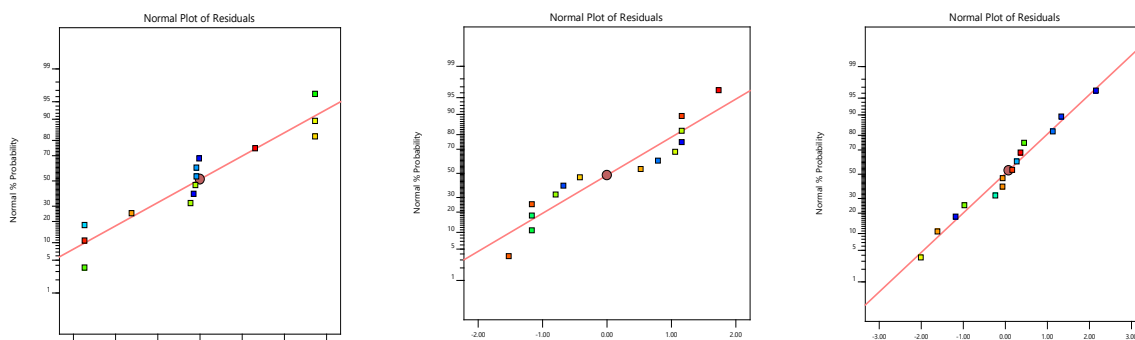


Figure 1. Normal plot for residual of Pyrene (a), Naphthalene (b) and Anthracene (c)

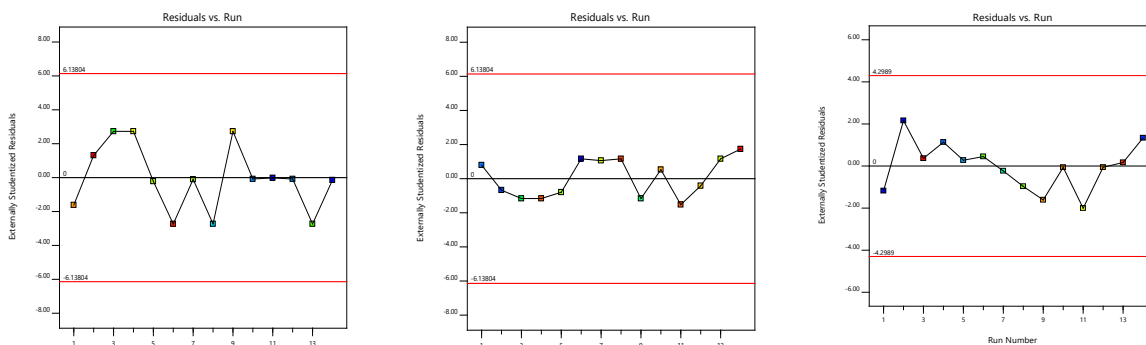


Figure 2. Residual vs Run plot for Pyrene(a), Naphthalene(b) and Anthracene(c)

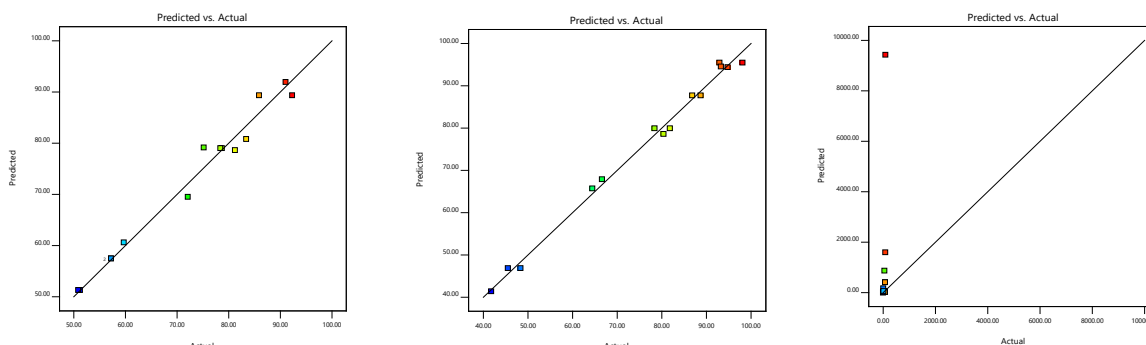


Figure 3. Predicted vs Actual plot for Pyrene(a), Naphthalene(b) and Anthracene(c)

### 3.8 Response Surface Plot

The equation model's current condition for each RE of the Pyrene, Naphthalene, and Anthracene is shown in Figure 5. The 3D areas' flat surfaces show that the equation is linear, it shows in the 3D that Pyrene, Naphthalene and Anthracene have flat surfaces. The red region of the figures represents the area where the adsorption process is occurring, while the blue region represents the area where the adsorption process is occurring the least, and the green region represents the area where the adsorption process is feasible. Comparing the 3D and contour of the Anthracene it is shown in the 3D of Anthracene that the red region and the green region are hidden.

## Adsorption Behaviour of Naphthalene, Anthracene and Pyrene in Aqueous Medium onto Rice Husk Ash: Removal Efficiency Optimization

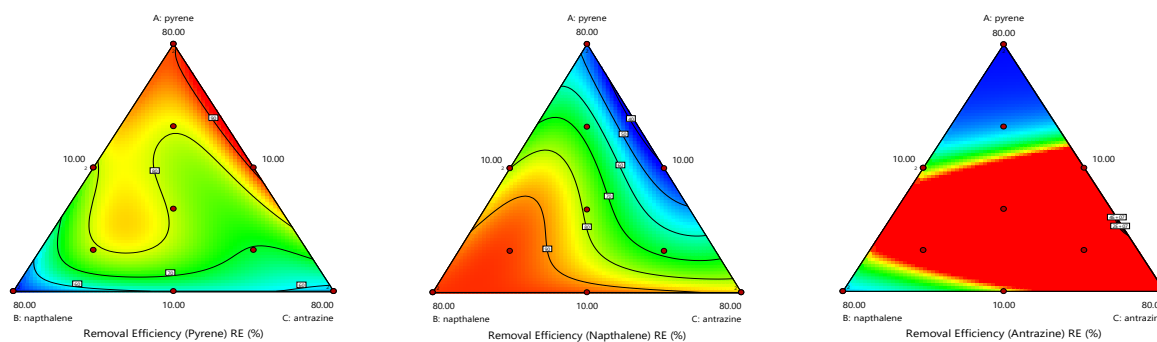


Figure 4: 2D view of the Removal Efficiency of Pyrene, Naphthalene and Anthracene

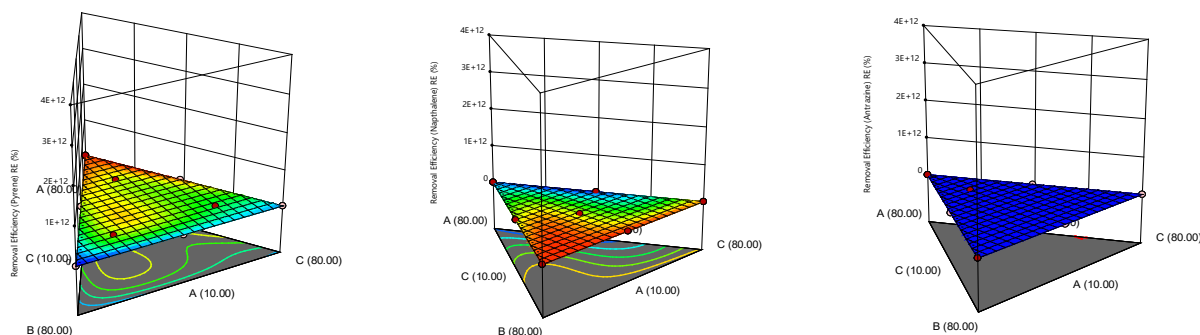


Figure 5: 3D view of the Removal Efficiency of Pyrene, Naphthalene and Anthracene

## CONCLUSION

Using the DOE optimal design tool, it was successfully examined how Rice Husk Ash (RHA) can remove Pyrene, Naphthalene, and Anthracene from wastewater. Pyrene, Naphthalene and Anthracene had the highest Removal efficiency of the RHA at runs 2, 14 and 3 corresponding with 92.31%, 98.12% and 92.06%. The Special quartic and Quadratic models were developed for process optimization and statistical experimental designs. The usefulness of these models for understanding and foreseeing the interactions between the selected process factors was demonstrated.

## REFERENCES

- Avani B.P., Shabnam S., Kunal R., Chirayu D., and Datta M., (2020). Polycyclic Aromatic Hydrocarbons: Sources, Toxicity, and Remediation Approaches. *Front. Microbiol.*, 05 November 2020, *Sec. Microbiotechnology*. <https://doi.org/10.3389/fmicb.2020.562813>.
- Humaira G.Z., Lavania B., Rajashekhar P, Pradeep K., Singa, S., Umer I., and Shamsul Rahman M.K., (2021). Produced Water Treatment with Conventional Adsorbents and MOF as an Alternative. *Materials*. 14(24): pp.7607.
- Hussein I.A. and Mona S.M.M. (2016). Polycyclic, aromatic hydrocarbons: source, environmental impact, effect on human health and remediation. *Egyptian Journal of Petroleum*, 25(1). <https://doi.org/10.1016/j.ejpe.2015.03.011>
- Jovan L., Magdalena Tomašević-Čanović, Milan Adamović, Dragana Kovačević, Sonja Milićević.(2007). Competitive adsorption of polycyclic aromatic hydrocarbons on organo-zeolites. *Microporous and Mesoporous Materials*. 105(3): pp. 317-323.
- Oluwafunmilayo O.O., Adetomi A.A., Olusoji, O.O., and Aladesida, A.A. (2018). Concentration of Polycyclic aromatic hydrocarbons and estimated human health risk of water samples around Atlas Cove, Lagos, Nigeria. *Journal of Health and Pollution* 8(20)pp. 210. <https://doi.org/10.5696/2156-9614-8.20.181210>.
- Teruhisa H., Michiru M., Yuji H., and Hironobu A. (2021) Simultaneous Methylene Blue Adsorption and pH Neutralization of Contaminated Water by Rice Husk Ash. *ACS Omega*. 16;6(33):pp 21604-21612.
- Yakout, S.M., Daifullah, A.A.M., and El-Reefy, S.A. (2013) Equilibrium and Kinetic studies of sorption of Polycyclic aromatic hydrocarbons from water using rice husk activated carbon. *Asian Journal of Chemistry*. 25(18): pp. 10037-10042.



## Study on Electrical and Thermal Conductivities of Optimised Rice Husk Particleboard

Lucas HAMIDU<sup>1</sup>, Umar AROKE<sup>2</sup>, Odeh OSHA<sup>3</sup> and Idris MUHAMMAD<sup>1</sup>

<sup>1</sup>Nigerian Building and Road Research Institute

<sup>2</sup>Abubakar Tafawa Balewa University, Bauchi

<sup>3</sup>University of Calabar

\*Corresponding author: [lucadohamidu@gmail.com](mailto:lucadohamidu@gmail.com)

### ABSTRACT

The study determined the electrical and thermal conductivities of the optimised particleboard produced from rice husk waste and R7AD2 adhesive produced from polystyrene waste. The electrical conductivity was determined using industrial insulation test resistance tester and the thermal conductivity was determined using Lee's disc method based on industrial standard. This was to ascertain the extent of the resistance of the particleboard to electrical conductivity and the thickness of the particleboard for energy conservation. The optimised RHP8 particleboard resistance ranges from  $1.52 \times 10^{10} \Omega$  to  $1.21 \times 10^{10} \Omega$ , while the corresponding power ranges from  $1.64 \times 10^{-5}$  to  $2.07 \times 10^{-3}$  Watts at 500 V and 5000 V test. The rate of heat transfer and thermal conductivity at RHP8  $20 \times 20$  thickness were 28.41 Watts and  $8.1 \times 10^{-4}$  W/m. K respectively. This inferred that the optimised RHP8 particleboard produced from rice husk using R7AD2 adhesive is highly resistant to electric shock and can conserve energy for thermal comfort of the user in structural environment at 20 mm thickness size as desired.

**Keywords:** Electrical conductivity, optimised, particleboard, rice husk, thermal conductivity.

### 1. INTRODUCTION

Waste generation from agro-based by product plays a vital role as industrial raw material in production of furniture such as particleboard. The usage of particleboard cut across divers systems like flooring, stair trends and underlayment (Pan *et al.*, 2007), interior and exterior applications, wall, ceiling panels, office dividers, bulletin boards, cabinets, counter and desks (Alam *et al.*, 2015) and other non-structural architectural applications (Harshavardhan & Muruganandam 2017).

In Nigeria, bulk of the rice husk generated at the milling sites are not harnessed for any industrial application, and therefore the end points are burning or dumped on the land. The research carried out on rice husk as raw material for particleboard production using different binders includes rice straw (Hussein *et al.*, 2018), rice husk (Temitope *et al.*, 2015; Da Silva Cesar *et al.*, 2017) and rice husk with R7AD2 adhesive (Hamidu *et al.*, 2021) among others.

Particleboard acceptability depends on characteristic properties such as water absorption, density, thickness swelling, resistance to electrical conductivity, thermal conductivity and mechanical properties among others for usage. Thus, the desired to determine electrical conductivity, rate of heat transfer and thermal conductivity of the optimised RHP8 particleboard was sort in this research as water absorption, thickness swelling, and density had been previously determined as reported by Hamidu *et al.*, (2021).

Electrical conductivity indicates the quality of a material to conduct electricity. Asha (2017) carried out electrical conductivity test on particleboard from rice husks, using wire connected between rice husk board and electric bulb, when the bulb failed to glow, it was concluded that the bulb does not conduct electricity, and so it is a bad conductor. However, the electrical resistance of an insulation material should be varied across several voltages to determine the extent of resistance other than the electric bulb lighting.

Thermal conductivity of a particleboard is a cardinal factor in energy conservation and its efficiency that could offer some resistance to heat in the build environment when used as furniture. Geankoplis (1978) defined thermal conductivity (k) as the time rate of heat flow through unit thickness expressed by Fourier's Law in terms of heat transfer. According to Samuel, Ramon & Johnson (2012) and Geankoplis (1978) Wood and corkboard exhibits lower thermal conductivities with excellent heat insulation properties compared to other building materials such as aluminum, iron, marble, glass and concrete as reported by (Aggrey-Smith, Preko & Owusu 2016) and papyrus fibers (Singhadej & Kumfu 2011). Previous researches on thermal conductivity of particleboard includes properties of wood-gypsum boards by (Bekhta & Dobrowolska 2006), sawdust additives to clay by (Folaranmi 2009), thin film materials using the  $\omega$  method by (Zhang, Behbahanian & Roberts 2020), hot plate method by (Wayne 1967), heat flow method by (Czajkowski *et al.*, 2016), flat



disc method by (Paul & Layi, 2014), Lees disc method by (Bakam *et al.*, 2020; Ebong, Attai & Joshua, 2016) and light flash process thermal diffusivity of commercial MDF by (Zhou *et al.*, 2013).

In this work, the Lees disc method was adopted in determination of thermal conductivity of optimized particleboard from rice husk by varying the thickness ( $\Delta x$ ) of the material. The process is the most effective in determination of thermal conductivity of a material with low thermal conductivity, being the easy-to-find parts that anyone can assemble, operate and to provide a better understanding of how to obtain desire output, than other methods reported (Theasy, Yulianto & Astuti, 2017).

## 2. METHODOLOGY

Three (3) specimens of optimised RHP8 particleboard produced from rice husk and R7AD2 adhesive (RHP8) (Hamidu *et al.*, 2021; 2022), was cut into 50 by 50 by 20 mm sizes for the electrical conductivity test using industrial standard insulation test resistance tester UNI-T Model UT513 (Electrical Construction and Maintenance, 2020) as employed by the electricity company as presented in Plate 1. The meter was set to test the resistances at 500, 1000, 2500 and 5000 Volt (V). While the current (I) passing through the optimised RHP8 particleboard was determined using Equation 1 and the electric power (P, Watts) was determined using Equation 2 (Paul & Layi, 2014).

$$V = I \cdot R \quad (1)$$

$$P = I^2 R \quad (2)$$

Where, P = Electric power (Watts), I = current passing through the optimised RHP8 particleboard (ampere) and R = resistance of the optimised RHP8 particleboard (ohm ( $\Omega$ )).



Plate 1: Determination of Insulation Property of RHP8 Particleboards

Thermal conductivity of the optimised RHP8 particleboard by (Hamidu *et al.*, 2022) was carried out using Lee's disc method according to (Antwi-Boasiako & Boadu 2017; Aggrey-Smith, Preko & Owusu, 2016). Two (2) specimen each of the optimized RHP8 particleboard was cut into a disc plate size using power flex jig saw to the thickness ( $\Delta x$ ) of  $20 \pm 0.01$  mm,  $15 \pm 0.01$  mm and  $10 \pm 0.01$  mm each having diameter of  $110 \pm 0.01$  mm Plate 2.



Plate 2: Disc Plates of the Optimised RHP8 Particleboard

In Plate 3, thermal conductivity experimental set-up using Lee's disc method is presented.

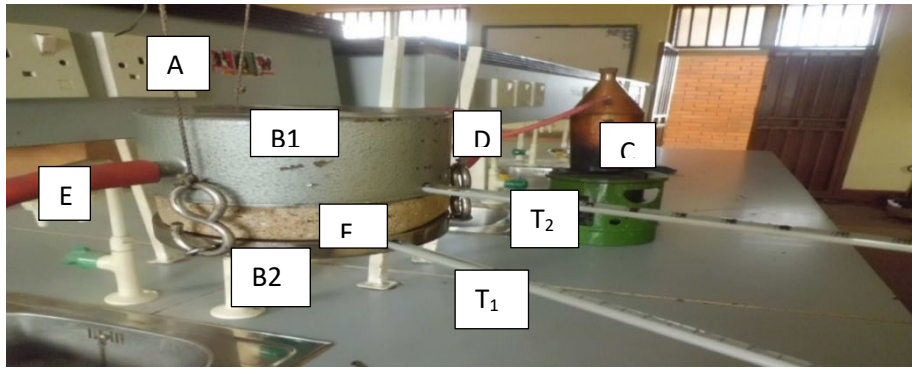


Plate 3: Determination of Thermal Conductivity of Optimised RHP8 Particleboard

Prior to start of experiment, ambient temperatures as  $T_1^\circ$  and  $T_2^\circ$  ( $^\circ\text{C}$ ) was recorded. The boiler labeled C was filled with water to  $\frac{3}{4}$  capacity by volume followed by insertion of thermometers at  $T_1$  and  $T_2$  and sandwiched with particleboard (F) in between and the steam chamber (B1) and copper brass disc (B2) supported on 3 stringed clamp stand (A). Then the boiler inlet (D) and outlet (E) were connected to the steam chamber (B1) and steam was passed through to heat the base and conducted across the copper brass disc (B2) through the particleboard disc (F). The temperatures at  $T_1$  and  $T_2$  began to rise steadily until steady state was reached and allowed to stabilize for 10 minutes before the temperatures value were recorded. Thereafter,  $T_1$  and  $T_2$  were swapped while heating continues until steady state to obtain the reverse temperatures at  $T_1$  and  $T_2$ .

Thereafter, the particleboard disc and steam chamber were removed while the copper brass disc (B2) was heated directly until the temperature was  $7^\circ\text{C}$  above  $T_1$  recorded at steady state. Then heating was disconnected and allowed to stabilize for uniform distribution of heat on the copper brass disc (B2) for 2 – 3 minutes. Followed by placement of particleboard disc (F) on the copper brass disc (B2) to start recording the cooling temperature at every 1 minute intervals until when the temperature fell to  $10^\circ\text{C}$  less than  $T_1$  at steady state as presented in Plate 4.

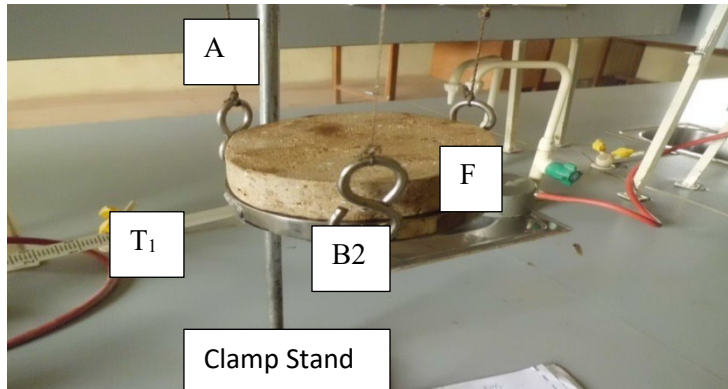


Plate 4: Cooling Time Study of Optimized RHP8 Particleboard

Equations 3 to 6 were used in determination of the thermal conductivity and rate of heat transfer of optimized rice husk particleboard (RHP8) at the tested thickness sizes. Area of particleboard was calculated using Equation 3 (Antwi-Boasiako & Boadu, 2017).

$$A = \frac{\pi d^2}{4} \quad (3).$$

where, A = cross sectional area normal to the direction of flow of heat ( $\text{mm}^2$ ).

The slope of the curves which is the change in temperature of the disc and time taken to cool were determined using Equation 4 (Aggrey-Smith, Preko & Owusu 2016).

$$S = \frac{dT}{dt} \quad (4).$$

where, S = slope of the cooling curve,  $dT$  = change in temperature as the disc cooled and  $dt$  = the differential in time as the copper brass disc cooled.

The rate of heat transfer through the disc was calculated using Equation 5 (Aggrey-Smith, Preko & Owusu 2016; Ojo *et al.*, 2009).

$$Q = mC_p \left( \frac{dT}{dt} \right) \quad (5).$$

where,  $Q$  = rate of heat transfer rate (W),  $m$  = mass of the copper brass disc (kg),  $C_p$  = specific heat capacity of the copper brass disc (J/kg. K).

Equation 6 was used to determine the thermal conductivity (Aggrey-Smith, Preko & Owusu 2016; Kharshiduzzaman *et al.*, 2019).

$$k = \frac{mC_p\Delta x}{A(T_2 - T_1)} S \quad (6)$$

where;  $k$  = thermal conductivity (W/m. K),  $\Delta x$  is the distance (m),  $T_2 - T_1$  = disc cooling temperature (K).

The error in slope and diameter of the disc were determined using Equations 7 and 8 (Aggrey-Smith, Preko & Owusu 2016).

$$S = \left( \frac{S_1 - S_2}{S_m} \right)^2 \quad (7)$$

$$d = \left( 2 \frac{d - d_m}{d} \right)^2 \quad (8)$$

Error in thickness was determined using Equation 9 (Aggrey-Smith, Preko & Owusu 2016).

$$\Delta x = \left( \frac{x - x_m}{x} \right)^2 \quad (9)$$

Error in Temperature reading was determined using Equation 10 (Aggrey-Smith, Preko & Owusu 2016; Antwi-Boasiako & Boadu 2017).

$$T = \left( \frac{\Delta T_2 + \Delta T_1}{T_2 - T_1} \right)^2 \quad (10)$$

And error in thermal conductivity was determined using Equation 11 (Antwi-Boasiako & Boadu 2017 p.74).

$$\Delta k = k\sqrt{S + d + \Delta x + T} \quad (11)$$

where;  $\Delta k$  = change in thermal conductivity.

### 3. RESULTS AND DISCUSSION

In this section, the results of optimised RHP8 particleboards based on the electrical and thermal conductivities variants were studied.

#### 3.1 Electrical Conductivity of Optimised RHP8 Particleboard

Electrical conductivity was carried out on the particleboard to determine its insulation property as presented in Figure 1 showing the relationship between the resistance and voltage at tested readings.

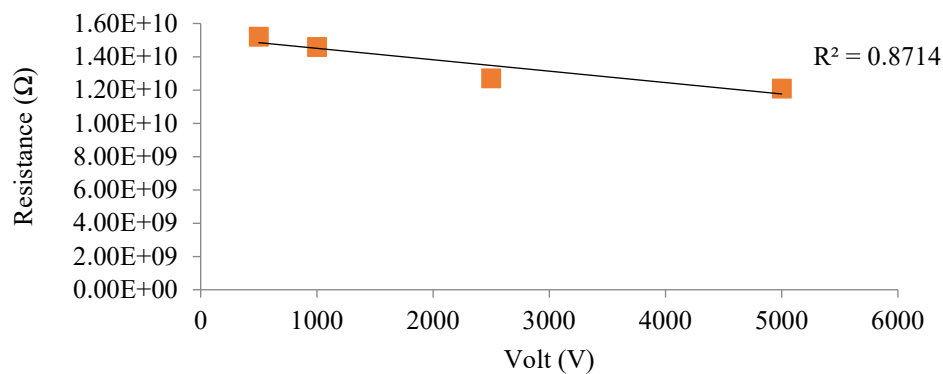


Fig. 1: Electrical Conductivity of Optimised RHP8 Particleboard

At 500 V and 5000 V, the resistances of the RHP8 were  $1.52 \times 10^{10} \Omega$ , and  $1.21 \times 10^{10} \Omega$  respectively. This implies that the optimised RHP8 particleboard produced from rice husk and R7AD2 adhesive (Hamidu *et al.*, 2021) has demonstrated high resistance to electrical conductivity which can withstand 5000 V as against the use of the electric light bulb for insulation test which ranges from 220 – 240 V by Asha (2017). It also inferred that the produced and optimised RHP8 particleboard had shown high resistance to electric shock. The regression values ( $R^2$ ) generated from the plots of voltage-resistance depicting the insulation property's relationship was 0.8714, which is adequate to predict the reliability of the RHP8 insulation up to 5000 Voltage as presented in Figure 2 for the particleboard.

The current-voltage relationship shows that, the lower the voltage, the lower is the current flowing through the optimised RHP8 particleboard. This implies current is directly proportional to the voltage and inversely proportional to the resistance. Thus, the RHP8 particleboard had demonstrated high insulation ability that can withstand voltage up to 5000 as electrical insulator with maximum current ( $I$ ) of  $4.13 \times 10^{-7}$  amp. The corresponding power ( $P$ , Watts) depicting the capacity of the particleboards were determined using several power factors such voltage-resistance and current-resistance. At the minimum voltage of 500, the power was  $1.64 \times 10^{-5}$  Watts and at the maximum voltage of 5000,  $2.07 \times 10^{-3}$  Watts

obtained for the RHP8 particleboard. This implies that the produced particleboard could serve as good insulation material for usage in the built environment as desired.

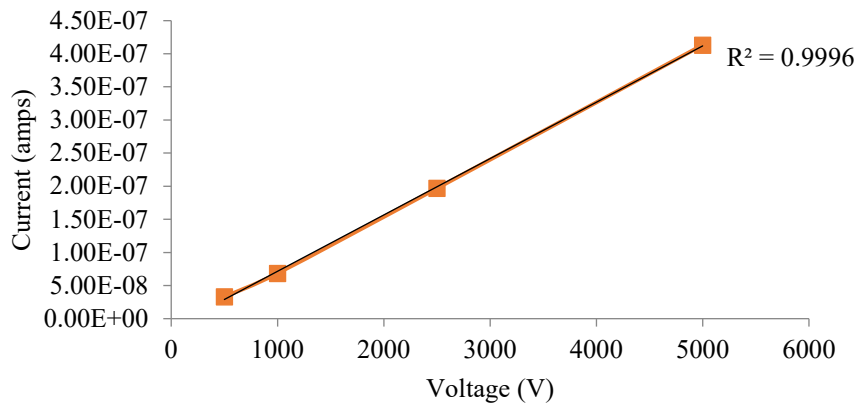


Fig. 2: Voltage versus Current of Optimised RHP8 Particleboard

### 3.2 Thermal Conductivity of RHP8 Particleboard

Thermal conductivities measurement at different thickness coded as: RHP8Δx20, RHP8Δx15 and RHP8Δx10 were carried out. The cooling curves based on individual thickness were determined from the slopes using Equation 4. The slopes (S) 0.0753, 0.2571 and 0.4063 for RHP8Δx20, RHP8Δx15 and RHP8Δx10 were determined from Figures (3 – 5). The slopes shows that low slope value was recorded at higher thickness with longer cooling period. This is due to silicate material in the rice husks and tendency to absorb more heat at higher thickness. The determined rate of heat transfer, slope values and thermal conductivities of the optimised RHP8 particleboard using the corresponding Equations (4 – 6) are as presented in Table 1.

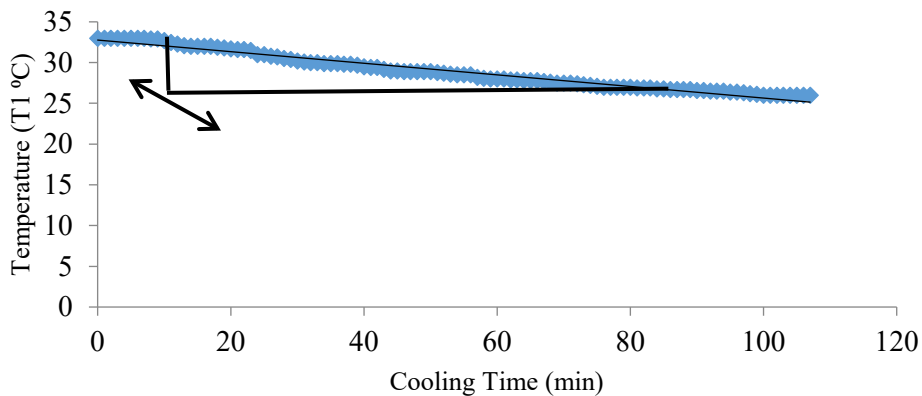


Fig. 3: Cooling Curve of RHP8Δx20 Particleboard

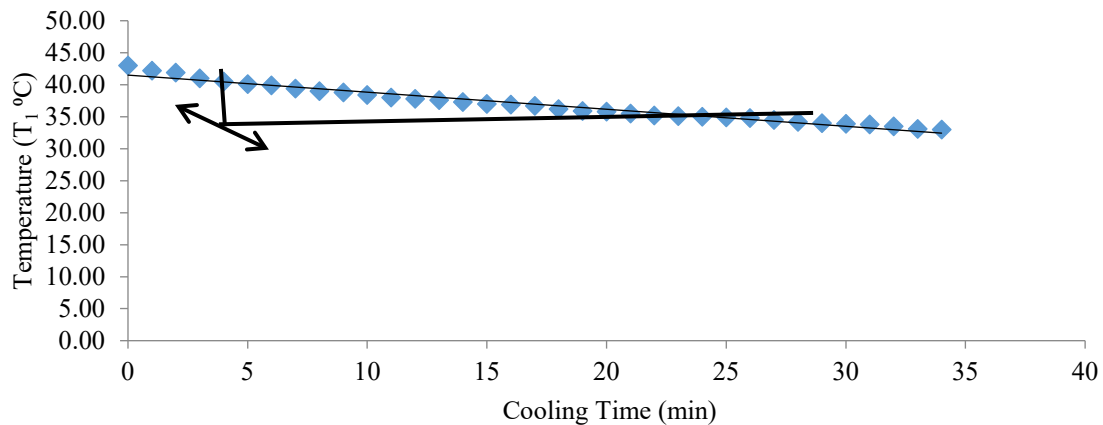


Fig. 4: Cooling Curve of RHP8Δx15 Particleboard

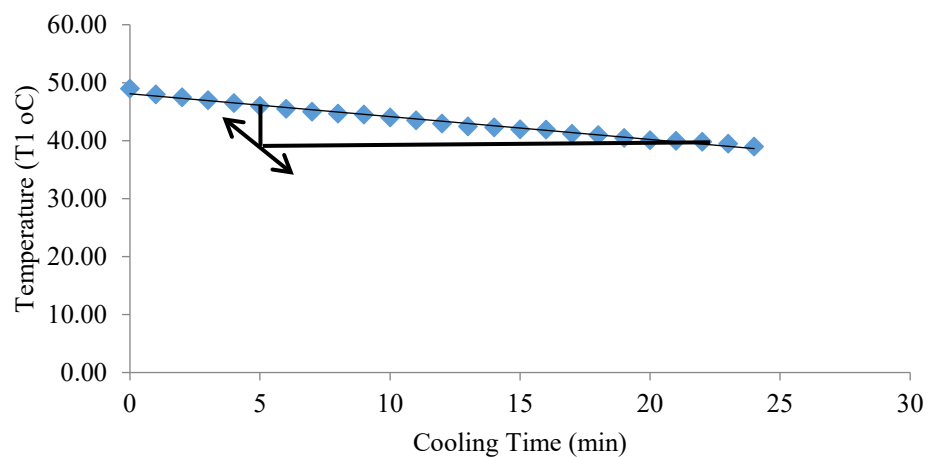


Fig. 5: Cooling Curve of RHP8Δx10 Particleboard

Table 1: Rate of Heat Transfer, Slope and Thermal Conductivities of Particleboards

Particleboard	Rate of Heat Trans. Q (Watts)	Slope (S)	Thermal Conductivity k (W/m. K)
RHP8Δx20	28.417	0.0753	$8.1 \times 10^{-4}$
RHP8Δx15	96.946	0.2571	$2.3 \times 10^{-3}$
RHP8Δx10	153.310	0.4063	$2.7 \times 10^{-3}$

Low-rate heat transfer and thermal conductivity was observed at RHP8Δx20 particleboard, while at RHP8Δx15 and RHP8Δx10 high rate of heat transfer and thermal conductivity was recorded. This implies that, the rate of heat transfer and thermal conductivity of the RHP8 particleboard varies with thickness sizes. According to Aggrey-Smith, Preko & Owusu (2016), lower thermal conductivity values equate to greater heat insulating properties of the material. This was also similar to reported polystyrene thermal conductivity for its insulation property which showed total resistant to the influence of water and good insulation properties, a situation where thermal conductivity decreases, the better the insulation property of the material (Ademović, Suljagić, & Zulić 2016). Therefore, the RHP8Δx20 particleboard size is the desired best fit size to use for the thermal comfort of occupants in the built and structural environment.

### 3.3 Thermal conductivity percentage errors

The thermal conductivity percentage errors for particleboards were calculated using Equations (7– 11) as presented in Table 2.

Table 2: Percentage Errors of Particleboard

%Error	RHP8Δx20	RHP8Δx15	RHP8Δx10
Slope	7.3E-03	1.89E-03	2.22E-04
diameter	2.98E-07	2.98E-07	1.322E-07
Thickness	6.25E-06	1.78E-06	1E-08
Temperature	3.102	4.851	6.493
Thermal conductivity	2.1E-04	6.05E-04	7.47E-04

The change in thermal conductivity  $\Delta k$  of the optimised RHP8 particleboard produced from rice husk and R7AD2 adhesive has shown negligible errors, which implies that ecofriendly and non-emitting particleboard is feasible from renewable biomass.

### 4. CONCLUSION

The optimised RHP8 particleboard produced from rice husk and R7AD2 adhesive studied for the electrical and thermal conductivities based on the industrial standard for safe usage as potential material in the office furniture, household and industrial applications. The results revealed that the electrical conductivity of the optimised RHP8 is highly resistance which can withstand up to 5000 volts (V) with a corresponding power capacity of  $2.07 \times 10^{-3}$  Watts. Furthermore, at thickness of RHP8Δx20 the thermal conductivity (k and the rate of heat transfer (Q)) of  $8.1 \times 10^{-4}$  W/m. K and 28.418 Watts were promising for application as a furniture for office partitioning. Thus, the optimised RHP8 particleboard is highly resistant to electric power shock and can conserve energy for usage as office furniture, household and industrial furniture. Y

### ACKNOWLEDGEMENT

The authors acknowledge Prof. Samson Duna, DG/CEO of Nigerian Building and Road Research Institute, for his financial assistance, Mr. Tanko Nanman Fanzhi (Physics Department, University of Jos) and Engr Alhassan Dali and his team of Jos Electricity Distribution Company for using their laboratory facilities and appliances.

### REFERENCES

- Ademović, Z, Suljagić, J & Zulić, J (2017) ‘Influence of Physical Properties on Thermal Conductivity of Polystyrene Insulation’ *Materials Contemporary Materials*, vol. 8, no. 1, pp. 42 – 47. Doi: 10.7251/COMEN1701042A.
- Aggrey-Smith, S, Preko, F & Owusu, F, W (2016) ‘Study of Thermal Properties of some Selected Tropical Hard Wood Species’, *International Journal of Materials Science and Application*, vol. 5, no. 3, pp. 143 – 150. Doi: 10.11648/j.ijmsa.20160503.15.
- Alam, D, M, N, Rahaman, S, K, Ratul, S, B, Sharmin, A, Islam, T, Hasan, M, A, W & Islam, M, N (2015) ‘Properties of Particleboard Manufactured from commonly used Bamboo (*Bambusa vulgaris*) Waste in Bangladesh’, *Advances in Research*, vol. 4, no.3, pp. 203 – 211.
- Antwi-Boasiako, C & Boadu, B, K (2017) ‘Thermal conductivity, resistance and specific heat capacity of chemically-treated, widely-used timber for building-envelope’, *High Temperature-High Pressure*, vol. 47, no. 1, pp. 65 – 84.
- Asha, A (2017) ‘Fabrication of Particleboards from Rice Husk’, *International Journal of Modern Engineering Research*, vol. 7, no. 5, pp. 30 – 38.
- Bakam, V, A, Mbishida, M, A, Danjuma, T, Zingfat, M, J, Hamidu, L, A, J & Pyendang, Z, S (2020) ‘Determination of Thermal Conductivity of Interlocking Compressed Stabilized Earth Block (CSEB)’, *International Journal of Recent Engineering Research and Development (IJRERD)* ISSN: 2455-8761 [www.ijrerd.com](http://www.ijrerd.com), vol. 5, no. 01, pp. 01-08.
- Bekhta, P & Dobrowolska, E (2006) ‘Thermal Properties of Wood-gypsum’, *Holz als Roh-und Werkstoff*, vol. 64, pp. 427 – 429. Doi 10.1007/s00107-005-0074-8.
- Czajkowski, L, Olek, W, Weres, J & Guzenda, R (2016) ‘Thermal Properties of Wood-Based Panels: Thermal Conductivity Identification with Inverse Modeling’, *Eur. J. Wood Prod.* Vol. 74, pp. 577–584. Doi 10.1007/S00107-016-1021-6.
- Da Silva César, A, A, Bufalino, L, Mendes, L, M, De Almeida Mesquita, R, G, De Paula Protásio, T, Mendes, R, F & Ferreira Andrade, L, M (2017) ‘Transforming Rice Husk into a High-Added Value Product: Potential for Particleboard Production’, *Ciência Florestal, Santa Maria*, vol. 27, no. 1, pp. 303-313.
- Ebong, S, T, Attai, E, S & Joshua, E, O (2016) ‘Measurement of Thermal Conductivity and Specific Heat Capacity of Three Major Geomorphological Units in Akwa Ibom State, Nigeria’, *British Journal of Applied Science & Technology*, vol. 12, no. 2, pp. 1-7, DOI: 10.9734/BJAST/2016/17834.

- Electrical Construction and Maintenance (2020) ‘Understanding Insulation Testing’, <https://www.ecmweb.com/maintenance> viewed on 26th November, 2020.
- Folaranmi, J (2009) ‘Effects of Additives on the Thermal Conductivity of Clay’, *Leonardo Journal of Science*, vol. 14, pp. 74 – 77.
- Geankoplis, C, J (1978) ‘Transport Processes and Unit Operations’, Allyn and Bacon, INC. Boston London Sydney Toronto, ISBN 0-205-05939-2.
- Hamidu, L, A, J, Aroke, U, O, Osha, O, A & Muhammad, I, M (2021) Modeling and Optimization of Particleboard from Rice Husk Waste Using R7AD2 Adhesive, Proceedings of the Nigerian Society of Chemical Engineers 51st Annual International Conference Lagos, Nigeria. 10th – 13th, November 2021, pp. 149 – 155.
- Hamidu, L, A, J, Aroke, U, O, Osha, O, A & Muhammad, I, M (2022) Modeling and Optimization of Particleboard from Rice Husk Waste Using R7AD2 Adhesive, *Journal of the Nigerian Society of Engineers*, vol. 37, no 1, pp. 66 – 74. DOI:10.51975/22370105.com.
- Harshavardhan, A & Muruganandam, L (2017) ‘Preparation and characteristic study of particle board from solid waste’, 14<sup>th</sup> ICSET IOP Conf. Series: Materials Science and Engineering, vol. 263 (2017) 032005 doi:10.1088/1757-899X/263/3/032005.
- Hussein, Z, Ashour, T, Khalil, M, H, Bahnasawy, A, H & Ali, A, S (2018) ‘Mechanical Properties of Particleboard Panels Made From Agricultural Wastes’, *Misr J. Ag. Eng.*, vol. 35, no. 1, pp. 319 – 338.
- Japanese Industrial Standard A.5908 (2003). Particleboards. *Japanese Standard Association*. Tokyo, Japan, 1 – 12.
- Kharshiduzzaman, M, D, Hossain, S, M, D, Ali, S & Ahmed, S (2019) ‘Determination of the Thermal Conductivity of Poor Conductive Materials in the Form of Disc by Self-Constructed Lee’s Disc Apparatus’, *AIP Conference Proceedings* 2121, 140008 (2019); <https://doi.org/10.1063/1.5115959>.
- Ojo, M, O, Adenodi, R, A, Alabi, O, O, Akinjogbin, I, O & Akinwale, B, F (2009) ‘Analysis of Thermal and Electrical Properties of Some Clay Samples: Implications on Residential Buildings in Ondo Town’, *Nigeria*, vol.14, pp. 1 – 6.
- Pan, Z, Zheng, Y, Zhang, R & Jenkins, B, M (2007) ‘Physical Properties of thin Particleboard made from Saline Eucalyptus’, *An International Journal of Industrial Crops and Products*, vol. 26, no. 1, pp. 185 – 194.
- Paul, P & Layi, F (2014) ‘Design of Lee’s Disc Electrical Method for Determining Thermal Conductivity of a Poor Conductor in the Form of a Flat Disc’, *International Journal of Innovation and Scientific Research*, vol. 9, no. 2, pp. 335-343 <http://www.ijisr-issr-journals.org>.
- Samuel, O, S, Ramon, B, O & Johnson, Y, O (2012) ‘Thermal Conductivity of Three Different Wood Products of Combretaceae Family; Terminalia superba, Terminalia ivorensis and Quisqualis indica’, *Journal of Natural Sciences Research*, vol. 2, no. 4, pp. 36-43.
- Singhadej, T & Kumfu, S (2011) ‘Particleboard from Papyrus Fibers as Thermal Insulation’, *Journal of Applied Sciences*, vol. 11, no. 14, pp. 2640 – 2645. Doi: 10.3923/jas.2011.2640.2645.
- Temitope, A, K, Onaopemipo, A, T, Olawale, A, A & Abayomi, O, O (2015) ‘Recycling Rice Husk into a Locally-Made Water Resistant Particleboard’, *Journal of Industrial Engineering Management*, vol. 4, no. 3, pp. 1 – 6.
- Theasy, Y, Yulianto, A & Astuti, B (2017) ‘Effect of Thickness on Thermal Conductivity Based on Waste Newspaper Particle Board’, *Journal of Natural Sciences and Mathematics Research*, vol. 3, no. 1, pp. 210 – 214. Doi: 10.21580/jnsmr.2017.3.1.1696.
- Wayne, C, L (1967) ‘Thermal Conductivity of Wood-Base Fiber and Particle Panel Materials’, Forest Products Laboratory, U. S. Department of Agriculture, 1967, pp. 1 – 14.
- Zhang, D, Behbahanian, A & Roberts, N. A (2020) ‘Thermal Conductivity Measurement of Supported Thin Film Materials Using the 3 $\omega$  Method Department of Mechanical and Aerospace Engineering’, Utah State University, Logan, UT (July 2, 2020).
- Zhou, J, Zhou, H, Hu, C & Hu, S (2013) ‘Measurement of Thermal and Dielectric Properties of Medium Density Fiberboard with Different Moisture Content’, *Journal of BioResources*, vol. 8, no. 3, pp. 4185 – 4192. Doi:10.15367/biores.8.3.4185 – 4192.



## Extraction of Keratin Protein from Chicken Feathers: An Optimization Study

Favour Oluwabukunmi KAYODE<sup>1</sup>, Benjamin ADEREMI<sup>2</sup>, Olayomi Abiodun FALOWO<sup>3,\*</sup>

<sup>1,2,3</sup>Department of Chemical Engineering, Landmark University Omu-Aran, Nigeria.

<sup>1</sup>[kayode.favour@lmu.edu.ng](mailto:kayode.favour@lmu.edu.ng), <sup>2</sup>[aderemi.benjamin@lmu.edu.ng](mailto:aderemi.benjamin@lmu.edu.ng), <sup>3</sup>[falowo.olayomi@lmu.edu.ng](mailto:falowo.olayomi@lmu.edu.ng)

\*Corresponding author: [falowo.olayomi@lmu.edu.ng](mailto:falowo.olayomi@lmu.edu.ng)

### ABSTRACT

*Box-Behnken design was used to model, optimize and examine the interplay of the process variables affecting the extraction of keratin protein. The variables used in the experimental design were Temperature (70°C - 90°C), extraction time (2-8 hrs), liquid-solid ratio (5-20 ml/g), and concentration of sodium sulfide (8-50 g/l). Biuret test was carried out on extracted keratin and Fourier Transform Infrared Spectroscopy (FTIR) and Scanning Electron Microscopy (SEM) were used to characterize the extracted keratin. The extraction was done and biuret test confirmed that the extract was indeed protein. From the FTIR analysis, the presence of functional groups such as amino and carbonyl groups confirmed the presence of protein backbone in the extracted keratin. The micrograph from the SEM analysis compared the appearance of keratin and the feather residue after keratin extraction. The optimal process conditions established for the keratin protein extraction are a temperature of 72°C, an extraction time of 2 hrs, a liquid-solid ratio of 5 ml/g, and a sodium sulfide concentration of 20.614 g/l. These conditions generated a protein yield of 86.92 wt.%.*

**Keywords:** Optimization, Keratin protein, Chicken feathers, Characterization, Extraction.

### 1. INTRODUCTION

One of the most abundant proteins in the bodies of mammals, birds, and reptiles is keratin. It is found in feathers, wool, horn, and nails and gives the body its strength. All keratins have an underlying structure made up of  $\alpha$ -helices and  $\beta$ -pleated sheets, and the cysteine in their backbones promotes the production of robust disulfide bonds that facilitate the construction of the helix and pleated sheets as well as the coiled coil structure (Khan et al., 2017). It was eventually determined that keratin comes in two varieties, type I and type II, which can be differentiated by their variations in secondary structures (Rouse & Van Dyke, 2010). The richest source of keratin is found in skin and its appendages, including nails, hair, feathers, wool, hooves, scales, and stratum corneum (Shah et al., 2019). Keratin, a filamentous protein, can be used for variety of purposes as a result of its good biodegradability, biocompatibility, cell adhesion performance, strong polarity, and high chemical activity, among other properties (Shavandi et al., 2017). Nowadays, the most popular and desirable usage of this protein is in hair cosmetics, for example keratin serum, shampoos and conditioners are now being utilized extensively to restore hair damage. Due to its filamentous shape, keratin is used in tissue engineering and controlled-release applications as a source of natural and synthetic biomaterial (Rajabi et al., 2020). Also, keratin is more stable and less soluble than the majority of other proteins (Donato & Mija, 2019). This characteristic makes the dissolution and extraction of keratin a difficult process compared to other natural polymers. Feather keratin is a potential source of cheap, eco-friendly and commercial biomaterial (Anbesaw, 2022). The processing of chicken meat for human consumption produces approximately 5 million tons of feathers per year as a waste stream (Šafarič et al., 2020). Chicken feathers consist of about 90% keratin and can be utilized for industrial applications (Kumawat et al., 2018). Recently, industrial applications of keratin led to the development of several means of keratin extraction as well as its modification for improved performance. The major methods used to isolate keratin from keratin-rich materials are alkali extraction, chemical hydrolysis, microwave irradiation, steam explosion, sulfitolysis, reduction, oxidation, and ionic liquids (Reddy et al., 2021). The reduction of disulfide bonds using mercaptoethanol (MEC) has been the standard method for keratin extraction with a good yield of keratin (Vineis et al., 2019). However, MEC is a toxic chemical and is undesirable commercially and environmentally due to its high cost and issues related to its toxicity to the environment, as such, it is rarely used. Sodium sulfite can be a good alternative to break down the sulfide bonds and extract keratin. This method of sulfitolysis has major industrial and analytical impacts on chicken feather processing as it prevents complete liquefaction of the substrate as well as pollutants reduction (Laba and Szczekala, 2013). Therefore, knowing the optimum sodium sulfite concentration and other process variables impacting keratin extraction is vital.

Optimization of the process variables influencing keratin extraction will aid keratin protein production by establishing optimum conditions for large scale application. The extraction of keratin protein from chicken feathers could be a strategic method to convert waste to wealth. Harnessing chicken feathers, technologically solves its waste disposal



problem and offers the possibility of novel products from chicken feathers. However, there is need to improve the extraction process at higher reducing agent concentration with the inclusion of liquid-solid ratios with the aim of increasing the keratin yield. This research project is in tandem with the Sustainable Development Goal (SDG) 9, which is to build resilient infrastructure, promote inclusive and sustainable industrialization and foster innovation.

## 2. MATERIALS AND METHODS

### 2.1. Materials

The Chicken Feathers used in this study were obtained from a poultry farm in Omu-aran and conveyed to the Chemical Engineering laboratory, Landmark University, Omu-aran, Kwara State. The chemicals and reagents used were all of analytical grade (AG).

### 2.2. Methods

#### 2.2.1. Chicken Feather Pre-treatment

The feathers were pre-treated following a modification of the method proposed by Oluba *et al.* (2021). The feathers were cleaned by washing with warm water, and were disinfected by soaking in sodium hypochlorite, rinsed and then air dried for 36 hrs. Then, the feathers were soaked in ethanol for 24 hrs, washed with detergent and rinsed thoroughly with water. The washed feathers were oven dried at 60°C for 24 hrs. Thereafter, the dried feathers were grounded into fine particles and stored for further use.

#### 2.2.2. Experimental Design and Optimization of Keratin Protein Extraction Process

Optimization of keratin extraction was done using design expert software (version 12), and Box-Behnken design model was used for the optimization of the extraction of the keratin process. The four independent variables and the ranges investigated is presented in Table 1.

Table 1: Variables for the experimental design

Factors (Independent variable)	Factors level		
	-1	0	1
Time (hrs)	2	5	8
Temperature (°C)	70	80	90
Concentration (g/l)	8	29	50
Liquid-Solid ratio	5	12.5	20

Twenty-nine experimental runs were generated with the keratin protein amount as the response. The experimental data were fitted into a polynomial quadratic model equation.

#### 2.2.3. Keratin Protein Extraction Process

The extraction process was carried out according to the experimental run generated. A known amount of the milled feather was weighed and added to a known volume of Na<sub>2</sub>S solution to form the liquid-solid ratio. The pH of the solution ranged between 12 and 13. The mixture was placed in 250 ml beakers with a foil seal on the top and then mechanically shaken on a desk top shaker for homogeneous mixing. Thereafter, it was placed in a water bath set to the appropriate temperature. The reaction time was imputed and varied according to the values generated by the experimental design. After cooling, the turbid solution was filtered using a muslin cloth to obtain the filtrate. The filtrate obtained was precipitated with 10% trichloroacetic acid (Sigma-Aldrich, UK). The precipitate was filtered out with a muslin cloth and washed under water. The precipitated keratin was oven-dried at 40°C for 15 hrs. The dried keratin was pulverized using a mortar and pestle and then stored for further analysis.

The yield of Keratin obtained was calculated using

$$\text{Keratin yield} = \frac{W_i}{W_o} \times 100 \quad (1)$$

Where,  $W_i$  is the weight of initial feather used as calculated from the liquid solid ratio and  $W_o$  is the weight of recovered keratin.

### 2.2.4. Biuret Test for Extracted Keratin Protein

The extracted keratin underwent Biuret test. The resulting solution from the biuret test was analyzed under UV-vis to obtain its absorbance at a wavelength of 540 nm.

### 2.2.5. Characterization of Extracted Keratin and Feather Residue

The extracted keratin collected after purification was analyzed using the FTIR to examine the functional groups present in the extract. Also, extracted keratin and the feather residue left after the extraction were analyzed using the scanning electron microscope to evaluate their surface structures (Oluba *et al.*, 2021).

## 3. RESULTS AND DISCUSSIONS

### 3.1. Pre-treatment of Waste Chicken Feathers

The feathers which were initially brown in colour and produced offensive odour became white and odourless upon pre-treatment. The addition of sodium hypochlorite for cleaning made the feathers white and upon ethanol addition, made them even whiter.

### 3.2. ANOVA Results of the keratin Extraction from Feathers

The results obtained from the conduction of keratin extraction from chicken feathers was presented in Table 2. Run 27 has the highest keratin recovery from the chicken feather while the lowest keratin protein was obtained in run 10.

Table 2: Box Behnken design of process variables and keratin yield

Run	Temp (°C)	Conc (g/l)	Time (hrs)	Liquid/Solid ratio	Keratin Yield (%)
1	70.00	50.00	5.00	12.5	24.875
2	90.00	29.00	2.00	12.5	53.125
3	80.00	8.00	8.00	12.5	35.750
4	80.00	29.00	5.00	12.5	41.500
5	80.00	8.00	2.00	12.5	68.130
6	80.00	29.00	8.00	5.00	56.800
7	90.00	29.00	8.00	12.5	19.250
8	80.00	50.00	8.00	12.5	16.125
9	80.00	29.00	5.00	12.5	41.500
10	80.00	50.00	5.00	20.00	3.400
11	80.00	50.00	5.00	5.00	45.800
12	80.00	29.00	5.00	12.5	41.500
13	70.00	8.00	5.00	12.5	60.250
14	80.00	50.00	2.00	12.5	52.875
15	80.00	8.00	5.00	20.00	47.200
16	80.00	8.00	5.00	5.00	26.500
17	90.00	29.00	5.00	5.00	62.850
18	70.00	29.00	2.00	12.50	61.625
19	80.00	29.00	2.00	5.00	72.400
20	80.00	29.00	2.00	20.00	50.000
21	70.00	29.00	8.00	12.50	40.500
22	80.00	29.00	5.00	12.50	41.500
23	90.00	8.00	5.00	12.50	38.125
24	80.00	29.00	8.00	20.00	21.400
25	90.00	50.00	5.00	12.50	13.000
26	80.00	29.00	5.00	12.50	41.500
27	70.00	29.00	5.00	5.00	73.450
28	90.00	29.00	5.00	20.00	20.200
29	70.00	29.00	5.00	20.00	42.600

The analysis of variance (ANOVA) shows that the model as well as the process variables (Liquid solid ratio, temperature, time and solvent concentration) were significant. Any model term having p value  $\leq 0.05$  indicates that the parameter is significant (Table 3). The **Model also has an F-value** of 21.88 which implies that there is only a 0.01% chance that an F-value this large could occur due to noise. Hence, this model's F-value further showed its significance. In this case A, B, C, D, BD, B<sup>2</sup> are significant model terms.

Table 3: Analysis of Variance for Reduced Quadratic model of Keratin Extraction

Source	Sum of Squares	df	Mean Square	F-value	p-value
Model	7985.48	6	1330.91	21.88	< 0.0001 significant
A-Temp	780.05	1	780.05	12.82	0.0017
B-Conc	1197.50	1	1197.50	19.69	0.0002
C-Time	2361.11	1	2361.11	38.82	< 0.0001
D-L/S ratio	1950.75	1	1950.75	32.07	< 0.0001
BD	995.40	1	995.40	16.36	0.0005
B <sup>2</sup>	700.68	1	700.68	11.52	0.0026
Residual	1338.23	22	60.83		
Lack of Fit	1338.23	18	74.35		
Pure Error	0.0000	4	0.0000		
Cor Total	9323.72	28			

Table 4 shows the adequate precision measure of 19.644. Adequate Precision measures the signal to noise ratio. A ratio greater than 4 is desirable. This means that the model had a strong signal to be used for optimization. The Predicted R<sup>2</sup> of 0.6651 is in reasonable agreement with the Adjusted R<sup>2</sup> of 0.8173; i.e. the difference is less than 0.2.

Table 4: Fits Statistics

Fits	Values
Std. Dev.	7.80
Mean	41.85
C.V. %	18.64
R <sup>2</sup>	0.8565
Adjusted R <sup>2</sup>	0.8173
Predicted R <sup>2</sup>	0.6651
Adeq Precision	19.6439

### 3.3. Final Equation in Terms of Coded Factors

The coefficient estimates were used to formulate the model equation

$$\text{Keratin yield(\%)} = 45.98 - 8.06A - 9.99B - 14.03C - 12.75D - 15.78BD - 9.98B^2 \quad (2)$$

Where A, B, C, D is temperature concentration, time, and liquid-solid ratio, respectively. The equation in terms of coded factors can be used to make predictions about the response for given levels of each factor. By default, the high levels of the factors are coded as +1 and the low levels are coded as -1. The coded equation is useful for identifying the relative impact of the factors by comparing the factor coefficients.

### 3.4 Graphical Plots

A normal probability plot of the residuals is a scatter plot with the theoretical percentiles of the normal distribution on the x axis and the sample percentiles of the residuals on the y axis. The normal plot of residuals (Figure 1) and the plot of predicted vs. actual (Figure 4) both indicated a straight line. This means there is close agreement in the actual and predicted response

# Extraction of Keratin Protein from Chicken Feathers: An Optimization Study

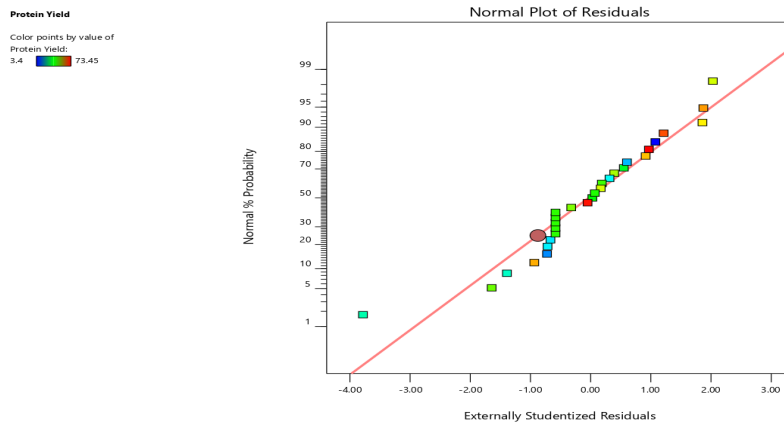


Figure 1: Normal Plot of Residuals Against Studentized residuals

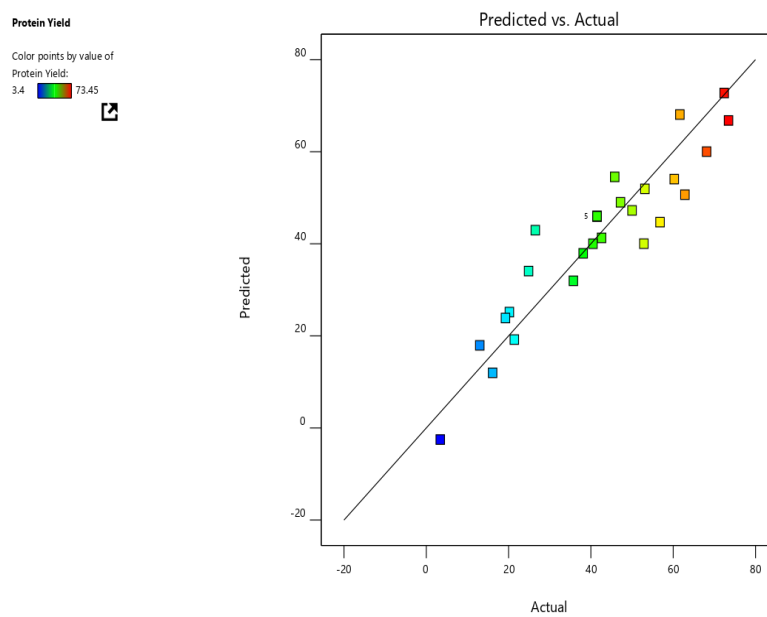


Figure 2: A Plot of Predicted against Actual keratin protein

The interactive effects of the process variables on the keratin yield (%) were examined using a three-dimensional surface curve (3D) against any two-independent variable while keeping the other variable constant. The 3D- graphs represents the effects of the independent variables and their interactions on the keratin yield. Where Figure 3 shows the effect of concentration of sodium sulfide and reaction temperature on the amount of keratin extracted. This plot shows that an increase in concentration along with increasing temperature initially leads to increase in the keratin yield but after a certain point, further increase of concentration and temperature to the highest level resulted into a decrease in protein yield. Figure 4 represents the effects of Sodium sulfide’s concentration and liquid-solid ratio on keratin yield. The plot shows that the keratin yield is majorly influenced by the changes in sulfide concentration, though a marginal increase was observed with increase in Liquid -solid ratio. Interaction between these two variables clearly show that concentration has a more domineering effect on the protein yield compared to the Liquid-solid ratio.

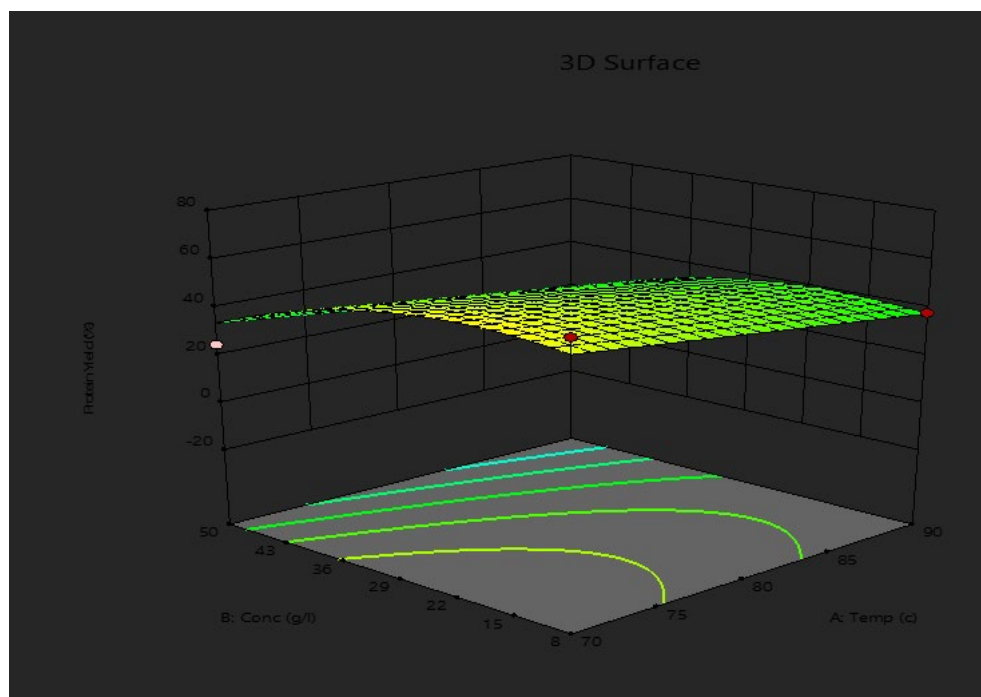


Figure 3: 3-D Response Surface Plot for the interaction of Temp and Concentration

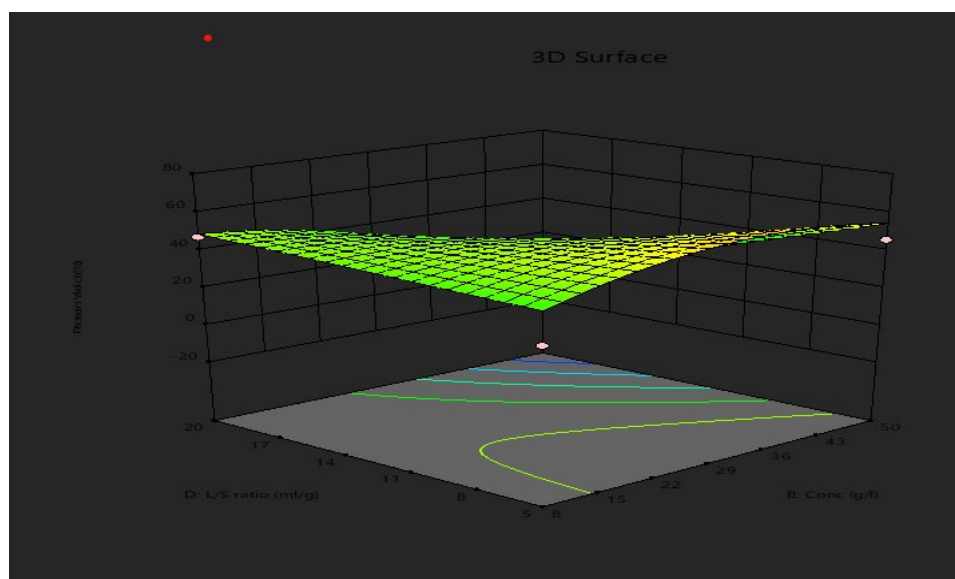


Figure 4: 3-D Response Surface Plot for the interaction of Concentration and L/S Ratio

### 3.4. Validation of Experiment

The optimal conditions predicted from the optimization of keratin protein extraction were temperature of 72 °C, Time of 2 hrs, L/S ratio of 5 ml/g and Concentration of 20.614 g/l. The experiment was carried out at this optimal conditions to validate the predicted optimal values. At these optimum conditions, the keratin yield was 86.92 w% which was higher than the highest keratin yield from the experimental runs.

### 3.5. Protein Characterization

The biuret test conducted on the extract from all the 29 experimental runs indicates a purple colour change in the final sample which confirmed the presence of protein in all the samples. Protein amount of each sample was obtained using a UV spectrophotometer following the method developed by Reinhold in 1953.

### 3.6. Structural Analysis of the Extract by FTIR

Figure 5 shows the results from the FTIR analysis. The FTIR characterization of keratin extracts have characteristic peaks corresponding to important functional groups like -CO-NH-, -NH<sub>2</sub>, -CNH, -C-H. The relatively broad peak in the region of 3314.552 cm<sup>-1</sup> corresponds to hydrogen-bonded -N-H and -O-H stretching motion out of amide functionality and absorbed water. The less intense peak in the region of 2900-3100 cm<sup>-1</sup> signifies -C-H and -N-H groups stretching vibrations. The carbonyl group of amide functionality occurs in the region of 1600-1700 cm<sup>-1</sup>. An observed peak at 1675.355 cm<sup>-1</sup> is assigned to amide carbonyl (-C=O) functional group stretching vibration. The observed peak at 1334.499 cm<sup>-1</sup> corresponds to -CNH group comprising -C-N- and -C-C- groups stretching vibrations and -N-H group bending vibration. The bending vibration of -CH<sub>2</sub> group occurred at 1452.65 cm<sup>-1</sup>. The intense sharp peak at 1532.649 cm<sup>-1</sup> corresponds to -C-N-H group bending vibration. These results showed the presence of characteristic peaks like amide -N-H, -C=O, -C-N- and -CNH functionalities which confirm building block amino acids forming peptide groups of keratin protein.

### 3.8. SEM Analysis

The SEM micrograph showed in Figure 6 indicated a compact porous-like structure for the extracted keratin (Figure 6a and Figure 6b) compared to the feather residue which showed a thread-like microstructure (Figure 7a and Figure 7b). The feather residue void of keratin did not indicate any form of porosity in its structure.

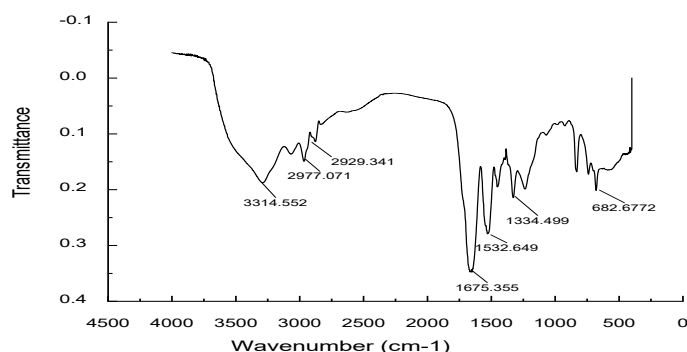


Figure 5: FTIR Analysis of extracted Keratin protein

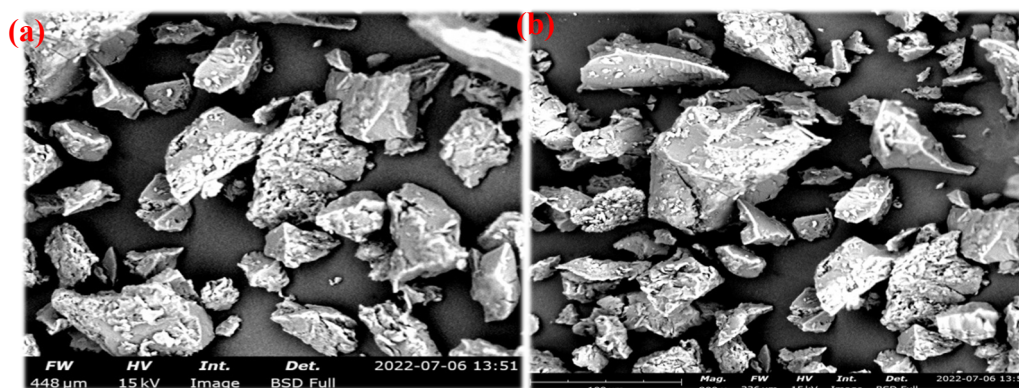


Figure 6: SEM Micrograph for (a) keratin 600x (b) Keratin 800x

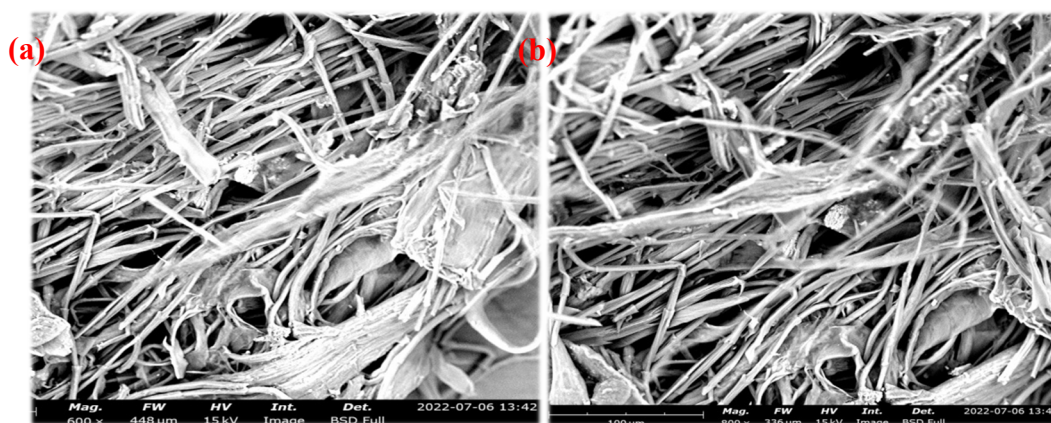


Figure 7: SEM Micrograph for (a) Feather Residue 600x (b) Feather Residue 800x

#### 4. CONCLUSION

The optimal process conditions established for keratin extraction were time: 2 hrs, temperature: 72°C, liquid-ratio: 5 ml/g and sodium sulfide concentration: 20.614 g/l respectively with a corresponding yield of 86.92 wt% of keratin protein. The results of the FT-IR analysis revealed that amino and carbonyl groups were the active functional groups present, which further confirmed that the extract obtained was made up of protein. The SEM micrograph indicated a compact microstructure for keratin while the feather residue showed a thread-like microstructure. The establishment of optimal process parameters could facilitate large scale extraction of keratin for industrial applications.

#### ACKNOWLEDGEMENTS

The authors appreciate the contribution of Prof Olarewaju Oluba of Department of Biochemistry and the technologists in the Department of Chemical Engineering, Landmark University for their technical assistance.

#### REFERENCES

- Anbesaw, M. S. (2022). Bioconversion of Keratin Wastes Using Keratinolytic Microorganisms to Generate Value-Added Products. *International Journal of Biomaterials*, 2022.
- Donato, R. K., & Mija, A. (2019). Keratin associations with synthetic, biosynthetic and natural polymers: An extensive review. *Polymers*, 12(1), 32.
- Khan, R. H., Siddiqi, M. K., & Salahuddin, P. (2017). Protein structure and function. *Basic biochemistry*, 5, 1-39.
- Kumawat, T. K., Sharma, A., Sharma, V., & Chandra, S. (2018). Keratin waste: the biodegradable polymers. In *Keratin*. IntechOpen.
- Łaba, W., & Szczekała K. B., (2013). Keratinolytic Proteases in Biodegradation of Pretreated Feathers. *Pol. Journal. Environ. Stud.*, 22, (4), 1101-1109
- Oluba, O. M., Osayame, E., & Shoyombo, A. O. (2021). Production and characterization of keratin-starch bio-composite film from chicken feather waste and turmeric starch. *Biocatalysis and Agricultural Biotechnology*, 33, 101996.
- Rajabi, M., Ali, A., McConnell, M., & Cabral, J. (2020). Keratinous materials: Structures and functions in biomedical applications. *Materials Science and Engineering: C*, 110, 110612.
- Reddy, C. C., Khilji, I. A., Gupta, A., Bhuyar, P., Mahmood, S., AL-Japairai, K. A. S., & Chua, G. K. (2021). Valorization of keratin waste biomass and its potential applications. *Journal of Water Process Engineering*, 40, 101707.
- Rouse, J. G., & Van Dyke, M. E. (2010). A review of keratin-based biomaterials for biomedical applications. *Materials*, 3(2), 999-1014.
- Šafarič, R., Fras Zemljič, L., Novak, M., Dugonik, B., Bratina, B., Gubelj, N., Bolka, S., & Strnad, S. (2020). Preparation and characterisation of waste poultry feathers composite fibreboards. *Materials*, 13(21), 4964.
- Shah, A., Tyagi, S., Bharagava, R. N., Belhaj, D., Kumar, A., Saxena, G., Saratale, G. D., & Mulla, S. I. (2019). Keratin production and its applications: current and future perspective. *Keratin as a protein biopolymer*, 19-34.
- Shavandi, A., Silva, T. H., Bekhit, A. A., & Bekhit, A. E.-D. A. (2017). Keratin: dissolution, extraction and biomedical application. *Biomaterials science*, 5(9), 1699-1735.
- Vineis, C., Varesano, A., Varchi, G., & Aluigi, A. (2019). Extraction and characterization of keratin from different biomasses. In *Keratin as a protein biopolymer* (pp. 35-76). Springer.



## Optimization of Avocado Seed Oil Extraction using Five-Level Response Surface Methodology Design

Saidat O. GIWA<sup>1\*</sup>, Fatima Y. Abdullahi<sup>2</sup>, Olukayode G. OLOYEDE<sup>3</sup>, Saidu IBRAHIM<sup>4</sup>, Abdulwahab GIWA<sup>5</sup>

<sup>1,2,3,4</sup>Department of Chemical Engineering, Abubakar Tafawa Balewa University, Bauchi, Nigeria

<sup>5</sup>Department of Chemical and Petroleum Engineering, Afe Babalola University, Ado-Ekiti, Ekiti State, Nigeria

<sup>1\*</sup>[sogiwa@atbu.edu.ng](mailto:sogiwa@atbu.edu.ng), <sup>2</sup>[Fatimayakmut@gmail.com](mailto:Fatimayakmut@gmail.com), <sup>3</sup>[ogoloyede.pg@atbu.edu.ng](mailto:ogoloyede.pg@atbu.edu.ng), <sup>4</sup>[saiduibrahim65@gmail.com](mailto:saiduibrahim65@gmail.com),  
<sup>5</sup>[agiwa@abuad.edu.ng](mailto:agiwa@abuad.edu.ng)

\*Corresponding author

---

### ABSTRACT

In this work, optimization of avocado seed oil extraction was carried out with the aid of Design Expert 7.0.0. The effects of particle size, extraction temperature and extraction time on the percentage yield of oil and cake were considered. Experiments were designed according to central composite method. With n-hexane as the solvent, each experimental run was carried out in a Soxhlet apparatus. Thereafter, experimental data were modelled. The analysis of variance results showed that the model developed for oil yield was statistically significant with p-value of 0.0277. The R-squared value of the model was found to be 0.6722 which was an indication that the quadratic model developed fairly represented the experimental data. The cake yield model was also significant and had an R-squared value of 0.6459. However, based on the adjusted R-squared value obtained, overall mean was observed to be a better predictor of the cake data. The numerical optimization results predicted 0.74 mm, 55°C and 5 h as the optimum conditions to achieve 13.21 % and 74.63 % oil and cake yields respectively. On validation using the same conditions, 17.54 % oil yield was obtained. The physicochemical properties of the extracted oil were also investigated.

**Keywords:** Avocado seed oil, extraction, Central Composite Design (CCD), cake weight, oil yield.

### 1. INTRODUCTION

In 2011, the global avocado production was about 4.4 million with 20% increase recorded between 2007 and 2011 (Duarte *et al.*, 2016). The rise in productivity of the plant can be linked to high nutrition value and various health-related claims.

Avocado is an energetic fruit with high nutritional value and is considered a major tropical fruit, since it is rich in protein and contains fat soluble vitamins lacking in other fruits, including Vitamins A and B, and median levels of vitamins D and E. It contains different oil levels in the pulp, thus it is widely used in pharmaceutical and cosmetic industries, and for obtaining commercial oils similar to olive oil, because of their similarity in fatty acid composition. In addition, this fruit has been recognized for its health benefits, especially due to the compounds present in the lipid fraction (Santos *et al.*, 2014).

Avocado oil is well known for its various health benefits. But the oil is mostly extracted from the pulp of the fruit while the skin and seeds are usually discarded (Gomez *et al.*, 2014). The seed of this plant is considered underutilised; thus, it attracts the attention of the researchers. Many of the works available on avocado seed involve extraction and/or optimization of phytochemicals (Gomez *et al.*, 2014; Adaramola *et al.*, 2016; Noorul *et al.*, 2017; Ong *et al.*, 2022). Also, there is a few studies on the seed oil extraction and its use for biodiesel production and the yield of oil extracted in these works were in the range of 3 % (Dagde, 2019) and 13.4 % (Deepalkshmi *et al.*, 2014). However, no work could be found on optimization of n-hexane extraction of avocado seed oil. Hence, the research was carried out to maximize the yield of oil extraction from the seed within the selected ranges of particle size, temperature and extraction time, using response surface methodology. The effects of variation of extraction factors on the yield of the cake was also investigated as the by-product can be valuable. Moreover, the extracted oil at the optimum conditions was characterized to evaluate the suitability of the oil for various applications.



## 2. MATERIALS AND METHODS

A short description of the materials and methods used must be included in this section.

### 2.1 Sample Collection and Preparation

Avocado fruits were procured from Muda Lawal market, in Bauchi metropolis. The seeds were ripped off from the fruit and were washed manually with water and sundried for 7 days followed by oven drying at 40°C for 72 h until their moisture content became constant, after which they were crushed and sieved to different particle sizes in the desired range given in Table 1.

### 2.2 Experimental Design and Oil Extraction

Previous study has shown that n-hexane extraction are significantly affected by particle size, extraction time and extraction temperature (Yahaya *et al.*, 2016). Based on this, 18 experiments were designed with the aid of Design Expert 7.0.0 using the central composite design (CCD) of Response Surface Methodology (RSM) for extraction of avocado seed oil. The maximum and the minimum levels of the factors used were as given in Table 1.

Table 1: Maximum and minimum level of experimental factors

Variable	Unit	Maximum	Minimum
Particle Size (A)	mm	1.18	0.3
Temperature (B)	°C	70.00	40.00
Time (C)	h	5.00	3.00

Thereafter, oil extraction experiments were performed according to the CCD matrix. For each experimental run, 10 g of the grounded avocado seed was wrapped in a filter paper and placed inside the thimble chamber which was placed into the extractor. A round bottom flask containing 150 ml n-hexane was coupled with the extractor connected to a condenser. Cool water (from a chiller at temperature of 10 °C ) was passed through the condenser to condense the evaporating solvent back into the flask. The extraction was carried out according to the conditions specified for each run in the design matrix. Thereafter, the resulting mixture of n-hexane and the extracted oil was separated by distillation to recover the solvent. At the end of each experiment, the yield of the oil was obtained in percentage by dividing the amount of oil extracted by the weight of the seed and multiplying by 100. Also, the cake obtained was dried and later weighed. The cake weight was expressed as percentage of the feedstock.

### 2.3 Analysis of Experimental Data and Optimization

The experimental data were entered into the design matrix and the modelling of both the oil and cake yield data were performed. Each of the responses was model using a second-order polynomial equation which was later modified to improve its statistical importance. The significance of these models was evaluated using Analysis of Variance (ANOVA) results. Based on the fact that, an experiment was performed at 0.74 mm, 55 °C and 5 h, numerical optimization criteria for particle size and temperature were set to be equal to 0.74 mm and 55°C respectively and that of time was set to be a target of 5 h. The objective of the oil yield was to maximize while the cake yield was set to be in range. This was done because our aim was to extract almost all the oil in feedstock.

### 2.4 Characterization of the Avocado Seed Oil

The physicochemical properties of the oil determined were density, viscosity, pour point, flash point, cloud point, free fatty acid, acid value, iodine value, peroxide value and saponification value. All the analyses were done according to various standards as explained by Adaramola *et al.* (2016)

## 3. RESULTS AND DISCUSSION

### 3.1 Oil Extraction

Conventionally, efficiency of extraction process which is usually defined using the yield of the product is affected by factors such as particle size of the solute, temperature and time. As shown in Table 2, at various extraction conditions, yield of both the oil and the cake was observed to vary. However, that of the former was more significant. The oil yield was in the range of 4.07 and 14.02%; the minimum and maximum cake yield obtained were 88.212 and 97.377%. As it can be noticed from Table 2, Run 1 gave the minimum amount of cake and maximum amount of oil, however, the sum of the two products is greater than 100 by 2.232. The increment may be as result of presence of residual n-hexane in both the cake and oil. Also, the cake might have more moisture. Similar trend can be observed in Run 2 where the minimum oil and maximum cake yields were obtained.

### 3.2 Statistical Analysis and Optimization

In order to understand the effects of the selected factors on the oil and cake yields, the experimental data were modelled using a second-order polynomial equation for each of the responses. The models were later modified to improve their performances. Given in Table 3 are the results of ANOVA obtained for oil yield. The reduced quadratic model was

significant based on the fact that the probability of error value ( $p$ -value= 0.0277) was less than 0.05 (on 95% confidence level). Also, using the same criterion, the significant terms for this model were C, AB, BC and  $C^2$  which implied that the oil extraction was significantly affected by variation of time at both linear and quadratic level, interaction of particle size and temperature, and interaction of temperature and time. Also, the model had predicted R-squared value of 0.6722, adjusted R-squared of 0.4934, Predicted R-squared of 0.2460 and adequate prediction of 7.951. Though, Predicted and adjusted R-squared were not very close, the results still demonstrated the validity of the model.

Table 2: The central composite design (CCD) experimental design matrix and the responses

Run No	A: Particle size (mm)	B: Temperature (°C)	C: Time (h)	Y <sub>1</sub> : Oil yield (%)	Y <sub>2</sub> : Cake Yield (%)
1	0.74	55.00	5.00	14.02	88.212
2	1.00	46.08	4.59	4.07	97.377
3	0.48	46.08	3.41	9.54	90.408
4	0.74	40.00	4.00	7.13	93.694
5	0.74	55.00	4.00	9.49	92.627
6	0.48	46.08	3.41	7.74	92.078
7	0.74	63.92	3.41	6.15	94.095
8	0.74	70.00	4.00	8.37	94.065
9	1.18	55.00	4.00	8.28	91.654
10	1.00	55.00	4.00	6.86	93.505
11	0.30	63.92	4.59	8.15	91.332
12	0.74	55.00	4.00	8.60	92.80
13	0.74	55.00	3.00	7.33	94.123
14	0.74	55.00	4.00	5.03	96.151
15	1.00	63.92	3.41	9.34	90.577
16	0.48	63.92	4.59	9.35	90.897
17	0.74	55.00	4.00	4.50	95.309
18	0.48	46.08	4.59	8.01	92.536

Table 3: ANOVA results for Oil Yield Model

Source	Sum of Squares	df	Mean Square	F Value	p-value Prob > F
Model	58.7	6	9.78	3.76	0.0277
A-Particle size	3.25	1	3.25	1.25	0.2876
B-Temperature	12.18	1	12.18	4.68	0.0534
C-Time	24.07	1	24.07	9.25	0.0112
AB	27.21	1	27.21	10.46	0.008
BC	16.64	1	16.64	6.39	0.028
$C^2$	19.15	1	19.15	7.36	0.0202
Residual	28.63	11	2.6		
Lack of Fit	8.15	7	1.16	0.23	0.9568

Similarly, the results of ANOVA obtained for cake yield model is given in Table 4. As it can be seen from the Table, the reduced quadratic model developed for the response was significant and had among its important terms, time (C), interaction of particle size and temperature (AB) and temperature and time (BC), indication that the variation of the selected factors affected the response. The R-squared, its adjusted and predicted values were 0.6459, 0.4527 and -0.0163 respectively. The wide margin between the adjusted and predicted R-squared values and the negative nature of the former can be attributed to the fact that obtained cake yield values were in close range. This means that the overall mean could be a better predictor of the cake yield data.

Numerical optimization carried out based on criteria explained earlier showed that the predicted optimum conditions for obtaining maximum yield of oil of 13.21% with the cake yield of 74.63.4% were 0.74 mm, 55 °C and 5 h of particle size, temperature and time respectively at 91.9% desirability. Validating these conditions experimentally yielded 17.54% oil yield. The obtained yield was observed to be close to 17.9% reported by Musa *et al.* (2016) who optimized avocado seed oil extraction using petroleum ether as solvent. Also, the optimum conditions achieved in this work were in agreement with 0.5 mm, 60 °C and 5 h of particle size, temperature and time obtained in the previous study (Musa *et al.*, 2016).

Table 4: ANOVA results for Cake yield Model

Source	Sum of Squares	Df	Mean Square	F-Value	p-value Prob > F
Model	59.47	7	8.5	3.44	0.0382
A-Particle size	0.66	1	0.66	0.27	0.6176
B-Temperature	10.29	1	10.29	4.17	0.0685
C-Time	13.71	1	13.71	5.55	0.0402
AB	27.91	1	27.91	11.31	0.0072
BC	12.95	1	12.95	5.24	0.045
A <sup>2</sup>	5.11	1	5.11	2.07	0.1806
C <sup>2</sup>	13.96	1	13.96	5.65	0.0388
Residual	24.69	10	2.47		
Lack of Fit	13.83	6	2.3	0.85	0.5925

### 3.3 Physicochemical Properties of Avocado Seed Oil

The characteristics of the oil extracted at the optimum conditions were investigated. The characterization results obtained were as given in Table 5. As it can be seen in the Table, the avocado seed oil extracted at 0.74 mm, 55 °C and 5 h with the yield of 17.54wt% had the density of 0.8709 g/cm<sup>3</sup>, kinematic viscosity of 27.1 cSt (2.71 mm<sup>2</sup>/s), cloud point of 6 °C, pour point -2 °C and flash point of 187°C. Based on the fact values of flash point, viscosity and density obtained were within EN 14214:2012 standard for biodiesel, the oil can be a good feedstock for biodiesel production or may be used as biodiesel if other fuel properties can be determined to conform to appropriate standards. However, the quantity of the oil in the seed may be its impediment for this application on industrial scale. The seed oil had free fatty acid of 1.592%, acid value of 3.168 mgKOH/g, peroxide value of 16.5 meq/kg, iodine value of 66.3 mgI/g, and saponification value of 143 mg KOH/g. The acid value and peroxide value obtained for this oil were higher than 0.6 mg KOH/g and up to 10 meq/kg specified standard for edible oil (Codex Stan 19-1981 Rev. 2-1999). The higher acid value may be associated with presence of unsaturated fatty acid which can make the oil to be susceptible to oxidative degradation (Negash *et al.*, 2019). Also, higher peroxide amount may indicate rancidity of the oil which can decrease the nutritional value of the oil (Negash *et al.*, 2019). High peroxide and acid values make the oil not a good choice for consumption.

Also, based on the fact that the saponification value of the oil was not to close 200 mg KOH/g, it may not be suitable for soap production (Musa *et al.*, 2016; Adaramola *et al.*, 2016). Thus, the extracted oil can be useful for cosmetics production as its saponification is close to that of baobab seed oil reported to be in the range of 140-205 mg KOH/g (Wright, 2021). Also, many studies (Adaramola *et al.*, 2016; Gomez *et al.*, 2014; Ong *et al.*, 2022) have confirmed that the seed extracts are rich in phytochemicals and antioxidants, thus the oil may be useful for manufacturing of body-friendly cosmetic products. However, the characteristic of the extracted oil obtained in this study were observed not to be in line with the ones reported by Musa *et al.* (2016). The difference in the parameters may be as a result of different solvent types used, petroleum ether was adopted for their study.

Table 5: Physicochemical properties of avocado seed oil

Parameter	Values obtained
Density (g/cm <sup>3</sup> )	0.8709
Kinematic Viscosity (mm <sup>2</sup> /s)	2.71
Cloud point ( °C)	6
Pour point (°C)	-2
Flash point (°C)	187
Free Fatty Acid (%)	1.592
Acid value (mgKOH/g)	3.168
Peroxide value (meq/kg)	16.5
Iodine value (mg I/g)	66.3
Saponification value (mgKOH/g)	143.055

## 4. CONCLUSION

In this study, Optimization of operating conditions for extraction of avocado seed oil was investigated using response surface methodology. The oil and the cake yields were found to be affected by the selected factors singly and/or interactively. Also, the models developed were observed to be statistically significant. The optimum conditions

determined for the oil extraction using n-hexane as solvent, were 0.74 mm, 55 °C and 5 h of particle size, temperature and time respectively. Experimentally, the maximum oil yield obtained was 17.54%. Analysis of the physicochemical properties of the oil obtained at the optimum conditions revealed that the oil was suitable for biodiesel and cosmetics production.

## REFERENCES

- Adaramola, B., Onigbinde, A. and Shokunbi, O. (2016). Phytochemical properties and antioxidant potentials of *Persea Americana* seed oil, *Chemistry International*, 2, 168-175
- Codex Stan 19-1981 Rev. 2-1999, available at <https://www.fao.org/3/y2774e/y2774e03.htm> . [Accessed on 24 August, 2022].
- Dagde, K. K., (2019). Extraction of vegetable oil from avocado seed oil for production of biodiesel, *J. Appl. Sci. Environ. Manage.*, 23 (2) 215-221.
- Deepalkshmi, S., Sivalingam, A., Thirumarimurugan, M., Yasvanthrajan, N. and Sivakumar, P. (2014). In-situ transesterification and process optimization of biodiesel from waste avocado seed, National Conference on Green Engineering and Technologies for Sustainable Future-2014, *Journal of Chemical and Pharmaceutical Sciences*, 115-118.
- Duarte, F. F., Borgas, C. D. and Mendonca, C. R. B. (2016). Avocado characteristics, health benefit and uses, *Food Technology. Cienc. Rural*, 46(4).
- Gomez, F. S., Peirosanchez, S., Iradi, M.G.G., Azman, N.A.M. and Almajano, M. P. (2014). Avocado seeds: extraction optimization and possible use as antioxidant in food, *Antioxidant*, 3, 439-454.
- Musa, U., Mohammed, I.A., Suleiman, B., Isah, A.G., Garba M.U., and Mohammed, A. (2016). Response surface optimization of avocado pear (*Persea Americana*) seed oil extraction and characterization as potential industrial feedstock. 37th Annual Conference and Annual General Meeting –Minna 2016 Proceedings Book, 590-596.
- Nagash, Y. A., Amare, D. E., Bitew, B. D. and Dagne, H. (2019). Assessment of quality of edible oils accessed in Gondar City, Northwest Ethiopia, *BMC Res. Notes*, 12, 793.
- Noorul, H., Mujahid, M., Badruddeen, Khalid, M., Vartika, S., Nesar, A., Zafar, K., Zohrameena, S. (2017). Physico-chemical analysis and estimation of total phenolic, flavonoids and proanthocyanidin content of *Persea Americana* (avocado) seed extracts, *World Journal of Pharmaceutical Sciences*, 5 (4), 70-77.
- Ong, E. S., Low, J., Tan, J. C. W., Foo, S. U., Leo and C. H. (2022). Valorisation of avocado seeds with antioxidant capacity using pressurized hot water extraction, *Scientific Reports*, 12, 13036.
- Santos, M.A.Z., Alicieo, T.V. R., Pereira, C. M.P. Ramis-Ramos, G. and Mendonca, C. R. B. (2014). Profile of Bioactive Compounds in Avocado Pulp oil Influence of drying process and extraction method, *Journal of the American Oil Chemists' Society*, 91(1), 3776-3779.
- Wright, R. (2021), Baobab Seed Oil, available at <https://www.botanicalformulations.com/oil-monographs/baobab-seed-oil>. [Accessed on 25 August, 2022].
- Yahaya, S., Giwa, S.O., Ibrahim, M. and Giwa, A. (2016). Extraction of oil from *Jatropha* seed kernels: Optimization and Characterization, *International Journal of Chemtech Research*, 9, 758-770.



## Design of Experiment as an Experimental Key in the Optimisation of the Oil Yield from Fluidised Catalytic Cracking of Oil Shale Using ZSM-5 Catalyst

B. O. Umeh<sup>1</sup>, P.E. Dim<sup>2</sup>, A. G. Olugbenga<sup>3</sup> and M.B. Baba<sup>4</sup>

<sup>1,2,3</sup>Department of Chemical Engineering, Federal University of Technology Minna, Niger State, Nigeria

<sup>4</sup>Department of Water Aquaculture and Fishery Technology WAFT, Federal University of Technology Minna, Niger State, Nigeria

<sup>1\*</sup>[bobbyfrank.umeh@st.futminna.edu.ng](mailto:bobbyfrank.umeh@st.futminna.edu.ng), <sup>2</sup>[pevdim@futminna.edu.ng](mailto:pevdim@futminna.edu.ng), <sup>3</sup>[grace.adeola@futminna.edu.ng](mailto:grace.adeola@futminna.edu.ng),

<sup>4</sup>[choiceangel@futminna.edu.ng](mailto:choiceangel@futminna.edu.ng)

\*Corresponding author

---

### ABSTRACT

Alternatively, an unconventional fuel oil is obtained by fluidised catalytic cracking of oil shale using abundant deposit of Kaolin Clay which serves as a local source for ZSM-5 Catalyst. Oil Shale is an unconventional source of energy which is abundantly present in some parts of Nigeria like Abakaliki, Bida, Adamawa, Benue, Borno and among others as reported. The material is significant to Nigeria's economic sustainability but yet to be tapped efficiently. The aim of this work is to improve the yield of fuel oil from shale oil via fluidised catalytic cracking using abundant locally sourced ZSM-5 as catalyst. In this research work, oil shale sample obtained from Lokpanta area of the Abakaliki anticlinorium in Ebonyi State, an epicenter in the Lower Benue trough. Prior to the fluidised catalytic cracking of oil shale using a fabricated fluidised bed reactor, proximate and ultimate analyses were carried out to investigate the obtained shale oil. The optimisation methodology involved the use of Design of Experiment (DOE) where the Central Composite Design (CCD) was adopted. The factorial indicates that the optimum yield is at point 5. Therefore, the experimental result shows that Lokpanta has a good organic matter which makes it fit for the optimisation of oil yield via a fluidised catalytic bed reactor along with other analytical assessment in subsequent research findings.

**Keywords:** Lokpanta Oil Shale, Zeolite Socony Mobil (ZSM-5) Catalyst, Design of Experiment (DOE), Central Composite Design (CCD) and Fluidised Catalytic Bed Reactor (FCBR).

### 1. INTRODUCTION

Nigeria is ranked the major oil producer in Africa and sixth largest oil producing country in the world, with an estimated crude oil production capacity of 2.5 million barrels in 24 hours. The nation appears to have a greater propensity to produce gas than oil. Nigeria's gas production capacity in the year 2000 was approximately 1,681.66 billion scf; 1,3715 billion scf was associated gas, while the other 310.16 billion was non-associated gas. Oil drilling falls into one of two basic categories: onshore drilling or offshore drilling methods. Onshore drilling deals with drilling sites located on land or swampy areas. About 70 percent of world oil production is derived from onshore drilling. Offshore drilling takes place within water bodies. Only 30 percent of the world's oil is obtained from offshore drilling. There were 37.2 billion barrels ( $5.91 \times 10^9$  m<sup>3</sup>) of inland oil reserves in Nigeria in the year 2011, which ranked the country as the largest producer of oil in Africa. A basin is a depression in the earth's surface, wholly or partially surrounded by higher land such as a river basin. Basins are formed in some ways like the other landforms of the world. One of the standard ways is the basins are manufactured through motion of earth's crust, known as plate tectonics. There are several sedimentary basins in Nigeria to mention a few are; Bida basin, Benue trough complex, Bomo/Chad basin, Eastern dahomey basin, Niger delta basin and Sokoto basin. Oil shale is organic-rich fine-grained sedimentary rock containing kerogen (a solid mixture of organic chemical compounds) from which liquid hydrocarbons are produced, called shale oil (not to be confused with tight oil-crude oil which occurs naturally in shale). Shale oil is a substitute for conventional crude oil. Shale oil extraction is an industrial process for atypical oil production. This process converts kerogen in oil shale into shale oil by pyrolysis, hydrogenation, or thermal dissolution (Daniel, 2016).

Pyrolysis is the thermal breakdown of materials (kerogen) at increased temperature in an inactive atmosphere. It encompasses a conversion of chemical composition and is irretrievable. The main product of pyrolysis of kerogen is hydrocarbons (liquid, solid and gas). Carbon dioxide and water are also formed in the process. The carbon dioxide content aids to predict whether or not kerogen will be expected to produce majorly oil, gas or both of them. Thus, by employing only the carbon dioxide and hydrocarbon pyrolysis yields of oil shale, the quantitative organic geochemistry of the rock

and its petroleum potential can be estimated. There are various pyrolysis techniques apply to oil shale evaluation. These are Rock-eval pyrolysis, open and close pyrolysis and Thermo-gravimetric Analysis (TGA). Rock-eval pyrolysis can be applied in determining the hydrocarbon potential of shale rock. Rock-eval is majorly applied for fast and preliminary screening of sedimentary rock. TGA (Thermo-gravimetric Analysis) is used to study sample weight loss due to thermal decomposition and the de-volatilization of organic matter. This is commonly applied in dynamic study and to predict thermal characteristics of oil shale. Open and close pyrolysis feigns hydrocarbon generation in source rock and are applied in more detailed evaluation of hydrocarbon generative prospect. These types of pyrolysis also permit one to determine product's compositions (Liive *et al.*; 2007).

## 2. METHODOLOGY

### 2.1. Design of Experiment

#### 2.1.1 Optimization of Shale oil Production Energy with a fluidized ZSM-5 Catalyst along with other catalyst using RSM

Design-Expert Software was used to analyse the experimental data of four different oil shale and catalyst so as to establish the design matrix. Numerical and graphical optimization techniques were used and the responses are mass and energy. Residence Times (**A**), Reaction Temperature (**B**) and Catalyst Dosage(**C**) are selected (based on pilot experiments) to describe this system with reasonable ranges as follows:

- a.  $5\text{mins} \leq \text{residence time (m)} \leq 20\text{mins}$
- b.  $300^{\circ}\text{C} \leq \text{reaction temperature (C)} \leq 800^{\circ}\text{C}$
- c.  $1\text{ratio} \leq \text{catalyst dosage} \leq 2\text{ratio}$

In this study, the test was based on a three- factor three level Central Composite Design (CCD), as presented in Table 1. An RSM was applied to the experimental data using **Design Expert Software Version.13**; polynomial equation generated fitted to the experimental data to obtain the regression equation for the Optimum Yield and energy. The statistical significance of the terms in the equation was examined using one-way anova.

Table 1: Build Information

Design Expert Version	
<b>File Version:</b> 13.0.5.0	
<b>Study Type:</b> Response Surface	<b>Subtype:</b> Randomized
<b>Design type:</b> Central Composite	<b>Runs:</b> 20.00
<b>Design Model:</b> Quadratic	<b>Blocks:</b> No Blocks

## 3. RESULTS AND DISCUSSION

The design is aimed at improving the yield of shale oil production in large scale with minimal energy consumption under the use of ZSM-5 catalyst.

### 3.1 Design of Experiment

Considering Table 2 and Fig. 1; the design of experiment (DOE) indicates that the optimum yield will be recorded at point 5, catalytic pyrolysis using synthesized ZSM-5 decreased the liquid oil yield (52%) with an increase in gases (17.7%) and char (30.1%) production. the produced char was 14.5% with ZSM-5 zeolite and its higher than 10.25% from thermal pyrolysis. In addition, gases produced were increased with ZSM-5 Zeolite catalyst 55%. Mason *et al.*, (2015) and Aleksander *et al.*, 2021.

Design of Experiment as an Experimental Key in the Optimisation of the Oil Yield from Fluidised Catalytic Cracking of Oil Shale Using ZSM-5 Catalyst

Table 2: Actual Experimental Data

Std	Run	TIME(M)	TEMP(C)	ZSM-5 CATALYST	Lokpanta oil%
17	1	12.5	550	1.5	11.98
3	2	5	800	1	11.41
18	3	12.5	550	1.5	11.98
12	4	12.5	970.448	1.5	11.98
8	5	20	800	2	12.42
14	6	12.5	550	2.3409	12.84
2	7	20	300	1	11.41
13	8	12.5	550	0.659104	11.12
9	9	9	-0.113446	550 1.5	11.98
20	10	12.5	550	1.5	11.98
19	11	12.5	550	1.5	11.98
1	12	5	300	1	11.41
15	13	12.5	550	1.5	11.98
4	14	20	800	1	11.41
16	15	12.5	550	1.5	11.98
5	16	5	300	2	12.42
11	17	12.5	129.552	1.5	11.98
7	18	5	800	2	12.42
6	19	20	300	2	12.42
10	20	25.1134	550	1.5	11.98

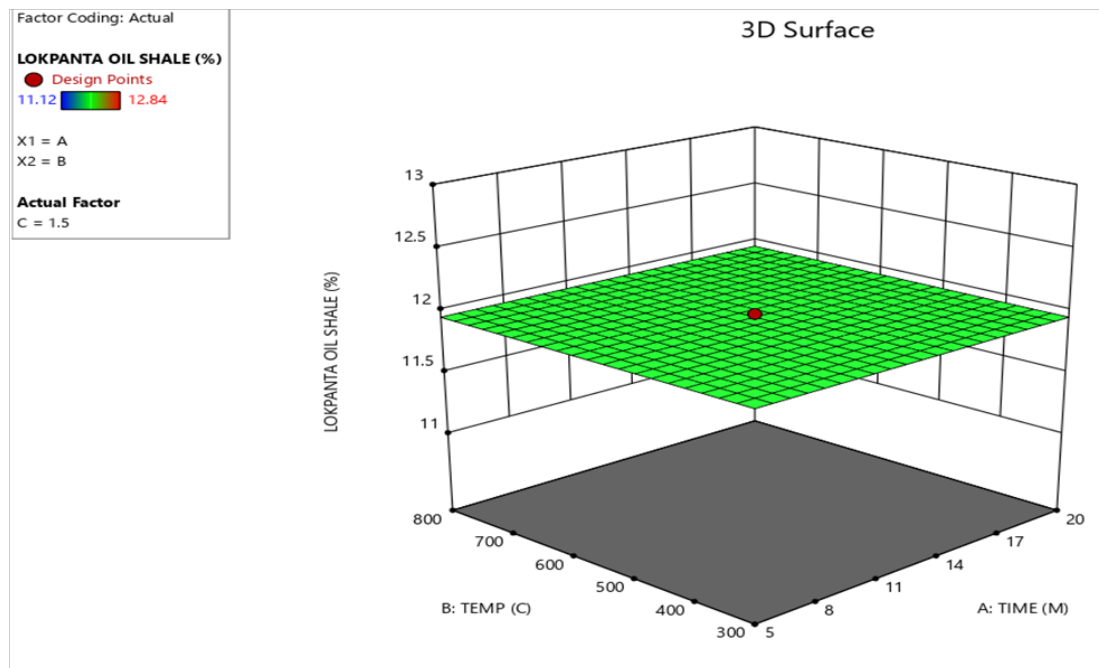


Figure 1: 3D ANOVA – Dimensional Analysis

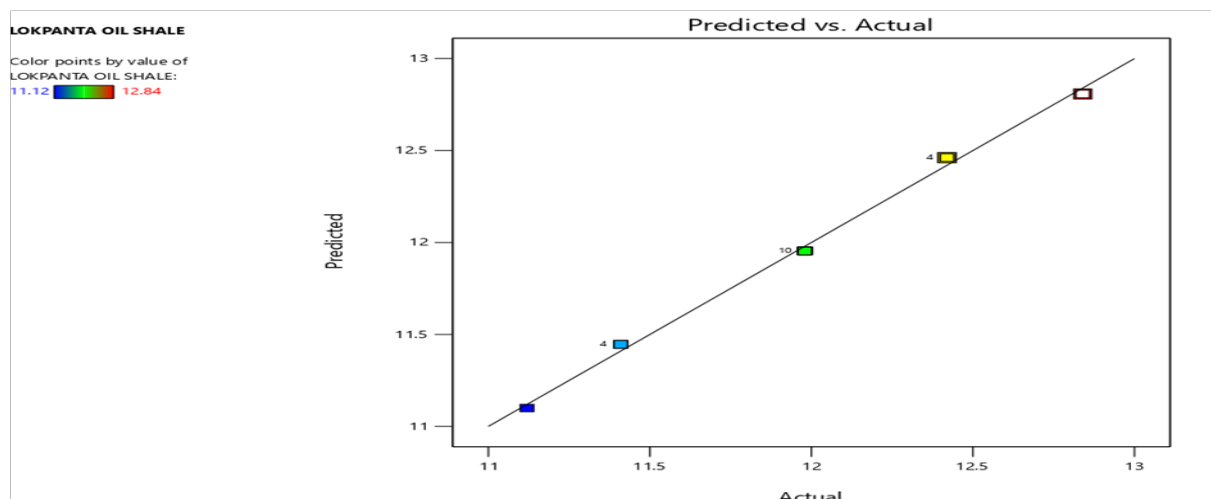


Figure 2: ANOVA Graph Plot

Table 3: ANOVA Linear Model  
Response1: Lokpanta Oil Shale

Source	Sum of Squares	df	Mean square	F-Valua	p -Value
<b>Model</b>	3.52	3	1.17	919.44	<0.0001
Significant					
A-TIME	0.0000	1	0.0000	0.0000	1.0000
B- TEMP	4.441 E-16	1	4.441 E-16	3.481E-13	1.0000
C-ZSM-5 CATALYST	3.52	1	3.52	2758.32	<0.00001
<b>Residual</b>	0.0204	16	0.0013		
Lack of fit	0.0204	11	0.0019		
Pure Error	0.0000	5	0.0000		
<b>C.Total</b>	3.54	19			

From Table 3, the following information are extracted:

- Factor coding is Coded.
- Sum of squares is Type III-Partial
- The Model F-valus is 919.44 implies the model is significant. There is only a 0.01% chance that an F-value this large could occur due to noise.

P-Values less than 0.0500 indicate model terms are significant. In this case C is a significant model term. Values greater than 0.1000 indicate the model terms are not significant. If there are many insignificant model terms (not counting those required to support hierarchy), model reduction may improve the model.

Table 3.3 ANOVA Statistics

Fit Statistics	
<b>Std Dev.</b> 0.0357	<b>R<sup>2</sup></b> 0.9942
<b>Mean</b> 11.95	<b>Adjusted R<sup>2</sup></b> 0.9932
<b>C.V %</b> 0.2988	<b>Predicted R<sup>2</sup></b> 0.9901
	<b>Adeq. Precision</b> 106.8893



## Design of Experiment as an Experimental Key in the Optimisation of the Oil Yield from Fluidised Catalytic Cracking of Oil Shale Using ZSM-5 Catalyst

The predicted  $R^2$  of 0.9901 is in reasonable agreement with the Adjusted  $R^2$  of 0.9932; i.e the difference is less than 0.2. Adequate precision measures the signal to noise ratio. A ratio greater than 4 is desirable. The obtained ratio of 106.889 indicates an adequate signal. This model can be used to navigate the design space.

Therefore, the experimental result shows that Lokpanta has a good organic matter which makes it fit for the optimisation of oil yield with an illustrative polynomial actual equation expressed below as:

$$y = 10.143100k - 9.11930e - 17t - 2.61562e - 18T + 1.01527L$$

Where:  $y$  = lokpanta oil shale,  $k$  = constant,  $t$  = time,  $T$  = temperature, and  $L$  = catalyst

## 4. CONCLUSION

The Design of Experiment (DOE) study shows that there is a great need for researchers to embark on the optimisation yield of oil from Lokpanta oil shale reserves; this will enable the comparison between actual and approximate results. The factorial indicates that the optimum yield is at point 5.

## ACKNOWLEDGEMENT

Authors wishing to acknowledge Step B Nanotech Lab and Department of WAFT Lab in the Federal University of Technology Minna.

## REFERENCES

- Aleksander Jankovic, Gaurav Chaudhary & Francesco Goia (2021) Designing the design of experiments (DOE)- An investigation on the influence of different factorial designs on the characterization of complex systems. :A Journal of Science Direct Elsevier Biglarbigi, K., Mohan, H., Crawford, P. & Carolus, M. (2007). Potential for Oil Shale Development in the United States. Society of Petroleum Engineers, SPE Paper 110590.
- Daniel, D. D. (2016). The Economic Feasibility of Oil Shale Development in Nigeria: A Case Study of Abakaliki Shale Deposit. Unpublished B.Eng. Project submitted to the Department of Chemical and Petroleum Engineering, University of Uyo, Nigeria.
- Ehinola, O. A., Sonibare, O. O. & Akanbi, O. A. (2005). Economic Evaluation, Recovery Techniques and Environmental Implications of the Oil Shale Deposit in the Abakaliki Anticlinoria, Southeastern Nigeria. Estonian Academy Publishers, 22(1):5-19. [3].
- Liive, S. (2007). Oil Shale Energetics in Estonia. Estonian Academy Publishers, 24(1):1-4.
- Mason, F., Lucija, A. & Sheila, M. (2015). The Economics of Shale Gas Development. RFF DP 14-42REV: November 2014, Revised February 2015.
- Olawuyi, D. S. (2014). Hydraulic Fracturing Technology and Shale Gas Production in Nigeria: Legal and Sustainability Assessment. Petroleum Technology Development Journal, 2(4):38-40
- Zaixing Jiang, Wenzhao Zhang, Chao Liang, Yongshi Wang, Huimin Liu and Xiang Chen (2016). Basic Characteristics and evaluation of Shale oil reservoirs. Petroleum Research: A Journal of Science Direct Elsevier.



## Modelling, Simulation and Optimization of a Reactive Distillation Column

Chinenye S. UKPAI<sup>1\*</sup>, Mufliah G. OMOFOYEWA<sup>2</sup>, Idowu I. OLATEJU<sup>3</sup>, Saidat O. GIWA<sup>4</sup>, Abdulwahab GIWA<sup>5,\*</sup>

<sup>1,2,3,5</sup>Department of Chemical and Petroleum Engineering, Afe Babalola University, Ado-Ekiti, Ekiti State, Nigeria

<sup>4</sup>Chemical Engineering Department, Faculty of Engineering and Engineering Technology, Abubakar Tafawa Balewa University, Tafawa Balewa Way, Bauchi, Nigeria

<sup>1</sup>[ukpaichinerve@yahoo.com](mailto:ukpaichinerve@yahoo.com), <sup>2</sup>[gomofoyewa@gmail.com](mailto:gomofoyewa@gmail.com), <sup>3</sup>[iolateju@abuad.edu.ng](mailto:iolateju@abuad.edu.ng), <sup>4</sup>[sogiwa@atbu.edu.ng](mailto:sogiwa@atbu.edu.ng), <sup>5,\*</sup>[agiwa@abuad.edu.ng](mailto:agiwa@abuad.edu.ng)

\*Corresponding author

---

### ABSTRACT

Reactive distillation (RD) is a technology for process intensification that combines chemical reaction and separation (distillation) into a single device. Separation of products from unconverted reactants enables high conversion in the reactive distillation system because product removal restores equilibrium and forces the reaction to completion. This method has numerous advantages; however, the combination of chemical reaction and separation in the same piece of equipment has created some difficulties in the process, and chemical engineers are still working on finding the best optimum parameters for the process. Consequently, this research has been carried out to determine the optimum values of the parameters required for a reactive distillation system involved in the production of biodiesel. Aspen HYSYS, Design Expert v13 and MATLAB were used respectively to create the steady state model of the system, design the experiments and develop the models for the optimization to estimate the optimum values. The optimum values of the simulation process were obtained to be a reflux ratio of 10 and a reboiler duty of 500000 kJ/s. The reactive distillation system was discovered to be capable of completing both processes in a single column with improved efficiency and yield.

**Keywords:** *Reactive distillation, esterification, Aspen HYSYS, Design Expert, MATLAB.*

### 1. INTRODUCTION

In recent decades, there has been a growing interest in developing alternative technologies to the oil economy that are based on what are known as renewable energy sources. This is due to the fact that the exhausts from currently used petroleum-based fuels have been found to have detrimental environmental effects. A usable biofuel made from plant oils and animal fats, for example, has the potential to replace petroleum fuels since it is renewable. Biodiesel is one of these renewable fuel types (Giwa *et al.*, 2021).

Biodiesel is a non-toxic, sulphur-free, and ecologically friendly alternative diesel fuel that is renewable and biodegradable. It is made up of fatty acid methyl (or ethyl) esters that are made from renewable resources such as vegetable oils, animal fats and restaurant grease. One of the appealing features of biodiesel is that it does not necessitate any-engine changes, therefore, the engine does not need to be dedicated to biodiesel use (Tat and Gerpen, 2002). Sulphur level, flash point, aromatic content, and biodegradability are all advantages of biodiesel fuel over diesel fuel. Moreover, biodiesel emits less pollutant than petroleum diesel, it does not contribute to an increase in the net carbon dioxide concentration in the atmosphere and reduces the intensity of greenhouse gas emissions (Ahmia *et al.*, 2014). The reaction involved in the production of biodiesel is esterification reaction. Esterification reaction is a reversible reaction in which alcohol and carboxylic acid react to generate an ester and water as a by-product (Ukpai, 2022).

The process of producing biodiesel can be carried out experimentally. Simulating the production process helps in predicting the yield and understanding the behaviour of the system prior to experimental implementation. Process simulation is a relatively old intelligent technology that has evolved into a powerful computing tool for chemical engineering design, original engineering transformation, and optimization in recent decades. As an example, one of the most widely used simulation systems is Aspen HYSYS (Ukpai, 2022).

For the oil and gas production, gas processing, petroleum refining and air separation industries, Aspen HYSYS is a market-leading process modelling solution for conceptual design, optimization, business planning, asset management,

and performance monitoring. Aspen HYSYS is a critical component of Aspen Tech's Aspen ONE Engineering software. The ability to mimic a process is crucial for chemical engineers (Chowdhury *et al.*, 2012). In the oil and gas refining business, Aspen HYSYS has shown to be a very intuitive and user-friendly process simulator. Users with no prior experience with Aspen HYSYS can pick it up and learn how to use it. A highly interactive process flow diagram for generating and navigating huge simulations is one of the very intuitive capabilities. Process design, equipment sizing, and preliminary cost estimation are all handled efficiently (Ambar *et al.*, 2012).

A very flexible and user-friendly distillation column modeling environment is also provided by the application. Furthermore, the interactive aspect of HYSYS allows users to quickly and effectively construct and use their models. For the oil and gas and refining industries, Aspen HYSYS provides a thorough thermodynamics basis for precise calculation of physical parameters, transport attributes, and phase behavior. In both steady state and dynamic contexts, a comprehensive library of unit operation models encompassing distillation, reactors, heat transfer processes, rotating equipment, controllers, and logical operations is available (Ambar *et al.*, 2012).

In applying Aspen HYSYS for the production of biodiesel, an integrated method, which is known as reactive distillation can be employed. Reactive distillation (RD) is a process intensification technique that combines chemical reaction and distillation in one device. In other words, reactive distillation entails a chemical reaction as well as multi-component distillation at the same time (Nwambuonwo and Giwa, 2015). The total capital cost of reactive distillation is lowered since two process steps are merged in a single unit. This type of integration is also advantageous in terms of lowering pump and other instrumentation costs. The reduction in total energy costs is owing to the exothermic nature of many chemical processes, which are advantageous in supplying heat for simultaneous component separation (Sakhre, 2019).

Due to high potential of biodiesel replacing petroleum-based fuel, coupled with advantages of reactive distillation, research has begun to predict the practical feasibility of biodiesel production via the integrated system by employing modelling and simulation approaches. For instance, Giwa and Giwa (2013) used a reaction-integrated distillation column to optimize the esterification process between myristic acid and isopropanol for the production of a biodiesel (isopropyl myristate), with the bottom mole fraction of isopropyl myristate as the objective function and the reflux ratio, the feed ratio, and the reboiler duty as the manipulated variables. HYSYS 3.2 and Response Surface Methodology were used to create the experimental setup and design the experimental simulations respectively. With the help of MATLAB R2012a, the constructed model was theoretically simulated and optimized, and the theoretical optimum parameters were used to run the experimental setup. The practical simulation with these values provided the bottom isopropyl myristate mole fraction of 0.9912, which compared very well with the theoretical simulation value of 1.0000, indicating that the theoretical optimum values derived with the aid of MATLAB R2012a were valid.

Similarly, Akomolafe *et al.* (2021) created and simulated steady-state and dynamic models for a reactive distillation process using Aspen Plus V11. The modelling and simulation of the process were presented using an esterification process as a case study, which produced ethyl acetate and water as a by-product of the interaction between acetic acid and ethanol. The input parameters of the developed model were modified to generate sets of data that were utilized to develop a set of dynamic models for the system using the System Identification Toolbox of MATLAB. The dynamic models were used to investigate how the outputs of the system were changing with time. The good correlation between the acquired results and those found in the literature demonstrated that the developed reactive distillation technology model was valid. Due to the consistent steady-state outputs and dynamic responses acquired, it was also determined that using Aspen Plus and MATLAB together produced stable models that could be successfully simulated for this complex process.

It has been identified that obtaining the appropriate purity of a product (biodiesel) in an industry is not very easy, and this has been determined to be due to insufficient optimum parameters for the system. As such, this research work has been carried out to estimate the optimum parameters for the production of methyl propanoate, which is a biodiesel, via reactive distillation process.

## 2. METHODOLOGY

In this work, Aspen HYSYS V10 (Aspen, 2019) was used for the simulation of the reactive distillation process for the production of biodiesel. The components (propionic acid, methanol, methyl propanoate and water) involved in the process were selected from the Aspen HYSYS database. NRTL model was chosen to carry out the property calculation.

### 2.1 Steady-State Simulation

The column had 30 stages, excluding the condenser and the reboiler. Thereafter, the streams and equipment used were obtained from the Model Palette after entering the Simulation Environment of the simulator and connected as shown in Figure 1.

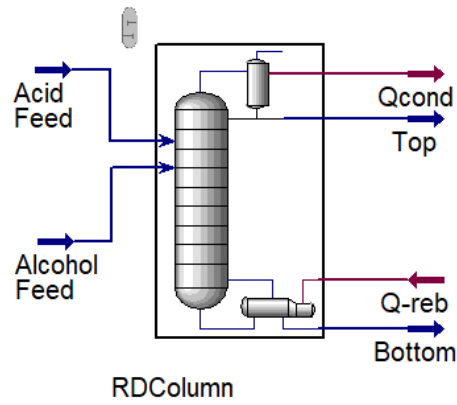
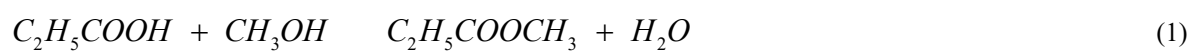


Figure 1: Aspen HYSYS model of the reactive distillation biodiesel production process

Then, the parameters for the input streams and reactive distillation column were specified as given in Table 1.

Table 1: Inlet and column conditions for the Reactive Distillation column

Description	Parameter
Inlet Streams	Acid Feed and Alcohol Feed
Acid feed temperature	350 °C
Acid feed pressure	5 atm
Acid feed flow rate	100000 kgmol/h
Alcohol feed temperature	150 °C
Alcohol feed pressure	1 atm
Alcohol feed flow rate	100000 kgmol/h
Number of column stages	30
Condenser type	Total
Condenser pressure	1 atm
Acid feed stage	8
Alcohol feed stage	19
Reboiler pressure	1 atm
Reboiler duty	600000 kJ/s
Reflux ratio	3
Reaction type (Equation 1)	Equilibrium
Solving method	Sparse Continuous solver



### 3.2 Experimental Design

The reflux ratio and the reboiler duty were utilized as the decision variables to design the experiments for the process synthesis using Design Expert 13. The design matrix given in Table 3, was generated according to central composite design of response surface methodology (RSM). The specified low and high bounds of the variables are given in Table 2 while the obtained experimental runs were as shown in Table 3.

Table 2: Low and high bounds of the manipulated variables

Factor	Name	Coded Low	Coded High
A or X <sub>1</sub>	Reflux Ratio	3	5
B or X <sub>2</sub>	Reboiler Duty	200000	500000

Table 3: Experimental runs

Std	Run	Reflux ratio	Reboiler duty (kJ/s)
1	1	3	200000
13	2	4	350000
8	3	4	562132
5	4	2.58579	350000
4	5	5	500000
2	6	5	200000
9	7	4	350000
10	8	4	350000
3	9	3	500000
7	10	4	137868
11	11	4	350000
6	12	5.41421	350000
12	13	4	350000

Thereafter, by using the conditions specified in each of the runs, the Aspen HYSYS model earlier developed was run to obtain mole fractions of both the top and the bottom products of methyl propanoate (biodiesel) and water as the responses. The responses were used to generate model equations for the system, which were used to carry out the optimization of the process.

### 2.3 Optimization

The optimization of the process was carried out with the aid of Optimization Toolbox of MATLAB R2021a using *fsolve* command and the developed model equations of the process. The decision variables of the optimization were the reflux ratio and the reboiler duty while the objective was the maximization of the mole fraction of the desired product (methyl propanoate) obtained from the reactive distillation column.

### 3. RESULTS AND DISCUSSION

After the steady state simulation, the reboiler duty and reflux ratio were used as decision variables to obtain different runs in Design expert which were then put in the HYSYS simulation to get the mole fractions of methyl propanoate and water obtained from the top and the bottom of the reactive distillation column as given in Table 4, respectively.

Table 4: Mole fractions of biodiesel and water obtained from the top and the bottom products

Run	Reflux Ratio	Reboiler Duty	Top		Bottom	
			Biodiesel	Water	Biodiesel	Water
1	3	200000	0.5465	0.3156	0.2569	0.4338
2	4	350000	0.6385	0.3597	0.2651	0.4291
3	4	562132	0.6779	0.3207	0.3013	0.5380
4	2.58579	350000	0.5654	0.2931	0.2809	0.5638
5	5	500000	0.6968	0.3018	0.2993	0.4913
6	5	200000	0.0000	0.0000	0.0000	0.0000
7	4	350000	0.6386	0.3597	0.2651	0.4291
8	4	350000	0.6386	0.3597	0.2651	0.4291
9	3	500000	0.6281	0.3377	0.2871	0.5606
10	4	137868	0.5942	0.3830	0.2325	0.3425
11	4	350000	0.6385	0.3597	0.2650	0.4291
12	5.41421	350000	0.6771	0.3213	0.2779	0.4238
13	4	350000	0.6386	0.3597	0.2650	0.4290

These mole fractions were used as responses together with the manipulated variables in the Design Expert to develop model equations for the system. However, the actual models could not be shown because they contained some terms that were aliased with one another. Further analysis revealed that the p-values of some of the model terms were greater than the significance level of 0.05. The very high values of the p-values of these factors made them to be insignificant. Consequently, the developed cubic model was modified and the modified model equations for the mole fractions of top methyl propanoate, top water, bottom methyl propanoate and bottom water were as shown in Equations (2) – (5).

$$x_{bt} = -1.85599 + 2.28619R - 4.83432E - 6Q - 2.82031E - 6RQ - 0.434041R^2 \dots + \dots + 2.64730E - 11Q^2 + 1.10005E - 6R^2Q - 7.07823E - 12RQ^2 \quad (2)$$

$$x_{wt} = -1.58232 + 1.62758R - 2.83247E - 6Q - 1.87317E - 6RQ - 0.291149R^2 \dots + \dots + 1.68682E - 11Q^2 + 6.86676E - 7R^2Q - 4.50581E - 12RQ^2 \quad (3)$$

$$x_{bb} = -0.232020 + 0.665575R - 2.46455E - 6Q - 7.77304E - 7RQ - 0.143862R^2 \dots + \dots + 1.00354E - 11Q^2 + 3.87004E - 7R^2Q - 2.67175E - 12RQ^2 \quad (4)$$

$$x_{wb} = -0.175374 + 0.849141R - 1.78182E - 6Q - 1.57437E - 6RQ - 0.190819R^2 \dots + \dots + 1.27464E - 11Q^2 + 5.69369E - 7R^2Q - 3.39011E - 12RQ^2 \quad (5)$$

Looking at the model equations very well, it would be discovered that some of the insignificant factors referred to before were still contained in the modified model equation owing to the hierarchical problem of the model. The analysis of variance of the modified model equation developed was also carried out and the results obtained showed that the situation was better in the sense that the overall model has a predicted R-Squared value of 0.8923.

The optimum values obtained from the optimization carried out, in which the objective function was the maximization of the biodiesel (methyl propanoate) present in the top product of the column, using the Optimization Toolbox of MATLAB were as shown in Table 5.

Table 5: Optimum values

Variable	Optimum value
Reflux ratio	5
Reboiler duty (kJ/s)	500000
Top methyl propanoate mole fraction	1

In order to validate the optimum values obtained theoretically, they were used to run an experiment in Aspen HYSYS, and the mole fraction of methyl propanoate given was found to be 0.8435. This value was found to compare favorably well with the theoretical one.

Thereafter, the temperature profile of the finally converged Aspen HYSYS simulation was plotted (Figure 2), and it was discovered that, as expected, the temperature of the condenser was less than that of the reboiler. However, during the simulation, very high temperature of the column was observed at the reaction section of the column. The high temperature observed at the reaction section was as a result of the exothermic nature of the esterification reaction taking place there.

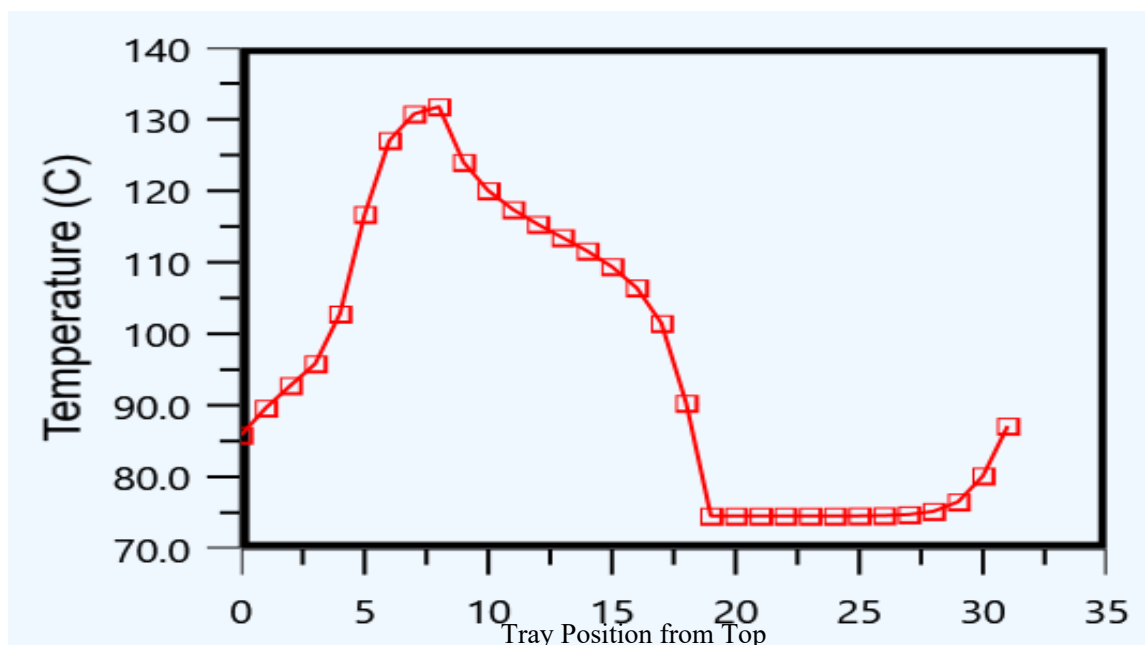


Figure 2: Temperature profile of the reactive distillation column

Also shown in Figure 3 were the composition profiles of the liquid being obtained from the column at steady state. As can be seen from the plots given in Figure 3, the component with the highest mole fraction at the top and second highest mole fraction at the bottom of the column was found to be the desired product (methyl propanoate – biodiesel).

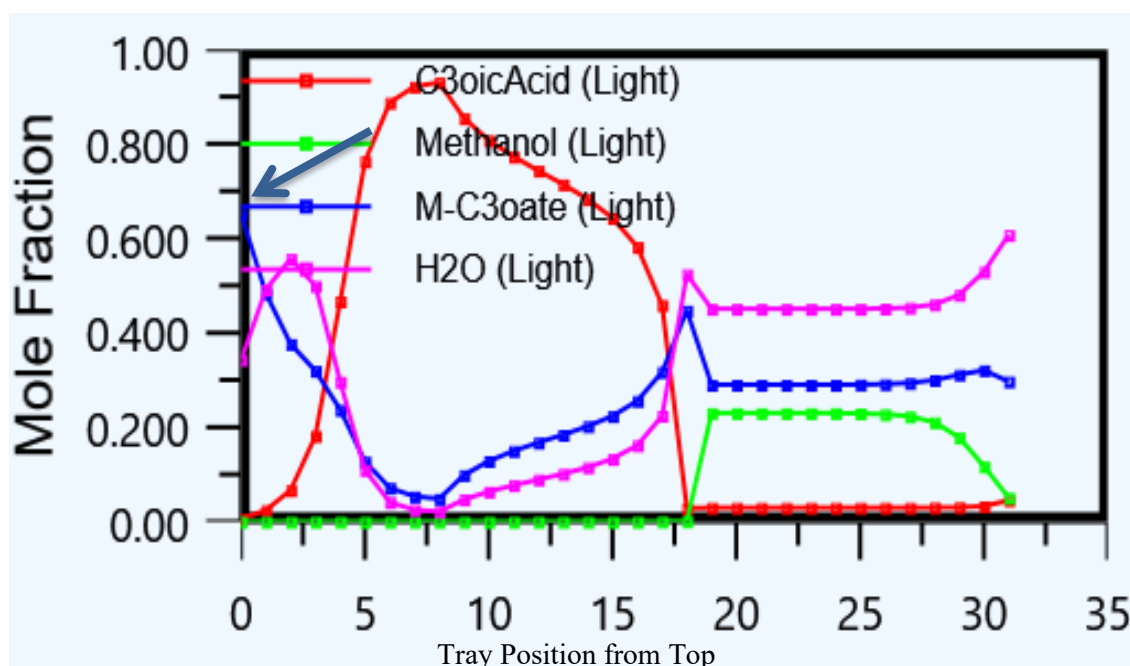


Figure 3: Steady state liquid mole fraction profiles of the components obtained from optimization

#### 4. CONCLUSION

The results obtained from the steady-state simulation carried out at different runs of the experiments designed with the aid of Design Expert revealed that a valid model that could be used to represent the reactive distillation process for the production of biodiesel was developed successfully with the aid of Aspen HYSYS. Furthermore, the models used for the optimization were also discovered to be significant enough for the system. The excellent convergence given by the simulation of the Aspen HYSYS model designed for the reactive distillation esterification process demonstrated the versatility of the process simulator in accurately representing the behaviour of a complex process like reactive distillation. The results also showed that achieving production of biodiesel of high purity could be possible when the optimum parameters with reflux ratio of 10 and reboiler duty of 500000 kJ/s are applied.

#### ACKNOWLEDGEMENTS

Special thanks go to Aare Afe Babalola, LL.B., FFPA, FNIALS, FCI Arb, LL.D., SAN, OFR, CON – The Founder and President, and the Management of Afe Babalola University, Ado-Ekiti, Ekiti State, Nigeria for providing a very conducive environment and the necessary materials that enabled the accomplishment of this research work.

#### REFERENCES

- Ahmia, A.C., Danane, F., Bessah, R. and Boumesbah I. (2014) 'Raw material for biodiesel production. Valorization of used edible oil', *Revue des Energies Renouvelables*, 17, pp. 335-343.
- Akomolafe, D.O., Olateju, I.I., Owolabi, J.O. and Giwa, A. (2021) 'Modelling and Simulation of Reactive Distillation Technology: A Case Study of Esterification process', 64(2), pp. 1-19.
- Ambar, T., Chavan, T., Kavale, M. and Walke, M.S. (2012) 'Simulation of Process Equipment by using Hysys', *International Journal of Engineering Research and Applications (IJERA)*, ISSN: 2248-9622.
- Aspen (2019). Aspen HYSYS V11. Aspen Technology, USA.
- Chowdhury, N.B., Hasan, Z., and Biplob A. H. M. (2012) 'HYSYS Simulation of a Sulfuric Acid Plant and Optimization Approach of Annual Profit', *Journal of Science (JOS)*, 2 (4).
- Giwa, A. and Giwa, S.O. (2013) 'Isopropyl Myristate Production Process Optimization Using Response Surface Methodology and MATLAB', 2(1), pp. 1-11.
- Giwa, S.O., Haggai, M.B., and Giwa, A. (2021) 'Production of Biodiesel from Desert Date Seed Oil Using Heterogeneous Catalyst', 53, pp. 180-189.
- Tat, M.E. and Gerpen, J.H. (2002) 'Physical Properties and Composition Detection of Biodiesel Fuel Blends', *The Society for engineering in agricultural, food and biological systems, An ASAE Meeting Presentation*, pp. 2-11.
- Nwambuonwo, S.C. and Giwa, A. (2015) 'Modelling, simulation and optimization of Fatty Acid Methyl Ester Reactive Distillation Process Using Aspen Hysys', 4(7), pp. 1-8.
- Sakhre, V. (2019) 'Reactive Distillation: Modeling, Simulation, and Optimization', in V. Steffen (ed.), *Distillation - Modelling, Simulation and Optimization*, IntechOpen, London. 10.5772/intechopen.85433.
- Ukpai, C.S. (2022) *Modelling and Optimization of a Reactive Distillation Column*. Bachelor of Engineering Project Report Submitted to Afe Babalola University, Ado-Ekiti, Ekiti State, Nigeria, 52 pp.





## Process Simulation and Optimization of Palm Oil from Spent Bleaching Earth via Supercritical Extraction for Sustainable Development

Wasiu A. OLADOSU<sup>1\*</sup>, Mohammed S. HARUNA<sup>1</sup>, Alaba A. SALAMI<sup>1</sup>

<sup>1</sup>National Agency for Science and Engineering Infrastructure (NASENI), Abuja

\*Corresponding author: wasiureal@gmail.com

### ABSTRACT

Vegetable oils undergo numerous refining steps to remove undesirable compounds and produce high quality, stable commercial products. Recovery of vegetable oil from spent bleaching earth is an area where ample opportunities exist for cleaner production and cost saving in the vegetable oil processing industry. Conventional oil extraction and refining processes, which involve multiple unit operations, have several disadvantages. These include complex separation steps, energy-intensive operations, the requirement for large amounts of water and hazardous chemicals and the potential of generating large quantities of wastes. Therefore, the objective of this study is to develop a process simulation and optimization for the recovery of palm oil from spent bleaching earth using supercritical fluid extraction (SFE). The methodology adopted for this study include applying experimental data to enable the development of a reliable simulation and optimization models of the supercritical fluid extraction to recover palm oil from spent bleaching earth. The result of the study shows that optimal total annual cost of US\$246 million at 10 MPa and 45 oC with optimum separation pressure of 2 MPa was obtained. The simulation and optimization for obtaining palm oil from spent bleaching earth via SFE will produce comparable and better oil recovery, using a significantly intensified process that is green and sustainable.

**Keywords:** Palm oil, Spent Bleaching Earth, Supercritical Fluid Extraction.

### 1. INTRODUCTION

Bleaching earth is used in the stage of oil bleaching during the refining process to remove colour, oxidized products, metals, and gum from the oil (Aziz *et al.*, 2015). After the vegetable oil bleaching, the spent bleaching earth (SBE) is separated from the oil by filtration and discharged as a waste product which is commonly disposed in solid waste landfill (Prokopov and Mechevov, 2013). Based on world oil production of 128.2 million metric tons in 2007, about 1.5 to 2 million of SBE was generated (Huang and Chang, 2010). The disposal of SBE in landfills may cause fire and pollution hazards due to the substantial oil content in the clay and its disposal constituted a significant economic waste and an environmental burden (Aladetuyi *et al.*, 2014). The residual oil in SBE should ideally be recovered and re-used for industrial applications in order to reduce cost in oil processing industry (Loh *et al.*, 2013). Conventional method is commonly used for extraction of palm oil from spent bleaching earth (Salea *et al.*, 2017). However, Supercritical CO<sub>2</sub> is a non-toxic with no solvent traces remain in the extracted oil (Fiori, 2010). Supercritical fluid technology is advantageously positioned as a sustainable and safe extraction option to produce vegetable oil and has been widely studied in a variety of applications during the last decades (de Melo *et al.*, 2008). Bhargava and Mohanty (2016) studied simulation of supercritical fluid extraction of essential oil from natural product. Manan *et al.* (2008) investigated modelling of a new supercritical fluid extraction process for palm oil refining using Aspen Plus commercial process simulator version 10.2.1 based on the Redlich-Kwong-Aspen (RKA) thermodynamic model. Lim *et al.* (2003) investigated the simulation and modelling of the phase behaviour of palm oil with supercritical CO<sub>2</sub> using Redlich – Kwong – Aspen (RKA) thermodynamic model implemented in Aspen Plus 10.21. The simulated model provides an efficient and cost-effective alternative for preliminary design and optimization of the supercritical fluid extraction process. Cabeza *et al.* (2016) studied the modelling of the SFE of oil from sesame seeds with ScCO<sub>2</sub>. Feng *et al.* (2015) presented mathematical modelling for the extraction of tea seed oil with supercritical CO<sub>2</sub> which was based on the differential mass balance. Process design and simulator such as Aspen Hysys and Aspen Plus can facilitate the scale up and cost analysis for the recovery of palm oil from spent bleaching earth (Nascimento *et al.*, 2016). Ciprés *et al.* (2016) reported an industrial design of supercritical fluid extraction process that produces an extract rich in glucosinolates and phenolic compounds from freeze-dried rocket salad using carbon dioxide. The objective of this work is to develop a new intensified process for the recovery of palm oil from spent bleaching using supercritical fluid extraction (SFE) and to evaluate the influence of extraction pressure and temperature on the total annual cost.

## 2. METHODOLOGY

A conceptual design of an industrial-scale application of the supercritical CO<sub>2</sub> extraction process to recover palm oil from spent bleaching earth using Aspen Plus V8.0 was simulated and validated using experimental data from the literature. The SFE plant has been designed for a processing capacity of 10,000 kg/hr of SBE. Before injecting carbon dioxide to the extraction vessel, the solvent was cooled to 5 °C to avoid pump cavitation in the compression stage. After this, the carbon dioxide was compressed to 10MPa, and temperature was raised to 45°C to reach supercritical condition. The supercritical CO<sub>2</sub> was passed through the extraction vessel with SBE. Redlich–Kwong Equation of State (RK-EoS) was used for the thermodynamic model. Keeping temperature and pressure constant during the extraction stage is necessary in order to maintain the right CO<sub>2</sub> density and viscosity and maximise the extraction yield. Two streams were obtained after the extraction process. The first stream includes the fraction of spent bleaching earth and the second stream include palm oil diluted with Supercritical CO<sub>2</sub>. It is important to depressurize the stream because the extract will be obtained at high pressure and separate the carbon dioxide from the palm oil. Two stages are involved in the depressurization, reducing the pressure to 2MPa and gasifying the carbon dioxide to avoid excessive cooling respectively. Valve was used to reduce the pressure at the desire separation pressure. This is important since palm oil losses will be avoided. However, the consequence of this is an easier recovery of palm oil extract (Moncada *et al.*, 2016). It was discovered that 99.6% of CO<sub>2</sub> was recovered from the extract and recycle at a depressurisation pressure of 2 MPa. Finally, CO<sub>2</sub> was cooled to 5 °C and then re-pressurized back to the extraction vessel. The material and energy balance from the specified operating conditions for each unit systems were calculated using Aspen PlusV8.0 software. Figure 1 depicts the process flow diagram for the recovery of palm oil from spent bleaching earth.

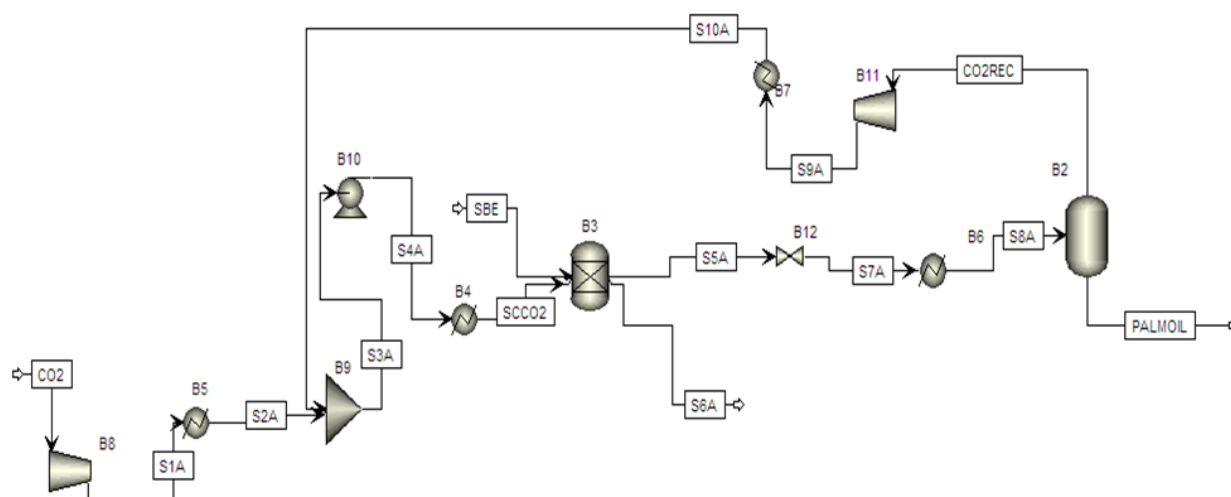


Figure 1: Process flow diagram for Supercritical Fluid Extraction of palm oil from Spent Bleaching Earth.

## 3.0 ECONOMIC ANALYSIS

An economic evaluation is performed to investigate effect of total annual cost of the process when optimizing the operating conditions. In the economic assessment, the capital and operating costs were calculated using Aspen Process Economic Analyzer. Sizing and costing on each equipment were evaluated using Aspen Process Economic Analyzer to estimate the total annual capital and operating cost. Equipment calculations were performed following the Aspen Process Economic Analyzer V8.0. The operating costs are the expenses related to the operation of the plant. They can be divided into cost of utilities, labour and cost of raw materials. The utilities needed for the operation of the SFE plant are electricity, heating and cooling. The breakdown of energy cost is summarized in Table 2.

Table 1: Result of Material balance for Supercritical Fluid Extraction of palm oil from Spent Bleaching Earth

Stream	SBE	SCCO <sub>2</sub>	S1A	S2A	S3A	S4A	S5A	S6A	S7A	S8A	S9A	S10A	CO <sub>2</sub> REC	PALM OIL
Temperature (°C)	45	45	66.8	5.0	4.22	10.04	45.99	45.99	-22.08	30	151.86	5	30	30
Pressure (MPa)	10	10	10	10	6	10	10	10	10	6	6	2	2	2
Mass flow(kg/hr)	10000	10000	42.979	42.97	10000	10000	10729	9271	10729	9957.0 2	9957.02	10729	9957.02	771.979
SiO <sub>2</sub>	7300	0.00	0.00	0.00	0.00	0.00	0.00	7300	0.00	0.00	0.00	0.00	0.00	0.00
C14:0	32.4	0.00	0.00	0.00	1.52e <sup>-15</sup>	1.5e <sup>-15</sup>	8.748	23.652	8.748	8.748	1.52e <sup>-15</sup>	1.52e <sup>-15</sup>	1.52e <sup>-15</sup>	8.748
C16:0	1201.5	0.00	0.00	0.00	1.2e <sup>-14</sup>	1.2e <sup>-14</sup>	324.405	877.095	324.405	324.40 5	1.9e <sup>-4</sup>	1.2e <sup>-14</sup>	1.2e <sup>-14</sup>	324.405
C18:0	137.7	0.00	0.00	0.00	1.9e <sup>-4</sup>	1.9e <sup>-4</sup>	37.179	100.521	37.179	37.179 1	1.9e <sup>-4</sup>	1.9e <sup>-4</sup>	1.9e <sup>-4</sup>	37.179
C18:1	137.7	0.00	0.00	0.00	6.32e <sup>-6</sup>	6.32e <sup>-6</sup>	281.394	760.806	281.394	281.39 4	6.31e <sup>-6</sup>	6.31e <sup>-6</sup>	6.31e <sup>-6</sup>	281.394
C18:2	286.2	0.00	0.00	0.00	2.36e <sup>-7</sup>	2.36e <sup>-7</sup>	77.274	208.926	77.274	77.274	2.36e <sup>-7</sup>	2.36e <sup>-7</sup>	2.36e <sup>-7</sup>	77.274
CO <sub>2</sub>	0.00	10000	42.979	42.97	10000	10000	10000	0.000	10000	10000	9957.02	9957	9957.02	42.979

Table 2: Energy cost for Supercritical Fluid Extraction (SFE) Plant

Utilities	Cost (US \$)/year
Electricity	244,327
Heating	154,101
Cooling	37,629

Table 3: Process Equipment cost for SFE Plant

Process Equipment	Cost (US \$)/year
Compressor	244,327
Heat Exchanger	154,101
Separator	37,629
Extraction Vessel	45,700

### 3. RESULTS AND DISCUSSION

The results show a good agreement with the experimental data, with 99.6% of CO<sub>2</sub> recovered as shown in Table 1. Techno-economic analysis was performed to assess the influence of operating conditions on the total annual cost. First, the effect of different extraction pressure on the total annual cost was evaluated. This can be shown in Figure 2, the higher the extraction pressure at constant temperature of 35°C, the higher the total annual cost, increase in extraction pressure from 10MPa to 20MPa causes increase in energy consumption which lead to increase in energy cost. Also, heating requirement for the throttling valve is higher when extraction pressure increases (del Valle *et al.*, 2014). The effect of extraction temperature on the total annual cost has also been investigated. As shown in Figure 3., the higher the extraction temperature at constant pressure of 10MPa, the lower the total annual cost. There is a significant decrease from 35°C to 45°C. But at 50 °C there was increase in total annual cost because at higher temperature, energy cost increases. Lower extraction temperature might be required to preserve the quality of the extracted oil (SeEVERS,1998). To sum up, the lowest total annual cost was obtained at 10 MPa and 45°C, at a separation pressure of 2 MPa.

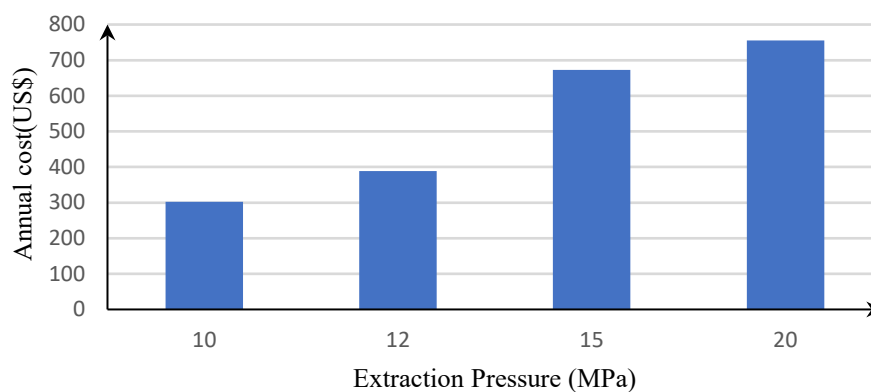


Figure 2: Effect of total annual cost on the extraction pressure at constant temperature of 35°C

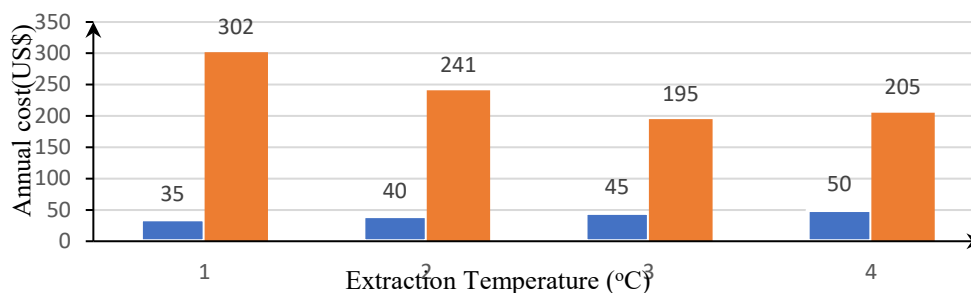


Figure 3: Effect of total annual cost on the extraction temperature at constant pressure of 10MPa

Figure 3:

#### 4. CONCLUSION

A conceptual design of an industrial supercritical fluid extraction process for the recovery of palm oil from spent bleaching earth has been developed. The base for calculation is a plant size able to process 10,000 kg/hr of SBE using Aspen Plus V8.0 for process simulation. The influence of the extraction pressure and the extraction temperature have been investigated, obtaining optimal total annual cost of US\$246 million at 10 MPa and 45 °C with optimum separation pressure of 2 MPa.

#### ACKNOWLEDGEMENT

The authors gratefully acknowledge the financial supports from Executive Vice Chairman of National Agency for Science and Engineering Infrastructure, Abuja.

#### REFERENCES

- Aziz, M.K.A., Morad, N.A., Muhamad, N.N.B., Okayama, T., Kose, R. (2015). Residual oil recovery using bio-ethanol from spent bleaching clay and its characterization. in Control Conference (ASCC), 2015 10th Asian IEEE.
- Prokopov, T. and Mechenov, G. (2013). Utilization of spent bleaching earth from vegetable oil processing. Ukrainian food journal, (2, Issue 4): 489-498.
- Huang, Y.P. and Chang, J.I. (2010). Biodiesel production from residual oils recovered from spent bleaching earth. Renewable Energy. 35(1): 269-274.
- Aladetuyi, A., Olatunji, G.A., Ogunniyi, D.S., Odeto, T.E., Oguntoye, S.O. (2014). Production and characterization of biodiesel using palm kernel oil; fresh and recovered from spent bleaching earth. Biofuel Research Journal. 1(4): 134-138.
- Loh, S.K., James, S., Ngatiman, M. (2013) Enhancement of palm oil refinery waste – Spent bleaching earth (SBE) into bio-organic fertilizer and their effects on crop biomass growth. Industrial Crops and Products. 49: 775-781.
- Salea, R. B., Veriansyah, B. and Tjandrawinata, R. R. (2017). Optimization and scale-up process for supercritical fluids extraction of ginger oil from *Zingiber officinale* var. *Amarum*. *The Journal of Supercritical Fluids*. 120: 285-294.
- Fiori, L. (2010). Supercritical extraction of grape seed oil at industrial scale: Plant and process design, modeling, economic feasibility. *Chemical Engineering and Processing: Process Intensification* 49(8): 866-872.
- de Melo, M.M.R., Oliveira, E.L.G., Silvestre, A.J.D., Silva, C. M. (2014). Scale-up studies of the supercritical fluid extraction of triterpenic acids from *Eucalyptus globulus* bark. *The Journal of Supercritical Fluids*. 95: 44-50.
- Bhargava, A.R. and Mohanty, B. (2016) Simulation of supercritical fluid extraction of essential oil from natural products. *Journal of Applied Research on Medicinal and Aromatic Plants*.
- Manan, Z. A., Lim, C. S., Abd Rahman, N. S. and Wan Alwi, S. R. (2008). Modelling of a new supercritical fluid extraction process for palm oil refining. *International conference on Science & Technology*.
- Lim, C. S., Manan, Z. A. and Sarmidi, M. R. (2003). Simulation modelling of the phase behavior of palm oil-supercritical carbon dioxide. *Journal of the American Oil Chemists' Society*, 2003. 80(11): 1147-1156
- Cabeza, A., Sobrón, F., García-Serna, J. and Cocero, M.J. (2016). Simulation of the supercritical CO<sub>2</sub> extraction from natural matrices in packed bed columns: User-friendly simulator tool using Excel. *The Journal of Supercritical Fluids*. 116: 198-208.
- Feng, J., Lei, H. and Ge, F. (2015). Modelling of the Extraction Process of Tea Seed Oil with Supercritical Carbon Dioxide. *Brazilian Journal of Chemical Engineering*. 32(4): 941-947.
- Nascimento, A. D. P., Soares, L. A. L., Stragevitch, L. and Danielski, L. (2016). Extraction of *Acrocomia intumescens* Drude oil with supercritical carbon dioxide: Process modelling and comparison with organic solvent extractions. *The Journal of Supercritical Fluids*. 111: 1-7
- Ciprés, M.S., Mirofci, S. and Bertucco, A. (2016). Production of phenolic and glucosinolate extracts from rocket salad by supercritical fluid extraction: Process design and cost benefits analysis. *Journal of Food Engineering*, 168: 35-41.
- Moncada, J., Tamayo, J. A. and Cardona, C. A. (2016). Techno-economic and environmental assessment of essential oil extraction from *Oregano* (*Origanum vulgare*) and *Rosemary* (*Rosmarinus officinalis*) in Colombia. *Journal of Cleaner Production*. 112: 172-181.
- del Valle, J. M., Núñez, G. A. and Aravena, R. I. (2014). Supercritical CO<sub>2</sub> oilseed extraction in multi-vessel plants. 1. Minimization of operational cost. *The Journal of Supercritical Fluids*, 92: 197-207.



## Investigation of Adsorption Capacity of Eggshell-based Chitosan in the Treatment of Multicomponent Aromatic Organic Pollutants

Azeez G. AKINYEMI<sup>1,2</sup>, Arinkoola O. AKEEM<sup>1</sup>, Shukurat B. OLABIYI<sup>1</sup>, Monsuru O. DAUDA<sup>1,2</sup>, Monsurat O. JIMOH<sup>1,2</sup>, Odunola D. AKINWUMI<sup>1</sup>, Sunday O. OYEKUNLE<sup>1</sup>, Tinuade J. AFOLABI<sup>1,2</sup> and Abass O. ALADE,<sup>1,2,3\*</sup>

<sup>1</sup>Department of Chemical Engineering, Ladoke Akintola University of Technology, P.M.B. 4000, Ogbomoso, Nigeria

<sup>2</sup>Bioenvironmental, Water and Engineering Research Group, (BWERG), Ladoke Akintola University of Technology, P.M.B. 4000, Ogbomoso, Nigeria

<sup>3</sup>Science and Engineering Research Group, (SEARG), Ladoke Akintola University of Technology, P.M.B. 4000, Ogbomoso, Nigeria

\*Corresponding Author: [aopalade@lautech.edu.ng](mailto:aopalade@lautech.edu.ng) +2347037885961

### ABSTRACT

Adsorption technology has been advocated for wastewater treatment to diminish the harmful effects of aromatic hydrocarbons (AHs) on the environment and human health. This work investigated the adsorption capacity of chitosan-based adsorbents developed from waste eggshells for the treatment of wastewater containing selected AHs. The eggshell was washed, sun-dried, oven-dried and milled to uniform sizes. The milled eggshell was deproteinized with 1 M NaOH at 60 °C for 2 h and then demineralized with 1.2 M HCl for 4 h to produce eggshell chitin, which was further deacetylated with 50 wt.% NaOH at 120 °C for 2 h to produce Eggshell Chitosan (ESC). The ESC (1 g) was mixed with a solution (100 ml) of selected AHs (phenol, acenaphthene, and pyrene) which were mixed at different concentration ratios (20-60 mg/L) based on the Simplex Centroid Design (SLD) of the Design-Expert (12.0.1) software. The batch adsorption process was conducted in 250 mL flasks, agitated on a rotary shaker at 150 rpm for 1 h at room temperature. The residual concentration was evaluated using a UV-VIS spectrophotometer at 274 nm, 303 nm, and 335 nm for the phenol, acenaphthene, and pyrene respectively. The data generated were statistically analyzed. The maximum adsorption capacity of phenol, acenaphthene and pyrene removal was 5.746 mg/g, 5.761 mg/g, and 5.840 mg/g, respectively. The eggshell-Chitosan adsorbent demonstrated satisfactory capacity for AHs adsorption.

**Keywords:** Adsorbent, Chitosan, Eggshell, Optimization, Organic Pollutants.

### 1. INTRODUCTION

Fast urbanization, industrialization, and population growth lead to the production and release of organic and inorganic pollutants into the environment, causing most water supplies to become contaminated and endangering the environment, human health, and ecological system (Awad *et al.*, 2020). Organic pollutants have been known to hurt the ecosystem for decades, according to Awad *et al.* (2020). Phenol and phenolic wastes are the most prevalent organic pollutants, which are mostly produced by the chemical, pharmaceutical, and petroleum processing industries (Ruifang *et al.*, 2020). The treatment of wastewater that contains phenol and other organic contaminants have been done using a variety of techniques such as oxidation, precipitation, ion exchange, photocatalytic degradation, solvent extraction, and adsorption are other techniques utilized to remediate wastewater overtime but research into alternate and inexpensive precursor materials for the production of adsorbent is receiving a lot of attention (Pandey & Mishra, 2011).

A statistical tool called the Design of Experiments (DoE) is used to organize and optimize experiments. The mixing designs (MDs) are one of the many experimental designs (Eds). Two or more ingredients are combined in a variety of ratios (Jain *et al.*; 2019). In MDs, the properties of the finished products are noted. The sum of a mixture's proportions in various elements or components is always 1 or 100%. This work's primary objective is to investigate the use of eggshell-based Chitosan for the adsorption of a few specific Aromatic Organic Compounds from an aqueous solution (Galvan *et al.*, 2014).

### 2. MATERIALS AND METHODS

#### 2.1 Materials/Reagents and Equipment

In this study, chemicals of analytical grade were used. The phenol (C<sub>6</sub>H<sub>6</sub>O, 99.5 percent), acenaphthene (C<sub>12</sub>H<sub>10</sub>, 99.5 percent), pyrene (C<sub>16</sub>H<sub>10</sub>, 95.0 percent), sodium hydroxide (NaOH, 40wt%), deionized water, and concentrated hydrochloric acid (HCl, 38%). The eggshell that was used to create chitosan was sponsored by the Ysluv Restaurant in Ogbomoso, Nigeria.

## 2.2 Pretreatment of Eggshell Sample

The eggshell was washed severally with distilled water to remove impurities and sun-dried for 12 h, the eggshell sample was then oven-dried for 3 h at 80 °C to remove surface and pore moisture and milled to enhance surface area (Brezeski *et al.*, 1982).

## 2.3 Preparation of Eggshell-Based Chitosan Adsorbent

The treated eggshell sample was deproteinized and completed using sodium hydroxide, NaOH (1 M), at 60°C with continuous stirring for 2 h. The sample was rinsed severally with distilled water to pH 7 before the demineralization process and dried to a constant weight. Hydrochloric acid (1.2 M) was used to demineralize the material, which was then neutralized and dried to a constant weight to produce chitin. The final step in the synthesis of chitosan from eggshells is the deacetylation technique, which entails the addition of 50% sodium hydroxide, NaOH, to the chitin produced on a magnetic stirrer set at 120 °C under continuous agitation for 2 h (Khanafari *et al.*, 2008).

## 2.4 Simulated Wastewater Preparation

Phenol, acenaphthene, and pyrene, (0.1 g) each based on the percentage purity, were separately dissolved in 1 L of distilled water to create simulated wastewater with a concentration of 100 mg/L. From these, simulated stock wastewater was created by combining the initially prepared wastewater based on various concentrations as provided by the Simplex Centroid feature of the Design Expert software version 12.1.0 with mixture ranges of 20 mg/L to 60 mg/L.

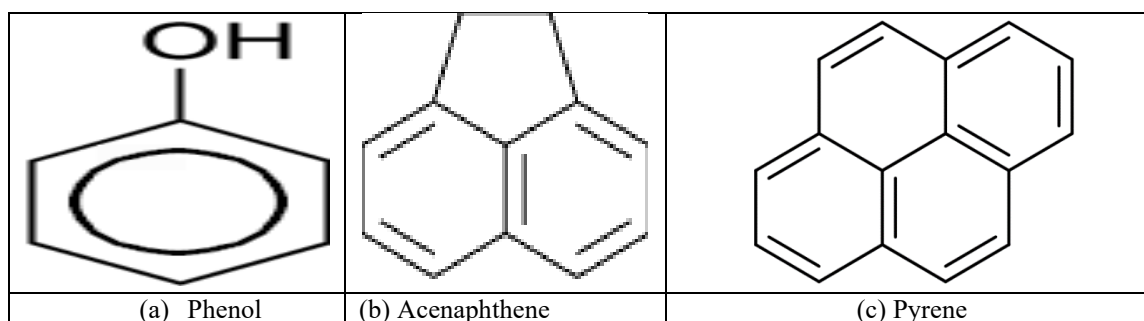


Figure 1: Chemical Structures of selected Aromatic Organic compounds

## 2.5 Adsorption Studies

A 250 mL glass conical flask was utilized as the reactor for laboratory-scale investigations, and the concentrations of the three pollutants were measured before and after each experiment. Then, for each run, 100 mL of the produced adsorbate and 1g of synthetic chitosan adsorbent were utilized. The reactor was mounted on a fixed, rotating shaker (150 rpm) for agitation of the adsorbate and adsorbent for the desired reaction period of 1 h. Samples were withdrawn and filtered and the filtrate was analyzed for residual concentration of the AHs. Using a UV-visible spectrophotometer set at a maximum wavelength of 274 nm, 303 nm, and 335 nm for phenol, acenaphthene, and pyrene, respectively. An individual experiment was run three times to reduce error. Average values were also used. Equation (2) was used to get the % removal efficiency of the organic compounds:

$$\text{Adsorption Capacity (mg/g)} = \frac{C_0 - C_F}{C_0} \times \frac{M}{V} \quad (1)$$

$$\text{Removal Efficiency (\%)} = \frac{C_0 - C_E}{C_0} \times 100 \quad (2)$$

Where  $C_0$  and  $C_F$  represent the respective initial and ultimate concentrations of the chosen organic components.

## 2.6 Simplex Centroid Experimental Design for the Batch Adsorption Studies

The mixing methodology based on a simplex centroid design was used in this study to generate 14 runs with 4 replicates (containing  $2 \times 2 = 4$  axial points and  $2^2 = 4$  design points), statistically analyze experimental data, and examine the relationship between the independent variable (concentration) and response (removal efficiency). Based on the elimination efficiency of phenol, acenaphthene, and pyrene, the responses, which served as the dependent variables, were selected. The combination content of phenol, acenaphthene and pyrene was considered a separate component, though. The lowest and maximum variables are shown in Table 1.

Table 1: Independent variable levels used in this research for experimental design

Component Name	Units	Minimum	Maximum
Phenol	mg/L	20.00	60.00
Acenaphthene	mg/L	20.00	60.00
Pyrene	mg/L	20.00	60.00

The second-order polynomial regression model for the variables is given as (Javid *et al.*, 2020)

$$Y = \alpha_0 + \sum_{j=1}^n \alpha_j x_j + \sum_{j=1}^n \alpha_{jj} x_{jj}^2 + \sum_{j=1}^{n-1} \sum_{i=1}^{n-1} \beta_{ij} x_j x_i + \varepsilon \quad (3)$$

Where, Y is the response;  $x_j$  and  $x_{jj}$  are independent variables that have an impact on Y;  $\alpha_0$  is the constant;  $\alpha_j$  and  $\alpha_{jj}$ , respectively, are the linear and second-order coefficients,  $n$  is the number of input variables;  $\beta_{ij}$  is the interaction effect, and  $\varepsilon$  is a random error (Kalali *et al.*, 2011). The levels were selected based on the preliminary adsorption experiments. The actual and coded values of factors and levels used in the experimental design are presented in Table 1. The adsorption capacity which is the dependent variable served as the response. The design of the experiment with 14 experimental runs is displayed in Table 2.

Table 2: Experimental design and responses value at different runs of the multi-component organic pollutant adsorption capacity

Run	Components			Adsorption Capacity (mg/g)		
	A: Phenol	B: Acenaphthene	C: Pyrene	Phenol	Acenaphthene	Pyrene
1	20.00	60.00	20.00	1.6437	5.7610	1.8404
2	26.67	26.67	46.66	2.2698	2.3798	4.4947
3	20.00	20.00	60.00	1.5489	1.6605	5.7019
4	20.00	60.00	20.00	1.6417	5.7607	1.8394
5	40.00	40.00	20.00	3.6886	3.7285	1.9296
6	40.00	40.00	20.00	3.6866	3.7291	1.7667
7	60.00	20.00	20.00	5.7455	1.6639	1.9319
8	20.00	40.00	40.00	1.5210	3.6021	3.7657
9	26.67	46.66	26.67	2.3247	4.3060	2.5750
10	40.00	20.00	40.00	3.6108	1.7853	3.7831
11	46.66	26.67	26.67	4.3576	2.3345	2.5872
12	33.33	33.33	33.33	2.9158	2.8796	3.1433
13	20.00	20.00	60.00	1.5509	1.6607	5.8404
14	60.00	20.00	20.00	5.7435	1.6634	1.9333

### 3. RESULTS AND DISCUSSION

#### 3.1 Phenol (PH), Acenaphthene (AC), and Pyrene (PY) Adsorption

The results of the selected AHs onto the synthetic eggshell chitosan adsorbent about adsorption capacity are shown in Table 2. For each pair of experimental runs 1 and 4, 3 and 13, 5 and 6, and 7 and 14 with the same process condition of concentration of phenol, acenaphthene, and pyrene, the results showed that the selected AHs had a higher adsorption capacity at a higher concentration than at a lower concentration. The influence of a single process factor on the adsorption capacity of the chosen AHs, (Figure 2), the factor plot provides a better visual depiction of the findings. As seen in Figure 2, the adsorption capacity of phenol increased and the adsorption capacities of acenaphthene and pyrene decreased by the chitosan adsorbent as the concentration of selected AHs increased gradually from a low level of 20 mg/L (coded value -0.4) to a high level of 60 mg/L (coded value 0.8) (Noreen *et al.*, 2017).

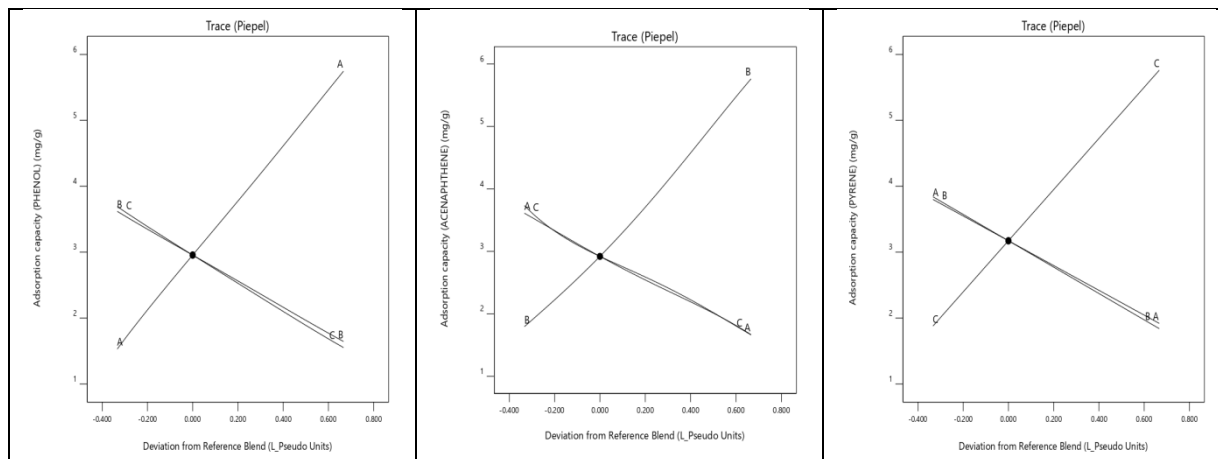
As shown in Figure 2, phenol's adsorption capacity grew with concentration, but that of acenaphthene and pyrene declined from a high level of 60 mg/L (coded value 0.8) to 20 mg/L (coded value -0.4). The chitosan adsorbent's best adsorption capability, however, is found at concentrations of 40 mg/L, 40 mg/L, and 20 mg/L for phenol, acenaphthene and pyrene. The increased availability of active binding sites on the surface of the adsorbent that is empty may be the cause of the high adsorption rate (Kanwal *et al.*, 2017).

#### 3.2 Regression Model and Analysis of Variance (ANOVA)

The coefficients of the model equation shown in Table 4 were obtained by fitting the adsorption experimental data to the special quartic, special quartic, and linear regression models using the Design Expert statistical software (12). The coefficient estimate represents the expected change in response per unit change in factor value when all other factors are held constant. The average response of all the runs is the intercept in an orthogonal design. to get Eq. (4-6) for Adsorption capacity as a function of Phenol, Acenaphthene, and Pyrene concentrations, the coefficients are modifications made around that average based on the factor settings. The significant model terms and the insignificant model terms are included in the equation.

$$\text{Adsorption Capacity}_{\text{Phenol}} = 5.75A + 1.64B + 1.55C - 0.0150AB - 0.1190AC - 0.2746BC - 1.65A^2BC + 1.63AB^2C + 1.65ABC^2 \quad (4)$$





$$\text{Adsorption Capacity}_{\text{Acenaphthene}} = 1.67A + 5.76B + 1.66C + 0.0751AB + 0.5195AC - 0.4080BC - 6.72A2BC - 6.65AB2C + 2.68ABC2 \quad (5)$$

$$\text{Adsorption Capacity}_{\text{Pyrene}} = 1.92A + 1.84B + 5.76C \quad (6)$$

Where, respectively, A, B, and C are phenol, acenaphthene, and pyrene. The Fischer test (F-value), probability value (p-value), and determination coefficient ( $R^2$ ) (being a measure of fit goodness) were established and assessed to test the models' fit (Table 5).

For phenol, acenaphthene, and pyrene, respectively, the model equation developed for their adsorption capacities is special quartic, special quartic, and linear with standard deviation,  $R^2$ , and Adjusted  $R^2$  values of (0.0283, 0.9999, and 0.9996), (1.36, 0.9758, and 0.9607), (0.0281, 0.9999, and 0.9996). The comparatively high values of  $R^2$  show that the experimentally observed values and anticipated values exhibit a strong association.

The model is sufficient because the "Pred  $R^2$ " values of 0.9999, 0.9758, and 0.9999 are in reasonable agreement with the corresponding "Adj  $R^2$ " values of 0.9996, 0.9607, and 0.9996 for phenol, acenaphthene, and pyrene, respectively. An Adequate (Adeq) Precision of 186.0268, 182.1855, and 144.4584 obtained for the adsorption capacity of phenol, acenaphthene, and pyrene, respectively, by the chitosan adsorbent, indicates an adequate signal because "Adeq Precision" measures the signal to noise ratio and a ratio greater than 4 is desirable. The regression models' high significance is indicated by the Model F-values of 4580.85, 4408.55, and 3877.74 for the adsorption capacities of phenol, acenaphthene, and pyrene, respectively, by the chitosan adsorbent (Table 5). There is only a 0.01% chance that a "Model F-value" this large could occur due to noise

Regression models' analysis of variances (ANOVA) revealed that the models were highly significant, which was demonstrated by the F test's low probability value ( $< 0.0001$ ). Model terms are considered significant when Prob  $> F$  values are less than 0.05, and inconsequential when values are more than 0.1000. The linear mixture terms are significant models in all of the regression model equations that were developed, according to the p values of the regression coefficients.

### 3.3 Adequacy of model

Several diagnostic data analyses based on actual and expected values were performed to determine whether or not the selected model gives an adequate approximation of the real system. The predicted values came from the model equations, whereas the actual values were obtained by experimentation. The model's anticipated and actual responses for the elimination of all organic pollutants are shown in Figures 1a, 2a, and 3a using a normal distribution. Figures 1b, 2b, and 3b, together with the outcome of plotting the expected value against the actual value, are the discrepancies between the actual and projected responses for the elimination of organic pollutants. Figure 2a shows a closer match between actual and projected values. The data are evenly distributed when all the data points are plotted in a straight line. The residuals are close, as seen in Figure 2b. Figures 3a, 3b, and 3c show the correlation between the 3D distribution of the chosen AHs using the created models. Additionally, it demonstrated how well the selected model approximates the actual system.



Table 4: Coefficient of model for Adsorption capacity of selected AHs

Component	Phenol				Acenaphthene				Pyrene			
	Coefficient Estimate	Standard Error	95% CI Low	95% CI High	Coefficient Estimate	Standard Error	95% CI Low	95% CI High	Coefficient Estimate	Standard Error	95% CI Low	95% CI High
A-PHENOL	5.75	0.0200	5.70	5.80	1.67	0.0198	1.61	1.72	0.0335	1.85	1.99	1.09
B-ACENAP	1.64	0.0200	1.59	1.70	5.76	0.0198	5.71	5.81	0.0335	1.77	1.91	1.09
C-PYRENE	1.55	0.0200	1.50	1.60	1.66	0.0198	1.61	1.71	0.0342	5.69	5.84	1.06
AB	-0.015	0.0979	-0.27	0.24	0.0751	0.0972	-0.17	0.32	NA	NA	NA	NA
AC	-0.119	0.1259	-0.44	0.20	0.5195	0.1250	0.20	0.84	NA	NA	NA	NA
BC	-0.275	0.1259	-0.60	0.05	-0.408	0.1250	-0.73	-0.09	NA	NA	NA	NA
A <sup>2</sup> BC	-1.65	2.79	-8.83	5.53	-6.72	2.77	-13.8	0.41	NA	NA	NA	NA
AB <sup>2</sup> C	1.63	2.79	-5.55	8.81	-6.65	2.77	-13.8	0.48	NA	NA	NA	NA
ABC <sup>2</sup>	1.65	2.83	-5.63	8.93	2.68	2.81	-4.54	9.91	NA	NA	NA	NA

Table 5: Results of ANOVA for selected AHs by synthesized Eggshell-based chitosan Adsorbent

	Phenol				Acenaphthene				Pyrene			
	Sum of Squares	Mean Square	F-value	p-value	Sum of Squares	Mean Square	F-value	p-value	Sum of Squares	Mean Square	F-value	p-value
Model	29.29	3.66	4580.85	<0.0001	27.79	3.47	4408.55	<0.0001	26.68	13.34	3877.74	<0.0001
Linear M	29.29	14.64	18320.27	<0.0001	27.74	13.87	17603.73	<0.0001	26.68	13.34	3877.74	<0.0001
AB	0.0000	0.0000	0.0236	0.8839	0.0005	0.0005	0.5974	0.4745	0.0378	0.0034	NA	NA
AC	0.0007	0.0007	0.8932	0.3880	0.0136	0.0136	17.28	0.0088	0.0150	0.0021	0.3744	0.8784
BC	0.0038	0.0038	4.76	0.0809	0.0084	0.0084	10.66	0.0223	0.0229	0.0057	NA	NA
A <sup>2</sup> BC	0.0003	0.0003	0.3504	0.5796	0.0046	0.0046	5.87	0.0600	26.72	NA	NA	NA
AB <sup>2</sup> C	0.0003	0.0003	0.3417	0.5842	0.0045	0.0045	5.75	0.0619	NA	NA	NA	NA
ABC <sup>2</sup>	0.0003	0.0003	0.3394	0.5854	0.0007	0.0007	0.9112	0.3836	NA	NA	NA	NA
Residual	0.0040	0.0008	NA	NA	0.0039	0.0008	NA	NA	NA	NA	NA	NA
L. of Fit	0.0040	0.0040	2002.27	<0.0001	0.0039	0.0039	45986.44	<0.0001	NA	NA	NA	NA
Pure Error	7.968E-06	1.992E-06	NA	NA	3.426E-07	8.566E-08	NA	NA	NA	NA	NA	NA
Cor Total	29.30	NA	NA	NA	27.79	NA	NA	NA	NA	NA	NA	NA

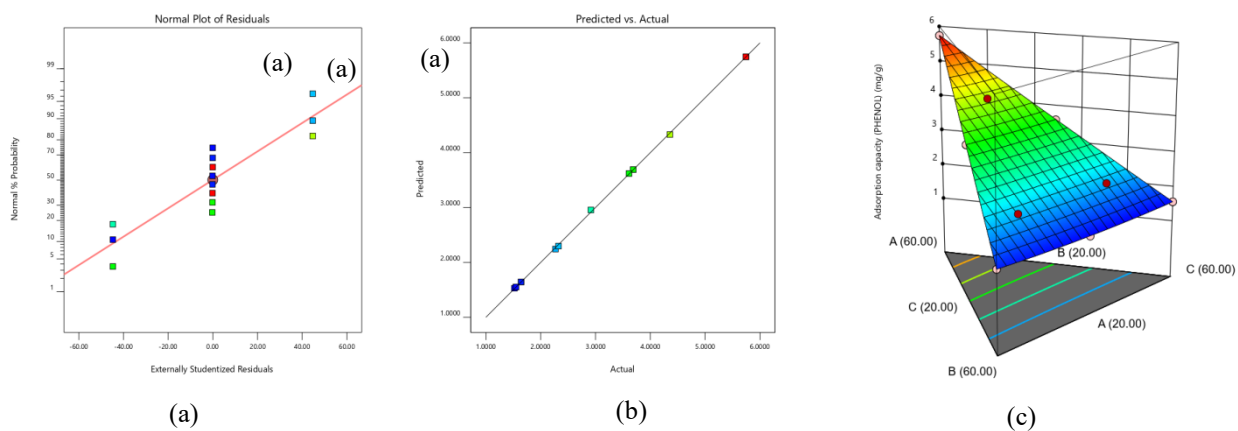


Figure 1: Phenol (a) Normal % probability versus Externally studentized residuals (b) Actual versus Predicted value and (c) 3D surface distribution respectively

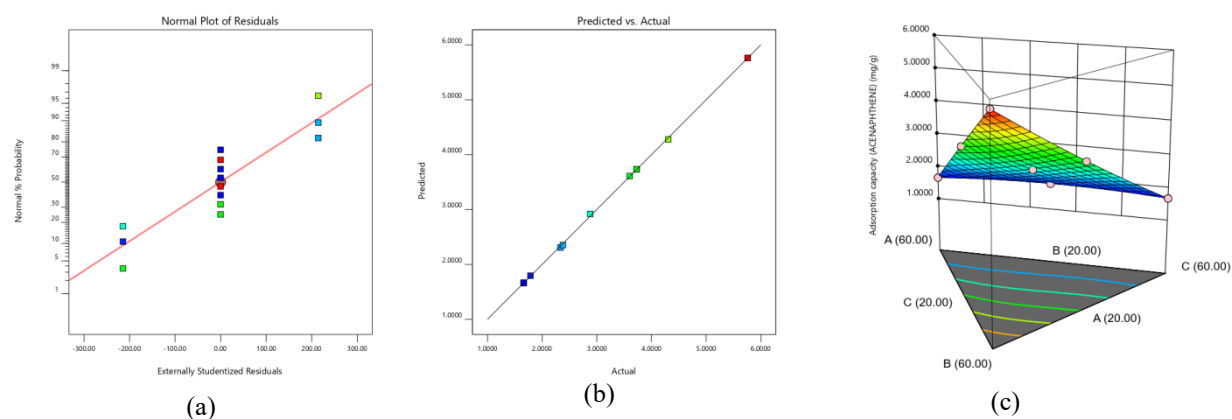


Figure 2: Acenaphthene (a) Normal % probability versus Externally studentized residuals (b) Actual versus Predicted value and (c) 3D surface distribution respectively

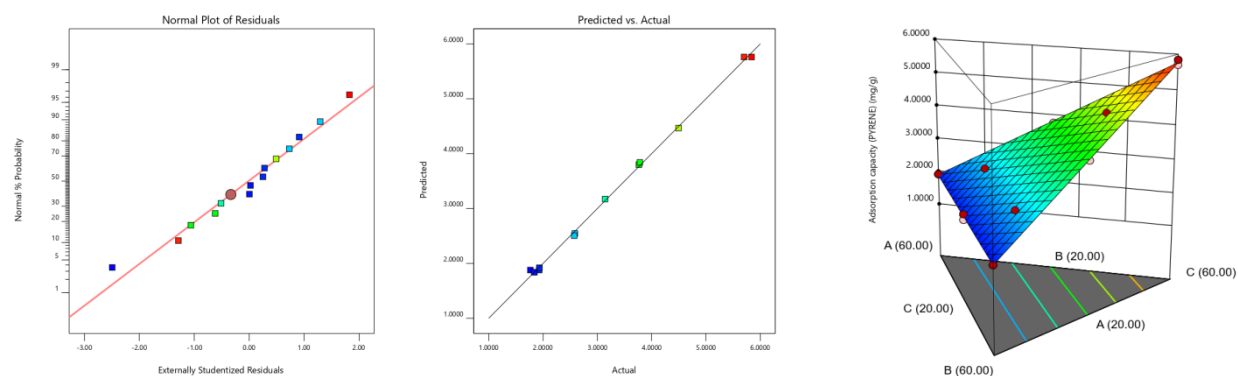


Figure 3: Pyrene (a) Normal % probability versus Externally studentized residuals (b) Actual versus Predicted value and (c) 3D surface distribution respectively.

#### 4. CONCLUSION

Utilizing Design Expert Software's Simplex Centroid of the Mixture approach, the adsorption of Phenol, Acenaphthene, and Pyrene was investigated as well as the individual and interacting effects of the concentration of the chosen AHs. The investigation has shown that a selective adjustment in the content of phenol, acenaphthene, and pyrene had a significant effect on the ability of the produced eggshell-based chitosan to adsorb the chosen AHs. The maximum adsorption capacities of phenol, acenaphthene and pyrene are demonstrated to be 5.746 mg/g, 5.761 mg/g, and 5.840 mg/g, respectively, at the optimum conditions reached 37.910 mg/L, 38.680 mg/L, and 23.409 mg/L with an optimal capacity of 3.116 mg/g. The models created (special quartic, special quartic, and linear) for each AH's adsorption capacity were useful in determining the best conditions for the adsorption process.

#### REFERENCE

- Awad A, Jalab R, Benamor A, Naser M, Ba-Abbad M, El-Naas M, Mohammad A (2020) Adsorption of organic pollutants by nanomaterial-based adsorbents: an overview. *J Mol Liq*. Pp. 112-135
- Brzeski, M.M. (1982) Concept of chitin chitosan isolation from Antarctic Krill (*Euphausia Superba*) shells on a technical scale. In Proceedings of the *Second International Conference on Chitin and Chitosan*; Hirano, S., Tokura, S., Eds.; *The Japan Society of Chitin and Chitosan: Sapporo*, pp. 15–29
- Galvan, D.; Orives, J.R.; Coppo, R.L.; Rodrigues, C.H.F.; Spacino, K.R.; Pinto, J.P.; Borsato, D.D. (2014) Study of oxidation kinetics of B100 biodiesel from soybean and pig fat: Activation energy determination. *Quim. Nova*, 37, pp. 244–248.
- Jain, A.; Hurkat, P.; Jain, S.K. (2019) Development of liposomes using formulation by design: Basics to recent advances. *Chem. Phys. Lipids*, 224, pp. 1–16.
- Javid A, Roudbari A, Yousefi N, Fard MA, Barkdoll B, Talebi SS, Nazemi S, Ghanbarian M, Ghadiri SK (2020). Modeling of chromium (VI) removal from aqueous solution using modified green graphene: RSM-CCD approach, optimization, isotherm, and kinetic studies. *J Environ Health Sci Eng* pp. 1-15.
- Kalali A, Ebadi T, Rabbani A, Moghaddam SS (2011) Response surface methodology approach to the optimization of oil hydrocarbon polluted soil remediation using enhanced soil washing. *Int J Environ Sci Technol* 8:pp. 389–400.
- Kanwal A, Bhatti H. N, Munawar I, and Noreen S, (2017). Basic Dye Adsorption onto Clay/MnFe<sub>2</sub>O<sub>4</sub> Composite: A Mechanistic Study, *Water Environment Research: A Research Publication of the Water Environment Federation* 89,(4):pp. 301–311.
- Khanafari, A.; Marandi, R.; Sanatei, S. (2008) Recovery of chitin and chitosan from shrimp waste by chemical and microbial methods. *Iran. J. Environ. Health Sci. Eng.*, 5, polycyclic aromatic hydrocarbons and total suspended particulate in indoor and outdoor atmosphere of a Taiwanese temple. *Journal of Hazardous Materials*, 95(1-2):pp. 1-12.
- Noreen S, Bhatti H. N, Zuber M, Zahid M, and Asgher M, (2017)“Removal of Actacid Orange-RL Dye Using Biocomposites: Modeling Studies,” *Polish Journal of Environmental Studies* 26,(5): pp 125–134.
- Pandey S, and Mishra S. B, (2011)“Organic-Inorganic Hybrid of Chitosan/Organoclay Bio Nanocomposites for Hexavalent Chromium Uptake,” *Journal of Colloid Interface Science* 361(2): pp. 509–520.
- Ruifang D, Dongyun C, Li N, Qingfeng X, Hua L, Jinghui H, Jianmei L (2020) Removal of phenol from aqueous solution using acid-modified *Pseudomonas putida*-sepiolite/ZIF-8 bio-nanocomposites. *Chemosphere* 239: pp. 124-138



## Impacts of Metal Recycling Plant Operations on Ambient Air and Noise Qualities

Bamidele S. FAKINLE<sup>1\*</sup>, Jacob A. SONIBARE<sup>2</sup>, Funso A. AKEREDOLU<sup>2</sup> and Ebenezer L. ODEKANLE<sup>3</sup>

<sup>1</sup>Department of Chemical Engineering, Landmark University, Omu-Aran, Nigeria

<sup>2</sup>Department of Chemical Engineering, Obafemi Awolowo University, Ile-Ife, Nigeria

<sup>2</sup>Department of Chemical and Mineral Resources Engineering, First Technical University, Ibadan, Nigeria

<sup>1\*</sup>[fakinle.bamidele@lmu.edu.ng](mailto:fakinle.bamidele@lmu.edu.ng), <sup>2</sup>[asonibar@yahoo.com](mailto:asonibar@yahoo.com), <sup>2</sup>[osnufy2k3@yahoo.co.uk](mailto:osnufy2k3@yahoo.co.uk), <sup>3</sup>[eodekanle@yahoo.com](mailto:eodekanle@yahoo.com)

\*Corresponding author

### ABSTRACT

*Air quality and noise levels assessment of an Iron and Steel company located, Ile-Ife, Osun State, a typical metal recycling plant in Southwest Nigeria was carried out within and around factory premises with a view to determining the impacts of the plant operation on ambient air quality. Relevant weather parameters, air pollutants and noise levels were determined accordingly and the results compared with relevant recommended limits. Measure meteorological parameters were in harmony with the historical climate data of Ile Ife. Of all the air pollutants, only CO and NH<sub>3</sub> (1.0 ppm) were detected within the factory, while SO<sub>2</sub>, NO, NO<sub>2</sub>, H<sub>2</sub>S and VOCs were not detected (< 1.0 ppm). However, in the surrounding, only NO was detected. 24-hour extrapolated concentrations were all within the recommended limits. The 24-hours extrapolated concentrations of PM<sub>10</sub> and TSP within the factory's premises as well as in the surrounding fell within their respective limits, Noise levels within the factory and some locations outside the factory were observed to exceed sleep disturbance limits recommended by WHO, while some other location outside the factory premises were within the recommended limit. Preventive and control measures to mitigate exposure to air pollutions and noise within and outside the factory were suggested.*

**Keywords:** Air pollution, Noise, Recycling, Air quality, microclimatic parameters

### 1. INTRODUCTION

Metal recycling is a continuously growing industry in Nigeria, possibly because it enhances daily economic welfare of the residents of the host community. Apart from this, iron and steel play a crucial role in the industrialization of any country, especially as it relates to construction industries as well as infrastructural development. The current non-functionality of Ajaokuta Steel Rolling Mill, Kogi State, Nigeria and Osogbo Steel Rolling Company, Osun State has left steel industries with almost dependence on recycling of scraps of metal (Ohimain and Jenakumo, 2013) and this in turn has led to some environmental challenges arising from emission from such recycling operation.

The nature of the operation of metal recycling plants is always characterized with the release of toxic air pollutants to the ambient air of the host community, apart from the possible noise pollution that can emanate from the within the facility. Emissions from metal recycling operation include but not limited to SO<sub>2</sub>; NH<sub>3</sub>; CO; H<sub>2</sub>S; NO<sub>x</sub> and particulate matters. The release of these pollutants into the atmosphere results into an increase in atmospheric pollution load and thus constitutes environmental and health threat (Olayinka *et al.*, 2015).

The study therefore focused on the impacts of metal recycling plant operation on ambient air quality. The results of the study will help in putting appropriate measures that will enhance environmental sustainability.

### 2. MATERIALS AND METHODS

#### 2.1 Sampling Area

A metal recycling plant located within its facility at Ile-Ife (latitude 7° 29' 0" - 7° 29' 30" N and longitude 4° 28' 0" E - 4° 28' 30" E), Osun State, Southwest Nigeria was used for this study. The factory is located few meters away from the expressway (Figure 1) and the regular emission of visible dark plume makes the area of interest for this study. The area is gradually becoming a residential area, with few commercial activities taking place in the vicinity. From all over the country, metal scraps are conveyed to the factory for recycling process and this has made the vicinity of the factory ever busy with activities. During recycling operation, dark plumes are emitted from the factory indiscriminately into the atmosphere, thus creating environmental threat for the residents.

## 2.2 Sampling equipment

In this study, microclimatic parameters (wind speed, wind direction, relative humidity, pressure and temperature) were measured with the aid of Weather Tracker Kestrel 4500.



Figure 1: Location of the study area (Fakinle *et al.*, 2020)

The device is incorporated with a PC interface which permits uploading of data for long-term storage, with the date and time of storage. It also has provision for chart mode where up to 250 measurements can be represented on graphs. Concentrations of SO<sub>2</sub>, NH<sub>3</sub>, CO and NO<sub>x</sub> were determined using an *insitu* single gas monitors by ToxiRAE, the Particulate matter (PM) was measured with GT-321 Particle Counter/Dust Monitor while Noise levels were measured with the aid of a digital battery-powered, sound pressure level meter. All the measurements were done for 15 minutes duration with each sampling cycle lasting for about 5 minutes. The average observation for each sampling location was recorded as well as the grand mean for both factory premises and surroundings

## 2.3 Sampling Procedure

To measure in the location of interest, monitoring devices were switched on and the values of parameters or concentrations of air pollutants to be measured were read directly on the screen of the monitor after capturing the pollutants. Each monitor was placed at least, 1.5- 2 m above the ground level at every location of interest. To measure the noise levels at any of the sampling locations, the sound level meter was placed at a distance of at least 3 m from any barrier or other sound reflecting sources and at about 1.5 m above ground level. Sampling was done in fifteen (15) different locations within the factory premises (designated as S1 to S16), while four locations (designated as S16- to S19) were chosen as sampling points within the host residential environment of the factory. Day-time noise measurement was also carried out.

To assess the impacts of the Iron and Steel recycling company on ambient conditions, especially as related to air quality and noise levels, the concentrations of the measured pollutants were compared with the National Ambient Air Quality Standards (NAAQS) of Nigeria as well as the Air Quality Standards of the World Bank (1995). Similarly, the measured noise levels were compared with the permissible noise levels of the Federal Ministry of Environment (FEPA 1991), the World Bank (2005), and that of the Guidelines values for Community Noise.

## 3.0 RESULTS AND DISCUSSION

### 3.1 Microclimatic Parameters

Presented in Table 1 are microclimatic parameters within the factory and the neighbourhood. These parameters included relative humidity, ambient temperature, atmospheric pressure, wind speed and oxygen level. In all the indoor and outdoor sampling locations covered within the factory's premises during the study, the relative humidity of the environment ranged between 62.1 and 73.2% with an average of 67.1% but outside the factory premises it was 54.6 – 66.4% with average of 61.4% which are all within the historical humidity of 66.5 – 89.9% of Ile-Ife, the project site location. The mean ambient temperature measured within the factory was 31.9 °C ranging between 28.6°C and 34.4°C while outside the factory it was 34.4°C ranging between 33.0 and 36.2°C. Like the trend in the relative humidity, the measured ambient

temperature during the study also agree with the historical ambient temperature of 27.8 – 34.1°C with an average 31.1°C reported for the area.

**Table 1:** Measured Microclimatic Parameters in the Factory during the Study

Sampling Location	Relative Humidity (%)	Ambient Temperature (°C)	Atmospheric Pressure (mbar)	Wind Speed (m/s)	Oxygen Level (%)
<b>Factory Premises</b>					
S1	69.5	28.6	985.0	Calm	20.9
S2	73.2	29.7	985.1	Calm	20.9
S3	69.9	30.5	985.5	Calm	20.8
S4	65.7	31.9	984.5	Calm	20.9
S5	72.8	30.7	984.3	1.4	20.9
S6	71.1	30.6	983.6	Calm	20.7
S7	66.8	32.0	983.7	0.5	20.8
S8	63.2	32.0	983.3	1.3	20.6
S9	68.5	33.3	983.0	0.9	20.9
S10	65.4	32.0	983.0	2.5	20.8
S11	66.9	33.0	982.5	Calm	20.8
S12	63.4	31.9	982.3	1.3	20.7
S13	65.2	33.3	982.2	0.6	20.8
S14	63.5	34.4	983.7	1.2	20.7
S15	62.1	34.0	981.3	1.1	20.9
<b>Mean</b>	<b>67.1</b>	<b>31.9</b>	<b>983.5</b>	<b>1.2</b>	<b>20.8</b>
<b>Factory Surroundings</b>					
S16	54.6	36.2	980.4	1.1	20.9
S17	63.2	35.2	981.6	1.2	20.9
S18	61.4	33.0	981.9	0.5	20.9
S19	66.4	33.1	982.2	Calm	20.9
<b>Mean</b>	<b>61.4</b>	<b>34.4</b>	<b>981.5</b>	<b>0.9</b>	<b>20.9</b>

Though some occasional calmness was observed during the fieldwork, the measured wind speed was 0.5 – 2.5 m/s with 1.2 m/s as average which are all within the historical wind speed data of 1.2 – 2.7 m/s with an average of 1.6 m/s. Generally, in the indoor environment of the factory, calm wind condition was predominant however all the locations where sampling took place were well ventilated as evident in the oxygen level of the factory which was between 20.6 and 20.9% with 20.8% as mean.

### 3.2 Air Quality

Although seven gaseous pollutants were monitored during the study, only CO and NH<sub>3</sub> were detected within the factory premises while SO<sub>2</sub>, NO, NO<sub>2</sub>, H<sub>2</sub>S and VOCs were not detected (< 1.0). In the two locations where detected, CO and NH<sub>3</sub> were measured to be 1.0 ppm. While CO was detected in the Furnace B South East End and the Gate House within the factory, NH<sub>3</sub> was detected in the Furnace B Charging Area and the Electric Power Generator. In the factory's surroundings, only NO was detected and it was measured to be 1.0 ppm in the only location where detected. When extrapolated to 24-hour concentrations, the measured CO and NH<sub>3</sub> in all the locations where detected within the factory premises was 0.4 ppm and outside the factory premises where NO was detected, the 24-hour extrapolated concentration of the measured concentration was also 0.4 ppm. It is important to note that CO and NH<sub>3</sub> were detected at each stage of charging, melting and tapping of molten scrap which take place in electric arc furnaces.

Within the factory premises, the ambient concentrations of SO<sub>2</sub>, NO, NO<sub>2</sub>, H<sub>2</sub>S and VOCs both in the indoor and outdoor environments being below the detection limits of the measuring instruments during the audit, implies that their concentrations are within the recommended limits. This implies that SO<sub>2</sub> in the environment is within its 0.01 ppm recommended limit of the Federal Ministry of Environment (FMENV) and NO/NO<sub>2</sub> in all the floors were within the FMENV recommended limit of 0.04 – 0.06 ppm. Similarly, the VOCs levels within factory were within the benzene's long-term limit of 1.5 ppm, within the toluene's long-term limit of 0.6 ppm, within the xylene's long term limit of 0.7 ppm and within the WHO guideline of 6.3 ppm and the FMENV limit of 1.9 ppm for VOCs. In this same factory premises, the 24-hour extrapolated CO level of 0.4 ppm is within the 10 ppm recommended limit of the FMENV for CO. Though Nigeria has no limit for NH<sub>3</sub> and H<sub>2</sub>S, the 24-hour extrapolated level of 0.4 ppm obtained from the measured NH<sub>3</sub> calls for no concern. The contribution from other sources such as domestic activities, vehicles and electric power generator were not considered.

In all the sampling locations, particulate matters were also detected and the measured concentrations are presented in Table 2. Within the factory premises, PM<sub>1</sub>, PM<sub>2.5</sub>, PM<sub>7</sub>, PM<sub>10</sub> and TSP concentrations were in the range of 0.7 – 19.8 µg/m<sup>3</sup>, 2.1 – 91.2 µg/m<sup>3</sup>, 4.3 – 121.4 µg/m<sup>3</sup>, 4.3 – 122.1 µg/m<sup>3</sup>, and 4.3 – 122.5 µg/m<sup>3</sup>, respectively with respective means of 4.8 µg/m<sup>3</sup>, 17.1 µg/m<sup>3</sup>, 24.7 µg/m<sup>3</sup>, 24.8 µg/m<sup>3</sup>, and 25.0 µg/m<sup>3</sup> while in the factory's surroundings, the concentrations' range were 3.0 – 12.7 µg/m<sup>3</sup>, 8.6 – 51.1 µg/m<sup>3</sup>, 14.1 – 70.0 µg/m<sup>3</sup>, 14.1 – 70.1 µg/m<sup>3</sup>, and 14.1 – 70.3 µg/m<sup>3</sup> for PM<sub>1</sub>, PM<sub>2.5</sub>, PM<sub>7</sub>, PM<sub>10</sub> and TSP respectively.

Table 2: 15-Minutes Measured Particulates within the Factory Premises and the Surrounding

Sampling Locations	Concentrations (µg/m <sup>3</sup> )				
	PM <sub>1</sub>	PM <sub>2.5</sub>	PM <sub>7</sub>	PM <sub>10</sub>	TSP
<b>Factory Premises</b>					
S1	3.6	11.0	14.0	14.0	14.0
S2	0.7	2.1	4.3	4.3	4.3
S3	12.5	49.3	65.8	66.3	66.5
S4	3.1	9.3	13.8	13.8	13.8
S5	1.8	4.7	8.8	8.8	8.8
S6	2.5	7.8	11.1	11.3	11.7
S7	1.3	3.5	6.0	6.0	6.0
S8	6.2	19.9	26.5	26.6	26.6
S9	1.9	5.2	8.2	8.2	8.2
S10	1.2	3.3	6.1	6.1	6.1
S11	7.0	22.0	28.6	28.6	29.7
S12	4.4	12.9	19.2	19.2	19.2
S13	19.8	91.2	121.4	122.1	122.5
S14	3.0	7.8	12.3	12.3	12.5
S15	2.8	7.1	24.5	24.6	24.6
<b>Factory Surrounding</b>					
S16	12.7	51.1	70.0	70.1	70.3
S17	4.3	12.1	18.8	19.1	19.1
S18	3.4	9.6	14.5	14.5	14.7
S19	3.0	8.6	14.1	14.1	14.1

On extrapolating these values to 24-hour concentrations, the measured particulate matters concentrations within the factory premises were 0.3 - 7.6 µg/m<sup>3</sup>, 0.8 – 35.0 µg/m<sup>3</sup>, 1.6 – 46.6 µg/m<sup>3</sup>, 1.6 – 46.8 µg/m<sup>3</sup>, and 1.6 – 47.0 µg/m<sup>3</sup> for PM<sub>1</sub>, PM<sub>2.5</sub>, PM<sub>7</sub>, PM<sub>10</sub> and TSP respectively with respective means of 1.8 µg/m<sup>3</sup>, 6.6 µg/m<sup>3</sup>, 9.5 µg/m<sup>3</sup>, 9.5 µg/m<sup>3</sup>, and 9.6 µg/m<sup>3</sup> but in the surroundings, the measured particulates concentrations became 1.2- 4.9 µg/m<sup>3</sup>, 3.3 – 19.6 µg/m<sup>3</sup>, 5.4 – 26.8 µg/m<sup>3</sup>, 5.4 – 26.9 µg/m<sup>3</sup>, and 5.4 – 27.0 µg/m<sup>3</sup> respectively for PM<sub>1</sub>, PM<sub>2.5</sub>, PM<sub>7</sub>, PM<sub>10</sub> and TSP with respective average of 2.2 µg/m<sup>3</sup>, 7.8 µg/m<sup>3</sup>, 11.3 µg/m<sup>3</sup>, 11.3 µg/m<sup>3</sup>, and 11.3 µg/m<sup>3</sup>. From the result obtained, it was noticed that the concentrations of the particulate matters were higher at the surrounding than the concentrations within the premises of the factory. While the concentrations within the factory premises for PM<sub>1</sub>, PM<sub>2.5</sub>, PM<sub>7</sub>, PM<sub>10</sub> and TSP were approximately 4.8; 17.0; 24.7; 24.8 and 25.0 µg/m<sup>3</sup>, respectively, concentrations of these pollutants within the neighbourhood of the factory (surroundings) were respectively 5.0, 20.4, 29.3, 29.5 and 29.6 µg/m<sup>3</sup>. This is an indication of diffusion of the pollutants from the source of emission to nearby environment and in most cases, the process is influenced by climatic conditions, especially the wind speed. The average wind speed within the factory premises was higher than that of the surrounding, hence it is thought that this enhanced the transport of the particulate from the source of the emission (factory premises) to the nearby surroundings. These values are higher than the previously reported figures on the same plant (Adeyeye *et al.*, 2017). This could be attributed to the increased production operation of the plant.

In none of the sampling locations was the PM<sub>10</sub> World Bank limit or the TSP FMENV limit breached either in the indoor or outdoor of the factory or in the surrounding communities. The detection of the highest particulate level in the North West Flank is an indication that the released air pollutants from Ife Iron and steel Limited can be transported outside the factory's premises. Efforts should therefore be intensified to ensure that air pollutants are contained within the factory premises by installing adequate air pollution control equipment.



### 3.3 Ambient Noise Level

Presented in Table 3 are the measured noise levels within the factory premises as well as its surrounding.

The minimum measured ambient noise levels within the factory premises were 48.8 – 78.2 dB(A) with a maximum range of 63.1 – 90.8 dB(A) while outside the factory premises, the measured minimum noise levels were 35.1 – 45.4 dB(A) with maximum levels of 47.2 – 79.6 dB(A).

Table 3: Measured Ambient Noise Levels in metal recycling Company

Sampling Location	Minimum	Maximum
<b>Factory Premises</b>		
S1	64.2	72.0
S2	78.1	84.0
S3	75.9	90.8
S4	75.7	85.1
S5	78.2	86.4
S6	71.9	78.4
S7	73.8	83.0
S8	71.1	78.8
S9	61.5	67.8
S10	51.7	63.1
S11	67.9	80.1
S12	70.4	90.6
S13	59.7	75.6
S14	48.8	76.9
S15	63.2	90.5
<b>Factory Surroundings</b>		
S16	45.4	79.6
S17	35.4	53.6
S18	45.1	68.2
S19	35.1	47.2

The minimum ambient noise levels within the factory did not exceed the 8-hour 90 dB (A) shop floor set limit of the Federal Ministry of Environment. On the other hand, measured maximum ambient noise levels in the Furnace A Charging Area, the Furnace B Scrap Yard and the Gate House exceeded the limit. In the factory's surroundings, both the minimum and maximum measured noise levels were within the set limit.

All the measured noise levels at the fifteen locations within the factory exceeded the sleep-disturbance limit.

World Health Organization (WHO) limit was also exceeded in all the sampling locations within the factory except in the South West Flank and the North East Flank where the minimum noise levels were within the limit. The measured minimum noise levels in the factory's surroundings were within the sleep disturbance limit in two of the four sampling locations and within the WHO limit in all but one while the measured maximum noise levels in these surroundings breached the sleep disturbance limit in all locations but breached the WHO limit in only two of these four locations.

It is therefore advocated that in all the sections where noise has been established to exceed the 8-hour 90 dB (A) limit, adequate efforts must be put in place for noise control (such as noise insulating system) and exposure-preventive measure such as adequate provision of ear muffs/plugs for workers; considering the fact that regular exposure to noise above the recommended level can result into occupationally-induced hearing loss and mental fatigue (Palmer *et al.*, 2002). It is therefore important to take safety precaution in order to avoid both short-term and long-term hearing loss as well as mental fatigue as a result of noise emanating from metal recycling plant operations. Some of the negative effects of being exposed to high noise level include disturbance of sleep, interruption of conversation, stress creation and annoyance in the general population.

#### 4.0 CONCLUSION

To investigate the impacts of metal recycling plant operation on ambient air quality, air quality and noise levels assessment of Ife Iron and Steel Ltd., Ife-Ibadan Expressway, Ile-Ife Osun State were carried out within and around the factory.

Only CO and NH<sub>3</sub> were detected within the factory premises and at 1.0 ppm. Particulates were detected in all the sampling locations considered within the factory premises and its surroundings. The 24-hours extrapolated concentrations of PM<sub>10</sub> within the factory's premises are 2.1 – 58.5% of the World Bank's 80 µg/m<sup>3</sup> limit while the TSP levels in the same environment are 0.7 – 18.8% of the Federal Ministry of Environment's limit of 250 µg/m<sup>3</sup> in all the locations. In none of the locations was the PM<sub>10</sub> World Bank limit or the TSP FMENV limit breached either in the indoor or outdoor of the factory and the surrounding communities. The measured minimum ambient noise levels within the factory premises were below the 8-hour 90 dB(A) shop floor set limit of the Federal Ministry of Environment in all the sampling locations while measured maximum ambient noise levels, the limit was breached in some areas within the factory.

#### REFERENCES

- Adeyeye, M.A., Akeredolu, F.A., Sonibare, J.A., Fakinle, B.S., Odekanle, E.L and Oloko-Oba, I.M. (2017). Emission inventory of air pollutants in a metal recycling facility". *American Journal of Environmental Protection* 5: 9-12
- Fakinle. B.S., Odekanle. E. L., Olalekan. A. P., Ije. H. E., Oke. D.O., Sonibare. J.A. (2020). Air pollutant emissions by anthropogenic combustion processes in Lagos, Nigeria. *Cogent Engineering* 7: 1808285
- FEPA. (1991). Guidelines to Standards for Environmental Pollution Control in Nigeria. Federal Environmental Protection Agency (FEPA), Lagos
- NIMET- Nigerian Meteorological Organization (2010). Climatic Variability and Change: Impacts, Science, Innovation and Policy. *Climate Review Bulletin*, 1-24.
- Ohimain, E.L and Jenakumo, C, B, (2013). Scrap recycling and valorization in Bayelsa State, Nigeria. *The Journal of Material Science*, 119:139-147
- Olayinka, O.O; Adedeji, O.H and Bolaji, Y. (2015). Air and heavy metal pollution around a steel foundry in Ogijjo, Ogun State, Nigeria. *Journal of Science Research*, 14: 8-15
- Palmer, K., T., Griffin, M., J., Syddall, H., E., Davis, A., Pannett, B. and Coggon, D. (2002). Occupational exposure to noise and the attributable burden of hearing difficulties in Great Britain. *Occupational and Environmental Medicine*. 59(9):634–9.
- World Bank (1999) Pollution Prevention and Abatement Handbook 1998: Toward Cleaner Production. The World Bank Group in Collaboration with the United Nations Environment Programme and the United Nations Industrial Development Organization. The World Bank Group, Washington DC., USA. 457 pp.
- WHO. (2005). Health effects of transport-related air pollution. *World Health Organisation Regional Publications, WHO Regional Office for Europe, Copenhagen*



## Air and Noise Quality Assessment Around Lube Blending and Insecticide Production Plant

Jacob A. SONIBARE<sup>1\*</sup>, Funso A. AKEREDOLU<sup>1</sup>, Ebenezer L. ODEKANLE<sup>2</sup> and Bamidele S, FAKINLE<sup>3</sup>

<sup>1</sup>Department of Chemical Engineering, Obafemi Awolowo University, Ile-Ife, Nigeria

<sup>2</sup>Department of Chemical and Mineral Resources Engineering, First Technical University, Ibadan Nigeria.

<sup>3</sup>Department of Chemical Engineering, Landmark University, Omu-Aran, Nigeria

<sup>1\*</sup>[asonibar@yahoo.com](mailto:asonibar@yahoo.com), <sup>1</sup>[osnufy2k3@yahoo.co.uk](mailto:osnufy2k3@yahoo.co.uk), <sup>2</sup>[eodekanle@yahoo.com](mailto:eodekanle@yahoo.com), <sup>3</sup>[fakinle.bamidele@lmu.edu.ng](mailto:fakinle.bamidele@lmu.edu.ng)

\*Corresponding author

---

### ABSTRACT

The air quality impacts of Lube Oil Blending and Insecticide Plants of an Oil company in Lagos Nigeria was carried out by measuring relevant microclimatic and air quality parameters as well as noise levels within and around the plant premises. The results were compared with the appropriate permissible limits. The results showed that the measured microclimatic parameters of the environment were within the historical climatic condition of Lagos. Furthermore, VOCs were detected in only nine of the seventeen sampling locations, while NH<sub>3</sub>, SO<sub>2</sub>, NO<sub>2</sub>, CO, and H<sub>2</sub>S were not detected at all. The extrapolated 24-hour concentrations of VOCs exceeded both the WHO guidelines and the FMENV limits only in the Fuel Loading Rack of the company. Particulates were detected in all the sampling locations and the 24-hours extrapolated concentrations of PM<sub>10</sub> were found to be about 5.0 - 11.9% of the World Bank's limit of 80 µg/m<sup>3</sup> while the TSP levels are 1.7 - 4.0 % of the Federal Ministry of Environment's limit of 250 µg/m<sup>3</sup> in all the sampling locations. Also, measured noise levels did not exceed the shopfloor 8-hour limit of the FMENV in all the locations, but it exceeded the sleep disturbance limit in all.

**Keywords:** Air quality; Lube Oil; Insecticide; noise level; microclimatic parameters

### 1. INTRODUCTION

Since the last few decades, urban air pollution is gradually becoming an environmental issue of public concern, considering the fact that the quality of the environment has a direct effect on the quality of the life of residents. Modern anthropogenic activities which could be a direct reflection of industrialization and population growth continue to be precursors to contamination of ambient air quality. Petroleum and petrochemical industries have been adjudged as one of the major emitters of toxic pollutants such as benzene, toluene, ethyl benzene, and xylene as well as the sources of emission of hydrocarbons like natural gas and light volatile fuels which are less toxic (Beckett *et al.*, 1998). They also emit criteria air pollutants such as particulate matter (PM), NO<sub>x</sub>, CO, H<sub>2</sub>S and SO<sub>2</sub> (Odekanle *et al.*, 2021). Despite the contribution of industrial and commercial utilization of refined products to the immense growth and development of Nigeria, manufacturing of such products often results in unacceptable levels of toxic emissions which deteriorate atmospheric air quality.

Lube oil, important petroleum product, which is blended to produce variety of lubricants, possesses a crucial role in increasing national economy (Utser *et al.*, 2013). These lubricants are therefore petroleum hydrocarbon-based and are obtained from vacuum distillation of atmospheric residue with appropriate blending (Ahmed, 2006). Blending of lube oil to produce lubricant is not without emission of significant air pollutant (Jacob, 2000; Utser *et al.*, 2013). Also, manufacture insecticide- a chemical manufactured from petroleum product traditionally used for insect control has been reported to be associated with the emission of air pollutants (Adetuyi *et al.*, 2012).

As part of research interest to assess the impact of industrial activities on air quality, the study seeks to investigate the contribution of lube oil blending and insecticide production to air quality. Lube Oil Blending and Insecticide Plants owned by ExxonMobil Oil Nigeria Plc was used as a case study. The company produces about 84 different kinds of lubricants and only one insecticide. In the Insecticide Plant, production activities include mixing, blending, filling, capping and packaging while the Lube Oil Plant has heating, blending, filling, capping and packaging as production activities. Within and around the plants, air quality and noise levels were measured accordingly and the results compared with the recommended limits. The result of the study will provide scientific basis for provision of pollutants 'mitigating measures.

## 2. MATERIALS AND METHODS

### 2.1 Study Location

For this study, Lube Oil Blending and Insecticide Plants of Mobil Oil Nigeria Plc., located within ExxonMobil complex in Apapa, Lagos State, Nigeria was used as study location (Figure 1).



Figure 1: Study location (Fakinle *et al.*, 2020)

The factory has three production facilities: a lube oil blending plant, a petroleum jelly plant, and an insecticide plant. Each production facility is equipped with its own basic utility equipment, as well as backup power devices. However during the study, only the lube oil blending plant and the insecticide plant were working. The petroleum jelly plant is temporary out of operation. Different grades of virgin oils including monograde, multigrade, marine lubricant, and industrial lubricants are produced in the lube oil blending plant from imported base oils. There about 84 of these different lubricants. In the insecticide plant, only mobil aerosol insecticide is produced. The other major facility in the company premises is the fuel storage and loading bay. The Insecticide Plant produces about 30,000 cartons of “Mobil Insecticide” per month while the Lube Oil Plant has an installed capacity of about 450,000 barrels (73.1 million litres) per annum.

### 2.2 Sampling equipment

Weather Tracker Kestrel 4500 was employed to measure climatic parameters (wind speed, wind direction, relative humidity, pressure and temperature). The device is capable of monitoring parameters such as Temperature, Wind Speed, Humidity, Wind Chill, Density, Altitude, Barometric Pressure, Dew Point, Heat Index and Wet Bulb. It also has a chart mode that allows users to recall and graph up to 250 measurements, along with the date and time of storage with a PC interface that allows data uploading for long-term storage, in-depth analysis and detailed charting. GT-321 Particle Counter/Dust Monitor was used to determine the level of Particulate matter (PM), an equipment from Met One Instruments. It is handheld, battery operated and completely portable device capable of measuring five mass ranges of particulate matters: PM<sub>1</sub>, PM<sub>2.5</sub>, PM<sub>7</sub>, PM<sub>10</sub>, and TSP. It has a concentration range of 0 – 1 mg/m<sup>3</sup> (with a resolution of 0.1 µg/m<sup>3</sup>), a sampling time of 2 minutes and a flow rate of 2.83 l/min. To measure, it is placed at 1 m above the ground level, switched on in the environment of interest and the measured concentration read directly on the screen after particle capturing. NO<sub>x</sub> concentrations were measured as NO<sub>2</sub> using an *insitu* single gas NO<sub>x</sub> monitor (ToxiRAE Model PGM-1110); SO<sub>2</sub> concentrations were measured an *insitu* single gas SO<sub>2</sub> monitor (ToxiRAE Model PGM-1130); CO and NH<sub>3</sub> measurements were taken using an *insitu* non-integrated single gas carbon monoxide monitor (ToxiRAE Model PGM-1150); while Hydrogen Sulphide (H<sub>2</sub>S) and Volatile Organic Compounds (VOCs) concentrations were measured using an *insitu* MultiRAE gas monitor (Model PGM50-5P). All these devices are similar both in configuration and modes of operation. The monitors are 9.3 cm x 4.9 cm x 2.2 cm measuring equipment weighing about 0.1 kg with an instantaneous direct readout displays through which current the respective pollutants’ concentrations can be continuously monitored in ppm (parts per million). With the exemption of monitor ToxiRAE Model PGM-1150 and MultiRAE gas monitor (Model PGM50-5P) which have detection ranges of 0 – 500 ppm with 1 ppm resolution. 0 – 200 ppm with 0.1 ppm resolution, respectively, all other monitors have detection ranges of 0 – 20 ppm and 0.1 ppm resolution. Each of the monitors has facility for Short Term Exposure Limit (STEL) from which the pollutants’ concentration for the last 15 minutes can be

determined; the Time Weighted Average (TWA) from which the accumulated reading of the gas concentration since the monitor was turned on is divided by 8 hours; and the Peak Reading, which is the highest reading since the monitor was turned on. For every field measurement, the “Auto-Zero at Start-up” calibration is required and this was carried out during the measurements. The levels of noise were determined noise using a digital, battery-powered, sound pressure level meter (EXTEC Instruments, US Model 407735). The monitor has high- and low-metering ranges of 35 – 100 dB and 65 – 130 dB, respectively. The meter is also equipped with a build-in calibration check (94 dB), tripod mount, and analog DC/AC conditioned outputs of 10mV/dB and utilized a 0.49 “ (12.3 mm) condenser microphone

### 2.3 Sampling Procedures

Sampling took place in seventeen locations in the production floors and the general company premises (Table 1). The parameters monitored were meteorological data: temperature, wind speed and direction; particulate matter concentrations including those with diameter less than 1 microns (PM<sub>1</sub>), 2.5 microns (PM<sub>2.5</sub>), 7 microns (PM<sub>7</sub>), 10 microns (PM<sub>10</sub>) and total suspended particulate (TSP), TSP; gaseous pollutants concentrations including carbon monoxide (CO), oxides of nitrogen in form of nitrogen dioxide (NO<sub>2</sub>), sulphur dioxide (SO<sub>2</sub>), hydrogen sulphide (H<sub>2</sub>S) and volatile organic compounds (VOCs); and noise levels. The monitors were switched on at the location of interest and the values of parameters were read directly on the screen of the monitor after capturing the pollutants. At each location, the sampling equipment was placed at a height of at a height between 1.5 to 2 m above the ground, depending on the topography of the sampling location. Similarly, noise level monitor were located 1.2 m above the ground and at least 3 m away from any obstruction or any sound reflecting object. A sampling period of 15 minutes was adopted for the measurement of gaseous pollutants while 15 seconds was adopted for noise measurements. As recommended Federal Ministry of Environment (FEPA, 1991).

Table1: Description of Sampling Locations around the Study Area

S/No	Station ID	Location	
		Name	Designation
1.	S1	Insecticide Plant Raw Material Section	Indoor
2.	S2	Insecticide Plant Production Area	Indoor
3.	S3	Insecticide Plant Warehouse	Indoor
4.	S4	LPG Tank Farm	Outdoor
5.	S5	Lube Plant Filling Area	Indoor
6.	S6	ABB Area	Indoor
7.	S7	Additives Tank Farm	Outdoor
8.	S8	Boiler Room	Indoor
9.	S9	Generator House	Indoor
10.	S10	Solid Waste Holding Area	Outdoor
11.	S11	Lube Plant Additive Warehouse	Indoor
12.	S12	Lube Plant Entrance	Outdoor
13.	S13	Fuel Oil Tank Farm	Outdoor
14.	S14	Base Oil Tank Farm	Outdoor
15.	S15	Pump House	Outdoor
16.	S16	Chemical Loading Rack	Outdoor
17.	S17	Fuel Loading Rack	Outdoor

The measured concentrations of air pollutants were extrapolated to 24-hour concentrations and then compared with the National Ambient Air Quality Standards (NAAQS) of Nigeria and the Air Quality Standards of the World Bank. The measured noise levels were compared with the permissible noise levels of the Federal Ministry of Environment, World Bank and that of the World Health Organization.

## 3.0 RESULTS AND DISCUSSION

### 3.1 Microclimatic Parameters

In all the sampling locations covered within the company premises both indoor and outdoor, the humidity of the environment ranged between 67.4 and 82% with an average of 71.8 % (Figure 1) which are all within humidity of 66.2 – 90.9% of Lagos area. The mean ambient temperature measured in the company premises during the study was 31.3 °C ranging between 27.3 and 32.9 °C (Figure 2). These also agree with the historical ambient temperature of 21.6 - 34.1 °C established for Lagos, Nigeria.

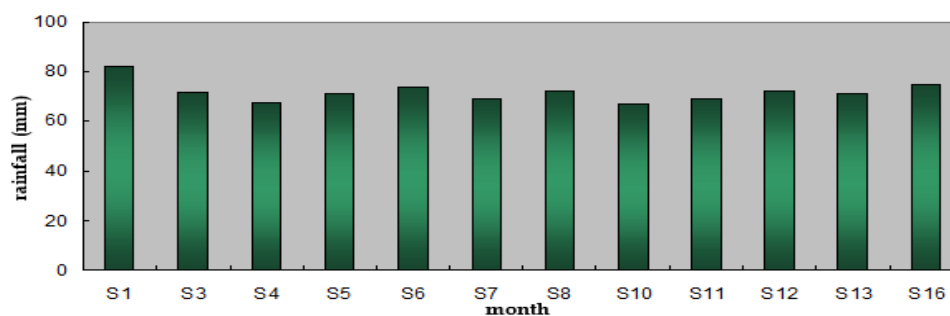


Figure 1: Measured Humidity in Mobil Nig. Plc., during the Study

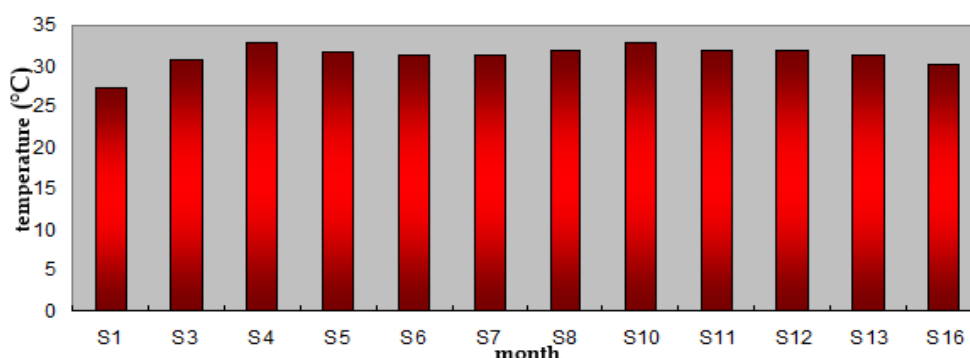


Figure 2: Measured Air Temperature in Mobil Nig. Plc., during the Study

### 3.2 Air Quality

The 15-minutes mean measured concentrations of gaseous pollutants in each of the sampling locations are summarized in Table 2. NH<sub>3</sub>, SO<sub>2</sub>, NO<sub>2</sub>, CO, and H<sub>2</sub>S were not detected in any of the seventeen sampling locations (i.e. < 0.1 ppm). However, VOCs were detected in nine of these location in the range 0.1 – 37.8 ppm with the minimum and maximum at S10 (Solid Waste Holding Area) and S17 (Fuel Loading Rack Area) respectively.

**Table 2:** 15-Minutes Measured Gaseous Pollutant Concentrations within the Factory

Sampling Locations	Concentrations (ppm)					
	SO <sub>2</sub>	NO <sub>2</sub>	CO	NH <sub>3</sub>	H <sub>2</sub> S	VOCs
S1	<0.1	<0.1	<1.0	<1.0	<0.1	<0.1
S2	<0.1	<0.1	<1.0	<1.0	<0.1	<0.1
S3	<0.1	<0.1	<1.0	<1.0	<0.1	<0.1
S4	<0.1	<0.1	<1.0	<1.0	<0.1	<0.1
S5	<0.1	<0.1	<1.0	<1.0	<0.1	0.3
S6	<0.1	<0.1	<1.0	<1.0	<0.1	0.5
S7	<0.1	<0.1	<1.0	<1.0	<0.1	0.8
S8	<0.1	<0.1	<1.0	<1.0	<0.1	0.6
S9	<0.1	<0.1	<1.0	<1.0	<0.1	0.4
S10	<0.1	<0.1	<1.0	<1.0	<0.1	0.1
S11	<0.1	<0.1	<1.0	<1.0	<0.1	<0.1
S12	<0.1	<0.1	<1.0	<1.0	<0.1	<0.1
S13	<0.1	<0.1	<1.0	<1.0	<0.1	<0.1
S14	<0.1	<0.1	<1.0	<1.0	<0.1	0.3
S15	<0.1	<0.1	<1.0	<1.0	<0.1	0.3
S16	<0.1	<0.1	<1.0	<1.0	<0.1	<0.1
S17	<0.1	<0.1	<1.0	<1.0	<0.1	37.8

The extrapolated 24-hour concentrations of VOCs in all the sampling locations where the pollutants were detected in the Company premises ranged between 0.1 and 19.4 ppm (Figure 3). These concentrations were found to exceed both the WHO guidelines and the FMENV limits only in S17 which is the Fuel Loading Rack of the company.

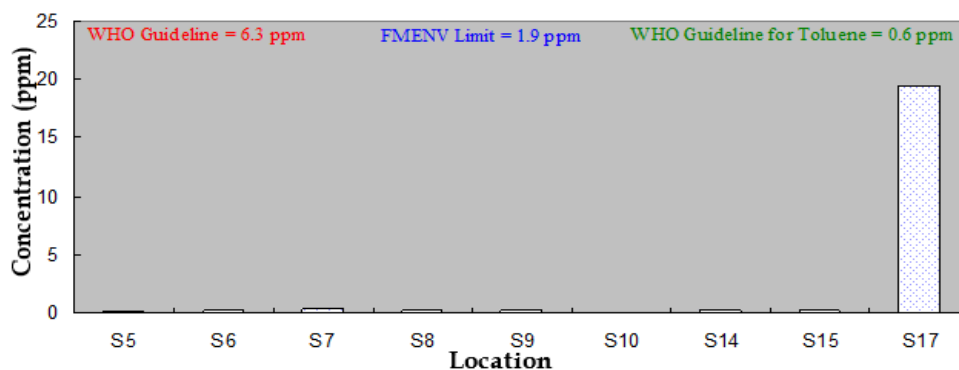


Figure 3: Extrapolated VOCs Concentrations Compared to Standards

In all the other locations where they were detected, they are just about 0.8 – 6.5% of the WHO limit and 2.7 – 21.6% of the Federal Ministry of Environment’s limit with the minimum from S10, that is the Solid Waste Holding Area and the maximum from S7 which is the Additives Tank Farm. Benzene, toluene and xylene (BTX) are the three major forms of VOCs that are of environmental concern. If the measured VOCs are considered in respect of benzene, the measured concentrations are below the short-term limit in all the sampling locations except in S17, the Fuel Loading Rack. However, its long-term limit was exceeded in S7, the Additives Tank Farm, in addition. If the consideration is in respect of toluene, the measured concentration then exceeded FMENV short-term limit in the Fuel Loading Rack while the long-term limit is exceeded in S6, S7, and S8 in addition to the Fuel Loading Rack. In all the sampling locations within the Company premises, the xylene short-term limit of the Federal Ministry of Environment is not exceeded except at the Fuel Loading Rack but its long-term limit was exceeded in all except if these VOCs are xylene, the FMENV short-term limit was exceeded in all locations where VOCs were detected except in S10, the Solid Waste Holding Area.

In the Insecticide Plant and the Lube Oil Plant, several materials blended for finished products are made of volatile organic compounds and their proper handling will be required to minimize release into the environment. The difference in sources is thought to be an indication of the difference in composition of the measured VOCs. Since VOCs from the Fuel Loading Rack are from gasoline and diesel vapour, they may be more of BTX. Prolonged exposures to benzene have been associated with haematotoxicity, genotoxicity and carcinogenicity (WHO, 2000). Chronic benzene exposure can result in bone marrow depression expressed as leukopenia, anaemia and/or thrombocytopenia, leading to pancytopenia and aplastic anaemia (Fakinle *et al.*, 2021). Similarly, haematological effects of varying severity have been reported in workers occupationally exposed to high levels of benzene while some studies have demonstrated chromosomal effects at mean workplace exposures as low as 1.4 – 2.2 ppm (WHO, 2000). The acute and chronic effects of toluene on the central nervous system are the effects of most concern (Tehrani *et al.*, 2020, Odekanle *et al.*, 2021). It may also cause developmental decrements and congenital anomalies in humans, including fetal development retardation, skeletal anomalies, low birth weight and developmental neurotoxicity (Mulenga and Siziya, 2019). The potential effects of toluene on reproduction and hormone balance in women, coupled with findings of hormone imbalances in exposed males, are also of concern (WHO, 2000). For these reasons, there is an urgent need for the control of VOCs release in the company’s premises. Concentrations of particulate matters measured in all the sampling locations are presented in Table 3.

These concentrations were in the range of 10.5 – 24.8  $\mu\text{g}/\text{m}^3$ , 8.7 – 20.8  $\mu\text{g}/\text{m}^3$ , 2.9 – 6.6  $\mu\text{g}/\text{m}^3$ , 0.4 – 1.2  $\mu\text{g}/\text{m}^3$ , and 10.9 – 26.4  $\mu\text{g}/\text{m}^3$  for  $\text{PM}_{10}$ ,  $\text{PM}_7$ ,  $\text{PM}_{2.5}$  and TSP respectively. When extrapolated to 24-hour concentrations, these measured concentrations become 4.0- 9.5  $\mu\text{g}/\text{m}^3$ , 3.3 – 8.0  $\mu\text{g}/\text{m}^3$ , 1.1 – 2.5  $\mu\text{g}/\text{m}^3$ , 0.2 – 0.5  $\mu\text{g}/\text{m}^3$ , and 4.2 – 10.1  $\mu\text{g}/\text{m}^3$ . The 24-hours extrapolated concentrations of  $\text{PM}_{20}$  are about 5.0 - 11.9% of the World Bank’s limit of 80  $\mu\text{g}/\text{m}^3$  while the TSP levels are 1.7 – 4.0 % of the Federal Ministry of Environment’s limit of 250  $\mu\text{g}/\text{m}^3$  in all the sampling locations.

Low particulate matter concentration measured in the factory premises are connected to the fact that materials being handled in the company are mostly liquid. Though dust re-suspension is a major source of particulates in the Chemical industries, it was observed that floor of company was well-kept and this made contribution of dust re-suspension in the company insignificant. Similarly, combustion activities in both the electric power generators and steam boilers are another expected source of particulate matter, however, low measured concentrations of particulate in this study is a reflection of proper maintenance of the electric power generation and steam boiler in the company.

**Table 3:** Measured Particulate Concentrations

Sampling Locations	Concentrations ( $\mu\text{g}/\text{m}^3$ )				
	PM <sub>10</sub>	PM <sub>7</sub>	PM <sub>2.5</sub>	PM <sub>1</sub>	TSP
S1	17.8	15.2	5.9	1.0	18.4
S2	21.6	17.9	6.4	1.2	24.5
S3	21.1	18.0	6.6	1.1	22.2
S4	21.5	19.5	6.6	1.0	24.8
S5	15.3	14.6	4.4	0.7	17.5
S6	16.1	14.7	3.9	0.6	17.7
S7	18.3	14.6	4.7	0.7	19.6
S8	11.9	9.7	2.9	0.4	13.4
S9	11.4	9.6	3.0	0.5	12.6
S10	12.9	11.0	3.4	0.5	14.1
S11	10.5	8.7	3.0	0.5	10.9
S12	10.7	9.8	3.0	0.5	12.2
S13	24.8	20.8	6.3	1.0	26.4
S14	17.8	16.4	5.1	0.8	21.0
S15	13.3	11.1	3.2	0.5	14.6
S16	15.6	14.8	4.2	0.6	18.0
S17	22.3	18.8	6.0	1.0	25.1

### 3.3 Ambient noise levels

The levels of noise in the ambient environment of the plant are represented in Figure 4. The minimum levels ranged from 41.9 to 82.6 dB(A) with the maximum levels ranged from 58.5 to 88.3 dB(A).

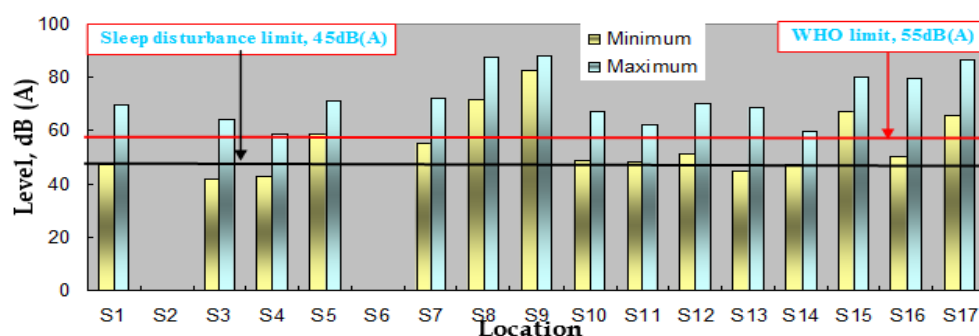


Figure 4: Ambient Noise Levels within Mobil Nig. Plc., Apapa

Although it was found that the shopfloor 8-hour limit of the FMENV (FEPA, 1991) was not exceeded in all the sampling locations by both the measured minimum and maximum noise levels, sleep disturbance limit was exceeded in 71% of the sampling locations by the measure minimum noise levels, while all measured maximum noise levels exceeded sleep disturbance limit. Furthermore, WHO limit (Berglund *et al.*, 1999) was exceeded in only 29% of the sampling locations by the measured minimum levels but the maximum levels exceeded WHO limit in all of the locations as shown in Figure 4.

## 4.0 CONCLUSION

Air and noise quality within and around the premises of Lube Oil Blending and Insecticide Plants of Mobil Oil Nigeria Plc, Lagos was investigated. In 17 locations within and around the plant, microclimatic and air quality parameters as well as noise levels were measured accordingly. The results showed that in all the sampling locations within and around the company premises, the humidity of the environment and the mean ambient temperature are within the historical humidity and ambient temperature of Lagos area. Furthermore, only VOCs that was detected in nine of the locations. Particulates were detected in all the sampling locations and the 24-hours extrapolated concentrations of PM<sub>20</sub> were found to be below the recommended limits. For the ambient noise, maximum levels exceeded WHO limits in all the sampling location. It can be concluded therefore that although, the impact of the plant on air quality currently poses no significant environmental threat, long exposure to VOCs by people around the plants should be avoided as this could complicate issues for those with existing health challenges and thus adequate measures should be taken to protect workers involved in fuel loading to reduce potential breathing of VOCs.



## REFERENCES

- Adetuyi, O.O., Ajekwene, K.K. and Jabar, J.M. (2012). Production and Performance Evaluation of Insecticide-based Coating. *Journal of Chemical Society of Nigeria*, 37:20-26
- Ahmed, N.S. (2006). Preparation and evaluation of some oil additive based on polyethylene glycol. *International Journal of Polymeric Materials*, 55: 761-771
- Beckett, K. P., Freer-Smith, P. H., and Taylor, G. (1998). Urban woodlands: Their role in reducing the effects of particulate pollution. *Environmental Pollution*, 99(3), 347–360. [https://doi.org/10.1016/S0269-7491\(98\)00016-5](https://doi.org/10.1016/S0269-7491(98)00016-5)
- Berglund, B., Lindvall, T., and Schwela, D (1999) Guidelines for Community Noise. World Health Organization (WHO), Geneva. pp. 141
- Fakinle. B.S., Odekanle. E. L., Olalekan. A. P., Ije. H. E., Oke. D.O., Sonibare. J.A. (2020). Air pollutant emissions by anthropogenic combustion processes in Lagos, Nigeria. *Cogent Engineering* 7: 1808285
- Fakinle, B.S., Olalekan, A.P., Odekanle, E.L., Bakut, C.B., Ogundokun, R.O., Sonibare, J.A., and Aremu, C.O (2021). Assessment of the contribution of hazardous air pollutants from Nigeria's petroleum refineries to ambient air quality. Part 1. *Cogent Engineering*, 8: 1870792. <https://doi.org/10.1080/23311916.2020.1870792>
- FEPA. (1991). Guidelines to Standards for Environmental Pollution Control in Nigeria. Federal Environmental Protection Agency (FEPA), Lagos.
- Giacosa, G.; Barnett, C.; Rainham, D.G.; Walker, T.R. (2022) Characterization of Annual Air Emissions Reported by Pulp and Paper Mills in Atlantic Canada. *Pollutants* 2:135–155. <https://doi.org/10.3390/pollutants2020011>
- Jacob, A. (2000). Continuous risk assessment for the process industries in Nigeria. *Proceeding of the 30<sup>th</sup> Annual Conference of MSChe*, pp 29-37
- Mulenga, D., and Siziya, S. (2019). Indoor air pollution related respiratory III health, a sequel of biomass use. *SciMedicine Journal*, 1(1), 30–37. <https://doi.org/10.28991/SciMedJ-2019-0101-5>
- Odekanle, E.L., Bakut, C.B., Olalekan, A.P., Ogundokun, R.O., Aremu, C.O, Sonibare. J.A, Akande. O.T., Olayanju, A.T and Fakinle. B.S (2021). Assessment of the contribution of TEX air pollutants from Nigeria's petroleum refineries to the ambient air quality: Part II. *Cogent Engineering* (2021), 8: 1947007 <https://doi.org/10.1080/23311916.2021.1947007>
- Tehrani, A. M., Bahrami, A., Leili, A., Poorolajal, J., Zafari, D., Samadi, M., and Mahri, A. (2020). Investigation of seasonal variation of probabilistic risk assessment of BTEX emission in municipal solid waste transfer station. *Int. Journal of Environmental and Analytical Chemistry*. <https://doi.org/10.1080/03067319.2020.1814269>
- Utser, J.T., Aho, M.I., Uungwa, S.T (2013). Lube Oil Recycling: Environmental and Economic Implication. *Energy, Science and Technology*, 6:73-78
- WHO (2000) Air Quality Guidelines for Europe (2<sup>nd</sup> Ed.) World Health Organization, Regional Office for Europe, Copenhagen, WHO Regional Publications, European Series, No. 91. 273 pp.
- World Bank (1999) Pollution Prevention and Abatement Handbook 1998: Toward Cleaner Production. The World Bank Group in Collaboration with the United Nations Environment Programme and the United Nations Industrial Development Organization. The World Bank Group, Washington DC., USA. 457 pp.



## Emission of Air Pollutants in the Paper Recycling Plants: Measurement Results from a Nigerian Major Paper Recycling Plant Production Floors

Funso A. AKEREDOLU<sup>1</sup>, Bamidele S. FAKINLE<sup>2\*</sup>, Ebenezer L. ODEKANLE<sup>3</sup> and Jacob A. SONIBARE<sup>1</sup>

<sup>1</sup>Department of Chemical Engineering, Obafemi Awolowo University, Ile-Ife, Nigeria

<sup>2</sup>Department of Chemical Engineering, Landmark University, Omu-Aran, Nigeria

<sup>3</sup>Department of Chemical and Mineral Resources Engineering, First Technical University, Ibadan Nigeria.

<sup>1</sup>[osnufy2k3@yahoo.co.uk](mailto:osnufy2k3@yahoo.co.uk), <sup>2\*</sup>[fakinle.bamidele@lmu.edu.ng](mailto:fakinle.bamidele@lmu.edu.ng), <sup>3</sup>[eodekanle@yahoo.com](mailto:eodekanle@yahoo.com), <sup>1</sup>[asonibar@yahoo.com](mailto:asonibar@yahoo.com)

\*Corresponding author

---

### ABSTRACT

To assess the contribution of paper recycling plants to atmospheric pollution load, meteorological parameters, and air emissions around paper recycling plant in Ikeja, Lagos, were measured during wet and dry season and, the results were compared with the permissible limits of the Federal Ministry of Environment (FMENV) and World Health Organization. The results indicated that the measured meteorological data were in agreement with the historical data of the study area. Furthermore, 24-hour extrapolated values of both gaseous air pollutants and particulate matters were within permissible limits, although wet season concentrations of the pollutants were lower than dry season concentrations. It was concluded that although, the air quality around the plant currently poses no threat to humans health, long exposure should be avoided.

**Keywords:** Air emission; anthropogenic activities; recycling; meteorological data.

### 1. INTRODUCTION

Historically, paper has been a medium of transmitting information and, its usage has continued to grow in recent decades due to the ever-growing rate of literacy and technological development. With paper, it is much easier to read, comprehend and identify errors in information than in electronic material. This advantage culminated in minimal reduction in the amount of paper production despite continuous advocate for paperless society. While air pollutants can exist naturally from volcanic eruption and wildfires, anthropogenic emissions from industrial activities, such as paper recycling process, produce great amount of toxic air pollutants (Ghosal et al., 2019). Globally, paper industry is considered as one of the major contributors to air and water pollution (Ono et al., 2020), possibly because its production and recycling processes are energy-consuming, which release several contaminants to the atmosphere (Giacosa et al., 2022). Air pollution from paper recycling plant is caused by the production of various sulphur-containing compounds and nitrogen oxides (Mandeep et al., 2019). Combustion of biomass/fuel during recycling process also emits particulate matters, gaseous pollutants and volatile organic compounds (VOCs) (Hoffman et al., 2017). Although several studies have reported impacts of paper recycling plant wastewater effluents on the environment (McMater et al., 2006; Adesida, 2020), there have been paucity of reported information on the contribution of paper recycling plant to air quality (Tong et al., 2018). This study therefore focused on the measurement of emission of air pollutants around paper recycling plant in order to ascertain the level of agreement with the permissible limits.

### 2. MATERIALS AND METHODS

#### 2.1 Study Area

A Paper recycling plant located in Ikeja, Lagos was used for this study. The company which was established in 1986, recycles waste paper such as old books, office paper and newspapers, most of which is converted into a large array of tissue paper products utilizing state of the art European machinery. These products include toilet, facial, pocket handkerchiefs, table napkins and kitchen towels.

#### 2.2 Sampling equipment

The various sampling equipment used for the study included Weather Tracker Kestrel 4500, GT-321 Particle Counter, ToxiRAE gas monitors, and MultiRAE gas. Weather Tracker Kestrel 4500 was used for the measurement of meteorological parameters. Levels of particulate matter (PM) were determined with the aid of GT-321 Particle Counter/Dust Monitor from Met One Instruments. NO<sub>2</sub>, SO<sub>2</sub>, CO, NH<sub>3</sub> and H<sub>2</sub>S/VOCs concentrations were measured using an *insitu* single gas NO<sub>x</sub> monitor (ToxiRAE Model PGM-1110); *insitu* single gas SO<sub>2</sub> monitor (ToxiRAE Model

PGM-1130); *insitu* non-integrated single gas CO monitor (ToxiRAE Model PGM-1150); *in situ* non-integrated single NH<sub>3</sub> monitor (ToxiRAE Model PGM-1150) and an *insitu* MultiRAE gas monitor (Model PGM50-5P), respectively.

## 2.2 Sampling Procedures

Measurements were done in eighteen different sampling stations in the production floors and the general company premises, as shown in Table 1. The parameters monitored were meteorological parameters: wind speed and direction, ambient air temperature, pressure and relative humidity; gaseous pollutants concentration: CO, NO<sub>2</sub>, SO<sub>2</sub>, H<sub>2</sub>S and VOCs; particulate matter concentrations: PM<sub>1</sub>, PM<sub>2.5</sub>, PM<sub>7</sub>, PM<sub>10</sub> and TSP. To measure, the air pollutants; monitors were placed at 1 m above the ground level, switched on in the environment of interest and the measured concentration read directly on the screen after particle capturing. For all the gaseous and particulates level measurements, a sampling period of 15 minutes was used.

Table 1: Sampling Locations for Meteorology, Air Quality and Noise

S/No	Sampling Location	Designation	Coordinates
1.	S1	Car Park in front of Admin Block	Latitude: 6° 37' 40.89 "N Longitude: 3° 21' 13.29 "E
2.	S2	Old Waste Paper Store (Bailing Section)	Indoor
3.	S3	Old Waste Paper Store (Sorting Section)	Indoor
4.	S4	Around the Pulping Section	Latitude: 6° 37' 44.59 "N Longitude: 3° 21' 13.31 "E
5.	S5	Proposed Expanded Site – NW Flank	Latitude: 6° 37' 46.63 "N Longitude: 3° 21' 12.36 "E
6.	S6	Proposed Expanded Site – NE Flank	Latitude: 6° 37' 47.49 "N Longitude: 3° 21' 13.90 "E
7.	S7	Proposed Expanded Site – SE Flank	Latitude: 6° 37' 43.84 "N Longitude: 3° 21' 14.97 "E
8.	S8	Proposed Expanded Site – Centre	Latitude: 6° 37' 45.53 "N Longitude: 3° 21' 14.11 "E
9.	S9	Existing Pulping Section	Indoor
10.	S10	Around the Pulping Machine	Indoor
11.	S11	Rewinder Machine	Indoor
12.	S12	Conversion Section	Indoor
13.	S13	Proposed Finished Good Store (Presently Conversion Section)	Indoor
14.	S14	Existing Boiler Room	Indoor
15.	S15	Existing Generator House	Indoor
16.	S16	Proposed Gate House by Wemco	Latitude: 6° 37' 48.77 "N Longitude: 3° 21' 08.34 "E
17.	S17	Proposed Warehouse	Latitude: 6° 37' 46.72 "N Longitude: 3° 21' 10.90 "E
18.	S18	Main Gate House	Latitude: 6° 37' 42.06 "N

Comparison of the measured ambient air quality parameters with the National Ambient Air Quality Standards (NAAQS) of Nigeria and that of the Air Quality Standards of the World Bank (Table 2) was also made.

Table 2: 24 -Hour Standards of Ambient Air Quality

Contaminant	Concentrations (ppm)	
	FMENV (FEPA, 1991)	World Bank (1999)
CO	10	
NO <sub>x</sub>	0.04 – 0.06	0.08
SO <sub>2</sub>	0.01	
PM <sub>10</sub>		80 µg/m <sup>3</sup>
TSP	250 µg/m <sup>3</sup>	80 µg/m <sup>3</sup>

### 3.0 RESULTS AND DISCUSSION

#### 3.1 Meteorological Parameters

The meteorology of the area is best discussed using long-term data measurements of Ikeja as obtained from the Nigeria Meteorological Agency (NIMET, 2011). Generally, Nigeria’s climate is characterized by the hot and wet conditions associated with the movement of the Inter-Tropical Convergence Zone (ITCZ) north and south of the equator. This Inter-Tropical Convergence Zone (ITCZ) appears as a band of clouds, usually thunderstorms that circle the globe near the equator; Nigeria is located just north of the equator. When the ITCZ is to the south of the equator, the north-east winds prevail producing the dry-season condition and whenever it moves into the Northern Hemisphere, the south westerly wind prevails to bring rainfall and the rainy (wet) season thus giving the proposed project area both the dry and wet seasons. For rainfall /relative humidity, the measured relative humidity of 61.3 – 70.7% and a mean of 65.8% obtained in the study (Figure 1) agreed with the historical data (NIMET, 2011). Ambient temperatures are generally high in the proposed project site with monthly minimum and maximum range of 20.0 – 24.7°C and 26.0 – 34.9°C respectively (Figure 2) which is usually attributed to the latitudinal location of the region within the tropics.

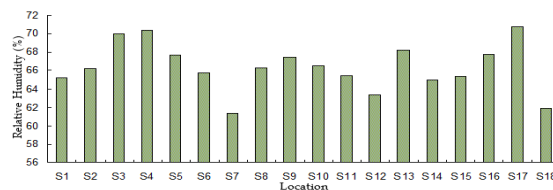


Figure 1: Measured Relative Humidity in the Study Area during Fieldwork

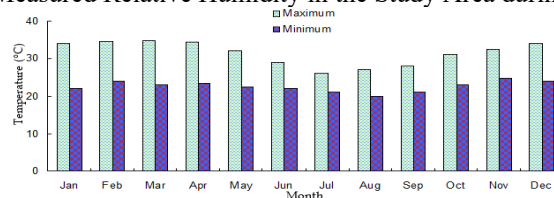


Figure 2: Monthly Air Temperature Distribution in the Study Area (NIMET, 2011)

The highest maximum temperature occurs in the months of February and March, the peak of the dry season, while the lowest is in the month of July at the peak of the wet season. Measured air temperatures in the area during the field work (29.9 – 34.5 °C) agree with the historical data (Figure 3).

The available data on surface wind distribution in the proposed project area shows a wind speed in the range of 2.0 – 3.1 m/s with the maximum in July - August (Figure 4) which are respectively the peaks of the rainy season. The prevailing wind directions as obtained from the historical data are the South-west and North-east (Figure 5) which agree with the observed wind characteristics during the field study (Table 3). There is some occasional calmness with insignificant wind speed in the area.

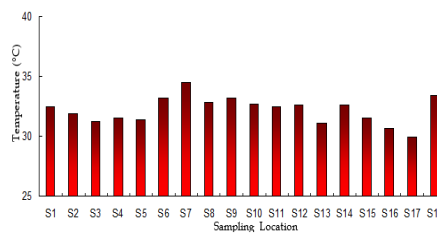


Figure 3: Measured Ambient Air Temperature in the Study Area

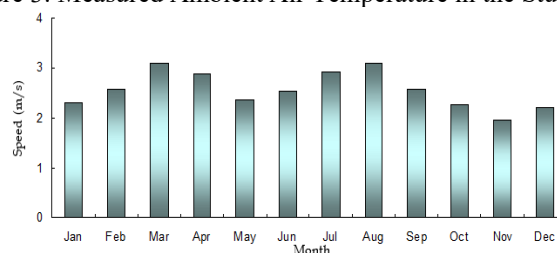


Figure 4: Mean Monthly Wind Speed Distribution in the Study Area (NIMET, 2011).

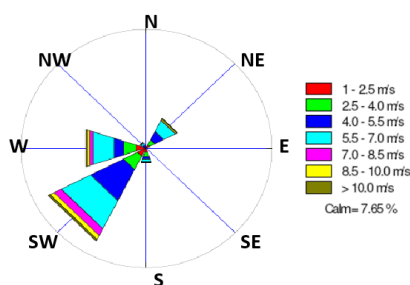


Figure 5: Wind Direction in the Area, 2000 – 2010 (Source: NIMET, 2011)

Table 3: Measured Wind Speed and Prevailing Direction of the Study Area

Sampling Location	Northeast Wind	Southwest Wind	Sampling Location	Northeast Wind	Southwest Wind
S1	0.5	0.8	S10	Calm	Calm
S2	0.4	0.4	S11	Calm	Calm
S3	Calm	Calm	S12	Calm	Calm
S4	0.8	0.3	S13	0.3	0.3
S5	1.8	1.3	S14	1.2	1.2
S6	0.8	1.9	S15	0.3	0.3
S7	2.1	0.8	S16	1.0	1.6
S8	1.0	1.0	S17	1.5	1.5
S9	Calm	Calm	S18	1.3	0.8

The mean surface wind speed and direction depends on the seasonal variation which also follows the migratory ITCZ with two main air masses alternate with the season. The northeast wind direction predominates during the dry season while the Southwest winds are dominant during the wet season.

### 3.2 Air Quality

Average measured gaseous concentrations are as summarized in Table 4. SO<sub>2</sub>, NO<sub>2</sub>, NO and H<sub>2</sub>S were not detected in any of the eighteen sampling locations in the wet season while NO was not detected in the dry season. In the locations where detected in the wet season (Main Gate House, S18), NO and NH<sub>3</sub> were 1.0 ppm while CO concentrations ranged from 1.0 to 6.0 ppm with an average of 2.2 ppm and VOCs were 0.1 – 0.3 ppm with average of 0.1 ppm where detected. However in the dry season, CO was 1 – 3 ppm with an average of 2 ppm, NH<sub>3</sub> and VOCS were 1 ppm and 0.1 ppm in the only locations where detected (Conversion Section). Also in the wet season, CO was detected in all the sampling locations except Around the Pulping Section (S4), Around the Pulping Machine (S10), the Proposed Finished Good Store, Presently Conversion Section (S13), and the Proposed Warehouse (S17) but in the dry season, it was detected in all except in the Proposed Gate House (S16). Volatile organic compounds were detected in five of the sampling locations in the wet season including the Car Park in front of Admin Block (S1), the Old Waste Paper Store - Bailing Section (S2), the Old Waste Paper Store - Sorting Section (S3), the Proposed Expanded Site – NW Flank (S5) and the Existing Generator House (S15) but in the dry season, it was detected in the Existing Boiler Room only.

When extrapolated to 24-hour concentrations (Table 5), the measured NO and NH<sub>3</sub> in factory premises in the only locations where detected were 0.4 ppm with CO and VOCs being 0.4 – 2.3 ppm and 0.1 ppm respectively, in the wet season but in the dry season, CO was 0.4 – 1.2 ppm with an average of 0.7 ppm, NH<sub>3</sub> and VOCS were 0.4 ppm and <0.1 ppm in the only locations where detected. With the ambient concentrations of SO<sub>2</sub>, NO<sub>2</sub>, and H<sub>2</sub>S being below the detection limits of the measuring instruments during the wet season and SO<sub>2</sub>, NO<sub>2</sub>, H<sub>2</sub>S and NO<sub>2</sub> being below these limits in the dry season, it is safe to conclude that their concentrations are within the recommended limits.

This implies that SO<sub>2</sub> in the environment is within the 0.01 ppm recommended limit of the Federal Ministry of Environment (FMENV) and NO/NO<sub>2</sub> is within the 0.04 – 0.06 ppm, the set limits. Nigeria has no limit for H<sub>2</sub>S in the ambient environment at present. Both the measured CO levels in the proposed project expansion site and its 24-hour extrapolated concentrations were within the 10 ppm limit of the Federal Ministry of Environment both in the wet and dry seasons. The three major forms of VOCs of environmental concern as mentioned earlier are benzene, toluene and xylene (BTX). If the measured VOCs were benzene, its long-term limit of 1.5 ppm was not exceeded in any of the sampling locations where detected in the two seasons. Also if they were toluene, its long-term limit of 0.6 ppm was not exceeded in any of the sampling locations by both the measured and the 24-hour extrapolated VOCs concentrations obtained in the factory in the two seasons.

Emission of Air Pollutants in the Paper Recycling Plants: Measurement Results from a Nigerian Major Paper Recycling Plant Production Floors

Table 4: Measured Gaseous Concentrations the Factory

Sampling Locations	Concentrations (ppm)													
	SO <sub>2</sub>		NO		NO <sub>2</sub>		CO		NH <sub>3</sub>		H <sub>2</sub> S		VOCs	
	Wet Seas on	Dry Seas on	Wet Seas on	Dry Seas on	Wet Seas on	Dry Seas on	Wet Seas on	Dry Seas on	Wet Seas on	Dry Seas on	Wet Seas on	Dry Seas on	Wet Seas on	Dry Seas on
S1	<0.1	<0.1	<1.0	<1.0	<0.1	<0.1	5	1	<1.0	<1.0	<0.1	<0.1	0.1	<0.1
S2	<0.1	<0.1	<1.0	<1.0	<0.1	<0.1	1	1	<1.0	<1.0	<0.1	<0.1	0.1	<0.1
S3	<0.1	<0.1	<1.0	<1.0	<0.1	<0.1	1	1	<1.0	<1.0	<0.1	<0.1	0.1	<0.1
S4	<0.1	<0.1	<1.0	<1.0	<0.1	<0.1	<1.0	3	<1.0	<1.0	<0.1	<0.1	<0.1	<0.1
S5	<0.1	<0.1	<1.0	<1.0	<0.1	<0.1	1	3	<1.0	<1.0	<0.1	<0.1	0.1	<0.1
S6	<0.1	<0.1	<1.0	<1.0	<0.1	<0.1	3	3	<1.0	<1.0	<0.1	<0.1	<0.1	<0.1
S7	<0.1	<0.1	<1.0	<1.0	<0.1	<0.1	6	1	<1.0	<1.0	<0.1	<0.1	<0.1	<0.1
S8	<0.1	<0.1	<1.0	<1.0	<0.1	<0.1	2	3	<1.0	<1.0	<0.1	<0.1	<0.1	<0.1
S9	<0.1	<0.1	<1.0	<1.0	<0.1	<0.1	1	1	<1.0	<1.0	<0.1	<0.1	<0.1	<0.1
S10	<0.1	<0.1	<1.0	<1.0	<0.1	<0.1	<1.0	1	<1.0	<1.0	<0.1	<0.1	<0.1	<0.1
S11	<0.1	<0.1	<1.0	<1.0	<0.1	<0.1	1	1	<1.0	<1.0	<0.1	<0.1	<0.1	<0.1
S12	<0.1	<0.1	<1.0	<1.0	<0.1	<0.1	1	1	<1.0	1	<0.1	<0.1	<0.1	<0.1
S13	<0.1	<0.1	<1.0	<1.0	<0.1	<0.1	<1.0	1	<1.0	<1.0	<0.1	<0.1	<0.1	<0.1
S14	<0.1	<0.1	<1.0	<1.0	<0.1	<0.1	1	3	<1.0	<1.0	<0.1	<0.1	<0.1	0.1
S15	<0.1	<0.1	<1.0	<1.0	<0.1	<0.1	2	3	<1.0	<1.0	<0.1	<0.1	0.3	<0.1
S16	<0.1	<0.1	<1.0	<1.0	<0.1	<0.1	1	<1.0	<1.0	<1.0	<0.1	<0.1	<0.1	<0.1
S17	<0.1	<0.1	<1.0	<1.0	<0.1	<0.1	<1.0	1	<1.0	<1.0	<0.1	<0.1	<0.1	<0.1
S18	<0.1	<0.1	1.0	<1.0	<0.1	<0.1	5	3	1.0	<1.0	<0.1	<0.1	<0.1	<0.1

Generally, the relative lower concentrations of air pollutants in the wet season than the dry season could be attributed to the rain “washout” that usually characterises the wet season in which air pollutants are removed from the atmosphere by rainfall.

Table 5: Extrapolated Gaseous Concentrations within the Factory

Sampling Locations	Concentrations (ppm)													
	SO <sub>2</sub>		NO		NO <sub>2</sub>		CO		NH <sub>3</sub>		H <sub>2</sub> S		VO Cs	
	Wet Seas on	Dry Seas on	Wet Seas on	Dry Seas on	Wet Seas on	Dry Seas on	Wet Seas on	Dry Seas on	Wet Seas on	Dry Seas on	Wet Seas on	Dry Seas on	Wet Seas on	Dry Seas on
S1	<0.1	<0.1	<1.0	<1.0	<0.1	<0.1	1.9	0.4	<1.0	<1.0	<0.1	<0.1	<0.1	<0.1
S2	<0.1	<0.1	<1.0	<1.0	<0.1	<0.1	0.4	0.4	<1.0	<1.0	<0.1	<0.1	<0.1	<0.1
S3	<0.1	<0.1	<1.0	<1.0	<0.1	<0.1	0.4	0.4	<1.0	<1.0	<0.1	<0.1	<0.1	<0.1
S4	<0.1	<0.1	<1.0	<1.0	<0.1	<0.1	<1.0	1.2	<1.0	<1.0	<0.1	<0.1	<0.1	<0.1
S5	<0.1	<0.1	<1.0	<1.0	<0.1	<0.1	0.4	1.2	<1.0	<1.0	<0.1	<0.1	<0.1	<0.1
S6	<0.1	<0.1	<1.0	<1.0	<0.1	<0.1	1.2	1.2	<1.0	<1.0	<0.1	<0.1	<0.1	<0.1
S7	<0.1	<0.1	<1.0	<1.0	<0.1	<0.1	2.3	0.4	<1.0	<1.0	<0.1	<0.1	<0.1	<0.1
S8	<0.1	<0.1	<1.0	<1.0	<0.1	<0.1	0.8	1.2	<1.0	<1.0	<0.1	<0.1	<0.1	<0.1
S9	<0.1	<0.1	<1.0	<1.0	<0.1	<0.1	0.4	0.4	<1.0	<1.0	<0.1	<0.1	<0.1	<0.1
S10	<0.1	<0.1	<1.0	<1.0	<0.1	<0.1	<1.0	0.4	<1.0	<1.0	<0.1	<0.1	<0.1	<0.1
S11	<0.1	<0.1	<1.0	<1.0	<0.1	<0.1	0.4	0.4	<1.0	<1.0	<0.1	<0.1	<0.1	<0.1
S12	<0.1	<0.1	<1.0	<1.0	<0.1	<0.1	0.4	0.4	<1.0	0.4	<0.1	<0.1	<0.1	<0.1
S13	<0.1	<0.1	<1.0	<1.0	<0.1	<0.1	<1.0	0.4	<1.0	<1.0	<0.1	<0.1	<0.1	<0.1
S14	<0.1	<0.1	<1.0	<1.0	<0.1	<0.1	0.4	1.2	<1.0	<1.0	<0.1	<0.1	<0.1	<0.1
S15	<0.1	<0.1	<1.0	<1.0	<0.1	<0.1	0.8	1.2	<1.0	<1.0	<0.1	<0.1	0.1	<0.1
S16	<0.1	<0.1	<1.0	<1.0	<0.1	<0.1	0.4	<1.0	<1.0	<1.0	<0.1	<0.1	<0.1	<0.1
S17	<0.1	<0.1	<1.0	<1.0	<0.1	<0.1	<1.0	0.4	<1.0	<1.0	<0.1	<0.1	<0.1	<0.1
S18	<0.1	<0.1	0.4	<1.0	<0.1	<0.1	1.9	1.2	0.4	<1.0	<0.1	<0.1	<0.1	<0.1

Table 6: Measured and 24-Hour Extrapolated Particulate Concentrations

Sampling Locations	Concentrations ( $\mu\text{g}/\text{m}^3$ )									
	PM <sub>1</sub>		PM <sub>2.5</sub>		PM <sub>7</sub>		PM <sub>10</sub>		TSP	
	Wet Season	Dry Season	Wet Season	Dry Season	Wet Season	Dry Season	Wet Season	Dry Season	Wet Season	Dry Season
<b>Measured Particulate Concentrations</b>										
S1	4.6	5.1	14.1	15.6	18.7	45.3	18.7	35.4	18.7	24.4
S2	1.7	4.3	4.8	11.7	7.6	17.6	7.7	28.9	7.7	42.1
S3	1.7	3.4	4.7	11.2	7.1	23.3	7.1	33.6	7.1	35.4
S4	1.2	3.4	3.3	13.4	5.1	25.4	5.1	28.7	5.1	29.6
S5	2.2	5.4	6.1	16.5	9.1	25.6	9.1	32.2	9.1	41.3
S6	1.1	4.0	3.1	16.6	6.2	27.5	6.2	18.7	6.2	27.6
S7	1.6	4.5	4.5	14.3	7.5	17.5	7.5	23.5	7.5	25.4
S8	1.7	4.5	4.6	12.7	7.0	18.5	7.0	31.2	7.0	41.2
S9	1.3	2.3	3.6	12.4	5.7	16.7	5.7	27.6	5.7	29.8
S10	1.4	4.2	3.9	14.3	5.4	21.3	5.4	28.8	5.4	31.1
S11	1.2	3.4	3.3	13.2	5.0	27.9	5.1	19.7	5.1	29.9
S12	0.8	2.3	2.4	12.3	3.9	23.2	3.9	16.7	3.9	31.9
S13	1.7	4.5	4.8	14.8	6.6	34.7	6.6	17.9	6.6	20.6
S14	1.4	5.4	4.0	11.4	5.9	35.7	5.9	29.4	5.9	33.3
S15	0.9	4.3	2.5	11.9	4.5	23.7	4.5	41.2	4.5	45.4
S16	1.2	3.4	3.5	12.2	5.3	34.3	5.3	13.3	5.3	21.1
S17	1.4	5.3	4.0	13.3	6.1	36.4	6.1	17.2	6.1	27.7
S18	0.9	4.5	2.7	13.2	4.4	29.8	4.4	36.2	4.4	39.9
<b>24-Hour Extrapolated Particulate Concentrations</b>										
S1	1.8	2.0	5.4	6.0	7.2	17.4	7.2	13.6	7.2	9.4
S2	0.7	1.6	1.8	4.5	2.9	6.7	3.0	11.1	3.0	16.1
S3	0.7	1.3	1.8	4.3	2.7	8.9	2.7	12.9	2.7	13.6
S4	0.5	1.3	1.3	5.1	2.0	9.7	2.0	11.0	2.0	11.4
S5	0.8	2.1	2.3	6.3	3.5	9.8	3.5	12.3	3.5	15.8
S6	0.4	1.5	1.2	6.4	2.4	10.5	2.4	7.2	2.4	10.6
S7	0.6	1.7	1.7	5.5	2.9	6.7	2.9	9.0	2.9	9.7
S8	0.7	1.7	1.8	4.9	2.7	7.1	2.7	12.0	2.7	15.8
S9	0.5	0.9	1.4	4.8	2.2	6.4	2.2	10.6	2.2	11.4
S10	0.5	1.6	1.5	5.5	2.1	8.2	2.1	11.0	2.1	11.9
S11	0.5	1.3	1.3	5.1	1.9	10.7	2.0	7.6	2.0	11.5
S12	0.3	0.9	0.9	4.7	1.5	8.9	1.5	6.4	1.5	12.2
S13	0.7	1.7	1.8	5.7	2.5	13.3	2.5	6.9	2.5	7.9
S14	0.5	2.1	1.5	4.4	2.3	13.7	2.3	11.3	2.3	12.8
S15	0.3	1.6	1.0	4.6	1.7	9.1	1.7	15.8	1.7	17.4
S16	0.5	1.3	1.3	4.7	2.0	13.2	2.0	5.1	2.0	8.1
S17	0.5	2.0	1.5	5.1	2.3	14.0	2.3	6.6	2.3	10.6
S18	0.3	1.7	1.0	5.1	1.7	11.4	1.7	13.9	1.7	15.3

Similarly, if xylene, the long-term limit of 0.7 ppm was not exceeded in all these locations. Both the WHO guideline of 6.3 ppm and the FMENV limit of 1.9 ppm for VOCs were not breached in any of these locations were detected in the two seasons.

Particulates were detected in all the sampling locations within the factory. In the wet season, these were of the range 0.8 – 4.6  $\mu\text{g}/\text{m}^3$ , 2.4 – 14.1  $\mu\text{g}/\text{m}^3$ , 3.9 – 18.7  $\mu\text{g}/\text{m}^3$ , 3.9 – 18.7  $\mu\text{g}/\text{m}^3$ , and 3.9 – 18.7  $\mu\text{g}/\text{m}^3$  for PM<sub>1</sub>, PM<sub>2.5</sub>, PM<sub>7</sub>, PM<sub>10</sub> and TSP respectively. But in the dry season, they were 2.3 – 5.4  $\mu\text{g}/\text{m}^3$ , 11.2 – 16.6  $\mu\text{g}/\text{m}^3$ , 16.7 – 45.3  $\mu\text{g}/\text{m}^3$ , 13.3 – 41.2  $\mu\text{g}/\text{m}^3$ , and 20.6 – 45.5  $\mu\text{g}/\text{m}^3$  for PM<sub>1</sub>, PM<sub>2.5</sub>, PM<sub>7</sub>, PM<sub>10</sub> and TSP, respectively. Both the measured and extrapolated concentrations of particulate matters are presented in Table 6. The measured concentrations now ranged 0.3 – 1.8  $\mu\text{g}/\text{m}^3$ , 0.9 – 5.4  $\mu\text{g}/\text{m}^3$ , 1.5 – 7.2  $\mu\text{g}/\text{m}^3$ , 1.5 – 7.2  $\mu\text{g}/\text{m}^3$ , and 1.5 – 7.2  $\mu\text{g}/\text{m}^3$  for PM<sub>1</sub>, PM<sub>2.5</sub>, PM<sub>7</sub>, PM<sub>10</sub>, and TSP respectively

## Emission of Air Pollutants in the Paper Recycling Plants: Measurement Results from a Nigerian Major Paper Recycling Plant Production Floors

in the wet season and 0.9 – 2.1  $\mu\text{g}/\text{m}^3$ , 4.3 – 6.4  $\mu\text{g}/\text{m}^3$ , 6.4 – 17.4  $\mu\text{g}/\text{m}^3$ , 5.1 – 15.8  $\mu\text{g}/\text{m}^3$ , and 7.9 – 17.4  $\mu\text{g}/\text{m}^3$  for the respective  $\text{PM}_{10}$ ,  $\text{PM}_{2.5}$ ,  $\text{PM}_7$ ,  $\text{PM}_{10}$  and TSP in the dry season.

These 24-hours extrapolated concentrations of  $\text{PM}_{10}$  are about 1.9 – 9.0% and 6.4 – 19.7% of the World Bank's limit of 80  $\mu\text{g}/\text{m}^3$  in the wet and dry seasons respectively while the TSP levels are 0.6 – 2.9 % and 3.2 – 7.0% of the Federal Ministry of Environment's limit of 250  $\mu\text{g}/\text{m}^3$  in the wet and dry seasons respectively in all the sampling locations.

### 4.0 CONCLUSION

Air quality within and around the premises of paper recycling plant in Ikeja, Lagos, was investigated to ascertain level of compliance of the company to emission permissible limits of environmental regulatory bodies. In 18 locations within and around the plant, microclimatic and air quality parameters as well as noise levels were measured accordingly and the results compared with the permissible limits. The results showed that the measured meteorological parameters were in agreement with historical weather condition of the factory area. The concentrations of air pollutants obtained in this study were within the permissible limit. Relatively lower concentrations of air pollutants were obtained during wet season than dry season. This could be attributed to 'wash out' effect during rainy season when pollutants are removed from the atmosphere by rainfall. It can be concluded therefore that, although emission around the recycling plant is within permissible limit and the air quality is considered safe, effort should always be made to ensure avoidance of long exposure to air pollutants, especially individuals with existing health issues.

### REFERENCES

- Adesida, A.A. (2020). Concurrent removal of organic and heavy metal contaminants in wastewater: A case study on a Pulp Mill effluents and leachate; *Dalhousie University: Halifax, NS, Canada*
- Berglund, B., Lindvall, T., and Schwela, D (1999) Guidelines for Community Noise. World Health Organization (WHO), Geneva. pp. 141
- FEPA. (1991). Guidelines to Standards for Environmental Pollution Control in Nigeria. Federal Environmental Protection Agency (FEPA), Lagos.
- Ghosal, V., Stephan, A., Weiss, J.F. (2019). Decentralized Environmental regulations and plant-level productivity. *Bus. Strateg. Environ.*, 29:998-1011.
- Giacosa, G., Barnett, C., Rianham, D.G. and Walker, T.R. (2022). Characterization of Annual Air Emission Reported by Pulp and Paper Mill in Atlantic Canada. *Pollutants*, 2:135-155
- Hoffman, E., Guernsey, J.R., Walker, T.R., Kim, J.S., Sherren, K., Andreou, P. (2017). Pilot study of investigating ambient air toxic emissions near a Canadian Kraft pulp and paper facility in Pictou County, Nova Scotia. *Environ. Sci. Pollution Research*, 24:20685-20698
- Mandeep, G.G.K., Liu, H., Shukla, P. (2019). Pulp and Paper industry-based pollutants, their health hazard and environmental risks. *Curr. Opin. Environ. Sci. Health*, 12:48-56
- McMaster, M.E., Hewitt, L.M., Parrott, J.L. (2006). A decade of research on environmental impacts of pulp and paper mill effluents in Canada: Field studies and Mechanistic Research. *J. Toxicol. Environ. Health-Part B. Crit. Rev.*, 9:319-339
- NIMET-Nigerian Meteorological Agency (2011). Nigerian Climate Review Bulletin 40p
- Ono, Y., Hayashi, M., Yokoyama, K., Okamura, T and Itsubo, N. (2020). Environmental Assessment of Innovative Paper Recycling Technology Using Product Lifecycle Perspectives. *Resources*, 2020,9: 23
- Tong, X., Shen, W., Chen, X., Corriou, J.P. (2018). Qualitative and Quantitative Analysis of Gaseous Pollutants for Cleaner Production in Pulp and Paper Mill. *J. Cleaner Prod*, 198: 1066-1075
- WHO (2000) Air Quality Guidelines for Europe (2<sup>nd</sup> Ed.) World Health Organization, Regional Office for Europe, Copenhagen, WHO Regional Publications, European Series, No. 91. 273 pp.
- World Bank (1999) Pollution Prevention and Abatement Handbook 1998: Toward Cleaner Production. The World Bank Group in Collaboration with the United Nations Environment Programme and the United Nations Industrial Development Organization. The World Bank Group, Washington DC., USA. 457 pp.





## Elemental Characterization of Pollutants Emanated from Combustion of Selected Agricultural Remnants

Temilade, T. ADEBISI<sup>1</sup>, Adejoke O. ALAMU<sup>2</sup>, Sunday A. ADEBANJO<sup>3</sup>, Olusesan A. OLU-AROTIOWA<sup>2</sup>, Kazeem K. SALAM<sup>2</sup>, Lukuman, A. JIMODA<sup>2</sup> and Abass O. ALADE,<sup>2\*</sup>

<sup>1</sup> Department of Science Laboratory Technology, Oyo State College of Agriculture and Technology, Igboora, Oyo State, Nigeria.

<sup>2</sup> Department of Chemical Engineering, Ladoké Akintola University of Technology, Ogbomosho, Oyo State, Nigeria.

<sup>3</sup> Chemical Engineering Department, Lagos State University, Epe Campus

\*Corresponding author: [aoalade@lautech.edu.ng](mailto:aoalade@lautech.edu.ng)

### ABSTRACT

Trace metals pose challenges to humanity especially when recommended limit is exceeded. This study considered agricultural remnants: Coconut Husk (CH), Groundnut Shell (GS) and Empty Palm Kernel Fruit Bunch (EPKFB) which were subjected to controlled combustion in a laboratory-scale combustion chamber. The concentration ( $\mu\text{g}/\text{m}^3$ ) range of heavy metals (K, Ca, Sc, Ti, V, Cr, Mn, Fe, Co, Ni, Cu, Zn, Ga, Ge, As, Se, Br, Kr and Rb) analyzed from TSP trapped filters were 0.47 - 464.31; 0.75 - 548.53 and 0.26 - 306.64, that from  $\text{PM}_{0.8}$  filters were 0.008 - 89.93; 0.076 - 89.021 and 0.083 - 75.34 while 0.083 - 82.40; 0.04 - 77.94 and 0.061 - 59.88 were obtained from 0.4  $\mu\text{m}$  size particles. In exemption of heavy metals analyzed on TSP trapped from GS emission, the concentration of K emitted from all the crop residues burnt significantly preceded others while Ga and Ge mostly have the least emission values. Although there were variations in all the experimental runs, it was discovered that CH emitted a larger elemental concentration compared to other crop wastes. Also, elemental concentrations increase with increasing particle size.

**Keywords:** Coconut Husk, Combustion, Empty Palm Kernel Fruit Bunch, Emission Groundnut Shell

### 1. INTRODUCTION

Open burning of biomass emits large amounts of pollutants (gases and particles) into the ambient air (Booth, 2012; Zhang *et al.* 2012). Studies have highlighted that these pollutants are among the main and the chief partaker of insecure air quality prediction and climatic change (Byun and Shere, 2006; Jain *et al.* 2014; Xiao *et al.* 2015; Andini *et al.* 2018; Zhang *et al.* 2018). Pollutants strongly influence many atmospheric processes among which the environmental effects include changes in visibility, solar radiation transfer (related to global warming), cloud formation, and acidification of clouds, rain and fog (Sahu *et al.*, 2011; Satsangi, *et al.*, 2014) which in turn poses serious health degradation to living organisms. However, atmospheric quality is a serious concern especially today when the consequences of human interventions are already evident.

Uncontrolled dispersion of open burning of biomass wastes emissions into the atmospheric air has also been recognized as a significant source of active trace species leading to atmospheric degradation, and change in the climatic system Zhang *et al.* (2012) and poses a serious threat to human's health and the environment (Kim *et al.* 2015). The International Agency for Research on Cancer (IARC) has listed many of these air pollutants among the cancer-causing pollutants (Vreeland *et al.* 2016). This study, therefore, characterized elemental pollutants that emanated from burning off some selected agricultural remnants.

### 2. MATERIALS AND METHODS

#### Materials/Reagents and Equipment

The filter papers that can retain particulate matter of aerodynamic diameter  $\leq 0.4$  ( $\text{PM}_{0.4}$ ), particulate matter of aerodynamic diameter  $\leq 0.8$  ( $\text{PM}_{0.8}$ ) and total suspended particulate matter (TSP) were kept in a desiccator for two hours, weighed and then wrapped in an aluminum foil, before use, as adopted by Anf and Emad (2014).

Three different crop residues: Coconut Husk (CH), Groundnut Shell (GS) and Empty Palm Kernel Fruit Bunch (EPKFB) procured from a farm in Igboora, Ibarapa Central Local Government Area of Oyo State were dried until a constant weight was attained and kept for further experimental use. The crop remnants of 100 g each were burnt using a laboratory-scale combustion chamber having cylindrical parts (0.175 m internal diameter and 0.225 m height) with a bottom side vent and a mounted 0.15 m height detachable inverted funnel-like part. Sequentially arranged in the

chamber filter holders to allow the deposition of varying PM emitted from the crop wastes burning process were filter papers that can withhold the TSP size of particles and two other filters of different aerodynamic diameters less than 0.8  $\mu\text{m}$  and 0.4  $\mu\text{m}$ . The emissions from the burning were directed by a one-stage vacuum pump of model VE115N having 2.0 CFM, 230 V/ 50-60 Hz. The process was halted after 20 mins of sampling and the PM-deposited filters were kept in a zip-lock bag for analysis.

Elemental compositions of PM trapped filter samples were performed using Energy Dispersive X-ray Fluorescence (EDXRF) Spectrometer brand name, Eclipse III supplied by AMTEK INC., U.S.A. having model XR-100CR high-performance X-ray detector system with a preamplifier and a thermoelectrically cooled Si-PIN photodiode at Obafemi Awolowo University (O.A.U), Ile Ife, Osun State, Nigeria.

### 3. RESULTS AND DISCUSSION

The concentration ( $\mu\text{g}/\text{m}^3$ ) of heavy metals obtained from the TSP-trapped filter for CH burning was as presented in Figure 1. K had the highest concentration of 464.31  $\mu\text{g}/\text{m}^3$  followed by Ca (396.43  $\mu\text{g}/\text{m}^3$ ), Ti (122.77  $\mu\text{g}/\text{m}^3$ ) and Zn (105.96  $\mu\text{g}/\text{m}^3$ ) while Se was characterized by the lowest concentration of 0.47  $\mu\text{g}/\text{m}^3$ .

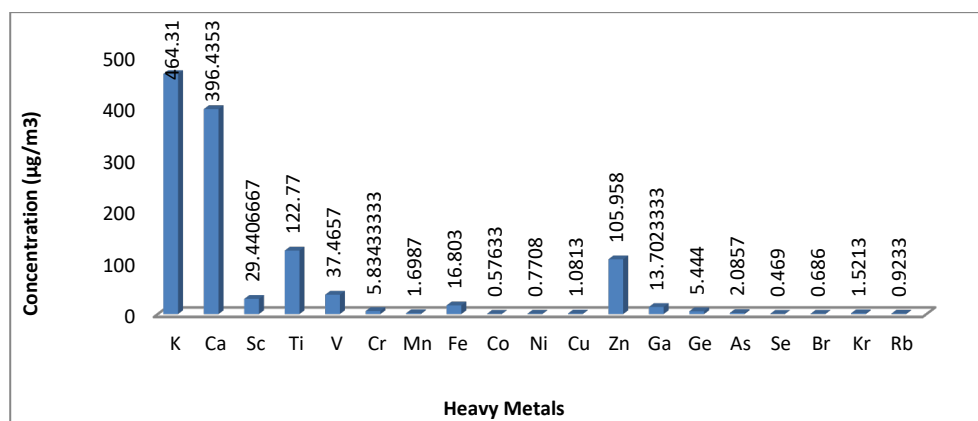


Figure 1: Elemental Compositions of TSP Emitted from Combustion of CH

However, Figure 2 described the analyzed elements in TSP collected from GS combustion. The range of the metals differs a bit from that of CH and EPKFB with the highest concentration observed in Ca (548.53  $\mu\text{g}/\text{m}^3$ ) emission, K (142.64  $\mu\text{g}/\text{m}^3$ ), Ti (28.182  $\mu\text{g}/\text{m}^3$ ) and Zn (26.59  $\mu\text{g}/\text{m}^3$ ) while Co (0.15) had the least emission value. Similarly, heavy metals characterized by trapped TSP emissions from EPKFB as depicted in Fig. 3 followed almost the same trend as that of CH emissions as K, Ca, Ti and Zn led the trend with the highest concentration. in descending order of 306.64  $\mu\text{g}/\text{m}^3 > 234.86 \mu\text{g}/\text{m}^3 > 63.76 \mu\text{g}/\text{m}^3 > 32.24 \mu\text{g}/\text{m}^3$ . The least concentration value was observed in Ga emission (0.26  $\mu\text{g}/\text{m}^3$ ) which was in contrast to the lowest metal emission (Se - 0.47  $\mu\text{g}/\text{m}^3$ ) from CH. The average heavy metal concentrations emitted from EPKFB were a bit lower than that emitted from CH and GS. The order of concentration is as follows: K > Ca > Ti > Zn > Sc > Kr > Fe > Cr > V > As > Rb > Mn > Ge > Cu > Br > Ni > Se > Co > Ga.

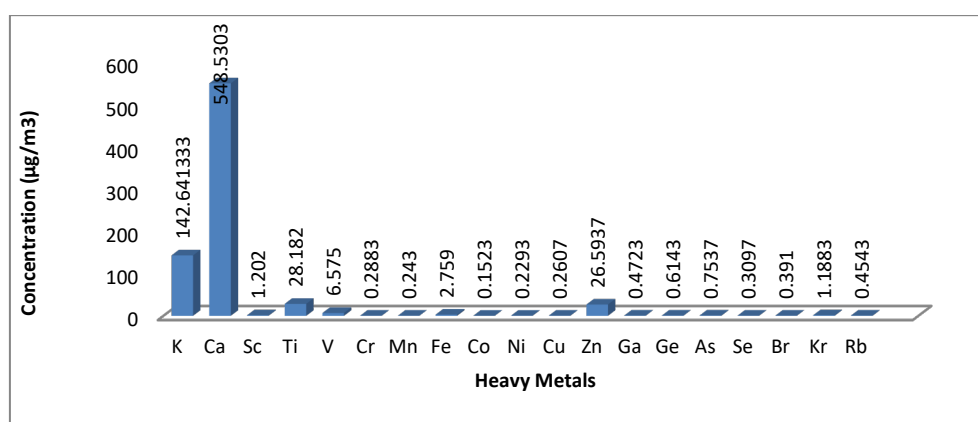


Figure 2: Elemental Compositions of TSP Emitted from Combustion of GS

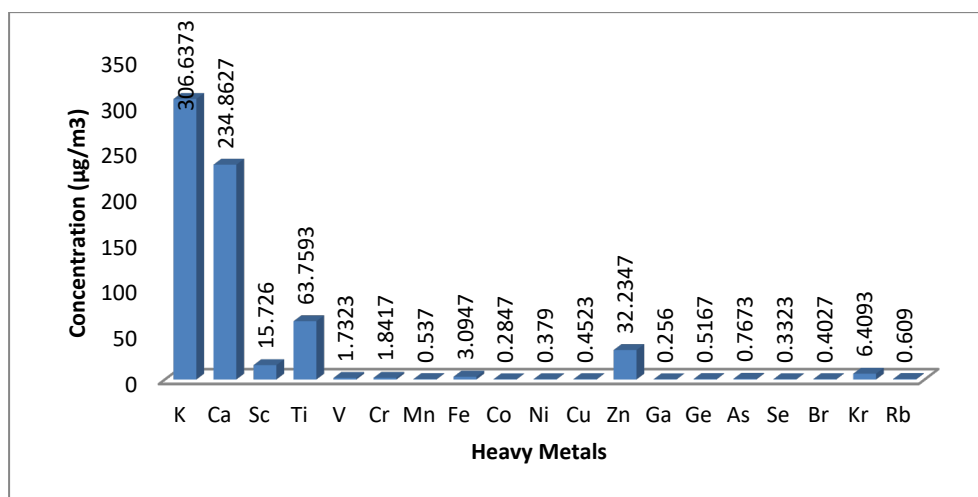


Figure 3: Elemental Compositions TSP Emitted from Combustion of EPKFB

Subsequently, the average concentration of elemental compositions from crop waste emissions trapped in a 0.8 µm sized filter is presented. The result (Fig. 4) revealed that the emission order for CH followed  $K > Ca > Fe > Rb > Kr > Ti > Sc > Zn > Br > Mn > Cu > Se > Co > Cr > Ga > Ni > V > As > Ge$ . This is meaningfully differed to that of GS revealed in Fig. 5;  $K > Ca > Sc > Ti > Br > Fe > V > Rb > Cu > Zn > Ni > Mn > Cr > Kr > Co > As > Se > Ge > Ga$  and to metal pollutants released from EPKFB;  $K > Ca > Sc > Fe > Ti > Zn > Kr > Rb > Mn > Cu > V > Ni > Ga > Co > Br > Cr > Se > As > Ge$  as in Fig. 6. In all the emission experiments conducted for CH, GS and EPKFB, it was brought to knowledge that, K (89.93; 89.02; 75.34) possesses the highest emission concentration value (µg/m³) followed by Ca (13.74; 6.04; 5.95) while the minimum emissions were detected as being  $As > Ge$ ;  $Ge > Ga$  and  $As > Ge$  for CH, GS and EPKFB. However, aside from K and Ca, the concentration values for other heavy metals emitted were slightly dissimilar to one another.

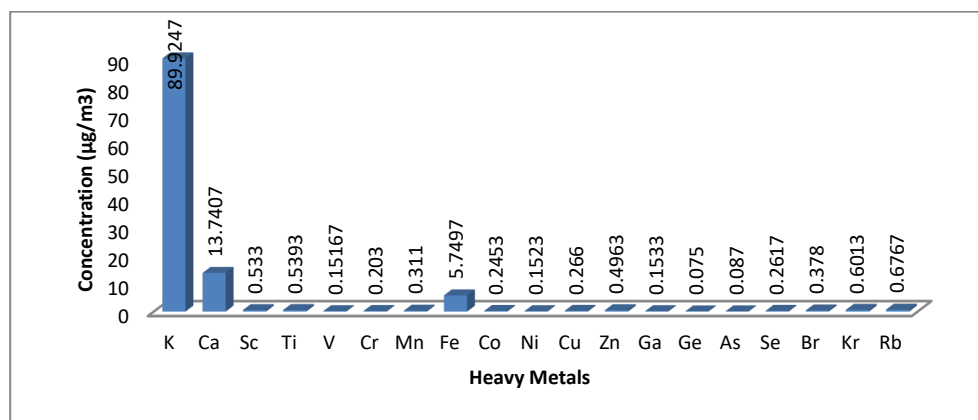


Figure 4: Elemental Compositions of PM<sub>0.8</sub> Emitted from Combustion of CH

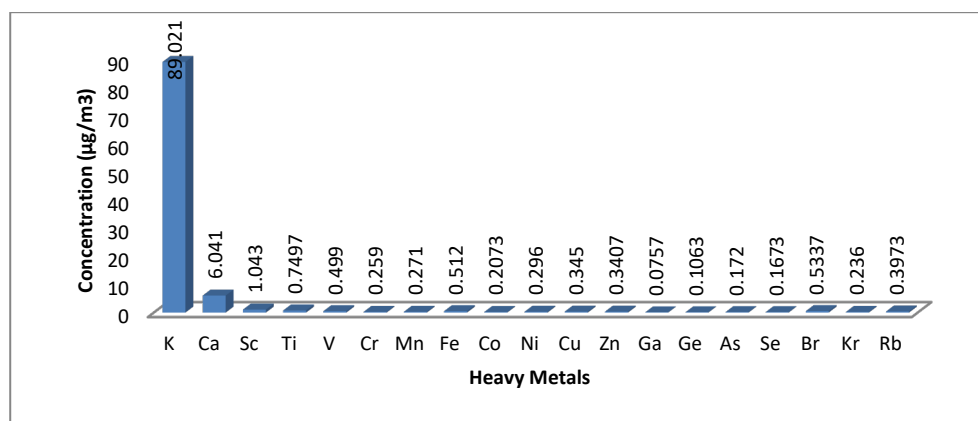
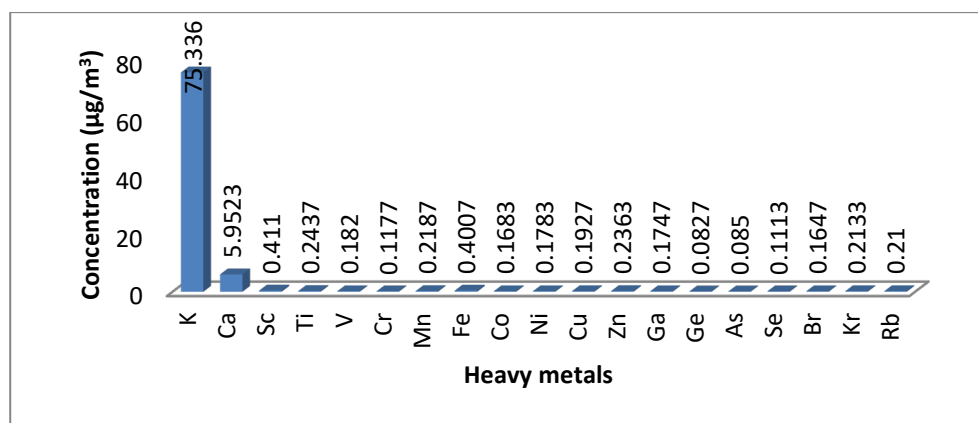
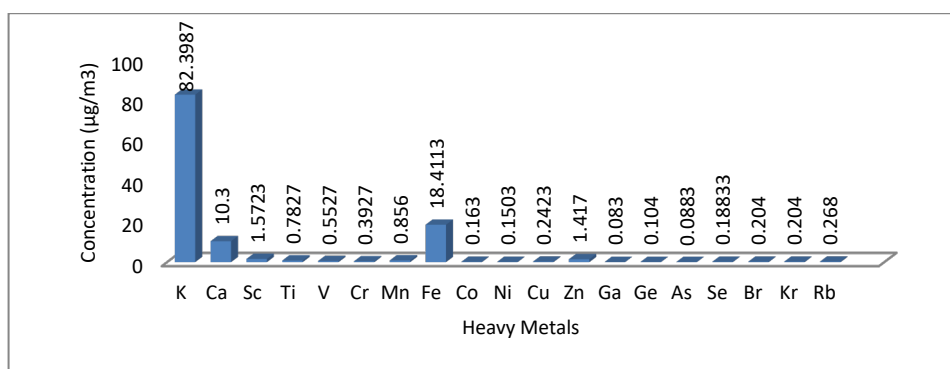
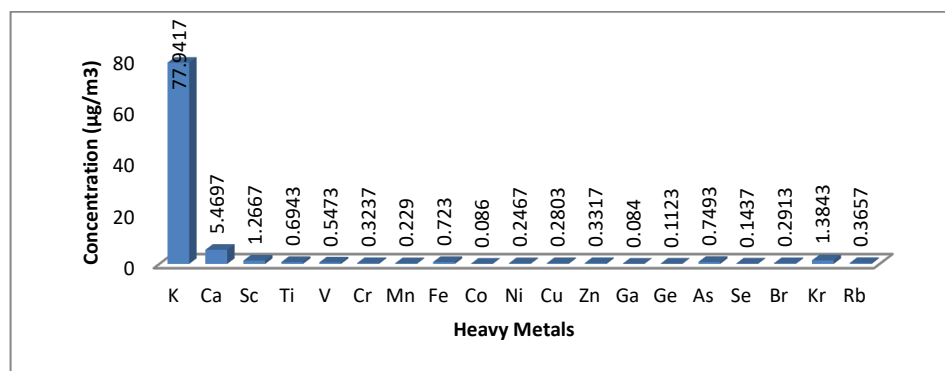


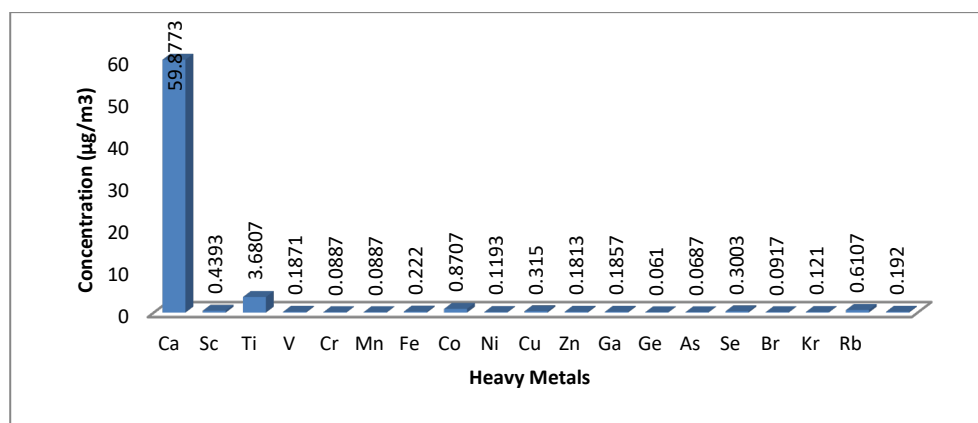
Figure 5: Elemental Compositions of PM<sub>0.8</sub> Emitted from Combustion of GS

Figure 6: Elemental Compositions of PM<sub>0.8</sub> Emitted from Combustion of EPKFB

Also, heavy metal concentrations ranged from 0.075 µg/m<sup>3</sup> – 89.93 µg/m<sup>3</sup>; 0.076 – 89.021 µg/m<sup>3</sup> and 0.083 – 75.336 µg/m<sup>3</sup> for CH, GS and EPKFB, respectively as presented in Figs. 4-6. CH (89.93 µg/m<sup>3</sup>) and GS (89.02 µg/m<sup>3</sup>) exhibit almost the same K concentration as the highest emission among the analyzed elements and its value was not significantly less than the emission released from EPKFB (75.37 µg/m<sup>3</sup>). CH was observed with the highest concentration of metals compared to other crop remnant samples burnt. Thus, the crop residue emissions trend was CH > GS > EPKFB.

However, considering the highest and the lowest metal emissions deposition on PM<sub>0.4</sub>-sized filters, a trend similar to CH was observed in GS and EPKFB as shown in Figs. 7-9. The three crop remains have K as the highest in order of CH (82.40 µg/m<sup>3</sup>) > GS (77.94 µg/m<sup>3</sup>) > EPKFB (58.88 µg/m<sup>3</sup>) and Ga, the least emissions in different order of GS (0.084 µg/m<sup>3</sup>) > CH (0.083 µg/m<sup>3</sup>) > EPKFB (0.061 µg/m<sup>3</sup>). Though, the 4th, 7th, 8th, 12th and 17th emitted elemental concentration might not be the same for CH and GS, but their order of emission (µg/m<sup>3</sup>) corresponds to one another with Sc (1.57) > Ti (0.78) > V (0.55) > Br (0.20) > Ge (0.10) and Sc (1.27) > Ti (0.69) > V (0.54) > Br (0.29) > Ge (0.11), respectively. EPKFB had the least average emitted metals (67.70 µg/m<sup>3</sup>) compared to two other crop wastes after which was GS (91.27), and the highest metal emission was characterized by CH (118.38). EPKFB emission trend did not conform to that of CH and GS.

Figure 7: Elemental compositions of PM<sub>0.4</sub> Emitted from Combustion of CHFigure 8: Elemental Compositions of PM<sub>0.4</sub> Emitted from Combustion of GS

Figure 9: Elemental Compositions of PM<sub>0.4</sub> Emitted from Combustion of EPKFB

Nevertheless, the K emitted from CH was significantly different from other metals emitted; this trend was as well observed in GS and EPKFB. The trend is thus,  $K > Fe > Ca > Sc > Zn > Mn > Ti > V > Cr > Rb > Cu > Br > Kr > Se > Co > Ni > Ge > As > Ga$  for CH,  $K > Ca > Kr > Sc > As > Fe > Ti > V > Rb > Zn > Cr > Br > Cu > Ni > Mn > Se > Ge > Co > Ga$  for GS and the trend for EPKFB was  $K > Sc > Fe > Kr > Ca > Ni > As > Mn > Rb > Ti > Zn > Cu > Br > Co > Se > V > Cr > Ge > Ga$ .

However, among the analyzed elements, a significantly higher concentration of K was observed in 0.8 µm (89.93 µg/m<sup>3</sup>, 89.02 µg/m<sup>3</sup>, 75.34 µg/m<sup>3</sup>) and 0.4 µm (82.40 µg/m<sup>3</sup>, 77.94 µg/m<sup>3</sup>, 59.88 µg/m<sup>3</sup>) size particles emitted from the three crop residues burnt, these values were beyond while that of other characterized elements ranging between 0.061 µg/m<sup>3</sup> to 18.41 µg/m<sup>3</sup> were below U.S. EPA and WHO set standard values of 35 µg/m<sup>3</sup> and 25 µg/m<sup>3</sup>, respectively. This report did not support the study of Adebajo *et al* (2019) where the concentration of all the characterized elements exceeded the standard. This could be a result of industrial and vehicular emissions not associated with the area where the crop remnant was sourced (Adebajo *et al*. 2019).

Subsequently, aside from TSP emission concentrations of K (464.31 µg/m<sup>3</sup> for CH, 142.64 µg/m<sup>3</sup> for GS, 306.69 µg/m<sup>3</sup> for EPKFB) which preceded the threshold limit, other metals concentrations analyzed from TSP trapped from CH such as Ca (396.44 µg/m<sup>3</sup>), Zn (105.96 µg/m<sup>3</sup>), V (37.47 µg/m<sup>3</sup>), Ti (122.77 µg/m<sup>3</sup>), Sc (29.44 µg/m<sup>3</sup>); TSP emitted from GS such as Ti (28.18 µg/m<sup>3</sup>) and TSP emitted from EPKFB like Ti (63.76 µg/m<sup>3</sup>) and Zn (32.24 µg/m<sup>3</sup>) were also higher than the set standard values. These values were in line with that of Adebajo *et al*. (2019).

## CONCLUSION AND RECOMMENDATION

It was observed that of the three sets of agricultural wastes burnt, TSP emissions were characterized as having the highest elemental concentration followed by PM<sub>0.8</sub> while elements concentration analyzed from PM<sub>0.4</sub> was the least. K concentration exceeds other trace metals whereas Ga and Ge mostly possess the lowest concentration. However, the use of crop residues being processed into valuable products should be encouraged to reduce crop emissions through the burning process.

## REFERENCES

- Adebajo, S.A., Jimoda, L.A., Alade, A.O. and Alagbe, E. (2019). Elemental Composition of Particulates Deposition in some Selected Industrial Areas of Ikeja, Lagos, Nigeria. *Journal of the Nigeria Society of Chemical Engineers*, **34** (1): pp. 62–70.
- Andini, A., Bonnet, S. and Rousset, P. (2018). Assessment of Climate Pollutants Emissions from Crop Residues Open Burning in Indonesia. *J. of Tech. and Inno. for Global Rev*, pp. 296-299.
- Booth, M.S. (2012). Biomass Energy in Pennsylvania : Implications for Air Quality, Carbon Emissions and Forests. By partnership for Public Integrity, Pennsylvania. Pp. 1-76.
- Byun, D.W. and Schere, K.L. (2006). Review of the Governing Equations, Computational Algorithms and other Components of the Models-3. Community Multiscale Air Quality (CMAQ) Modeling System. *Applied Mechanics Review*, **59**: pp. 51-57.
- Jain, N., Bhatia, A. and Pathak, H. (2014). Emission of Air Pollutants from Crop Residue Burning in India. *Aerosol and Air Quality Research*, **14**: pp. 422-430.
- Kim, P S., Jacob, D.J., Mickley, L.J., Koplitz, S.N., Marlier, M.E., Defries, R.S., Myers, S.S., Chew, B.N. and Mao, Y.H. (2015). Sensitivity of Population Smoke Exposure to Fine Locations in Equatorial Asia. *Atmospheric Environment*, **102**: pp. 11-17.

- Sahu, L.K., Kondo, Y., Miyazaki, Y., Pongkiatkul, P. and Kim Oanh, N. T. (2011). Seasonal and Diurnal Variations of Black Carbon and Organic Carbon Aerosols in Bangkok. *Journal of Geophysical Research (USA)*, **116** (15): pp 15302.
- Satsangi, P.G., Chavan, S.P., Rao, P.S.P. and Safai, P.D. (2014). Chemical Characterization of Particulate Matter at Sinhagad, a High-Altitude Station in Pune, India. *Indian Journal of Radio and Space Physics*, **43**: pp.284-292.
- Vreeland, H., Schauer, J.J., Russell, A.G., Marshall, J.D., Fushimi, A., Jain, G., Sethuraman, K., Verma, V., Tripathi, S.N. and Bergin, M.H. (2016). Chemical Characterization and Toxicity of Particulate Matter Emissions from Roadside Trash Combustion in Urban India. *Atmospheric Environment*, **147**: pp. 22-30.
- Xiao, Q., Saikawa, E., Yokelson, R.J., Chen, P., Li, C. and Kang, S. (2015). Indoor Air Pollution from Burning Yak Dung as a Household fuel in Tibet. *Atmospheric Environment*, **102** (1): pp. 406-412.
- Zhang, H., Wang, S., Hao, J., Wan, L., Jiang, J., Zhang, M., Mestl, H.E.S., Alnes, L.W.H., Aunan, K. and Mellouki, A.W. (2012). Chemical and Size Characterization of Particles Emitted from Burning of Coal and Wood in Rural Household in Quizhou, China. *Atmospheric Environment*, **51pp.** : 94-99.
- Zhang, X., Lu, Y., Wang, Q and Qian, X. (2018). A high-resolution Inventory of Air Pollutants Emissions from Crop residues burning in China. *Journal of Atmospheric Chemistry and Physics*, pp.1-19.



## Air Emissions from Stepwise Co-Pyrolysis of Plastic Mixtures

Atilade A. OLADUNNI<sup>1\*</sup>, Oludare J. ODEJOBI<sup>2</sup>, Jacob A. SONIBARE<sup>2</sup>

<sup>1</sup>Department of Chemical Sciences, Ajayi Crowther University, Oyo, Nigeria

<sup>2</sup>Department of Chemical Engineering, Obafemi Awolowo University, Ile-Ife, Nigeria

<sup>1\*</sup>[aa.oladunni@acu.edu.ng](mailto:aa.oladunni@acu.edu.ng), <sup>2</sup>[dareodejobi@oauife.edu.ng](mailto:dareodejobi@oauife.edu.ng), <sup>3</sup>[asonibar@yahoo.com](mailto:asonibar@yahoo.com)

\*Corresponding author

---

### ABSTRACT

Stepwise air emissions of Hydrocarbon, carbon II oxide (CO), carbon IV oxide (CO<sub>2</sub>), nitrogen II oxide (NO), nitrogen IV oxide (NO<sub>2</sub>), oxides of nitrogen (NO<sub>x</sub>), Sulphur IV oxide (SO<sub>2</sub>), and hydrogen sulphide (H<sub>2</sub>S) from co-pyrolysis of Low-density polyethylene (LDPE), Polystyrene (PS) and Polyethylene terephthalate (PET) were studied between 50 °C - 450 °C using E8500 plus combustion analyzer. The maximum air emissions measured were compared with available Ambient Air Quality Guidelines from World Health Organization and National Environmental Standards and Regulations Enforcement Agency. The result showed that HC, CO, and NO were detected while CO<sub>2</sub>, NO<sub>2</sub>, SO<sub>2</sub>, and H<sub>2</sub>S were not. Co-pyrolysis of plastic mixture comprising 50% LDPE, 0%PS and 50% PET gave the highest HC emission of 16,567 mg/m<sup>3</sup> at 400-450 °C, while co-pyrolysis of 100% LDPE, 0% PS and 0% PET gave the highest CO emission of 16239.85 mg/m<sup>3</sup> and NO emission of 138.44 mg/m<sup>3</sup> at 50-100, and 250-300 °C respectively. The maximum measured emission of CO far exceeded the maximum allowable standards which implied toxic ambient air within the vicinity of operation.

**Keywords:** Co-pyrolysis, Air emission, Ambient air quality, mixtures, plastic valorisation.

### 1. INTRODUCTION

Thermal degradation of plastics by means of pyrolysis results in depolymerization to yield solid, liquid and gaseous products of high energy value (Miandad *et al.*, 2019). Gaseous emissions from this process oftentimes contain air pollutants which could be hazardous to human health if emitted at high quantity (Kehinde *et al.*, 2020).

Although, the acceptance of co-pyrolysis as a thermochemical method of treating plastics has increased across the globe in recent years; rare studies have been conducted to characterize the emissions associated with co-pyrolysis of LDPE, PS and PET.

This study seeks to characterize and quantify the emissions associated with the co-pyrolysis of LDPE, PS and PET through experimental simulation of the process in the laboratory at stepwise increase in temperature in comparison with Ambient Air Quality standards.

### 2. MATERIALS AND METHODS

Low-density polyethylene(LDPE), Polystyrene(PS) and Polyethylene terephthalate(PET) materials were shredded into an approximate uniform size of 10×10 cm and air-dried to minimize energy requirement for drying in the experiment before usage (Yuliansyah *et al.*, 2015).

#### 2.1 Experimental Design

Experimental design showing standard mixture ratios for the co-pyrolysis of LDPE, PS and PET are shown in Table 1. Four experimental points were three-component mixtures, three experimental points were two-component mixtures, and the remaining three experimental points were pure components. The components of the mixtures were calculated in grams and the total weight of each mixture was 60g. The percentage mass fractions of the mixtures are shown in Table 1. The unique mixtures were coded A-J for easy identification. The mixtures were loaded into the reactor according to the mixture fractions and the co-pyrolysis were performed at 50 - 450 °C for 90 min at a constant heating rate of 6 °Cmin<sup>-1</sup> (Demirbas, 2004; Onwudili *et al.*, 2009; Patni *et al.*, 2013).

Table 1: The sample codes and percentage of mass fraction at the experimental design points

Run	Run codes	LDPE (%)	PS(%)	PET(%)	Total (%)
1	A	17.00	17.00	66.00	100
2	B	17.00	66.00	17.00	100
3	C	100.00	0.00	0.00	100
4	D	50.00	0.00	50.00	100
5	E	33.33	33.33	33.33	100
6	F	0.00	0.00	100.00	100
7	G	50.00	50.00	0.00	100
8	H	0.00	100.00	0.00	100
9	I	0.00	50.00	50.00	100
10	J	66.00	16.00	16.00	100

## 2.2 Experimental Set-up and Procedure

The representation of the entire pyrolysis system is shown in Figure 1. The batch reactor was cylindrical and made of stainless-steel material (American Society for Metals, 1980) with a height of 25cm and external diameter of 16cm. Gasket sheet of 0.2 cm thickness was positioned between the cover and the flanges of the reactor to prevent gas leakage. The reactor was loaded and unloaded through a circular opening (12 cm diameter) sealed off by a 13 × 13 cm square plate at the center of the cover. The internal temperature of the reactor was measured by type-K thermocouple controlled by a 1200 °C range temperature controller. The reactor was placed in a double walled lagged vessel to prevent heat loss. Probe of E8500 plus combustion analyzer was positioned inside the ground end of the Liebig condenser to have a direct contact with the gaseous emissions from the co-pyrolysis process.

The characterized emissions from the co-pyrolysis of the polymeric wastes include, Hydrocarbons (HCs), carbon II oxide (CO), carbon IV oxide (CO<sub>2</sub>), nitrogen II oxide (NO), nitrogen IV oxide (NO<sub>2</sub>), oxides of nitrogen (NO<sub>x</sub>), sulphur IV oxide (SO<sub>2</sub>), and hydrogen sulphide (H<sub>2</sub>S) in accordance with EPA provisional reference methods (EPA-CTM-022, 1995; ICAC, 1999; EPA, 2017). The emissions of the co-pyrolysis of each mixture were measured in milligram per cubic meter (mg/m<sup>3</sup>) at a 50 °C stepwise increase in temperature from 50 - 450 °C for all the air emissions, and the time taken for each period of measurements were recorded in seconds (s)

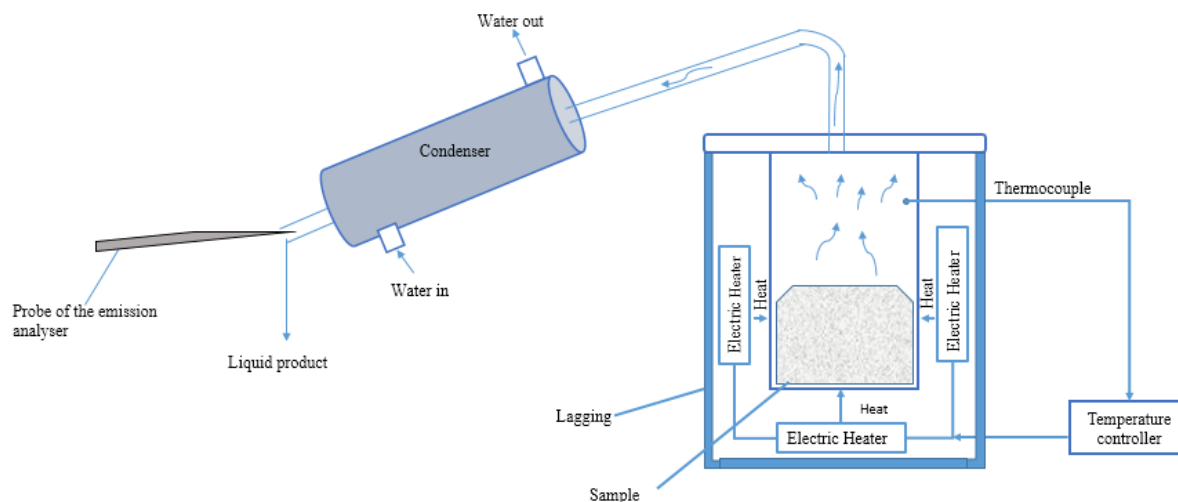


Figure 1: Sketch of experimental set up

## 2.3 Comparison of Emissions with Air Quality Standards

The emissions from the co-pyrolysis process were compared with various air quality standards by World Health Organization (WHO), National Environmental Standards and Regulations Enforcement Agency (NESREA) and US environmental protection Agency (EPA) to determine compliance with the standard limits.



### 3.0 RESULTS AND DISCUSSION

#### 3.1 Air Emissions at stepwise 50 °C increase in temperature in the co-pyrolysis of LDPE, PS and PET

No emissions of CO<sub>2</sub>, NO<sub>2</sub>, SO<sub>2</sub> and H<sub>2</sub>S were detected in all the mixtures studied between 50-450°C. However, there was detection of HC, CO, and NO. Oxides of nitrogen, NO<sub>x</sub> measured as summation of NO and NO<sub>2</sub> have the same value as NO since NO<sub>2</sub> was not detected. The graphical presentation of the detected emissions are shown in Figure 2, 3, and 4.

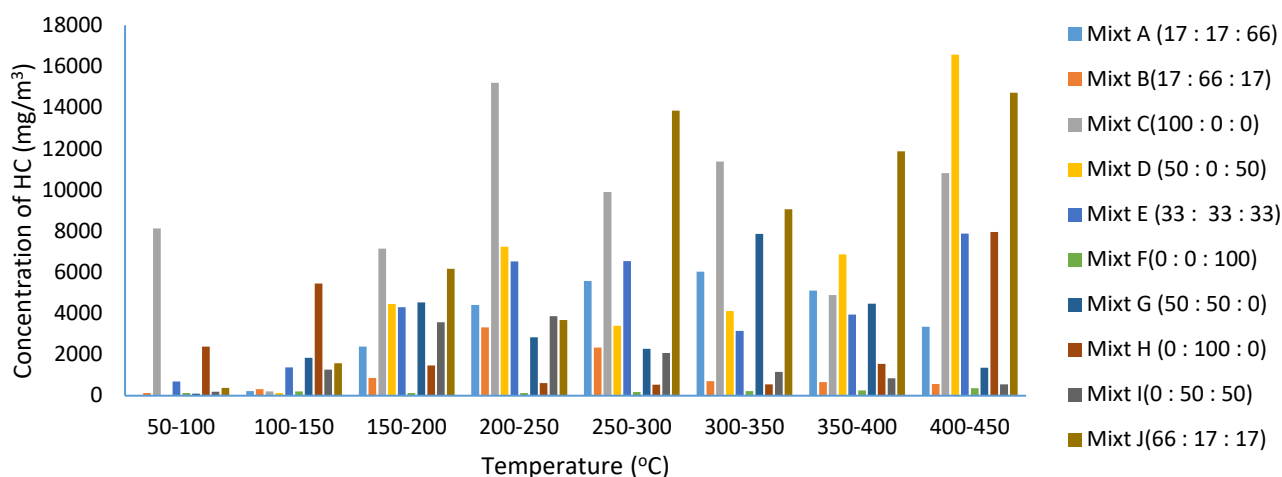


Figure 2: Hydrocarbon emissions at 50 °C stepwise increase in temperature from 50-450 °C for different mixture compositions during Co-pyrolysis of LDPE, PS and PET

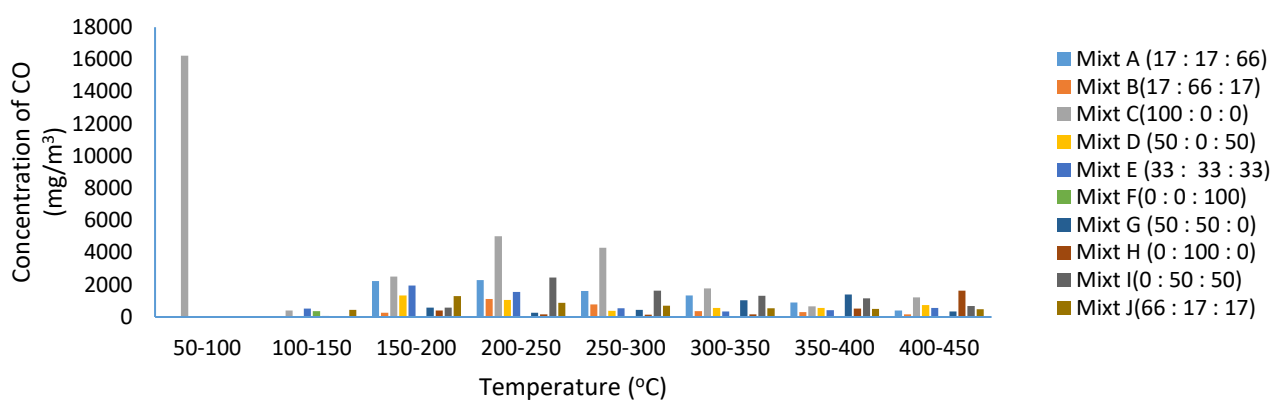


Figure 3: Carbon (II) oxide emissions at 50 °C stepwise temperature increase from 50-450 °C for different mixture compositions during Co-pyrolysis of LDPE, PS and PET

##### 3.1.1 Emissions of HC at 50 °C stepwise increase in temperature in the co-pyrolysis of LDPE, PS and PET

Figure 2 shows the emissions of HC for all the mixture compositions. At 50-100 °C, mixture A and D did not emit any HC. While mixtures B, C, E, F, G, H, I and J gave HC emissions with values ranging from 100 mg/m<sup>3</sup> to 8119.93 mg/m<sup>3</sup>. At 100-150 °C, all the mixture emitted HC with emission from mixture H being the highest at 5450 mg/m<sup>3</sup> and that from mixture D being the lowest at 124.92 mg/m<sup>3</sup>. At 150-200 °C, all mixture compositions emitted HC with the highest emissions recorded from mixture C as 7144 mg/m<sup>3</sup> and lowest emission from mixture F as 124.92 mg/m<sup>3</sup>. At 200-250 °C, all mixtures emitted HC with mixture C having the highest emission of 15,209 mg/m<sup>3</sup> which also doubled as the highest emission of HC for mixture C throughout the co-pyrolysis, and mixture F still having the lowest emission of HC at 124.92 mg/m<sup>3</sup>. At 250-300 °C, Mixture J has the highest emission of HC at 13,850 mg/m<sup>3</sup> and mixture F the lowest emission of HC at 176.97 mg/m<sup>3</sup>. At 300-350 °C, mixture C emitted the highest HC at 11,373 mg/m<sup>3</sup> and mixture F the lowest emission of HC at 230.33 mg/m<sup>3</sup>. At 350-400 °C, mixture J gave the highest emission of HC at

11,876 mg/m<sup>3</sup> and mixture F gave the lowest emission of HC at 249.84 mg/m<sup>3</sup>. At 350-400 °C, mixture J gave the highest emission of HC at 11,876 mg/m<sup>3</sup>. At 400-450 °C, mixture D gave the highest HC emission of 16,567 mg/m<sup>3</sup> (the highest observed HC emission in all the experiments) and mixture F gave the lowest HC emission of 367.83 mg/m<sup>3</sup>.

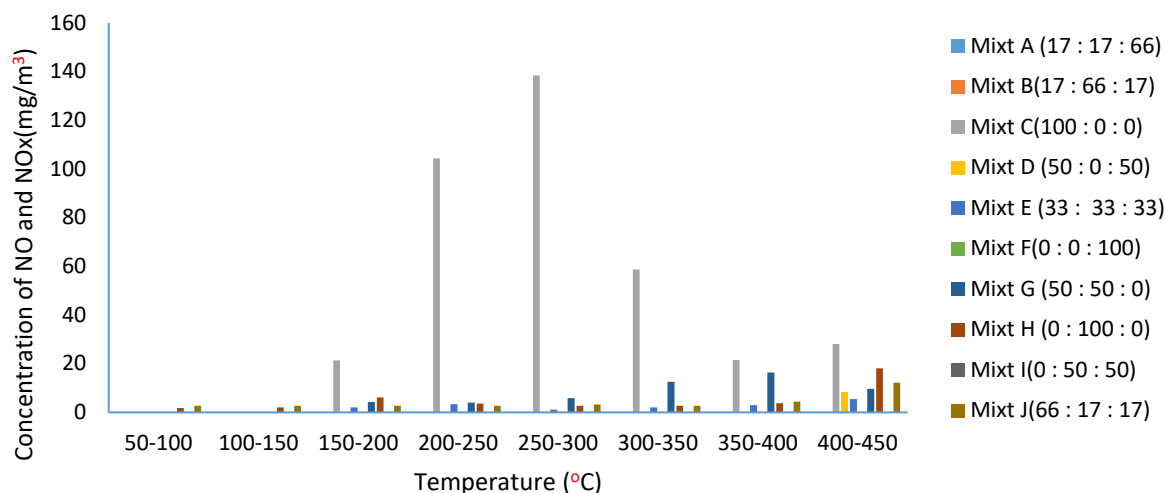


Figure 4: Measured concentrations of Nitrogen II oxide and oxides of Nitrogen at 50 °C stepwise temperature increase from 50-450 °C for different mixture compositions in the Co-pyrolysis of LDPE,

### 3.1.2 Emissions of CO at 50 °C stepwise increase in temperature in the co-pyrolysis of LDPE, PS and PET

Figure 3 shows the emissions of CO by the various mixtures. At 50 -100 °C, only mixtures C, E, H and J emitted CO and mixture C was distinctively higher than others with an emission of 16239.85 mg/m<sup>3</sup>. At 100-150 °C, all mixtures except B and D emitted CO. However, the CO emissions for all the mixture compositions were less than 100 mg/m<sup>3</sup>. At 150-200 °C, all mixture compositions emitted CO. The highest emission was recorded from mixture C as 2517.93 mg/m<sup>3</sup> for CO. At 200-250 °C, all of the mixtures also emitted CO with mixture C having the highest emission of 5014.21 mg/m<sup>3</sup>. At 250-300 °C, only mixture F did not emit CO. Mixture C still has the highest emissions of CO of 4306.37 mg/m<sup>3</sup>. Furthermore, at 300-350 °C, all mixtures emitted CO with mixture C emitting the highest of 1,779.06 mg/m<sup>3</sup>. At 350-400 °C, mixture G gave the highest CO emission of 1401.06 mg/m<sup>3</sup>. At 400-450 °C, mixture H gave the highest CO emission of 1,629.70 mg/m<sup>3</sup>.

### 3.1.3 Emissions of NO and NOx at 50 °C stepwise increase in temperature in the co-pyrolysis of LDPE, PS and PET

In Figure 4, the emissions of NO and NO<sub>x</sub> by the various mixtures are displayed. At 50 -100 °C, only two mixtures H and J emitted NO and NO<sub>x</sub>. Meanwhile, at 100-150 °C, only two mixture compositions H and J emitted NO and NO<sub>x</sub> and their emissions were less than 10mg/m<sup>3</sup> each. At 150-200 °C, Mixtures C, E, G, H, and J emitted NO and NO<sub>x</sub> with C having the highest value of 21.42 mg/m<sup>3</sup>. At 200-250 °C, only mixtures C, E, G, H and J emitted NO and NO<sub>x</sub>. Mixture C had the highest emission of 104.40 mg/m<sup>3</sup>. At 250-300 °C mixture C gave the highest emission of 138.45 mg/m<sup>3</sup> and lowest emission of 2.68 mg/m<sup>3</sup> at mixture H. Meanwhile there is no emission for mixtures A, B, D, E, F and I. At 300-350 °C, Mixture C, E, G, H, and J emitted NO and NO<sub>x</sub> with C having the highest emissions of 58.8mg/m<sup>3</sup>. At 350-400 °C, mixture C gave highest emission and NO<sub>x</sub> emission of 28.2mg/m<sup>3</sup>. None of the mixtures emitted CO<sub>2</sub>, H<sub>2</sub>S and SO<sub>2</sub>. Mixture F had HC emissions lower than 400 mg/m<sup>3</sup> throughout the process with its highest emission of 368 mg/m<sup>3</sup>. Mixtures A and B did not emit any NO and NO<sub>x</sub> throughout the process.

## 3.2 Comparison of Emissions with Air Quality standards

There are no existing distinct emission standards for pyrolysis processes (Taylor, 2021). The highest measured emissions of the gaseous species investigated (Table 2) were expressed in part per million (ppm) and compared with EPA regulations for small municipal solid waste incinerators (MSWIs) operating at < 250 tons/day (Schwartz *et al.*, 2020) and point source maximum emission limits for facilities and processes set by National Environmental Standards and Regulations Enforcement Agency (NESREA, 2014). There was limits available for air emissions of HCs. Maximum measured CO far exceeded the maximum allowable limits of 50 and 400ppm for EPA and NESREA. Maximum emitted NO on the other hand was lower than EPA and NESREA limits for NO<sub>x</sub> from small MSWIs and point source emission for facilities and processes respectively. This implies that the point source emission from the co-pyrolysis operation could be regarded as very toxic with respect to emission of CO and not safe for human health.

Table 2: Comparison of highest air emissions measured from the co-pyrolysis of LDPE, PS and PET with WHO and NESREA point source maximum emission limits for facility and processes.

Air emission	Max value recorded (mg/m <sup>3</sup> )	Max value recorded (ppm)	Mixt. Comp. LDPE:PS:PET (%)	Temp. Range (°C)	EPA OSWI (ppm)	NESREA AQS (ppm)
HC <sub>Max</sub>	16567.23	25253.7	50:0:50	400-450	-	-
CO <sub>Max</sub>	16239.85	14175.8	100:0:0	50-100	50	400
NO <sub>Max</sub>	138.45	112.799	100:0:0	250-300	*500	**244
NO <sub>2</sub>	nd	nd	-	-	*500	**244
CO <sub>2</sub>	nd	nd	-	-	-	-
SO <sub>2</sub>	nd	nd	-	-	30	-
H <sub>2</sub> S	nd	nd	-	-	-	5.0

nd-No detection; \* NO<sub>x</sub> from new source; \*\* emission standard for NO<sub>x</sub> (NESREA, 2014; Schwartz *et al.*, 2020)

#### 4.0 CONCLUSION

The study established the presence of air pollutants during co-pyrolysis of LDPE, PS and PET. It also showed that during the co-pyrolysis of LDPE, PS and PET; HC, CO, and NO were detected while NO<sub>2</sub>, CO<sub>2</sub>, SO<sub>2</sub> and H<sub>2</sub>S were not at 50 °C - 450 °C. The study revealed that co-pyrolysis of plastic mixture composition comprising 50% LDPE, 0%PS and 50% PET gave the highest HC emission of 16,567 mg/m<sup>3</sup> at 400-450 °C, when compared to all other mixture compositions and temperature range investigated. On the other hand, plastic mixture composition comprising 100% LDPE, 0% PS and 0% PET gave the highest value of 16239.85 mg/m<sup>3</sup> and 138.44 mg/m<sup>3</sup> for CO and NO emissions at temperature range 50-100, and 250-300 °C respectively. The maximum measured emission of CO far exceeded the maximum allowable limits by EPA and NESREA for small MSWIs and point source emission for facilities and processes respectively. Emitted pollutants observed during the co-pyrolysis process can be addressed by installing air pollution control device to trap HC, CO and NO which can further be separated for various applications.

#### ACKNOWLEDGEMENT

The authors would like to thank the Environmental Engineering Laboratory, Department of Chemical Engineering, Obafemi Awolowo University for making available relevant technical assistance in the course of the research.

#### REFERENCES

- American Society for Metals (1980) *Metals Handbook. 9th Ed. Vol. 3. Properties and Selection Stainless Steels Tool Materials & Special-purpose Metal, Neuroscience.* ASM 1980. Available at: <http://www.pubmedcentral.nih.gov/articlerender.fcgi?artid=2854659&tool=pmcentrez&rendertype=abstract>
- Demirbas, A. (2004) 'Pyrolysis of municipal plastic wastes for recovery of gasoline-range hydrocarbons', 72, pp. 97–102. Available at: <https://doi.org/10.1016/j.jaap.2004.03.001>.
- EPA-CTM-022 (1995) 'Epa Ctm-022', pp. 1–16.
- EPA (2017) *Method 25B - Determination Of Total Gaseous Organic Concentration Using A Non-dispersive Infrared Analyzer.*
- ICAC (1999) *Test Method - Determination of Oxygen, Carbon Monoxide and Oxides of Nitrogen from Stationary Sources.* 1660 L Street, NW, Suite 1100 Washington DC 20036.
- Kehinde, O. *et al.* (2020) 'Plastic wastes: environmental hazard and instrument for wealth creation in Nigeria', *Heliyon*, 6(10), p. e05131. Available at: <https://doi.org/10.1016/j.heliyon.2020.e05131>.
- Miandad, R. *et al.* (2019) 'Catalytic pyrolysis of plastic waste: Moving toward pyrolysis based biorefineries', *Frontiers in Energy Research*, 7(MAR), pp. 1–17. Available at: <https://doi.org/10.3389/fenrg.2019.00027>.
- NESREA (2014) *National Environmental (Air Quality Control) Regulations.* 142. Lagos, Nigeria.
- Onwudili, J.A., Insura, N. and Williams, P.T. (2009) 'Journal of Analytical and Applied Pyrolysis Composition of products from the pyrolysis of polyethylene and polystyrene in a closed batch reactor : Effects of temperature and residence time', 86, pp. 293–303. Available at: <https://doi.org/10.1016/j.jaap.2009.07.008>.
- Patni, N. *et al.* (2013) 'Alternate Strategies for Conversion of Waste Plastic to Fuels', *ISRN Renewable Energy*, 2013, pp. 1–7. Available at: <https://doi.org/10.1155/2013/902053>.
- Schwartz, N.R. *et al.* (2020) 'Analysis of emissions from combusting pyrolysis products', *Fuel*, 274(January), p. 117863. Available at: <https://doi.org/10.1016/j.fuel.2020.117863>.
- Taylor, O.A. (2021) *US EPA Federal Register.*
- Yuliansyah, A.T. *et al.* (2015) 'Pyrolysis of plastic waste to produce pyrolytic oil as an alternative fuel', *International Journal of Technology*, 6(7), pp. 1076–1083. Available at: <https://doi.org/10.14716/ijtech.v6i7.1241>.



## Modeling of Gaseous Pollutant Emissions from Savannah Vegetation Fires

Khadijat A. ABDULRAHEEM<sup>1,2</sup>, Jamiu A. ADENIRAN<sup>3</sup> and Adeniyi S. AREMU<sup>1</sup>.

<sup>1</sup> Department of Civil Engineering, University of Ilorin, Ilorin, Nigeria.

<sup>2</sup> Department of Water Resources and Environmental Engineering, Ahmadu Bello University, Zaria, Nigeria.

<sup>3</sup> Environmental Engineering Research Laboratory, Department of Chemical Engineering, University of Ilorin, Ilorin, Nigeria.

### ABSTRACT

The concentration and transport dynamics of emissions during savannah vegetation fires are not well-understood. This study aims at modelling the ground level concentrations (GLC) of gaseous pollutants on the receptor environment using the American Meteorological Society/Environmental Protection Agency Regulatory Model (AERMOD). Three (3) scenarios were investigated based on the vegetation density of the savannah grasses. The model revealed that the 24-hour averaging period for CO, NO<sub>2</sub>, SO<sub>2</sub> and volatile organic compounds (VOC) ranges from 50 – 5,046 µg/m<sup>3</sup>; 0.049 – 4.97 µg/m<sup>3</sup>; 0.6 – 55.9 µg/m<sup>3</sup> and 63 – 6,253 µg/m<sup>3</sup> for Scenario 1; 288 – 28,825 µg/m<sup>3</sup>; 0.08 – 8.31 µg/m<sup>3</sup>; 2 – 203 µg/m<sup>3</sup> and 65 – 6,498 µg/m<sup>3</sup> for Scenario 2; 394 and 39,435 µg/m<sup>3</sup>; 0.2 and 22.3 µg/m<sup>3</sup>; 4 – 419 µg/m<sup>3</sup>; and 118 – 11,782 µg/m<sup>3</sup> for Scenario 3, respectively. The study revealed that the World Health Organization (WHO) guideline of 4 mg/m<sup>3</sup> for the 24-hour concentration of CO was breached under Scenarios 2 and 3 by 150%. The findings of this study will help in the accurate estimation of emissions from the savannah fires and in the development of appropriate mitigation strategies for emission control.

**Keywords:** Ground level concentrations; gaseous pollutants; modeling; emissions.

### 1. INTRODUCTION

Vegetation fires have been identified as one of the sources of gaseous pollutants in the environment. Gaseous pollutants such as CO, SO<sub>2</sub>, NO<sub>2</sub>, and VOCs emitted during vegetation fires change the chemical composition of the atmosphere which has detrimental effects on the environment, human health, and climate. Savannah landscapes are noted to experience the highest frequency and intensity of fires globally (Sun *et al.*, 2019) with about 20% of nitrogen oxides (NO<sub>x</sub>) and one-third of global CO emissions attributed to it (Andreae, 2019). Abdulraheem *et al.* (2022) reported that approximately 167 Tg of CO and 10 Tg of NO<sub>x</sub> were emitted from savannah vegetation fires in the West Africa region between 1990 – 2019 while Akagi *et al.* (2011) disclosed that the vegetation fire is the second largest contributor of volatile organic carbons to the atmosphere.

High concentrations of gaseous pollutants in the atmosphere have adverse effects on the environment and human health when above the thresholds established by air quality regulatory bodies. The short-term Air Quality Guideline levels recently released by the WHO 2021 have replaced the 2005 levels where tolerable pollutants levels were reviewed. To ascertain the concentrations of pollutants emitted during vegetation fires on the receptor environment, dispersion models have been employed by researchers. One of such models is the American Meteorological Society/Environmental Protection Agency Regulatory Model (AERMOD) as recommended by the United States Environmental Protection Agency (USEPA) (de Ferreyro Monticelli *et al.*, 2020). AERMOD is a near-field steady-state Gaussian Plume model that is based on planetary boundary layer (PBL) structure and scaling concepts over simple and complex terrains (Holmes and Morawska, 2006; ul Haq *et al.*, 2019). AERMOD calculates meteorological profiles with the use of measurements and similarity parameterizations to estimate adjacent vertical measurements (Cimorelli *et al.*, 2005). The model is relevant to a variety of pollutant sources in a wide range of settings such as rural, urban, flat, and complex terrain (Jampana *et al.*, 2004). The model has been used to analyze pollutant emissions in the environmental impact assessment study (Seangkiatiyuth *et al.*, 2011).

Researchers have used AERMOD models in the past for the determination of GLC of pollutants. In the study of Adeniran *et al.* (2018), air quality at the Ibese Cement factory in Ogun state Nigeria was assessed using the AERMOD model under four scenarios. The results revealed that particulates and gaseous pollutants from simultaneous operations of all point sources of air emissions are within stipulated limits in the neighboring communities except for the 24-h concentration values of NO<sub>x</sub> and SO<sub>2</sub> which breached their limits in a few locations. Afzali *et al.* (2017) predicted air pollutant concentrations from multiple sources with the use of AERMOD coupled with Weather Research Forecasting. Their findings indicated good agreement between predicted and observed concentrations. Rangel *et al.* (2018) estimated the concentrations of air pollutants emitted from the burning of sugarcane biomass using AERMOD software in Brazil. The study revealed that the highest dispersion was observed in February while April was observed to have the highest concentrations of pollutants.

Annual burning of vegetation is a prevalent practice in the savannah region of the country. The concentrations and transport dynamics of the pollutants emitted during this process are fairly understood and might exceed the acceptable levels stipulated by the regulatory guidelines. Therefore, this study aims at determining the GLC of pollutants emitted during savannah vegetation fires and their impacts on the receptor environment.

## 2. METHODOLOGY

The AERMOD model is a steady-state Gaussian dispersion model developed for air quality regulations. The gaseous pollutants emitted during the burning of savannah grasses were simulated using the AERMOD model over a flat/undulated terrain and under known meteorological conditions in three different scenarios. The impacts on receptor locations were observed under each scenario. The AERMOD model flowchart process is presented in Figure 1.

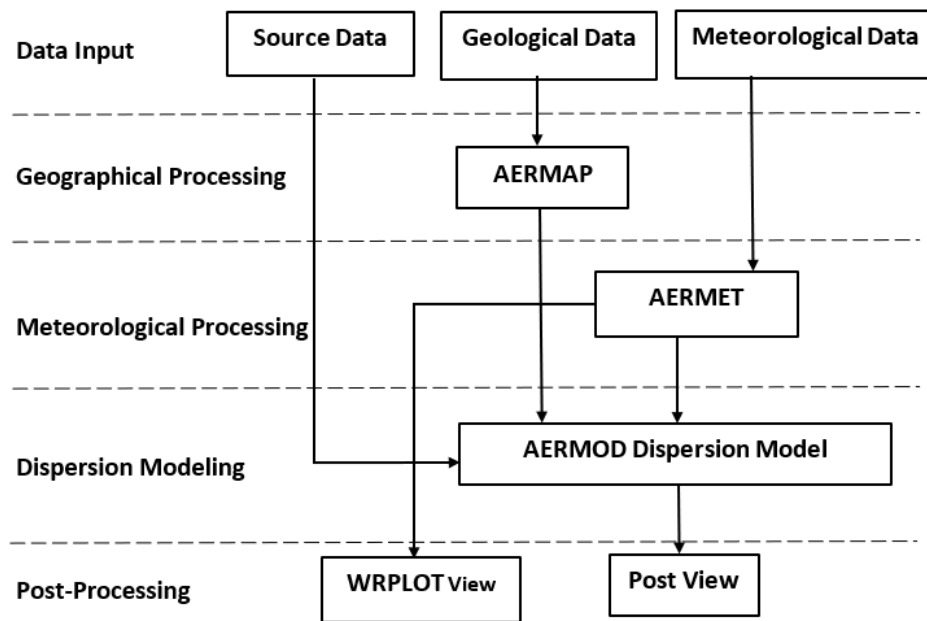


Figure 1: Process Flowchart for AERMOD model  
Adapted from: Seangkiatiyuth *et al.* (2011)

The licensed version of Lakes Environmental AERMOD View (version 8.9) was used for simulation in this study. The input data includes the source data, geological data i.e., the map of source location, and the meteorological data that are defined under various pathways. The source location selected for modeling was selected based on the Moderate Imaging Spectroradiometer (MODIS) satellite observations detected by the Aqua satellite which shows the active fire hotspots. For this study, the savannah region that is susceptible to annual vegetation fires in Nigeria was used for the modeling. The area source was selected in the Mariga Local Government Area of Niger State, at a geographical location of 10.508°N and 5.853°E. Figure 2 shows the active fire hotspots detected in Niger State in the first week of January 2021 and the selected source location used for the AERMOD model.

The model input includes the air emission rate, release height, area of dimension, orientation angle, and base elevation. The air emission rate is given as:

$$AE = \frac{EF \times FC}{t} \quad (1)$$

where  $AE$  = Area emission rate ( $\text{g}/\text{m}^2 \text{ s}$ );  $EF$  = Emission Factor ( $\text{g}/\text{kg}$ );  $FC$  = Fuel consumption ( $\text{kg}/\text{m}^2$ ) and  $t$  = average burning time (sec).

For the determination of GLC of pollutants from burning of savannah grasses using the AERMOD model, three (3) scenarios of air emission from savannah burnings were considered in this study which was based on the emission rate and grass density, they are: Low Emission - Scenario 1; Moderate Emission – Scenario 2; and High Emission - Scenario 3.

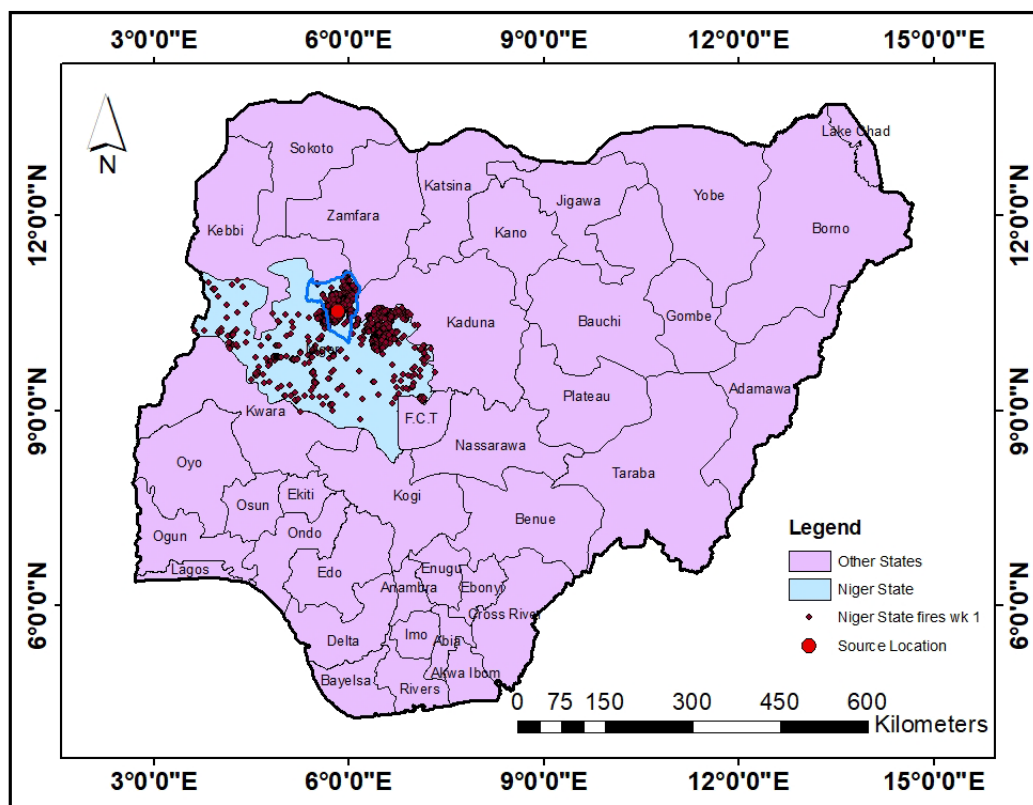


Figure 2: Map of Nigeria showing the source location used for the AERMOD model

### 3. RESULTS AND DISCUSSION

The AERMOD air quality dispersion model was performed to predict the GLC of CO, NO<sub>2</sub>, SO<sub>2</sub>, and VOC around the selected burned area in Niger State, Nigeria. The GLCs CO, NO<sub>2</sub>, SO<sub>2</sub>, and VOC were considered for the 1-hour, 8-hour, and 24-hour averaging period using the Industrial Source Complex (ISC)-AERMOD view. The minimum and maximum GLC of the pollutants from burned vegetation were computed and compared with the NAAQS - FMEnv and NESREA; WHO Air Quality Guidelines; and the NAAQS - USEPA to determine their level of compliance.

Scenario 1: The minimum 1-hour averaging concentration for CO, NO<sub>2</sub>, SO<sub>2</sub>, and VOC are 908, 0.8, 11 and 986 µg/m<sup>3</sup>, respectively while the maximum of 90835, 84.9, 1110, and 98637 µg/m<sup>3</sup> were observed, respectively. The minimum 8-hour averaging concentration for CO, NO<sub>2</sub>, SO<sub>2</sub>, and VOC are 140, 0.1, 2, and 201 µg/m<sup>3</sup>, respectively while the maximum of 14011, 11.8, 185, and 20135 µg/m<sup>3</sup> are observed respectively. The minimum 24-hour averaging concentration for CO, NO<sub>2</sub>, SO<sub>2</sub>, and VOC are 50, 0.049, 0.6, and 63 µg/m<sup>3</sup> while the maximum of 5046, 4.97, 55.9, and 6,253 µg/m<sup>3</sup> are observed respectively. The isopleth of the 24-hour averaging of the predicted concentrations of CO in Scenario 1 is shown in Figure 3.

Scenario 2: For CO, the 1-hour averaging concentration ranges from 3,761 – 376,061 µg/m<sup>3</sup>; the 8-hour averaging concentration ranges from 1,242 – 124,160 µg/m<sup>3</sup> while the 24-hour averaging concentration ranges from 288 – 28,825 µg/m<sup>3</sup>. For NO<sub>2</sub>, the 1-hour averaging concentration ranges from 2 – 151 µg/m<sup>3</sup>; the 8-hour averaging concentration ranges from 0.3 – 25.2 µg/m<sup>3</sup> while the 24-hour averaging concentration ranges from 0.08 – 8.31 µg/m<sup>3</sup>. For SO<sub>2</sub>, the 1-hour averaging concentration ranges from 41 – 4,103 µg/m<sup>3</sup>; the 8-hour averaging concentration ranges from 6 – 586 µg/m<sup>3</sup> while the 24-hour averaging concentration ranges from 2 – 203 µg/m<sup>3</sup>. For VOC, the 1-hour averaging concentration ranges from 1,495 – 149,473 µg/m<sup>3</sup>; the 8-hour averaging concentration ranges from 188 – 18,759 µg/m<sup>3</sup> while the 24-hour averaging concentration ranges from 65 – 6,498 µg/m<sup>3</sup>. Figure 4 shows the isopleth of the 24-hour averaging of the predicted concentrations of CO in Scenario 2.

Scenario 3: The 1-hour, 8-hour and 24-hour averaging concentrations of CO was observed to be between 6,271 and 627,140 µg/m<sup>3</sup>; 1,045 and 104,523 µg/m<sup>3</sup>; 394 and 39,435 µg/m<sup>3</sup>, respectively. For NO<sub>2</sub>, the 1-hour, 8-hour, and 24-hour averaging concentrations observed are between 4 and 433 µg/m<sup>3</sup>; 0.7 and 67 µg/m<sup>3</sup>; 0.2 and 22.3 µg/m<sup>3</sup>, respectively. For SO<sub>2</sub>, the concentrations were in the range of 90 – 8,961 µg/m<sup>3</sup>; 15 – 1,493 µg/m<sup>3</sup>; and 4 – 419 µg/m<sup>3</sup> for 1-hour, 8-hour and 24-hour averaging, respectively. Lastly, the 1-hour, 8-hour and 24-hour averaging concentration for VOC are

observed to be between 2,606 and 260,555  $\mu\text{g}/\text{m}^3$ ; 412 and 41,237  $\mu\text{g}/\text{m}^3$ ; 118 and 11,782  $\mu\text{g}/\text{m}^3$ , respectively. The isopleth of the 24-hour averaging of the predicted concentrations of CO is shown in Figure 5.

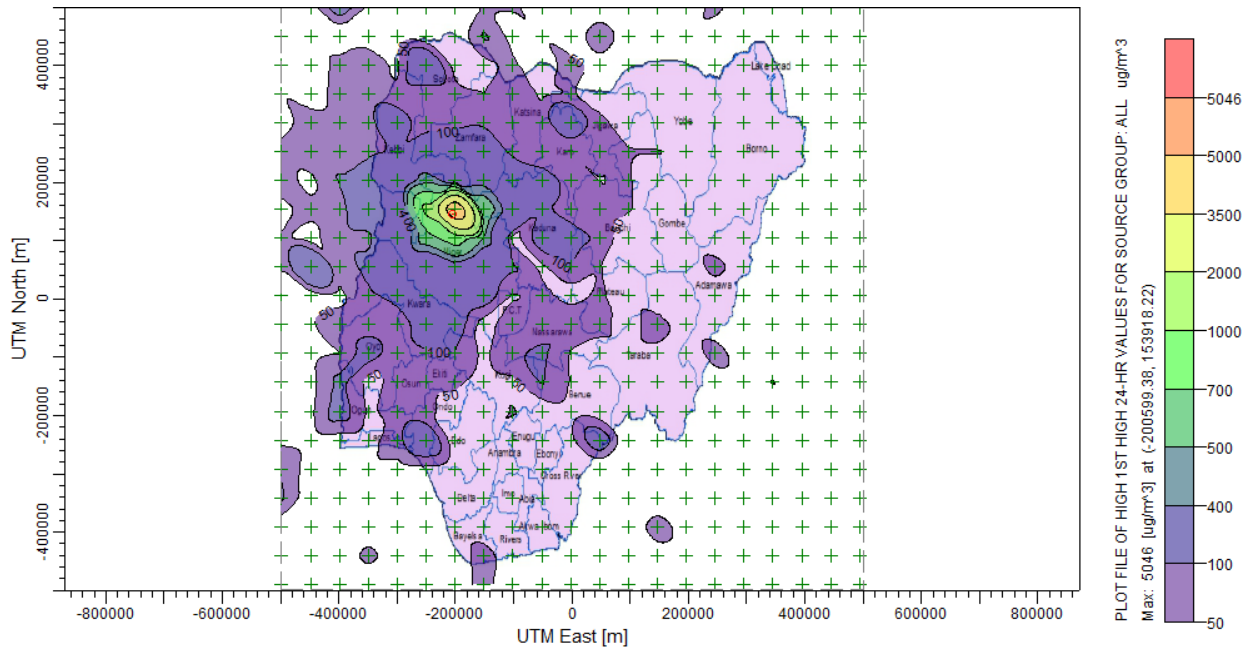


Figure 3: CO concentration profile for 24-hr averaging for Scenario 1

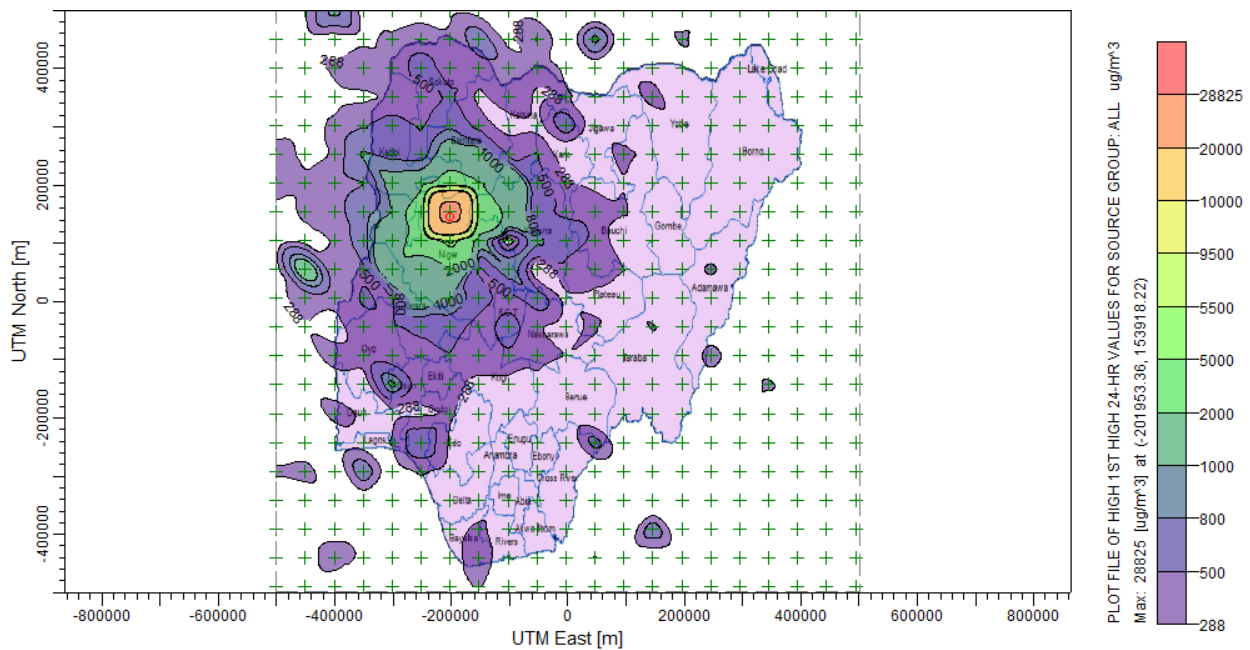


Figure 4: CO concentration profile for 24-hr averaging for Scenario 2

The distances from the source point to the receptor locations are shown in Table 1. It was observed that the dispersion of pollutants was in all directions of burned area for all the pollutants investigated. The pollutants disperse to several states in Nigeria and their concentrations depended on the distances between the source and the receptor states. The closest states to the source such as Kebbi, Zamfara, and Kaduna were observed to have the highest impacts.

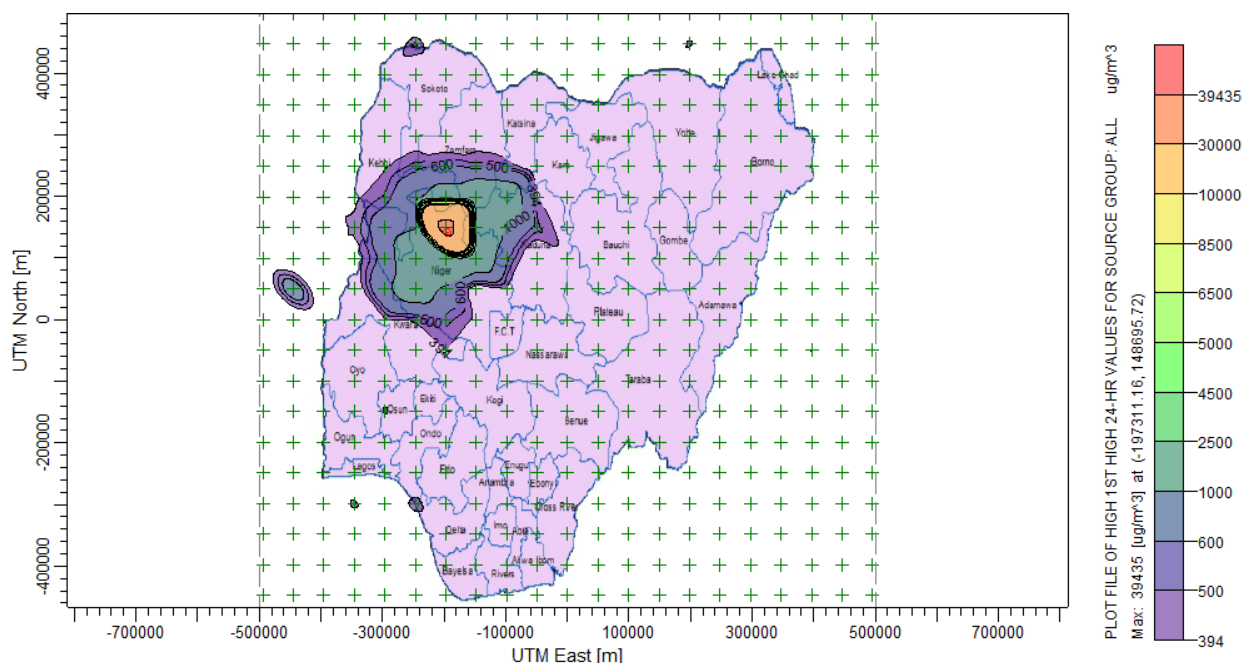


Figure 51: CO concentration profile for 24-hr averaging for Scenario 3

Table 1: The Nigerian States and their average distance from the source location

State	The average distance from the source (km)	State	The average distance from the source (km)
Kwara	197.33	Kano	272.6
Ekiti	307.62	Plateau	329.65
FCT	199.23	Kogi	261.24
Kebbi	61.93	Nasarawa	274.52
Sokoto	146.76	Osun	318.43
Kaduna	41.47	Oyo	270.45
Jigawa	376.34	Ondo	334
Bauchi	326.95	Benue	408.05
Katsina	152.75	Gombe	525.8
Ogun	468.114	Yobe	568.89
Zamfara	47.75		

In Table 2, the minimum and maximum GLC of the pollutants considered under the three scenarios are shown. The impacts of vegetation burning in the savannah on ambient air quality were investigated by comparing the hourly, 8-hourly, and daily maximum GLC of each of the investigated pollutants with the Nigerian NAAQS of the FMEnv and NESREA, WHO Air Quality Guidelines, and the NAAQS of the USEPA. For Scenario 1, the 1-hour, 8-hour and 24-hour maximum emission emitted for CO, NO<sub>2</sub>, and SO<sub>2</sub> were within the standards sets by the regulatory organizations. Statutory guidelines for VOCs are not available, hence GLC of VOCs was not compared.

For Scenario 2, the 1-hour, 8-hour and 24-hour maximum emission emitted for NO<sub>2</sub> and SO<sub>2</sub> were within the standards sets by the regulatory organizations. The WHO guideline of 4 mg/m<sup>3</sup> for the 24-hour concentration of CO was breached under this scenario by 150% in Kebbi, Kaduna, and Zamfara States whereas the USEPA standards of 9 ppm (approximately 10.3 mg/m<sup>3</sup>) for the 8-hour concentration of CO was breached by 387% in Kebbi and Kaduna states and by 193% in Zamfara State. The breakdown of the percentage increase in average concentrations of CO above the WHO and USEPA thresholds is presented in Table 3.



Table 2: Ground-level concentrations of pollutants ( $\mu\text{g}/\text{m}^3$ ) from the AERMOD model

	Pollutant concentrations ( $\mu\text{g}/\text{m}^3$ )					
	Scenario 1		Scenario 2		Scenario 3	
	Min	Max	Min	Max	Min	Max
CO (1-hr)	908	90,835	3761	376,061	6,271	627,140
CO (8-hr)	140	14,011	1,045	104,523	1,242	124,160
CO (24-hr)	50	5,046	288	28,825	394	39,435
NO <sub>2</sub> (1-hr)	0.8	84.9	2	151	4	433
NO <sub>2</sub> (8-hr)	0.1	11.8	0.3	25.2	0.7	67
NO <sub>2</sub> (24-hr)	0.049	4.97	0.08	8.31	0.2	22.3
SO <sub>2</sub> (1-hr)	11	1,110	41	4,103	90	8,961
SO <sub>2</sub> (8-hr)	2	185	6	586	15	1,493
SO <sub>2</sub> (24-hr)	0.6	55.9	2	203	4	419
VOC (1-hr)	986	98,637	1,495	149,473	2,606	260,555
VOC (8-hr)	188	18,759	201	20,135	412	41,237
VOC (24-hr)	63	6,253	65	6,498	118	11,782

Table 3: Percentage increase in average concentrations of CO above regulatory guidelines

States	WHO guideline - 4 mg/m <sup>3</sup> (24-hr)			USEPA Standards - 10 mg/m <sup>3</sup> (8-hr)		
	Scenario 1	Scenario 2	Scenario 3	Scenario 1	Scenario 2	Scenario 3
Kebbi		150%	150%		387%	385%
Kaduna		150%	150%		387%	191%
Zamfara		150%	138%		193%	191%

For Scenario 3, the 24-hour concentration of CO breached the WHO guideline of 4 mg/m<sup>3</sup> and the 8-hour concentration of USEPA standard of 10.3 mg/m<sup>3</sup> in the three closest states to the source location as presented in Table 3.

This study observed high concentrations of CO in the 24-hour averaging concentrations in scenarios 2 and 3 which exceeded the WHO and USEPA statutory guidelines. The high concentrations of this pollutant may be attributable to the size of biomass burned and the season of burning i.e. dry season. The severity of biomass burning in a location is usually measured with the concentration of CO (Kganyago and Shikwambana, 2020) since CO emission is generally an indicator of biomass burning (Scholes *et al.*, 1996). CO and other non-methane volatile organic carbon are often released during the smoldering stage of a burning process whereas a significant fraction of well-oxidized species such as CO<sub>2</sub> or NO<sub>x</sub> is released during the flaming stage (Manojkumar and Srimuruganandam, 2019). The burning season in Nigeria coincides with the dry harmattan period associated with narrow planetary boundary layer and poor mixing of air masses causing high concentrations of atmospheric gases including CO. Besides, low inversion and low wind speed usually experienced during the burning season reduce ventilation and dispersion of pollutants (Toro *et al.*, 2018) leading to their high concentrations. Increased concentrations of CO in the atmosphere may impact significantly on human health through the displacement of oxygen in the bloodstream and deprivation of the heart, brain, and other vital organs of oxygen which may lead to loss of consciousness and suffocation (Kampa and Castanas, 2008).

Smoke from wildfire plumes not only impacts the immediate environment but also has impacts on far locations at high concentrations. Alonso-Blanco *et al.* (2017) revealed that substantial concentrations of pollutants were observed in an area of Leon city in Spain, about 70km away from the source of fire due to intense subsidence inversion caused by a high-pressure system that prevented vertical dispersion. A similar observation was noted in this study, Kebbi State is approximately 62km away from the fire location and had a CO concentration of 1.5 folds of the WHO guideline for the 24-hr average concentration.

#### 4. CONCLUSION

High concentrations of CO in the 24-hour averaging were detected from the AERMOD dispersion model in Scenarios 2 and 3. These values exceeded the WHO guideline of 4 mg/m<sup>3</sup> for 24-hr and the USEPA standard of 10 mg/m<sup>3</sup> for 8-hr which have negative implications on human health and the environment. The findings from this study have significantly advanced the understanding of savannah ecosystem and the characteristics of the pollutants emitted during biomass burning. The results would be useful in the estimation of emissions specific to the region and help in the development of appropriate mitigation strategies for control.

#### REFERENCES

- Abdulraheem, K., Adeniran, J., & Aremu, A. (2022). Carbon and precursor gases emission from forest and non-forest land sources in West Africa. *International Journal of Environmental Science and Technology*, 1-16.
- Adeniran, J. A., Yusuf, R. O., Fakinle, B. S., & Sonibare, J. A. (2019). Air quality assessment and modeling of pollutants emission from a major cement plant complex in Nigeria. *Atmospheric Pollution Research*, 10(1), 257-266.
- Afzali, A., Rashid, M., Afzali, M., & Younesi, V. (2017). Prediction of air pollutants concentrations from multiple sources using AERMOD coupled with WRF prognostic model. *Journal of Cleaner Production*, 166, 1216-1225.
- Akagi, S., Yokelson, R. J., Wiedinmyer, C., Alvarado, M., Reid, J., Karl, T., Crounse, J., & Wennberg, P. (2011). Emission factors for open and domestic biomass burning for use in atmospheric models. *Atmospheric Chemistry and Physics*, 11(9), 4039-4072.
- Alonso-Blanco, E., Castro, A., Calvo, A. I., Pont, V., Mallet, M., & Fraile, R. (2018). Wildfire smoke plumes transport under a subsidence inversion: Climate and health implications in a distant urban area. *Science of the Total Environment*, 619, 988-1002.
- Andreae, M. O. (2019). Emission of trace gases and aerosols from biomass burning—an updated assessment. *Atmospheric Chemistry and Physics*, 19(13), 8523-8546.
- Cimorelli, A. J., Perry, S. G., Venkatram, A., Weil, J. C., Paine, R. J., Wilson, R. B., Lee, R. F., Peters, W. D., & Brode, R. W. (2005). AERMOD: A dispersion model for industrial source applications. Part I: General model formulation and boundary layer characterization. *Journal of applied meteorology*, 44(5), 682-693.
- de Ferreyro Monticelli, D., Santos, J. M., Dourado, H. O., Moreira, D. M., & Reis Jr, N. C. (2020). Assessing particle dry deposition in an urban environment by using dispersion models. *Atmospheric Pollution Research*, 11(1), 1-10.
- Holmes, N. S., & Morawska, L. (2006). A review of dispersion modeling and its application to the dispersion of particles: an overview of different dispersion models available. *Atmospheric Environment*, 40(30), 5902-5928.
- Jampana, S. S. (2004). *Comparison, Evaluation and Use of AERMOD Model for Estimating Ambient Air Concentrations of Sulfur Dioxide, Nitrogen Dioxide and Particulate Matter for Lucas County*. University of Toledo.
- Kampa, M., & Castanas, E. (2008). Human health effects of air pollution. *Environmental pollution*, 151(2), 362-367.
- Kganyago, M., & Shikwambana, L. (2021). Did COVID-19 Lockdown Restrictions have an Impact on Biomass Burning Emissions in Sub-Saharan Africa? *Aerosol and Air Quality Research*, 21(4), 200470.
- Manojkumar, N., & Srimuruganandam, B. (2019). Assessment of gaseous emissions and radiative forcing in Indian forest fires. *International Journal of Environmental Studies*.
- Rangel, M. G. L., Henríquez, J. R., Costa, J. A., & de Lira Junior, J. C. (2018). An assessment of dispersing pollutants from the pre-harvest burning of sugarcane in rural areas in the northeast of Brazil. *Atmospheric Environment*, 178, 265-281.
- Scholes, R., Ward, D., & Justice, C. (1996). Emissions of trace gases and aerosol particles due to vegetation burning in southern hemisphere Africa. *Journal of Geophysical Research: Atmospheres*, 101(D19), 23677-23682.
- Seangkiatiyuth, K., Surapipith, V., Tantrakarnapa, K., & Lothongkum, A. W. (2011). Application of the AERMOD modeling system for environmental impact assessment of NO<sub>2</sub> emissions from a cement complex. *Journal of Environmental Sciences*, 23(6), 931-940.
- Sun, Q., Miao, C., Hanel, M., Borthwick, A. G., Duan, Q., Ji, D., & Li, H. (2019). Global heat stress on health, wildfires, and agricultural crops under different levels of climate warming. *Environment international*, 128, 125-136.
- Toro, R., Kvakić, M., Klaić, Z. B., & Koračin, D. (2019). Exploring atmospheric stagnation during a severe particulate matter air pollution episode over complex terrain in Santiago, Chile. *Environmental pollution*, 244, 705-714.
- ul Haq, A., Nadeem, Q., Farooq, A., Irfan, N., Ahmad, M., & Ali, M. R. (2019). Assessment of AERMOD modeling system for application in complex terrain in Pakistan. *Atmospheric Pollution Research*, 10(5), 1492-1497.



## Three-box Sequential Modelling of the Emission, Decay and Transportation of Volatile Organic Compounds in Beauty Shops

Sarat Ayodele ATANDA<sup>1\*</sup>, Jamiu Adetayo ADENIRAN<sup>1</sup>, Tunmise Latifat ADEWOYE<sup>1</sup>

<sup>1</sup>Department of Chemical Engineering, University of Ilorin, Nigeria

<sup>1\*</sup> [sarat.morenikeji@gmail.com](mailto:sarat.morenikeji@gmail.com), <sup>2</sup> [adeniran.ja@unilorin.edu.ng](mailto:adeniran.ja@unilorin.edu.ng), <sup>3</sup> [adewoye.tl@unilorin.edu.ng](mailto:adewoye.tl@unilorin.edu.ng)

\*Corresponding author

---

### ABSTRACT

The concentration of Volatile Organic Compounds (VOCs) in indoor environments such as beauty shops where numerous essential oil and scented products are used depends on their emission rate, decay and transportation. Consequently, a better understanding of the dynamic behaviour of this pollutant in the indoor environment improves estimates of human exposure to indoor air pollutants. Single-zone-based models are easy to simulate but are inadequate for predicting exposure in indoor spaces where the source of the pollutant is near. In this study, a three sequential box model which accounts for the mass transfer process in the air, emission from indoor sources, decay and transportation was developed with the assumption of perfect mixing. The *dsolve* package in MATLAB R2019a software was used to solve model equations. Finally, the results of the study revealed that as the VOCs concentration in the box that contains the emission source decreases the concentration in other boxes increases and has a correlation coefficient of 0.9401 with the measured value. Hence, a suitable control strategy can be developed to reduce VOCs concentration in indoor environments.

**Keywords:** Indoor air quality, sequential box model, VOCs, MATLAB and validation.

### 1. INTRODUCTION

Numerous researches and campaigns have been carried out across the globe to quantify, model the dynamic behaviour and determine health risks associated with exposure to Volatile Organic Compounds (VOCs) in the indoor environment. Beauty shops use a lot of cosmetic products such as hair spray, hair dyes, shampoo, creams, lotions, mascara, perfumes, relaxers and many more which contain VOCs (Baghani *et al.*, 2018). Exposure to VOCs in indoor environment where people spend more than 80% of their time (Cetin & Sevik, 2016; Höllbacher, Ters, Rieder-Gradinger, & Srebotnik, 2017; Huang *et al.*, 2016; Hussain, He, Mohamad, & Tao, 2015; Liagkouridis, Cousins, & Cousins, 2014; Paciência, Madureira, Rufo, Moreira, & Fernandes, 2016) where its concentration is higher have direct impacts on human health (Attia, Swasy, Ateia, Alexis, & Whitehead, 2019; Katsoyiannis, Leva, & Kotzias, 2008; Paciência *et al.*, 2016) and the environment (Hussain *et al.*, 2015; Liagkouridis *et al.*, 2014; Zhu, Shena, & Luo, 2020). Every year, there are about 4.2 million deaths as a result of ambient air pollution and 3.8 million deaths as a result of indoor air pollution (WHO, 2021). Given the dangers posed by VOCs both to human health and to the environment, strict regulations have been put in place to regulate VOCs by developed countries (Zhu *et al.*, 2020). Effective control of the level of VOCs in indoor environment require the development of a robust model that describes the dynamic behavior of the pollutant in the indoor air.

Models account for sources of pollutants, the amounts of pollutants emitted, chemical reaction transformations, different meteorological conditions, topographical features and other factors that affect dispersion of pollutants (Babusiaux, 2003). Such models can be used for calculating pollutant concentrations at any given point and for experiments simulations. An air quality model can be simple or complex depending on the assumptions used in formulating them. There are two main types of VOCs models available in literature: physical (analytical) and empirical models.

Physical model is a mass transfer-based model which takes into account the inflow, outflow, deposition and emission sources of the pollutant (Hu, Zhang, Wang, & Little, 2007). Physical model when validated can predict VOC emission for a wide range of conditions using known physical parameters (Hu *et al.*, 2007). Physical model can be formulated by considering the system as either one box or multibox (sequential box). One box model as shown in Figure 2.1 considers the whole space as a masks the three-dimensional variability in exposure and underestimates source proximate exposure intensity (Oladokun & Lin, 2019). One box model presented in Equation 2.1 is suitable in cases

where we have a complete mixing within the whole room or indoor space, uniform source emission and a long time frame modelling (Akintola & Sonibare, 2022; Li & Niu, 2007; Oladokun & Lin, 2019; Ryan, Splengler, & Halfpenny, 1988; Wei, Mandin, & Ramalho, 2018).

A multibox model consists of multiple or sequential boxes as presented in Figure 1.2 which can be arranged horizontally or vertically to exhibit the characteristics of the whole system (Oladokun & Lin, 2019). The sequential box model gives option for the limitations associated with one-box models because it takes into account with preferred direction of flow and the different sources of the pollutant within each box (Ryan *et al.*, 1988). Multibox model as illustrated in Equation 2.2 gives adequate information for pollutant dispersals when compared with full-scale experiments (Oladokun & Lin, 2019) and can be used in the design of predictive controllers. It consists of multiple (sequential) boxes that contain the features of a one-box model; hence, the contaminant in each box is assumed to be well-mixed. Also, each box interacts with the box next to it. Jensen *et al.* (2018) compared one-box, two-box and three-box model for aerosol dispersion, the three box model gave better estimate of the concentrations and the timing of the peaks for fluctuating concentrations. To the best of my knowledge there is no study that modeled the dynamic behavior of VOCs in beauty shops. This study focuses on the three box modeling of VOCs in indoor environment.

## 2. MATERIAL AND METHODS

### 2.1 Model Development

An unsteady state diffusion of VOCs in a typical beauty shop in Nigeria was considered in this research. Most beauty shops consist of different sections which include hair styling, manicure, massage, makeup many more. The beauty shop was divided into three boxes of equal volumes as presented in Figure 2.1 where  $d_1$ ,  $d_2$ , and  $d_3$

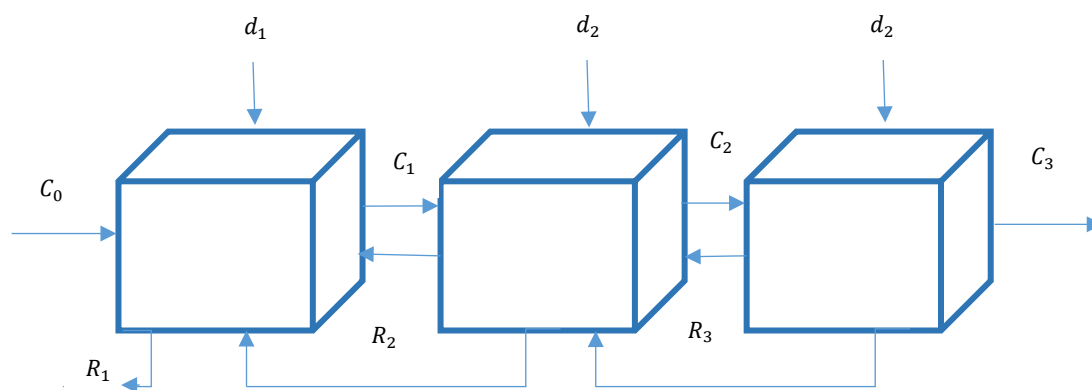


Figure 1: schematic representation of Three-box model

The following assumptions were made in the model development:

1. The boxes have equal volumes  $V_1 = V_2 = V_3$
2. No interaction between the boxes that are far apart; that is there is only interaction between boxes that are beside each other.
3. Deposition in each of the boxes is considered to be negligible due to the volatile nature of the pollutant
4. Flow rate in the boxes are uniform
5. Emission of the VOC in the indoor environment is from box 1

From the first principle the differential equation which governs the generation and decay of VOCs, based on mass balance consideration as shown in Equation 1

$$\text{Rate of change pollutant} = \text{inflow from outdoor} - \text{outflow to outdoor} - \text{deposition rate} + \text{emission rate} + \text{infiltration from adjacent box} - \text{return} \quad (1)$$

The rate of change of concentration of VOCs in box 1, 2 and 3 are represented by Equations 2, 3 and 4, respectively.

$$V_1 \frac{dc_1}{dt} = C_0 F_0 - C_1 F_1 + e_1 - d_1 - R \quad (2)$$

$$V_2 \frac{dc_2}{dt} = C_1 F_1 - C_2 F_2 + e_2 - d_2 - R \quad (3)$$

$$V_3 \frac{dc_3}{dt} = C_2 F_2 - C_3 F_3 + e_3 - d_3 - R \quad (4)$$

Where

$C_0$ =initial concentration of VOCs in box 1

$C_1, C_2$  and  $C_3$ = concentration of VOCs leaving box 1, 2 and 3 respectively

$V_1, V_2$  and  $V_3$ =volume of the box 1, 2 and 3 respectively

$F_0$ =flowrate into the box 1 from outdoor air  
 $F_1, F_2$  and  $F_3$ =flowrate out of the box 1, 2 and 3, respectively  
 $d_1, d_2$  and  $d_3$ =deposition rate in box 1, 2 and 3  
 $R$ =return  
 $e_1$ =emission from box 1, 2 and 3

The emission rate of VOCs in the indoor environment from the surface source to the gas phase is given by Equation 5

$$E_i = h_m A (C_s - C_i) \quad (5)$$

Where  $E_i$  is the emission from the box but for simplicity it was that the pollutant was emitted in the first box only.  $h_m$  is the specific source /air mass transfer coefficient which can be estimated with Equation 6-9.  $D_a$  represents the diffusion coefficient ( $m^2/s$ )

$$h_m = \frac{D_a}{l} \times Sh \quad (6)$$

$$Sh = 0.664 Sc^{1/3} Re^{1/2} \quad (7)$$

$$\text{Where } Sc = \left( \frac{\mu}{\rho D_a} \right) \quad (8)$$

$$Re = \frac{\rho ul}{\mu} \quad (9)$$

$L(m)$  is the length, and  $\mu$  kg/ms is the dynamic viscosity of the air (Wei *et al.*, 2018). The values of this parameters used in the simulation

VOCs convert spontaneously to secondary pollutants in the presence of light. we can assume that most of the emitted Semi Volatile Organic Compounds (SVOC) will sorb onto available surfaces that will act as secondary continuous sources. This chemical reaction may significantly reduce the concentration of VOCs and increase the concentration of the reaction product (Wei, Mandin, & Ramalho, 2017). Only the surface sources were considered in the model and some of the VOCs lost as a result of chemical reaction for this case was taken to be first order. The rate of disappearance of VOCs is given by Equation 10 and the rate constant was calculated from concentration data obtained in the experiment described in the next subsection.

$$R = K C_i \quad (10)$$

Considering all the parameters the general Equation becomes Equation 11

$$V_i \frac{dC_i}{dt} = C_i F_i - C_{i+1} F_{i+1} - h_m A (C_s - C_i) - K C_i \quad (11)$$

## 2.2 Experimental Procedure

An unhabited room ( $2.72 \times 2.82 \times 2.00$ )  $m^3$  with an air conditioning unit was chosen as the experimental room because it has no major indoor and outdoor pollution generating sources except the aerosols being released from the hair spraying products. Five bestselling brands of hair spray products were used separately to carry out the experiment. Measurements were taken in the experimental room under atmospheric conditions. The hair sprays were sprayed at the centre of the room at the height of 1.5 m above the ground and the samplers were placed 40 cm away from where it is sprayed the total VOCs were measured with an insitu MultiRAE gas monitor (Model PGM50-5P) with detection limit of 0-2,000 ppm measurement of VOCs with 0.1 ppm resolution Instantaneous readings were taken initially when it was sprayed, 15 min, 1 hr, and 3hrs after spraying.

## 3.0 RESULTS AND DISCUSSION

### 3.1 MATLAB Solution of the Three-box Model

The solution to the sequential box model proposed in this study computes the spatial variation of the concentration with a time of the sequential box model using the *dsolve* (solver) package for simultaneous ordinary differential equation in MATLAB 2019a environment. The model solution was obtained for 1h and 24 h for three scenarios where the source of pollution is in one box, or two boxes and all the three boxes simulations were presented in Figures 2 and 3, respectively. The first scenario consists of three cases that are when the pollutant is either in boxes 1, 2 or 3, three cases were also considered for the second scenario which includes the pollutant emission source in boxes 1 and 2, 2 and 3 and 1 and 3. In all scenarios considered the profile of the box that contained the pollutant source showed a correlation with the experimental values obtained.

## Scenario 1

### Case 1: when the emission source is in box 1

The change in concentration with time when the source of the pollutant is from the first box only is presented in Figures 4.1 and 4.2 following an hour and 24 h from the start of the VOCs emission under room temperature and pressure. It was observed from Figure 4.1 that the highest concentration of the VOCs was  $5.6 \times 10^5 \mu\text{g}/\text{m}^3$  and was obtained at box 1 where the VOC emission source is located. The concentration continued to decrease for about 20 mins to a value of  $5.0 \times 10^5 \mu\text{g}/\text{m}^3$  while boxes 2 and 3 showed a sharp rise in concentration before they begin to decrease as a result of ventilation. It was found that the concentration of the VOCs in box 2 is higher than what was obtained in box 3 because it was closer to the emission source of the VOCs. The concentration in box 2 and 3 were higher than what was obtained in box 1 between 10 to 20 mins indicating that with dispersion and photocatalytic oxidation of VOCs the concentration of areas closer to the source decreases while that farther away from the source increase as reported by Davardsoot and Kahfooroushan (2018). The concentration of VOCs became stable with time in each of the boxes.

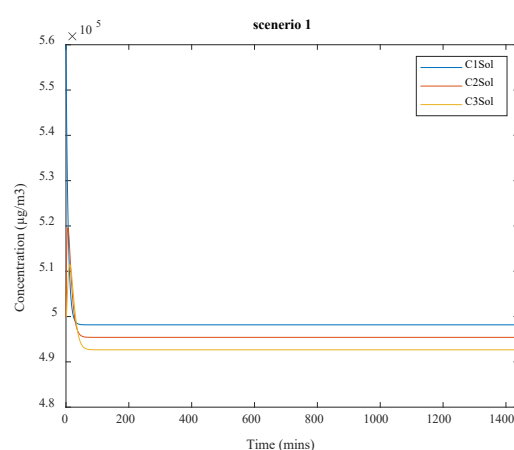
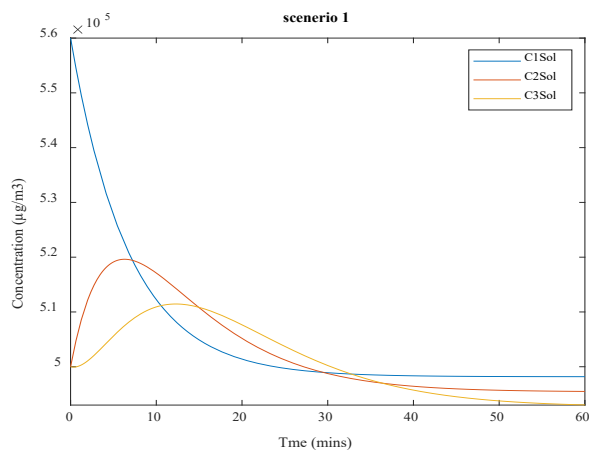


Figure 2: Predicted concentration up to 1h Figure 3: Predicted concentration up to 24h

### Case 2: when the pollutant emission source is in box 2

When the emission source was in the second box only the result obtained for the simulation was shown in Figures 4 and 5 following an hour and 24 hours from the start of the VOCs emission under atmospheric conditions. As observed in case 1 the highest concentration was obtained in box 2 as shown in Figures 6 and 7 The concentration value declined for about 15 mins while box 3 showed a sharp rise in concentration before they begin to decrease due to ventilation. The concentration VOC on the other hand in Box1 showed only a slight difference, this can be attributed to the preferred direction of wind flow (Ryan *et al.*, 1988) and photocatalytic degradation of the VOCs in that box.

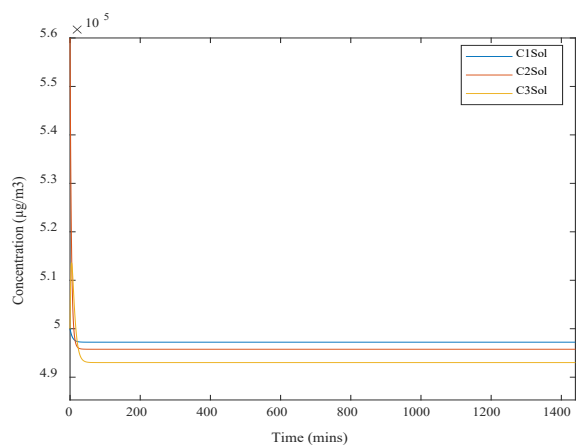
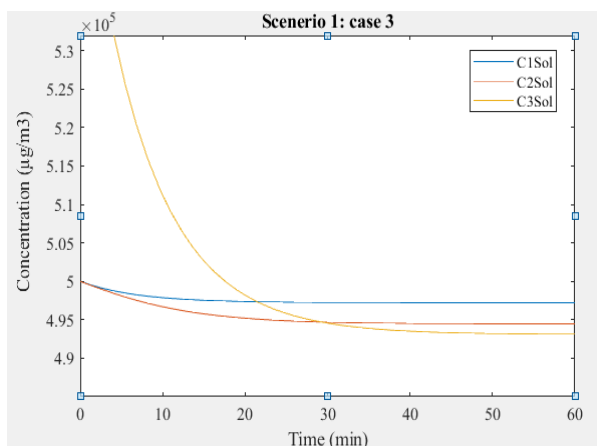


Figure 4: Predicted concentration up to 1hr Figure 5: Predicted concentration up to 24h

### Case 3: when the pollutant source is in box 3

Figures 6 and 7 showed when the source of pollutant in box 3 it was observed that box 3 showed a decrease in concentration while boxes 1 and 2 did not show a significant difference in concentration which can also be attributed to the direction of air. It can be deduced from this result that The dispersion of VOCs has a strong relationship with the ventilation and airflow because it is the only means of mixing the VOCs in confined spaces apart from convection. The result obtained from this study agrees with the findings of Jensen *et al.* (2018).

## Three-box Sequential Modelling of the Emission, Decay and Transportation of Volatile Organic Compounds in Beauty Shops

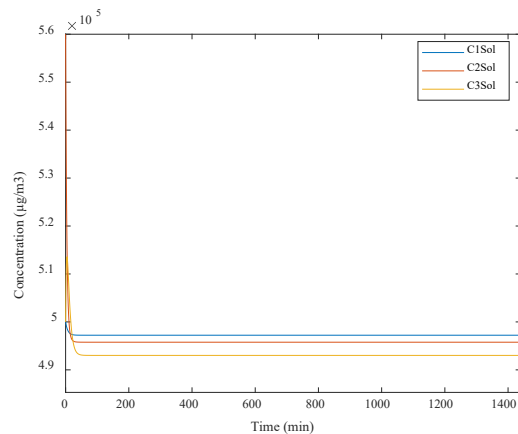


Figure 6: Predicted concentration for 1h

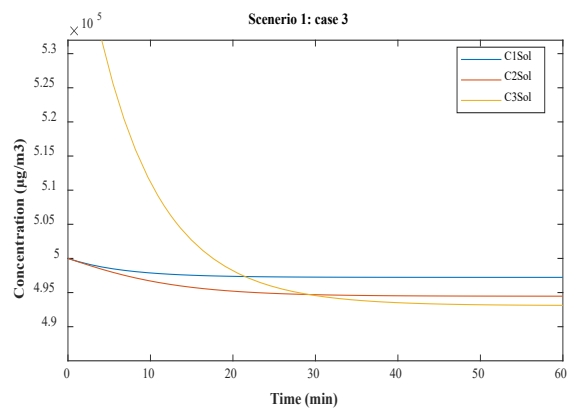


Figure 7: Predicted concentration for 24h

### Scenario 2 (emission source is from two boxes)

The solution obtained when the source of the pollutant is in boxes 1 and 2 is presented in Figures 4.7 and 4.8. the concentration of VOCs decreased until it attained a steady state at about 25 mins. A sharp rise was observed in box 3 until there was a decrease in the concentration.

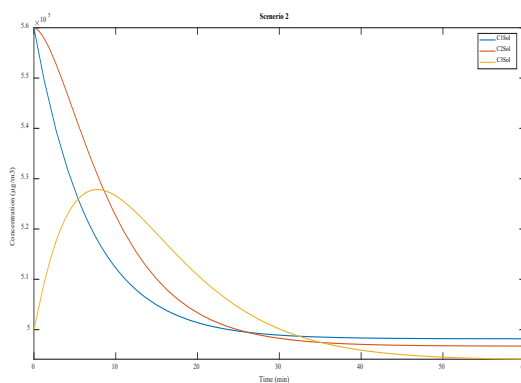


Figure 8: Predicted concentration up to 1h

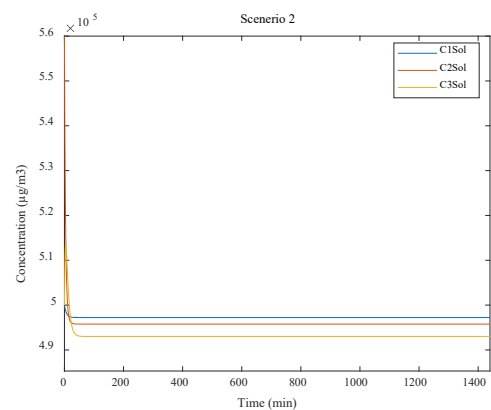


Figure 9: Predicted concentration up to 24h

### Scenario 3 emission source is from three boxes

The concentration of VOCs as shown in Figure 4.10 and 4.11 obtained in scenario 3 decreased slowly in boxes 1 and 2 up to 10 mins before attaining a steady state. There was a sharp decrease in box 3 on the other hand which can be attributed to its closeness to a ventilation source.

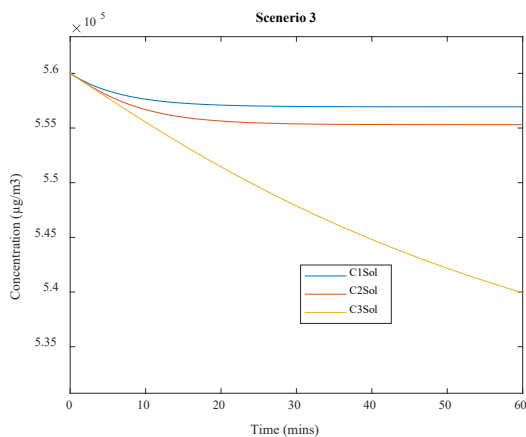


Figure 10: Predicted concentration up to 1h

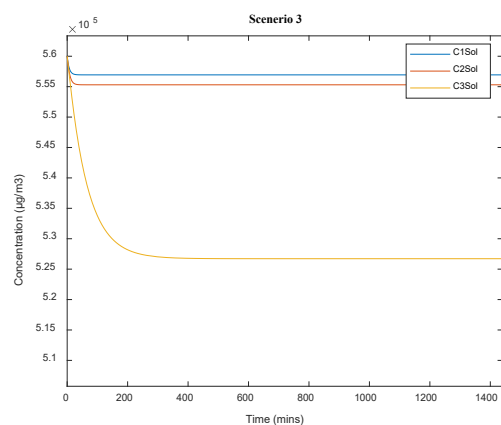


Figure 11: Predicted concentration up to 24h

The measured concentration from the experiment and predicted concentrations from the model developed are shown in Figure 12. The Pearson's correlation coefficient ( $R^2$ ) was obtained to be 0.9401 indicating a strong association between the VOCs concentration measured and predicted concentration. The concentration profile to what was obtained for all scenarios is similar to what was obtained in the experiment which conform with what was obtained by Jensen *et al.* (2018). It can be deduced that the predicted concentration from the three boxes agrees with the measured concentration from the experimental room. The performance of the three-box model may be ascribed to exchange velocity and other dynamical parameters (Dai, Cai, Zhong, & MacKenzie, 2021). An increase in the number of local concentration gradients gives a better description of the flux balance in the multi-box model and better modelling results.

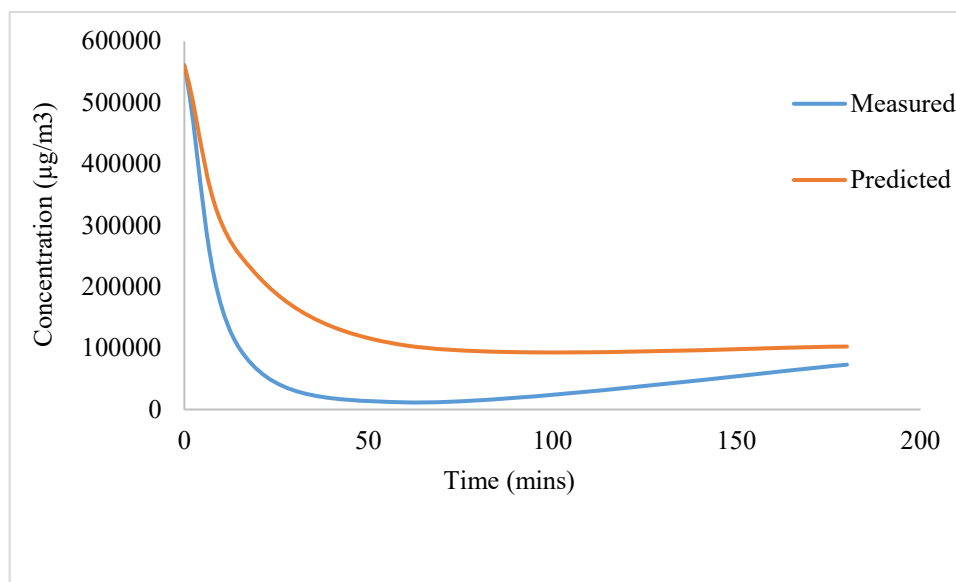


Figure 12: Measured and predicted concentration of VOCs

#### 4. CONCLUSION

Sequential box models can be used to quantify the effect of air pollutants on human health and design/propose a suitable control strategy. Ordinary Differential Equations with a solution of concentrations varying with time can give an insight into the dynamic behaviour of VOCs in an indoor environment. These model equations developed contain either emission or reaction term or both terms using the mass balance approach. The *dsolve* solver in Matlab 2019a gave a result which has the same profile as the experimental results obtained in the experimental room considered in this study in obtaining numerical solutions when studying the dynamic behaviour of VOCs in confined spaces. The concentrations of air pollutants decrease with time in the box that contains the emission source and remains constant at a point when a steady state is attained. The boxes that did not contain the emission showed a rise and then reduced gradually until a steady state is attained. The dispersion of the VOCs was through a preferred direction of flow. Further study should be carried out on the influence of different ventilation modes

#### REFERENCES

- Akintola, O., & Sonibare, J. (2022). Advection-diffusion model for indoor-outdoor exchange of air pollutants from electric power generators servicing buildings. *Cogent Engineering*, 9(1), 2076321.
- Attia, M., Swasy, M., Ateia, M., Alexis, F., & Whitehead, D. (2019). Periodic mesoporous organosilica nanomaterials for rapid capture of VOCs. *communication*, 1-3.
- Babusiaux, D. (2003). Allocation of the CO<sub>2</sub> and Pollutant Emissions of a Refinery to Petroleum Finished Products. *Oil & Gas Science and Technology*, 58(6), 685-695.
- Baghani, A. N., Rostami, R., Arfaenia, H., Hazrati, S., Fazlzadeh, M., & Delikhoon, M. (2018). BTEX in indoor air of beauty salons: risk assessment, levels and factors influencing their concentrations. *Ecotoxicology and Environmental Safety*, 159, 102-108.
- Cetin, M., & Sevik, H. (2016). Measuring the impact of selected plants on indoor CO<sub>2</sub> concentrations. *Polish Journal of Environmental Studies*, 25(3), 973-979.
- Dai, Y., Cai, X., Zhong, J., & MacKenzie, A. R. (2021). Modelling chemistry and transport in urban street canyons: Comparing offline multi-box models with large-eddy simulation. *Atmospheric Environment*, 264, 118709.
- Davardsoot, F., & Kahfooroushan, D. (2018). Modelling the dispersion of Volatile Organic Compounds in indoor environment. *chemical engineering and technology*, 1-22.



- Höllbacher, E., Ters, T., Rieder-Gradinger, C., & Srebotnik, E. (2017). Emissions of indoor air pollutants from six user scenarios in a model room. *Atmospheric Environment*, *150*, 389-394.
- Hu, H. P., Zhang, Y. P., Wang, X. K., & Little, J. C. (2007). An analytical mass transfer model for predicting VOC emissions from multi-layered building materials with convective surfaces on both sides. *International Journal of Heat and Mass Transfer*, *50* 2069–2077.
- Huang, Y., Hang, S. S., Lu, Y., Niu, R., Xu, L., Cao, J., & Lee, S. (2016). Removal of Indoor Volatile Organic Compounds via Photocatalytic Oxidation: A Short Review and Prospect. *molecules*, *21*(56), 1-20.
- Hussain, M., He, Y.-L., Mohamad, A. A., & Tao, W.-Q. (2015). A new hybrid algorithm for numerical simulation of VOC emissions using single-layer and multilayer approaches *Taylor and Francis*, *67*, 211-229.
- Jensen, A. C., Dal Maso, M., Koivisto, A. J., Belut, E., Meyer-Plath, A., Van Tongeren, M., . . . Toftum, J. (2018). Comparison of geometrical layouts for a multi-box aerosol model from a single-chamber dispersion study. *Environments*, *5*(5), 52.
- Katsoyiannis, A., Leva, P., & Kotzias, D. (2008). VOCs and carbonyl emission from carpets: A comparative study using four types of environmental chambers. *Journal of hazardous material*, *152*, 671-675.
- Li, F., & Niu, J. (2007). Control of volatile organic compounds indoors—development of an integrated mass-transfer-based model and its application. *Atmospheric Environment*, *41*(11), 2344-2354.
- Liagkouridis, L., Cousins, I. T., & Cousins, A. P. (2014). Emissions and fate of brominated flame retardant in indoor environment: A critical review of modelling approaches. *Elsevier*, 1-20.
- Oladokun, M., & Lin, Z. (2019). Dynamic sequential box modelling of inhalation exposure potential in multibed patient ward: Validation and baseline case studies. *Building and Environment*, *161*(106241), 1-14.
- Paciência, I., Madureira, J., Rufo, J., Moreira, A., & Fernandes, E. d. O. (2016). A Systematic Review of Evidence and Implications of Spatial and Seasonal Variations of Volatile Organic Compounds (VOC) in Indoor Human Environments *Journal of toxicology and environmental Health*, 1-15.
- Ryan, B., Splengler, J., & Halfpenny, P. (1988). Sequential box model for indoor air quality: application to airliner cabin quality *Atmospheric Environment*, *22*(6), 1031-1038.
- Wei, W., Mandin, C., & Ramalho, O. (2017). Reactivity of semivolatile organic compounds with hydroxyl radicals, nitrate radicals, and ozone in indoor air. *International Journal of Chemical Kinetics*, *49*(7), 506-521.
- Wei, W., Mandin, C., & Ramalho, O. (2018). Influence of indoor environmental factors on mass transfer parameters and concentrations of semi-volatile organic compounds. *Chemosphere*, *195*, 223-235.
- WHO. (2021). Air pollution. Retrieved from [https://www.who.int/health-topics/air-pollution#tab=tab\\_1](https://www.who.int/health-topics/air-pollution#tab=tab_1)
- Zhu, L., Shena, D., & Luo, K. (2020). A critical review on VOCs adsorption by different porous materials: Species, mechanisms and modification methods *Journal of Hazardous Materials*, *389*(122102), 1-23.



## Fuzzy Logic Controller Design for Temperature Control of Servo Systems using Simulink

Ajiboye OSUNLEKE<sup>1\*</sup>, Ayorinde BAMIMORE<sup>1,2</sup>, Sunrise EZEKIKWU<sup>2,3</sup>, Ismail OYEHAN<sup>1,4</sup>, Nafees SANNI<sup>1,5</sup>

<sup>1</sup>Department of Chemical Engineering, Obafemi Awolowo University, Ile-Ife, Nigeria

<sup>2</sup>Andela, USA

<sup>3</sup>Department of Process and Operations, Dangote Petroleum Refinery and Petrochemicals FZE, Lagos

<sup>1\*</sup>[aosunlek@oauife.edu.ng](mailto:aosunlek@oauife.edu.ng), <sup>2</sup>[abamimore@oauife.edu.ng](mailto:abamimore@oauife.edu.ng), <sup>3</sup>[ezesunrise@gmail.com](mailto:ezesunrise@gmail.com), <sup>4</sup>[oyesmiling@gmail.com](mailto:oyesmiling@gmail.com),

<sup>5</sup>[nafeesolaitan@gmail.com](mailto:nafeesolaitan@gmail.com), <sup>6</sup>[ibrahimabiolabdmus@yahoo.com](mailto:ibrahimabiolabdmus@yahoo.com)

\*Corresponding author

---

### ABSTRACT

*In this paper, the versatility in the applications of a fuzzy logic controller (FLC) in control systems was utilized in the temperature control of a servo system using Simulink. Servo system is one of the automatic control systems employed in manipulating the rotation angle (or displacement) of the controlled object so that it can automatically, continuously, and accurately respond to the input command in a feedback control loop. A servo control loop is one which responds to a change in setpoint which changes as a function of time, and in which the controlled variable must track the setpoint. The aim of this work is to employ fuzzy logic modelling approach to design controllers for temperature control of heat chamber, CSTR and Distillation columns. Model of a fuzzy logic controller was designed using the Fuzzy Logic Toolbox in MATLAB and the models of the systems required test the performance of the controller designed were built using Simulink. The performance of the fuzzy controller was evaluated based on the rise time, overshoot, and steady state error. Simulations were carried out for each system with step changes of +1, -1, +5 and -5 applied to the setpoint. The results obtained indicated that the controllers designed using Fuzzy Logic were robust and can be utilized successively for temperature control of systems.*

**Keywords:** Fuzzy logic controller, Servo system, Simulink, Temperature control, Non-isothermal CSTR.

### 1. INTRODUCTION

Temperature is one of the most important quantities measured and controlled in the industry and household appliances as most physical, electronic, chemical, mechanical, and biological systems are affected by temperature. A good performance servo system requires high displacement accuracy, good stability, high positioning accuracy, fast response, wide speed range among others. It is usually a closed-loop control system with negative feedback, and in some cases open-loop control can be used to achieve its function. Some processes work well only within a narrow range of temperatures while others perform best within wide temperature ranges; in order to keep temperature of processes within specified limits or constant values, controllers are often used (Ramanathan, 2014). Different types of controllers can be applied to a temperature control process which include fuzzy logic controller (FLC), Proportional Integral derivative (PID) controller, neural networks, and other classical controllers. Of all these controllers, fuzzy logic controllers have some advantages compared to other classical controllers in terms of high stability of control, low cost, and the possibility to design without knowing the exact mathematical model of the process.

A fuzzy controller is based on fuzzy logic built on the use of fuzzy set theories (Aguilar *et al.*, 2014; Zimmermann, 2001; Bharathi and Kumar, 2016; Abdo-Allah *et al.*, 2018; Awelewa *et al.*, 2021; Castillo *et al.*, 2020). The controller method constitutes a way of converting linguistic control strategy into an automatic control strategy by generating a rule base which controls the behaviour of a system. Fuzzy logic provides a remarkably simple way to draw definite conclusions from vague, ambiguous, or imprecise information.

Fuzzy logic controllers have been applied in control systems ranging from household appliances to industrial processes. A fuzzy logic controller implements human reasoning that has been programmed into fuzzy logic language (fuzzification, membership functions, rules and defuzzification) for controlling a plant (Castillo *et al.*, 2020).

## 2. MODEL DEVELOPMENT

The design of the fuzzy controller was characterised by the fuzzy methodology. For designing a fuzzy control system from scratch, more or less heuristic methods are available. The steps used in designing the fuzzy logic control system are as follows.

- i. Identify the variables of the plant which includes its inputs, outputs, and states.
- ii. Partition the universe of discourse of each variable into a number of fuzzy subsets, assigning each a linguistic label.
- iii. Assign or determine a membership function for each fuzzy subset.
- iv. Assign the fuzzy relationships between the inputs or states' fuzzy subsets and the outputs' fuzzy subsets, thus forming the rule base.
- v. Fuzzify the inputs to the controller.
- vi. Use fuzzy approximate reasoning to infer the output contributed from each rule.
- vii. Aggregate the fuzzy outputs recommended by each rule.
- viii. Apply defuzzification to form a crisp output.

The design and simulation of the fuzzy controller was supported by specific components characteristic of a fuzzy logic controller (FLC). The control system structure for the fuzzy controller is shown in Figure 1.

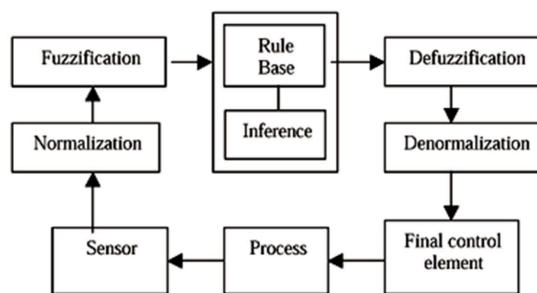


Figure 1: Fuzzy logic control structure

The fuzzy logic toolbox in MATLAB was used in defining the parameters of the controller. There are primarily five graphical user interface (GUI) tools for the building, editing, and observing of the fuzzy inference system in the toolbox. These are the Fuzzy Inference System (FIS) editor, Membership Function (MF) editor, Rule Editor, Rule Viewer, Surface Viewer. These GUIs are dynamically linked such that if changes are made in any one of the editors, the effect is implemented and seen on other GUIs. The input variables of the fuzzy logic controller for a thermal system are the temperature error ( $e$ ) and the rate of change of the error,  $\frac{\partial e}{\partial t}$ . The output variables are the heating (Heat) and cooling (Cool) system voltages to the actuator of the final control element of the control system. Both the error variable and its derivative variables were taken into consideration. It won't be an accurate measurement of its real-time nature especially with its rapid change in response of the error variable if the controller works with the consideration of error variable alone.

Reference point command is to be set in order to derive the first input variable, error,  $e$ , which is the difference between the set-point (reference point) and the current temperature of the system (in terms of feedback from the encoders over the sampling time). The second input variable defined to be the error derivative,  $\left(\frac{\partial e}{\partial t}\right)$ , is the rate of change of error parameter which contributes to the inference mechanism and the overall algorithm by providing an indicative estimate rate of change of temperature of the system over the last sampling time interval. Although it is possible to use a single instantaneous error parameter without knowing its rate of change, this cripples the system's ability to minimize overshoot for step inputs.

$$\frac{\partial e}{\partial t} = \frac{\partial(\text{sp} - T(t))}{\partial t} \quad (1)$$

The universe of discourse for the input variables error and error change are partitioned into seven and five intervals respectively. The universe of discourse for the output variables Heat and Cool are partitioned into five variables each. The linguistic variables for the inputs and outputs are

Error: Negative Large (NL), Negative Medium (NM), Negative Small (NS), Zero (Z), Positive Small (PS), Positive Medium (PM) and Positive Large (PL)

Error change: Negative Large (NL), Negative Small (NS), Zero (Z), Positive Small (PS) and Positive Large (PL)

Heat: Close (C), Steady (S), Heat Slow (HS), Heat Medium (HM) and Heat Fast (HF)

Cool: Close (C), Steady (S), Cool Slow (CS), Cool Medium (CM) and Cool Fast (CF).

The membership function for the inputs (error and error rate) and the output is the triangular membership function (trimf) and trapezoidal membership function (trapmf). These membership functions are defined as:

$$\text{TRIMF: } \mu_x(x; a, b, c) = \begin{cases} (x-a)/(b-a) & a < x < b \\ (c-x)/(c-b) & b < x < c \\ 0 & \text{otherwise} \end{cases} \quad (2)$$

$$\text{TRAPMF: } \mu_x(x; a, b, c, d) = \begin{cases} (x-a)/(b-a) & a < x < b \\ 1 & b < x < c \\ (d-x)/(d-c) & c < x < d \\ 0 & \text{otherwise} \end{cases} \quad (3)$$

The rule base for the controller is tabulated in Table 1 while the membership functions are represented in Figures 2 and 3.

Table 1: Rule base for the fuzzy logic controller\*

Error → Error Change ↓	NL	NM	NS	Z	PS	PM	PL
NL	C	C	CM	C	CS	C	CS
NS	C	C	CM	C	C	S	C
Z	C	C	CM	C	C	HS	C
PS	C	C	CS	C	S	C	C
PL	C	C	S	C	C	C	HS

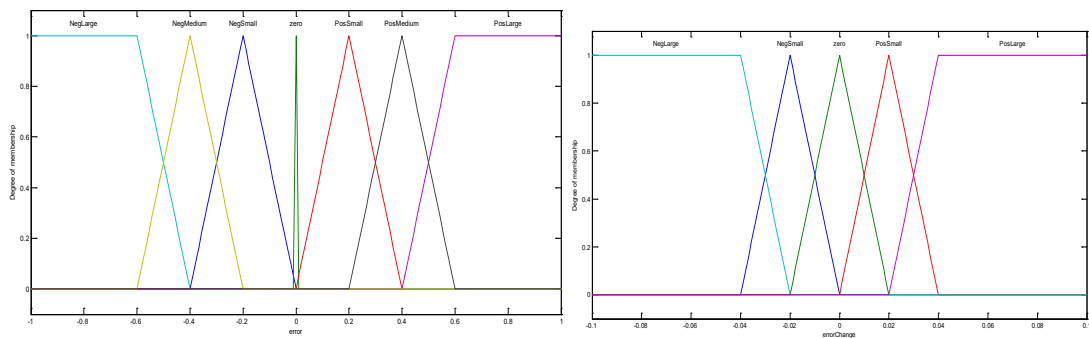


Figure 2: Membership function for (a) the input 'error' and (b) Error change

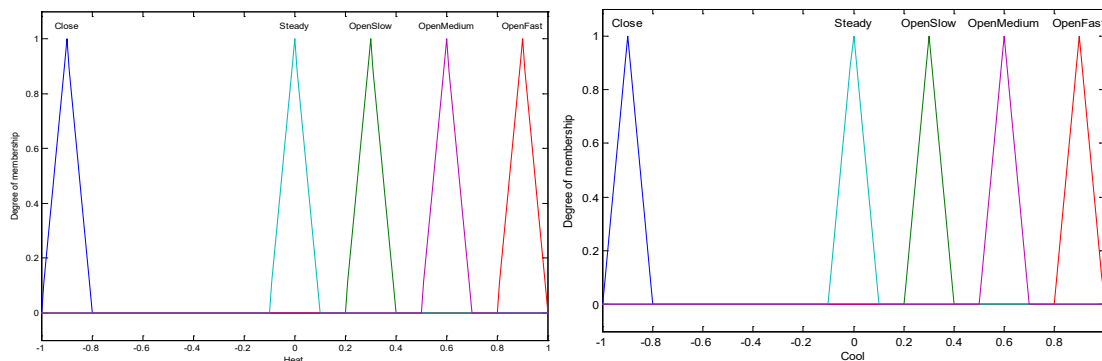


Figure 3: Membership function for (a) the output 'Heat' and (b) the 'Cool'

The fuzzy surface view illustrating the fuzzy rules are shown in Figure 4.

\* The first in each column represents the command for 'Heat' while the second represents the command for 'Cool'

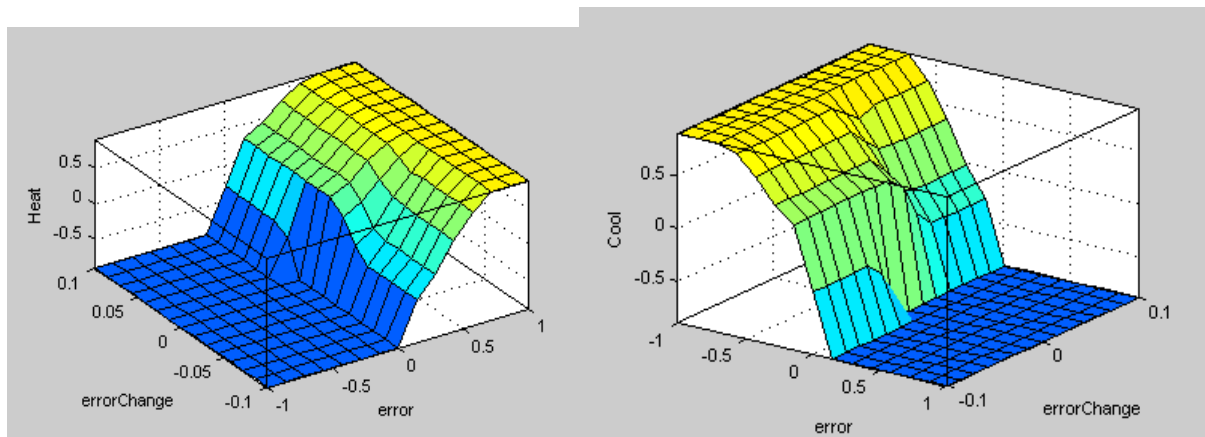


Figure 4: Fuzzy surface for the output (a) 'Heat' and (b) 'Cool'

### 3. CASE STUDIES

The dynamic simulation software, Simulink, in MATLAB was exploited in the development of models of practical dynamic systems with the FLC controller in place. The systems developed possess varying dynamics. The dynamic equations were obtained by mathematical modelling of the systems from first principle with appropriate assumptions. These systems include:

#### 3.1 A Heat Chamber

A closed chamber with a derived dynamic equation given by:

$$\frac{dT}{dt} = \frac{F_h}{V_C} (T_h - T) + \frac{F_c}{V_C} (T_h - T) + \frac{\rho_{Co2} C_{pCo2} F_{Co2}}{\rho C_p V_C} (T_{Co2} - T) \quad (4)$$

#### 3.2 A Heat exchanger

A stirred steam-heated vessel () with a derived dynamic equation given by:

$$\frac{dT}{dt} = \frac{F}{V_l} (T_i - T) + \frac{\lambda_s}{\rho_l C_{pl} V_l} S \quad (5)$$

#### 3.3 A non-isothermal CSTR for the reaction:



$$r_C = -r_A = \frac{dC_A}{dt} = k C_A C_B \quad (6)$$

$$k = k_0 e^{-E/R(1/300 - 1/T)} \quad (7)$$

with a derived dynamic equation given by:

$$\frac{dT}{dt} = \frac{F}{V} (T_0 - T) + \frac{H_R k C_A^2}{\rho_l C_p} - \frac{U A_H}{\rho_l C_p V} (T - T_j) \quad (8)$$

The properties of these systems were stored in MATLAB's M-files, wherefrom the simulations were initiated. The systems were simulated using Simulink. Varying step changes in set-point were applied to each system and the response of the systems' output variables with time were obtained. Figures 5-7 show the systems in Simulink blocks.

## 4. RESULTS AND DISCUSSION

Based on the existing MATLAB Fuzzy Logic Toolbox, the controller was implemented and simulated successfully in Simulink and the results were obtained as shown in the figures below. As noted, the performance of the fuzzy controller was evaluated based on the following indices: rise time, overshoot, and steady state error. The results obtained from the simulations of all the cases considered are shown in Table 2.

The various output responses of the cases considered are shown in Figures 8 through 15. Simulation of the chamber model gave an overshoot of 0% of the step change for all step changes of +1, -1, +5 and -5. The rise times were 7.6s, 8.1s, 26.1s and 27.0s for a step change in set-point of +1, -1, +5 and -5 respectively. The responses showed that the system is robust to set-point tracking.

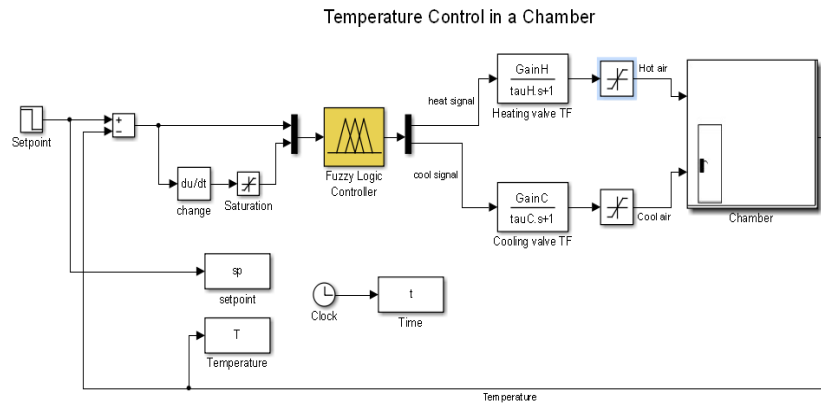


Figure 5: Fuzzy logic temperature-controlled Simulink model of a chamber

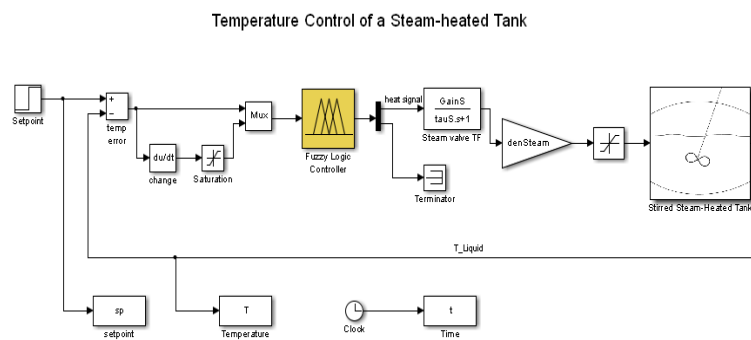


Figure 6: Simulink model of a fuzzy logic-controlled steam-heated vessel

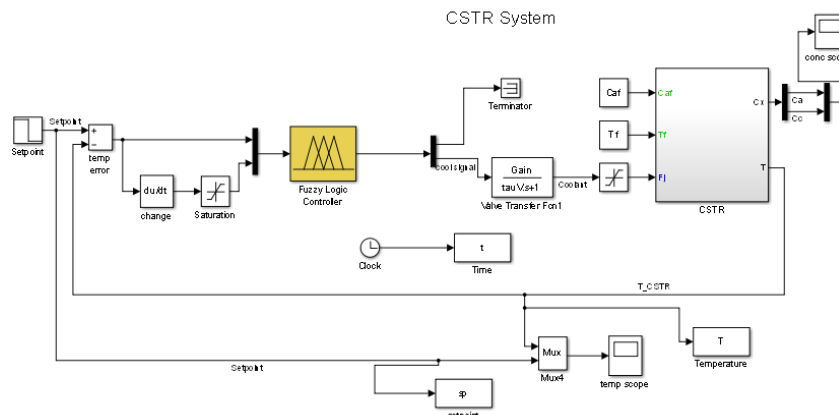


Figure 7: Simulink model of a fuzzy logic-controlled of a non-isothermal CSTR

Table 2: Result obtained for a change in set-point of the systems

Model	Overshoot (%)				Rise time (s)				Settling time (s)			
	+1	-1	+5	-5	+1	-1	+5	-5	+1	-1	+5	-5
Chamber	0.0	0.0	0.0	0.0	9.3	7	18	15.8	8	10	28	25.5
House	0.1	0.2	0.8	0.3	4.0	11.0	5.0	57.0	4.4	17	6.3	57.2
CSTR	8.0	8.0	0	4.0	10.0	2.0	50.0	4.0	10	2.5	52	6

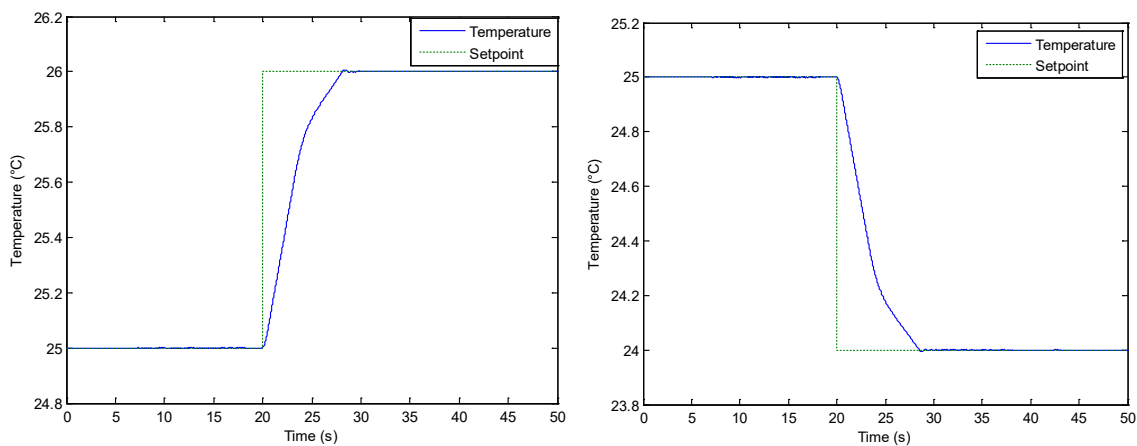


Figure 8: Unit step change of (a) (+1) and (b) (-1) in closed chamber set-point temperature

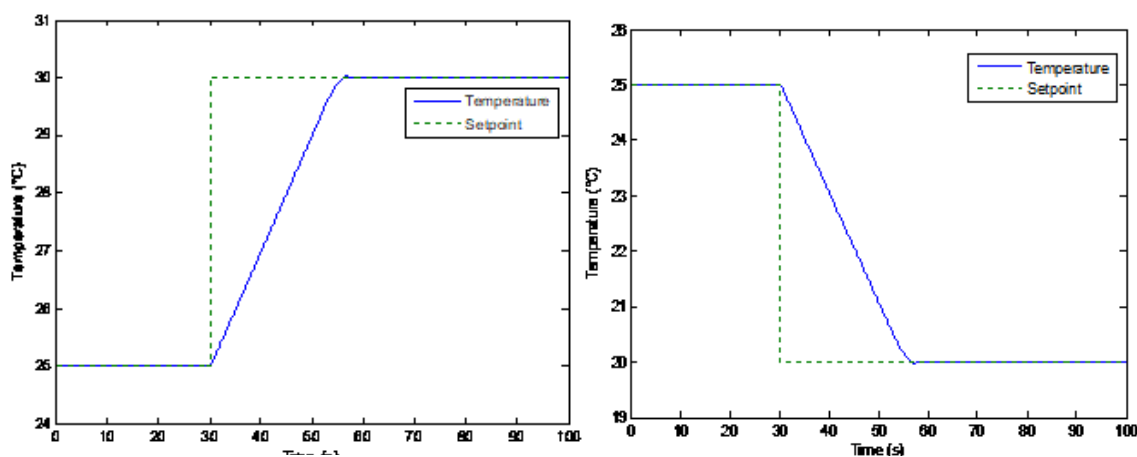


Figure 9: (a) Step change (+5), (b) Step change (-5) in closed chamber set-point temperature

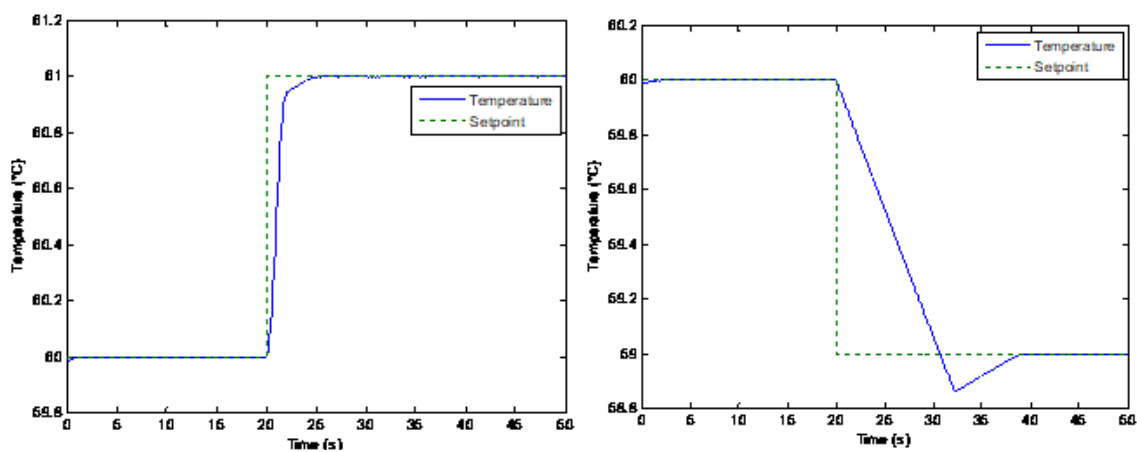


Figure 10: Unit step change of (a) (+1) and (b) (-1) in in set-point temperature (stirred steam-heated vessel)

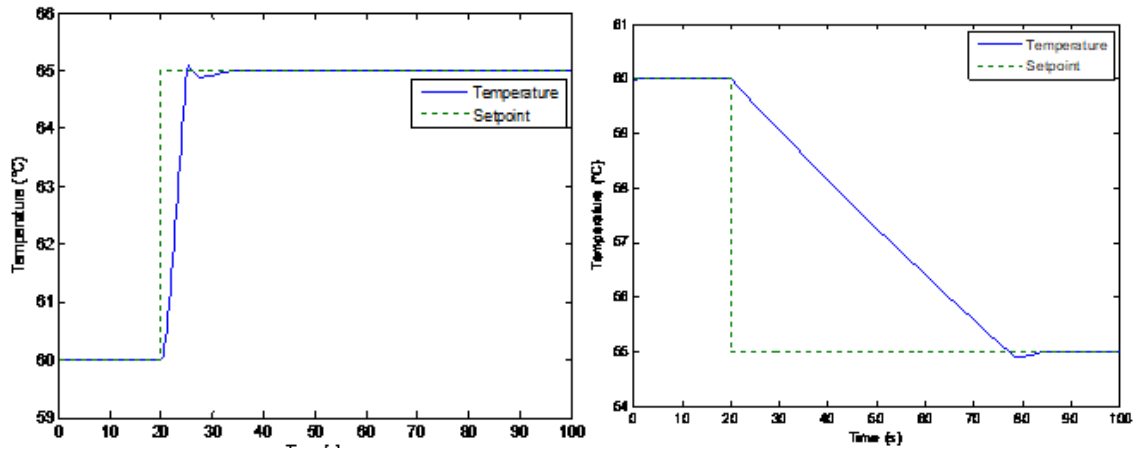


Figure 11: Unit step change of (a) (+5) and (b) (-5) in in set-point temperature (stirred steam-heated vessel)

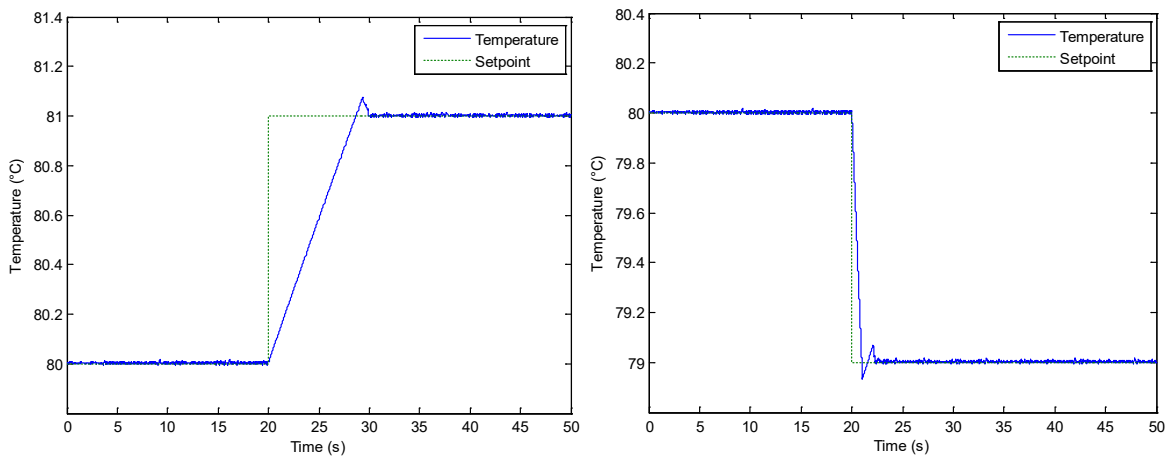


Figure 12: Step change of (a) (+1) and (b) (-1) in set-point temperature (Non-isothermal CSTR)

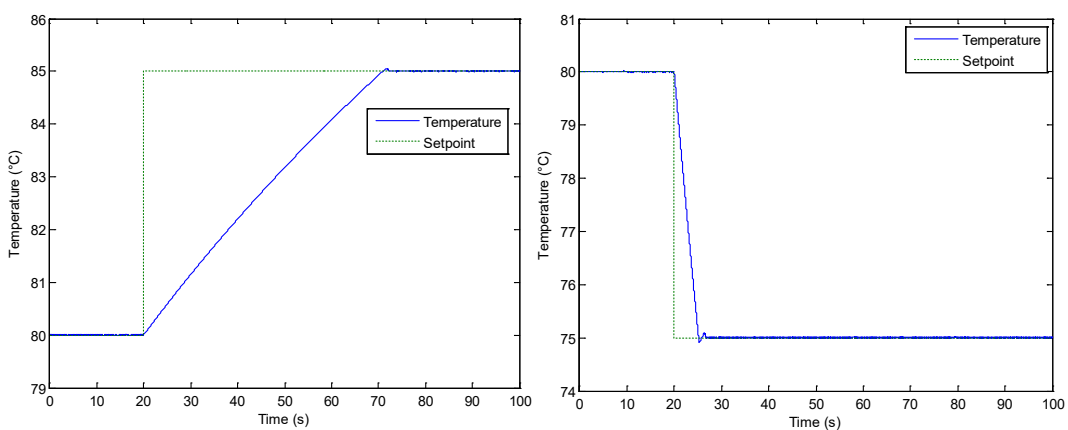


Figure 13: Step change of (+5) (a) and (b) (-5) in set-point temperature (Non-isothermal CSTR)

Simulation of the chamber model in Figures (8) and (9) gave an overshoot of 0% of the step change for all step changes of +1, -1, +5 and -5. The rise time were 9.3s, 7.0s, 18.0s, and 15.8s respectively for a step change of +1, -1, +5 and -5 in set-point. These responses correspond to a robust system characterised by zero overshoot.

On simulation of the stirred steam-heated vessel model, overshoots of 0.1%, 0.2%, 0.8%, and 0.3% of the step change were respectively observed for step changes of +1, -1, +5 and -5. The rise times were 4.4s for a unit step change of +1,



11.0s for a unit step change of -1, 5.0s for a step change of +5 and 57.2 for a step change of -5. This indicates that the system responds in a very short time to increase in set-point and vice-versa. This occurs because the only means of temperature decrease is the heat transfer by convection to the feed.

The non-isothermal CSTR model in Figures (10) and (11) gave an overshoot of about 8% of the step change for a unit step change of +1, 8% for a unit step change of -1, 0% for a step change of +5 and 4% for a step change of -5. The rise times were respectively 10s, 2s, 50s, and 4s. The system was observed to settle in 10.0s, 2.5s, 52s and 6.0s. This shows that the system responds very fast to decrease in set-point as opposed to an increase in set-point. This is as a result of the passive action of the controller during heat-up as it functions as a coolant controller.

In all the foregoing, the fuzzy controller showed good performance to a great extent as some of the most important features we would normally expect to find in acceptable closed-loop reference trajectories- no steady-state offset, quick, stable response, having little or no overshoot, a dynamic response which the process is capable of achieving and a mathematical form which is as simple as possible were obtained.

## 5. CONCLUSIONS

The implementation of fuzzy logic controller design for temperature control of servo systems is accomplished in this work. The closed-loop responses obtained for all the systems considered revealed that robust tracking and control of the systems can be achieved with fuzzy logic controller design. This work has shown the applicability of fuzzy logic methodology in controlling the temperature of thermal systems. The enhancement of the performance of the controller by the use of output scaling gain improves the rise time of the controller thereby showing that the controller can effectively respond to set-point changes in temperature within a short time.

## REFERENCES

- Aguilar, R.M., Muñoz, V. and Callero, Y. (2012). Control Application Using Fuzzy Logic: Fuzzy Inference System - Theory and Applications, Dr. Mohammad Fazle Azeem (Ed.), InTech.
- Abdo-Allah, A., Iqbal, T., and Pope K. (2018). 'Modeling, Analysis, and Design of a Fuzzy Logic Controller for an AHU in the S.J. Carew Building at Memorial University', *Journal of Energy*, vol. 2018, Article ID 4540387, 11 pages. <https://doi.org/10.1155/2018/4540387>.
- Awelewa, A., Omiloli, K., Olajube, A. and Samuel I. (2021). 'Design and Optimization of an Intelligent Fuzzy Logic Controller for a Nonlinear Dynamic System', *2021 International Conference on Decision Aid Sciences and Application (DASA)*, Online.
- Bharathi, T. and Kumar, M. M. (2016). 'A Study on Fuzzy Logic Controller', *International Journal of Engineering Science Invention Research & Development*; Vol. II (XII), pgs (800-804).
- Castillo, O., Cortés-Antonio, P., Melin, P. and Valdez, F. (2020). 'Type-2 fuzzy control for line following using line detection images', *Journal of Intelligent & Fuzzy Systems: Applications in Engineering and Technology*, Vol 39 (5), pp 6089–6097.
- Ramanathan P. (2014). 'Fuzzy Logic Controller for Temperature Regulation Process', *Middle-East Journal of Scientific Research*, 20 (11).
- Sivanandam, S. N., Sumathi, S. and Deepa S. N. (2007). *Introduction to Fuzzy Logic using MATLAB*. Springer, Berlin.
- Wood, R.K. and Berry, M.W. (1973). 'Terminal composition control of a binary distillation column'. *Chemical Engineering Science*, 28 (9).
- Zimmermann, H. J. (2001). *Fuzzy Set Theory – and its applications*, 4<sup>th</sup> edition, Springer Science + Business Media, New York.



## Fuzzy Logic Controller Design: A General Appraisal

Ajiboye OSUNLEKE<sup>1\*</sup>, Ayorinde BAMIMORE<sup>1,2</sup>, Ayodeji AJANI<sup>1,3</sup>, Nafees SANNI<sup>1,4</sup>, Ibrahim Abimbola BADMUS<sup>2,5</sup>

<sup>1</sup>Department of Chemical Engineering, Obafemi Awolowo University, Ile-Ife, Nigeria

<sup>2</sup>Department of Process and Operations, Dangote Petroleum Refinery and Petrochemicals, FZE Lagos, Nigeria

<sup>1\*</sup>[aosunlek@oauife.edu.ng](mailto:aosunlek@oauife.edu.ng); <sup>2</sup>[abamimore@oauife.edu.ng](mailto:abamimore@oauife.edu.ng); <sup>3</sup>[u1269949@utah.edu](mailto:u1269949@utah.edu); <sup>4</sup>[nafeesolaitan@gmail.com](mailto:nafeesolaitan@gmail.com);

<sup>5</sup>[ibrahimabimolabadmus@yahoo.com](mailto:ibrahimabimolabadmus@yahoo.com)

\*Corresponding author

---

### ABSTRACT

*This research work aims at presenting the general appraisal of fuzzy logic control (FLC) in its application in controller design. The method used involves the formulation of a general design algorithm for constructing a fuzzy logic controller for a single-input single-output system as well for a multivariable system. The Fuzzy Logic Toolbox feature in MATLAB and Simulink is utilized for system design and simulation. Nonlinear water tank model, continuous stirred tank reactor; and a steam-heated stirred tank are considered as case studies for this appraisal. The performance criteria taken into consideration are overshoot, rise time, settling time and steady state error. The results obtained largely show that fuzzy logic control gave results over its conventional counterpart, giving absolutely no overshoots, little or no oscillations, better rise and settling times in most cases with minimal differences in the few cases where it was not. It can be concluded that FLC handles nonlinear systems well and when compared with conventional control, can provide better transient response performance.*

**Keywords:** Fuzzy logic control, controller design, PID.

### 1. INTRODUCTION

Fuzzy logic theory and control has emerged as one of the most active and applied areas of research in recent time. The pioneering research in this field was by Zadeh (1965) who established the theory of fuzzy sets. Zadeh (1965) defined fuzzy sets as a class of objects with a continuum of grades of membership, where such sets are characterized by membership (or characteristic) functions. A membership function assigns to each object a grade of membership, ranging between zero and one. Fuzzy logic is an extension of ordinary logic where fuzzy sets is used for the membership of a variable. It forms the theoretical foundation for fuzzy logic control. It is a set of linguistic control rules (algorithms) that can be converted into an automatic control strategy. Fuzzy Logic Controllers (FLCs) are rule-based systems that successfully incorporate the flexibility of human decision-making by means of the use of fuzzy set theory (Gupta and Tsukamoto, 1980; Lee, 1990). The important questions that remain subjects of ongoing research in this field are how FLC compares with conventional control in terms of versatility, applicability and performance (which is one of the objects of this research); whether FLC is better as a standalone control or in combination with conventional control; and lastly, there are only a few methods available to analyze the stability of FLC systems (Eze *et al.*, 2014; Sravya and Aswini, 2020).

### 2. MODEL FORMULATION

The appraisal of the fuzzy logic control method was done by constructing models and assessing its performance with the models. The first step was to formulate algorithms that guide the design of a fuzzy logic controller for single input-single output and multiple input-multiple output systems. The systems were then represented as models. The models were built and implemented in MATLAB and Simulink, using the Fuzzy Logic Toolbox to formulate fuzzy membership functions and fuzzy rules. The models were nonlinear and were applied to both single input-single output and multiple input-multiple output systems and of different types like second order, first-order-plus-time-delay systems, to demonstrate the wide range of application of FLC. The basic architecture of a FLC system was as shown in Figure 1. The conventional controllers used for comparison were P, PI or PID controllers. The models built for FLC were implemented within the conventional framework, and the results were compared. The criteria for performance are steady state error, overshoot, rise time and settling time.

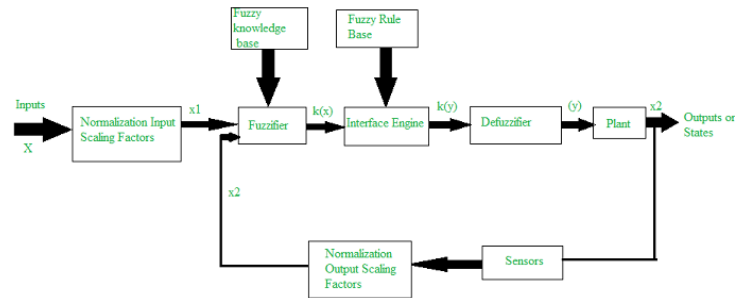


Fig. 1: Basic architecture of a FLC system

The conventional controllers used for comparison were P, PI or PID controllers. The models built for FLC were implemented within the conventional framework, and the results were compared. The criteria for performance are steady state error, overshoot, rise time and settling time.

The general algorithm in the design of a fuzzy logic controller is outlined thus:

- i. Determination of condition (input) variables and specification of the fuzzy sets describing them.
- ii. Determination of action (output) variables and specification of the fuzzy sets describing them.
- iii. Derivation of membership functions.
- iv. Formulation of 'IF-THEN' rules.

Fuzzy rules for the case of a multiple-input-single-output (MISO) system:

$$R_1: \text{if } u \text{ is } A_1 \text{ and } v \text{ is } B_1 \text{ then } y \text{ is } C_1$$

$$R_2: \text{if } u \text{ is } A_2 \text{ and } v \text{ is } B_2 \text{ then } y \text{ is } C_2$$

... ..

$$R_n: \text{if } u \text{ is } A_n \text{ and } v \text{ is } B_n \text{ then } y \text{ is } C_n$$

where  $i = 1, 2, \dots, n$ ;

$u, v$  are linguistic variables and  $y$  is the control variable;

$A_i, B_i$ , and  $C_i$  are the values of the linguistic and control variables respectively and;

fuzzy relation is defined as  $R_i \triangleq (A_i \text{ and } B_i) \rightarrow C_i$

- v. Conversion of precise inputs to fuzzy inputs, known as fuzzification:
 
$$u = \text{fuzzifier}(u_0) \quad (1)$$

- vi. Conversion of fuzzy inputs into fuzzy outputs, known as fuzzy inference.

- vii. Conversion of fuzzy outputs into precise inputs, known as defuzzification:
 
$$y_0 = \text{defuzzifier}(y) \quad (2)$$

## 2.1 FLC Design for MIMO Systems

Belarbi *et al.* (2006) introduced a methodology based on fuzzy controllers for single variable systems and a fuzzy compensator of interactions acting in feedforward. The fuzzy controllers are set for each subsystem without considering the interactions. These are then considered as measurable disturbances and the feedforward fuzzy compensator is used to compensate their effect at each subsystem. The following procedure is used:

- i. Design a decoupling matrix.
- ii. Design single-input single-output (SISO) controllers for decoupled system.
- iii. Fuzzy controllers are set for each system without taking into account interactions.
- iv. Fuzzy compensator compensates for the effect of disturbances on the subsystem.

## 2.2 PID Conventional Controller Design

The PID is defined by the s-domain transfer function

$$g_c = K_c \left( 1 + \frac{1}{\tau_I s} + \tau_D s \right) \quad (3)$$

where  $K_c$  is the proportional gain,  $\tau_I$  is the integral time or reset time and  $\tau_D$  is the derivative time constant.

The performance criteria to be employed for comparison are rise time, settling time and overshoot. It is expected that the systems are stable for an effective closed loop response, and that the systems' output ultimately attain the desired set point value, that is, negligible or no steady state error.

### 3. SIMULATION WITH PRACTICAL EXAMPLES

The examples considered are nonlinear water tank, one case for continuous stirred tank reactor and steam heated stirred tank.

#### 3.1 Water Tank

A nonlinear tank in which water level is controlled was considered as single-input single-output and flow into the system is represented by  $F_i$ . The flow out  $F_o$  is dependent on the square root of height  $h$ , with  $c$  being the constant of proportionality. The system is nonlinear with respect to height  $h$  and the constant cross-sectional area of the tank is given as  $A$ . The conserved quantities are mass, energy and momentum and the physical properties of water like density, specific heat and thermal conductivity remain constant. Using the law of conservation of mass, the differential equation representing the system is given as

$$\frac{dh}{dt} = \frac{1}{A}(F_i - c\sqrt{h}) \tag{4}$$

The FLC system was modelled as a single input-single output system as shown in Fig. 2. Membership functions for the input variable into the controller is termed 'Error' and the output variable is 'Height'. The error ranges from 0-20 and the height ranges from 0-20. The error variable has three triangular membership functions: small, zero and large. The height variable has three triangular membership functions: low, desired, and high.

The fuzzy linguistic rules are defined thus:

- i. If (Error is small) then (Height is low)
- ii. If (Error is large) then (Height is high)
- iii. If (Error is zero) then (Height is desired)

The PID control system is achieved by tuning heuristically with the following parameters:  $K_c = 1, \tau_I = 1$  and  $\tau_D = 0.2$ . This is implemented by replacing the FLC block in Fig. 2 with a PID block with the parameters specified.

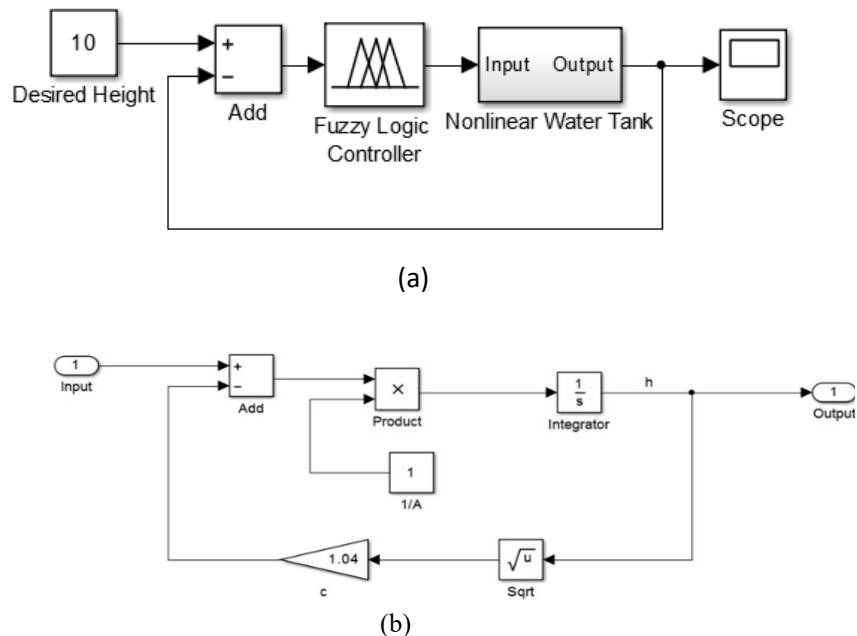
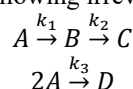


Fig. 2: Simulink model of (a) FLC system, (b) nonlinear tank model

#### 3.2 A CSTR with Van de Vusse Reaction

The Van de Vusse reaction scheme consists of the following irreversible reactions (Vusse, 1964):



Assumptions include constant density and volume. The material balance modelling equations for components  $A$ ,  $B$ ,  $C$  and  $D$  are respectively

$$\frac{dC_A}{dt} = \frac{F}{V}(C_{Af} - C_A) - k_1 C_A - k_3 C_A^2 \quad (5)$$

$$\frac{dC_B}{dt} = -\frac{F}{V} C_B + k_1 C_A - k_2 C_B \quad (6)$$

$$\frac{dC_C}{dt} = -\frac{F}{V} C_C + k_2 C_B \quad (7)$$

$$\frac{dC_D}{dt} = -\frac{F}{V} C_D + \frac{1}{2} k_3 C_A^2 \quad (8)$$

Since component balance on  $A$  and  $B$  do not depend on  $C$  and  $D$  - they only depend on  $A$  and  $B$ . Thus, both equations will be treated for the design of the control strategy. Using the case study developed by Bequette (1998):  $C_{As} = 6.0870 \frac{\text{mol}}{\text{L}}$ ,  $C_{Bs} = 1.117 \frac{\text{mol}}{\text{L}}$ , and  $F/V = 2.8744 \text{ min}^{-1}$ .

The state space model is obtained as:

$$A = \begin{bmatrix} -5.7367 & 0 \\ 0.8333 & -4.5411 \end{bmatrix}, B = \begin{bmatrix} 3.9130 \\ -1.1170 \end{bmatrix},$$

and the transfer function is realized as

$$g(s) = \frac{-1.1170s - 3.1472}{s^2 + 10.2778s + 26.0508} \quad (9)$$

The FLC design for the feedback control scheme is shown in Fig. 3. The input to the system is a step input and the process is described by the transfer function and controlled using a fuzzy logic controller, with the inputs to the controller being error and derivative of error, and the signal being amplified by a gain block, to reduce oscillations.

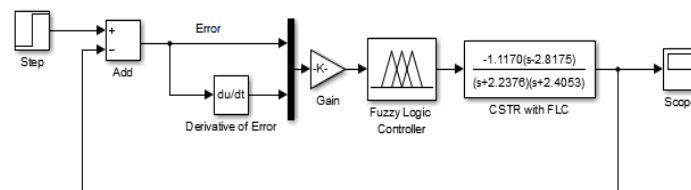


Fig. 3: Simulink model of CSTR with FLC (Van de Vusse)

The inputs and outputs are each defined by seven membership functions, namely: Negative Big (NB), Negative Medium (NM), Negative Small (NS), Zero (Z), Positive Small (PS), Positive Medium (PM) and Positive Big (PB). The error ranges from 0 to 1, derivative of error ranges from 0 to 0.1 and the concentration ranges from 0 to 3.42. The corresponding PID controller is designed using the Simulink PID auto-tuning feature and the resulting parameters are:  $K_c = 1.40$ ,  $\tau_I = 1.71$  and  $\tau_D = 0.01$ .

### 3.3 A Steam-Heated Stirred Tank

This is a multiple-input multiple-output system with the model equations, assuming constant density and volume given as

$$\text{Tank: } \frac{dT}{dt} = \frac{F}{V}(T_i - T) + \frac{Q}{V\rho c_p} \quad (10)$$

$$\text{Jacket: } \frac{dT_j}{dt} = \frac{F_j}{V_j}(T_{ji} - T_j) + \frac{Q}{V_j\rho_j c_{pj}} \quad (11),$$

$$\text{where: } Q = UA(T_j - T) \quad (12)$$

and  $A$  = heat transfer area,  $c_p$  = heat capacity,  $F$  = volumetric flow rate,  $\rho$  = density,  $T$  = temperature,  $t$  = time,  $Q$  = heat transfer rate,  $U$  = heat transfer coefficient,  $V$  = volume,  $i$  = inlet,  $j$  = jacket and  $ji$  = jacket inlet.

Equations (10) and (11) were modelled in Simulink as a subsystem and this is shown in Fig. 4.

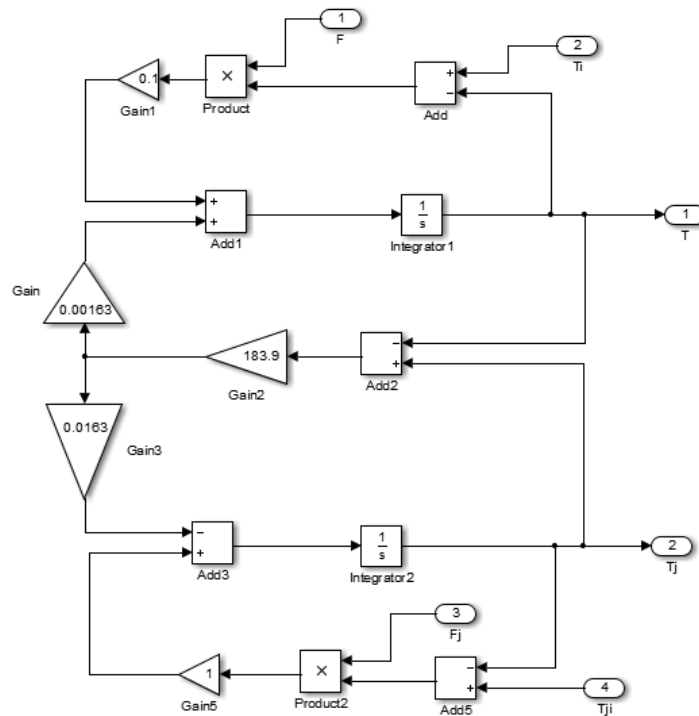


Fig. 4: Simulink model of steam-heated stirred tank modelling equation

### 3.4 FLC MIMO Design

The FLC design for a MIMO system as described in the methodology involves designing controllers for the controlled variables in the system as though designing for a SISO system, and a fuzzy compensator, which compensates for the effect of disturbances in the subsystem. Thus, the control system shown in Fig. 5 consists of controller FLC1 designed to control variable  $T$ , controller FLC2 to control variable  $T_j$ , and a third controller FC to act as a fuzzy compensator.

The inputs to FLC1 and FLC2 are error and derivative of error. The outputs signals,  $uf_1$  from FLC1 and  $uf_2$  from FLC2 are attenuated by saturation blocks, and then set as inputs into the FC,  $uc_2$  and  $uc_1$ . The outputs of the fuzzy compensator are then added to the controlled signals to form  $u_1$  and  $u_2$ , which serve as inputs to the subsystem.

The temperature of the tank and the jacket are both set to  $100^\circ\text{C}$ . The membership functions defined for the inputs and outputs to controllers FLC1 and FLC2 are essentially the same. The error ranges from -100 to 100, the derivative of error from -10 to 10 and the output ( $uf_1$  for FLC1 or  $uf_2$  for FLC2) ranges from 0-200. The error and derivative of error variables have three triangular membership functions: Negative (N), Zero (Z) and Positive (P). The output has three triangular membership functions: Small (S), Medium (M) and Big (B).

The fuzzy inference system used for FLC1 and FLC2 is Mamdani. The rules for FLC1 are given in the form of a rule table shown in Table 2.

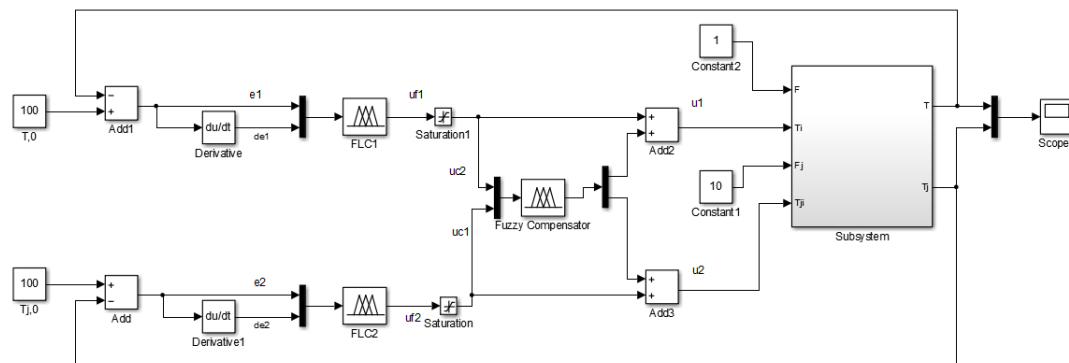


Fig. 5: Simulink model of steam-heated stirred tank with FLC

Table 2: Rule Table for Steam-heated Stirred Tank Fuzzy Logic Controllers

		Derivative of Error		
		<b>N</b>	<b>Z</b>	<b>P</b>
Error	<b>N</b>	S	M	S
	<b>Z</b>	M	B	M
	<b>P</b>	S	M	S

The fuzzy inference system used for the fuzzy compensator FC is Sugeno. The inputs into the FC are  $uc_2$  and  $uc_1$ , and the outputs are  $ufc_1$  and  $ufc_2$ . The inputs range from -1 to 1 while the outputs range from 0 to 1. Each input and output have three Gaussian membership functions: Negative (N), Zero (Z) and Positive (P). The rule table is given in Table 3.

The corresponding PID design was achieved by tuning heuristically to the following parameters,  $K_c = 1$ ,  $\tau_I = 0.6$  and  $\tau_D = 0.2$ . This design was implemented by replacing the FLC block in Fig. 5 with a PID block with the parameters specified without the derivative of error, saturation and compensator blocks.

Table 3: Rule Table for Steam-heated Stirred Tank Fuzzy Compensator

<b>uc1</b>	<b>uc2</b>	<b>ufc1</b>	<b>ufc2</b>
N	N	N	N
N	Z	Z	N
N	P	P	N
Z	N	N	Z
Z	Z	Z	Z
Z	P	P	Z
P	N	P	N
P	Z	P	Z
P	P	P	P

## 4. RESULTS AND DISCUSSION

The simulation results for examples considered using FLC and PID controllers are compared using the following performance criteria:  $M_p$  (%), settling time  $t_s$  (s), rise time  $t_r$  (s) and steady state error  $e_s$ .

### 4.1 Water Tank

The responses obtained for simulation of both FLC and PID designs for the nonlinear water tank is shown in Fig. 6, while the comparison in performance criteria for both designs is shown in Table 4. Evidently, fuzzy logic controller exhibited zero overshoot and shorter settling time when compared with conventional control. The steady state error is approximately zero in both cases. The rising time is a little higher than that of PID. Also, the FLC exhibited no oscillation. Overall, the model responds better under fuzzy control than under PID control.

In the design and simulation of the FLC, it was found that if the area specified for the subsystem (in the form  $1/A$ ) is large, the rise time is slow; for example, for  $1/A = 0.1$  or  $A = 10$ , the rise time for the FLC was  $t_r = 14.88s$ . Conversely, smaller areas led to faster rise times, for example, for  $1/A = 10$  or  $A = 0.1$ ,  $t_r = 0.16s$ . An intermediate value of  $1/A = 1$  was used in the design.

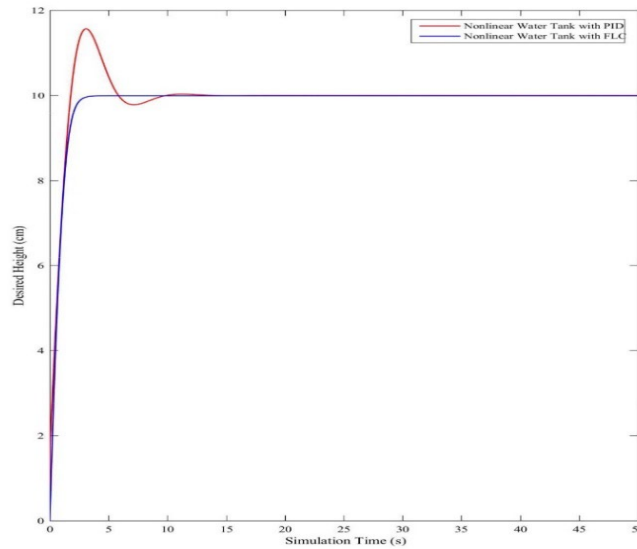


Fig.6: Transient response of nonlinear water tank system

Table 4: Transient Response Parameters for Nonlinear Water Tank

Criteria	FLC	PID
$M_p$ (%)	0.00	15.63
$t_s$ (s)	2.97	8.68
$t_r$ (s)	1.49	1.45
$e_s$	0.01	0.00

The system is said to be nonlinear with respect to height  $h$ , with  $F_o = c\sqrt{h}$ . It was found that values of  $c < 1.00$  gave undesirable transient responses characterized by ever-increasing amplitudes while values of  $c > 1.10$  gave large offsets. Optimal transient response was found at  $c = 1.04$ .

#### 4.2 CSTR: Van de Vusse Reaction

The transient responses from simulation of the continuous stirred tank reactor in which a *Van Vusse Reaction* is occurring, using FLC and PID designs are shown in Fig. 7 and the corresponding performance criteria parameters are given in Table 5.

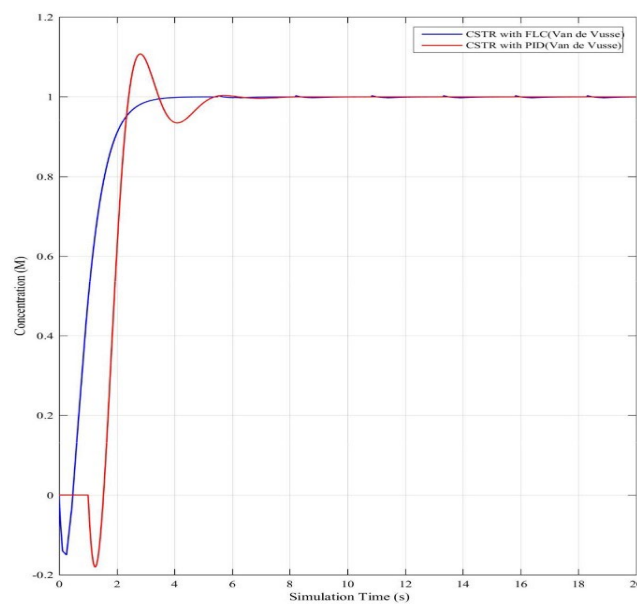


Fig. 7: Transient response of CSTR (Van de Vusse Reaction)



Table 5: Transient Response Parameters for CSTR (Van de Vusse Reaction)

CRITERIA	FLC	PID
$M_p$ (%)	0.00	10.73
$t_s$ (s)	3.14	5.11
$t_r$ (s)	1.38	0.65
$e_s$	0.00	0.00

From the responses and performance criteria, it was seen that the FLC design out-performed the conventional controller by giving no overshoot, better settling time, and no steady state offset. However, the rise time of the PID was faster than that of the FLC. Overall, the fuzzy logic controller remains a better choice.

### 4.3 Steam-Heated Stirred Tank

The results obtained from simulation of the steam-heated stirred tank using FLC and PID for temperature of the tank,  $T$  and Jacket,  $T_j$  are shown in Fig. 8 while the corresponding criteria parameters are given in Table 6 and 7 respectively. For the tank temperature, the FLC gave a mixed performance, giving no overshoot and a better settling time, but giving a slower rise time and a steady state offset; while for the jacket temperature, the FLC outperformed the conventional PID controller by giving no overshoot, better settling and rise times, but with steady state offset of 0.5. The steady state offset may be attributed to the disturbances associated with the multivariable system.

Considering the system holistically, FLC gave an average performance in controlling the tank temperature but an excellent performance with the jacket temperature. The performance of the FLC may further be improved by reducing the effect of disturbances in the system. One way this can be done is by designing a more complex fuzzy compensator with more fuzzy rules and membership functions. Another improvement may be by adding an integral of error block as an additional input to both fuzzy controllers, leading to more fuzzy rules and consequently, better control and zero steady state offset. Overall, the advantages offered by fuzzy logic control to the system outweighs the drawbacks. Compared to the conventional PID controller, it offers a better choice if factors such as fast settling times, minimal oscillations, and zero overshoot, are vital.

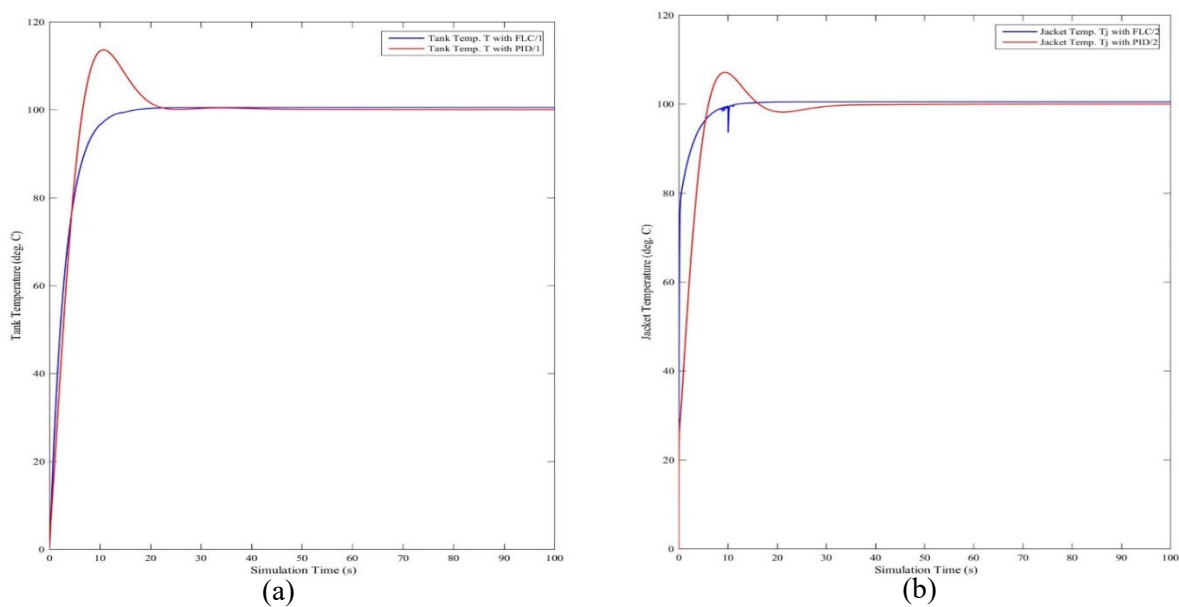


Fig. 8: Transient response of (a) tank and (b) Jacket temperature for stirred tank

Table 5: Transient Response Parameters of Tank Temperature for Stirred Tank

CRITERIA	FLC	PID
$M_p$ (%)	0.00	13.67
$t_s$ (s)	13.07	21.00
$t_r$ (s)	6.55	5.01
$e_s$	0.50	0.00

Table 6: Transient Response Parameters of Jacket Temperature for Stirred Tank

CRITERIA	FLC	PID
$M_p$ (%)	0.00	7.16
$t_s$ (s)	10.25	26.78
$t_r$ (s)	2.54	4.60
$e_s$	0.50	0.00

## 5. CONCLUSIONS

Fuzzy logic control algorithms were developed by determination of input and output variables, specifying their fuzzy sets, derivation of membership functions, formulation of IF-THEN rules, fuzzification, fuzzy inference and defuzzification. The algorithm developed for a MIMO system involves the design of a decoupling matrix, design of SISO controllers for decoupled system, setting fuzzy controllers for each system, and design of fuzzy compensator. The control algorithms developed were implemented on models like water tank, a CSTR and steam-heated stirred tank, using the Fuzzy Logic Toolbox. The design and simulation of the systems were accomplished using Simulink.

The results obtained from the design and simulations of key nonlinear systems like the nonlinear water tank, the two cases considered for the continuous stirred tank reactor; and multivariable system like the steam-heated stirred tank, largely show that fuzzy logic control gave favorable results over its conventional counterpart. The performance metrics taken into consideration are overshoot, rise time, settling time and steady state error. The general observations from the results were that FLC provide no overshoots, and little or no oscillations. For the systems considered, the rise and settling times were better than conventional control in most cases, and the differences were minimal in the few cases where it was not. The steady state error was zero for all cases except for the steam-heated stirred tank system, and this may be attributed to the disturbances associated with the multivariable system. It can be concluded that FLC handles nonlinear and stochastic systems well and when compared with conventional control, can provide better transient response performance.

## REFERENCES

- Belarbi, K., Belhani, A., & Fujimoto, K. (2006). Multivariable fuzzy logic controller based on a compensator of interactions and genetic tuning. *International Journal of Innovative Computing, Information and Control*, 1207–1217.
- Bequette, B. (1998). *Process Dynamics: Modelling, Analysis and Simulation*. New Jersey: Prentice Hall.
- Eze, U.F., Emmanuel, I., Stephen, E. (2014). Fuzzy Logic Model for Traffic Congestion. *IOSR Journal of Mobile Computing & Application (IOSR-JMCA)* e-ISSN: 2394-0050, P-ISSN: 2394-0042. Volume 1, Issue 1 (May.-Jun 2014), PP 15-20
- Gupta, M., & Tsukamoto, Y. (1980). Fuzzy Logic Controllers - A Perspective. *Proc. Joint Automatic Control Conf.*, FA10-C.
- Lee, C. (1990). Fuzzy Logic in Control Systems: Fuzzy Logic Controller-Parts I & II. *IEEE Transactions on Systems, Man and Cybernetics*, 404-435.
- Sravya1, T. and Aswini, K. (2020). Analysis and Comparison of Conventional and Interleaved DC/DC CUK Converter using Fuzzy Logic Controller. *International Journal for Research in Applied Science & Engineering Technology (IJRASET)* ISSN: 2321-9653; 8(5). DOI: <http://doi.org/10.22214/ijraset.2020.5460>
- Vusse, V. (1964). *Chemical Engineering Science*. London: Pergamon.
- Zadeh, L. A. (1965). Fuzzy Sets. *Intl J. Information Control*, 338-353.



## A New Implicit Model for Predicting Economic Pipe Diameter in a Fully Developed Turbulent Single-phase Pipe Flow

Joseph U. OKON<sup>1</sup>, Emmanuela O. AINERUA<sup>1</sup>, Innocent O. OBOH<sup>\*1</sup> and Anselm I. IGBAFE<sup>2</sup>

<sup>1</sup>Department of Chemical and Petroleum Engineering, University of Uyo, Uyo, Nigeria

<sup>2</sup>Department of Chemical and Petroleum Engineering, Afe Babalola University, Ado-Ekiti, Ekiti State, Nigeria

<sup>1</sup>[utibe.okonyahoo.com](mailto:utibe.okonyahoo.com), <sup>1</sup>[emmanuelainerua@uniuyo.edu.ng](mailto:emmanuelainerua@uniuyo.edu.ng), <sup>1\*</sup>[innocentoboh@uniuyo.edu.ng](mailto:innocentoboh@uniuyo.edu.ng), <sup>2</sup>[igbafesai@abuad.edu.ng](mailto:igbafesai@abuad.edu.ng).

\*Corresponding author

---

### ABSTRACT

The cost of a piping system accounts for about 20% of the plant's total cost and could run higher than that for pipeline transporting crude or petroleum products through a thousand kilometres of distance hence the need to accurately select the optimal size during the design stage of such a project. This paper presents an implicit correlation for optimization of economic pipe diameter based on the simple economic balance approach first used by Genereaux. A new model was developed and is implicit in  $D$  (Economic pipe diameter) which has been found to give superior estimates over existing correlations. The computations of the economic diameter of brass, stainless steel and aluminium pipes were carried out using the developed implicit model. A plot of effect of pipe roughness on economic diameter was obtained with a coefficient of determination of  $R^2 = 0.909$ . Results from the study showed that heavier fluids would require larger diameter.

**Keywords:** *Implicit model, piping systems, Economic pipe diameter, Turbulent single-stage pipe flow.*

### 1. INTRODUCTION

Fluid is a general name for any substance that can flow (basically liquid and gas). It can be transported through pipes. The use of pipe for moving fluid has a long history in engineering. Pipes have been made in a round cylindrical form for a great number of reasons. One reason given for this is that a circular cross-section results in the least surface area per unit of volume and reduces fluid stagnation (Whitesides, 2008).

In a chemical process plant, fluid flows through pipe networks from one operating unit to another. The piping system for any particular plant is therefore an important integral part of the overall plant. Pumps and compressors are used to provide the pressure for the fluid to flow. However, due to pressure losses along the pipe length caused by the pipe roughness, sudden contractions or expansions and pipe fittings such as elbows, bend etc., additional pumps or compressors may be required at intervals along the pipe length to keep the fluid flowing or a bigger capacity may have to be installed altogether (McCabe *et al.*, 2005). This increases the operating cost of the piping system. Since piping systems can run up to 20% and above of the total plant cost (Genic *et al.*, 2012), it is therefore important that a good consideration should be given to this area when there is a need to optimise cost.

Frictional head loss has been found to increase with decrease in pipe diameter, meaning an increase in pumping or compressing cost, while the annualised fixed cost of a piping system increases with diameter (Peters and Timmerhaus, 1991). Therefore, there exists an optimum economic pipe diameter which gives the lowest possible total annualised cost. Several publications have been done on this subject in which formulae and nomographs for estimation of economic pipe diameter were proposed (Genereaux, 1937; Peters and Timmerhaus, 1968; Peters and Timmerhaus, 1991). The basic development of this relationship combines the concepts of fluid flow in pipes, plant economics of the piping system and simple optimization procedure.

Genereaux (1937) is a pioneer as far as the subject of economic pipe diameter is concerned. The Genereaux Equation though covering a wider aspect (including analysis on tax) is not without its own shortcomings, the main reason being that it was derived based on hydraulically smooth pipes (Genic *et al.*, 2012). Before now, Peters and Timmerhaus (1991) had reproduced a somewhat simple but more accurate correlation for new carbon steel pipe for both laminar and turbulent

flow regime which has been plotted as a non-linear nomograph. Their correlation was an improvement to the pioneering Genereaux equation. Apart from showing that different results could be obtained for laminar and turbulent flow in a new commercial still pipe, it also accounted for the pressure losses due to pipe fittings, by assuming it as a fraction of the pressure drop due to the actual pipe length. Depending on the complexity of the attached fittings a value of 0.5 can be used (Genic *et al.*, 2012).

The investment on piping accounts for a good part of the total investment for industrial chemical plants, consequently equations are available for calculating the economic size of pipe (which is a direct function of its diameter) that gives the least possible cost implication (Akintola, 2003). These equations are represented on nomograph from which the economic pipe size or diameter can be obtained manually with associated problems of accuracy and limited applicability (Peters and Timmerhaus, 1991). Already published formulae were based on smooth pipe and a few have approximated the effect of pipe roughness (Genic *et al.*, 2012). In view of this setback, there is need to modify these models to accommodate the effect of both pipe roughness and Reynolds number on the pressure drop and hence the operating cost for any pipe material operating in the turbulent flow regime. Moody's Chart gives distinct flow regimes. Genic *et al.* (2012) showed that a different set of economic diameters can be obtained for the region of complete turbulence where the friction factor depends only on the pipe relative roughness. However, none of the available models can be applied on the region of Moody's Chart where the friction factor depends on both the pipe roughness and Reynolds number (Bratland, 2009).

The economic pipe size here denotes the best possible pipe diameter when considering the economic investment and operating cost. Since the cost of pumping is proportional to pressure drop, to accurately estimate the pressure drop implies using an effective friction factor which accounted for both pipe roughness and Reynolds number effect in the turbulent flow regime, hence the choice of the Altshul's friction factor for the new model. This paper will develop a model for estimating economic pipe diameter for an incompressible fluid flow in the turbulent regime based on the Altshul (1975) power law friction factor correlation which is given as

$$\lambda = 0.11\left(R_r + \frac{68}{Re}\right)^{0.25} \quad (1)$$

Also, a comparison of the developed model and the nomograph for the economic diameters of some selected piping materials will be done.

## 2. METHODOLOGY

### 2.1 Assumptions

The following assumptions hold in the present approach to the solution of the problem:

- i. The total annual operating cost is the sum of the annualized capital cost of the pipe and the annual pumping or operating cost.
- ii. The Altshul(1975) equation covers completely the area of moody's chart as colebrook's implicit model ( $4000 \geq Re \geq 108$ ;  $0 \geq R_r \geq 0.05$ )
- iii. Minor frictional loss is a fraction of the frictional loss due to pipe length.
- iv. Fluid is incompressible and Newtonian.
- v. Greater percentage of the annual operating cost is dominated by the annual pumping cost.

### 2.2 Model Development

The cost of piping system in a plant is examined based on two cost components: its annual operating cost and the fixed annualized capital charges. It is assumed that a greater percentage of the annual operating cost is dominated by the annual pumping cost. For fluid flow through pipe, the annual pumping cost is given by (Alamu *et al.*, 2002):

$$C_p = \frac{AEQ}{100\eta} \Delta P_T (\$/myr) \quad (2)$$

This shows that the operating cost is influenced by; the plant attainment A (hr/yr), the cost of electricity E (\$/KWh), pump efficiency  $\eta$  and the flow rate of the fluid Q (m<sup>3</sup>/s). A higher pressure drop due to friction will give rise to a corresponding increase in the pumping cost. However, the effective pressure drop is the frictional pressure drop due to pipe length ( $\Delta P$ ) and that caused by frictional loss due to fittings and bends ( $\Delta P_M$ ) expressed as equivalent fractional loss in a straight pipe (J).

$$\Delta P = \frac{\lambda L \rho V^2}{2D} \quad (3)$$

For one meter length of pipe:

$$\Delta P = \frac{\lambda \rho V^2}{2D} \quad (4)$$

Where  $\lambda$  is the Darcy-Weisbach friction factor which is approximated by the Altshul's power law Equation (Brkić, 2011).

Although the logarithmic correlation for estimating friction factor gives a more accurate result the power law form is used here for simplicity. Also, equation (1) has been found to produce a close approximation of the Colebrook's friction factor (Brkić, 2011). This equation shows the dependency of friction factor on both the Reynolds number and the relative roughness of the pipe used. This flow regime lies between the rough flow (fully turbulent) and the turbulent region of Moody's chart. The absolute roughness,  $\varepsilon$  (m) has been shown to vary with the piping material (Perry and Green 2008), and the Reynolds number is

$$\text{Re} = \frac{DV\rho}{\mu} \quad (5)$$

The velocity of fluid flow through pipe is inversely proportional to the pipe internal diameter and is given as:

$$V = \frac{Q}{A} = \frac{4Q}{\pi D^2} \quad (6)$$

Reynolds in terms of flow rate, fluid viscosity and density is given by

$$\text{Re} = \frac{4\rho Q}{\pi D\mu} \quad (7)$$

Let  $\Delta P_T = \Delta P + \Delta P_M = \Delta P(1 + J)$

After proper substitution, we have

$$\Delta P_T = \left[ \left( \frac{0.88^4}{\pi^8} \right) \varepsilon \rho^4 Q^8 D^{-21} + 17 \left( \frac{0.99^4}{\pi^8} \right) \mu \pi \rho^3 Q^7 D^{-19} \right]^{0.25} [1 + J] \quad (8)$$

On substituting the total pressure drop into the annual pumping cost the following equation is arrived at:

$$C_p = \frac{AE}{1000\eta} [1 + J] \left[ \left( \frac{0.88^4}{\pi^8} \right) \varepsilon \rho^4 Q^{12} D^{-21} + 17 \left( \frac{0.99^4}{\pi^8} \right) \mu \pi \rho^3 Q^{11} D^{-19} \right]^{0.25} \quad (9)$$

Take

$$M = \left( \frac{0.99^4}{\pi^8} \right) \varepsilon \rho^4 Q^{12}; H = 17 \left( \frac{0.99^4}{\pi^8} \right) \mu \pi \rho^3 Q^{11}; Z = \frac{AE}{1000\eta} [1 + J],$$

Then let

$$C_p = Z[MD^{-21} + HD^{-19}]^{0.25} \quad (10)$$

Again let

$$U = MD^{-21} + HD^{-19} \quad (11)$$

$$C_p = ZU^{0.25} \quad (12)$$

Then

$$\frac{\partial C_p}{\partial D} = -0.25ZU^{-0.75}D^{-22}[21M + 19HD^2] \quad (13)$$

The annualized cost for the installed piping system evaluated on a one-meter length basis as been given by Genic (2012) as:

$$C_c = XD^x(1 + F)(a + b) \quad (14)$$

On taking the partial derivative of (15) with respect to the pipe diameter:

$$\frac{\partial C_c}{\partial D} = xXD^{x-1}(1 + F)(a + b) \quad (15)$$

The value of D is minimum at the point where the sum of (13) and (15) equals zero.

$$\frac{\partial C_p}{\partial D} + \frac{\partial C_c}{\partial D} = 0 \quad (16)$$

Making D the subject results in

$$D = \left[ \frac{-0.25ZU^{-0.75}(21M+19HD^2)}{xX(1+F)(a+b)} \right]^{\left( \frac{1}{x+21} \right)} \quad (17),$$

which is implicit in D and require iteration to evaluate the final numerical value of D in meters.

Equation 17 is the proposed correlation for estimating economic pipe diameter for incompressible fluid flow in the turbulent regime of fluid flow.

The parameters for solving Equation (17) were obtained from Table 1. It was assumed that the system will operate 24 hours a day and 7 days a week which puts the plant attainment A at 8760 hr/yr. The fraction of the pipe that accounted for minor losses due to pipe fittings and valves was taken as 0.5 while the combine pump and motor efficiency  $\eta$  was also taken as 0.5.

### 2.3 Calculation of D for Different Material and Fluid

Equation (17) which is implicit in D, it was solved by enabling a computational iterative tool in Microsoft Office Excel. First, the SAE R40 data was used as given in Table 1. The volume flow rate was varied from 0.001 to 1.0 (m<sup>3</sup>/s) and D in Equation (18) was calculated for carbon steel, stainless steel, aluminium and brass pipe based on 2008 costing. At each flow rate, a corresponding calculation is done with the Peters and Timmerhaus nomograph model for carbon steel pipe only. This procedure was also repeated with automotive gas oil (AGO) and the results were recorded accordingly. Figure

1 shows sample calculation on Microsoft Excel window indicating the optimal economic pipe diameter for a specific flow case. With similar steps D was calculated for carbon steel and stainless-steel pipes based on 1998 costing and AGO as fluid.

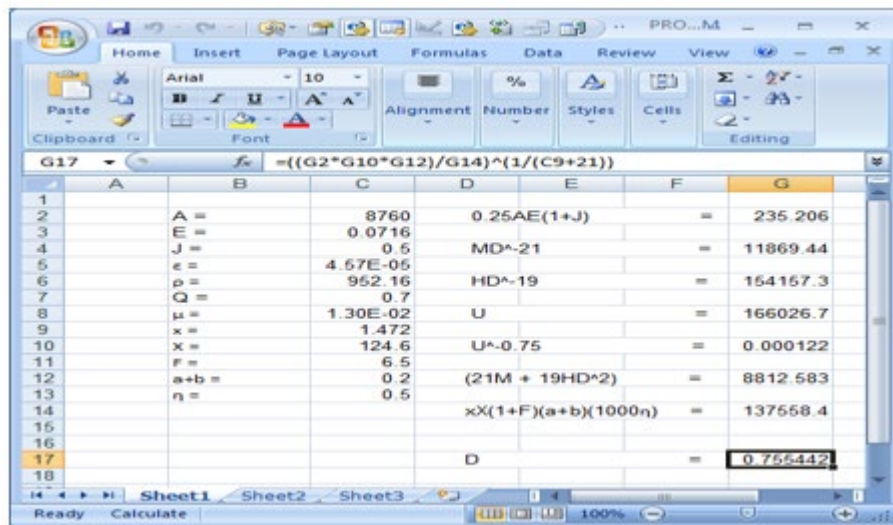


Figure 1: Sample calculations on Microsoft Excel Window

#### 2.4 Calculation of D for Different Value of Absolute Roughness of Carbon Steel Pipe

Lubricating oil was used as fluid, with the volume flow rate fixed, the absolute roughness of carbon steel pipe was spread from slightly rough to severely rough and D was recorded for every value of absolute roughness.

Table 1: Parameters in Equation (17)

Terms	Carbon steel	Stainless steel	Aluminium	Brass	Fluid	$\rho$ ( $kg/m^3$ )	$\mu$ (PaS)
x (2008)	1.472	0.9240	0.769	0.907			
(1998)	1.350	0.7793	-----	-----	Lube Oil	870.24	5.865E-3
X (2008)	124.6	301.9	182.09	311.3			
(1998)	481.6	1076.6	-----	-----	SAE	952.16	1.295E-2
(a + b)	0.2	0.2	0.2	0.2			
E (2008)	0.0716	0.0716	0.0716	0.0716			
(1998)	0.0488	0.0488	0.0488	0.0488			
F (2008)	6.5	7.4	7.1	7.2			
(1998)	6.7	7.5	-----	-----	AGO	849.56	3.700E-3
$\epsilon$ (m)	4.57E5	1.5E-5	1.2E-6	1.0E-6			

Source: Durand et al., 2010; Odeunmi, 2002

### 3. RESULTS AND DISCUSSION

From Table 2 it can be seen that the developed model is able to estimate economic pipe diameter not only for carbon steel pipe, but also for other piping materials such as stainless steel, aluminium, and brass. It shows that for a particular fluid flow rate, viscosity, density and pipe roughness, that the pipe diameter varies according to how expensive the material is. Brass being the most expensive takes the least diameter while carbon steel being the least expensive takes on the highest diameter (Durand et al., 2010).

The results also suggested that a high-density fluid require a larger economic pipe diameter and first cost compared to a low-density fluid at the same flow conditions. This was so because higher operating cost will be required for heavier fluid hence a compromise which leads to favoring the annualized capital cost will be reached and vice versa. Meanwhile, the diameters calculated from the derived model for the 1998 cost data shows that when the capital cost of the pipe increases, the economic diameter tends to reduce in size. This is as expected since the optimal size lies between larger line sizes for a lower operating cost (Whitesides, 2008). Hence, when the unit cost of carbon steel pipe decreased in 2008

as compared to its relative high cost in 1998, it is reasonable that the design size should increase anticipating a rather low capital investment against operating cost.

Using Lube Oil, the effect of roughness on the optimal economic diameter of carbon steel pipe was examined and Table 5 shows the various possible degree of roughness of carbon steel pipe during its service life. Figure 2 indicates that for a constant volume flow rate that the line size can be directly correlated with the absolute roughness of a pipeline which can be given as

$$D = 25.64\varepsilon + 0.736 \tag{18}$$

Similarly, linear correlations of the optimum economic diameter for particular fluids were obtained for brass, stainless steel and aluminum pipes. However, these linear relations can only provide approximate result as the main new implicit model is not a linear equation. However, since their R2 values are close to unity they can be used in this manner.

Table 2: Economic pipe size when SAE oil was used, based on 2008 costing

SN	Q (m <sup>3</sup> /s)	Carbon Steel (2008) D (m)	Stainless Steel (2008) D (m)	Aluminium (2008) D (m)	Brass (2008) D (m)	Carbon Steel (m) D <sub>n</sub>	ΔP <sub>T</sub> (Pa) Carbon Steel 2008	C <sub>P</sub> Carbon steel 2008 (\$/m yr)	C <sub>C</sub> Carbon Steel 2008 (\$/year)
1	0.001	0.04166	0.02789	0.02871	0.0276	0.0171	427.00	0.5357	1.737
2	0.005	0.08488	0.06084	0.06404	0.0604	0.0354	243.40	1.5265	4.952
3	0.010	0.11533	0.08513	0.09045	0.0845	0.0483	191.00	2.3961	7.777
4	0.030	0.18749	0.14500	0.15637	0.1442	0.0792	130.10	4.8959	15.900
5	0.050	0.23502	0.18574	0.20170	0.1849	0.0997	108.80	6.8258	22.180
6	0.080	0.28934	0.23326	0.25493	0.2323	0.1231	92.32	9.2654	30.120
7	0.100	0.31935	0.25991	0.28491	0.2590	0.1318	85.41	10.714	34.820
8	0.400	0.58968	0.50893	0.56846	0.5080	0.2541	52.61	26.396	85.890
9	0.700	0.75534	0.66752	0.75127	0.6669	0.3268	43.26	37.987	23.700
10	1.000	0.88446	0.79350	0.89739	0.7931	0.3838	38.19	47.907	156.000

Table 3: Economic pipe sizes when AGO was used, based on 2008 costing

S/N	Q (m <sup>3</sup> /s)	Carbon Steel (2008) D (m)	Stainless Steel (2008) D (m)	Aluminium (2008) D (m)	Brass (2008) D (m)	Carbon Steel (m) D <sub>n</sub>	ΔP <sub>T</sub> (Pa) carbon Steel 2008	C <sub>P</sub> Carbon Steel 2008 (\$/m yr)	C <sub>C</sub> Carbon Steel 2008 (\$/year)
1	0.001	0.0393	0.0261	0.0267	0.0257	0.0164	386.10	0.4844	1.594
2	0.005	0.0801	0.0569	0.0600	0.0563	0.0338	220.60	1.3834	4.547
3	0.010	0.1088	0.0797	0.0842	0.0788	0.0461	173.70	2.1790	7.137
4	0.030	0.1770	0.1358	0.1455	0.1345	0.0756	118.30	4.4514	14.610
5	0.050	0.2220	0.1739	0.1877	0.1724	0.0952	98.83	6.1986	20.390
6	0.080	0.2734	0.2184	0.2372	0.2166	0.1176	83.84	8.4138	27.710
7	0.100	0.3018	0.2434	0.2651	0.2414	0.1300	77.56	9.7299	32.040
8	0.400	0.5578	0.4766	0.5290	0.4736	0.2426	47.80	23.983	79.150
9	0.700	0.7148	0.6252	0.6992	0.6217	0.3121	39.31	34.522	114.000
10	1.000	0.8373	0.7432	0.8351	0.7394	0.3665	34.69	43.522	143.900

Table 4: Economic pipe size when AGO was used, based on 1998 costing

S/N	Q (m <sup>3</sup> /s)	Carbon Steel (1998) D (m)	Stainless Steel (1998) D (m)	Carbon Steel 1998 D <sub>n</sub> (m)	C <sub>p</sub> Carbon Steel 1998 (\$/m yr)	C <sub>c</sub> Carbon steel 1998 (\$/year)
1	0.001	0.0277	0.0179	0.0126	1.640	5.855
2	0.005	0.0574	0.0399	0.0264	4.341	15.660
3	0.010	0.0785	0.0563	0.0363	6.627	23.890
4	0.030	0.1290	0.0973	0.0602	12.930	46.720
5	0.050	0.1626	0.1254	0.0761	17.600	63.860
6	0.080	0.2011	0.1585	0.0944	23.450	85.080
7	0.100	0.2224	0.1771	0.1046	26.880	97.460
8	0.400	0.4164	0.3529	0.1976	62.450	227.300
9	0.700	0.5363	0.4662	0.2555	87.840	319.800
10	1.000	0.6303	0.5567	0.3009	109.100	397.700

Table 5: Effect of absolute roughness on Economic pipe diameter (lube oil)

S/N	Q (m <sup>3</sup> /s)	P (Kg/m <sup>3</sup> )	ε (m)	D (m)	ΔP (Pa)	C <sub>p</sub> (\$/m yr)	Degree of Pipe Roughness
1	0.7	870.24	5.0E-5	0.7276	40.570	35.62	Slightly
2	0.7	870.24	9.0E-5	0.7320	40.565	35.62	Rough
3	0.7	870.24	1.3E-4	0.7359	40.560	35.61	
4	0.7	870.24	1.7E-4	0.7392	40.610	35.66	Moderately
5	0.7	870.24	4.57E-4	0.7560	40.998	36.00	Rough
6	0.7	870.24	9.0E-4	0.7710	41.627	36.55	
7	0.7	870.24	1.0E-3	0.7735	41.765	36.67	
8	0.7	870.24	1.7E-3	0.7870	42.511	37.32	Severely
9	0.7	870.24	2.4E-3	0.7963	43.086	37.83	Rough
10	0.7	870.24	2.9E-3	0.8015	43.444	38.14	

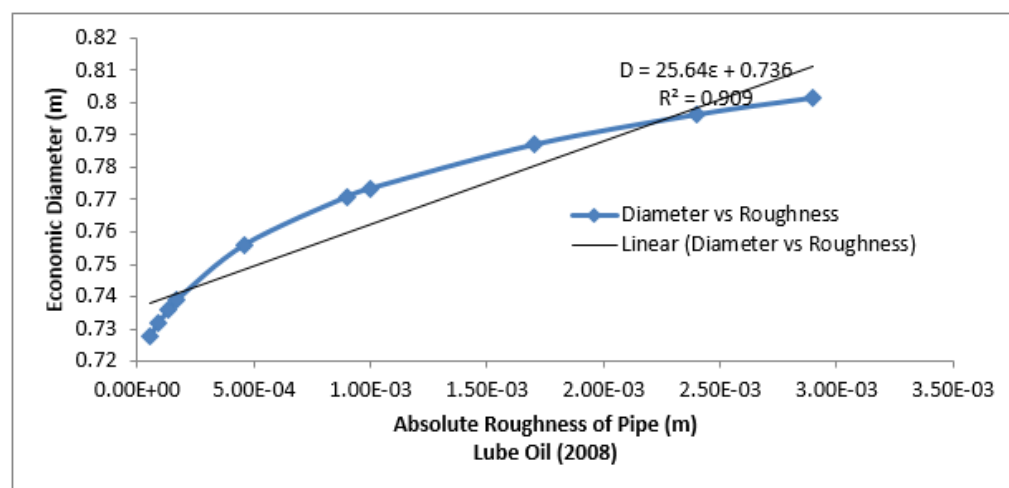


Figure 2: Effect of Pipe Roughness on Economic Diameter

Table 6: Linear correlations of the optimum economic diameter for particular fluids and materials.

S/N	Linear Correlation	Material, fluid (2008)
1	$D = 0.806Q + 0.158$	Carbon Steel, SAE,
2	$D = 0.843Q + 0.129$	Aluminum, SAE,
3	$D = 0.740Q + 0.120$	Stainless Steel, SAE
4	$D = 0.784Q + 0.120$	Aluminum, AGO
5	$D = 0.690Q + 0.112$	Brass, AGO



### 3.1 Statistical Analysis

To test the accuracy of the new implicit model, experimental results from Genic et al (2012) was used. The experimental data was obtained from 2008 costing (which includes the cost per meter length of carbon steel pipes, valves cost of electricity etc.). A plot of the economic diameters obtained from the new model ( $D_{pred}$ ) and that of Genic ( $D_{exp}$ ) was done at the same flow conditions. The accuracy was then ascertained with the value of  $R^2$ .

$R^2$  was calculated as follows:

$$R^2 = 1 - \frac{SSerr}{SStot} \tag{19}$$

$$SSerr = \sum(D_{exp} - D_{pred})^2 \tag{20}$$

$$SSreg = \sum(D_{pred} - D_{expave})^2 \tag{21}$$

$$SStot = SSreg + SSerr \tag{22}$$

Table 7 shows the values of the diameters used for the validation. Diameters calculated from Equation 17 were used as the predicted values ( $D_{pred}$ ) while those from Genic et al (2012) were the experimental values ( $D_{exp}$ ).

Table 7: Economic Diameters of Water Flow in Carbon Steel Pipe

S/N	Q (m <sup>3</sup> /s)	$D_{exp}$	$D_{pred}$
1	0.001	0.041000	0.038490
2	0.002	0.056000	0.052378
3	0.005	0.084000	0.078705
4	0.010	0.114000	0.107105
5	0.020	0.155000	0.145775
6	0.050	0.234000	0.219106
7	0.100	0.319000	0.298233
8	0.200	0.434000	0.405957
9	0.500	0.653000	0.610314
10	1.000	0.890000	0.830861

Density of water = 1000Kg/m<sup>3</sup>,

### 3.2 Comparison of the New Implicit Model with the Peters and Timmerhaus (2005) Model

Tables 2 through 4 shows the economic diameter ( $D$ ) computed with the new model and that calculated from the Nomograph model. The variation between the two models is shown in Figure 3. It can be observed that though the curves have the same pattern, a remarkable disparity exist between the new model and the Nomograph model even though the same parameters were used. This difference can be explained by the fact that the approximation given by Genereaux for new carbon steel pipe (assumed smooth flow) cannot adequately predict the flows in the region of Moody’s chart which is influenced by both Reynolds number and relative roughness. It is this approximation that has been used by previous researchers including Peters and Timmerhaus (2005) (Genic et al, 2012).

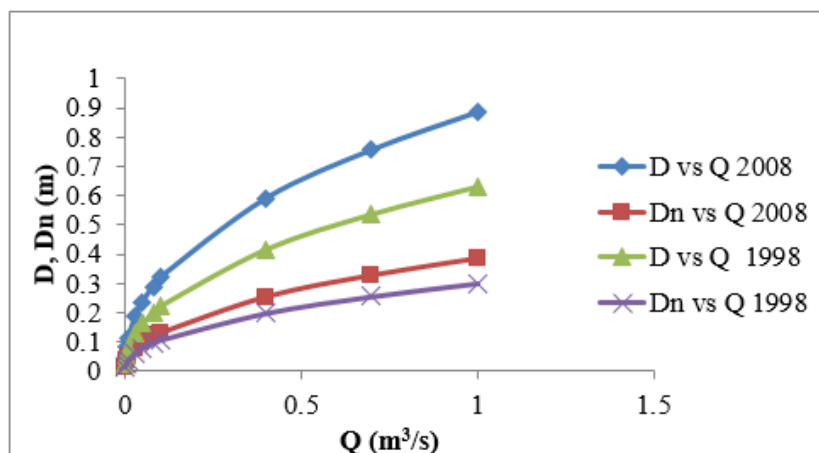


Figure 3: A plot of flow rate against diameter of carbon steel for the new model ( $D$ ) and the Nomograph model ( $D_n$ )

### 3.3 Comparison of Experimented Against Predicted Results

Since the new correlation covers flow on both fully turbulent and turbulent regime of the Moody’s chart the calculated economic diameter when compared with the Genic et al (2012) data (Table 7) for rough flow at the same flow conditions using water as fluid and carbon steel pipe shows that the model has high accuracy. This is ascertained from the  $R^2$  value

of 0.994636000 (Table 8) which is close to unity. A plot of the experimental economic diameters and the predicted ones against flow rate shown on Figure 4 indicates a very little deviation of the model from experimental results.

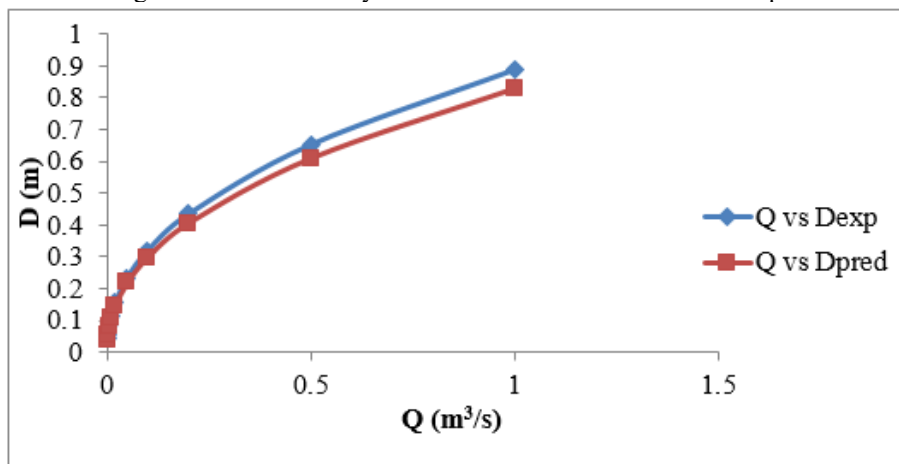


Figure 4: Plot of Predicted and Experimental Economic Diameter against Volume Flow rate.

Table 8: Validation Results calculated from Table 7

S/N	Index	Value
1	SS <sub>err</sub>	0.003441702
2	SS <sub>reg</sub>	0.634739000
3	SS <sub>tot</sub>	0.641623000
4	R <sup>2</sup>	0.994636000

#### 4. CONCLUSION

The cost of pipe run for transporting fluid through long distances or within a plant area in which fluids are moved from one process unit to another is a very significant factor when estimating the cost of project at the design stage. Any decision taken at this stage would be very crucial as it may not be possible to redeem any possible miscalculation after the execution of such project. An implicit correlation for predicting economic pipe diameter for turbulent flow in pipelines was simulated using Microsoft excels. Results obtained from the validation of the developed model showed that economic pipe diameter increases with fluid density. It was also found that the optimum pipe diameter increases with pipe roughness and Reynolds number. It can be concluded that the developed model made it possible to calculate the economic pipe diameter.

#### Nomenclature

a	Capital amortization factor yr <sup>-1</sup> .
A	Plant attainment (h/year)
b	Maintenance costs as fraction of installed capital yr <sup>-1</sup> .
CP	Annual pumping cost (\$/m yr)
CC	Annualized cost for the installed piping system (\$/year)
D	Pipe internal diameter (m)
E	Cost of electricity (\$/KW h)
F	Ratio of the total cost for fittings, valves and installation to the purchase cost for the new pipe.
J	Ratio of minor pressure losses and friction pressure drop
L	Pipe length (m)
Q	Volumetric flow rate [(m) <sup>3</sup> /s)
Re	Reynolds number
Rr	Relative pipe roughness (m)
v	Average fluid velocity (m/s)
x	Constant whose value depends on the pipe type.
X	Purchase cost of new pipe per meter length which depends on the piping material used.

#### Greek symbols

$\lambda$	Darcy-Weisbach friction factor
-----------	--------------------------------

$\Delta P$	Pressure drop (Pa)
$\varepsilon$	Absolute roughness of pipe internal surface (m)
$\eta$	Combine pump and motor efficiency (fraction).
$\rho$	Fluid density ( $\text{kg}/\text{m}^3$ )
$\mu$	Fluid viscosity taken at $30^\circ\text{C}$ during calculation PaS

## REFERENCES

- Akintola, T.A. (2003). "Optimum Pipe Size Selection for Turbulent Flow". *Journal of Science and Technology Research* 14, p.112-123.
- Alamu, O.J., Adigun O.J. and Durowoju M.O. (2002) Computer Aided Optimum Pipe Size Selection for Non Viscous Flow, *Annals of Engineering Analysis*, 1(4): .p.30 – 39.
- Altshul, A. D. and P.G. Kiselev (1975). *Hydraulics and Aerodynamics*, Stoisdat Publishing House, Moscow USSR.
- Bratland, Ove (2009) Pipe Flow 1. Single Phase Flow Assurance. [Online] (1). p. 6- 40. Available from: [www.drbratland.com](http://www.drbratland.com). [Accessed: 8th October, 2022].
- Brkić, D., (2011) Review of explicit approximation to the Colebrook relation for flow friction. *Journal of Pet. Science and Engineering* 77, 34-48.
- Durand A.A., Casas, M.V., Cornejo A.S., Carranza, D.J., Pacheco Roman, F.J., Espinoza, Juan Sampieri and Parra, L.V. (2010) Updating the rules for pipe sizing. *Chemical Engineering*. 116 (1) 48–50.
- Genereaux, R. P. (1937) Fluid-Flow Design Methods, *Industrial and Engineering Chemistry* 29 385–388.
- Genic, S.B., Jacimovic, B.M and Genic, V.B. (2012) Economic optimization of pipe diameter for complete turbulence. *Journal of Energy and Building* 45, 335–338.
- McCabe, W. L., Smith, J. C. and Harriott, Peter. (2005) *Unit Operation of Chemical Engineering*, 7th edition. Singapore: McGraw-Hill.
- Odebunmi, (2002) Characterization of Crude Oils and Petroleum Products. *Chemical Society of Ethiopia* 16 (2) .p. 115-132.
- Perry, R.H. and Green, D. W. (2008) *Perry's Chemical Engineers' Handbook*, McGraw-Hill,
- Peters, M. S. and Timmerhaus, K. D. (1968) *Plant Design and Economics for Chemical Engineers*, 2nd ed. (McGraw-Hill).
- Peters, M. S. and Timmerhaus, K. D. (1991). *Plant Design and Economics*, 4th Edn. (McGrawHill).
- Peters, M. S. and Timmerhaus, K. D. (2004). *Plant Design and Economics*, 5th Edn. (McGrawHill).
- Whitesides, R. W. (2008) Selecting the Optimum Pipe Size. PDHonline Course M270 (12PDH). [Online] (12). p.1-50. Available from: [www.pdhonline.org/./m270content](http://www.pdhonline.org/./m270content). [Accessed: 8th October, 2022]



## Modelling of Liquefied Natural Gas and Propane Production using Nonlinear Autoregressive with Exogenous Input Neural Network

Azubuike Shedrack ASHINZE<sup>1\*</sup>, Adekunle Tirimisiyu ADENIYI<sup>1</sup>, Abdulwahab GIWA<sup>1</sup>

<sup>1</sup>Department of Chemical and Petroleum Engineering, College of Engineering, Afe Babalola University, KM. 8.5, Afe Babalola Way, Ado-Ekiti, Ekiti state, Nigeria.

<sup>1\*</sup>[azubuika@abuad.edu.ng](mailto:azubuika@abuad.edu.ng), <sup>1</sup>[adenivia@abuad.edu.ng](mailto:adenivia@abuad.edu.ng), <sup>1</sup>[agiwa@abuad.edu.ng](mailto:agiwa@abuad.edu.ng)

\*Corresponding author

### ABSTRACT

Natural gas is used globally for the production of liquefied natural gas (LNG) and propane. In this paper, a Nonlinear Autoregressive with exogenous inputs (NARX) neural network model was built in MATLAB R2021a in a bid to capture the time-behaviour of the LNG and propane production process. Five input parameters and three output parameters were chosen from the daily production report of a natural gas handling facility in southern Nigeria which were tabulated/saved in Excel, and then incorporated into a written transfer function generation algorithm and used to develop a Simulink model. The simulation generated input-output time series datasets representing the dynamics of the natural gas liquefaction plant. Furthermore, the datasets were imported into the NARX Graphical User Interface (GUI) in MATLAB R2021a to create the neural network model. The NARX model developed was trained iteratively, and its performance was evaluated using mean squared error (MSE) and regression (R) values as the criteria. MSE values of approximately 0.7357, 0.7819, 0.8398 and R-values of approximately 0.9981, 0.9979, 0.9977 were obtained after training, validation, and testing respectively, which depicted the efficacy of the model in capturing the dynamics of the production process as well as forecasting future values of LNG and propane.

**Keywords:** Natural gas, liquefied Natural Gas (LNG), artificial neural network (ANN), graphical user interface (GUI), nonlinear autoregressive with exogenous inputs (NARX).

### 1.0 INTRODUCTION

Natural gas is contained in pressure-filled rock reservoirs in the earth's crust. It is formed from decomposed organic matter (biomass) which accumulated in thick layers on the earth's surface and ocean floors millions of years ago and were buried underground over time. The buried organic matter transformed into natural gas due to its exposure to extremely high heat.

Natural gas is extracted from these rock reservoirs alone just like crude oil or dissolved in crude oil (Bakar and Ali, 2010; EIA, 2020). The main component of natural gas is methane (CH<sub>4</sub>), although it may also, in traces, contain additional kinds of paraffin (C<sub>n</sub>H<sub>2n+2</sub>) with n>1, cyclic hydrocarbon compounds, aromatic hydrocarbon compounds, and non-hydrocarbon gases (Abdel-Aal *et al.*, 2003; Mokhatab *et al.*, 2006; Mezni, 2015; Speight, 2017). It is colourless and odourless in its purest form. The global use of natural gas is fast rising owing to its environmental benefits as well as its less labour-intensive processing compared to other fossil fuels (Bakar and Ali, 2010; Nejad and Farzi, 2014; Mezni, 2015; ElBadawy *et al.*, 2017; Owolabi *et al.*, 2020). After extraction, natural gas is sent to industry via pipelines, where it is employed as a direct chemical feedstock for a variety of uses. These uses include the production of hydrates, electricity, clean fuels, plastic precursors or methanol, aluminium, cement, iron bars, and processing to obtain other useful products (Mokhatab *et al.*, 2006; EIA, 2020).

The industrial processing of natural gas is a time-consuming and expensive operation. It consists of gas treatment, which includes gas sweetening (removal of all impurities and contaminants in the natural gas such as acid gases (H<sub>2</sub>S and CO<sub>2</sub>), dehydration (removal of water vapour), removal of inert gases, and cooling of the natural gas in a cryogenic unit (liquefaction unit) to produce propane and liquefied natural gas (LNG). The cryogenic equipment records high propane recovery of about 90 to 98% when operating at temperatures below -100 °F, and the process involved is widely acknowledged as the most practical way of recovering a significant portion of propane. Cryogenic refrigeration process is the name given to the procedure that takes place in the cryogenic unit, and it is similar to the procedure in contemporary home refrigerators but on a far larger scale (Finn, 2002; Mokhatab *et al.*, 2006; Aronsson, 2012; Alsohbi, 2015; Bhran, 2016; Ekejiuba and Ikoku, 2021). Liquefied natural gas (LNG) is a form of natural gas that is obtained when natural gas

has been cooled to a temperature of about -162 °C and assumes a volume of approximately 1/600 of its volume at room temperature (20 - 30 °C) while propane is a paraffinic hydrocarbon ( $C_nH_{2n+2}$ ) with the chemical formula  $C_3H_8$ .

Liquefied compressed natural gas (LCNG) is produced by compressing liquefied natural gas to a pressure of roughly 200 bar (2900 psig). When natural gas is compressed to a pressure between 1800 psig and 3600 psig and it assumes a volume smaller than 1% of the volume it occupies at standard atmospheric pressure (760 mmHg or 101,325 Pa), compressed natural gas (CNG) is produced. Hydrogen compressed natural gas (HCNG) is created by mixing compressed natural gas (CNG) with a predetermined amount of hydrogen. The near future is expected to be quite promising for emerging trends like LCNG and HCNG (Mokhatab *et al.*, 2006; Yadav and Sircar, 2017).

Artificial neural network (ANN) models can be thought of as non-linear information processing and estimation models made up of interconnected processing elements known as neurons that are useful for data compression, data classification, pattern recognition, fault detection, and time prediction in addition to being used to represent the correlation between input-output data of a process (Himmelblau, 2000; Giwa *et al.*, 2015; Gupta *et al.*, 2019). Each neuron in the ANN is similar to a biological neuron in terms of structure and function. Artificial neural networks are very powerful tools for providing multiple solutions to real-life problems in diverse fields such as medicine, sciences, finances, engineering and various other industries, and they are classified as static neural networks and dynamic neural networks.

Static neural networks include multilayer feed-forward neural networks and fuzzy neural networks while examples of dynamic neural networks are nonlinear autoregressive neural networks, nonlinear autoregressive neural networks with exogenous (external) input, and nonlinear input-output neural networks (Diaconescu, 2008; Akhoondzadeh *et al.*, 2014; Abounoori *et al.*, 2016).

The use of Nonlinear Autoregressive with exogenous input (NARX) neural network in capturing the dynamics of a natural gas liquefaction process is yet to be investigated. To fill this gap and contribute to the literature, the process occurring in a natural gas liquefaction plant is modeled and simulated using the Nonlinear Autoregressive with exogenous input (NARX) neural network to robustly represent the time behavior of the process and predict the amount of LNG and propane produced at the output of the neural network in vector format.

## 2.0 COMPUTATIONAL MODELLING AND SIMULATION

### 2.1 Data acquisition

The data used for the dynamic modeling were acquired from the daily production report of a natural gas liquefaction plant situated in southern Nigeria. The data, which were primary in nature had a time span of sixty-nine (69) days. The plant was involved in the daily liquefaction of processed natural gas to liquefied natural gas, propane, and gas condensates.

### 2.2 Model Development

Five (5) parameters were selected from the acquired dataset while three (3) parameters were selected as the output parameters. The selected parameters were tabulated and saved in Microsoft Excel 2019 (Microsoft, 2019). The saved file was incorporated in a written transfer function generation algorithm in MATLAB R2021a (MathWorks, 2021) *mfile* environment which could be simulated with the aid of a transfer function model developed in MATLAB/Simulink to relate the input parameters and the output parameters obtained from the daily production report. This simulation generated time series inputs and targets using random number blocks at the inputs, which output a normally (Gaussian) distributed random signal with the aid of varying odd number seeds of 0, 3, 5, 7, and 9 for blocks U1, U2, U3, U4, and U5 respectively, a sample time of 0.01 and stop time of 500 s. The output was made repeatable for a given seed. A time series dataset is mathematically expressed as:

$$y(t), t = 0, 1, 2, \dots \quad (1)$$

Where  $t$  is the time elapsed for a set of discrete output parameters  $y$ .

The time series dataset obtained which comprised of 5001 samples were then imported to MATLAB R2021a workspace from the Microsoft Excel software and used to develop a Non-linear AutoRegressive with eXogenous inputs (NARX) model with the aid of the NARX neural network graphical user interface (GUI) available in the time series application of the program. The NARX model methodology is mathematically defined as:

$$y(t) = f[u(t-1), u(t-2), \dots, u(t-du), y(t-1), y(t-2), \dots, y(t-dy)] \quad (2)$$

Where  $y$ = model outputs,  $u$ =exogenous data,  $f$ = a nonlinear function representing the mapping performed by the neural network,  $du$ = delay order of input  $u$  and  $dy$ = delay order of input  $y$ .

The NARX neural network GUI in MATLAB R2021a is characterised by a sigmoid transfer function in the hidden layer and purelin transfer function in the output layer (MathWorks, 2021). The parameters used in formulating the NARX neural network are shown in Table 1.

Table 1: Parameters used in formulating the three dynamic neural network models

S/N	Parameter	Value/Description
1.	Number of time series inputs	5
2.	Number of time series outputs	3
3.	Number of layers	3
4.	Number of hidden neurons	10
5.	Number of delays	2
6.	Training algorithm	Levenberg Marquardt

### 3.0 RESULTS AND DISCUSSION

After launching the time series application and feeding the necessary parameters to the NARX neural network GUI, the model was developed, then trained and retrained iteratively to obtain progress results and predict desired output parameters. The progress results obtained included the mean squared error values presented in Table 2. The mean squared error is an indication of the difference between the actual data and the predicted data. It is a measure of the performance of the model in learning the dataset as the lower the MSE computed by the model, the better the model in learning the dataset.

Table 2: MSE and R values for the NARX model

Description	Target Value	Epoch	R	MSE
Training	10503	24	0.9981	0.7357060
Validation	2250	24	0.9979	0.781932
Testing	2250	24	0.9977	0.839765

A plot of the validation efficiency between the number of epochs and the mean squared error (performance) is presented in Figure 1, and this shows a decrease in training error, validation, and testing until iteration 24 was attained, thereby signifying that there was no element of occurrence of overfitting. The best performance was taken from the epoch with the lowest validation error (dotted circle).

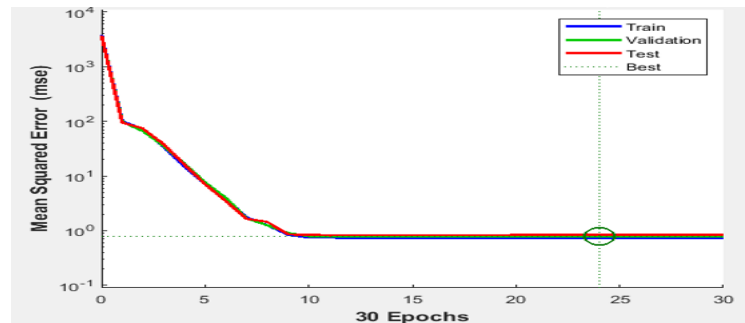


Figure 1: Dependence of the mean squared error on the number of epochs for the trained NARX model

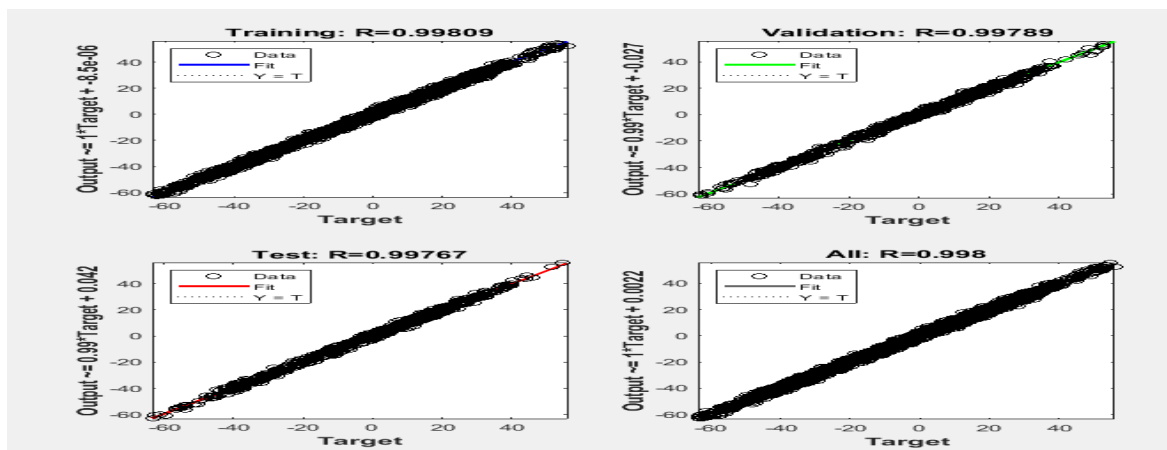


Figure 2: Regression plots for the trained NARX model

Four distinct regression plots are presented in Figure 2. The regression (R) value helps to ascertain the relationship between the outputs and the targets. A regression value of 0 would imply a random relationship while a regression value of 1 would imply a close relationship between the outputs and the targets. The solid straight lines represent the linear regression line that best fitted the data between the outputs and the training targets (blue), validation targets (green), testing targets (red) and overall targets (black). The overlap of the actual target and expected output along the 45° solid straight line indicates a close relationship between the target and the output values, which serves as evidence of the efficacy of the NARX model.

The error autocorrelation function, which shows how the prediction errors are related in time, is shown in Figure 3 to validate the performance of the trained network. For a prediction model to be adjudged as an accurate one, the error autocorrelation function of value should only be one non-zero, and it should arrive at zero lag, which is the mean squared error. In the plot, a significant correlation was observed between the prediction errors, and most of the trained network fell within the red confidence limits, leaving an opportunity for improvement (probably by increasing the number of neurons and delays further). Apart from the correlation that hit the zero lag, all the other correlations were considerably shorter and nearly all of them fell within the red confidence limits that signified that the network had been properly trained.

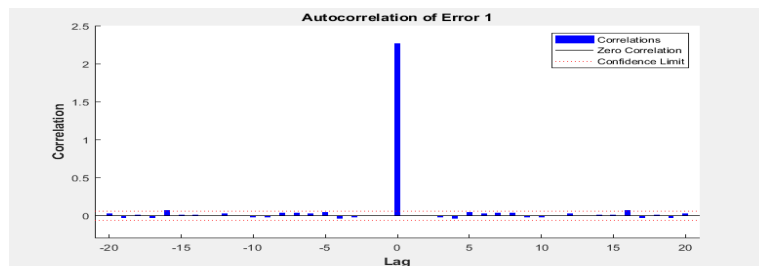


Figure 3: Error autocorrelation for the trained NARX model

The input-error cross-correlation function is seen in Figure 4 and provides additional verification of the network performance by demonstrating how the errors are correlated with the input sequences  $u(t)$ . For an accurate prediction model, all the correlations should be zero. In the plot, correlations were observed between the input and the error, which indicated that there was opportunity to enhance prediction, probably by increasing the number of delays in the tapped delay lines.

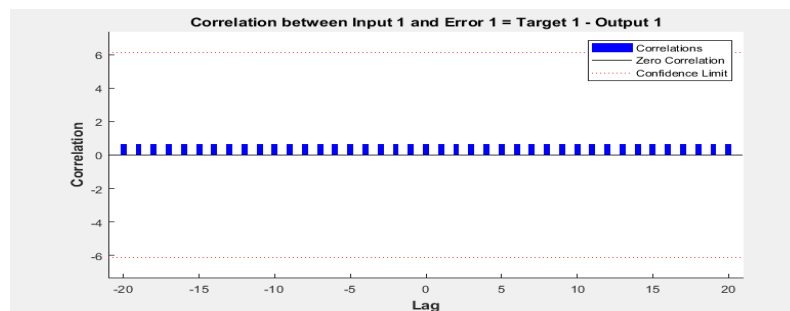


Figure 4: Input error cross-correlation for the trained NARX model

Figure 5 displays the outputs, targets, and errors against time and shows the time points that were chosen for training, testing, and validation. It is a plot of the errors between a target time series and an output time series on the same axis. The plot required numerous target pairs, which typically defined the output and the targets for training, validation and testing.

The training state and error histogram of the created NARX model are depicted in Figure 6 and Figure 7, respectively. Figure 6 shows the variation of the gradient coefficient with the number of epochs and presents the final value of the gradient coefficient as 1.0295 at epoch 30, which was found to be close to zero (0). The total error of the NARX neural network was split up into 20 smaller vertical bins in Figure 7. The y-axis displays the number of data points from the entire dataset in a particular bin. The bin in the middle of the plot was found to correspond to an error of -0.2545. The corresponding height of each segment of the bin notified that the numerous samples from the different datasets had errors that were within that range.

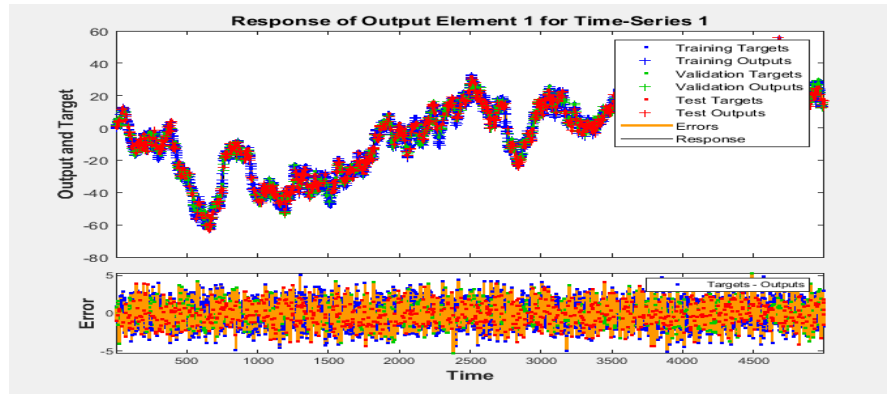


Figure 5: Time series response for the trained NARX model

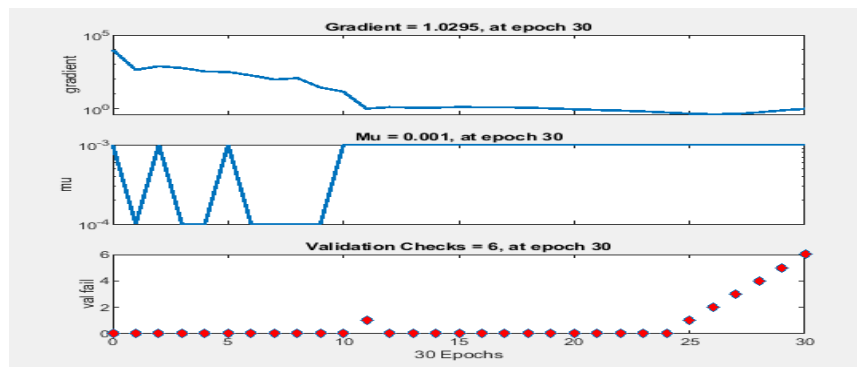


Figure 6: Training state for the trained NARX model

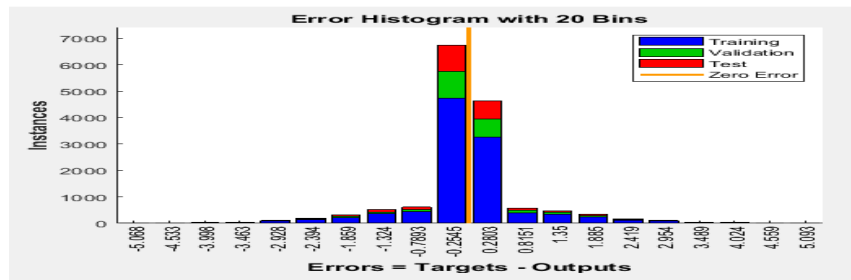


Figure 7: Error histogram for the developed NARX model

#### 4.0 CONCLUSION

The results obtained from the simulation of the NARX neural network model developed showed that the model could represent the process very well because values of the mean squared error and the correlation coefficient were very close to zero (0) and unity (1), respectively. Therefore, the NARX neural network model can be used to represent the dynamics of a natural gas liquefaction plant successfully.

#### REFERENCES

- Abdel-Aal, H.K., Aggour, M. and Fahim, M.A. (2003) *Petroleum and Gas Field Processing*. New York: Marcel Dekker, Inc.
- Abounoori, A.A., Naderi, E., Alikhani, N.G. and Mohammadali, H. (2016) ‘Comparative Study of Static and Dynamic Artificial Neural Network Models in Forecasting of Tehran Stock Exchange’. A Research Project Financed by the Islamic Azad University Central, Tehran Branch. *International Journal of Business and Development Studies (IJBS)*, 8(1), pp 43-59. Available at: [https://ijbds.usb.ac.ir/article\\_2635\\_6ec4858c51fc98ddca15dcf14a32b695.pdf](https://ijbds.usb.ac.ir/article_2635_6ec4858c51fc98ddca15dcf14a32b695.pdf) (Accessed: 5th October, 2021).
- Akhoondzadeh, M., Shahrivand, M. and Sharifi, M. A. (2014) ‘Detection of Gravity Changes before Powerful Earthquakes in GRACE Satellite Observations’, *Annals of Geophysics*, 57(5), pp. 2-12. Available at: 0.4401/ag-6612.
- Alsohbi, S. (2015) *Modeling and Optimization of Natural Gas Processing and Production Networks*. A thesis presented to the University of Waterloo in fulfilment of the thesis requirement for the degree of Doctor of Philosophy in Chemical Engineering. Available at:



- [https://uwspace.uwaterloo.ca/bitstream/handle/10012/9522/Alsobhi\\_Saad.pdf;jsessionid=066847342D5317B B106810596A464066?sequence=3](https://uwspace.uwaterloo.ca/bitstream/handle/10012/9522/Alsobhi_Saad.pdf;jsessionid=066847342D5317B B106810596A464066?sequence=3) (Accessed: 15th March, 2022).
- Aronsson, E. (2012) *FLNG Compared to LNG Carriers-Requirements and Recommendations for LNG Production Facilities and Re-gas Units*. A thesis submitted to the Department of Shipping and Marine Technology, Division of Marine Design, Chalmers University of Technology, Gothenburg, Sweden for the Degree of Master of Science, Report No. X12/279, pp 1-38. Available at: <https://publications.lib.chalmers.se/records/fulltext/162630.pdf> (Accessed: 4<sup>th</sup> June 2022).
- Bakar, W. A. W. A. and Ali, R. (2010) *Natural Gas*. Edited by Primoz Potocnik, London: IntechOpen.
- Bhran, A.A. Hassanean, M.H., and Helal, M.G. (2016) ‘Maximization of Natural Gas Liquid Production from an Existing Gas Plant’, *Egyptian Journal of Petroleum*, 25, pp 333-341. Available at: <https://www.infona.pl/resource/bwmeta1.element.elsevier-7ae86205-66a8-3c82-abea-0a075861b719> (Accessed: 5<sup>th</sup> June 2022).
- Diaconescu, E. (2008) ‘The use of NARX model to predict chaotic time series’, *WEAS Transactions on Computer Research*, 3(3), pp 182-191. Available at: <https://www.researchgate.net/publication/228571349>, (accessed 15<sup>th</sup> March 2022).
- Ekejiuba, A. and Ikoku, C.U. (2021) ‘Viability of Producing LPG and LNG from the Nigerian Gas Flare Stream’, *Inter-world Journal of Science and Technology (IJST)*, 2(1), pp 1-32. Available at: [https://www.researchgate.net/publication/350790144\\_VIABILITY\\_OF\\_Producing\\_LPG\\_and\\_LNG\\_From\\_The\\_Nigerian\\_Flare\\_Gas\\_Stream](https://www.researchgate.net/publication/350790144_VIABILITY_OF_Producing_LPG_and_LNG_From_The_Nigerian_Flare_Gas_Stream) (Accessed 5th June, 2022).
- ElBadawy, K.M., Teamah, A.M., Shehata, I.A. and Hanfy, A.A. (2017) ‘Simulation of Liquefied Petroleum Gas Production from Natural Gas Using Fractionation Towers’, *International Journal of Advanced Scientific and Technical Research (IJASTR)*, 6(7), pp 148-153. Available at: <https://dx.doi.org/10.26808/rs.st.i7v6.16> (Accessed: 8th June, 2022).
- Finn, A.J. (2002) ‘Effective LNG Production Offshore’, pp 1-19. Available at: [https://www.researchgate.net/publication/237557652\\_EFFECTIVE\\_LNG\\_PRODUCTION\\_OFFSHORE](https://www.researchgate.net/publication/237557652_EFFECTIVE_LNG_PRODUCTION_OFFSHORE), (Accessed: 4<sup>th</sup> June 2022).
- Giwa, A., Bello, A. and Giwa, S.O. (2015) ‘Artificial Neural Network Modelling of a Reactive Distillation Process for Biodiesel production’, *International Journal of Scientific and Engineering Research*, 6(1), pp 1175-1191. Available at: [https://www.researchgate.net/publication/271852041\\_Artificial\\_Neural\\_Network\\_Modeling\\_of\\_a\\_Reactive\\_Distillation\\_Process\\_for\\_Biodiesel\\_Production](https://www.researchgate.net/publication/271852041_Artificial_Neural_Network_Modeling_of_a_Reactive_Distillation_Process_for_Biodiesel_Production), (Accessed: 15<sup>th</sup> June, 2022)
- Gupta, A., Salau, A., Akinola, A.S., Chaturvedi, P. and Nwulu, I.N. (2019) ‘Artificial Neural Networks: Its techniques and Applications to Forecasting’, *IEEE International Conference on Automation, Computation and Technology Management (ICACTM)*, pp 320-324. Available at: <https://www.researchgate.net/publication/335340306ArtificialneuralnetworksitstechniquesandApplicationstoforecasting> (Accessed: 3<sup>rd</sup> February, 2022).
- Himmelblau, D. M. (2000) ‘Applications of Artificial Neural Networks in Chemical Engineering. *Korean Journal of Chemical Engineering*, 17(4), pp 373-392. Available at: <https://www.cheric.org/PDF/KJChE/KC17/KC17-4-0373.pdf>, (Accessed: 3<sup>rd</sup> February, 2022).
- MathWorks [Online] 2021 Neural Networks. Available at: <https://www.mathworks.com/discovery/neural-network.html>, (accessed: 11th October 2021).
- MathWorks, 2021. MATLAB R2021a. The MathWorks, Inc.
- Mezni, M. (2015). *LPG Recovery Unit Optimization*. Thesis for: Dipôme National d'Ingénieur en Chimie Industrielle, pp 1-84. Available at: [https://www.researchgate.net/publication/317840680\\_LPG\\_Recovery\\_Unit\\_Optimization](https://www.researchgate.net/publication/317840680_LPG_Recovery_Unit_Optimization) (Accessed: 1<sup>st</sup> June 2022).
- Microsoft, 2019. Excel software, 2019. Microsoft Corporation.
- Mokhatab, S., Poe, W.A., and Mak, J.Y. (2006) *Handbook of Natural Gas Transmission and Processing. Principles and Practices*. Fourth Edition, Gulf Professional Publishing, MA, USA 1-5.
- Nejad, A.T. and Farzi, A. (2014) ‘Simulation and Optimization of LNG Production Unit for Energy Conservations’, *Iranica Journal of Energy and Environment*, 5(1), pp 67-72. Available at: [https://www.ijee.net/article\\_64510\\_be35d9e75faa4847436bafa769a4b6b5.pdf](https://www.ijee.net/article_64510_be35d9e75faa4847436bafa769a4b6b5.pdf) (Accessed: 4<sup>th</sup> June 2022).
- Owolabi, J.O., Kila, O.O. and Giwa, A. (2020) ‘Modelling and Simulation of a Natural Gas Fractionation System Using Aspen HYSYS’, *International Journal of Engineering Research in Africa (IJERA)*, 49, pp 1-14. Available at: 10.4028/www.scientific.net/IJERA.49.1 (Accessed: 18<sup>th</sup> February, 2022).
- United States Energy Information Administration (2020) *Annual Energy Outlook with projectionsto2050*. Available at: <https://www.eia.gov/aeo>, (accessed 13<sup>th</sup> October 2021).
- Yadav, K. and Sircar, A. (2017) ‘Hydrogen Compressed Natural Gas and Fuel Compressed Natural Gas: Fuels for Future’, *Journal of Energy and Management*. Available at: <https://www.researchgate.net/publication/321183186>, (accessed 29<sup>th</sup> April 2022).



## Evaluation of Natural Gas Liquefaction Process using Nonlinear Autoregressive Neural Network and Nonlinear Input-Output Neural Network: A Comparative Study

Azubuike Shedrack ASHINZE<sup>1\*</sup>, Adekunle Tirimisiyu ADENIYI<sup>1</sup>, Abdulwahab GIWA<sup>1</sup>

<sup>1</sup>Department of Chemical and Petroleum Engineering, College of Engineering, Afe Babalola University, KM. 8.5, Afe Babalola Way, Ado-Ekiti, Ekiti state, Nigeria.

<sup>1\*</sup>[azubuikea@abuad.edu.ng](mailto:azubuikea@abuad.edu.ng), <sup>1</sup>[adeniyia@abuad.edu.ng](mailto:adeniyia@abuad.edu.ng), <sup>1</sup>[agiwa@abuad.edu.ng](mailto:agiwa@abuad.edu.ng)

\*Corresponding author

---

### ABSTRACT

The simulation modelling of artificial neural network models to evaluate a natural gas liquefaction process has been carried out in this work. Five input parameters gas feed volume, gas feed flow rate, gas feed temperature, gas feed pressure and volume of fuel gas utilized in the gas turbine power plant and three output parameters volume of Liquefied Natural Gas produced, volume of propane produced, and volume of gas condensates produced were chosen from the raw data obtained from a liquefaction facility in southern Nigeria. These parameters were arranged in Excel before being incorporated into an m-file transfer function algorithm and transfer function model in MATLAB R2021a to generate a time series dataset. The input and output parameters were imported into the time series application available in MATLAB R2021a and trained using the Levenberg Marquardt algorithm. The Nonlinear Autoregressive (NAR) model gave 0.758528, 0.820267 and 0.857507 while the Nonlinear Input-Output (NIO) model gave 33.16290, 35.68165 and 36.05067 as the Mean Squared Error (MSE) values for training, validation and testing, respectively. Thus, for the Autoregressive two neural network models considered, the NAR model outperformed the NIO model in the evaluation of natural gas liquefaction process perceptible in the lower MSE values returned.

**Keywords:** *Liquefaction, MATLAB, nonlinear autoregressive, nonlinear input-output, simulation modelling.*

### 1.0 INTRODUCTION

Natural gas is a fossil fuel extracted from underground rock reservoirs in gas or crude oil fields. Its formation can be linked to decomposed organic matter, which accumulated in thick layers on the earth's surface and ocean floors millions of years ago. Over time, the organic matter was covered gradually by sediments and layers of rocks where they became compressed. As they moved deeper into the earth's crust, they became subjected to extremely high heat and pressure to form natural gas. The natural gas extracted from the gas or crude oil fields is transported to industries for processing to produce solids such as natural gas hydrates formed by mixing natural gas with water at 80 to 100 bar and 2 to 10 °C, liquids such as syncrude methanol and ammonia by converting the natural gas to syngas and then employing a Fischer-Tropsch process (in the presence of a catalyst) or an oxygenation method in the presence of a suitable catalyst, and commodities such as aluminium, glass and Iron bars using the energy, thermal or electrical power from the natural gas (Bakar and Ali, 2010; Nejad and Farzi, 2014; Mezni, 2015; ElBadawy *et al.*, 2017; Owolabi *et al.*, 2020). The processing of the extracted natural gas in the industries is a complex process involving the treatment of the gas to remove impurities such as hydrogen sulphide and carbon (IV) oxide that may be present, dehydration of the gas to remove water and water vapour, removal of inert gases and liquefaction of the gas to produce liquefied natural gas (LNG) and propane.

Liquefaction is the conversion of natural gas to liquid state by chilling the natural gas to a temperature of 260 °F (-162 °C), and this occupies approximately 1/600 of its original volume at room temperature (Cameron LNG, 2018). The liquefaction process is a large-scale cryogenic refrigeration process like the process in contemporary home refrigerators that makes use of a variety of refrigeration cycles including cascade, mixed refrigerant and turbo-expander refrigeration cycles. During the liquefaction process, propane (a lower paraffin hydrocarbon with the chemical formula C<sub>3</sub>H<sub>8</sub> can be produced as a by-product (Finn, 2002; Mokhtab *et al.*, 2006; Aronsson, 2012; Alsobhi, 2015; Bhran *et al.*, 2016; Vikse *et al.*, 2018, Ekejiuba and Ikpku, 2021; Sun *et al.*, 2022).

Liquefied Natural Gas (LNG) is produced to ease the storage of natural gas in well-insulated cryogenic tanks and cylinders to enable economized and safe transportation of the product around the world for various uses. Similarly, propane is produced in a liquid state and stored in well-insulated tanks and low-pressure cylinders for ease of storage and safe transport around the world. LNG and propane are useful as fuels in transport, heating and cooking in homes, power

generation, and a chemical feedstock in other industrial applications. They are crucial natural gas products for optimizing a country's natural gas reserve and growing a country's economy (Rafiq *et al.*, 2011; Nejad and Farzi, 2014; Mezni, 2015; Ubani and Ani, 2016; FMPR, 2017; Cameron LNG, 2018; Borelli *et al.*, 2021; CTCN, 2022).

The evaluation of the natural gas liquefaction process for various unique purposes through modelling and simulation has been carried out by various researchers during the past decade using different nonconventional and conventional models implemented with the aid of various specialized chemical engineering application software. Trigilio *et al.* (2012) modelled and simulated a natural gas liquefaction process in a stationary state using cycles with mixed refrigerant (MR) and cascade cycles with pure refrigerants with the aid of Peng-Robinson equation of state in Aspen HYSYS software and routines in MATLAB software. The heat and powers of the cycle were derived after the modelling and simulation were performed and through sensitivity analysis, the high pressure of the external cycle (for the cascades) and the high pressure of the simple cycle with mixed refrigerant were found to be the most affecting variables. The authors further proposed an optimization approach using compositions found in the literature for the simple cycle as a means of maximizing the coefficient of performance. Nejad and Farzi (2014) simulated the process of converting natural gas to LNG with the aid of Aspen HYSYS software aimed at minimizing the energy consumption per ton of LNG produced. The results obtained showed that the energy consumption of the LNG liquefaction plant can be minimized by optimizing the outlet pressure from the compressor and obtaining the best mass fraction for the refrigerants used in the three-stage heat exchanger. Mezni (2015) performed a simulation of the propane refrigeration unit of a natural gas processing plant using Aspen HYSYS software to check the performance of the unit in recovering propane from the processed natural gas feed. The results obtained showed that hydrates were formed in the propane chiller tubes while all equipment was working well which prompted the author to suggest the installation of spray nozzles in the chiller tubes that can decrease the hydrates formation temperature and improve propane recovery. The author also proposed that the efficiency of propane recovery from natural gas was essential to the characteristics of the LNG produced from the processing plant. The simulation of human intelligence by technology, particularly computers, is known as artificial intelligence. An artificial intelligence architecture called an artificial neural network was created to simulate the structure and neurological processing capabilities of the human brain. They can be viewed as nonlinear empirical models, and like a human brain, they are made up of interconnected processing units known as neurons that allow them to accurately learn and represent input-output data, compress data, classify data, identify patterns, find errors and predict outcomes in real time (Hajjar *et al.*, 2018; Sansa and Bellaaj, 2018; Gupta *et al.*, 2019). Based on the information obtained from the literature, different types of artificial neural networks have been used to investigate different processes rooted in chemical engineering. For example, Giwa and Karacan (2012) used delayed neural networks, namely the Nonlinear Autoregressive (NAR) neural network, Nonlinear Autoregressive with exogenous input (NARX) neural network and Nonlinear Input-Output (NIO) neural network available in MATLAB R2010b software to model a reactive packed distillation column for production of ethyl acetate to predict the top and the bottom section temperatures of the column. The authors obtained satisfactory results for the NAR and NARX model while the results from the NIO were unsatisfactory. Bolaji *et al.* (2019) developed NARX and NIO models with the aid of MATLAB software to study and relate both steady state and transient characteristics of pollution mortality using simulated and operational data to demonstrate the usefulness of artificial neural networks in capturing complicated nonlinear dynamics. Their findings suggested that both models developed were capable of accurately capturing the dynamic dataset being modelled to an acceptable level.

There exist a gap in the literature regarding the application of Artificial Neural Networks in capturing the time behaviour and underlying trends among process parameters in a time series dataset from a gas liquefaction facility producing Liquefied Natural Gas (LNG) and propane due to the fact that time series datasets for a natural gas liquefaction process cannot be readily obtained. Hence, this research work has been carried out to generate time series datasets for a natural gas liquefaction process and apply Nonlinear Autoregressive (NAR) neural networks and Nonlinear Input-Output (NIO) neural network available in MATLAB R2021a (MathWorks, 2021) software to model the liquefaction process which can be helpful in predicting the next values of LNG and propane produced at the output of the facility to a certain degree of acceptance. The selected input parameters for modelling the process were the natural gas feed volume, natural gas feed flow rate, natural gas feed temperature, natural gas feed pressure and volume of fuel gas utilized in the gas turbine power plant attached to the liquefaction plant while the selected output parameters were the volume of LNG produced, the volume of propane produced and the volume of gas condensates produced.

## 2.0 METHODOLOGY

The main tool used in accomplishing this work was MATLAB R2021a (MathWorks, 2021), a research tool used to analyse data, develop algorithms and create models. The data used were obtained in a steady-state form in real-time from a working liquefaction plant in southern Nigeria. Input and output parameters were selected from the raw data and arranged in cell arrays in Microsoft Excel software (Microsoft, 2019) before being converted to nonlinear dynamic data by incorporating the selected parameters into a developed transfer function generation algorithm and transfer function model in the MATLAB/Simulink environment. The set-up, configuration, and simulation of the developed Simulink transfer function model and written MATLAB *m-file* algorithm produced 5001 samples of time series input-output dataset comprising six input parameters (time was automatically introduced to the initially selected input parameters) and three

output parameters. The diagram of the transfer function model developed in the Simulink workspace using random number blocks with varying odd number seeds is shown in Figure 1.

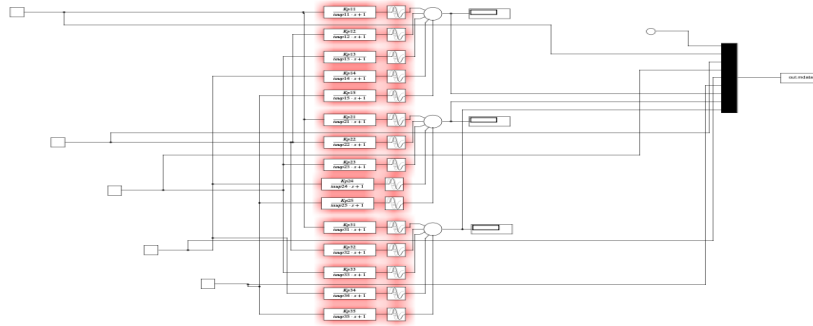


Figure 1: Developed simulink transfer function model

After the time series, and input-output dataset has been generated, the input and output datasets were fed into the MATLAB neural network time series application and used to set up as well as configure the structure of each neural network model to be developed. The structure of each neural network model was made up of 3 layers (the input, the hidden and the output layers), 10 hidden neurons, a time delay of 2 and Levenberg Marquardt as the optimization/training algorithm.

The output dataset served as the target dataset and the models were iteratively trained to evaluate their performance in predicting the next value of the target dataset. The accuracy and performance of each of the neural network models in learning and generalizing the relationships that exist in the nonlinear dynamic dataset were ascertained by the Mean Squared Error (MSE) values and regression (R) values presented by the neural network model at the end of training respectively. The MSE showed the difference between the target parameters and the predicted output parameters while the R-values informed about the closeness or randomness that exist between the target parameters and the predicted output parameters (MathWorks, 2021). MSE values close to 0 signify good performance of a model in learning, generalization and prediction while regression values close to 1 indicate close relationships between the predicted output data and target data. The best MSE value (performance) for each neural network model was taken from the epoch with the lowest validation error (dotted circle).

The mathematical definitions of the neural networks to be built are Nonlinear Autoregressive (NAR) and Nonlinear Input-Output (NIO).

### 2.1 Nonlinear Autoregressive (NAR)

$$y(t) = f[ y(t - 1), y(t - 2), \dots, y(t - dy) ] \tag{1}$$

Where  $y$ = model outputs,  $f$  = a nonlinear function which represents the mapping performed by the neural network,  $t$ = time elapsed and  $dy$ = delay order of output  $y$ .

MATLAB R2021a illustration of the guiding principle of the NAR model is shown in Figure 2 while the open loop architecture and closed loop architecture of the NAR model are shown in Figure 3 and Figure 4 respectively.

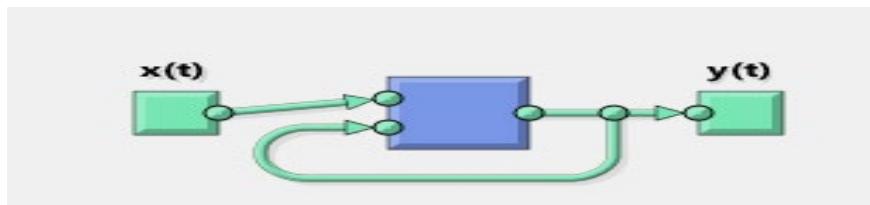


Figure 2: The guiding principle of the NAR model neural network model

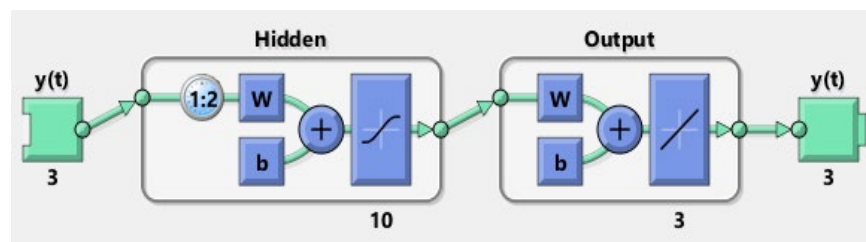


Figure 3: The overview of the open-loop architecture of the developed NAR model

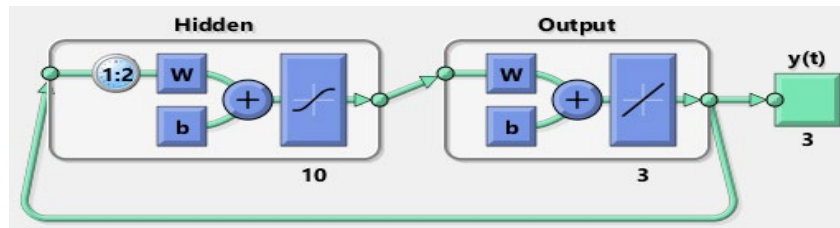


Figure 4: The overview of the closed-loop of the developed NAR model

### 2.2 Nonlinear Input-Output (NIO):

$$y(t) = f[u(t - 1), u(t - 2), \dots, u(t - du)] \tag{2}$$

Where  $u$ = model external inputs,  $f$  = a nonlinear function which represents the mapping performed by the neural network,  $t$ =time elapsed and  $du$ = delay order of input  $u$ .

MATLAB R2021a illustration of the guiding principle of the NIO model is shown in Figure 5 while the open loop architecture of the developed NIO model is shown in Figure 6.

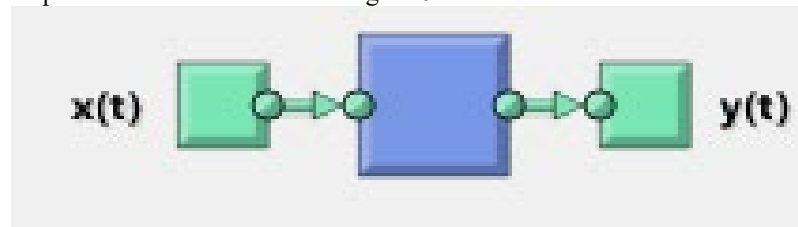


Figure 5: The guiding principle of the NAR model neural network model

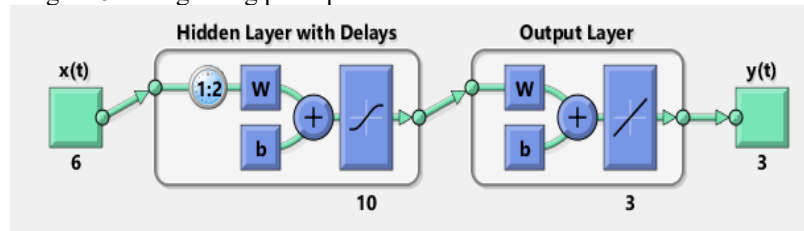


Figure 6: The overview of the open-loop architecture of the developed NIO model

### 3.0 RESULTS AND DISCUSSION

The MSE values and regression (R) values presented by the developed NAR and NIO neural network models after training are given in Tables 1 and 2 respectively while a plot of the validation efficiency between the number of epochs and the mean squared error (performance) for the NAR model and NIO model are shown in Figures 7 and 8 respectively.

The training errors, validation errors, testing errors and regression values of the trained neural network models were computed in an open-loop manner, although the NAR model is a closed-loop neural network.

Table 1: MSE and R values for the NAR model

Description	Target Value	Epoch	R	MSE
Training	10503	8	0.9980	0.758528
Validation	2250	8	0.9976	0.820267
Testing	2250	8	0.9978	0.857507

R=Regression MSE=Mean Squared Error

Table 2: MSE and R values for the NIO model

Description	Target Value	Epoch	R	MSE
Training	10503	27	0.906493	33.16290
Validation	2250	27	0.905761	35.68165
Testing	2250	27	0.904721	36.05067

R=Regression MSE=Mean Squared Error

From the MSE and R values recorded in Table 1 and Table 2, the lower MSE values (closer to 0) recorded for the NAR model in Table 1 indicate increased efficiency in predicting output parameters having minimal differences with the target parameters by the NAR model compared to the efficiency of the NIO model whose predicted output parameters substantially differ from the target parameters evident in the larger MSE values (farther from 0) recorded in Table 2. The higher R values (closer to 1) recorded for the NAR model in Table 1 commensurate with the MSE values recorded as they denote close relationships between the predicted output parameters and target parameters compared to the R values (farther from 1) recorded in Table 2 for the NIO model which denote random relationships between the predicted output parameters and target output parameters.

Figures 7 and 8 demonstrated that the training error, the validation error and the testing error decreased until epoch 8 was reached (for the NAR model) and epoch 27 was reached (for the NIO model), which served as evidence that no element of over fitting occurred. An epoch refers to one cycle through the full training dataset.

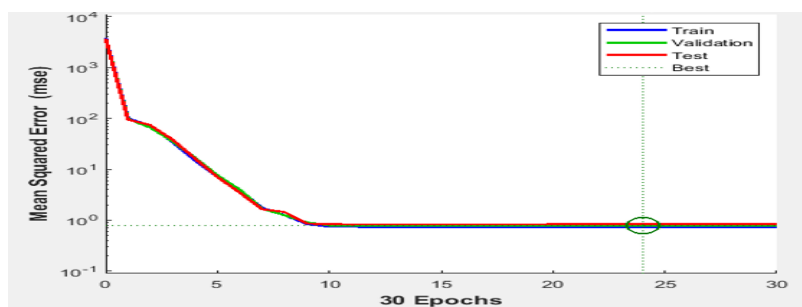


Figure 7: Mean squared error versus the number of epochs for the NAR model

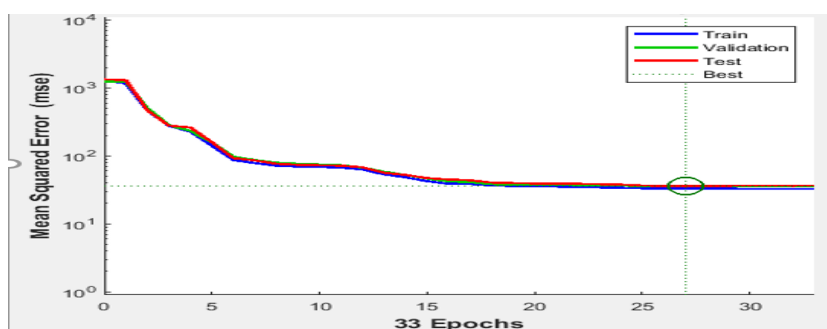


Figure 8: Mean squared error versus the number of epochs for the NIO model

#### 4.0 CONCLUSION

The results obtained in this work showed revealed the competence of the NAR and NIO models in representing the natural gas liquefaction process. The NAR model was found to outperform the NIO model in simulation and prediction owing to its lower MSE values (closer to 0) and its higher R values (closer to 1) compared to the MSE and R values of the NIO model. This outperformance by the NAR model was found to be connected with the fact that the NAR model made use of past values of the predicted output which converted it from an open-loop neural network to a closed-loop neural network unlike the NIO model which was an open loop neural network. The ideas and findings from the research work can be used by Chemical Engineers working in liquefaction plants to generate time series datasets which represent the liquefaction process. They can also serve as a guide to the Chemical Engineers for sound decision making and during the conceptual design and optimization of the crucial parameters involved in natural gas liquefaction process as well as in controlling the natural gas liquefaction process. In addition, they can help in lowering the high costs that would otherwise be incurred by the Management of liquefaction plants if experiments were to be carried out to obtain such results.

#### ACKNOWLEDGEMENT

Special thanks go to Aare Afe Babalola, LL.B, FFPA, FNIALS, FCI Arb, LL.D, SAN, OFR, CON – The Founder and President, and the University Management of Afe Babalola University, Ado-Ekiti, Ekiti State, Nigeria for providing a very conducive environment and the necessary materials that enabled the accomplishment of this research work.

## REFERENCES

- Alsobhi, S. (2015) *Modeling and Optimization of Natural Gas Processing and Production Networks*. A thesis presented to the University of Waterloo in fulfillment of the thesis requirement for the degree of Doctor of Philosophy in Chemical Engineering. Available at: [https://uwspace.uwaterloo.ca/bitstream/handle/10012/9522/Alsobhi\\_Saad.pdf;jsessionid=066847342D5317B106810596A464066?sequence=3](https://uwspace.uwaterloo.ca/bitstream/handle/10012/9522/Alsobhi_Saad.pdf;jsessionid=066847342D5317B106810596A464066?sequence=3) (Accessed: 15th March, 2022).
- Aronsson, E. (2012) *FLNG Compared to LNG Carriers-Requirements and Recommendations for LNG Production Facilities and Re-gas Units*. A thesis submitted to the Department of Shipping and Marine Technology, Division of Marine Design, Chalmers University of Technology, Gothenburg, Sweden for the Degree of Master of Science, Report No. X12/279, pp 1-38. Available at: <https://publications.lib.chalmers.se/records/fulltext/162630.pdf> (Accessed: 4<sup>th</sup> June 2022).
- Bakar, W.A. W.A. and Ali, R. (2010) *Natural Gas*. Edited by Primoz Potocnik, London: IntechOpen.
- Bhran, A.A. Hassanean, M.H., and Helal, M.G. (2016) ‘Maximization of Natural Gas Liquid Production from an Existing Gas Plant’, *Egyptian Journal of Petroleum*, 25, pp 333-341. Available at: <https://www.infona.pl/resource/bwmeta1.element.elsevier-7ae86205-66a8-3c82-abca-0a075861b719> (Accessed: 5<sup>th</sup> June 2022).
- Bolaji, B.A., Olawale, A.O. and Ayotunde, A.I. (2019) ‘Evaluation of Pollution Mortality Using NARX and NIO Time Series Predictive Algorithm on MATLAB’, *International Journal of Engineering Applied Sciences and Technology*, 4(7), pp 99-107. Available at: [10.33564/IJEST.2019.v04i07.015](https://www.ijest.org/Vol4Issue7/1033564-IJEST.2019.v04i07.015) (Accessed: 5<sup>th</sup> June 2022).
- Borelli, D., Devia, F., Schenone, C., Silenzi, F. and Tagliafico, A.L. (2021) ‘Dynamic Modelling of LNG Powered Combined Energy Systems in Port Areas’, *Energies*, 14, pp 1-18. Available at: [https://mdpi-res.com/d\\_attachment/energies/energies-14-03640/article\\_deploy/energies-14-03640-v2.pdf?version=1624201953](https://mdpi-res.com/d_attachment/energies/energies-14-03640/article_deploy/energies-14-03640-v2.pdf?version=1624201953) (Accessed: 4<sup>th</sup> June, 2022).
- Cameron LNG [Online] (2018) Natural Gas and the Liquefaction Process. Available at: <https://cameronlng.com/wp-content/uploads/2018/10/Natural-Gas-and-the-Liquefaction-Process-CLNG.pdf>, (Accessed: 1<sup>st</sup> June 2022).
- Ekejiuba, A. and Ikpku, C.U. (2021) ‘Viability of Producing LPG and LNG from the Nigerian Gas Flare Stream’, *Inter-world Journal of Science and Technology (IJST)*, 2(1), pp 1-32. Available at: [https://www.researchgate.net/publication/350790144\\_VIABILITY\\_OF\\_PRODUCING\\_LPG\\_AND\\_LNG\\_FROM\\_THE\\_NIGERIAN\\_FLARE\\_GAS\\_STREAM](https://www.researchgate.net/publication/350790144_VIABILITY_OF_PRODUCING_LPG_AND_LNG_FROM_THE_NIGERIAN_FLARE_GAS_STREAM) (Accessed 5th June, 2022).
- ElBadawy, K.M., Teamah, A.M., Shehata, I.A. and Hanfy, A.A. (2017) ‘Simulation of Liquefied Petroleum Gas Production from Natural Gas Using Fractionation Towers’, *International Journal of Advanced Scientific and Technical Research (IJASTR)*, 6(7), pp 148-153. Available at: <https://dx.doi.org/10.26808/rs.st.i7v6.16> (Accessed: 8th June, 2022).
- Finn, A.J. (2002) ‘Effective LNG Production Offshore’, pp 1-19. Available at: [https://www.researchgate.net/publication/237557652\\_EFFECTIVE\\_LNG\\_PRODUCTION\\_OFFSHORE](https://www.researchgate.net/publication/237557652_EFFECTIVE_LNG_PRODUCTION_OFFSHORE), (Accessed: 4<sup>th</sup> June 2022).
- Giwa, A. and Karacan, S. (2012) ‘Modelling and Simulation of a Reactive Packed Distillation Column Using Delayed Neural Networks’, *Chaotic Modelling and Simulation (CMSIM)*, 1: pp 101-108. Available at: [https://www.researchgate.net/publication/235766810\\_Modeling\\_and\\_Simulation\\_of\\_a\\_Reactive\\_Packed\\_Distillation\\_Column\\_Using\\_Delayed\\_Neural\\_Networks/link/0fcfd5135a680bd232000000/download](https://www.researchgate.net/publication/235766810_Modeling_and_Simulation_of_a_Reactive_Packed_Distillation_Column_Using_Delayed_Neural_Networks/link/0fcfd5135a680bd232000000/download) (Accessed: 15th June, 2022).
- Gupta, A., Salau, A., Akinola, A.S., Chaturvedi, P. and Nwulu, I.N. (2019) ‘Artificial Neural Networks: Its techniques and Applications to Forecasting’, *IEEE International Conference on Automation, Computation and Technology Management (ICACTM)*, pp 320-324. Available at: [https://www.researchgate.net/publication/335340306\\_Artificial\\_neural\\_networks\\_its\\_techniques\\_and\\_applications\\_to\\_forecasting](https://www.researchgate.net/publication/335340306_Artificial_neural_networks_its_techniques_and_applications_to_forecasting) (Accessed: 3<sup>rd</sup> February, 2022).
- Hajjar, Z., Tayebbi, S. and Ahmadi, M.H.E. (2018). Application of AI in Chemical Engineering. IntechOpen document, Chapter 20. Available at: <https://cdn.intechopen.com/pdfs/60761.pdf> (Accessed: 5<sup>th</sup> May 2022).
- MathWorks, 2021. MATLAB R2021a. The MathWorks Inc.
- Mezni, M. (2015). *LPG Recovery Unit Optimization*. Thesis for: Dipôme National d'Ingénieur en Chimie Industrielle, pp 1-84. Available at: [https://www.researchgate.net/publication/317840680\\_LPG\\_Recovery\\_Unit\\_Optimization](https://www.researchgate.net/publication/317840680_LPG_Recovery_Unit_Optimization) (Accessed: 1<sup>st</sup> June 2022).
- Microsoft, 2019. Excel 2019 software. Microsoft Corporation.
- Ministry of Petroleum Resources, Federal Government of Nigeria (2017) National Gas Policy. Nigerian Government Policy and Actions. Available from: <http://www.petroleumindustrybill.com/wp-content/uploads/2017/06/National-Gas-Policy-Approved-By-FEC-in-June-2017.pdf> (Accessed: 11th September, 2021).
- Mokhatab, S., Poe, W.A., and Mak, J.Y. (2006) *Handbook of Natural Gas Transmission and Processing. Principles and Practices*. Fourth Edition, Gulf Professional Publishing, MA, USA 1-5.
- Nejad, A.T. and Farzi, A. (2014) ‘Simulation and Optimization of LNG Production Unit for Energy Conservations’, *Iranica Journal of Energy and Environment*, 5(1), pp 67-72. Available at:

- [https://www.ijee.net/article\\_64510\\_be35d9e75faa4847436bafa769a4b6b5.pdf](https://www.ijee.net/article_64510_be35d9e75faa4847436bafa769a4b6b5.pdf) (Accessed: 4<sup>th</sup> June 2022).
- Owolabi, J.O., Kila, O.O. and Giwa, A. (2020) 'Modelling and Simulation of a Natural Gas Fractionation System Using Aspen HYSYS', *International Journal of Engineering Research in Africa (IJERA)*, 49, pp 1-14. Available at: 10.4028/www.scientific.net/IJERA.49.1 (Accessed: 18<sup>th</sup> February, 2022).
- Rafiq, A., Majed, A., Osama El-Majzoub Det, M., Maros, H., Amir, S.F. and Muhammad U. (2011) *Fractionation of Natural Gas Liquids to Produce LPG*. A document submitted to Prof. Jon Steinar Gudmundsson, Department of Petroleum Engineering and Applied Geophysics, Norwegian University of Science and Technology. Available at: <https://fddocuments.us/document/fractionation-of-natural-gas-liquids-to-produce-lpg.html> (Accessed: 13<sup>th</sup> October 2021).
- Sansa, I. and Bellaaj, N.M. (2018) *Solar Radiation Prediction using NARX Model*. Chapter 13 of *Advanced application for Artificial Neural Network*, London: INTECH.
- Sun, H., Geng, J., Na, F., Rong, G. and Wang, C. (2022) 'Performance Evaluation and Comparison of Commonly Used Optimization Algorithms for Natural Gas Liquefaction Processes', *Elsevier Energy Reports*, 8, pp 4787-4800. Available at: <https://doi.org/10.1016/j.egy.2022.03.164> (Accessed: 13<sup>th</sup> October, 2021).
- Trigilio, A., Bouza, A. and Scipio, S.D. (2012) 'Modelling and Simulation of Natural Gas Liquefaction Process', *Journal on Advances in Natural Gas Technology*, pp 213-234. Available at: [https://www.researchgate.net/publication/224830180\\_Modelling\\_and\\_Simulation\\_of\\_Natural\\_Gas\\_Liquefaction\\_Process/figures?lo=1](https://www.researchgate.net/publication/224830180_Modelling_and_Simulation_of_Natural_Gas_Liquefaction_Process/figures?lo=1), (accessed 28<sup>th</sup> May, 2022).
- Ubani, C., and Ani, G.O. (2016). Natural Gas Utilization and its Effect on Nigeria's Economic. *International Journal of Scientific Engineering and Technology (IJSET)*, 5(12), pp. 532-536. Available at: 10.17950/ijset/v5s12/1202 (Accessed 2<sup>nd</sup> June, 2022).
- United Nations Climate Technology Centre and Network (2022) *LPG and LNG for Household and Commercial Cooking*. Available at: <https://www.ctc-n.org/technologies/lpg-and-lng-household-and-commercial-cooking> (Accessed: 28<sup>th</sup> May 2022).
- Vikse, M., Watson, H.A.J., Kim, D., Barton, P.I. and Gundersen, T. (2020) 'Optimization of a Dual-mixed Refrigerant Process using a Nonsmooth Approach', *Energy*, 196, pp 1-12. Available at: [https://www.researchgate.net/publication/338820524\\_Optimization\\_of\\_a\\_dual\\_mixed\\_refrigerant\\_process\\_using\\_a\\_nonsmooth\\_approach](https://www.researchgate.net/publication/338820524_Optimization_of_a_dual_mixed_refrigerant_process_using_a_nonsmooth_approach) (Accessed: 4<sup>th</sup> April, 2022).





## Design and Development of Arduino-Based Temperature Monitoring System for a Portable Haemodialysis System

Aminah A. SULAYMAN<sup>1\*</sup>, Dauda O. ARAROMI<sup>1</sup>, Olugbenga E. AYODELE<sup>2</sup>

<sup>1</sup> Department of Chemical Engineering, Ladoké Akintola University of Technology, Ogbomoso, Oyo State, Nigeria

<sup>2</sup> Department of Medicine, Ladoké Akintola University of Technology, Ogbomoso, Oyo State, Nigeria

<sup>1\*</sup> [aasulayman@lautech.edu.ng](mailto:aasulayman@lautech.edu.ng), <sup>1</sup> [doararomi@lautech.edu.ng](mailto:doararomi@lautech.edu.ng), <sup>2</sup> [gbengaayox@yahoo.ca](mailto:gbengaayox@yahoo.ca)

\* Corresponding author

---

### ABSTRACT

Haemodialysis (HD) is a life-saving treatment option for end-stage kidney disease patients to remove excess fluid, substances and waste products through a semi-permeable membrane (dialyser, also known as the artificial kidney). This makes HD a perfect illustration of the synergy between chemical engineering principles and medical care. Although commercial haemodialysis machines are available, high cost, large space consumption, and accessibility to poor masses are significant concerns. This work develops an Arduino-based temperature monitoring system for a low-cost portable haemodialysis machine. In vitro HD system design was verified by experiment using porcine blood, and it can monitor blood and dialysate temperature in real-time using Arduino microcontroller. The accuracy of the designed HD system was determined using Urea Reduction Ratio (URR) and Creatinine Reduction Ratio (CRR). Results of the URR and CRR obtained were 71.97% and 65.29%, respectively. The developed HD system can be used to monitor temperature during haemodialysis.

**Keywords:** Haemodialysis, Kidney disease, Accuracy, real-time monitoring, dialyser

### 1. INTRODUCTION

Kidney failure results in the accumulation of fluid and toxic or metabolic wastes in the body. About 10% of the world's population is affected by chronic kidney disease, and the mortality rate increases yearly due to inaccessible affordable treatment (World Kidney Day, 2015). Kidney replacement therapy is the therapeutic option for patients diagnosed with kidney failure, which can be either dialysis or kidney transplantation.

Dialysis treatment can be done either by haemodialysis or peritoneal dialysis. Haemodialysis is an extracorporeal blood purification process whereby blood is circulated out of the body, cleansed and balanced for its constituents such as electrolytes, fluid concentration and fluid concentration through an external device called a dialyser and thereafter returned to the body (Muhammadu *et al.*, 2020). The intermittent haemodialysis method is a commonly recognized treatment in hospitals. However, complications such as intradialytic hypotension (low blood pressure) usually arise and may be associated with high mortality rates (Panhwar *et al.*, 2018).

Most haemodialysis machines available are expensive and require large water treatment plants. These limitations led to the development of an arduino-based monitoring device for a low-cost, portable haemodialysis system. This improvement can potentially monitor some haemodynamic properties in real-time to improve the patient's quality of life and reduce dialysis costs for patients and healthcare providers.

Real-time monitoring requires the instrumentation of a system using microcontrollers. Arduino is open-source, cross-platform software with a programming circuit board called a microcontroller and a set of development boards known as Arduino Integrated Development Environment (IDE). Arduino developed software can support MATLAB, which allows one to obtain and plot real-time data directly from the command window. This helps to construct a real-time monitoring haemodialysis system (Gao *et al.*, 2021; Shin & Jeon, 2017; SNikilla, 2016).

## 2. METHODOLOGY

### 2.1 Process Description

The *in vitro* haemodialysis system constructed has two glass jars of 1L capacity that served as the storage tanks for blood and dialysate storage in the experimental rig. Two peristaltic pumps with model TA7291P were used to pump blood and dialysate. Pump flow rates can be adjusted between 10 and 250 ml/min. A dialyser of type ELISIO™ – 17L (Low Flux) served as an artificial kidney. Two Arduino DS18B20 temperature sensors simultaneously measured the blood temperature and dialysate during the dialysis session. A heating unit adjusted and stabilised the dialysate temperature at 37 °C. The pumps, probes and sensors were calibrated before the start of dialysis. MATLAB ® 2019 served as the hardware-software interface and coordinated different activities during the experiment.

The instrumentation unit was constructed as an assembly of electronic components, which housed a microcontroller, conductivity readers, temperature readers and developmental boards. This unit was built to synchronise the activities of the two peristaltic pumps and measuring devices used in the experiment. The Process Flow Diagram of the haemodialysis process is shown in Figure 1. MATLAB 2019 simulation software was used for simulation.

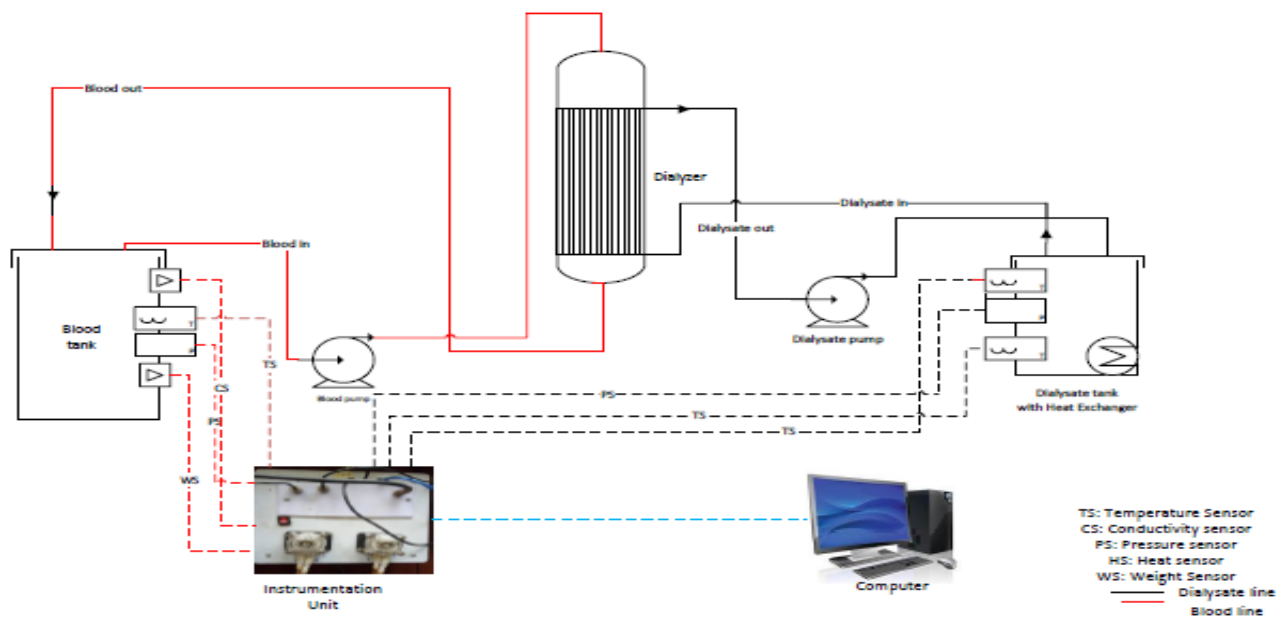


Figure 1: Process flow diagram of haemodialysis process

### 2.2 Preparation of Solution

The dialysate solution was prepared by mixing acid concentrate for haemodialysis (NIPROSOL 324A) and sodium hydrogen bicarbonate concentrate ( $\text{NaHCO}_3$ ) with deionized water at a volumetric ratio of 1:1.72:42.28. Porcine blood was chosen as a substitute for human blood because its haematological constants are close to human blood. The specific gravity of human and porcine blood is 1.05-1.06 and 1.005-1.06, respectively, and both have a relative viscosity of 4 - 5 (Panhwar *et al.*, 2018). The blood was obtained from an abattoir. A dose of 3.5–7.0 USP/mL heparin was immediately added to the blood to prevent clotting (Olson, 2009). The heparinised porcine blood was then transferred to the laboratory in an insulated vessel. The heparinised porcine blood sample was treated by adding 5.76g of creatinine and 0.9g of urea to 500 mL of heparinised blood since high blood urea nitrogen and creatinine are significantly elevated in patients with uraemia. The treated blood sample is a substitute for human blood samples of patients with uraemia (Panhwar *et al.*, 2018).

### 2.3 Instrumentation Unit

The main component in the instrumentation unit used for the experimental set-up is the Arduino microcontroller. Arduino was used because it is easy and economical to create a project relating to digital electronics embedded systems (Aqeel, 2018). Arduino contains a programmed circuit board called microcontroller and a set of development boards that contains hardware and software libraries called Arduino Integrated Development Environment (IDE). The microcontrollers deliver information by connecting to a computer with the help of USB cable while Integrated Development Environment was used in programming (C programming language). Arduino board interprets commands in the instrumentation system and then sends appropriate signals to the various units for proper action.

## 2.4 Haemodialysis Experiment

Bloodline was rinsed with normal saline to remove exhaust gas in the bloodline. During the experiment, blood is pumped from the blood tank and sent to a dialyser for purification. In the dialyser, there was a mass transfer of solutes (Blood Urea Nitrogen (BUN) and creatinine) from the sample blood to the dialysate. The mass transfer occurred by diffusion through a semi-permeable membrane inside the dialyser. The dialysate temperature was kept at 37 °C and passed through the dialysate pump to the dialyser, where the diffusion occurs. The experiment was carried out at blood and dialysate flow rates of 100, 120 ml/min (FL1) and 120, 150 ml/min (FL2) for 60 min. The haemodialysis experimental setup is shown in Figure 2 while its Simulink interface is shown in Figure 3.

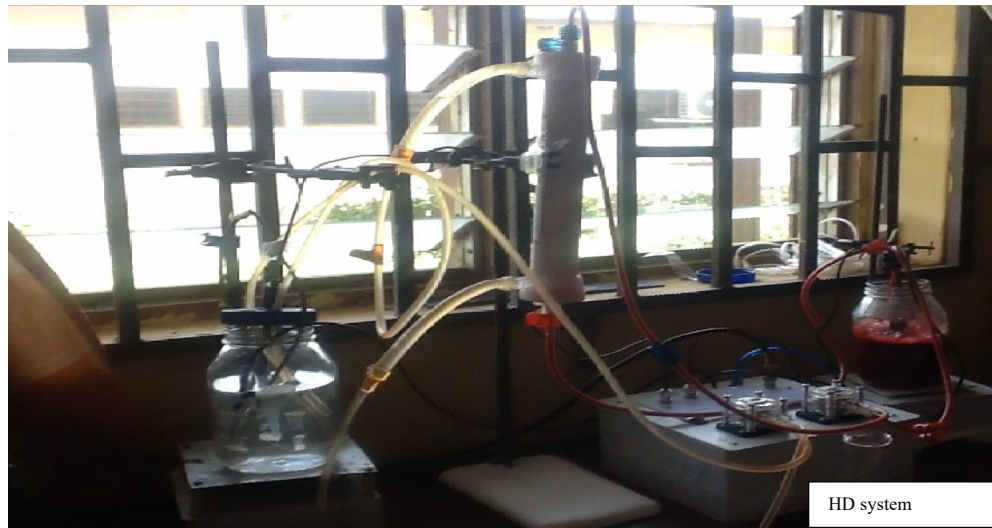


Figure 2: An *In-vitro* haemodialysis system

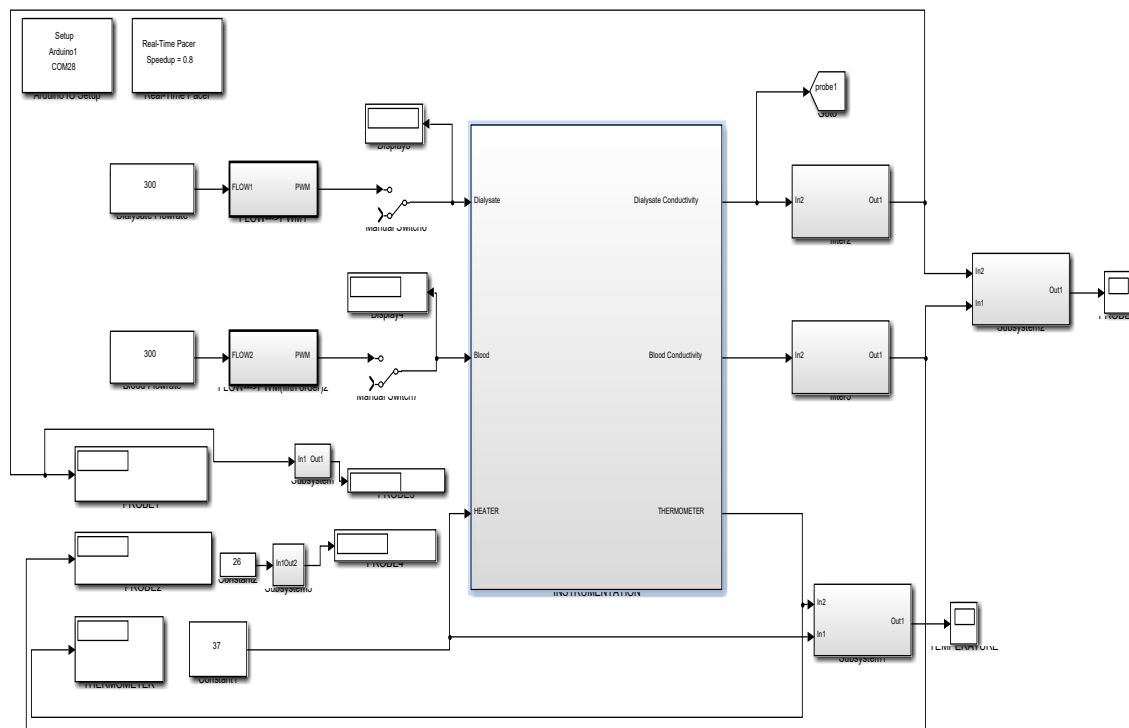


Figure 1: Simulink interface for haemodialysis experimental set-up

## 2.5 Method of Analysis

Intradialytic blood samples of 1ml at 10 min intervals were taken for BUN and creatinine analysis. BUN and creatinine analyses were carried out using SPM-23A Spectrophotometer using Berthelot and Jeff's method, respectively. Haemodialysis process adequacy was determined using Urea Reduction Ratio (URR) and Creatinine Reduction Ratio (CRR). The National Kidney Foundation Guidelines (DOQI) and the European Renal Association (ERA) have set

standards for the adequacy of haemodialysis treatment. The threshold for adequate URR and CRR is 65% (Nafisi *et al.*, 2011; Panhwar *et al.*, 2018). The URR and CRR were determined using Equation 1.

$$R = 100(1 - \frac{C_t}{C_o}) \quad (1)$$

Where  $R$ = Reduction Ratio (BUN or creatinine),  $C_t$ = concentration (BUN or creatinine) at time  $t$ ,  $C_o$ = initial concentration (BUN or creatinine).

### 3. RESULTS AND DISCUSSION

The results of BUN and creatinine analysis of the *in vitro* haemodialysis system designed are shown in Tables 1 and 2, respectively. Table 1 shows the BUN analysis of FL1 and FL2 before haemodialysis and at 10 mins intervals for 60 mins. Results of BUN analysis of fresh blood collected in FL1 and FL2 were 12.1 mg/dL and 28.0 mg/dL, respectively. BUN of treated blood samples (fresh blood added with BUN and creatinine) for FL1 and FL2 were 70.9 mg/L and 113.1 mg/dL, respectively, before the commencement of haemodialysis. It is observed from the table that a high removal rate of BUN occurred within 10 mins of the dialysis session in both experiments. However, removal rates were low after 10 mins in both experiments.

The result of creatinine analysis shown in Table 2 revealed a high removal rate of creatinine in the 10 mins of dialysis in both FL1 and FL2. However, FL1 had a low creatinine removal rate from 10 minutes to 40 minutes before the oscillatory response. FL2 showed a steady removal rate for 30 mins, and a higher creatinine response was obtained at 40 mins before its decline. The fluctuations in the BUN and creatinine analysis results were due to the analyser used in their analysis. Low removal rates in BUN and Creatinine results were caused by dialysate recirculation. This is because recirculation uses less dialysate, but less mass transfer rate from the blood to dialysate due to a smaller concentration gradient (Olson, 2009).

Table 1: Blood Urea Nitrogen Analysis Result of *in vitro* Haemodialysis Process

Sampling Time (min)	FL1 (mg/dL)	FL2 (mg/dL)
Pre-dialytic	70.9	113.1
10	41.1	43
20	39.7	38.3
30	38.3	31.3
40	37.3	32.2
50	36.4	31.9
60	36.7	31.7

Table 2: Creatinine Analysis Result of *in vitro* Haemodialysis Process

Sample Time	FL1 (mg/dL)	FL2 (mg/dL)
Pre-dialytic	41.2	36.3
10	18.9	16.7
20	18.3	19.3
30	15.2	11.9
40	15.4	14.8
50	17.1	14.2
60	16.7	12.6

The results obtained in this study were compared with Olson (2009) and Chen *et al.* (2014) results. A 70% removal rate of BUN was achieved by Chen *et al.* (2014) at 29 mins using deionised water for dialysate preparation and 12 mins using plasmon-induced dialysate comprising Au nanoparticles (NPs)-treated (AuNT) water for dialysate preparation.

Olson (2009) could not achieve a 70% removal rate at 60 mins using deionised water for dialysate preparation. In this research work, FL2 achieved a 70% removal rate at 25 mins; however, FL1 could not achieve a 70% removal rate at the end of 60 mins. The result showed that micro solutes such as BUN and creatinine were successfully removed through the *in vitro* haemodialysis process experiment and FL2 gave the best removal rate.

The chart of the adequacy of the haemodialysis process evaluated using URR and CRR is shown in Figures 4 and 5, respectively. The trend of the URR chart shown in Figure 4 showed that FL1 attained 65.1% URR at 30 min and was reduced to 62.6% at the end of dialysis. However, FL2 has an adequate haemodialysis process with a final URR of 71.97%. The CRR chart in Figure 5 indicated that the creatinine removal rate was fast at the onset of haemodialysis. However, the removal rate fluctuated during the haemodialysis session, which may be due to the recirculation of dialysate during the dialysis period. The final CRR obtained in FL1 and FL2 at the end of the dialysis session are 59.5% and 65.3%. Since adequate haemodialysis process is obtained at URR or CRR > 65%, it can be concluded that FL2 with a blood pump of 120 ml/min and dialysate pump of 150 ml/min is efficient for the haemodialysis process.

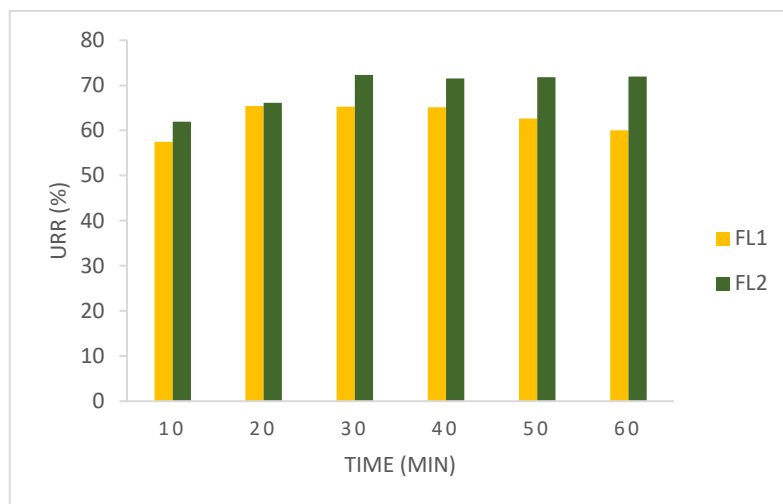


Figure 4: Urea reduction ratio of haemodialysis process

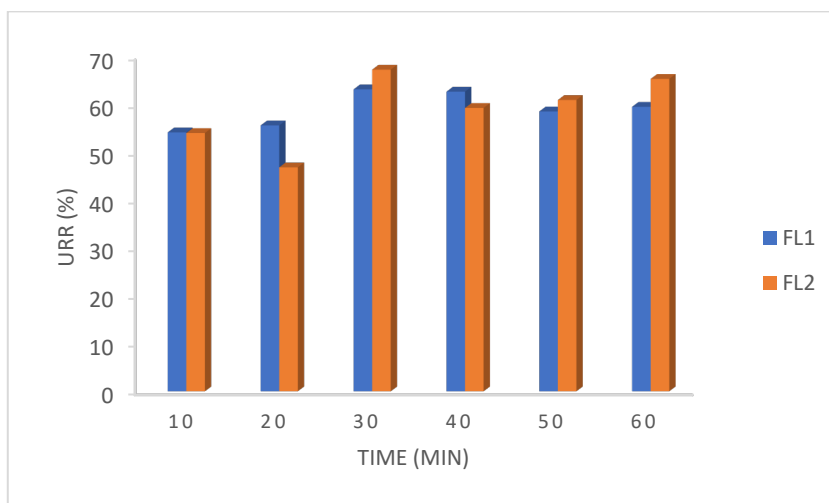


Figure 5: Creatinine reduction ratio of haemodialysis process

Hypotension can occur during a dialysis session. In response to the low blood pressure (hypotension), there is generalised vasoconstriction, which can make the patient complain of coldness and shivering. The blood and dialysate temperatures were monitored in real-time during the haemodialysis process to monitor the patient's condition. The plot of blood and dialysate temperatures monitored in real-time during *in vitro* haemodialysis session is shown in Figure 5. The dialysate temperature was set at a constant temperature of 37°C at the start of the haemodialysis session. The heating unit automatically regulated the dialysate temperature as indicated in the dialysate temperature graph. The dialysate temperature was used to regulate the blood temperature. This is because as blood passes through the inner membrane of the dialyser while the dialysate passes countercurrently to the outer layer of the dialyser; thus temperature gradient occurs. There was no increase in the blood temperature from the start of the dialysis session at 32.8 °C, and

this was because the dialysate temperature regulated the dialysate surface line in the dialyser. As the time increases, the blood temperature increases while regulating the dialysate temperature across the 37°C set temperature. The result showed that the dialysate heating unit could regulate the dialysate temperature across 37 °C set temperature. With this observation, it is possible to manipulate the dialysate temperature to control the patient's blood temperature.

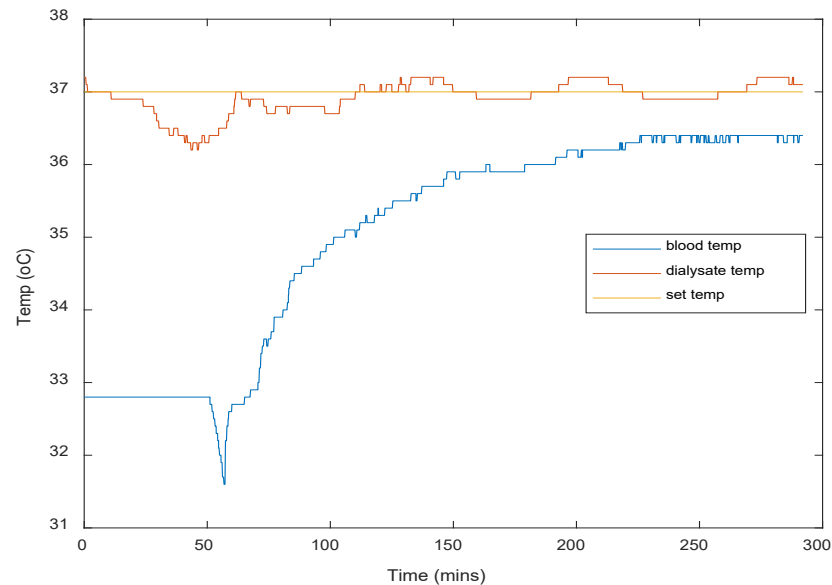


Figure 6: Blood and dialysate temperature curves

#### 4. CONCLUSION

The designed *in vitro* haemodialysis system mimicked the clinical haemodialysis system and removed toxic micro solutes (BUN and creatinine) accumulated in the blood. Experimental results of the designed *in vitro* haemodialysis system showed that real-time temperature monitoring was successfully achieved at different blood flow rates. Optimum flow rates of blood and dialysate were achieved at 120 ml/min and 150 ml/min, respectively, at URR and CRR at 71.97% and 65.29%.

#### REFERENCES

- Aqeel, A. (2018). Introduction to Arduino Nano. The Engineering Projects, 1-4 [accessed 22<sup>nd</sup> November, 2021]
- Chen, H.C, Lin, H.C, Chen, H.H., Mai, F.D., Liu, Y.C., Lin, C.M., Chang, C.C., Tsai, H.Y., and Yang, C.P, (2014). Innovative Strategy with Potential to Increase Haemodialysis Efficiency and Safety. *Scientific Reports*, 1 – 4.
- Gao, W., Luo, X., Liu, Y., Zhao, Y. and Cui, Y. (2021). Development of an Arduino-based Integrated System for Sensing of Hydrogen Peroxide. *Sensors and Actuators Reports*, 3, p.100045.
- Muhammadu, S.K., Revanth, M., Sakthiel, M., Sanjay, K.S. and Thamarai, K. V. (2020). Portable Dialyzer – A Safety Engineering on the Design of Haemodialysis System, *International Journal of Innovative Research in Advanced Engineering*, 7(3), pp. 39 – 42.
- Olson, J. C., (2009). Design and Modelling of a Portable Haemodialysis System. *Unpublished Masters Thesis*, Georgia Institute of Technology.
- Panhwar, M. A., Panhwar, F., Zhao, G., and Pirzada, N. (2018). A Low-cost Portable Device for Combined Haemodialysis and Ultrafiltration. *International Journal of Applied Engineering Research*, 13(7), 5400–5403.
- Shin, H.S. and Jeon, J.-C., (2017). Data Acquisition System using Arduino and MATLAB. *Journal of Innovative Research in IT & Computer Science*, 01(01), pp.6–9
- SNikilla, R., (2016). Real Time Health Monitoring System using Arduino. *South Asian Journal of Engineering and Technology*, 2(18), pp.52–60.
- World Kidney Day (2015). Chronic Kidney Disease. <http://www.worldkidneyday.org/fags/kidney-disease> [accessed 10<sup>th</sup> July, 2022].



## Fuzzy Logic Control of Tomato Conversion in a Triple-Effect Evaporator

Mojirade M. OLORUNTOBA<sup>1\*</sup> and Folahan P. IBITOYE<sup>1</sup>

<sup>1</sup>Department of Research and Development, Prototype Engineering Development Institute, Ilesa, Nigeria

<sup>1\*</sup>[mojitoba@yahoo.com](mailto:mojitoba@yahoo.com), <sup>1</sup>[folaitoye@yahoo.com](mailto:folaitoye@yahoo.com).

\*Corresponding author

---

### ABSTRACT

Triple-effect evaporator used in tomato paste industry is one of the largest evaporation process which may be found in an industry. The economy of tomato paste manufacturing depends strongly on the triple-effect evaporator. The implementation of Fuzzy Logic Control in triple-effect evaporator for a 5 ton/h processed tomato juice initially at 5% concentration to 35% tomato paste concentration was adequately studied. It was concluded that most of the output parameters, such as tomato paste concentration; water removed; volumetric flow rate; and area decrease with increasing steam economy (SE); only mass of flow rate increases with increasing SE. Also, the tomato paste concentration increases as the number of effect (NE) increases. The choice of the SE and the NE which is needed was determined with the assistance of the Fuzzy Logic Control considered before the design of tomato paste production facility.

**Keywords:** Fuzzy Logic Control, Steam Economy, Tomato, Facility, Concentration.

### NOMENCLATURES

*TomatopasteConc:* Tomato concentration

*SE:* Steam economy

*NE:* Number of Effects

*VolumetricFlowRate:* Volumetric flow rate

*MassFlowRate:* Mass flow rate

*VH:* Very-High

*MH:* Medium-High

*VL:* Very-Low

*ML:* Medium-Low

### 1. INTRODUCTION

The tomato processing industry has since evolved with a range of technologies which are able to convert tomatoes into products such as paste, sauces and ketchup. In the industrial market, tomato paste is used globally as an ingredient in preparing meals and food products; valued in household for thickening and adding depth of flavour to sauces and stews and used as basis for a wide range of other products (Oloruntoba *et al.*, 2016). It is technically classified according to its dry matter content. Single concentrate having 12-14% of dry matter; double concentrate (the most common form of tomato paste) with 28-30% dry matter and triple concentrate with 36-38% dry matter.

George and Kyatanavar, 2006, conducted research on Multiple-effect evaporator used in sugar industry has the biggest and most complex evaporation process which may be met in an industry. The economy of sugar manufacturing depends strongly on the multiple effect evaporator. It is therefore of interest to optimize this process in order to decrease energy consumption as well as to enhance the quality of sugar. Such an optimization can be achieved by applying efficient techniques like the Taguchi Method. The research discusses the modeling and optimization of a quadruple effect evaporator used in sugar industries. Modeling has been performed in MATLAB and a Simulink file has been prepared with the data collected from Bhogawati Sugar Industry, Kolhapur, MS, India. For optimization of the evaporation process, Taguchi technique integrated with Fuzzy logic was employed. A Multi Response Performance Index (MRPI) has been calculated for optimization. The evaporation parameters viz. Feed temperature, Feed flow rate and Steam flow rate have been optimized with consideration of multiple performance characteristics. In recent years, fuzzy logic has been used to solve many complex problems by developing intelligent systems. Fuzzy logic has proved to be a powerful tool for decision-making systems, such as expert and pattern classification systems and Fuzzy set theory has been used in some chemical process (George and Kyatanavar, 2006).

In traditional rule-based approaches, knowledge is encoded in the form of antecedent consequent structure. When new data are encountered, it is matched to the antecedent's clause of each rule, and those rules where antecedents match a data exactly are fired, establishing the consequent clauses. This process continues until the desired conclusion is reached, or no new rule fired. In the past decade, fuzzy logic has proved to be useful for intelligent systems in chemical engineering (Emami, 2010) and since its inception, fuzzy logic has attracted an incredible amount of interest, and this interest continues to grow at an exponential rate. As such, scientists, researchers, educators and practitioners of fuzzy logic continue to expand on the applicability of what and how fuzzy can be utilised in the real-world (Carter, *et al.*, 2021).

The major objectives of an evaporator control system are smooth operation and accurate control of brix, these can be stated in other ways using economic analysis (George *et al.*, 2016). The economic objective is the delivery of the maximum amount of high-quality product to the downstream factory. In the tomato paste factory, this quality is determined by the tomato concentration. The amount of tomato paste that can be delivered is constrained by the rate at which tomato juice arrives at the station, and there is also an upper limit on the tomato concentration in order to avoid spontaneous nucleation or excessive deposition and scaling. The choice of Steam Economy (SE) and the number of Effects can be properly decided through the implementation of the Fuzzy Logic Control and the relationships between the production parameters can be properly studied. The aim of the research is to investigate the effect of variations of SE and NE on tomato paste concentration in triple-effect evaporator.

## 2. METHODOLOGY

### 2.1 Fuzzy Controller Design of the Triple-Effect Evaporator

The basic structure of a fuzzy controller includes a fuzzification interface, rule base, inference engine and defuzzification interface (Figure 1). In order to study the tomato conversion in a triple-effect evaporator, Multiple-Inputs-Multiple-Output (MIMO) was adopted. The control factors used include: the Steam Economy (SE), Number of Effects (NE), tomato concentration (TomatopasteConc), water removed (WaterRemoved), volumetric flow rate (VolumetricFlowRate), mass flow rate (MassFlowRate) and Area.

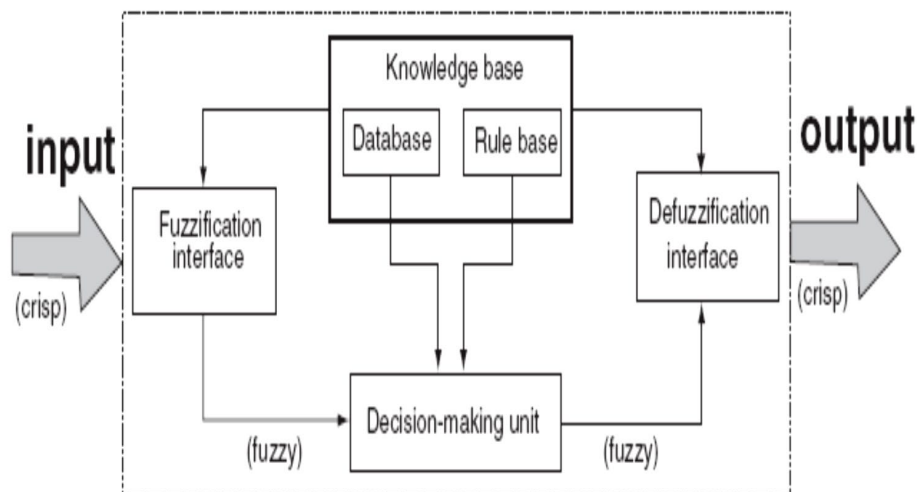


Figure 1: Fuzzy inference system

The MIMO includes the Steam Economy (SE) and Number of Effects (NE) as the inputs and tomato concentration (TomatopasteConc), water removed (WaterRemoved), volumetric flow rate (VolumetricFlowRate), mass flow rate (MassFlowRate) and Area as the outputs.

#### 2.1.1 Linguistic Value

The number of linguistic values affects the complexity and efficacy of a typical system, in studying the tomato conversion in triple-effect evaporator, the number of linguistic variables was set to four with corresponding symbols. The four linguistic values include Very-Low (VL), Medium-Low (ML), Very-High (VH) and Medium-High (MH).

#### 2.1.2 Membership Functions

The fuzzy controller in this design for the Triple-Effect evaporator used the Gaussian-type, and trapezoidal membership functions.



### 2.1.3 Fuzzy Rule Base

The fuzzy rules were based on expert knowledge and practical evidence from previous studies of Oloruntoba *et al.*, 2016 which was used to create the fuzzy condition inference. In the fuzzy control, the fuzzy rule is the core of the fuzzy controller, directly affecting the performance of the control system; the specific rules are shown Table 1.

Table 1: Fuzzy Rules for the Triple-Effect Evaporator

SE	NE	TomatoPasteConc	WaterRemoved	MassFlowRate	VolumetricFlowRate	Area
VL	-	VH	VH	VL	VH	VH
VH	-	VL	VL	VH	VL	VL
-	VH	VH	-	-	-	-
-	VL	VL	-	-	-	-
ML	-	MH	MH	ML	MH	MH
MH	-	ML	ML	MH	ML	ML
-	MH	MH	-	-	-	-
-	ML	ML	-	-	-	-

### 2.1.4 Establishment of Fuzzy Model

In order to debug and set up the fuzzy controller quickly, fuzzy tool in MATLAB (Fuzzy Inference System Editor, Membership function Editor, Rule Viewer, Surface Viewer, The MathWork Inc. Natick, Mass.) was used as shown in Figure 2. This tool was used to establish fuzzy inference system, complete the fuzzy controller design, and establish the rules. The fuzzy rule browser and surface view was used to observe and debug the constructed fuzzy system, correct the relevant parameters for the membership function and verify whether its function was consistent with expectations (Figures 3 and 4).

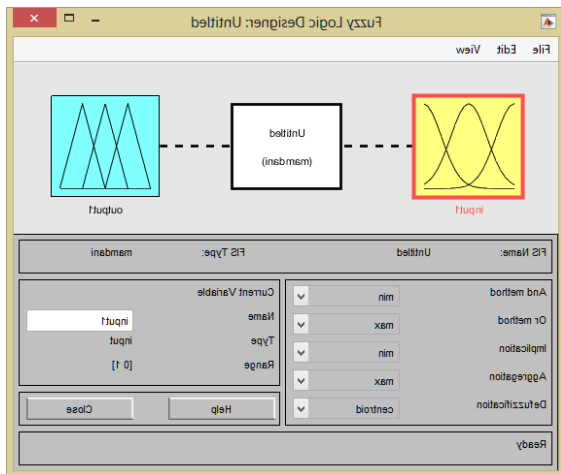


Figure 2: Fuzzy Logic Toolbox

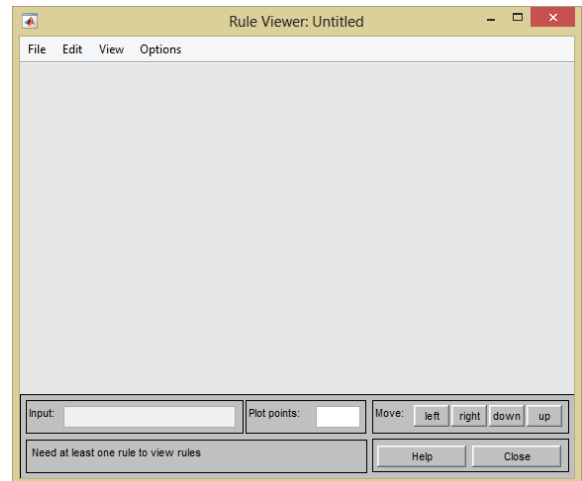


Figure 3: Fuzzy Rule browser

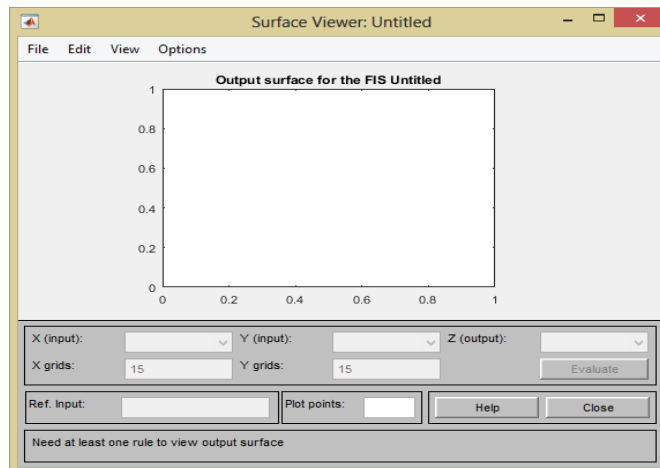


Figure 4: Surface Viewer

### 3. RESULTS AND DISCUSSION

All the completed final draft articles should be submitted by uploading through the Conference Management Toolkit. The inputs (Steam Economy (SE), the Number of Effects (NE)) and the outputs (tomato concentration (TomatopasteConc), water removed (WaterRemoved), volumetric flow rate (VolumetricFlowRate), mass flow rate (MassFlowRate) and Area) with mamdani model are shown in Figure 5. Figures 6 - 7 show the membership functions graph for input variables SE and the NE with four linguistic variables (Very-Low (VL), Medium-Low (ML), Medium-High (MH) and Very-High (VH)) while Figures 8 - 12 show the membership functions graph for output variables “tomato concentration (TomatopasteConc), water removed (WaterRemoved), volumetric flow rate (VolumetricFlowRate), mass flow rate (MassFlowRate) and Area” with four linguistic variables (Very-Low, Medium-Low, Medium-High and Very-High), the degree of membership for the inputs (SE and the NE) and outputs (tomato concentration (TomatopasteConc), water removed (WaterRemoved), volumetric flow rate (VolumetricFlowRate), mass flow rate (MassFlowRate) and Area) ranges from 2 - 4, 0 - 3, 0 - 0.4, 0 – 1600 kg/h, 0 – 18000m<sup>3</sup>/s, 0 – 5000kg/h and 0 – 400m<sup>2</sup>.

Fuzzy Logic Control (FLC) surface viewer with various inputs and outputs are shown in Figures 13 – 19. Figure 13 shows the 3-D relationship between input variables (SE and NE) and output variable “tomato concentration (TomatopasteConc)”, Figure 14 shows the relationship between the input variable “Steam Economy (SE)” and output variable tomato paste concentration (TomatopasteConc), Figure 15 shows the relationship between input variable “Steam Economy (SE)” and output variable “Water Removed (WaterRemoved)”, Figure 16 shows the relationship between input variable “Steam Economy (SE)” and output variable “Volumetric Flow Rate (VolumetricFlowRate)”, Figure 17 shows the relationship between input variable “Steam Economy (SE)” and output variable “Mass Flow Rate (MassFlowRate)”, Figure 18 shows the relationship between input variable “Steam Economy (SE)” and output variable “Area (Area)”, Figure 19 shows the relationship between input variable “Number of Effects (NE)” and output variable “Tomato paste concentration (TomatopasteConc)”. TomatopasteConc, WaterRemoved, VolumetricFlowRate and Area attains the values of 0.35, 400 kg/h, 1600 m<sup>3</sup>/s and 350m<sup>2</sup> respectively which are the maximum values, when SE is minimum with value of 2. Tomato paste concentration attains a maximum value of 0.35, when the Number of Effects (NE) attains maximum value of 3. Figures 20 and 21 show the rules and the rule viewer for MIMO (Multiple Input Mingle Output) with input variables SE and NE.

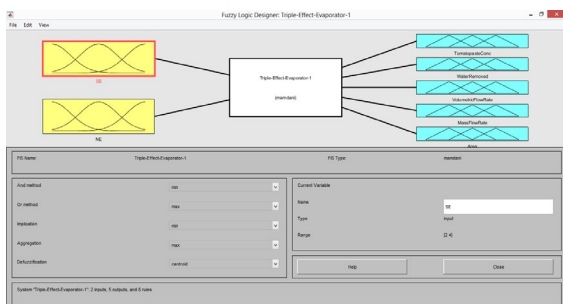


Figure 5: Fuzzy Inference System

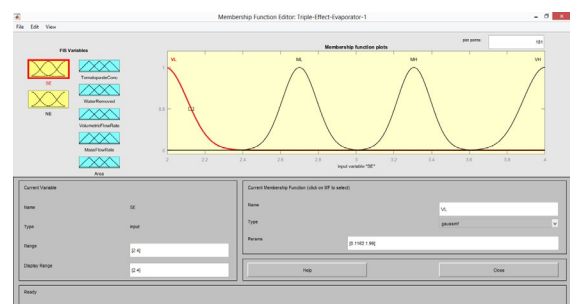


Figure 6: Membership function SE

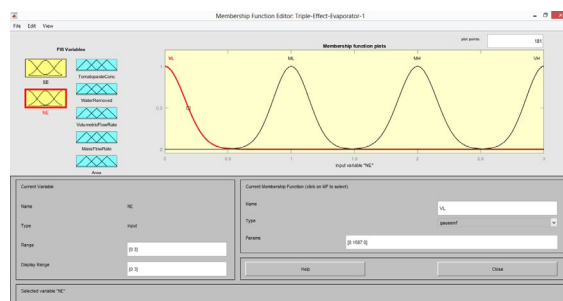


Figure 7: Membership for NE

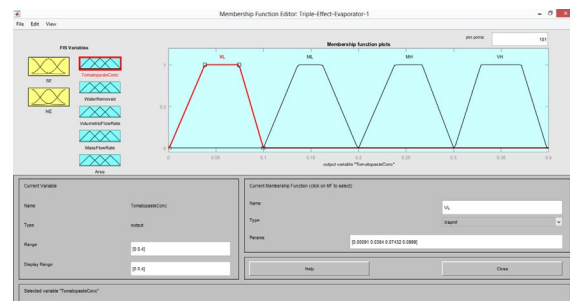


Figure 8: Membership for TomatopasteConc

# Fuzzy Logic Control of Tomato Conversion in a Triple-Effect Evaporator

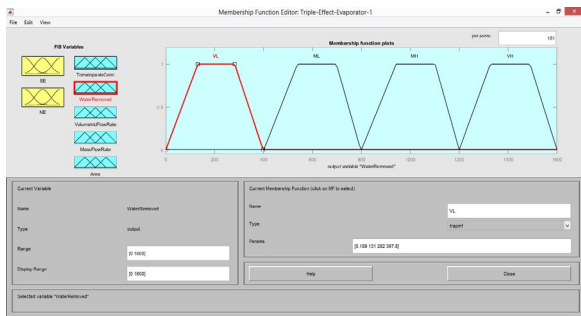


Figure 9: Membership for “WaterRemoved”

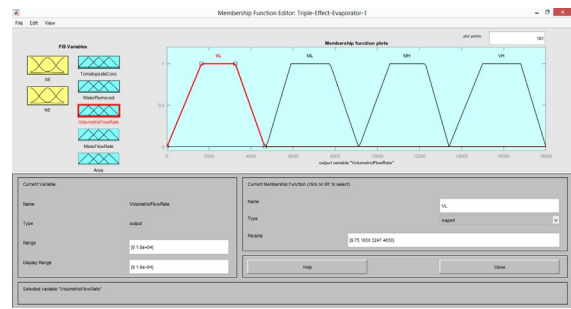


Figure 10: Membership for “VolumetricFlowRate”

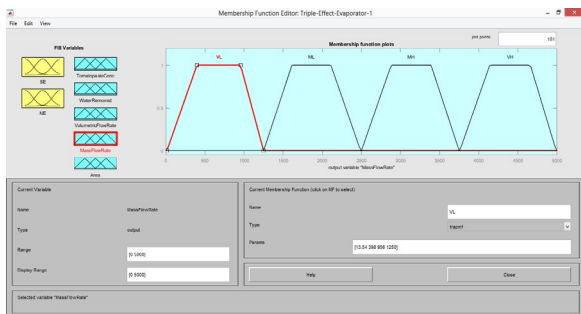


Figure 11: Membership for “MassFlowRate”

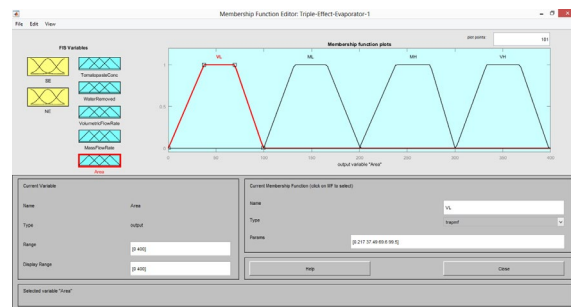


Figure 12: Membership for “Area”

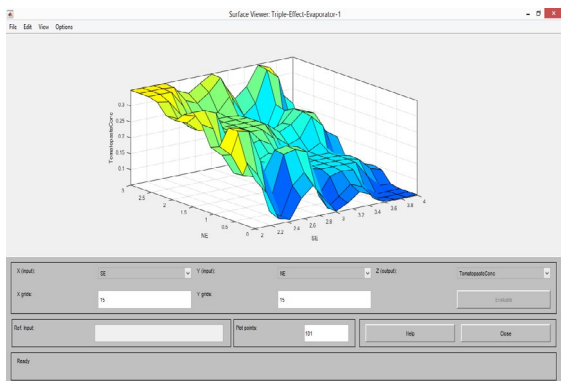


Figure 13: NE vs SE vs TomatopasteConc

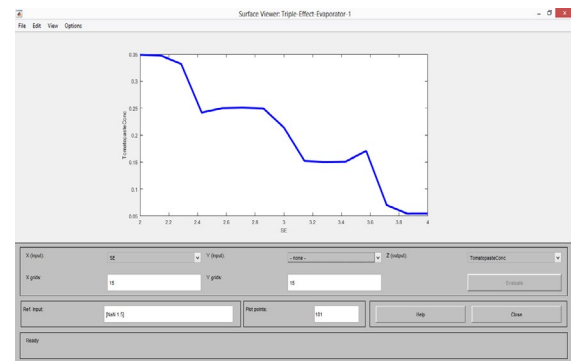


Figure 14: SE vs TomatopasteConc

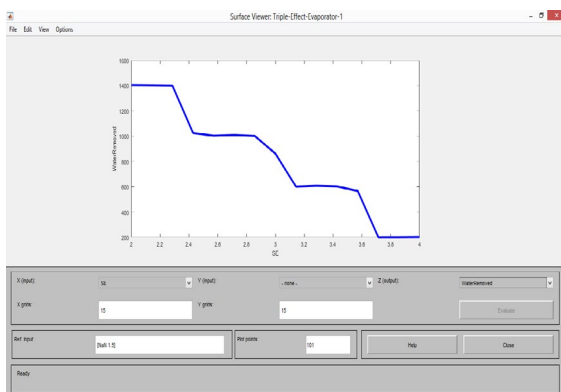


Figure 15: SE vs WaterRemoved

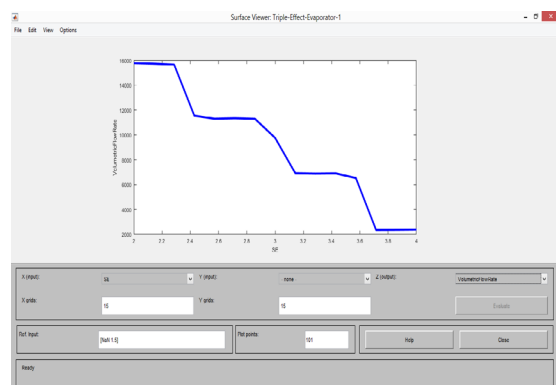


Figure 16: SE vs VolumetricFlowRate

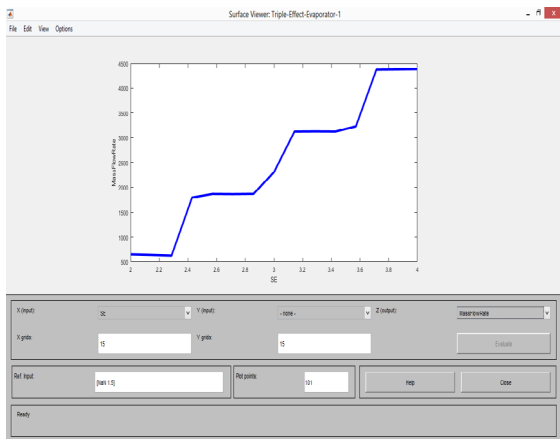


Figure 17: SE vs MassFlowRate

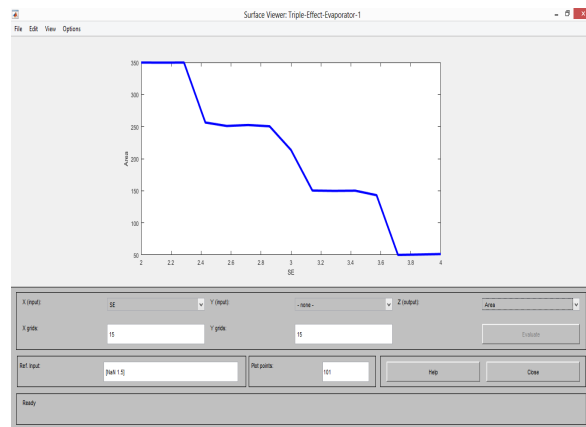


Figure 18: SE vs Area

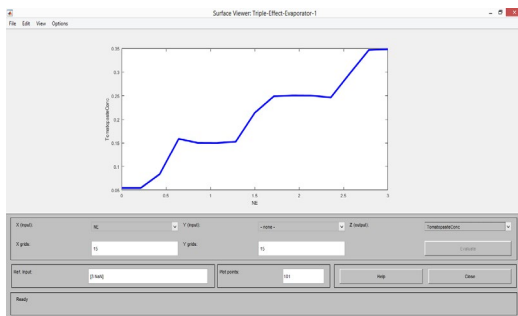


Figure 19: NE vs TomatopasteConc

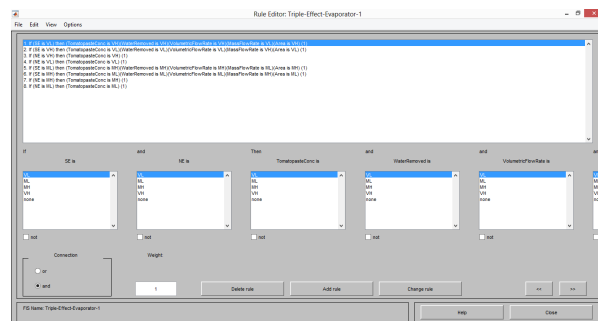


Figure 20: Rules display for MIMO with Inputs and Outputs

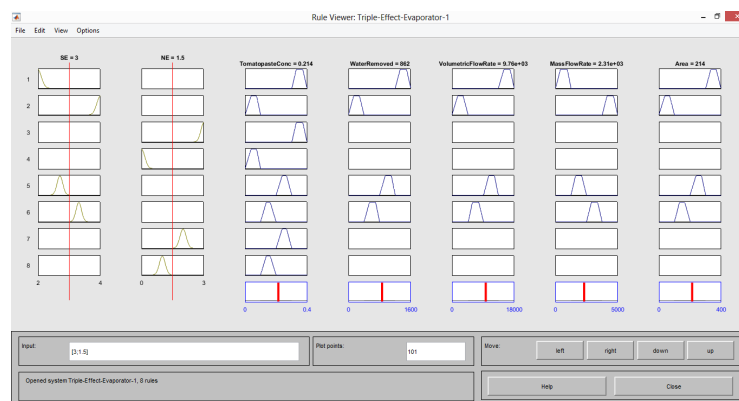


Figure 21: Rule Viewer Showing Selected values for design algorithm using MIMO with Input Variables “SE and NE”

#### 4. CONCLUSION

The implementation of Fuzzy Logic Control in triple-effect evaporator for a 5 ton/h processed tomato juice initially at 5% concentration to 35% tomato paste concentration was adequately studied. The effect of Steam Economy (SE) was studied on the tomato paste concentration. The desired tomato paste concentration of 35% was obtained in the third effect. Simulation results confirmed the applicability of fuzzy control to maintain tomato paste concentration and ensure energy savings.

## REFERENCES

- Smith, P. D. Cleswatz, S. Harrison, T.L. (2000) Control and Optimization of a multiple effect evaporator. In: Proceedings of S Afr Sug Technol Ass :74, pp 274-279.
- Emami, M. R. S. (2010). Fuzzy Logic Applications in Chemical Processes. *The Journal of Mathematics and Computer Science*, 1(4), 339-348.
- Ranganath M. and Elamin E. K. (2013) Fuzzy Logic Control of pH neutralization process. In: *IEEE international Conference on Electronics circuits and systems: ICESC*, pp. 1066-1069
- George, S. and Kyatanavar D. N. (2016). Optimization of Multiple Effect Evaporator Using Fuzzy Logic Integrated with Taguchi Technique. *International Conference on Electrical, Electronics, and Optimization Techniques (ICEEOT)*, 978-1-4673-9939-5/16, 1415-1419
- Oloruntoba, M. M., Olunlade, B. A. and Ibitoye, F.P. (2016). Effects of Input Variables on the Conversion of 5Ton/h Processed Tomato Juice in a Triple-Effect Evaporator, *Biotechnology Journal International*, 16(4), Article no.BJI.29320.
- Carter, J., Chiclana, F., Khuman, A. and Chen, T. (2021). Fuzzy Logic Recent Applications and Developments: Recent Applications and Developments. 10.1007/978-3-030-66474-9.



## Process Development for the Production of Lower Olefins from Levulinic Acid using 2 Sec-Butyl Phenol Recovery Strategy

Aramide A. ADESINA<sup>1,2,3\*</sup>, David LOKHAT<sup>1</sup> and Kamilu F. OYEDEKO<sup>2</sup>

<sup>1</sup>Discipline of Chemical Engineering, University of KwaZulu-Natal, Durban 4001, South Africa

<sup>2</sup>Department of Chemical Engineering, Lagos State University, Lagos, Nigeria

<sup>3</sup>ORCID 0000-0002-8689-3879

<sup>1\*</sup>[aramide.adesina@lasu.edu.ng](mailto:aramide.adesina@lasu.edu.ng), <sup>2</sup>[lokhat@ukzn.ac.za](mailto:lokhat@ukzn.ac.za), <sup>3</sup>[kamilu.oyedeko@lasu.edu.ng](mailto:kamilu.oyedeko@lasu.edu.ng)

\*Corresponding author

---

### ABSTRACT

This work presents a technical evaluation of a potential second-generation biorefinery process aimed at the production of ethylene and propylene as lower olefins from lignocellulosic biomass using an alternative levulinic acid recovery strategy. The process development was carried out through the coupling of various catalytic processes involving hydrolysis, hydrogenation, decarboxylation, and cracking. Additional alternative configurations were developed as an improvement to the base case process using the combustion of all generated hydrocarbons and solid by-products. The proposed bio-olefin production route was evaluated using the target product yield and energy efficiencies. The results revealed that 40 ktonne/yr of lower olefins can be produced from the process at a plant processing capacity of 701 ktonne of sugarcane bagasse per year with a base case energy efficiency of 41%. Therefore, the developed process is a viable option for the production of ethylene and propylene from lignocellulosic biomass.

**Keywords:** Biorefinery, lower olefins, 2-sec-butylphenol, process development.

### ABBREVIATIONS

LA	Levulinic acid
FA	Formic acid
5-HMF	5-Hydroxymethylfurfural
GVL	Gammavalerolactone
2-MTHF	2-Methyltetrahydrofuran
NRTL-HOC	Non-random two-liquid-Hayden-O'Connell
WHSV	Weight hourly space velocity
2-SBP	2-Sec-butylphenol

### 1. INTRODUCTION

The replacement of fossil-based fuels and chemicals with their bio-based counterparts has continued to be an area of research focus due to the depletion of fossil resources, the rising environmental concerns over their non-degradability and continued depletion of the ozone layer. Consequently, research (Hu *et al.*, 2022; 2020, Zhang *et al.*, 2021) has exploited the upgrading of biomass-based platform molecules to fuels and commodity chemicals. One such platform molecule is levulinic acid (LA). Although in recent times, the United States Department of Energy screened out LA as one of the bioproducts with upcoming potential due to issues with market attractiveness (Bidy *et al.*, 2016), it was tagged as one of the 12 main building blocks for producing value-added chemicals and fuels by the United States Department of Energy (Werpy *et al.*, 2004).

LA is produced via the hydrolysis of the cellulosic fraction of different biomass feedstock but for sustainability, the lignocellulosic type of biomass has been exploited as a promising feedstock starting from the 20th century (Pizzolitto *et al.*, 2020). The process of hydrolyzing lignocellulosic biomass to LA is carried out over homogeneous and heterogeneous catalysts with or without solvents. However, the major bottleneck of this process is that a series of reactions take place due to the complexity of the lignocellulosic biomass. The hexose sugars in the cellulose fraction break down to form formic acid (FA) and LA while the pentose sugars in the hemicellulose are degraded to furfural. The hexose sugars in the hemicellulose are also hydrolyzed to 5-Hydroxymethylfurfural (5-HMF) and then further to LA and FA (Fitzpatrick, 1990) while the lignin component is degraded to humins. Another drawback in the hydrolysis of lignocellulosic biomass to LA is the production of LA in low concentrations making recovery difficult (Morone *et al.*, 2015).

Consequently, several recovery strategies using extracting solvents have been investigated for the recovery of LA from the resulting biomass hydrolysate of the hydrolysis reaction. One of such strategies is the use of gamma-valerolactone (GVL) as a green solvent for the one-pot conversion of lignocellulosic biomass to LA and the selective recovery of LA from the biomass hydrolysate (Alonso *et al.*, 2013). Organic solvents such as butanol, o-cresol, and methyl isobutyl ketone have also been exploited for the recovery of LA and the subsequent upgrade of LA to liquid hydrocarbon fuels. However, a major drawback of the use of solvents is the large volume of solvents used and the cost of solvent recovery (Morone *et al.*, 2015). This drawback has led to the hunt for the application of novel solvents at a low cost to aid industrial applicability (Adesina and Lokhat, 2022).

Accordingly, Adesina and Lokhat (2022) adopted the o-cresol-based strategy for the recovery of LA and its subsequent use for the production of lower olefins. One of the potential shortcomings of the afore-developed strategy is the inclusion of two distillation columns for the recovery of the extracted LA from the solvent prior to the next hydrogenation reaction. Also, Alonso *et al.* (2011) developed the 2-sec-butylphenol (2-SBP) strategy, also called the alkylphenol strategy, for the recovery of LA and its subsequent hydrogenation to GVL. This approach tends to address the drawback of having to use distillation columns for solvent recovery before the next catalytic hydrogenation stage. However, the 2-SBP recovery approach used by Alonso *et al.* (2011) was only used to intensify the process of the catalytic upgrading of LA to liquid hydrocarbon fuels.

For the 2-SBP recovery system, the technical evaluation of its application for the industrial processing of LA to lower-range hydrocarbons such as ethylene and propylene has not been explored. Presently, fully integrated biopropylene plants are lacking and the available bioethylene plants are operated via the dehydration of dilute ethanol solutions which require a large amount of energy to anhydriy the ethanol (Rossetti *et al.*, 2015). This limits the sustainability of the use of ethanol as a feedstock for commercial bioethylene production (Rossetti *et al.*, 2019). Consequently, the simulation of alternative processes for the industrial production of ethylene and propylene needs to be further explored. The application of the 2-SBP recovery strategy for the industrial processing of LA to ethylene and propylene could be explored as an alternative lower olefin production strategy. Hence, this work aims to carry out the process development of the catalytic upgrade of LA for the production of lower olefins using a 2-SBP recovery strategy for LA recovery.

## 2. METHODOLOGY

The strategy for the process development of lower olefins, from lignocellulosic biomass, involves the coupling of processes involving hydrolysis, hydrogenation, decarboxylation, and cracking to a liquid-liquid extraction process. The LA formed during the hydrolysis of lignocellulosic biomass is extracted using 2-SBP. The sulphuric acid does not partition into the organic phase and can be recycled back into the hydrolysis stage. This approach prevents the negative impact of sulphuric acid on the hydrogenation catalyst in the next stage. The impacts include a reduction in the conversion of LA to GVL, turnover frequency, and selectivity of LA to GVL (Braden *et al.*, 2011). Furthermore, the adopted approach also reduces the amount of fresh sulphuric acid required for the hydrolysis process. The extracted LA can then be converted to ethylene and propylene via the reaction stages described in section 2.1.2 to 2.1.4 below.

### 2.1 Technology overview

#### 2.1.1 Hydrolysis of lignocellulosic biomass

Ethylene and propylene can be produced from lignocellulosic biomass via GVL intermediate compound. For the production of GVL, lignocellulosic biomass is first hydrolysed to LA and FA using sulphuric acid as a catalyst. The reaction is a complex network of reactions involving the formation of other compounds such as furfural, 5-HMF and unwanted degradation productions called humins (Liang *et al.*, 2018). At an optimum reaction time of 6 h, an acid concentration of 0.55 M and a temperature of 158 °C, a yield of 56% LA can be achieved using a feed-to-liquor ratio of 0.1. Another product which is formed from the reaction is glucose (Adesina and Lokhat, 2018). The produced LA can then be hydrogenated to GVL.

#### 2.1.2 Hydrogenation of LA

The catalytic hydrogenation of LA to GVL takes place in the presence of a hydrogen donor such as water, FA and hydrogen gas. Using a LA concentration of 2 M and an H<sub>2</sub> feed flow rate of 329 kg/h, 99% GVL can be obtained over RuSn<sub>4</sub>/C catalyst at 200 °C, a weight hourly space velocity (WHSV) of 2.2 h<sup>-1</sup>, and a pressure of 35 bar H<sub>2</sub> (Alonso *et al.*, 2011). Other compounds such as water, and 2-methyltetrahydrofuran (2-MTHF) are formed as side products of the reaction. GVL can be further decarboxylated to butene which is subsequently cracked to ethylene and propylene as target products.

#### 2.1.3 Decarboxylation of GVL

The decarboxylation of GVL proceeds via a two-step process of (1) The ring-opening of GVL to a mixture of isomeric pentenoic acids and (2) The decarboxylation of the pentenoic acids to butene and CO<sub>2</sub> (Bond *et al.*, 2010b). The decarboxylation reaction can be carried out using an aqueous feed of 60 wt% GVL at 375 °C over SiO<sub>2</sub>/Al<sub>2</sub>O<sub>3</sub> catalyst in

a fixed bed reactor with an optimum conversion of 100%. A 98% selectivity to a mixture of butene can be obtained (Bond *et al.*, 2010a).

### 2.1.4 Cracking of butene

The mixture of butene comprising mainly of 1-butene can be cracked at lower pressures to favour the production of ethylene and propylene as lower hydrocarbons. However, the cracking reaction is complicated as a network of side reactions occurs with the main reaction. Possible side reactions include the hydrogen transfer reactions to aromatics and higher alkanes and the dehydrogenation-aromatization reaction to aromatics and hydrogen gas. Consequently, 1-butene can be cracked using ZSM-5 catalyst with a much stronger acid site. Ethane, methane, benzene, pentane, hydrogen, and toluene can also be formed as side products of the reaction (Lin *et al.*, 2014).

## 2.2 Process assumptions, feedstock selection and plant size

Sugarcane bagasse is chosen as the feedstock for lower olefin production because of its high glucan composition (Figure 1.) and its availability as agricultural waste. This work uses the same lignocellulosic biomass feedstock processing rate of 773000 dry U.S ton/year amounting to 2000 tonne/day used for the o-cresol-based strategy and a similar plant operating time of 8410 hours per year.

The developed process is an nth-plant design based on the scale-up of experimentally determined yields and selectivities without performance loss. Also, all operating conditions such as temperature and pressure are set to that of experimental conditions. The developed process design follows the developed National renewable energy laboratory (NREL) benchmark case of the process design of biorefinery products from lignocellulosic biomass (Davis *et al.*, 2018).

Aspen Plus V10 was used for modelling the process. All physical properties of components used were in the Aspen databank. Physical properties of all components which were not present in the Aspen data bank (HMF, sugarcane bagasse) were sourced from the NREL-developed process for the conversion of Lignocellulosic biomass to hydrocarbon fuels and coproducts (Davis *et al.*, 2018). The NRTL-HOC thermodynamic model was adopted for modelling the different sections aside from the decarboxylation and cracking sections. This thermodynamic package is best suited to handle the non-ideality of polar and non-polar compounds including organic acids. For the latter, the Soave-Redlich-Kwong (SRK) thermodynamic model was adopted to determine the thermodynamic properties of the light hydrocarbons.

All reaction stoichiometry and conversions for modelling the reaction processes in Aspen plus are presented in Table 1.

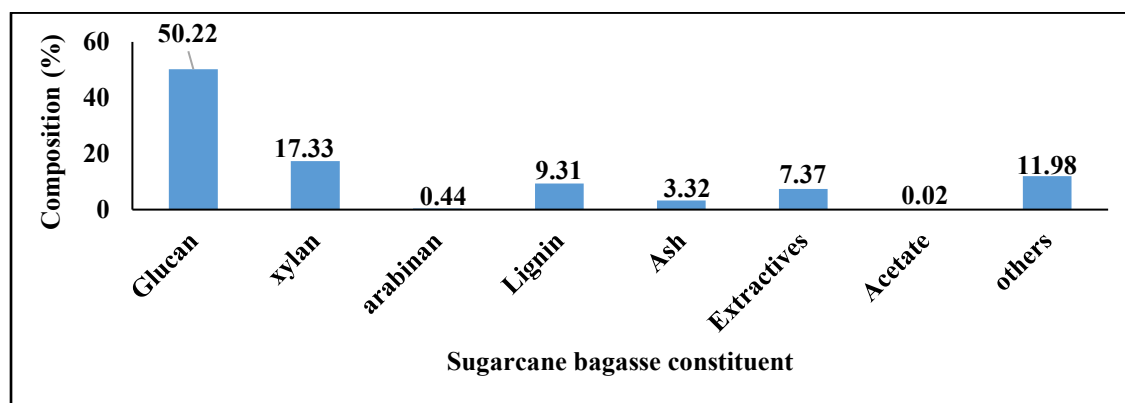


Figure 1: Compositional analysis of sugarcane bagasse (Adesina and Lokhat, 2022)

## 2.3 Process synthesis

The process flow sheet of the developed process is presented in Figure 2. Washed sugarcane bagasse feedstock is fed into the hydrolysis reactors (R101-R104) in area S-100 at 10% solids loading where the hexose sugars are converted to LA and FA. The pentose sugars present in the feedstock are assumed to be converted to degradation products called humins (Girisuta *et al.* 2013). The reactors are operated at 158 °C, and a pressure of 5.2 atm for 6 h to give a 56% yield of LA. Full details of the reaction stoichiometry and operating conditions used are in Table 1. At the end of the hydrolysis reaction, the hydrolysate is discharged and flashed (F101) to remove a fraction of the water from the hydrolysate. Further removal of water, however, takes place in the evaporator (E101) to reduce the solvent requirement in the next extraction section (S-200).

The top product from E101 contains a large portion of water and FA because the distribution coefficient of the 2-SBP solvent for FA is relatively low compared to that of LA. Consequently, FA has to be removed from the system in the evaporator (E101) to prevent a build-up in the system. FA could be used for the further production of on-site hydrogen gas. A little amount of LA is also flashed alongside the water. The bottom product from E101 consisting of a concentrated



LA solution is pumped into a centrifuge (C101) for the separation of the solids from the hydrolysate liquor. It is assumed that the percentage efficiency of the centrifuge is 99.5% with a loss of 0.5 % of the hydrolysate liquor. In this stage 0.5 wt% LA and FA are lost. The separated solids called humins are further washed with water in separator S101 to remove any remaining concentrated acid. The humins can be further used for heat and electricity generation for the plant. The hydrolysate liquor from evaporator E101 is then pumped into the extractor (EX201) in area S-200 where LA is extracted using 2-SBP.

Table 1: Reaction stoichiometry and conversions for modelling the reaction processes in aspen plus

Products	Conversion
<b>Conversions for biomass hydrolysis at 5 atm, 154 °C, 6 hr (Adesina and Lokhat, 2018)</b>	
Glucan + water → glucose	0.002
Glucan + 0.335 water → humins	0.435
Glucan → HMF + 2water	0.000
Glucan → LA + FA	0.563
Glucose → HMF + 3water	0.000
HMF + 2water → LA + FA	0.999
HMF + 2.336water → humins	0.000
Glucose → humins + 0.664034water	0.389
Glucose → LA + FA + water	0.610
Arabinan + 0.999water → tar	1
<b>Products</b>	<b>Conversion</b>
Xylan + 0.999water → tar	1
Extractive → tar + 1.666water	1
Acetate + 5water → tar	1
<b>Conversions for LA hydrogenation at 0.18 h<sup>-1</sup>, 200 °C, 35 bar (Alonso <i>et al.</i>, 2011)</b>	
LA + FA → GVL + H <sub>2</sub> O	0.0379
LA + H <sub>2</sub> → GVL + H <sub>2</sub> O	0.9521
LA + 3H <sub>2</sub> → 2MTHF + 3H <sub>2</sub> O	0.01
<b>Conversions for GVL decarboxylation at 2.2 h<sup>-1</sup>, 375 °C, 36 bar (Bond <i>et al.</i>, 2010a)</b>	
GVL → butene + CO <sub>2</sub>	0.98
GVL → 1-octene + ethyl benzene	0.02
Pentenoic acid → butanol + CO <sub>2</sub>	1
Levulinic acid → MEK + CO <sub>2</sub>	1
<b>Conversions for butene cracking at 6 h<sup>-1</sup>, 500 °C, 1 bar (Lin <i>et al.</i>, 2014)</b>	
1-Butene → Ethylene	0.157805
5.250 1-Butene → Benzene + 3 Pentane	0.174819
1- Butene → 1.33335 Propylene	0.342505
2.820 1-Butene → 2 Benzene + Hydrogen	0.083179
1.928 1-Butene → Toluene + methane	0.012429
1.928 1-Butene → Benzene + Ethane	0.012429

The extractor is operated at 16 bar and 80 °C. The value for parameter  $a$ , in the aspen-built-in liquid-liquid distribution coefficient ( $K_{LL}$ ) correlation (equation 1) for the extractor (EX201) is presented in Table 2.

$$\ln K_{LL} = a + \frac{b}{T} + C \ln(T) + dT \quad (1)$$

Where  $a$ ,  $b$  and  $c$  are the correlation constants and  $T$  is the temperature

A 99.9% recovery of LA was achieved at 16 bar using 21 stages and a solvent mass flow rate of 44000kg/h. The organic phase from the extractor containing mainly the solvent, LA and a little amount of FA flows to the next hydrogenation reactor (R301) while the aqueous phase consisting of water, a little amount of FA and sulphuric acid is recycled back into the hydrolysis reactor (R101-R104).

The hydrogenation reactors (R301-R305) handle the hydrogenation of LA to GVL in 2-SBP. The organic phase from section S-200 is pumped to the reactors (R301-R305) where LA is hydrogenated to GVL over RuSn<sub>4</sub>/C catalyst. CO<sub>2</sub>, H<sub>2</sub>O, and 2-MTHF are also formed as by-products of the reaction. Although FA in the feed stream is used to hydrogenate LA to GVL, additional hydrogen gas is required since the 2-SBP cannot extract an equimolar amount of FA required for the complete reaction of LA. At 200 °C, 35 bar and a WHSV of 2.2 h<sup>-1</sup>, a 100% conversion of LA was achieved without

## Process Development for the Production of Lower Olefins from Levulinic Acid using 2 Sec-Butyl Phenol Recovery Strategy

the hydrogenation of the solvent. The reaction stoichiometry and performance data used for the hydrogenation process are presented in Table 1. At the end of the hydrogenation reaction, to reduce the energy requirement of the direct use of utilities, the reactor content is first flashed (F301) to remove the excess hydrogen gas and some water vapour as the top product. The bottom product consisting of water, GVL, and 2-MTHF is pumped into a distillation column (D301) for the recovery of GVL from the product stream. Using optimum conditions of 28 stages, a mole reflux ratio of 1.9 and at a feed stage of 10, a 99% recovery of GVL as the distillate and a 96% recovery of the solvent in the bottom is achieved. The top product from the distillation column (D301) consists of GVL, water, with a little amount of 2-MTHF and 2-SBP solvent. The bottom product which consists mainly of the solvent is recycled back into the extractor (EX201). The top product from the distillation column (D301) is then sent to the decarboxylation section for the production of butene.

The aqueous GVL stream is preheated (E401) to the reaction temperature of 375 °C and then fed into the decarboxylation reactors (R401-R405) where GVL is decarboxylated to butene over  $\text{SiO}_2/\text{Al}_2\text{O}_3$  catalyst at 36 bar, 375 °C and a WHSV of  $0.9 \text{ h}^{-1}$  as explained in section 2. Water is introduced into the feed stream going into the reactors (R601-R605) to give a GVL concentration of 60 wt%. Reaction conditions, as well as the performance data used to model the reactors, are found in Table 1. The product from the decarboxylation reactors is flashed to remove the liquid hydrocarbon by-products. The top stream, which consists mainly of butene and  $\text{CO}_2$  is separated in the next distillation column D401. Using 14 stages, a feed stage of 7 and a mole reflux ratio of 2, a 99.9% recovery of butene in the bottom and a 99.9% recovery of  $\text{CO}_2$  as the distillate was achieved. The recovered butene flows into the cracking section where it is converted to ethylene, propylene and a mixture of other hydrocarbons at 500 °C, 1 bar and a WHSV of  $6 \text{ h}^{-1}$ . The product from the cracking reactors (R501-R503) is then sent to a series of distillation columns where pure ethylene and propylene are recovered as target products. Reaction conditions, performance data and the flow sheet configuration used for the cracking section are presented in Table 1 and Figure 1.

The design of the subsidiary units (waste water treatment, utilities and boiler) is similar to the afore-mentioned NREL design of these units.

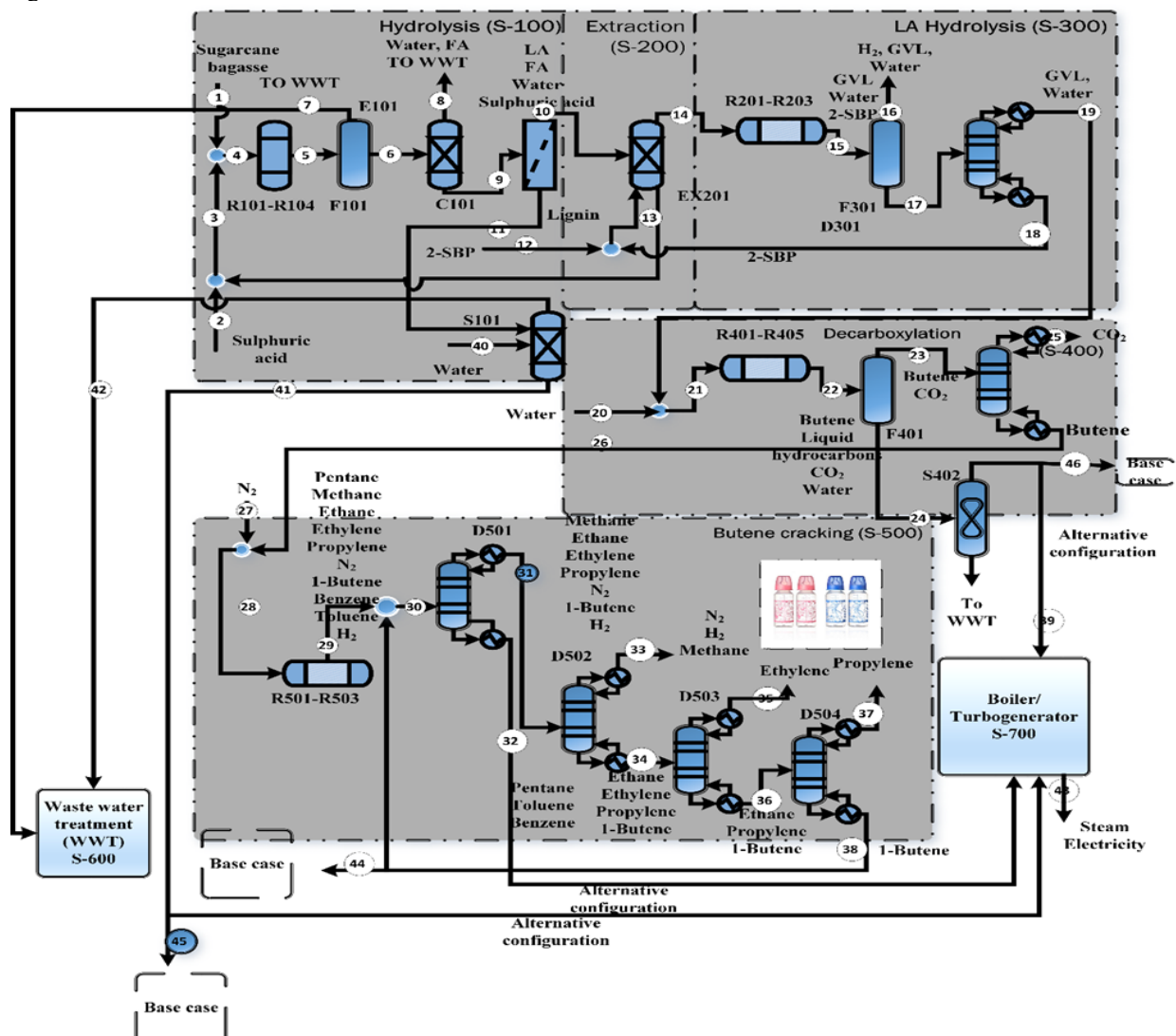


Figure 2: Process flow diagram of the production of lower olefins using a 2-SBP recovery strategy

Table 2: Reaction stoichiometry and conversions for modelling the reaction processes in aspen plus

Component	Value of coefficient (a)
LA	2.82342
FA	-0.27827
Water	-20.3596
2-SBP	24.4814
Sulphuric acid	-18.2805
Glucose	-13.8682
HMF	-9.58665
GVL	5.60787

## 2.4 Heat integration

To reduce the total utility requirement for the process, heat integration was performed by matching the process hot streams against the cold streams. Using an initial value of the minimum temperature difference ( $\Delta T_{min}$ ), a heat exchanger network design (HEN) was developed using Aspen Energy Analyzer. The total annualized cost of the HEN was determined from the sum of the annual operating cost and capital cost using equations 2 & 4.

$$\text{Total capital cost of a heat exchanger} = a + b * (A_{min})^c \quad (2)$$

Where  $a$ ,  $b$ , and  $c$  are the cost law coefficient which depends on the specifications of the heat exchanger and  $A_{min}$  is the total minimum heat exchanger requirement.  $A_{min}$  is calculated using equation 3

$$A_{min} = \sum_i \frac{\Delta Q_i}{U_i \Delta T_{LMi}} \quad (3)$$

$\Delta Q_i$ ,  $U_i$  and  $\Delta T_{LMi}$  are the heat exchanger load, overall heat transfer coefficient and the change in logarithmic mean temperature difference for any stream  $i$ .

$$\text{Total operating cost} = \text{sum cost of hot streams} + \text{sum cost of cold streams} \quad (4)$$

Specifically, for the design of the heat exchangers in the hydrolysis section, stainless steel SS 316 was chosen as the material of construction to provide additional resistance to mineral acids. The value for coefficients  $a$ ,  $b$ , and  $c$  used were 30800, 1644 and 1 respectively (Hojjati *et al.*, 2004). The material of construction for the HEN for other sections of the process was assumed to be carbon steel and the default values for  $a$ ,  $b$  and  $c$  in Aspen energy analyzer were used for these other sections.

To further determine the optimum value of  $\Delta T_{min}$  for which the total annualized cost of the HEN is minimized, the value of  $\Delta T_{min}$  was varied between 0.1 to 100 °C and the corresponding effect on the total annualized cost of the HEN was determined. The optimization toolbox of the Aspen energy analyzer was further used to generate an optimized HEN design by targeting the minimum total annualized cost of the HEN design.

## 2.5 Alternative configuration

To reduce the usage of non-renewable fuels to generate heat and electricity for the plant, the solid residue and the generated hydrocarbon by-products are used to power the plant. The liquid hydrocarbons generated in areas S-400 and S-500, and the solid degradation products from S-100 are all sent to the combustor in a combined heat and power system for the co-generation of heat and electricity for the plant.

## 3. RESULTS AND DISCUSSION

### 3.1 Mass balance results

The mass balance result for the base case design is presented in Table 3. 1544 kg/h of ethylene and 3360 kg/h of propylene are produced. This would amount to a total lower olefin yield of 41 ktonne/yr. Consequently, it will increase the global production capacity of biopolymers. Comparatively, a higher yield of lower olefins was obtained than that of the o-cresol based-process of 30 ktonne/yr previously developed by the authors (Figure 3). Also, the number of hydrocarbon by-products generated (3234 kg/h) is lower than the o-cresol-based process (5125 kg/h).

In terms of the CO<sub>2</sub> produced by this process, 6260 kg/h of CO<sub>2</sub> is produced. However, only 277 kg/h of the total produced CO<sub>2</sub> is from the hydrogenation process. About 96% of the produced CO<sub>2</sub> is from the decarboxylation section which is produced at very high pressures (36 bar) making CO<sub>2</sub> capture and storage feasible under this condition.

## Process Development for the Production of Lower Olefins from Levulinic Acid using 2 Sec-Butyl Phenol Recovery Strategy

Other by-products include hydrocarbons and solid products. The solid products consist mainly of the lignin component of the feedstock and the solid decomposition products called humins. Lignin can be used for the production of green solvents (Kim and Han, 2016) while the whole solid products can also serve as a source of steam and electricity generation for biorefineries. Consequently, these solid and liquid hydrocarbon by-products are used for the onsite generation of heat and electricity in the alternative configuration.

Table 3: Mass balance result for the base case design for the 2-SBP strategy

Materials	Mass (kg/h)
<b>Input</b>	
Bagasse	83333
Water used up in	2749
Hydrogen (A600)	271
<b>Total input</b>	<b>86353</b>
<b>Output</b>	
Target products	
Ethylene	1544.27
Propylene	3360.34
By-products	
Solid residue and organic liquids	
Lignin	9264.48
Glucose	3.09
HMF	0.32
LA	377.39
FA	6437.51
Tar	31564.90
Humins	18807.20
Liquid and gaseous hydrocarbons	3234.21
Non-hydrocarbon gases	
CO <sub>2</sub>	6260.79
H <sub>2</sub>	10.39
Water produced	5488.11
<b>Total output</b>	<b>86353</b>
<b>Recycling rate</b>	
Fresh o-cresol in	44000
o-cresol recycling rate	96.40%
H <sub>2</sub> SO <sub>4</sub> in	8216
H <sub>2</sub> SO <sub>4</sub> recycled rate	99.30%
<b>Inert (ktonne/yr)</b>	
Nitrogen rate	29739

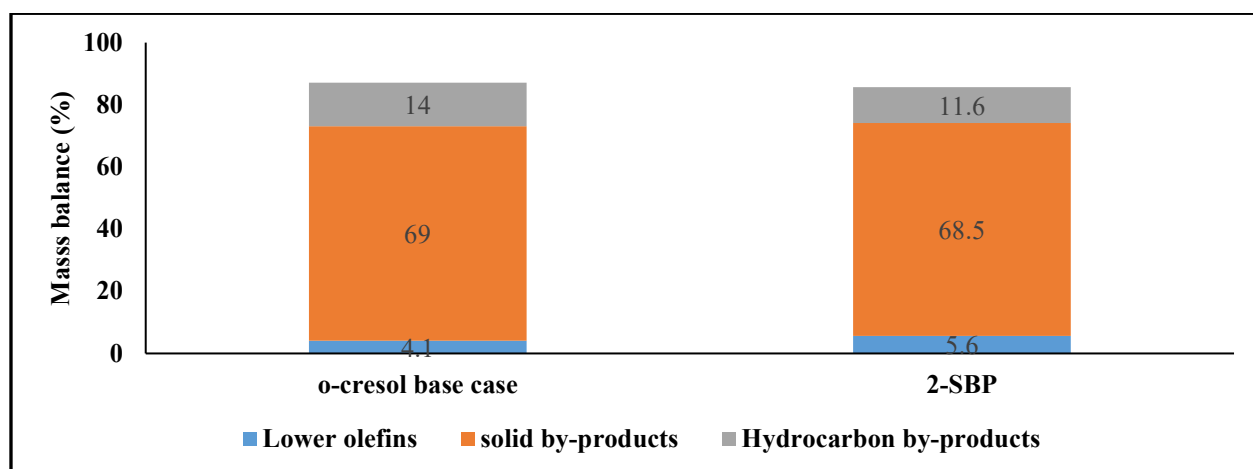


Figure 3: Comparison of mass yield of different products obtained from the 2-SBP process to literature

### 3.2 Energy balance results

The result of the energy balance for the process is first presented in terms of the heat requirement of the process, 515 MW of heating and 548 MW of cooling (Table 4) are required where the hydrolysis process accounts for about 85% of the total heating requirement. This is due to a large amount of heat (368MW) required to achieve a design specification of 90% evaporation of the water in the hydrolysis section prior to extraction, to reduce the quantity of solvent used for the liquid-liquid extraction process. In comparative terms, the overall heat requirement for the 2-SBP extraction strategy is about 18% lower than the *o*-cresol-based process. The overall heat requirement of the process was further reduced by the exchange of heat between the hot and cold process streams using heat integration. The diagram for the HEN is presented as Fig. S1 (see associated supplementary information).

Accordingly, using an initial  $\Delta T_{\min}$  of 10 °C, the total annualized cost of the HEN was \$ 1.089/s. At an optimum  $\Delta T_{\min}$  value of 12 °C, the total annualized cost of the HEN was minimized (\$ 1.087/s). The integrated process led to a 23% decrease in the total utility demand of the process. To further reduce the external energy demand of the integrated base case process, all solids and hydrocarbon by-products were combusted in a combined heat and power system as an alternative configuration. This led to a 26.7% reduction in the earlier energy demand of the base case process.

Regarding the energy efficiency of the developed process, the process efficiency of the base case process is 41%.

Table 4: **Energy balance result for the developed processes**

Heat demand for the base case Section	Heating requirement (MW)	Cooling requirement (MW)
S-100-Hydrolysis	435	470
S-200-Extraction	-	5
S-300-Hydrogenation	24	18
S-400-Decarboxylation	13	10
S-500-Cracking	14	24
S-600-Wastewater treatment	1.8	16
S-700-Boiler	25	4
S-800-Utilities (Process water)	4.2	-
<b>Total</b>	<b>517</b>	<b>547</b>
<b>Heat demand after integration (MW<sub>thermal</sub>)</b>	<b>400</b>	<b>426</b>
<b>Heat demand for the alternative configuration (MW<sub>thermal</sub>)</b>		
Heat from by-product combustion		107
External heat supply		293
Electricity generation (MW <sub>elec</sub> )		114
On-site electricity usage		24
Electricity export (MW <sub>elec</sub> )		109
Process Efficiency (%HHV)		41

### 4. CONCLUSION

The work presented here involves the development of a process for the production of ethylene and propylene from lignocellulosic biomass. Further technical performance of the developed process has been assessed with the process producing 4904 kg/h olefins, accounting for an annual production of 41 ktonnes/yr. The developed 2-SBP based-strategy resulted in a higher yield compared to that of the formerly developed *o*-cresol-based strategy. Furthermore, the developed alternative configuration strategy led to a 26% reduction in the utility requirement compared to the base case strategy for producing the lower olefins.

However, despite the technical assessment of the different strategies for the production of lower olefins to determine the feasibility of the developed processes, a full economic evaluation of the process is further required to determine the commercial feasibility of the use of these approaches for ethylene and propylene production.

### ACKNOWLEDGEMENT

This work was supported by the South African National Research Foundation (Grant number 101068).

## REFERENCES

- Adesina, A. & Lokhat, D. 2018. Kinetic Model Development and Bi-objective Optimization of Levulinic Acid Production from Sugarcane Bagasse. *The Role of Exergy in Energy and the Environment*. Springer.
- Adesina, A. & Lokhat, D. 2022. Process development for the production of ethylene and propylene from lignocellulosic biomass via the chemical route using an o-cresol-based recovery strategy. *Biomass Conversion and Biorefinery*, 1-18.
- Alonso, D. M., Wettstein, S. G., Bond, J. Q., Root, T. W. & Dumesic, J. A. 2011. Production of Biofuels from Cellulose and Corn Stover Using Alkylphenol Solvents. *ChemSusChem*, 4, 1078-1081.
- Alonso, D. M., Wettstein, S. G., Mellmer, M. A., Gurbuz, E. I. & Dumesic, J. A. 2013. Integrated conversion of hemicellulose and cellulose from lignocellulosic biomass. *Energy & Environmental Science*, 6, 76-80.
- Biddy, M. J., Scarlata, C. & Kinchin, C. 2016. Chemicals from biomass: a market assessment of bioproducts with near-term potential. National Renewable Energy Lab.(NREL), Golden, CO (United States).
- Bond, J. Q., Alonso, D. M., Wang, D., West, R. M. & Dumesic, J. A. 2010a. Integrated catalytic conversion of  $\gamma$ -valerolactone to liquid alkenes for transportation fuels. *Science*, 327, 1110-1114.
- Bond, J. Q., Alonso, M. D., West, R. M. & Dumesic, J. A. 2010b.  $\gamma$ -Valerolactone Ring-Opening and Decarboxylation over  $\text{SiO}_2/\text{Al}_2\text{O}_3$  in the Presence of Water. *Langmuir*, 26, 16291-16298.
- Braden, D. J., Henao, C. A., Heltzel, J., Maravelias, C. C. & Dumesic, J. A. 2011. Production of liquid hydrocarbon fuels by catalytic conversion of biomass-derived levulinic acid. *Green Chemistry*, 13, 1755-1765
- Broeren, M. 2013. Production of Bio-ethylene. *IEA-ETSAP and IRENA© Technology-Policy Brief*, 13.
- Davis, R.E., Grundl, N.J., Tao, L., Biddy, M.J., Tan, E.C., Beckham, G.T., Humbird, D., Thompson, D.N. & Roni, M.S. 2018. Process design and economics for the conversion of lignocellulosic biomass to hydrocarbon fuels and coproducts: 2018 biochemical design case update; biochemical deconstruction and conversion of biomass to fuels and products via integrated biorefinery pathways (No. NREL/TP-5100-71949). National Renewable Energy Lab.(NREL), Golden, CO (United States).
- Finkenrath, M. 2011. Cost and performance of carbon dioxide capture from power generation.
- Fitzpatrick, S. W. 1990. *Lignocellulose degradation to furfural and levulinic acid*. United States patent application 186,234.
- Girisuta, B., Dussan, K., Haverty, D., Leahy, J. & Hayes, M. 2013. A kinetic study of acid catalysed hydrolysis of sugar cane bagasse to levulinic acid. *Chemical engineering journal*, 217, 61-70.
- Haro, P., Ollero, P. & Trippe, F. 2013. Technoeconomic assessment of potential processes for bio-ethylene production. *Fuel Processing Technology*, 114, 35-48.
- Hojjati, M. R., Omidkhah, M. R. & Panjeh Shahi, M. H. 2004. Cost effective heat exchanger network design with mixed materials of construction. *Iranian Journal of Chemistry and Chemical Engineering (IJCCCE)*, 23, 89-100.
- Hu, W., Zhou, L., & Chen, J. H. 2022. Conversion sweet sorghum biomass to produce value-added products. *Biotechnology for Biofuels and Bioproducts*, 15(1), 1-11.
- Kim, S. & Han, J. 2016. A catalytic biofuel production strategy involving separate conversion of hemicellulose and cellulose using 2-sec-butylphenol (SBP) and lignin-derived (LD) alkylphenol solvents. *Bioresource technology*, 204, 1-8.
- Liang, C., Hu, Y., Wang, Y., Wu, L. & Zhang, W. 2018. Production of levulinic acid from corn cob residue in a fed-batch acid hydrolysis process. *Process Biochemistry*, 73, 124-131.
- Lin, L., Qiu, C., Zhuo, Z., Zhang, D., Zhao, S., Wu, H., Liu, Y. & He, M. 2014. Acid strength controlled reaction pathways for the catalytic cracking of 1-butene to propene over ZSM-5. *Journal of Catalysis*, 309, 136-145.
- Machado, P. G., Walter, A. & Cunha, M. 2016. Bio-based propylene production in a sugarcane biorefinery: A techno-economic evaluation for Brazilian conditions. *Biofuels, Bioproducts and Biorefining*, 10, 623-633.
- Morone, A., Apte, M. & Pandey, R. A. 2015. Levulinic acid production from renewable waste resources: Bottlenecks, potential remedies, advancements and applications. *Renewable and Sustainable Energy Reviews*, 51, 548-565.
- Rossetti, I., Lasso, J., Compagnoni, M., De Guido, G., & Pellegrini, L. A. 2015.  $\text{H}_2$  production from bioethanol and its use in fuel-cells. In ICheaP12 International Conference on Chemical & Process Engineering, 229-234.
- Rossetti, I., Tripodi, A., Frosi, M., Ramis, G., & Mahinpey, N. 2019. Bio-ethylene production: from reaction kinetics to plant scale. *Arabia*, 2(106), 4.
- Vasiliadou, E. S. & Lemonidou, A. A. 2016. Production of Biopropylene Using Biomass-Derived Sources. *Encyclopedia of Inorganic and Bioinorganic Chemistry*, 1-12.
- Tullo A. 2011. Notes On Dow's Brazilian Biopolymers Project. [Online]. <http://cenblog.org/the-chemical-notebook/2011/07/447/>. [Accessed:23-Apr-2019].
- Werpy, T., Petersen, G., Aden, A., Bozell, J., Holladay, J., White, J., Manheim, A., Eliot, D., Lasure, L. & Jones, S. 2004. Top value added chemicals from biomass. Volume 1-Results of screening for potential candidates from sugars and synthesis gas. Department of Energy Washington DC.
- Zhang, S., Wang, J., & Jiang, H.. 2021. Microbial production of value-added bioproducts and enzymes from molasses, a by-product of sugar industry. *Food chemistry*, 346, 128860.



## Response Modelling and Optimization of Produced Particleboards from Sawdust Softwood using R7AD2 Adhesive

Lucas HAMIDU<sup>1</sup> and Umar AROKE<sup>2</sup>

<sup>1</sup>Nigerian Building and Road Research Institute

<sup>2</sup>Abubakar Tafawa Balewa University, Bauchi

\*Corresponding author: [lucadohamidu@gmail.com](mailto:lucadohamidu@gmail.com)

### ABSTRACT

This work presents the modelling and optimisation of produced particleboards from sawdust softwood using R7AD2 adhesive, focusing on conversion of wastes into wealth for a sustainable environment. Mixture design of experiment (DOE) using Design Expert Software, Version 6.0.8 were employed in the process formulation for the production of particleboards due to compatibility. The produced particleboards were characterised for the responses water absorptions (WA) at 2 and 24 hours and density, and optimised. The analysis of variance (ANOVA) and sequential model sum of squares (SMSS) were used to validate the responses. Based on the results of the optimised responses, the sawdust softwood particleboard formulation 8 (SDP8) which has ratio of 0.32 softwood sawdust (SD) to 0.68 R7AD2 adhesive with the characteristic values of 17.23%WA at 2 hours, 90.48%WA at 24 hours and 647.28 kg/m<sup>3</sup> density was found best fit among others, placing the produced particleboard in the medium density category. The overall process revealed that Cubic model best fit the design based on the statistical analysis. The R7AD2 adhesive and the sawdust softwood particleboard (SDP8) formulation had shown better water repellent at 24 hours immersion which had met the standard specification.

**Keywords:** Modelling, optimisation, particleboards, R7AD2 adhesive, sawdust.

### 1. INTRODUCTION

Forest reserve is beneficial to humanity as it absorbs emitted carbon dioxide (CO<sub>2</sub>) which is stored in trees and soil thereby releasing oxygen into the atmosphere in the form of fresh air (Alan 2019). Green leaves provide conducive atmosphere for habitat as the surrounding temperature diffused to maintain stable environment, which can be achieved through planting of trees and other economic plants. Due to high demand for lignocellulosic biomass utilization as feedstock in the production of composite materials such as particleboard by the manufacturing industry, the forest resources are diminishing (Aigbodion *et al.* 2012). The use of wood on daily basis in building and construction sectors is creating scarcity of raw materials for furniture, the development which has led to deforestation, climate change and global warming.

Elbadawi *et al.* (2015) reported that the global demand for particleboard is over 23 million metric cube meters per annum. Particleboard is known to be cost reflective and affordable due to its dynamic nature, softness, and flexibility, moisture resistant, denser and is resistant to thermal conductivity which can provide comfort for the user in built environment (Fiorelli *et al.*, 2014). It is also used as an insulator due to its poor electrical conduction (Asha 2017) and reported to have low water absorption and thickness swelling for indoor use (Idris *et al.*, 2011). It is also used as energy efficient material in household and office accommodation and flooring systems, stair trends and underlayment (Pan *et al.*, 2007), wall, ceiling panels, office partition and cladding (Olawale *et al.*, 2020), bulletin boards, cabinets and desks (Alam *et al.*, 2015).

Peter *et al.* (2017) projected wastes from wood pellets/chips to be about 80 million tons by 2020 from the third world countries as import based by the European Commission. If such waste is harnessed into production of composite material such as particleboard, it would be of economic value and maintenance of clean environment instead of burning. Research on sawdust waste in the production of particleboard is still at infant stage due to variation in some properties observed below the international standard. Some of this previous research in the production of particleboards includes: the production of particleboard from plantain residue, cacao pad stem and Ceiba by Mitual *et al.* (2020), rice husk by Da Silva Cesar *et al.* (2017) wood chips or spices by Abdulkareem and Adeniyi (2017), sawdust and agricultural waste by (Abdulkareem *et al.*, 2017) and reed by (Flores-Yepes *et al.*, 2012). Others are low density sugar bagasse by (Liao *et al.*, 2016), wood waste and cashew nutshell by (Mari and Villena, 2016), wheat straw by (Zhang *et al.*, 2011), recycled low density polyethylene in wood composite by (Atuanya *et al.*, 2011). Low-density Binderless particleboard from Kenaf core, reinforced and characterized with fibre-woven sheets by (Xu *et al.*, 2004; Xu, Widyorini and Kawai 2005) among

others. Pan *et al.* (2007) reported that medium size mesh (20 – 40) gave higher particleboard qualities, than the smaller size (40–60 mesh) and larger size (10–20 mesh).

Modelling is usually employed in process formulation with essentials relying best on the responses (Roffel and Betlem, 2006), which can be verified experimentally to determine the best desired product using mathematical model equation (Mari and Villena, 2016). While statistical data from different models are used in the decision for selecting the best fit (Richard, 2007). This use of software such as design expert in modelling and optimisation will bring into limelight technological innovation in the selection of the best produced particleboard among several formulations.

## 2. METHODOLOGY

### 2.1 Design of Experiment

Mixture Design of Experiment (DOE) Equation 1 (Silva, Vianna & Neubert 2014) was used in the formulation of particleboards production from sawdust softwood (SD) with R7AD2 adhesive which had eight (8) experimental runs.

$$A + B = 1.0 \tag{1}$$

where, A= Sawdust and B= R7AD2 Adhesive

Boundary conditions:  $0.30 \leq A \leq 0.40$  and  $0.60 \leq B \leq 0.70$

The characterised responses water absorption and density as presented in Table 1 at 2 and 24 hours, and density for the produced particleboards from sawdust softwood with R7AD2 adhesive by Hamidu *et al.* (2021).

Table 1: Sawdust Softwood Particleboards Water Absorption and Density

Sawdust Particleboards	Percentage Water Absorption (%WA)		Density ( $\rho$ )
	2 hours	24 hours	kg/m <sup>3</sup>
SDP1	20.53	104.51	669.64
SDP2	43.10	105.79	808.00
SDP3	81.93	118.77	732.50
SDP4	112.58	151.24	907.14
SDP5	80.78	131.22	806.38
SDP6	41.94	103.97	848.98
SDP7	20.82	106.93	677.94
SDP8	30.95	96.65	685.71

### 2.2 Response Modelling and Optimisation of the particleboards

The responses water absorptions at 2 and 24 hours, and densities in Table 1 were modelled and optimised using Mixture design due to its compatibility based on the constraint factors for 2 components and 3 responses according to the standard procedure (Richard, 2007). The design matrix for constraints bounds for low and high values to authenticate the data captured is as presented in Table 2 for the boundary condition.

Table 2: Sawdust Particleboards Design Matrix Using Mixture Composition

Components	Name	Low Actual	High Actual	Low Coded	High Coded
A	Sawdust softwood	0.30	0.40	0.000	1.000
B	R7AD2 Adhesive	0.60	0.70	0.000	1.000

The optimisation process was focused on the goals to minimise water absorption within the density range as the basic requirement for commercial particleboard based on JIS A5908 (2003). Each response was evaluated using model equations that describe the process as either, linear mixture or special cubic mixture or cubic mixture or quadratic mixture model in validation of the analysis of variance. Other factors used were the regression values for both adj. and pred. R<sup>2</sup>, standard deviation (Std. Dev.) and precision adequacy, based on the model equations generated by the software for statistical analyses and followed by sum of squares analysis for each model (Richard, 2007).



## RESULTS AND DISCUSSION

The analysis of variance (ANOVA) and sequential model sum of squares (SMSS) were used in for the analysis in determining the best fit.

Table 3 present the sawdust particleboard responses analysis of variance (ANOVA) for water absorption and density generated by the design expert software. The ANOVA for 2 hours water absorption had the Model F-value of 914.74 and Prob < F value of 0.0001 which is less than 0.0500 implying that the model is significant. Other significant model terms which had high F-Values and Prob > F values less than 0.0500 satisfied the model criteria. However, according to Miller (1984), when more model terms are significant as the case in the ANOVA, the model with high polynomial value which is not aliasing becomes the desired model. Thus, the polynomial model Equation 2 generated by the software for the response %WA at 2 hours were used for the analysis of variance in terms of pseudo components.

$$SDP\ Y1 = +42.74 * SD + 20.90 * AD2 + 203.50 * SD * AD2 + 377.11 * SD * AD2 * (SD - AD2) \quad (2)$$

where, SDP Y1 = water absorption at 2 hours and SD = sawdust and AD2 = R7AD2 adhesive

Table 3: Sawdust Particleboard Responses Analyses of Variance for Water Absorption and Density

Source	Sum of Squares	DF	Mean Square	F Value	Prob > F	
<b>SDP Y1 (2 hrs %WA)</b>						
Model	7933.96	3	2644.65	914.74	< 0.0001	significant
Linear Mixture	1586.91	1	1586.91	548.89	< 0.0001	
SDAD2	4125.03	1	4125.03	1426.78	< 0.0001	
SDAD2(SD-AD2)	2222.02	1	2222.02	768.56	< 0.0001	
Residual	11.56	4	2.89			
Pure Error	1.38	3	0.46			
Cor Total	7945.53	7	1135.08			
<b>SDP Y2 (24 hrs %WA)</b>						
Model	2207.99	3	736.00	29.17	0.0035	significant
Linear Mixture	145.81	1	145.81	5.78	0.0740	
SDAD2	717.25	1	717.25	28.43	0.0060	
SDAD2(SD-AD2)	1344.93	1	1344.93	53.31	0.0019	
Residual	100.92	4	25.23			
<b>SDP Y3 (Density)</b>						
Model	49947.50	3	16649.17	13.72	0.0143	significant
Linear Mixture	39221.47	1	39221.47	32.33	0.0047	
SDAD2	1499.79	1	1499.79	1.24	0.3285	
SDAD2(SD-AD)	9226.24	1	9226.24	7.60	0.0510	
Residual	4853.18	4	1213.29			

Figure 1 shows the diagnostic case plot for the predicted versus the actual experimental values. The points were not cluster either above or below the diagonal line, which implies there were no problems of over prediction and/or under prediction from the experimental design.

The ANOVA modeling for water absorption at 24 hours presented in Table 3 implies that "Model F-value" of 29.17 with "Prob > F" of 0.0035 which is less than 0.0500 are significant model terms. However, Linear Mixture model with 5.78 "F-value" and 0.0740 "Prob > F" value which is greater than 0.0500 implies that the model is not significant. While other models SD\*AD2 which had "F-value" of 28.43 and "Prob > F" value of 0.0060, and SD\*AD2 (SD-AD2) with "F-value" of 53.31 and "Prob > F" value of 0.0019 are significant model terms for the P > F value is less than 0.0500. Where more significant models exist, the model with highest polynomial values that is not aliasing becomes the significant model (Richard 2007). The model Equation 3 for the analysis of variance in terms of pseudo components generated by the software and the corresponding diagnostic case plot in Figure 2 showing the model relationship between the predicted and actual values used.

$$SDP\ Y2 = +105.18 * SD + 106.02 * AD2 + 84.86 * SD * AD2 + 293.39 * SD * AD2 * (SD - AD2) \quad (3)$$

The points were cluster below the line showing under prediction of the values, nevertheless; above the curve it shows that the predicted and actual values indicate adequate precision in the formulation, signifying adequate phase contact between the R7AD2 adhesive and (SD) sawdust softwood in the mat formation. The sawdust particleboard ANOVA modeling for density revealed that the Model had "F-Value" of 13.72 with "Prob > F" value of 0.0143 which is less than 0.0500", this implies that the model is significant. Linear Mixture model has 32.33 "F-Value" and 0.0047 "Prob > F" value implies the significant of model, which satisfied the criteria for navigation in the design (Shari 2018). Furthermore,

the model was analyzed based on the predicted and actual experimental values from the design and calculated using pseudo component Equation 4 generated by the software and the diagnostic case plot presented in Figure 3.

$$SDP Y3 = +830.97 * SD + 676.27 * AD2 + 122.71 * SD * AD2 + 768.43 * SD * AD2 * (SD - AD2) \quad (4)$$

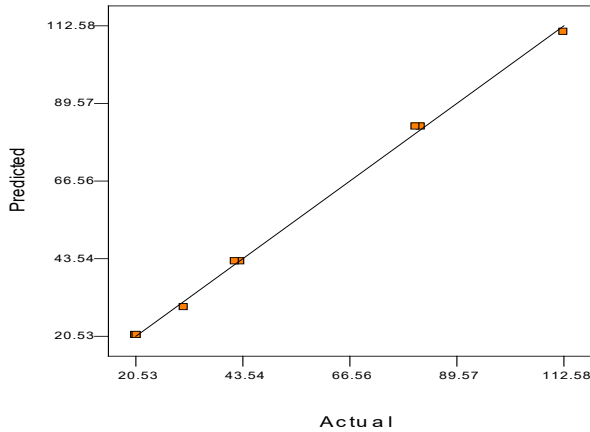


Fig. 1: Predicted versus Actual Values of Sawdust Particleboard Water Absorption at 2 hours

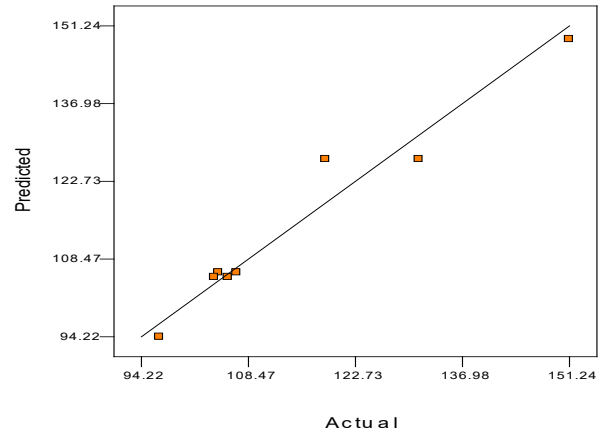


Fig. 2: Predicted versus Actual Values of Sawdust Particleboard Water Absorption at 24 hours

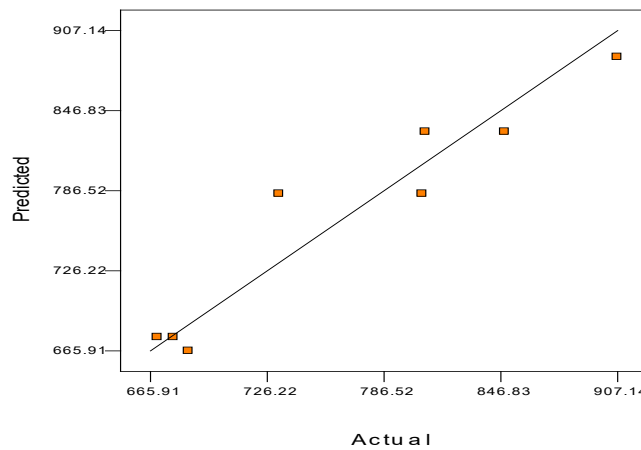


Fig. 3: Predicted versus Actual Values of Sawdust Particleboard Density

The diagnostic case plot shows cluster points and also scatter at the middle below the plot, implying there was under prediction of the values for the particleboard density, however; towards the middle the scattered points occur showing slight deviation between the predicted and actual values as the density increases resulting to high PRESS value and 34.83 value for std. dev. (Shari 2018). Based on the analyses of ANOVA, the models were significant, but specific optimization model was not identified and thus, the used of sequential model sum of squares (SMSS). SMSS were analyzed using three (3) models (Linear, Quadratic and Cubic) to determine the best model that fits the design as presented in Table 4 for the responses water absorption at 2 and 24 hours and density generated by the design expert software.

The percentage water absorption at 2 hours shows that both Linear and Quadratic models had "F-Value" of 1.50 and 9.23 "F-Value", "Prob > F" value of 0.2669 and 0.0288 respectively which reveals that the models were insignificant. While Cubic model with high "F-Value" of 768.56 and "Prob > F" value of 0.0001 which is in agreement with the suggested ANOVA model was the desired significant model that fits the design. The suggested Cubic model had standard deviation of 1.70, PRESS value of 77.84, adjusted R<sup>2</sup> of 0.9985 and predicted R<sup>2</sup> of 0.9975 respectively as against Linear and Quadratic models that had high standard deviations, high PRESS values and low R<sup>2</sup> values and are not fit to suggest the significance of the model. Thus, Cubic model satisfy the criteria which suggested the model as significant with "Prob > F" value is less than 0.0500 based on the standard (Gryze, Langhans & Vandebroek 2007).

The SMSS summary statistics for 24 hours water absorption was analysed using Cubic, Linear and Quadratic models. Amongst these models, Cubic model was suggested as the desired model which had std. dev. of 5.02, while Linear and for Quadratic models had std. devs. of 18.99 and 17.00 respectively. Other criterion includes PRESS value of 323.36 being the least among the 3 models tested. Similarly, the high R<sup>2</sup> values confirmed that Cubic model was the best fitted

to model the percentage water absorption at 24 hours. This follows the trends that, the higher the F-Value in modeling the more adequate and significant the model. A fitted model is acceptable only when the R<sup>2</sup> values for adjusted and predicted values are in agreement of not more than 0.2000 differences (Gryze, Langhans & Vandebroek 2007; Miller 1984). The R<sup>2</sup> values for the suggested Cubic model ranged from 0.8599 – 0.9563 which is close to unity. The result was further validated using std. dev., PRESS values and precision adequacy “focusing on predicted R<sup>2</sup> and adjusted R<sup>2</sup> values to maximize model navigation in the design space”.

Table 4: Sawdust Particleboard Response Sequential Model Sum of Squares for Water Absorption and Density

SDP Y1 (2 hours %WA)					
Source	Mean	Linear	Quadratic	Cubic	Total
Sum of Squares	23396.09	1586.91	4125.03	2222.02	31341.62
DF	1	1	1	1	8
Mean Square	23396.09	1586.91	4125.03	2222.02	3917.70
F value		1.50	9.23	768.56	
Prob > F		0.2669	0.0288	< 0.0001	
Std. Dev.		32.55	21.14	1.70	
R <sup>2</sup>		-0.4024	0.4551	0.9902	
R <sup>2</sup> Adjusted		0.1997	0.7189	0.9985	
R <sup>2</sup> Predicted		0.0663	0.6064	0.9975	
PRESS		11142.80	4329.83	77.84	
Precision Adeq.	74.767			Suggested	
SDP Y2 (24 hours %WA)					
Source	Mean	Linear	Quadratic	Cubic	Total
Sum of Squares	1.056E+005	145.81	717.25	1344.93	1.079E+005
DF	1	1	1	1	8
Mean Square	1.056E+005	145.81	717.25	1344.93	13487.18
F value		0.40	2.48	53.31	
Prob > F		0.5483	0.1761	0.0019	
Std. Dev.		18.99	17.00	5.02	
R <sup>2</sup>		-0.5665	-0.2250	0.8599	
R <sup>2</sup> Adjusted		0.0631	0.3738	0.9563	
R <sup>2</sup> Predicted		-0.0930	0.1233	0.9235	
PRESS		3616.94	2828.32	323.36	
Precision Adeq.	15.370			suggested	
SDP Y3 (Density)					
Source	Mean	Linear	Quadratic	Cubic	Total
Sum of Squares	4.707E+006	39221.47	1499.79	9226.24	4.762E+006
DF	1	1	1	1	8
Mean Square	4.707E+006	39221.47	1499.79	9226.24	5.952E+005
F value		15.11	0.53	7.60	
Prob > F		0.0081	0.4982	0.0510	
Std. Dev.		50.96	53.06	34.83	
R <sup>2</sup>		0.5403	0.4646	0.6639	
R <sup>2</sup> Adjusted		0.7157	0.7431	0.9114	
R <sup>2</sup> Predicted		0.6683	0.6403	0.8450	
PRESS		25194.61	29339.31	18421.21	
Precision Adeq.	8.990			suggested	

The SMSS summary statistics for density shows that, the suggested Cubic model that had F-Value of 7.60 and P > F value of 0.0510 was not adequate. Nevertheless, the highest order polynomial was selected when additional terms are significant since the model is not aliasing. Based on the analyses carried out using the 3 models, it shows that the suggested Cubic model had std. dev. of 34.83, being the least compared to 50.96 for Linear model and 53.06 for Quadratic model respectively. Furthermore, the PRESS values for the models were low in Cubic which had 18421.21, while Linear and Quadratic models had 25194.61 and 29339.31 values respectively. The corresponding R<sup>2</sup> values for both predicted and adjusted are higher in Cubic model than the Linear and Quadratic models. Therefore, the model is best fitted using Cubic model for sawdust particleboard density due the low standard deviation between the experimental and actual values, and the F values and Prob > F values were adequate. The final process revealed a single numerical solution as presented in Table 5 for the model.

Table 5: Numerical Solution for Sawdust Particleboard Modeling

Number	SD	Ri7AD2	Y1	Y2	Y3	Desirability	
1	0.32	0.68	17.2773	90.4809	647.279	0.704	Selected

The produced sawdust particleboard formulation coded SDP8 best fit the design, with the characteristic values for water absorption at 2 hours = 17.23%; at 24 hours = 90.48% and density = 647.28 kg/m<sup>3</sup>. Although the characterized response results in Table 1 for 2- and 24-hours water absorption and density varied with the numerical optimisation solution but based on the factors used in selection of the desired model, the range values for the responses fell within the Japanese Industrial Standard 2003, and thus, placing the particleboard in medium density category. The desirability factor for models analyses selection is presented in Figure 4 showing 8 experimental runs including duplicates.

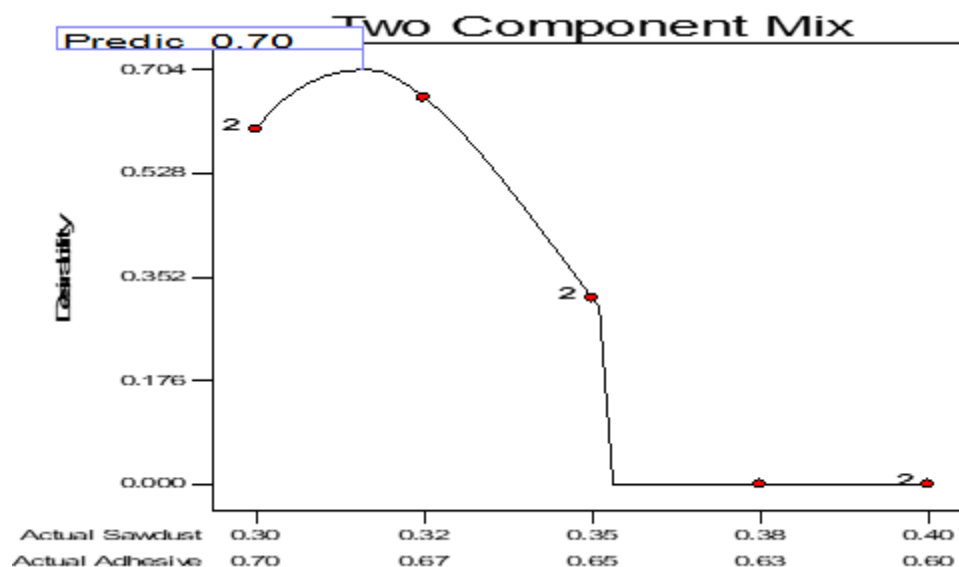


Fig.4: Sawdust Particleboard Numerical Solution Desirability

Out of the numbers of particleboards produced from sawdust softwood using R7AD2 adhesive as binder, a single solution was found based on the responses: water absorption at 2 hours, 24 hours and density, and the desirability factor of 0.704 achieved was adequate to predict the model for navigation in the design space. The model shows that formulation SDP8 which has better water repellent met the international standard quality of particleboard.

#### 4. CONCLUSION

The conclusions drawn from this work are as follows: the use of software in selection of the best among several formulations is a good innovation especially in highly constrained design such as this. Also the use of statistical tools in identification of the model that fit the best design was demonstrated in the produced particleboards from softwood sawdust using R7AD2 adhesive, the modelled responses based on numerical solution for %WA and density shows that SDP8 was the best particleboard produced with the desirability factor of 0.704. This has come with technological innovations in process formulation in the production of particleboard.

#### ACKNOWLEDGEMENTS

The Authors acknowledged University of Jos, North central Nigeria, Nigerian Building and Road Research Institute, North Central Zonal office Jos and Abubakar Tatari Ali Polytechnic, Bauchi, North Eastern Nigeria for using their facilities in this work.

#### REFERENCES

- Abdulkareem, S, A & Adeniyi, A, G 2017, ‘Production of Particleboard Using Polystyrene and Bamboo Wastes’, *Nigerian Journal of Technology*, vol. 36, no. 3, pp. 788 – 793.
- Abdulkareem, S, A, Raji, A, S & Adeniyi, A, G 2017, ‘Development of Particleboard from Waste Styrofoam and Sawdust’, *Nigerian Journal of Technological Development*, vol. 14, no. 1, pp. 18 – 22. Doi:<http://dx.doi.org/10.4314/njtd.v14i1.3>.
- Aigbodion, V, S, Idris, U, D, Gadzama, R, M & Ahmed, T, Y 2012, ‘Suitability of Maize Cob Particles and Recycled Low Density Polyethylene for Particleboard Manufacturing’, *Journal of Material Science*, vol. 8, no. 1, pp. 34 – 37.

- Alam, D, M, N, Rahaman, S, K, Ratul, S, B, Sharmin, A, Islam, T, Hasan, M, A W & Islam, M, N 2015, 'Properties of Particleboard Manufactured from commonly used Bamboo (*Bambusa vulgaris*) Waste in Bangladesh,' *Advances in Research*, vol. 4, no. 3, pp. 203 – 211. Available online at [www.sciencedomain.org](http://www.sciencedomain.org).
- Alan, B 2019, 'Examining the Viability of Planting Trees to Help Mitigate Climate Change', *NASA's Jet Propulsion Laboratory*, Featured November 7, 2019, viewed on 23<sup>rd</sup> May, 2021.
- Asha, A 2017, 'Fabrication of Particleboards from Rice Husk', *International Journal of Modern Engineering Research*, vol. 7, no. 5, pp. 30 – 38.
- Atuanya, C, U, Ibadode, A, O, A & Igboanugo, A, C 2011, 'Potential of using Recycled Low-density Polyethylene in Wood Composites Board', *African Journal of Environmental Science and Technology*, vol. 5, no. 5, pp. 389-396, available online at <http://www.academicjournals.org/AJEST>.
- Da Silva César, A, A, Bufalino, L, Mendes, L, M, De Almeida Mesquita, R, G, De Paula Protásio, T, Mendes, R, F & Ferreira Andrade, L, M 201, 'Transforming Rice Husk into a High-Added Value Product: Potential for Particleboard Production', *Ciência Florestal, Santa Maria*, vol. 27, no. 1, pp. 303-313.
- Elbadawi, M, Osman, Z, Paridah, T, Nasroun, T & Kantiner, W 2015, 'Mechanical and Physical Properties of Particleboards made from Ailanthus Wood and UF resin Fortified by Acacias Tannins Blend', *Journal of Materials and Environmental Sciences* vol. 6, no. 4, pp. 1016 – 1021.
- Fiorelli, J, Ramos, R, D, Sayama, J, T, Barrero, N, G & Palone, E, J, A 2014, 'Particleboards with waste wood from reforestation', *Acta Scientiarum Technology Maringa*, vol. 36, no. 2, pp. 251 – 256.
- Flores-Yepes, J, Pastor-Perez, J, Gimeno-Blanes, F & Rodriguez-Guisado, I 2012, 'Full Recovery of Arunda Donax Particleboard from Swelling Test without Waterproofing Additives', *BioResources*, vol. 7, no. 4, pp. 5222 – 5235.
- Gryze, D, S, Langhans, I & Vandebroek, M 2007, 'Using the correct intervals for predictions', A tutorial on tolerance intervals of ordinary least regression. *Chemometrics and Intelligent Laboratory System*, vol. 87, no. 2, pp. 147 – 154.
- Hamidu, L, A, J, Aroke, U, O, Osha, O, A & Muhammad, I, M 2021, 'Characterization of Physical Properties of Particleboard produced from Sawdust using R7AD2 Adhesive', *Proceedings of the 51<sup>st</sup> International Conference and Annual General Meeting of the Nigerian Society of Engineers*, Lagos Nigeria, 10<sup>th</sup> – 13<sup>th</sup> November, 2021, Pages 162 – 168.
- Idris, U, D, Aigbodion, V, S, Gadzama, R, M & Abdullahi, J 2011, 'Eco-Friendly (Watermelon Peels) Alternatives to Wood-based Particleboard Composites', *The Pacific Journal of Science and Technology*, vol. 12. No. 2, pp. 112 – 119.
- Japanese Industrial Standard A.5908 (2003), Particleboards. Japanese Standard Association. Tokyo, Japan, pp. 1 – 12.
- Liao, R, Xu, J & Umemura, K 2016, 'Low Density Sugarcane Bagasse Particleboard Bonded with Citric Acid and Sucrose: Effect of board density and additive content', *Peer-reviewed, Journal of BioResources*, vol. 11, no. 1, pp. 2174 – 2185.
- Mari, E, L & Villena, E, M 2016, 'Properties of Particleboard from Wood Wastes and Cashew Nut Shell Residue', *Philippine Journal of Science*, vol. 145, no. 1, pp. 1 – 8.
- Miller, D 1984, 'Reducing Transformation Bias in Curve Fitting', *The American Statistician*, vol. 38, no. 2, pp. 124 – 126.
- Olawale, O, Akinyemi, B, A & Attabo, F 2020, 'Optimization of the Mixing Ratio for Particleboard Production from Groundnut Shell and Rice Husk', *Acta Technologica Agriculturae 4 Nitra, Slovaca Universitas Agriculturae Nitriae*, 2020, pp. 168–175 DOI: 10.2478/ata-2020-0027.
- Pan, Z, Zheng, Y, Zhang, R & Jenkins, B, M 2007, 'Physical Properties of thin Particleboard made from Saline Eucalyptus', *An International Journal of Industrial Crops and Products*, vol. 26, no. 1, pp. 185 – 194.
- Peter, A, Albert, O & Anthony, U 2017, 'Nigerian Wood Waste: A Potential Resource for Economic Development', *Journal of Allied Science Environmental Management*, vol. 21, no. 2, pp. 246 – 251. <http://dx.doi.org/10.4314/jasem.v21i2.4>.
- Richard, B 2007, 'Mathematical Learning Support Center', Design Expert 7 Tutorial, 1 – 10.
- Roffel, B & Betlem, B 2006, *Process Dynamics and Control Modeling for Control and Prediction*, Copyright © 2006 John Wiley & Sons Ltd, the Atrium, Southern Gate, Chichester, West Sussex PO19 8SQ, England Telephone (+44) 1243 779777.
- Silva, F, B, M, Vianna, R, F & Neubert, E, I 2014, 'Study of Adhesion Properties of Natural Rubber - Based Pressure Sensitive Adhesive with Variation of Tackifier Resin and Plasticizers Agents', *Area tematica: Engenharia de Materiais e Nanotecnologia*; vol. 1, pp. 1 – 8.
- Xu, J, Sugawara, R, Widyorini, R, Han, G & Kawai, S 2004, 'Manufacture and Properties of Low-density Binderless Particleboard from Kenaf Core', *Journal of Wood Science*, vol. 50, no. 1, pp. 62 – 67.
- Xu, J, Widyorini, R & Kawai, S 2005, 'Properties of Kenaf Core Binderless Particleboard Reinforced with Kenaf Bast Fiber-woven Sheets', *Journal of Wood Science*, vol. 51, no. 4, pp. 415 – 420.
- Zhang, Y, Gu, J, Tan, H, Di, M, Zhu, L & Weng, X 2011, 'Wheat Straw Based Particle Board Bonded with Composite Adhesives', *Peer-Reviewed, Journal of BioResources*, vol. 6, no. 1, pp. 464 – 476.



## ANN Prediction of Selected Oleophilic Bacterial Growth in Crude Oil Bioremediation

Ajiboye S. OSUNLEKE<sup>1\*</sup>, Nafees O. SANNI<sup>1</sup>, Mumeenah O. Mustapha<sup>2</sup>, Elizabeth F. ARANSIOLA<sup>1</sup>

<sup>1</sup>Department of Chemical Engineering, Obafemi Awolowo University, Ile-Ife, Nigeria

<sup>2</sup>Department of Microbiology, Kwara State University, Malete, Nigeria

<sup>1\*</sup>[aosunlek@oauife.edu.ng](mailto:aosunlek@oauife.edu.ng), <sup>2</sup>[nafeesolaitan@gmail.com](mailto:nafeesolaitan@gmail.com), <sup>3</sup>[momustapha91@gmail.com](mailto:momustapha91@gmail.com), <sup>4</sup>[aransiolaef@gmail.com](mailto:aransiolaef@gmail.com)

\*Corresponding author:

---

### ABSTRACT

Crude oil spillage during exploration of oil causes a menace to the marine ecosystem and threatens the aquatic lives so it must be cleaned to restore the marine environment to its natural state. Bioremediation is the most environmentally friendly restorative approach to employ in mitigating these spills. A good number of effective oleophilic micro-organisms have been isolated by researchers for bioremediation. This work investigates the interactive effect of various parameters on bacterial growth rate and how these physicochemical parameters (temperature, pH, number of days, inoculum size and crude oil percentage) can be varied to predict bacteria growth rates. Hydrocarbon-degrading bacteria were isolated from an auto-mechanic workshop and growth rate tests were carried out to screen for the two most effective bacteria isolates. Parameters were then varied for the best performing isolates and growth rates were measured periodically for twenty-five (25) days. An artificial neural network (ANN) was employed in training the data and the network parameters were tuned to predict the response from the input factors. The correlation parameter ( $R^2$ ) obtained was greater than 0.91 which demonstrated that the training was successful, and the network could predict closely related values to that of the experimentally obtained values.

**Keywords:** Physicochemical properties, Bioremediation, ANN, Crude oil

### 1. INTRODUCTION

Crude oil and petroleum products are useful for transportation, heating, residential and industrial electricity generation; however, the accidental spillage of petroleum in water bodies during exploration and transportation causes severe damage to aquatic life and harms the coastal population of the affected areas (Silva, et al., 2022), which if not handled correctly, can cause economic meltdown, ecological degradation and public hazards.

Oil spills are among the most catastrophic events to marine ecosystems (Bôto *et al.*, 2021). Such pollution to water has increased due to the increasing demand for crude oil-based energy and petroleum products (Ojewumi *et al.*, 2018) which has necessitated offshore drilling due to the global population growth. The effects are experienced not only in the area of the spill, but it stretches wide to near regions to negatively impact shorelines and terrestrial wildlife thousands of meters away from the site of the spill (Agarwal, 2021). Such pollution can also harm human health because of its carcinogenic, mutagenic and teratogenic properties. Uncontained oil is toxic to plants, animals and humans and spilled oil needs to be cleaned up to prevent further damage to life and the environment. (French and Terry, 2020). Spilled oil affects plants and animals either directly from the oil covering their habitat or from the cleanup process which is why a suitable clean-up process must be selected.

Various methods are available for cleaning up oil spills such as booms, skimming, burning of oil, dispersant, adsorbent, solidifiers and biodegradation (Silva, *et al.*, 2022). Some of these oil clean-up methods, even though they clean up the oil, are not environmentally friendly and can cause more environmental damage, which in turn increases the time required by the ecosystem to recover. Bioremediation is an alternative clean-up action that is safer for the environment than other chemical or physical solutions. The microorganisms used for bioremediation are either already living in the affected environment or are brought into the environment (Caitlin, 2018). Bioremediation can deal with a lower concentration of petroleum compounds, where cleanup by conventional physical methods is ineffective and expensive (Khanpour-Alikelayeh, 2020)

Oleophilic bacteria are known with the ability to degrade a wide range of oil components and are widely distributed in soil and marine environment; nevertheless, they exist in low abundance in marine environments (Abdulsalam *et al.*, 2012). Some conditions can be put in place to increase the rate of biodegradation, which includes bio-augmentation; however, the efficacy of biodegradation is influenced by several factors such as bioavailability, fertilizers, quality and quantity of contaminants, temperature, pH and oxygen (Yusuf *et al.*, 2021).

Previous researchers had studied the effect of parameters such as Khanpour-Alikayeleh (2020) reported that the significant factors for crude oil bioremediation as salinity, crude oil concentration and pH, Yusuf (2021) studied the effects of pH, temperature and nitrogen source on bioremediation and (Torimiro *et al.*, 2020) studied the effect of pH, soil organic matter and conductivity. However, most of the works employed the OFAT method i.e., varying One Factor At a Time which could not be used to ascertain interactive effects of the parameters.

Optimization of parameters is crucial in chemical and biological processes as it saves time, money and makes cleanup more efficient. An effective optimization procedure requires good modelling and for the biodegradation process. Each micro-organism is unique and do not conform to the same models, it thus become imperative to work on suitable models for accurate modelling and prediction; hence, the need for an artificial neural network. Artificial neural network (ANN)s outperforms other statistical analysis programs due to its adaptive learning, parallel operation and also fault tolerance, this makes them excellent for pattern recognition (Kukreja *et al.*, 2016). An artificial neural network consists of three layers; an input layer of neurons, a hidden layer(s) and a final layer of output neurons (DeVore *et al.*, 2021). Each connection is associated with a numeric number called weight.

The neural network equation is

$$Z = W_0 + W_1X_1 + W_2X_2 + \dots + W_nX_n \quad (1)$$

Where  $Z$  is the activation function, the  $W$ s, are the weights and  $X$ s, are the independent variables or the inputs, and  $W_0$  is the bias. The purpose of the activation function is to introduce nonlinearity into the neural network (DeVore *et al.*, 2021).

This work, therefore, developed procedures for isolating crude oil-degrading bacteria, evaluating their growth potential, varying temperature, pH, inoculum size, and crude oil concentration to assess the effects on growth rate and employed artificial neural network to effectively predict the growth rate based on the input factors.

## 2. MATERIALS AND METHODS

The soil was aseptically collected from an auto mechanic workshop along Obafemi Awolowo University Campus Gate, Ile-Ife into a sterilized glass bottle with spatula by scraping off the top soil and collecting the soil beneath. The study area (Ile-Ife) is located in Osun-State, South-Western Nigeria. The crude oil was collected from the Warri refinery. They were all transported to the laboratory for microbial analysis.

Other materials and equipment used for the project include a colorimeter, UV spectrophotometer (Shimadzu Corp 70743 Model UV-1800), conical flasks, pH meter, test tubes, microtubes, spatula, Petri dishes, weighing balance, an autoclave (Express equipment) and thermal incubators (Gallenkamp, England). Two media were prepared for use in this work: Minimal Salt Medium and Nutrient Agar. Minimal Salt Medium was prepared according to Yusuf *et al.* (2021) and the Nutrient Agar was prepared according to the manufacturer's instructions.

### 2.1 Isolation Screening and of Hydrocarbon-Degrading Bacteria from the Soil Samples

Ninety (90) ml of Minimal Salt Medium (MSM) was put into a 250 ml flask and 10 ml of crude oil was added. The flask was then sterilized in an autoclave for 30 minutes. Ten grams (10 g) of the soil sample was added to the flask containing the medium and crude oil and incubated for 24 hours. A serial dilution of the soil solution of up to  $10^{-5}$  was carried out and the pour plate method of isolation was done by pipetting 1 ml each from the  $10^{-4}$  and  $10^{-5}$  tubes into Petri dishes with enough nutrient agar added, the Petri dishes were incubated at 37 degrees.

This was repeated daily for 3 days and ended up with 6 agar plates. A distinct colony was marked in each of the plates and sub cultured into 6 labelled fresh Petri dishes of nutrient agar with the aid of an inoculating needle which was flamed at each turn/use. All 6 plates were incubated at 37 °C for 24 hours and they formed pure cultures. The isolated bacteria plates were coded and labelled as: 24-01, 24-02, 48-01, 48-02, 72-01 and 72-02. The pure colonies were physically and morphologically characterized.

## 2.2 Preliminary Growth Profile Assessment of Potential Hydrocarbon Degraders

Peptone water was prepared according to the manufacturer's instructions and 5 ml each was dispensed into six sterile test tubes. With the aid of a flamed inoculating loop, isolates were transferred into the test tubes, labelled accordingly and incubated at 37 °C for 24 hours. This was done to help the bacteria grow.

The contents of the test tubes were aseptically transferred into sterilized conical flasks of 45 ml Minimal Salt Medium (MSM) and 0.5 ml crude oil to serve as 1% of the 50 ml mixture (Karthika *et al.*, 2014). The flasks were incubated for 7 days, withdrawing 1 ml aliquots daily for analysis using the Ultraviolet spectrophotometer. The 7th flask that served as the control flask with no inoculated bacteria was used to calibrate the Ultraviolet spectrophotometer.

## 2.3 Response Surface Methodology (RSM) to Generate and Randomize Factor Values

The experimental design was generated using Design-Expert software version 6.0.8 (Stat-Ease Inc., USA). Each factor was analyzed at three levels. Four factors were varied (inoculum size, crude oil percentage, temperature and pH). Three levels of each of the factors were determined and using Response Surface Methodology, randomization of values of all factors was obtained. This generated 28 runs with six (6) centre points which were manually adjusted.

## 2.4 Obtaining the Growth Rate of Isolated Bacterial Strains under Varying Conditions

Minimal Salt Medium (MSM) was prepared and divided into three (3) flasks. These flasks were adjusted to pH values of 5,7 and 9 respectively.

Twenty-eight (28) clean 100 ml conical flasks were labelled based on the order of runs for each of the two isolates. Thirty (30) ml of MSM of the pH corresponding to each flask was dispensed in all 28 flasks, the volume of crude oil correlating to each flask was dispensed and the flasks were sterilized at 121°C.

To attain uniformity in the inoculum size of the two bacterial isolates, fresh 24-hour-old cultures of the two bacteria were inoculated into sterilized test tubes containing normal saline and standardized with the use of a colorimeter to 0.5 McFarland Standard. The standardized isolates were added to each flask, with the volumes also correlating to the order of runs.

The flasks were divided into three groups according to temperatures (25, 30 and 37 °C) and these were placed in incubators with shakers at each of the temperatures for 25 days withdrawing 1 ml from each flask every 5 days for UV analysis at 600 nm wavelength.

## 2.5 Artificial Neural Network

The generalized artificial neural network system of MATLAB 2021, (Math Works, Inc., USA), was adopted as the training method. A genetic algorithm was used as the input optimization method starting with one hidden layer. This network was trained using Mean Square Error and by varying the number of neurons (hidden layers), epoch and validation checks to get the optimal combination of neurons and epochs that predicts the model best, using the value of regression parameter ( $R^2$ ) obtained from training the network at a different number of neurons as the efficiency check. Generally, the higher the  $R^2$  value, the better the model.

## 3. RESULTS AND DISCUSSION

### 3.1 Characterization of the Isolates

The six bacterial isolates were subjected to biochemical tests and the results are shown in Table 1.

Table 1: Bio-Chemical test of Isolates

	Catalase	Oxidase	Citrate	Mr	Vp	Nitrate	Sulphide	Indole	Motility
24-01	+VE	+VE	+VE	-VE	+VE	+VE	-VE	-VE	+VE
24-02	+VE	-VE	-VE	+VE	+VE	+VE	-VE	-VE	-VE
48-01	+VE	-VE	+VE	+VE	+VE	+VE	+VE	-VE	+VE
48-02	+VE	+VE	+VE	+VE	+VE	+VE	+VE	-VE	+VE
72-01	+VE	-VE	+VE	+VE	+VE	+VE	-VE	-VE	-VE
72-02	+VE	+VE	+VE	+VE	+VE	+VE	+VE	-VE	+VE



### 3.2 Selection of the best isolates by Growth Rate

Samples were withdrawn 24-hourly from each of the six flasks containing the isolated bacteria and the salt media supplemented with crude oil, these were subjected to growth analysis by a UV-Spectrophotometer at a fixed wavelength of 600 nm. The measured turbidity values of the bacteria isolates obtained from the ultraviolet spectrophotometer were plotted against the days as shown in Figure 1. The culture plates of each isolate are shown in Plate 1.

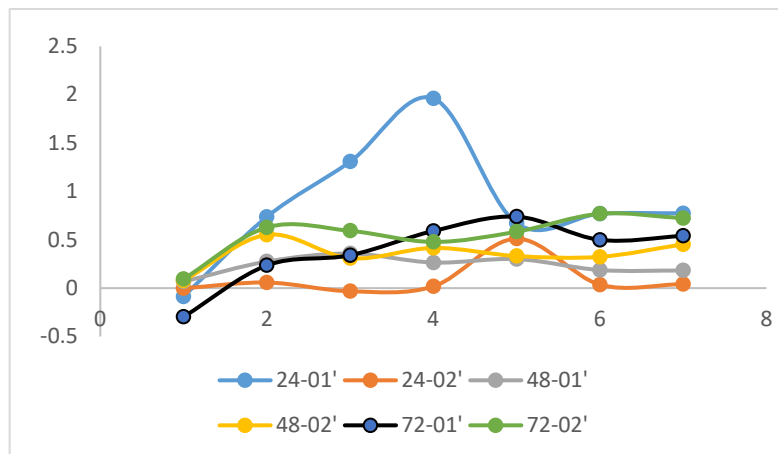


Figure 1: Growth Potential of the six isolates

The figure depicts the two bacteria samples coded as 24-01 and 72-02 as the ones with the best growth and they were picked for further analysis.

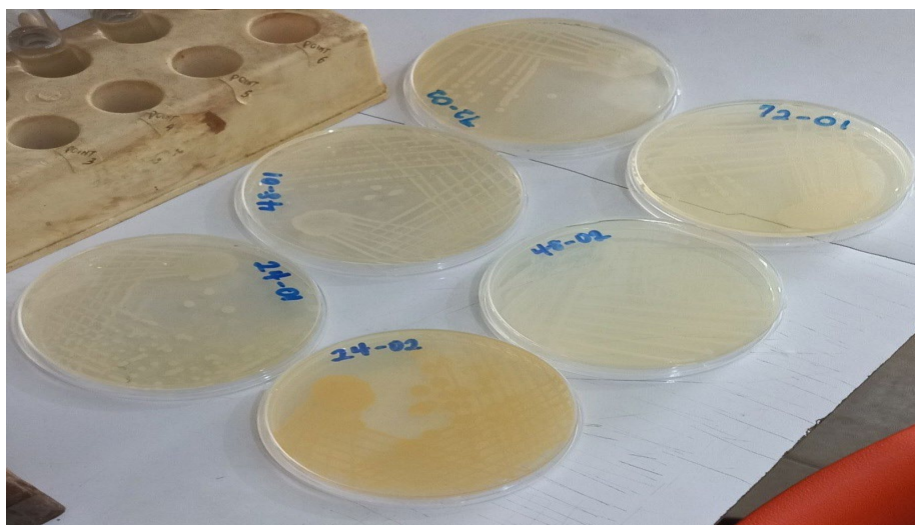


Plate 1: Culture plates of each isolate

### 3.2 Interactive Effects of Physicochemical Parameters

Four (4) factors were varied: McFarland standardized inoculum (0.5ml, 1ml and 1.5ml), pH (5, 7 and 9), temperature (25, 30 and 37 °C), and crude oil percentage (0.5%, 1%, 1.5%) of the 30 ml salt media, this translated to 0.15 ml, 0.3 ml and 0.45 ml respectively). Samples were withdrawn from each of the 28 flasks every 5 days for twenty-five (25) days and subjected to OD analysis via an Ultraviolet spectrophotometer which resulted in time being a fifth factor.

The Optical Density results (growth rate) for each of the bacteria are presented in Tables 2 and 3.

Table 2: Experimental growth rate of bacteria 24-01

Factor 1	Factor 2	Factor 3	Factor 4	OPTICAL DENSITY/BACTERIA GROWTH				
Inoc. Size (CFU/ml)	pH	Crude oil conc. (%)	Temp. (°C)	Day 5	Day 10	Day 15	Day 20	Day 25
1.5	5	0.5	25	1.0285	1.685	1.298	1.6045	1.626
1.5	5	0.5	37	2.114	2.059	1.579	1.412	1.5775
0.5	7	0.5	25	1.7455	1.6845	1.4395	1.853	1.458
1.5	9	1	30	1.8975	1.27	0.787	1.0925	1.1285
0.5	9	1.5	25	2.376	2.771	2.43875	1.956	2.012
1	7	1	37	1.829	2.296	1.4245	1.296	1.296
0.5	9	0.5	37	1.6436	2.1017	2.0117	1.6635	1.81
1	9	1	30	0.8885	1.2265	0.892	1.149	0.601
1.5	5	1.5	25	1.556	1.573	1.215	1.339	1.9735
1	7	1	25	1.7055	1.557	1.07475	2.67	3.908
0.5	7	1	30	2.651	1.778	1.53233	1.644	1.446
0.5	9	0.5	25	1.554	1.518	1.183	1.5365	2.388
1	7	1	30	1.692	1.816	1.5095	1.678	1.4005
1	9	1.5	25	0.6545	1.5765	0.858	1.288	1.176
1.5	7	1.5	37	2.037	2.1925	1.59	1.8667	1.937
1.5	7	0.5	30	2.0325	1.8925	0.791	1.036	1.002
1	9	0.5	37	1.9705	2.786	2.525	2.9643	3.387
1	7	1.5	25	1.414	1.9225	1.5205	1.642	1.1543
0.5	7	1.5	37	1.7173	2.071	1.9875	1.923	2.064
0.5	5	1.5	25	1.279	1.6235	1.34433	1.51	2.4045
1.5	5	1	37	1.9645	1.8925	1.9585	1.83	2.1165
1	5	1	37	1.5425	1.908	1.923	1.74	2.004
1.5	7	1.5	30	2.2405	2.3085	1.0075	2.293	2.5775
1.5	9	0.5	37	2.157	2.168	1.9205	1.6805	1.943
1	7	0.5	25	2.319	2.83	2.70775	3.1593	3.9345
0.5	5	0.5	37	2.0805	2.6755	3.07767	3.5243	4
1	5	0.5	30	1.8	1.5295	1.0195	1.273	1.2375
0.5	5	1.5	37	2.067	1.958	1.2405	1.618	1.899

Table 3: Experimental growth rate of bacteria 72-02

Factor 1	Factor 2	Factor 3	Factor 4	OPTICAL DENSITY/BACTERIA GROWTH				
A: Inoc. Size (CFU/ml)	B: pH	C: Crude oil conc. (%)	D: Temp. (°C)	Day 5	Day 10	Day 15	Day 20	Day 25
1.5	5	0.5	25	1.5865	1.625	1.2555	1.3743	1.475
1.5	5	0.5	37	0.241	0.058	1.492	2.758	3.2346667
0.5	7	0.5	25	1.125	1.7835	1.0675	1.28	1.379
1.5	9	1	30	2.111	2.4045	1.4865	1.9385	2.78
0.5	9	1.5	25	1.497	2.325	1.891	1.9575	2.78
1	7	1	37	0.128	0.262	0.3515	1.525	2.145
0.5	9	0.5	37	2.4875	2.2557	2.2	2.111	2.2375
1	9	1	30	1.433	2.342	1.543	2.017	2.0355
1.5	5	1.5	25	1.6415	2.054	1.6105	3.2326	4
1	7	1	25	1.823	2.396	1.9635	2.32433	2.7675
0.5	7	1	30	2.189	2.2745	1.601	1.84267	1.896
0.5	9	0.5	25	1.5465	2.0715	1.0005	1.7176	1.5865
1	7	1	30	1.594	1.78	1.31	1.6345	1.545
1	9	1.5	25	0.7755	1.3925	1.263	1.586	2.2295
1.5	7	1.5	37	0.447	0.4785	1.1	1.22367	2.148
1.5	7	0.5	30	1.599	1.828	1.2605	1.6195	1.723
1	9	0.5	37	2.103	2.2805	1.615	1.53233	1.879
1	7	1.5	25	1.3895	1.774	1.50467	1.967	2.4835
0.5	7	1.5	37	0.2327 5	0.158	1.61	1.756	2.246
0.5	5	1.5	25	2.0265	2.0195	1.6405	2.012	3.843
1.5	5	1	37	0.274	1.0165	1.4165	1.417	1.6523
1	5	1	37	0.186	0.2205	0.673	1.13	1.9705
1.5	7	1.5	30	1.915	2.0065	1.481	1.781	1.8475
1.5	9	0.5	37	1.775	1.966	2.122	2.3525	2.9267
1	7	0.5	25	1.132	1.8645	1.3215	1.525	1.754
0.5	5	0.5	37	0.092	0.19	0.22	0.53667	1.374
1	5	0.5	30	2.025	1.7795	1.2265	1.495	1.5045
0.5	5	1.5	37	0.26	0.403	1.7515	1.8545	1.9893

### 3.4 Effectiveness of the Trained Artificial Neural Networks

Two neural networks were trained using the MATLAB neural network toolbox for each of the bacteria as the performance of each of the bacteria differed from the others. The Neural networks were developed with one (1) hidden layer and 10 neurons and were trained using the Levenberg-Marquardt training algorithm. The data set was trained by randomly dividing the data set into 70 % for training, 15 % for validation and 15 % for testing. The number of epochs was varied

multiple times until acceptable R2 were obtained (> 0.91). Figure 3 represent the regression plots of network 24-01 with correlation parameters of 88.937%, 98.23%, and 97.225% for training, test and validation respectively and 91.803% as overall. Figure 5 represent the regression plots of network 72-02 with correlation parameter of 93.127%, 85.463%, and 88.166% for training, test and validation respectively and 91.345% as overall.

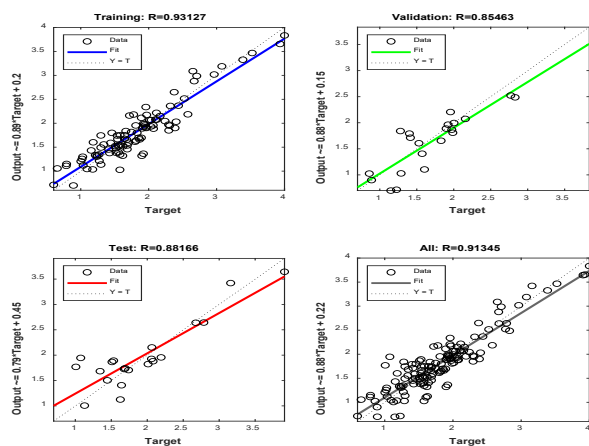


Figure 3: Neural Network regression plot for 24-01

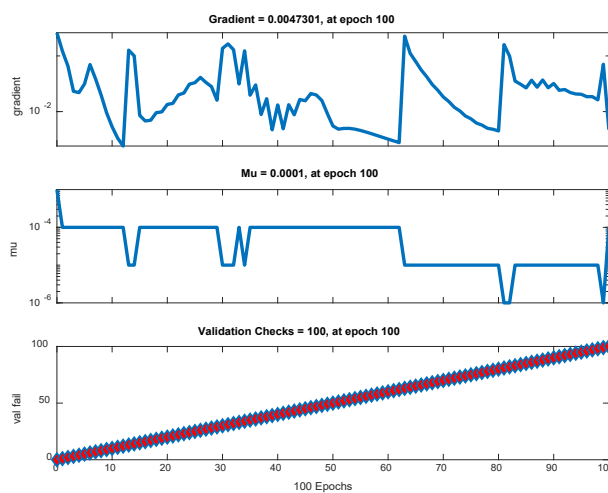


Figure 4: Training Performance Plots of the neural network for 24-01

Figures (4) and (6) are the performance training plots that correspond to the highest correlation coefficient ( $R^2$ ).

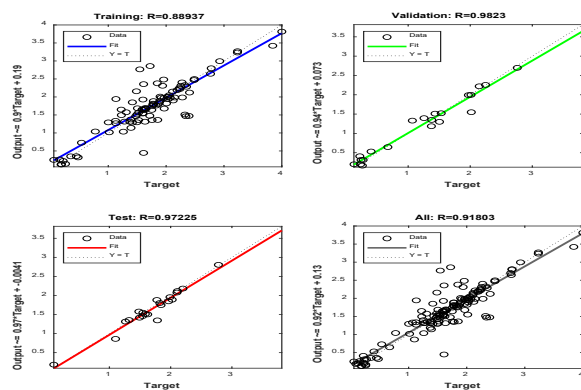


Figure 5: Neural Network regression plot for 72-02

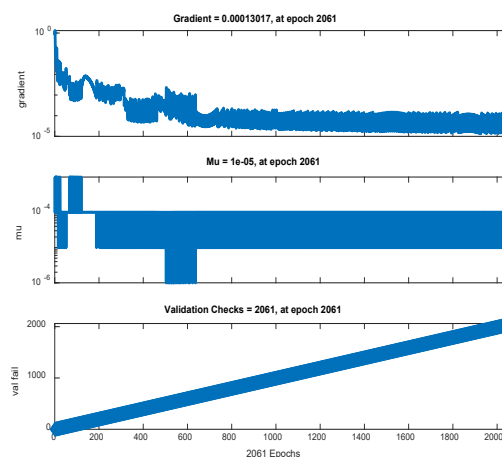


Figure 6: Training Performance Plots of the neural network for 72-02

The network output was compared with the experimental output and the error was minimal. This validates the effectiveness of the neural network in response prediction.

## REFERENCES

- Silva, I. A., Almeida, F. C., Souza, T. C., Bezerra, K. G., Durval, I. J., Converti, A., & Sarubbo, L.A. (2022). Oil spills: impacts and perspectives of treatment technologies with focus on the use of green surfactants. *Environmental Monitoring and Assessment*, 194(3), 1-29.
- Bôto, M. L., Magalhães, C., Perdigão, R., Alexandrino, D. A., Fernandes, J. P., Bernabeu, A. M., and Mucha, A. P. (2021). Harnessing the potential of native microbial communities for bioremediation of oil spills in the Iberian Peninsula NW coast. *Frontiers in microbiology*, 12; 633659.
- Ojewumi, M. E., Okeniyi, J. O., Ikotun, J. O., Okeniyi, E. T., Ejemen, V. A., & Popoola, A. P. I. (2018). Bioremediation: Data on *Pseudomonas aeruginosa* effects on the bioremediation of crude oil polluted soil. *Data in brief*, 19, 101-113.
- Agarwal, M. (2021). <https://www.marineinsight.com/environment/10-methods-for-oil-spill-cleanup-at-sea/> [Accessed 20<sup>th</sup> October, 2022]
- French, K. E., Zhou, Z., & Terry, N. (2020). Horizontal 'gene drives' harness indigenous bacteria for bioremediation. *Scientific reports*, 10(1), 1-11.
- Caitlin, B. (2018). Bioremediation as a Tool for Resiliency in Oil Spills Science Buzz.
- Khanpour-Alikelayeh, E., Partovinia, A., Talebi, A., & Kermanian, H. (2020). Investigation of *Bacillus licheniformis* in the biodegradation of Iranian heavy crude oil: A two-stage sequential approach containing factor-screening and optimization. *Ecotoxicology and Environmental Safety*, 205, 111103.
- Abdulsalam, S., Adefila, S., Bugaje, I.M. and Ibrahim, S. (2012). Bioremediation of Soil Contaminated with Used Motor Oil in a Closed System. *Journal of Bioremediation and Biodegradation*, 3:172.
- Olabisi Omolola Yusuf *et al.* (2021) Evaluation of the effect of Physicochemical Parameters on the Biodegradation of spent engine oil using selected Oleophilic Bacteria IOP Conf. Ser.: *Earth Environ. Sci.* 655 01209
- Torimiro, N., Akhigbe, G. E., & Adebisi, F. M. (2020). Bioprospecting of potential petroleum hydrocarbon degraders using bacterial strains isolated from soils around transformer installation areas. *Energy Sources, Part A: Recovery, Utilization, and Environmental Effects*, 1-14.
- Kukreja, H., Bharath, N., Siddesh, C. S., & Kuldeep, S. (2016). An introduction to artificial neural network. *Int J Adv Res Innov Ideas Educ*, 1, 27-30.
- DeVore, R., Hanin, B. and Petrova, G. (2021). Neural network approximation. *Acta Numerica*, 30; 327-444.
- Karthika, R., Gopinath, L. R., Archaya, S., and Bhuvaneshwari, R. (2014). Isolation of diesel degrading bacteria, identification of Catechol gene and its biogas production. *Journal of environmental Science, Toxicology and Food Technology*, 8 (10):76-82.



## Thermodynamics Studies of Adsorption of Selected Antibiotics Mixture from Aqueous Solution using *Delonix regia* Pod

Ilesanmi A. OJO<sup>1,2,3</sup>, Ayobami O. AJANI<sup>1,2</sup>, Wasiat O. BELLO<sup>1,2</sup>, Tinuade J. AFOLABI<sup>1,2</sup>, Abdulrazaq, ABDULLAHI<sup>1,2</sup>, Akeem O. OLAYIWOLA<sup>4</sup>, Ameen N AKINSOLA<sup>3</sup>, and Abass O. ALADE<sup>1,2,5\*</sup>

<sup>a</sup> Department of Chemical Engineering, Faculty of Engineering, Ladoké Akintola University of Technology, Ogbomoso, Nigeria

<sup>b</sup> Bioenvironmental, Water and Engineering Research Group (BWERG), Ladoké Akintola University of Technology, Ogbomoso, Nigeria

<sup>c</sup> Science Laboratory Unit, Al-Hikmah University, Ilorin, Nigeria

<sup>d</sup> Department of Pure and Applied Chemistry, Ladoké Akintola University of Technology, Ogbomoso, Nigeria

<sup>e</sup> Science and Engineering Research Group (SAERG), Ladoké Akintola University of Technology, Ogbomoso, Nigeria

\*Corresponding Author: [aolade@lautech.edu.ng](mailto:aolade@lautech.edu.ng)

### ABSTRACT

The thermodynamic properties of batch adsorption of antibiotics mixture in aqueous solution onto *Delonix regia* Pod (DRP) activated, under the effect of temperature, was investigated in this study. The raw DRPs were processed, activated with KOH, carbonised at 500 °C for 40 mins and then used for the treatment of wastewater containing a multi-component mixture of amoxicillin, tetracycline and ampicillin, in a batch mode at varying temperatures (40-60 °C). Thermodynamic parameters, such as Gibb's Free Energy ( $\Delta G^0$ ), Enthalpy Change ( $\Delta H^0$ ), Entropy Change ( $\Delta S^0$ ), Isosteric Heat of Adsorption ( $\Delta H_x$ ), Activation Energy ( $E_a$ ), Sticking Probability ( $S^*$ ), Surface Coverage ( $\theta$ ) and Hopping Number ( $n$ ) were calculated, which are indicators of the possible nature of adsorption. The most suitable adsorption temperature was 40 °C with maximum adsorption capacities of 5.1, 5.3 and 4.5 mg/g and the corresponding removal efficiency of 85.91, 91.24 and 78.67 %, were obtained for amoxicillin, tetracycline and ampicillin respectively. The  $\Delta H$ ,  $\Delta S$ ,  $E_a$  and  $S^*$  values were -314.30, -72.74 and -364.12 kJ/mol; 7.8459, 16.2522 and 2.7079 kJ/mol; 69.0885, 6.7706 and 150.824  $\text{gmol}^{-1}$ ; and 0.6909, 0.8606 and 0.4842 for amoxicillin, tetracycline and ampicillin respectively. These values confirm that the adsorption process is favourable and exothermic.

**Keywords:** Activation Energy, Antibiotics, *Delonix regia* Pod, Thermodynamic, Wastewater.

### 1. INTRODUCTION

Industrial wastewater is discharged into the environment, without adequate treatment and ends up in the receiving waters and thus degrading the environment with adverse consequences for plants and animals (Dube *et al.* 2019). The pharmaceutical industry has developed widely and a wide variety of pharmaceutical products that are produced for the treatment of diverse infections, illnesses and diseases confronting humans. However, careless disposal of pharmaceutical residues to the environment after consumption, ends up on the surface of river bodies, thus posing a potential danger to human health. Gabriela *et al.* (2020) reported that 80 % of the world's wastewater is discarded without previous treatment.

Every year, about 1 billion people get diseases caused by untreated water and more than 200 different species of marine life are harmed (Zhou *et al.*, 2020). Among the various pharmaceutical compounds, antibiotics have been paid particular attention to because of their potential role in the development of antibiotic-resistant bacteria. Most antibiotics tested to date are known to be bio-recalcitrant under aerobic conditions (Azarpira *et al.*, 2019). It is essential to remove pharmaceutical residues in industrial wastewater before being discharged into the environment. Removal of pollutants from industrial wastewater using conventional methods is expensive and has significant disadvantages such as requirements and production of toxic sludge, and incomplete removal of waste products that require further disposal (Renugadevi and Krishnaveni, 2021). Hence, conventional methods do not suit the needs of developing countries. Adsorption has been reported as an effective technology for the treatment of contaminated wastewater (Azarpira *et al.*, 2019), despite there is an ongoing search for eco-friendly, efficient, renewable and cheap agricultural residues to be used for the production of adsorbents to reduce the cost of using the adsorption technology.

*Delonix regia* pod is a soft biomass residue that litter the environment as solid waste, particularly around the vicinity of the parent tree (Iwar *et al.*, 2020). This development necessitates the need for conversion of this waste into useful and

value-added products such as adsorbents which can be used for the removal of pollutants in wastewater (Abulude and Adejayan, 2017). The adsorption technique can be operated in batch or continuous modes. Both modes are influenced by various operational factors such as initial concentration and pH of the pollutant, particle size and dosage of the adsorbent as well as temperature, agitation and contact time of the process. In this research, a cheap and eco-friendly adsorbent was developed from the waste DRP, used for the removal of antibiotics mixture from an aqueous solution, under the effect of changing temperatures and the adsorption thermodynamic parameters relating to the adsorption process was investigated (Renugadevi and Krishnaveni, 2021).

## 2. MATERIALS AND METHODS

The DRPs residues were washed and rinsed with distilled water to remove surface-adhered particles attached to the pod. They were cut into smaller pieces, sun-dried to remove the moisture, ground and sieved (425-850  $\mu\text{m}$ ) sieves using a sieve shaker (Dada *et al.*, 2020). The DRP sample (10 g) was soaked in 100 ml of 1.0 M KOH at room temperature for 24 h and later boiled off. The resulting mixture was cooled and washed with distilled water to a pH range of 6.9-7.1. The activated DRPs were oven-dried at 105  $^{\circ}\text{C}$  overnight and cooled in a desiccator containing silica gel (Dada *et al.*, 2020). The activated DRP (10 g) was charged into the muffle furnace at 500  $^{\circ}\text{C}$  for 40 min (Ravichandran *et al.*, 2018; Nomngongo and Chaba 2019). The char obtained was washed and oven dried to constant weight. The selected antibiotics used were amoxicillin, tetracycline and ampicillin. All the reagents used are analytical grades and were used as received.

### 2.1 Batch Adsorption Studies

Samples (100 ml) of the antibiotic's solution were mixed with 1 g of the DRP-activated carbon in a 250 ml flask. The flask and its contents were placed in a rotary shaker housed in an incubator to agitate at 180 rpm for 60 mins at a varying temperature between 40 and 60  $^{\circ}\text{C}$  intervals of 5  $^{\circ}\text{C}$ . Then the flasks were withdrawn from the shaker and the solution was decanted, the supernatant was centrifuged at 1500 rpm for 10 mins. The absorbance of the unadsorbed antibiotics in the centrifuged content was determined with the use of a UV-Vis Spectrophotometer at wavelengths of 287, 288 and 361 nm (Hasan *et al.*, 2014). The Adsorption capacity and percentage removal were determined accordingly as indicated in Equations 1 and 2 (Okoye *et al.*, 2018).

$$q_e = \frac{V(C_o - C_e)}{W} \quad (1)$$

$$R_e = \frac{(C_o - C_e)}{C_o} \times 100\% \quad (2)$$

where  $v$  is the volume of antibiotics mixture in contact with the DRP;  $C_o$  and  $C_e$  are initial and final concentrations of the adsorbate (mg/L);  $w$  is the amount of adsorbent usually expressed as dry weight.

### 2.2 Adsorption Thermodynamics Properties

The thermodynamic properties of the selected antibiotic adsorption onto the DRP-activated carbon developed were investigated based on the existing adsorption thermodynamics models. These properties often give insight into the nature (physisorption or chemisorption) and the impact of the temperature-prompted energy of the adsorption process (Sahmoune, 2018).

#### 2.2.1 Gibb's free energy, enthalpy change and entropy change

Gibb's free energy, enthalpy change and entropy change of the adsorption study were investigated based on Equations 3-6. The values of  $\Delta H^{\circ}$  and  $\Delta S^{\circ}$  are evaluated from the slope and intercepts of the linear plot of  $\ln K_c$  against  $1/T$  (Batool *et al.*, 2018).

$$k_c = \frac{C_o}{C_e} \quad (3)$$

$$\Delta G^{\circ} = -RT \ln K_c \quad (4)$$

$$\Delta G^{\circ} = \Delta H - T\Delta S \quad (5)$$

$$\ln k_c = \frac{\Delta S}{R} - \frac{\Delta H}{RT} \quad (6)$$

Where  $R$  is the gas constant (8.314 J/molK),  $T$  is the temperature,  $k_c$  is the equilibrium constant (Distribution coefficient),  $C_o$  and  $C_e$  are the concentration of the adsorbed adsorbate and the concentration of remaining antibiotics in solution (mg/L).

#### 2.2.2 Isotheric heat of adsorption

The Isotheric heat of adsorption is essential in the characterization of adsorption processes and it is based on the Clausius-Clapeyron Equation

$$\frac{d \ln C_e}{dT} = \frac{-\Delta H_x}{RT^2} \quad (7)$$

On integration and rearrangement

$$\ln C_e = -\frac{\Delta H_x}{R} \frac{1}{T} + K \quad (8)$$

Where  $\Delta H_x$  is the isotheric heat of adsorption ( $\text{kJ mol}^{-1}$ ).

The values of  $\Delta H_x$  and K were determined from the slope and intercept, respectively from the plot of  $\ln C_e$  against  $\frac{1}{T}$ .

### 2.2.3 Surface coverage versus the hopping number

The Hopping number is defined as the feasible number of hopping performed by the adsorbate molecule while locating an unoccupied site on the surface of the targeted adsorbent during the adsorption process (Menkiti *et al.*, 2014). The surface coverage is expressed in Equation 9 while the relationship between the  $\theta$  versus n is expressed in Equation 10.

$$\theta = \left(1 - \frac{C_e}{C_o}\right) \quad (9)$$

$$n = \frac{1}{(1-\theta)\theta} \quad (10)$$

### 2.2.4 Activation energy and sorption probability

Activation energy is defined as the minimum energy needed for a specific adsorbate-adsorbent interaction such as chemical reaction. The Sorption probability is a thermodynamic parameter that is related to the ability of an adsorbate to stick to the surface of an adsorbent indefinitely. The  $E_a$  and  $S^*$  were evaluated from Equations 11 and 12 based on the plot of  $\ln(1-\theta)$  against  $1/T$  where the intercept and slope are  $\ln S^*$  and  $\frac{E_a}{R}$  respectively.

$$\ln(1-\theta) = \ln S^* + \frac{E_a}{RT} \quad (11)$$

$$\ln\left(\frac{C_o - C_e}{C_o}\right) = \frac{E_a}{RT} + \ln S^* \quad (12)$$

Where;  $\theta$  is the surface coverage and  $E_a$  is the activation energy.

### 2.2.5 Eyring equations

The thermodynamic properties ( $\Delta H^-$  and  $\Delta S^-$ ) of the Eyring equation from Equations 13 and 14. The values of ( $\Delta H^-$ ) and ( $\Delta S^-$ ) were calculated from the slope and intercept of the plot of  $\ln \frac{k}{T}$  versus  $1/T$  (Ebelegi, *et al.*, 2020).

$$\ln \frac{k}{T} = \left(\ln \frac{k_B}{h} + \frac{\Delta S^-}{R}\right) - \frac{\Delta H^-}{RT} \quad (13)$$

$$\ln \frac{k}{T} = -\frac{\Delta H^-}{R} \frac{1}{T} + \left(\ln \frac{k_B}{h} + \frac{\Delta S^-}{R}\right) \quad (14)$$

Where  $k_B$  is the Boltzmann constant ( $1.3807 \times 10^{-23} \text{ J K}^{-1}$ ) and h is the Plank constant ( $6.6261 \times 10^{-34} \text{ Js}$ ) and R is the universal gas constant ( $8.314 \text{ J mol}^{-1} \text{ K}^{-1}$ ).

## 3. RESULTS AND DISCUSSION

### 3.1 Effect of temperature on the adsorption

The adsorption process decreased as the temperature increased from 40 to 60 °C (Figures 1a-b). The most suitable adsorption temperature was 40 °C which suggested that lower solution temperatures favour selected antibiotics mixture removal by the biomass and lower temperature makes the adsorption easier. The selected antibiotics mixture exhibited the inclination to migrate to the bulk solution from the solid phase as the temperature of the solution increased. This, coupled with the increase in the rate of desorption of adsorbed antibiotics mixture from the adsorbent surface, could result in a decrease in the adsorption (Marczewski, *et al.*, 2016). The decrease in concentrations with increasing temperature indicates a low energy requirement for the selected antibiotics mixture adsorption onto the DRP. This trend is similar to the report of Ifeuebuegu and Edet (2020) for phosphate adsorption with an increase in temperature using Recycled Brick Waste.

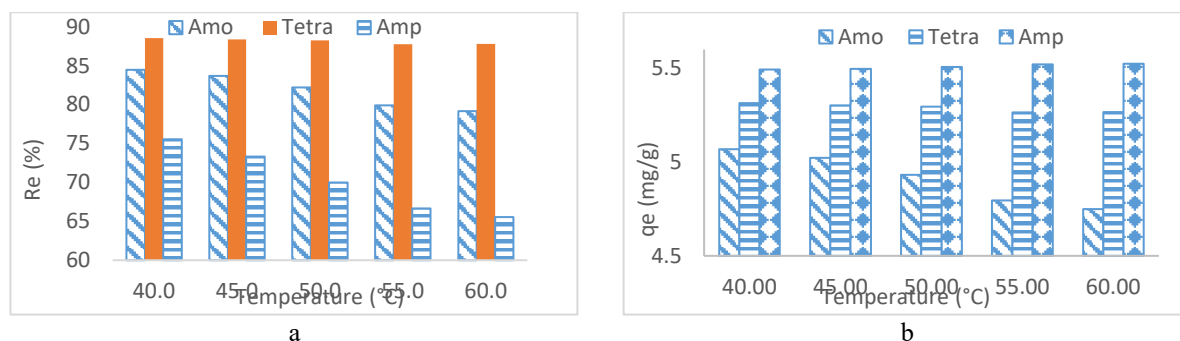


Figure 1: The plot of (a) Removal efficiency against temperature (b) Adsorption capacity against temperature for the removal of amoxicillin, tetracycline and ampicillin on DRP



### 3.2 Thermodynamics Studies

#### 3.2.1 Enthalpy change, Entropy change, and Gibb's free energy

Thermodynamics parameters such as Enthalpy change ( $\Delta H$ ), Entropy change ( $\Delta S$ ), and Gibb's free energy ( $\Delta G$ ) (Table 1) were determined from the intercept and slope of the plots of  $\ln k_c$  against  $1/T$  for different temperatures used as shown in Figure 2. Negative values obtained for  $\Delta G$  at all temperatures confirm the feasibility of the process and the spontaneous nature of the adsorption of the antibiotics mixture onto DRP. Higher negative values were obtained at higher temperatures suggesting the affinity of antibiotics on the DRP adsorption process and were more spontaneous at higher temperatures. The values of  $\Delta G$  suggest a chemisorption process as values of  $\Delta G$  for the physisorption process are generally between  $-2770.0690$  and  $-1265.8506$  kJ/mol. The negative values of  $\Delta H$   $-314.30$ ,  $-72.74$  and  $-364.12$  kJ/mol for amoxicillin, tetracycline and ampicillin, respectively, suggest that the adsorption process is exothermic. The positive  $\Delta S$  value  $7.8459$ ,  $16.2522$  and  $2.7079$  kJ/mol for amoxicillin, tetracycline and ampicillin, respectively, indicates that the adsorption process increases randomly at the solid-solution interface during the adsorption of antibiotic mixture onto DRP, and there is an affinity for the adsorbent used in this study. The values gotten for  $\Delta H$ ,  $\Delta S$ , and  $\Delta G$  fell between the ranges of the compared studies which indicates that the adsorption of antibiotics unto DRP is a feasible process. The results are similar to those obtained by (Chakraborty *et al.*, 2021).

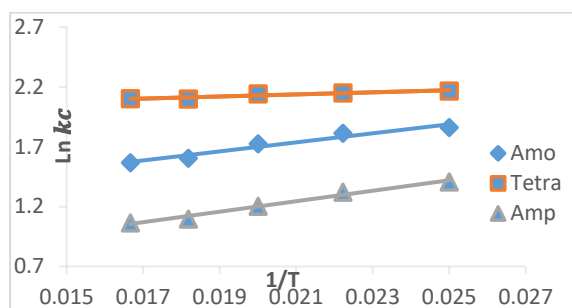


Figure 2: Plots of  $\ln k_c$  versus  $1/T$

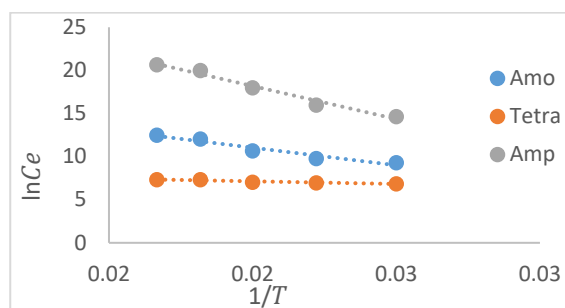


Figure 3: Plots of  $\ln C_e$  against  $1/T$

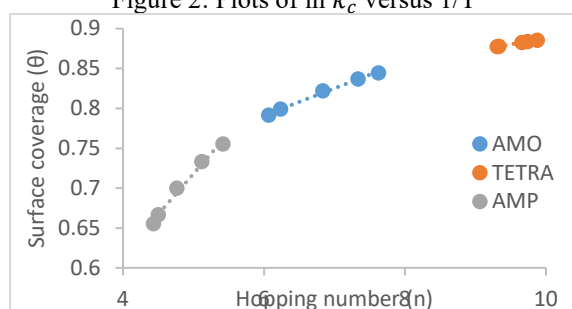


Figure 4: Surface coverage vs hopping number

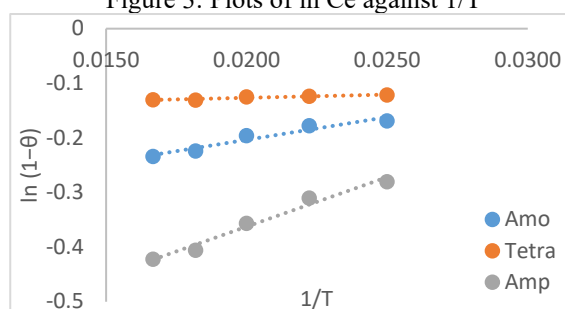


Figure 5: The plot of  $\ln(1-\theta)$  against  $1/T$

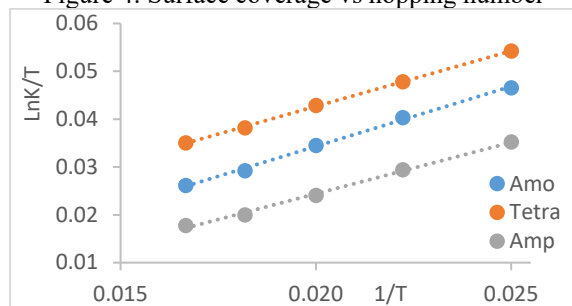


Figure 6: The plot of  $\ln \frac{k}{T}$  versus  $\frac{1}{T}$

#### 3.2.2 Isotheric heat of adsorption

The values of  $\Delta H_x$  were obtained from the slope of a plot of  $\ln C_e$  versus  $1/T$ , which were found to be linear (Figure 3). The  $R^2$  values of the isosteres and the corresponding  $\Delta H_x$  values are listed in Table 2. The magnitude of  $\Delta H_x$  value gives information about the adsorption mechanism as chemical ion exchange or physical adsorption. For physical adsorption,  $\Delta H_x$  should be below  $80$  kJ mol $^{-1}$  and for chemical adsorption, it ranges between  $80$  and  $400$  kJ.mol $^{-1}$  (Neimark, *et al.*, 2017). In this research, the values of  $\Delta H_x$  were  $33.936$ ,  $51.679$  and  $63.764$  kJ mol $^{-1}$  for amoxicillin, tetracycline and ampicillin, respectively (Figure 3), indicating that the adsorption of antibiotics onto DRP-activated carbon was a physical process. It gives some indication about the surface energetic heterogeneity.

Table 1: Antibiotic uptake dynamic thermodynamic parameters

Adsorbate / Parameters	Amoxicillin	Tetracycline	Ampicillin
$R^2$	0.9539	0.8924	0.9845
$\Delta H$ (KJ/mol)	-314.3000	-72.7400	-364.1200
$\Delta S$ (J/ gmol K)	7.8459	16.2522	2.7079
$\Delta G$ (KJ/mol) at 313.0	-2770.0690	-5159.6786	-1211.6926
$\Delta G$ (KJ/mol) at 318.0	-2809.2990	-5240.9396	-1225.2321
$\Delta G$ (KJ/mol) at 323.0	-2848.5280	-5322.2006	-1238.7716
$\Delta G$ (KJ/mol) at 328.0	-2887.7580	-5403.4616	-1252.3111
$\Delta G$ (KJ/mol) at 333.0	-2926.9870	-5484.7226	-1265.8506

Table 2: Isosteric heat of adsorption, sticking probability and activation energy parameters

Adsorbate / Parameters	Amoxicillin	Tetracycline	Ampicillin
$\Delta H_x$ (KJ/mol)	33.936	51.679	63.764
K	19.20	8.38	33.52
$R^2$	0.9429	0.8883	0.9790
$E_a$ (g mol <sup>-1</sup> )	69,0885	9,7706	150.842
$S^*$	0.6909	0.8606	0.4842

### 3.2.3 Surface coverage versus the hopping number

The plot of surface coverage versus hopping number (Figure 4), indicates that the movement of the selected antibiotics to the vacant sites on the adsorbent surface increased with an increase in the surface coverage. The difference observed in  $\theta$  and  $n$  for amoxicillin, tetracycline and ampicillin indicated the ease with which ampicillin found a binding site when compared with amoxicillin and tetracycline. The hopping number describes how fast an adsorption process happens, thus the smaller the hopping number ( $n$ ) the faster the sorption process. These findings are consistent with the reports of Menkiti *et al.* (2014).

### 3.2.4 Sticking probability and activation energy

The  $E_a$  values calculated from the slope of the plot (Figure 5) were 69.0885, 6.7706 and 150.824 gmol<sup>-1</sup> for amoxicillin, tetracycline and ampicillin, respectively. The results shown in Table 2 indicate that the probability of adsorbate sticking to the DRP surface is  $0 < S^* < 1$  for all antibiotics studied. These values confirm that the adsorption process is favourable, with sticking of adsorbate to adsorbent and physisorption mechanism predominant. The sticking probability is a function of the adsorbate/adsorbent system under consideration but must lie in the range  $0 < S^* < 1$  and is dependent on the temperature of the system (Ebelegi, *et al.*, 2020). The positive values of  $E_a$  indicate that the process is endothermic and relatively high values of  $E_a$  suggests that antibiotics adsorption is not a diffusion-controlled process (Ebelegi *et al.*, 2020).

### 3.2.5 Eyring equations

The large positive values of  $\Delta G^-$  suggests that energy was required in the process to convert reactants into products. The negative values of  $\Delta H^-$  (-20.832, -19.261 and -17.869) mol<sup>-1</sup> for amoxicillin, tetracycline and ampicillin, respectively, indicate an exothermic process (Figure 6). The negative value of  $\Delta S^-$  -197.370, -197.270 and -197.39 K<sup>-1</sup> (Table 4) suggest that antibiotics adsorption onto DRP-activated carbon is an associative mechanism (Abechi, 2018).

Table 4: Antibiotic uptake of Eyring equations parameters

Adsorbate / Parameters	Amoxicillin	Tetracycline	Ampicillin
$R^2$	0.9975	0.9995	0.9966
$\Delta H^-$ (KJ/mol)	-20.832	-19.261	-17.869
$\Delta S^-$ (KJ/mol)	-197.370	-197.270	-197.39
$\Delta G^-$ (KJ/mol) at 313.0	61755.9776	61726.249	61765.2
$\Delta G^-$ (KJ/mol) at 318.0	62742.8276	62712.599	62752.2
$\Delta G^-$ (KJ/mol) at 323.0	63729.6776	63698.949	63739.1
$\Delta G^-$ (KJ/mol) at 328.0	64716.5276	64685.299	64726.1
$\Delta G^-$ (KJ/mol) at 333.0	65703.3776	65671.649	65713

#### 4. CONCLUSION

Removal of the antibiotic mixture from an aqueous solution was carried out using activated carbon developed from agricultural residues of the DRP. The removal of the selected antibiotics mixture using matured DRP was a function of temperature. The decrease in concentrations with increasing temperature indicates a low energy requirement for the selected antibiotics mixture adsorption onto the DRP. The adsorption process was spontaneous, feasible, exothermic, increases randomly at the interface, and there is an affinity for the adsorbent used in this study. Considering the data and analysis presented in this study, it is suggested that DRPs would be well suited for the adsorption of industrial effluents containing pharmaceutical residues. DRP constitutes a promising material for the development of low-cost adsorption technology for the removal of antibiotics from effluents.

#### ACKNOWLEDGEMENT

Authors are grateful to all Academic staff of the Department of Chemical Engineering, Faculty of Engineering and Technology, Ladoke Akintola University of Technology, Ogbomoso, Oyo State, Nigeria for supervisory guidance.

#### REFERENCES

- Abechi, S. E. (2018). Studies on the Mechanism of Adsorption of Methylene Blue onto Activated Carbon Using Thermodynamic Tools. *Science World Journal*, 13(2), pp. 17-19.
- Abulude, F. O. and Adejayan, A. W. (2017). Nutritional values of flamboyant (*Delonix regia*) seeds obtained in Akure, Nigeria. *Science and Education Development*, 1(4), pp. 1-18.
- Azarpira, H., Balarak, D., Joghatayi, A. and Mostafapour, F. K. (2019). Biosorption of Amoxicillin from Contaminated Water onto Palm Bark Biomass. *International Journal of Life Science and Pharmaceutical Research*, 7(1), pp. 9-16.
- Batool, F., Akbar, J., Iqbal, S., Noreen, S., Syed, N. and Bukhari, A. (2018). Study of Isothermal, Kinetic, and Thermodynamic Parameters for Adsorption of Cadmium: An Overview of Linear and Nonlinear Approach and Error Analysis. *Bioinorganic Chemistry and Applications*, 2018, Article ID 3463724, pp. 1-11.
- Dada, E. O., Ojo, I. A., Alade, A. O., Afolabi, T. J., Amuda, O. S. and Jameel, A. T. (2020). Biosorption of Bromophenol Blue from Aqueous Solution Using Flamboyant (*Delonix regia*) Pod. *Chemical Science International Journal*, 29(5), pp. 32-50.
- Dube, S., Kebede, T. G. and Nindi, M. M. (2019). Removal of Antibiotic Drugs from Wastewater Using *Moringa stenopetala* Seeds. *Water Journal*, 11(9), pp. 1-13.
- Gabriela, S. d., Alaor, V. F., Raïssa, X. K., Luana, V. T. and André Ricardo, F. d. (2020). Preparation and Characterization of Activated Carbon Obtained from Water Plant Sludge for Removal of Cationic Dye from Wastewater. *Processes*, 8(13), pp. 1-13.
- Ifelebuegu, A. O. and Edet, U. A. (2020). Kinetics, Isotherms, and Thermodynamic Adsorption of Phosphates from Wastewater Using Recycled Brick Waste. *Processes*, 8(6), pp. 1-15.
- Iwar, R. T., Utsev, J. T. and Ifyalem, K. J. (2020). Adsorption of Methylene Blue from Aqueous Solution onto *Delonix regia* Pod: Batch Isotherm, Kinetic and Thermodynamic Studies. *Journal of Materials and Environmental Science*, 11(7), pp. 1058-1078.
- Marczewski, A. W., Seczkowska, M., Deryło-Marczewska, A. and Blachnio, M. (2016). Adsorption equilibrium and kinetics of selected phenoxyacid pesticides on activated carbon: effect of temperature. *Adsorption*, 22(1), pp. 777-790.
- Menkiti, M. C., Aneke, M. C., Ejikeme, P. M., Onukwuli, O. D. and Nwasinachi, U. M. (2014). Adsorptive treatment of brewery effluent using activated *Chrysophyllum albidum* seed shell carbon. *Springer Plus*, 3(1), pp. 1-19.
- Neimark, A. V., Ravikovitch, P. I., Kowalczyk, P. and Cimino, R. T. (2017). Determination of Isothermic Heat of Adsorption by Quenched Solid Density Functional Theory. *American Chemical Society, Langmuir*, 33(1), pp. 1769-1779.
- Okoye, C. C., Okey-Onyesolu, C. F., Chime, D. C. and Achike, C. C. (2018). Adsorptive Removal of Bromophenol Blue Dye from Aqueous Solution using Activated Clay. *International Journal of Scientific Research and Management*, 6(3), pp. 2321-3418.
- Ravichandran, P., Sugumaran, P., Seshadri, S. and Basta, A. H. (2018). Optimizing the route for production of activated carbon from *Casuarina equisetifolia* fruit waste. *Royal Society of Chemistry*, 5(9), pp. 1-12.
- Renugadevi, N. and Krishnaveni, J. (2021). Thermodynamics studies of Adsorption of Methylene Blue dye from Aqueous Solution Using Dried Algae. *Research Expo International Multidisciplinary Research Journal*, 2(3), pp. 1250-1263.
- Sahmoune, M. N. (2018). Evaluation of thermodynamic parameters for adsorption of heavy metals by green adsorbents. *Environmental Chemistry Letters*, 17(4), pp. 1-9.
- Sen, T. K. (2014). Review on Dye Removal from Its Aqueous Solution into Non-Conventional Adsorbents. *Journal of Chemical and Process Engineering*, 1(3), pp. 1-11.
- Zhou, J. L., Ahmad, M. B., Ngo, H. H. and Wenshan, G. (2020). Adsorptive removal of antibiotics from water and wastewater: Progress and challenges. *Science of the Total Environment*, 5(32), pp. 112-126.



## Equilibrium Study of Methylene Blue Adsorption by *Vitex Doniana* Activated Carbon

Kevin S. OTOIKHIAN<sup>1</sup>, Oluwadayo A. FRANCIS<sup>2\*</sup>, Emeka C. NWORIE<sup>3</sup>

<sup>1,2</sup>Department of Chemical Engineering, Edo State University, Uzairue, Nigeria

<sup>3</sup>Department of Chemical Engineering Technology, Auchi Polytechnic, Auchi, Nigeria

<sup>1</sup>otoikhian.kevin@edouniversity.edu.ng, <sup>2\*</sup>Francis.asokogene@edouniversity.edu.ng, <sup>3</sup>nocyka2016@gmail.com

\*Corresponding author

### ABSTRACT

*Vitex doniana* activated carbon modified with zinc chloride (VDZnCl<sub>2</sub>) was synthesized for the removal of methylene blue. VDZnCl<sub>2</sub> was characterized for textural properties, surface morphology and surface chemistry. The textural properties revealed increased surface area from 14.02 to 933.25 m<sup>2</sup>/g, the surface morphology showed pores with widened cavities, and the surface chemistry showed the inclusion of O-H group and characteristics C=C group commonly found in carbonaceous materials. Adsorption study showed increased removal of methylene blue as concentration increased from 1 to 800 mg/L until equilibrium was attained. The Sips isotherm model had the best fittings with the equilibrium data ( $R^2 = 0.938$  and  $SSE = 7016.14$ ), thereby suggesting physical adsorption onto the heterogeneous surface of VDZnCl<sub>2</sub>. However, the maximum adsorption capacity was 238 mg/g. The performance put up by VDZnCl<sub>2</sub> suggested that it is a possible and suitable alternative adsorbent for textile and dyeing industries' wastewater.

**Keywords:** Activated carbon, synthesized, adsorbent, methylene blue, characterized

### 1. INTRODUCTION

Most paper, pulp, textile and dyeing industries either permanently or temporarily empty their waste into water bodies, which in turn contaminates them and other adjoining streams and tributaries, thereby reducing the dissolved oxygen and restricting the penetration of sunlight and aerobic activities. These phenomena render the waters unfit for drinking and irrigation, ultimately posing serious hazards to human life and aquatic system (Asokogene *et al.*, 2019; Piriya *et al.*, 2021). Exposure to dyes results in several health challenges like dyscrasia, leukocytosis, anaemia, cyanosis, vomiting, convulsion, methemoglobinemia, liver, heart, spleen, kidney, lungs, and bone damage, (Alipour *et al.*, 2019; Piriya *et al.*, 2021). Methylene blue (C<sub>16</sub>H<sub>18</sub>ClN<sub>3</sub>S) is a cationic dye commonly used in textile industries for cotton, wool and silk (Thakur, Pandey, and Arotiba, 2016). Therefore, its treatment in wastewater has become an issue of great concern.

Notably, the treatment methods for methylene blue in wastewater include extraction, membrane separation, coagulation, ozonation, flocculation and adsorption (Luo *et al.*, 2017; Wang *et al.*, 2017; Asokogene *et al.*, 2019). Adsorption is low cost, possesses the potential to selectively adsorb certain molecules and is excellent at dyes removal from wastewater (Asokogene *et al.*, 2019; Pandey *et al.*, 2020; Piriya *et al.*, 2021).

The quest for low-cost, and available adsorbents has made scientists turn to a variety of natural and synthetic biomass waste materials as adsorbents. Activated carbon, has gained wide attention as an adsorbent due to its high content of hydroxyl functional group which reflects the significant potential for the removal of several aquatic pollutants. It also possesses high surface area and good pore architectures (Afshin *et al.*, 2019). Activated carbon can be made from several biomass waste materials such as coconut shells (Aljebori *et al.*, 2017), bamboo (Zhao *et al.*, 2017), palm shells (Zhao *et al.*, 2018), woods (Nowicki, 2016), sawdust (Zhu *et al.*, 2014), apricot stones (Djilani *et al.*, 2015), grape seeds (Okman *et al.*, 2014), rice husk (Li *et al.*, 2015) and empty fruit bunch (Zaini and Shaid, 2016).

Research has shown that activated carbon adsorbents that are chemically modified with metal salt possess improved porosity, better specific surface area and better adsorption potential for dyes, metals and other aqueous contaminants (Piriya *et al.*, 2021). Rangabhashiyam and Selvaraju (2015), reported that ZnCl<sub>2</sub>-activated carbon derived from sterculia gulata shells showed an adsorption capacity of 90.90 mg/g, compared to 45.45 mg/g of its precursor for hexagonal chromium removal from wastewater. Zhang *et al.*, 2020 also found that ZnCl<sub>2</sub>treated activated carbon from rice husks had a larger surface area than its precursor at a 1:1 impregnation ratio.

Meanwhile, *Vitex doniana* seeds and its modified adsorbent have not gained wide recognition in dye (methylene blue) removal from wastewater, except as activated carbon adsorbent for Zn (II) and Pb (II) removal (Ameh, Odoh and Oluwaseye 2012), and as phosphoric acid (H<sub>3</sub>PO<sub>4</sub>) modified activated carbon for Cr (II) removal (Yusuf, Muhammed and Grace, 2020) from wastewater. However, the availability at little cost of *Vitex doniana* seeds (Kapooria and Aime, 2005) which are the raw materials for this adsorbent could be a promising alternative to present-day adsorbents. Therefore, this work was aimed at evaluating the adsorptive characteristics of zinc chloride (ZnCl<sub>2</sub>) activated *Vitex doniana* for methylene blue removal from wastewater. The activated carbon adsorbent was characterized and its adsorption for methylene blue in batch mode was performed. Equilibrium isotherm models were adopted to evaluate the adsorption data, from which the possible adsorption behaviour was discussed.

## 2. MATERIALS AND METHODS

Seeds of *Vitex doniana* were collected around Auchi Polytechnic community in Edo State, Nigeria. Methylene blue powder (98.5%) was supplied by BDH, England and zinc chloride pellet (99%) was supplied by Merck, Germany. All chemicals are of analytical reagent grade.

### 2.1 Adsorbent preparation and characterization

The exocarp and associated impurities of *Vitex doniana* seed were washed off with running water. The seed was sun-dried for seven days, crushed, ground and sieved to 355 µm (Ameh *et al.*, 2012). A 100 g pulverized *Vitex doniana* was chemically activated using ZnCl<sub>2</sub> (VDZnCl<sub>2</sub>) at 800°C for 2 h in a TT-EF-12 muffle furnace (Techmel, USA). The activated sample was allowed to cool before it was soaked in HCl (3 wt.%) for 12 h to remove surface ash and then washed in distilled water to a pH of 7 (Mkungunugwa *et al.*, 2021).

The surface functional groups of VDZnCl<sub>2</sub> and VDC adsorbent samples were determined using an FTIR analyser from Thermo Scientific Nicolet ISI 10, USA at a wavenumber range of 4000-500 cm<sup>-1</sup>. The textural properties were measured using a Thermo Scientific, USA model surface area analyser (single point Brunauer-Emmett-Teller (BET) method. The SEM image of the adsorbent surface and texture was obtained by Karl Zeiss (Germany) instrument.

### 2.2 Batch Adsorption Studies

One gram (1 g) of methylene blue powder was dissolved in 1000 mL of distilled water to make stock solution. Following that, working concentrations of 1–800 mg/L were created by serial dilution. In Beatson bottles, 50mL of each concentration was added to 50 mg of adsorbent, the bottles were sealed, shaken, and kept at 28°C for 72 h. The contact time was assumed to be long enough to achieve equilibrium adsorption (Asokogene *et al.*, 2019). The residual concentrations were obtained by measuring absorbance at 620 nm with an Angstrom Advanced Inc. (model 752) scientific ultraviolet-visible (UV-Vis) spectrophotometer. The pH of the methylene blue solution was kept in its natural form of 4.8±0.3. The adsorption capacity,  $q_e$  (mg/g), was determined from a mass balance equation,

$$q_e = \left( \frac{C_o - C_e}{m} \right) \times V \quad (1)$$

Where;  $C_o$  and  $C_e$  (mg/L) are the initial and equilibrium concentrations, respectively,  $V$  (L) is the volume of the solution, and  $m$  (g) is the mass of the adsorbent.

## 3. RESULTS AND DISCUSSION

### 3.1 Adsorbent Characterization

Figure 2 presents the FTIR spectra of VDZnCl<sub>2</sub> and VDC adsorbents across a frequency range of 4000-500 cm<sup>-1</sup>, revealing the surface functional groups.

The functional groups contained in VDZnCl<sub>2</sub> and VDC revealed that the majority of the peaks in both adsorbent materials were comparable, except for a peak at 1551.37 cm<sup>-1</sup> (VDZnCl<sub>2</sub>) which corresponds to C=C stretching vibrations in the aromatic ring of alkenes and is commonly detected in carbonaceous materials like activated carbon (Mkungunugwa *et al.*, 2021). The signals at 3625.27 cm<sup>-1</sup> and 3605.53 cm<sup>-1</sup> in the FTIR spectrum of VDZnCl<sub>2</sub> and VDC, respectively, correspond to the intermolecular hydrogen bonding of polymeric compounds such as alcohols, phenols, and carboxylic acids, showing the presence of free hydroxyl groups on the carbon surface. C=C stretching vibration of alkenyl, unconjugated ketone, carbonyl, and ester groups has a peak at 2611.08 cm<sup>-1</sup> (VDZnCl<sub>2</sub>) and 1903.27 cm<sup>-1</sup> (VDC).

Table 1 presents the textural properties of VDZnCl<sub>2</sub> and VDC. The surface area of VDZnCl<sub>2</sub> increased dramatically from 14.02 to 933.3 m<sup>2</sup>/g. This pattern is consistent with other materials after activation (Mistar, Alfatah and Supardan, 2020). Accordingly, the pore volume increased by about three times, from 0.07 to 0.21 cm<sup>3</sup>/g. After activation, the pore size increased from 0.92 to 18.9Å. Therefore, VDZnCl<sub>2</sub> will allow for pore fillings of numerous molecules inside its carbon matrix during adsorption (Mistar, Alfatah and Supardan, 2020).

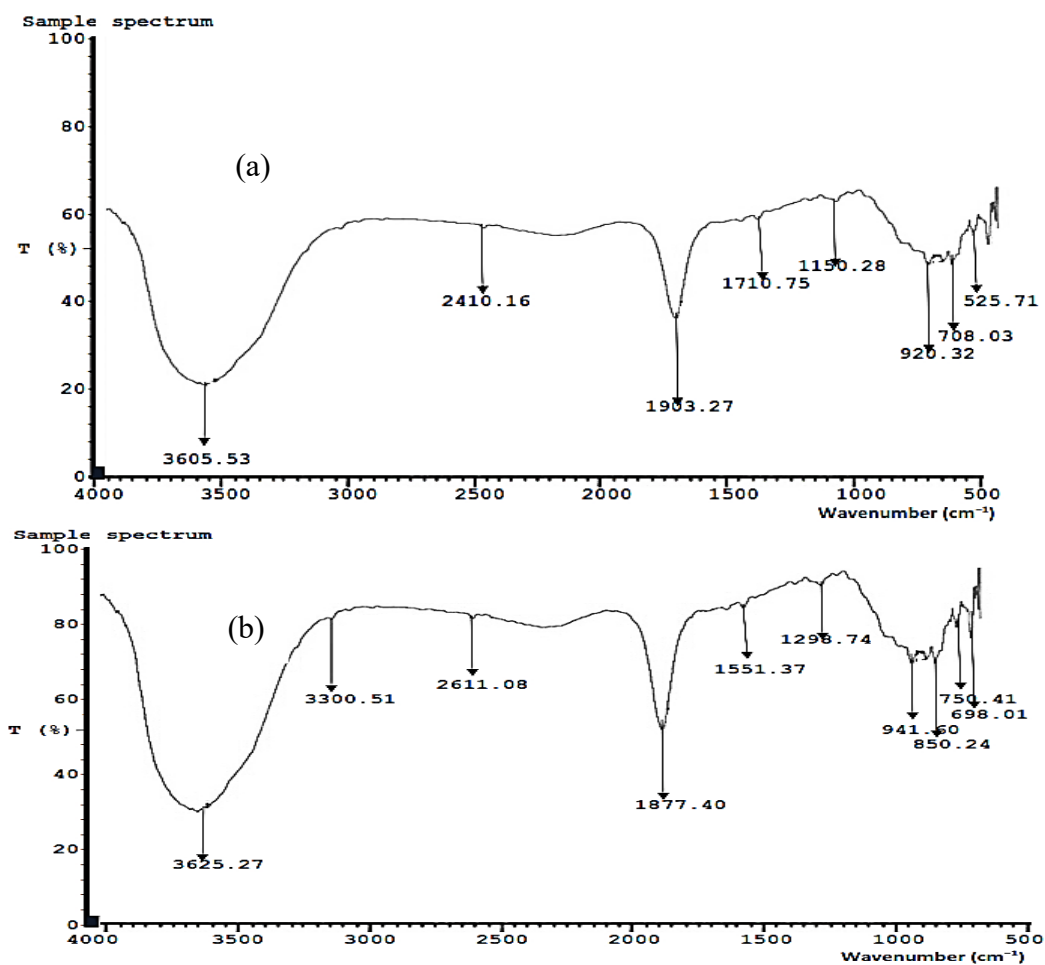


Figure 2: FTIR spectra of (a) Vitex doniana (VDC) and (b) its derived activated carbon (VDZnCl<sub>2</sub>)

Table 1: Surface Textural Properties of VDZnCl<sub>2</sub> and VDC

BET Parameters	Samples	
	VDC	VDZnCl <sub>2</sub>
Surface area (m <sup>2</sup> g <sup>-1</sup> )	14.02	933.3
Pore volume (cm <sup>3</sup> g <sup>-1</sup> )	0.07	0.21
Pore size (Å)	0.92	18.9

The SEM result of the VDZnCl<sub>2</sub> adsorbent material which was characteristic of its surface morphology and texture at ×500 magnification is shown in Figure 3.

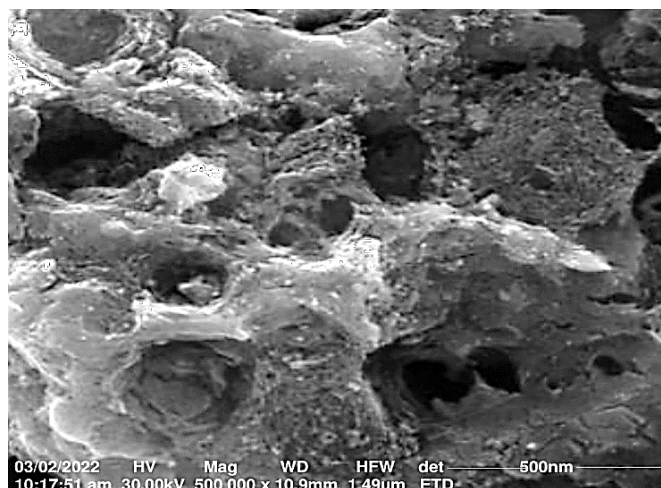


Figure 3: VDZnCl<sub>2</sub> adsorbent SEM micrograph

The SEM micrograph showed thin plant boundary walls due to modification and the presence of varieties of pores with widened cavities which could be due to the removal of volatile matter and the production of fixed carbon after activation (Ohimor, Temisa, and Ononiwu, 2021).

### 3.2 Equilibrium Adsorption Isotherm

Figure 4 presents the adsorption isotherm model fittings of methylene blue onto VDZnCl<sub>2</sub> when 50 mg of adsorbent was brought into contact with 50 mL of the solution (1–800 mg/L) at 28°C for 72 h, while the summarized models' constants are presented in Table 2. Until maximum methylene blue adsorption occurred and adsorption equilibrium was reached, there was increased adsorption capacity as the solution concentration increased from 1 to 400 mg/L. This is because active adsorption sites of adsorbent were easily occupied and saturated by adsorbate molecules at low initial concentrations, resulting in low adsorption capacity; meanwhile, at high initial concentrations, a higher fractional adsorbent-adsorbate adsorption ratio occurred which resulted in increased methylene blue adsorption (Luo *et al.*, 2019; Zhao *et al.*, 2022).

Nonlinear Langmuir, Freundlich, and Sips isotherm models were used for the validation of the adsorption experimental data. Equations (2), (3), and (4), respectively, define these models, and Microsoft Excel Solver 2019 was used to solve the model equations through non-linear regression.

$$q_e = \frac{Q_m K_L C_e}{1 + K_L C_e} \quad (2)$$

$$q_e = K_F C_e^{\frac{1}{n}} \quad (3)$$

$$q_e = \frac{Q_m (K_S C_e)^{n_s}}{1 + (K_S C_e)^{n_s}} \quad (4)$$

Where;  $q_e$  (mg/g) is the amount of dye removed by the adsorbent,  $C_e$  (mg/L) is the equilibrium dye concentration in solution,  $K_L$  (L/mg) is the Langmuir equilibrium constant;  $Q_m$  (mg/g) is the maximal monolayer adsorption capacity. The Freundlich adsorption constant of adsorption capacity and the frequency of surface heterogeneity are defined as  $K_F$  (mg/g) (L/mg)<sup>1/n</sup> and  $1/n$ , respectively. The sips constant is  $K_S$  (L/mg), and surface heterogeneity is  $n_s$ . The Langmuir isotherm model assumes a one-molecule thick adsorbed layer and sorbate removal at defined and definite sites with no lateral or steric interference. Only low concentrations and multilayer adsorption are covered by the Freundlich isotherm model. Sips isotherm model combines Langmuir and Freundlich models in forecasting heterogeneous surface adsorption (Vhahangwele and Mugeru, 2015).

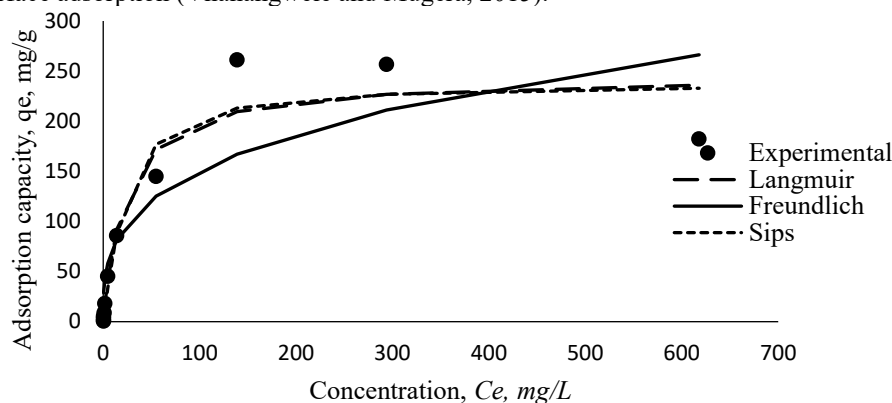


Figure 4: Equilibrium curve of methylene blue adsorption (Lines and isotherm models)

Both the Langmuir and Sips models fit the experimental data well; However, the Sips isotherm model fit better due to its closeness to the experimental data under experimental conditions (Figure 4), its highest regression coefficient ( $R^2$ ) value of 0.938, and least error function (SSE) value of 7016.14. (Table 2). As a result, the Sips model best described this adsorption behaviour at equilibrium, implying a heterogeneous methylene blue adsorption process onto VDZnCl<sub>2</sub> involving pore filling and ionic interaction (Luo *et al.*, 2019; Mistar, Alfatah and Supardan, 2020). Maximum adsorption capacity ( $Q_m$ ) of methylene blue was, 238 mg/g.

Table 2: Parameters of Isotherm Models for Methylene Blue Adsorption on VDZnCl<sub>2</sub>

Isotherm model	Parameters	Adsorbent (VDZnCl <sub>2</sub> )
Langmuir	$Q_m$ (mg/g)	244.901
	$K_L$ (L/mg)	0.043
	$R^2$	0.936
	$R_L$	0.087
	$SSE$	7240.47
Freundlich	$K_f$ (mg/g)(L/mg) <sup>1/n</sup>	35.988
	1/n	0.311
	$R^2$	0.813
	$SSE$	22663.4
Sips	$Q_m$ (mg/g)	237.631
	$K_s$ (L/mg)	0.046
	$n_s$	1.168
	$R^2$	0.938
	$SSE$	7016.14

#### 4. CONCLUSIONS

Zinc chloride-modified activated carbon adsorbent (VDZnCl<sub>2</sub>) was synthesized from *Vitex doniana* (black plum) seed for methylene blue removal from simulated wastewater. The textural properties and functional group of VDZnCl<sub>2</sub> revealed increased surface area from 14.02 to 933.25 m<sup>2</sup>/g and porosity, and the inclusion of O-H group and a characteristic C=C group commonly found in carbonaceous materials, respectively. Adsorption study showed increased removal of methylene blue as concentration increased from 1 to 800 mg/L until equilibrium was attained. The maximum adsorption capacity was 238 mg/g. The Sips isotherm model had the best fittings with the equilibrium data.

#### ACKNOWLEDGEMENT

We wish to acknowledge the scientific and financial support made by our 2022 project students and the department of Chemical Engineering laboratory of Auchi Polytechnic Auchi, Edo State, Nigeria

#### REFERENCES

- Afshin, S., Rashtbari, Y., Shirmardi, M., Vosoughi, M. and Hamzehzadeh, A., 2019. Adsorption of basic violet 16 dye from aqueous solution onto mucilaginous seeds of *Salvia sclarea*: kinetics and isotherms studies. *Desalination and Water Treatment*, 161, pp. 365–375.
- Alipour, M., Vosoughi, M., Mokhtari, S.A., Sadeghi, H., Rashtbari, Y., Shirmardi, M. and Azad, R., 2021. Optimising the basic violet 16 adsorption from aqueous solutions by magnetic graphene oxide using the response surface model based on the Box–Behnken design. *International Journal of Environmental Analytical Chemistry*, 101(6), pp. 758–777.
- Aljeboree, A.M., Alshirifi, A.N. and Alkaim, A.F., 2017. Kinetics and equilibrium study for the adsorption of textile dyes on coconut shell activated carbon. *Arabian journal of chemistry*, 10, pp. S3381–S3393.
- Ameh, P. O., Odoh, R. and Oluwaseye, A., 2012. Equilibrium study on the adsorption of Zn(II) and Pb(II) ions from aqueous solution onto *Vitex doniana* nut. *International Journal of Modern Chemistry*, 3(2), pp. 82–97
- Asokogene, F. O., Muhammad, A. A. Z., Misau, M. I., Surajudeen, A. and El-Nafaty, A. U., 2019. Methylene Blue Adsorption onto Neem Leave/Chitosan Aggregates: Isotherm, Kinetics and thermodynamics Studies. *International Journal of Chemical Reactor Engineering*, pp. 1–16.
- Djilani, C., Zaghoudi, R., Djazi, F., Bouchekima, B., Lallam, A., Modarressi, A. and Rogalski, M., 2015. Adsorption of dyes on activated carbon prepared from apricot stones and commercial activated carbon. *Journal of Taiwan Institute of Chemical Engineering*, 53, pp. 112–121.
- Kapooria, R. G. and Aime, M. C., 2005. Report of oliverscutula on *Vitex doniana* in Zambia. *Africa Journal of Science and Technology*, 3, pp. 57–60.
- Imran, M., Islam, A. U., Tariq, M. A., Siddique, M. H., Shah, N. S., Khan, Z. U. H., Amjad, M., Din, S. U., Shah, G. M., Naeem, M. A., Nadeem, M., Nawaz, M. and Rizwan, M., 2019. Synthesis of magnetite-based nanocomposites for effective removal of brilliant green dye from wastewater. *Environmental Science and Pollution Research*, 26 (24), pp. 24489–24502.



- Li, W., Ma, T., Zhang, R., Tian, Y. and Qiao, Y., 2015. Preparation of porous carbons with high- and low-pressure CO<sub>2</sub> uptake by KOH activation of rice husk char *Fuel*, 139, pp. 68–70.
- Luo, L., Wu, X., Li, Z., Zhou, Y., Chen, T., Fan, M. and Zhao, W., 2019. Synthesis of activated carbon from biowaste of fir bark for methylene blue removal. *Royal Society Open Science*, 6(190523), pp. 1-14
- Luo, X. P., Fu, S. Y., Du, Y. M., Guo, J. Z. and Li, B., 2017. Adsorption of methylene blue and malachite green from aqueous solution by sulfonic acid group modified MIL-101. *Microporous and Mesoporous Materials*, 237, pp. 268–274.
- Mistar, E. M., Alfatah, T. and Supardan, M. D., 2020. Synthesis and characterization of activated carbon from *Bambusa vulgaris striata* using two-step KOH activation. *Journal of Materials Research and Technology*, 9(3), pp. 6278-6286.
- Mkungunugwa, T., Manhokwe, S., Chawafambira, A. and Shumba, M., 2021. Synthesis and characterisation of activated carbon obtained from Marula (sclerocaryabirrea) nutshell. *Journal of Chemistry*.
- Nowicki P., 2016. Effect of heat treatment on the physicochemical properties of nitrogen-enriched activated carbons. *Journal of Thermal Analysis and Calorimetry*, 125(3), pp. 1017-1024.
- Ohimor, E. O., Temisa, D. O. and Ononiwu, P. I., 2021. Production of activated carbon from carbonaceous agricultural waste material: coconut fibres. *Nigerian Journal of Technology*, 40(1), pp. 19-24.
- Okman, I., Selhan, K., Tay, T. and Erdem, M., 2014. Activated carbons from grape seeds by chemical activation with potassium carbonate and potassium hydroxide. *Applied Surface Science*, 293, pp. 138-142.
- Pandey, S., Do, J. Y., Kim, J. and Kang, M., 2020. Fast and highly efficient catalytic degradation of dyes using κ-carrageenan stabilized silver nanoparticles nanocatalyst. *Carbohydrate Polymers*, 230, pp. 115597.
- Piriya, R. S., Jayabalakrishnan, R. M., Maheswari, M., Boomiraj, K. and Oumabady, S., 2021. Coconut shell derived ZnCl<sub>2</sub> activated carbon for malachite green dye removal. *Water Science & Technology*, pp 1-16
- Rangabhashiyam, S. and Selvaraju, N., 2015. Adsorptive remediation of hexavalent chromium from synthetic wastewater by a natural and ZnCl<sub>2</sub>-activated *Sterculia guttata* shell. *Journal of Molecular Liquids*, 207, pp. 39-49.
- Thakur, S., Pandey, S. and Arotiba, O. A., 2016. Development of a sodium alginate-based organic/inorganic superabsorbent composite hydrogel for adsorption of methylene blue. *Carbohydrate Polymers*, 153, pp. 34-46.
- Vhahangwele, M. and Mugeru, G. W., 2015. The potential of ball-milled South African bentonite clay for attenuation of heavy metals from acidic wastewater: simultaneous sorption of CO<sub>2</sub><sup>+</sup>, Cu<sup>2+</sup>, Ni<sup>2+</sup>, Pb<sup>2+</sup> and Zn<sup>2+</sup> ions. *Journal of Environmental Chemical Engineering*, 3 (4), pp. 2416–2425.
- Wang, F., Zhang, L., Wang, Y., Liu, X., Rohani, S. and Lu, J., 2017. Fe<sub>3</sub>O<sub>4</sub> @ SiO<sub>2</sub> @ CS-TETA functionalized graphene oxide for the adsorption of methylene blue (MB) and Cu(II). *Applied Surface Science*, 420, pp. 970–981.
- Yusuf, J., Muhammed, M. and Grace, B.T., 2020. Preparation of activated carbon from *syzygiumcumini* seed for the removal of chromium (II) ion from aqueous solution. *Bayero Journal of Pure and Applied Sciences*, 13(1), pp. 158 - 163
- Zaini, M. A. A., Shu-Hui, T., Lin-Zhi, L. and Alias, N., 2016. Fate of chemical activators in the aqueous environment: What should we do about it? *Aceh International Journal of Science and Technology*, 5(1), pp. 18-20.
- Zhang, S., Zhu, S., Zhang, H., Liu, X. and Xiong, Y., 2020. Synthesis and characterization of rice husk-based magnetic porous carbon by pyrolysis of pre-treated rice husk with FeCl<sub>3</sub> and ZnCl<sub>2</sub>. *Journal of Analytical and Applied Pyrolysis*, 147, pp. 104806.
- Zhao, H., Zhong, H., Jiang, Y., Li, H., Tang, P., Li, D. and Feng, Y., 2022. Porous ZnCl<sub>2</sub>-activated carbon from Shaddock peel: methylene blue adsorption behaviour. *Materials*, 15(895), pp. 1-16
- Zhao, W., Luo, Lu., Wang, H. and Fan, M., 2017. Synthesis of bamboo-based activated carbons with super-high specific surface area for hydrogen storage. *Bioresources*, 12, pp. 1246–1262.
- Zhao, W., Luo, L., Chen, T., Li, Z., Zhang, Z. and Fan, M., 2018. Activated carbons from oil palm shell for hydrogen storage. *Material Science Engineering*, 368, pp. 012031.
- Zhu, X., Wang, P., Peng, C., Yang, J. and Yan, X., 2014. Activated carbon produced from paulownia sawdust for high-performance CO<sub>2</sub> sorbents. *Chin. Chem. Lett.*, 25, pp. 929–932.



## Thermodynamic Activity Coefficient Modelling of Liquid-Liquid Equilibrium Data for Tropical Almond Oil Biodiesel System

Kenneth K. ADAMA\*<sup>1</sup>, Rilva S. SANTIAGO-AGUIAR<sup>2</sup>, Regiane S. PINHEIRO<sup>2</sup>, Robson A. C. da SILVA<sup>2</sup>, Emmanuel O. ALUYOR<sup>1,3</sup>, Thomas O.K. AUDU<sup>3</sup>

<sup>1</sup> Department of Chemical Engineering, Edo State University Uzairue, P.M.B 04, Auchi, Edo State, Nigeria

<sup>2</sup> Chemical Engineering Department, Federal University of Ceara, Pici Campus, Bl. 709, CEP 60455 – 760, Fortaleza, CE Brazil

<sup>3</sup> Department of Chemical Engineering, University of Benin, P.M.G 1154, Ugbowo, Benin City, Edo State, Nigeria

\*Corresponding author: [adama.kenneth@edouniversity.edu.ng](mailto:adama.kenneth@edouniversity.edu.ng)

### ABSTRACT

In this study, the liquid-liquid equilibrium (LLE) data of system containing tropical almond oil biodiesel/methanol/glycerol was used to evaluate the performance of four thermodynamic activity coefficient models of Non-Random Two-Liquid (NRTL), Universal Quasichemical Activity Coefficient (UNIQUAC), Universal quasichemical Functional group Activity Coefficient (UNIFAC) and Analytical Solutions of Group (ASOG). The evaluated system formed the significant components at the conclusion of the methanolysis reaction of tropical almond oil and its subsequent purification. Using average global deviations, the accuracy of the models was evaluated. The experimental data were correlated satisfactorily. The order of prediction accuracy was established as: 3.72 UNIQUAC > 3.84 NRTL > 5.26 UNIFAC > 5.37 ASOG. In this regard, the activity coefficient models could be used for process simulation of biodiesel production, purification, separation and equipment design.

**Keywords:** Biodiesel system, Liquid-liquid equilibrium, Activity coefficient, Temperature, Thermodynamic modelling.

### 1. INTRODUCTION

In recent times, there has been greater interest in the development and use of sustainable and renewable energy sources (Atabani *et al.*, 2013). Biodiesel production from renewable energy sources has increased tremendously which has created healthy competition for diesel obtained from fossil energy sources. Renewable biodiesel sources are of remarkable benefits which include minimal emissions of particulate matters and hazardous gases and being environmentally benign. Biodiesel, as a renewable energy source, can be used as an alternative diesel fuel due to its biodegradability and non-toxicity (Atabani *et al.*, 2013; Do Carmo *et al.*, 2014; Adama *et al.*, 2021).

The challenges encountered in the separation and purification of high quality biodiesel is still a major issue in the commercial production of the product. The production process involves phase separation and purification which forms part of the integral process in determining the economic viability of the process (Adama *et al.*, 2021; Toledo *et al.*, 2019; Merzougui *et al.*, 2015; Esipovich *et al.*, 2018). In-depth understanding of the process requires the knowledge of the phase equilibrium of the liquid-liquid equilibrium system (Santos *et al.*, 2018; Wales *et al.*, 2016; Homrich *et al.*, 2016). Adequate knowledge and understanding of the equilibrium phase behaviour of any biodiesel/glycerol/alcohol ternary system is important in the design of efficient and effective separation and purification techniques for biodiesel production process (Adama *et al.*, 2021; Esipovich *et al.*, 2018; Cavalcanti *et al.*, 2018; Zhang *et al.*, 2016; Asoodeh *et al.*, 2019). In this regard, to successfully and conveniently describe the phase equilibria behaviour of products and mixtures from the transesterification reactions, several thermodynamic models have been developed. One of such model is the Universal quasichemical Functional group Activity Coefficient (UNIFAC) model which is used to model LLE of ternary biodiesel systems. Others include Non Random Two-Liquid (NRTL), Universal Quasichemical Activity Coefficient (UNIQUAC), Universal quasichemical Functional group Activity Coefficient – Liquid-Liquid Equilibrium (UNIFAC-LLE), Universal quasichemical Functional group Activity Coefficient – Dortmund (UNIFAC-Dortmund), Analytical Solutions of Group (ASOG) and several cubic-equations of state (EoS) models. These thermodynamic models find applications in the correlation of ternary mixtures and vapour-liquid equilibrium (VLE) of most binary mixtures (Merzougui *et al.*, 2015; Reynel-Avila *et al.*, 2019; Shaahmadi *et al.*, 2018; Mehrabam *et al.*, 2018; Weidlich and Gmehling 1987; Guggenheim 1952; Fredenslund *et al.*, 1975; Renon and Prausnitz 1968; Abrams and Prausnitz 1975; Tochigi and Kojima 1983; Dadfar and Biria 2015; Prausnitz *et al.*, 1998; Gupte and Daubert 1986; Gani 1989; Sorensen *et al.*, 1979).

There are several published studies on LLE data for different model systems with different fatty alkyl esters, methanol or ethanol and glycerol at several different temperatures (Do Carmo *et al.*, 2014; Noriega *et al.*, 2016; Sena and Pereira 2017; Espovich *et al.*, 2018; Toledo *et al.*, 2019; Adama *et al.*, 2021; Bazooyar *et al.*, 2021). These studies compared their experimental data results with different thermodynamic models with varying degrees of predictive ability, success and satisfaction. However, only a single published work presently exists for component distribution associated with phase separation and purification of tropical almond oil biodiesel/methanol/glycerol system at different temperatures (Adama *et al.*, 2021). This study presented experimentally determined LLE data at temperatures of (20, 30 and 40) °C without thermodynamic modelling of the experimental LLE data which would have assisted in the optimization and simulation of activity coefficient models and experimental data and predict outcomes of the phase behaviour.

Tropical almond oil is obtained from a large tropical tree known botanically as *Terminalia catappa*. It belongs to the *leadwood* tree family called *Combretaceae*. Its oil is used in the production of tropical almond biodiesel because it contains about 34-60% bland, yellow, semi-drying oil (Adama *et al.*, 2021; Campo *et al.*, 2017).

The use of thermodynamic modelling for the experimental liquid-liquid equilibrium (LLE) data of tropical almond oil biodiesel ternary system is implemented in this work through the application of four activity coefficient models: NRTL (Renon and Prausnitz 1968), UNIQUAC (Abrams and Prausnitz 1975), ASOG (Tochigi and Kojima 1983) and UNIFAC (Fredenslund *et al.*, 1975). Currently, no published literature exists on assessing the performance of thermodynamic models in correlating experimentally obtained LLE data from tropical almond oil biodiesel/methanol/glycerol system at any known temperature. Hence, the novelty of this research.

## 2. MATERIALS AND METHODS

All analytical and experimental techniques applied in this work were same used in our previous study (Adama *et al.*, 2021). The thermodynamic modelling of the experimental liquid-liquid equilibrium data was performed and predicted using local composition concepts approaches of NRTL (Renon and Prausnitz 1968) and UNIQUAC (Abrams and Prausnitz 1975) and group contribution concepts approaches of ASOG (Tochigi and Kojima 1983) and UNIFAC (Fredenslund *et al.*, 1975) respectively. The procedures are highlighted as follows for the different thermodynamic models.

The four activity coefficient models of NRTL, UNIQUAC, UNIFAC and ASOG were obtained using the flash and liquid-liquid equilibrium calculations performed using the software program TML-LLE 2.0 developed by Stragevitch 1997. The procedure is based on the simplex method proposed by (Nelder and Mead 1965), which consists of minimizing an objective function (OF) on the basis of the concentration of the components, as defined by objective function (Sorensen *et al.*, 1979):

$$F.O. = \sum_k^D \sum_j^M \sum_i^{N-1} \left\{ \left( x_{ijk}^{I,exp} - x_{ijk}^{I,calc} \right)^2 + \left( x_{ijk}^{II,exp} - x_{ijk}^{II,calc} \right)^2 \right\} \quad (1)$$

Where D = number of data set, N = number of components for each data set, M = tie-lines for each data set, superscripts 'I' and 'II' denote the LLE phases in equilibrium, superscript "exp." and "calc." denote experimental and calculated phases.

The interaction parameters were calculated using the above procedure while the comparison of experimental and calculated composition of each component in either the biodiesel or glycerol phase was evaluated using the root mean square (rms) deviations given by the expression:

$$\Delta x = 100 \sqrt{\frac{\sum_i^M \sum_j^N \left( x_{ij}^{I,exp} - x_{ij}^{I,calc} \right)^2 + \left( x_{ij}^{II,exp} - x_{ij}^{II,calc} \right)^2}{2MN}} \quad (2)$$

## 3. RESULTS AND DISCUSSION

Experimental LLE data phase diagram (tie line plots) involving the tie-line compositions for the system tropical almond biodiesel + methanol + glycerol at (20, 30 and 40) °C are presented in Figure 1 as previously reported in our earlier work (Adama *et al.*, 2021).

Thermodynamic Activity Coefficient Modelling of Liquid-Liquid Equilibrium Data for Tropical Almond Oil Biodiesel System

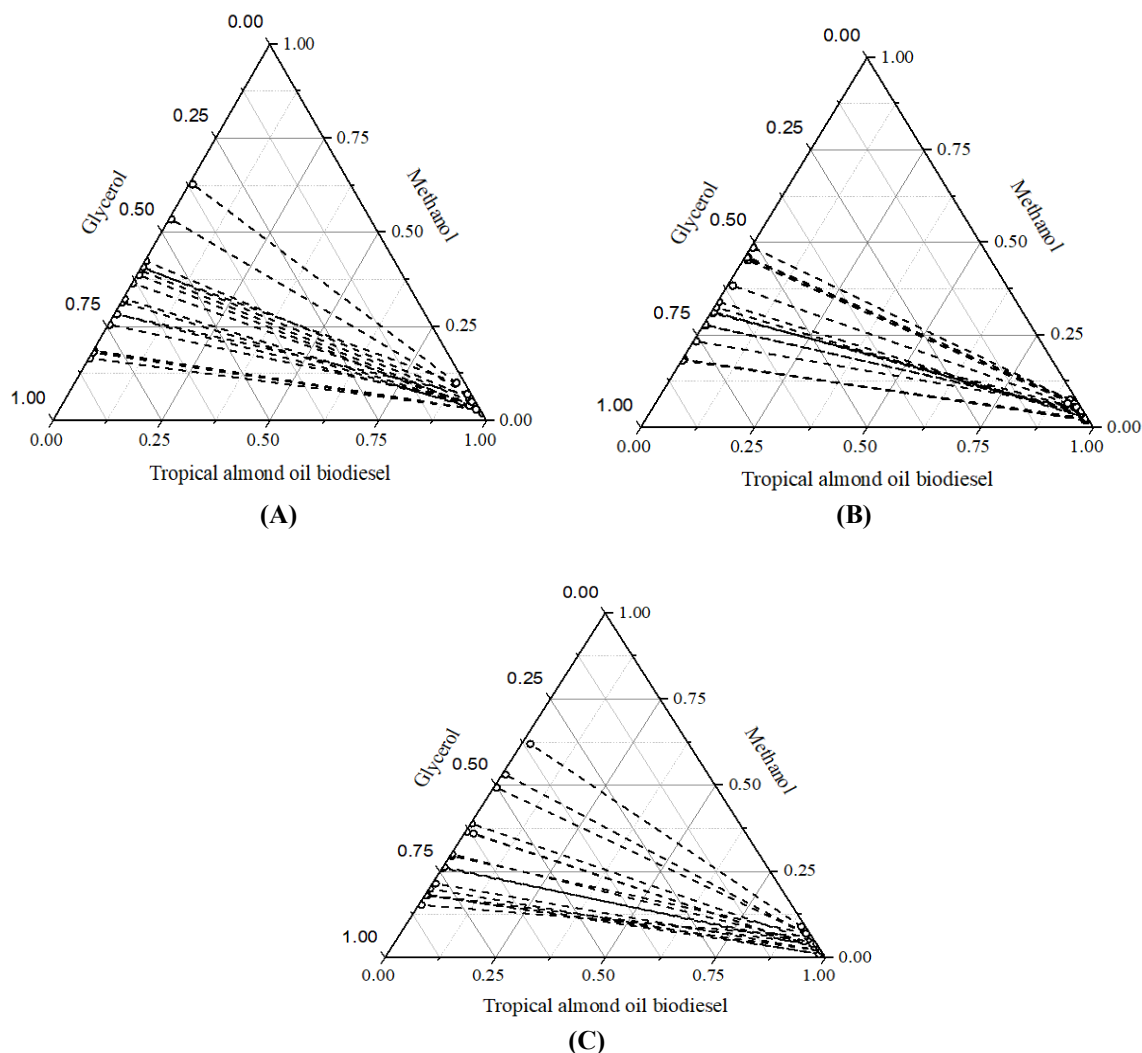
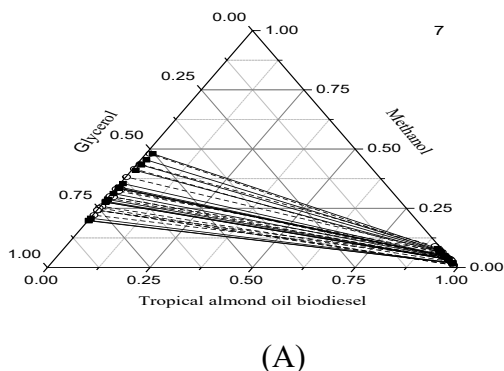


Figure 1: Tie-line analysis of experimental biodiesel-rich and glycerol-rich phase composition for tropical almond oil biodiesel/methanol/glycerol system at (A) 20 °C (B) 30 °C (C) 40 °C (Adama *et al.*, 2021)

The analysis of the experimental tie-lines of Figure 1 for the tropical almond biodiesel/methanol/glycerol system at the various temperatures revealed that the concentration of biodiesel component was higher in the biodiesel-rich phase as expected than glycerol due to density difference between the biodiesel and glycerol components. The concentration of biodiesel in the glycerol-rich phase was evenly distributed at the investigated temperatures and this increased with increasing temperatures. This is due to the fact the methanol readily solubilized the glycerol and so was more in the glycerol-rich phase than in the biodiesel-rich phase at the investigated conditions (Adama *et al.*, 2021; Campos *et al.*, 2017; Maghami *et al.*, 2016; Dagostin *et al.*, 2015). The influence of higher concentration of methanol in the glycerol-rich phase can be seen in the slope of the tie-lines in the LLE diagrams of Figure 1 at the various investigated temperatures.



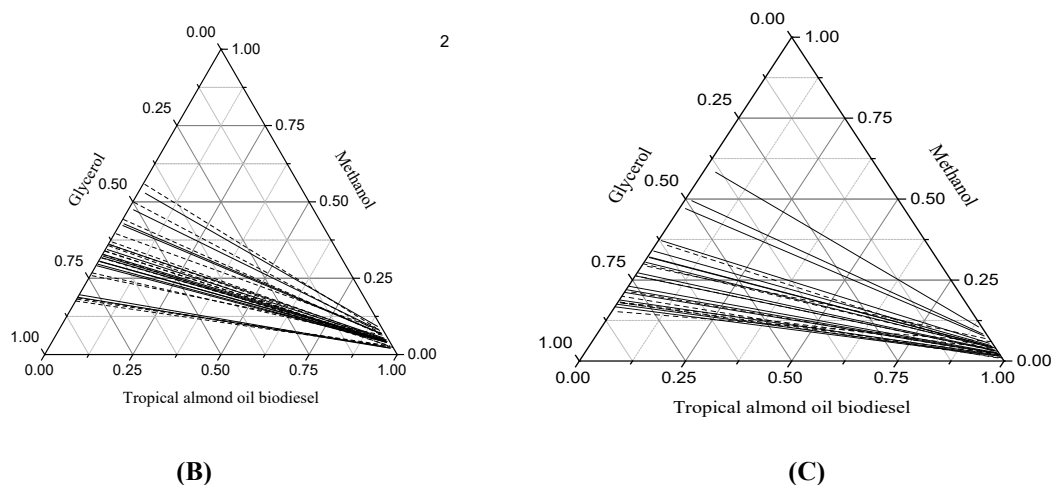


Figure 2: Tie-line analysis of biodiesel-rich and glycerol-rich phase composition for tropical almond oil biodiesel/methanol/glycerol system at (A) 20 °C (B) 30 °C (C) 40 °C. ---o--- experimental data; —■— calculated results by the NRTL model.

Figure 2 shows a comparison between experimental data with predictions outputted by the NRTL model at the different temperatures

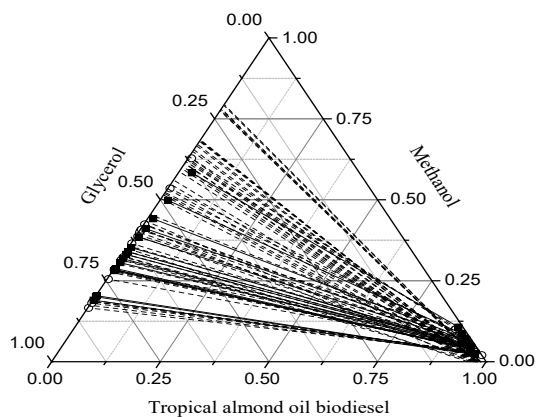


Figure 3: Tie-line analysis of biodiesel-rich and glycerol-rich phase composition for tropical almond oil biodiesel/methanol/glycerol system at 20 °C ---o--- experimental data; —■— calculated results by the NRTL, —x— calculated results by the UNIQUAC, —△— calculated results by the UNIFAC, —□— calculated results by the ASOG model

Figure 3 illustrate a comparison between tie-lines data calculated using NRTL, UNIQUAC, UNIFAC and ASOG models and compared with experimental tie-lines at 20 °C. NRTL and UNIQUAC binary interaction parameters between tropical almond biodiesel, methanol and glycerol are listed in Table 1. Experimental LLE data were used to determine these parameters. RMSD data are presented in Table 2 and the mean global deviation of all systems studied was established as 3.8416%, 3.7211 %, 5.258 % and 4.375 %) respectively, using the NRTL, UNIQUAC, UNIFAC and ASOG models.

Table 1: NRTL and UNIQUAC interaction parameters between tropical almond oil biodiesel (1) + methanol (2) + glycerol (3) at 20 °C, 30 °C and 40 °C

Pair ij	Thermodynamic model							
	NRTL				UNIQUAC			
	$A_{ij}$	$A_{ji}$	$B_{ij}$ (1/K)	$B_{ji}$ (1/K)	$A_{ij}$	$A_{ji}$	$B_{ij}$ (1/K)	$B_{ji}$ (1/K)
1 2	113.82	-261.21	-2.2952	6.7746	2411.3	204.84	-7.3894	4.9279
13	-10358	2339.6	37.296	1.5681	-646.67	3796.5	1.8418	-10.171
23	1623.3	-33.995	-6.5596	-1.0518	2570.4	481.49	-9.7473	0.54465

Table 2: Summary of the thermodynamic modelling calculations performed for all the systems

T (°C)	NRTL $\Delta w$ (%)	UNIQUAC $\Delta w$ (%)	UNIFAC $\Delta w$ (%)	ASOG $\Delta w$ (%)
Tropical almond oil biodiesel (1) + methanol (2) + glycerol (3)				
20	4.1963	4.0420	6.1659	5.3129
30	2.8589	2.8885	5.3090	4.5497
40	4.4819	4.6568	4.9835	4.1723
Global deviation of the correlation	3.8416	3.7211	5.2580	4.3751

## CONCLUSION

Liquid-liquid equilibrium data for the novel biodiesel system composed of tropical almond biodiesel + methanol + glycerol were obtained experimentally and correlated using thermodynamic models of NRTL, UNIQUAC, UNIFAC and ASOG with reasonable global deviations. The work compared the predictive ability of the four thermodynamic activity coefficient models and established that the local composition concept approach model had the best prediction represented by UNIQUAC (3.72%) while the group contribution concept approach had the best prediction represented by UNIFAC (5.26%). However, all thermodynamic models showed good prediction ability with the order of prediction accuracy given as: UNIQUAC>NRTL>UNIFAC>ASOG.

## REFERENCES

- Abrams D.S., Prausnitz J.M. Statistical Thermodynamics of Liquid Mixtures: A New Expression for the Excess Gibbs Energy of Partly or Completely Miscible Systems, *AICHE J* 21 (1975) 116-128.
- Adama K.K., Aluyor E.O., Audu T.O.K. Component Distribution Associated with Phase Separation and Purification of Tropical Almond Biodiesel at Different Temperatures, *Renew. Energy* 165 (2021) 67-76.
- Asoodeh A., Eslami F., Sadrameh S.M. Liquid-Liquid Equilibria of Systems Containing Linseed Oil Biodiesel + Methanol + Glycerol: Experimental Data and Thermodynamic Modelling, *Fuel* 253 (2019) 460-473
- Atabani A.E., Silitonya A.S., Irfan A.B., Mahlia T.M.I., Masjuki H.H., Mekhilef S.A. Comprehensive Reviews on Biodiesel as an Alternative Energy Source and its Characteristics, *Renew. Sustain. Energy Rev.*, 16 (2013) 2070-2093
- Bazooyar B., Shaahmadi F., Anbaz M.A., Jomekian A. Intelligent Modeling and Analysis of Biodiesel/Alcohol/Glycerol Liquid-Liquid Equilibria, *J. Mol. Liquids* 322 (2021) 114972
- Campo C.E., Cabarcas M., Gonzalez-Delgado A., Sanchez T.E., Ojeda D.K. Liquid-Liquid Equilibrium for Ternary Mixtures Methanol-Glycerol-Biodiesel from *Jatropha urcas*, *International J. ChemTech. Res.*, 10(4), (2017) 245-254
- Cavalcanti R.N., Oliveira M.B., Meirelles A.J.A. Liquid-Liquid Equilibria for Systems Containing Fatty Acid Ethyl Esters, Ethanol and Glycerol at 333.15 and 343.15 K: Experimental Data, Thermodynamic and Artificial Neural Network Modelling, *Brazilian J. Chem. Eng.* 35 (2018) 2 819-834
- Dadfar B., Biria D. Application of Group Contribution-NRTL Model with Closure to Predict LLE Behavior of an Oil/Brine/Surfactant System, *J. Chem. Eng. Data* 60 (2015) 2575-2584
- Dagostin J.L.A., Mafra M.R., Ramos L.P., Corazza M.L. Liquid-Liquid Phase Equilibrium Measurements and Modeling for Systems Involving (Soybean oil + Ethyl esters + (Ethanol + Water), *Fuel* 141 (2015) 164-172
- Do Carmo F.R., Evangelista N.S., De Santiago-Aguiar R.S., Fernandes F.A.N., De Sant'Ana H.B. Evaluation of Optimal Activity Coefficient Models for Modeling and Simulation of Liquid-Liquid Equilibrium of Biodiesel + Glycerol + Methanol Systems, *Fuel* 125 (2014) 57-65
- Esipovich A.L., Rogozhin A.E., Belousov A.S., Kanokov E.A., Otopkova K.V., Danov S.M. Liquid-Liquid Equilibrium in the Systems of FAMES + Vegetable oil + Methyl alcohol and FAMES + Glycerol + Methyl Alcohol, *Fuel* 217 (2018) 31-37
- Fredenslund A., Jones R.L., Prausnitz J.M. Group-contribution Estimation of Activity Coefficients in Non-ideal Mixtures, *AICHE J* 21 (1975) 1086-1099
- Gani R. A knowledge-based System for the Selection of Thermodynamic Models, *Comput. Chem. Eng.* 13 (1989), 397-404
- Guggenheim E.A. *Mixtures: The Theory of the Equilibrium Properties of Some Simple Cases of Mixtures, Solutions, and Alloys* (1952), Clarendon Press

- Gupte P.A., Daubert T.E. Prediction of Low-Pressure Vapour-Liquid Equilibria of Non-Hydrocarbon-Containing Systems-ASOG or UNIFAC, 1986, 481-486.
- Homrich P.O., Ceriani R. Liquid-Liquid Equilibrium Data for the Pseudoternary Model System of Refined Sunflower Seed Oil + (n-hexanal, or 2-nonenal, or 2, 4-decadienal + Anhydrous Ethanol) at 298.15 K, *J. Chem. Eng. Data* 61 (2016) 3069-3076
- Maghami M., Yousefi Seyf J., Sadrameh S.M., Haghtalab A. Liquid-Liquid Equilibrium in Ternary Mixture of Waste Fish Oil Biodiesel-Methanol-Glycerol: Experimental Data and Thermodynamic Modeling, *Fluid Phase Equilib.* 409 (2016) 124-130
- Mehraban M., Anbaz M.A., Shaahmadi F., Bazooyar B. Property Estimation of Water/Alcohol/Ionic Liquid Ternary Systems: Density, *J. Mol. Liq.* 264 (2018) 88-97
- Merzougui A., Bonilla-Petriciolet A., Hasseine A., Laiadi D., Labed N. Modeling of Liquid-Liquid Equilibrium of Systems Relevant for Biodiesel Production using Backtracking Search Optimization, *Fluid Phase Equilib.* 388 (2015) 84-92
- Nelder, J. A., Mead, R. A Simplex Method for Function Minimization. *Comput. J.* 1965, 7, 308–313.
- Noriega M.A., Narvaez P.C., Imbachi A.D., Cadavid J.G., Habert A.C. Liquid-Liquid Equilibrium for Biodiesel-Glycerol-Methanol or Ethanol Systems using UNIFAC Correlated Parameters, *Energy* 111 (2016) 841-849
- Prausnitz J.M., Linchtenthaler R.N., de Azevedo E.G. *Molecular Thermodynamics of Fluid-Phase Equilibria*, Prentice Hall, 1998
- Renon H. Prausnitz J.M. Local Compositions in Thermodynamic Excess Functions for Liquid Mixtures, *AIChE J* 14 (1968) 135-144
- Reynel-Avila H.E., Bonilla-Petriciolet A., Tapia-Picazo J.C. An Artificial Neural Network-based NRTL Model for Simulating Liquid-Liquid Equilibria of Systems Present in Biofuels Production, *Fluid Phase Equilib.* 483 (2019) 153-164
- Santos T., Gones J.F., Puna J. Liquid-Liquid Equilibrium for Ternary System Containing Biodiesel, Methanol and Water, *J. Environ. Chem. Eng.* 6 (2018) 984-990
- Sena S.R.C., Pereira C.G. Melon Seed Oil Utilization for Biodiesel Production and Analysis of Liquid-Liquid Equilibrium for the System Biodiesel + Methanol + Glycerine, *Environ. Prog. Sustain. Energy* 36 (2017) 325-332
- Shaahmadi F., Anbaz M.A., Bazooyar B. The Analysis of Liquid-Liquid Equilibria (LLE) of Toluene + Heptane + Ionic Liquid Ternary Mixture Using Intelligent Models, *Chem. Eng. Res. Des.* 130 (2018) 184-198
- Sorensen J.M., Magnussen T., Rasmussen T., Fredenslung A. Liquid-Liquid Equilibrium Data: Their Retrieval, Correlation and Prediction Part II: Correlation, *Fluid Phase Equilib.*, 3, (1979) 47-82
- Stragevitch L. *Liquid-Liquid Equilibrium in Non-Electrolyte Systems*, State University of Campinas: Campinas, 1997
- Tochigi K., Kojima K. *Prediction of High Pressure Vapor-Liquid Equilibria by the ASOG Method*, Elsevier Scientific Pub. Co (1983)
- Toledo I.E.P., Ferreira-Pinto L., Voll F.A.P., Cardozo-Filho L., Meili L., De Coelho D.G., *et al.* Liquid-Liquid Equilibrium of the System (Peanut biodiesel + Glycerol + Ethanol) at Atmospheric Pressure, *J. Chem. Eng. Data* 64 (2019) 2207-2212
- Venkatalakshmi P., Vadivel V., Brindha P. Phytopharmacological Significance of Terminalia Catappa L: An Updated Review. *Int. J. Res. Ayurveda Pharm.* 7 (2) (2016)
- Wales M.D., Huang C., Joos L.B., Probst K.V., Vadlani P.V., Anthony J.L., Rezac M.C. Liquid-Liquid Equilibria for Ternary Systems of Water + Methoxycyclopentane + Alcohol (Methanol, Ethanol, 1-propanol, or 2-propanol), *J. Chem. Eng. Data* 78 (2016) 3 37-41
- Weidlich U., Gmehling J. A modified UNIFAC model. 1. Prediction of VLE, hE and LLE. *Ind. Eng. Chem. Res.* 26 (1987) 1372-1381
- Zhang C., Luo H., Xia S., Ma P. Liquid-Liquid Equilibrium for the Ternary System of Methyl laurate/Methyl myristate + Ethanol +Glycerol at 318.15 and 333.15 K, *J. Chem. Eng. Data* 61 (2016) 1868-1872



## Profit Making Through Pinch Analysis of Feed Gas Circuit in Liquefaction System of Natural Gas

BABATUNDE O. OLALEYE<sup>1\*</sup>, Micheal S. OLAKUNLE<sup>2</sup>, Adegboyega S. OLAWALE<sup>3</sup>

<sup>1,2,3</sup>Department of Chemical Engineering, Ahmadu Bello University, Zaria, Kaduna, Nigeria

<sup>1\*</sup>[olatunde9200@gmail.com](mailto:olatunde9200@gmail.com), <sup>2</sup> [molakunles@gmail.com](mailto:molakunles@gmail.com), <sup>3</sup> [asolawale@yahoo.com](mailto:asolawale@yahoo.com)

\*Corresponding author

---

### ABSTRACT

In this study pinch technology was used to determine the reduction of total annual cost for feed gas circuit in cryogenic liquefaction system of natural gas. Reduction of the total annual cost was achieved by determining the optimum minimum temperature difference through a trade-off between the capital cost target and operating cost target. The total annual cost of the base case at minimum temperature difference of 5°C was compared with the optimized case. At the end of the HEN design total annual cost of \$1024920 was saved per annum through optimum temperature difference of 4.1°C.

**Keywords:** Cryogenic liquefaction system, Gas liquefaction, Natural gas, Pinch analysis.

### 1. INTRODUCTION

Gas liquefaction is an important area of cryogenic study since many important scientific and engineering processes at ultralow temperatures depend on liquefied gases. (Rosen *et al.*, 2013). Cryogenic liquefaction system is used to drive a gas from extremely superheated state through combinations of isothermal compressions process, counter current cooling process, and isenthalpic or adiabatic expansion processes to be withdrawn as liquid at saturated liquid state. (Zohuri, 2018).

There are various types of gas liquefaction system e.g., simple linde hampson liquefaction cycle, pre-cool linde hampson liquefaction cycle (Yilmaz *et al.*, 2019) and claudeliquefaction cycle (Sham *et al.*, 2019). Gases at ambient condition are extremely at superheated state, i.e., they are above critical temperature but have pressures below their critical pressures. Then if a gas is required to be liquefied then it is taken through saturated liquid and vapor state, withdrawn as liquid down the saturated liquid line (Winterbone, 1997). Natural gas is composed primarily of methane and tiny amounts of other hydrocarbons, as well as nitrogen, carbon dioxide, helium, and other trace gases (Rosen *et al.*, 2013). The relevance of liquefying natural gas stems from the economics of carrying it in bulk liquid form, which takes up just 1/600th of the volume of gaseous form. One of the biggest challenges that affect the production of LNG is high required cost of energy in the process (Mehrpooya *et al.*, 2015).

Pinch analysis is a technique for reducing chemical process energy consumption by determining thermodynamically viable energy targets (lowest energy consumption) and realizing them by optimizing heat recovery systems, energy supply techniques, and process operating parameters. (Gujar *et al.*, 2016). Pinch analysis is applicable in many chemical processing industries e.g refinery (Afeeq *et al.*, 2018), Brewing process (Tibasilma *et al.*, 2017), Cement industry (Verma *et al.*, 2017) and sugar cane wax accelerated solvent extraction process (Scolpap *et al.*, 2018). Study of pinch analysis on existing design of FCC of Kaduna Refinery Petrochemical Company was done by (Abubakar, 2020).

Pinch technology was used to save 18.4% of the total annual cost which is equivalent to \$1.6 million. (Gabr, 2018) HEN design remains adequate tools used to increase energy harnessed and reduce external utilities used. (Ateeq *et al.*, 2014) 46% energy consumption was saved in ADU of AL-Basra refinery through HEN design. (Tibalisma *et al.*, 2017) conducted pinch analysis on a brewing plant which shows potential savings of 21.5% of energy savings. (Skolpap *et al.*, 2018).

In this study the focus is to minimize the total annual cost target of the feed gas circuit of the liquefaction system of natural gas. This was achieved by determining the optimum minimum temperature difference through pinch analysis that gives the best trade of between capital cost targets and operating cost targets.



## 2. MATERIALS AND METHODS

### 2.1 Materials

The material and energy balance was carried out on this work through aspen hysis plus. The process description, operating parameters was obtained from the liquefaction and fractionation manual of natural gas.

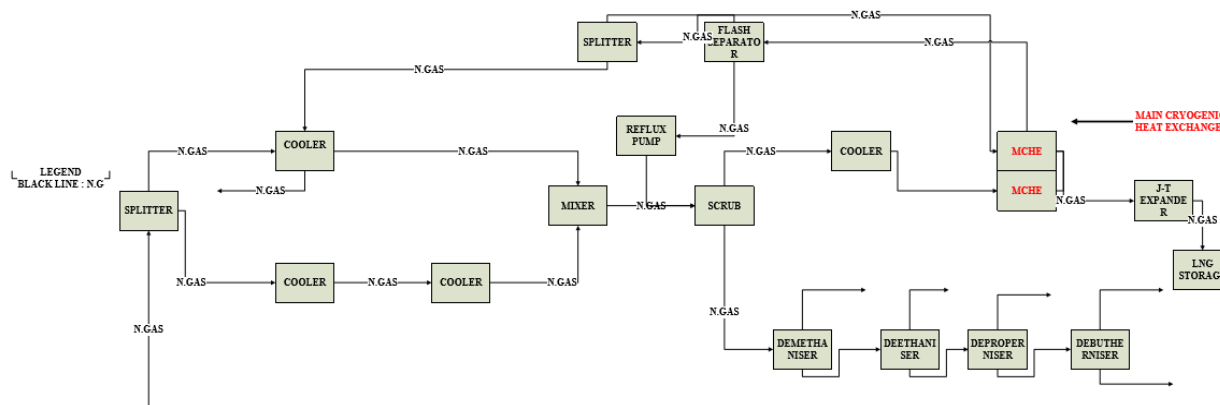


Figure 4: Block flow diagram for typical feed gas circuit in cryogenic liquefaction system of natural gas.

Extremely superheated gas at temperature of 23°C and pressure of 49.5bar g was spitted into two portion, one portion of the feed gas temperature was reduced to 10°C and pressure of 49.5 barg partially condensed by cold vapor from the overhead of the scrub column through high pressure propane evaporator E1406. The other portion was cooled by high pressure propane evaporator E102 and medium pressure evaporator E103 respectively to temperature of 15°C and 10°C. The cooled feed gas was mixed with the feed gas from fuel gas then feed gas sent to the scrub column C1401 at pressure of 48.barg for separation into light and heavy fraction. The light fraction was cooled to a temperature of -100°C and -112°C respectively through the scrub column condenser E-1404 and cooled bundle of the MCHE E-1405. The two phase stream exiting the cooled bundle of the MCHE was recycled back as feed at temperature of -114°C to the flash separator .The flash separator separates the feed gas into light and heavy fraction, however the light fraction was cooled by MCHE from temperature of -100°C to -120°C by the cooled bundle of MCHE. However GT-1401 joule Thompson expander sub cooled the feed gas temperature to -162°C. Heavy fraction from flash separator V-1401 was refluxed back to the scrub C-1401 at temperature of -100°C. The heavy fraction from the scrub column was sent as feed at temperature of -90°C, -88°C, -86°C and -84°C respectively through de-methaniser column C-1540, de-ethaniser column C-1560, de-propaniser column C-1570 and de-butaniser column C-1580 for further separations.

### 2.2 Methods

#### 2.2.1 Construction Of Composite Curve

In this study Graphical method was utilized. To generate a composite using the equation 1 below

$$(\sum Cp_h - \sum Cp_c) \tag{1}$$

Where

$\sum Cp_h$  =sum of heat capacities of hot stream on the scale within their ranked temperatures.

$\sum Cp_c$  =sum of heat capacities of cold stream on the scale within their ranked temperatures.

Cps of hot and cold stream that fell within the range of real temperatures using the equation 1 above stated by (Gabr, 2018) were used and multiplied by real temperature change to obtain heat load. Heat load of each hot and cold stream was calculated using equation 2 below

$$H = C_p \Delta T = m C_p \Delta T \tag{2}$$

$C_p$  = Heat capacity (KJ/Kg)

$\Delta T$  = Change in temperature (C)

$m$  = mass flow rate (Kg/h)

H= Enthalpy (Kw)

Then the plot of heat load against real temperature for hot and cold composite curve. On the plot three sections is given respectively. The overlap is the pinch point, non-overlap on the right is the minimum heating utility and the non-overlap on the left is minimum cooling utility.

### 2.2.2 Construction of Grand Composite Curve

$$\text{Hot streams } T_i = T_r - \frac{\Delta T_{min}}{2} \quad (3)$$

$$\text{Cold streams } T_i = T_{act} + \frac{\Delta T_{min}}{2} \quad (4)$$

Divide all temperature range into intervals and apply equation 3 and 4 stated by (Gabr,2018) to shift the temperature for a given  $\Delta T_{min}$ , carry out an energy balance around each temperature intervals using equation 2 stated by (Abubakar,2020) to obtain the positive heat value (surplus) and negative heat load (deficit).then add the heat load value down the cascade such that to eliminate all negative value of heat load. Then make a plot of the temperature shift against the heat loads obtained.

### 2.2.3 Heat Exchanger Network Design

Various designs were suggested in this work through the use of pinch technology. To obtain the best design a trade-off between the capital cost target and operating cost target was used to obtain the best reduction of total annual cost. The following are the governing equations used for economic analysis in this work. The surface area was calculated by what (Gabr, 2018) used shown below

$$A = \frac{Q}{U \cdot \Delta T_m} \quad (5)$$

A = Heat transfer area ( $m^2$ )

Q = heat load (Kw)

U = overall heat transfer coefficient.

$\Delta T_m$  = log mean temperature difference ( $^{\circ}C$ )

$$A_{min} = \sum A \quad (6)$$

The equation above was used in this work stated by (Abubakar, 2020) to calculate the total surface area above and below the pinch.

The equation 7 below HEN capital cost equation stated by (Abubakar, 2020) was used to calculate capital cost for HEN.

$$C_{HEN}(\$) = [N_{min} \left( a + b \left( \frac{A_{min}}{N_{min}} \right)^c \right)]_{AP} + C_{HEN}(\$) = [N_{min} \left( a + b \left( \frac{A_{min}}{N_{min}} \right)^c \right)]_{BP} \quad (7)$$

Where,

$C_{HEN}(\$)$  = Heat Exchanger Network Design capital cost.

$N_{min}$  = Minimum number of units.

$A_{min}$  = Minimum number of area required for heat transfer.

## 3. RESULTS AND DISCUSSION

The table 1 and table 2 below shows the thermal data of thirteen process stream and utility stream in feed gas circuit of cryogenic liquefaction system of natural gas. The thermal data is made up of seven hot stream and six cold streams that cut across various minimum temperature difference from 3  $^{\circ}C$  to 5 $^{\circ}C$  stated by (Linnhoff, 2018).

Figure 1 and Figure 2 shows the composite curve and the ground composite curve at assumed initial minimum temperature difference of 5 $^{\circ}C$ . The composite curve shows the minimum hot utility requirement and cold utility requirement to be 99220000KJ/h and 21400000KJ/h respectively. However, Figure 2 contains the ground composite curve which shows pinch point temperature to be 91.1 $^{\circ}C$ .

Table 1: Thermal data for process stream in cryogenic liquefaction system of natural gas

Stream Name	Stream Type	Ts°C	Tt°C	M(Kg/H)	Cp(Kj/K)	Mcp	Enthalpy(K)
S1 to S7	HOT	23	7.7	57430	-1.322		2481000
S8 to S14	HOT	-91	-109	267000	-1.901		6601000
To Condenser @ B14 to S17	HOT	-95.3	-95.4	94020	2.216		15840000
To Reboiler @ B17 to S32	COLD	-88.3	-70.4	94020	1.905		3073000
To Condenser @ B17 to S33	HOT	-95.2	-95.7	94020	1.823	79910000	3352000
To Reboiler @ B14 to S26	COLD	-93.3	-90.2	94020	12.581		40930000
To Condenser @ B16 to S31	HOT	-95.2	-95.7	610200	62.165	58120000	113800000
To Reboiler @ B15 to S29	COLD	-90.8	-88.1	158800	503.14		39960000
To Condenser @ B15 to S28	HOT	-95.2	-95.7	382300	31.775	58110000	78960000
To Reboiler @ B16 to S30	COLD	-88.9	-79.7	317600	503.136		79910000
B13 heater	COLD	-112	-100	520600	-2460.622	200100	128100000
B7 heater	HOT	-22.2	-91	228800	24.475	1911000	39760000

Table 2: Thermal data for hot utility stream and cold utility stream of feed gas circuit in cryogenic liquefaction system of natural gas.

STREAM NAME			Ts °C	Tt °C	COST INDEX(\$/KJ)	ENTHALPY(Kw)
Refrigerant generation	3	Hot	-64	-65	-5816000	233700000
Refrigerant		Cold	-25	-24	2739000	8178000
Refrigerant 4		Cold	-103	-102	8531000	42900000
Very low temperature	low	Cold	-270	-269	8900000	377700000

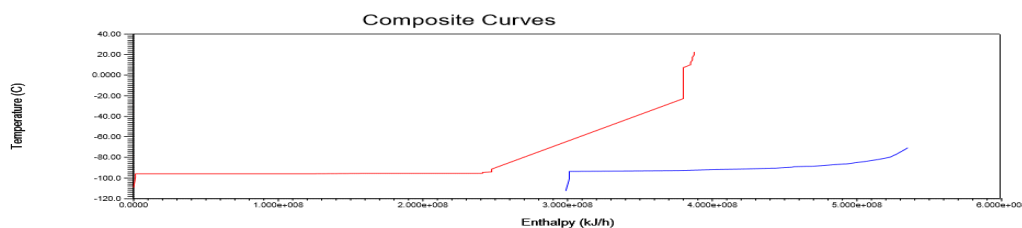


Figure 1: Combine composite curve of base case scenario for existing feed gas circuit of Cryogenic liquefaction system of natural gas at  $\Delta T_{min}$  of 5°C.

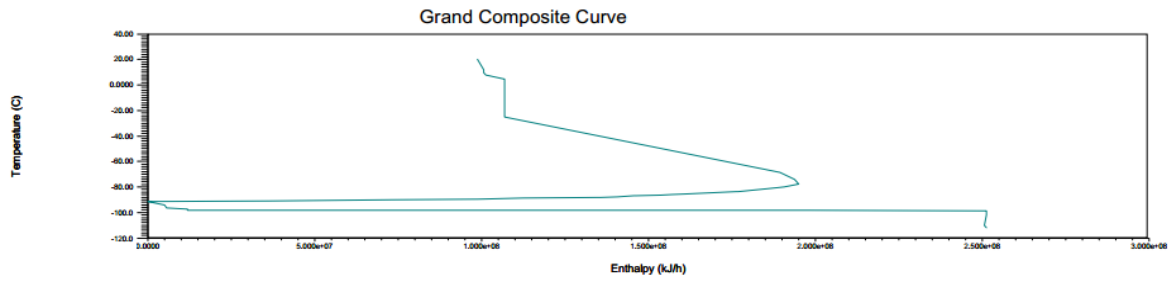


Figure 2: Grand composite curve of base case scenario for existing feed gas circuit in Cryogenic liquefaction system of natural gas. at  $\Delta T_{min}$  of 5°C.

Figure 3 below contains the trade of between the capital cost target and the operating cost target as a function of optimum minimum temperature difference of 4.1°C.

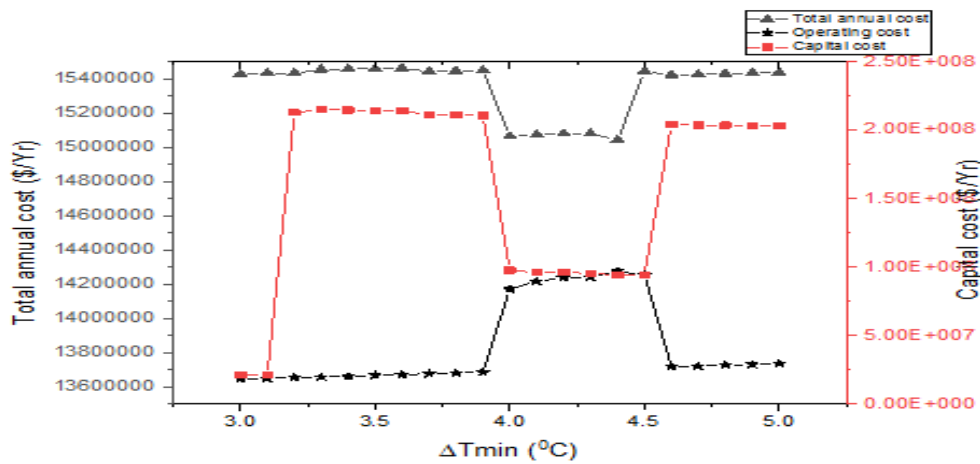


Figure 3: Cost target summary at different  $\Delta T_{min}$  3°C -5°C.

Table 4 contain the energy cost target, cost index target and cost savings respectively obtained from carrying out pinch analysis on feed gas circuit of cryogenic liquefaction system of natural gas.

**Table 3:** Energy and cost target summary for base case and optimized case scenario for feed gas circuit in cryogenic liquefaction system of natural gas.

	Base case $\Delta T_{min}$ of 5.0°C	Targets $\Delta T_{min}$ of 4.1°C	Savings	% Savings
Heating (KJ/h)	99220000	104600000	-5380000	5.14
Cooling (KJ/h)	251400000	256800000	-5400000	2.10
Area (m <sup>2</sup> )	377420	11920	365500	96.84
Capital cost index(\$/year)	203281056000000	94513392000000	108767664000000	53.50
Operating cost index(\$/year)	13737081.6	14254272	517190.4	3.6
Total annual cost (\$/year)	15436872	15042672	394200	2.55

## CONCLUSIONS

In this study pinch technology was used to evaluate the following stated below

- i. when initial minimum temperature difference of was 5.0°C assumed for the HEN Design process, Total annual cost value of base case scenario of existing feed gas circuit of liquefaction system was found to be 15436872\$/year.
- ii. The optimum temperature difference was found to be 4.1°C
- iii. A total annual cost value of 15042672\$/year was achieved at optimum minimum temperature difference of 4.1°C.
- iv. A 2.55% reduction of total annual cost was achieved at minimum temperature difference of 4.1°C.

## REFERENCES

- Abubakar, A., 2020. Cost Reduction of Fluid Catalytic Cracking Unit in Kaduna Refining and Petrochemical Company using Pinch Technology. *Nigerian Journal of Technological Development*, 17(3), pp. 189-196.
- Ateeq AA, Taher, M.A, Al-Salam FA., 2017 Energy Saving in Atmospheric Distillation Unit by Retrofit Design of Heat Exchanger networks of Al-Basra Refinery. *International Journal of Engineering Research and Technology*, 6(4), pp 425- 430.
- Dincer, I. Rosen M.A., Energy, environment and sustainable development. *Applied energy*, 64(1-4):427-440
- Eldemerdashe, U., 2011. Technology review of natural gas liquefaction processes. *Journal of Applied Sciences*.
- Gabr, E. M. 2018. Step by step for designing an optimum heat exchanger network. *International Journal of Scientific & Engineering Research*, 9(7).
- GUJAR, S., UPKARE, M., and SATPUT, S., 2016. Pinch Analysis of Xylene Fractionation and CCR-Plate forming Process Using Aspen Plus. *Chemical Science*, 5(3), pp00-00.
- Mehrpooya, M. and Ansarinassab, H. 2015. Exergoeconomic evaluation of single mixed refrigerant natural gas liquefaction processes. *Energy conversion and management*, 99, 400-413.
- Skolpap, W. Owat, N., 2018 Pinch Analysis of a Commercial-Scale Sugarcane Wax Accelerated-Solvent Extraction and Purification Process. *The International Journal of Engineering and Science*.2018;7(7):25-34
- Tibasiima, N. and Okullo, A., 2017. Energy targeting for a brewing process using pinch analysis. *Energy and Power Engineering*. 9(1):11-21
- March, L., 1998. Introduction to pinch technology. Targeting House, Gadbrook Park, Northwich, Cheshire, CW7UZ, England.
- Yilmaz, C., (2019). Thermodynamic performance analysis of gas liquefaction cycles for cryogenic applications. *Journal of Thermal Engineering*, 5(1), 62-75.